Copyrighted Material

Edited by
Ricardo S. Sussmann

CVD Diamond
for Electronic Devices and Sensors

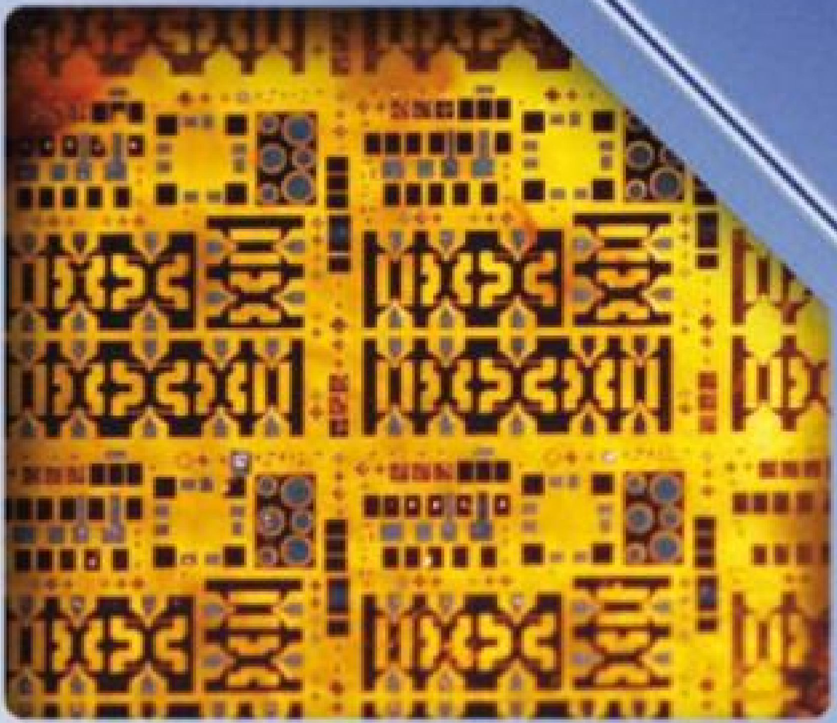

WILEY

Wiley Series
in Materials for
Electronic
& Optoelectronic
Applications

Copyrighted Material

VISIT…

LANZAROTE
Caliente.COM

CVD Diamond for Electronic Devices and Sensors

CVD Diamond for Electronic Devices and Sensors Edited by Ricardo S. Sussmann
© 2009 John Wiley & Sons, Ltd. ISBN: 978-0-470-06532-7

Wiley Series in Materials for Electronic and Optoelectronic Applications

Series Editors

Dr. Peter Capper, SELEX Sensors and Airborne Systems Infrared Ltd., Southampton, UK

Professor Safa Kasap, University of Saskatchewan, Saskatoon, Canada

Professor Arthur Willoughby, University of Southampton, Southampton, UK

Published Titles

Bulk Crystal Growth of Electronic, Optical and Optoelectronic Materials, Edited by P. Capper

Properties of Group-IV, III–V and II–VI Semiconductors, S. Adachi

Charge Transport in Disordered Solids with Applications in Electronics, Edited by S. Baranovski

Optical Properties of Condensed Matter and Applications, Edited by J. Singh

Thin Film Solar Cells: Fabrication, Characterization and Applications, Edited by J. Poortmans and V. Arkhipov

Dielectric Films for Advanced Microelectronics, Edited by M. R. Baklanov, M. Green and K. Maex

Liquid Phase Epitaxy of Electronic, Optical and Optoelectronic Materials, Edited by P. Capper and M. Mauk

Molecular Electronics: From Principles to Practice, M. Petty

Luminescent Materials and Applications, Edited by A. Kitai

Forthcoming Titles

Photovoltaic Materials: From Crystalline Silicon to Third-Generation Approaches, Edited by G. J. Conibeer

Silicon Photonics: Fundamentals and Devices, M. J. Deen and P. K. Basu

Zinc Oxide Materials for Electronic and Optoelectronic Device Applications, Edited by C. Litton, D. C. Reynolds and T. C. Collins

Mercury Cadmium Telluride: Growth, Properties and Applications, Edited by P. Capper and J. Garland

CVD Diamond for Electronic Devices and Sensors

Edited by

Ricardo S. Sussmann,
Kings College London, London, UK

WILEY
A John Wiley and Sons, Ltd., Publication

This edition first published 2009
© 2009 John Wiley & Sons Ltd

Registered office
John Wiley & Sons Ltd, The Atrium, Southern Gate, Chichester, West Sussex, PO19 8SQ, United Kingdom

For details of our global editorial offices, for customer services and for information about how to apply for permission to reuse the copyright material in this book please see our website at www.wiley.com.

The right of the author to be identified as the author of this work has been asserted in accordance with the Copyright, Designs and Patents Act 1988.

All rights reserved. No part of this publication may be reproduced, stored in a retrieval system, or transmitted, in any form or by any means, electronic, mechanical, photocopying, recording or otherwise, except as permitted by the UK Copyright, Designs and Patents Act 1988, without the prior permission of the publisher.

Wiley also publishes its books in a variety of electronic formats. Some content that appears in print may not be available in electronic books.

Designations used by companies to distinguish their products are often claimed as trademarks. All brand names and product names used in this book are trade names, service marks, trademarks or registered trademarks of their respective owners. The publisher is not associated with any product or vendor mentioned in this book. This publication is designed to provide accurate and authoritative information in regard to the subject matter covered. It is sold on the understanding that the publisher is not engaged in rendering professional services. If professional advice or other expert assistance is required, the services of a competent professional should be sought.

The Publisher and the Author make no representations or warranties with respect to the accuracy or completeness of the contents of this work and specifically disclaim all warranties, including without limitation any implied warranties of fitness for a particular purpose. The advice and strategies contained herein may not be suitable for every situation. In view of ongoing research, equipment modifications, changes in governmental regulations, and the constant flow of information relating to the use of experimental reagents, equipment, and devices, the reader is urged to review and evaluate the information provided in the package insert or instructions for each chemical, piece of equipment, reagent, or device for, among other things, any changes in the instructions or indication of usage and for added warnings and precautions. The fact that an organization or Website is referred to in this work as a citation and/or a potential source of further information does not mean that the author or the publisher endorses the information the organization or Website may provide or recommendations it may make. Further, readers should be aware that Internet Websites listed in this work may have changed or disappeared between when this work was written and when it is read. No warranty may be created or extended by any promotional statements for this work. Neither the Publisher nor the Author shall be liable for any damages arising herefrom.

Library of Congress Cataloging-in-Publication Data

CVD diamond for electronic devices and sensors / Ricardo S. Sussmann [editor].
p. cm. – (Wiley series in materials for electronic and optoelectronic applications)
Includes bibliographical references and index.
ISBN 978-0-470-06532-7 (cloth : alk. paper)
1. Electronics–Materials. 2. Diamonds, Artificial. 3. Chemical vapor deposition.
I. Sussmann, Ricardo S.
TK7871.15.D53C94 2009
621.381–dc22
2008033267

British Library Cataloguing in Publication Data

A catalogue record for this book is available from the British Library

ISBN 978-0-470-06532-7 (HB)

Typeset in 10/12 Times by Laserwords Private Limited, Chennai, India
Printed and bound in Great Britain by Antony Rowe Ltd, Chippenham, Wiltshire

I would like to dedicate this book to my wife Silvia (for much more than sorting out my computer) and to my son Sebastian who lent me many good books that served as welcome distractions from the long hours of editing work.

Contents

Series Preface xi

Preface xiii

List of Contributors xxi

Basic Properties, Defects and Impurities, Surface properties and Synthesis

1 **Basic Properties of Diamond: Phonon Spectra, Thermal Properties, Band Structure** 3
Gordon Davies

2 **Transport Properties of Electrons and Holes in Diamond** 29
Jan Isberg

3 **Point Defects, Impurities and Doping** 49
Alison Mainwood

4 **Surface Conductivity of Diamond** 69
Lothar Ley

5 **Recent Progress in the Understanding of CVD Growth of Diamond** 103
J.E. Butler, A. Cheesman and M. N. R. Ashfold

6 **Heteroepitaxial Growth** 125
M. Schreck

Radiation Sensors

7 **Detectors for UV and Far UV Radiation** 165
Alan T. Collins

8 Diamond Radiation Sensors for Radiotherapy **185**
Mara Bruzzi

9 Radiation Sensors for High Energy Physics Experiments **207**
H. Kagan and W. Trischuk

10 CVD-Diamond Detectors for Experiments with Hadrons, Nuclei, and Atoms **227**
E. Berdermann and M. Ciobanu

11 Neutron Detectors **257**
G. Verona-Rinati

Active Electronic Devices

12 High-Power Switching Devices **277**
Jan Isberg

13 H-Terminated Diamond Field-Effect Transistors **289**
Makoto Kasu

14 Doped Diamond Electron Devices **313**
E. Kohn and A. Denisenko

15 Optoelectronic Devices Using Homoepitaxial Diamond p–n and p–i–n Junctions **379**
Toshiharu Makino and Hiromitsu Kato

Electrochemical and Biological Sensors

16 Biofunctionalization of Diamond Surfaces: Fundamentals and Applications **401**
J. A. Garrido

17 Diamond Electrochemical Sensors **439**
John S. Foord

Micro-Electro-Mechanical Systems

18 CVD Diamond MEMS **469**
J. Kusterer and E. Kohn

Superconductivity in CVD Diamond

19 Superconductivity in Diamond **549**
Yoshihiko Takano

Index **563**

Series Preface

WILEY SERIES IN MATERIALS FOR ELECTRONIC AND OPTOELECTRONIC APPLICATIONS

This book series is devoted to the rapidly developing class of materials used for electronic and optoelectronic applications. It is designed to provide much-needed information on the fundamental scientific principles of these materials, together with how these are employed in technological applications. The books are aimed at (postgraduate) students, researchers and technologists, engaged in research, development and the study of materials in electronics and photonics, and industrial scientists developing new materials, devices and circuits for the electronic, optoelectronic and communications industries.

The development of new electronic and optoelectronic materials depends not only on materials engineering at a practical level, but also on a clear understanding of the properties of materials, and the fundamental science behind these properties. It is the properties of a material that eventually determine its usefulness in an application. The series therefore also includes such titles as electrical conduction in solids, optical properties, thermal properties, and so on, all with applications and examples of materials in electronics and optoelectronics. The characterization of materials is also covered within the series in as much as it is impossible to develop new materials without the proper characterization of their structure and properties. Structure-property relationships have always been fundamentally and intrinsically important to materials science and engineering.

Materials science is well known for being one of the most interdisciplinary sciences. It is the interdisciplinary aspect of materials science that has led to many exciting discoveries, new materials and new applications. It is not unusual to find scientists with chemical engineering backgrounds working on materials projects with applications in electronics. In selecting titles for the series, we have tried to maintain the interdisciplinary aspect of the field, and hence its excitement to researchers in this field.

Peter Capper
Safa Kasap
Arthur Willoughby

Preface

> I am accustomed to sleep, and in my dreams to imagine the same things that lunatics imagine when awake.
> *Rene Descartes, Meditations on First Philosophy*

> When one of your dreams come true, you begin to look at the others more carefully.
> *Anon*.

The discovery of diamond synthesis by Chemical Vapour deposition (CVD) in the early 1980s opened a large range of new applications for diamond. Among these, and the one that motivated much of the early and current research, is the use of CVD diamond for electronic devices and sensors. It is the aim of this book to review the state of the art on this subject. Within this scope I have aimed to include the widest possible range of devices even at the risk of stretching the conventional meaning of an electronic device. Therefore in addition to the 'classics' such as rectifying diodes and transistors, I have included radiation sensors (for a wide range of radiation ranging from photons to high energy particles, heavy ions and neutrons), electrochemical and biological sensors, micro-electro-mechanical systems (MEMS), and a chapter on the recently discovered superconductivity effect in diamond.

When I was approached by Professor Willoughby and his colleagues from Wiley in the spring of 2006, with the proposition to edit a book on diamond electronics, I had serious reservations as there are already several very good books and review articles covering this subject. In addition it was then over 16 years since I had started my involvement with CVD diamond and, realistically, one could not claim that diamond electronic devices had been a rolling commercial success. Despite early claims that diamond would replace silicon as the key electronic material, there are only a few niche applications currently on the market (mostly radiation and electrochemical sensors), a far cry from the industry that would be worth over 2000 million dollars by 2010 as projected in the late 1980s and early 1990s. On further reflection, I concluded that the important advances achieved since the turn of the Twenty-first century had taken CVD diamond technology into a second phase of development and that this progress needed to be properly reviewed. A book like this would therefore not only be a positive addition to the current body of work, but also might help to clarify the future market for diamond electronic devices.

What were the events that led to the current phase of development?

Many of the superlative physical and chemical properties of diamond have been known since the mid 1940s, almost four decades before the momentous experiments by the NIRIM (National Institute for Research in Inorganic Materials) team in Japan, who demonstrated the feasibility of CVD diamond synthesis. It was known that diamond, a wide band-gap semiconductor, was the hardest and most rigid (highest Young's modulus) material, the most thermally conductive (at room temperature); that it was inert to chemical attack; that (when free of nitrogen) it was transparent in the UV, visible and infrared part of the spectrum (except for the two and three phonon bands between 2 and 7 micrometres wavelength); that it could be used as a radiation detector and that the electron and hole mobilities were very respectable. Later on it was also learned that diamond could be doped with boron to become a p-type semiconductor and rudimentary rectifiers and transistors were demonstrated. All this was achieved using, first, natural diamond stones and later, diamond synthesised by the high-pressure and high-temperature (HPHT) process.

Heroic attempts were made during the pre-CVD era to use diamond in high technology applications outside the abrasive and cutting tool industry that was, and still is, superbly served by natural and HPHT diamond. A good example was the UV diamond window (18.2 mm in diameter and 2.8 mm thick) made out of a natural Type-IIa stone used for the main pressure cell of the Venus space probe launched in August 1978. The price of this window at that time was close to $250 000, equivalent to over $1 million today. Also, small pieces of IIa diamond were sold as heat sinks (or heat spreaders) to mount diode lasers but the price was too high and the size too small to consider these as heat sinks for high-power electronic circuits. Whatever scientists thought of the electronic devices that were made using natural or HPHT diamond, it was clear that there was no hope whatsoever of developing significant commercial electronic devices if the only materials available were small natural stones of irreproducible properties, or similar-sized HPHT diamond mostly contaminated with nitrogen or metal catalysts.

In view of the above, it should come as no surprise that a great deal of excitement was generated when scientists from NIRIM in Japan reported that it was possible to synthesise diamond from the gas phase, at sub-atmospheric pressures in a continuous way on a nondiamond substrate. These achievements were reported between 1982 and 1984, using firstly hot filament and later microwave plasma assisted reactors. Extrapolating (probably too enthusiastically) from what was known of gas phase epitaxial techniques used for the growth of high electronic quality Si and III–V materials, some sectors of the scientific community concluded that we were witnessing the dawn of an era where wafer size electronic quality diamond could be grown. Further extrapolation led to the rather extravagant claims about diamond replacing Si and the very large size of the markets mentioned above. All this resulted in a substantial amount of funding from government agencies throughout the 1990s and a brave attempt by at least one Japanese company to open research sites in the UK and USA for the specific task of developing commercial diamond electronic devices. Alas, well before the century was over, most of the funding (at least in USA) had dried up (being diverted mostly to the wide gap III–V nitrides and SiC), and the industrial research sites in Europe and USA mentioned above were closed down. There was nonetheless a positive outcome from all these activities: very good research was done and the considerable know-how that was acquired has been invaluable for all the further developments in diamond electronics that will be described in this book.

More realistic expectations were harboured by different groups of scientists who were interested in the optical, mechanical and thermal properties of diamond, and who believed that CVD technology could open the way to large, affordable windows and heat spreaders, and that CVD diamond could also contribute to the cutting-tool industry with either thick diamond layers or diamond coatings on tungsten carbide tool inserts. These expectations met with considerably more success. High quality diamond windows up to 100 mm in diameter and 1–2 mm thick have been commercially available now for over a decade, and have been used routinely for the transmission of high-power CO_2 lasers, broad band transmission from Synchrotron infrared beam lines, and the transmission of MW power from microwave tubes for use in thermonuclear fusion reactors, just to name a few. Whilst not cheap, these windows are affordable. The Venus probe window, for instance, if made by CVD diamond, would cost no more than $10 000. Furthermore, these windows met all the technical specifications that were expected for pure Type-IIa diamond. The notion of a piece of high quality diamond over 100 mm in diameter, 2 mm thick ($\sim$280 carats) that could be routinely available for technological applications at an affordable price would have been considered a wild dream before the advent of CVD diamond technology. In addition, diamond heat sinks of about 1 cm^2 are routinely used in the packaging of high-power rf transistors, and the CVD diamond tool industry has found interesting applications in providing a very useful complement to HPHT diamond. All this progress was achieved in just over a decade, which is good going for a new technology.

I believe we are currently witnessing a renewed impetus in what I call the second development phase in diamond electronics, and this is due to two major factors.

One derives from diamond being a very adaptable material. New attributes and properties have been discovered over the past couple of decades, such as the large voltametric potential and the possibility of functionalising the surface. These have opened exciting possibilities for biological and electrochemical sensors. Although doping has been, and continues to be, the most serious hurdle in the realisation of diamond electronic devices, the discovery of a surface p-type conductive layer in hydrogenated surfaces, and the possibility of implementing delta doping, have resulted in diamond FETs with very attractive performances. The fact that diamond is a superb ceramic material with a very high Young's modulus that can be made electrically conductive and can be grown as nanocrystalline layers with smooth surfaces, has motivated considerable interest in the development of Micro-Electro-Mechanical Systems (MEMS).

The other factor is the considerable progress that has been achieved in crystal growth technology resulting, for instance, in the synthesis of very high purity and crystalline quality homoepitaxial single crystal specimens that exhibit considerably greater values of electron and hole mobilities, as well as dielectric breakdown, compared with values previously reported. Size, nonetheless, still remains a problem since even in the most optimistic case crystal sizes are not much above 8–10-mm squares. There has however been much progress in the understanding of heteroepitaxial synthesis, which offers a glimmer of hope for the synthesis of large size single crystal diamond wafers.

The first part of this book (Chapters 1 to 6) reviews the basic properties of diamond with emphasis on what is new and relevant for many of the new developments. Gordon Davies (Chapter 1) reminds us about the basic physics: lattice structure, phonon spectra, elastic, thermal and other properties, including some of the recent understanding on isotopic effects. In Chapter 2, Jan Isberg reviews the current knowledge of free carrier transport, describing for instance the experimental evidence for the very high reported values of electron and hole mobilities. The topic of defects and impurities in diamond is reviewed by Alison Mainwood in Chapter 3, which gives a comprehensive account of the impurity centres in diamond either as single elements or as complexes, and discusses their possible role in electronic properties including some recent work on shallow dopants. The topic of surface conductivity exhibited by hydrogenated diamond surfaces is treated by Lothar Ley in Chapter 4, a fascinating account of how the understanding of this phenomenon, unique to diamond, has developed. The chemistry of crystal growth, including a description of the new experimental techniques that are being used for the analysis of the growth chemistry, is given in Chapter 5 by Jim Butler, A. Cheesman and Michael Ashford whilst the last chapter in this part (Chapter 6 by Matthias Schreck) summarises the progress in heteroepitaxial growth: the quest for a wafer size single crystal diamond.

The second part (Chapters 7 to 11) is devoted to the various applications where diamond has been used as a radiation detector. This field of application is particularly interesting for diamond because in most devices the active layer consists of intrinsic diamond. By removing the need to use doped active layers the device structures not only become simpler but it also becomes possible to preserve the optimum properties of diamond such as the large electron and hole mobilities, long recombination lifetimes and large dielectric breakdown voltages. This is one reason why radiation sensors have been investigated since the early days of diamond research and were one of the first electronic applications actively pursued since the early 1990s in CVD diamond for the various areas of use: far UV, high-energy photons (X- and gamma-rays) and high-energy nuclear particles. In this part, these applications are reviewed. Because of its wide band gap, diamond has been proposed as an ideal solar blind UV and soft X-ray detector for solar space missions, and because of its tolerance for radiation, as a candidate for detectors in deep-UV photolithography. These applications are discussed by Alan Collins in Chapter 7. There are several attributes that make diamond attractive for radiation detectors in medical radiotherapy applications, an area of application where diamond has been investigated for nearly five decades, well before CVD, and is probably one of the few examples where the only commercially available device is still made from a natural diamond stone. The use of CVD diamond in this application has been studied since the early days, first using polycrystalline and, more recently, single crystal specimens. The progress achieved and current status is reviewed by Mara Bruzzi in Chapter 8. The high predicted radiation hardness of diamond and the possibility of realising large area and affordable detectors using CVD diamond motivated a long and fruitful research collaboration between industry and scientists from CERN (RD 42 Collaboration), which started in about 1994. In many ways, this collaboration was the driving force for the improvement in the quality of CVD diamond, resulting in an increase in collection distance from under 10 micrometres to the current value of over 250 micrometres (in polycrystalline material) and much larger in single crystals. The other outcome of this research activity was the confirmation that diamond is indeed radiation hard, better than silicon by at least a factor of ten. It has been announced recently that CVD diamond detectors will be used as beam monitors in the new Large Hadron Collider, a modest but nonetheless rewarding outcome from these many years of research. Chapter 9 by Harris Kagan and William Trischuk describes the achievements in this field. The detection of heavy ions is one application where diamond seems to excel: the signals are good because a large amount of charge is generated, the detectors can be very fast and, of course, radiation hard. Another close collaboration between industry and the Institute for Research in Heavy Ions (Gesellschaft für Schwerionenforschung, GSI) in Darmstadt has resulted in many different applications for CVD diamond detectors (using both polycrystalline and single crystal material), and has also been a driving force for the improvement of material quality and the development of specialised electronics. This progress is described in Chapter 10 by Eleni Berderman and Mircea Ciobanu. We finish this section on radiation detectors with Chapter 11 by Gianluca Verona-Rinati, who describes a neutron detector made from single crystal CVD diamond. This device is able to detect both thermal and energetic neutrons and has undergone prolonged periods of test in TRIGA RC-1, a fusion research reactor, and in the Joint European Torus, a magnetic confinement fusion reactor, exhibiting negligible degradation and confirming the high radiation tolerance of diamond.

Chapters 12 to 15 are dedicated to what are recognised in the electronic industry as the major active devices: rectifiers and high power switches, transistors and opto-electronic devices. The underlying thread in all these chapters is the creative effort that is being made to overcome what seems to be a fundamental limitation of diamond as an electronic material: the difficulty of doping. Chapter 12 by Jan Isberg summarises the efforts in the development of efficient rectifiers and switches for the control of high powers. In Chapter 13, Makoto Kasu describes some of the very impressive results that have been achieved using the surface p-type layer in hydrogenated diamond as the active layer for the fabrication of field-effect transistors (FETs). In these devices, long-term stability still seems to be a limitation. The use of boron doped diamond as the active layer would in principle remove the stability problem. In Chapter 14, Erhard Kohn and Andrej Denisenko describe how the major limitation of low boron activation may be overcome by the use of a delta-doped layer. They extend their brief by commenting also on how this concept may be used for high power rectifiers and other devices, and give a very comprehensive description of the technologies that need to be used for the processing of diamond in the fabrication of devices. Boron incorporates easily into the diamond lattice and, although it results in a relatively deep acceptor level at 0.37 eV, it can be used to make either semiconducting or almost metallic diamond by increasing the concentration. N-Type doping is considerably more difficult. So far the only reliable n-type dopant that has been found is phosphorus, which is more difficult to incorporate and results in an even deeper defect centre near 0.6 eV. As a consequence, n-type doping has not so far been very useful for conventional p–n type devices, either rectifiers or transistors. One exception seems to be light-emitting devices. Although diamond is an indirect band material, by making use of exitonic emission, interesting UV light emitting diodes have been demonstrated as described in Chapter 15 by Toshiharu Makino and Hiromitsu Kato.

Part 4 addresses biological and electrochemical sensor applications. Following the work on surface modification by hydrogen or oxygen, it was discovered that the surface of diamond could be functionalised to accept different types of protein. This has opened a seemingly vast field of potential applications, which, if successful, being mostly in the medical diagnostics field, could result in large markets. This subject is described by Jose Garrido in Chapter 16. Relatively early in the development of CVD diamond applications, it was found that electrically conductive diamond had interesting and promising properties as an electrochemical electrode. It combined a relatively large voltametric potential with the established chemical inertness of diamond. Further work showed that these properties could be used to make electrodes for a number of applications ranging from water purification to chemical analysis. The subject is complicated because CVD diamond prepared by different techniques behaves very differently. The scope of this application with emphasis on electrochemical sensors is described in Chapter 17 by John Foord.

Chapter 18, by Joachim Kusterer and Erhard Kohn, concerns the numerous MEMS (micro-electro-mechanical systems) that have been made from CVD diamond using either conventional polycrystalline material or some of the finer grain versions such as nano- or ultrananocrystalline diamond. The group led by Erhard Kohn at the University of Ulm has been at the forefront of this technology and has developed an impressive range of different actuators and sensors, using almost all of the possible advantages that the different types of CVD diamond material are able to offer. This chapter discusses how and in which areas diamond might be able to replace silicon in the MEMS field.

Finally, I thought that we should include in a book on diamond electronics an account of a relatively newly discovered property of boron-doped diamond: superconductivity. If combined with the other attractive properties of diamond the possibility remains open to the development of superconductive devices, although these have not yet been demonstrated. This subject is presented in Chapter 19 by Yoshihiko Takano.

The question remains as to whether CVD diamond will ever become a major money earner as an electronic material or whether it will continue to address only low volume niche applications. Some of the serious limitations of diamond are relatively well known: the difficulty in doping, size of single crystal specimens and, not least, the added hurdle of having to compete with the successful advances achieved in the other wide-gap materials: SiC and the III–V nitrides. In a series of publications by Alan Collins over a period of almost a decade from 1989 to 1998, some of the hurdles in developing a successful market for diamond electronics are analysed. These papers make sobering reading and should, I suggest, be compulsory for anyone wishing to invest in this technology. I am not sure if any of the chapters in this book succeed 100 % in proving Alan Collins wrong. However I believe they do succeed in showing possible avenues that may be successful in the future. What is also apparent from all the contributions in this book is that there is still a very considerable motivation to continue the research and development activities in diamond electronics. Although diamond is behind the other wide-gap semiconductors in terms of successful applications it still has the allure of being an elemental material with none of the stoichiometry problems and related defects of compound materials. In this regard it may be interesting to note that one of the major CVD diamond producers (E6) has recently started a joint venture (Diamond Microwave Devices) to develop and exploit CVD diamond RF devices. I would not like to speculate as to whether the creation of this company is in response to a product they believe to be close to market or a leap of faith, only time will tell, but I am sure I am joined by the rest of the CVD diamond community in wishing them every possible success. The dream is clearly alive and most certainly continues.

The editing of this book has been for me a highly rewarding activity. It has been a pleasure and privilege to be at the receiving end of so many erudite and fascinating accounts on different aspects of diamond as a potential electronic material. I have certainly learned a great deal and I cannot find sufficient words to thank all the contributors for the hard and conscientious work they have devoted to these chapters. Another aspect that has been very rewarding and is of special personal importance is to see that many of the collaborative research projects that I started while at the head of the CVD R&D group at De Beers Industrial Diamonds Divisions (now E6) have flourished and continue to deliver so many promising applications for CVD diamond. I am grateful to all the scientists that have been involved in these developments that have enriched this book and with whom I have shared so many interesting discussions. Since I retired from industry, Kings College London has kindly allowed me to become a Senior Research Fellow of the College. The benefits of being able to enjoy the frequent contact with colleagues in the Department of Physics and the attachment to the College have been invaluable for all my recent activities in the CVD diamond field including, needless to say, the editing of this book. I am particularly grateful to Alison Mainwood, Gordon Davies and Alan Collins from Kings College Physics Department for their friendship, support and encouragement during all these years. Finally, I would like to thank Alexandra Carrick, Richard Davies and Emma Strickland from John Wiley & Sons for their patient help and guidance during the preparation of this book.

Ricardo S. Sussmann,
May 2008

List of Contributors

M.N.R. Ashfold
School of Chemistry, University of Bristol, Bristol BS8 1TS, UK

E. Berdermann
Gesellschaft für Schwerionenforschung (GSI) mbH, Planckstr. 1, 64291 Darmstadt, Germany

M. Bruzzi
Dipartimento di Energetica 'S. Stecco', Via S. Marta 3, 50139 Firenze, Italy

J.E. Butler
Chemistry Division, Naval Research Laboratory, Washington DC 20375, USA

A. Cheesman
School of Chemistry, University of Bristol, Bristol BS8 1TS, UK

M. Ciobanu
Gesellschaft für Schwerionenforschung (GSI) mbH, Planckstr. 1, 64291 Darmstadt, Germany

A.T. Collins
Physics Department, King's College London, Strand, London WC2R 2LS

G. Davies
Physics Department, King's College London, Strand, London WC2R 2LS

A. Denisenko
Department of Electron Devices, University of Ulm, Albert Einstein Allee 45, D-89081 Ulm, Germany

J.S. Foord
University of Oxford, Department of Chemistry, Chemistry Research Laboratory, Mansfield Road, Oxford, OX1 3TA, UK

J.A. Garrido
Walter Schottky Institut, Technische Universität München, Germany

J. Isberg
Division for Electricity Research, Uppsala University, P.O. Box 534, SE-751 21, Uppsala, Sweden

H. Kagan
Department of Physics, Ohio State University, Columbus, OH 43210 USA

H. Kato
Nanotechnology Research Institute, National Institute of Advanced Industrial Science and Technology, Tsukuba, Ibaraki 305-8568, Japan

M. Kasu
NTT Basic Research Laboratories, NTT Corporation, 3-1 Morinosato-Wakamiya, Atsugi 243-0198, Japan

E. Kohn
Department of Electron Devices, University of Ulm, Albert Einstein Allee 45, D-89081 Ulm, Germany

J. Kusterer
Department of Electron Devices, University of Ulm, Albert Einstein Allee 45, D-89081 Ulm, Germany

L. Ley
Technical Physics, University of Erlangen, Erwin-Rommel-Str. 1, D-91058 Erlangen, Germany

A. Mainwood
King's College London, Physics Department, Strand, London, WC2R 2LS, UK

T. Makino
Nanotechnology Research Institute, National Institute of Advanced Industrial Science and Technology, Tsukuba, Ibaraki 305-8568, Japan

M. Schreck
Universitat Augsburg, Institut fur Physik, Universitatsstr. 1/Geb.Nord 86135 Augsburg,Germany

Y. Takano
National Institute for Materials Science (NIMS),1-2-1 Sengen, Tsukuba 305-0047, Japan

W. Trischuk
Department of Physics, University of Toronto, Toronto, ON, Canada

G. Verona-Rinati
Dipartimento di Ingegneria Meccanica, Università di Roma 'Tor Vergata', Via del Politecnico 1, I-00133 Roma, Italy

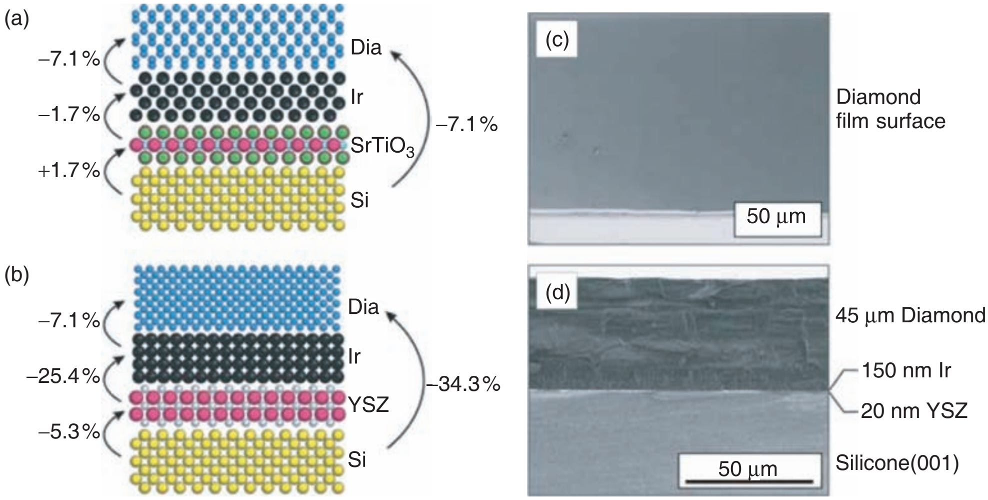
(a)
−7.1%
−1.7%
+1.7%
Dia
Ir
SrTiO3
Si
−7.1%
(b)
−7.1%
−25.4%
−5.3%
Dia
Ir
YSZ
Si
−34.3%
(c)
Diamond film surface
50 µm
(d)
45 µm Diamond
150 nm Ir
20 nm YSZ
Silicone(001)
50 µm

Plate 1 (Figure 6.22)

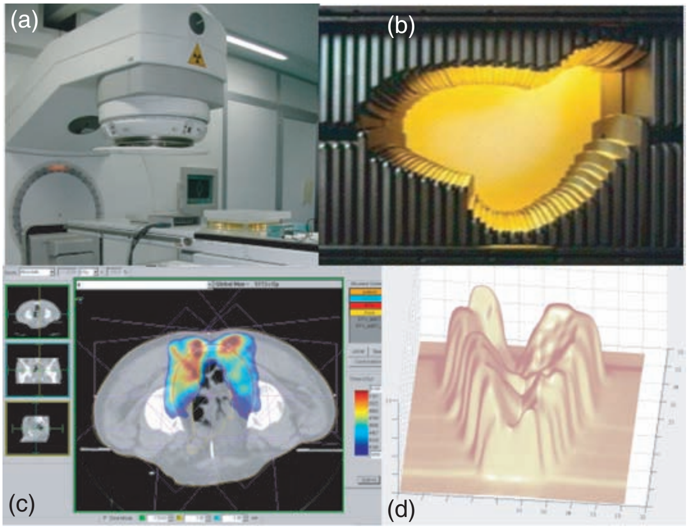

Plate 2 (Figure 8.2)

CVD Diamond for Electronic Devices and Sensors Edited by Ricardo S. Sussmann
© 2009 John Wiley & Sons, Ltd. ISBN: 978-0-470-06532-7

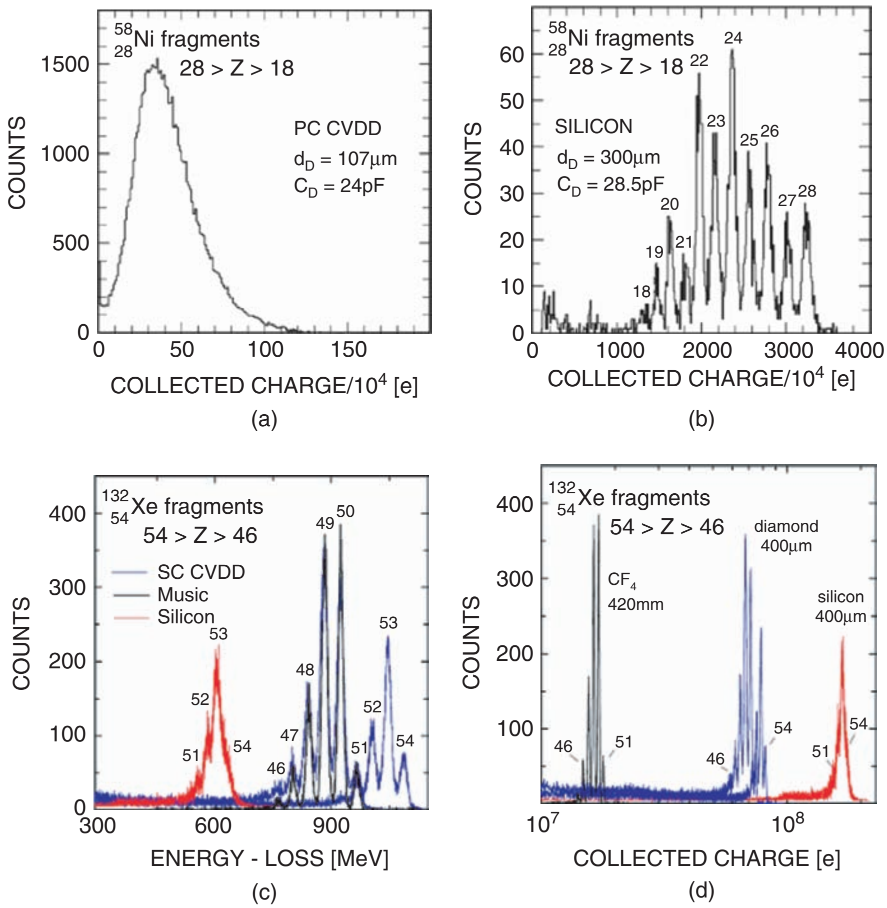

(a)

(b)

(c)

(d)

Plate 3 (Figure 10.9)

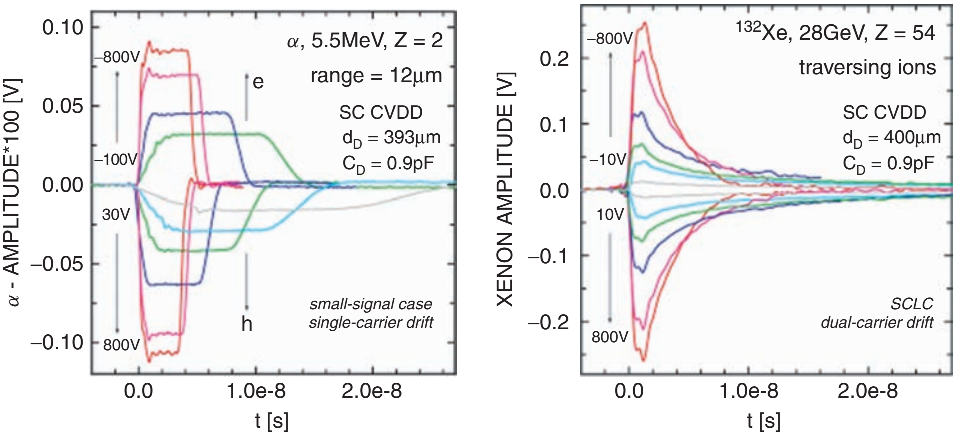

(a) (b)

Plate 4 (Figure 10.10)

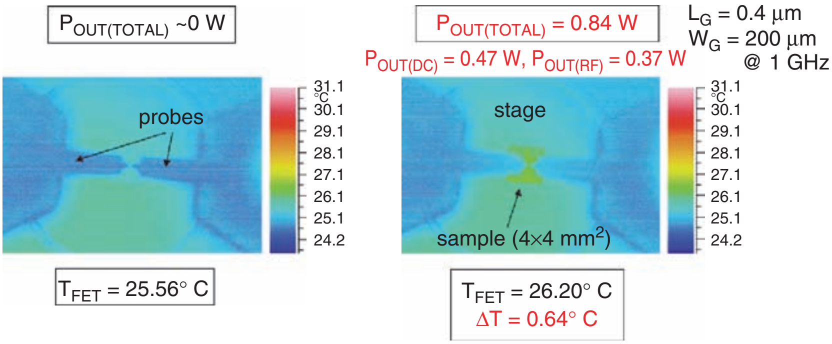
$P_{OUT(TOTAL)}$ ~0 W
probes
31.1
°C
30.1
29.1
28.1
27.1
26.1
25.1
24.2
T_{FET} = 25.56° C
$P_{OUT(TOTAL)}$ = 0.84 W
$P_{OUT(DC)}$ = 0.47 W, $P_{OUT(RF)}$ = 0.37 W
L_G = 0.4 µm
W_G = 200 µm
@ 1 GHz
stage
sample (4×4 mm^2)
31.1
°C
30.1
29.1
28.1
27.1
26.1
25.1
24.2
T_{FET} = 26.20° C
ΔT = 0.64° C

Plate 5 (Figure 13.18)

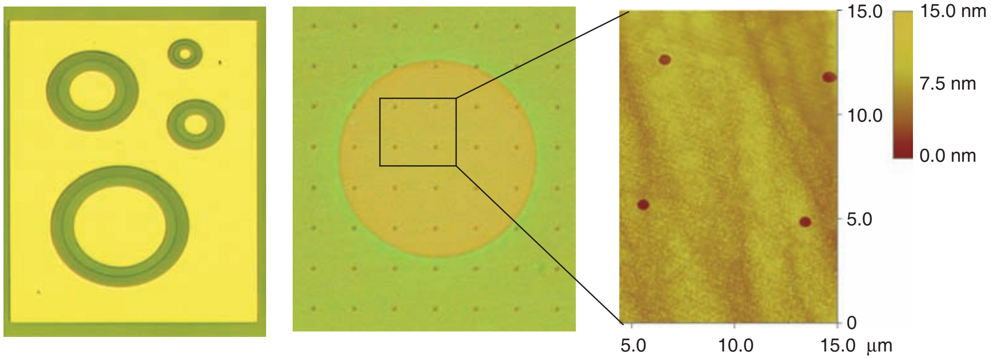
15.0
10.0
5.0
0
5.0
10.0
15.0 µm
15.0 nm
7.5 nm
0.0 nm

Plate 6 (Figure 14.35)

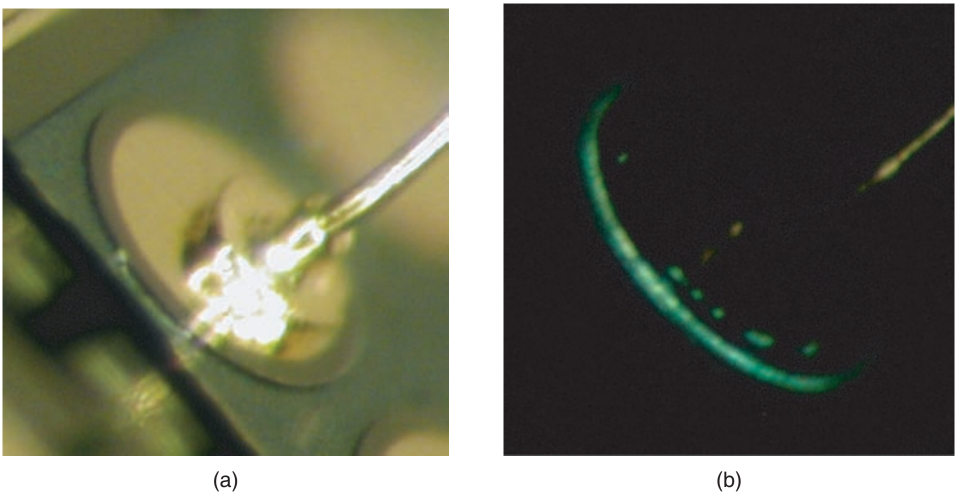

Plate 7 (Figure 15.6)

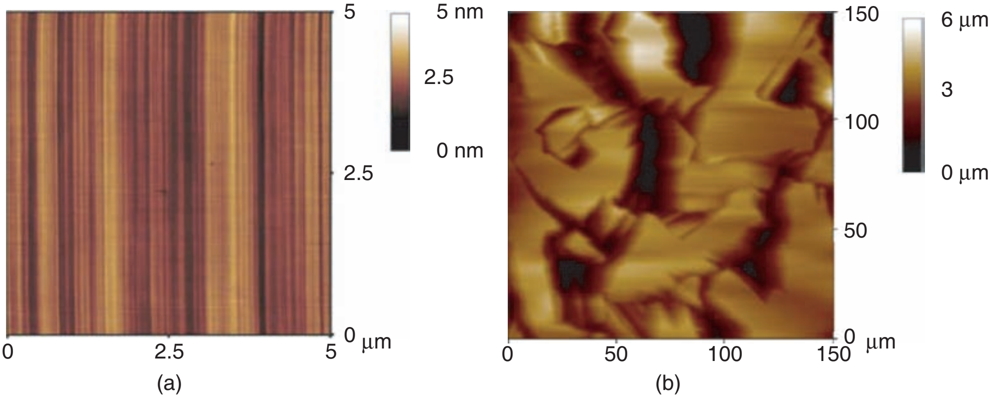
5
2.5
0
0
2.5
5
µm
5 nm
2.5
0 nm
(a)
150
100
50
0
0
50
100
150
µm
6 µm
3
0 µm
(b)

Plate 8 (Figure 16.1)

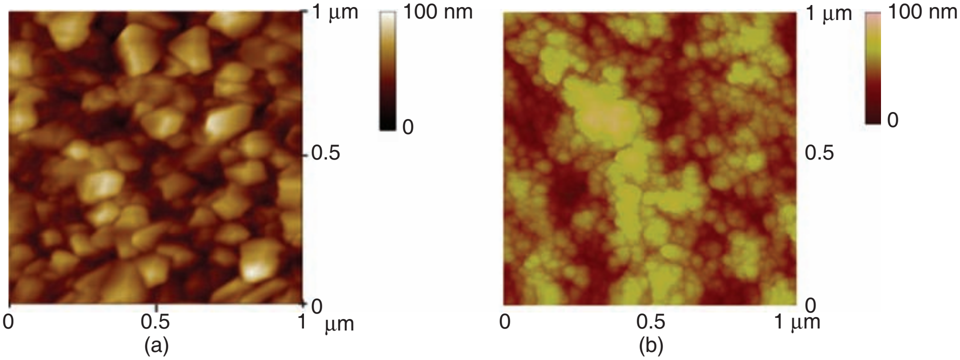
1 µm
0.5
0
0
0.5
1
µm
100 nm
0
(a)
1 µm
0.5
0
0
0.5
1 µm
100 nm
0
(b)

Plate 9 (Figure 16.2)

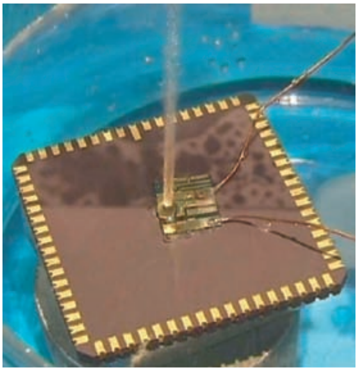

Plate 10 (Figure 18.1)

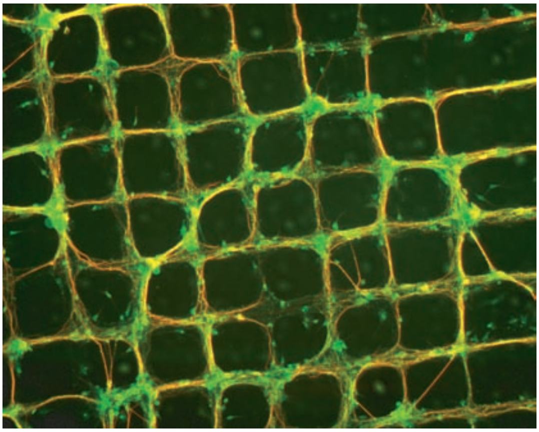

Plate 11 (Figure 18.14)

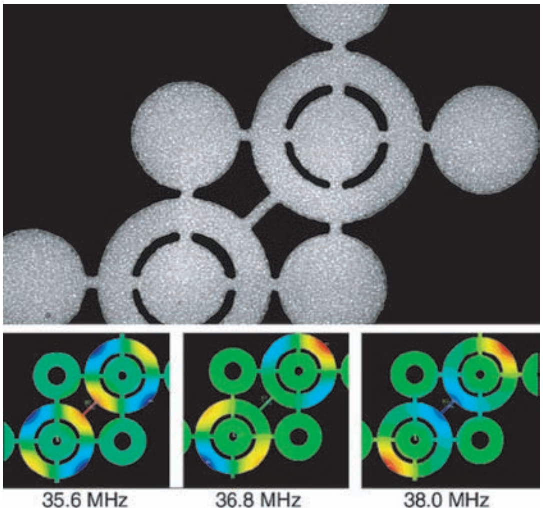
35.6 MHz
36.8 MHz
38.0 MHz

Plate 12 (Figure 18.37)

Part 1

Basic Properties, Defects and Impurities, Surface properties and Synthesis

CVD Diamond for Electronic Devices and Sensors Edited by Ricardo S. Sussmann

© 2009 John Wiley & Sons, Ltd. ISBN: 978-0-470-06532-7

1 Basic Properties of Diamond: Phonon Spectra, Thermal Properties, Band Structure

GORDON DAVIES

Physics Department, King's College London, UK

1.1 Introduction 3
1.2 The static lattice 4
  1.2.1 Dimensions of the lattice 4
  1.2.2 Thermal expansion of the lattice 5
  1.2.3 Isotope effects on the dimensions of the lattice 6
  1.2.4 Elastic constants 7
1.3 Vibrations 9
  1.3.1 Dispersion curves and the density of phonon states 10
  1.3.2 Special values of **k**: the Raman frequency 11
  1.3.3 Special values of **k**: other modes 13
  1.3.4 Two- and three-phonon processes 14
  1.3.5 Isotope effects 16
  1.3.6 Specific heat 17
  1.3.7 Thermal conductivity 18
1.4 Electronic energy states 20
  1.4.1 Dispersion curves 20
  1.4.2 Temperature dependence and isotope dependence of the lowest energy gap 22
  1.4.3 Exciton states and electron-hole condensates 23
  1.4.4 Dielectric properties 24
1.5 Summary 25
  References 25

1.1 INTRODUCTION

Diamond has been known for over two thousand years. For most of that time it was only valued for its appearance and for its mechanical properties. With the rapid increase in the control of its synthesis, new possibilities have arisen to exploit its electrical and

CVD Diamond for Electronic Devices and Sensors Edited by Ricardo S. Sussmann
© 2009 John Wiley & Sons, Ltd. ISBN: 978-0-470-06532-7

optical properties. Diamond has the largest electronic energy gap among the elemental semiconductors, and one of the largest known energy gaps of all semiconductors. It has high diffusion energies for impurities and defects, and stable surfaces. The combination of light atomic mass and strong chemical bonding results in diamond having relatively high vibrational frequencies compared with other semiconductors. Related to this, at room temperature and above, the ability of diamond to conduct heat from an active area is unusually high. These properties should allow diamond to be used increasingly in a range of applications, from surface-mediated processes to high-power devices [1]. Developments of the use of diamond require knowledge of a very wide range of properties. Some have been known for many years, such as the thermal expansion of diamond, which is required to make a heterogeneous structure of diamond and another material. Other properties have only been mapped out recently. For example, to obtain complete control of the lattice we need to know the effects not only of impurities but also of the disorder from the isotope content of the lattice. In yet other areas, exploiting high speed (terahertz) or small dimensions (nanometre), there is still much to learn.

In this chapter, our current understanding of the basic properties of diamond is outlined, focusing primarily on the experimental data.

1.2 THE STATIC LATTICE

The carbon in a natural diamond has two stable isotopes, ^{12}C in 98.9 % natural abundance, and ^{13}C at 1.1 % abundance. The nuclear spins are respectively zero and one-half. The simple chemical nature of diamond allowed its chemistry to be determined very early on [2], while the high crystalline quality of many natural diamonds permitted the crystal structure of diamond to be determined in the pioneering X-ray diffraction studies [3].

Diamond crystallises in a face-centred cubic lattice structure with a cube edge length denoted by a_0. Each lattice site in the face-centred cubic lattice is populated by two atoms, separated by $\sqrt{3/4}a_0$, approximately equal to 0.154 nm. The interatomic spacing is small compared with other semiconductors (compare the more typical 0.234 nm for silicon).

1.2.1 Dimensions of the lattice

A critical discussion of precision X-ray diffraction measurements on natural diamonds suggests that the cube edge length a_0 of pure diamond, measured at room temperature (approximately 20 °C), with natural isotope content, is [4] given by:

$$a_0 = 0.356710(4)\ \text{nm}. \tag{1.1}$$

The actual value for a particular diamond will depend on its impurity level, its isotope content and its temperature. To give a feeling of scale, a change in a_0 by 1 part in 10^5 would result if the temperature of the sample were to change by 12 °C, or if 7 % of the atoms were ^{13}C, or if 0.03 atomic-percent of the atoms were nitrogen atoms in the common pair (‘A’) form. Specifically, Lang and Pang [4] estimate that an atomic fraction

$c_{\mathrm{N(A)}}$ of nitrogen in the A form will produce a lattice expansion of:

$$\frac{\Delta a_0}{a_0} = 0.036 c_{\mathrm{N(A)}}. \tag{1.2}$$

For nitrogen in the single-substitutional form, commonly found in as-grown synthetic diamonds, they estimate that an atomic fraction $c_{\mathrm{N(C)}}$ of nitrogen in this dispersed (‘C’) form produces what can be a very significant effect:

$$\frac{\Delta a_0}{a_0} \sim 0.1 c_{\mathrm{N(C)}}. \tag{1.3}$$

The effect of pressure on the lattice is discussed in Section 1.2.4.

1.2.2 Thermal expansion of the lattice

Atomic vibrations in diamond are not precisely harmonic. For a typical chemical bond we expect the energy required to compress it by a small amount to be greater than the energy to lengthen it by the same amount. As the atoms vibrate, they can lengthen the bond more easily than compressing it. With increasing temperature, the vibrational amplitude increases, and the asymmetry becomes more pronounced. The lattice expands with increasing temperature, as a result of the anharmonicity in the vibrations.

In diamond, the cube edge length a_0 increases monotonically as the temperature increases. Recommended values of the coefficient of linear expansion (α) have been compiled by Slack and Bartram [5] based on work on natural diamonds. Up to a temperature of 500 K, α may be accurately parameterised as a function of the temperature T in kelvin by:

$$\alpha = 1.08 \times 10^{-11} T^2, \tag{1.4}$$

such that a_0 increases as the cube of T; the expansion (caused by vibrational anharmonicity) is proportional to the specific heat (resulting from the harmonic vibrations, see Section 1.3.6). With increasing T, α is expected to saturate to a constant value, and above 500 K a good parameterisation is:

$$\alpha = 7.95 \times 10^{-6} \times (1 - \exp[-T/1220]). \tag{1.5}$$

Wild and Koidl [6] have reported measurements of the expansion of polycrystalline, chemical-vapour-deposited (CVD) diamond, from 20 to 500 °C. Their data are a few (<5) percentage points higher than the recommended values of Slack and Bartram [5]. Wild and Koidl [6] describe their data using the temperature t in °C as:

$$\alpha = 8.19 \times 10^{-7} + 1.107 \times 10^{-8} t - 1.48 \times 10^{-11} t^2 + 1.08 \times 10^{-14} t^3, \quad 20 < t < 500. \tag{1.6}$$

The coefficient α of lattice expansion has been accurately calculated up to 400 K in the *ab initio* model of lattice vibrations of Pavone *et al.* [7]. The coefficient has very similar values to those of other semiconductors when the temperature is scaled [5] by an effective Debye temperature (~2240 K for diamond), but α is always positive for diamond in contrast to cubic silicon and germanium, where the lattice initially contracts (e.g. for $T < 120$ K for silicon).

1.2.3 Isotope effects on the dimensions of the lattice

The cube edge length a_0 has been measured in a series of diamonds synthesised at high pressure and high temperature, with five different atomic fractions x of ^{13}C, the remainder being ^{12}C. The variation in a_0 was found to be linear in x, following [8]:

$$a_0 = 0.356714 - 5.4 \times 10^{-5}x \text{ nm}. \tag{1.7}$$

The data are for 25 °C, and the value for $x = 0$ is in agreement with Equation (1.1). The fractional change for complete substitution, at $x = 1$, is then given by:

$$\frac{\Delta a_0}{a_0} = -1.5 \times 10^{-4}. \tag{1.8}$$

In contrast, Yamanaka *et al.* [9] have reported a nonlinear variation with x,

$$a_0 = 0.356712 - 9.0 \times 10^{-5}x + 3.7 \times 10^{-5}x^2 \text{ nm}. \tag{1.9}$$

The change in the volume is another consequence of the anharmonicity of the vibrations and may be calculated *ab initio* [10]. The physical basis is as follows. If we imagine a diamond made of ^{12}C that is at 0 K, and the atoms are static (there is no zero-point motion), then the chemical bonding will result in a certain inter-atomic spacing as a result of minimising the energy. We now allow the atoms to vibrate in their zero-point motion. In the harmonic approximation, the zero point motion of the ith mode is $\frac{1}{2}\hbar\omega_i$. All the modes therefore increase the energy by $\frac{1}{2}\sum_i \hbar\omega_i$. However, the modes are not strictly harmonic, and a change (usually an increase) in the bond length lowers the zero-point energy (Section 1.3.3). To minimise the vibrational energy, the lattice expands, but that expansion stretches the chemical bonds, and so increases the elastic energy of the lattice. A balance is reached where the decrease in vibrational energy is balanced by the increase in elastic energy. If we now repeat the argument for a ^{13}C diamond, the same processes occur, but now the vibrational frequencies are all smaller by a factor of $\sqrt{12/13}$, and so the zero-point energy is smaller. Expansion produces a smaller reduction in energy (because each $\hbar\omega_i$ is smaller), and so there is less energy to be saved by an expansion – starting from the imaginary static lattice, a ^{13}C diamond would not expand as much as a ^{12}C diamond. The value of a_0 is therefore smaller for a ^{13}C diamond than for a ^{12}C diamond. To calculate the effect, we need to know the change in frequency of each mode with the bond-length, how many modes we have at each frequency, and the elastic constants of diamond. The first is not well known (Section 3.3), the second and third are known (Sections 3.1 and 2.4). This argument applies at low temperatures (or at room temperature for diamond). In the limit of high temperature, the energy in each vibrational mode becomes the Boltzmann value of k_BT, which is independent of the frequency of the mode, and so is independent of its mass. At a very high temperature, a ^{13}C diamond would have the same lattice spacing as a ^{12}C diamond.

The content of ^{13}C in natural diamonds is slightly variable, with changes in ^{13}C of a few parts per thousand being observed. The variation is significant in geological studies but not likely to be of concern here.

1.2.4 Elastic constants

Diamond is well known to have large elastic constants. Because diamond has a face-centred cubic lattice, we can define Cartesian coordinates x, y, z with respect to the lattice, and the repeat distance along x, y or z is a_0. For a *macroscopic* diamond, any physical property measured along one of the cubic axes will have the same value along either of the others. This result produces a major simplification in the elastic constants: for a cubic crystal, there are only three elastic constants. We denote a strain generally by e. If we compress the crystal along the x axis, the fractional change in length along the x axis, the strain, is e_{xx}. This compression will cause the crystal to expand in the y and z directions, through the 'Poisson's ratio' effect, producing strains e_{yy} and e_{zz} in those directions. The stress, s, required to produce this particular deformation is given by the force acting in the x direction, on an area whose normal is in the x direction, and so is denoted s_{xx}. The relationship between the stress and the strains is given in terms of the elastic constants c_{11} and c_{12} as:

$$s_{xx} = c_{11}e_{xx} + c_{12}e_{yy} + c_{12}e_{zz}. \tag{1.10}$$

A different type of distortion is a shear, for example, when a cube face normal to y is sheared in the z direction to give a strain e_{yz}. To achieve this strain requires a shear stress, which is a force acting in the z direction on a unit-area face whose normal is in the y direction:

$$s_{yz} = c_{44}e_{yz}. \tag{1.11}$$

The numerical subscripts denote the combinations $1 = xx$, $2 = yy$, $3 = zz$, $4 = yz$, $5 = zx$, $6 = xy$. Equation (1.10) may be rewritten with a cyclic permutation of x, y and z, but using the same elastic constants (i.e. for the cubic crystals, $c_{11} = c_{22} = c_{33}$). Similarly, Equation (1.11) may be written for zx and xy shears, and $c_{44} = c_{55} = c_{66}$).

Brillouin scattering provides one method of measuring the elastic constants. It occurs when a photon is scattered into a new direction in the crystal, with the wave vector being conserved by emitting a phonon. The wave vector of the phonon is therefore known, and the change in energy of the scattered photon gives the frequency of the phonon. Hence the speed of the phonon (the speed of that sound wave) is known, and the speed of sound is linked to the elastic constants. The values at room temperature, for natural isotope abundance diamond, have been measured by Brillouin scattering [11]:

$$c_{11} = 1080.4 \pm 0.5, c_{12} = 127.0 \pm 0.7, c_{44} = 576.6 \pm 0.7 \text{ GPa}. \tag{1.12}$$

The 'bulk modulus' K $(= V\mathrm{d}P/\mathrm{d}V)$ is then given by:

$$K = (c_{11} + 2c_{12})/3 = 444.8 \text{ GPa}. \tag{1.13}$$

With increasing temperature from 300 K, each elastic constant c decreases from its value c_0 given immediately above, the change depending on the square of the temperature. The effect may be parameterised by:

$$c = c_0 + k(T^2 - 9.0 \times 10^4), \tag{1.14}$$

where the term k is the best-fitting parameter to the data, and T is in kelvin. For c_{11}, the value of k is $(-29 \pm 8)\times 10^{-6}$, for $c_{12}, k = (-3 \pm 18)\times 10^{-6}$, and for $c_{44}, k = (-22 \pm 7)\times 10^{-6}$ GPa K^{-2} [12].

Brillouin scattering measurements have been reported by Jiang *et al.* [13] for CVD diamond films, oriented with a $\langle 110\rangle$ direction normal to the surface of the sample, giving results, within their uncertainty, of the values in Equation (1.12). If the size of the diamond crystal is not macroscopic in all dimensions, the elastic constants would be expected to remain at their bulk values until the crystal shrinks to a few atoms in size. However, the wavelengths of the sound waves are ~100 nm, illustrating that the point when a crystal stops being macroscopic is dependent on the technique in use.

Macroscopic (beam-bending) measurements of the elastic properties of polycrystalline diamond have been reported by Szuecs *et al.* [14]. In many applications it is convenient to be able to calculate the effect of stress by using a simple 'Young's modulus' E which is defined in terms of the applied stress s and the applied strain e as $E = s/e$. However, the elastic properties are not isotropic. If the diamond is compressed by a stress s acting directly along the x axis, so that $s_{xx} = s$ and all other $s_{ij} = 0$, then the strains are known from the three equations like Equation (1.10), and Young's modulus is:

$$E_{001} = \left(c_{11}^2 + c_{11}c_{12} - 2c_{12}^2\right)/(c_{11} + c_{12}). \tag{1.15a}$$

In contrast, a stress s acting directly down a $\langle 111\rangle$ axis has stress components $s_{ij} = s/3$ for all i, j, and

$$E_{111} = 3c_{44}(c_{11} + 2c_{12})/(c_{11} + 2c_{12} + c_{44}). \tag{1.15b}$$

These values are, respectively, the minimum and maximum values of E for diamond. The values in Equation (1.12) give $E_{001} = 1054$ GPa and $E_{111} = 1208$ GPa, a variation of ~10 % about the mean. A polycrystalline sample would be expected to have a Young's modulus in this range, if the elastic properties of the material are not determined by the grain boundaries, a condition readily achieved in current CVD diamond: Szuecs *et al.* [14] report values for E at room temperature of 1143 GPa, with a 2.5 % scatter. The value is irreversibly reduced by degradation of the material when it is heated above 1000 K (700 °C) for the best quality, optical-grade, CVD diamond used. Below this transition point, they reported that Young's modulus for CVD diamond decreases with temperature T (in K) over the range 300 to 1000 K, at a sample-dependent rate that was significantly higher than that reported for single-crystal diamond (Equation 1.14). The rate was fitted by a linear dependence [14]:

$$E(T) = E(300)[1 + k(T - 300)], k \sim -1 \times 10^{-4}\text{K}^{-1}. \tag{1.16}$$

Data at high pressure are important, for example, when diamond is used in a high-pressure anvil cell. Occelli *et al.* [15] have measured the lattice size, using X-ray diffraction, up to

140 GPa as a function of pressure P (in GPa, determined from the ruby pressure scale). They find that P and the molecular volume V (in $\text{cm}^3\ \text{mol}^{-1}$) accurately follow the Vinet equation:

$$P = 3K_0(1 - X)X^{-2}\exp[3(K_0' - 1)((1 - X)/2], \tag{1.17}$$

where $X = (V/V_0)^{1/3}$. The subscript 0 indicates values at atmospheric pressure, and K_0' is the pressure derivative of the bulk modulus. The experimental value for the constants, valid up to a stated 140 GPa, were $V_0 = 3.4170(8)\ \text{cm}^3\ \text{mol}^{-1}$, $K_0 = 446(1)$ GPa, essentially as in Equations (1.1) and (1.13), and $K_0' = 3.0(1)$. However, the pressure calibration has been criticised; theoretical calculations predict [16]:

$$K_0' = 3.72 \text{ to } 3.8. \tag{1.18}$$

We have seen that the lattice spacing for ^{13}C diamond is smaller than for ^{12}C diamond (Section 2.3). There is a corresponding increase in the elastic constants. Ramdas *et al.* [17] report that for ^{13}C diamond at room temperature the following holds:

$$c_{11} = 1083.3 \pm 0.5,\ (c_{11} + 2c_{12} + 4c_{44})/3 = 1218.7 \pm 0.5 \text{ GPa}. \tag{1.19}$$

The value of the second term in ^{12}C diamond is 1214 GPa from Equation (1.12). Ramdas *et al.* [17] suggest that ^{13}C diamond is arguably the hardest known material.

The combination of the small interatomic distance and the high elastic constants results, qualitatively, in very high strain energies when most impurity atoms are placed into diamond, causing natural diamonds to be surprisingly pure.

1.3 VIBRATIONS

The vibrational dispersion curves, plotting the frequencies (ω) of vibrations against their wavevector ($\mathbf{k}$), are well established for most semiconductor materials. For silicon and germanium, the curves have very similar shapes and may be closely superimposed after linear scaling. The dispersion curves of diamond are distinctly different. The acoustic modes in Si and Ge have long regions near the zone boundaries in which ω varies little with $\mathbf{k}$, resulting in pronounced peaks in the phonon densities of states for the acoustic modes; diamond does not show this behaviour. Further, in contrast to Si and Ge, the maximum vibrational frequency is not at the zone centre.

Even at the limit of low temperature, atomic vibrations are occuring in a crystal as a result of zero-point motion. Consequently, all processes in a crystal involve the vibrations of the lattice. For example, when, at 0 K, an electron is excited between two ‘electronic’ states A and B; the process involves taking the crystal from the zero-point vibrational level with the electron in state A to the zero-point vibrational level with the electron in state B. Because the electronic state has changed, those vibrational states may not be identical. Some effects are small: at 0 K, it is estimated that the zero-point motion in the anharmonic potential results in the lattice parameter a_0 being about 0.5 % larger than would be the case for a static lattice [18]. More obviously, the temperature dependence of the lattice size (Section 1.2.2) and of the elastic constants (Section 1.2.4) arises primarily through the population of lattice modes (assuming a lightly doped or pure diamond, with negligible electronic excitation).

A *harmonic* vibration of angular frequency ω has energy levels $(n + \frac{1}{2})\hbar\omega$ and a Bose Einstein population at temperature T given by:

$$\overline{n} = 1.0/[\exp(\hbar\omega/k_{\mathrm{B}}T) - 1]. \tag{1.20}$$

$\overline{n}$ has the physical meaning that it is the mean value of n, the mean quantum state occupied. At high T, $k_{\mathrm{B}}T > \hbar\omega$, the population of a mode becomes $\overline{n} = k_{\mathrm{B}}T/\hbar\omega$, and the energy in that mode is $k_{\mathrm{B}}T$, which is independent of the frequency of the mode. Thermally induced effects therefore tend to be linear in T at high T. At the limit of low temperature, all vibrational states are populated in their zero-point level, $\frac{1}{2}\hbar\omega$, which is independent of T. The difference between the value of a property observed as $T \to 0$, and the value extrapolated to $T = 0$ from the high-temperature values is frequently referred to as the zero-point renormalisation, and controls, for example, much of the isotope dependence of the property.

When a transition involves the creation or destruction of a phonon, the probabilities, P_e and P_a, of emitting or absorbing a phonon of frequency ω depend on temperature through:

$$P_e \propto [1 + \overline{n}],\ P_a \propto \overline{n}. \tag{1.21}$$

At low T, only states of small ω can be populated, any thermal effect is weighted towards the vibrations of low frequency, and the high frequency vibrations are irrelevant. In diamond, the maximum lattice frequency of 1335 cm^{-1} has an energy quantum $\hbar\omega$ equal to $k_{\mathrm{B}}T$ at 1900 K, requiring the use of high temperatures if all the vibrational modes are to be thermally populated.

To understand the vibrational properties of diamond we need to know the values of the frequencies and how many modes of vibration we have in each small frequency interval.

1.3.1 Dispersion curves and the density of phonon states

As expected for a simple crystal, the vibrational dispersion curves of diamond were among the first to be measured by neutron scattering [19]. However, these data were limited to room temperature and pressure, and some key data were sparse: for example, only one measurement was made for the highest frequency optic modes with $\mathbf{k} \parallel \langle 001\rangle$. Subsequently, it was observed that the two-phonon Raman spectrum (Section 1.3.3) showed a peak at a frequency shift about 3 cm^{-1} greater than twice the Raman frequency [20–23], as a result of the vibrational frequency for the highest energy ('longitudinal optic') modes increasing slightly in frequency as $\mathbf{k}$ moves away from the zone centre. That maximum has been confirmed by inelastic X-ray scattering measurements for $\mathbf{k} \parallel \langle 001\rangle$ [24]. Burkel *et al*. [25] have also reported on the dispersion curve of the longitudinal acoustic mode along $\langle 001\rangle$, confirming the neutron data. The increase in frequency in the dispersion curves for the optic mode on moving away from the zone centre is a result of the unusually strong next-nearest-neighbour force interactions in diamond compared to other zinc blende and elemental semiconductors [7].

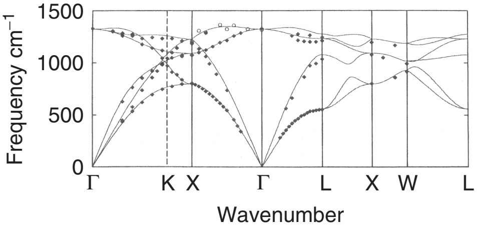

Figure 1.1 Phonon dispersion curves calculated by Pavone *et al.* [7], for phonon wavevectors **k** parallel to the major crystallographic axes. Point Γ has $\mathbf{k} = 0$, and X, L and K are respectively at the ⟨001⟩, ⟨111⟩ and ⟨110⟩ zone boundaries. The filled circles are neutron scattering data [19] and the open circles are X-ray scattering data [24], at room temperature

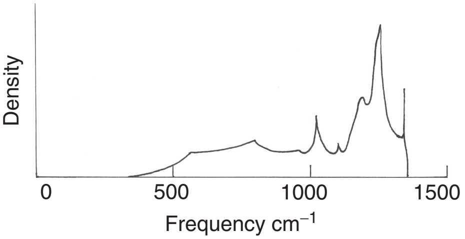

Figure 1.2 The phonon density of states, calculated by Pavone *et al.* [7], for diamond at room temperature

The measured dispersion curves provide a check for calculated dispersion curves, now available at high accuracy (e.g. Refs [7, 26], and Figure 1.1). Calculations of the vibrational frequencies allow, effectively, interpolation between the measured data, so that the number of modes of vibration $g(\omega)\mathrm{d}\omega$, which lie between angular frequencies ω and $\omega + \mathrm{d}\omega$, may be found (Figure 1.2). Inelastic X-ray scattering from diamond powders, of 3 to 5 μm size, has been used to derive the density of phonon states more directly from experiment [27]. The results are in very close agreement with the calculated density [7, 26], the major difference being a smaller measured peak in $g(\omega)$ at the highest frequencies compared with calculation.

1.3.2 Special values of k: the Raman frequency

Since diamond is a homopolar solid, a pure macroscopic diamond does not have any electrostatic dipole moments. The derivative of the dipole moment with respect to any deformation is also zero, and so diamond does not satisfy the necessary condition for first-order absorption of infrared radiation with the creation of one phonon in a pure bulk sample; impurities allow absorption with the creation one phonon, as would nano-scale dimensions. Pure diamond may absorb radiation with the involvement of more than one phonon. Qualitatively, one phonon can be thought to distort the lattice, creating instantaneous dipoles, to which the infrared radiation may couple, creating a second phonon. The optical absorption spectrum is then measuring combinations of phonons rather than single phonons. However, the creation of one phonon is allowed in Raman spectroscopy.

Pure diamond has one Raman-active mode, producing a sharp peak of full width at half height, at room temperature, in high quality crystals, of $\Gamma \sim 1.2$ cm^{-1}, at $\omega_R = 1332.4(1)$ cm^{-1}. Micro-Raman measurements, extrapolated to 0 K, give a limiting line width of 1.10(3) cm^{-1} [28]. The line width is determined, in a crystal, by lifetime broadening. A third-order perturbation approach [29], in which the Raman mode decays into two phonons, has predicted a decay time of 5.2 ps and so $\Gamma = 1.0$ cm^{-1}. Direct observation of the decay of the Raman line has been reported by pumping a pure diamond with 395 nm light, and observing a small (parts per million) oscillation in the reflection coefficient, the time period of the oscillation being equal to the Raman frequency [30]. The oscillations decayed at room temperature with an exponential decay time of 6.9 ps. Because the acoustic branches in diamond rise to a high value relative to the optic modes compared with other semiconductors (Section 1.3), there is a high density of acoustic modes at half the Raman energy. The Raman phonon predominantly decays into two acoustic phonons of similar energy [29], as in the 'Klemens' model [31].

The high intensity and sharpness of the Raman line has allowed detailed measurements to be made on it. With these data, the Raman line may be used to measure the temperature of a diamond, or to measure a high pressure that the diamond is subjected to. For example, the pressure in a diamond anvil cell may be measured using the exact frequency of the Raman line from a ^{13}C diamond chip that has been included in the working volume of the cell [32], or by using the Raman signal from a ^{13}C isotopically enhanced diamond anvil [33].

The dependence of a frequency of vibration on the volume V of the crystal is usually expressed through the 'Grüneisen parameter' γ of the mode:

$$\frac{\Delta\omega}{\omega} = -\gamma\frac{\Delta V}{V}. \tag{1.22}$$

Data have been presented by many workers [34–38] using the hydrostatic compressive stress P as the controlled variable, with agreement for several data sets now up to 140 GPa at [15]:

$$\frac{\Delta\omega}{\Delta P} = 2.7 \text{ to } 2.9 \text{ cm}^{-1}/\text{GPa}, \tag{1.23}$$

corresponding, via Equation (1.13), to $\gamma = -0.90$ to -0.97. Occelli *et al.* [15] have taken the pressure sufficiently high that nonlinear effects are very pronounced, giving, with P in GPa:

$$\omega = 1333.0 + 2.83P - 3.65 \times 10^{-3}P^2 \text{ cm}^{-1}. \tag{1.24}$$

The Grüneisen parameter is effectively constant at $\gamma = -0.97(1)$ throughout the range. Values of $\gamma = -0.92$ to -0.99 have been calculated using quantum Monte Carlo calculations [16].

The full width of the Raman line at half its width is sample dependent, for example, through the variations in strain fields, but has a minimum value of ~1.2 cm^{-1} in the limit of low temperature (essentially below room temperature). The decay at low T is reported above to be into two modes of equal energy, hence 667 cm^{-1}, and the probability of emitting those phonons increases as $\overline{n}$, see Equation (1.20). Above room temperature, the line width increases with temperature. Data for the line width up to 900 K, by Liu *et al.* [39], agree with the third-order perturbation calculation of Debernardi *et al.* [29] and are less temperature dependent than earlier data [40, 41].

The Raman frequency is triply degenerate in diamond, and so is split into a nondegenerate state and a doubly degenerate state when the symmetry is lowered by compression along the $\langle 111\rangle$ and $\langle 001\rangle$ axes. The splittings [42, 43] are $\Delta\omega = 2.2 \pm 0.2$ cm^{-1} GPa^{-1} for $\langle 111\rangle$, $\Delta\omega_{001} = 0.73 \pm 0.1$ cm^{-1} GPa^{-1} for $\langle 001\rangle$, comparable with the values in Equation (1.23). Note that for the same applied stress, the fractional changes $\Delta\omega/\omega$ are typically two orders of magnitude smaller for vibrations than for electronic states. Nevertheless, the splitting can be used to probe the stress inhomogeneities in diamond anvil cells [44].

A uniaxial stress produces a perturbation with even parity, while an electric field has odd parity: reducing the symmetry by an electric field allows the Raman frequency to be observed in optical absorption, the intensity of absorption increasing as the square of the applied field, and with a spectrometer-corrected line width of $\sim$1.5 cm^{-1} [45].

The small width of the Raman line allows it to be studied as a function of temperature. At high temperature, the temperature of the sample may be measured using the ratio of the probabilities of emitting (Stokes) or absorbing (anti-Stokes) a phonon in the Raman processes. The intensity I of the Raman line depends on the fourth power of its photon energy, and so the ratio is given by Equation (1.21) modified by a term containing the laser excitation frequency ω_L:

$$\frac{I_e}{I_a} = \left(\frac{\omega_L - \omega_R}{\omega_L + \omega_R}\right)^4 \exp\left(\frac{\hbar\omega_R}{k_B T}\right). \tag{1.25}$$

Data by Zouboulis and Grimsditch [40] for the Raman frequency from room temperature to 1850 K are in close agreement with data by Herschen and Capelli [41], who fitted their measurements to the simple expression:

$$\omega_R(T) = \omega_R(0) - 0.00777T - 1.075 \times 10^{-5}T^2, \quad 300 < T < 1850 \text{ K} \tag{1.26}$$

where $\omega_R(0) = 1334.5$ cm^{-1}.

The origin of the shift is partly caused by the expansion of the lattice, which, above room temperature, may be represented by a power series (Equation 1.6), as in Equation (1.26). However, evaluation using the Grüneisen parameter, after Equation (1.23), shows that the expansion accounts for only about one third of the observed effect, the remainder being caused by the anharmonicity of the vibrations.

Raman scattering is frequently used in assessing the crystallinity of chemical-vapour deposited diamond, by considering the ratio of the Raman lines from diamond and from noncrystalline (or nondiamondiferous) material [46]. The efficiency of exciting the two Raman features varies with the excitation wavelength, with UV favouring diamond and near infrared favouring nondiamond [47].

1.3.3 Special values of k: other modes

When, at low temperature, an electron is excited to the conduction band, it will de-excite rapidly (in picoseconds) to the minimum in the conduction band, located at a wave vector

$\mathbf{k} = 0.76 \pm 0.002$ of the zone-boundary value along the $\langle 001 \rangle$ axes. The hole will similarly de-excite, to its minimum energy state in the valence band at $\mathbf{k} = 0$. Recombination of the electron and hole in the pure diamond requires the wave vector to be conserved by emitting a phonon with $\mathbf{k}_{001} = 0.76 \pm 0.002$. Selection rules result in three of the phonons at that wave vector being identifiable: the transverse acoustic, transverse optic and longitudinal optic. The energy ($h\nu$) of the photon emitted by the recombination of the electron and hole is then reduced from the free-exciton band-gap energy E_b by the energy $\hbar\omega$ of each phonon: $h\nu = E_b - \hbar\omega$. However, because the recombination without involving a phonon is forbidden, there is uncertainty in the value of $\hbar\omega$. It may be measured from the onset of the equivalent absorption process, at $h\nu = E_b + \hbar\omega$ [48]:

$$\hbar\omega_{\mathrm{TA}} = 700 \pm 15, \hbar\omega_{\mathrm{TO}} = 1137 \pm 15, \hbar\omega_{\mathrm{LO}} = 1315 \pm 10, \mathrm{cm}^{-1}. \tag{1.27}$$

One problem with using the recombination of the free exciton is that the exciton has kinetic energy as a result of its thermal energy, leading to a line width of $1.8k_{\mathrm{B}}T$ [49]. More precise values may be determined by using the excitons that are weakly bound to the shallow boron acceptor, if we assume that the localisation does not affect the energy of the phonons involved. The localisation does, however, induce a zero-phonon component, providing a useful origin in the energy scale from which to measure the phonon energies. By this method, the energies in natural diamond are [50]:

$$\hbar\omega_{\mathrm{TO}} = 1139 \pm 5, \hbar\omega_{\mathrm{LO}} = 1315 \pm 5, \ \mathrm{cm}^{-1}. \tag{1.28}$$

The width of the phonon-assisted transitions in the bound-exciton luminescence allows the dispersion in k-space of those modes to be detected [51].

1.3.4 Two- and three-phonon processes

The two-phonon Raman scattering spectrum of diamond is well known [11, 20] and has been fitted closely, using five parameters to describe the second-order polarisability [22]. By definition, the multi-phonon processes involve combinations of (usually different) phonons. Identifications of the individual phonons involved have been attempted by associating peaks in the two-phonon absorption spectrum with peaks in the density of phonon states, either from an experimental matching or, more formally, from the calculated spectra. For example, Tables III of Ref. [23] and II of Ref. [22] contain extensive identifications. To avoid using combinations of modes, Klein *et al.* [52] have used the one-phonon, defect-induced, infrared absorption in imperfectly grown chemical-vapour deposited diamonds to pick out critical points in the one-phonon density of states.

Measurements [53] on the two-phonon Raman spectrum under hydrostatic stress (of <2.4 GPa) have given shift rates for the combined modes of 5.6 to 8.6 ± 0.6 cm^{-1} GPa^{-1}; we note that the same work resulted in a shift rate for the Raman line of about 20 % larger than the values of Equation (1.24), and so a 20 % reduction in the shift rates should probably be applied. The data are in overall agreement with the results of *ab initio* calculations of the Grüneisen parameters (Figure 1.3). These calculations suggest that the

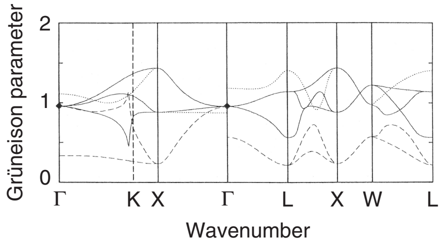

Figure 1.3 Grüneisen parameters for diamond at room temperature, as calculated by Pavone *et al.* [7]. The dashed lines are transverse acoustic modes, dotted lines are longitudinal acoustic modes, and solid lines are optic modes. The experimental data for the Raman mode are shown by diamonds

Grüneisen parameters γ for transverse acoustic, longitudinal acoustic and optic modes lie in the approximate ranges:

$$0.2 < \gamma_{\mathrm{TA}} < 1.1, 1.0 < \gamma_{\mathrm{LA}} < 1.4, 0.5 < \gamma_{\mathrm{TA}} < 1.4. \tag{1.29}$$

We noted that photons may be absorbed by a perfect diamond with the creation of two or more phonons. The shape of the absorption spectrum is well known experimentally (see, for example, Ref. [54]), but has not yet been closely simulated by theory. We would expect that the combinations of phonons must conserve wave vector, and that peaks in the two-phonon spectrum would follow the peaks in the two-phonon density of states. However, the band shape is strongly dependent on the transition probability for creating each pair of phonons. The absorption features move to lower energy as the temperature increases, as a result of the anharmonicity of the vibrations [55] and the lattice expansion. Typically lattice expansion accounts for about half of the total shift, and a simple parameterisation for the total change in energy E is of the form:

$$\Delta E = C/[\exp(\hbar\omega/k_{\mathrm{B}}T) - 1], \tag{1.30}$$

where $\hbar\omega$ is an effective, (lowest energy), phonon involved in the process. All the distinctive features of the two-phonon spectrum move to lower energy at approximately the same *fractional* rates:

$$\Delta E/E \sim -0.027/[\exp(860\ \mathrm{cm}^{-1}/k_{\mathrm{B}}T) - 1]. \tag{1.31}$$

For the well-defined features produced by the creation of two phonons, the absorption coefficient $A(\nu, T)$ increases with temperature T, as expected from Equation (1.21):

$$A(\nu, T) = a(\nu, 0)[1 + n(E_1, T)][1 + n(E_2, T)], \tag{1.32}$$

where E_1 and E_2 are the phonon energies, and of course $h\nu = E_1 + E_2$.

An especially important two-phonon absorption process is that at 10.6 μm, 943 cm^{-1}, the frequency of a $\mathrm{CO_2}$ laser. The absorption in pure diamond is $\sim$0.03 cm^{-1} at 300 K, but increases very rapidly, being a factor of 9 larger at 800 K [54]. Since wave vector and energy must be conserved, the two phonons involved must have, from the dispersion curves, energy quanta of $E_1 = 400 \pm 30$ cm^{-1} and $E_2 = 540 \mp 30$ cm^{-1}. The temperature dependence of the absorption with these two phonons being created is then given by Equation (1.32) and amounts to a factor of 2.8 increase between 300 and 800 K, and not the factor of 9 observed. The difference is caused partly by the two-phonon process at 943 cm^{-1} involving the destruction of one phonon and the creation of a second. From the dispersion curves, wave vector and energy may be conserved by destroying one low-energy acoustic mode of $E_1 = 335 \pm 35$ cm^{-1} and creating an optic mode of $E_2 = 1272 \pm 35$ cm^{-1}. The absorption coefficient of this process then increases with temperature as (see Equation 1.22):

$$A(\nu, T) = a(\nu, 0)n(E_1, T)[1 + n(E_2, T)], \tag{1.33}$$

and the low value of E_1 produces considerable temperature dependence. A further process contributing to the rapid rise in absorption with T at 943 cm^{-1} is that the phonon frequencies drift downwards as T increases (Equation 1.30), moving the stronger absorption that occurs at higher energy down to 943 cm^{-1}. Finally, with increasing T, the low-energy, three-phonon, processes (discussed next) become significant. The very strong temperature dependence can therefore be understood explicitly in terms of known components.

For the three-phonon processes, the allowed combinations of phonons are apparently sufficiently large that one may simply use the density $g_3(\omega)$ of three-phonon states, derived by twice convoluting the one-phonon density with itself. The absorption coefficient $A(\nu)$ at photon frequency ν is then found to be proportional to the combined density g_3 multiplied by the fourth power of ν. With increasing temperature, the probability of emitting each phonon increases as in Equation (1.21), but in practice it is sufficient to use a frequency $\nu/3$ for each of the phonons. The absorption then depends on the photon frequency and the temperature T as [54]:

$$A(\nu) \propto \nu^4 g_3(\nu)[1 + n(\nu/3)]^3. \tag{1.34}$$

1.3.5 Isotope effects

Multi-phonon Raman and infrared absorption measurements on isotopically modified diamonds produce the same band shapes but with the frequency scale modified essentially in accordance with the 'virtual crystal approximation', in which the mean mass of the lattice atoms is used [23]. Thus, for a mixture of x parts of ^{13}C and $(1 - x)$ parts of ^{12}C, the mean mass is $12 + x$ and the frequencies in this approximation are:

$$\omega(x) = \omega_{12}\sqrt{\frac{12}{12 + x}}. \tag{1.35}$$

For $\omega_{12} = 1332.8$ cm^{-1}, $\omega(x) = 1332.8 - 55.5x + 3.5x^2$. Precise measurements may be made on the one-phonon Raman line [23, 56–58]. The peak frequency is fitted with:

$$\omega(x) = 1332.82 - 34.77x - 16.98x^2 \text{ cm}^{-1}. \tag{1.36}$$

The shift is made up of the dominant virtual crystal term, plus the static lattice contraction affecting the frequency of the mode (the Grüneisen effect). Additionally, isotope disorder increases the scattering of phonons (Section 3.7 below). Ruf *et al.* [59] give a simple description of the effect by representing it in terms of a two-level model. One level, say the Raman phonon, interacts with other modes, represented by the second level, which is located at about the mean of the density of phonon states. Since the Raman frequency is greater than that mean, the interaction produced by the isotope disorder will force the Raman frequency higher. Measurement and theory [59] show that the disorder contributes a shift to the Raman line of between +4 and +7 cm^{-1} at $x \sim 0.5$. The disorder effects occur through the minority isotope species. For example, at high x the scattering atoms are ^{12}C, which raise the frequency of the active modes relative to the values in the pure ^{13}C crystal. The scattering modes are close to the Raman energy and produce a large positive shift. In contrast, at small x, the 'impurity' atoms are ^{13}C, which lower the frequency of the active modes away from the Raman energy. The disorder shift is asymmetric, maximising near $x = 0.6$ in this case [57]. From the measured disorder broadening, at $x = 0$ the line width Γ is expected to change at the rate $\mathrm{d}\Gamma/\mathrm{d}x = 2$ meV, so that in a natural diamond the isotope disorder contributes about 0.16 cm^{-1}, or over 10 %, to the line width.

The phonons that play an important role in the band-gap optical transitions at 0.76 of the $\langle 001 \rangle$ zone boundary are shifted, within experimental error, in accordance with the virtual crystal approximation when a complete change of isotope is made ($x = 0$ to $x = 1$) [50, 59]. Since the transverse optic mode lies below the mean in the density of states, the disorder interaction will now move that mode to lower energy [59], giving a disorder contribution at $x = 0.5$ of about -4 cm^{-1}.

1.3.6 Specific heat

Knowing the density of phonon states, $g(\omega)$ (Figure 1.2), and the probability of occupying them (Equation 1.19), the energy stored in the vibrations is given by:

$$E(T) = \int_0^{\omega_{\max}} \mathrm{d}\omega g(\omega) n(\omega), \tag{1.37}$$

and the specific heat is $C \propto \mathrm{d}E/\mathrm{d}T$. If $g(\omega)$ is known, the calculation is simple. For example, a very good fit to the experimental data results from using $g(\omega)$ obtained by inelastic X-rays (Figure 6 of Ref. [27]).

At low T, only the low frequency acoustic modes are thermally populated, with $\omega \propto k$. Consequently, the density of states $g(\omega) \propto \omega^2$. This form leads to the convention of using the Debye approximation, in which the density $g(\omega) \propto \omega^2$ is assumed to apply to all the modes. The expression for the specific heat may then be fitted to the experimental data at *any* temperature by choosing the appropriate value of $\omega_{\max}$ in the integral. The value of $\omega_{\max}$ is expressed conventionally in terms of the Debye temperature, $\Theta_D = \hbar\omega_{\max}/k_B$. The Debye temperature defined from specific heat measurements is $\Theta_D = 1865 \pm 10$ K in the range 300 to 800 K, corresponding to an increase in the specific heat C from 6.19 J g-atom^{-1} K^{-1} at 300 K to 19.29 J g-atom^{-1} K^{-1} at 800 K [60], that is from 0.5 J g^{-1} K^{-1} at room temperature to 1.6 J g^{-1} K^{-1} at 500 °C. To approach 90 % of the classical value of $C = 3R$, temperatures in excess of 1300 K would be required. Below 300 K, C decreases rapidly as fewer vibrational modes may be thermally populated [61, 62]. The rapid decrease away from the classical value of $C_v = 3R$, known since 1875

[63], is historically important as being the data that led Einstein to develop his quantum theory of specific heats [64].

The specific heat of chemical-vapour deposited diamond will depend on the quality of the films. However, the colour of diamond may be determined by very low concentrations of impurities, of the level of parts per million, which are irrelevant to bulk specific heat measurements. The specific heat of 'black' CVD diamond has been reported to be within 1 % (the experimental uncertainty) of that of bulk diamond [65].

There is a significant dependence of the specific heat of diamond on its isotope content. When the isotopic content is changed by increasing the fraction of ^{13}C, the predominant effect is that the frequencies of vibration are reduced in accordance with the virtual crystal approximation, and so at low temperature, where the frequency of the modes is most important, the specific heat is increased. Predictions by Sanati *et al.* [66] have been closely verified by measurements of the specific heat over the range 75 to 300 K [67]. At 170 K, the specific heat of ^{13}C is about one-sixth larger than for ^{12}C [67].

1.3.7 Thermal conductivity

The standard approach to the thermal conductivity κ of a solid is to use the analogy to conductivity in a gas:

$$\kappa = \tfrac{1}{3}Cv^2\tau, \tag{1.38}$$

where C is the specific heat, v is the speed of the heat carriers (phonons in diamond), and τ is the mean time between scattering events for the carriers. In diamond, there will be different contributions from the different frequencies of the phonons, requiring a sum over all the densities of state [68].

The specific heat increases from zero at 0 K, becoming a constant at high temperature (Section 1.3.6). With increasing T, there is an increase in the number of phonons available to transport the heat, and those phonons have increasing frequencies as T increases. However, with the increased populations of phonons, the probability of interacting with another phonon increases, and the probability of decaying into other phonons also increases (Equation 1.21). These intrinsic processes result in the phonon population being $\sim\hbar\omega/k_BT$ at high T, and so $\tau \propto T^{-1}$. At sufficiently high T, approximately above room temperature, this process will dominate in any diamond, and the thermal conductivity will be independent of the sample. Below about 100 K, only relatively low frequency (long wavelength) phonons are thermally excited. At this limit, the dimensions of the sample determine the scattering time; for example, polycrystalline diamond films could, therefore, have an anisotropic thermal conductivity. Finally, at intermediate temperatures, $T \sim 50$ to 300 K, the scattering time τ is determined by the impurities or other crystalline imperfections in the diamond, including isotope disorder. Although its peak thermal conductivity is at 70 K, the thermal conductivity of diamond at room temperature is still higher than for any other solid, and over four times that of pure copper.

These processes imply that the value of κ is, below 300 K, highly dependent on the specific sample used. There are now many techniques in use for determining the thermal conductivity, as reviewed by Reichling and Hartmann [69]. In general terms, high quality, 'pure' (type IIa) natural diamonds have their maximum thermal conductivity of

$\sim$15 000 W m^{-1} K^{-1} at $\sim$70 K [70–72]. Above 100 K, in high quality natural samples, κ decreases approximately inversely with T, to $\sim$600 W m^{-1} K^{-1} at $\sim$1000 K [70–72]. Diamonds are likely to contain atomic-sized defects and impurities, which act as scattering centres. They are most important in reducing the thermal conductivity in the central range, where neither the crystal size nor the phonon–phonon scattering is dominant. For example, reductions in the maximum value of κ by an order of magnitude are easily obtained in natural 'type Ia' diamonds with concentrations of nitrogen of a few parts per thousand. Similarly, radiation damage introduces additional thermal resistance in proportion to the concentration of vacancies [73].

Isotope disorder creates significant scattering of the phonons, reducing the thermal conductivity. Again, at the limits of low and high temperatures, κ is expected to be independent of the isotope content. However, an isotopic 'impurity', such as a ^{13}C atom in a predominantly ^{12}C diamond, is expected to increase the scattering rate τ^{-1} in proportion to the concentration of the isotopic impurity, and as the fourth power of the phonon frequency. The thermal conductivity is substantially reduced by the disorder near its maximum values (typically between 30 and 200 K). Isotopically enhanced diamond, with only 0.1 % ^{13}C has a peak value of κ some three times larger than diamond of natural isotope abundance [74], and the peak is shifted slightly, but possibly usefully, to higher T, to about 90 K. Isotopically pure diamond (^{13}C less than 0.001 %) would probably have a thermal conductivity of more than an order of magnitude greater than a diamond of natural isotope abundance.

In polycrystalline films, which have nucleated at many points on the surface of the substrate, the thermal conductivity may be highly anisotropic. A typical cross-section of the film will show many small crystallites at the nucleation surface, of which only a small proportion will grow into elongated crystals to the surface of the film. In such a sample, we could expect that the thermal conductivity measured through the thickness of the film, along a single crystal, may be significantly higher than in the lateral direction, where the heat flow has to jump across grain boundaries [75]. In this case, the resistance κ_F^{-1} to heat flow in the plane of the film is then made up of the resistance κ^{-1} inside the (pure) diamond grain, plus the resistance from the grain interfaces:

$$\kappa_F^{-1} = \kappa^{-1} + \frac{R_{\text{th}}}{a}. \tag{1.39}$$

Here, R_{th} is the resistance of one interface, and a is the mean grain size. For example, in samples investigated by Hartmann *et al.* [76], the interfacial resistance was 2×10^{-9} m^2 K W^{-1}, and so became increasingly important at grain sizes of $a < 20$ μm. For this value of R_{th}, the room temperature value of κ_F^{-1} decreases by a factor of two between 9 and 2.5 μm. However, if the first 30 to 40 μm of the CVD crystal growth is removed from the samples, and good quality material is used, the thermal conductivity in the plane of the CVD film and perpendicular to that plane have been found to be equal, within a measuring accuracy of 8 % [77]. Room-temperature values of κ of up to 2220 W m^{-1} K^{-1} were reported [77], which very closely approach the value for good natural crystals ($\sim$2265 W m^{-1} K^{-1}). Twitchen *et al.* [77] observed an excellent correlation in their samples between the thermal conductivity and the concentration of the carbon–hydrogen complexes identified by the absorption in the vibrational transitions at 2760 to 3030 cm^{-1}; these complexes appeared to be the dominant extrinsic source of thermal resistance. In earlier work, in some batches of polycrystalline films contaminated with nondiamond carbon, the ratio of the Raman signals from the diamond and nondiamond components was found to be a good indicator of the lateral thermal conductivity [78]: an example of how the limitations of materials decrease as the technology improves. As for single crystal diamond, isotope disorder in films can have a measurable effect on the thermal conductivity, and Belay *et al.* [79] have reported a lateral thermal conductivity three times lower in a 50 % ^{13}C sample compared with a sample of natural isotopes.

At the nanoscale, the surfaces become extremely significant, both in terms of surface contaminants and the intrinsic ability of carbon to rehybridise, and so the method of preparation is a key factor. The sparse data available to date show that the surfaces present significant barriers to thermal diffusion, resulting in very low thermal conductivity ($\sim$0.1 W cm^{-1}K^{-1} at room temperature [28]).

1.4 ELECTRONIC ENERGY STATES

1.4.1 Dispersion curves

The valence bands in diamond have their maxima at $\mathbf{k} = 0$, and the minimum in the first conduction band at $\mathbf{k} = 0.76$ of the zone boundary in the $\langle 001 \rangle$ directions [48]. The energy gap at low temperature is 5.49 eV, much larger than the other Group IV semiconductors, while the spin-orbit splitting at the maximum of the valence band is particularly small at $\sim$12 meV [80].

Experimental data have been derived mainly from optical measurements of absorption, luminescence, reflectance and ellipsometry. Given the indirect nature of the lowest band gap, optical absorption must involve the creation or (at high enough temperature) the destruction of a wave-vector-conserving phonon (Section 1.3.3). The absorption coefficient of pure diamond increases rapidly with photon energy, as discussed by Clark *et al.* [81]. Diamond is effectively opaque at photon energies just above the indirect band gap, but data on the band structure were obtained many years ago by using reflection spectra up to 35 eV [82, 83]. From the reflection spectra, the real (reflectance) and imaginary (absorbance) parts of the dielectric function can be obtained. Sharp features in the function derive primarily from the joint (valence and conduction band) density of states, and so relate to either the extreme of a band or to energy–wave vector plots of the valence and conduction bands running parallel to each other in **k**-space. Distinguishing between them relies on band structure analyses (Figure 1.4). The lowest direct gap is located at 7.2 eV above the valence band maximum. Good fits to the dielectric function between 5 and 25 eV are given by Papadopoulos and Anastassakis [84].

The width of the valence band has been measured using photoelectron spectroscopy by several groups. The width of the valence band, as determined by photoexcitation [85], is 23.0 ± 0.2 eV, greater than the width of 21.5 ± 0.2 eV predicted by local-density functional theory [86, 87], which does not include the many-particle contributions to the excitation. The exact shapes of the bands near the valence band maximum and first conduction band minimum have been predicted [88].

Formally, the effective mass of an electron or hole is given by the inverse curvature of the dispersion plots, $m^{\star}_{ij} = \hbar^2/(d^2E/dk_i dk_j)$. For the electron at the minimum of the conduction band, two masses are required, corresponding to motion longitudinal ($\mathbf{k} || \langle 001 \rangle$

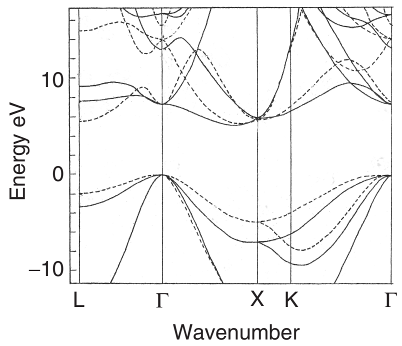

Figure 1.4 Electronic energy bands in pure diamond, for wave vectors **k** parallel to the major crystallographic axes. Point Γ has $\mathbf{k} = 0$, and X, L and K are respectively at the ⟨001⟩, ⟨111⟩ and ⟨110⟩ zone boundaries. The lines are calulated by L.R. Saravia and D. Brust, *Phys. Rev*. **170**, 683 (1968)

for the ⟨001⟩ minimum) or to transverse motion. Experimental masses for the electron have been calculated from the electron drift velocity by Nava *et al.* [89], yielding:

$$m^\star_{t,e} = 0.36m_0, m^\star_{l,e} = 1.4m_0, \tag{1.40}$$

in terms of the vacuum mass m_0 of the electron. One application of the masses is their use in predicting the higher energy levels of electrons bound to donors, using effective mass theory. A fit to experimental data for the energy levels of the phosphorus donor yields [90] $m^\star_{t,e} = 0.31m_0$, and $m^\star_{l,e} = 1.8m_0$ in reasonable agreement. Further, a detailed theoretical investigation of the band extrema [88] results in $m^\star_{t,e} = 0.34m_0$, and $m^\star_{l,e} = 1.5m_0$, in close agreement with Equation (1.40).

The valence band maximum is complicated by being composed of p atomic orbitals, giving, in atomic language, spin–orbit split states of $j = 3/2$ (lower energy hole states) and $j = 1/2$. The spin–orbit splitting is small, so that both the $j = 3/2$ and the $j = 1/2$ states need to be considered in any physical process, such as the formation of the bound states of the hole at the boron acceptor. Further, the $j = 3/2$ states split into $m_j = \pm 3/2, m_j = \pm 1/2$ pairs when the symmetry is reduced by having $k \neq 0$. To obtain different values of the energy at the same value of **k** requires different values of the curvature of the valence band for the $j = 3/2$ states, and hence two masses, a heavy hole (smaller hole energy) and a light hole. The tensor property of the effective mass is a further complication. Values derived theoretically for motion along the ⟨001⟩, ⟨111⟩ and ⟨110⟩ directions are, for the heavy hole [88]:

$$m^\star_{001} = 0.43m_0, m^\star_{111} = 0.78m_0, m^\star_{110} = 0.69m_0, \tag{1.41}$$

and for the light hole

$$m^\star_{001} = 0.37m_0, m^\star_{111} = 0.26m_0, m^\star_{110} = 0.28m_0. \tag{1.42}$$

The split-off spin-orbit state has a mass $0.4m_0$ [88].

The value of the spin–orbit interaction has been subject to some controversy. Considering *only* the maximum of the valence band, the atomic properties to consider are the angular momentum of the p orbitals, and the spin of the electron. They couple to give the $j = 3/2$ and $j = 1/2$ states, split at $\mathbf{k} = 0$ by the spin–orbit interaction λ. In an experiment, further interactions may be involved. For example, when a free exciton is created (Section 1.4.3 below), the hole at the valence band maximum interacts with an electron, which has at least angular momentum in its spin. Exchange coupling between the spins of the hole and the electron, of magnitude Δ, would, in the absence of spin–orbit coupling, create a spin singlet, $S = 0$, and a spin triplet, $S = 1$. These two interactions need to be considered together. A re-analysis by Cardona *et al.* [80] of data by Sauer *et al.* [91] suggests that the spin–orbit interaction is:

$$\lambda = 11.7 \text{ meV}, \tag{1.43}$$

in close agreement with theoretical calculations [88].

The lowest (indirect) energy gap moves to higher energy under hydrostatic pressure P at the rate, at room temperature and from $P = 0$ to $P = 2.3$ GPa, of [92]:

$$\mathrm{d}E/\mathrm{d}P = 6.0 \text{ meV/GPa}, \tag{1.44}$$

an order of magnitude larger than the shifts for the phonons (Equation 1.23).

When an electron has been excited from the maximum in the valence band to an energy state with more than twice the direct energy gap, its lifetime in that state has been estimated (from lifetime broadening) to be a few times 10^{-16} s [93]. The high energy state allows de-excitation of the electron through electron–electron interactions.

In nano-diamond, the surface properties become highly significant, in addition to the dimensions of the sample. For example, the band gap is predicted to decrease in diamond nanowires relative to bulk diamond, the extent depending on these properties [94].

1.4.2 Temperature dependence and isotope dependence of the lowest energy gap

With increasing temperature T, the lowest (indirect) energy gap at 5.49 eV moves monotonically to lower energy [81]. A shift of -110 meV is reported by 675 K. The effect is partly made up of the effect of lattice expansion (Section 1.2.2). A volume change of ΔV produces a shift:

$$\Delta E_{\mathrm{exp}} = -a(c_{11} + 2c_{12})\Delta V/V, \tag{1.45}$$

where the elastic constants are known (Section 1.2.4). There is uncertainty in a, the change in energy of the energy gap per unit hydrostatic pressure, with $a \sim 5$ to 6.4 meV/GPa [50, 95]. However, the lattice expansion term accounts for less than 10 % of the total observed shift. The majority of the shift comes from electron–phonon interactions. These have been discussed in detail by Zollner *et al.* [96], showing that total electron–phonon coupling in the valence band is about double that in the conduction band, and the coupling is predominantly in the optic modes. Their calculation reproduces the measured data. The electron–phonon coupling may be parameterised in terms of the density $g(\omega)$ of phonon states (Section 1.3.1), and the Bose–Einstein population term $n(\omega)$ (Equation 1.20). A simple empirical expression shows that the coupling term is proportional to the frequency ω of the phonon, giving:

$$\Delta E_{\mathrm{e-p}} = c \int \mathrm{d}\omega \omega g(\omega) n(\omega), \tag{1.46}$$

where the integral is over all the frequencies. This expression allows the energy-gap renormalisation energy to be found (~370 meV), which is required for discussion of the isotope effects. However, for practical purposes, the expression of O'Donnell and Chen [97] provides a simpler fit: the shift between 100 and 700 K is given by $-S\hbar\omega[\coth(\hbar\omega/kT) - 1]$ with $S = 2.31$ and $\hbar\omega = 94$ meV. Based on extraordinarily high precision measurements in single-isotope silicon, Cardona *et al.* [67] have proposed a universal law to the effect that the energy gap will change as T^4 at very low (liquid helium) temperatures.

Closely related to the temperature dependence is the isotope dependence. The total shift of the lowest indirect energy gap from natural to ^{13}C diamond is measured, at low T to be [50]:

$$E_{13} - E_{12} = 13.6 \pm 0.2 \text{ meV}. \tag{1.47}$$

Measurements by Ruf *et al.* [98] of luminescence from excitons weakly bound to boron acceptors show that their energies, which closely follow the lowest indirect energy gap, change linearly with the ^{13}C isotopic fraction x at a shift rate of $\mathrm{d}E/\mathrm{d}x = +14.6 \pm 0.5$ meV.

The shift is again partly caused by the contraction of the lattice that occurs when the isotope is changed (Section 1.2.3), but this is a small contribution of 3 ± 1.3 meV to the total shift [50]. Most of the shift can be identified as a result of changing the vibrational frequencies in Equation (1.46), and by using the value of c from the temperature dependence, a contribution of $+13.5 \pm 2$ meV was estimated to come from the electron–phonon term. A very similar value of +18.4 meV was predicted *ab inito* by Zollner *et al.* [96].

The temperature dependence of the first direct energy gap is similar to that of the lowest indirect gap [99].

1.4.3 Exciton states and electron-hole condensates

When one electron is excited to the conduction band, creating one electron at the conduction band minimum and one hole at the valence band maximum, separated in space by a distance r, there is a coulombic attraction between them of $V = -e^2/4\pi\varepsilon r$ for the two particles. At low temperature, a pseudo-hydrogenic system can be created with the electron and hole orbiting each other in a 'exciton' state, with a binding energy $E_{\mathrm{ex}} = e^2/8\pi\varepsilon a_{\mathrm{ex}}$. The binding energy of the exciton is measured as 80 meV and, together with the static dielectric constant $\varepsilon_\infty = 5.70$ from experiment [100], yields an effective radius for the exciton of:

$$a_{\mathrm{ex}} = 1.58 \text{ nm}. \tag{1.48}$$

The lifetime of the exciton has been measured as 2.3 μs [101]. The recombination of the electron and hole must involve a wave-vector conserving phonon (Equation 1.27), and so involves three particles plus the emitted photon (see Section 1.3.3). In silicon, free excitons may survive for tens of microseconds. In diamond, the exciton's lifetime is long enough for diffusion to take place, even at liquid helium temperature, from its random creation point to be trapped, for example, at a boron atom, when boron is present at concentrations of over $\sim 10^{17}$ cm^{-3}. Since the exciton's lifetime is determined partly by the rate of capture at impurities, any experimental value should be regarded as a lower limit.

With increasing excitation power, many electrons and holes may be created before the first pair recombines. As long as sufficent power is placed in a pure diamond without appreciable heating of the sample (T less than about 165 K [102]), the attraction of the oppositely charged particles lowers their energy sufficiently for an 'electron-hole condensate' to be created within 'several tens of picoseconds' [102], analogous to a liquid being formed in preference to a gas (the free excitons). Luminescence from the electron-hole condensate still involves transitions across the indirect energy gap, and so involves the phonons of Equation (1.27). The electron–hole attraction lowers the available electronic energy relative to the 5.49 eV energy gap by an amount that depends on the concentration of the electrons and holes, and hence on the excitation power. Luminescence, which grows rapidly with excitation power, is then observed in the range 5.1 to 5.25 eV, involving the transverse-optic phonon [103]. The concentration of electrons and holes in the condensate depends on the excitation and temperature, but is of the order of 10^{20} cm^{-3} [102, 103]. The decay time of the condensate, measured as $\sim$1 ps at 15 K, is significantly shorter than the lifetime (2.3 μs quoted above) of the free exciton, and is consistent with quenching by the Auger process [102]. In ^{13}C, luminescence from the electron–hole condensate is shifted by about 14 meV relative to ^{12}C, as expected from Equation (1.47) [103]. A thorough account of the electron–hole condensate is given by Sauer *et al.* [104].

Finally, we note the electronic states of an exciton, whether free or weakly bound to boron or phosphorus, sample a volume of the crystal given by $V = 4\pi a_{\text{ex}}^3/3$, where a_{ex} is known (Equation 1.46). Random isotopes inevitably broaden those states, at a rate determined by the isotope dependence of the energy gap, $\mathrm{d}E/\mathrm{d}x = 13.6$ meV (Equation 1.47). The full width at half height of an optical transition in natural diamond, $x = 0.01$ is then given by:

$$\Gamma = 2.36\frac{\mathrm{d}E}{\mathrm{d}x}\left[\frac{x(1-x)}{\rho V}\right]^{1/2} = 0.2\ \text{meV}, \tag{1.49}$$

where $\rho = 1.76\times10^{28}$ m^{-3} is the atomic density of diamond. This value is significantly smaller than the smallest width of bound exciton lines detected to date [51], of $\sim$1 meV, and indicates the potential still to be achieved in material quality.

1.4.4 Dielectric properties

When there is no absorption in a sample, the refractive index n is related to the real part ε_1 of the dielectric constant by $n = \sqrt{\varepsilon_1}$. Measurements of the static dielectric constant, by capacitance techniques with frequencies of 1 to 10 kHz, gave $\varepsilon_\infty = 5.70$ [100] at room temperature, consistent with the prediction of 5.72 from the *ab initio* calculation of Pavone *et al.* [7]. For $\varepsilon_1 = 5.7, n = 2.39$. At higher, optical, frequencies the refractive index increases to 2.72 for photons just below the indirect energy gap. The dependence on wavelength λ is [105]:

$$n^2 = 1 + \frac{0.3306\lambda^2}{\lambda^2 - \lambda_1^2} + \frac{4.3356\lambda^2}{\lambda^2 - \lambda_2^2}, \tag{1.50}$$

where $\lambda_1 = 175$ nm and $\lambda_2 = 106$ nm.

The dielectric constant varies with temperature T as [106]:

$$\varepsilon_1 = 5.701 - 5.35 \times 10^{-5}T + 1.66 \times 10^{-7}T^2. \tag{1.51}$$

Equivalently, Ruf *et al.* [98] have measured the refractive index up to 925 K, and can fit the temperature variation in terms of a Bose–Einstein factor (Equation 1.20), with a single effective frequency of 711 cm^{-1}.

One immediate practical application of the refractive index is to the reflection coefficient R at normal incidence, which in the absence of absorption is $R = (n - 1)^2/(n + 1)^2$. The reflection coefficient increases from 17 % in the infrared and visible to 21 % in the near UV. At higher energies [106], near 12.6 eV, R exceeds 50 %. Other aspects of the optical data have been reviewed fully by Mainwood [107], to which we add recent rationalisation of the photoelastic constants, which are important for determining strains in diamond [108]. The optical data are essential for the design of optical components fabricated from diamond. For example plano-convex lenses, of diameters of 2 to 5 mm and focal lengths of 3.2 to 5.2 mm, have been made by chemical vapour deposition of diamond into spherical depressions in a substrate, followed by polishing flat the growth surface [109].

1.5 SUMMARY

All aspects of the basic properties of pure diamond cannot be reviewed in a short chapter. For example, we have not touched on electron transport in the bulk (which is discussed in this book by J. Isberg), surface properties, or the properties of nano-diamond. It is striking that many scientific properties of diamond have been known for considerably longer than for almost any other crystalline material, and they have played significant roles in the development of condensed matter research. However, because diamond is a simple, prototype material, its science is constantly being revisited at both the experimental and theoretical levels as new techniques become available. It will be fascinating to see how far future improvements in the growth of diamond will extend its already unique properties.

REFERENCES

[1] R.S. Balmer, I. Friel, S.M. Woollard, C.J.H. Wort, G.A. Scarsbrook, S.E. Coe, H. ElHaji, A. Kaiser, A. Denisenko, E. Kohn and J. Isberg, *Phil. Trans. R. Soc.* **366**, 251 (2008).

[2] A. Lavoisier, Traité élémentaire de chimie, Paris Chez Cuchet 1789, reprinted Bruxelles: Culture et Civilisations, 1965.

[3] W.H. Bragg and W.L. Bragg, *Proc. R. Soc A* **89**, 277 (1913).
[4] A.R. Lang and G. Pang, *Phil Trans. R. Soc. Lond. A* **356**, 1397 (1998).
[5] G.A. Slack and S.F. Bartram, *J. Appl. Phys.* **46**, 89 (1975).
[6] C. Wild and P. Koidl, in Properties, Growth and Applications of Diamond, M.H. Nazaré and A.J. Neves (Eds), INSPEC, p. 351 (2001).
[7] P. Pavone, K. Karch, O. Schütt, W. Windl, D. Strauch, P. Giannozzi and S. Baroni, *Phys. Rev. B* **48**, 3156 (1993).
[8] H. Holloway, H.C. Hass, M.A. Tamor, T.R. Anthony and W.F. Banholzer, *Phys. Rev. B* **44**, 7123 (1991).
[9] T. Yamanaka, S. Morimoto and H. Kanda, *Phys. Rev. B* **49**, 9341 (1994).
[10] P. Pavone and S. Baroni, *Sol. State Commun.* **90**, 295 (1994).
[11] R. Vogelgesang, A.K. Ramdas, S. Rodriguez, M. Grimsditch and T.R. Anthony, *Phys. Rev B* **54**, 3989 (1996).
[12] E.S. Zoulboulis, M. Grimsditch, A.K. Ramdas and S. Rodriguez, *Phys. Rev. B* **57**, 2889 (1998).
[13] X. Jiang, J.V. Harzer, B. Hillebrands, Ch. Wild and P. Koidl, *Appl. Phys. Lett.* **59**, 1055 (1991).
[14] F. Szeucs, M. Werner, R.S. Sussmann and C.S.J. Pickles, *J. Appl. Phys.* **86**, 6010 (1999).
[15] F. Occelli, P. Loubeyre and R. Letoullec, *Nature Mat.* **2**, 151 (2003).
[16] R. Maezono, A. Ma, M.D. Towler and R.J. Needs, *Phys. Rev. Lett.* **98**, 025701 (2007).
[17] A.K. Ramdas, S. Rodriguez, M. Grimsditch, T.R. Anthony and W.F. Banholzer, *Phys. Rev. Lett.* **71**, 189 (1993).
[18] C.P. Herrero and R. Ramirez, *Phys. Rev. B* **63**, 024103 (2001).
[19] J.L. Warren, J.L. Yarnell, G. Dolling and R.A. Cowley, *Phys. Rev.* **158**, 805 (1967).
[20] S.A. Solin and A.K. Ramdas, *Phys. Rev. B* **1**, 1687 (1970).
[21] M.A. Washington and H.Z. Cummings, *Phys. Rev. B* **15**, 5840 (1977).
[22] W. Windl, P. Pavone, K. Karch, O. Schütt, D. Strauch, P. Giannozzi and S. Baroni *Phys. Rev. B* **48**, 3164 (1993).
[23] R. Vogelgesang, A.D. Alvarenga, H. Kim, A.K. Ramdas, S. Rodrigues, M. Grimsditch and T.R. Anthony, *Phys. Rev. B*, **58**, 5408 (1998).
[24] E. Burkel, pp. 61–64 in *Inelastic Scattering of X-rays with Very High Energy Resolution*, Springer tracts in Modern Physics, Vol. **125**, Springer, Berlin, 1991.
[25] E. Burkel, B. Dorner, Th. Illini and J. Peisl, *Rev. Sci. Instrum.* **60**, 1671 (1989).
[26] N. Mounet and N. Marzan, *Phys. Rev. B* **71**, 205214 (2005).
[27] A. Bosak and M. Krisch, *Phys. Rev. B* **72**, 224305 (2005).
[28] W.L. Liu, M. Shamsa, I. Calizo and A.A. Balandin, *Appl. Phys. Lett.* **89**, 171915 (2006).
[29] A. Debernardi, S. Baroni and E. Molinari, *Phys. Rev. Lett.* **75**, 1819 (1995).
[30] K. Ishioka, M. Hase and M. Kitajima, *Appl. Phys. Lett.* **89**, 231916 (2006).
[31] P.G. Klemens, *Phys. Rev.* **148**, 845 (1966).
[32] D. Schiferi, M. Nicol, J.M. Zaug, S.K. Sharma, T.F. Cooney, T.R. Anthony and J.F. Fleischer, *J. Appl. Phys.* **82**, 3256 (1997).
[33] P.A. Baker, Y.K. Vohra, R.S. Peterson and S.T. Weir, *Appl. Phys. Lett.* **83**, 1734 (2003).
[34] S.S. Mitra, O. Brafman, W.B. Daniels and R.K. Crawford, *Phys. Rev. B* **186**, 942 (1969).
[35] E. Whalley, A. Lavergne and P.T.T. Wong, *Rev. Sci. Instrum.* **47**, 845 (1976).
[36] M. Hanfland, K. Syassen, S. Fahy, S.G. Louie and M.L. Cohen, *Phys. Rev. B* **31**, 6896 (1985).
[37] H. Boppart, J. van Straaten and I.F. Silvera, *Phys. Rev. B* **32**, 1423 (1985).
[38] A.F. Goncharov, I.N. Makarenko and S.M. Stishov, *JETP Lett.* **41**, 184 (1985).
[39] M.S. Liu, L.A. Bursill and S. Prawer, *Phys. Rev. B* **61**, 3391 (2000).
[40] E.S. Zouboulis and M. Grimsditch, *Phys. Rev. B* **43**, 12490 (1991).
[41] H. Herschen and M.A. Capelli, *Phys. Rev. B* **43**, 12490 (1991).
[42] M.H. Grimsditch, E. Anastassakis and M. Cardona, *Phys. Rev. B* **18**, 901 (1978).

[43] E. Anastassakis, A. Cantarero and M. Cardona, *Phys. Rev. B* **41**, 7529 (1990).
[44] Y. Akahama and H. Kawamura, *J. Appl. Phys.* **98**, 083523 (2005).
[45] J.F. Angress, C. Cooke and A.J. Maiden, *J. Phys. C* **1**, 1769 (1968).
[46] J. Wagner, C. Wild, W. Mullersebert and P. Koidl, *Appl. Phys. Lett.* **61**, 1284 (1992).
[47] J. Wagner, C. Wild and P. Koidl, *Appl. Phys. Lett.* **59**, 779 (1991).
[48] P.J. Dean, E.C. Lightowlers and D.R. Wight, *Phys. Rev.* **140** A352 (1965).
[49] G. Davies, *J. Phys. Chem. Solids* **31**, 883 (1970).
[50] A.T. Collins, S.C. Lawson, G. Davies and H. Kanda, *Phys. Rev. Lett.* **65**, 891 (1990).
[51] S.J. Sharp, A.T. Collins, G. Davies and G.S. Joyce, *J. Phys. C: Condens. Matter* **9**, L451 (1997).
[52] C.A. Klein, T.M. Hartnett and C.J. Robinson, *Phys. Rev. B* **45**, 12854 (1992).
[53] B.J. Parsons, *Proc. R. Soc. Lond. A* **352**, 397 (1976).
[54] C. Piccirillo, G. Davies, A. Mainwood, S. Scarle, C.M. Penchina, T.P. Mollart, K.L. Lewis, M. Nesládek, Z. Remes and C.S.J. Pickles, *J. Appl. Phys.* **92**, 756 (2002).
[55] J. Menéndez and M. Cardona, *Phys. Rev. B* **29**, 2051 (1984).
[56] R.M. Chrenko, *J. Appl. Phys.* **63**, 5873 (1988).
[57] K.C. Haas, M.A. Tamor, T.R. Anthony and W.F. Banholzer, *Phys. Rev. B* **45**, 7171 (1992).
[58] J. Spitzer, P. Etchegoin, M. Cardona, T.R. Anthony and W.F. Banholzer, *Solid State Commun.* **88** 509 (1993).
[59] T. Ruf, M. Cardona, H. Sternschulte, S. Wahl, K. Thonke, R. Sauer, P. Pavone and T.R. Anthony, *Solid State Commun.* **105**, 311 (1998).
[60] A.C. Victor, *J. Chem. Phys.* **36**, 1903 (1962).
[61] W. DeSorbo, *J. Chem. Phys.* **21**, 1903 (1962).
[62] J.E. Desnoyers and J.A. Morrison, *Phil. Mag.* **3**, 42 (1958).
[63] H.E. Weber, *Philos. Mag.* **49**, 161 (1875).
[64] A. Einstein, *Ann. Phys.* **22**, 180 (1907).
[65] J.E. Graebner, *Diamond Rel. Mater.* **5**, 1366 (1996).
[66] M. Sanati, S.K. Estreicher and M. Cardona, *Solid State Commun.* **131**, 229 (2004); M. Cardona, R.K. Kremer, M. Sanati, S.K. Estreicher and T.R. Anthony, *Solid State Commun.* **133**, 465 (2005).
[67] M. Cardona, T.A. Meyer and M.L.W. Thewalt, *Phys. Rev. Lett.* **92**, 196403 (2004).
[68] J. Calloway, *Phys. Rev.* **113**, 1046 (1959).
[69] M. Reichling and J. Hartmann, in *Properties, Growth and Applications of Diamond*, M.H. Nazaré and A.J. Neves (Eds), INSPEC, p. 55 (2001).
[70] J.W. Vandersande, *Phys. Rev. B* **13**, 4560 (1976).
[71] R. Berman, P.R.W. Hudson and M. Martinez, *J. Phys. C. Solid State Phys.* **8**. L430 (1975).
[72] E.A. Burgemeister, *Physica B & C* **93**, 165 (1978).
[73] E.A. Burgemeister, C.A. Ammerlaan and G. Davies, *J. Phys. C: Solid St. Phys.* **13**, L691 (1980).
[74] L. Wei, P.K. Kuo, R.L. Thomas, T.R. Anthony and W.F. Banholzer, *Phys. Rev. Lett.* **70**, 3764 (1993).
[75] J.E. Graebner, S. Jin, G.W. Kammlott, J.A. Herb and C.F. Gardinier, *Nature* **359**, 401 (1992).
[76] J. Hartmann, M. Costello and M. Reichling, *Phys. Rev. Lett.* **80**, 117 (1998).
[77] D.J. Twitchen, C.S.J. Pickles, S.E. Coe, R.S. Sussmann and C.E. Hall, *Diamond Rel. Mater.* **10**, 731 (2001).
[78] E. Woerner, J. Wagner, W. Mueller-Sebert, C. Wild and P. Koidl, *Appl. Phys. Lett.* **68**, 1482 (1996).
[79] K.I. Belay, Z.Y. Etzel, D.G. Onn and T.R. Anthony, *J. Appl. Phys.* **79**, 8336 (1996).
[80] M. Cardona, T. Ruf and J. Serrano, *Phys. Rev. Lett.* **86**, 3923 (2001).
[81] C.D. Clark, P.J. Dean and P.V. Harris, *Proc. R. Soc. Lond. A* **277**, 312 (1964).
[82] H.R. Philipp and E.A. Taft, *Phys. Rev.* **A136**, 1445 (1964).

[83] R.A. Roberts and W.C. Walker, *Phys. Rev.* **161**, 730 (1967).

[84] A.D. Papadopoulos and E. Anastassakis, *Phys. Rev. B* **43**, 5090 (1991).

[85] I. Jiménez, L.J. Terminello, D.G.J. Sutherland, J.A. Carlisle, E.L. Shirley and F.J. Himpsel, *Phys. Rev. B* **56**, 7215 (1997).

[86] M. Hybertsen and S.G. Louie, *Phys. Rev. B* **34**, 5390 (1986).

[87] M. Rohlfing, P. Kruger and J. Pollmann, *Phys. Rev. B* **48**, 17791 (1993).

[88] M. Willatzen, M. Cardona and N.E. Christensen, *Phys. Rev. B* **50**, 18054 (1994).

[89] F. Nava, C. Canali, C. Jacobini, L. Reggiani and S.F. Kozlov, *Solid State Commun.* **33**, 475 (1980).

[90] E. Gheeraert, N. Casanova, S. Koizumi, T. Teraji and H. Kanda, *Diamond Rel. Mater.* **10**, 444 (2001).

[91] R. Sauer, H. Sternschulte, S. Wahl, K. Thonke and T.R. Anthony, *Phys. Rev. Lett.* **84**, 4172 (2000).

[92] A. Onodera, M. Hasegawa, K. Furuno, M. Kobayashi and Y. Nisida, *Phys. Rev. B* **44**, 12176 (1991).

[93] F.J. Himpsel, J.F. van der Veen and D.E. Eastman, *Phys. Rev. B* **22**, 1967 (1980).

[94] A.S. Barnard, S.P. Russo and I.K. Snook, *Phys. Rev. B* **69**, 235407 (2003).

[95] P.E. van Camp, V.E. Van Doren and J.T. Devreese, *Phys. Rev. B* **34**, 1314 (1986).

[96] S. Zollner, M. Cardona and S. Gopalan, *Phys. Rev. B* **45**, 3376 (1992).

[97] K.P. O'Donnell and X. Chen, *Appl. Phys. Lett.* **58**, 2924 (1991).

[98] T. Ruf, M. Cardona, C. Pickles and R. Sussmann, *Phys. Rev. B* **62**, 16578 (2000).

[99] S. Logothetidis, J. Petalas, H.M. Polatoglou and D. Fuchs, *Phys. Rev. B* **46**, 4483 (1992).

[100] J. Fontanella, R.L. Johnston, J.H. Colwell and C. Andeen, *Appl. Opt.* **16**, 2949 (1977).

[101] A. Kujii, K. Takiyama, R. Maki and T. Fujita, *J. Lumin.* **94**, 355 (2001).

[102] R. Shimano, M. Nagai, K. Horiuch and M. Kuwata-Gonokami, *Phys. Rev. Lett.* **88**, 057404 (2002).

[103] K. Thonke, R. Schielsing, N. Teofilov, H. Zacharias, R. Sauer, A.M. Zaitsev, H. Kanda and T.R. Anthony, *Diamond Rel. Mater.* **9**, 428 (2000).

[104] R. Sauer, N. Teofilov and K. Thonke, *Diamond Rel. Mater.* **13**, 691 (2004).

[105] F. Peter, *Z. Phys.* **15**, 358 (1923).

[106] W.C. Walker and J. Osantowski, *Phys. Rev.* **134**, A153 (1964).

[107] A. Mainwood, Optical constants of diamond, in *Properties and Growth of Diamond*, G. Davies (Ed.), Electronic Materials Information Service Data Reviews Series, INSPEC, London, 1994.

[108] L.S. Hounsome, R. Jones, M.J. Shaw and P.R. Briddon, *Phys. Stat. Sol. (a)*, **203**, 3088 (2006).

[109] E. Woerner, C. Wild, W. Mueller-Sebert and P. Koidl, *Diamond Rel. Mater.* **10** 557 (2001).

2 Transport Properties of Electrons and Holes in Diamond

JAN ISBERG

Division for Electricity Research, Uppsala University, Sweden

---

2.1 Introduction 29
2.2 Conductivity and carrier concentration 30
2.3 Scattering mechanisms 33
  2.3.1 Phonon scattering 34
  2.3.2 Acoustic phonon scattering 34
  2.3.3 Optical phonon scattering 35
  2.3.4 Intervalley scattering 35
  2.3.5 Ionised impurity scattering 35
  2.3.6 Neutral impurity scattering 36
  2.3.7 Scattering at dislocations 37
  2.3.8 Surfaces and grain boundaries 37
2.4 Drift velocity measurements 38
2.5 Velocity saturation 40
2.6 Space–charge limited current 41
2.7 Hall effect measurements 42
  2.7.1 Photo-Hall measurements 43
  2.7.2 Hall measurements on phosphorus-doped diamond 44
  2.7.3 Hall measurements on boron-doped diamond 44
2.8 Summary 46
References 46

2.1 INTRODUCTION

In a semiconductor, electrons in the conduction band and holes in the valence band are free to move under the influence of an applied force. It is the response of free carriers to applied forces, in particular from electric fields, which determines the electric transport properties of a material. This, for the case of diamond, is the subject of this chapter.

CVD Diamond for Electronic Devices and Sensors Edited by Ricardo S. Sussmann
© 2009 John Wiley & Sons, Ltd. ISBN: 978-0-470-06532-7

Free carriers can be supplied by several means. For example, they can be injected through a junction; generated by some form of radiation or supplied through doping, i.e. by the addition of foreign atoms that become thermally ionised. The concentration of carriers in diamond together with their motion in an externally applied electric field determines the conductivity. This is discussed in the first section. The motion of free carriers is never completely unimpeded. Carriers are constantly scattered by lattice vibrations and lattice defects. Important scattering mechanisms in diamond and their influence on carrier transport are treated in the second section. The latter half of this chapter reviews carrier drift velocity and Hall effect measurements on diamond.

2.2 CONDUCTIVITY AND CARRIER CONCENTRATION

Due to the wide band gap of diamond (5.47 eV), the intrinsic carrier concentration is very low at room temperature and consequently pure diamond is an excellent insulator. The resistivity of pure diamond can exceed 10^{16} Ω cm [1]. Extrinsic semiconductivity in diamond can be achieved through doping [see Chapter 3, ‘Point defects, impurities and doping’ by A Mainwood in this book]. With boron (B), the most thoroughly studied dopant in diamond, extrinsic p-type conduction can be observed at doping concentrations below 3 and 10^{19} atoms/cm^3. At very high boron concentrations the activation energy approaches zero and conduction becomes metallic type. A room temperature resistivity of about 10^{-3} Ω cm can be achieved for boron concentrations above 10^{21} cm^{-3}. Superconductivity in heavily boron-doped diamond was reported for the first time in 2004 [2]. For CVD diamond, boron can effectively be introduced into the diamond lattice during deposition. Extrinsic n-type conductivity in diamond can also be achieved, e.g. by doping with phosphorus (P).

Dopants in wide-band-gap semiconductors such as diamond, tend to have higher ionisation energies than in narrow-band-gap semiconductors. For example, in 4-H silicon carbide the shallowest acceptor is aluminium with ionisation energy 0.19 eV. In diamond, known dopants have even higher ionisation energies, resulting in low activation at room temperature. Boron has an ionisation energy of 0.36 eV and phosphorus has an ionisation energy of about 0.57 eV. Reports claiming that sulfur (S) or oxygen (O) constitute reasonably shallow donors remain to be substantiated at the time of writing. A boron–deuterium complex has also been reported to constitute a reasonably shallow donor, but the long-term stability of this complex is uncertain. The lack of known, genuinely shallow, donors in diamond has led some investigators to conclude that its prospects for use in electronic devices are poor. It is true that the lack of known shallow dopants restricts the capability of diamond but, on the other hand, the extreme material properties of diamond do expand the capability in other directions. Diamond is the most extreme wide-band-gap semiconductor with respect to material properties but has high dopant ionisation energies. Therefore, conventional device designs cannot automatically be expected to work well in diamond. Instead a more creative approach is required and one should develop new types of device that exploit the material advantages of diamond, rather than trying to adopt more conventional devices designs. Examples of this approach are delta-doped FETs and Schottky diodes with intrinsic layers [3, 4], see also Chapters 12 and 14 in this book. In these types of devices the carriers are supplied from a highly doped region, while the active region consists of intrinsic diamond.

To achieve a high activation in a doped semiconductor it is necessary to have a low degree of compensation. For p-doped diamond, for instance, the amount of compensating donors (shallow or deep) must be kept to a minimum. This puts strict demands on the impurity concentration of the material, especially at low doping concentrations.

At low electric fields the conductivity σ is proportional to the hole concentration p in a p-type semiconductor:

$$\sigma = q\mu_p p \tag{2.1}$$

where q is the elementary charge and μ_p is the drift mobility for holes. In a crystal with cubic symmetry, e.g. diamond, conductivity (and mobility) is always isotropic so that a scalar conductivity makes sense. If both acceptors and compensating donors are present with concentrations N_A and N_D, respectively, and with $N_A > N_D$, then in a nondegenerate semiconductor the hole concentration p can be calculated from:

$$\frac{p(p+N_D)-n_i^2}{N_A-N_D-p-n_i^2/p} = \frac{N_V}{g_a}\exp(-E_A/kT) \tag{2.2}$$

where n_i is the intrinsic carrier concentration, N_V the valence band effective density of states, g_a the spin degeneracy factor, E_A the acceptor ionisation energy, k the Boltzmann constant and T the absolute temperature. In Equation (2.2) the influence of excited impurity states has been neglected. Expressions for more complex models, including several acceptor and donor levels and excited states, can be found in, for example, Ref. [5]. The intrinsic carrier concentration n_i equals:

$$n_i = \sqrt{N_C N_V}\exp(-E_g/2kT) \tag{2.3}$$

Here E_g is the band-gap and N_C the conduction band effective density of states. For diamond the intrinsic concentration can normally be neglected for temperatures below 1000 K due to the large band-gap. N_V and N_C are given by:

$$N_V = 2\left[\frac{2\pi m_{h,dos}kT}{h^2}\right]^{3/2} \qquad N_C = 2\left[\frac{2\pi m_{e,dos}kT}{h^2}\right]^{3/2} \tag{2.4}$$

where h is Planck's constant and $m_{h,dos}$ ($m_{e,dos}$) the density of states effective hole (electron) mass.

Figure 2.1 shows the hole concentration in boron-doped diamond with a deep compensating donor (e.g. nitrogen) for a particular case $N_A = 3 \times 10^{16}$ cm^{-3}, $N_D = 1 \times 10^{14}$ cm^{-3}. Note that the acceptor is completely ionised only at very high temperatures, above 1000 K. The carrier concentration exhibits four qualitatively different behaviours in different temperature intervals.

In the figure, behaviour (i) applies very low temperatures when $p \ll N_D$, $p \ll N_A - N_D$ and $p \gg n_i$, the acceptor is incompletely ionised and the compensating donor is only partially ionised and Equation (2.2) reduces to:

$$p = \frac{N_A - N_D}{N_D}\cdot\frac{N_V}{g_a}\exp\left(\frac{-E_A}{kT}\right) \tag{2.5}$$

At somewhat higher temperatures (ii), when $N_A \gg p \gg N_D$ and $p \gg n_i$, the acceptor is still incompletely ionised but the donor is fully ionised. In this case Equation (2.2) yields:

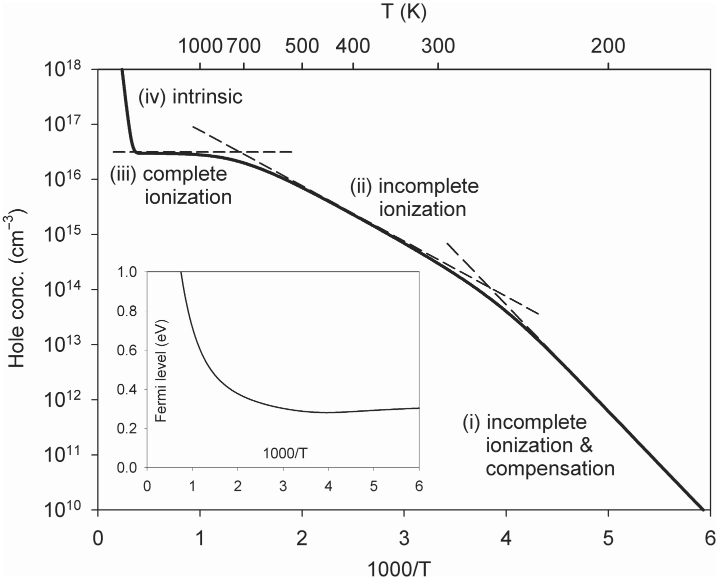

Figure 2.1 Hole concentration in diamond for the case $N_A = 3 \times 10^{16}$ cm^{-3}, $N_D = 10^{14}$ cm^{-3} calculated from Equation (2.2), with $E_a = 0.36$ eV, $g_a = 6$, $m_{e,dos} = 0.56m_e$, $m_{h,dos} = 0.8m_e$. Inset shows the variation of the Fermi level with inverse temperature

$$p = \sqrt{(N_A - N_D)\frac{N_V}{g_a}} \exp\left(\frac{-E_A}{2kT}\right) \tag{2.6}$$

In the case of (iii), for still higher temperatures, where $E_A \gg kT$ and $p \gg n_i$, complete ionisation of the acceptor occurs. In this region the carrier concentration is independent of the temperature:

$$p = N_A - N_D \tag{2.7}$$

If the temperature is further increased (iv), the intrinsic carrier concentration will dominate so that p $\approx n_i$ where n_i is given by Equation (2.3).

The degree of boron activation at 300 K is plotted in Figure 2.2, which shows the hole concentration for different acceptor and compensating donor concentrations. However, if the boron concentration is increased above 10^{19} cm^{-3} and the insulator–metal transition is approached, the activation increases rapidly almost to completion.

The valence band in common semiconductors consists of a light hole branch and a heavy hole branch, doubly degenerate at the Brillouin zone centre, and a split-off branch. This split-off branch is separated from the other branches by a certain energy Δ at the Brillouin zone centre, due to spin–orbit coupling. In most semiconductors the spin–orbit coupling is relatively strong and Δ exceeds kT for all temperatures of interest, and consequently the split-off valence band is not populated by holes. For example, in Si this splitting is 44 meV and in GaAs even higher at 340 meV.

The case is very different in diamond as the spin–orbit coupling is uncommonly weak. Because of this the split-off band can also play a role in hole transport in diamond. The

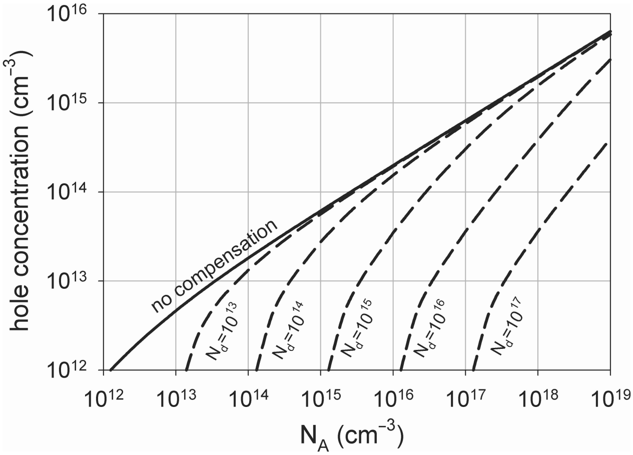

Figure 2.2 Hole concentration against dopant concentration (N_A) of boron doped diamond at 300 K for different concentrations of compensating donors (N_D)

experimental value $\Delta = 6$ meV was reported [6], but *ab initio* band structure calculations suggest a different value for Δ of 13 meV [7]. Considering that the splitting is weak compared with the ionisation energy, the spin degeneracy factor g_a should be set to 4 for low temperatures and to 6 for high temperatures, as suggested by Collins [8]. Fontaine [9] assumes a Boltzmann distribution of carriers, and suggests using the following expression:

$$g_a = 4 + 2\exp(-\Delta/kT) \tag{2.8}$$

2.3 SCATTERING MECHANISMS

As electrons and holes travel through a semiconductor, they are frequently scattered by collisions with, for example, impurity atoms, crystal defects, phonons or other carriers. These collisions tend to counteract the increase in momentum and energy that carriers attain in an electric field. Scattering therefore acts as a kind of friction that rapidly relaxes the increase of momentum and energy and limits the mobility of the carriers.

In the relaxation time approximation, the relaxation of carrier momentum is described by the momentum relaxation time τ_m, which can be thought of as the average time between two collisions. τ_m generally depends on the carrier momentum. If several independent scattering mechanisms are involved the total relaxation time can be written:

$$\tau_m^{-1} = \sum_i \tau_{m,i}^{-1} \tag{2.9}$$

where $\tau_{m,i}$ is the momentum relaxation time for the individual processes. The low-field drift mobility μ is then given by:

$$\mu = \frac{q}{m_c}\langle\tau_m\rangle \tag{2.10}$$

where m_c is the conduction effective mass and the angle brackets denote the average over the momentum distribution of the carriers. However, in many situations the exact carrier momentum distribution may not be known. Therefore, a proposition known as Mathiessen's rule is often used to estimate the total mobility when several independent scattering mechanisms are involved. Mathiessen's rule states:

$$\mu^{-1} = \sum_i \mu_i^{-1} \tag{2.11}$$

where μ_i is the mobility for a scattering mechanisms considered separately. However, it should be pointed out that this rule only holds if the individual scattering processes have the same momentum dependence (since, in general, $\langle \tau_m \rangle^{-1} \neq \langle \tau_m^{-1} \rangle$). This is rarely the case. Nevertheless, Mathiessen's rule is often useful for obtaining a rough estimate of the total mobility. Under quite general assumptions, even outside the relaxation time approximation, it can be shown that Mathiessen's rule holds as an inequality:

$$\mu^{-1} \geq \sum_i \mu_i^{-1} \tag{2.12}$$

2.3.1 Phonon scattering

Scattering by lattice waves includes the absorption or emission of either acoustic or optical phonons. Since the phonon density in a solid normally increases with temperature, the time between carrier–phonon collisions decreases with temperature. Consequently, the mobility can also be expected to drop with increasing temperature whenever phonon scattering is the dominant scattering mechanism. Since the wavelengths of thermalised carriers in a solid are many times larger than the lattice spacing, carriers only interact with phonons of relatively long wavelength. Optical phonons with long wavelengths carry an energy $\hbar\omega_{LO} = 163$ meV, which is exchanged with the carrier, and therefore the scattering is inelastic. In contrast, long wavelength acoustic phonons carry little energy and cause predominantly elastic scattering events.

2.3.2 Acoustic phonon scattering

In a nonpolar semiconductor, like diamond, the interaction between carriers and acoustic phonons can be considered as arising from the periodic variations in lattice spacing induced by long wavelength longitudinal phonons. This variation in lattice spacing gives rise to a shift in the band-gap, which in turn leads to carrier scattering. Assuming parabolic bands, this acoustic deformation potential (ADP) model gives rise to a carrier mobility that drops as $T^{-3/2}$ with increasing temperature. The mobility μ_{ADP} is given by:

$$\mu_{ADP} = \frac{2\sqrt{2\pi} q \hbar^4 c_l}{3 D_A^2 (m_{dos})^{3/2} m_c (kT)^{3/2}} \tag{2.13}$$

where c_l is the bulk longitudinal elastic constant, m_c the conductivity effective mass and D_A the band edge energy shift per unit strain. In reality the deviations from this simple model can be quite large. For example, in high purity silicon, phonon scattering leads to a hole mobility $\mu_h \sim T^{-2.2}$, and an electron mobility $\mu_e \sim T^{-2.4}$, instead of the $\mu \sim T^{-1.5}$ behaviour expected from Equation (2.13). Several other scattering mechanisms (including ionised impurity scattering, if the ionised impurity concentration varies with temperature) also cause mobility to decrease with increasing temperature, as seen below. Therefore, observation of a $\mu \sim T^{-1.5}$ dependency in drift mobility data is not sufficient evidence that phonon scattering is the dominating scattering mechanism.

2.3.3 Optical phonon scattering

For low-energy carriers only nonpolar optical phonon *absorption* is energetically allowed. This is in contradistinction to hot carriers accelerated by high electric fields, which can also emit optical phonons. This is a highly probable transition that limits carrier velocities at high fields, and leads to velocity saturation. For low-energy carriers the scattering rate is roughly proportional to the concentration of optical phonons, which increases exponentially for temperatures below approximately 30 % of the Debye temperature Θ. In diamond, the Debye temperature is very high, about 2240 K. Therefore, with increasing temperature, an exponential drop in mobility is expected for $T < 600$ K, if optical phonons are dominating the scattering. The resulting mobility can be estimated by using a deformation potential formalism for longitudinal phonons in analogy with the acoustic deformation potential, yielding:

$$\mu_{NPO} = \frac{4\sqrt{2\pi}q\rho\hbar^2\sqrt{k\Theta}}{3D_o^2(m_{dos})^{3/2}m_c}\phi(T) \tag{2.14}$$

where ρ is the material density, D_o the optical deformation potential and $\phi(T)$ a function that has a nearly exponential decrease for temperatures well below the Debye temperature and approaches unity for T above Θ.

2.3.4 Intervalley scattering

Indirect band-gap semiconductors, like diamond, have several conduction band minima (valleys) at symmetrically equivalent directions in the Brillouin zone. In diamond the minima lie along the six [100] directions at 73 % of the distance to the zone boundary. Intervalley scattering, i.e. scattering of electrons between two valleys, involves a large change in momentum and therefore requires phonons with wave vectors near the zone boundary. Such phonons, either acoustic or optical, have energy below the longitudinal optical phonon energy $\hbar\omega_{LO}$. Intervalley scattering has a similar influence on the electron scattering rate to that of optical phonon scattering. However, this scattering mechanism requires less energetic phonons and it will therefore dominate over optical phonon scattering at lower temperatures.

2.3.5 Ionised impurity scattering

When ionised impurities are present in a solid, holes and electrons are scattered due to their long range coulomb interaction with the charged defect. For this type of scattering slow carriers are more strongly scattered than fast carriers, and consequently the scattering cross-section decreases with increasing thermal carrier velocities. The scattering rate also depends on the concentration of free carriers, as these tend to screen the charge in the impurities. Obviously the scattering rate also depends on the concentration of ionised impurities. If the ionised impurity concentration is independent of the temperature, e.g. for a shallow completely ionised dopant, the mobility due to ionised impurity scattering typically increases as $\mu \sim T^{3/2}$. This behaviour is often taken as an indication that ionised impurity scattering is the dominant scattering mechanism. For diamond, with its deep impurity levels, a constant ionised impurity concentration is not easily achieved and this can give rise to an entirely different temperature dependence. The classical expression for the momentum relaxation time due to ionised impurity scattering is the Brooks–Herring [10] expression:

$$\tau_m = \frac{16\sqrt{2m_c}\pi\varepsilon^2}{Z^2q^4N_I}(\ln(1+b) - b/(1+b))E^{3/2}, \quad \text{with } b = 8m_cL_D^2E/\hbar^2 \tag{2.15}$$

Here ε is the dielectric constant for the medium, N_I the concentration of the ionised impurity, Z its degree of ionisation, L_D the Debye length and E the energy of the carrier. By averaging over carrier momentum, as in Equation (2.10), assuming parabolic bands, and by neglecting the weak dependence on energy through b, the mobility can be written:

$$\mu_{BH} = \frac{128\sqrt{2\pi}\varepsilon^2(kT)^{3/2}}{Z^2q^3\sqrt{m_c}N_I(\ln(1+b') - b'/(1+b'))}, \quad \text{with } b' = 24m_cL_D^2kT/\hbar^2 \tag{2.16}$$

In the absence of screening, for very low carrier densities, the Debye length diverges and a similar expression due to Conwell and Weisskopf [11] can be used instead.

For the case of, for example, boron acceptors in the presence of compensating donors, the ionised impurity concentration N_I in Equation (2.16) equals $p + 2N_D$. Since p is strongly temperature dependent (Equation 2.2), so is N_I. The mobility therefore deviates strongly from the $\mu \sim T^{3/2}$ behaviour, with the exception of very high temperatures when the boron is fully ionised (so that p is independent of temperature) and for very low temperatures (so that p is small compared to N_D). It has been suggested [12, 13] that this is the cause of the rapid decrease in mobility with increasing temperature observed in boron-doped diamond samples by several groups [1, 14–17] for temperatures in the interval 350–500 K, rather than the more obvious candidates, optical phonon scattering or intervalley scattering.

2.3.6 Neutral impurity scattering

Neutral impurities have a scattering cross-section that is roughly the size of the impurity atom, since there is no net charge. Typically, the scattering cross-sections for neutral impurities are several orders of magnitude smaller than for charged impurities. However, if the density of neutral impurities is several orders of magnitude higher than the ionised impurity density, neutral density scattering can still be a dominating mechanism. For example, in diamond doped with boron to high concentrations (but below the Mott transition), say 10^{19} boron atoms per cubic centimetre, less than one in a thousand dopant atoms are ionised at room temperature. In this example the vast majority of boron impurities are therefore neutral and will contribute substantially to carrier scattering. A simple expression for the mobility resulting from neutral impurity scattering was given by Erginsoy [18]:

$$\mu_{ERG} = \frac{q^3 m_{dos}}{8\pi^3 \hbar^3 \varepsilon N^0} \tag{2.17}$$

where N^0 is the neutral impurity concentration. Thus (at least in the Erginsoy approximation) there is no dependence of the mobility on temperature, except for any dependence that is implicit in the neutral impurity density. Nearly temperature independent Hall mobilities over the temperature interval 200–300 K have been observed in some boron-doped diamond samples [19, 20]. It is however not apparent at this time whether this observation can be attributed to neutral impurity scattering.

2.3.7 Scattering at dislocations

Dislocations can have a major influence on carrier transport in diamond. Deep states are localised at the core of the dislocation and less sharply localised strain induced states are also present in the forbidden band [21]. Depending on the position of the Fermi level, these states may attract electrons or holes resulting in a charged dislocation. If present, free charges screen the charge trapped at the dislocation, thereby containing the induced electric field to a cylinder with a radius roughly equal to the Debye length. In contradistinction to, for instance, phonon or impurity scattering, aligned dislocations can create anisotropy in the low-field carrier transport. The mobility measured perpendicularly to an array of aligned dislocations is typically lower than when measured in parallel with the array. CVD grown polycrystalline diamond generally exhibits very high dislocation densities, above 10^{11} cm^{-2}, while dislocation densities in natural IIa diamond often exceed 10^7 cm^{-2}. In homoepitaxial single crystal CVD diamond, dislocations tend to appear in bundles emanating from the substrate. Material with average dislocation bundle densities of less than 10^2 cm^{-2} and with approximately 100 dislocations per bundle can now be produced [22]. Such dislocation bundles are roughly aligned with the direction of growth, leading to anisotropy in the observed carrier mobility.

2.3.8 Surfaces and grain boundaries

If conduction takes place in the vicinity of an external surface, e.g. in narrow channel devices such as MOSFETs, the surface can have a strong influence on the carrier transport. External surfaces affect carrier transport by surface scattering. They also contain recombination centres and traps. In polycrystalline and nanocrystalline material a strong reduction in carrier mobility due to the presence of grain boundaries is generally observed. Grain boundaries invariably contain a high density of lattice defects such as defect clusters and dislocations. Dangling and sp^2 bonds can also have a strong influence on the transport properties. Charging of the grain boundaries can also occur due to trapping of carriers at the interface. Screening of the interface charge by free carriers creates a space-charge triple layer, producing a potential barrier between the different grains. For these reasons the effective mobility in polycrystalline diamond is lower than for single crystal diamond, and fine-grained material generally has a lower mobility than coarse-grained material.

2.4 DRIFT VELOCITY MEASUREMENTS

The drift velocity of carriers can be measured directly by the time-of-flight (ToF) technique. This is based on a measurement of the time that charge carriers take to cross a sample of known thickness d. The basic set-up is shown in Figure 2.3. Electron-hole pairs are created in the sample by a suitable source of radiation. Ideally, the electron-hole pairs are created by a short pulse near one surface at a range that is much shorter than d. For example, alpha particles are commonly used for excitation. Alternatively, pulsed electron beams or strongly absorbed laser pulses can be used. These sources have the advantage that an external trigger is readily available. When a bias is applied across the sample, carriers of one type will drift towards the bottom electrode where they are collected. Carriers of the other type are collected at the top electrode after drifting a distance much shorter than d. In the simplest case (neglecting trapping, carrier recombination and space charge in the sample) carriers of the first type drift in a uniform electric field with an average velocity v and spend a time $\tau = d/v$ traversing the sample. In this case a constant current $I = Qv/d$ can be measured at the electrodes during the time of transit. Here Q is the total charge of each carrier type. Thus by measuring the duration of the current pulse we find the drift velocity at the applied bias voltage. The time required for electrons (holes) to thermalise in the conduction (valence) band is less than 1 ps. This holds even for highly energetic excitation sources [23]. This time is normally much shorter than the transit time. By a careful analysis of the transient current ToF experiments may, in addition to measuring carrier drift velocities, also yield useful information on trapping, recombination and electric field distribution in a sample [see e.g. 24–27].

Depending on the magnitude of the total charge Q (of either carrier type) generated by the irradiation, the current transient phenomena can be classified into three types:

(i) The space charge free (SCF) transient for which Q is much smaller than is required to alter the electric field in the solid appreciably. That is $Q \ll CV$, where C is the sample capacitance and V the applied bias voltage.
(ii) The space charge limited (SCL) transient for which Q is large enough to create a charge reservoir near the irradiated electrode, $Q \gg CV$.
(iii) The space charge perturbed (SCP) transient for which Q is intermediate between the SCF and SCL cases.

The space charge limited case in the presence of trapping was first treated by Many and Rakavy [28]. Several models of transient currents can be found in [29].

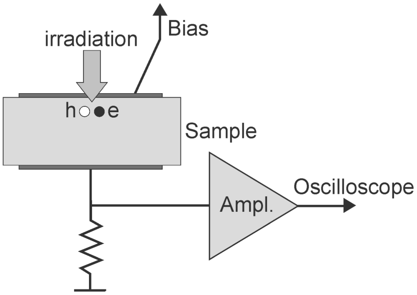

Figure 2.3 Basic set-up for time-of-flight drift velocity measurements

The time-of-flight method has been used to measure drift velocities in insulators and strongly depleted semiconductors. Early drift velocity measurements using β-particle irradiation were performed by Yamakawa in 1951 on silver bromide (AgBr) [30] and by Brown in 1955 on silver chloride crystals (AgCl) [31]. Pulsed electron beams were used by Spear in 1957 for ToF measurements on amorphous selenium [32] and by Canali *et al.* in 1971. They used a 40-keV pulsed electron beam to measure drift mobilities for electrons and holes in silicon [33]. Measurements on several III–V and II–VI semiconductors, using the same excitation source are described by Alberigi Quaranta *et al.* [34]. Tove and coworkers described the use of a pulsed laser as the excitation source used for ToF measurements on silicon in the SCF regime in 1970 [35], and in the SCL regime in 1973 [36].

Nava *et al.* [37] and Reggiani *et al.* [38, 39] applied the ToF technique to measure the drift mobility in several samples of natural diamond. They measured a low-field electron drift mobility of 2500 cm^2/Vs for electrons and 2100 ± 50 cm^2/Vs for holes at 300 K. The carriers were generated using a pulsed electron gun. For temperatures below 400 K at $\mu \sim T^{-3/2}$ dependence was observed for both carrier types. This was interpreted as indicative of acoustic phonon scattering. A steeper dependence observed at higher temperatures was attributed to intervalley scattering for electrons and to optical phonon scattering for holes. By measuring drift velocity at high fields they also found, by extrapolation, an electron saturation velocity of $1.5 \pm 0.1 \times 10^7$ cm/s and a hole saturation velocity of $1.1 \pm 0.1 \times 10^7$ cm/s for temperatures below 300 K in both the $\langle 100 \rangle$ and the $\langle 110 \rangle$ directions.

Measurements on homoepitaxially grown layers of single-crystal CVD diamond have subsequently yielded higher values for both the hole and the electron drift mobilities. ToF measurements by Isberg *et al.* in the SCL regime, using pulsed UV laser excitation on four samples, showed mobilities between 3500 to 4500 cm^2/Vs for electrons and 2600 to 3800 cm^2/Vs for holes. Carrier lifetimes of several microseconds were also observed [40, 41]. Measurements for injected carrier densities in the SCF regime have yielded lower values, in particular for the electron mobility. For holes, Isberg *et al.* [42] reported SCF–ToF measurements on single-crystal CVD diamond with a room temperature mobility $\mu_h = 3400 \pm 400$ cm^2/Vs. Over the temperature interval 150–350 K a $\mu_h \sim T^{-1.55}$ dependence was observed. Above 350 K, mobility decreased rapidly with increasing temperature, $\mu_h \sim T^{-3.4}$ (see Figure 2.4). Substantial variations in mobility between samples of different material quality (i.e. impurity concentration and dislocation density) have been observed by the present author as well as by other groups. Pernegger *et al.* measured low-field drift mobilities $\mu_e = 1714$ cm^2/Vs and $\mu_h = 2064$ cm^2/Vs for electrons and holes respectively, using α-particle excitation [27] in 2005. Higher mobilities were measured by Pomorski *et al.* [43, 44] also using α-particles. They found a low-field electron mobility with values in the range $\mu_e = 1300$–3100 cm^2/Vs and hole mobilities with less variation between samples, i.e. $\mu_h = 2330$–2400 cm^2/Vs. After irradiation of the samples with 26 MeV protons at a dose of 10^{16} cm^{-2}, the current transit could no longer be observed. By annealing at 1000 °C the signal improved and it could be almost completely restored by priming with ^{90}Sr-electrons. Irradiation with a dose of 10^{13} cm^{-2} had little effect on the drift velocities, indicating the creation of mainly neutral defects. In 2007, Deferme *et al.* [45] reported samples with $\mu_e = 2100$ cm^2/Vs and $\mu_h = 2250$ cm^2/Vs, and Tranchant *et al.* [46] found $\mu_e = 2500$ cm^2/Vs and $\mu_h = 2050$ cm^2/Vs. The latter also found a

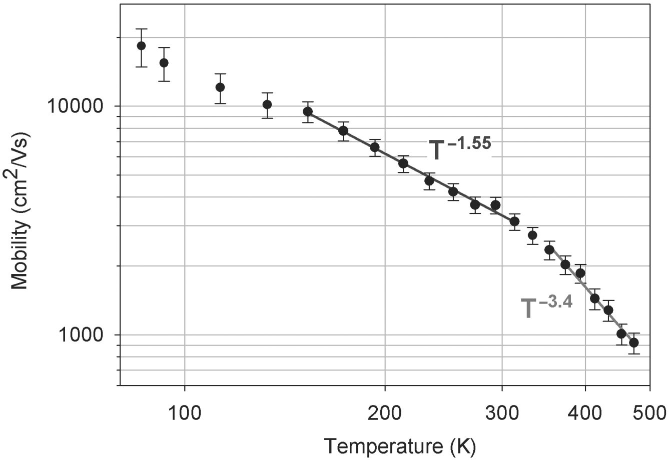

Figure 2.4 Hole drift mobility in single-crystal CVD diamond, measured by SCF-ToF using pulsed 213 nm UV laser excitation [42]

$\mu_e \sim T^{-1.4}$, $\mu_h \sim T^{-1.5}$ temperature dependence below 350 K and a $\mu_e \sim T^{-3.2}$, $\mu_h \sim T^{-2.8}$ dependence above 350 K.

2.5 VELOCITY SATURATION

At high electric fields carriers rapidly lose energy to the crystal lattice by the emission of optical phonons. Together with other scattering mechanisms this effect limits the drift velocity of carriers to some maximum velocity (the saturation velocity v_s) that cannot be exceeded. v_s may be different for electrons and holes. The saturation velocity is an important factor in limiting the performance of high-frequency devices, such as field-effect transistors. High v_s is therefore desirable in this type of device application. The saturation velocity, taking only optical phonon emission into account, is given by:

$$v_s = \sqrt{\frac{8E_{opt}}{3\pi m_{dos}}\tanh(E_{opt}/2kT)} \tag{2.18}$$

where E_{opt} is the energy of zero momentum optical phonons. High optical phonon energy and low effective mass therefore leads to a high saturated carrier velocity. Diamond has the highest optical phonon energy, $E_{opt} = 163$ meV, of any semiconductor because of strong covalent bonds and low atomic mass. For diamond the saturation velocity, from Equation (2.18), equals:

$$v_s = (m_{dos}/m_e)^{-1/2} \cdot 1.56 \cdot 10^7 \text{cm/s} \tag{2.19}$$

where m_e is the electron mass. A more detailed analysis was performed by Ferry [47], who solved the Boltzmann equation including all the scattering mechanisms discussed earlier and calculated $v_{s,e} = 2.3 \times 10^7$ cm/s for electrons. Osman [48] found a lower value by Monte-Carlo simulations: $v_{s,e} = 1.5 \times 10^7$ cm/s.

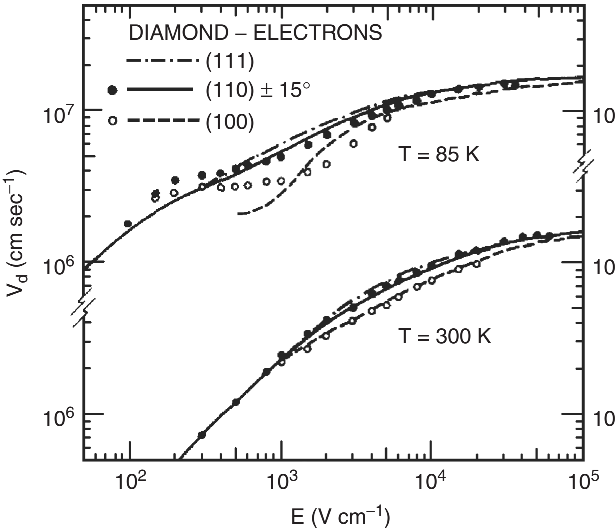

Figure 2.5 Electron drift velocity in natural diamond showing velocity saturation at high electric fields [37]. Closed and open circles refer to experiments performed along ⟨110⟩ and ⟨100⟩ crystallographic directions, respectively. The solid and dashed curves are according to theoretical calculations. Reprinted from solid State Communication, Electron effective masses and lattice scattering in natural diamond by F. Nava, C. Canali, C. Jacoboni, L. Reggiani and S.F. Koslov, 33,4, by permission of Elsevier, copyright 1980

Experimentally determined values of v_s also exhibit some variation. Nava *et al.* [37] and Reggiani *et al.* [39] performed drift velocity measurements on natural diamond for fields up to 6×10^4 V/cm, enough to reach velocity saturation. They found $v_{s,e} = (1.5 \pm 0.1) \times 10^7$, $v_{s,h} = (1.1 \pm 0.1) \times 10^7$ cm/s in both the ⟨100⟩ and ⟨110⟩ directions and for all temperatures between 85 and 300 K. In CVD diamond, Pernegger *et al.* [27] found saturation velocities of $v_{s,e} = 0.96 \times 10^7$ cm/s and $v_{s,h} = 1.41 \times 10^7$ cm/s, and Pomorski *et al.* [43, 44] reported $v_{s,e} = 1.9 \times 10^7$ cm/s and $v_{s,h} = 1.4 \times 10^7$ cm/s. Both these groups assumed a velocity field dependence of the form:

$$v(E) = \frac{\mu E}{1 + \mu E / v_s} \tag{2.20}$$

and used this to fit to the drift velocity data in order to find v_s. In [27] the drift velocity was measured for fields up to 1.5×10^4 V/cm, and in [43, 44] up to 3×10^4 V/cm.

2.6 SPACE–CHARGE LIMITED CURRENT

When carriers are injected from a metal contact or a highly doped region into a low-doped or undoped region in a semiconductor, the charge density can become high enough to change the electric field in this region appreciably. The presence of this space–charge affects the electric field distribution so as to oppose further increase of the current. In this situation the current is said to be space–charge limited. Space–charge limited current (SCLC) measurements can be used to probe the energetic distribution of traps in the band gap. If the current is space–charge limited, it can be shown [49], assuming field-independent mobility and neglecting diffusion, that the current–voltage relationship obeys a scaling law of the form:

$$\frac{j}{d} = f\left(\frac{V}{d^2}\right) \tag{2.21}$$

where j is the current density, V the bias voltage and f some arbitrary function. Observation of a current–voltage relationship that obeys Equation (2.21) for several different values of the film thickness d, gives a strong indication that the current is indeed space charge limited.

In diamond, SCLC measurements have been used to study density and distribution of traps in polycrystalline CVD diamond by several groups [50–52]. These groups all found an exponential distribution of traps near the valence band edge. For theory on spectroscopy of bulk traps using SCLC, see [53].

If the concentration of traps is low enough, SCLC predominantly due to free carriers can be observed. In this case the current obeys the Mott–Gurney law [54]:

$$j = \frac{9}{8}\varepsilon\mu\frac{V^2}{d^3} \tag{2.22}$$

Note that Equation (2.22) obeys the scaling law Equation (2.21) with $f(x) = 9/8\varepsilon\mu x^2$. This situation is similar to the SCLC in thermionic vacuum diodes, which, due to the ballistic transport of electrons in vacuum, instead obey the analogous Child–Langmuir relation. SCLC due to free holes has been observed in high purity CVD diamond films [3, 40, 55].

2.7 HALL EFFECT MEASUREMENTS

The Hall effect in metals was first reported in 1879 [56]. For extrinsic semiconductors, the Hall effect has become one of the most important characterisation techniques. This is mainly due to its ability to determine carrier type, carrier concentration and, in combination with a resistivity measurement, also carrier mobility. Although special samples are required, such as Hall bars or samples with the van der Pauw contact geometry, these are usually not difficult to prepare and the measurements only make moderate demands on experimental equipment. In intrinsic semiconductors, carriers can be generated throughout a sample by photoexcitation, so-called photo-Hall measurements. Because of the presence of both holes and electrons, the interpretation of data is more complicated in this case, and accumulation of space charge can also cause problems.

The Hall coefficient R_H is determined experimentally as:

$$R_H = \frac{dV_H}{BI} \tag{2.23}$$

where V_H is the Hall voltage, I the current through the sample, B the magnetic field and d the thickness of the sample. For extrinsic p-type material the hole carrier concentration p is given by:

$$p = \frac{r}{qR_H} \tag{2.24}$$

Table 2.1 Values of the Hall scattering factor r for different scattering mechanisms

Scattering mechanism	s	r
Neutral impurities	0	1
Ionised impurities	−3/2	1.93
Acoustic phonons	1/2	1.18

where the Hall scattering factor r depends on the details of the scattering process that limits drift mobility. Since the presence of the magnetic field tends to perturb carrier motion, r also depends on B but approaches unity for very strong magnetic fields when $\mu B \gg 1$. For weak magnetic fields ($\mu B \ll 1$) r may differ appreciably from unity. To obtain an accurate value for p it is obviously necessary to know r. Often, in presenting Hall data, r is assumed to equal unity. The absolute value of the Hall coefficient multiplied by the sample conductivity σ is known as the Hall mobility, μ_H, which is also equal to r multiplied by the drift mobility μ:

$$\mu_H \equiv |R_H \sigma| = r\mu \tag{2.25}$$

Thus, if the drift mobility is known independently, e.g. from time-of-flight measurements, the scattering factor can be calculated as the ratio of Hall and drift mobilities. Alternatively the Hall scattering factor can be inferred by comparing Hall measurements for low and high (where $r \approx 1$) magnetic fields. This may require a magnetic field of 10 T or more, which is not easily attained.

By assuming simple power law dependencies of the relaxation time on energy $\tau(E) \sim E^{-s}$ for the scattering mechanism, the relaxation time approximation gives the values of r shown in Table 2.1 (for the derivation see, for example, Ref. [57]).

However, these values, which have the merit of simplicity, must be adopted with a certain care. For example in the Brooks–Herring mobility expression for ionised impurity scattering Equation (2.16), the screening factor multiplies the power law term. Thus, the overall energy dependence is no longer of the power law form. This modifies r quite significantly [58]. Also, nonparabolicity of the bands and deviations from the relaxation time approximations also lead to deviations. Reggiani *et al.* [59] report measurements on natural diamond that indicate that the Hall scattering factor for phonon scattering is less than unity for all temperatures between 100 and 1000 K and that $r = 0.6$–0.8 at 300 K. This was also supported by pseudo-potential band-structure calculations. These data therefore imply that for holes in pure diamond, the Hall mobility is substantially less than the drift mobility.

2.7.1 Photo-Hall measurements

Photo-Hall mobility measurements of carrier mobility in natural diamond were first reported by Redfield in 1954 [60]. He found that both the electron and hole mobilities varied as $\mu \sim T^{-3/2}$, which he notes is consistent with acoustic phonon scattering. Redfield measured an electronic mobility of 1800 cm^2/Vs and a hole mobility of 1200 cm^2/Vs at 300 K. Denham *et al.* reported a hole mobility of 2800 cm^2/Vs in natural

IIa diamond at 290 K [61] but also states that it is difficult to estimate the reliability of this result due to the likely inhomogeneity in the distribution of donors. Remes *et al.* [62] used photo-Hall to measure mobility in P-, N- and B-doped CVD diamond. They found an enhanced mobility at low lattice temperatures when carriers are photoexcited, and proposed that this effect is due to the increase of the average kinetic energy of photoexcited carriers as enhanced kinetic energy of the carriers can effectively reduce the ionised impurity scattering rates.

2.7.2 Hall measurements on phosphorus-doped diamond

Phosphorus is a relatively deep donor in diamond with an activation energy of $E_a = 0.57$ eV [63]. It was first successfully incorporated during epitaxy on $\langle 111 \rangle$ substrates by Koizumi *et al.* in 1996 [64]. They confirmed n-type conduction using Hall measurements and found a quite low mobility, 23 cm^2/Vs at 500 K, in their films. Subsequently the crystalline quality of P-doped films has improved. The highest room temperature mobility in P-doped films reported until now is 660 cm^2/Vs, measured in a sample with a phosphorus concentration of 6.8×10^{16} cm^{-3} and a compensation ratio of 13 %. In the temperature interval 300–430 K, mobility varied as $\mu \sim T^{-1.4}$, and in the interval 450–873 K a steeper dependence $\mu \sim T^{-2.6}$ was reported. At higher P concentration, 5×10^{17} cm^{-3}, room temperature mobility decreased to 410 cm^2/Vs [63]. Pernot *et al.* reported [65] fits of Hall mobility measurements in the range 293–873 K to theoretical expressions for neutral impurity, ionised impurity, acoustic phonon and intervalley scattering, using Mathiessen's rule.

2.7.3 Hall measurements on boron-doped diamond

Most authors agree that the ionisation energy for boron acceptors in diamond is $E_a =$ 0.36–0.37 eV. For example Tsukioka and Okushi [20] found, for samples with a low or medium doping level, $E_a = 0.365$ eV. They also measured the temperature dependence of the Hall mobility in the temperature range 140 to 870 K for nine boron-doped homoepitaxial CVD diamond films. Fitting expressions for the different scattering rates to the mobility data, yielded an optical deformation potential D_0 of $(1.2 \pm 0.2) \times 10^{12}$ eV/m.

High Hall mobilities in lightly boron-doped CVD diamond have been reported by several groups. Fox *et al.* in 1995 reported a RT Hall hole mobility of 1370 cm^2/Vs and a hole concentration of 10^{14} cm^{-3} in a sample with a boron concentration of 5.9×10^{16} cm^{-3} and a compensating donor concentration of 2.9×10^{15} cm^{-3} [66]. They also reported several samples with mobilities larger than 1000 cm^2/Vs for samples with boron concentrations up to 10^{18} cm^{-3}. Hatta *et al.* reported in 1999 [19] a sample with a RT mobility of 1600 cm^2/Vs at a boron concentration of 7×10^{16} cm^{-3} and a compensation ratio of 6 %. Teraji *et al.* [14] report a Hall mobility of 1620 cm^2/Vs at 290 K and 2750 cm^2/Vs at 215 K. The boron concentration was 6.4×10^{16} cm^{-3} and the compensation ratio 1.1 %. The hole concentration was measured as 3.5×10^{14} cm^{-3} at 290 K. The variation of the mobility in this sample decreased with T as $\mu \sim T^{-1.3}$ to $\text{T}^{-1.6}$ for temperatures below 270 K. Above this temperature the mobility decreased very rapidly, i.e. $\mu \sim T^{-4.0}$ to $T^{-4.5}$. The former behaviour was attributed to acoustic phonon scattering, while the origin of the latter rapid decrease with temperature remains unclear. The highest RT hole

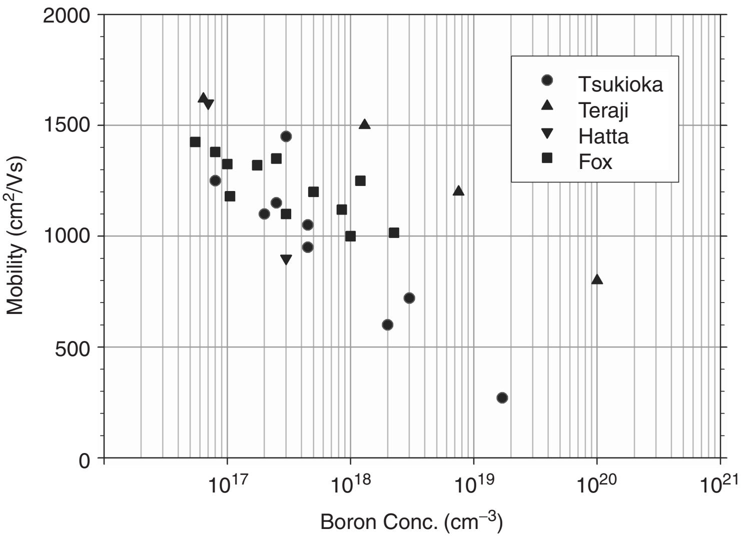

Figure 2.6 Hall mobility at room temperature against dopant concentration in boron-doped, single-crystal, CVD diamond. The data are from Refs [14, 19, 20, 66]

mobility reported to date in boron-doped homoepitaxial CVD films is 1840 cm^2/Vs [67] at a hole concentration of 2×10^{14} cm^{-3}. At 170 K the mobility was measured to 3370 cm^2/Vs. The compensation ratio in this film was about 0.4 %. Figure 2.6 shows several recently reported Hall mobilities as a function of the boron concentration.

At high impurity concentrations, when the average acceptor (or donor) separation is comparable to the Bohr radius of the ground state, the dopant levels form a band and conduction in this band occurs together with the normal conduction band transport. If the density of impurities is increased to a level where delocalisation occurs at the Fermi level, metallic conduction is observed (Figure 2.7). In boron-doped diamond, this Mott transition occurs at an acceptor density of about 3×10^{20} atoms cm^{-3}. Metallic conduction in boron-doped diamond is associated with relatively low hole mobility. For example, Tavares *et al.* [68] observed a temperature independent hole concentration $p = 10^{21}$ cm^{-3} in the temperature range 300–900 K and a temperature independent mobility of 1 cm^2/Vs in a highly boron-doped sample. Borst and Weis [1] found an almost constant hole mobility of 3–4 cm^2/Vs over the interval 180–950 K in a sample with a B concentration of 3×10^{20} cm^{-3} and a carrier concentration also equal to 3×10^{20} cm^{-3}.

At somewhat lower impurity densities, impurity levels are localised and conduction can occur by tunnelling. This hopping conduction is often observed in Hall data on boron-doped diamond. At room temperature, hopping dominates in the concentration range $3 \times 10^{19} - 3 \times 10^{20}$ atoms cm^{-3}, but at low temperatures it can be observed at much lower doping concentrations. When a sample is cooled, the Hall coefficient R_H increases as the carrier concentration drops, but then goes through a maximum and then decreases as hopping conduction starts to dominate. When this occurs, the standard analysis of the Hall factor in terms of conduction band transport breaks down and models including the hopping transport must be used for the interpretation. Examples of this behaviour in Hall data can be seen in Borst and Weis [1] or Tsukioka and Okushi [20], where a contribution of hopping conduction in the low temperature range is observed.

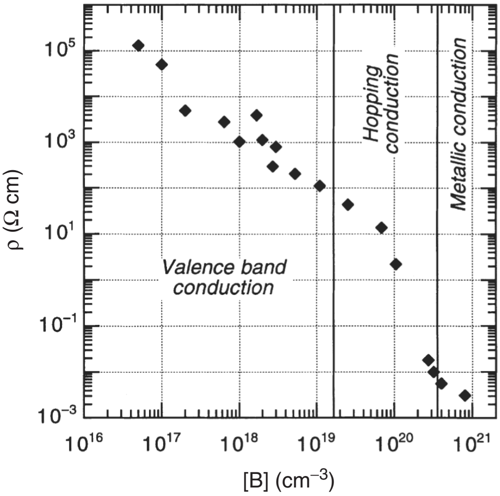

Figure 2.7 Room-temperature resistivity of homoepitaxial boron-doped films [69]. With increasing dopant concentration, conduction shifts from thermally activated band conduction to metallic conduction. Reprinted from Diamond and Related Materials, Activation energy in low compensated homoepitaxial boron-doped diamond films by J. P. Lagrange, A. Deneuville and E. Gheeraert, 7, 9 by permission of Elsevier, copyright 1998

2.8 SUMMARY

In this chapter we have reviewed transport properties of electrons and holes that determine the macroscopic electrical characteristics of diamond. These transport properties are governed not only by diamond's intrinsic properties (e.g., by phonon scattering) but also by various imperfections (e.g., lattice dislocations, grain boundaries or impurities). Due to the rapid progress in the synthesis of CVD diamond, such material now exhibits properties that greatly surpass natural diamond. In particular, substantially lower impurity and dislocation densities as well as higher carrier mobilities have been achieved. By doping with boron, diamond exhibits extrinsic p-type conduction. For high boron concentrations the activation energy approaches zero and conduction becomes of the metallic type. Phosphorus doping, on the other hand, results in n-type conduction.

REFERENCES

[1] T.H. Borst and O. Weis, *Phys. Status Solidi A*, **154**, 423–444 (1996).
[2] E.A. Ekimov, V.A. Sidorov, E.D. Bauer, N.N. Mel'nik, N.J. Curro, J.D. Thompson and S.M. Stishov, *Nature*, **428**, 542–545 (2004).
[3] D.J. Twitchen, A.J. Whitehead, S.E. Coe, J. Isberg, J. Hammersberg, T. Wikstrom and E. Johansson, *IEEE Trans. Electr. Dev.*, **51**, 826–828 (2004).
[4] A. Denisenko and E. Kohn, *Diam. Rel. Mater.*, **14**, 491–498 (2005).
[5] J.S. Blakemore, Semiconductor Statistics, Pergamon Press, New York, 1962.
[6] C.J. Rauch, in: *Proceedings of the International Conference on the Physics of Semiconductors*, A.C. Stickland (Ed.), The Institute of Physics and the Physical Society, Exeter, p. 267, 1962.
[7] M. Willatzen, M. Cardona and N.E. Christensen, *Phys. Rev. B*, **50**, 18054–18059 (1994).

[8] A. Collins, in *Thin Film Diamond*, A. Lettington and J.W. Steeds (Eds.), Chapman & Hall, London, 1994.

[9] F. Fontaine, *J. Appl. Phys.*, **85**, 1409–1422 (1999).

[10] H. Brooks, in *Advances in Electronics and Electron Physics*, L. Marton (Ed.), Academic Press, New York, p. 158, 1955.

[11] E. Conwell and V.F. Weisskopf, *Phys. Rev.*, **77**, 388 (1950).

[12] K. Somogyi, *Appl. Phys. Lett.*, **75**, 1911–1913 (1999).

[13] K. Somogyi, *Diam. Rel. Mater.*, **11**, 686–691 (2002).

[14] T. Teraji, H. Wada, M. Yamamoto, K. Arima and T. Ito, *Diam. Rel. Mater.*, **15**, 602–606 (2006).

[15] D.M. Malta, J.A. von Windheim and B.A. Fox, *Appl. Phys. Lett.*, **62**, 2926–2928 (1993).

[16] N. Fujimori, H. Nakahata and T. Imai, *Jpn. J. Appl. Phys.*, **29**, 824–827 (1990).

[17] H. Kiyota, E. Matsushima, K. Sato, H. Okushi, T. Ando, J. Tanaka, M. Kamo and Y. Sato, *Diam. Rel. Mater.*, **6**, 1753–1758 (1997).

[18] C. Erginsoy, *Phys. Rev.*, **79**, 1013–1014 (1950).

[19] A. Hatta, S. Sonoda and T. Ito, *Diam. Rel. Mater.*, **8**, 1470–1475 (1999).

[20] K. Tsukioka and H. Okushi, *Jpn. J. Appl. Phys., Part 1*, **45**, 8571–8577 (2006).

[21] N. Fujita, A.T. Blumenau, R. Jones, S. Oberg and P.R. Briddon, *Phys. Status Solidi A*, **203**, 3070–3075 (2006).

[22] D.J. Twitchen, G.C. Summerton, I. Friel, J.O. Hansen, G.K. Barry, M.P. Gaukroger, P.M. Martienau, R.C. Burns, S.C. Lawson and T.P.G. Addison, Patent No. patnoWO2007066215, 14th June 2007.

[23] B. Ziaja, R.A. London and J. Hajdu, *J. Appl. Phys.*, **97**, 064905–1-9 (2005).

[24] J. Isberg, M. Gabrysch, A. Tajani and D.J. Twitchen, *Semicond. Sci. Technol.*, **21**, 1193–1195 (2006).

[25] J. Isberg, A. Tajani and D.J. Twitchen, *Phys. Rev. B*, **73**, 245207–1-4 (2006).

[26] D. Menichelli, D. Serafini, E. Borchi and G. Toci, *Nucl. Instrum. Methods Phys. Res., Sect. A*, **476**, 614–620 (2002).

[27] H. Pernegger, S. Roe, P. Weilhammer, V. Eremin, H. Frais-Kolbl, E. Griesmayer, H. Kagan, S. Schnetzer, R. Stone, W. Trischuk, D. Twitchen and A. Whitehead, *J. Appl. Phys.*, **97**, 073704–1-9 (2005).

[28] A. Many and G. Rakavy, *Phys. Rev.*, **126**, 1980–1988 (1962).

[29] W.E. Spear, *J. Non-Cryst. Solids*, **1**, 197–214 (1969).

[30] K.A. Yamakawa, *Phys. Rev.*, **82**, 522–527 (1951).

[31] F.C. Brown, *Phys. Rev.*, **97**, 355–362 (1955).

[32] W.E. Spear, *Proceedings of the Physical Society, Section B*, **70**, 669–675 (1957).

[33] C. Canali, G. Ottaviani and A. Alberigi Quaranta, *J. Phys. Chem. Solids*, **32**, 1707–1720 (1971).

[34] A. Alberigi Quaranta, C. Jacoboni and G. Ottaviani, *Rivista del Nuovo Cimento*, **1**, 445–495 (1971).

[35] P.A. Tove, G. Andersson, G. Ericsson and R. Lidholt, *IEEE Trans. Electr. Dev.*, **17**, 407–412 (1970).

[36] P.A. Tove and L.G. Andersson, *Solid-State Electron.*, **16**, 961–962 (1973).

[37] F. Nava, C. Canali, C. Jacoboni, L. Reggiani and S.F. Kozlov, *Solid State Commun.*, **33**, 475–477 (1980).

[38] L. Reggiani, S. Bosi, C. Canali, F. Nava and S.F. Kozlov, *Solid State Commun.*, **30**, 333–335 (1979).

[39] L. Reggiani, S. Bosi, C. Canali, F. Nava and S.F. Kozlov, *Phys. Rev. B*, **23**, 3050–3057 (1981).

[40] J. Isberg, J. Hammersberg, E. Johansson, T. Wikstrom, D.J. Twitchen, A.J. Whitehead, S.E. Coe and G.A. Scarsbrook, *Science*, **297**, 1670–1672 (2002).

[41] J. Isberg, J. Hammersberg, D.J. Twitchen and A. Whitehead, *Diam. Rel. Mater.*, **13**, 320–324 (2004).

[42] J. Isberg, A. Lindblom, A. Tajani and D. Twitchen, *Phys. Status Solidi A*, **202**, 2194–2198 (2005).

[43] M. Pomorski, E. Berdermann, A. Caragheorgheopol, M. Ciobanu, M. Kis, A. Martemiyanov, C. Nebel and P. Moritz, *Phys. Status Solidi A*, **203**, 3152–3160 (2006).

[44] M. Pomorski, E. Berdermann, W. de Boer, A. Furgeri, C. Sander and J. Morse, *Diam. Rel. Mater.*, **16**, 1066–1069 (2007).

[45] W. Deferme, A. Bogdan, G. Bogdan, K. Haenen, W. De Ceuninck and M. Nesladek, *Phys. Status Solidi A*, **204**, 3017–3022 (2007).

[46] N. Tranchant, M. Nesladek, D. Tromson, Z. Remes, A. Bogdan and P. Bergonzo, *Phys. Status Solidi A*, **204**, 3023–3029 (2007).

[47] D.K. Ferry, *Phys. Rev. B*, **12**, 2361–2369 (1975).

[48] M.A. Osman, M. Imam and N. Nintunze, *Diffusion Coefficient of Electrons in Diamond*, Elsevier Science, New York, NY, USA, Auburn, AL, USA, 1991.

[49] M.A. Lampert and P. Mark, Current Injection in Solids, Academic Press, London, 1970.

[50] M. Werner, O. Dorsch, A. Hinze, E. Obermeier, R.E. Harper, C. Johnston, P.R. Chalker and I.M. Buckley-Golder, *Diam. Rel. Mater.*, **2**, 825–828 (1993).

[51] Y. Matsumae, Y. Akiba, Y. Hirose, T. Kurosu and M. Iida, *Jpn. J. Appl. Phys.*, **33**, L702–L704 (1994).

[52] K. Srikanth, S. Ashok, A. Badzian, T. Badzian and R. Messier, *Thin Solid Films*, **164**, 187–190 (1988).

[53] S. Nespurek and J. Sworakowski, *J. Appl. Phys.*, **51**, 2098–2102 (1980).

[54] N.F. Mott and R.W. Gurney, *Electronic Processes in Ionic Crystals*, Oxford University Press, New York, 1940.

[55] M. Yamamoto, T. Watanabe, M. Hamada, T. Teraji and T. Ito, *Appl. Surf. Sci.*, **244**, 310–313 (2005).

[56] E.H. Hall, *Am. J. Mathematics* **2**, 287–292 (1879).

[57] M. Lundstrom, *Fundamentals of Carrier Transport*, Cambridge University Press, Cambridge, 2000.

[58] R. Mansfield, *Proc. Phys. Soc., Section B*, **69**, 862–865 (1956).

[59] L. Reggiani, D. Waechter and S. Zukotynski, *Phys. Rev. B*, **28**, 3550–3555 (1983).

[60] A.G. Redfield, *Phys. Rev.*, **94**, 526–537 (1954).

[61] P. Denham, E.C. Lightowlers and P.J. Dean, *Phys. Rev.*, **161**, 762–768 (1967).

[62] Z. Remes, C. Uzan-Saguy, E. Baskin, R. Kalish, Y. Avigal, M. Nesladek and S. Koizumi, *Diam. Rel. Mater.*, **13**, 713–717 (2004).

[63] M. Katagiri, J. Isoya, S. Koizumi and H. Kanda, *Appl. Phys. Lett.*, **85**, 6365–6367 (2004).

[64] S. Koizumi, M. Kamo, Y. Sato, H. Ozaki and T. Inuzuka, *Appl. Phys. Lett.*, **71**, 1065–1067 (1997).

[65] J. Pernot, C. Tavares, E. Gheeraert, E. Bustarret, M. Katagiri and S. Koizumi, *Appl. Phys. Lett.*, **89**, 122111-1-3 (2006).

[66] B.A. Fox, M.L. Hartsell, D.M. Malta, H.A. Wynands, C.T. Kao, L.S. Plano, G.J. Tessmer, R.B. Henard, J.S. Holmes, A.J. Tessmer and D.L. Dreifus, *Diam. Rel. Mater.*, **4**, 622–627 (1995).

[67] S. Yamanaka, D. Takeuchi, H. Watanabe, H. Okushi and K. Kajimura, *Phys. Status Solidi A*, **174**, 59–64 (1999).

[68] C. Tavares, F. Omnes, J. Pernot and E. Bustarret, *Diam. Rel. Mater.*, **15**, 582–585 (2006).

[69] J.P. Lagrange, A. Deneuville and E. Gheeraert, *Diam. Rel. Mater.*, **7**, 1390–1393 (1998).

3 Point Defects, Impurities and Doping

ALISON MAINWOOD

Department of Physics, King's College London, UK

3.1 Introduction 50
3.2 Dopants 51
  3.2.1 Boron 51
  3.2.2 Nitrogen 52
  3.2.3 Phosphorus 52
  3.2.4 Sulfur 53
  3.2.5 Other substitutional dopants 54
  3.2.6 Interstitial dopants 54
  3.2.7 Impurity complexes as dopants 54
  3.2.8 Dopant – vacancy complexes 55
  3.2.9 The nitrogen vacancy centre 56
3.3 Hydrogen 57
  3.3.1 Dopant – hydrogen complexes 57
  3.3.2 The B – D shallow donor 58
3.4 Defects that Trap and Scatter Carriers 58
  3.4.1 Vacancy and interstitial centres 59
  3.4.2 The vacancy – hydrogen (VH) and nitrogen – vacancy – hydrogen (NVH) centres 60
  3.4.3 Silicon 60
  3.4.4 Experiments on the trapping of carriers by defects 61
3.5 Other Impurities 61
  3.5.1 Nickel defects 61
  3.5.2 Cobalt defects 62
  3.5.3 Other transition metals 62
3.6 Discussion 62
3.7 Conclusions 63
Acknowledgements 63
References 63

CVD Diamond for Electronic Devices and Sensors Edited by Ricardo S. Sussmann
© 2009 John Wiley & Sons, Ltd. ISBN: 978-0-470-06532-7

3.1 INTRODUCTION

There have been many reviews over the last 30 or more years covering a great deal of research on defects in diamond [1–4]. However, since this book is on the electronic properties of diamond, this review will be focused on the impurities and point defects that affect those electronic properties. Extended defects – dislocations, grain boundaries, inclusions of graphitic or disordered carbon for example – also trap and scatter carriers, but these are outside the scope of this review.

If diamond is to be used in conventional electronic devices both shallow donors and acceptors are necessary. Boron (although its ionisation energy of 0.37 eV is not shallow by the standards of conventional semiconductors) is the acceptor that is usually used. Donors are more of a problem; only phosphorus is acceptably soluble and its ionisation level of 0.6 eV [5, 6] is too deep to be of great use except in high temperature devices or for UV optoelectroncs (see Makino's chapter in this volume). The search for a shallower donor has been going on for many years, both from theoretical [7] and experimental [8] approaches. In Section 3.2, below, I review the dopant issues, including the passivation of the dopants by vacancies (which may be grown into the diamond or produced by implantation of the dopants). There has been a strong interest in diamond as a host for qubits in Quantum Information Processing (QIP) [9] because of the stability of the defects and the low electron–phonon coupling for many of them. The NV centre is a leading candidate for a qubit and, therefore, has been exhaustively researched recently [9]. Because this is an application not addressed in the following sections of this volume, the review in Section 3.2.9 is brief but should explain the relevant properties of the defect itself.

Hydrogen is known to passivate dopants in diamond [10] as it does in silicon, but because CVD diamond is grown in a hydrogen-rich atmosphere, it is an effect that cannot be ignored. The effects of hydrogen on boron-doped diamond are more complex than passivation, though – a shallow donor appears under certain conditions [11]. The effects of hydrogen are reviewed in Section 3.3.

Other defects are known to trap carriers, or at least many occur in two charge states, so trapping must occur. Some of these are ubiquitous in diamond, either because they are intrinsic or contain nitrogen, the most common impurity. The vacancy, nitrogen, and the nitrogen vacancy centre (NV) spring to mind here. Little is known about their properties as traps, partly because it is difficult to identify the traps from DLTS (Deep Level Transient Spectroscopy) or TSC (Thermally Stimulated Current) experimental data with their chemical identity. Section 3.4 reviews the intrinsic and nitrogen-related defects, many of which trap carriers.

Section 3.5 contains a brief explanation of the transition metal impurities that are incorporated into diamonds grown by high pressure, high temperature (HPHT) synthesis where these metals are used as solvent catalysts, and of other impurities found in diamond.

This review will not attempt to discuss the hydrogen-induced surface conductivity, which can be exploited for electronic devices – that is covered in reviews by Ley and Kasu in this volume. Nor will this review cover many of the defects most commonly seen in natural diamonds (or produced by irradiating and/or annealing natural diamonds) some of which are of interest because of their effect on the colour of gems.

3.2 DOPANTS

3.2.1 Boron

Boron's acceptor level is deep by the standards of silicon (0.37 eV) [12]. It is found in natural diamond (Type IIb); it can be implanted successfully [13], and when a boron compound is introduced into the gas phase when diamond is grown using CVD processes, it is readily grown into the polycrystalline or single crystal material [14].

Theoretical models of boron in diamond are quite reliable. Acceptors are intrinsically easier to model than donors because the occupied electronic levels in most atomistic schemes are self-consistent, while the unoccupied levels are not, so the hole in an acceptor occupies a reliable self-consistent state. Density Functional Theory (DFT) calculations show that the boron stays on-site or very close to its site, perhaps with a dynamic, trigonal Jahn–Teller distortion [15]. Its ionisation energy is predicted to be 0.39 eV [16] or 0.5 eV [17], in excellent agreement with the experimental value of 0.37 eV [12]. The acceptor state is effective**-mass-like**, with a modest central cell correction; the excited states calculated from a simple effective**-mass-like** model correspond closely to those observed [18, 19]. Boron pairs are not expected to be more stable than the separated single boron atoms [20].

Experimentally, boron-doped diamond is well understood. Some of its characteristic features, at low concentrations, include an oscillatory nature of the photoconductivity signal, due to its ionisation with absorption of up to about 10 optical phonons [21, 22]. In absorption, at low energies (1282 cm^{-1}) a local vibrational state can be seen below the two-phonon spectrum of pure diamond. Overlapping with the three-phonon spectrum and above it, at 2453.5 cm^{-1} and in the range 2665–3050 cm^{-1} are 28 or more sharp lines that have been identified with electronic excitations of the boron, and in the ranges 3600–5500 cm^{-1} there are phonon replicas of these. All this amounts to a very characteristic absorption spectrum [23, 24]. Its infrared one-phonon spectrum includes a Fano resonance at 165 meV (1332.5 cm^{-1}) [25] due to the overlap of localised phonon vibrations with electronic transitions on the boron. These features make its concentration easy to determine using the infrared absorption in the peak at 0.348 eV (2800 cm^{-1}) [26], and concentrations as low as 1 ppb can be detected by Fourier transform photocurrent spectroscopy and photocurrent isothermal spectroscopy [27]. It appears that when B-doped diamond is grown by CVD methods an approximately equal ratio of boron to carbon grows into the crystal as that in the gas phase [28].

At higher concentrations of boron, the acceptor level broadens out to a band [see Kohn's chapter in this volume], and a Fano resonance is seen in the Raman spectrum at 165 meV [29], which appears to have a different origin to that observed in the infrared spectrum [30]. Above 3.9×10^{21} cm^{-3}, a metal–insulator transition takes place as the band starts to overlap with the valence band [31, 32].

A recent exciting discovery was that heavily boron-doped diamond is superconducting – the first elemental semiconductor to display superconductivity [33]. This was quickly followed up by simulation, which showed that a strong electron–phonon coupling occurs [34, 35]. The superconducting transition temperature depends on the boron concentration [36] and can be as high as 11 K [37] in homoepitaxial samples.

3.2.2 Nitrogen

Nitrogen is the most common impurity in diamond. Its presence led to the classification scheme for diamonds – Type 1 diamonds contain nitrogen, Type II do not (or at least only very small concentrations). In natural diamond the nitrogen is normally aggregated (Type Ia), but in synthetic diamonds it is mainly in the form of single substitutional atoms (Type Ib). Although in this form it is a donor, its ionisation energy is far too great for it to be a useful donor (1.7 eV) [38, 39], so my review of the properties of nitrogen will be brief here. There are many reviews that give more detail (for example chapters within Refs [1–4, 40]. Many of the theoretical models are reviewed by Lombardi *et al.* [41], who also present their own model of nitrogen in diamond. It seems apparent, from experimental data, that the nitrogen moves strongly off-site in a $\langle 111 \rangle$ direction away from one of its carbon neighbours, and most of the unpaired electron resides on that unique carbon neighbour. The distortion is not driven by a Jahn–Teller effect, and the defect is well modelled by Density Functional Theory [41–44], in the right hands. Nitrogen, whether aggregated, or as single atoms or even ionised as N^+, leads to infrared absorption in the one phonon region (below about 1325 cm^{-1}), which is characteristic of its form. Concentrations of nitrogen in its various forms, including the positive ion, can be determined accurately by deconvolving these spectra [45]. This is the method of choice unless the concentrations are very low, when the electron paramagnetic resonance of what is called the P1 defect (single N) can be used to determine concentrations of the neutral species [3].

The nitrogen interstitial [46] is probably not electrically active, but appears to occupy a (001) split site [47] with an infrared signature at 1450 cm^{-1} [46, 47]. The A aggregate consists of a pair of nearest neighbour substitutional nitrogen atoms and is a deep donor, with the level near the middle of the bandgap [40]. The fascinating subject of the aggregation of nitrogen under geological conditions in natural stones, or at high temperatures under stabilising pressure in the lab, is covered in detail by Evans [48], and was modelled with surprising success [49]. Other commonly encountered nitrogen or nitrogen vacancy complexes are discussed by Davies *et al.* [50] and in Refs [1, 2] and we will return for a brief review of the nitrogen-vacancy (NV) defect in Section 3.2.9.

3.2.3 Phosphorus

When the obvious donor in diamond, nitrogen, proved not to be of much use electronically, attention turned to the next Group V element in the periodic table – phosphorus – and it has proved to be the most successful donor so far. Phosphorus-doped diamond was first grown and proved to be electrically active by Koizumi *et al.* in 1995 [5]. Since then, several groups have grown P-doped diamond by CVD methods [8, 51]. It has a deep acceptor level of 0.6 eV [19]. Most earlier successful phosphorus-doped diamond was grown by CVD on the $\langle 111 \rangle$ surfaces of diamond substrates [8], but more recently $\langle 100 \rangle$ homoepitaxial growth [52–54] and polycrystalline heteroepitaxy have both produced high quality P-doped material. The best material has mobilities of up to 660 $cm^2\ V^{-1}s^{-1}$ [6] for concentrations in the 10^{-16} cm^{-3} range. Both phosphine in the growth gas, and more recently, TBP (tertiarybutylphosphine) lead to successful growth [55]. The concentration of phosphorus in the doped film is usually determined by SIMS.

A clear characteristic P bound exciton luminescence can be seen in the best quality samples [56], and Barjon *et al.* [57, 58] have demonstrated a calibration based on the ratio of the intensities of the phosphorus bound exciton and the free exciton peaks seen in cathodoluminescence.

Most theoretical models of phosphorus in diamond located it at the tetrahedral site with a large outward distortion of the lattice to accommodate the phosphorus atom [16, 59]. In addition to this, some found a small trigonal distortion (C_{3v}) [44]. However, recent EPR data [60] identifies a tetragonal 'signal with the phosphorus donor. The signal disappears at temperatures above about 18 K. Renewed theoretical investigations [61–63] show that the phosphorus in the tetrahedral site has a triply degenerate ground state, which is occupied by a single electron, and is therefore subject to a Jahn–Teller distortion. This is the origin of the tetragonal distortion, which arises when the four carbon neighbours are displaced outwards a short distance along a cube axis (D_{2d}). Because there is also a large symmetric (A_1) outward relaxation, the elastic restoring force is strong, and the tetragonal distortion is very small. Consequently, the energy barrier between equivalent distortions is only about 20 meV, and the defect will reorient readily above about 15 K, leading to the disappearance of the tetragonal EPR signal, as has been observed [60]. The large elastic distortion indicates why the solubility of phosphorus is low [61].

Despite its large ionisation energy, phosphorus acts as a shallow donor, so one would expect effective-mass-like excited states, which are, indeed, observed [18, 51].

The electronic properties of high quality P-doped layers were analysed by admittance spectroscopy [64, 65]. The thermal ionisation energy was found to be 0.54 ± 0.02 eV and the capture cross-section was $4.5 \pm 2.0 \times 10^{-17}$ cm^2. The thermal ionisation energy is lower than the optical one because excitations into the effective-mass-like excited states, close to the conduction band edge, may allow tunnelling (or thermal excitation) into the conduction band itself. Two explanations of the deviation of the conductance-frequency curve from Shockley–Read–Hall statistics are given: (i) that there is a long Debye tail of electron distribution at the depletion layer edge [64, 65], or (ii) that the deep donor cannot maintain the equilibrium ionisation state under high frequency modulation [66, 67]. Suzuki *et al.* [66, 67] achieved an active phosphorus ratio of 0.75 of the concentration of 8.3×10^{17} cm^{-3}, and in this sample, the built in potential was 4.0 eV.

As-grown phosphorus-doped diamond often displays high compensation ratios – a large number of other defects are created having deep states that trap the electrons. However, annealing some samples at 1300 K activates the donors [68].

3.2.4 Sulfur

The production of n-type diamond doped with sulfur was announced in 1999 [69], but the claims were shown to be mistaken [70]. Although several groups have attempted to produce sulfur-doped diamond since then, success has been elusive [71]. However, the modelling of this potential double donor has had rather more success [16, 17, 44, 59], although the results are not very consistent. The sulfur has a trigonal distortion, lowering its energy by 0.22 eV [16] or 0.27 eV [59] from its energy on site, and elongating one C–S bond by 27 % [16] to 30 % [59]. Its ionisation energy is 0.77 eV [16], 1.1 eV [59], 1.2 eV [17] or 1.4 eV [44]. It is a double donor, and the (++/+) energies are quoted by these authors. None of the recent models support the disputed experimental assertion that it is a shallower donor than phosphorus. Li *et al.* [72] have had some success in incorporating sulfur into diamond when co-doped with boron. These authors quote donor energies of 0.52 to 0.39 eV as increasing concentrations of sulfur were incorporated. The samples displayed n-type conductivity, but it is unclear whether the donor is isolated sulfur or a B–S complex.

3.2.5 Other substitutional dopants

Theoretical models have suggested a number of species that should be shallow donors (and acceptors), but so far, there has been no success in growing diamond doped with the more promising species [73]. Sque, Goss and coworkers [17, 44] explored a range of elements in the same columns of the periodic table as nitrogen (pnictogens) and sulfur (chalcogens). They concluded that there is a trend towards lower ionisation energies for the elements further down the column of the periodic table. Among the chalcogens, which tend to have the same trigonal structure as sulfur, the ionisation energy of selenium is about the same as that predicted for sulfur, 1.4 eV, but tellurium is shallower (1.2 eV) so all of these could be donors. The higher pnictogens (donors, again) lie on-site. Arsenic is predicted to have an ionisation energy of 0.4 eV, and antimony of 0.3 eV. However, both atoms are a great deal larger than the carbon atom they displace, and the large distortion required to accommodate them in the lattice and the resultant elastic energy implies that they are unlikely to be soluble in the concentrations required to dope diamond effectively. Sque *et al.* point out, however, that a large lattice distortion is necessary around substitutional phosphorus, and this species grows into diamond due to the surface chemistry in the CVD growth.

Aluminium would be expected to be an acceptor, and from the trend observed above, might be expected to be shallower than boron. Lombardi and Mainwood [74] show that this is not the case – they predict an ionisation energy of about 1 eV, and a strong distortion in the lattice around the atom, which itself relaxes along a (111) axis like nitrogen. They also modelled substitutional sodium and lithium, each of which had very deep mid-band-gap levels, and could not be described as shallow dopants [74].

3.2.6 Interstitial dopants

Interstitial halogens have also been suggested as shallow donors [43]. Theory predicts lithium to be a shallow donor, with an ionisation energy of 0.6 eV [74, 75], 0.35 eV [76] or 0.5 to 0.6 eV [77, 78]. However, each of these three models predicts that lithium's activation energy for diffusion is predicted to be small so that it would be very mobile under processing conditions and, therefore, is likely to anneal out [75] or form complexes [76–78]. Lombardi *et al.* [75] suggested that interstitial sodium was a more promising candidate for a stable donor, with an ionisation energy of 0.6 eV, like lithium, but with a larger migration energy. However, Goss and coworkers [77, 78] found that it had a mid-gap electronic level and much the same migration and aggregation properties as lithium. Experimental efforts to incorporate either species have been inconclusive or contradictory, with poor solubility, some evidence of clustering of the species, and no clear n-type electrical activity [79–81].

3.2.7 Impurity complexes as dopants

Here again, the theoretical models have been ahead of the experimentalists. A number of increasingly complex impurity clusters have been suggested as shallow dopants, but it is often unclear how they could be produced in sufficient concentrations to be electronically useful, and most have not been produced experimentally at all. For example, the complex consisting of a substitutional nitrogen bonded to four silicon substitutional atoms is predicted to have a donor energy of only 0.09 eV [82]. Miyasaki and Yamasaki [83] have compared the N–H–N defects (see Section 3.3) with some other complexes that had previously suggested as shallow donors, such as N–Al–N [84] or N–B–N (or N–N–B) [85], and concludes that they have considerably deeper ionisation energies than N–H–N.

However, a review of many of the complexes that could be considered as shallow donors was carried out by Eyre *et al.* [86] who found that very few can be expected to have lower ionisation energies than phosphorus. Those involving second row elements are unbound, and only the nitrogen complexes are stable. The most promising dopant complexes they found were N–B–N, N–Al–N, N–Ga–N and N–In–N. Although the authors showed the last two of these to have shallow donor levels, they calculated that the Ga–N–N and N–N–In structures, respectively, would be more stable. They concluded that it is unlikely to be possible to grow or anneal diamond to create any of the complexes studied to form shallow donors. I am not aware of any experimental work that has been successful in creating n-type doping from impurity complexes.

3.2.8 Dopant – vacancy complexes

One of the problems in using many of the exotic species mentioned above is that they are insoluble in diamond. In silicon, implantation is used to introduce dopants, and annealing at temperature of a few hundred degrees Celsius is sufficient to heal much of the damage and to allow the dopant to migrate and form any complex that might be stable. Implantation is a good method for controlling the spatial distribution of dopants, too, allowing devices of dimensions smaller than micrometres to be fabricated. Diamond can rarely be treated in this way for four reasons:

(i) Because it is only one of the stable allotropes of carbon, implantation damage may form complex graphitic or amorphous regions (either spontaneously or after annealing), rather than recovering the diamond structure, even on a scale of a few atoms.
(ii) Very high temperatures are required to allow substitutional atoms to migrate – ~1500 °C for nitrogen, and at that temperature annealing has to be done at a stabilising high pressure – not an easy process.
(iii) The bonds in diamond are so short that few atoms can be accommodated in the lattice without substantial strain, and it is usually true that a more stable complex forms when a vacancy is captured by (or forms during growth beside) the defect.
(iv) The residual radiation damage or complexes formed on annealing tend to compensate the implanted dopants [87].

In practice, implanted diamond (whether the implanted species is B, P or C) leads to deep energy levels in the band gap, which can be photoexcited to release holes into the valence band [88]. Low energy implantation has been successful in producing the NV centre (see Section 3.2.9), but here the damage (in the form of vacancies) is exploited to create the final product. Implantation of boron also produces p-type conduction with an acceptable hole mobility [89].

Goss *et al.* [90, 91] modelled a large range of impurities that may capture vacancies. In most cases, the impurity atom is located in the centre of a divacancy – a structure that is energetically favourable for larger impurity atoms, often called the semi-divacancy or split-vacancy structure. This is known experimentally to be a stable structure for some large atoms (Ni, Si, Co). These papers report on calculations of the binding energies of the dopant-vacancy (XV) complexes using this equation (or the equivalent for charged defects):

$$\mathrm{X} + \mathrm{V} \rightarrow \mathrm{XV}$$

According to their calculations, *no* dopant-vacancy complex has shallow electronic levels.

It is important to understand what these binding energies are indicating:

- The XV complex is stable (bound) if $E_{\mathrm{XV}} < E_{\mathrm{X}} + E_{\mathrm{V}}$ where E_{X}, E_{XV} and E_{V} are total energies as calculated (or enthalpies) associated with the dopant X, complex XV and the vacancy respectively.
- The complexes are likely to form as the dopant grows into the diamond in preference to the isolated dopant provided that $E_{\mathrm{XV}} + E_{\mathrm{C}} < E_{\mathrm{X}}$, where E_{C} is the energy of the displaced carbon on a lattice site in the diamond.
- However, the complex will not be formed spontaneously unless $E_{\mathrm{XV}} + E_{\mathrm{I}} < E_{\mathrm{X}}$ where E_{I} is the energy of the displaced carbon interstitial, which is approximately 12 eV.
- In implanted diamond, annealed above about 700 K, vacancies are available and mobile, so these vacancy complexes would be expected to form in implanted diamond, in preference to the isolated dopant atom whenever $E_{\mathrm{XV}} < E_{\mathrm{X}} + E_{\mathrm{V}}$ applies (which it does for all the species, X, which the papers model). All calculations relate to absolute zero temperature, so in most cases all entropic considerations are neglected.

3.2.9 The nitrogen vacancy centre

The nitrogen-vacancy centre (NV) has two charge states with zero phonon lines in absorption or luminescence at 2.156 eV (575 nm) (neutral) [92] and 1.945 eV (637 nm) (negative) [93]. The negatively charged defect has an EPR signal with spin 1 (W15), but its neutral version has only been detected in its excited state (spin 3/2) by EPR [94]. NV centres are found in as-grown CVD diamond if a small amount of nitrogen enters the growing chamber. In addition, if vacancies are present, due to irradiation or implantation, annealing will result in their being trapped by nitrogen, forming the NV centres as required. They will be negatively charged if there is a sufficient concentration of nitrogen also present due to the reaction:

$$\mathrm{N}^0 + \mathrm{NV}^0 \rightarrow \mathrm{N}^+ + \mathrm{NV}^-$$

This reaction can be induced by light of energy greater than about 2.4 eV [95].

Because of its high luminescent efficiency (~70 %) and luminescent lifetime of 13 ns, the negatively charged version is a leading candidate for a solid state qubit for use in Quantum Information Processing (QIP). NV^- has a $^3\mathrm{A}$ ground state and a $^3\mathrm{E}$ excited state, with a $^1\mathrm{A}$ state located in between them, to which transitions are (nearly) forbidden because of the spin flip. It is the optical transitions between the excited ^3E states split by a magnetic field, which is at the heart of the qubit. A useful review has been published by Wrachtrup and Jelezko [9]. The production of a lattice of optimally separated defects is a major problem. Implantation of helium ions into N-doped diamond (and 600 °C annealing to trap the vacancies produced on the nitrogen) has been investigated and has set limits on the doses and damage that would be acceptable [96]. The nitrogen present can be a source of decoherence. A very fine balance of the defects needs to be maintained.

3.3 HYDROGEN

Goss [97] reviews the theoretical predictions of hydrogen and its complexes in diamond. His review compares the theoretical predictions with the experimental data available up to 2003. Hydrogen occupies a bond-centred position in the diamond lattice, which is stable in negatively charged, neutral and positively charged states (in the latter case the C–H–C bond is buckled). However, its migration energy depends on its charge state: 2.0, 1.6 and 0.2 eV [97, 98] are predicted in the negative, neutral and positive charge states respectively. The experimental value found in B-doped diamond (positively charged H) is 0.35 eV [99] with that for the other charge states being higher [100]. An interesting aspect of the theoretical models of hydrogen in diamond (or any material) is that quantum effects may be significant in the structure and stability of the defects. Kerridge and coworkers [101, 102] have addressed these ideas by treating the hydrogen as a quantum, rather than classical, object. They show that tunnelling is significant in at least one hydrogen-containing defect in diamond (see Section 3.4.3). However, it is probable that quantum effects could occur in other hydrogen defects.

3.3.1 Dopant – hydrogen complexes

It is energetically favourable for a single nitrogen to capture a hydrogen atom, but this is predicted to produce a deeper donor level than that of nitrogen [97, 98]. Similarly, phosphorus, boron and sulfur all capture hydrogen [15, 41, 59, 103]. What is not apparent from these theoretical models (all performed at absolute zero) is the thermodynamic considerations that show that the complexes dissociate at higher temperatures. Mainwood and Goss [104] have shown that in boron-doped diamond, at temperatures of a few hundred degrees, there is a dynamic equilibrium between the boron−hydrogen complex and isolated B^- and H^+ ions in the diamond. The H^+ ions are mobile, and it is energetically favourable for them to form hydrogen gas (H_2) if they migrate to the surface, so the observed outgassing of hydrogen takes place above about 1000 K (compare this with the experimental value of about 820 K [99, 105]). The lower solubility and much higher migration energy of (neutral and) negatively charged hydrogen make it much more difficult to perform the same experiments on N- or P-doped diamond. Chevallier [100] has succeeded in plasma treating P-doped diamond and observed that a temperature of over 1000 °C is required [100, 106]. They observed an infrared absorption peak at 3107 cm^{-1} that they identify as a N–H vibration, but argue that the hydrogen is not captured by phosphorus.

If the A aggregate of nitrogen, which consists of a pair of nitrogen atoms, captures a hydrogen atom, which sits between the nitrogens (N–H–N), then Miyazaki *et al.* [107]

predict that a donor with ionisation energy of 0.6 eV will be formed. This is one of the complexes that it may be possible to produce in a sufficient concentration for electronic purposes, using our knowledge of the aggregation of nitrogen. Synthetic diamond containing a high concentration of single substitutional nitrogen, can be annealed to produce A aggregates [48]. If hydrogen can be diffused into the diamond from a plasma, then it could be trapped by the A aggregates to form the N–H–N complexes. The viability of the latter process is supported by the observation of muons (effectively a light version of a proton) being trapped by A aggregates [108]. I am not aware of any experimental attempt to produce this N–H–N complex.

3.3.2 The B – D shallow donor

Chevallier and Saguy and coworkers [99, 100, 105, 106] have been using a hydrogen plasma to in-diffuse hydrogen into diamond for some time. They showed, very persuasively, that hydrogen is very mobile in the positively charged state, and it passivates the boron acceptor in p-type diamond. However, it was with some surprise that Teukam *et al.* showed [11] that not only was the p-type behaviour eliminated as deuterium diffused into the diamond (as expected), but some samples started to show n-type conduction. At higher temperatures (above 550 °C) the effect reversed and the sample became p-type again as the deuterium outgassed. The effect has been reproduced by several teams [109–111], but it appears to be very dependent on the sample and even on the region in the sample, implying that it only occurs in regions with low (or high) concentrations of some other defect. The donor produced was shallow with an ionisation energy of about 0.23 eV, and appears where SIMS shows approximately equal concentrations of boron and deuterium. I am not aware that it has been observed when hydrogen, rather than deuterium, has been used. It appears that the shallow donor is only stable below about 200 °C [110].

Theorists have struggled to find an explanation [59, 103] – certainly the obvious candidate, the B–D complex is not a shallow donor. Goss *et al.* [103] suggested that is a surface effect, but the experimental evidence does not support this [110].

Although this shallow donor looks to be a very attractive one for electronics, it is not yet clear if it is reproducible, stable or reliable enough to be used in real devices.

3.4 DEFECTS THAT TRAP AND SCATTER CARRIERS

The experimental techniques that could be used to explore trapping, such as Deep Level Transient Spectroscopy (DLTS) and Thermally Stimulated Currents (TSC) are difficult to perform on diamond, and rather few defects have been investigated in this way. However, it is known that several defects are present in two (and perhaps more) charge states, and that the nonequilibrium charge state may have a long lifetime. We can therefore suggest that these defects must act as deep traps for carriers. In other semiconductors, quite high charge states of defects exist – for example in silicon, diamond's closest relation, doubly charged defect states are common. However, in diamond, despite its wider band gap, only singly charged and neutral states have so far been identified. Any defect disrupts the lattice of a crystal, though, so even if defects do not trap carriers, they are likely to scatter them.

One of the common defects which is seen in two charge states is the NV centre described in Section 3.2.9. It is present in one or both charge states in almost all CVD diamond, and may be expected to trap electrons or holes accordingly:

$$NV^0 + e^- \rightarrow NV^-$$

$$NV^- + h^+ \rightarrow NV^0$$

3.4.1 Vacancy and interstitial centres

The vacancy in diamond, usually produced by radiation damage, is a very intensely studied defect [3, 4, 40, 50, 112], and the reader is referred to these reviews and references therein for details. There is some evidence that vacancies also form at the surface of CVD diamond as it grows [113, 114] (although most of those vacancies will anneal out during growth at any temperature above about 650 °C). To summarise the properties of the vacancy – it gives rise to absorption bands with zero phonon lines at 1.673 eV (GR1) in its neutral charge state and 3.150 eV (ND1) in its negative charge state. There are further transitions (called GR2-8) to closely spaced, higher excited states of the neutral vacancy at 2.88–3.07 eV [115]. These, and ND1, give rise to photoconductivity, implying that the excited states are close to the band edges, while the ground states are in the middle of the band gap. ND1, as expected leads to n-type photoconductivity [116], but in GR2-8, holes are released into the valence band [115], contrary to intuition. GR1 and ND1 are seen predominantly in Type 1a (containing aggregated nitrogen, with a mid-gap Fermi level) and Type 1b (containing deep N donors) diamond, respectively. In p-type samples neither is seen, implying that there is a positively charged vacancy. This can be detected by optically detected DLTS (see Section 3.4.4) with a (−/0) ionisation level 1.25 eV above the valence band [117, 118]. EPR signals from the negative vacancy and excited states of the neutral vacancy allow its concentration to be quantified and to calibrate the optical absorption. Some photochroism of these centres is seen, and it has been shown that the negative vacancy must lose its electron in order to migrate [50].

The activation energy for migration is 2.3 eV, which means that it is mobile above about 700 °C. Mobile vacancies are readily trapped by nitrogen, to form the NV centres, by the A aggregate of nitrogen, to form the H3 or H2 centres (N–V–N) and by the B aggregate of nitrogen (4 Ns around a vacancy) to form the H4 centre, all of which are detected by their characteristic absorption signals. If nitrogen is scarce in the sample, the vacancies may form divacancies (the TH5 optical centre and the R4 EPR centre) or become trapped at other defects. The H3 centre, with a zero phonon line at 2.463 eV [115] has a negative charge state (H2) with a zero phonon line at 1.257 eV [119]. None of the defects involving aggregated nitrogen are likely to be found in synthetic diamond, unless it has been annealed deliberately in order to aggregate the nitrogen [48] and to produce the centres [50].

The interstitial in diamond has been identified with the R2 EPR signal [120] and a zero phonon line at 1.685 eV [121]. It is mobile at lower temperatures than the vacancy, with an activation energy of about 1.7 eV (∼400 °C) [122]. It forms pairs (the R1 EPR defect) [123] and threes (O3) [124] and probably larger aggregates and platelets [125–127]. So far all the identified interstitial defects are seen in just one charge state, so they are not necessarily traps for carriers, but they will be scattering centres. Because of the low migration energy of the interstitial (mobile below the growth or processing temperatures for CVD diamond), it is likely that only the more stable interstitial aggregates are present in most diamond.

3.4.2 The vacancy – hydrogen (VH) and nitrogen – vacancy – hydrogen (NVH) centres

Recently, Glover *et al.* [128, 129] have identified EPR signals that originate from defects in which the vacancy and NV defects have trapped hydrogen atoms. It is unclear as to whether the centre is formed complete during growth or whether the V or NV forms and traps the hydrogen later. Both the VH and NVH centres are in the negative charge state – only observed in diamond with enough nitrogen to donate its electron to the defect, which indicates that each may have an unobserved neutral charge state in nitrogen-free diamond. Both defects are oriented along a $\langle 111 \rangle$ axis. Here there is a discrepancy with the model of NVH, which predicts that the hydrogen should be bonded to one of the carbon neighbours to the vacancy [130] (which would yield a lower symmetry), not to the nitrogen. This has been resolved by showing that the hydrogen tunnels rapidly between the three stable carbon-bonded states such that the experimentally observed axis is $\langle 111 \rangle$ [101]. The NVH^- centre is present in diamond in quite surprisingly high concentrations, only limited by the nitrogen concentration [128] ($\sim$2 ppm) two orders of magnitude greater than the concentration of NV^-. An infrared peak in the absorption spectrum at 3123 cm^{-1} is believed to be a vibration of the NVH defect (probably in its negative charge state) [131]. Because of their concentration, their presence in unirradiated diamond, and their charge state, we would expect these defects to be important traps for carriers.

3.4.3 Silicon

Silicon is often used as a substrate for the non- or hetero-epitaxial growth of polycrystalline diamond and it too enters the lattice as a substitutional atom. However, it is a lot larger than the carbon atom it replaces, and the defects that have been identified as containing silicon (usually from silicon isotope data) locate the silicon in the semi-divacancy structure. The best known of these has a PL peak at 1.682 eV, a $\langle 111 \rangle$ orientation, and is in its negative charge state [132, 133]. It is a ubiquitous defect in polycrystalline CVD diamond, and is probably one of the more important traps for carriers – certainly very high quality homoepitaxial diamond with high mobilities [134] has very low concentrations of this defect. The neutral charge state of the Si–V defect has been observed in EPR (called KUL1) [135, 136], and a version in which it has trapped a hydrogen atom has also been identified [135]. The production of the $Si–V^-$ defect is enhanced by irradiating and annealing at 900 °C CVD diamond, which implies that there are also unidentified substitutional silicon atoms in the lattice that can trap vacancies and then be detected. Because silicon is isoelectronic with carbon, no band-gap levels (hence optical or EPR signature) would be expected from substitutional silicon, but some infrared absorption in the severely strained lattice is expected, and indeed a peak at 1338 cm^{-1} is reported [137] (as well as other PL peaks which may be associated with other Si-related defects).

3.4.4 Experiments on the trapping of carriers by defects

DLTS (Deep Level Transient Spectroscopy) has been a powerful technique for identifying the electronic level of defects in the band gap for semiconductors like silicon. However, because of diamond's large band gap, rather little reliable conventional DLTS data is available. In boron-doped diamond, though, optically detected DLTS (O-DLTS) has shown that there is a deeper electronic level than the boron acceptor at 1.25 eV above the valence band [138]. This trap was identified as the positive charged vacancy, and the optically induced transition between the boron and the vacancy at 0.9 eV was observed as well as the direct ionisation of the vacancy [117, 118]. It was also possible to use this technique to see the passivation of boron after deuteration (as discussed in Section 3.3.2), although the shallow donor was not seen. Charge-based-DLTS (Q-DLTS) has been used to detect a number of trapping levels, of which few have been identified with specific defects. One, at 0.36 eV, is clearly boron and it has a capture cross-section of $1.3 \times 10^{-13}\text{cm}^{-2}$ [139]. To put this into context, this indicates that any electron coming within about 20 Å of the neutral boron will be captured by it. Traps with similar cross-sections to the boron, above, and activation energies of 1.14 eV and 1.23 eV been observed using Thermally Stimulated Currents (TSC) with concentrations around 10^{16} cm^{-3} [140], but these are not definitely identified with any obvious defects, although the positively charged vacancy is a good candidate.

3.5 OTHER IMPURITIES

Most diamond produced by High Pressure, High Temperature (HPHT) synthesis is grown with a transition-metal solvent catalyst. Nickel, cobalt and iron are the most common. In order to reduce the nitrogen content of HPHT diamond, nitrogen getters are used – often titanium or zirconium. All these transition metals (TMs) may be expected to enter the lattice as point defects, but in practice only nickel- and cobalt-containing defects have been positively identified [141]. In CVD or natural diamond, TMs are rare, but one of the Ni–N complexes (grown in deliberately) is another defect which might be suitable for quantum information processing as a single photon source, and therefore is worth discussing briefly in Section 3.5.1 below.

3.5.1 Nickel defects

Nickel appears to be quite readily soluble in diamond (usually HPHT unless nickel has been deliberately introduced into the source gases for CVD growth), despite the size of the atom [141]. It is present predominantly in the $\langle 111 \rangle$ growth sectors. It is known to be present in the form of an interstitial (Ni_i) or substitutional atom (Ni_s). On annealing, it forms a semi-divacancy (Ni–V) structure by ejecting carbon interstitials (which then enhance the aggregation of nitrogen) [142]:

$$\text{Ni}_\text{i} \rightarrow \text{Ni}_\text{s} + \text{C}_\text{i}$$

$$\text{Ni}_\text{s} \rightarrow \text{Ni–V} + \text{C}_\text{i}$$

The charged states actually observed (and identified) are Ni_i^+ (the NIRIM-1 EPR centre) [143, 144], Ni_s^- (2.56 eV luminescence centre, and W8 EPR signal) [145] and Ni–V

(NE4 semi-divacancy EPR defect), but it is likely that other charged states of these exist. Under further annealing, the nickel captures nitrogen, and a complex family of defects has been identified by EPR (NE1-NE8, AB5) and optical spectroscopy [146, 147], in which the nickel is at the semi-divacancy site with its six carbon neighbours replaced by increasing numbers of nitrogen atoms [148, 149].

The defect called NE8 has the nickel in the split vacancy site surrounded by four nitrogen atoms, in a planar arrangement. It is produced by annealing nickel-containing diamond, which also contains nitrogen, at 1700–2000 K such that the mobile nitrogen is trapped by the nickel. The other $Ni–N_n$ defects are created at the same time, of course. NE8 has very low electron–phonon coupling and the zero-phonon line (at 802 nm, eV) in luminescence at room temperature is very narrow (1.5 nm). It has promise as a single photon emitter due to its excellent photostability [9].

3.5.2 Cobalt defects

Lawson *et al.* [150] identified a series of PL peaks that were present in HPHT diamond grown with cobalt. They have, like nickel, been seen predominantly in ⟨111⟩ growth sectors [151]. Johnston *et al.* [152] identified the PL at 2.367 eV from a $Co_s–N_s$ complex, which has a level about 4.4 eV below the conduction band [153]. Twitchen *et al.* [154] identified a defect containing cobalt in a split vacancy with a neighbouring nitrogen ($Co–V–N^-$) in the same sample by EPR (O4). It is likely, therefore, that a family of cobalt–nitrogen defects similar to the nickel defects forms on annealing.

3.5.3 Other transition metals

Several theorists [155–157] have surveyed the first transition series, and variously shown that other TMs should be present in diamond. There are also a few experimental identifications of other TMs [158], but few are accepted. It seems surprising that while there are so many nickel defects, there are no common ones containing the other TMs.

3.6 DISCUSSION

The main conclusions from all this work on point defects in diamond are that shallow donors are still a problem and are likely to remain so. The new species that have been suggested have either proved on further theoretical investigation not to be shallow after all (e.g. S, N–B–N, N–Al–N, etc.), are going to be extremely difficult to produce (e.g. As, Sb), or are unlikely to be stable under processing conditions (e.g. the B–D donor, N–Ga–N, Li_i). It may be worth trying the very careful implantation techniques developed in order to produce the NV centre to dope with As or Sb, but since these species are a great deal more stable when they have captured a vacancy, it is not a very promising prospect. In fact, the passivation of dopants by hydrogen or a vacancy (which often produces a deep electronic state that then compensates remaining dopants) is another reason why doping diamond has been such an intractable problem. It is one that can be circumvented in several ways (e.g. by using unipolar devices, or the deep P donor) and these are discussed in the following chapters.

Secondly, although the identity, structure, and optical and magnetic properties of many of the defects are well understood, very little is known about how they trap carriers. We have suggested that those that are present in several charge states must be traps and discussed some of the relevant defects, but capture cross-sections are only very rarely known. Vacancies are part of many of these trapping centres that are seen in high concentrations (V–H, NV, N–V–H) – another reason why implantation of dopants into diamond may be counter productive. Carriers are scattered by charged defects and by the phonons associated with them (in addition to the scattering mechanisms for the perfect lattice), and by dislocations – these limit the mobility below the values theoretically attainable for pure diamond. The theoretical limit has not, to my knowledge, been calculated, nor has the effect of defects, dopants and impurities on the mobility been assessed.

3.7 CONCLUSIONS

This review has summarised some of the problems associated with the use of diamond in electronic devices, by considering point defects and impurities. Dopants, even boron, tend to be so deep that there are few free carriers except at high temperatures. Donors, of which the best candidate is still phosphorus, have even deeper levels, and other species of donor are not promising. Implantation is seldom successful in producing electrically active dopants. Finally, there is very little understanding of the defects and processes that lead to trapping of carriers in diamond, so it is difficult to understand which defects need to be reduced or eliminated in order to improve the electronic properties of the material.

Despite all these difficulties, extremely good quality material, with high electron and hole mobilities, is now being grown. Devices are being designed that exploit the strengths of diamond as an electronic material, rather than being limited by its problems. Those strengths are formidable, and the potential for diamond devices is excellent, some of which will be explained in the following pages.

ACKNOWLEDGEMENTS

This work has been supported by the EPSRC (GR/S96784) and the EU-funded Research Training Network DRIVE (MRTN-CT-2004-512224)

REFERENCES

[1] J.E. Field, *The Properties of Diamond*. 1979, London: Academic Press.

[2] J.E. Field, *The Properties of Natural and Synthetic Diamond*. 1992, London: Academic Press.

[3] G. Davies, *Properties and Growth of Diamond*. 1994, London: INSPEC, Institute of Electrical Engineers.

[4] M.H. Nazare and A.J. Neves, *Properties, Growth and Applications of Diamond*. 2001, London: INSPEC, Institute of Electrical Engineers.

[5] S. Koizumi, M. Kamo, Y. Sato, H. Ozaki and T. Inuzuka, *Appl. Phys. Lett.*, **71**, 1065 (1997).

[6] S. Koizumi and M. Suzuki, *Phys. Stat. Sol. (a)*, **203**, 3358 (2006).

[7] A. Mainwood, *J. Mater. Sci.–Mater. Electronics*, **17**, 453–458 (2006).

[8] M. Nesladek, *Semi. Sci. Technol.*, **20**, R19–R27 (2005).

[9] J. Wrachtrup and F. Jelezko, *J. Phys.: Condens. Matt.*, **18**, S807–S824, Special issue (2006).

[10] J. Chevallier, Hydrogen Diffusion and Acceptor Passivation in Diamond, in *Thin-Film Diamond II*. Academic Press, 2004. pp. 1–35.

[11] Z. Teukam, J. Chevallier, C. Saguy, R. Kalish, D. Ballutaud, M. Barbe, F. Jomard, A. Tromson-Carli, C. Cytermann, J.E. Butler, M. Bernard, C. Baron and A. Deneuville, *Nature Materials*, **2**, 482–486 (2003).

[12] P.A. Crowther, P.J. Dean and W.F. Sherman, *Phys. Rev.*, **154**, 772 (1967).

[13] C. Uzan-Saguy, R. Kalish, R. Walker, D.N. Jamieson and S. Prawer, *Diam. Relat. Mater.*, **7**, 1429 (1998).

[14] N. Fujimori, H. Nakahata and T. Imai, *Jpn J. Appl. Phys.*, **29**, 824 (1990).

[15] J.P. Goss, P.R. Briddon, R. Jones, Z. Teukam, D. Ballutaud, F. Jomard, J. Chevallier, M. Bernard and A. Deneuville, *Phys. Rev.B*, **68**, 235209 (2003).

[16] L.G. Wang and A. Zunger, *Phys. Rev.B*, **66**, 161202 (2002).

[17] J.P. Goss, P.R. Briddon, R. Jones and S. Sque, *Diam. Relat. Mater.*, **13**, 684–690 (2004).

[18] E. Gheeraert, S. Koizumi, T. Teraji and H. Kanda, *Solid State Commun.*, **113**, 577 (2000).

[19] E. Gheeraert, S. Koizumi, T. Teraji, H. Kanda and M. Nesládek, *Diam. Relat. Mater.*, **9**, 948 (2000).

[20] J.P. Goss and P.R. Briddon, *Phys. Rev.B*, **73**, 085204 (2006).

[21] A.T. Collins and E.C. Lightowlers, *Phys. Rev.*, **171**, 843 (1968).

[22] L. Allers and A.T. Collins, *J. Appl. Phys.*, **77**, 3879–3884 (1995).

[23] S.D. Smith and W. Taylor, *Proc. Roy. Soc. (London) A*, **79**, 1142 (1962).

[24] H.J. Kim, A.K. Ramdas, S. Rodriguez and T.R. Anthony, *Sol. St. Commun.*, **102**, 861–865 (1997).

[25] C. Piccirillo, G. Davies, A. Mainwood and C.M. Penchina,. *Diam. Relat. Mater.*, **11**, 338–341, Special Issue (2002).

[26] A.T. Collins and A.W.S. Williams, *J. Phys. C*, **4**, 1789 (1971).

[27] R. Kravets, M. Vanecek, C. Piccirillo, A. Mainwood and M.E. Newton, *Diam. Relat. Mater.*, **13**, 1785–1790 (2004).

[28] M. Suzuki, H. Yoshida, N. Sakuma, T. Ono, T. Sakai, M. Ogura, H. Okushi and S. Koizumi, *Diam. Relat. Mater.*, **13**, 198–202 (2004).

[29] R. Locher, J. Wagner, F. Fuchs, M. Maier, P. Gonon and P. Koidl, *Diam. Relat. Mater.*, **4**, 678–683 (1995).

[30] C. Piccirillo, A. Mainwood, G. Davies, C.M. Penchina, A. Tajani, M. Bernard and A. Deneuville. *Phys. Stat. Sol. A*, **193**, 529–534 (2002).

[31] A. Deneuville, Boron Doping of Diamond Films from the Gas Phase, in *Thin-Film Diamond I*. Academic Press, 2003. pp. 183–238.

[32] T. Tshepe, C. Kasl, J.F. Prins and M.J.R. Hoch, *Phys. Rev.B*, **70**, 245107 (2004).

[33] E.A. Ekimov, V.A. Sidorov, E.D. Bauer, N.N. Mel'nik, N.J. Curro, J.D. Thompson and S.M. Stishov, *Nature*, **428**, 542–545 (2004).

[34] X. Blase, C. Adessi and D. Connetable, *Phys. Rev. Lett.*, **93**, 237004 (2004).

[35] Y.M. Ma, J.S. Tse, T. Cui, D.D. Klug, L.J. Zhang, Y. Xie, Y.L. Niu and G.T. Zou, *Phys. Rev.B*, **72**, 014306 (2005).

[36] T. Klein, P. Achatz, J. Kacmarcik, C. Marcenat, F. Gustafsson, J. Marcus, E. Bustarret, J. Pernot, F. Omnes, B.E. Sernelius, C. Persson, A.F. da Silva and C. Cytermann, *Phys. Rev.B*, **75**, 165313 (2007).

[37] Y. Takano, T. Takenouchi, S. Ishii, S. Ueda, T. Okutsu, I. Sakaguchi, H. Umezawa, H. Kawarada and M. Tachiki, *Diam. Relat. Mater.*, **16**, 911–914 (2007).

[38] R.G. Farrer, *Solid State Commun.*, **7**, 685 (1969).

[39] B.B. Li, M.C. Tosin, A.C. Peterlevitz and V. Baranauskas, *Appl. Phys. Lett.*, **73**, 812 (1998).

[40] G. Davies, *Carbon*, **13**, 1 (1977).

[41] E.B. Lombardi, A. Mainwood and K. Osuch,. *Diam. Relat. Mater.*, **12**, 490–494 (2003).

[42] P.R. Briddon, M.I. Heggie and R. Jones, *Mater. Sci. Forum*, **83–87**, 457 (1992).
[43] S.A. Kajihara, A. Antonelli, J. Bernholc and R. Car, *Phys. Rev. Lett.*, **66**, 2010 (1991).
[44] S.J. Sque, R. Jones, J.P. Goss and P.R. Briddon, *Phys. Rev. Lett.*, **92**, 017402 (2004).
[45] S.C. Lawson, D. Fisher, D.C. Hunt and M.E. Newton, *J. Phys.:Condens. Matt.*, **10**, 6171–6180 (1998).
[46] I. Kiflawi, A. Mainwood, H. Kanda and D. Fisher, *Phys. Rev.B*, **54**, 16719–16726 (1996).
[47] J.P. Goss, Nitrogen Interstitial. *Private communication* (2006).
[48] T. Evans, *The Properties of Natural and Synthetic Diamond*, J.E. Field, (Ed.) 1992, London: Academic Press. p. 259.
[49] A. Mainwood, *Phys. Rev.B*, **49**, 7934–7940 (1994).
[50] G. Davies, S.C. Lawson, A.T. Collins, A. Mainwood and S.J. Sharp, *Phys. Rev.B*, **46**, 13157–13170 (1992).
[51] K. Haenen, K. Meykens, M. Nesládek, G. Knuyt, L.M. Stals, T. Teraji and S. Koizumi, *Phys. Stat. Sol. (a)*, **181**, 11 (2000).
[52] H. Kato, T. Makino, S. Yamasaki and H. Okushi, *J. Phys. D*, **40**, 6189–6200 (2007).
[53] H. Kato, H. Watanabe, S. Yamasaki and H. Okushi,. *Diam. Relat. Mater.*, **15**, 548–553, Special Issue (2006).
[54] H. Kato, S. Yamasaki and H. Okushi, *Diam. Relat. Mater.*, **16**, 796–799 (2007).
[55] T. Kociniewski, J. Barjon, M.A. Pinault, F. Jomard, A. Lusson, D. Ballutaud, O. Gorochov, J.M. Laroche, E. Rzepka, J. Chevallier and C. Saguy, *Phys. Stat. Sol. (a)*, **203**, 3136–3141 (2006).
[56] R. Sauer, N. Teofilov, K. Thonke and S. Koizumi, *Diam. Relat. Mater.*, **13**, 727–731 (2004).
[57] J. Barjon, P. Desfonds, M.A. Pinault, T. Kociniewski, F. Jomard and J. Chevallier, *J. Appl. Phys.*, **101**, 113701 (2007).
[58] J. Barjon, M.A. Pinault, T. Kociniewski, F. Jomard and J. Chevallier, *Phys. Stat. Sol. (a)*, **204**, 2965–2970 (2007).
[59] E.B. Lombardi, A. Mainwood and K. Osuch, *Phys. Rev.B*, **70**, 205201 (2004).
[60] J. Isoya, M. Katagiri, T. Umeda, S. Koizumi, H. Kanda, N.T. Son, A. Henry, A. Gali and E. Janzen, *Physica B*, **376**, 358–361 (2006).
[61] B. Butorac and A. Mainwood, in prep*aration* (2007).
[62] R.J. Eyre, J.P. Goss, P.R. Briddon and J.P. Hagon,. *J. Phys.:Condens. Matt.*, **17**, 5831–5837 (2005).
[63] N. Orita, T. Nishimatsu and H. Katayama-Yoshida, *Jpn J. Appl. Phys.* **46**, 315–317 (2007).
[64] Y. Koide, S. Koizumi, H. Kanda, M. Suzuki, H. Yoshida, N. Sakuma, T. Ono and T. Sakai, *Diam. Relat. Mater.*, **14**, 2011–2014 (2005).
[65] Y. Koide, S. Koizumi, H. Kanda, M. Suzuki, H. Yoshida, N. Sakuma, T. Ono and T. Sakai, *Applied Physics Letters*, **86**, 232105 (2005).
[66] M. Suzuki, S. Koizumi, M. Katagiri, H. Yoshida, N. Sakuma, T. Ono and T. Sakai, *Diam. Relat. Mater.*, **13**, 2037–2040 (2004).
[67] M. Suzuki, H. Yoshida, N. Sakuma, T. Ono, T. Sakai and S. Koizumi, *Applied Physics Letters*, **84**, 2349–2351 (2004).
[68] J. Chevallier, C. Saguy, M. Barbe, F. Jomard, D. Ballutaud, T. Kociniewski, B. Philosoph, B. Fizgeer and S. Koizumi, *Phys. Stat. Sol. (a)*, **202**, 2141–2147 (2005).
[69] I. Sakaguchi, M.N. Gamo, Y. Kikuchi, E. Yasu, H. Haneda, T. Suzuki and T. Ando, *Phys. Rev. B*, **60**, R2139 (1999).
[70] R. Kalish, A. Reznik, C.U. Saguy and C. Cytermann, *Appl. Phys. Lett.*, **76**, 757 (2000).
[71] J.A. Garrido, C.E. Nebel, M. Stutzmann, E. Gheeraert, N. Casanova and E. Bustarret, *Phys. Rev.B*, **65**, 165409 (2002).
[72] R.B. Li, X.J. Hu, H.S. Shen and X.C. He, *Materials Letters*, **58**, 1835–1838 (2004).
[73] P.W. May *Private communication* (2006).
[74] E.B. Lombardi and A. Mainwood, *Diam. Relat. Mater*., to be published, (2007).
[75] E.B. Lombardi, A. Mainwood and K. Osuch, *Phys. Rev. B*, **76**, 155203 (2007).

[76] H. Yilmaz, B.R. Weiner and G. Morell, *Diam. Relat. Mater.*, **16**, 840–844 (2007).

[77] J.P. Goss and P.R. Briddon, *Phys. Rev.B*, **75**, 075202 (2007).

[78] J.P. Goss, R.J. Eyre and P.R. Briddon, *Phys. Stat. Sol. (a)*, **204**, 2978–2984 (2007).

[79] T.H. Borst and O. Weis, *Diam. Relat. Mater.*, **4**, 948 (1995).

[80] H. Sachdev, R. Haubner and B. Lux,. *Diam. Relat. Mater.*, **6**, 494 (1997).

[81] R. Zeisel, C.E. Nebel, M. Stutzmann, H. Sternschulte, M. Schreck and B. Stritzker, *Phys. Stat. Sol. (a)*, **181**, 45 (2000).

[82] D. Segev and S.H. Wei, *Phys. Rev. Lett.*, **91**, 126406 (2003).

[83] T. Miyazaki and S. Yamasaki, *Applied Physics Letters*, **86**, 261910 (2005).

[84] B.D. Yu, Y. Miyamoto and O. Sugino, *Appl. Phys. Lett.*, **76**, 976 (2000).

[85] H. Katayama-Yoshida, T. Nishimatsu, T. Yamamoto and N. Orita, *Phys. Stat. Sol. (a)*, **210**, 429 (1998).

[86] R.J. Eyre, J.P. Goss, P.R. Briddon and M.G. Wardle, *Phys. Stat. Sol. (a)*, **204**, 2971–2977 (2007).

[87] C. Saguy, A. Reznik, E. Baskin, Z. Remes and R. Kalish, *Diam. Relat. Mater.*, **13**, 722–726 (2004).

[88] C. Saguy, E. Baskin and R. Kalish, *Diam. Relat. Mater.*, **14**, 344–349, Special Issue (2005).

[89] F. Fontaine, C. Uzan-Saguy, B. Philosoph and R. Kalish, *Appl. Phys. Lett.*, **68**, 2264 (1996).

[90] J.P. Goss, P.R. Briddon, M.J. Rayson, S.J. Sque and R. Jones, *Phys. Rev.B*, **72**, 035214 (2005).

[91] J.P. Goss, P.R. Briddon, M.J. Rayson, S.J. Sque and R. Jones, *Phys. Rev.B*, **73**, 199904 (2006).

[92] Y. Mita, *Phys. Rev. B*, **53**, 11360 (1996).

[93] G. Davies and M.F. Hamer, *Proc. Roy. Soc. (London) A*, **348**, 285 (1976).

[94] S. Felton, A.M. Edmonds, M. Newton, P. Martineau, D. Fisher and D. Twitchen, Neutral NV Excited State. Private communication, (2007).

[95] T. Gaebel, M. Domhan, C. Wittmann, I. Popa, F. Jelezko, J. Rabeau, A. Greentree, S. Prawer, E. Trajkov, P.R. Hemmer and J. Wrachtrup, *Applied Physics B*, **82**, 243–246 (2006).

[96] F.C. Warldermann, P. Olivero, J. Nunn, K. Surmacz, Z.Y. Wang, D. Jaksch, R.A. Taylor, I.A. Walmsley, M. Draganski, P. Reichart, A.D. Greentree, D.N. Jamieson and S. Prawer, *Diam. Relat. Mater.*, **16**, 1887–1895 (2007).

[97] J.P. Goss, *J. Phys.:Condens. Matt.*, **15**, R551–R580 (2003).

[98] J.P. Goss, R. Jones, M.I. Heggie, C.P. Ewels, P.R. Briddon and S. Oberg, *Phys. Rev.B*, **65**, 115207 (2002).

[99] J. Chevallier, B. Theys, A. Lusson, C. Grattepain, A. Deneuville and E. Gheeraert, *Phys. Rev.B*, **58**, 7966–7969 (1998).

[100] J. Chevallier, F. Jomard, Z. Teukam, S. Koizumi, H. Kanda, Y. Sato, A. Deneuville and M. Bernard, *Diam. Relat. Mater.*, **11**, 1566–1571 (2002).

[101] A. Kerridge, A.H. Harker and A.M. Stoneham, *J. Phys.:Condens. Matt.*, **16**, 8743–8751 (2004).

[102] M.J. Shaw, P.R. Briddon, J.P. Goss, M.J. Rayson, A. Kerridge, A.H. Harker and A.M. Stoneham, *Phys. Rev. Lett.*, **95**, 105502 (2005).

[103] J.P. Goss, P.R. Briddon, S.J. Sque and R. Jones, *Phys. Rev.B*, **69**, 165215 (2004).

[104] A. Mainwood and J.P. Goss, in preparation, (2008).

[105] J. Chevallier, D. Ballutaud, B. Theys, F. Jomard, A. Deneuville, E. Gheeraert and F. Pruvost, *Phys. Stat. Sol. A*, **174**, 73–81 (1999).

[106] C. Saguy, C. Cytermann, B. Fizgeer, V. Richter, Y. Avigal, N. Moriya, R. Kalish, B. Mathieu and A. Deneuville, *Diam. Relat. Mater.*, **12**, 623–631 (2003).

[107] T. Miyazaki, H. Okushi and T. Uda, *Phys. Rev. Lett.*, **88**, 066402 (2002).

[108] I.Z. Machi, S. Connell, J.M. Baker, J.P.F. Sellschop, K. Bharuth-Ram, C.G. Fischer, R.W. Nilen, S.F.J. Cox and J.E. Butler, *Physica B*, **507**, 489 (2000).

[109] J. Chevallier, T. Kociniewski, C. Saguy, R. Kalish, C. Cytermann, M. Barbe, D. Ballutaud, F. Jomard, A. Deneuville, C. Baron, J.E. Butler and S. Koizumi, Some Recent Advances on the n-type Doping of Diamond, in *Gettering and Defect Engineering in Semiconductor Technology XI*. Trans Tech Publications Ltd, 2005. pp. 703–708.

[110] C. Saguy, R. Kalish, J. Chevallier, F. Jornard, C. Cytermann, B. Philosoph, T. Kociniewski, D. Ballutaud, C. Baron and A. Deneuville, *Diam. Relat. Mater.*, **16**, 1459–1462 (2007).

[111] C. Saguy, R. Kalish, C. Cytermann, Z. Teukam, J. Chevallier, F. Jomard, A. Tromson-Carli, J.E. Butler, C. Baron and A. Deneuville, *Diam. Relat. Mater.*, **13**, 700–704 (2004).

[112] G. Davies, B. Campbell, A. Mainwood, M. Newton, M. Watkins, H. Kanda and T.R. Anthony, *Phys. Stat. Sol. A*, **186**, 187–198 (2001).

[113] Y. Baryam and T.D. Moustakas, *Nature*, **342**, 786–787 (1989).

[114] L. Allers and A. Mainwood, *Diam. Relat. Mater.*, **7**, 261–265 (1998).

[115] J. Walker, L.A. Vermeulen and C.D. Clark, *Proc. Roy. Soc. (London) A*, **341**, 253 (1974).

[116] R.G. Farrer and L.A. Vermeulen, *J. Phys. C*, **5**, 2762 (1972).

[117] C.E. Nebel, R. Zeisel and M. Stutzmann, *Diam. Relat. Mater.*, **10**, 639–644, Special Issue (2001).

[118] R. Zeisel, C.E. Nebel, M. Stutzmann, E. Gheeraert and A. Deneuville, *Phys. Rev.B*, **60**, 2476–2479 (1999).

[119] S.C. Lawson, G. Davies, A.T. Collins and A. Mainwood, *J. Phys.:Condens. Matt.*, **4**, 3439–3452 (1992).

[120] D.C. Hunt, D.J. Twitchen, M.E. Newton, J.M. Baker, T.R. Anthony, W.F. Banholzer and S.S. Vagarali, *Phys. Rev.B*, **61**, 3863–3876 (2000).

[121] H.E. Smith, G. Davies, M.E. Newton and H. Kanda, *Phys. Rev.B*, **69**, 045203 (2004).

[122] D.J. Twitchen, D.C. Hunt, C. Wade, M.E. Newton, J.M. Baker, T.R. Anthony and W.F. Banholzer, *Physica B*, **274**, 644–646 (1999).

[123] D.J. Twitchen, M.E. Newton, J.M. Baker, T.R. Anthony and W.F. Banholzer, *J. Phys.: Condens. Matt.*, **13**, 2045–2051 (2001).

[124] D.C. Hunt, D.J. Twitchen, M.E. Newton, J.M. Baker, J.K. Kirui, J.A. van Wyk, T.R. Anthony and W.F. Banholzer, *Phys. Rev.B*, **62**, 6587–6597 (2000).

[125] J.P. Goss, B.J. Coomer, R. Jones, C.J. Fall, C.D. Latham, P.R. Briddon and S. Oberg, *J. Phys.:Condens. Matt.*, **12**, 10257–10261 (2000).

[126] J.P. Goss, B.J. Coomer, R. Jones, T.D. Shaw, P.R. Briddon and S. Oberg, *Diam. Relat. Mater.*, **10**, 434–438, Special Issue (2001).

[127] J.P. Goss, B.J. Coomer, R. Jones, T.D. Shaw, P.R. Briddon, M. Rayson and S. Oberg, *Phys. Rev.B*, **6319**, 195208 (2001).

[128] C. Glover, M.E. Newton, P. Martineau, D.J. Twitchen and J.M. Baker, *Phys. Rev. Lett.*, **90**, 185507 (2003).

[129] C. Glover, M.E. Newton, P.M. Martineau, S. Quinn and D.J. Twitchen, *Phys. Rev. Lett.*, **92**, 135502 (2004).

[130] J.P. Goss, P.R. Briddon, R. Jones and S. Sque, *J. Phys.:Condens. Matt.*, **15**, S2903–S2911, Special Issue (2003).

[131] R.J. Cruddace, M. Newton, H.E. Smith, G. Davies, P. Martineau and D. Twitchen, *Private communication*, (2007).

[132] C.D. Clark, H. Kanda, I. Kiflawi and G. Sittas, *Phys. Rev.B*, **51**, 16681–16688 (1995).

[133] J.P. Goss, R. Jones, S.J. Breuer, P.R. Briddon and S. Oberg, *Phys. Rev. Lett.*, **77**, 3041–3044 (1996).

[134] J. Isberg, J. Hammersberg, D.J. Twitchen and A. Whitehead, *Diam. Relat. Mater.*, **13**, 320–324 (2004).

[135] A.M. Edmonds, M. Newton, P. Martineau and D. Twitchen, *Private communication* (2007).

[136] K. Iakoubovskii and A. Stesmans, *Phys. Rev. B*, **66**, 195207 (2002).

[137] D.J.F. Evans, C.J. Kelly, P. Leno, P. Martineau and A.J. Taylor, *Private communication* (2006).

[138] C.E. Nebel, R. Zeisel and M. Stutzmann, *Phys. Stat. Sol. A*, **174**, 117–127 (1999).

[139] V.I. Polyakov, A.I. Rukovishnikov, N.M. Rossukanyi and V.G. Ralchenko, *Diam. Relat. Mater.*, **10**, 593–600, Special Issue (2001).

[140] M. Bruzzi, D. Menichelli, S. Sciortino and L. Lombardi, *J. Appl. Phys.*, **91**, 5765–5774 (2002).

[141] A.T. Collins, *Diam. Relat. Mater.*, **9**, 417–423 (2000).

[142] I. Kiflawi, H. Kanda and A. Mainwood, *Diam. Relat. Mater.*, **7**, 327–332 (1998).

[143] M.H. Nazare, A.J. Neves and G. Davies, *Phys. Rev. B*, **43**, 14196 (1991).

[144] J. Isoya, H. Kanda and Y. Uchida, *Phys. Rev.B*, **42**, 9843–9852 Part A (1990).

[145] M.H. Nazare, P.W. Mason and G.D. Watkins, *Phys. Rev.*, **51**, 16741 (1995).

[146] A.P. Yelisseyev, J.W. Steeds, Y.V. Babich and B.N. Feigelson, *Diam. Relat. Mater.*, **15**, 1886–1890, Special Issue (2006).

[147] R.N. Pereira, W. Gehlhoff, A.J. Neves, N.A. Sobolev, L. Rino and H. Kanda, *Phys.:Condens. Matt.*, **15**, S2941–S2949, Special Issue (2003).

[148] K. Johnston and A. Mainwood, *Diam. Relat. Mater.*, **12**, 516–520 (2003).

[149] R. Larico, J.F. Justo, W.V.M. Machado and L.V.C. Assali, *Physica B*, **376**, 292–295 (2006).

[150] S. Lawson, H. Kanda, H. Watanabe, I. Kiflawi, K. Sato and A.T. Collins, *J. Appl. Phys.*, **79**, 4348 (1996).

[151] X. Jia, S. Hayakawa, W. Li, Y. Gohshi and M. Wakatsuki, *Diam. Relat. Mater.*, **8**, 1895–1899 (1999).

[152] K. Johnston, A. Mainwood, A.T. Collins, G. Davies, D. Twitchen, J.M. Baker and M. Newton, *Physica B*, **274**, 647–650 (1999).

[153] I.N. Kupriyanov, V.A. Gusev, Y.N. Pal'yanov, Y.M. Borzdov and A.G. Sokol, *Diam. Relat. Mater.*, **10**, 59–62 (2001).

[154] D.J. Twitchen, J.M. Baker, M.E. Newton and K. Johnston, *Phys. Rev.B*, **61**, 9–11 (2000).

[155] G.W. Ludwig and H.H. Woodbury, *Solid State Physics*, **13**, 223 (1962).

[156] M. Watkins and A. Mainwood, *J. Phys.:Condens. Matt.*, **15**, S2913–S2927, Special Issue (2003).

[157] K. Johnston and A. Mainwood, *Physica B-Condensed Matter*, **308**, 565–568 (2001).

[158] A. Yelisseyev and H. Kanda, *New Diamond and Frontier Carbon Technology*, **17**, 127–178 (2007).

4 Surface Conductivity of Diamond

LOTHAR LEY

University of Erlangen, Germany

4.1 Introduction 69
4.2 Basic concepts 73
  4.2.1 Hydrogen termination and negative electron affinity 73
  4.2.2 Band profile and carrier density 77
  4.2.3 Charge transfer between diamond and adsorbed molecules 83
4.3 Fullerene induced surface conductivity 85
4.4 Air induced surface conductivity: The electrochemical transfer doping model 92
Acknowledgements 98
References 98

4.1 INTRODUCTION

Diamond with a band gap of 5.5 eV is a bona fide insulator when undoped. The intrinsic conductivity is below $10^{-16}\ \Omega^{-1}\ \mathrm{cm}^{-1}$. Thus it came as no little surprise when, in 1989, Landstrass and Ravi reported a conductivity of about $10^{-6}\ \Omega^{-1}\ \mathrm{cm}^{-1}$ for CVD diamond (Landstrass and Ravi 1989) and for single crystal IIa diamond after it had been exposed to a hydrogen plasma. From the beginning it was evident that this type of conductivity was intimately related to hydrogen at or just below the surface because mild annealing at ~300 °C in air or oxidation in $CrO_3 + H_2SO_4$ removed the conductivity (Grot *et al.* 1990; Gildenblat *et al.* 1991). A first indication that holes in a subsurface layer are responsible for this unexpected conductivity came from Seebeck-effect measurements and the analysis of current voltage characteristics of a rudimentary MISFET (metal insulator semiconductor field effect transistor) based on hydrogenated diamond (Maki *et al.* 1992). Hence the term surface conductivity (SC).

SC of diamond might have remained a curiosity had it not been for the work of Kawarada *et al.* who demonstrated that a particularly simple enhancement mode field

CVD Diamond for Electronic Devices and Sensors Edited by Ricardo S. Sussmann
© 2009 John Wiley & Sons, Ltd. ISBN: 978-0-470-06532-7

affect transistor (FET) could be realized on H-terminated diamond (Kawarada *et al.* 1994). Two gold pads provide ohmic contacts with the conducting hole channel, and an aluminium gate electrode forms a Schottky barrier with diamond such that the underlying hole channel is totally depleted in the unbiased mode. Applying a positive voltage to the Al-gate controls the channel conductance. Transconductances as high as 200 μS/mm had already been obtained in these first devices and that figure was improved to 110 mS/mm five years later (Umezawa *et al.* 1999).

In subsequent years, these particularly simple metal–semiconductor FETs (MESFETs) were developed in various directions emphasising high power and high frequency operation (Gluche *et al.* 1997; Aleksov *et al.* 2002; Kasu *et al.* 2005; Ueda *et al.* 2006), control of individual hole transport (Tachiki *et al.* 2002), or, most recently, as ion and pH-sensitive devices that are about to enter the biological and medical sector (Kawarada *et al.* 2001; Song *et al.* 2004; Yang and Hamers 2004; Rezek *et al.* 2006; Yang *et al.* 2006; Song *et al.* 2007).

In these device applications surface hydrogenation of diamond serves a double purpose: it is a crucial ingredient in providing the surface conductive channel, as will be explained below, and it simultaneously reduces the density of surface and interface states to a level sufficiently low for the diamond/metal barrier heights to follow the metal work function (Mott–Schottky limit). Consequently, for a p-type conductive channel, Au with a high work function of 5.1 eV has a very low Schottky barrier of <0.2 eV and thus serves as an ohmic contact whereas Al with a work function of 4.2 eV forms a Schottky barrier of 0.9 eV with H-terminated diamond (Aoki and Kawarada 1994).

By 1997, key factors of the SC were firmly established through temperature dependent conductivity and Hall measurements that remain valid up to the present (Hayashi *et al.* 1996; Hayashi *et al.* 1997). The sheet conductivity $\sigma_\square$ of hydrogenated diamond is of the order of 10^{-4} to 10^{-5} Ω^{-1} at RT for polycrystalline and nanocrystalline CVD films, homoepitaxial diamond, and single crystals alike. The only case where SC is not observed is heavily N-doped (type Ib) diamond (Jiang and Ito 1999) and the reason was explained by Riedel and coworkers (Ristein 2001; 2002). The areal density of the p-type carriers lies between 10^{12} and 10^{13} cm^{-2} and is hardly temperature dependent between 400 and 120 K (Hayashi *et al.* 1997; Jiang and Ito 1999). The mobility μ shows the largest variation between different samples and values between 30 and 70 cm^2 eV^{-1} s^{-1} are typical. As in conventional semiconductors, the mobility is not only a function of sample quality but also of carrier concentration: the lower the concentration the higher is μ (Looi *et al.* 1998). The highest mobility measured so far at RT is for homoepitaxial C(100) layers and amounts to 335 cm^2 V^{-1} s^{-1} for a carrier concentration of 7×10^{11} cm^{-2} (Rezek *et al.* 2006).

The temperature coefficients of μ are generally small and positive between ~150 and 400 K for samples with $\mu \leqslant 100$ cm^2 V^{-1} s^{-1}. They have either been interpreted by a power law dependence of μ on T [$\mu \sim T^{1.1}$ (Hayashi *et al.* 1997)] or by exponentials with activation energies in the range of 7 to 24 meV, depending on sheet carrier density (Jiang and Ito 1999). Only for the highest quality samples with $\mu \sim 200$ cm^{-2} V^{-1} s^{-1} at RT a shallow maximum is observed around 260 K with μ dropping off to either side. The corresponding slopes have been ascribed to the low and high temperature power laws expected for mobilities that are dominated by ionized impurity scattering ($T^{+3/2}$ below 260 K) and phonon scattering ($T^{-3/2}$ above 260 K), respectively, as in conventional, bulk-doped, semiconductors (Rezek *et al.* 2006; Isberg, Chapter 2 in this book).

The depth distribution and the origin of the holes responsible for SC have been discussed controversially over the years. Initially, borrowing from experience with more conventional semiconductors (Pankove and Johnson 1991) it was assumed that hydrogen would diffuse during plasma treatment into diamond and thereby passivate deep lying defects that were supposed to compensate unspecified shallow acceptors in the non-hydrogenated case (Landstrass and Ravi 1989; Albin and Watkins 1990; Maki *et al.* 1992). However, the etching experiments of Grot *et al.* clearly excluded that option because SC was removed without attacking diamond (Grot *et al.* 1990).

Shirafuji and Sugino were the first to suggest that a hole accumulation layer below the surface is responsible for the SC (Shirafuji and Sugino 1996). Based on XPS and Kelvin-probe measurements, they suggested that electrons from diamond were transferred into acceptor-like surface states present on the H-terminated diamond surface, yielding the required hole accumulation layer and a concomitant upward band bending. After oxidation by oxidizing acids, for example, the acceptor states are replaced by donor-like surface defects, which take up the excess holes rendering the diamond surface insulating. Indeed, the I–V characteristics of surface-channel field-effect transistors were successfully modelled either with a two-dimensional, fully ionized, acceptor layer right on the surface or by a depth distribution of ionized acceptors extending up to 10 nm into the diamond (Tsugawa *et al.* 1999).

In the limit of a quasi-two-dimensional acceptor layer at or up to 30 nm below the surface, the observed hole density of $\sim 10^{13}$ cm^{-2} requires a subsurface band profile such that the Fermi level position lies within a few $k_B T$ of the valence band maximum (VBM) right at the surface (Tsugawa *et al.* 1999).

With these results the notion that hydrogen would passivate deep defects and thereby recover an unspecified p-doped surface layer could no longer be maintained. Instead it was assumed that hydrogen itself would form particular, as yet unspecified, acceptor-like defects (Hayashi *et al.* 1997). The nature of these hydrogen induced acceptors could, however, not be substantiated. Instead, Ri *et al.* demonstrated that the SC depends sensitively on the kind of atmosphere in which the diamond sample is kept. Exposed to acidic vapours the SC increases, whereas it drops over basic solutions (Ri *et al.* 1995; 1999). Based on these experiments, Ri *et al.* were the first to suggest the reduction of H_3O^+ by electrons from diamond as the origin of SC.

The crucial experiment that clarified the respective roles of hydrogen termination and atmospheric conditions for the SC of diamond was published in 2000 by Maier *et al.* (Maier *et al.* 2000). They placed various hydrogen terminated, undoped single crystal diamonds and epitaxial diamond (100) layers into ultrahigh vacuum (UHV) where they could measure the conductivity *in situ* by a two-point probe. They then removed the hydrogen termination by mild electron bombardment from one half of the sample and removed thereby the SC on that half as well. Annealing the sample at 410 °C for 15 min in UHV removed the surface conductivity on the nonirradiated half without removing the hydrogen. The intact hydrogen termination was confirmed by total photoelectron yield spectroscopy which showed the steeply rising yield at the band gap energy of 5.5 eV, which is characteristic for the negative electron affinity (NEA) of a hydrogen terminated diamond as shown in the inset of Figure 4.1 (Cui *et al.* 1999). After this treatment, both halves of the sample had a conductance below 10^{-10} Ω^{-1}, i.e. neither showed any surface conductivity, and this remained so as long as they were kept in UHV. However, once the sample was brought up to air the conductance of the hydrogenated half of the sample rose

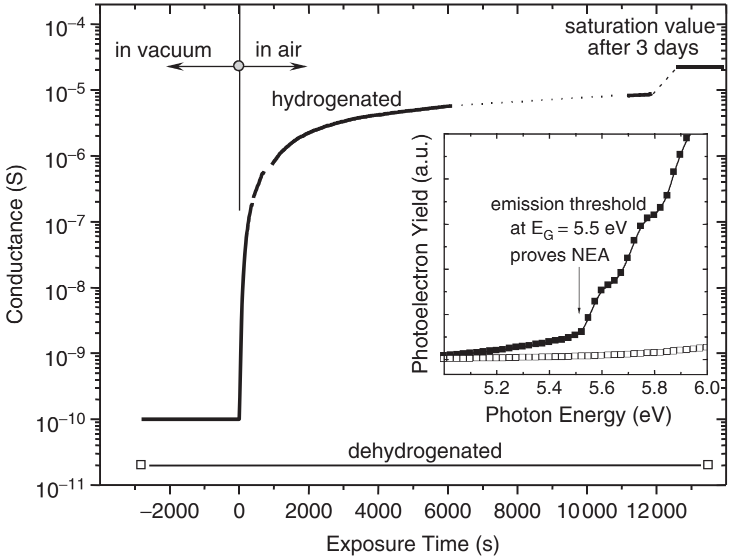

Figure 4.1 Surface conductivity of hydrogenated and nonhydrogenated diamond in ultrahigh vacuum and during exposure to air. The inset shows the yield spectra of the two samples. Only the hydrogenated surface exhibits the steep rise in quantum yield at the band gap energy of 5.5 eV that is characteristic for a surface with negative electron affinity (NEA). (Adapted from (Maier, Riedel *et al.* 2000)

rapidly by 4 orders of magnitude within the first 20 min of exposure and reached a typical SC value of $2 \times 10^{-5}\ \Omega^{-1}$ after 3 days (Figure 4.1). By contrast, the dehydrogenated part of the sample remained in the low conductance state with no change whatsoever.

Maier *et al.* drew the only possible conclusion from this experiment, namely, that hydrogenation of the diamond surface is a necessary albeit not a sufficient condition for SC. Instead, additional, acceptor-like, air-borne species are necessary to induce SC on hydrogen-terminated diamond.

On the basis of this experiment and elaborating on ideas first presented by Ri *et al.*, Maier *et al.* developed an electrochemical transfer doping model that is not only able to account for virtually all experimental findings concerning SC of diamond but also gives a natural explanation for the fact that diamond is the only semiconductor that exhibits this kind of surface conductivity. Most important, the crucial role of hydrogen was identified albeit not as an acceptor but rather as a means to lower the ionization energy of diamond sufficiently to allow transfer doping. This model and its implications will be the topic of Section 4.4.

Once the basic mechanism underlying the air-induced SC of diamond was understood, a deliberate search for alternate surface acceptors was started by the Erlangen group. Success came in the form of fullerene molecules (C_{60}) and their fluorinated derivatives, the fluorofullerenes ($C_{60}F_x, x = 18, 36, 48$). When evaporated onto hydrogen-terminated diamond they induce p-type SC as well by accepting electrons from the valence band of diamond into their lowest unoccupied molecular orbital (LUMO) (Strobel *et al.* 2004; Strobel *et al.* 2005). For $C_{60}F_{48}$ a doping efficiency of unity is obtained, i.e. for each $C_{60}F_{48}$ molecule on the surface a hole is created up to a maximum concentration of about

10^{13} cm^{-2}. Since this type of transfer doping is easier to discuss than the air-induced SC, I shall start my discussion of SC with the fullerenes in Section 4.3. However, before I do so, I shall recall some basic features of transfer doping and the hole accumulation layer in diamond that are independent of the details of the doping process because the acceptors are in each case situated outside the diamond.

4.2 BASIC CONCEPTS

In this section I shall outline some basic concepts and fundamental results concerning the transfer doping mechanism and the resulting charge carrier density in diamond. These considerations are so general that they apply equally to the electrochemical doping mechanism and the fullerene induced SC. I shall start, however, with a brief review of the connection between hydrogen termination and the lowering of the electron affinity and ionisation potential that is at the heart of the role of hydrogen in the transfer doping of diamond.

4.2.1 Hydrogen termination and negative electron affinity

The quantum yield of hydrogen terminated diamond, i.e. the number of electrons emitted per absorbed photon, sets in right at the band gap energy of 5.5 eV, follows the absorption coefficient, and reaches a high value of more than 60 % for photon energies about 8 eV above threshold. All this has been measured by Himpsel *et al.* in the late seventies and was interpreted correctly as being due to the negative electron affinity (NEA) of the hydrogenated diamond surface (Himpsel *et al.* 1979). These observations were, over the years, confirmed and elaborated upon by others (Bandis and Pate 1995; Cui *et al.* 1999; Takeuchi *et al.* 2006). NEA means that the vacuum level E_{VAC} lies energetically below the conduction band minimum E_{C} and hence the electron affinity $\chi = E_{\mathrm{VAC}} - E_{\mathrm{C}} < 0$. Consequently, electrons, once excited into the conduction band, can escape into vacuum without experiencing a barrier while the opposite applies to virtually all other semiconductors for which $\chi > 0$. This explains the onset of electron emission for photon energies equal to the band gap of diamond as shown, for example, in the inset of Figure 4.1. The extremely high quantum yield above the threshold, which, for geometric reasons, cannot exceed 0.5 (only half the electrons travel in the forward direction if no other factors intervene), is due to the large electron escape depth in diamond with NEA. Hot electrons with energies well above E_{C} lose their energy within picoseconds due to a cascade of electron–electron and electron–phonon scattering events until they thermalize at the conduction band minimum. The diffusive mean free path travelled by an electron during the thermalization time lies in the range of a few to a few tens of Å for excess energies up to few hundred eV. Hence, this is the typical electron escape depth for materials with positive electron affinity (PEA) where electrons have to have a finite energy in order to overcome the surface barrier $\chi > 0$. Because the electron mean free path is short compared to the photon absorption length (of the order of micrometres near threshold), the quantum yield for PEA surfaces remains correspondingly small. If the surface barrier is absent, however, electrons thermalized to the conduction band minimum are able to escape and their escape depth equals the diffusion length of thermalized electrons which is governed by their lifetime of the order of microseconds. Consequently, escape depths exceeding 2 μm have been estimated for both electrons and excitons provided the surfaces have NEA (Bandis and Pate 1995; Ristein *et al.* 1997). Cui *et al.* have demonstrated that the escape depth drops by more than 5 orders of magnitude when the surface turns from NEA to PEA (Cui *et al.* 1999). Consequently, both, the yield threshold at 5.5 eV and the higher magnitude of the electron yield of a hydrogenated compared to a non-hydrogenated or even oxidized diamond surface has been taken as a fingerprint for NEA.

Now, the observation is that only surfaces with NEA show SC. However, for a proper understanding of SC it is not so much the negative electron affinity that is crucial but rather the ionization energy $I = E_{\mathrm{VAC}} - E_{\mathrm{V}}$ where E_{V} is the valence band maximum. Obviously, $I - \chi = E_{\mathrm{g}}$ and any lowering of χ is accompanied by the same reduction in I. Hence, a quantitative determination of χ and thus I as a function of hydrogen coverage is of the essence.

The corresponding measurements were made by Cui *et al.* for C(111) and by Maier *et al.* for C(100) (Cui *et al.* 1999; Maier *et al.* 2001). They measured the electron affinity and hence, implicitly, the ionization energy as a function of hydrogen coverage by combining work function measurements with a determination of the surface Fermi level position in the band gap through C1s core level spectra. In this way, a minimum electron affinity of −1.3 eV and a corresponding ionisation energy of 4.2 eV have been obtained for the fully hydrogen covered (111) as well as the (100) surface, whereas the corresponding values for the hydrogen-free surfaces are +0.4 and 5.9 eV, respectively.

The data for C(111) are shown in Figure 4.2 as solid squares. They have been fitted successfully by adopting a simple electrostatic dipole model as depicted schematically in Figure 4.3. The partially ionic $C^{\delta-} - H^{\delta+}$ bonds at the surface form a dipole layer that causes a potential drop ΔV perpendicular to the surface over a distance equal to the C–H bond length of 1.1 Å. The sign of the potential step is such that it raises the inner potential of diamond relative to E_{VAC} by $e\Delta V$ where e is the elementary charge. The reduction in

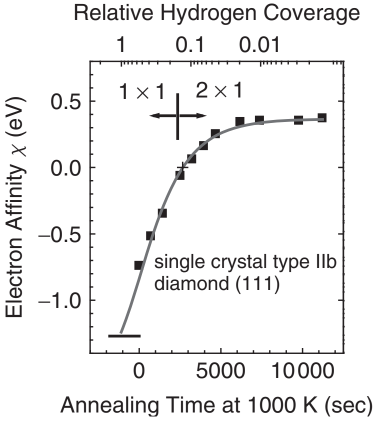

Figure 4.2 Electron affinity as a function of hydrogen coverage for a single crystal diamond (111) surface. The solid squares give the electron affinity as it was measured in a series of isothermal annealing steps starting with a fully hydrogenated surface. The solid line is a fit assuming first-order desorption kinetics for hydrogen. From the fit the hydrogen coverage (upper abscissa) and a value for the C−H dipole moment of 0.09 eÅ was obtained. The surface reconstruction changes from 1 × 1 (unreconstructed) to 2 × 1 as hydrogen desorbs. (Adapted from (Cui, Ristein *et al.* 1999)

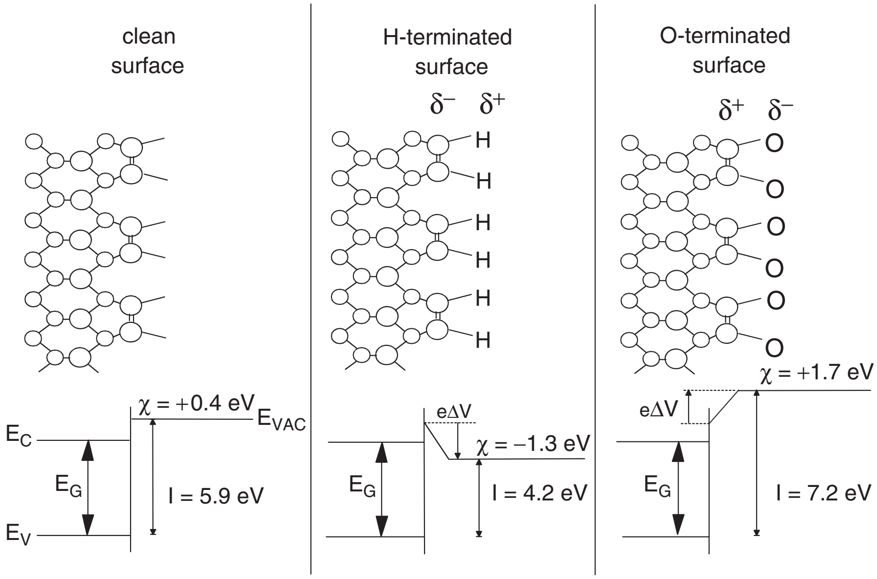

Figure 4.3 Schematic cross-sections through diamond perpendicular to the surface: non-terminated and terminated with H or O. The dipole layers that are formed on account of the partially ionic C–H and C–O bonds give rise to the band diagrams shown at the bottom. Relative to the non-terminated surface, the vacuum level E_{VAC} is lowered or raised by an amount $e\Delta V$, where $e\Delta V$ is the potential step associated with the two dipole layers of opposite sign.

χ from its value χ_0 for the nonhydrogenated and reconstructed surface is thus equal to $-e\Delta V$. ΔV in turn depends on the areal density π of the dipoles and the magnitude $p_\perp$ of the dipole moment perpendicular to the surface:

$$\chi - \chi_0 = -e \cdot \Delta V = -\frac{e \cdot \pi \cdot p_\perp}{\varepsilon_0} \cdot f(\pi)$$

where ε_0 is the dielectric constant of free space and f(π) a function that takes the depolarization of dipoles for high dipole densities into account (Topping 1927). With this model, and assuming first-order desorption kinetics for hydrogen from C(111):H, Cui *et al.* were able to describe the measured changes in χ as function of annealing time quantitatively as shown by the solid line in Figure 4.2. The magnitude of the dipole moment, $p_\perp$, required to obtain the best fit was 0.09 e·Å. A simple estimate for $p_\perp$ is based on the C–H bond length $d = 1.09$ Å (Vidali *et al.* 1983) and the charge transfer Δq from H to C: $p = p_\perp = d \cdot \Delta q$ where I use the fact that the C–H bonds stand perpendicular to the surface (Vidali *et al.* 1983). The charge transfer is estimated on the basis of Pauling's electronegativities for C (2.55) and H (2.2) according to Mönch (1995) and one obtains $\Delta q = 0.07e$ yielding $p = 0.08\ e \cdot$ Å in excellent agreement with the fit result. This lends considerable credibility to the model that must be correct in its essential features.

With reference to Figure 4.3 it appears that electrons leaving a hydrogenated surface see a small triangular barrier when crossing from E_C into vacuum for $\chi < \chi_0$. This barrier is, at most, 0.4 eV high and less than 0.5 Å wide and can obviously be crossed easily by quantum mechanical tunnelling.

Calculations of the electron affinities by methods of varying sophistication yield affinity values of -2.2 and $+0.8$ eV (Zhang *et al.* 1995), and -2.0 and $+0.35$ eV (Rutter and Robertson 1998) for the hydrogen-saturated and hydrogen-free C(111) surfaces, respectively.

For further reference it should be emphasized that $I = 4.2$ eV is the lowest ionization energy of any common semiconductor; for silicon, $I = 5.2$ eV, for example. A lowering of I by hydrogenation is furthermore only possible for diamond. Among all relevant elements, it is only carbon that has an electronegativity higher than that of hydrogen. For all other elements, the H-termination results in an increase in I and χ rather than a reduction.

When the diamond surface is terminated with oxygen instead of hydrogen, a dipole layer of opposite sign is expected to form on the surface because of the higher electronegativity of O (3.5) compared with C (2.5) on the Pauling scale. This expectation is born out by the data in Figure 4.4, where χ of the oxidized surface rises up to $+1.7$ eV (Maier *et al.*

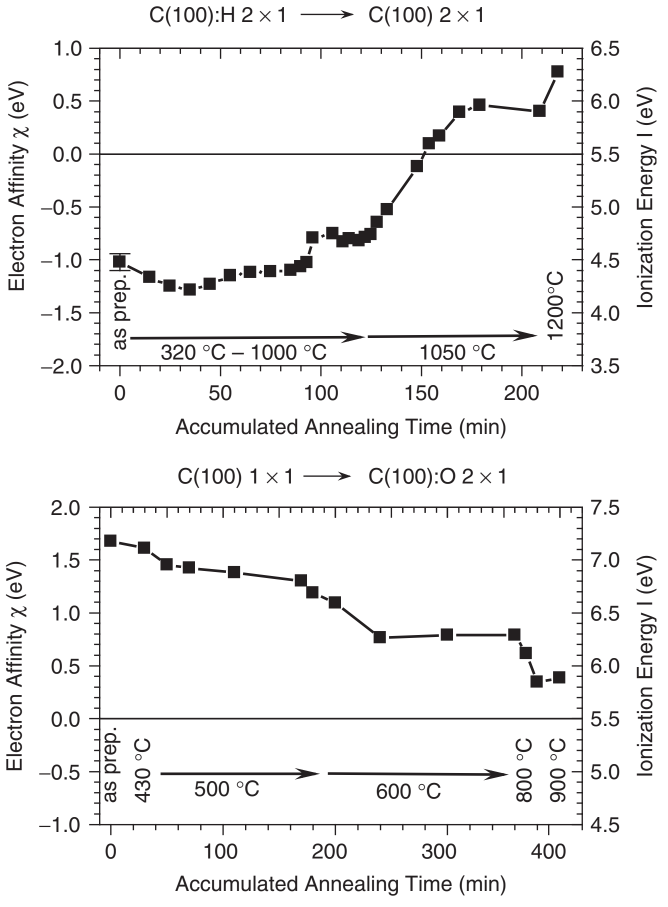

Figure 4.4 Electron affinity and ionization energy of diamond (100) as a function of H and O coverage. Starting from a fully hydrogen-covered (by hydrogen plasma, top panel) or a fully oxygen-covered surface (by oxidizing acids, bottom panel), the coverage is reduced to zero by annealing in ultra high vacuum. (Adapted from Maier, Ristein *et al.* 2001)

2001). Hence, by just changing the surface termination, the electron affinity of diamond can be varied by about 3 eV from −1.3 to +1.7 eV!

There are other ways to induce a NEA surface in diamond (Pickett 1994; Wang *et al.* 2000; Loh *et al.* 2002). This is because for semiconductors or insulators with very large band gaps there is a tendency for the vacuum level to lie close to the conduction band minimum. Therefore, adlayers with comparatively small dipole moments of the right sign suffice to lower E_{VAC} below E_C. What makes the hydrogen-terminated diamond surface special in this respect are the ease with which the H-termination is achieved (a good polish with olive oil suffices in many instances), the immense stability of this kind of termination, and its passivating nature. You can take a hydrogen terminated diamond sample out of the drawer after a year, put it into your vacuum chamber, anneal it at 300 °C to drive physisorbed hydrocarbons off, and you will find a clean surface with NEA. These are, of course, crucial aspects for the application of SC on diamond. I already mentioned in the Introduction the importance of the double role of surface hydrogenation for the operation of MESFETs based on the SC of diamond: an electronic surface passivation by hydrogen in addition to its role in lowering the ionization energy to enable SC in the first place.

4.2.2 Band profile and carrier density

In this section I shall derive the connection between the band profile and the carrier density as they arise in diamond as a result of surface acceptors. Combined with the carrier (here hole) mobility the carrier density gives the surface conductivity as an experimentally accessible quantity.

The situation is schematically depicted by the energy diagram on the left hand side of Figure 4.5 where a molecular layer of acceptors is shown in front of an undoped, hydrogen-terminated diamond surface. Each molecule is characterized by a series of molecular orbitals which are assumed for simplicity to be nondegenerate. They are filled

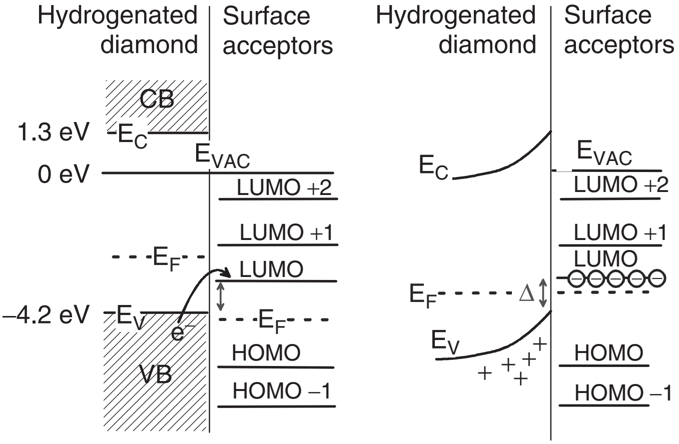

Figure 4.5 Schematic energy diagram of a diamond surface and a molecule: left – before charge exchange; right – after charge exchange when both are in thermodynamic equilibrium. For details see text

with two electrons each, up to the highest occupied orbital (HOMO) and empty above. Between HOMO and LUMO (lowest unoccupied orbital) lies the Fermi level $E_{F,m}$. The diamond is characterized by valence (E_V) and conduction band (E_C) edges separated by the gap $E_g = 5.5$ eV, an electron affinity $\chi = E_{VAC} - E_C = -1.3$ eV as appropriate for hydrogenated diamond, and the Fermi energy $E_{F,d,}$ which is situated close to midgap for undoped diamond. The vacuum level, E_{VAC}, is the common reference level for both systems before equilibrium is achieved by charge exchange. It is taken as the zero of energy and it corresponds to the energy of an electron just outside of diamond or the acceptor molecule; hence it constitutes the natural reference energy for both systems. A final quantity of crucial importance is Δ, the energy difference between LUMO and the valence band edge E_V.

Once acceptors and diamond are brought into contact, i.e. charge exchange is made possible, the situation just described is no longer an equilibrium situation because the chemical potentials of electrons in diamond and the acceptor layer, i.e. the respective Fermi levels, differ. As a result, electrons are being transferred from the valence band of diamond into the LUMO of the acceptors. This leads to space charges in diamond and the acceptor layer in the form of spatially separated holes and electrons, respectively, which will in turn give rise to an electric field and a spatially varying electrostatic potential. When the potential is added to the bands or molecular orbitals, a band bending will result as depicted schematically on the right-hand side of Figure 4.5. The net charge exchange will come to a halt when the Fermi levels in diamond and the acceptor layer coincide. Note that at the interface, the relative alignment of all energy levels in diamond and the molecules remains unaffected by the addition of the space-charge induced potential because the latter is a smooth function of the space coordinate perpendicular to the interface. The alignment of energy levels across the interface is determined by the atomic structure of the interface and is thus established over distances of Å, whereas the potential varies typically over hundreds of Å.

As it turns out, the overwhelming fraction of the total band bending is accommodated in the diamond and I shall therefore proceed to give expressions for the potential profile and the hole concentration in diamond as derived by Ristein *et al.* (Ristein 2004; Ristein *et al.* 2004; Ristein 2006).

The treatment is one-dimensional and assumes a semi-infinite diamond in the direction perpendicular to the surface. It disregards all but the holes as sources of space charges, that is in particular dopands and deep defects. It further assumes that thermally excited electrons do not contribute to the space charge either. This is equivalent to the assumption of a unipolar semiconductor with an infinite band gap.

Electrostatic potential V and space charge density ρ are related via Poisson's equation

$$\frac{d^2V(x)}{dx^2} = -\frac{\rho(x)}{\varepsilon\varepsilon_0} \tag{4.1}$$

where ε is the relative dielectric constant of diamond ($\varepsilon = 5.8$), ε_0 the vacuum permittivity ($\varepsilon_0 = 8.85 \times 10^{-12}\text{AsV}^{-1}\ \text{m}^{-1}$), and x the coordinate perpendicular to the surface. $\Psi(x) = -e \cdot V(x)$ is the potential energy of an electron in potential V and that is the quantity that has to be added to all band energies, in particular to E_V and $E_{C,}$ yielding the commonly plotted band bending $E_{V,C}(x) = E_{V,C} + \Psi(x)$ (compare Figure 4.5). For convenience, we shall shift the origin of $\Psi(x)$ in such a way that the zero of energy corresponds to $E_{\mathrm{F,d}}$. The resulting quantity $u(x) \equiv E_{\mathrm{V}}(x) - E_{\mathrm{F}}$ is <0 for most of the space charge region and we have

$$\frac{d^2u(x)}{dx^2} = \frac{e}{\varepsilon\varepsilon_0} \cdot \rho(x) \tag{4.2}$$

instead of Equation (4.1).

The space charge density $\rho(x)$ is the result of a diffusive equilibrium. It is established between the diffusion current density of holes $\vec{j}_d$ from their point of creation at the diamond surface into the diamond bulk on the one hand, and the field current density $\vec{j}_f$ that is the result of the electric field $\frac{1}{e}\frac{du}{dx}$ connected with the potential $u(x)$ on the other:

$$\begin{gathered} \vec{j}_d = -\vec{j}_f \\ -D \cdot \frac{dp}{dx} = -\mu \cdot p(x) \cdot \frac{1}{e} \cdot \frac{du}{dx} \end{gathered} \tag{4.3}$$

Here D is the diffusion constant for holes in diamond, μ their mobility, and $p(x) = \frac{1}{e} \cdot \rho(x)$ the hole density.
Straightforward manipulations of Equation (4.3):

$$D \cdot \frac{dp}{du} \cdot \frac{du}{dx} = \mu \cdot p(u(x)) \cdot \frac{1}{e} \cdot \frac{du}{dx} \tag{4.3a}$$

gives a differential equation for $p(u)$:

$$\frac{dp}{du} = \frac{\mu}{eD} \cdot p(u) \tag{4.4}$$

with the solution

$$p(u) = p_0 \exp\left(\frac{\mu}{eD} \cdot u\right) \tag{4.5}$$

Using Einstein's relation $\dfrac{\mu}{D} = \dfrac{e}{k_BT}$ and replacing the integration constant p_0 by the effective density of valence states N_{v} ($N_{\mathrm{v}} = 2.7 \times 10^{19}$ cm^{-3} for diamond at RT) we recognize Equation (4.6)

$$p(u) = N_V \exp\left(\frac{1}{k_BT} \cdot u\right) \equiv N_V \cdot \exp\left\{-(E_{F,d} - E_V(x))/k_BT\right\} = p(x) \tag{4.6}$$

as the usual expression for the hole concentration in a semiconductor in the Boltzmann approximation. We could have started with this expression from the outset but that would have raised the question about the time it would take before carriers reached thermal equilibrium across a gap of 5.5 eV. Inserting Equation (4.6) into Equation (4.2) yields a second order differential equation for $u(x)$:

$$\frac{d^2u}{dx^2} = \frac{e^2N_V}{\varepsilon\varepsilon_0} \exp\left(\frac{u}{k_BT}\right) \tag{4.7}$$

with the solution for the potential $u(x)$:

$$u(x) = -2\ k_B T \ln(\sqrt{N_V/p_0} - x/\lambda)^{1/2} \tag{4.8}$$

Here, $\lambda = \sqrt{2\ k_B T \varepsilon\varepsilon_0/(e^2 N_V)}$ is a semiconductor-specific length scale that amounts to 7.7 Å for diamond at RT. Consecutive differentiation of Equation (4.8) yields the electric field:

$$F(x) = \frac{2\ k_B T}{\lambda \cdot e} \frac{1}{(\sqrt{N_V/p_0} - x/\lambda)} \tag{4.9}$$

and the hole density:

$$p(x) = \frac{\rho(x)}{e} = N_V \frac{1}{(\sqrt{N_V/p_0} - x/\lambda)^2} \tag{4.10}$$

A further quantity of interest is the depth integrated carrier density $s(x)$:

$$s(x) = \int_{-\infty}^{x} dx p(x) = \frac{\varepsilon \cdot \varepsilon_0}{e} F(x) \tag{4.11}$$

$$= \frac{\varepsilon \cdot \varepsilon_0 \cdot 2\ k_B T}{\lambda \cdot e^2} \frac{1}{\left(\sqrt{\frac{N_V}{p_0}} - x/\lambda\right)}. \tag{4.11a}$$

Here p_0 is the hole density at $x = 0$.

These equations fulfil one boundary condition, namely that the hole density and the electric field vanish in the bulk of diamond ($x \to -\infty$), which implies $u(x \to -\infty) \to -\infty$. The latter is a necessary consequence of the unipolar treatment of diamond (infinite band gap), which, strictly speaking, can never be neutral.

Equations (4.8) through (4.11) constitute universal, unipolar diffusion profiles for an undoped semiconductor provided the appropriate values for N_v, ε, and λ are inserted. As such their use is not limited to diamond.

A second boundary condition is required to fix the second integration constant. This will be either the surface potential u_s, the surface field strength F_s or, most often, the total integrated hole density $s_\mathrm{s} = s(x_\mathrm{s})$. Thereby the coordinate scale x is fixed as well, with x_s the coordinate of the surface and $x < x_\mathrm{s}$ for positions further into the bulk.

The universal character of the potential, field, and carrier profiles is further accentuated when we adopt the following reduced quantities:

$$\tilde{x} = -\left(\frac{x}{\lambda} - \sqrt{N_V/p_0}\right) \tag{4.12a}$$

$$\tilde{u} = u/2k_B T \tag{4.12b}$$

$$\tilde{p} = p/N_V \tag{4.12c}$$

$$\tilde{F} = F/(2k_BT/(\lambda \cdot e)) \tag{4.12d}$$

$$\tilde{s} = s/N_V \cdot \lambda \tag{4.12e}$$

That is to say, we measure x in terms of the characteristic length λ, change the sign so that x increases towards the bulk and shift the x-scale by $\sqrt{N_V/p_0}$ in order to bring the singularities in u, p, and F to $x = 0$. The energy $u = E_V - E_F$ is measured in units of $2k_BT \cong 50$ meV at RT; the hole density is scaled in terms of the effective valence band density of states N_V; the electric field strength is expressed in terms of a characteristic field that equals the unit potential drop over the characteristic distance λ. Finally, the integrated areal hole density $\tilde{s}(\tilde{x}) = \int_x^{+\infty} \tilde{p}(\tilde{x}) \cdot d\tilde{x}$ is measured in units of $N_V \cdot \lambda$. With this the universal, semi-infite diffusion profiles take on particularly simple forms as plotted in Figure 4.6:

$$\tilde{u} = -\ln \tilde{x}; \quad \tilde{p} = \frac{1}{\tilde{x}^2} \tag{4.13}$$

$$\tilde{F} = \frac{1}{\tilde{x}}; \quad \tilde{s} = \frac{1}{\tilde{x}}$$

In addition to the universal reduced quantities, the scales in Figure 4.6 are also labelled in conventional units, as they are appropriate for diamond at RT. Since we adopted the Boltzmann approximation, the profiles are valid only for $\tilde{u} < 0$ in the limit $T = 0$ as indicated by the horizontal line in Figure 4.6. For $\tilde{u} = 0$ $\tilde{x} = 1$ and the integrated areal hole density amounts to $\lambda \cdot N_V = 2.1 \times 10^{12}$ cm^{-2} in diamond. This is a typical hole density as measured for surface-conducting diamond, and it implies that the Fermi level coincides with the valence band maximum ($u = E_V - E_F = 0$) at the surface. The $\tilde{s}(\tilde{x})$ profile tells us that 90 % of the holes are confined within ~8 nm below the surface. The electric field strength at the surface is unity in reduced units for this case, which amounts to about 6×10^5 V/cm.

For greater hole concentrations (~10^{13} cm^{-2}) that are not uncommon in diamond, the Fermi level has to move into the valence band, i.e. $u = (E_v - E_F) > 0$ at the surface. Clearly that situation is not covered by the profiles in Figure 4.6 because we are dealing now with the degenerate case that requires Fermi–Dirac statistics in Equation (4.6) instead of the Boltzmann approximation. Ristein has expanded the foregoing treatment to include the degenerate case as well, and the results of numerical integrations of the Poisson equation are given in Figure 4.7 (Ristein 2006). As before, a boundary condition at the surface fixes the depth scale and allows reading off of all other relevant parameters. For example, the highest total areal hole density that has been reported is about 5×10^{13} cm^{-2}. This puts the surface coordinate at $x = -0.8\ \lambda$ in Figure 4.7. The surface Fermi level is under these conditions pushed into the valence band to a position ~1 eV below E_V($u = E_V - E_F = 1000$ meV), as can be read off the upper left-hand ordinate of Figure 4.7, and is in agreement with experimental data (Rezek *et al.* 2003). The electric field at the surface is 1.5×10^7 V cm^{-1} (bottom right ordinate), and is in the range of the breakdown field reported for diamond (Collins 1994). Whether this fact is the limiting factor for the surface hole density in diamond achieved by transfer doping remains to be seen.

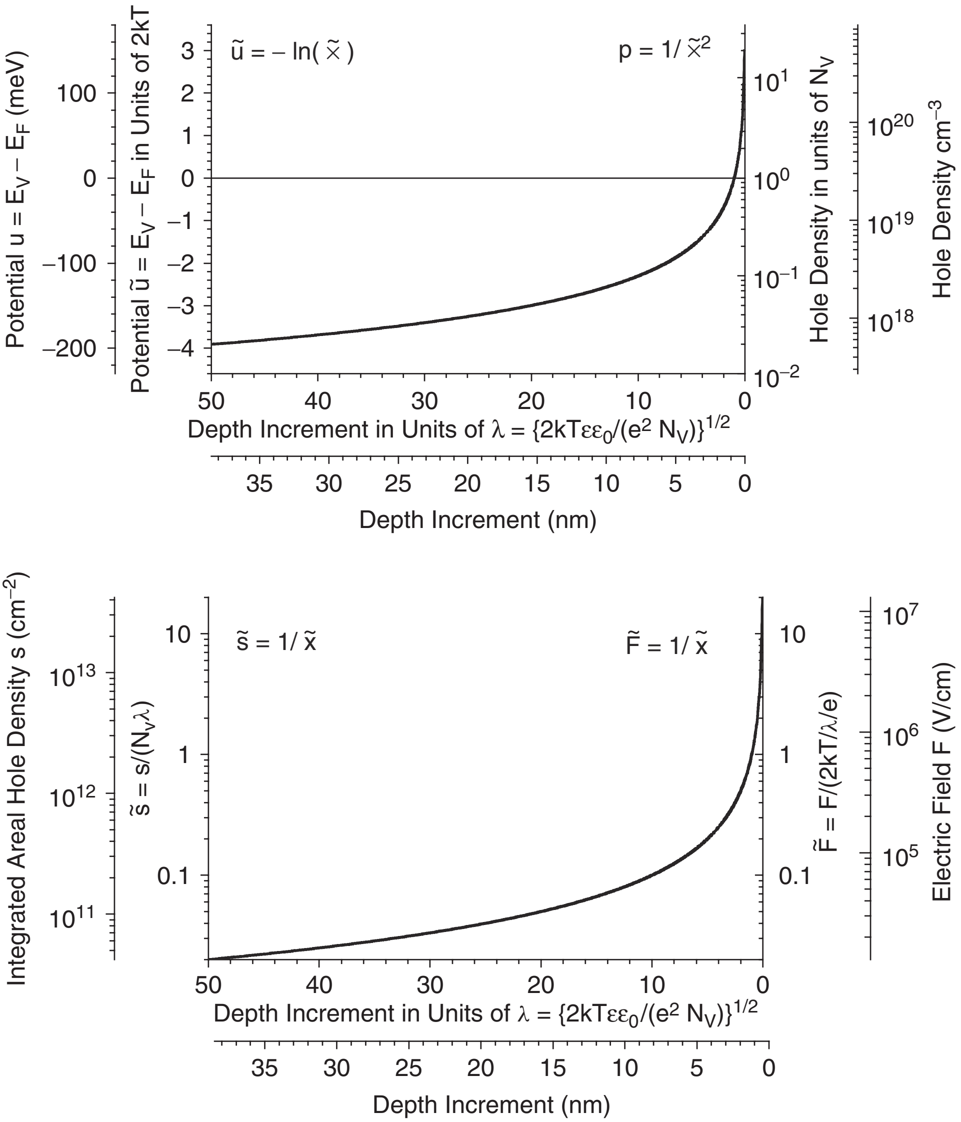

Figure 4.6 Universal hole diffusion profile for a semi-infinite semiconductor calculated in the Boltzmann approximation. Plotted are the reduced potential $\widetilde{u}$, the reduced carrier concentration $\widetilde{p}$, the reduced field strength $\widetilde{F}$, and the depth integrated hole concentration $\widetilde{s}$ as a function of the normalized depth coordinate $\widetilde{x} = x/\lambda$. In addition, the values of these quantities in conventional units appropriate for diamond at RT are given by the outer coordinates. (Adapted from Ristein, Riedel *et al.* 2004)

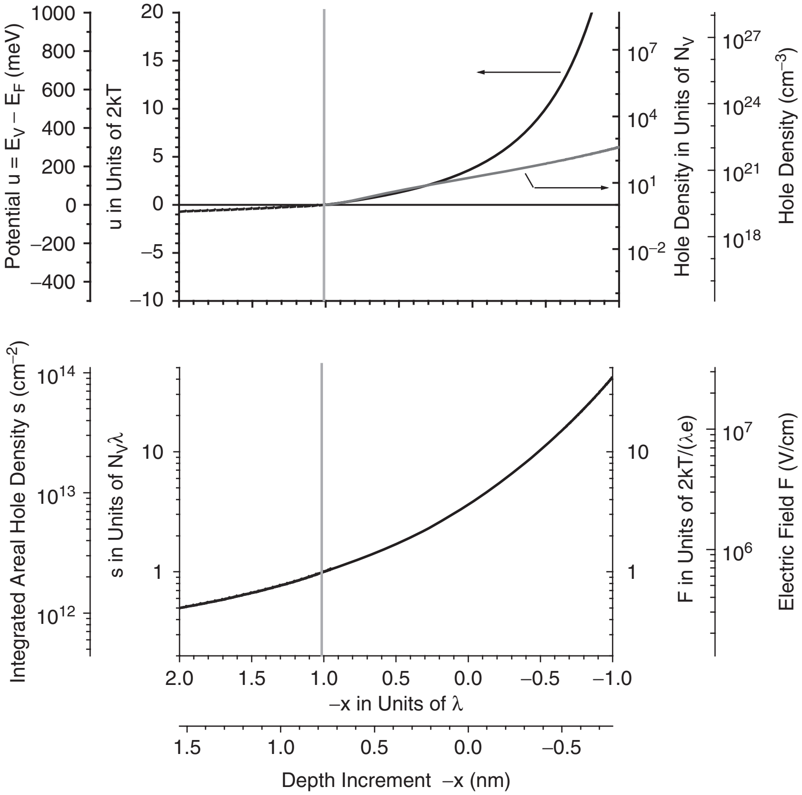

Figure 4.7 Expanded view of Figure 4.6 near $\widetilde{u} = 0$. For the degenerate case ($u > 0$) a numerical solution of the diffusion problem using the correct Fermi–Dirac statistics is also given (Adapted from Ristein 2006)

4.2.3 Charge transfer between diamond and adsorbed molecules

For the case of molecular adsorbates as surface donors, the analysis can be carried further. Three requirements have to be met:

(i) Charge neutrality requires that the depth integrated areal hole density in diamond

$$\begin{aligned} s(x_s) = s(u_s) &\equiv \lambda \cdot N_V \cdot \exp\left\{(E_{F,d} - E_V)_s/(2k_BT)\right\} \\ &= \lambda \cdot N_V \cdot \exp\{(u_s)/(2k_BT)\} \end{aligned} \tag{4.14}$$

equals the areal electron density n_C in the molecule layer:

$$s(u_s) = n_C(N_C, \Delta) \tag{4.15}$$

Here we have indicated that the latter depends on the *areal* density of molecules N_C and the ‘activation energy’ Δ which corresponds to $E_{LUMO} - E_V$ at the interface (compare Figure 4.5).

(ii) In thermal equilibrium the chemical potentials of electrons in diamond ($E_{\mathrm{F,d}}$) and the molecular layer ($E_{\mathrm{F,m}}$) have to be equal:

$$E_{F,d} = E_{F,m} \tag{4.16}$$

(iii) The sheet conductivity $\sigma_\square$, finally, is given by:

$$\sigma_\square = s(u_s) \cdot e \cdot (\mu_p + \mu_n) \tag{4.17}$$

where μ_{p} and μ_{n} are the mobilities of holes in diamond and electrons in the molecular layer, respectively. In principle, both types of carrier contribute to the surface conductivity. However, as it turns out, the hole mobility in diamond is about 70 $\mathrm{cm}^2\ \mathrm{V}^{-1}\ \mathrm{s}^{-1}$, whereas the electron mobility in fullerite (fullerene solids) does not exceed 10^{-1} $\mathrm{cm}^2\ \mathrm{V}^{-1}\ \mathrm{s}^{-1}$ (Haddon *et al.* 1995). Hence, we shall drop the electron contribution to $\sigma_\square$ in what follows.

The areal electron concentration in the molecular layer is given by:

$$n_C(N_C) = N_C \left\{ \sum_{i=1}^{l} g_i f(E_i, E_{F,m}, T) \right\} \tag{4.18}$$

where the sum extends over all molecular orbitals i with energy E_{i} and degeneracy g_{i}, respectively, and $f(E_i, E_{F,m}, T)$ is the Fermi–Dirac occupation function. For fullerenes the gap, i.e. the energy separation between LUMO and HOMO, is discussed controversially in the literature and values between 1.5 and 2.0 eV for isolated molecules (Yang *et al.* 1987) and 2.3 to 3.5 eV for a multilayer C_{60} film (fullerite) have been reported (Lof *et al.* 1992). In either case, the gap energy is large compared with $k_{\mathrm{B}}T$ so that the $T \to 0$ limit applies, viz. the HOMO is fully occupied and the LUMO and all higher MOs are empty. Because the LUMO+1 is at least 1 eV higher in energy, it suffices to consider charge transfer into the LUMO alone. With this we obtain for n_{C}, the electron concentration in the molecule layer:

$$n_C = N_C \cdot g_{LUMO} \cdot \frac{1}{1 + \exp\left(\frac{E_{LUMO} - E_{F,m}}{k_B T}\right)} \tag{4.19}$$

The degeneracy of the LUMO, g_{LUMO}, equals 12 in $C_{60,}$ including the spin degree of freedom. In thermodynamic equilibrium, that is $E_{\mathrm{F,m}} = E_{\mathrm{F,d}}$, the exponent in Equation (4.19) may be rephrased using the system-inherent quantity $\Delta = E_{\mathrm{LUMO}} - E_{\mathrm{V}}$:

$$E_{LUMO} - E_{F,m} = \underbrace{E_{LUMO} - E_V}_{\Delta} + \underbrace{E_V - E_{F,d}}_{u_s}$$
$$= \Delta + u_{\mathrm{s}}$$

In this way a connection is made between the areal electron density in the molecular layer:

$$n_C = N_C \cdot g_{LUMO} \cdot \frac{1}{1 + \exp\left(\frac{\Delta + u_s}{k_B T}\right)} \tag{4.19a}$$

on the one side and the areal hole density in diamond on the other:

$$s(u_s) = \lambda \cdot N_V \cdot \exp(u_s/(2k_B T)) \tag{4.14}$$

via the surface potential u_s and the material constant Δ, the latter being characteristic for the diamond/molecule interface.

Combining Equation (4.17) with (4.15) and (4.19a), we obtain an expression for the surface conductivity $\sigma_\square$ induced by a molecular layer of areal density N_C with Δ as the material specific parameter:

$$\sigma_\square = e \cdot \mu_p \frac{N_C \cdot g_{LUMO}}{\exp((\Delta + u_s)/k_B T) + 1} \tag{4.20}$$

4.3 FULLERENE INDUCED SURFACE CONDUCTIVITY

Based on their experience with air induced SC, the Erlangen group started to look for an alternative surface acceptor that would avoid some if not all of the idiosyncrasies of the propitious, if somewhat ill-defined, water layer that is at the heart of air-induced SC. It was clear at the outset that the key property to look for was a high electron affinity in the range of 3–4 eV. The fullerene molecule C_{60} is known by chemists to be a strongly oxidizing species which implies a high electron affinity. Although the electron affinity of C_{60} is measured at only 2.7 ± 0.1 eV (Yang *et al.* 1987), Goss and coworkers obtained evidence for an electron transfer from diamond to C_{60} in a cluster calculation of fullerene in contact with hydrogenated diamond (Goss *et al.* 2001; Sque *et al.* 2005). Higher electron affinities have been measured for the fluorinated fullerenes $C_{60}F_{18}$, $C_{60}F_{36}$, and $C_{60}F_{48,}$ whose structure and electron affinities are shown in Figure 4.8. Strobel *et al.* did indeed demonstrate that $C_{60,}$ and in particular the fluorofullerenes, induce a SC comparable in magnitude to the air induced one (Strobel *et al.* 2004; Strobel *et al.* 2005; Strobel *et al.* 2006).

The experiments were performed on IIa single crystals and undoped homoepitaxial layers grown on synthetic Ib substrates, all of (100) orientation. Prior to each experiment, the diamond samples were plasma hydrogen terminated after removing metallic and graphitic contaminations by boiling them in a H_2SO_4:HNO_3 mixture. After transferring the samples into the ultrahigh vacuum chamber of a combined photoemission–evaporation chamber, they were annealed a 300 °C for a few minutes in order to remove the air induced SC (see Section 4.4). Fullerene molecules were deposited by electron beam evaporation under the

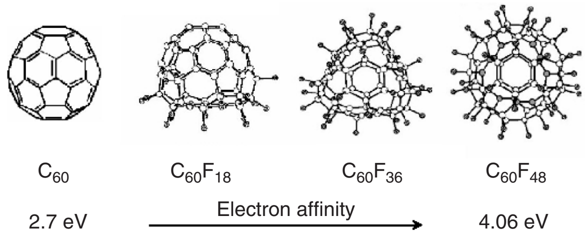

Figure 4.8 Structure and electron affinities of different fluorofullerenes as they are used to induce SC in diamond. The fluorine atoms are represented by the solid spheres outside the C_{60} cage. (Adapted from Boltalina and Strauss)

control of a flux monitor. The evaporation rate was calibrated by measuring the thickness and composition of the fullerene layers by X-ray induced photoelectron spectroscopy (XPS). Conductivities were obtained during, as well as after, evaporation by a two-probe set-up *in situ* without exposing the sample to air.

Figure 4.9 shows the C1s core level spectra of different $C_{60}F_x$ layers on diamond. Notice that there are significant chemical shifts between the C1s line of diamond and those of C_{60} and the fluorofullerenes. This allows easy identification of the stoichiometry of the different fluorofullerenes on account of the relative intensities of the chemically shifted C1s components. More importantly, as demonstrated in Figure 4.9a, from the intensities of the fullerene-derived lines relative to that of the diamond substrate, an accurate determination of the $C_{60}F_x$ overlayer thickness down to a tenth of a monolayer (ML) is possible. This is done by using standard formulas for the attenuation of the diamond substrate C1s signal by the $C_{60}F_x$ overlayer (Seah and Dench 1979). Using this information to calibrate the flux monitor, fullerene coverages down to 5×10^{-4} ML have been determined reliably.

Figure 4.10 shows the evolution of the surface conductivity as a function of coverage for C_{60}, $C_{60}F_{18}$, and $C_{60}F_{48}$, respectively. Prior to $C_{60}F_x$ evaporation, the samples were in the nonconducting state with sheet conductivities below 10^{-12} Ω^{-1}. With increasing C_{60} or $C_{60}F_x$ coverage, the sheet conductivity rises in all cases by more than six orders of magnitude and saturates between 5×10^{-6} and 5×10^{-5} Ω^{-1}. Control experiments using silica glass and oxidized instead of hydrogenated diamond surfaces, failed in all cases to show any sign of conductivity, which proves that the observed conductivity is not

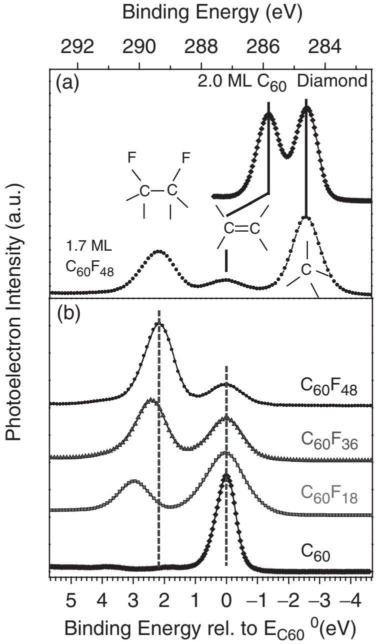

Figure 4.9 C1s photoemission core level spectrum of 1.7 monolayers $C_{60}F_{48}$ on diamond (a), and C1s spectra of thick C_{60}, $C_{60}F_{18}$, $C_{60}F_{38}$, and $C_{60}F_{48}$ layers (b). (Adapted from Strobel, Riedel *et al.* 2005)

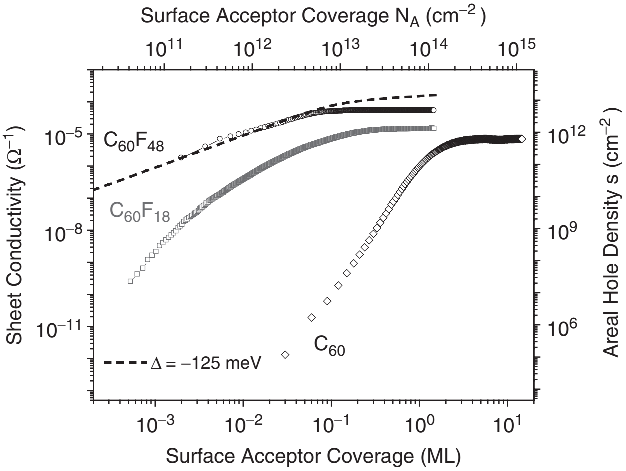

Figure 4.10 Evolution of the surface conductivity as a function of (fluoro-)fullerene coverage, given in monolayers (ML) along the bottom abscissa. It is recalculated in terms of absolute coverage for $C_{60}F_{48}$ on the upper abscissa. The areal hole density on the right hand ordinate is calculated from the conductivity by assuming a hole mobility of 70 cm^2 V^{-1} s^{-1}. (Adapted from Strobel, Riedel *et al.* 2005)

due to transport through the (fluoro-)fullerene layer, and that a lowering of the diamond ionization energy by hydrogenation is a necessary condition for fullerene induced SC. The former point was recently confirmed by *in situ* Hall measurements that confirmed holes with a mobility around 40–80 cm^2 V^{-1} s^{-1} as the dominant charge carriers (Strobel personal communication). Two aspects are apparent in Figure 4.10. The coverage necessary to achieve a given conductivity decreases dramatically with increasing fluorine content and so does the coverage where saturation in $\sigma_\square$ sets in. The saturation conductivity increases by an order of magnitude between C_{60} and $C_{60}F_{48}$, and the latter is higher than the air-induced SC by a factor of about three. For further reference, in Figure 4.10 the conductivity scale (left-hand ordinate) is recalculated in terms of the areal hole density $s = \sigma_\square/(e \cdot \mu)$ (right-hand ordinate) by using an average hole mobility of $\mu = 70$ cm^2 V^{-1} s^{-1}. Similarly, the coverage is recalculated from monolayers (ML) to absolute coverage for $C_{60}F_{48}$ (upper abscissa) by using a molecular density of 7.8×10^{13} $C_{60}F_{48}$ molecules cm^{-2} for a coverage of 1 ML.

It is obvious from the data in Figure 4.10 that the fullerenes are more efficient as surface acceptors the higher their electron affinity is. In fact, $C_{60}F_{48}$ with an electron affinity of 4.06 eV (Jin *et al.* 1994) has a doping efficiency $\eta = 1$ below saturation, that is, there is one hole for each adsorbed $C_{60}F_{48}$ up to a maximum of about 5×10^{12} cm^{-2}. The molecular transfer doping model as discussed in Section 4.2 does describe the carrier concentration by electron transfer from the valence band of diamond into the LUMO of $C_{60}F_{48}$ quite well, as demonstrated by the dashed line in Figure 4.10. That includes the saturation in $\sigma_\square$, which is a consequence of the degeneracy of the hole gas as the Fermi level comes close to and falls below the valence band maximum E_V of diamond. A fit to the data with Δ, the energy separation of LUMO and valence band maximum, as the sole parameter yields $\Delta = -125$ meV, i.e. the LUMO of $C_{60}F_{48}$ lies 125 meV below the valence band maximum of diamond. In conventional semiconductor language, that would correspond to a negative activation energy. Combining $\Delta = -125$ meV with the electron affinity of $C_{60}F_{48}$, of 4.06 eV (Jin *et al.* 1994) yields 3.9 and −1.6 eV for the ionization energy and electron affinity of hydrogen terminated diamond. The latter value is 0.3 eV lower than the one measured by Cui *et al.* (Cui *et al.* 1999), which appears to be acceptable in view of the combined uncertainties of all experimental values.

C_{60}, at the other extreme, constitutes a special case. An attempt to fit the hole density versus coverage in the molecular surface acceptor model of Section 4.2 with a fixed activation energy Δ fails. The maximum conductivity achieved for a coverage of about 5 ML requires $\Delta = 0.24$ eV. This in turn corresponds to a rather weak coverage dependence of $\sigma_\square$ and s as demonstrated by the dashed line in the upper panel of Figure 4.11, while the actual conductivity drops by 8 orders of magnitude as the coverage is reduced to a tenth of a monolayer. A perfect fit as shown by the solid line requires a gradual increase of Δ from 0.24 eV for the high coverage to 1.5 eV for the lowest coverage (compare the lower panel in Figure 4.11). Values of Δ for a second C_{60} sample are also given in Figure 4.11 and they exhibit a very similar coverage dependence, proving that this is a

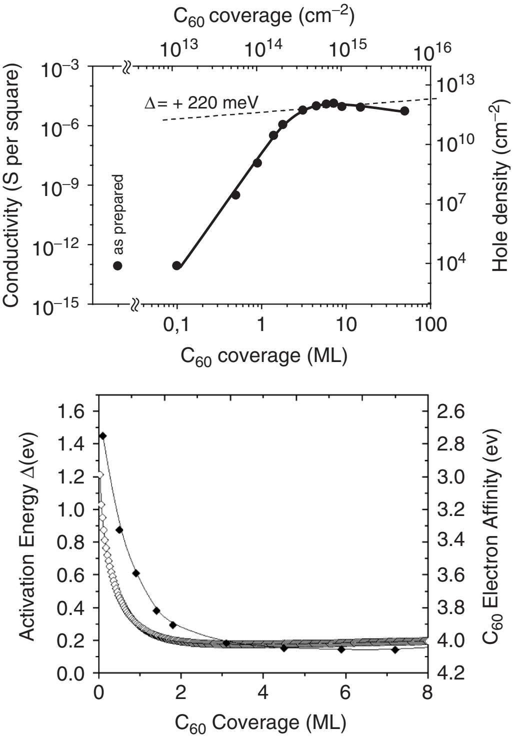

Figure 4.11 Upper panel: Same as Figure 4.10 for a C_{60} sample. The dashed line corresponds to a simulation of the hole density with a fixed activation energy of $\Delta = 0.24\ eV$. The solid line is a fit to the data with a coverage-dependent activation energy. Lower panel: variation of the activation energy Δ, i.e. the energy difference between the LUMO of C_{60} and E_V of diamond, as a function of coverage as it is necessary to describe the C_{60} data above (solid diamonds) and those of Figure 4.10 (open diamonds) in terms of the molecular surface acceptor model. (Adapted from Strobel, Riedel *et al.* 2004)

general phenomenon. In essence, Figure 4.11 shows that it costs about 0.2 eV to transfer an electron from the diamond valence band maximum into the LUMO of a C_{60} layer several monolayers thick, whereas the same transfer costs 1.5 eV if it takes place into an isolated C_{60} molecule. Phrased differently, the electron affinity of C_{60} increases by 1.3 eV when going from a single C_{60} molecule to fullerite, i.e. the C_{60} solid.

The electron affinity is, strictly speaking, the difference of two total energies, namely that of the system in its N-electron ground state $E(N)$ and that of the $N+1$ electron system also in its ground state $E(N+1)$. The difference $E(N) - E(N+1) = \chi$ is a true many-electron quantity that depends on the size of the system. The same holds, of course, for the ionisation energy $I = E(N-1) - E(N)$. For the sake of argument, it is convenient to split the many-electron expression into a difference of one-electron energies ($E_{\mathrm{VAC}} - E_{\mathrm{LUMO}}$ for χ), and a many-body correction that is usually termed the effective correlation energy U. This energy involves the Coulomb interaction of the additional electron brought into the lowest accessible electronic state of the system with all the other electrons already present. As such, U is reduced by the relaxation of the electrons already present. The relaxation in turn depends strongly on the polarizability of the system or, put somewhat less scientifically, how well the electrons can get out of the way in order to reduce their Coulomb repulsion with the new arrival. Clearly, that works better for a solid than for an isolated molecule. Consequently, the effective correlation energy is significantly lower for an electron brought to the conduction band minimum of C_{60} in the solid phase than into the LUMO of an isolated C_{60} molecule. For the molecule, theory gives values between 2.7 and 3.1 eV for the correlation energy whereas an experimental estimate yields a slightly larger value of 3.3 eV (Gunnarson 1997 and references therein). The same quantity for the solid state was found between 0.8 and 1.3 eV, theoretically, and between 1.4 and 1.6 eV experimentally (Gunnarson 1997). The difference $\delta U \approx 1.8 \pm 0.2$ eV in effective correlation energy is in reasonable agreement with the change of 1.3 eV in Δ derived above. In fact, electrons and holes in the transfer doping process have only to be separated across the width of the diamond space charge layer plus the C_{60} layer thickness. This leaves a finite though hard to specify Coulomb energy, by which the 'band offset' energy Δ should be lowered as compared with the estimate obtained from the diamond ionization potential and the C_{60} electron affinity. The remaining Coulomb energy is expected to decrease with increasing C_{60} layer thickness, and the decrease in Δ should indeed be smaller than δU by this difference.

One might ask why the same does not apply to $C_{60}F_{48}$. With reference to Figure 4.10, it is clear that the negative 'activation energy' in this case suffices to achieve a degree of ionization equal to unity. Hence, conductivity and hole density are driven into saturation for coverages well below a monolayer and the question of a solid state related reduction in Δ does not arise. It should be emphasized, finally, that hydrogenation of the diamond surface is necessary. For atomically clean surfaces or oxidized surfaces, the ionization energy of diamond is 1.7 or even 3 eV higher than for the hydrogenated surface (compare Figure 4.4) Hence, the activation energy Δ would reach values of 1.5 or 2.9 eV, much too large to allow even the smallest measurable charge transfer.

At the outset of this section I mentioned that one of the reasons to look for an alternative to the air-induced SC was to find a SC with better reproducibility and stability in view of electronic applications in power and high frequency FETs, for example. For this reason, the thermal stability of the $C_{60}F_x$ layer is of importance as well. Strobel *et al.* have explored this issue (Strobel *et al.* 2006). There are actually two issues: the thermal stability of the

$C_{60}F_x$ layer, and the necessary hydrogen termination on diamond. It has been demonstrated that the hydrogen termination is stable on diamond up to about 700 °C in vacuum (Su and Lin 1998; Cui *et al.* 1999). In contrast, hydrogen chemisorbed on diamond is not stable in air for temperatures exceeding ∼230 °C due to an exchange reaction with oxygen (Mantel *et al.* 2001). Therefore, the thermal stability of the hydrogen termination is the limiting factor for fullerene as well as for air induced SC. Consequently, Strobel *et al.* concentrated on the thermal stability in vacuum. Here, the fullerenes are the limiting factor due to their rather high vapour pressures. In general, the vapour pressure increases with fluorine content and consequently $C_{60}F_{48}$ has the highest vapour pressure (Boltalina and Strauss 2004). The amount that suffices to drive the surface conductivity into saturation (∼0.5 ML) is lost after two weeks *in vacuo* at RT. At the other extreme, thin C_{60} layers require a temperature of about 200 °C for sublimation to commence *in vacuo*. This is significantly more stable than the air induced SC that is lost in vacuo within minutes at temperatures exceeding 60 °C (Riedel *et al.* 2004b).

The first attempt to increase the thermal stability was to cover the $C_{60}F_x$ layer by different dielectrics, such as SiO, Si_3N_4, or CaF_2, in order to prevent evaporation (Strobel *et al.* 2006). Representative results are shown in the upper panel of Figure 4.12, where the evolution of the SC as a function of processing steps is shown for two samples. All start with the hydrogen-terminated surface that exhibits a SC of a few times $10^{-4}\ \Omega^{-1}$. After annealing at 300 °C, the air induced SC is lost and $\sigma_\square$ drops to below $3 \times 10^{-11}\ \Omega^{-1}$, only to recover to a value in excess of $10^{-4}\ \Omega^{-1}$ after $C_{60}F_{48}$ has been evaporated. Subsequently, one sample was protected by thermal evaporation of 100 nm SiO. Both samples retained their SC in air, while the unprotected sample lost it in vacuum at an annealing temperature of 250 °C. In contrast, the SC of the protected sample started to drop significantly only after a 300 °C anneal. Similar results were obtained with protection by CaF_2 and SiO/Si_3N_4 (Strobel *et al.* 2006). An important aspect of this work is that the dielectrics have no effect on the SC.

An entirely different way to achieve higher thermal stability of the fullerene layer is by light- and oxygen-induced polymerization of C_{60}. C_{60} is known to polymerize under pressure at elevated temperatures by cycloaddition reactions (Nunez-Regueiro *et al.* 1995). However, Strobel *et al.* recognized a different path to polymerization that is mediated by oxygen (Ristein *et al.* 2006). The polymerization takes place under 10^{-2} mbar of oxygen and UV illumination by a mercury lamp within about 6 h. The UV illumination most likely serves to create ozone and oxygen radicals, which are much more reactive than O_2. C1s and O1s core level spectra prove that, on average, 1.6 oxygen atoms are bonded to each C_{60}. Assuming bridging ketone configurations for O between the C_{60} cages, this corresponds to an average covalent coordination of 3.2 C–O bonds per C_{60}, indicating the development of an oxygen-linked C_{60} polymer. This is nicely confirmed by photoemission valence-band spectra, which undergo a drastic change of the electronic structure of the C_{60} layer with the topmost occupied states being most affected. Simultaneously, the C_{60} induced SC is not only maintained but its thermal stability is extended to a record 500 °C in ultrahigh vacuum (UHV, $p < 10^{-9}$ mbar) and to 250 °C in air as shown in the lower panel of Figure 4.12. The lower trace represents the conductance of an oxygen-terminated surface that has undergone the same treatment as the hydrogen-terminated one. The lack of SC is proof that even after oxygen-mediated polymerisation, conductance is still via transfer doping requiring the low ionization energy of the hydrogen terminated surface.

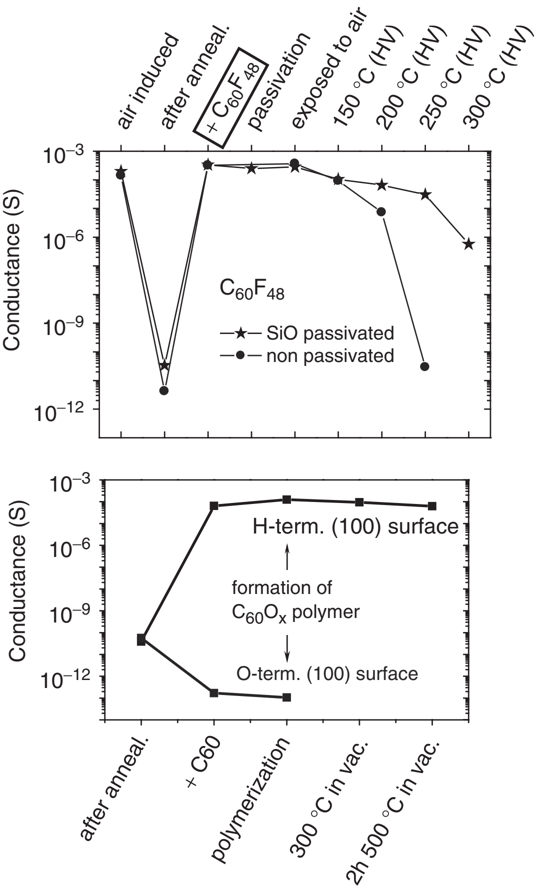

Figure 4.12 Upper panel: Thermal stability of $C_{60}F_{48}$-induced surface conductivity with and without passivation by about 100 nm of SiO as a protecting layer (HV: high vacuum: 10^{-7} mbar). Lower panel: same as upper panel for an oxygen-mediated polymerization of the C_{60} layer. The lack of conductance for an oxygen-terminated diamond surface proves that the surface transfer doping is still active on C (1000):H even after C_{60} polymerization. (Adapted from Strobel, Ristein *et al.* 2006)

In summary, C_{60} and the fluorofullerenes constitute a particularly simple surface acceptor system for hydrogenated diamond. Hole concentration and conductivity are well described in terms of the transfer-doping model as outlined in Section 4.2. There is only one material-specific parameter, namely Δ, the energy difference between the valence band top of hydrogen-terminated diamond and the LUMO of the molecular adlayer that determines the hole concentration as a function of coverage. The range of Δ from −125 meV for $C_{60}F_{48}$ to +1.5 eV for isolated C_{60} molecules follows the trend expected from the respective electron affinities of the (fluoro-)fullerenes. Protective dielectric coatings or oxygen-linked polymerization of C_{60} provide the necessary thermal stability to make the C:H/$C_{60}F_x$ system a viable alternative to the air induced SC as a basis for surface channel FETs based on diamond.

4.4 AIR INDUCED SURFACE CONDUCTIVITY: THE ELECTROCHEMICAL TRANSFER DOPING MODEL

As mentioned in the introduction, the first observation of SC in diamond was one that forms spontaneously in air on hydrogen-terminated surfaces and disappears upon mild annealing. The experiments of Maier *et al.* (Maier *et al.* 2000) and Cui *et al.* (Cui *et al.* 1998) (see Figure 4.1) prove unambiguously that hydrogen is not directly responsible for the hole accumulation but rather serves to lower the electron affinity and thereby the ionization energy of diamond from about 5.9 eV to 4.2 eV. Consequently, an airborne species has to be responsible for the surface doping analogous to the $C_{60}F_x$ discussed in the previous section. With areal hole densities of 10^{12} to 10^{13} cm^{-2}, the acceptor level (LUMO) has to coincide with the valence band maximum of diamond or, phrased differently, the electron affinity of the acceptor species has to be about 4.2 eV or higher. Electron affinities of common atmospheric molecules (N_2, O_2, H_2O, CO_2, etc.) are below 2.3 eV and even the most electronegative halogen radical, chlorine, has an electron affinity of 'only' 3.6 eV, insufficient to account for the hole density (Lide 1996). In this situation, Maier *et al.* suggested solvated ions within a thin aqueous wetting layer that forms spontaneously on all surfaces in air as surface acceptors. The doping mechanism no longer involves a simple electron transfer from diamond to an adsorbed molecule. Instead, two partial redox reactions lead to the required charge exchange. One half-reaction involves diamond:

$$\text{diamond} \leftrightarrow \text{diamond}^{\,2+(\text{holes})} + 2e^- \tag{4.21a}$$

the other the electrolyte on the surface:

$$2H_3O^+ + 2e^- \leftrightarrow H_2 + 2H_2O \tag{4.21b}$$

yielding the overall redox reaction

$$\text{diamond} + 2H_3O^+ \leftrightarrow \text{diamond}^{\,2+(\text{holes})} + H_2 + 2H_2O \tag{4.22}$$

The reduction of hydronium to H_2 was the reaction suggested by Maier *et al.* (2000) but others have been proposed subsequently that will be considered below. The half reaction involving diamond corresponds formally to the oxidation of diamond. In contrast to the common electrolytic oxidation of metals where positive metal ions go into solution, diamond is not corroded; on the contrary, the positive charge remains and contributes to the hole accumulation layer that forms below the diamond surface.

The direction in which the redox reaction (Equation 4.22) proceeds depends on the electrochemical potentials μ_e in the two subsystems. In diamond, μ_e is the Fermi level $E_{F,d}$ which is referred to the band edges E_V and E_C. In the electrolyte it is the electrochemical potential μ_e appropriate for the particular redox reaction under consideration. In electrochemistry μ_e is referred to the redox potential μ_0 of the standard hydrogen electrode (SHE). Aside from a sign convention for the charge to be exchanged, both quantities $E_{F,d}$ and μ_e, refer to the same physical property and can thus be placed on a common scale. In Figure 4.13, the band diagram of diamond plotted on the so-called 'physical scale' has been aligned with the electrochemical scale using the vacuum level E_{VAC} as the common

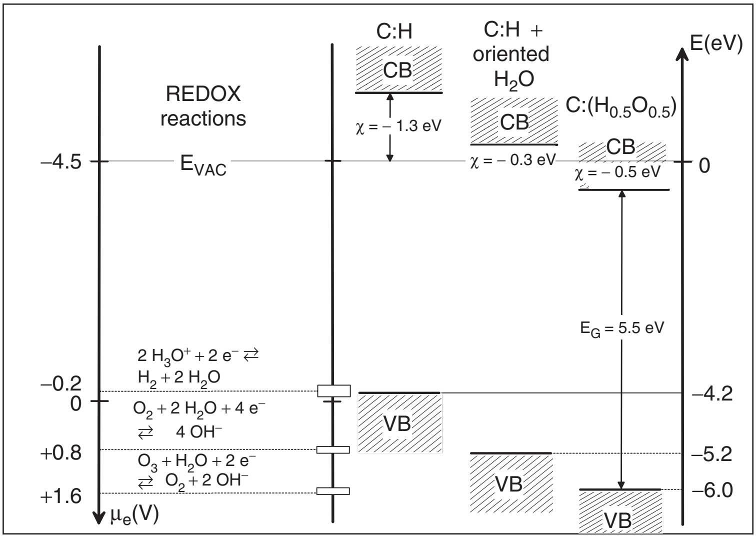

Figure 4.13 Electrochemical potential μ_e and the band energies of hydrogenated diamond, hydrogenated diamond with an oriented water layer on top, and diamond with a mixed termination of equal amounts of hydrogen and oxygen referred to the vacuum level E_{VAC} as the common reference energy. Also given are the electrochemical potentials of redox reactions that have been considered in connection with the air induced surface conductivity of diamond

reference level by adopting the recommended value of −4.44 eV for the SHE chemical potential relative to E_{VAC} on the physical scale (Trasatti 1986; Sato 1998)].

Electrochemical potentials depend on the concentrations of the participating species according to Nernst's equation. For a simple redox reaction:

$$n \cdot OX + ze^- \rightleftarrows m \cdot RED \tag{4.23}$$

where n, m are the number of participating molecules and z the number of electrons exchanged, Nernst's equation reads:

$$\mu = \mu_s - \frac{k_B T}{z} \cdot \ln\left[\frac{([OX]/[OX]_s)^n}{([RED]/[RED]_s)^m}\right] \tag{4.24}$$

The square brackets denote the concentrations of the oxidized and reduced species, respectively, and the index s refers to 'standard' conditions, i.e. to room temperature and standard concentrations (1 mol/kg for species in solution and 1 bar partial pressure for species participating from the gas phase in equilibrium with the electrolyte). The sign in Equation 4.24 has been adapted to the 'physical scale' of Figure 4.13, i.e. changes in μ are appropriate for electrons and are thus opposite to those in standard electrochemistry texts where the exchange of positive charges are considered. Applied to the hydronium reduction, Equation (4.24) reads:

$$\mu = \mu_0 - \frac{k_B T}{2} \ln\left[\frac{\left([H_3O^+]/[H_3O^+]_{SHE}\right)^2}{[H_2]/[H_2]_{SHE}}\right] \tag{4.25}$$

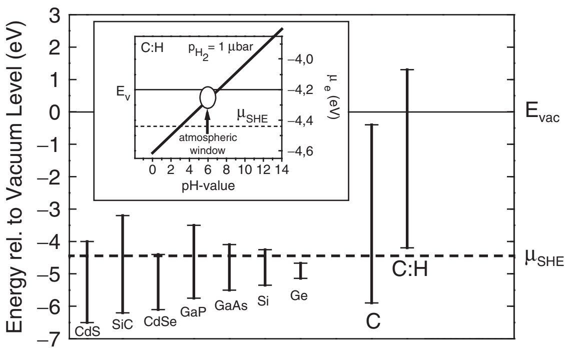

Figure 4.14 Band gaps and band edge energies of common semiconductors and of bare and hydrogen-terminated diamond relative to the vacuum level E_{VAC}. The inset shows the variation in the electrochemical potential μ_e of the H_3O^+/H_2 redox couple as a function of pH according to Nernst's equation. μ_{SHE} and E_V refer to the electrochemical potential of the standard hydrogen electrode and the valence band edge of hydrogenated diamond, respectively

where $\mu_o = -4.44$ eV is the chemical potential of the SHE and $[H_3O^+]_{SHE}$ and $[H_2]_{SHE}$ are the corresponding hydronium and hydrogen concentrations, respectively. The H_2O concentration does not enter in Equation (4.25) because, on account of its large volume, it effectively remains constant during the redox reaction. Replacing $[H_2]$ by the H_2 partial pressure p_{H_2} and $[H_3O^+]$ by the pH value of the aqueous wetting layer yields at RT:

$$\mu_e = -4.44\ eV + \frac{58\ meV}{2}\left[2pH + \log\left(\frac{p_{H_2}}{bar}\right)\right] \tag{4.26}$$

In the inset of Figure 4.14, this chemical potential is plotted as a function of pH for a realistic hydrogen partial pressure of 10^{-6} bar. Assuming a water layer with a pH between 5 and 7 due to dissolved CO_2, yields values between −4.2 and −4.3 eV for the chemical potential μ_e of the hydronium-redox couple. The valence band maximum E_V of hydrogen-terminated diamond falls into that window. Hence, for a Fermi level in diamond above E_V, an electron transfer from diamond into the electrolyte is thermodynamically possible. It comes to a halt when E_F and μ_e coincide or, referring to Figure 4.14, if E_F coincides with $E_V = -4.2$ eV to within a few tens of a meV. According to the discussion in Section 4.2 and Figures 4.6 and 4.7, this corresponds to a situation where the observed areal hole density of $10^{12} \ldots 10^{13}$ cm^{-2} is to be expected. Hence, the electrochemical transfer-doping model of Maier *et al.* appears to be a viable explanation for the air induced SC of diamond. A schematic depicting the hydrogen-terminated diamond surface with the wetting layer, and three band diagrams illustrating the evolution of the band bending as a function of charge transfer, are given in Figure 4.15. Figure 4.14 also provides an explanation as to why the air induced SC is only observed in hydrogenated diamond and in no other semiconductor; no other has a valence band maximum even close to μ_O.

In one instance, the Fermi level was found to lie 0.7 eV below the valence band maximum using Kelvin probe experiments (Rezek *et al.* 2003), and the upward subsurface band bending was unambiguously confirmed by Takeuchi *et al.* on the basis of yield

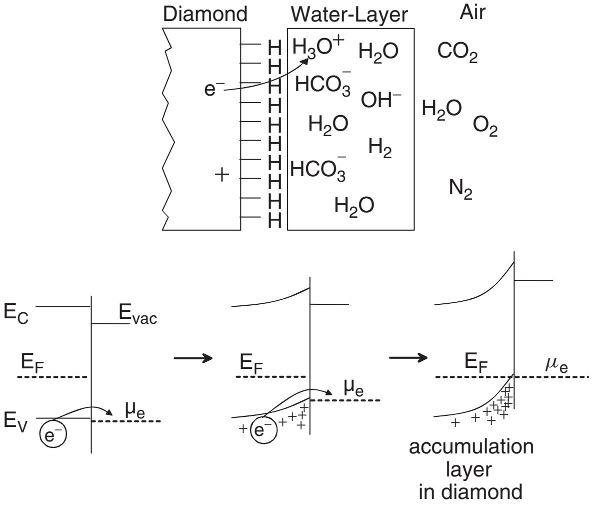

Figure 4.15 Upper panel: schematic of the triple layer diamond–water–atmosphere and the molecular species that are responsible for the surface conductivity of diamond according to the electrochemical transfer doping model of Maier *et al.* Lower panel: schematic band diagrams before, during, and after equilibration between diamond and the water layer

experiments (Takeuchi *et al.* 2003). According to Equation (4.22) and as indicated in Figure 4.15, each positive charge in the hole accumulation layer is compensated by an anion, HCO_3^-, that is no longer balanced in the electrolyte by H_3O^+ after the reduction of $2H_3O^+$ to H_2. In a chemical sense, diamond and HCO_3^- form a special kind of salt while in the language of semiconductor physics HCO_3^- is the ionized acceptor. Consequently, once the charge transfer is completed and the thermodynamic equilibrium is established, the water layer is no longer needed. This is nicely confirmed by two types of experiment. In one, the acceptors are simply 'washed off' under running water and the SC vanishes, only to recover after a while when the sample is removed from the tap. In the other experiment (see Figure 4.16) a conducting diamond is brought into vacuum and the conductivity is fully maintained up to about 60 °C, i.e. under conditions where water is long evaporated from the diamond surface *in vacuo*. At around 100 °C the anions start to desorb as well and the SC is completely lost after a 150 °C anneal. When the diamond is brought back to air after the 150 °C anneal, the wetting layer reforms, the redox reaction commences, and the SC is fully recovered (Riedel *et al.* 2004b). Also, in air the thermal stability of the SC is not limited by that of the water layer but rather by the deterioration of the hydrogen termination, which disappears at temperatures above 230 °C due to a reaction with oxygen, as has been demonstrated spectroscopically by Mantel *et al.* (Mantel *et al.* 2001).

The influence of gas exposures right after plasma hydrogenation was explored by Foord *et al.* (Foord *et al.* 2002) and by Snidero *et al.* (Snidero *et al.* 2003) who found that SC is only observed if water vapour and air or acidic vapours are both admitted to the freshly hydrogenated surface, whereas each ingredient alone has no effect on the conductivity. This is, of course, expected for the electrolytic transfer-doping model.

The relative alignment of chemical potentials determines in principle only the direction of the charge transfer and its eventual equilibrium. Even if thermodynamically allowed, charge exchange may be kinetically hindered. I have already pointed out in connection

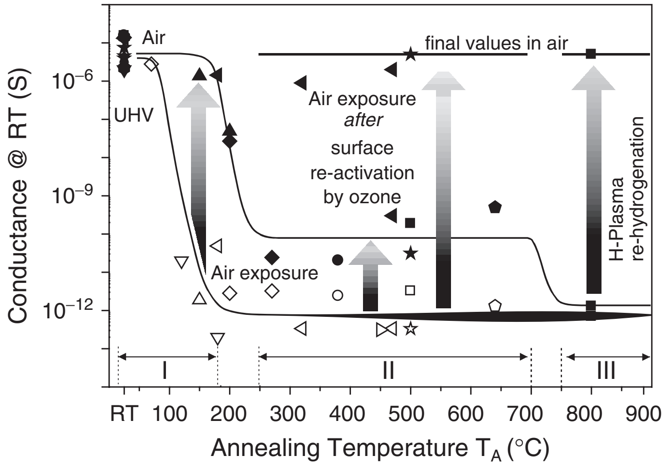

Figure 4.16 Loss and recovery of surface conductivity of diamond after thermal annealing in ultra high vacuum. Each annealing step starts with a sample that shows full SC in air. There are three distinct temperature regimes that are marked by roman numerals at the bottom. In regime I ($T_A <\sim 150\,^\circ C$), the SC is recovered fully after the sample is reexposed to air. In regime II ($250\,^\circ C < T_A < 700\,^\circ C$) exposure to air alone leads only to a partial recovery of SC. Only after the samples have been exposed to ozone prior to air is the SC fully recovered. This observation has been taken as evidence that oxygen-related catalytic centres are required in addition to hydrogen to enable charge transfer in finite times. In regime III ($T_A > 700\,^\circ C$), the SC is irretrievably lost due to the loss of hydrogen termination. (Adapted from Riedel, Ristein *et al.* 2004)

with Figure 4.1, the rather long time it takes for the full SC to develop after a hydrogenated sample is exposed to air. This effect was investigated in more detail by Riedel *et al.* and Snidero *et al.* (Riedel *et al.* 2004b; Snidero, *et al.* 2004). Comprehensive investigations of the SC recovery after annealing *in vacuo* (see Figure 4.16) have indicated that the electron transfer between the solvated ions in the wetting layer and diamond may require oxygen-related catalytic centres on diamond, with concentrations that lie well below 10^{-3} monolayers and are thus difficult to identify spectroscopically (Riedel *et al.* 2004b). Since these centres are created most effectively under UV illumination in the presence of atmospheric oxygen, as demonstrated by the same authors, they may also account for reports of the beneficial action of UV light for the SC of diamond [(Snidero *et al.* 2003).

In the original electrochemical transfer doping model of Maier *et al.*, the H_3O^+/H_2 redox couple was chosen as the electron acceptor because its chemical potential when referred to the vacuum level matches the ionization energy of the perfectly hydrogen-terminated diamond surface (4.2 eV), as discussed in Section 4.2.1. There is evidence, however, that other redox couples might actually be active when these ideal conditions are not met. Because oxygen termination increases the electron affinity and the ionization energy of diamond (Maier *et al.* 2001), a partial oxidation of an otherwise hydrogenated surface will render the hydronium/hydrogen couple ineffective as an acceptor in the framework of the electrochemical doping model. Upon tuning the ionization energy of diamond deliberately from 4.2 eV to 7.2 eV by replacing successively more of the surface hydrogen by oxygen, Riedel *et al.* identified a second redox couple, namely $O_3/O_2 + OH^-$, with a chemical potential of -6.1 eV relative to E_{VAC} for pH 7 (see Figure 4.13) that is able to

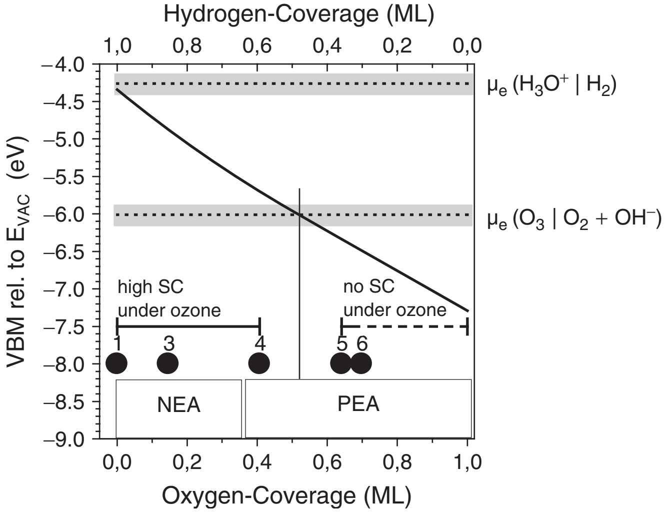

Figure 4.17 Tuning the ionization energy of diamond between 4.2 and 7.2 eV by successively replacing hydrogen with oxygen as surface termination. In an ozone-rich atmosphere, SC is observed for ionization energies as high as 5.7 eV (data point 4) which corresponds to a positive electron affinity (PEA) of +0.2 eV. The redox reaction believed to be active is $O_3 + H_2O + 2e^- \rightleftarrows O_2 + 2OH^-$ with an electrochemical potential corresponding to −6 eV on the physical scale. (Adapted from Riedel, Ristein *et al.* 2004)

maintain SC on diamond with a mixed H/O coverage of up to about 1:1 in an ozone-rich atmosphere as shown in Figure 4.17 (Riedel *et al.* 2004).

Another factor that might render the hydronium/hydrogen couple ineffective is a layer of oriented water molecules that forms at the diamond/water interface. Piantanida *et al.* have estimated that the contribution of the oriented H_2O dipoles increases the ionization energy by 0.8 eV to about 5.0 eV when diamond is brought into contact with water (Piantanida *et al.* 2001). Differential capacitance measurements on the interface of hydrogenated diamond and electrolytes of known electrochemical potentials (Mott–Schottky measurements) confirm this notion and give a slightly higher ionization energy of 5.2 eV for C:H in contact with water (compare Figure 4.13) (Pleskov *et al.* 1987). Under these circumstances, the hydroxyl/oxygen couple has been suggested as being yet another redox reaction responsible for SC on diamond (Foord *et al.* 2002, Chakrapani *et al.* 2007):

$$O_2 + 2H_2O + 4e^- \rightleftarrows 4OH^-, \tag{4.27}$$

where the electrons again come from diamond and result in the hole conducting layer.

The corresponding chemical potential for an oxygen partial pressure of 0.2 bar and a pH between 5 and 7 is marked in Figure 4.13 with $\mu_e \approx -5.3$ eV.

In a series of brilliantly devised experiments employing diamond nanocrystals Angus *et al.* (Chakrapani *et al.* 2007) were able to confirm all predictions of the electrochemical transfer doping model provided the hydroxyl/oxygen redox couple is assumed to be active. On account of the large surface area of the nanocrystals, the macroscopic chemical effects rather than the conductivity could be followed as a function of charge exchange. In this way, the increase in pH as the reaction in Equation (4.27) proceeds, as well as the concomitant depletion of dissolved oxygen, has been confirmed. It thus appears that the hydroxyl/oxygen redox couple is the more realistic candidate for the air-induced SC of diamond. The counter charges of the holes are then provided by the hydroxyl ions produced according to Equation (4.27).

Note added to proof

The controversy over whether the hydrogen-hydronium couple or the oxygen-hydroxyl couple is responsible for the charge transfer leading to the hole accumulation in diamond was recently addressed by Zhang et al. (Zhang et al. 2008). They measured the open circuit voltage of hydrogenated diamond immersed in an aqueous electrolyte vs. Ag/AgCl as a function of pH. The value for the open circuit voltage lies between that of the reversible oxygen potential and the reversible hydrogen potential. In other words, both redox couples contribute to the electron exchange between hydrogen-terminated diamond electrodes and an aqueous electrolyte. The very low initial exchange current densities of the order of 10^{-15} *A/cm*^{2} *furthermore account for the long equilibration times that are necessary to establish SC in diamond. In an accompanying paper (Ristein et al. 2008) the same authors analyzed the transfer characteristics of a diamond-based solution-gate field effect transistor and arrive among other things at a value of* -0.50 ± 0.02 *eV for the electron affinity of hydrogenated diamond in an aqueous electrolyte. The increase by 0.8 eV compared to UHV is in excellent agreement with the estimate of Piantanida et al. for the contribution of an oriented* H_2O *layer to the potential step at the hydrogenated diamond surface in contact with water. (Piantanida et al. 2001)*

Zhang, Wenjing, Jürgen Ristein, Lothar Ley (2008). Hydrogen-terminated diamond electrodes. II. Redox activity. Physical Review E78: 041603

Ristein, Juergen, Wenjing Zhang, Lothar Ley (2008). Hydrogen-terminated diamond electrodes. I. Charges, potentials, and energies. Physical Review E 78: 041602

ACKNOWLEDGEMENTS

I would like to thank my former and current coworkers and students J.B. Cui, F. Maier, B. Mantel, M. Stammler, M. Riedel, P. Strobel, and especially J. Ristein for years of stimulating and successful cooperation. This review is the essence of our common endeavour in the field of diamond surface conductivity. I am particularly indebted to J. Angus for generously making his experimental material available to me prior to publication.

Last but not least, I would like to thank the members of the Institute of Advanced Studies at LaTrobe University, Melbourne, for their generous hospitality during the last stages of this work.

REFERENCES

Albin, S. and L. Watkins (1990). Electrical properties of hydrogenated diamond. *Applied Physics Letters* **56**(15): 1454–1456.

Aleksov, A., A. Denisenko, *et al*. (2002). RF performance of surface channel diamond FETs with sub-micron gate length. *Diamond and Related Materials* **11**(3–6): 382–386.

Aoki, M. and H. Kawarada (1994). Electric properties of metal/diamond interfaces utilising hydrogen-terminated surfaces of homoepitaxial diamonds. *Japanese Journal of Applied Physics Part 2–Letters & Express Letters* **33**(5B): L708–L711.

Bandis, C. and B. B. Pate (1995). Photoelectric-emission from negative-electron-affinity diamond(111) surfaces – exciton breakup versus conduction-band emission. *Physical Review B* **52**(16): 12056–12071.

Boltalina, O. V. and S. H. Strauss (2004). *Encyclopedia of Nano-Science and Nanotechnology*: DOI 10.1081/EENN 120013608.

Chakrapani, V., JC Angus *et al.* (2007). Charge transfer equilibria between diamond and an aqueous oxygen electrochemical redox couple. Science **318** (5855): 1424–1430.

Collins, A. T. (1994). Breakdown field and saturated carrier velocity in diamond. *Properties and Growth of Diamond*. G. Davies. London, INSPEC: 288.

Cui, J. B., J. Ristein and L. Ley (1998). Electron affinity of the bare and hydrogen covered single crystal diamond (111) surface. *Phys. Rev. Lett.* **81**: 429–432.

Cui, J. B., J. Ristein, *et al*. (1999). Low-threshold electron emission from diamond. *Physical Review B* **60**(23): 16135–16142.

Foord, J. S., C. H. Lau, *et al*. (2002). Influence of the environment on the surface conductivity of chemical vapor deposition diamond. *Diamond and Related Materials* **11**(3–6): 856–860.

Gildenblat, G. S., S. A. Grot, *et al*. (1991). The electrical properties and device applications of homoepitaxial and polycrystalline diamond films. *Proceedings of the IEEE* **79**(5): 647–668.

Gluche, P., A. Aleksov, *et al*. (1997). Diamond surface-channel FET structure with 200 V breakdown voltage. *IEEE Electron Device Letters* **18**(11): 547–549.

Goss, J. P., B. Hourahine, *et al*. (2001). p-type surface doping of diamond: a first-principles study. *Journal of Physics–Condensed Matter* **13**(40): 8973–8978.

Grot, S. A., G. S. Gildenblat, *et al*. (1990). The effect of surface treatment on electrical properties of metal contacts to boron doped homoepitaxial diamond films. *IEEE Electron Device Letters* **11**: 100–102.

Gunnarson, O. (1997). Superconductivity in fullerides. *Review of Modern Physics* **69**: 575–606.

Haddon, R. C., A. S. Perel, *et al*. (1995). C-60 thin-film transistors. *Applied Physics Letters* **67**(1): 121–123.

Hayashi, K., S. Yamanaka, *et al*. (1996). Study of the effect of hydrogen on transport properties in chemical vapor deposited diamond films by Hall measurements. *Applied Physics Letters* **68**(3): 376–378.

Hayashi, K., S. Yamanaka, *et al*. (1997). Investigation of the effect of hydrogen on electrical and optical properties in chemical vapor deposited on homoepitaxial diamond films. *Journal of Applied Physics* **81**(2): 744–753.

Himpsel, F. J., J. A. Knapp, *et al*. (1979). Quantum photoyield of diamond(111) – a stable negative-affinity emitter. *Physical Review B* **20**(2): 624.

Jiang, N. and T. Ito (1999). Electrical properties of surface conductive layers of homoepitaxial diamond films. *Journal of Applied Physics* **85**(12): 8267–8273.

Jin, C., R. L. Hettich, *et al*. (1994). Attachment of two electrons to $C_{\{60\}}F_{\{48\}}$: Coulomb barriers in doubly charged anions. *Physical Review Letters* **73**(21): 2821.

Kasu, M., K. Ueda, *et al*. (2005). 2W/mm output power density at 1 GHz for diamond FETs. *Electronics Letters* **41**(22): 1249–1250.

Kawarada, H., M. Aoki, *et al*. (1994). Enhancement mode metal-semiconductor field effect transistors using homoepitaxial diamonds. *Applied Physics Letters* **65**(12): 1563–1565.

Kawarada, H., Y. Araki, *et al*. (2001). Electrolyte-solution-gate FETs using diamond surface for biocompatible ion sensors. *Physica Status Solidi A – Applied Research* **185**(1): 79–83.

Landstrass, M. I. and K. V. Ravi (1989a). Hydrogen passivation of electrically active defects in diamond. *Applied Physics Letters* **55**: 1391.

Landstrass, M. I. and K. V. Ravi (1989b). Resistivity of chemical vapor deposited diamond films. *Applied Physics Letters* **55**: 975.

Lide, D. R. (Ed.) (1996). *CRC Handbook of Chemistry and Physics*. New York, CRC Press, Inc.

Lof, R. W., M. A. van Veenendaal, *et al*. (1992). Band gap, excitons, and Coulomb interaction in solid $C_{\{60\}}$. *Physical Review Letters* **68**(26): 3924.

Loh, K., X. Xie, *et al*. (2002). A spectroscopic study of the negative electron affinity of cesium oxide-coated diamond (111) and theoretical calculation of the surface density-of-states on oxygenated diamond (111) *Diamond and Related Materials* **11**: 1379–1384

Looi, H. J., R. B. Jackman, *et al*. (1998). High carrier mobility in polycrystalline thin film diamond. *Applied Physics Letters* **72**(3): 353–355.

Maier, F., M. Riedel, *et al*. (2000). Origin of surface conductivity in diamond. *Physical Review Letters* **85**(16): 3472–3475.

Maier, F., J. Ristein, *et al*. (2001). Electron affinity of plasma-hydrogenated and chemically oxidized diamond (100) surfaces. *Physical Review B* **64**(16): 165411.

Maki, T., S. Shikama, *et al*. (1992). Hydrogenation Effect of Single Crystal Diamond Surface. *Japanese Journal of Applied Physics Part 2 – Letters & Express Letters* **31**(10A): L1446–L1449.

Mantel, B. F., M. Stammler, *et al*. (2001). The correlation between surface conductivity and adsorbate coverage on diamond as studied by infrared spectroscopy. *Diamond and Related Materials* **10**(3–7): 429–433.

Mönch, W. (1995). *Semiconductor Surfaces and Interfaces*. Berlin, Springer-Verlag.

Nunez-Regueiro, M., L. Marques, *et al*. (1995). Polymerized fullerite structures. *Physical Review Letters* **74**(2): 278–281.

Pankove, J. I. and N. M. Johnson (Eds.) (1991). *Hydrogen in Semiconductors. Semiconductors and Semimetals*. Boston, Academic Press.

Piantanida, G., A. Breskin, *et al*. (2001). Effect of moderate heating on the negative electron affinity and photoyield of air-exposed hydrogen-terminated chemical vapor deposited diamond. *Journal of Applied Physics* **89**(12): 8259–8264.

Pickett, W. E. (1994). Negative electron affinity and low work function surface: cesium on oxygenated diamond (100). *Physical Review Letters* **73**(12): 1664 LP–1667.

Pleskov, Y. V., A. Y. Sakharova, *et al*. (1987). *Journal of Electroanalytical Chemistry* **228**: 19.

Rezek, B., C. Sauerer, *et al*. (2003). Fermi level on hydrogen terminated diamond surfaces. *Applied Physics Letters* **82**(14): 2266–2268.

Rezek, B., H. Watanabe, *et al*. (2006a). High carrier mobility on hydrogen terminated ⟨100⟩ diamond surfaces. *Applied Physics Letters* **88**(4): 042110.

Rezek, B., H. Watanabe, *et al*. (2006b). Ion-sensitive field effect transistor on hydrogenated diamond. *Diamond and Related Materials* **15**(4–8): 673–677.

Ri, S. G., T. Mizumasa, *et al*. (1995). Formation mechanism of p-type surface conductive layer on deposited diamond films. *Japanese Journal of Applied Physics Part 1–Regular Papers Brief Communications & Review Papers* **34**(10): 5550–5555.

Ri, S. G., K. Tashiro, *et al*. (1999). Hall effect measurements of surface conductive layer on undoped diamond films in NO2 and NH3 atmospheres. *Japanese Journal of Applied Physics Part 1-Regular Papers Brief Communications & Review Papers* **38**(6A): 3492–3496.

Riedel, M., J. Ristein, *et al*. (2004a). The impact of ozone on the surface conductivity of single crystal diamond. *Diamond and Related Materials* **13**(4–8): 746–750.

Riedel, M., J. Ristein, *et al*. (2004b). Recovery of surface conductivity of H-terminated diamond after thermal annealing in vacuum. *Physical Review B* **69**(12).

Ristein, J. (2004). Structural and electronic properties of diamond surfaces. *Thin Film Diamond*. J. R. C. E. Nebel. Amsterdam, Elsevier. **2:** 37–93.

Ristein, J. (2006). Surface transfer doping of diamond. *Journal of Physics D-Applied Physics* **39**(4): R71–R81.

Ristein, J., M. Riedel, *et al*. (2001). Surface conductivity of diamond as a function of nitrogen doping. *Physica Status Solidi A – Applied Research* **186**(2): 249–256.

Ristein, J., M. Riedel, *et al*. (2002). Surface conductivity of nitrogen-doped diamond. *Diamond and Related Materials* **11**(3–6): 359–364.

Ristein, J., M. Riedel, *et al*. (2004). Electrochemical surface transfer doping – The mechanism behind the surface conductivity of hydrogen-terminated diamond. *Journal of the Electrochemical Society* **151**(10): E315–E321.

Ristein, J., W. Stein, *et al*. (1997). Defect spectroscopy and determination of the electron diffusion length in single crystal diamond by total photoelectron yield spectroscopy. *Physical Review Letters* **78**(9): 1803–1806.

Ristein, J., P. Strobel, *et al*. (2006). Surface conductivity of diamond: a novel doping mechanism. *Advanced Science and Technology* **48**: 93–102.

Rutter, M. J. and J. Robertson (1998). Ab initio calculation of electron affinities of diamond surfaces. *Physical Review B* **57**(15): 9241–9245.

Sato, N. (1998). *Electrochemistry at Metal and Semiconductors Electrodes*. Amsterdam, Elsevier.

Seah, M. P. and W. A. Dench (1979). *Surface and Interface Analysis.* **1**: 2.

Shirafuji, J. and T. Sugino (1996). Electrical properties of diamond surfaces. *Diamond and Related Materials* **5**(6–8): 706–713.

Snidero, E., D. Tromson, *et al*. (2003). Influence of the postplasma process conditions on the surface conductivity of hydrogenated diamond surfaces. *Journal of Applied Physics* **93**(5): 2700–2704.

Snidero, E., D. Tromson, *et al*. (2004). Dynamical aspects of the surface layer build up on diamond and improvement of the conductivity stability. *Diamond and Related Materials* **13**(4–8): 761–764.

Song, K. S., M. Degawa, *et al*. (2004). Surface-modified diamond field-effect transistors for enzyme-immobilized biosensors. *Japanese Journal of Applied Physics Part 2 – Letters & Express Letters* **43**(6B): L814–L817.

Song, K. S., T. Hiraki, *et al*. (2007). Miniaturized diamond field-effect transistors for application in biosensors in electrolyte solution. *Applied Physics Letters* **90**(6).

Sque, S. J., R. Jones, *et al*. (2005). First-principles study of C-60 and C60F36 as transfer dopants for p-type diamond. *Journal of Physics – Condensed Matter* **17**(2): L21–L26.

Strobel, P. Private communication.

Strobel, P., M. Riedel, *et al*. (2004). Surface transfer doping of diamond. *Nature* **430**(6998): 439–441.

Strobel, P., M. Riedel, *et al*. (2005). Surface transfer doping of diamond by fullerene. *Diamond and Related Materials* **14**(3–7): 451–458.

Strobel, P., J. Ristein, *et al*. (2006). Surface conductivity induced by fullerenes on diamond: passivation and thermal stability. *Diamond and Related Materials* **15**(4–8): 720–724.

Su, C. and J. C. Lin (1998). Thermal desorption of hydrogen from the diamond C(100) surface. *Surface Science* **406**(1–3): 149–166.

Tachiki, M., H. Seo, *et al*. (2002). Fabrication of single-hole transistors on hydrogenated diamond surface using atomic force microscope. *Applied Physics Letters* **81**(15): 2854–2856.

Takeuchi, D., C. E. Nebel, *et al*. (2006). Photoelectron emission properties of hydrogen terminated intrinsic diamond. *Journal of Applied Physics* **99**: 086102.

Takeuchi, D., M. Riedel, *et al*. (2003). Surface band bending and surface conductivity of hydrogenated diamond. *Physical Review B* **68**(4).

Topping, J. (1927). *Proc. R. Soc. London* **A114**: 67.

Trasatti, S. (1986). The absolute electrode potential: an explanatory note. *Pure and Applied Chemistry* **58**(7): 955–966.

Tsugawa, K., K. Kitatani, *et al*. (1999). High-performance diamond surface-channel field-effect transistors and their operation mechanism. *Diamond and Related Materials* **8**(2–5): 927–933.

Ueda, K., M. Kasu, *et al*. (2006). Characterization of high-quality polycrystalline diamond and its high FET performance. *Diamond and Related Materials* **15**(11–12): 1954–1957.

Umezawa, H., K. Tsugawa, *et al*. (1999). high-performance diamond metal-semiconductor field-effect transistor with 1micrometer gate length. *Japanese Journal of Applied Physics Part 2 – Letters & Express Letters* **38**(11A): L1222–L1224.

Vidali, G., M. W. Cole, *et al*. (1983). Helium as a probe of the (111) surface of diamond. *Physical Review Letters* **51**(2): 118.

Wang, Y. M., K. W. Wong, *et al*. (2000). Recent studies on diamond surfaces. *Diamond and Related Materials* **9**(9–10): 1582–1590.

Yang, J. H., K. S. Song, *et al*. (2006). Characterization of direct immobilized probe DNA on partially functionalized diamond solution-gate field-effect transistors. *Japanese Journal of Applied Physics Part 2 – Letters & Express Letters* **45**(42–45): L1114–L1117.

Yang, S. H., C. L. Pettiette, *et al*. (1987). UPS of buckminsterfullerene and other large clusters of carbon. *Chemical Physics Letters* **139**(3–4): 233–238.

Yang, W. S. and R. J. Hamers (2004). Fabrication and characterization of a biologically sensitive field-effect transistor using a nanocrystalline diamond thin film. *Applied Physics Letters* **85**(16): 3626–3628.

Zhang, Z., M. Wensell, *et al*. (1995). Surface-structures and electron-affinities of bare and hydrogenated diamond C(100) surfaces. *Physical Review B* **51**(8): 5291–5296.

5 Recent Progress in the Understanding of CVD Growth of Diamond

J.E. BUTLER

Chemistry Division, Naval Research Laboratory, Washington DC 20375, USA

A. CHEESMAN AND M.N.R. ASHFOLD

School of Chemistry, University of Bristol, Bristol UK BS8 1TS

5.1 Introduction 103
5.2 Gas-phase chemistry 104
5.3 Modeling of MW activated gas mixtures 105
5.4 Optical diagnosis of MW activated gas mixtures 108
5.5 Surface chemical growth mechanisms 108
  5.5.1 Insertion into dimer reconstruction 111
  5.5.2 Insertions across dimer troughs 112
  5.5.3 Etching 114
  5.5.4 Migration 115
5.6 Large growth models 117
5.7 Summary 120
Acknowledgements 120
References 121

5.1 INTRODUCTION

Diamond growth by chemical vapor deposition (CVD), e.g. growth from low pressure gases, has been reported [1, 2] since the mid-Twentieth century (see also Ref. 16 in [3]). It became an active and extensive area of research beginning in the 1980s, leading to the industrial manufacture and use of diamond materials in many applications. There are many summary and review articles on the growth of diamond by CVD in the literature [3–20]. This overview focuses on 'recent progress' that have appeared since the extensive chapter on the 'Theory of Diamond Chemical Vapor Deposition' by Goodwin and Butler

CVD Diamond for Electronic Devices and Sensors Edited by Ricardo S. Sussmann
© 2009 John Wiley & Sons, Ltd. ISBN: 978-0-470-06532-7

(G&B) in 1997 [11]. In addition, many of the previous reviews are worth your attention [3, 4, 7, 8, 11, 16].

The focus of this review is primarily the growth of diamond on diamond single-crystal surfaces, ignoring the spontaneous formation of diamond nuclei, since the vast majority of growth of diamond materials by CVD is on diamond particles seeded on a substrate with dimensions from nanometers to centimeter(s). Whether the resultant diamond material is classified as ultrananocrystalline (UNCD), nanocrystalline (NCD), microcrystalline (MCD), or single crystal, the local chemical environment around a growth site, e.g. within 100s of atoms of the growth site, has a single crystal structure (including possible structural defects such as twin planes, etc.). We shall not address the issues of spontaneous nucleation of diamond seeds on a nondiamond surface in this review, but refer readers to References [9, 18, 21].

At the time of the G&B review [11] the 'standard model' of diamond CVD [8, 22] was already well developed. In this model, atomic hydrogen plays a critical role in the gas phase and surface chemical reactions, stabilizing the diamond surface with CH bonds, and creating reactive hydrocarbon species and surface radical sites where the reactive hydrocarbon species can attach. This model was based on *in situ* diagnostics of the chemical species in the growth environment, measurements of the surface chemistry and structure *ex situ*, and extensive previous research and understanding of organic chemistry. The 'standard' model has worked extremely well in explaining most of the general features of diamond CVD. In the 'standard' model, the hydrogen atoms are made either by thermal dissociation on hot surfaces ($>1800\,^\circ$C), e.g. on a hot filament (HF) of W or Ta, or in low pressure plasmas, e.g. a microwave (MW) excited plasma, by various processes such as electron impact excitation or collisional energy transfer. The reactive H atoms are subsequently lost to reaction at walls and surfaces, reactions with the gaseous hydrocarbon reactants, and homogeneous recombination. The rate of the carbon coated wall (or surface) reactions is highly dependant on temperature, ranging from very low (*ca* 0.001) on cold surfaces (<600 K) to a value of ~ 0.16 estimated for the heterogeneous recombination coefficient, γ_H, (defined as the ratio of the H atom loss rate to the overall collision rate) on a CVD diamond surface at $T_{sub} \sim 1200$ K [23].

5.2 GAS-PHASE CHEMISTRY

Methane is commonly used as the reactant gas, but as will be seen, it does not really matter what the starting hydrocarbon is. The H atoms present in the gas phase from the hot filament or plasma dissociation of H_2 drive the formation and equilibration of CH_x ($x = 3, 2, 1, 0$) species with rapid hydrogen abstraction and recombination reactions. C_2H_x species are formed by CH_y radical recombinations, e.g.:

$$\begin{aligned} CH_3 + CH_3 &\xrightarrow{(M)} C_2H_6 \\ &\longrightarrow C_2H_5 + H \end{aligned} \tag{5.1}$$

(where M is a third body). C_2H_x species also cycle through a series of H-shifting reactions, with C_2H_2 being the thermodynamically favored hydrocarbon at high T_{gas}. At the time of the G&B review, it was recognized that the growth environment also supported $C_2H_x \rightarrow CH_y$ conversions, but the mechanism by which C_2H_x species broke down to CH_y species was unclear. Heterogeneous conversions, on the reactor walls or the growing diamond surface, were proposed as possible explanations. More recently, spatially resolved, resonance enhanced multiphoton ionization (REMPI) measurements have since shown that the CH_3 radical density profiles in HF activated CH_4/H_2 and C_2H_2/H_2 gas mixtures were essentially identical [24]. These findings suggest that $C_2H_x \rightarrow CH_y$ conversion must occur via gas phase chemistry, and complementary modeling studies [25] showed the importance of (third body stabilized) gas phase addition reactions of the form:

$$C_2H_x + H(+M) \rightleftharpoons C_2H_{x+1}(+M) \quad x \geqslant 2 \tag{5.2}$$

as a means of hydrogenating unsaturated C_2H_x species (most notably C_2H_2) in cooler regions of the reactor. The fate of the resulting C_2H_{x+1} species depends on their subsequent transport in the reactor. In the cooler regions ($T_{gas} \sim 1000$ K), e.g. away from the HF or plasma ball in a MW activated gas mixture, where H atom densities are still normally $>10^{14}$ cm^{-3}, each of the steps Equation (5.2) in the sequence $C_2H_2 \rightarrow C_2H_3 \rightarrow C_2H_4 \rightarrow C_2H_5$ lies in the forward direction. The ultimate $H + C_2H_5$ reaction step favors formation of two CH_3 radicals and thence CH_4. C_2H_x species that are transported back into regions of high T_{gas} will undergo an analogous sequence of H-shifting abstraction reactions:

$$C_2H_x + H \rightleftharpoons C_2H_{x-1} + H_2, \quad x \leqslant 6 \tag{5.3}$$

favoring C_2H_2, and radical species derived there from like C_2H and C_2 [25, 26]. Since all reactors used for diamond CVD contain steep temperature gradients in the gas phase, it follows that the total gas phase number densities, the H atom densities, the various CH_y and C_2H_x species densities, and thus all of the reaction rates for interconversion between these species, are sensitive functions of location within the reactor. This complexity is further compounded by gas–surface reactions (at the growing diamond surface and at the walls of the reactor) and by gas transport and residence times. Recent progress towards unraveling this complexity has been driven by a combination of modeling and (laser based) *in-situ* gas phase diagnostic measurements.

MW plasma-enhanced CVD is now widely used as the method of choice for growth of high quality diamond, and the remainder of this section will concentrate on experimental and modeling studies of the gas-phase chemistry underpinning MW-activated diamond CVD that have appeared since the earlier review. For completeness, however, we note a number of recent papers detailing spectroscopic measurements (of H atoms, and CH, C_2 and C_3 radicals) and modeling studies of the gas phase chemistry and composition in arc jets used for diamond deposition both at Stanford Research Institute [27–31] and at Bristol [32–38]. The results of such studies have proved very useful in developing and testing understanding and modeling of the fast radical interconversions occurring in regions of high T_{gas}.

5.3 MODELING OF MW ACTIVATED GAS MIXTURES

In the vanguard of recent advances in the optical diagnosis and modeling of the gas phase chemistry and composition in MW plasma-enhanced CVD reactors have been Gicquel and colleagues at LIMHP, Université Paris-Nord, and the Bristol–Moscow collaboration. The former have reported self-consistent model calculations based on a cylindrically symmetric bell-jar reactor, operating over a range of input powers, pressures and thus microwave power densities ($\leqslant 30$ W cm^{-3}), both for pure H_2 and for hydrocarbon/H_2 gas mixtures [39–45]. Inevitably, calculations of the (simpler) MW activated H_2 plasma are more exact. These highlight the different routes to forming H atoms, and ions (i.e. plasma), and the way their relative importance varies with pressure, p, and input power, P (and thus T_{gas}). For example, at low p, H atom production is predominantly by electron impact excitation of internal energy levels of H_2, the population of which is promoted through successively higher vibrational levels to dissociation. Increasing p leads to smaller mean free paths, collisional energy transfer from the electrons to H_2 causes more gas heating, the $H_2 - H_2$ collision frequency increases and, once $p > 100$ torr, thermally driven dissociation is usually the dominant H atom formation mechanism [41]. The relative importance of different plasma forming mechanisms is similarly sensitive to process conditions. Direct ionization (Equation 5.4), and the reaction sequence of Equation (5.5), involving electronically excited states of atomic hydrogen (H*), both play important roles at $T_{gas} < 3000$ K but, at higher T_{gas} (and thus higher [H]/[H_2] number density ratios) most ionization is attributable to reactions shown in Equations (5.5b) and (5.5c). Electron loss is primarily by dissociative attachment (Equation 5.6) or, at low p, by transport (to the walls).

$$H_2 + e \rightarrow H_2^+ + 2e \tag{5.4}$$

$$H_2 + e \rightarrow 2H + e \tag{5.5a}$$

$$H + e \rightarrow H^* + e \tag{5.5b}$$

$$H^* + H_2 \rightarrow H_3^+ + e \tag{5.5c}$$

$$H_3^+ + e \rightarrow H + H_2(\text{or } 3H) \tag{5.6}$$

Figure 5.1 displays illustrative 2-D (r, z) model outputs of the absorbed microwave power density (Figure 5.1a), T_{gas} for a MW plasma operating with $p(H_2) = 18.75$ torr and an input power, $P = 500$ W (Figure 5.1b), the electron energy distribution function (EEDF, which, though not strictly Maxwellian, is usually approximated by an electron temperature, T_e, Figure 5.1c), and the electron density (n_e) (Figure 5.1d). Both the p and P values used in these calculations are low relative to those used in most contemporary MW CVD reactors. So too, therefore, are the quoted values for all of the above parameters, but the plots serve to illustrate a number of features that are common to most such reactors. Power is absorbed preferentially near the substrate surface (Figure 5.1a), where the local power density is more than twice the average power density in the plasma. The T_e distribution (Figure 1c) follows the absorbed power distribution closely; its profile is similarly determined, primarily by the electron source terms. The T_{gas} distribution (Figure 5.1b) is smoother and peaks further from the substrate surface, reflecting the role of conduction and diffusion in transporting energy (heat) from the point of maximum power deposition. The n_e distribution (Figure 5.1d) also exhibits a more smoothly varying spatial distribution, emphasizing the importance of transport (ambipolar diffusion) in establishing the electron density balance.

The addition of a small amount of hydrocarbon to a H_2 plasma has relatively little effect on the electromagnetic field and plasma distributions. If the input power is maintained constant, the typical effect of introducing a small hydrocarbon fraction is for the distributions

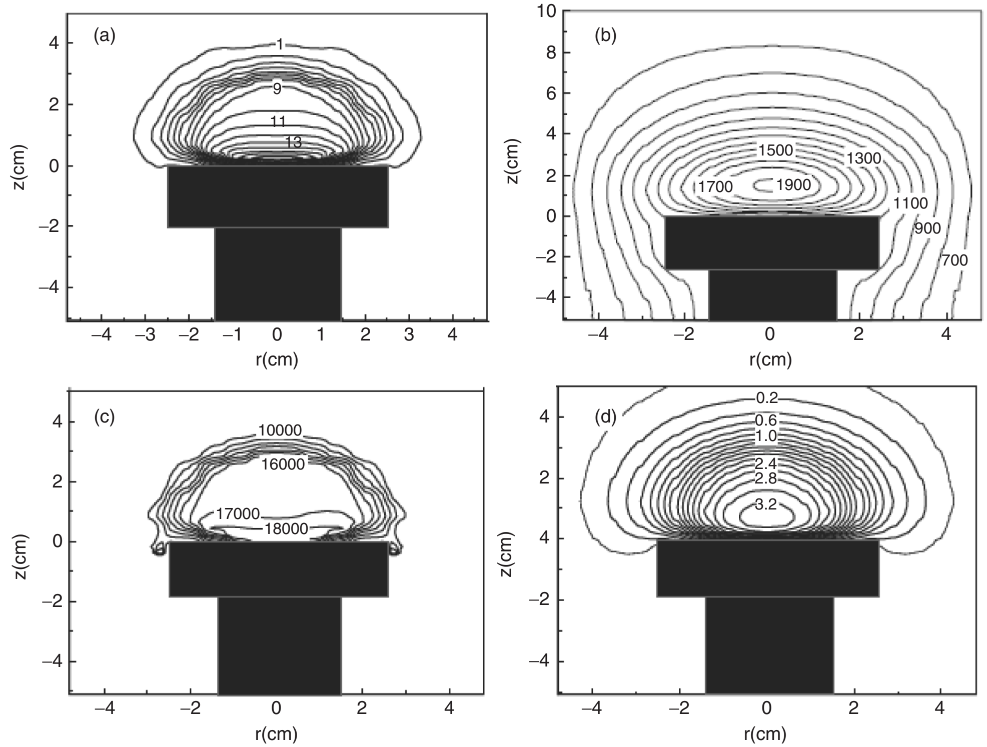

Figure 5.1 -D (r versus z) model distributions of (a) the absorbed microwave power (in W cm^{-3}), (b) T_{gas} (in K), (c) T_e (in K) and (d) n_e (in units of $10^{11}cm^{-3}$) above the top of the substrate holder (shaded black) for a MW activated H_2 plasma at $p = 18.75$ torr and an input power of 500 W (from Ref. [45], with permission). Reprinted from Plasma Sources Science and Technology, Overview of the differing aspects in modeling moderate pressure H_2 and H_2/CH_4 microwave discharges by K. Hassouni, G. Lombardi, X. Duten, G. Haagelar, F. Silva, A. Gicquel, T.A. Grotjohn, M. Capitelli, J. Ropcke, Vol 15, Iss 125, pg 117, copyright (2006) Institute of Physics

to shrink slightly. This reflects the lower ionization potentials and thus greater ionization probabilities of hydrocarbons (principally C_2H_2) relative to H_2 or Ar, and suggests that $C_2H_2^+$ and $C_2H_3^+$ will be the most abundant ions in most MW activated hydrocarbon/H_2 plasmas [43]. Despite much progress, the development of fully self-consistent models for MW activated hydrocarbon/H_2 plasmas remains challenging, on account of: (i) the numerous species and collisional processes that demand inclusion, (ii) the large spatial variation in T_{gas} and T_e (and thus in the densities of the many different hydrocarbon species), and (iii) the strong space and time dependence of the chemistry (which renders numerical solution of the relevant 2-D transport equations very time consuming).

Nonetheless, much progress has been made, in the context of both MW[43–46] and DC arc jet [38] plasmas. These calculations, and experimental measurements [46, 47] all show that CH_4 is rapidly converted to C_2H_2 in regions of high [H] and high T_{gas}, and is thus the major hydrocarbon species in the plasma. The dominant reactions responsible for cycling gas-phase carbon between C_2H_2 and the various radical species in this region are all thermal in nature, and fast. As a result, neutral hydrocarbon species in the plasma region are in partial chemical equilibrium, with relative abundances that are dictated by T_{gas} and the local H atom density. A thin temperature and compositional boundary layer separates the bulk plasma from the growing diamond surface. Modeling the chemical composition within this layer remains a major challenge. T_{gas} falls on approaching the substrate surface, steeply, and typically by several hundred Kelvin, in the case of contemporary high pressure, high power MW reactors. The substantial diffusive transfer driven by such gradients dictates that the local composition must be highly nonequilibrium. The relative densities of all radical species will surely fall as the surface is approached – not least because of reactive loss of such species by gas–surface chemistry – but many of the details remain to be quantified.

5.4 OPTICAL DIAGNOSIS OF MW ACTIVATED GAS MIXTURES

Many of the recent experimental advances in the diagnosis of diamond CVD plasmas have centered on two families of laser absorption spectroscopy methods. Stable hydrocarbon species (e.g. CH_4, C_2H_2 and C_2H_6) and CH_3 radicals have been monitored by direct line-of-sight infrared (IR) absorption methods using tunable diode lasers [7, 48–50] and/or (the more recently developed [51]) quantum cascade lasers [46, 47]. CH_3 radicals have also been measured by line-of-sight absorption via their ultraviolet (UV) absorption [52], but most of the latest measurements of radical species like C_2 and CH, and of electronically excited H atoms [32–34, 37, 46, 53, 54] have involved use of pulsed tunable dye lasers (in the visible and near-UV spectral regions) and cavity enhanced absorption methods (particularly cavity ring down spectroscopy, CRDS [55]). Both IR and CRDS methods offer a major advantage if diagnosis involves use of a well-characterized spectroscopic transition: analysis can yield *absolute* densities of the species of interest. However, the density returned is a *column* density (usually along r). The probed column spans a wide range of T_{gas} (typically from ~3000 K in the plasma ball to ~300 K immediately inside the view-ports mounted on the reactor wall), and thus a very inhomogeneous distribution of the target species. The determination of local *number* densities in the case of molecular species is further complicated by the temperature dependence of the rovibrational partition function; the fraction of the total density in any probed quantum state will depend on T_{gas} and thus on r. In the context of understanding the gas-phase chemistry underpinning diamond CVD, therefore, experiment and theory are both essential and symbiotic. Experimental measurements (e.g. spatially resolved column density measurements, as a function of process conditions) are essential for validating model calculations, but model outputs (e.g. the r dependence of T_{gas} and the various species mole fractions) are also essential for quantitative interpretation of the experimental data.

IR column density measurements of MW activated hydrocarbon/H_2 gas mixtures [46, 47] reveal efficient conversion of any input hydrocarbon (including C_2H_2) into CH_4 under the (relatively) high [H] and lower T_{gas} conditions that are typically found where the process gas enters the reactor, and serve to confirm theoretical predictions [43–45] regarding the conversion of CH_4 to C_2H_2 in the plasma (high [H] and high T_{gas}).

5.5 SURFACE CHEMICAL GROWTH MECHANISMS

The recent advancements in computational power and techniques, have made accurate computational modeling an accessible option for probing reactions occurring at the gas–

Table 5.1 The scaling of the activation energies, E_a with associated rates at 1000 K, with an assumed prefactor, A, of 10^{13}s^{-1} Reprinted from [45], Copyright (2006), Institute of Physics

E_a/kJ mol^{-1}	exp($-E_a/RT$)	*rate*
20	9×10^{-2}	9×10^{11}
50	2×10^{-3}	2×10^{10}
100	6×10^{-6}	6×10^{7}
200	4×10^{-11}	3×10^{2}
300	2×10^{-16}	2×10^{-3}

surface interface and the subsequent surface reactions. In recent years, computational modeling of diamond has drifted away from semiempirical methods and adopted higher levels of theory, with the preferred types of calculation being based upon density functional theory methodologies, or a Hartree–Fock based method including electron correlation corrections.

Throughout this section of the review, we will use a simple kinetic model to interpret the feasibility and competition between reaction pathways, as care must be taken in the inference of kinetic processes, such as growth, from thermodynamic energy calculations. The majority of chemical reactions occurring within a CVD growth environment are either bimolecular gas–surface site reactions or unimolecular surface rearrangement/migration reactions.

For unimolecular processes, the reaction rate constant can be calculated from the activation energy, E_a, and the temperature by the Arrhenius equation ($k = A\exp(-E_a/RT)$). The upper limit to A, the Arrhenius prefactor, will be of the same order as a vibrational period ($\sim10^{13}$ s^{-1}), with A being reduced for reactions involving anything other than a simple single bond fission. Table 5.1 shows that at a typical surface temperature of 1000 K any unimolecular process with an activation energy $>$200 kJ mol^{-1} will not be feasible.

Bimolecular reactions are more complex as the reaction rate constants depend upon the collisional frequency between the two reagents, as well as the activation energy. Under the typical microwave plasma CVD reactor conditions used at Bristol [47] and using simple collisional theory [56], atomic hydrogen and methyl radical collision frequencies with a hydrogen-terminated diamond surface site (C_S–H) (assuming bulk carbon–carbon bond length) are computed to be $\sim6\times10^4$ s^{-1} site^{-1} and 80 s^{-1} site^{-1} respectively, several orders of magnitude slower than unimolecular processes. The inclusion of activation barriers further reduces the reaction rate constant and reactions with activation barriers greater than 50 kJ mol^{-1} will be unlikely events, as the barrier height reduces the bimolecular rate constant by three or more orders of magnitude.

The key quantity determining reaction rates and equilibria is the Gibbs free energy. Diamond CVD substrate (and growth surface) temperatures typically span the range 1000–1400 K. Entropic effects will make a significant contribution to the free energy profile at these temperatures – particularly in steps that involve loss or production of a gas phase species. By way of illustration, a step like B → C in Figure 5.2, where a gas phase CH_3 species is accommodated at the surface, will have an associated Δ_rS of ~-100 J mol^{-1}K^{-1}. The entropic contribution, $T\Delta_rS$, will thus be $\sim$120 kJ mol^{-1} at typical CVD growth temperatures and sufficient to render formation of weaker C–C bonds improbable.

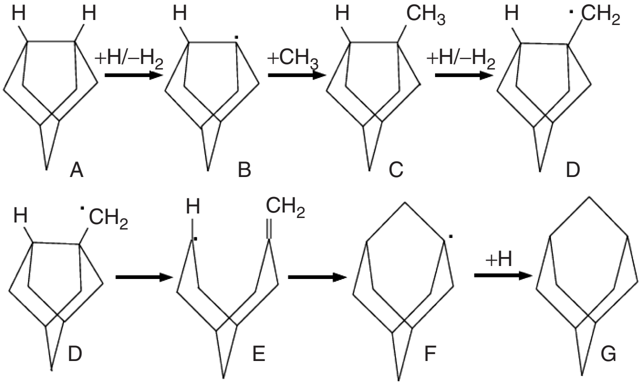

Figure 5.2 The mechanism by which methyl radicals can be incorporated into a dimer reconstruction

Most of the work performed on modeling the reactions on diamond surfaces is based on reactions occurring upon the hydrogen terminated reconstructed 2 × 1 {100} surface since {100} surfaces are prevalent (along with {111}) in most CVD diamond growth and it is the preferred surface for homoepitaxial single crystal growth. Since the surface chemistry is driven by hydrogen abstractions, the energetics and kinetics of individual reaction steps on the {100} reconstructed surface are similar to those on other surfaces. However, steric effects due to local stereochemistry of different sites may impact specific reaction sequences, so caution is advised when applying such sequences to growth along a different crystallographic axis. Since the G&B review [11], much work has focused upon the reinvestigation of CH_3 reactions due to its large abundance in the gas phase.

Modeling of the CVD growth of diamond has focused upon radical-based chemistry occurring between gas-phase radicals and the diamond surface, particularly the addition of carbon containing radicals to numerous sites on a diamond surface and the subsequent reactions by which these pendant species are incorporated into the different diamond faces or step edges.

In order for the addition of carbon containing radicals, the surface requires the formation of a surface radical (a dangling bond). This is usually realized by abstraction of a hydrogen atom from a surface CH bond, for example, the hydrogen pendant on the dimer reconstruction, by a gaseous species (A →B, Figure 5.2). Atomic hydrogen, being the most abundant radical species, is commonly modeled as abstracting a surface hydrogen to form gaseous molecular hydrogen, but this abstraction can also occur by gaseous carbon-containing radicals with similar energetics. Surface site activation can also be initiated by a fast migration of a surface hydrogen to a neighboring radical site upon a previous abstraction or incorporation. Either process requires a hydrogen abstraction event by a gas-phase species and hence will occur over similar timescales.

Methyl radicals can diffuse from the gas phase towards the diamond surface and form strong bonds to the surface radical sites. For example, on the (100) 2 × 1 surface, the resulting bound methyl group can be incorporated by forming a second C–C bond in two different places, either by formation of a carbon–carbon bond at the neighboring end of a reconstructed dimer bond to which the methyl group is bound, or by addition to the neighboring reconstructed carbon dimer by bridging the trough between the two dimer rows.

Table 5.2 Comparison of energetics for methyl incorporation into a dimer reconstruction (to be read in conjunction with Figure 5.2). Reaction energies (ΔE) and activation energies (E_a) for the relevant transition states (defined relative to the relevant reactants) are quoted in kJ mol^{-1}. Reprinted from [45], Copyright (2006), Institute of Physics

	Cheesman *et al.* [61]	Kang and Musgrave [58]	Tamura and Gordon [59]		Brown *et al.* [73, 74]	Oleinik *et al.* [72]	Skokov *et al.* [67, 68]
	B3LYP QM/MM	B3LYP	CASSCF (3,3)	MRMP2	MP2	DFT hybrid	PM3
A →B	−0.7	–	17.3	−1.7	11.3 [73]	−36.7	–
E_a	*26.4*	28.0	*94.6*	*51.1*	*46.0* [73]		
B →C	−373.2	−351.6	−372.4	−372.4		−311.7	−307.9 [68]
E_a	*0.0*	–	*0.0*	*0.0*			*0.0* [68]
C →D	−30.1	−37.7	−20.5	−34.7	−27.2 [74]	−79.1	–
E_a	*29.5*	*25.1*	*83.3*	*45.2*	*48.6* [74]		–
D →E	28.0	−2.1	83.3	74.1			51.9 [67]
E_a	*43.4*	*40.2*	*20.2*	*15.1*			*64.0* [67]
E →F	−78.4	−41.9	−78.7	−72.4			−100.4 [68]
E_a	*53.1*	*59.0*	*72.4*	*50.6*			*51.5* [68]
D →F		−44.0				−29.3	
E_a		*206.8*				*54.4*	

5.5.1 Insertion into dimer reconstruction

Figure 5.2 shows the mechanism for the process for CH_3 insertion into the dimer bond on (100) 2 × 1-2H surface, (A), initially proposed by Garrison *et al.* from molecular dynamics studies of diamond surfaces [57]. The process is initiated by hydrogen abstraction from a pendant surface-bound CH_3 (i.e. C →D in Figure 5.2). The newly formed CH_2 radical then incorporates into the diamond structure via a ring opening mechanism (D → E → F, Figure 5.2) rather than by direct insertion of CH_2 into the C–C bond which has a very large barrier (~200 kJ mol^{-1}) [57, 58]. The mechanism has been studied with numerous different environments including isolated clusters [58], larger QM/MM clusters [59–61] and under periodic boundary conditions [62, 63] and the energies (ΔE) and activation energies (E_a) for the various elementary steps from these comparable investigations are summarized in Table 5.2. The ring opening and closing mechanism for incorporation can also model lateral {100} diamond growth from a step on the {111} surface [64].

Frenklach and collaborators have been at the forefront of the development of a consistent model for the growth of CVD diamond. Within the calculations performed by Frenklach *et al.* [64], the diamond surface is modeled using a two region system with an inner core described using the semi-empirical PM3 method [65] and the outer perimeter using an empirical potential parameterized to PM3 [66]. There have been various size models for the PM3 region ranging from an isolated cluster describing one reconstruction (C_9H_{14}) to two rows of reconstructed dimers describing a 3 × 2 section of the diamond surface ($C_{40}H_{52}$). Local minima on the potential energy surfaces (PES) were calculated using unrestricted Hartree–Fock theory in conjunction with the combined-force molecular dynamics (CFMD) method for the outer perimeter. The energetics obtained from these calculations have been used to calculate rate constants using nonvariational transition-state theory (TST), and these rate constants form the basis for their large scale model of diamond growth using Kinetic Monte Carlo (KMC) techniques, which are discussed later.

The main growth species considered within these studies are the methyl radical [67, 68] and acetylene [69–71]. The modeling shows that methyl addition to a pristine diamond surface is a barrierless process, but that there may be energy barriers for CH_3 radical addition at sites adjacent to previous incorporations. The results for CH_3 addition were used to infer that the ring opening/closing mechanism is the more favorable process due to the inherent kinetic and thermodynamic stability of methyl adsorption upon the pristine diamond surface. C_2H_2 addition to a surface radical is calculated to be a feasible process resulting in the formation of the surface bound $C{=}CH_2$ species.

The work of Oleinik *et al.* [72] has been included for comparison, as these energetics confirm the etching mechanism for the KMC models of Battaile *et al.* [60]. Contrary to other results presented within the literature, Oleinik *et al.* found that the incorporation mechanism occurs through a direct process with a single transition state, yet the barrier height reported is comparable to that of the ring-closing step. The exothermicity for the ring opening/closing step $D \rightarrow E \rightarrow F$ is also 2-times smaller than other reported values (Table 5.2). This has the implication of enhancing the significance of the reverse reaction, which is a key part in the etching process in the Battaile KMC model (discussed below).

Caution should be taken with interpreting MP2 calculations as high activation energies are reported for the hydrogen abstraction activation reactions by Brown *et al.* [73, 74]. Tamura and Gordon [59] also dramatically overestimate certain activation barriers and calculate that the overall ring opening/closing process is essentially thermoneutral.

Using the simple kinetic arguments outlined above, it follows that the overall rate limiting steps in the incorporation of methyl species into the 2 × 1{100} diamond surface is the addition and subsequent activation of the methyl to an activated site (Figure 5.2: Steps $A \rightarrow D$). This involves a sequence of three 'bimolecular' reactions involving a gas-phase species colliding with the surface (the slowest having an estimated rate of only about 80 s^{-1}), and is generally likely to be slower than the alternative 'bottle-neck' – the ring opening/closing process (Figure 5.2: Steps $D \rightarrow E \rightarrow F$) – suggested elsewhere [57, 71].

5.5.2 Insertions across dimer troughs

An additional mechanism for the incorporation of carbon into the growing surface is for methyl radicals to react with the neighboring 2 × 1 dimer reconstruction across the trough between them. This reaction scheme is known as the Harris or 'HH' mechanism [75]. In essence, the process involves the formation of a bridging methylene group across the

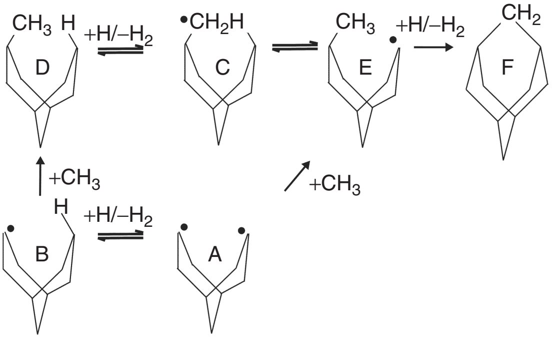

Figure 5.3 The modified 'HH' mechanism by which carbon can be incorporated into the {100} surface across a dimer row

trough between dimer rows (Figure 5.3). This can occur by two possible mechanisms: a biradical pathway (Figure 5.3: A → E), or a sterically hindered addition (Figure 5.3: B → D). The actual mechanism shown in Figure 5.3 is a modification of the trough bridging mechanism of Harris, which avoids the sterically unfavorable hydrogen abstraction from the diamond surface by a hydrogen migration from the surface to the pendant CH_2 radical (C → E) [61]. The resultant methyl group can undergo a further hydrogen abstraction resulting in ring closure.

Studies by Cheesman *et al.* [61] have found that methyl addition to the single radical site is a barrierless process similar to CH_3 addition to a perfect 2×1 reconstructed {100} diamond surface with no neighboring incorporations. Addition to the energetically favourable biradical site is assumed to occur by a similar mechanism. This suggests that CH_3 addition to the surface is only affected by the strength of the resulting carbon–carbon bond, which is determined by the local chemical environment. These results are in direct contradiction to the finding of Skokov *et al.*, who found activation barriers for methyl addition to a radical site that has a previous insertion into the dimer bond [68] (structure F in Figure 5.2). (Likely origins for the apparent activation barrier for this process are discussed further in Ref. [61].) The presence of activation barriers for methyl addition to the sterically hindered site has been used to favor the biradical pathway as a major growth process. However the recent calculations from Cheesman *et al.* show that *both* the steric and biradical reaction pathways are energetically feasible, and since both processes involve the same number of gas–surface bimolecular steps, they should occur over similar time scales.

Diatomic carbon, C_2 (ground electronic state), has been considered as a growth species. We are not aware of any reports of C_2 incorporation by addition to an isolated radical site (analogous to the mechanism shown in Figure 5.2). However, C_2 radicals have been shown to incorporate, exothermically, into a reconstructed dimer bond on a fully reconstructed (H-free) diamond surface via an 'end-on' geometry and subsequently rearrange to form a cyclobutane ring on the surface [76, 77]. These 'clean' surfaces have no surface-bound hydrogen and the resultant electronic dependences are satisfied by the formation of partial double bonds on the individual reconstructions. Analogous insertion and rearrangement reactions are possible on the hydrogen-terminated surface (the energetics of the addition of C_2 to the dimer bond calculated using the B3LYP/6-31G* basis set are $\Delta E \sim -545.6$ kJ mol^{-1}) [76]. Mechanisms involving multiple adjacent adsorbed C_2 species [78] have to be considered highly improbable due to the low abundance of gas-phase C_2 species and the lack of C_2 surface migration reactions.

5.5.3 Etching

CVD diamond growth has been conceived as a delicate balance between the incorporation and etching rates of carbon species [3]. Numerous experimental surface studies have looked at the effective 'cleaning' of hydrogen from the diamond surface by thermal desorption. Within these studies, molecular hydrogen desorbs from the surface at a temperature above 825 °C [79, 80]. Carbon removal studies, looking at the effects of hydrogen etching upon a diamond surface, show that methane is the predominant carbon-containing species etched [81]. Etching usually occurs along and across the diamond surface, resulting in the formation of small, shallow (~1-nm deep) pits upon the surface [82].

Published computational modeling does not describe the experimental carbon etching findings highlighted above. The most common method proposed for the removal of C_1H_x species is the unimolecular dissociation of a pendant CH_3 species from the surface into the gas phase. This pendant species can be formed by the reversal of the insertion reaction (G → B, Figure 5.2). This desorption reaction is thermodynamically unfavorable. The entropic contribution to the free energy change associated with methyl desorption into the gas phase at typical CVD diamond surface temperatures, $T\Delta_r S$, is ~150 kJ mol^{-1} and is insufficient to overcome the endothermicity (~370 kJ mol^{-1}) associated with breaking the strong C–C bond (Step C → B in Figure 5.2). Similar arguments hold for surface radical induced methyl expulsion. This process is initiated by the abstraction of the neighboring hydrogen on the dimer, leaving a radical site which forces the methyl group to dissociate from the diamond surface by the formation of a double bond resulting in a 'bare' reconstruction [70]. This expulsion is similar to the *beta scission* reaction, which etches any surface pendant $C_nH_x (n \geqslant 2, x \geqslant 3)$ species with the expulsion of a C_2H_x species ($x = 0$, 2, 4), discussed more fully later [83].

Methane desorption from the surface has also been proposed to occur by a radical displacement reaction on a pendant methyl group instigated by an incident H [59]. This is calculated to be an exothermic process with a large activation energy barrier ($\Delta E = -69.3$ kJ mol^{-1}; $E_a = 133.2$ kJ mol^{-1}) that dramatically reduces the reaction rate and makes this reaction insignificant under typical CVD growth conditions.

Kanai *et al* have proposed a hydrogen etching mechanism for diamond and graphite using DFT methods [84]. The etching process is initiated by H-atom addition to a surface dimer carbon atom resulting in the cleavage of the surface carbon−carbon bond ($\Delta E = -112$ kJ mol^{-1}, $E_a = 53$ kJ mol^{-1}). Further H addition to this dihydride carbon results in the formation of a pendant methyl group ($\Delta E = 39$ kJ mol^{-1}, $E_a = 229$ kJ mol^{-1}), which dissociates into the gas phase as methane by a radical displacement reaction with atomic gas-phase hydrogen, with the surface reforming carbon−carbon bonds ($\Delta E = -501$ kJ mol^{-1}, $E_a = 119$ kJ mol^{-1}) [84]. However, applying the simple kinetic ideas (Table 5.1) to each of these steps, it is clear that this process is extremely slow due to the prohibitively large activation barriers. This is in contrast to the exothermic etching of a sheet of graphene by a similar mechanism, where only one activation barrier is detected, namely that for the second hydrogen insertion ($\Delta E = 48$ kJ mol^{-1}, $E_a = 113$ kJ mol^{-1}). This particular step is endothermic, with a significant barrier, due to the hydrogen inserting into a sp^2 carbon−carbon bond in the plane of the graphene sheet [84].

The only thermodynamically [85] and kinetically feasible model for carbon removal from the diamond surface is the *beta-scission* mechanism. This process requires the addition of a second C_1H_x species, typically a methyl radical to a pendant methyl radical or methylene radical (structure D, Figure 5.2). Hydrogen abstraction from the terminal carbon leads to formation of a pendant – $CH_2CH_2^{\bullet}$ radical, which dissociates from the surface to form a gas-phase species (ethylene) and a surface radical site by the breaking of the bonding *beta* (or two carbon atoms away from the radical site) – thereby preventing longer alkyl chains from growing on the diamond surface [11, 83, 86].

5.5.4 Migration

Frenklach and Skokov proposed that surface migration of carbon species might lead to the observed smooth diamond surfaces [87]. Their studies were performed at similar theory levels to their carbon incorporation energetics studies. In general, the results show that hydrogen atoms cannot migrate across a pristine diamond surface to a surface vacancy, as the migration process is prohibited by a large activation energy barrier (calculated to be $E_a = 277$ kJ mol^{-1}, which is likely to be an underestimate). This barrier originates from the large separations along and between the dimer rows on the reconstructed $2 \times 1\{100\}$ surface. However, when the distance between a radical species and an H atom is reduced (i.e. between a dimer reconstruction and an insertion or a pendant carbon species and a surface radical site), the movement of the atomic hydrogen to the adjacent carbon becomes a favorable process. Also, hydrogen can only migrate from bulk defect sites to the surface when there is a surface radical site available, thus reducing the number of surface activated sites [88]. These migration steps reduce the lifetime of single radical species at certain sites on the surface and thus reduce the feasibility of the trough-bridging mechanism.

The surface migration of carbon species such as CH_2 and $C{=}CH_2$ is possible when a biradical site is formed from two neighboring hydrogen abstractions. The proposed mechanism for the migration of a CH_2 group begins with the incorporated methylene group (F from Figure 5.2) adjacent to a neighboring radical site. The incorporated CH_2 group undergoes a ring opening process to form an unsaturated methylene group with a radical upon either side (15a in Figure 5.4). This intermediate either reforms the dimer reconstruction (15b) or forms a bridging carbon–carbon bond across the dimer trough (15c). The previous steps move the two radicals close enough to form a bond resulting in the strained intermediate, which can open in two ways, one of which reverts to the original configuration, and the other leads to the migrated species. Also, the formation of a pendant CH_2 radical allows migration in two dimensions, both along dimer chains as well as along dimer rows. The rate of transportation is only limited by the hydrogen abstraction/addition processes as the migration processes are unimolecular. These carbon migration reactions are most favorable upon a pristine surface but the process becomes less favorable with increasing levels of neighboring carbon incorporations as the steric interactions from the pendant CH_2 groups increases the activation energy for the migration reactions to unreasonable levels. The movement of carbon species upon the diamond surface typically ends when proximate radical species coalesce.

The work of the Frenklach group provides a guide to surface migrations of C_1H_x. Reinvestigations of these mechanisms at higher levels of theory confirm the energy profiles, feasibility, and rates at which CH_2 species can migrate across and along a pristine diamond surface [61]. However, one should be careful not to over extend the role of surface migrations in CVD processes, for example, the migration length of these species under diamond growth conditions is suggested to be only about 10 Å [87].

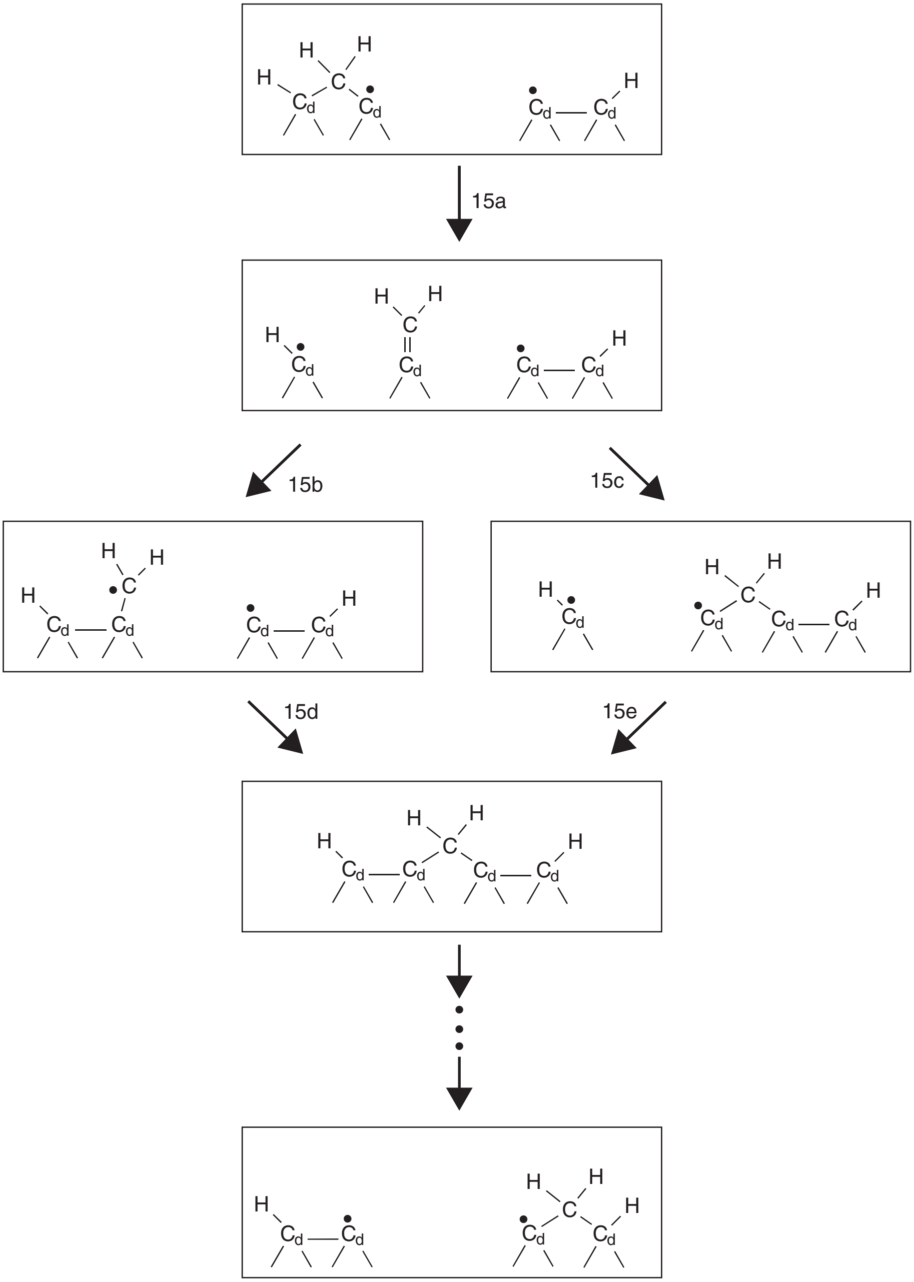

Figure 5.4 Mechanisms for the migrations of methylene along a dimer row (from [87]). Reprinted from Journal of Physical Chemistry B, Surface Migration in Diamond Growth by M. Frenklach, S. Skokov, Vol 101, Iss 16, pg 3025, copyright (1997) American Chemical Society

The well-known observation of rows of reconstructed dimer has been a hallmark of diamond growth upon the {100} surface. Skokov *et al.* [89] have proposed that under the right conditions, the surface migrations of $C{=}CH_2$ species can result in the formation of the dimer pattern. They showed that there is no preference for adsorption of a gaseous methyl at the two common step edges (S_A, S_B) present on the reconstructed diamond $2 \times 1\{100\}$ surface, and that $C{=}CH_2$ species can also be incorporated into the dimer trough forming a new reconstruction, and that this process is reversible.

5.6 LARGE GROWTH MODELS

Due to the large number of gas-phase and surface reactions possible, Kinetic Monte Carlo (KMC) protocols have been used to see how the reaction energetics affect the growth of {100} diamond. The KMC modeling process uses a time-based probability algorithm to weight the potential pathway from all the possible reactions. For a given initial condition, a complete table of the possible events at a given temperature is prepared and the simulation then randomly chooses an event (as weighted by the relative rates) and advances the time clock by a characteristic time (see [90] for more details). The weaknesses of the KMC approach are: (i) the process does not offer direct insight into new mechanisms; (ii) the model can be readily distorted by missing or erroneous processes; and (iii) the results generated can only be validated by suitable experimental data.

The initial kinetic investigations of diamond growth looked at the direct incorporation of incident carbon species using simple adsorption models for carbon species [91, 92]. These models mapped the available experimentally published growth rates well, but offered little insight into the surface chemistry. However, the shortcomings of these initial models has led to an expansion of the modeling to include more complex reaction dynamics like surface migrations [93] and etching of surface atoms [60].

The Frenklach implementation of KMC modeled diamond growth [93] has methyl radicals as the sole growth species with the incorporation into the diamond surface described by means of the ring opening/closing mechanism. CH_2 migration along and across the dimer reconstructions was included as well as the reforming of the surface reconstruction bonds from two suitable adjacent surface radical sites. Etching was only considered to occur at isolated incorporated CH_2 groups and reconstructed dimers. The former etching process is described by the removal of CH_2 by the reverse of the ring opening/closing incorporation mechanism and the removal of isolated dimer reconstructions by a one- or two-carbon removal process.

The energetics and kinetic data for these reactions are sourced from numerous calculations and experimental measurements in hydrocarbon chemistry. The initial model failed to produce continuous rows of incorporated CH_2 species (a similar observation is obtained in [94]). All subsequent reports [93] include a compensatory term to ensure saturation of these sites. This compensation is parameterized by the optimization of the growth rate [93].

The Frenklach work [93] highlights the positive effect that the surface migration has upon the growth rates of diamond, giving a roughly one order of magnitude enhancement of the growth rate over that for adsorption only growth. The KMC model has studied the effects of numerous process conditions, including abundance of reagents and substrate temperature [93].

The resultant films ‘grown’ under these KMC conditions show wide variations in surface roughness, with the formation of {111} domains, most unlike the pristine starting diamond surface. The results do not show smooth terrace growth of diamond and suggest that the growth process is similar to island-type growth. However, upon closer examination of the mechanisms proposed, there is no direct mechanism for forming the dimer reconstructions. Instead, dimer formation is suggested to occur as a by-product of migration of incorporated CH_2, or as the coalescence of two neighboring carbon surface radicals.

The Frenklach growth model [93] also shows that, without the growth species present, the etching reactions on the rough {100} diamond surface can produce the experimentally observed smooth surfaces. The time frame for this process is short enough to occur with the annealing that can happen during the process of shutting down the reactor. However, the model lacks feasible etching processes for CH_x species, as the only process included is the expulsion of CH_3 by the fission of a strong surface carbon–carbon bond. There is also no provision for a *beta-scission* etching reaction.

Overall, the Frenklach model suggests that carbon, in the form of CH_3, can randomly incorporate into a diamond surface and undergo migration across the surface until multiple species coalesce. During this process, the substrate surface can act as a template for migrating species to form new dimer reconstructions and, in combination with etching (especially under post-growth conditions), can result in the smooth surface growth observed [95].

The KMC modeling work by Battaile *et al.* [96–101] is based upon previously reported energetics in the literature and considers diamond growth occurring by methyl radicals via the trough bridging incorporation mechanism (discussed in conjunction with the

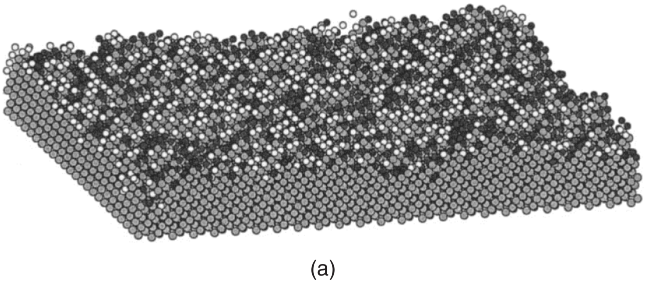

(a)

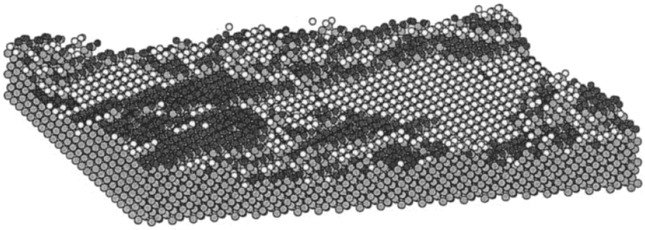

(b)

Figure 5.5 Images of {100} films during simulated growth at 1200 K (a) without and (b) with etching. Light grey atoms are carbons in the diamond film. The hydrogen atoms are shaded according to their height. Two gray levels (dark grey and white) are used, and cycle every two layers (from [96]). Reprinted with permission from Journal of Applied Physics, A kinetic Monte Carlo method for the atomic-scale simulation of chemical vapour deposition by C.C. Battaile, D.J. Srolovitz, J.E. Butler, Vol 82, Iss 12, pg 6293, copyright (1997) American Institute of Physics

incorporation of acetylene). These studies highlight the importance of substrate orientations and the roles of C_2H_2 in controlling the growth rate. By including the possibility of etching within the KMC calculations due to CH_3 dissociation from the surface (calculated at the PM3 theory level), large smooth terraces upon the {100} diamond surface can be produced, as illustrated in Figure 5.5 [60]. This KMC work has also indirectly highlighted the effects that 'new layer nucleation' has upon the growing crystal morphology [97]. Modeling of 'off axis' growth upon the {111} face predicted structures comparable with 'step-flow' growth showing the faster rate for lateral growth over new layer nucleation [98]. This effect is highly surface specific as misalignment upon the {100} face had minimal effect upon the morphology.

Grujicic and Lai have modeled a hot-filament CVD growth reactor using an expanded KMC protocol by directly coupling a gas-phase reactor model to provide the calculated number densities for various surface sites on both the {111} [102] and {100} [103] surfaces shown in Figures 5.6 and 5.7 respectively. Despite the identical gas-phase and gas-surface chemistry used in both scenarios, the {111} model produces a rough surface showing a higher concentration of defects, including twinning, kinks and vacancies. The model has large smooth terraces, attributed to the poor rate of nucleation of the next layer of growth (see also [83]). The {100} surface, however, is rough on the atomic scale, shows no long-range structure or defects, and is lacking the dimer reconstructions.

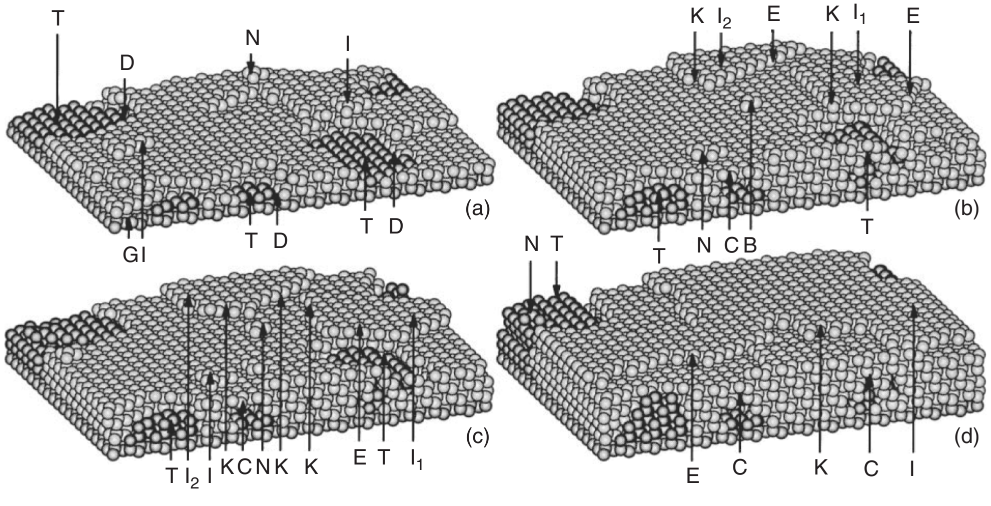

Figure 5.6 Top view of a (111)-oriented diamond film simulated under the following CVD conditions in the reactor: reactive gas at the reactor inlet (0.4 % CH_4, 92.5 % H_2), $T_{\text{heater}} = 2000$ K, $T_{\text{substrate}} = 1000$ K, $p = 20.25$ torr. Heater-to-substrate distance = 1.3 cm. Deposition times: (a) 0.87 s; (b) 1.81 s; (c) 2.07 s and (d) 2.85 s. Nomenclature: B, 3-carbon bridge; C, twin covered by regular crystal; D, dislocation loop; E, edge; G, Gap; I, island; K, kink; N, nucleus; T, twin; V, void (from [103]). With kind permission from Springer Science+Business Media: Reprinted from Journal of Materials Science, Multi-length scale modeling of CVD diamond pt II, a combined atomic-scale/grain-scale analysis by M. Grujicic, S.G. Lai, vol 35, Iss 21, pg 3571, copyright (2000) Springer

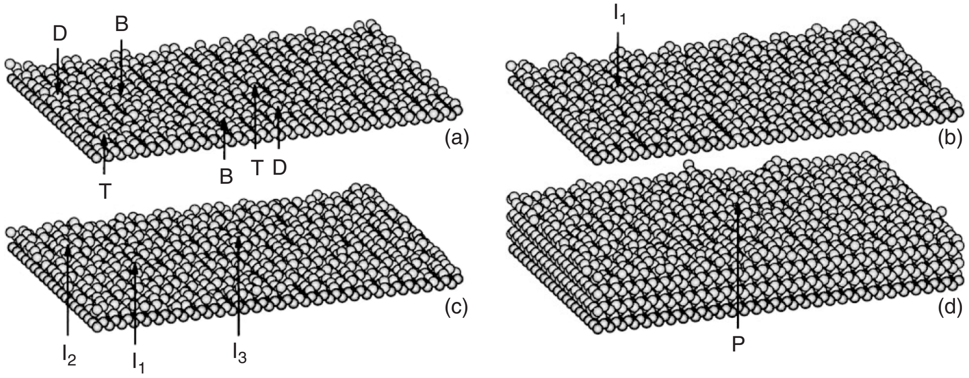

Figure 5.7 Top view of four (100) surface configurations obtained under the CVD conditions identical to the ones listed in Figure 5.6. Deposition times: (a) 0.01 s; (b) 0.018 s; (c) 0.032 s and (d) 0.208 s. Nomenclature: B, BCN mechanism (i.e. CH_3 insertion across a trough by the HH mechanism); D, dimer insertion mechanism; P, pit; I, island; T, trough (from [103]). With kind permission from Springer Science+Business Media: Reprinted from Journal of Materials Science, Multi-length scale modeling of CVD diamond pt II, a combined atomic-scale/grain-scale analysis by M. Grujicic, S.G. Lai, Vol 35, Iss 21, pg 3571, copyright (2000) Springer

5.7 SUMMARY

This review highlights much of the progress in understanding diamond growth environment since the review of Goodwin and Butler in 1997 [11]. Major improvements have been made in the *in-situ* measurements of gaseous reactants, plasma and reactor modeling, and the details of surface chemical growth mechanisms. However, there is still a lot that is poorly understood. For example, what is the impact of trace impurities, such as dopants, on the growth mechanisms, film morphology, and quality? What is the role of substrate imperfections on film growth? How do common gaseous impurities (or intentionally added species) such as nitrogen, oxygen, halogens, or rare gases impact each element of the growth process? As our knowledge base and experimental capabilities improve, one expects that many of these issues will be addressed.

ACKNOWLEDGEMENTS

The Bristol authors are most grateful to EPSRC for funding via the portfolio award LASER, the Royal Society for a Joint Project Grant, Element Six Ltd for the long-term loan of various CVD reactors designed for laser diagnosis, Dr Yu.A. Mankelevich (Moscow State University) for enduring and fruitful collaboration, and Bristol colleagues Jie Ma, K.N. Rosser and Drs P.W. May, J.N. Harvey and J.A. Smith for their many contributions to aspects of the work described herein. J.E. Butler acknowledges the support of ONR/NRL, and thanks Dr M.E. Newton and the members of his group at Warwick for fruitful discussions during his stay in 2007.

REFERENCES

[1] J. C. Angus, H. A. Will, W. S. Stanko, *Journal of Applied Physics* (1968) **39**, 2915.

[2] B. V. Deryagin, B. V. Spitsyn, A. E. Aleksenko, A. E. Gorodetskii, A. P. Zakharov, R. I. Nazarova, *Doklady Akademii Nauk SSSR* (1973) **213**, 1059.

[3] J. C. Angus, C. C. Hayman, *Science* (1988) **241**, 913.

[4] J. C. Angus, Y. X. Wang, M. Sunkara, *Annual Review of Materials Science* (1991) **21**, 221.

[5] K. E. Spear, *Journal of the American Ceramic Society* (1989) **72**, 171.

[6] W. A. Yarbrough, R. Messier, *Science* (1990) **247**, 688.

[7] F. G. Celii, J. E. Butler, *Annual Review of Physical Chemistry* (1991) **42**, 643.

[8] J. E. Butler, R. L. Woodin, *Philosophical Transactions of the Royal Society of London Series a – Mathematical Physical and Engineering Sciences* (1993) **342**, 209.

[9] P. E. Pehrsson, J. E. Butler, in *Diamond Films and Coatings* (Ed: R. Davis), Noyes Publications (1993) p. 68.

[10] H. R. Thorsheim, J. E. Butler, in *Synthetic Diamond: Emerging CVD Science and Technology*, (Eds: K. Spear, J. Dismukes), Wiley Interscience (1994) p. 193.

[11] D. G. Goodwin, J. E. Butler, in *Handbook of Industrial Diamonds and Diamond Films* (Eds: M. A. Prelas, G. Popovici, L. K. Biglow), Marcel Dekker, Inc., NY (1997) p. 527.

[12] J. E. Butler, H. Windischmann, *MRS Bulletin* (1998) **23**, 22.

[13] D. M. Gruen, *Annual Review of Materials Science* (1999) **29**, 211.

[14] T. A. Railkar, W. P. Kang, H. Windischmann, A. P. Malshe, H. A. Naseem, J. L. Davidson, W. D. Brown, *Critical Reviews in Solid State and Materials Sciences* (2000) **25**, 163.

[15] P. W. May, *Philosophical Transactions of the Royal Society of London Series a – Mathematical Physical and Engineering Sciences* (2000) **358**, 473.

[16] V. P. Varnin, V. A. Laptev, V. G. Ralchenko, *Inorganic Materials* (2006) **42**, S1.

[17] O. A. Williams, M. Nesladek, *Physica Status Solidi a – Applications and Materials Science* (2006) **203**, 3375.

[18] D. Das, R. N. Singh, *International Materials Reviews* (2007) **52**, 29.

[19] W. D. Man, J. H. Wang, C. X. Wang, Z. B. Ma, *New Carbon Materials* (2002) **17**, 62.

[20] S. N. Marinkovic, in *Chemistry and Physics of Carbon*, Vol. **29** (2004) 71.

[21] H. Liu, D. S. Dandy, *Diamond Chemical Vapor Deposition – Nucleation and Early Growth Stages*, Noyes Publications, Park Ridge, NJ (1995).

[22] J. C. Angus, A. Argoitia, R. Gat, Z. Li, M. Sunkara, L. Wang, Y. Wang, *Philosophical Transactions of the Royal Society of London Series a – Mathematical Physical and Engineering Sciences* (1993) **342**, 195.

[23] L. N. Krasnoperov, I. J. Kalinovski, H. N. Chu, D. Gutman, *Journal of Physical Chemistry* (1993) **97**, 11787.

[24] J. A. Smith, E. Cameron, M. N. R. Ashfold, Y. A. Mankelevich, N. V. Suetin, *Diamond and Related Materials* (2001) **10**, 358.

[25] Y. A. Mankelevich, N. V. Suetin, M. N. R. Ashfold, J. A. Smith, E. Cameron, *Diamond and Related Materials* (2001) **10**, 364.

[26] M. N. R. Ashfold, P. W. May, J. R. Petherbridge, K. N. Rosser, J. A. Smith, Y. A. Mankelevich, N. V. Suetin, *Physical Chemistry Chemical Physics* (2001) **3**, 3471.

[27] J. Luque, W. Juchmann, J. B. Jeffries, *Journal of Applied Physics* (1997) **82**, 2072.

[28] J. Luque, W. Juchmann, E. A. Brinkman, J. B. Jeffries, *Journal of Vacuum Science & Technology A* (1998) **16**, 397.

[29] W. Juchmann, J. Luque, J. B. Jeffries, *Applied Optics* (2000) **39**, 3704.

[30] G. W. Faris, E. A. Brinkman, J. B. Jeffries, *Optics Express* (2000) **7**, 447.

[31] W. Juchmann, J. Luque, J. B. Jeffries, *Applied Optics* (2005) **44**, 6644.

[32] J. B. Wills, J. A. Smith, W. E. Boxford, J. M. F. Elks, M. N. R. Ashfold, A. J. Orr-Ewing, *Journal of Applied Physics* (2002) **92**, 4213.

[33] C. J. Rennick, J. A. Smith, M. N. R. Ashfold, A. J. Orr-Ewing, *Chemical Physics Letters* (2004) **383**, 518.

[34] C. J. Rennick, A. G. Smith, J. A. Smith, J. B. Wills, A. J. Orr-Ewing, M. N. R. Ashfold, Y. A. Mankelevich, N. V. Suetin, *Diamond and Related Materials* (2004) **13**, 561.

[35] C. J. Rennick, R. Engeln, J. A. Smith, A. J. Orr-Ewing, M. N. R. Ashfold, Y. A. Mankelevich, *Journal of Applied Physics* (2005) **97**, 113306.

[36] C. J. Rennick, J. Ma, M. N. R. Ashfold, A. J. Orr-Ewing, Y. A. Mankelevich, *Plasma Sources Science & Technology* (2006) **15**, 432.

[37] C. J. Rennick, J. Ma, J. J. Henney, J. B. Wills, M. N. R. Ashfold, A. J. Orr-Ewing, Y. A. Mankelevich, *Journal of Applied Physics* (2007) **102**, 063309.

[38] Y. A. Mankelevich, M. N. R. Ashfold, A. J. Orr-Ewing, *Journal of Applied Physics* (2007) **102**, 063310.

[39] K. Hassouni, O. Leroy, S. Farhat, A. Gicquel, *Plasma Chemistry and Plasma Processing* (1998) **18**, 325.

[40] K. Hassouni, T. A. Grotjohn, A. Gicquel, *Journal of Applied Physics* (1999) **86**, 134.

[41] K. Hassouni, A. Gicquel, M. Capitelli, J. Loureiro, *Plasma Sources Science & Technology* (1999) **8**, 494.

[42] G. J. M. Hagelaar, K. Hassouni, A. Gicquel, *Journal of Applied Physics* (2004) **96**, 1819.

[43] G. Lombardi, K. Hassouni, G. D. Stancu, L. Mechold, J. Ropcke, A. Gicquel, *Journal of Applied Physics* (2005) **98**, 053303.

[44] G. Lombardi, K. Hassouni, G. D. Stancu, L. Mechold, J. Ropcke, A. Gicquel, *Plasma Sources Science & Technology* (2005) **14**, 440.

[45] K. Hassouni, G. Lombardi, X. Duten, G. Haagelar, F. Silva, A. Gicquel, T. A. Grotjohn, M. Capitelli, J. Ropcke, *Plasma Sources Science & Technology* (2006) **15**, 117.

[46] J. Ma, *PhD thesis*, University of Bristol (2008).

[47] A. Cheesman, J. A. Smith, M. N. R. Ashfold, N. Langford, S. Wright, G. Duxbury, *Journal of Physical Chemistry A* (2006) **110**, 2821.

[48] F. G. Celii, P. E. Pehrsson, H. T. Wang, J. E. Butler, *Applied Physics Letters* (1988) **52**, 2043.

[49] G. Lombardi, F. Benedic, F. Mohasseb, K. Hassouni, A. Gicquel, *Plasma Sources Science & Technology* (2004) **13**, 375.

[50] G. Lombardi, K. Hassouni, F. Benedic, F. Mohasseb, J. Ropcke, A. Gicquel, *Journal of Applied Physics* (2004) **96**, 6739.

[51] G. Duxbury, N. Langford, M. T. McCulloch, S. Wright, *Chemical Society Reviews* (2005) **34**, 921.

[52] H. Toyoda, M. A. Childs, K. L. Menningen, L. W. Anderson, J. E. Lawler, *Journal of Applied Physics* (1994) **75**, 3142.

[53] P. John, J. R. Rabeau, J. I. B. Wilson, *Diamond and Related Materials* (2002) **11**, 608.

[54] J. R. Rabeau, P. John, J. I. B. Wilson, Y. Fan, *Journal of Applied Physics* (2004) **96**, 6724.

[55] M. D. Wheeler, S. M. Newman, A. J. Orr-Ewing, M. N. R. Ashfold, *Journal of the Chemical Society – Faraday Transactions* (1998) **94**, 337.

[56] P. Atkins, J. de Paula, *Atkins Physical Chemistry*, Oxford University Press (2006).

[57] B. J. Garrison, E. J. Dawnkaski, D. Srivastava, D. W. Brenner, *Science* (1992) **255**, 835.

[58] J. K. Kang, C. B. Musgrave, *Journal of Chemical Physics* (2000) **113**, 7582.

[59] H. Tamura, M. S. Gordon, *Chemical Physics Letters* (2005) **406**, 197.

[60] C. C. Battaile, D. J. Srolovitz, I. Oleinik, D. G. Pettifor, A. P. Sutton, S. J. Harris, J. E. Butler, *Journal of Chemical Physics* (1999) **111**, 4291.

[61] A. Cheesman, J. N. Harvey, M. N. R. Ashfold, *Journal of Physical Chemistry A.* (2008) **112**, 11436.

[62] H. Tamura, H. Zhou, Y. Hirano, S. Takami, M. Kubo, R. V. Belosludov, A. Miyamoto, A. Imamura, M. N. Gamo, T. Ando, *Physical Review B* (2000) **62**, 16995.

[63] M. Kaukonen, P. K. Sitch, G. Jungnickel, R. M. Nieminen, S. Poykko, D. Porezag,T. Frauenheim, *Physical Review B* (1998) **57**, 9965.

[64] M. Frenklach, S. Skokov, B. Weiner, *Nature* (1994) **372**, 535.

[65] J. J. P. Stewart, *Journal of Computational Chemistry* (1989) **10**, 209.

[66] S. Skokov, C. S. Carmer, B. Weiner, M. Frenklach, *Physical Review B* (1994) **49**, 5662.

[67] S. Skokov, B. Weiner, M. Frenklach, *Journal of Physical Chemistry* (1994) **98**, 8.

[68] S. Skokov, B. Weiner, M. Frenklach, *Journal of Physical Chemistry* (1994) **98**, 7073.

[69] S. Skokov, B. Weiner, M. Frenklach, *Journal of Physical Chemistry* (1995) **99**, 5616.

[70] D. Y. Huang, M. Frenklach, *Journal of Physical Chemistry* (1991) **95**, 3692.

[71] D. Huang, M. Frenklach, M. Maroncelli, *Journal of Physical Chemistry* (1988) **92**, 6379.

[72] I. I. Oleinik, D. G. Pettifor, A. P. Sutton, J. E. Butler, *Diamond and Related Materials* (2000) **9**, 241.

[73] R. C. Brown, C. J. Cramer, J. T. Roberts, *Journal of Physical Chemistry B* (1997) **101**, 9574.

[74] R. C. Brown, C. J. Cramer, J. T. Roberts, *Diamond and Related Materials* (2001) **10**, 39.

[75] S. J. Harris, *Applied Physics Letters* (1990) **56**, 2298.

[76] D. M. Gruen, P. C. Redfern, D. A. Horner, P. Zapol, L. A. Curtiss, *Journal of Physical Chemistry B* (1999) **103**, 5459.

[77] M. Sternberg, P. Zapol, L. A. Curtiss, *Molecular Physics* (2005) **103**, 1017.

[78] M. Sternberg, P. Zapol, L. A. Curtiss, *Physical Review B* (2003) **68**, 205330.

[79] D. D. Koleske, S. M. Gates, B. D. Thoms, J. N. Russell, J. E. Butler, *Journal of Chemical Physics* (1995) **102**, 992.

[80] D. D. Koleske, S. M. Gates, B. D. Thoms, J. N. Russell, J. E. Butler, *Surface Science* (1994) **320**, L105.

[81] J. S. Foord, K. P. Loh, R. B. Jackman, *Surface Science* (1998) **399**, 1.

[82] R. E. Stallcup, Y. Mo, T. W. Scharf, J. M. Perez, *Diamond and Related Materials* (2007) **16**, 1727.

[83] J. E. Butler, I. Oleynik, *Philosophical Transactions of the Royal Society a-Mathematical Physical and Engineering Sciences* (2008) **366**, 295.

[84] C. Kanai, K. Watanabe, Y. Takakuwa, *Physical Review B* (2001) **63**, 235311.

[85] A. Cheesman, J. N. Harvey, M. N. R. Ashfold, *Physical Chemistry Chemical Physics* (2005) **7**, 1121.

[86] S. J. Harris, D. G. Goodwin, *Journal of Physical Chemistry* (1993) **97**, 23.

[87] M. Frenklach, S. Skokov, *Journal of Physical Chemistry B* (1997) **101**, 3025.

[88] C. Kanai, Y. Shichibu, K. Watanabe, Y. Takakuwa, *Physical Review B* (2002) **65**, 153312.

[89] S. Skokov, B. Weiner, M. Frenklach, T. Frauenheim, M. Sternberg, *Physical Review B* (1995) **52**, 5426.

[90] C. C. Battaile, D. J. Srolovitz, *Annual Review of Materials Research* (2002) **32**, 297.

[91] M. Frenklach, H. Wang, *Physical Review B* (1991) **43**, 1520.

[92] M. E. Coltrin, D. S. Dandy, *Journal of Applied Physics* (1993) **74**, 5803.

[93] A. Netto, M. Frenklach, *Diamond and Related Materials* (2005) **14**, 1630.

[94] R. C. Brown, J. T. Roberts, *Journal of Physical Chemistry B* (2000) **104**, 8420.

[95] R. E. Stallcup, L. M. Villarreal, S. C. Lim, I. Akwani, A. F. Aviles, J. M. Perez, *Journal of Vacuum Science & Technology B* (1996) **14**, 929.

[96] C. C. Battaile, D. J. Srolovitz, J. E. Butler, *Journal of Applied Physics* (1997) **82**, 6293.

[97] C. C. Battaile, D. J. Srolovitz, J. E. Butler, *Diamond and Related Materials* (1997) **6**, 1198.

[98] C. C. Battaile, D. J. Srolovitz, J. E. Butler, *Journal of Crystal Growth* (1998) **194**, 353.

[99] C. C. Battaile, D. J. Srolovitz, J. E. Butler, *Journal of Electronic Materials* (1997) **26**, 960.

[100] D. J. Srolovitz, D. S. Dandy, J. E. Butler, C. C. Battaile, Paritosh, *JOM – Journal of the Minerals Metals & Materials Society* (1997) **49**, 42.
[101] C. C. Battaile, D. J. Srolovitz, J. E. Butler, *Journal of Materials Research* (1999) **14**, 3439.
[102] M. Grujicic, S. G. Lai, *Journal of Materials Science* (1999) **34**, 7.
[103] M. Grujicic, S. G. Lai, *Journal of Materials Science* (2000) **35**, 5371.

6 Heteroepitaxial Growth

M. SCHRECK

University of Augsburg, Germany

6.1 Introduction 126
6.2 The nucleation procedures 127
  6.2.1 Nucleation enhancement by scratching techniques 128
  6.2.2 Nucleation by ion bombardment 128
  6.2.3 Heteroepitaxial nucleation 129
6.3 Oriented diamond growth on various substrates and crystal faces 130
  6.3.1 c-BN: nucleation without pretreatment 130
  6.3.2 Sapphire: diamond nucleation and growth by laser ablation 130
  6.3.3 Cobalt, nickel, platinum: nucleation by diamond seeding and annealing 130
  6.3.4 TiC: BEN on a metal carbide 131
  6.3.5 Si, β-SiC: BEN on a semiconductor crystal and its carbide 131
  6.3.6 Re, Ir: BEN on non-carbide-forming metals 131
6.4 Heteroepitaxial diamond films on Si and β-SiC 132
  6.4.1 Diamond nucleation on Si: phenomenology of the BEN process 132
  6.4.2 Diamond nucleation on Si: models proposed for the explanation of the BEN process 133
  6.4.3 Diamond nucleation on Si: the aspect of epitaxy 135
  6.4.4 Reduction of the mosaic spread by textured growth 137
  6.4.5 Limitations for the structural perfection in the systems Dia/Si and Dia/β-SiC 138
6.5 Heteroepitaxial diamond growth on iridium 141
  6.5.1 BEN on iridium: nucleation under etching conditions and pattern formation 141
  6.5.2 The topographic signature of the domains 142
  6.5.3 The internal structure of the BEN layer 143
  6.5.4 The temporal development of the domain patterns during BEN 145
  6.5.5 Models describing the nucleation 146

CVD Diamond for Electronic Devices and Sensors Edited by Ricardo S. Sussmann
© 2009 John Wiley & Sons, Ltd. ISBN: 978-0-470-06532-7

6.5.6 Mechanisms of texture improvement 147
6.5.7 Strategies for a scaling-up: large oxide single crystals versus silicon based multi-layer structures 151
6.6 Properties and applications of heteroepitaxial diamond layers 152
6.7 Concluding remarks 154
References 154

6.1 INTRODUCTION

The unique combination of unrivalled material properties has been a permanent challenge for scientists and engineers who had tried to synthesize diamond crystals for centuries. Since the successful invention in 1954 of the high pressure–high temperature (HPHT) method [1], large quantities of synthetic diamond crystals have been produced mainly for mechanical applications. Even after 50 years the constraints imposed by growth environment and growth rate still limit the size of HPHT crystals to volumes of about 1 cm^3 [2].

The introduction of chemical vapour deposition (CVD) techniques opened up new possibilities such as the synthesis of thin films on large area substrates. Meanwhile protective coatings on tools and freestanding discs of polycrystalline diamond serving as heat spreaders or laser windows have entered the market as commercial products [3].

The most challenging applications for diamond are to be found in the field of electronic devices or detectors (see chapters elsewhere in this book). Here the ultimate performance can only be obtained by minimizing the density of chemical and structural defects. The latter aspect calls for single crystal samples in which the influence of grain boundaries is absent.

Homoepitaxial layers grown by CVD on HPHT single crystals can fulfil these quality requirements, as has been proved by the ultimate electron and hole mobility values that have recently been measured [4]. Various modified concepts based on the increase of single crystal substrates by homoepitaxial growth are currently under evaluation. They comprise the increase of the growth rate using nitrogen [5], the sequential application of many high rate growth steps in specifically designed sample holders [6] or the use of multiple seeds (mosaic growth) [7]. However, up to now, wafer-size homoepitaxial single crystals have not been demonstrated.

For other materials like GaN suffering from a similar lack of large single crystals, heteroepitaxy has turned out to be a viable alternative [8, 9]. Heteroepitaxy means oriented growth of one crystalline material on the surface of another one. The orientation relationship is usually given by designating for both crystals: (i) the lattice planes that form the interface, and (ii) two coinciding lattice vectors within these planes. Early work on heteroepitaxy was based on the assumption that oriented growth is only possible below a certain misfit in the lattice parameters [10]. In the meantime, many epitaxial systems with huge misfit have been demonstrated, which proves that this parameter does not yield a serious criterion for exclusion. Nevertheless, the usual aim is to minimize the mismatch since it controls the misfit dislocation network at the interface and thus influences the defect structure and mosaic spread of the grown layer.

While searching for an appropriate diamond growth substrate several aspects have to be considered:

(i) stability in the diamond growth environment;
(ii) chemistry, i.e. binding between carbon and substrate material, carbide formation and dissolution of carbon in the substrate material;
(iii) geometry, i.e. crystal structure and lattice mismatch;
(iv) availability in high quality and as large area samples.

Concerning diamond heteroepitaxy, it turned out that completely different materials can provide a template for oriented growth. They span from insulators like sapphire [11] over elemental [12] and compound semiconductors [13] to carbide-forming [14] and noncarbide-forming metals [15].

This review begins with a description of various nucleation procedures that have been developed for generating diamond nuclei on foreign substrates, followed by an overview of the different material combinations that have yielded oriented diamond growth. In order to permit critical assessing of the grain alignment and the resulting potential of a specific film/substrate combination, thicker layers and texture data are required. These are available only in few cases. Therefore this review firstly focuses on silicon and silicon carbide, two systems with a high potential for scaling-up that have been examined intensively. According to the available literature, neither ever yielded real single crystal diamond layers. The limiting factors are discussed. Currently iridium layers seem to be most seminal concerning single crystal diamond wafer technology and therefore take up most of the space in this chapter, which, furthermore compares different models for the description of epitaxial nucleation processes on Ir as well as current concepts for scaling-up via dedicated multilayer structures.

6.2 THE NUCLEATION PROCEDURES

In classical nucleation theory the critical cluster size above which further growth of a particle is more probable than its decay is called the nucleus size [16]. For homogeneous nucleation of a spherical particle with radius r, the critical size is given by the change in the free energy between the gas phase and the solid phase, which is composed of a bulk contribution ($\propto r^3$) and a surface contribution ($\propto r^2$). For a positive supersaturation, the bulk contribution is negative, i.e. condensation of particles is energetically favourable. In contrast, formation of a free surface gives a positive energy contribution. The sum of both yields a maximum in the free energy at a small radius, which corresponds to the formation energy of the nucleus. In heterogeneous nucleation, i.e. when condensation takes place on a solid surface, the surface energy of the substrate and the interface energy deposit/substrate have to be taken into consideration as additional contributions.

A simple transfer of this concept to diamond is hampered by the complexity of diamond CVD, since it involves a metastable phase that has to be stabilized and requires conditions that suppress nucleation and growth of the thermodynamically stable graphite phase. In diamond, breaking bonds and forming a free surface costs a high amount of energy (about

6 J/m^2 [17]). Reconstruction and surface termination can significantly modify this value. However, the generally low nucleation densities ($<10^6$ cm^{-2}) on untreated nondiamond substrates confirm the existence of a high energy barrier for nucleus formation. Only on c-BN with its similar crystal structure, bonding and surface energy is the barrier apparently low enough for spontaneous nucleation with appreciable density to occur [18, 19].

A huge amount of studies has been performed to find correlations between substrate properties and diamond nucleation. In these studies, without surface pretreatment two general trends were found. Firstly, carbon concentration at the surface and its evolution with process time is controlled by the diffusion of carbon into the bulk and by carbide formation properties of the substrate material. Thus, carbide formation and low diffusion accelerate the emergence of a surface carbon concentration sufficient to allow nucleation [20]. Secondly, the actual nucleation mainly occurs at defect structures on the surfaces.

For most technical applications nucleation densities of 10^9-10^{11} cm^{-2} are indispensable [21]. These can only be obtained by additional nucleation enhancement procedures. While a large variety of pretreatment methods have been studied, two methods turned out to be most efficient: the treatment with diamond powder, e.g. by mechanical scratching or ultrasonic scratching, and the bias enhanced nucleation (BEN) procedure. Due to their relevance, the present article is mainly restricted to these two methods. An extensive overview of earlier studies in this field may be found in the literature [22, 23].

6.2.1 Nucleation enhancement by scratching techniques

Mechanical scratching of substrate surfaces with diamond powder or paste and ultrasonic treatment with a diamond powder suspension can increase the nucleation density up to 10^{11} cm^{-2}. The particle size of the powder is typically 0.1–20 μm. By explaining the predominant mechanism of this treatment, creation of defect sites and diamond residues have been discussed. A first indication for the fact that the main contribution stems from seeding diamond residues arose from the observation that treatments with alternative powders containing SiC, Al_2O_3, ZrO_2, or nitrides, were always significantly less effective. Further strong evidence for this interpretation was obtained from a very careful transmission electron microscopy (TEM) study in which the density of diamond residues was clearly correlated with the diamond grain density grown on the samples [24]. As a consequence, in current CVD work, treatment with diamond powder became established as the predominant technique if the only requirement is nucleation with high area density. Refined techniques using nanodiamond from the detonation synthesis were also developed [25].

6.2.2 Nucleation by ion bombardment

In 1991 Yugo *et al.* introduced a new method, later termed bias enhanced nucleation (BEN), in a microwave plasma (MWPCVD) set-up [26] (for a description of different CVD diamond growth techniques see Chapter 5 in this book). The authors applied bias voltages between +100 and −200 V for 2 to 15 min to an unscratched silicon substrate. The concentration of methane in hydrogen was varied between 1 and 40 %. They found that threshold values of −70 V and 5 % methane are required for the generation of nucleation densities up to 10^{10} cm^{-2}. In the aftermath it turned out that nucleation enhancement can be achieved at negative as well as at positive voltages [27]. Using high methane concentrations enhancement was observed at DC voltages down to ±20 V [27]. Meanwhile another fact was discovered, namely that there is no clear threshold value for the methane concentration: heteroepitaxial diamond nucleation on silicon was realized at CH_4 concentrations as low as 1 % [28]. Finally, biasing with AC voltage [29] and repetitive pulse bias [30] were introduced as means to increase the fraction of oriented diamond crystals and to improve the homogeneity of epitaxial diamond films on silicon, respectively. Among all these technological variants, negative DC biasing using moderately increased methane concentrations represents the most established technique.

To excite the gas phase thermally by using a hot filament (HF) does not generate sufficient charge carriers to allow a significant current flow under low bias voltage. At higher voltages a discharge is ignited, and under careful control of the process conditions it is possible to nucleate heteroepitaxial diamond [31, 32]. By introducing a grid above the filament, the technique has been refined and allowed to generate a defined stable discharge by applying a second bias voltage between filament and grid [33].

Sawabe *et al.* combined a DC plasma CVD setup with a second DC biasing discharge for nucleation of diamond on silicon and iridium [15].

Applying a negative voltage in HF-, MW- or DC-plasma CVD is always accompanied by a localized discharge above the substrate. The simplest way to achieve this nucleation promoting discharge is to use only the DC voltage and increase it until a self-sustaining glow discharge is ignited. This promising technique was successfully applied for the epitaxial nucleation of diamond on 1-inch Ir/MgO substrates [34, 35].

Triggered by the awareness that the bombardment with positive ions may be the key mechanism of diamond nucleation by BEN, pure low energy ion beams were also employed to deposit carbon films and to generate diamond nuclei [36]. In principle this technique should allow a much better control of the local bombarding parameters like ion energy, ion-to-neutral ratio, and particle fluxes. However, the experimental results reported up to now neither reached the nucleation density nor the epitaxial alignment that can be easily obtained by BEN in MWPCVD.

6.2.3 Heteroepitaxial nucleation

All the nucleation techniques described above were at first developed for depositing polycrystalline films. In order to achieve oriented nucleation it was necessary to make the following modifications:

(i) For the seeding technique e.g. on Co, Ni and Pt, a careful control of the deposition conditions [37–39] and the accomplishment of specific post-treatment procedures [40–42] allowed initially random oriented seeds to be converted into heteroepitaxial diamond grains.
(ii) The key parameter for obtaining oriented nucleation by BEN on Si turned out to be the duration of the biasing procedure. Epitaxial diamond crystallites are only observed within a well-defined process time window [43].
(iii) For all nucleation and deposition techniques – even for systems that do not require a surface pretreatment – it is important to choose textured growth conditions adapted for the specific growth surface, e.g. (001) or (111). Otherwise, renucleation and

twinning cause polycrystalline films that cover the initially oriented nuclei at the interface.

6.3 ORIENTED DIAMOND GROWTH ON VARIOUS SUBSTRATES AND CRYSTAL FACES

This section briefly overviews the rich variety of growth substrates that served as a basis for heteroepitaxially oriented diamond crystal deposition.

6.3.1 c-BN: nucleation without pretreatment

A system most particularly characterized and for which oriented diamond growth without surface pretreatment has been observed is c-BN [44–47]. It was selected due to the low lattice mismatch of 1.3 %, the close relationship of its zinc-blende structure to that of diamond, and the high interfacial adhesion energy [48]. On the boron-terminated $\{111\}_B$ facets, a carbonaceous layer first decorates the terrace edges followed by a nucleation of isolated three-dimensional islands, which grow laterally and coalesce. On the opposite nitrogen-terminated $\{111\}_N$ facets, the different chemistry does not allow an oriented nucleation. On c-BN{001}, pyramidal diamond crystallites were observed that formed a closed layer within few minutes. The crystallographic orientation relationship on {111}, as well as on {001}, is always cube-on-cube. Thick epitaxial layers up to 10 µm have been prepared. In spite of the absence of X-ray diffraction (XRD) texture data, the studies indicate an excellent alignment. Nevertheless, due to the small size of available c-BN crystals, the system does not provide a viable concept for the growth of large diamond single crystals.

6.3.2 Sapphire: diamond nucleation and growth by laser ablation

Diamond growth on a sapphire (0001) surface by laser ablation of graphite in an oxidizing environment has been reported by Yoshimoto *et al.* [11]. This work proved the possibility of hydrogen-free diamond growth and demonstrated (111)-oriented diamond grains with clear azimuthal alignment. Up to the present there have been no attempts to grow thick layers or to determine texture data reported.

6.3.3 Cobalt, nickel, platinum: nucleation by diamond seeding and annealing

In search of new substrates suitable for diamond heteroepitaxy, the Group VIII transition metals Co, Ni, and Pt were mainly chosen due to their rather good lattice fit with diamond (diamond: 0.3567 nm, β-Co (above 417 °C): 0.3554 nm, Ni: 0.3517 nm, Pt: 0.3923 nm). For these three materials diamond seeding followed by high temperature annealing and growth steps yielded oriented diamond growth. In all cases it was speculated that a mixed metal–carbon–hydrogen phase was involved in the orientation formation mechanisms.

On the (111) surface of Co single crystals, the experimental results were limited to isolated epitaxial diamond crystals [40]. In contrast, for nickel, oriented nucleation and growth of 30-µm-thick coalesced diamond films were achieved on (001) and (111) surfaces [41, 42, 49].

Pt(111) was intensively studied by Kobashi *et al.* [50]. The authors used Pt single crystals and epitaxial Pt layers. In extended studies they were able to clarify the mechanisms of orientation formation consisting of the sequence dissolution, movement, alignment and recrystallization of the diamond seeds. They highlighted the intrinsic problem of double positioning for (111) oriented growth [51] and made first approaches to avoid the second variant rotated by 60° by using off-axis substrates [52]. Extensive XRD texture studies also allowed the appraisal of the structural properties of the films. Minimum values for the tilt of 1.1° (FWHM) were reported for diamond layers on Pt/Ir/Pt/sapphire(0001) without information about the in-plane angular spread (twist) [53].

6.3.4 TiC: BEN on a metal carbide

In a survey study with refractory metal substrates, Wolter *et al.* found a strong correlation between the efficiency of the BEN process and the carbide forming nature of the metal [54]. For one of these metal carbides, TiC(111), they later demonstrated successful nucleation of epitaxially aligned diamond crystals [14].

6.3.5 Si, β-SiC: BEN on a semiconductor crystal and its carbide

Compared with carbide-forming refractory metals [54], silicon is a strong carbide former, yielding the highest diamond nucleation densities of nearly 10^{11} cm^{-2}. For epitaxial growth the lattice mismatch could not be worse: $a_{\mathrm{Si}}/a_{\mathrm{Dia}} = 0.5431/0.3567 = 1.522$ and $a_{\mathrm{SiC}}/a_{\mathrm{Dia}} = 0.4360/0.3567 = 1.22$. Nevertheless, oriented nucleation by BEN was first carried out on β-SiC [13] and shortly afterwards on Si [12]. Extensive studies of BEN on Si and β-SiC yielded a lot of insight into the nucleation process and the textured growth of epitaxial diamond. This is described more precisely in Section 6.4.

6.3.6 Re, Ir: BEN on non-carbide-forming metals

The hcp metal rhenium and the fcc metal iridium are two non-carbide-forming elements for which epitaxial nucleation by BEN has been shown. On the Re(0001) surface, BEN generated diamond crystals with an area density of 2×10^8 cm^{-2} [55]. A small fraction of them was epitaxially aligned. The hexagonal symmetry of the substrate caused the occurrence of two equivalent variants rotated by 60° about the surface normal of the (111) contact plane. The resulting diamond films showed tilt and twist values of 4.8° and 3° (FWHM), respectively. The rather poor adhesion indicated a weak interaction between diamond and Re. Under the harsh ion bombardment, the Re took up carbon well above the saturation limit and released it later under pure hydrogen plasma conditions.

Iridium is another metal that neither forms a carbide nor takes up any significant amount of carbon, even under intense ion bombardment during BEN [56]. The nucleation density is extremely high, usually only oriented grains are found and the binding to diamond is

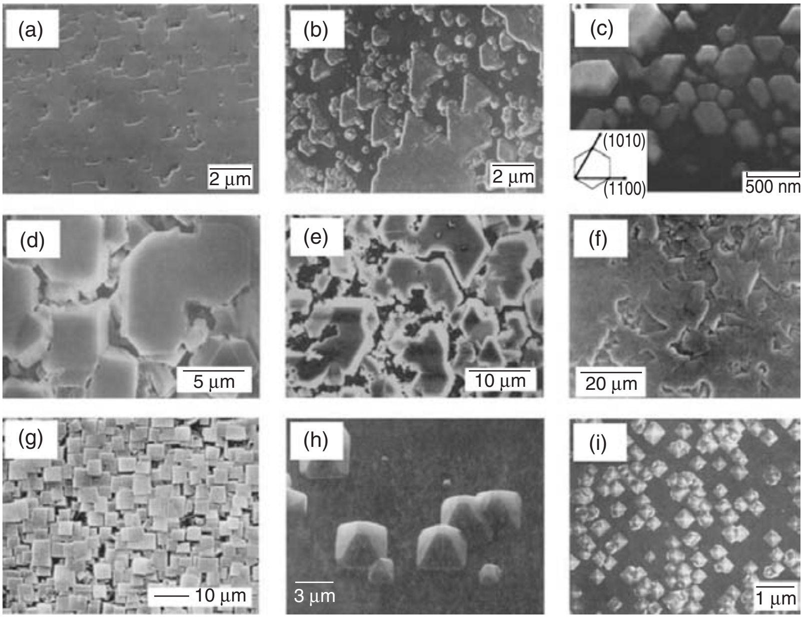

Figure 6.1 Survey of epitaxial diamond growth on different substrate materials: (a) c-BN(001); (b) c-BN(111); (c) Al_2O_3(0001); (d) Ni(001); (e) Ni(111); (f) Pt(111); (g) Si(001); (h) β-SiC(001); (i) Ir/MgO(001). (a) and (b) reprinted from [47] with permission from Elsevier. (c) reprinted from [11], copyright Nature Publishing. (d) and (e) reproduced from [42] by permission of the American Institute of Physics. (f) reprinted from [39] with permission from Elsevier. (g) reprinted from [12] by permission of the American Institute of Physics. (h) reprinted from [13] by permission of the American Institute of physics. (i) reprinted from [15] by permission of the Japanese Society of Applied Physics

very strong. As elaborated on in Section 6.5, diamond nucleation on Ir completely differs from the processes taking place on any other material.

The list of substrate materials that facilitated oriented deposition of at least isolated diamond grains can be completed by Cu [37], BeO [57], Ni_3Si [58], graphite and 6H-SiC [59]. Figure 6.1 presents a compilation of different systems.

6.4 HETEROEPITAXIAL DIAMOND FILMS ON Si AND β-SiC

Primarily BEN has been developed as an alternative to the scratching procedure. The majority of studies that aimed for a clarification of the BEN mechanisms were done on Si substrates in microwave plasmas. The following two sections therefore summarize general findings and models concerning diamond nucleation by biasing on silicon. In the subsequent sections, the aspect of epitaxial alignment will be considered.

6.4.1 Diamond nucleation on Si: phenomenology of the BEN process

On silicon, the nucleation process by BEN is typically done for 10–60 min at increased CH_4 concentration (e.g. 5 % in H_2) using bias voltages between −100 and −300 V, and

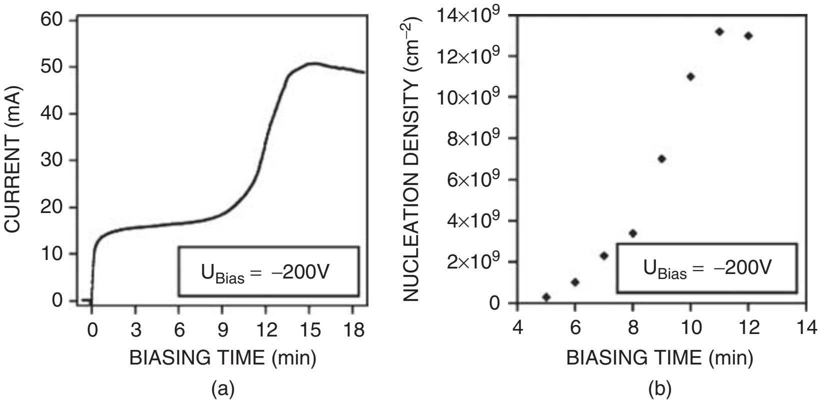

Figure 6.2 (a) Temporal development of the biasing current, and (b) the density of diamond grains during the biasing procedure on Si(001). Reprinted from [72] with permission from MYU KK

the process can be directly monitored by recording the biasing current. Figure 6.2 shows the current during the first 20 min after applying a negative DC bias voltage of −200 V to a mirror-polished silicon substrate in a gas mixture of 9 % CH_4 in H_2. After a short delay time of about 9 min, the current increases steeply and saturates after 15 min. While the absolute values of time constants and current levels depend on the chosen process parameters and the reactor geometry, these current versus time characteristics represent the typical signature for a successful BEN process [60]. The density of diamond grains (see Figure 6.2(b)) follows the increase of current.

Figure 6.3 shows the microwave plasma discharge (a) without bias, (b) with bias applied to pure Si, and (c) with bias applied to a diamond-covered surface. The course of the optical emission intensity during negative biasing in Figure 6.3(d) exhibits local maxima 1.95 and 0.8 mm above the pure silicon and diamond-covered surface, respectively. Stark effect measurements of the hydrogen Balmer lines (see in Figure 6.3(e) the splitting of the line in the biasing field) confirm that actually the major fraction of the applied bias voltage drops within the 1–2 mm wide cathode sheath [61]. Compared with this, the voltage drop within the plasma ball only yields a minor contribution. The resulting field enhancement with values of several kV/cm directly above the negatively biased substrate surface allows a strong acceleration of positively charged ions. They reach kinetic energies of more than 100 eV, as measured by Katai *et al.* [62], in spite of a gas kinetic mean free path in the range of 10 μm. In a glow discharge the width of the cathode fall is controlled by pressure, gas type and the electron yield of the cathode material [63]. For hydrogen terminated diamond with its negative electron affinity the yield for ion-induced electron emission is exceptionally high [64], which explains the steep rise in biasing current with the successive coverage of the silicon surface by diamond (see Figure 6.2(a))

6.4.2 Diamond nucleation on Si: models proposed for the explanation of the BEN process

Local changes in the gas phase activation were initially considered as one possible mechanism of nucleation enhancement by BEN [65]. However, biasing on micro-patterned

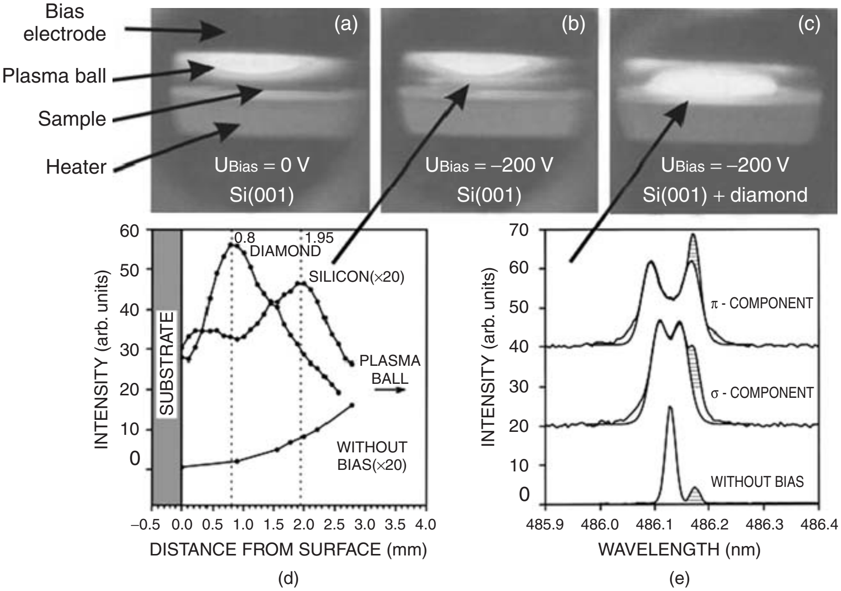

Figure 6.3 Images of a microwave plasma discharge: (a) Discharge above a silicon substrate without applied bias; (b) modification of the MW discharge after application of a negative bias of −200 V above a mirror polished Si substrate; (c) the same discharge after coverage of the silicon with a closed diamond film; (d) the optical emission intensity shows a sharp maximum 2 mm above the clean silicon and 0.8 mm above the diamond covered substrate; (e) the Stark splitting of the hydrogen Balmer line H_β is compatible with a field strength of 3.5 kV/cm above the diamond covered substrate. Reprinted from [61] by permission of Elsevier

silicon wafers clearly revealed the crucial role of directional ion bombardment: nucleation was only obtained on planar areas while the side walls, parallel to the preferential direction of accelerated ions, remained free of nuclei [66].

For describing the crucial processes stimulated by hyperthermal particle bombardment two basically different types of models were considered: (i) surface processes and (ii) subsurface processes.

The suggestion of enhanced surface diffusion due to ion bombardment as a critical step in BEN was deduced from nearest-neighbour distance distribution measurements [67]. The data showed a shift towards larger distances between grains as compared with a statistical distribution that was interpreted in terms of depletion zones at the substrate surface around existing diamond grains. Another effect evoked by ion bombardment on the very surface was the creation of defects serving as nucleation sites.

The majority of alternative models are based on the fact that carbon and hydrocarbon ions with energies of several tens up to ∼100 eV are capable of penetrating the surface of a carbon layer (15–20 eV [68]), displacing atoms in graphite (15–20 eV) and also from a diamond lattice (30–48 eV) [69]. In brief, they can induce all the elementary processes that play a role in the deposition of hard amorphous carbon films with high sp^3 fraction. According to the subplantation model, carbon atoms that are shallowly implanted densify the carbon matrix. Driven by compressive stress and/or preferential displacement processes – carbon atoms bound in graphite can be more easily displaced than those in a diamond environment – sp^2 bonded carbon is transformed into sp^3. Spontaneous bulk nucleation of diamond embryo clusters that are able to grow continuously by ion-bombardment-induced preferential displacement processes, was suggested as an explanation for diamond nucleation under these conditions [70]. The ion-bombardment-induced growth mechanism is supported by the direct experimental observation of transformation processes from fullerene and graphite to diamond under particle irradiation as reported by Banhart *et al.* [69].

6.4.3 Diamond nucleation on Si: the aspect of epitaxy

In general the process of diamond nucleation on silicon consists of two steps: the nucleation by BEN and the ensuing growth. Both steps have to fulfil certain requirements in order to ensure that the procedure yields heteroepitaxial grains and not just a high nucleation density (10^{10}–10^{11} cm^{-2}), which is easy to obtain.

The first factor refers to the biasing procedure. As it turned out epitaxial orientation is a transient phenomenon, i.e. oriented films can only be obtained within a well-defined process time window. Figures 6.4(a) and (b) show varying diamond film textures measured by XRD and imaged by SEM as a function of the duration of the BEN process and the current increase [71, 72]. There are three different regimes to be distinguished. For the process conditions chosen, below 5 min the biasing treatment is too short: only few grains appear. Together with the first rise of the biasing current a transition to regime II occurs. In this regime epitaxial diamond is observed. The optimum in epitaxial orientation (biasing time t_{opt}) and the minimum in mosaic spread is rapidly passed when the current rises steeply. After 12 min BEN, the epitaxial orientation has vanished completely.

Using a systematic variation of the bias voltage, the existence of a process time window for epitaxial diamond nucleation was deduced (see Figure 6.4(c)). While the absolute values for the voltages and the width of the window heavily depend on the specific setup and the plasma parameters, two general trends were found:

(i) The process time window rapidly narrows towards higher bias voltages (at −300 V the width reduces to 70 s and the optimum duration is 20 s).
(ii) Towards lower voltages the window widens and the mosaic spread improves (see also Figure 6.6). Unfortunately this positive trend is stopped abruptly when the voltage drops below the threshold value that is necessary to induce diamond nucleation by BEN.

It is essential that the growth conditions promote the survival of epitaxial grains. Even if some reports in the literature mention a fraction of 90 % oriented diamond grains on Si(001) [73] usually the majority of grains on silicon and SiC are nonepitaxial. Consequently, in order to avoid successfully formed (001)-oriented epitaxial diamond grains being immediately overgrown and buried by nonepitaxial crystals, (100)-textured growth conditions should be chosen. Substrate temperature, gas composition, and also the addition of traces of gas phase impurities like nitrogen [74, 75] are suitable parameters for this tuning process.

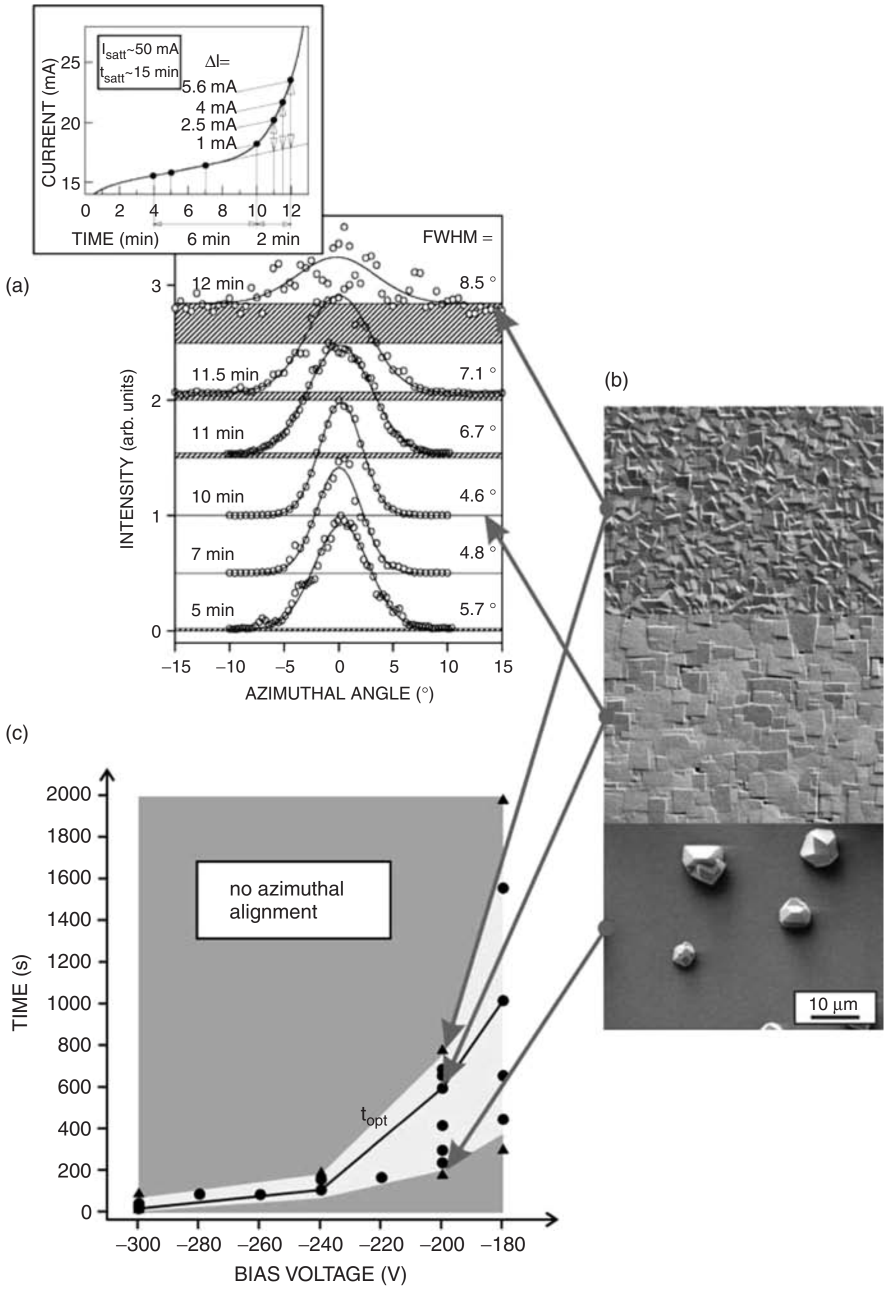

Figure 6.4 The process time window of epitaxial diamond nucleation on silicon. (a) Biasing current and XRD azimuthal scans of diamond films after BEN and 20 h growth. (b) SEM micrographs of the corresponding diamond films that were grown after different duration of the BEN process. (c) Map of the biasing time–bias voltage parameter space. Epitaxial alignment is only observed within the light grey area. Reprinted from [71] with permission from MYU KK

6.4.4 Reduction of the mosaic spread by textured growth

For diamond on silicon the epitaxial orientation relationship is Dia(001) [100] | | Si(001) [100]. This means that on both sides of the hetero-interface the contact is formed by (001) planes. In addition the azimuthal orientation is identical for diamond and silicon. An analogous cube-on-cube orientation applies to the system Dia/β-SiC.

As mentioned in the previous section, an appropriate textured growth step ensures that epitaxial diamond grains survive and that nonepitaxial crystals are overgrown. A careful analysis with respect to a thickness dependence of the texture data results in the conclusion of grain coarsening also having an impact on the orientation distribution of epitaxial grains. Figure 6.5 shows the variation of the mosaic spread decomposed into the polar component (tilt) and the azimuthal component (twist) with film thickness [76]. The tilt continuously improves towards higher thickness while the twist remains almost constant. First of all, this result indicates that a simple overgrowth of unfavourably oriented grains by favourably oriented ones controls the observed texture improvement (for more details see Section 6.5.6) Furthermore, this observation entails two important consequences:

(i) The constancy of the twist component imposes severe limitations for structure improvement of epitaxial diamond films on Si by mere growth of thick films.

(ii) The twist provides an ideal quantitative quality parameter (and the only meaningful one) for a systematic study of the BEN process, since it is essentially independent of nucleation density and duration of the growth process. The restriction of the data analysis to the twist component as presented in Figure 6.4 was based on this observation.

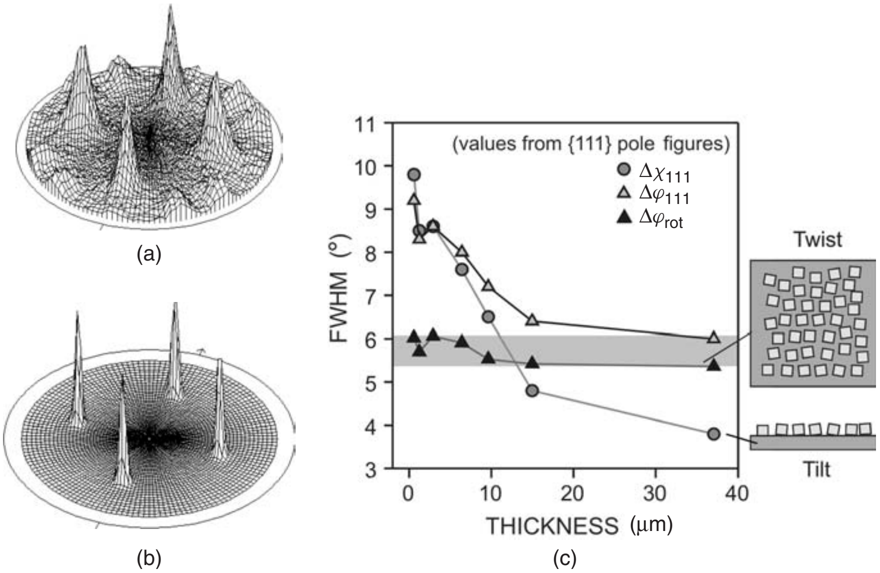

Figure 6.5 Diamond {111} pole figures of (a) a 0.6-µm thick, and (b) a 37-µm thick epitaxial diamond film on silicon. (c) FWHM of tilt and twist for epitaxial diamond films on silicon versus film thickness. $\Delta\chi_{111}$ and $\Delta\varphi_{111}$ correspond to the polar and azimuthal width of the pole density maxima in the pole figure. $\Delta\varphi_{\mathrm{rot}}$ represents the pure azimuthal angular spread [76]

6.4.5 Limitations for the structural perfection in the systems Dia/Si and Dia/β-SiC

In extensive parameter studies, epitaxial diamond films have been obtained for a wide range of substrate temperatures, gas pressures, and gas compositions (including the addition of oxygen [77]). Figure 6.6(a) summarizes the texture data for two completely different sets of process parameters [71]. As a fundamental result, it was concluded that epitaxy does not require a clearly defined narrow set of process parameters but a carefully controlled duration of the BEN procedure.

Interpreted in absolute numbers, the lowest twist value reported in literature for diamond on Si(001) was 3.9° (see Figure 6.6(a)). This indicated that growth of diamond on silicon may not provide a route to real single-crystal diamond films. TEM studies confirmed that heteroepitaxial diamond films on silicon always consist of individual crystallites [78, 79].

On β-SiC the database is less comprehensive and complete. The surface of epitaxial diamond films grown on on-axis and off-axis β-SiC substrates is comparable to that of a homoepitaxial layer, i.e. individual grains cannot be distinguished any more (Figure 6.7) [80]. According to the available reports, the mosaic spread for diamond might be ~50 % lower than on Si [80, 28], still meaning a significant misorientation.

Various reasons were suggested to explain the large angular spread. The most common referred to the huge lattice misfit between diamond and silicon (52 %) or diamond and β-SiC (22 %). Early models assumed that accommodation of the mismatch for diamond on β-SiC should result in preferred tilt and twist angles [81]. Only one publication presented

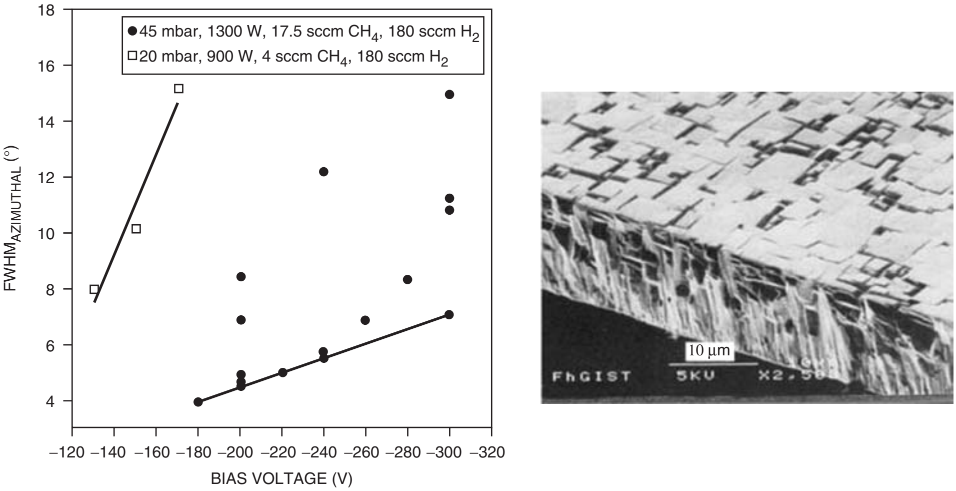

(a) (b)

Figure 6.6 (a) In-plane angular spread of epitaxial diamond films on silicon versus bias voltage for two different parameter sets (gas pressure, MW power, methane concentration). The scatter for each voltage results from the systematic variation of the epitaxial alignment within the process time window. The data point at −180 V corresponds to the minimum twist value that has been reported up to now for diamond on silicon films. Reprinted from [71] by permission of the American Institute of Physics. (b) Surface and cross section SEM image of a state of the art epitaxial diamond film on Si(001) [73]

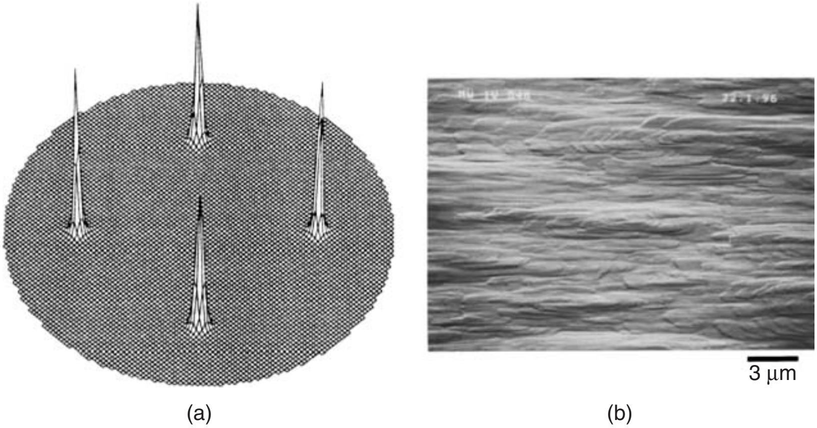

Figure 6.7 High quality epitaxial diamond layer on β-SiC(001) with a film thickness of 20 µm: (a) {111} pole figure, and (b) SEM image of the film surface. Reprinted from [80] by permission of the American Institute of Physics

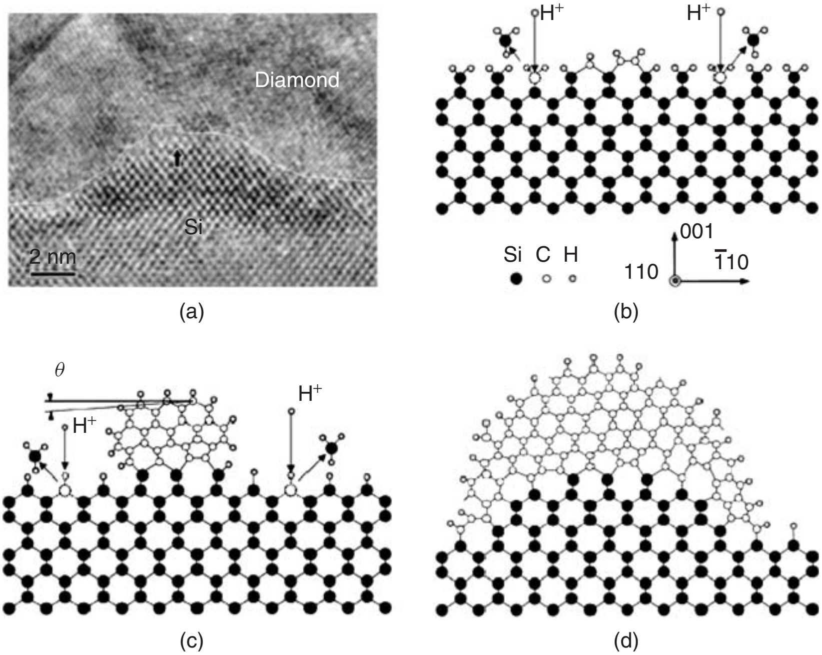

Figure 6.8 (a) High resolution TEM lattice image of a diamond grain with a tilt angle of about 6° located on top of a hillock that is believed to be the point where the nucleation occurred. (b), (c), (d) Schematics of the diamond nucleation on silicon. During interaction with the plasma, the deposition of carbon competes with the etching of silicon by hydrogen. The resulting roughening of the silicon surface causes the formation of tilted diamond nuclei. Reprinted from [85] by permission of the American Physical Society

experimental XRD data that indicated such a preferential misorientation for diamond on Si(001) [82]. In contrast, the majority of XRD [28] and also AFM data [83] revealed statistical orientation distributions that could be nicely fitted by Gaussian distributions, with the maximum corresponding to the perfect alignment. In TEM studies, imaging the interface of epitaxial diamond grains on Si(001), a well-defined crystalline interface structure was observed with a density of misfit dislocations that corresponded to the 3:2 lattice mismatch. The angular deviation in slightly misaligned grains was realized by an appropriate combination of interface dislocations [84]. Whereas this serves as a possible description for their geometric arrangement, it does not provide an explanation of why the grains show such a high misorientation. As a major driving force the same authors later proposed the asymmetric strain provoked by roughening of the silicon surface around the diamond nucleus (see Figure 6.8) [85]. Avoiding this roughening was suggested as an efficient strategy in order to minimize the misorientation in the films. Experimental proof for the viability of this concept is still missing.

Most authors reported a thin β-SiC interlayer between Si and diamond [86, 87]. The defective nature of this interlayer was supposed to contribute to the total mosaic spread of the epitaxial diamond layers on silicon [28].

Ion bombardment was identified as another source of mosaic spread [88]. In homoepitaxial growth experiments, additional biasing could either completely destroy the orientation by renucleation or introduce a steadily increasing mosaic spread by continuously forming defects [28, 89]. Since ion bombardment is an indispensible feature in heteroepitaxial diamond nucleation by BEN, the main experimental challenge is the minimization of its detrimental influence on the substrate surface and on the growing diamond grains.

The schema in Figure 6.9 summarizes the major effects that contribute to the limited crystalline quality of heteroepitaxial diamond films on silicon.

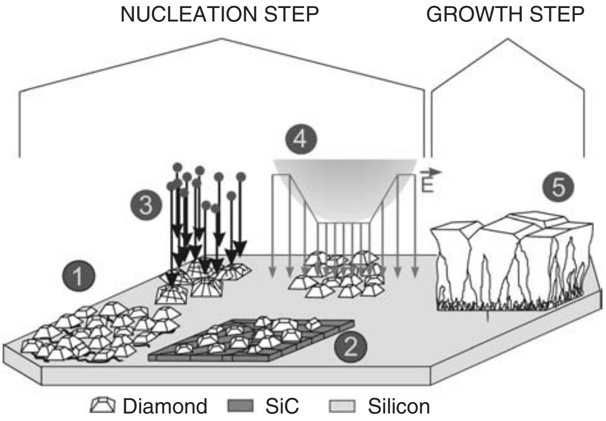

Figure 6.9 Schema summarizing the different processes that control the epitaxial alignment of diamond on silicon. (1) Diamond in direct contact with a roughened Si surface. (2) Diamond on top of a defective β-SiC buffer layer. (3) Defect and mosaicity formation due to ion bombardment. (4) Enhancement of the biasing field due to the feedback of the growing diamond layer. (5) Texture modification during growth

6.5 HETEROEPITAXIAL DIAMOND GROWTH ON IRIDIUM

The first report on diamond heteroepitaxy on iridium using Ir/MgO(001) as a substrate was presented by Sawabe's group in 1996 [15]. Ion bombardment in a DC plasma set-up was used in order to generate nuclei. The diamond films on Ir differed from all other systems (excluding c-BN) scrutinized until that time because of the extraordinarily high density of aligned diamond grains (see Figure 6.10(a)–(d)) with a negligible fraction of nonepitaxial crystals. This facilitated smooth epitaxial layers at extremely low film thickness (see Figure 6.10(e))[90]. Shortly after, the low mosaic spread deduced from XRD data for Dia/Ir/$SrTiO_3$(001) multilayer structures revealed the unique epitaxial alignment of diamond on Ir [91]. In both cases – MgO and $SrTiO_3$ – the iridium films were grown by e-beam evaporation at elevated temperature (750 °C and 950 °C, respectively) on the surface of the oxide single crystals.

Over the following ten years, iridium emerged as the most promising substrate for a heteroepitaxial diamond wafer technology. Its actual realization requires a profound control and understanding of the nucleation process, of the textured growth process and a concept for the scaling up. These three issues are discussed in the following sections.

6.5.1 BEN on iridium: nucleation under etching conditions and pattern formation

BEN on Ir requires a slightly higher bias voltage than on Si or β-SiC (e.g. 250–300 V instead of 200 V). The first peculiarity already observable during a successful BEN process on iridium is the marginal change in biasing current [72]. On silicon, the current increase by up to one order of magnitude was attributed to the immediate growth of the nuclei during BEN and to the gradual coverage of the substrate by a diamond layer. For standard BEN conditions on Si, diamond grains also grow in thickness.

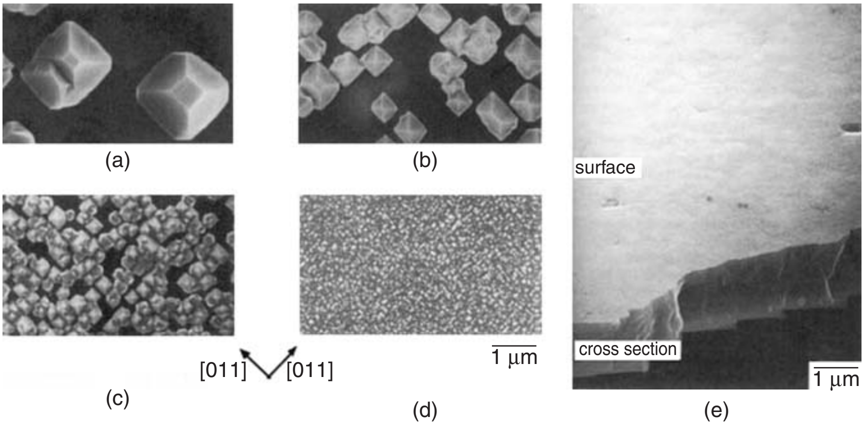

Figure 6.10 Variation of the diamond grain density on Ir/MgO(001) versus biasing current: (a) 70 mA/cm^2; (b) 105 mA/cm^2; (c) 140 mA/cm^2; (d) 175 mA/cm^2. (e) Flat epitaxial diamond film of ~1 μm thickness grown on Ir/MgO(001) [90]. (a)–(d) reprinted from [94] with permission from MYU KK, Copyright 2002; (e) reprinted from [90] by permission of the Japanese Society of Applied Physics

After BEN on Ir, extended diamond grains are not visible. Particles with a size of 5–10 nm, which are often found on top of a 3-nm-deep roughened Ir surface by SEM and AFM, were identified by TEM as iridium nanoparticles [92]. In a reference experiment, dispersed 100-nm large diamond crystals on an iridium surface completely vanished after 60 min BEN [93]. Thus, nucleation apparently proceeds under conditions for which the bulk phase of diamond is unstable. Nucleation under etching conditions is incompatible with classical nucleation theory (see Section 6.2) where a positive supersaturation ensures that clusters, after having overcome the nucleation barrier, can grow without further limitation. The suppression of diamond growth under BEN on Ir can also account for the absence of a process time window as found on Si [72].

Three changes of the iridium surface are usually observed after the BEN procedure:

(i) surface roughening;
(ii) the presence of a carbon layer of about 1 nm thickness;
(iii) a pattern consisting of extended islands that show a bright contrast in SEM.

Ir surface roughening has been reported by several groups [93, 94, 95]. The etch structures are aligned along the low index crystal directions of the iridium. Depending on the process parameters, the preferential orientation can switch between $\langle 100\rangle$ and $\langle 110\rangle$ [96]. Some TEM work suggests that diamond nucleates on top of the roughened structures [97]. However, the less common case of successful nucleation without roughening exists beside the observation of pronounced Ir surface roughening without successful diamond nucleation. The role of Ir surface roughening in the diamond nucleation process and, in particular, its meaning for the alignment of the films (see the discussion for diamond on Si) is completely unclear.

After BEN, the iridium surface is covered by a thin carbon layer. First measurements by elastic recoil detection analysis (ERD) of BEN layers deposited using isotopically enriched ^{13}C methane in the gas phase, yielded a value of 0.7 nm for the thickness of the carbon films assuming the atomic density of diamond [98]. The coverage showed only a weak variation with biasing time. Measurements of the carbon coverage by X-ray photoelectron spectroscopy (XPS) [99] and of the geometric carbon film thickness by TEM [100] gave similar results, of the order of 1–2 nm.

The most striking pecularity of the nucleation layer on iridium is reflected in the formation of characteristic patterns [95, 101–104]. Monitoring the surface by SEM with the in-lens detector allows bright islands of homogeneous contrast with clear border lines to be distinguished (Figure 6.11). Imaging the same area with the standard secondary electron detector, which is more sensitive to topographic features, yields extremely weak (or often no) contrast. The initial presumption, that diamond nuclei are located within the bright areas, was confirmed by measuring one and the same spot immediately after BEN and after a subsequent growth step (Figure 6.11(b) and (c)). For the bright islands containing the diamond nuclei after BEN the term ‘domains’ has been proposed.

6.5.2 The topographic signature of the domains

For a long time the existence of topographic features in AFM images that could be unequivocally correlated with the diamond nucleation structures was rather unclear. Golding *et al.* described nanometer size dots forming a regular pattern with a close-packed arrangement that they identified as epitaxial diamond crystals [99].

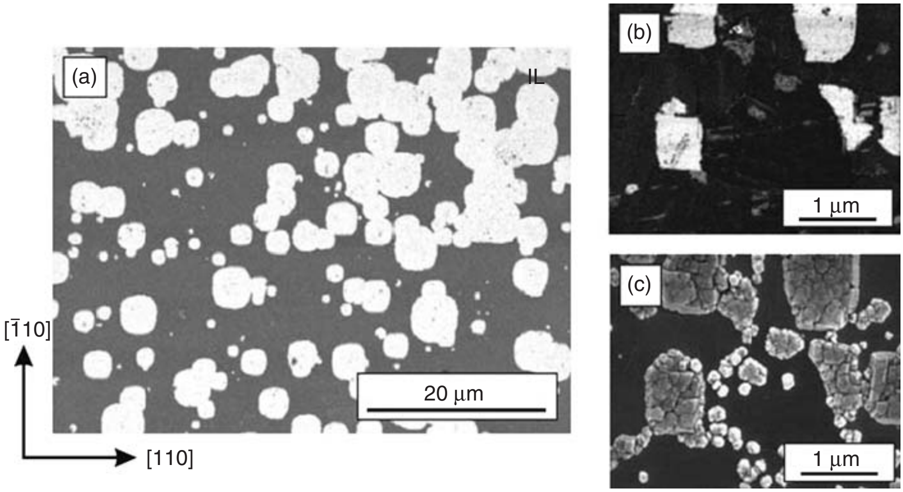

Figure 6.11 (a) SEM image of an iridium surface after BEN treatment taken with the in-lens detector. (b) Local spot imaged by SEM after BEN, and (c) after subsequent growth step

In other AFM work a successful identification of domain areas was achieved for the first time on a BEN layer without surface roughening [105]. Figure 6.12 shows SEM images and the corresponding AFM measurements. Surprisingly, there is a downward step of about 1 nm when crossing the sharp border between the nucleation-free area and the inner part of a domain. No further characteristic fine structure other than the one stemming from the underlying Ir film is visible within the domains. In comparative experiments, imaging identical spots by SEM and AFM, a similar height contrast was also found on roughened iridium films [105].

6.5.3 The internal structure of the BEN layer

Appropriate techniques for clarifying the crystalline structure of a 1-nm thick layer are reflection high energy electron diffraction (RHEED), low energy electron diffraction (LEED) or high resolution TEM. For RHEED, one report on successful diamond detection [103] contrasts with several other studies in which no diamond related spots were observed [15, 94, 107]. Neither with LEED [106, 107] nor with HRTEM have crystalline diamond structures been found up to now [100]. Figure 6.13 shows TEM images of two samples – one with roughening of the Ir surface and one without. The nucleation layer formed by BEN was intentionally coated by 10 nm Ir in order to protect it during TEM sample preparation and to facilitate the measurement of its thickness. In both samples, only amorphous structures were observed within the 1-nm thick carbon layer.

X-Ray photoelectron diffraction (XPD), which is based on the forward scattering of photoelectrons in an ordered matrix, is currently the only scattering technique that allows a reproducible detection of crystalline order due to the diamond nuclei in a BEN layer [99, 106–108]. Figure 6.14(a) shows azimuthal scans of the photoelectron intensity for different polar angles of a bias-treated Ir/MgO sample. The authors report that the anisotropy values deduced from these scans for different BEN processes could be correlated with the crystalline quality of the epitaxial diamond layers subsequently grown out of them

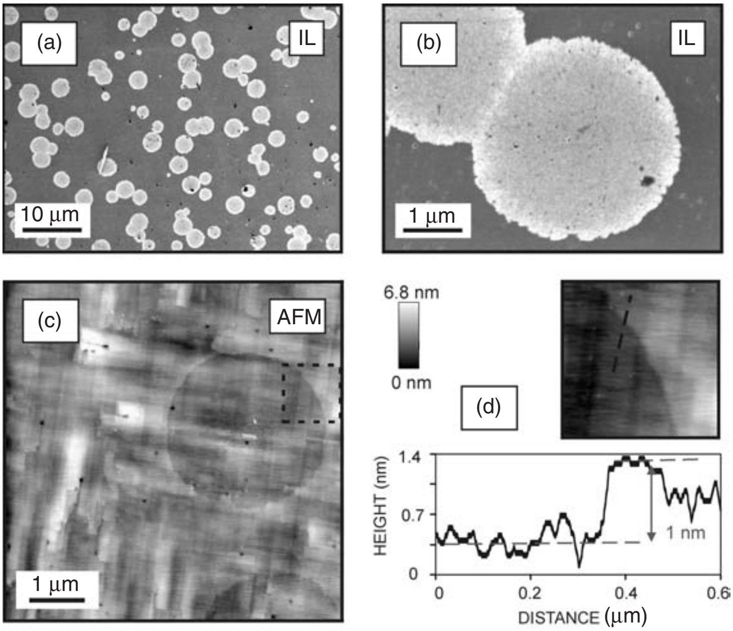

Figure 6.12 (a) Low and b) high magnification SEM images of the domains on an Ir(001) surface after BEN. The negligible roughening of the Ir substrate allows identification of the domains directly in the AFM images (c) and (d). Reprinted from [105] by permission of Elsevier

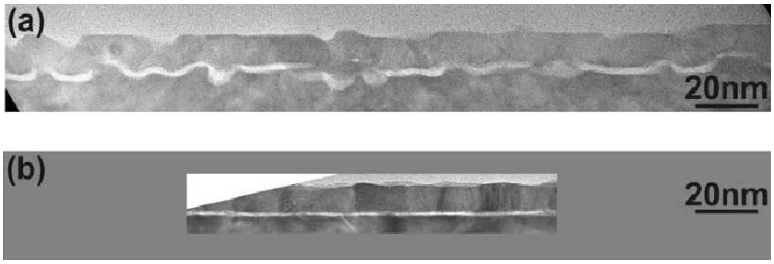

Figure 6.13 Cross-section TEM images of the carbon layer (bright slit) formed by BEN on Ir/SrTiO$_3$(001) samples. To protect the thin BEN layer, a 10-nm thick iridium layer was deposited before TEM sample preparation. (a) Roughened and (b) non-roughened iridium. Reprinted from [100] by permission of Elsevier

[108]. In Figure 6.14(b) and (c), full XPD patterns are plotted for two samples deposited on Ir/SrTiO$_3$(001) substrates [107]. The pattern in (c) was taken from a sample for which no domains were observed after the BEN process. The sample in (b) was covered by domains, which proves that the pattern stems from the crystalline structures within the domains.

A laterally resolved measurement of the carbon bonding structure was made by X-ray absorption near-edge structure (XANES) combined with an X-ray photoemission electron microscope (X-PEEM) [109]. In Figure 6.15(b), the dip around 303 eV, one of the most

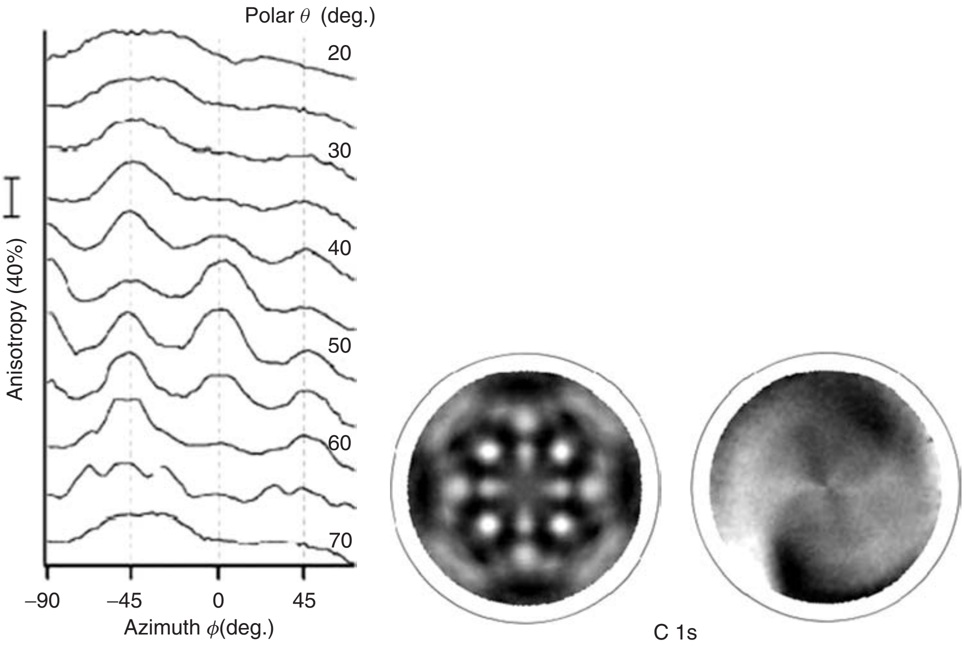

(a) (b) (c)

Figure 6.14 XPD measurements of the C1s photoelectrons from the carbon layers formed during BEN on iridium. (a) Azimuthal scans for a carbon layer on Ir/MgO(001) deposited by BEN in a DC plasma setup. Reprinted from [106] by permission of Elsevier; (b) and (c) Photoelectron diffraction patterns of two carbon layers formed by BEN in a microwave plasma discharge. The sample in (b) contained a high density of domains and in (c) no domains were observed [107]

prominent features in the spectra and a fingerprint for diamond, is only present within the domains and absent outside. Laterally resolved Auger spectra yield identical results.

In conductive AFM measurements it turned out that the surface is completely covered by a continuous film that is highly resistive both outside and inside the domains [105].

6.5.4 The temporal development of the domain patterns during BEN

A key requirement for a convincing model explaining diamond nucleation on Ir is its ability to describe also the domain formation. Important information concerning this question was deduced from an experiment in which the temporal development of the domain shapes was studied by exposing a BEN layer, after imaging the patterns by SEM, to a second biasing step [105]. Two different spots −5 mm apart – were chosen. At the first spot, the shape of the domains was nearly identical before and after the second BEN treatment having only increased in size. At the second spot, the size had decreased and small domains had vanished. The most important conclusion from this experiment is that the growth (or shrinkage, when the local biasing conditions are not appropriate) is a continuous process, which rules out the possibility that nucleation is a spontaneous event after switching off the bias as supposed in Ref. [104].

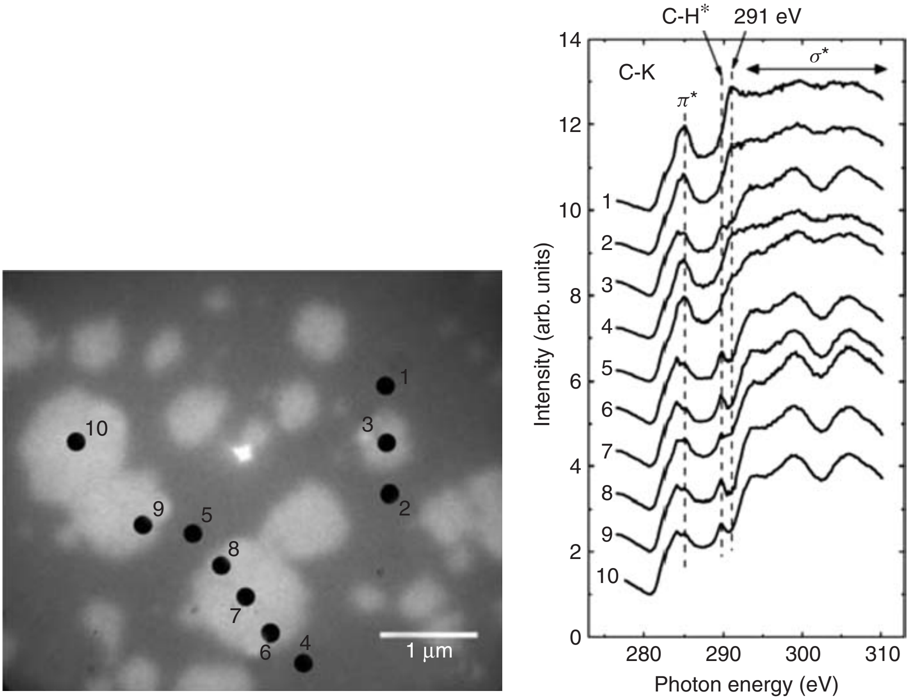

(a)

(b)

Figure 6.15 (a) PEEM image of a diamond nucleation layer formed by BEN on Ir/$SrTiO_3$(001) taken at the C–K edge using 275 eV photons. (b) XANES spectra taken at the different spots indicated in (a). Reprinted from [109] by permission of the Japanese Journal of Applied Physics

6.5.5 Models describing the nucleation

One detailed model of diamond nucleation on Ir was proposed by Golding *et al.* [104]. Its central part assumes a highly excited nonequilibrium carbon phase, which is present at the iridium surface during the ion bombardment stage. The termination of the BEN treatment causes quenching and in the supercooled condensate self-organisation creates ordered structures.

A typical value for the biasing current density on Ir is 100 mA/cm^2. Right above the cathode the current is primarily carried by ions (see current distribution in a glow discharge [63]). The particle flux density of (single-charged) positive ions hitting the surface is therefore 6×10^3 $nm^{-2}s^{-1}$. Taking the parameters from the thermal spike model [110], i.e. a projected surface area of 1–10 nm^2 for the collision cascade, one can calculate that every volume is hit with a maximum repetition rate of 6×10^4 s^{-1}. Thermalization occurs after about 1 ps, which means that each impact can be considered as individual event, well separated in time and distance, giving rise to a gradual development of the film structure. Instead of being in a highly excited state, the layer is, most of the time, in thermal equilibrium with the substrate during BEN.

An alternative scenario for the nucleation and domain formation comprises a sequence of five steps:

(i) After applying the bias voltage the ion bombardment results in the deposition of carbon on the iridium surface. The amount of carbon quickly reaches a saturation value, which is controlled by a dynamic equilibrium between deposition and etching. The equivalent thickness is about 1 nm. It is an amorphous, highly resistive, carbon layer without crystalline structures or inclusions.

(ii) Spontaneous nucleation of crystalline diamond structures occurs accordingly to models proposed for diamond nucleation by ion bombardment on other nondiamond substrates. The model described in Ref. [70] suggests that the formation probability of a diamond embryo cluster in a dense amorphous hydrogenated carbon matrix is extremely low. Under the harsh bombardment conditions on Ir, the probability is even lower. The exceptionally high proportion of epitaxial grains observed in subsequent growth experiments indicates that the nucleation event takes place at the iridium/carbon layer interface.

(iii) The nuclei immediately try to grow in the same way as on other substrates. Due to the higher bias voltage (as compared to BEN on Si) the growth perpendicular to the surface is supressed. However, lateral crystal growth close to the iridium interface is still possible.

(iv) The lattice misfit and the resulting stress [111] on the one hand, and the defect formation due to the ion bombardment on the other, cause a tendency in the laterally growing crystal to splitting into subunits, which later represent the nuclei. Repulsive interaction forces stabilize the crystalline subunits at a distance of about 25 nm [112]. The higher density of the carbon matrix within the domains as compared with the surrounding a-C:H layer might explain the step at the domain edge.

(v) After switching off the bias voltage, the highly defective crystalline matrix between the nuclei is completely etched away within 10 s [112]. This defective carbon phase was formed and stabilized by the ion bombardment. Simultaneously the nuclei start to grow as isolated diamond crystals that coalesce when their size reaches a value equal to their lateral distance. For domains with a lateral size of the order of 1 µm, one can estimate that only one or very few nuclei are created in real nucleation events. More than 99 % were formed by two-dimensional lateral growth followed by a splitting process.

6.5.6 Mechanisms of texture improvement

On a densely nucleated surface, coalescence of the diamond grains and the formation of a closed layer occur at a thickness below 100 nm in the subsequent growth step. At this stage individual grains can still be seen clearly. When the growth of thicker films continues this feature gets lost progressively.

The plan view TEM images in Figure 6.16 illustrate the change in internal structure for a sequence of 0.6 µm, 8 µm and 34 µm thick epitaxial diamond layers on Ir/$SrTiO_3$(001) [113]. The thinnest sample clearly consists of individual grains with a size of 300 nm. In the layer of 8 µm, grain coarsening has increased the extension of perfect single crystal areas to about 1 µm. These are separated by a closed network of grain boundaries. In the 34-µm sample, the closed network has vanished and at the same time the polycrystalline character of the diamond film got lost. Short defect bands now aligned along $\langle 100 \rangle$ directions are the residues of the former grain boundaries within an extended (defective) single crystal.

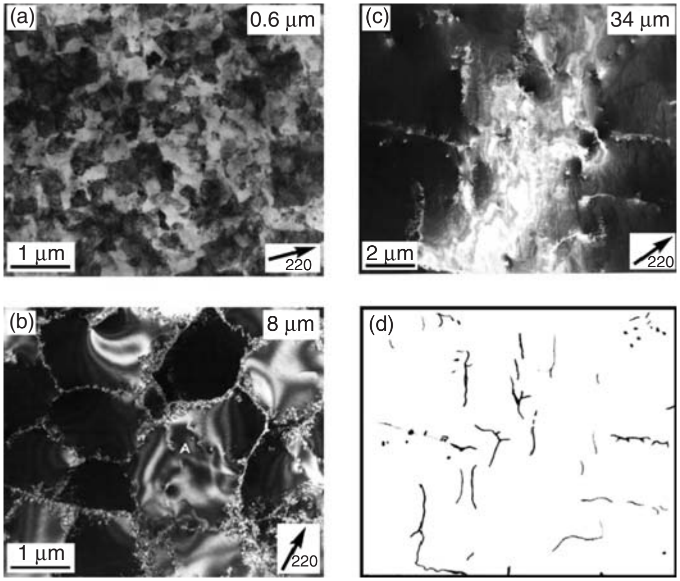

Figure 6.16 (a), (b), (c) Plan-view TEM images of epitaxial diamond layers on Ir/$SrTiO_3$(001) with different thicknesses. (d) Schematic drawing of the defect lines in the TEM image shown in (c). Reprinted from [113] by permission of the American Institute of Physics

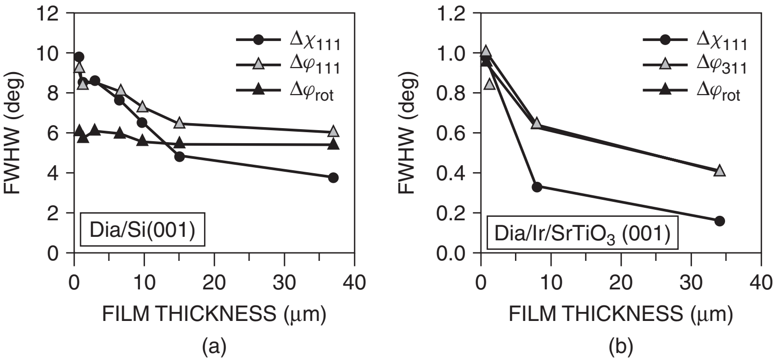

Figure 6.17 Comparison between the reduction in mosaic spread in epitaxial diamond films on silicon and on Ir/$SrTiO_3$(001). Reprinted from [113] by permission of the American Institute of Physics

The dramatic improvement in crystalline quality was also monitored by X-ray texture measurements. Figure 6.17 compares the development of tilt and twist with film thickness in epitaxial diamond films on Si(001) and Ir/$SrTiO_3$(001). As already discussed in Figure 6.5 for Dia/Si(001), tilt improves significantly with film thickness when appropriate growth conditions are chosen. At the same time, the twist remains nearly changeless. For diamond on iridium the situation differs fundamentally: both components of the mosaic spread decrease with film thickness.

Extremely narrow distributions of the polar angular spread with an FWHM down to 0.8° can be obtained in purely fibre-textured films grown from randomly oriented seeds, provided that appropriate growth conditions are chosen [114]. The principle of evolutionary selection [115, 116] provides a perfect quantitative description of this phenomenon in polycrystalline films by means of the growth parameter α ($\alpha = \sqrt{3}\frac{v_{100}}{v_{111}}$ with v_{100}, and v_{111} being the growth rates on the corresponding faces).

In epitaxial diamond films on silicon, overgrowth of unfavourably oriented grains by more favourably oriented ones also seems to be a dominating process in grain coarsening and texture improvement. However, the simple geometric model in which the growth rates on {111} and {100} facets are constant, i.e. only a function of temperature and gas composition but independent of their orientation and the local environment (neighbouring faces), cannot be reconciled with many observations.

As a first example, narrowing of the FWHM for the tilt in polycrystalline films down to less than 4° would require a growth parameter α close to 3. However, in heteroepitaxial diamond films on silicon, a FWHM of 3.9° for the tilt was experimentally obtained by growth with an α value of 2.5 [117]. For the films on iridium with minimum tilt values below 0.2°, the deviations from the pure geometric concept are even more pronounced [118].

As a further inconsistency, the shape of the {100} facets differs strongly for ⟨100⟩ fibre textured films and epitaxial diamond layers on Si(001). In Figure 6.18(a) the azimuthally random distributed {001} facets are square shaped. In contrast, for the oblong facets in the epitaxial diamond film on Si (Figure 6.18(b)) the aspect ratio is completely different from unity. A possible mechanism is indicated in Figure 6.18(c): the edges formed between well-aligned neighbouring grains can act as a source of new lattice planes. Similarly to the reentrant grooves formed by twinning [119], this specific geometry accelerates growth on the facets forming the edge. However, in the present situation the kink is removed with progressive growth leaving behind an elongated rectangular {001} facet.

Jiang *et al.* suggested a modified type of overgrowth by a step-flow mechanism in epitaxial diamond films on silicon [120]. In addition, they observed the merging of initially individual grains with only a slight difference in orientation. The grain boundary stops at a certain point in the film and growth continues as a single crystal (Figure 6.19). The remaining crystal defect is called a disclination. When a partial wedge disclination is formed instead of a grain boundary, the misorientation between grains is partially accommodated by elastic deformation. Michler *et al.* considered elastic energy associated with grain boundaries and disclinations [79] and found that the latter is energetically only preferred for small grains with low misorientation.

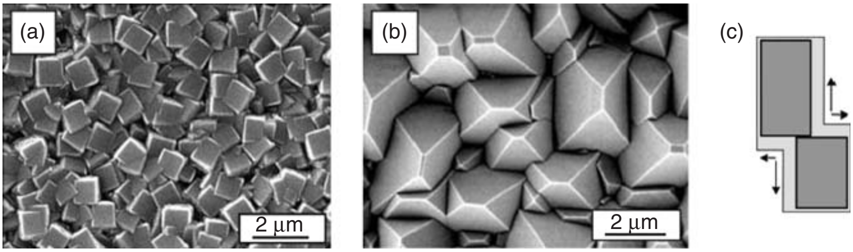

Figure 6.18 (a) (100) fibre textured diamond film. (b) Epitaxial diamond on Si(001). (c) Schema showing how the corners formed during merging of grains preferentially accelerate the growth rates on the neighbouring facets

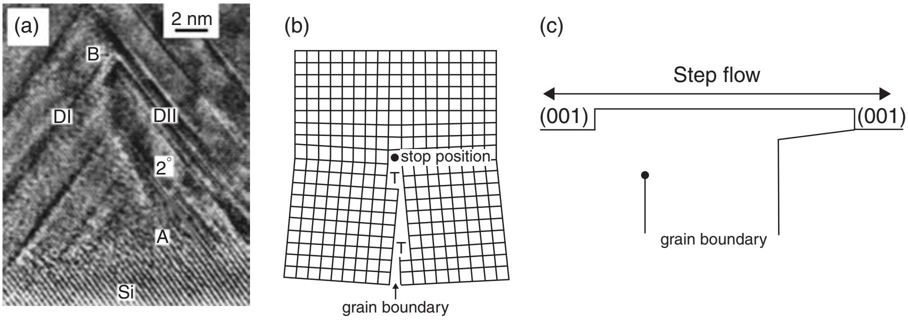

Figure 6.19 (a) Cross-section TEM image of the grain boundary region between two diamond grains on silicon. The 2° low-angle grain boundary disappears towards the upper edge of the image. (b) Schematic representation of the stopping of the grain boundary by introduction of a disclination. (c) Schematic representation of the lateral overgrowth by the step-flow growth mechanism. Reprinted from [120] by permission of the American Institute of Physics

The disclination concept was later applied successfully in order to explain quantitatively the different behaviour in texture improvement (presented in Figure 6.17) for Dia-on-Si and Dia-on-Ir [118]. Figure 6.20(e) first compares the elastic energy density of a grain boundary and of a disclination for different grain sizes (0.1 μm and 1 μm). For misorientation angles below the intersection point, disclinations represent the energetically favourable configuration; above this point grain boundaries are more stable. The intersection defines a critical angle, which is plotted in Figure 6.20(f) against the grain size. Transferring this result to the texture data in Figure 6.17 allows the following conclusion: on silicon, the maximum density of epitaxial diamond grains was of the order of $\sim 10^9$ cm^{-2} corresponding to a size of about 300 nm when the epitaxial grains meet and start to coalesce. According to Figure 6.20(f) this requires misorientation angles below 1° to favour substitution of the grain boundaries by disclinations. However, texture measurements of thin films typically yield an angular spread of 5–10° (FWHM), which results in grain boundary angles of about 5°. Thus, merging of grains by disclination formation is supposed to contribute only marginally to grain coarsening and texture improvement of epitaxial diamond films on silicon. The same arguments applied to the Dia-on-Ir layers suggest that the disclination mechanism is extremely effective.

By means of simple numerical simulations it was also possible to substantiate the slower reduction in the FWHM of the twist component, as compared with the tilt in terms of a competition between grain coarsening by lateral overgrowth and by the upper grain merging mechanism [118]. As an important conclusion, relevant to technology, the simulation also suggests that for efficient improvement of the in-plane angular spread, the coalescence of the top {001} facets should be delayed as long as possible during textured growth.

The previous discussion referred to structure and texture improvement by the mere optimization of growth parameters. Sawabe and coworkers introduced another concept to influence the density and local distribution of structural defects (such as dislocations) by means of a targeted patterning of the BEN layer [121]. Similarly to the situation during epitaxial lateral overgrowth (ELO), high quality crystalline material is laterally grown starting from small defect-rich regions thus reducing the overall defect density.

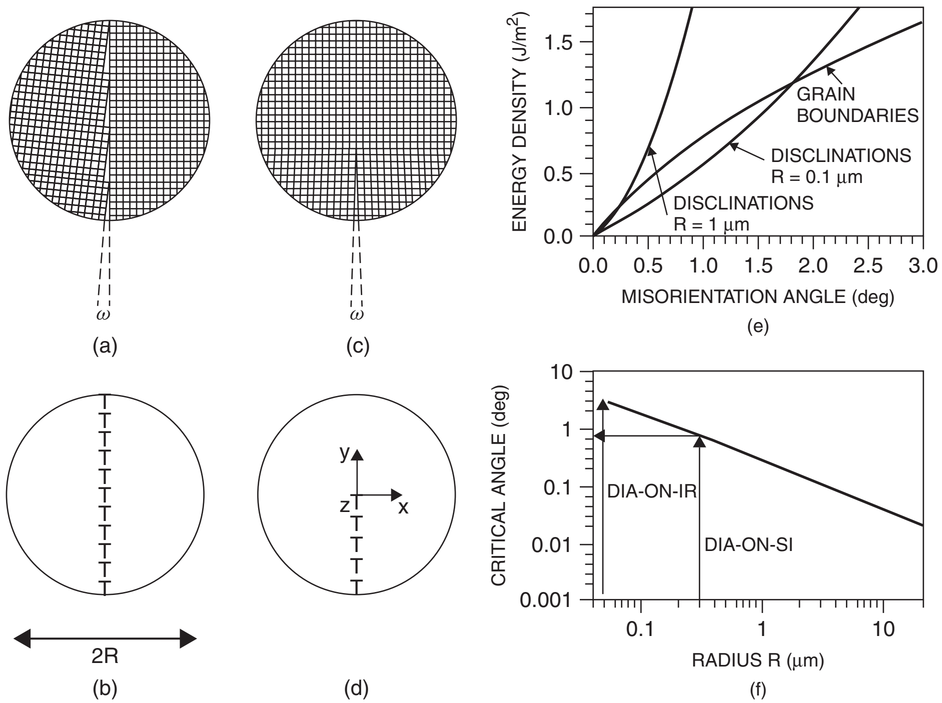

Figure 6.20 Schematic view of (a), (b) a grain boundary separating two slightly misaligned grains, and (c), (d) its substitution by a wedge disclination located in the particle centre at the end of the incomplete low-angle boundary [79]. (e) Energy density of a grain boundary and of disclinations for two different particle sizes (0.1 μm and 1 μm) versus the misorientation angle [118]. The intersection between the curve for grain boundary and disclination define a critical angle. Below this value, grain merging by disclination formation is energetically preferred. (f) Critical angle versus particle size. (a)-(d) reprinted from [79] by permission of the American Institute of Physics, (e) and (f) reprinted from [118] by permission of the American Institute of Physics

6.5.7 Strategies for a scaling-up: large oxide single crystals versus silicon based multi-layer structures

Growth on iridium always means on iridium layers grown epitaxially on another substrate. Bulk single crystals of this precious metal have no relevance in technology. Up to now, mainly oxides like MgO [15], $SrTiO_3$ [91, 122] and sapphire [123] have been used as growth substrates for iridium buffer layers. For future diamond wafer technology, the size of available substrates is an important issue. Two-inch substrates are available for $SrTiO_3$ and MgO and at least 4-inch substrates for sapphire. Sawabe *et al.* have recently shown Dia-on-Ir layers grown on MgO of 1 inch in diameter [35].

Besides the dimensions of the single crystal substrate, its coefficient of thermal expansion (CTE) is of similar importance. Figure 6.21 compares the thermal stress induced in a thin diamond layer on a thick substrate after cooling down from deposition temperature [124]. The vertical line and the numbers at the right-hand side indicate the values for a rather low deposition temperature of 700 °C. Nevertheless, the compressive stress for the oxide single crystals varies from −4 GPa for sapphire to more than −8 GPa for the MgO.

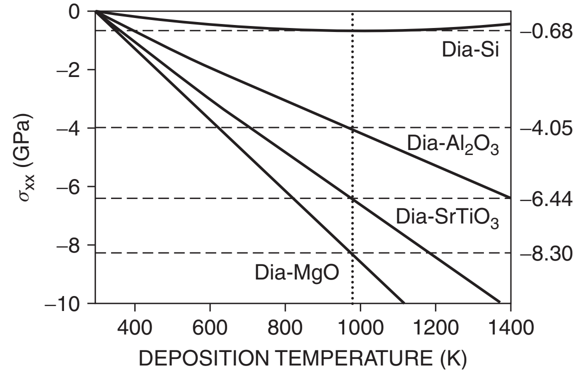

Figure 6.21 Thermal stress σ_{xx} in diamond layers on different substrates versus deposition temperature. Reprinted from [124] by permission of the American Institute of Physics

Diamond layers thicker than a few micrometres are therefore prone to delamination. In contrast, with −0.68 GPa, the thermal stress on silicon is comparatively low. It even decreases for higher deposition temperatures.

Deposition of iridium directly on silicon seems unrealistic due to the chemical reactivity of the two elements which can form a variety of iridium silicides with different crystal structures of low symmetry, some of them with low melting points [125]. A first attempt with CaF_2 buffer layers between Ir and Si yielded oriented Ir films and diamond grains [126], but the insufficient thermal stability of the fluoride films turned out to be a drawback.

Oxide buffer layers represent a viable alternative. The epitaxial deposition of stable oxides, like yttria-stabilized zirconia (YSZ) on silicon, has previously been studied in the context of HTc superconductors [127] and ferroelectrics [128] growth. The mosaic spread in these oxide buffer layers is typically above 1° (FWHM). Nevertheless, single-crystal iridium films with a one order of magnitude lower angular spread can be grown on top [129]. For Ir/$SrTiO_3$/Si(001) [130] and Ir/YSZ/Si(001) [124] the nucleation and growth of high quality epitaxial diamond films has been shown. Figure 6.22 shows the schematical set-up of these two multilayer structures as well as SEM images of the surface and the cross section for a Dia/Ir/YSZ/Si(001) sample. FWHM values of 0.16° and 0.34° for the polar and azimuthal angular spread, respectively, have been measured for this system on an area of 10 cm^2 [131]. They currently represent the state of the art for Dia-on-Ir layers. Scaling-up of the Ir/YSZ/Si(001) substrates to 4-inch wafer dimensions has successfully been shown [131] (Figure 6.23) and the transfer of the BEN process to 4-inch substrates is in progress.

6.6 PROPERTIES AND APPLICATIONS OF HETEROEPITAXIAL DIAMOND LAYERS

A multitude of attempts to explore the technological potential of heteroepitaxial diamond and to develop devices using this material has been reported.

Epitaxial Dia-on-Si layers were used to build a large variety of electromechanical, electrothermal, and electrochemical sensor and actuator devices [132–134]. In this field the

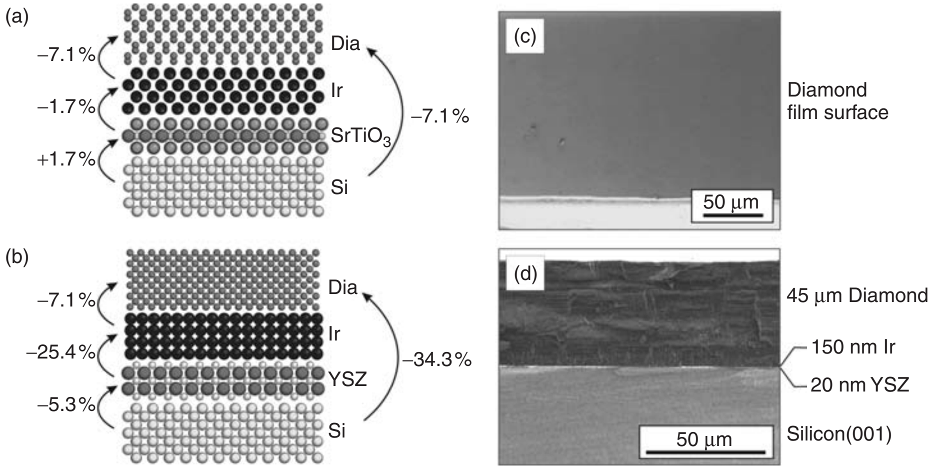

Figure 6.22 Schematic view of the epitaxial multilayer structures (a) Dia/Ir/$SrTiO_3$/Si(001), and (b) Dia/Ir/YSZ/Si(001). (c) Surface and (d) cross-section SEM images of a Dia/Ir/YSZ/Si(001) sample. Reprinted from [124] by permission of the American Institute of Physics. See plate 1

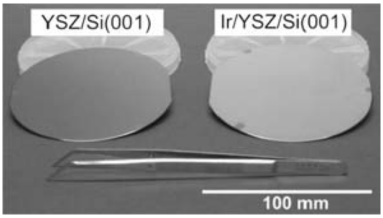

Figure 6.23 Epitaxial YSZ and Ir/YSZ layers on 4-inch diameter Si(001) substrates

epitaxial samples profit from a lower roughness compared with polycrystalline layers. In comparison with smooth nanocrystalline films they preserve the high thermal conductivity of diamond and contain fewer structural defects. The lower grain boundary density has also been quoted as an explanation of the higher sensitivity of ultraviolet detectors made from epitaxial diamond on Si as compared with randomly oriented polycrystalline films [135].

Low mosaicity diamond layers grown on 4° off-axis β-SiC were used to fabricate p-channel field effect transistors showing transconductance values similar to homoepitaxial devices and a nearly perfect pinch-off [136].

In electron emission experiments, heteroepitaxial diamond films on iridium revealed a higher homogeneity and a lower turn-on voltage than did comparable polycrystalline layers [137]. Hall-effect measurements on boron doped diamond films grown on Ir layers yielded mobility values of 340 cm^2/Vs [138]. These are higher than the 165 cm^2/Vs [139] measured at room temperature for heteroepitaxial layers on silicon but are still by a factor of 5 below the typical values for high quality homoepitaxial diamond. In another study, p-type surface channel field effect transistors (FETs) have been successfully fabricated on a diamond quasi-substrate grown on Ir/$SrTiO_3$ [140]. Finally, Dia-on-Ir films were investigated as detector material for heavy-ion tracking [141]. While the energy resolution of 18 % cannot reach the minimum values measured for the homoepitaxial layers, their excellent time resolution close to 10 ps qualifies them as promising candidates for timing applications.

6.7 CONCLUDING REMARKS

For almost two decades heteroepitaxy has been one of the main topics in diamond research. The first years were dominated by the search for the optimum substrate and by studies on the improvement of crystalline quality by means of appropriate textured growth steps. Concerning the search for an optimum substrate, iridium gained a special position among all potential materials. The mechanism that causes the formation of diamond nuclei with ultrahigh density at its surface is unique, and neither conforms with standard nucleation theory nor with the processes observed for BEN on any other material. These special properties result in outstanding epitaxial alignment of Dia-on-Ir layers, which can be transformed into (defective) single crystals by textured growth. The experimental data acquired for other competing substrates (Si, β-SiC and Pt) and our current understanding of mosaicity reduction mechanisms in epitaxial diamond films suggest that diamond layers on the latter substrates may not reach the quality of the Dia-on-Ir films, even if grown to extremely high film thickness.

First attempts to scale-up the diamond films on iridium buffer layers yielded epitaxial diamond areas of more than 10 cm^2, thus providing a clear route towards wafer size samples. Nevertheless, the proof of a controlled reproducible nucleation and stable growth of thick diamond layers over substrates with a diameter of several inches is lacking. At the same time it is important to evaluate further the mechanical, electrical, optical and thermal properties of this promising material in order to find out whether or not it can really approach the properties of high quality HPHT crystals or homoepitaxial CVD layers. In real applications it will have to compete with both polycrystalline diamond (which is easier to prepare) and with homoepitaxially grown single-crystal diamond, with its high crystalline quality but, still, significantly smaller size.

REFERENCES

[1] K. Nassau, Synthesis of Bulk Diamond: History and Present Status, in *Diamond Films and Coatings*, R.F. Davis (Ed.), Noyes Publications, Park Ridge, 1993, p. 31–67.

[2] R. Abbaschian, H. Zhu, and C. Clarke, High pressure–high temperature growth of diamond crystals using split sphere apparatus, *Diamond Relat. Mater.*, **14**, 1916–1919 (2005).

[3] M.A. Prelas, G. Popovici, and L.K. Bigelow (Eds), *Handbook of Industrial Diamonds and Diamond Films*, Marcel Dekker, New York, 1997.

[4] J. Isberg, J. Hammersberg, E. Johansson, T. Wikström, D.J. Twitchen, A.J. Whitehead, S.E. Coe, and G.A. Scarsbrook, High carrier mobility in single-crystal plasma-deposited diamond, *Science*, **297**, 1670–1672 (2002).

[5] C.S. Yan, Y.K. Vohra, H.K. Mao, and R.J. Hemley, Very high growth rate chemical vapor deposition of single-crystal diamond, *Proc. Natl. Acad. Sci.*, **99**, 12523–12525 (2002).

[6] Y. Mokuno, A. Chayahara, Y. Soda, Y. Horino, and N. Fujimori, Synthesizing single-crystal diamond by repetition of high rate homoepitaxial growth by microwave plasma CVD, *Diamond Relat. Mater.*, **14**, 1743–1746 (2005).

[7] K. Kobashi *et al.*, R&D of diamond films in the Frontier Carbon Technology Project and related topics, *Diamond Relat. Mater.*, **12**, 233–240 (2003).

[8] L. Liu and J.H. Edgar, Substrates for gallium nitride epitaxy, *Mat. Sci. Eng.*, **R 37**, 61–127 (2002).

[9] J.H. Edgar, S. Strite, I. Akasaki, H. Amano, and C. Wetzel (Eds), *Properties, Processing and Applications of Gallium Nitride and Related Semiconductors*, Emis Datareviews Series **23**, Inspec, London, 1999.

[10] D.W. Pashley, A historical review of epitaxy, in *Epitaxial Growth Part A*, J.W. Matthews (Ed), Academic Press, New York, 1975, p. 1–27.

[11] M. Yoshimoto, K. Yoshida, H. Maruta, Y. Hishitani, H. Koinuma, S. Nishio, M. Kakihara, and T. Tachibana, Epitaxial diamond growth on sapphire in an oxidizing environment, *Nature*, **398**, 340–342 (1999).

[12] X. Jiang, C.-P. Klages, R. Zachai, M. Hartweg, and H.-J. Füsser, Epitaxial diamond thin films on (001) silicon substrates, *Appl. Phys. Lett.*, **62**, 3438–3440 (1993).

[13] B.R. Stoner and J.T. Glass, Textured diamond growth on (001) β-SiC via microwave plasma chemical vapor deposition, *Appl. Phys. Lett.*, **60**, 698–700 (1992).

[14] S.D. Wolter, M.T. McClure, J.T. Glass, and B.R. Stoner, Bias induced nucleation of highly oriented diamond on titanium carbide (111) substrates, *Appl. Phys. Lett.*, **66**, 2810–2812 (1995).

[15] K. Ohtsuka, K. Suzuki, A. Sawabe, and T. Inuzuka, Epitaxial growth of diamond on iridium, *Jpn. J. Appl. Phys.*, **35**, L1702–L1074 (1996).

[16] L. Ickert and H.G. Schneider, *Wachstum einkristalliner Schichten*, VEB Deutscher Verlag für Grundstoffindustrie, Leipzig, 1983.

[17] J.E. Field, *The Properties of Diamond*, Academic Press, London, 1979.

[18] S. Koizumi, T. Murakami, T. Inuzuka, and K. Suzuki, Epitaxial growth of diamond thin films on cubic boron nitride {111} surfaces by dc plasma chemical vapor deposition, *Appl. Phys. Lett.*, **57**, 563–565 (1990).

[19] S. Koizumi and T. Inuzuka, Initial growth process of epitaxial diamond thin films on cBN single crystals, *Jpn. J. Appl. Phys.*, **32**, 3920–3927 (1993).

[20] R. Haubner, A. Lindlbauer, and B. Lux, Diamond nucleation and growth on refractory metals using microwave plasma deposition, *Int. J. Refract. Met.*, **14**, 119–125 (1996).

[21] Exceptions are applications where coarse grained films with low grain boundary density are required so that a low density of seeds is beneficial.

[22] H. Liu and D.S. Dandy, Studies on nucleation process in diamond CVD: An overview of recent developments, *Diamond Relat. Mater.*, **4**, 1173–1188 (1995).

[23] P.E. Pehrsson, F.G. Celii, and J.E. Butler, Chemical mechanisms of diamond CVD, in *Diamond Films and Coatings*, R.F. Davis (Ed), Noyes Publications, Park Ridge, 1993, p. 68–146.

[24] M. Ihara, H. Komiyama, and T. Okubo, Correlation between nucleation site density and residual diamond dust density in diamond film deposition, *Appl. Phys. Lett.*, **65**, 1192–1194 (1994).

[25] O.A. Williams, O. Douheret, M. Daenen, K. Haenen, E. Osawa, and M. Takahashi, Enhanced diamond nucleation on monodispersed nanocrystalline diamond, *Chem. Phys. Lett.*, **445**, 255–258 (2007).

[26] S. Yugo, T. Kanai, T. Kimura, and T. Muto, Generation of diamond nuclei by electric field in plasma chemical vapor deposition, *Appl. Phys. Lett.*, **58**, 1036–1038 (1991).

[27] M. Katoh, M. Aoki, and H. Kawarada, Plasma enhanced diamond nucleation on Si, *Jpn. J. Appl. Phys.*, **33**, L194–196 (1994).

[28] K.-H. Thürer, M. Schreck, and B. Stritzker, Limiting processes for diamond epitaxial alignment on silicon, *Phys. Rev. B*, **57**, 15454–15464 (1998).

[29] S.D. Wolter, T.H. Borst, A. Vescan, and E. Kohn, The nucleation of highly oriented diamond on silicon via an alternating current substrate bias, *Appl. Phys. Lett.*, **68**, 3558–3560 (1996).

[30] A. Flöter, H. Güttler, G. Schulz, D. Steinbach, C. Lutz-Elsner, R. Zachai, A. Bergmaier, and G. Dollinger, The nucleation and growth of large area, highly oriented diamond films on silicon substrates, *Diamond Relat. Mater.*, **7**, 283–288 (1998).

[31] F. Stubhan, M. Ferguson, H.-J. Füsser, and R.J. Behm, Heteroepitaxial nucleation of diamond on Si(001) in hot filament chemical vapor deposition, *Appl Phys. Lett.*, **66**, 1900–1902 (1995).

[32] Q. Chen, J. Yang, and Z. Lin, Synthesis of oriented textured diamond films on silicon via hot filament chemical vapor deposition, *Appl Phys. Lett.*, **67**, 1853–1855 (1995).

[33] X.T. Zhou, H.L. Lai, H.Y. Peng, C. Sun, W.J. Zhang, N. Wang, I. Bello, C.S. Lee, and S.T. Lee, Heteroepitaxial nucleation of diamond on Si(001) via double bias-assisted hot filament chemical vapor deposition, *Diamond Relat. Mater.*, **9**, 134–139 (2000).

[34] Y. Ando, J. Kuwabara, K. Suzuki, and A. Sawabe, Patterned growth of heteroepitaxial diamond, *Diamond Relat. Mater.*, **13**, 1975–1979 (2004).

[35] A. Sawabe, S. Maeda, K. Watanabe, Y. Ando, and K. Suzuki, Growth and characterization of free-standing heteroepitaxial diamond wafer of 1 inch in diameter, Invited talk at the workshop *Surface and bulk defects in CVD diamond films XI*, 22-24 Feb. 2006, Hasselt, Belgium.

[36] W.J. Zhang, Y.S. Sun, H.Y. Peng, N. Wang, C.S. Lee, I. Bello, and S.T. Lee, Diamond nucleation enhancement by direct low-energy ion-beam deposition, *Phys. Rev. B*, **61**, 5579–5586 (2000).

[37] Y. Sato, I. Yashima, H. Fujita, T. Ando, and M. Kamo, Epitaxial growth of diamond from the gas phase, in *New Diamond Science and Technology*, R. Messier, J.T. Glass, J.E. Butler, and R. Roy (Eds), Mater. Res. Soc. Symp. Int. Proc. NDST-2, Pittsburg, PA, 1991, p. 371–376.

[38] Y. Shintani, Growth of highly (111)-oriented, highly coalesced diamond films on platinum (111) surface: A possibility of heteroepitaxy, *J. Mater. Res.*, **11**, 2955–2956 (1996).

[39] T. Tachibana, Y. Yokota, K. Nishimura, K. Miyata, K. Kobashi, and Y. Shintani, Heteroepitaxial diamond growth on platinum (111) by the Shintani process, *Diamond Relat. Mater.*, **5**, 197–199 (1996).

[40] W. Liu, D.A. Tucker, P. Yang, and J.T. Glass, Nucleation of oriented diamond particles on cobalt substrates, *J. Appl. Phys.*, **78**, 1291–1296 (1995).

[41] P.C. Yang, W. Zhu, and J.T. Glass, Nucleation of oriented diamond films on nickel substrates, *J. Mater. Res.*, **8**, 1773–1776 (1993).

[42] W. Zhu, P.C. Yang, and J.T. Glass, Oriented diamond films grown on nickel substrates, *Appl. Phys. Lett.*, **63**, 1640–1642 (1993).

[43] M. Schreck, K.-H. Thürer, and B. Stritzker, Limitations of the process time window for the bias enhanced nucleation of heteroepitaxial diamond films on silicon in the time domain, *J. Appl. Phys.*, **81**, 3092–3095 (1997).

[44] S. Koizumi, T. Murakami, T. Inuzuka, and K. Suzuki, Epitaxial growth of diamond thin films on cubic boron nitride {111} surfaces by dc plasma chemical vapor deposition, *Appl. Phys. Lett.*, **57**, 563–565 (1990).

[45] S. Koizumi and T. Inuzuka, Initial growth process of epitaxial diamond thin films on cBN single crystals, *Jpn. J. Appl. Phys.*, **32**, 3920–3927 (1993).

[46] A. Argoitia, J.C. Angus, J.S. Ma, L. Wang, P. Pirouz, and W.R.L. Lambrecht, Heteroepitaxy of diamond on c-BN: Growth mechanisms and defect characterization, *J. Mater. Res.*, **9**, 1849–1865 (1994).

[47] T. Inuzuka, S. Koizumi, and K. Suzuki, Epitaxial growth of diamond thin films on foreign substrates, *Diamond Relat. Mater.*, **1**, 175–179 (1992).

[48] W.R.L. Lambrecht and B. Segall, Electronic structure of (diamond C)/(sphalerite BN) (110) interfaces and superlattices, *Phys. Rev. B*, **40**, 9909–9919 (1989).

[49] P.C. Yang, C.A. Wolden, W. Liu, R. Schlesser, R.F. Davis, J.T. Prater, and Z. Sitar, Coalesced oriented diamond films on nickel, *J. Mater. Res.*, **13**, 1120–1123 (1998).

[50] T. Tachibana, Y. Yokota, K. Miyata, K. Kobashi, and Y. Shintani, Heteroepitaxial diamond growth process on platinum (111), *Diamond Relat. Mater.*, **6**, 266–271 (1997).

[51] T. Tachibana, Y. Yokota, K. Kobashi, and Y. Shintani, X-ray diffraction pole figure measurements of diamond films grown on platinum (111), *J. Appl. Phys.*, **82**, 4327–4330 (1997).

[52] T. Tachibana, Y. Yokota, K. Hayashi, K. Miyata, and K. Kobashi, Growth of (111)-oriented diamond films on off-axis platinum (111), in *Proceedings of ADC/FCT '99*, August 31–September 3, 1999, Tsukuba, Japan, M. Yoshikawa, Y. Koga, Y. Tzeng, C.-P. Klages, and K. Miyoshi (Eds), p. 79–82.

[53] T. Tachibana, Y. Yokota, K. Hayashi, and K. Kobashi, Growth of {111}-oriented diamond on Pt/Ir/Pt substrate deposited on sapphire, *Diamond Relat. Mater.*, **10**, 1633–1636 (2001).

[54] S.D. Wolter, J.T. Glass, and B.R. Stoner, Bias induced diamond nucleation studies on refractory metal substrates, *J. Appl. Phys.*, **77**, 5119–5124 (1995).

[55] T. Bauer, M. Schreck, S. Gsell, F. Hörmann, and B. Stritzker, Epitaxial rhenium buffer layers on Al_2O_3(0001): A substrate for the deposition of (111)-oriented heteroepitaxial diamond films, *Phys. Stat. Sol. (a)*, **199**, 19–26 (2003).

[56] Th. Bauer, M. Schreck, F. Hörmann, A. Bergmaier, G. Dollinger, and B. Stritzker, Analysis of the total carbon deposition during the bias enhanced nucleation of diamond on Ir/$SrTiO_3$(001) using ^{13}C-methane, *Diamond Relat. Mater.*, **11**, 493–498 (2002).

[57] A. Argoitia, J.C. Angus, L. Wang, X.I. Ning, and P. Pirouz, Diamond grown on single-crystal beryllium oxide, *J. Appl. Phys.*, **73**, 4305–4312 (1993).

[58] D.A. Tucker, D.-K. Seo, M.-H. Whangbo, F.R. Sivazlian, B.R. Stoner, S.P. Bozeman, A.T. Sowers, R.J. Nemanich, and J.T. Glass, Comparison of silicon, nickel, and nickel silicide (Ni_3Si) as substrates for epitaxial diamond growth, *Surf. Sci.*, **334**, 179–194 (1995).

[59] T. Suzuki, M. Yagi, K. Shibuki, Growth of oriented diamond particles on 6H-type of SiC and graphite flakes, in *Advances in New Diamond Science and Technology*, S. Saito, N. Fujimori, O. Fukunaga, M. Kamo, K. Kobashi, and M. Yoshikawa (Eds), MYU, Tokyo, 1994, pp. 271–274.

[60] In the case of a diamond covered sample holder a completely different behaviour may be observed when the diamond coating outside the substrate attracts the major current flow. Under these conditions the current usually decreases at the beginning.

[61] M. Schreck, T. Baur, and B. Stritzker, Optical characterization of the cathode plasma sheath during the biasing step for diamond nucleation on silicon, *Diamond Relat. Mater.*, **4**, 553–558 (1995).

[62] Sz. Kátai, A. Kováts, I. Maros, and P. Deák, Ion energy distributions and their evolution during bias-enhanced nucleation of chemical vapor deposition of diamond, *Diamond Relat. Mater.*, **9**, 317–321 (2000).

[63] Y.P. Raizer, *Gas Discharge Physics*, Springer, Berlin, 1991.

[64] O. Ternyak, E. Cheifetz, S. Shchemelinin, A. Breskin, R. Chechik, H. Zhang, I. Avigal, and A. Hoffman, Ion-induced electron emission (IIEE) from undoped and B-doped diamond films induced by 1–10KeV H^+ and Ar^+, *Diamond Relat. Mater.*, **16**, 861–866 (2007).

[65] B.R. Stoner, G.H. Ma, S.D. Wolter, W. Zhu, Y-C. Wang, R.F. Davis, and J.T. Glass, Epitaxial nucleation of diamond on β-SiC via bias-enhanced microwave plasma chemical vapor deposition, *Diamond Relat. Mater.*, **2**, 142–146 (1993).

[66] X. Jiang, M. Paul, C.P. Klages, and C.L. Jia, Studies of heteroepitaxial nucleation and growth of diamond on silicon, *Electrochemical Society Proceedings*, vol. **95-4**, *Diamond Materials IV*, K.K. Ravi, J.P. Dismukes (Eds), The Electrochemical Society, Inc., Pennigton, NJ 1995, p. 50.

[67] X. Jiang, K. Schiffmann, and C.-P. Klages, Nucleation and initial growth phase of diamond thin films on (100) silicon, *Phys. Rev. B*, **50**, 8402–8410 (1994).

[68] J. Robertson, Deposition mechanisms for promoting sp^3 bonding in diamond-like carbon, *Diamond Relat. Mater.*, **2**, 984–989 (1993).

[69] M. Zaiser, Y. Lyutovich, and F. Banhart, Irradiation-induced transformation of graphite to diamond: A quantitative study, *Phys. Rev. B*, **62**, 3058–3064 (2000).

[70] Y. Lifshitz, Th. Köhler, Th. Frauenheim, I. Guzmann, A. Hoffman, R.Q. Zhang, X.T. Zhou, and S.T. Lee, The mechanism of diamond nucleation from energetic species, *Science*, **297**, 1531–1533 (2002).

[71] M. Schreck, K.-H. Thürer, R. Klarmann, and B. Stritzker, Influence of the nucleation process on the azimuthal misorientation of heteroepitaxial diamond films on Si(001), *J. Appl. Phys.*, **81**, 3096–3102 (1997).

[72] M. Schreck, F. Hörmann, H. Roll, T. Bauer, and B. Stritzker, Heteroepitaxial diamond films on silicon substrates and on iridium layers: Analogies and differences in nucleation and growth, *New Diam. Front. Carbon Technol.*, **11**, 189–205 (2001).

[73] X. Jiang and C.-P. Klages, Recent developments in heteroepitaxial nucleation and growth of diamond on silicon, *Phys. Stat. Sol. (a)*, **154**, 175–183 (1996).

[74] C. Wild, R. Kohl, N. Herres, W. Müller-Sebert, and P. Koidl, Oriented CVD diamond films: Twin formation, structure and morphology, *Diamond Relat. Mater.*, **3**, 373–381 (1994).

[75] R. Locher, C. Wild, N. Herres, D. Behr, and P. Koidl, Nitrogen stabilized $\langle 100 \rangle$ texture in chemical vapor deposited diamond films, *Appl. Phys. Lett.*, **65**, 34–36 (1994).

[76] R. Hessmer, M. Schreck, S. Geier, B. Rauschenbach, and B. Stritzker, The influence of the growth process on the film texture of epitaxially nucleated diamond on silicon(001), *Diamond Relat. Mater.*, **4**, 410–415 (1995).

[77] M. Schreck, K.-H. Thürer, C. Christensen, M. Müller, and B. Stritzker, Effect of oxygen on the bias enhanced nucleation of diamond on silicon, *Diamond Relat. Mater.*, **8**, 160–165 (1999).

[78] N. Bozzolo, S. Barrat, I. Dieguez, and E. Bauer-Grosse, Crystalline quality of highly oriented diamond films grown on (100) silicon studied by conventional TEM, *Diamond Relat. Mater.*, **6**, 41–47 (1997).

[79] J. Michler, Y. von Kaenel, J. Stiegler, and E. Blank, Complementary application of electron microscopy and micro-Raman spectroscopy for microstructure, stress, and bonding defect investigation of heteroepitaxial chemical vapor deposited diamond films, *J. Appl. Phys.*, **83**, 187–197 (1998).

[80] H. Kawarada, C. Wild, N. Herres, R. Locher, P. Koidl, and N. Nagasawa, Heteroepitaxial growth of highly oriented diamond on cubic silicon carbide, *J. Appl. Phys.*, **81**, 3490–3493 (1997).

[81] W. Zhu, X.H. Wang, B.R. Stoner, G.H.M. Ma, H.S. Kong, M.W.H. Braun, and J.T. Glass, Diamond and β-SiC heteroepitaxial interfaces: A theoretical and experimental study, *Phys. Rev. B*, **47**, 6529–6542 (1993).

[82] T. Tachibana, K. Hayashi, and K. Kobashi, Azimuthal rotation of diamond crystals epitaxially nucleated on silicon {001}, *Appl. Phys. Lett.*, **68**, 1491–1492 (1996).

[83] K. Schiffmann and X. Jiang, Investigation of heteroepitaxial diamond films by atomic force and scanning tunnelling microscopy, *Appl. Phys. A*, **59**, 17–22 (1994).

[84] C.L. Jia, K. Urban, and X. Jiang, Heteroepitaxial diamond films on silicon (001): Interface structure and crystallographic relations between film and substrate, *Phys. Rev. B*, **52**, 5164–5171 (1995).

[85] X. Jiang and C.L. Jia, Direct local epitaxy of diamond on Si(001) and surface-roughening-induced crystal misorientation, *Phys. Rev. Lett.*, **84**, 3658–3661 (2000).

[86] D. Wittorf, W. Jäger, C. Dieker, A. Flöter, and H. Güttler, Electron microscopy of interfaces in chemical vapour deposition diamond films on silicon, *Diamond Relat. Mater.*, **9**, 1696–1702 (2000).

[87] P. Wurzinger, N. Fuchs, P. Pongratz, M. Schreck, R. Heßmer, and B. Stritzker, TEM investigations on the heteroepitaxial nucleation of CVD diamond on (001) silicon substrates, *Diamond Relat. Mater.*, **6**, 752–757 (1997).

[88] X. Jiang, W.J. Zhang, M. Paul, and C.-P. Klages, Diamond film orientation by ion bombardment during deposition, *Appl. Phys. Lett.*, **68**, 1927–1929 (1996).

[89] M. Schreck, C. Grunick, C. Haug, R. Brenn, and B. Stritzker, Bias assisted growth on diamond single crystals: The defect formation due to ion bombardment studied by ion channelling, electron backscatter diffraction, and micro-Raman spectroscopy, *Diamond Relat. Mater.*, **11**, 487–492 (2002).

[90] K. Ohtsuka, H. Fukuda, K. Suzuki, and A. Sawabe, Fabrication of epitaxial diamond thin film on iridium, *Jpn. J. Appl. Phys.*, **36**, L1214–L1216 (1997).

[91] M. Schreck, H. Roll, and B. Stritzker, Diamond/Ir/$SrTiO_3$: A material combination for improved heteroepitaxial diamond films, *Appl. Phys. Lett.*, **74**, 650–652 (1999).

[92] F. Hörmann, Th. Bauer, M. Schreck, S. Gsell, and B. Stritzker, TEM analysis of nanometer-size surface structures formed by bias enhanced nucleation of diamond on iridium, *Diamond Relat. Mater.*, **12**, 350–355 (2003).

[93] F. Hörmann, M. Schreck, and B. Stritzker, First stages of diamond nucleation on iridium buffer layers, *Diamond Relat. Mater.*, **10**, 1617–1621 (2001).

[94] A. Sawabe, T. Yamada, H. Okamura, M. Katagiri, and K. Suzuki, Epitaxial growth of diamond thin films on Ir(001)/MgO(001) stacking by two-step dc plasma chemical vapor deposition and their characterization, *New Diam. Front. Carbon Technol.*, **12**, 343–353 (2002).

[95] T. Tsubota, M. Ohta, K. Kusakabe, S. Morooka, M. Watanabe, and H. Maeda, Heteroepitaxial growth of diamond on an iridium (100) substrate using microwave plasma-assisted chemical vapor deposition, *Diamond Relat. Mater.*, **9**, 1380–1387 (2000).

[96] Th. Bauer, S. Gsell, F. Hörmann, and B. Stritzker, Surface modifications and first stages of heteroepitaxial diamond growth on iridium, *Diamond Relat. Mater.*, **13**, 335–341 (2004).

[97] A. Sawabe, H. Fukuda, T. Suzuki, Y. Ikuhara, and T. Suzuki, Interface between CVD diamond and iridium films, *Surf. Science*, **467**, L845–L849 (2000).

[98] Th. Bauer, M. Schreck, F. Hörmann, A. Bergmaier, G. Dollinger, and B. Stritzker, Analysis of the total carbon deposition during the bias enhanced nucleation of diamond on Ir/$SrTiO_3$(001) using ^{13}C-methane, *Diamond Relat. Mater.*, **11**, 493–498 (2002).

[99] S. Kono, M. Shiraishi, N.I. Plusnin, T. Goto, Y. Ikejima, T. Abukawa, M. Shimomura, Z. Dai, C. Bednarski-Meinke, and B. Golding, X-ray photoelectron diffraction study of the initial stages of CVD diamond heteroepitaxy on Ir(001)/$SrTiO_3$, *New Diam. Front. Carbon Technol.*, **15**, 363–371 (2005).

[100] M. Schreck, F. Hörmann, S. Gsell, Th. Bauer, and B. Stritzker, Transmission electron microscopy study of the diamond nucleation layer on iridium, *Diamond Relat. Mater.*, **15**, 460–464 (2006).

[101] T. Saito, S. Tsuruga, N. Ohya, K. Kusakabe, S. Morooka, H. Maeda, A. Sawabe, and K. Suzuki, Epitaxial nucleation of diamond on an iridium substrate by bias treatment, for microwave plasma-assisted chemical vapor deposition, *Diamond Relat. Mater.*, **7**, 1381–1384 (1998).

[102] M. Schreck, Th. Bauer, S. Gsell, F. Hörmann, H. Bielefeldt, and B. Stritzker, Domain formation in diamond nucleation on iridium, *Diamond Relat. Mater.*, **12**, 262–267 (2003).

[103] T. Fujisaki, M. Tachiki, N. Taniyama, M. Kudo, and H. Kawarada, Initial growth of heteroepitaxial diamond on Ir(001)/MgO(001) substrates using antenna-edge-type microwave plasma assisted chemical vapor deposition, *Diamond Relat. Mater.*, **12**, 246–250 (2003).

[104] B. Golding, C. Bednarski-Meinke, and Z. Dai, Diamond heteroepitaxy: Pattern formation and mechanisms, *Diamond Relat. Mater.*, **13**, 545–551 (2004).

[105] S. Gsell, M. Schreck, G. Benstetter, E. Lodermeier, and B. Stritzker, Combined AFM-SEM study of the diamond nucleation layer on Ir(001), *Diamond Relat. Mater.*, **16**, 665–670 (2007).

[106] S. Kono, T. Takano, T. Goto, Y. Ikejima, M. Shiraishi, T. Abukawa, T. Yamada, and A. Sawabe, Effect of bias treatment in the CVD diamond growth on Ir(001), *Diamond Relat. Mater.*, **13**, 2081–2087 (2004).

[107] S. Gsell, S. Berner, T. Brugger, M. Schreck, R. Brescia, M. Fischer, T. Greber, J. Osterwalder, and B. Stritzker, Comparative electron diffraction study of the diamond nucleation layer on Ir(001), *Diamond Relat. Mater.*, **17**, 1029–1034 (2008).

[108] T. Aoyama, N. Amano, T. Goto, T. Abukawa, S. Kono, Y. Ando, and A. Sawabe, Characterization of planar-diode bias-treatment in DC-plasma hetero-epitaxial diamond growth on Ir(001), *Diamond Relat. Mater.*, **16**, 594–599 (2007).

[109] P. Bernhard, Ch. Ziethen, G. Schoenhense, M. Schreck, T. Bauer, S. Gsell, and B. Stritzker, Structural properties of the diamond nucleation layer on iridium analyzed by latterally resolved X-ray absorption spectroscopy, *Jpn. J. Appl. Phys.*, **45**, L984–L986 (2006).

[110] H. Hofsäss, H. Feldermann, R. Merk, M. Sebastian, and C. Ronning, Cylindrical spike model for the formation of diamondlike thin films by ion deposition, *Appl. Phys. A*, **66**, 153–181 (1998).

[111] R. Brescia, M. Schreck, J. Michler, S. Gsell, and B. Stritzker, Interaction of small diamond islands on iridium: A finite element simulation study, *Diamond Relat. Mater.*, **16**, 705–710 (2007).

[112] R. Brescia, M. Schreck, S. Gsell, M. Fischer, and B. Stritzker, Transmission electron microscopy study of the very early stages of diamond growth on iridium, *Diamond Relat. Mater.*, **17**, 1045–1050 (2008).

[113] M. Schreck, F. Hörmann, H. Roll, J.K.N. Lindner, and B. Stritzker, Diamond nucleation on iridium buffer layers and subsequent textured growth: A route for the realization of single-crystal diamond films, *Appl. Phys. Lett.*, **78**, 192–194 (2001).

[114] R. Locher, C. Wild, W. Müller-Sebert, R. Kohl, and P. Koidl, Optical reflection and angle-resolved light scattering from textured polycrystalline diamond films, *Diamond Relat. Mater.*, **2**, 1248–1252 (1993).

[115] A. Van der Drift, Evolutionary selection, a principle governing growth orientation in vapour-deposited layers, *Philips Res. Rep.*, **22**, 267–288 (1967).

[116] C. Wild, P. Koidl, W. Müller-Sebert, H. Walcher, R. Kohl, N. Herres, R. Locher, R. Samlenski, and R. Brenn, Chemical vapour deposition and characterization of smooth {100}-faceted diamond films, *Diamond Relat. Mater.*, **2**, 158–168 (1993).

[117] M. Schreck and B. Stritzker, Nucleation and growth of heteroepitaxial diamond films on silicon, *Phys. Stat. Sol. (a)*, **154**, 197–217 (1996).

[118] M. Schreck, A. Schury, F. Hörmann, H. Roll, and B. Stritzker, Mosaicity reduction during growth of heteroepitaxial diamond films on iridium buffer layers: Experimental results and numerical simulations, *J. Appl. Phys.*, **91**, 676–685 (2002).

[119] J.C. Angus, M. Sunkara, S.R. Sahaida, and J.T. Glass, Twinning and faceting in early stages of diamond growth by chemical vapor deposition, *J. Mater. Res.*, **7**, 3001–3009 (1992).

[120] X. Jiang and C.L. Jia, The coalescence of [001] diamond grains heteroepitaxially grown on (001) silicon, *Appl. Phys. Lett.*, **69**, 3902–3904 (1996).

[121] Y. Ando, J. Kuwabara, K. Suzuki, and A. Sawabe, Patterned growth of heteroepitaxial diamond, *Diamond Relat. Mater.*, **13**, 1975–1979 (2004).

[122] C. Bednarski, Z. Dai, A.-P. Li, and B. Golding, Studies of heteroepitaxial growth of diamond, *Diamond Relat. Mater.*, **12**, 241–245 (2003).

[123] Z. Dai, C. Bednarski-Meinke, R. Loloee, and B. Golding, Epitaxial (100) iridium on A-plane sapphire: A system for wafer scale diamond heteroepitaxy, *Appl. Phys. Lett.*, **82**, 3847–3849 (2003).

[124] S. Gsell, T. Bauer, J. Goldfuß, M. Schreck, and B. Stritzker, A route to diamond wafers by epitaxial deposition on silicon via iridium/yttria-stabilized zirconia buffer layers, *Appl. Phys. Lett.*, **84**, 4541–4543 (2004).

[125] K. Maex and M. van Rossum (Eds), *Properties of Metal Silicides*, INSPEC, London, 1995.

[126] Y. Wu, J. Qi, C.H. Lee, L.S. Hung, W.J. Zhang, I. Bello, Y. Lifshitz, and S.T. Lee, Diamond growth on Ir/CaF_2/Si substrates, *Diamond Relat. Mater.*, **12**, 1675–1680 (2003).

[127] A. Lubig, Ch. Buchal, J. Schubert, C. Copetti, D. Guggi, C.L. Jia, B. Stritzker, Epitaxial growth of $YBa_2Cu_3O_{7-x}$ thin films on Si(100) with zirconia buffers for varying crystalline quality and structure, *J. Appl. Phys.*, **71**, 5560–5564 (1992).

[128] R. Ramesh, H. Gilchrist, T. Sands, V.G. Keramidas, R. Haakenaasen, and D.K. Fork, Ferroelectric La-Sr-Co-O/Pb-Zr-Ti-O/La-Sr-Co-O heterostructures on silicon via template growth, *Appl. Phys. Lett.*, **63**, 3592–3594 (1993).

[129] S. Gsell, M. Fischer, R. Brescia, M. Schreck, P. Huber, F. Bayer, B. Stritzker, and D.G. Schlom, Reduction of mosaic spread using iridium interlayers: A route to improved oxide heteroepitaxy on silicon, *Appl. Phys. Lett.*, **91**, 061501–061501-3 (2007).

[130] T. Bauer, S. Gsell, M. Schreck, J. Goldfuß, J. Lettieri, D.G. Schlom, and B. Stritzker, Growth of epitaxial diamond on silicon via iridium/$SrTiO_3$ buffer layers, *Diamond Relat. Mater.*, **14**, 314–317 (2005).

[131] M. Fischer, S. Gsell, M. Schreck, R. Brescia, and B. Stritzker, Preparation of 4-inch Ir/YSZ/Si(001) substrates for the large-area deposition of single crystal diamond, *Diamond Relat. Mater.*, **17**, 1035–1038 (2008).

[132] E. Kohn, W. Ebert, M. Adamschik, P. Schmid, and A. Denisenko, Diamond based MEMS devices, *New Diam. Front. Carbon Technol.*, **11**, 81–100 (2001).

[133] E. Kohn, P. Gluche, and M. Adamschik, Diamond MEMS – a new emerging technology, *Diamond Relat. Mater.*, **8**, 934–940 (1999).

[134] S. Ertl, M. Adamschik, P. Schmid, P. Gluche, A. Flöter, and E. Kohn, Surface micromachined diamond microswitch, *Diamond Relat. Mater.*, **9**, 970–974 (2000).

[135] J. Achard, A. Tardieu, A. Kanaev, A. Gicquel, M.C. Castex, Y. Yokota, K. Hayashi, T. Tachibana, and K. Kobashi, Photoconductivity of highly oriented and randomly oriented diamond films for the detection of fast UV laser pulses, *Diamond Relat. Mater.*, **11**, 423–426 (2002).

[136] H. Kawarada, C. Wild, N. Herres, P. Koidl, Y. Mizuochi, A. Hokazono, and H. Nagasawa, Surface morphology and surface p-channel field effect transistor on the heteroepitaxial diamond deposited on inclined β-SiC(001) surfaces, *Appl. Phys. Lett.*, **72**, 1878–1880 (1998).

[137] T. Yamada, J. Maede, and A. Sawabe, Electron emission from a heteroepitaxial diamond planar emitter, *Jpn. J. Appl. Phys.*, **38**, L902–L903 (1999).

[138] K. Kusakabe, A. Sobana, K.-I. Sotowa, T. Imato, and T. Tsubota, Electrical properties of boron-doped diamond films synthesized by MPCVD on an iridium substrate, *Diamond Relat. Mater.*, **12**, 1396–1401 (2003).

[139] B.R. Stoner, Chien-teh Kao, D.M. Malta, and R.C. Glass, Hall effect measurements on boron-doped, highly oriented diamond films grown on silicon via microwave plasma chemical vapour deposition, *Appl. Phys. Lett.*, **62**, 2347–2349 (1993).

[140] M. Kubovic, A. Aleksov, M. Schreck, Th. Bauer, B. Stritzker, and E. Kohn, Field effect transistor fabricated on hydrogen-terminated diamond grown on $SrTiO_3$ substrate and iridium buffer layer, *Diamond Relat. Mater.*, **12**, 403–407 (2003).

[141] A. Stolz, M. Behravan, M. Regmi, and B. Golding, Heteroepitaxial diamond detectors for heavy ion beam tracking, *Diamond Relat. Mater.*, **15**, 807–810 (2006).

Part 2

Radiation Sensors

CVD Diamond for Electronic Devices and Sensors Edited by Ricardo S. Sussmann
© 2009 John Wiley & Sons, Ltd. ISBN: 978-0-470-06532-7

7 Detectors for UV and Far UV Radiation

ALAN T. COLLINS

Physics Department, King's College London, UK

7.1	Introduction	165
	7.1.1 UV and EUV lithography	166
	7.1.2 ESA Solar Orbiter	166
7.2	Photoconductivity Basics	166
	7.2.1 Contacts	167
	7.2.2 Photoconductivity due to defects	168
	7.2.3 Scattering and trapping by defects	169
7.3	Detectors Based on Polycrystalline CVD Diamond	170
7.4	Detectors based on Single-crystal CVD Diamond	174
7.5	Summary	177
7.6	Future Prospects for Diamond UV Detectors	178
	7.6.1 UV and EUV lithography	179
	7.6.2 ESA Solar Orbiter	180
7.7	Concluding Remarks	181
	References	181

7.1 INTRODUCTION

Diamond has an indirect energy gap of 5.5 eV, corresponding to a wavelength of 225 nm. At room temperature intrinsic diamond, therefore, exhibits a photoconductive response at wavelengths λ shorter than 236 nm (there is some phonon-assisted absorption at energies just below the energy gap) and has a negligible response to visible (400 to 700 nm) and near-ultraviolet radiation. Photoconductivity is well known in natural diamond, but is very variable. Indeed, Robertson *et al.* (1934) divided diamonds into type I or type II; in that study, type I diamonds absorbed in the ultraviolet (UV) region at energies above approximately 3.7 eV ($\lambda < 335$ nm) and were poor photoconductors whereas type II diamonds transmitted to 5.49 eV and were good photoconductors.

CVD Diamond for Electronic Devices and Sensors Edited by Ricardo S. Sussmann
© 2009 John Wiley & Sons, Ltd. ISBN: 978-0-470-06532-7

The ability to grow diamond by chemical vapour deposition (CVD) allows material to be produced with very low concentrations of impurities, compared with the impurity concentrations in type I natural diamonds. CVD diamond, therefore, has the apparent potential to be used as a sensitive detector of ultraviolet radiation for $\lambda < 230$ nm, and recent research into diamond UV detectors has been driven by two possible applications.

7.1.1 UV and EUV lithography

The continual shrinking of features in silicon semiconducting devices necessitates using ever-shorter wavelengths to carry out the lithography. Excimer lasers with $\lambda = 193$ nm are currently used, and it is envisaged that the trend to shorter wavelengths will continue towards the extreme ultraviolet (EUV). For efficient operation the lithography machines require robust solid-state UV detectors for direct beam monitoring and photoresist exposure dosimetry. Whitfield *et al.* (2001) stated that no detectors commercially available at that time could fully meet all the specifications required for these applications. Silicon detectors were said to suffer from rapid performance degradation and unacceptably high attenuation in the surface metallisation and passivation layers. However, Whitfield *et al.* proposed that a diamond UV detector would perform satisfactorily in this application.

7.1.2 ESA Solar Orbiter

In 2015 the European Space Agency (ESA) plans to launch the Solar Orbiter. This will be placed in an elliptical orbit around the sun, with a minimum approach distance of 48 solar radii, enabling it to obtain images of the sun at unprecedented resolution. The BOLD (Blind to Optical Light Detectors) international initiative has been set up to investigate and develop novel imaging detectors for solar observations at ultraviolet wavelengths (Hochedez *et al.* 2001, 2002). Diamond and/or $Al_xGa_{(1-x)}N$ are the materials most favoured for this application.

In the rest of this chapter we will review some of the research that has been carried out on the development and characterisation of diamond UV detectors, and conclude by examining the future prospects of CVD diamond in the above applications.

7.2 PHOTOCONDUCTIVITY BASICS

Illumination of diamond with a photon having energy higher than that of the band gap leads to the generation of an electron in the conduction band and a hole in the valence band. Until the electron and hole recombine they will cause an increase in the electrical conductivity. The application of an electric field will cause a current to flow, and, for a beam of photons that is fully absorbed in the diamond, the photoconductive signal I_{ph} (the difference between the current measured under illumination and in the dark) is given by:

$$I_{ph} = qF_0\eta\mu\tau E/d \tag{7.1}$$

where q is the electronic charge, F_0 is the number of incident photons, η is the quantum efficiency ($0 < \eta < 1$), $\mu\tau$ is the mobility-lifetime product, E is the electric field and d is the electrode spacing. Defining the photoconductive gain G as the ratio between the charge collection distance $L = \mu\tau E$ and d, the external quantum efficiency EQE is given by:

$$\mathrm{EQE} = I_{\mathrm{ph}}/(qF_0) = \eta L/d = \eta G \tag{7.2}$$

The mobility and lifetime used to define L are average values, and the full expression may be written as:

$$L = (\mu_{\mathrm{e}}\tau_{\mathrm{e}} + \mu_{\mathrm{h}}\tau_{\mathrm{h}})E \tag{7.3}$$

where the subscripts e and h refer to electrons and holes, respectively (Mainwood 2000). If $L > d$, EQE can have values greater than unity. Values of G greater than unity can be interpreted in terms of an electron flowing round the circuit several times before it recombines with a photo-generated hole (McKeag *et al.* 1997).

Diamond is an indirect gap semiconductor, and when an electronic transition occurs between the top of the valence band and the bottom of the conduction band, the wave vector is conserved by the absorption or emission of phonons (Clark *et al.* 1964). The room-temperature absorption spectrum of type IIa diamond shows clear thresholds at energies $E_{\mathrm{gx}} - \hbar\omega_{\mathrm{TO}}$, $E_{\mathrm{gx}} + \hbar\omega_{\mathrm{TA}}$ and $E_{\mathrm{gx}} + \hbar\omega_{\mathrm{TO}}$, where E_{gx} is the exciton energy gap and ω_{TO} and ω_{TA} are the energies of the transverse optical and transverse acoustic phonons with wave vectors at the lowest minimum of the conduction band. Using the mean room-temperature values of $E_{\mathrm{gx}} = 5.400$ eV, $\omega_{\mathrm{TO}} = 143$ meV and $\omega_{\mathrm{TA}} = 83$ meV, these thresholds occur at 5.257, 5.483 and 5.543 eV (235.8, 226.1 and 223.6 nm), respectively.

Initially the photoconductivity spectrum follows the structure in the absorption spectrum, and the three threshold energies observed in absorption can be clearly seen in the photoconductivity spectrum (Denham *et al.* 1967). The photocurrent increases rapidly at energies above 5.543 eV ($\lambda < 223.6$ nm) and reaches a maximum once most of the photons are absorbed. At higher energies, the penetration depth of the photons decreases and, because the carriers are generated closer to the surface, where there is a greater probability of recombination, the photocurrent decreases with increasing photon energy.

7.2.1 Contacts

The majority of investigations of diamond UV detectors have used the metal–semiconductor–metal (MSM) structure. Alternative configurations use a combination of p-type diamond, intrinsic diamond and n-type diamond to produce p–i–n or p–i–metal structures; a p–i–n device will be discussed in more detail in Section 7.4. Depending on the application, the contact configuration for an MSM device may be either coplanar or transverse. Coplanar contacts, deposited on the top (growth) surface, may simply comprise a pair of electrodes with a gap between them, or several strip electrodes, none of which is connected to another, or interdigitated electrodes in which every other electrode is connected in common (Figure 7.1a). For one-dimensional imaging applications, an interdigitated array, in which the 'odd' electrodes are connected in common and the 'even' electrodes are connected individually (Figure 7.1b), may be used (Lansley *et al.* 2002). For transverse measurements a continuous electrode is deposited on the bottom (substrate) surface, two top electrodes are connected and the photons focused on the gap between

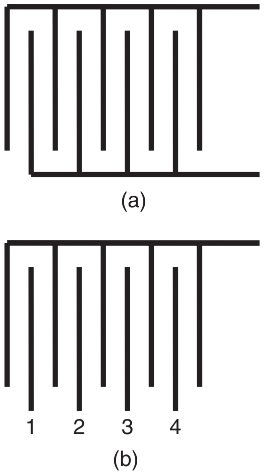

Figure 7.1 Coplanar contacting configurations: (a) interdigitated contacts, (b) interdigitated contacts with individual read-out for one-dimensional imaging

this pair (Mainwood 2000). Alternatively a single semitransparent metal layer may be used for the top contact; Allers and Collins (1995), for example, used a 25-nm gold layer.

As-grown, CVD diamond usually has a hydrogenated surface that behaves as a p-type semiconductor (Hokazono *et al.* 1997), and this must be removed by cleaning the diamond in oxidising reagents or by exposure to an oxygen plasma before making electrical contacts. Most applications require ohmic contacts. The generally adopted procedure is to evaporate or sputter a metal such as Ti, followed by Pt followed by a thicker layer of gold. On heating at 450 °C, the Ti forms a carbide, and connection to an external circuit may be made by bonding to the gold pad. The Pt serves as a diffusion barrier (Werner 2003). Where a blocking (rectifying) contact is needed, an evaporated layer of Al may be used. Isberg *et al.* (2004), for example, used standard lithographic techniques to produce semitransparent Al mesh contacts on their specimens.

7.2.2 Photoconductivity due to defects

In addition to the intrinsic excitation process described above, sub-band-gap photocurrents can be produced by various defects. Where it is required that the detector is blind to visible and near-ultraviolet photons, the growth process must be carefully controlled to minimise the incorporation of these defects.

Nitrogen is readily incorporated into CVD diamond and produces optical absorption and photoconductivity for energies above approximately 2.2 eV ($\lambda < 563$ nm), right up to the energy gap at 5.5 eV (Nebel 2003). Boron is also readily incorporated, and, if present as the major impurity, gives rise to photoconductivity starting at 380 meV in the near-infrared spectral region. The response reaches a maximum at approximately 550 meV (2.25 μm), and then progressively decreases at higher energies (Collins *et al.* 1969). Boron is an acceptor and, unless added intentionally, is present only at low concentrations (probably $\ll$ 1 part per million (ppm)); consequently, in many cases, any B present would be compensated by nitrogen donors, and not produce any photoconductivity.

Allers and Collins (1995) reported an extrinsic photoconductivity spectrum, which is seen only in CVD diamond. This exhibits a sharp onset at ~ 1.5 eV (825 nm) with a structured band to higher energy. Measurements were made between 1.5 and 2.6 eV (825 and 475 nm), and at the higher energies the photocurrent showed a small increase; this may be due to nitrogen. The structure in the band arises from the same mechanism that produces oscillatory features in the photoconductivity spectrum due to the boron acceptor. Although the photocurrent was too small in some specimens to measure the spectrum, all specimens showed some extrinsic photoconductivity when illuminated with a He/Ne laser (632.8 nm). Four samples for which it was possible to obtain an absorption spectrum had an absorption line at 1.681 eV (737 nm), which is attributed to a silicon-vacancy centre (Collins *et al.* 1990). Although this centre did not produce any photoconductivity, it is possible that the photoconductivity with a threshold at 1.5 eV is produced by a silicon-related defect (Martineau 2007).

Radiation damage creates vacancies in diamond, and also introduces a broad photoconductivity band, extending beyond the range 350 to 750 nm (Vermeulen 1976; Farrer and Vermeulen 1972). The higher excited states, GR2 to GR8, of the neutral vacancy, and the ND1 band associated with the negative vacancy, also produce photoconductivity signals (Farrer and Vermeulen 1972). Although vacancies can be detected in CVD diamond (Allers and Mainwood 1998), their concentration is unlikely to be high enough to produce substantial photoconductivity signals.

7.2.3 Scattering and trapping by defects

Diamond has been extensively investigated as a UV detector and as a particle detector, and many investigators report problems associated with scattering and trapping of the charge carriers. The situation is more severe with, but not unique to, CVD diamond. In polycrystalline CVD diamond, the grains grow in columns, and are smallest on the substrate side and largest on the growth surface. The grain size on the growth surface is typically 15 % of the thickness of the layer (Bergonzo *et al.* 2001). One indicator of the quality of a sample is the width of the Raman line at 1332 cm^{-1}; as the grains become larger the width of the Raman line decreases, indicating a lower level of strain in the grains. The charge collection distance increases considerably for line widths less than 2.5 cm^{-1} (Bergonzo *et al.*). Several other authors (e.g. McKeag and Jackman, 1998; Hammersberg *et al.* 2001; Isberg *et al.* 2004) have noted that the $\mu\tau$ product decreases as the grain size decreases. This suggests strongly that the grain boundaries scatter the charge carriers and/or act as traps for the charge carriers.

Some detectors exhibit a very slow recovery after illumination with UV. Nebel (2003) describes a persistent photocurrent in polycrystalline CVD diamond. After illuminating the sample for 10 min at 300 K the source was switched off and the sample left in the dark for 30 min. At the end of this period the dark current was only slightly smaller than the photocurrent. The persistent photocurrent could be annealed out by heating the sample for typically 100 s at 600 K. Analysis of the data indicated a trap with an activation energy of 1.4 eV, and a relaxation time of 6000 years at 300 K. These are just a few examples of phenomena associated with the scattering and trapping of charge carriers. Further examples will be given below.

7.3 DETECTORS BASED ON POLYCRYSTALLINE CVD DIAMOND

Jackman's group at University College London was one of the first to produce a UV detector that met some of the desirable criteria (McKeag *et al.* 1997). They chose the coplanar interdigitated contact structure shown in Figure 7.1(a). The spacing of the electrodes (20 μm) was comparable with the grain size at the growth surface. At energies above the diamond band gap, the penetration depth of the photons into the free-standing layer of diamond is much less than the thickness of the specimen, and the carriers are predominantly generated in large grains. Although the diamond layers were carefully cleaned in a strongly oxidising solution before the contacts were prepared, the performance of the devices was initially disappointing. As fabricated, the devices showed high dark current levels that were variable and in the range 1 to 200 μA for bias voltages in the range 0.1 to 10 volts. Illumination with photons in the wavelength range 180 to 800 nm produced an increase in this current at all wavelengths, although the greatest changes were for $\lambda < 225$ nm and $\lambda > 740$ nm. However, after heating at 700 °C for 1 h in methane, followed by heating at 400 °C for 1 h in air, the sub-band-gap photoconductivity was dramatically reduced, as shown in Figure 7.2. The ratio of the UV response to the visible response is now approximately 10^6:1 and the dark current has been reduced to < 0.1 nA. The responsivity as a function of the electric field varied as shown in Figure 7.3, and it is clear that this is approaching saturation at $E = 0.5$ V $(\mu\text{m})^{-1}$.

In a subsequent investigation, McKeag and Jackman (1998) studied the sensitivity and speed of three categories of diamond specimens. Categories I, II and III had thicknesses of 280, 110 and 70 μm and grain sizes at the growth surface of 40–60, 20–40 and 10–30 μm, respectively. Interdigitated contacts 20 μm wide and 40 μm spacing were applied, and the contacted specimens were subjected to the gas treatments described above. For the large-grain-size category I specimens, McKeag and Jackman reported that the photoelectric gain varied from 10^3 to $> 10^5$ as the bias increased from 0.1 to 50 volts. The maximum value of the gain implies that the charge collection distance L is

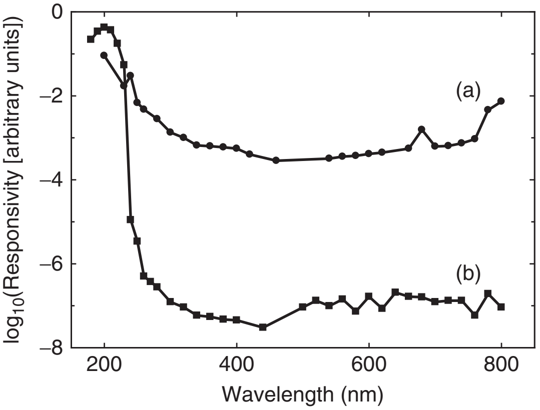

Figure 7.2 Photoconductivity spectrum of an interdigitated device based on polycrystalline CVD diamond (a) as constructed, and (b) after heating in methane at 700 °C and in air at 400 °C. (Redrawn from McKeag *et al.* 1997)

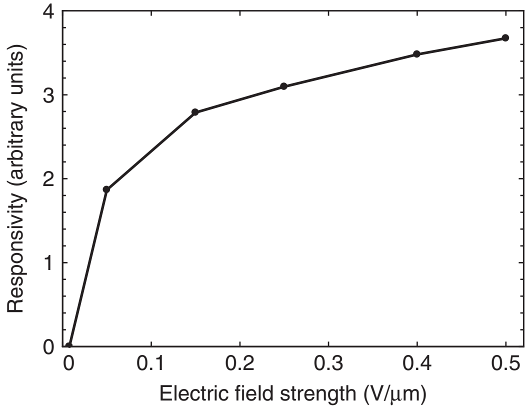

Figure 7.3 Responsivity of an interdigitated device based on polycrystalline CVD diamond as a function of the electric field. (Redrawn from McKeag *et al.* 1997)

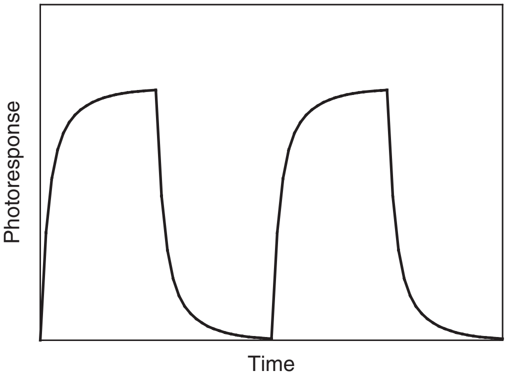

Figure 7.4 Generic shape of the photoconductivity signal as a function of time as the ultraviolet illumination is switched on and off. The build-up and decay of the signal are characterised by two or more time constants

in excess of 2 m, which is an unreasonably high value. Data from Section 7.4, below, substituted into Equation (7.3) suggest that a value of $L \sim 1$ mm is a realistic value for polycrystalline diamond. It is important to be aware of misleading conclusions in early investigations of diamond photodetectors.

McKeag and Jackman examined the time responses of their devices by illuminating the detectors at 200 nm for several seconds and then switching off the illumination. The characteristic behaviour is illustrated in Figure 7.4. When the illumination is switched on, the signal initially rises rapidly, followed by a slower increase; when the illumination is switched off the signal drops rapidly, followed by a slower decrease. This behaviour is typical of a material that contains trapping centres, and the variation of the photo-signal with time depends on the nature of the trap, the intensity of the illumination, the electric field, and temperature (Heijne 1966). Frequently a material will contain various types of trap; the response curves then correspond to a superposition of the curves for each kind of trap. This makes it difficult, if not impossible, to derive, from the observed curves, unambiguous data on the concentration and on the nature of the traps (Heijne 1966).

McKeag *et al.* certainly found that the turn-on and turn-off times were a function of the electric field, although no systematic trends emerged. The gain of the large-grain devices (category I) was greater than those of categories II or III, but the response speed was lower. In particular, the turn-off time for the large-grain detectors was of the order of 10 s. The time response of a detector based on material of category II was considerably shortened by further heat treatment.

Although many of these phenomena were inadequately understood, the development of a process that ‘worked’ led to a diamond UV detector being marketed by Centronic (UK). This had a sensitive region just over 2 mm square, with an interdigitated electrode structure on the growth surface, using electrodes approximately 17 μm wide and spaced at approximately 50 μm.

Hiscock and Collins (1999) carried out a detailed study of a Centronic detector together with five other ‘strip’ detectors made from free-standing diamond layers approximately 300 μm thick. For these latter specimens, electrodes 50 μm wide spaced at 100 μm were formed on the growth surfaces, using the standard Ti, Pt, Au evaporations, followed by annealing at 450 °C. Some specimens also had a continuous electrode on the substrate surface. With this geometry, photoconductivity measurements could be made either between a pair of contacts on the top surface, or through the bulk of the specimen, using a top contact and the bottom contact. In all cases an electric field of 0.2 to 0.3 V $(\mu\text{m})^{-1}$ was used.

The turn-on and turn-off times of all the detectors examined by Hiscock and Collins were of the order 1 s, and photoconductivity spectra could be obtained using a scanning monochromator provided the scan speed was sufficiently slow. These authors also investigated the spatial uniformity of the photoconductive responses of the strip detectors and the Centronic detector by focusing an image approximately 35 μm square from the monochromator onto the diamond detector. The detector was mounted in an electrically screened enclosure on an X–Y stage, which enabled the spot of focused UV radiation to be rastered over the area of interest.

Hiscock and Collins found that the photoconductivity spectra from the Centronic detector, and from the strip detectors using coplanar contacts, were very similar to those obtained by Denham *et al.* (1967) on natural type IIa diamond. However, for some of the strip detectors the spectrum measured transversely through the bulk of the diamond was very different from that measured on the same diamond with coplanar contacts, as illustrated in Figure 7.5. (Note that Hiscock and Collins did not correct the spectra for the response of the optical system, which decreases with decreasing wavelengths.) Some detectors also exhibited a substantial photoresponse at energies below 5.3 eV ($\lambda >$ 234 nm) when the field was applied between the top and bottom contacts. This extrinsic photoresponse, and the variability of the bulk response were attributed to the presence of low-quality, small-grain-size, CVD diamond at the substrate surface.

Hiscock and Collins also demonstrated that there were huge variations in the photoresponse as a function of position, both for the strip detectors and the Centronic detector. The latter had a few regions where the sensitivity was very high, and the response from the rest of the detector was relatively low and inhomogeneously distributed. The ratio of the sensitivities in the most sensitive and the least sensitive areas was more than 100. In view of the findings of McKeag *et al.* (1997), outlined briefly above, this is not surprising. They found that the average gain for their device made with large-grain-size material is

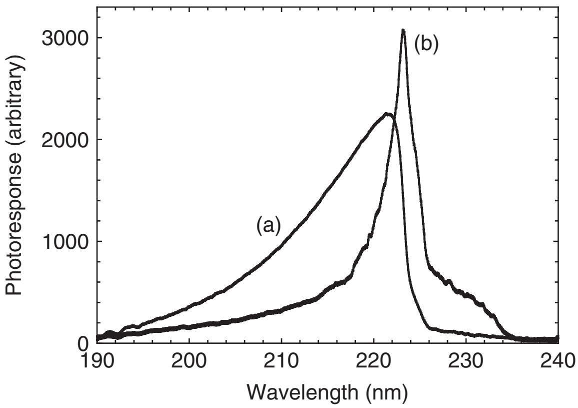

Figure 7.5 Photoconductivity spectra of a diamond strip detector measured (a) at the top surface using coplanar electrodes, and (b) through the bulk, using electrodes on the top and bottom surfaces, at the same electric field. The spectra have not been corrected for the response of the optical system, which decreases as the wavelength decreases. (Plotted using data from Hiscock and Collins 1999)

more than 100-times higher than that observed for the detector using small-grain-size diamond. On any one detector, however, there is a considerable variability in grain size. Furthermore, some grains are contacted by both electrodes, whereas in other regions of the detector the gap between the electrodes is crossed by one or more grain boundaries.

Hiscock and Collins compared the signal at 220 nm from the most sensitive region of the Centronic detector with that from a UV-enhanced silicon photodiode. The latter had a quantum efficiency of 0.65. The signal from the diamond detector at a bias of 9 V (corresponding to a field of about 0.27 V $(\mu\text{m})^{-1}$) was approximately 40-times larger than that from the Si detector, indicating that the most sensitive region of the Centronic detector had a quantum efficiency of ~25. However, despite this higher efficiency, the signal-to-noise ratio was higher for the Si detector by a factor of ~4. The response of the Si detector was also uniform (within ±10 %) over its entire surface area, and had much faster turn-on and turn-off times. Comparison of the Centronic and Si detectors produced useful information about what can be achieved with polycrystalline CVD diamond, but to the author's knowledge the Centronic detector is no longer commercially available.

The final important finding by Hiscock and Collins was that, although all the detectors they examined exhibited only a small sensitivity to visible light using the coplanar electrodes, after exposure to UV radiation the detectors exhibited a large *transient* response to white light. A typical transient, produced by illumination from an unfiltered tungsten lamp, is shown in Figure 7.6. These authors also noted that simultaneous illumination with visible and UV radiation produced a total photocurrent that was larger than the sum of the separate signals. These effects were attributed to unspecified charge-trapping phenomena.

Pace *et al.* (2000) investigated detectors, based on layers of polycrystalline diamond approximately 40 μm thick, deposited on a silicon substrate. Gold interdigitated contacts were deposited on the growth surface, and a continuous electrode was deposited on the back of the silicon substrate. The quantum efficiency of these detectors was measured in the range 125 to 1100 nm. It was found that the contacts were very non-ohmic, and the sensitivity and time response of a detector were very different when the polarity of the bias was reversed. In either case the signal levels took many tens of seconds to settle. It

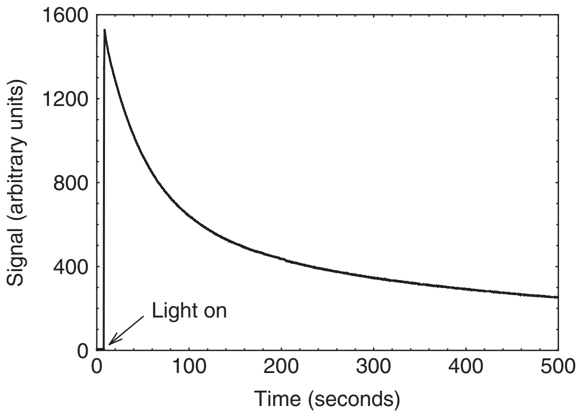

Figure 7.6 Transient photoconductivity signal produced by illuminating, with light from a tungsten lamp, an interdigitated device based on polycrystalline CVD diamond, following earlier exposure to above-band-gap ultraviolet radiation. 'Light on' indicates the time at which the tungsten lamp was switched on

was found that a negative bias applied to the back contact improved the time response somewhat. A surprisingly large quantum efficiency of ∼100 was found at 225 nm.

7.4 DETECTORS BASED ON SINGLE-CRYSTAL CVD DIAMOND

In an important contribution, using the photocurrent produced by illumination at 223 nm, Isberg *et al.* (2004) compared the charge collection distances $\mu\tau E$ in polycrystalline and single-crystal CVD diamond, extending the earlier work of Hammersberg *et al.* (2001), which investigated polycrystalline material only. UV radiation at 223 nm only penetrates ∼25 μm, and by using blocking contacts on the top and bottom of the diamond layers Hammersberg *et al* and Isberg *et al.* were able to measure the $\mu\tau$ products separately for electrons and holes. Their results are summarised in Table 7.1. For material with low nitrogen concentrations ($<10^{15}$ cm^{-3}) the $\mu\tau$ product is higher in polycrystalline diamond with larger average grain sizes. For specimens containing as little as 10^{15} to 10^{16} cm^{-3} nitrogen, the $\mu\tau$ product is lower (for $\mu_h\tau_h$) or considerably lower (for $\mu_e\tau_e$) than in the very pure material with comparable grain size. Although there is some unexplained variability, the $\mu\tau$ values for the high-purity single-crystal material are higher by 2 to 3 orders of magnitude. The current versus electric field for polycrystalline diamond approaches saturation at a field of 0.5 V (μm)$^{-1}$, similar to the results shown in Figure 7.3. For the single-crystal specimens, fields less than 0.01 V (μm)$^{-1}$ are sufficient to collect most of the carriers. The large improvement in charge collection distance clearly indicated that the most sensitive diamond UV detectors would be obtained using single-crystal CVD diamond.

Teraji *et al.* (2004) reported studies of several detectors based on homoepitaxial CVD diamond. These specimens were only ∼20 μm thick and were not removed from the type Ib diamond substrate (grown by high-pressure, high-temperature synthesis). Cathodoluminescence studies of the homoepitaxial layers showed no evidence of the nitrogen-vacancy emission at 575 nm, from which it was concluded that the nitrogen content in the specimens was negligible. Interdigitated contacts were applied to three specimens P1, P2 and

Table 7.1 $\mu\tau$ products for electrons (μ_e, τ_e) and holes (μ_h, τ_h) in polycrystalline CVD diamond with different grain sizes and in single crystal (SC) CVD diamond. The influence of small concentrations of nitrogen in polycrystalline material is shown for specimens 3 and 4. (Data from Hammersberg *et al.* 2001, and Isberg *et al.* 2004)

Sample number	Grain size on substrate side (µm)	Grain size on growth side (µm)	Average grain size (µm)	Thickness (µm)	Nitrogen content (cm^{-3})	$\mu_e\tau_e$ (10^{-6} cm^2 V^{-1})	$\mu_h\tau_h$ (10^{-6} cm^2 V^{-1})
1	15	34	25	95	$<10^{15}$	0.6	0.6
2	9	54	32	227	$<10^{15}$	3.1	1.8
3	29	49	39	202	$10^{15} - 10^{16}$	0.1	0.8
4	44	52	48	225	$10^{15} - 10^{16}$	0.6	1.7
5	107	113	110	98	$<10^{15}$	3.8	3.7
6	SC			690	$<10^{15}$	1700	650
7	SC			496	$<10^{15}$	3300	1400
8	SC			550	$<10^{15}$	1700	700

P3, with electrode spacings of 20, 50 and 100 µm, respectively. Detectors P1 and P3 showed the highest and lowest sensitivities, respectively, and P3 had the lowest dark current. All of the detectors had a response at 400 nm that was at least 4 orders of magnitude lower than that at 220 nm. The most important fact to emerge was that detector P2 had a noise equivalent power four orders of magnitude lower than that of a UV-enhanced Si photodiode This clearly demonstrated that very high detectivities can be obtained in the UV with single-crystal diamond devices. However, no details were presented about the response speed of the detectors.

De Sio *et al.* (2005) presented results for a detector produced from a free-standing single-crystal diamond layer 500 µm thick, using both coplanar and transverse electrode geometries. They measured the EQE at wavelengths from 150 to 250 nm with electric fields of 1 and 5 V (µm)$^{-1}$ in the coplanar configuration, and 1 and 2 V (µm)$^{-1}$ in the transverse configuration. The spectral shapes are similar in all cases. Data for the transverse configuration are shown in Figure 7.7, and we see that the EQE is ~300 at 225 nm; this compares with an EQE of ~ 2 for a field of 5 V (µm)$^{-1}$ in the coplanar configuration. All things being equal, greater EQE values would be expected in the coplanar device because of the closer contacts and the short absorption lengths at 225 nm. The lower efficiency observed may be a result of a high surface recombination rate, resulting from mechanical damage produced by the polishing of the diamond layer after growth (De Sio *et al.*).

Two disturbing points emerge from the work of De Sio *et al.* The UV response was determined by opening and closing a shutter in front of the device. On opening the shutter it took approximately 200 s for the photocurrent to reach a steady state, and when the shutter was closed it took a similar length of time to reach a steady-state value of the dark current. This behaviour is similar to that reported by McKeag and Jackman (1998) for their polycrystalline material, but with turn-on and turn-off times longer by 1 or 2 orders of magnitude in the detectors made by De Sio *et al.* The second observation from the work by De Sio *et al.* is that, at 250 nm, the photoresponse has dropped by only 3 orders of magnitude, compared with the 6 orders of magnitude obtained by McKeag *et al.*

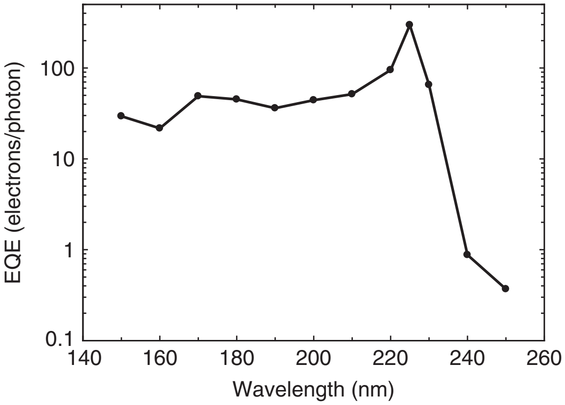

Figure 7.7 Photoconductive response from a single-crystal CVD diamond 500 μm thick in the transverse contact configuration with an electric field of 2 V $(\mu m)^{-1}$. (Redrawn from De Sio *et al.* 2005)

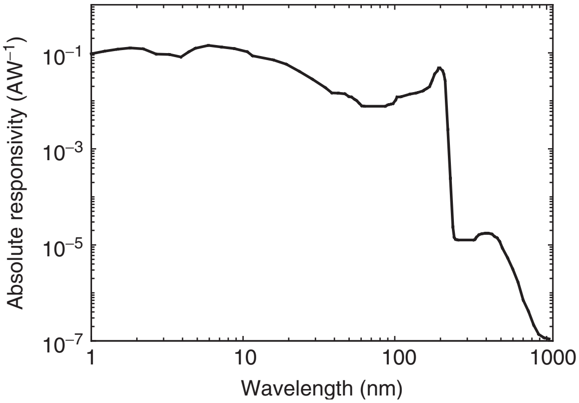

Figure 7.8 Photoconductive response of an MSM device, based on a single-crystal diamond layer 0.8 μm thick with interdigitated coplanar contacts. (Redrawn from BenMoussa *et al.* 2006)

(1997) for polycrystalline diamond. This may be because De Sio *et al.* introduced about 2 ppm of nitrogen into the gas phase when growing their specimen.

Finally, in this section, we consider two types of detector fabricated from homoepitaxial diamond reported by BenMoussa *et al.* (2006). An MSM photoconductor used a 0.8-μm thick CVD diamond layer grown on a type IIa natural diamond substrate. Interdigitated electrodes with a spacing of 15 μm were applied to the surface of this layer, and the ohmic properties were improved by laser annealing. By using a range of sources, the response of the detector was measured from the soft X-ray region ($\lambda = 1$ nm) through to 1000 nm in the near-infrared region. The absolute response in A W^{-1} is shown in Figure 7.8, and it is clear that the response varies by no more than a factor of 20 between 1 and 215 nm. In the visible region the response is four to five orders of magnitude lower than at 215 nm.

BenMoussa *et al.* also describe a p–i–n photodiode detector. Unlike all the photoconductive detectors described above, a p–i–n device generates a voltage when it is illuminated, and is operated at zero bias. A boron-doped layer was deposited on a type Ib diamond substrate produced by high-pressure, high temperature synthesis. This substrate with the p-type layer was then transferred to a second growth chamber where the intrinsic and phosphorus-doped (n-type) epitaxial layers were deposited. Contact was made to the top layer with a thin Al layer; the optical transmittance of this layer was estimated as 20 to 50 %. As with the MSM device, this detector had a good response at 220 nm, and a useful, but rather lower response between 1 and 20 nm. For reasons that are not understood, the signal from the detector reported by BenMoussa *et al.* became negative between 17 and 165 nm.

The signal stability of each device was determined by measuring the response as a shutter in front of the detector was opened and closed. The p–i–n device responded quickly to the signal change and returned to its initial dark-signal values after a relatively short (125 s) irradiation at 200 nm. The MSM device responded rapidly to the signal change but did not return to its initial dark signal values after the irradiation. BenMoussa *et al.* noted that the initial dark current seemed to be dependent on the duration and the flux of previous exposures.

The lateral homogeneity of response of both types of detector was determined by carrying out horizontal (x) and vertical (y) line scans at different wavelengths. At 200 nm the response as a function of position changed in a smooth fashion and did not vary by more than a factor of 2 for $-2 < x < 2$ or $-2 < y < 2$ (mm). In principle this is far more satisfactory for imaging applications than the extreme variability noted with detectors based on polycrystalline CVD diamond (Hiscock and Collins 1999).

7.5 SUMMARY

The history of development and characterisation of UV detectors based on CVD diamond has been followed using some representative papers from the wide range available in the literature. This work has shown that detectors based on polycrystalline diamond can be used to detect ultraviolet radiation at wavelengths shorter than 225 nm, and that a relative response of less than 10^{-6} in the visible region can be achieved. However, the response of such detectors as a function of position is very nonuniform, and is completely unsuitable for imaging applications. Furthermore, the rough as-grown surface on thick polycrystalline layers makes high-resolution lithography impossible (McKeag and Jackman 1998). Unfortunately, polishing the surface frequently introduces mechanical damage, which greatly increases the surface recombination velocity and so reduces the efficiency of the detector (De Sio *et al.* 2005).

It should be noted here that different authors use different units when plotting the response of their detectors. The quantum efficiency is shown *per photon* (e.g. De Sio *et al.* 2005), but the response may also be plotted as AW^{-1} or mAW^{-1} (e.g. BenMoussa *et al.* 2006). Table 7.2 compares the photosensitivity and EQE for the detectors described in this chapter. The spread of values is an indication of the immaturity of this technological field.

The absence of grain boundaries in single-crystal material results in a $\mu\tau$ product which is two to three orders of magnitude higher than in polycrystalline CVD diamond, allowing detectors to be fabricated with a high gain in the transverse contact configuration. Furthermore, detectors can be fabricated in which the response does not vary by more than a factor of 2 over an area 4×4 mm^2. In principle, UV imaging detectors could be made using such material.

Table 7.2 Comparisons of the photo sensitivity and external quantum efficiency (EQE) for some of the detectors described in this chapter

Authors	Diamond/ electrode types	Wavelength (nm)	Photo sensitivity (mA W^{-1})	EQE
McKeag *et al.* (1997)	Poly/coplanar	220	1064	6*
Pace *et al.* (2000)	Poly/coplanar	225	18000	100*
Pace *et al.* (2000)	Poly/coplanar	150	24	0.2*
Hochedez *et al.* (2001)	Poly/coplanar	4.4	0.2	0.06*
Hochedez *et al.* (2001)	Poly/coplanar	2	0.45	0.28*
Teraji *et al.* (2004)	SC/coplanar	220	177*	1
De Sio *et al.* (2005)	SC/coplanar	225	400	2.2*
De Sio *et al.* (2005)	SC/coplanar	150	31	0.26*
De Sio *et al.* (2005)	SC/transverse	225	54000	300*
De Sio *et al.* (2005)	SC/transverse	150	3100	29*
BenMoussa *et al.* (2006)	SC/coplanar	200	27*	0.17
BenMoussa *et al.* (2006)	SC/coplanar	150	16*	0.13
BenMoussa *et al.* (2006)	SC/coplanar	50	12*	0.28
BenMoussa *et al.* (2006)	SC/coplanar	10	120*	15
BenMoussa *et al.* (2006)	SC/coplanar	1	95*	118
BenMoussa *et al.* (2006)	p-i-n photodiode	200	27*	0.17

*These values of photosensitivity or EQE have been read from graphs, or are stated in the text, in the publications cited. They have then been used to calculate the values in the alternative units.
SC: Single crystal

However, there are problems with charge trapping and detrapping, both in polycrystalline and single-crystal material, which are not properly understood. These can lead to extremely long time constants and persistent photoconductivity. Some of these phenomena may be associated with non-ohmic contacts (Pace *et al.* 2000). In addition, detectors can become sensitised to visible light following exposure to above-band-gap irradiation. These are all issues that need to be addressed if diamond is to be used successfully for ultraviolet detector applications.

7.6 FUTURE PROSPECTS FOR DIAMOND UV DETECTORS

Yoder (1994) states that ‘The end product based on diamond must fulfill a function much better or less expensively than existing technology’. He also reminds researchers that developments in competing materials and systems are not dormant. Bergonzo *et al.* (2001) make a similar point: ‘One of the difficulties in using diamond for radiation detection ... is that the direct competitor to diamond – namely silicon – is generally cheaper, more efficient, more stable, more readily available and in possession of perfect homogeneity ... This consequently reduces diamond interests to areas where there exist several constraints which could only be overcome with the extreme superior properties of diamond’.

Two important properties of diamond for the applications being considered are that it is a wide band-gap material, and is more radiation hard than silicon. However, it is not the only material in this category. The Group III nitrides have become extremely prominent

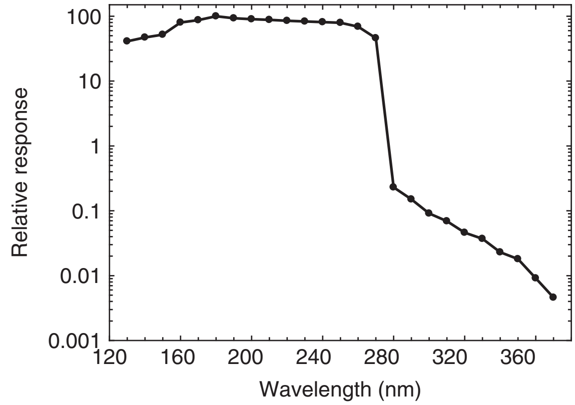

Figure 7.9 Relative photoconductive response for an AlGaN detector. (Redrawn from data on the Boston Electronics Corporation website,[1] and based on work by Chow *et al.* 2001)

in recent years. The blue-light emitting diode (LED) based on GaN has progressed from a laboratory prototype to a ubiquitous Christmas tree decoration in the space of 15 years. GaN lasers are incorporated in the 'Blu-Ray' high-density DVD players. These huge markets have enabled substantial investments to be made in the research and development of devices based on the Group III nitrides, including UV LEDs and UV detectors based on $Al_xGa_{(1-x)}N$. The response curve of an AlGaN detector, based on the work of Chow *et al.* (2001), is shown in Figure 7.9, and exhibits a useful range from 130 to 270 nm with the sensitivity dropping by at least 4 orders of magnitude for wavelengths longer than 360 nm. Ongoing research in this area has led to detectors responding to wavelengths in the extreme UV (see Section 6.1). Potential applications for diamond UV detectors, outlined in Section 7.6.1, need to be reconsidered in the light of these and other developments, taking into account progress made in the development of diamond devices reported in this chapter.

7.6.1 UV and EUV lithography

Developments in lithography for silicon devices have not progressed as anticipated by Whitfield *et al.* (2001). The size of features has been reduced, not by using a shorter wavelength laser, but by continuing to use an ArF excimer laser (193 nm) with 'immersion technology'.[2] This replaces the air between the lens and the wafer with a liquid to improve depth of focus and enable higher numerical apertures. ASML, the world's leading provider of lithography systems for the semiconductor industry, states that this technology will eventually enable feature sizes to be reduced to 45 nm. To progress to even smaller features the industry has developed prototype lithography systems using a plasma light source with $\lambda = 13.5$ nm. One ASML prototype is in place at the Inter-university Microelectronics Centre (IMEC) in Leuven, Belgium. Research on this equipment is being carried out by Joachim John. He has demonstrated robust 13.5 nm UV detection with an AlGaN-based device for the first time, and claims that it is a radiation-hard detector, which is superior in comparison to a reference silicon diode (Extance 2007). Detectors based on homoepitaxial CVD diamond also exhibit a good response at 13.5 nm (BenMoussa *et al.* 2006), but the present author is not aware of any comparisons that have been made between diamond-based and AlGaN-based detectors for this application.

---

[1] Some information in this paragraph has been obtained from the ASML website: www.asml.com

[2] http://www.boselec.com/products/documents/UVbrochurebackcoverspectralresponse.pdf

It is important to recognise that AlGaN devices are not without their problems. Defects that cause carrier trapping, and very slow transients with persistent photoconductivity produced by sub-band-gap illumination, have been reported by Dang *et al.* (1998), and continue to be topics of ongoing research (Seghier and Gislason 2008). It remains to be seen which, if either, of diamond or AlGaN, is used to replace Si as the detector material of choice in these advanced lithography systems.

It is interesting to note that, since Whitfield *et al.* (2001) drew attention to the shortcomings of silicon detectors for use in lithography equipment, substantial improvements have been made to overcome these problems. Hamamatsu (2006) is marketing a silicon detector (type S10043), which shows a negligible degradation after 10^7 shots from an ArF (193 nm) laser. (This is based on a laser with 0.1 mJ cm^{-2} per pulse, with a pulse width of 15 ns and an operating frequency of 100 Hz.) These diodes have a photoresponse down to 150 nm, and so would be equally suitable for use with lasers operating at 157 nm, had the semiconductor industry gone down that road. This development amply reinforces the comment by Yoder (1994) that competing materials and systems continue to progress.

7.6.2 ESA Solar Orbiter

One of the objectives of the Solar Orbiter mission is to obtain UV images of the sun at unprecedented resolution. This requires an imaging detector that responds well at the wavelengths of interest and is blind to radiation in the visible and near ultraviolet regions. As Hochedez *et al.* (2001) point out '... it is unlikely to attain straight away a solar-blind 2000 × 2000 UV imager with sub-micrometer pixel and 100 % QE in the EUV range'.

One scheme proposed for a diamond imager is to manufacture an array of Schottky diodes with $x-y$ addressing. Columns of p^+-doped diamond would be deposited on a type Ib substrate. These columns would be over-deposited with a layer of intrinsic diamond and rows of metal electrodes deposited on top of the intrinsic diamond layer (Hochedez *et al.* 2002). Although this might work with a small number of pixels, it is inconceivable that a 4-megapixel array could be fabricated in this way on a $6 \times 6\ \text{mm}^2$ substrate.

A further consideration that applies to any UV detector is that, in the UVC band (20–121 nm), for example, the photon flux from the sun is about 6 orders of magnitude lower than the integrated flux at wavelengths longer than 225 nm. Although the detectors may be nominally blind in the latter region, efficient filters will nevertheless be required to prevent the unwanted radiation being detected and/or causing transient changes and persistent photoconductivity (as observed in work on diamond by Hiscock and Collins 1999, and in work on AlGaN by Dang *et al.* 1998).

Progress on imaging detectors is at a more advanced stage for AlGaN. Long *et al.* (2002) describe 128 × 128 and 320 × 256 pixel arrays for the spectral region 300 to 365 nm, and 320 × 256 pixel arrays for the spectral region 240 to 285 nm. The smaller arrays used mesa diodes on a 38 μm pitch and the larger arrays used mesa diodes on a 30 μm pitch. The diode arrays were hybridised to silicon read-out circuits. The systems exhibited low noise and high sensitivity; however not all of the devices built for the

240–285 nm band worked, and in all cases the quality of the image was not as good as that recorded in the 300 to 365 nm band. These results are encouraging, but there is still a long way to go to meet the objectives required by the Solar Orbiter.

If a wide band-gap semiconductor ultimately proves suitable for imaging applications in the Solar Orbiter, the current state of the art suggests that this will be AlGaN, rather than diamond.

7.7 CONCLUDING REMARKS

There is no doubt that UV detectors, with a very low response to visible light, can be made from CVD diamond. Detectors made from polycrystalline material exhibit a nonuniform response over their active area, and are suitable neither for quantitative photometric purposes nor for imaging applications. Detectors fabricated from single-crystal CVD diamond can exhibit a spatial response that is reasonably uniform, but the realistic maximum area of such devices limits the resolution that can be achieved with an imaging detector. Diamond detectors, whether based on polycrystalline or single-crystal diamond, frequently contain trapping centres and/or have imperfect electrodes. As a result, many detectors described in the literature have a response that varies slowly with time, a dark current that takes a long time to settle (persistent photoconductivity), and exhibit a transient response to visible light after illumination with ultraviolet radiation.

Silicon devices continue to improve, and there is intense research and development being carried out on the Group III nitrides. Trapping centres are also an issue with the latter materials, but the development of imaging detectors is at a more advanced stage than that of imaging detectors based on diamond.

Despite its early promise, it therefore seems unlikely that visible-blind UV detectors based on CVD diamond will be employed, other than possibly in a very few esoteric applications.

REFERENCES

Allers L. and A.T. Collins (1995) Photoconductive spectroscopy of diamond grown by chemical vapour deposition, *J. Appl. Phys.*, **77**, 3879–3884.

Allers L. and A. Mainwood (1998) Surface vacancies in CVD diamond, *Diamond Relat. Mater.*, **7**, 261–265.

BenMoussa A. (2006) and 15 other authors, Diamond detectors for LYRA, the solar VUV radiometer on board PROBA2, *Diamond Relat. Mater.*, **15**, 802–806.

Bergonzo P., A. Brambilla, D. Tromson, C. Mer, B. Guizard, F. Foulon and A. Amosov (2001) CVD diamond for radiation detection devices, *Diamond Relat. Mater.*, **10**, 631–638.

Chow P.P., J.J. Klaassen, R.E. Vest, J.M. Van Hove, A.M. Wowchak and C. Polley (2001) AlGaN Schottky diodes for short wavelength UV applications, in *Photodetectors: Materials and Devices VI*, G.G. Brown and M. Razeghi (Eds), Proceedings of SPIE, **4288**, 230–237.

Clark C.D., P.J. Dean and P.V. Harris (1964) Intrinsic edge absorption in diamond, *Proc. Roy. Soc. A*, **277**, 312–329.

Collins A.T., E.C. Lightowlers and P.J. Dean (1969) Role of phonons in the oscillatory photoconductivity spectrum of semiconducting diamond, *Phys. Rev.*, **183**, 725–730.

Collins A.T., M. Kamo and Y. Sato (1990) A spectroscopic study of optical centers in diamond grown by microwave-assisted chemical vapour deposition, *J. Mater. Res.*, **5**, 2507–2514.

Dang X.Z., C.D. Wang, E.T. Yu, K.S. Boutros and J.M. Redwing (1998) Persistent photoconductivity and defect levels in n-type AlGaN/GaN heterostructures, *Appl. Phys. Lett.*, **72**, 2745–2747.

Denham P., E.C. Lightowlers and P.J. Dean (1967) Ultraviolet intrinsic and extrinsic photoconductivity of natural diamond, *Phys. Rev.*, **161**, 762–768.

De Sio A., J. Achard, A. Tallaire, R.S. Sussmann, A.T. Collins, F. Silva and E. Pace (2005) Electro-optical response of a single-crystal diamond ultraviolet photoconductor in transverse configuration, *Appl. Phys. Lett.*, **86**, 213504.

Extance A. (2007) AlGaN detectors suit EUV lithography, http://optics.org/cws/article/research/31771.

Farrer R.G. and L.A. Vermeulen (1972) Photoconductivity in irradiated diamond, *J. Phys. C: Solid State Phys.*, **5**, 2762–2768.

Hamamatsu, *Si photodiodes selection guide*, May 2006.

Hammersberg J., J. Isberg, E. Johansson, T. Lundström, O. Hjortstan and H. Bernhoff (2001) Injection dependent long carrier lifetimes in high quality CVD diamond, *Diamond Relat. Mater.*, **10**, 574–579.

Heijne L. (1966) Physical principles of photoconductivity II, *Philips Tech. Review*, **27**, 47–61.

Hiscock J. and A.T. Collins (1999) Comparison of diamond and silicon ultraviolet photodetectors, *Diamond Relat. Mater.*, **8**, 1753–1758.

Hochedez J.-F. (2001) and 22 other authors, Diamond UV detectors for future solar missions, *Diamond Relat. Mater.*, **10**, 673–680.

Hochedez J.-F. (2002) and 24 other authors, Recent progress of the BOLD investigation towards UV detectors for the ESA Solar Orbiter, *Diamond Relat. Mater.*, **11**, 427–432.

Hokazono A., A. Ishikura, T. Nakamura, S. Yamashita and H. Kawarada (1997) Enhancement/depletion MESFETs of diamond and their logic circuits, *Diamond Relat. Mater.*, **6**, 339–343.

Isberg J., H. Bernhoff, D.J. Twitchen and A.J. Whitehead (2004) Charge collection distance measurements in single and polycrystalline diamond, *Diamond Relat. Mater.*, **13**, 872–875.

Lansley S.P., O. Gaudin, H. Ye, N. Rizvi, M.D. Whitfield, R.D. McKeag and R.B. Jackman (2002) Imaging deep UV light with diamond-based systems, *Diamond Relat. Mater.*, **11**, 433–436.

Long J.P., S. Varadaraajan, J. Matthews and J.F. Schetzina (2002) UV detectors and focal plane imagers based on AlGaN p-i-n photodiodes, *Opto-electronics Review*, **10**, 251–260.

Mainwood A. (2000) Recent developments of diamond detectors for particles and UV radiation, *Semiconductor Sci. Technol.*, **15**, R55–R63.

McKeag R.D. and R.B. Jackman (1998) Diamond UV detectors: sensitivity and speed for visible blind applications, *Diamond Relat. Mater.*, **7**, 513–518.

McKeag R.D., R.D. Marshall, B. Baral, S.S.M. Chan and R.B. Jackman (1997) Photoconductive properties of thin film diamond, *Diamond Relat. Mater.*, **6**, 374–380.

Martineau P. (2007) Personal communication.

Nebel C.E. (2003) Electronic properties of CVD diamond, *Semiconductor Sci. Technol.*, **18**, S12–S19.

Pace E., R. Di Benedetto and S. Scuderi (2000) Fast stable visible blind and high sensitivity CVD diamond for laboratory and space applications, *Diamond Relat. Mater.*, **9**, 987–993.

Robertson R., J.J. Fox and A.E. Martin (1934) Further work on two types of diamond, *Proc. Roy. Soc. A*, **157**, 579–593.

Seghier D. and H.P. Gislason(2008) Opto-electric characterization of electrically active point defects in $Al_xGa_{(1-x)}N$, *J. Phys. D: Applied Phys.*, **41,** 095109.

Teraji T., S. Yoshzaki, H. Wada, M. Hamada and T. Ito (2004) Highly sensitive UV photodetectors fabricated using high-quality single-crystalline CVD diamond films, *Diamond Relat. Mater.*, **13**, 858–862.

Vermeulen L.A. (1976) Photo-Hall effect in irradiated type IIb diamonds, *Diamond Research 1976* (Industrial Diamond Information Bureau, Ascot), pp. 22–25.

Werner M. (2003) Diamond metallization for device applications, *Semiconductor Sci. Technol.*, **18**, S41–S46.

Whitfield M.D., S.P. Lansley, O. Gaudin, R.D. McKeag, N. Rizvi and R.B. Jackman (2001) Diamond photodetectors for the next generation 157-nm deep-UV photolithography tools, *Diamond Relat. Mater.*, **10**, 693–697.

Yoder M.N. (1994) The vision of diamond as an engineered material, in *Synthetic Diamond: Emerging CVD Science and Technology*, K.E. Spear and J.P. Dismukes (Eds), The Electrochemical Society, Inc., Pennington, New Jersey.

8 Diamond Radiation Sensors for Radiotherapy

MARA BRUZZI

Dipartimento di Energetica 'S. Stecco', Firenze, Italy

8.1 Introduction 185
8.2 Radiation dosimeters 187
8.3 Diamond sensors in radiotherapy 190
  8.3.1 Diamond sensors in on-line configuration 191
  8.3.2 Diamond sensors in off-line configuration 199
8.4 Conclusions 203
  Acknowledgements 203
  References 204

8.1 INTRODUCTION

Cancer is a major social problem, currently the cause of 12 % of all deaths worldwide [1]. Combating cancer is thus a major societal and economic issue, to be faced through a strong mobilization of both the scientific community and industrial manufacturers. In the treatment of cancer, radiotherapy plays an essential role: more than half of all cancer patients are nowadays treated by radiotherapy thanks to the technical advances in irradiation equipment achieved over the last sixty years [2]. For some cancer treatments (see, for example, the case of prostate cancer) radiotherapy treatment achieves the same long-term survival and quality of life as conventional surgery [3].

Historically, radiotherapy is divided in three main branches: external beam radiotherapy, brachytherapy and unsealed source radiotherapy. This latter relates to the use of radioactive substances that are administered to the body by injection or ingestion. In brachytherapy, the radioactive source is placed inside or next to the area requiring treatment, and it is usually extracted afterwards. In external beam radiotherapy (EBRT), the patient body is irradiated with an irradiation beam produced externally. This technique, from now on referred more simply as RT, became generally accepted therapy in the 1950s for clinically localized and locally advanced tumours with the advent of cobalt-60 sources [4, 5], and with linear accelerators capable of producing highly penetrating megavoltage

CVD Diamond for Electronic Devices and Sensors Edited by Ricardo S. Sussmann
© 2009 John Wiley & Sons, Ltd. ISBN: 978-0-470-06532-7

(MV) photon beams [6, 7]. Other very promising RT modalities are hadrontherapy, first proposed by founder of Fermilab, Robert Wilson [8] and radiosurgery [9, 10], also known as stereotactic radiotherapy: a medical procedure that allows noninvasive treatment by means of directed beams of ionizing radiation. The word 'stereotactic' describes a minimally invasive form of surgical intervention that makes use of a three-dimensional coordinate system to locate small targets inside the body.

The main aim in radiotherapy is to deliver a maximum effective dose of radiation to a designated tumour site while sparing the surrounding healthy tissue as much as possible. Figure 8.1 compares the relative dose versus penetration depth in tissue for a 6-MV photon beam, a 6-MeV electron beam and a 170-MeV proton beam [11, 12]. Compared to X-photons, the electron beam depth–dose curve exhibits a higher surface dose, which then builds up to a maximum at a certain depth and drops off rapidly for greater depths. These features offer a distinct clinical advantage over X-ray RT in the treatment of superficial tumours. Protons, on the other hand, deposit most of their energy at a specific depth that depends on their energy (Bragg peak). A beam of protons or light ions thus allows a highly conformal treatment of deep-seated tumours with millimetre accuracy, giving minimal doses to surrounding tissues and sparing the deeper located organs that might be at risk as well as the healthy tissue [13, 14].

X-Photon RT is usually carried out with more than one radiation beam in order to achieve a uniform dose distribution inside the target volume and a dose as low as possible in healthy tissues surrounding the target. Intensity-modulated radiotherapy (IMRT), first suggested by Brahme *et al.* around 1982 [15], represents a major development in this respect, being able to deliver a highly conformed dose to an irregularly shaped target volume. By means of a multileaf collimator (MLC) placed in the treatment head of the linac (see Figures 8.2a and b), the dose delivered on each point of the tumour can be precisely modulated in a 3-D way and a steeper dose gradient between the tumour and the healthy organs at risk can be obtained [16–19]. In IMRT, computerized treatment planning

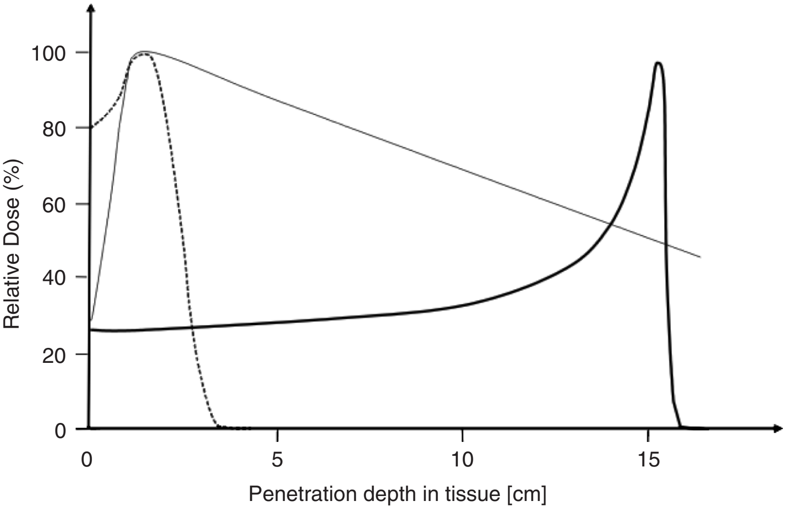

Figure 8.1 Relative dose versus penetration depth in tissue. Dashed curve: electron beams with energy 6 MeV; thin solid curve: photon beam of 6 MV; thick solid curve: 170-MeVproton beam [11]

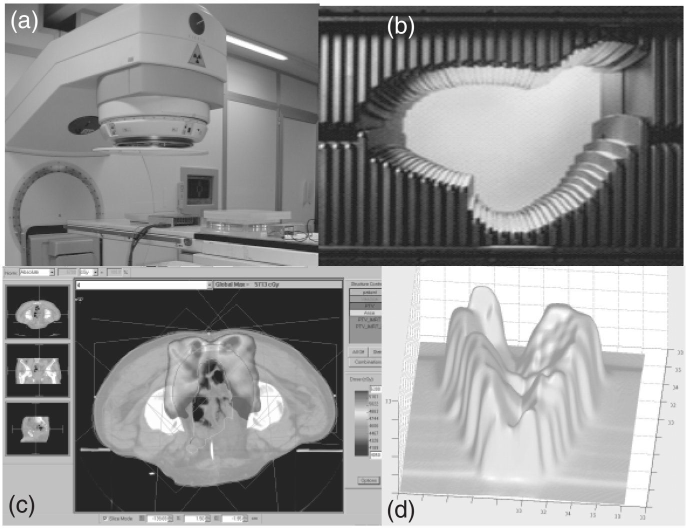

Figure 8.2 (a) Linear accelerator ELEKTA PRECISE for IMRT equipped for R&D studies on dosimeters; (b) VARIAN multileaf collimator for IMRT; (c) dose distribution for one IRMT application on prostate cancer; (d) body axial section in a Treatment Planning System (TPS) (Images a, c and d supplied courtesy of Dipartimento di Fisiopatologia, Università degli Studi di Firenze, Italy. Image b courtesy of Varian Medical Systems of Palo Alto, California. Copyright (2008), Varian Medical Systems. All right reserved. See plate 2)

systems (TPSs) are used to generate 3-D beam shapes and dose distributions where patient anatomy and tumour targets are represented as 3-D models [11]. Figure 8.2(c) shows as an example a body axial section in a Treatment Planning System (TPS) and Figure 8.2(d) shows a typical dose distribution for one IRMT application on prostate cancer.

The effective implementation of intensity modulated radiotherapy, stereotactic radiosurgery and hadron therapy represents a major challenge for the next generation of dosimeters that will be required for real-time dose monitoring, dose pretreatment verifications and large bidimensional fields. High-dose gradients and the elevated variability in space and time of the dose rate and of the beam spectral composition require detectors of small dimensions and high sensitivity, with a fast and stable response, independent of energy and dose rate. Moreover, to cover large bidimensional fields in IMRT and proton-therapy pretreatment verifications, segmented devices of high spatial resolution are needed [20].

Many of the outstanding chemical and physical properties of diamond makes this material potentially attractive for applications in radiotherapy dosimetry. This chapter will discuss the most important research work recently performed in this field, focusing in particular on Chemical Vapour Deposited (CVD) diamond.

8.2 RADIATION DOSIMETERS

A radiation dosimeter is a device capable of providing a measure of the average absorbed dose deposited in its sensitive volume by ionizing radiation. Radiation dosimeters can be used in *off-line* and *on-line* configurations. The latter refers to direct-reading dosimeters, such as ionization chambers (ICs) and semiconductor-based devices. An ionization chamber is basically a gas filled cavity surrounded by a conductive outer wall, equipped with a central collecting electrode. Irradiation causes the formation of a number of primary ions, proportional to the energy deposited by the charged-particle tracks in the detector volume, which are collected at the electrodes by the action of an externally applied potential difference. In a semiconductor device, radiation promotes electrons from the valence to the conduction band, thus generating free electron–hole (e–h) pairs in the bulk of the dosimeter, which are collected at the electrodes under the action of the electric field either due to the intrinsic potential (silicon diodes in photovoltaic mode), or to an externally applied potential difference (diamond dosimeters). Off-line configuration is used for passive dosimeters, such as thermoluminescence dosimeters (TLDs) and radiographic X-ray films, which are read after beam exposure. Thermoluminescence (TL) is the thermally stimulated emission of light following the previous absorption of energy from radiation [21]. A thermoluminescent material during exposure to ionizing radiation at a sufficiently low temperature stores charge (electrons or holes) in relatively deep energy levels within the forbidden gap. When the carriers are released by heating they can recombine, either directly or in most cases through a recombination centre, with the emission of light (luminescence).

Radiation dosimeters must exhibit the following characteristics:

- *Accuracy and precision:* The precision of a dosimeter is set by the degree of reproducibility of the measurements under similar conditions and can be estimated from the data obtained in repeated measurements. The accuracy of the measurement is the proximity of their expectation value to the 'true value' of the absorbed dose. A high signal-to-noise ratio is desirable to guarantee sufficient sensitivity to the measurement and to increased precision and accuracy.
- *Linearity with dose:* The dosimeter measurement should be proportional to the absorbed dose (usually referred to water). In reality, each radiation dosimeter presents a finite range of absorbed doses where linearity occurs that depends on its physical characteristics.
- *Independent of the dose rate:* Ideally, the response of a dosimeter should be independent of the dose rate. In reality, the dose rate may influence the dosimeter readings and appropriate corrections are necessary, for instance, recombination corrections must be applied for ionization chambers in pulsed beams.
- *Energy Response and tissue equivalence:* The response of a dosimeter system generally depends on the radiation beam quality (energy) [11]. For this reason it is important for the dosimeter to be made of a material characterized by absorption and scattering properties for a given radiation that sufficiently match those of biological tissue; such a material is considered to be a *tissue equivalent substance*. It is well known that, when a photon beam interacts with matter, the photoelectric effect predominates at low photon energies, the Compton one at intermediate energies and pair production at high photon energies, with relative predominance depending both on $h\nu$, photon energy, and Z, atomic number, as shown in Figure 8.3 [11].

Often the material is made of a mixture of different elements, as in case of biological tissue. An effective atomic number is then defined the better to describe the interaction of the photon beam with matter [22]. In the case of the photoelectric effect dominant over

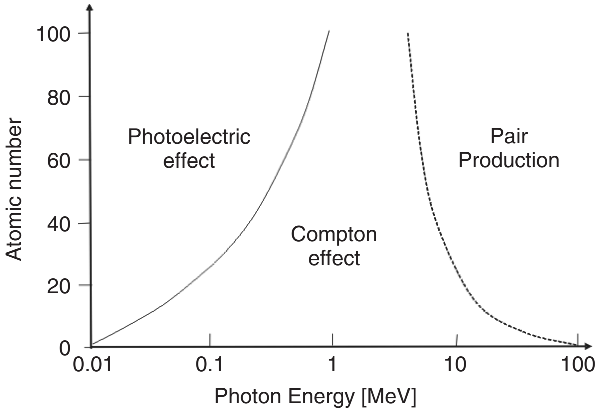

Figure 8.3 Regions of relative predominance of the three main forms of photon interaction with matter. (—) line of equal atomic coefficients for photoelectric and Compton effects (---) line of equal atomic Compton and pair production coefficients [11]

Compton and if pair production events cannot occur, Z_{eff} of a mixture is defined by:

$$Z_{\mathrm{eff}} = \sqrt[3.5]{\sum_i a_i Z_i^{3.5}} \tag{8.1}$$

Where a_i is the mass fraction of ith constituent element and Z_i its atomic number. Table 8.1 shows the effective atomic numbers for human tissue and bones together with that of a few materials used in radiotherapy, calculated using this relationship.

For photon beams, tissue equivalency implies a match in mass–energy absorption coefficient, mass stopping power and mass scattering power. This is approximately achieved if the material has the same electron density and the same atomic number as water, the most universal soft tissue substitute material.

Table 8.1 Effective atomic numbers of fat, tissue, bone and of a few materials used for dosimetry in radiotherapy

Material	Z_{eff}
Air	7.78
Water	7.51
Muscle	7.64
Fat	6.46
Bone	12.31
C	6
Si	14
LiF	8.14

- *Spatial Resolution and Physical Size:* Since the dose is a point quantity, the dosimeter should allow the determination of the dose from a very small volume. Further, a small sensing volume size means that high spatial resolution dosimeters can be realized following the Bragg–Gray cavity theory [23]. This theory relates the absorbed dose in the dosimeter's sensitive medium (cavity) to the absorbed dose in the surrounding medium containing the cavity. The cavity must be small as compared with the range of charged particles incident on it, so that its presence does not perturb the fluence of charged particles in the medium.
- *Dynamic response:* To be reliable, direct reading dosimeters must be characterized by a fast and reproducible dynamic response, with fast rise/decay times when beam is switched on/off.
- *Long term stability of response:* Ideally, the on-line dosimeter response must be stable during irradiation, and the response of a passive dosimeter must be, as far as possible, independent of time and storage conditions after the irradiation. Moreover, the response of the dosimeter should not depend on the dose accumulated during previous exposures. Often, as in silicon dosimeters, the accumulated dose is responsible for the formation of radiation-induced defects, which decrease the lifetime of minority carriers reducing the sensitivity of the device [24]. To overcome this problem, such a device must be frequently recalibrated [25].

8.3 DIAMOND SENSORS IN RADIOTHERAPY

Pioneering works on clinical radiotherapy applications of diamond dosimeters can be traced back to the early eighties [26–31]. Because diamond has an atomic number $Z = 6$, comparable to the effective atomic number of soft tissue, it is considered to be an almost tissue-equivalent material. This is an important advantage over, for instance, silicon, as the diamond response is almost energy independent for a wide energy range of photons. As a consequence, no energy dependent factor has to be applied to the diamond response when used with different energies, while Si dosimeters suffer from this drawback. Moreover, diamond is not fragile and can be heat sterilized. Diamond can be used both as on-line and off-line dosimeter. In one possible configuration for on-line measurements, a transverse geometry, two electrodes are deposited on opposite sides of the diamond plate, the incident radiation generates a current in the biased structure and the reading of this current during exposure to the beam can be used for real-time monitoring of the absorbed dose. Diamond dosimeters are solid state devices and as such, in comparison with ICs, have the advantage of a much higher sensitivity (18 000 times) for the same volume, and an ionization energy that is approximately 10-times smaller than that required in a gas. This in principle opens the way to the use of diamond in stereotactic and IMRT applications. Table 8.2 compares electronic properties of diamond and silicon that are relevant for dosimetric applications [32]. In silicon, an energy of 3.6 eV is required for the production of an e–h pair, leading to a generation constant of $4.2 \times 10^{13} \frac{pairs}{cGycm^3}$ [33]. In diamond the energy to generate an e–h pair is about 13 eV, and the generation constant is therefore about a factor of 3.6 lower than in silicon, resulting in a lower sensitivity per unit volume.

The large band gap makes diamond an excellent electrical insulator, as a result of which a large electric field can be applied without producing significant leakage current. Thus, there is no need for a reverse biased pn-junction as there is for silicon. Ohmic contacts

Table 8.2 Electronic properties of diamond and silicon relevant for dosimetric applications [32]

Property	Diamond	Si
Bandgap [eV]	5.5	1.12
Breakdown Field [V/cm]	10^7	310^5
Electron mobility [cm^2/Vs]	1800	1450
Hole mobility [cm^2/Vs]	1200	450
Saturation velocity [cm/s]	2.2×10^7	0.8×10^7
Effective atomic number z_{eff}	6	14
Dielectric constant ε_r	5.7	11.9
e-h creation energy [eV]	13	3.6
minority carrier lifetime [s]	10^{-9}	2.5×10^{-3}
Wigner Energy [eV]	43	13–20

on diamond are manufactured through the vacuum deposition of metals such as Ti/Au, Cr/Au or Ti/W followed in some cases by thermal annealing to ensure the formation of a carbide interface [34]. The high cohesive energy of the diamond lattice, which correlates with a much higher Wigner energy value (the energy needed to remove an atom from its lattice site to produce a vacancy) in diamond than in silicon, is responsible for the higher radiation hardness of diamond compared with silicon. Further, diamond has a smaller dielectric constant than silicon, yielding a smaller capacitance in transverse geometry and, therefore, better noise performance of the associated front-end electronics.

8.3.1 Diamond sensors in on-line configuration

On-line dosimeters fabricated with natural diamond stones have already been commercialized by PTW [35]. Suitable natural diamond crystals for dosimetry are of the colourless Type-IIa [28, 36] with a nitrogen concentration less than 10^{19} cm^{-3}: The production of devices made from natural diamond with interesting dosimetry characteristics requires a careful selection among available IIa diamond stones. Hence, these detectors are highly priced and long delivery times are usual. Moreover, a poor reproducibility between these devices has been observed [37], which is due to differences in the material itself. To overcome this practical constraint, the scientific research soon focused on the possible application of synthetic diamond to radiotherapy. Both polycrystalline [38, 39] and single crystal [39] chemical vapour deposited (CVD) diamond devices have been proposed, since they can potentially be produced with high purity, at a reduced cost compared with natural stones, and with reproducible properties.

When ionizing radiation is absorbed, a change in electrical conductivity is induced by the production of electrons and holes that have sufficient energy to freely move through the diamond lattice [40]. If D_r is the absorbed radiation per unit mass and unit time then the generated density of free electron–hole pairs per unit volume and time can be written as $f = QD_r$, with Q proportionality coefficient. The free carriers (electrons for instance) will recombine with an effective relaxation time τ_e and at steady state the concentration of free electrons will be given by:

$$n = QD_r\tau_e, \tag{8.2}$$

The electrical conductivity (due to electrons) increases as:

$$\sigma = n\ e\ \mu, \tag{8.3}$$

It is also well known [41] that the effective relaxation time is inversely proportional to the concentration of recombination centres N as:

$$\tau_e = \frac{1}{vsN} \tag{8.4}$$

With s the capture cross-section and v the thermal velocity. In a pure (intrinsic) semiconductor the electrons can only recombine with holes and therefore $N = p$ (where p is the density of holes) and because in this case $p = n$, then:

$$\tau_e = \frac{1}{vsn} \tag{8.5}$$

And therefore from Equations (8.2), (8.3) and (8.5) the increase in conductivity is given by:

$$\sigma = \sqrt{\frac{QD_r}{vs}e\mu}. \tag{8.6}$$

So in the case of a perfect intrinsic semiconductor, the photocurrent is expected to vary as the square root of the deposited dose rate. Since for an ideal dosimeter we seek a linear current–dose/rate response, this is clearly not suitable. In practice, however, most semiconductors and diamond, in particular (even in the most pure form available), have considerable concentrations of recombination centres and transport properties are dominated by these defects [42]. In this case the relaxation time is given by Equation (8.4), where $N \gg n, p$. In this case τ_e is independent of n and the conductivity can be expressed as:

$$\sigma = \frac{QD_r}{vsN}e\mu \tag{8.7}$$

which is linear with dose rate D_r. This condition results in a linear current response with dose rate, as it is actually required for the use of diamond in radiotherapy dosimetry.

Diamond detectors for tracking applications are generally operated using an electric field of 1 V/μm to saturate the drift velocity [43, 44]. A high electric field is also important for dosimetric applications, as the diamond sensitivity depends on the average internal electric field E, through the mobility (see Equation 8.7). Evidence of an increase of the dosimetric sensitivity due to increased external applied voltage has been reported [45]. In the same work it was also reported that the average electric field within the sensor is altered by charge carriers trapped at defects, acting in a direction opposite to the applied field: an effect known as polarization [46, 47]. Polarization is due to the progressive charging of traps, which generates a space charge in the bulk of the detector, resulting in non-ohmic I–V characteristics similar to those of a back-to-back Schottky device. Figure 8.4(a) shows the background current of a state-of-art polycrystalline CVD diamond film used for dosimetric characterization, and Figure 8.4(b) shows its I–V characteristics

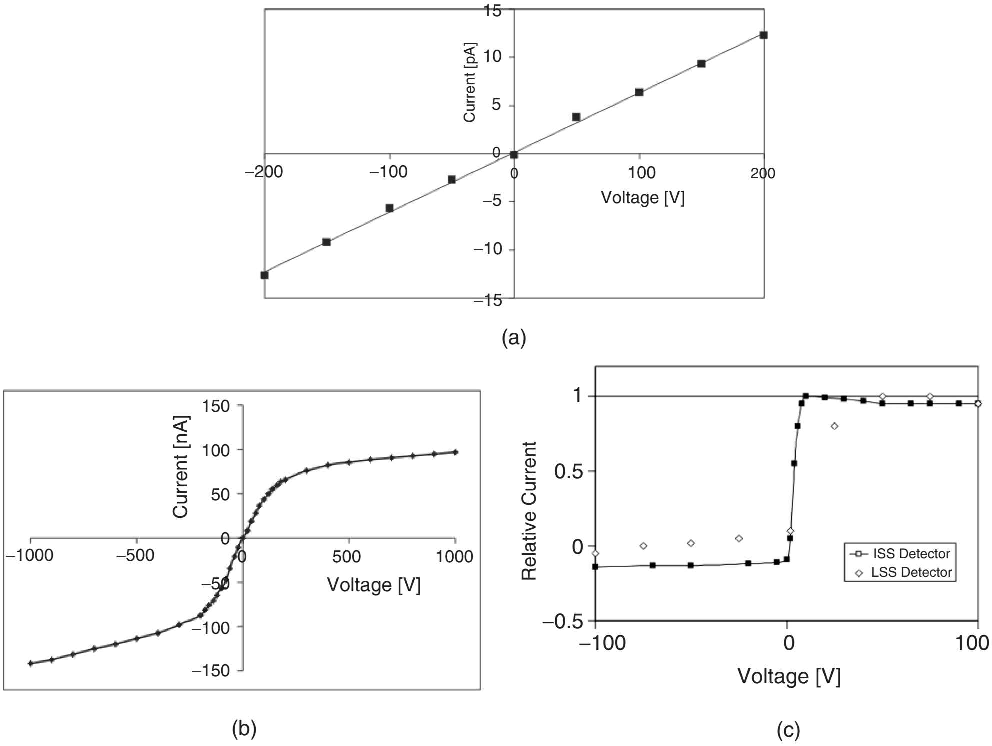

Figure 8.4 (a) I–V beam-off I–V characteristics of a CVD-diamond dosimeter in conventional set-up for radiotherapy dosimetry measurements; (b) I–V for same device under exposure to a 25-MV X-beam with dose rate 1.7 Gy/min [48]; (c) I–V curves for two PTW natural diamond detectors obtained with 6-MV X-rays radiotherapy beam [37]

during exposure to a 25-MV X-photon beam at 1.7 Gy/min dose-rate. These graphs show evidence that, while the beam-off (background) current exhibits indeed an ohmic behaviour, during beam exposure the I–V characteristics are non-ohmic [48]. Figure 8.4(c) shows the I–V characteristics of two natural PTW diamond detectors, under a 6-MV X-photon beam irradiation [37], demonstrating clearly a non-ohmic trend, characterized by a plateau in the high voltage range. Usually, the applied voltage during a dosimetric measurement is fixed within this plateau region in such a way to maximize the current response.

The negligible background current of diamond devices at room temperature is another advantage in their use as on-line dosimeters. The thermally activated leakage current I in semiconductor devices is given by [49]:

$$I(T)\alpha T^2 \exp\left(-\frac{E}{KT}\right) \tag{8.8}$$

where E is a typical activation energy characterizing the main electrical conductivity process in the semiconductor bulk, and K is the Boltzmann constant. Due to the large band gap of diamond, E is usually rather high and thus the leakage current at room temperature is very low (typically less than 1 pA), not affecting the operation of the device when it is biased with an high voltage. A negligible leakage current means a possibility of working with a high applied bias to maximize the active volume of the device and thus its sensitivity. Conversely, silicon diodes for dosimetry applications work unbiased, in a photovoltaic mode, to reduce the electronic noise associated with the leakage current. This noise increases proportionally to the square root of the applied voltage and, in a fully depleted device, linearly with the fluence of irradiation [50]. Thus the active volume of a silicon dosimeter is essentially governed by the minority diffusion length, typically of the order of 60 μm after pretreatments used to harden the detector volume against irradiation [25].

The greater active thickness of a diamond dosimeter compared with a silicon one partially compensates for the higher generation constant of silicon compared with diamond, and so the sensitivity per unit volume of diamond and silicon dosimeters are often comparable. Table 8.3 shows typical sensitivities of ICs and silicon diode commercial dosimeters, compared with diamond devices [51].

Another important advantage of diamond compared with silicon is that when the accumulated dose is increased, the leakage current of diamond usually does not change or if anything, decreases [52]. This can be attributed to the fact that irradiation results in the creation of energy levels deeper than the native ones that lead to an increase of the effective activation energy E and consequently a further decrease of I. We finally observe that, as diamond dosimeters are operated under an applied external voltage, care must be taken to eliminate the air ionization contribution to the photocurrent. This is achieved by either operating the device under vacuum or, more practically, by embedding the device in a tissue equivalent epoxy resin.

One important effect attributed to trapping of charge within the diamond sensor is the observed increase in current response under steady irradiation conditions during the early stages of exposure. This phenomenon, called *priming* or *pumping*, is probably related to an increase in the free-carrier lifetime caused by the passivation of deep native traps, which are filled with the electrons (holes) produced in the semiconductor bulk by the radiation. If the activation energy of these traps is sufficiently high, their rate of thermal ionization will be low and they will remain passivated for long periods of time. Polycrystalline CVD diamonds kept in the dark have been observed to remain pumped for months, while exposure to room light ionizes the traps and results in a rapid depumping [44]. For this reason, a diamond dosimeter should be pre-irradiated before first operation and then kept in the dark to preserve its electronic stability and to get a stable current response during successive operations. The current response of a CVD diamond dosimeter under first exposure to a 25V X-photon beam with dose rate 1.7 Gy/min, is shown in Figure 8.5(a):

Table 8.3 Typical sensitivity of ICs and silicon diode commercial dosimeters compared with that of some diamond devices in literature [51]

Device	bias [V]	Vol. [mm^3]	S per unit volume [nC/(Gy mm^3)]
Standard Farmer Ionisation chamber	300	600	0.036
Miniature EXTRADIN T1 Ionisation chamber	300	50	0.028
Scanditronix GR-p BS Silicon	0	0.295	474
Scanditronix SFD stereotactic Silicon	0	0.017	353
CVD Diamond	400	4.7	90–700

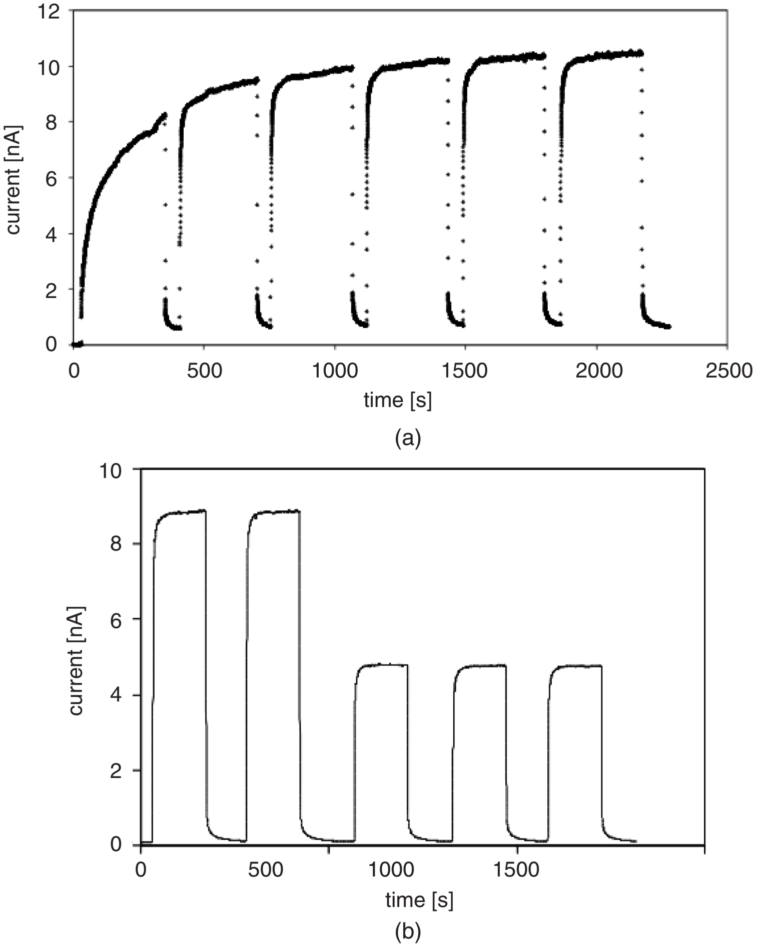

Figure 8.5 Current response of a CVD-diamond dosimeter (a) under first exposure to a 25-MV X-photons beam with dose rate 1.7 Gy/min, showing the priming effect during the first six successive irradiations (applied voltage = 100 V, Au contacts, room temperature) [53]; (b) under exposure to the same beam, and changing dose rates from 1.7 Gy/min to 0.85 Gy/min, after saturation of priming [54]

the priming effect during the first six successive irradiations is clearly visible [53]. After about 10–50 Gy (depending on the diamond crystalline quality), a stabilization of the response is achieved: Figure 8.5(b) shows the 'pumped' diamond under exposure to the same beam, measured at two different dose rates [54].

After priming, further long-term stability of response is a basic requirement for dosimetry, in both conventional and highly conformal radiotherapy treatments. The response of CVD diamond detectors that have been reported in the literature show considerable variability: some authors [45] claim a very good stability of the signal after priming, while others [55, 56] observed a loss of stability when the detector was not irradiated, even if the irradiation was off for only a few minutes.

In recent studies made on CVD polycrystalline diamond of state-of-the-art quality [48], the percentage standard deviation under a 10-MV X-photon beam was 0.3 % at 1 Gy: a good repeatability level for practical purposes. Recent work on the characteristics of the PTW natural diamond detector [37, 57] showed that preliminary irradiation was also required to stabilize the sensitivity: the variability with time after stabilization is approximately 0.1 %. Conversely, a first dosimetric evaluation of single crystal CVD diamond detectors, reported in [37], shows that no pre-irradiation is needed to reach signal stabilization and a repeatability better than 0.1 %, a result that is, in principle, in agreement with the higher purity and crystalline quality of CVD single crystal diamond compared with natural stones and polycrystalline CVD diamond.

Once a stable condition has been achieved, diamond dosimeters have been shown to be relatively insensitive to the accumulated dose typically encountered in radiotherapy applications. No changes, short or long term, have been observed in the calibration for doses as high as 9 kGy [26], a further demonstration of the radiation hardness of diamond.

The response of a dosimetric device should be sufficiently fast in order to follow in real time the changes of intensity of the radiation beam. This requires a time of response of the order of 1 second or even less for IMRT applications, where typical irradiation rates of 200 MU/min (Monitor Unit = MU usually corresponds to 1 cGy in standard irradiation conditions), means that one monitor unit is delivered approximately every 0.3 s [58]. It has been suggested that the observed current rise and fall times (after switching the beam on and off) in many CVD diamond dosimeters is influenced by the charging of relatively shallow defect levels that can be thermally ionized at room temperature [55, 59]. This pumping–depumping effect produces a smearing of the dynamic curve with a duration of several seconds. The rise and decay times of the response of CVD polycrystalline diamond dosimeters under an on–off beam of 10-MV X-photons, have been evaluated and compared with the response of an IC [48]: results are shown in Figure 8.6. When the beam is switched on, the dynamic response is the same as that of the IC up to 90 % of the equilibrium signal. After that, the CVD diamond response slows down to produce a shoulder of a few seconds (2–8 s) before reaching the equilibrium value [48, 54]. As the beam is switched off, the signal of the diamond sensor sharply decreases down to about 10 % of the equilibrium signal, following the response of the IC, but after this it decays slowly, exhibiting a persistent photocurrent (of a few tens of pA, above the dark current) that takes a few minutes to decay. The rise and fall times of CVD polycrystalline and single crystal diamond dosimeters have been found to be of the order of 2 s [39].

A slow dynamic response and the difficulty in achieving sufficient signal stability are clear hurdles for the use of diamond in clinical dosimetry. It has recently been shown that the dynamic performance of polycrystalline CVD-diamond on-line dosimeters can be substantially improved by irradiation with fast neutrons up to a fluence of 5×10^{14} n/cm^2 [60]. This improvement has been correlated with a decrease of more than one order of magnitude in the concentration of relatively shallow defect levels with activation energies in the range 0.8–1.4 eV. These are thought to be the levels responsible for the slow dynamic response observed in unirradiated devices. As a consequence of the neutron irradiation, a faster and more reproducible dynamic response is observed under the radiation of a 6-MV photon beam from a linear accelerator and also from a ^{60}Co source [60, 54]. Due to the creation of radiation-induced deep traps by the neutron irradiation (which enhances carrier recombination), the resulting sensitivity of diamond is reduced. However, the sensitivity is still higher than that of standard ionization chambers, and

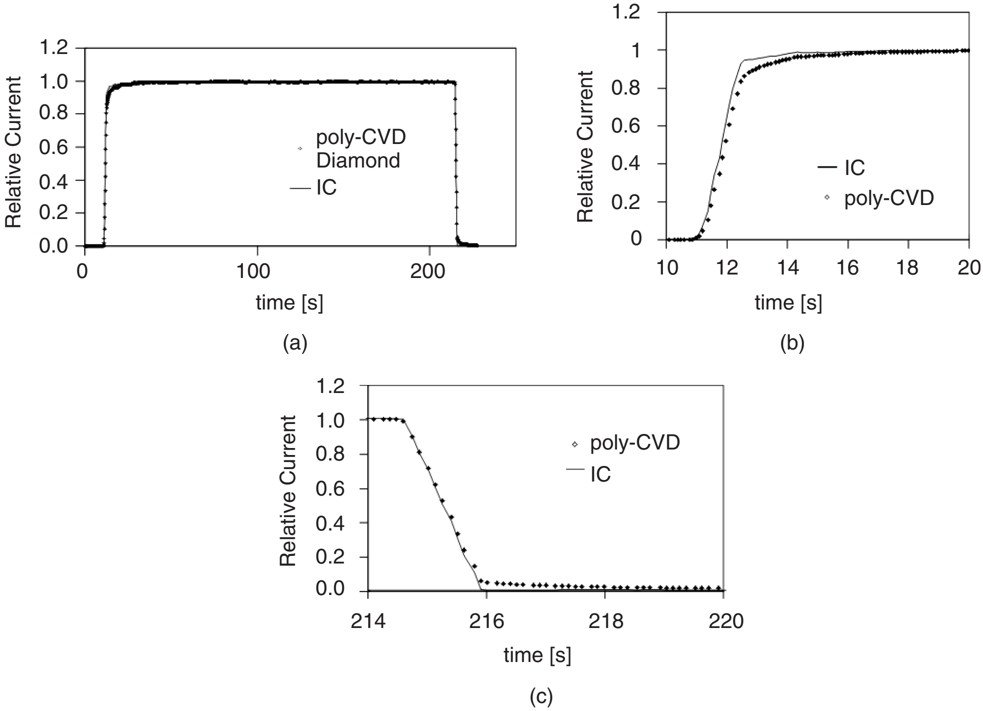

Figure 8.6 (a) Dynamic response of a polycrystalline diamond relative to the response of an ionization chamber, tested with a 10-MV X-photon; details of relative (b) rise, and (c) decay, times [48]

compares favourably with standard silicon dosimeters and with the best-quality natural diamond devices. The dynamic response before and after irradiation with 5×10^{14} fast neutrons/cm^2 of a polycrystalline CVD-diamond on-line detector produced at the University of Florence is shown in Figure 8.7 during exposure to a 6-MV photon radiotherapy beam [54]. Another method for avoiding the unwanted effect of defects on response dynamics has been recently suggested, which consists in the use of the CVD-diamond dosimeters at moderate temperatures (70–100 °C) [55]. This method improves the device rise time as a consequence of the faster emission coefficient of the dominant ~1-eV traps, and the almost complete ionization of shallower defects that takes place at higher temperatures. However, this method is strongly dependent on the specific trap parameters (energy, concentration cross-section) of the shallow defects involved, which can vary significantly from sample to sample. Moreover, the temperatures that are required to decrease the decay time are higher than 100 °C and at these temperatures the dark current increases to unacceptable levels [61].

The global dynamic performance of a CVD diamond device for IMRT applications has been studied [48] using a 6-MV photon IMRT clinical field, planned for the treatment of the head and neck and obtained by the step-and-shoot technique with 21 irradiation segments. The signal of the diamond dosimeter was observed to decay down to zero in a longer time than it was needed to rearrange the leaves (a few seconds) between two consecutive segments. Due to this slow dynamic response, the diamond dosimeter was

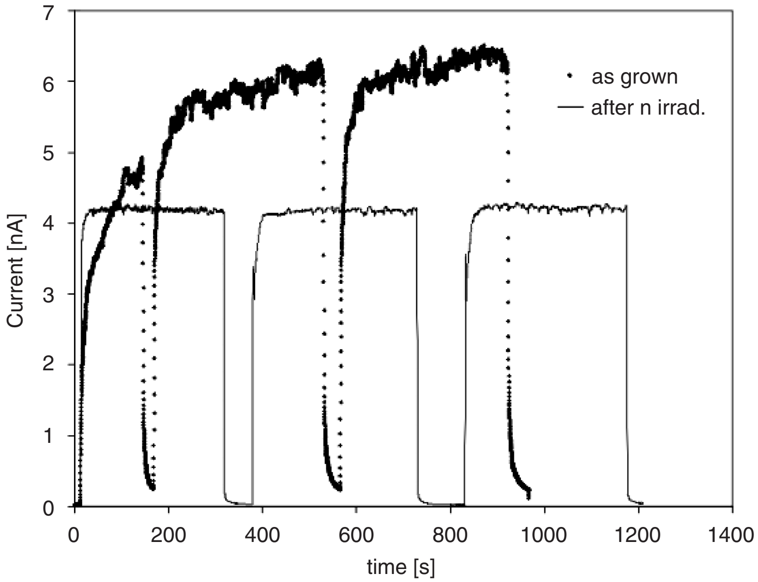

Figure 8.7 Medium-quality polycrystalline CVD diamond used in on-line configuration under irradiation with a 6-MV X-photon beam (solid dots) as grown and (—) after irradiation with fast neutrons up to the fluence of 5×10^{14} n/cm^2 (signal multiplied by 5 for better comparison) [54]

unable to follow the rapid dose-rate changes typical of an IMRT treatment: this rendered the device unsuitable for an accurate dosimetry in this case.

Once the stability of the signal has been achieved, in order to attain a measurement of the dose the diamond dosimeter current signal is monitored and integrated in time as a function of the absorbed dose. Figure 8.8(a) shows the collected charge versus dose in the range 1–10 Gy, measured at constant dose rate for a polycrystalline CVD diamond device [48]: a good linearity is observed. However, the same authors point out that the slope is slightly different from that measured in the range 0.1–1 Gy (2 % lower for the low-dose range). A more detailed study involving residual analysis (Figure 8.8b) shows that, for low doses, the deviations from linearity can be quite large, reaching almost 20 % for doses close to 0.1 Gy. This behaviour can be attributed to the dynamics of the device, which take a few seconds to reach the steady state (equilibrium current), while nonoptimal dynamic response does not influence linearity for doses above about 0.3 Gy.

A linear current versus dose/rate dependence is equivalent to a charge–dose response independent of dose rate. In the case of solid-state dosimeters in on-line configuration equipped with ohmic contacts, it is possible to apply the Fowler model [62]:

$$I = I_{dark} + RD_r^{\Delta} \tag{8.9}$$

where D_r is the dose rate, I_{dark} is the dark current, R and Δ are fitting parameters, where in particular Δ describes the deviation from linearity. In the case of a pure semiconductor without any traps, the model predicts a value $\Delta = 0.5$; for a uniform trap distribution $\Delta = 1$, and in intermediate cases $0.5 < \Delta < 1$ is expected, following from Equations (8.2–8.7). Different Δ values have been measured in diamond sensors of different origins. For PTW natural diamond devices, Δ values are of the order of 0.98–0.99, so the deviation

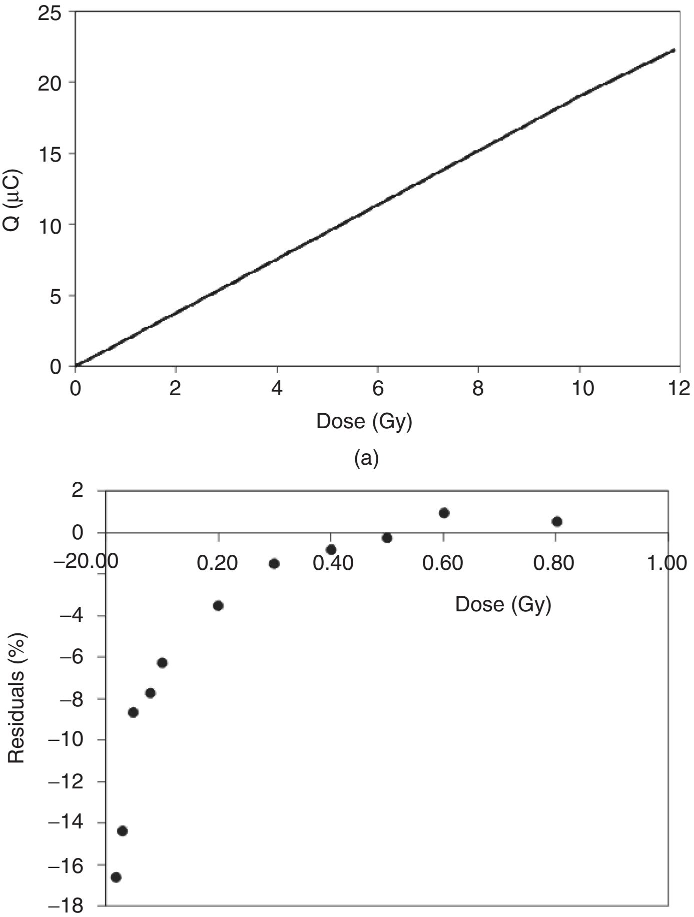

(a)

(b)

Figure 8.8 (a) Linearity of a CVD device for doses in the range 1–12 Gy; (b) residual plot against dose values in the range 0.1–1.0 Gy [48]

from linearity is very low [37]. Polycrystalline CVD diamond devices exhibit, in most cases, lower values of Δ, in the range 0.88–0.98, depending on the origin of the CVD diamond and the applied electric field. In fact, the value of Δ can be significantly increased by increasing the applied electrical field [45]: for instance a 7 % increase in Δ was observed as the electric field was increased from 0.2 to 2 V/μm [57]. CVD polycrystalline and single crystal diamond devices made at CEA, France, have been reported to have values of Δ of 0.97 ± 0.02 and 0.98 ± 0.07 respectively [39].

8.3.2 Diamond sensors in off-line configuration

Diamond films, natural and synthetic, can also be used as off-line dosimeters, by measuring their thermoluminescence response to radiation after beam exposure at room temperature and during a controlled heating scan. Natural diamond was the first material in which

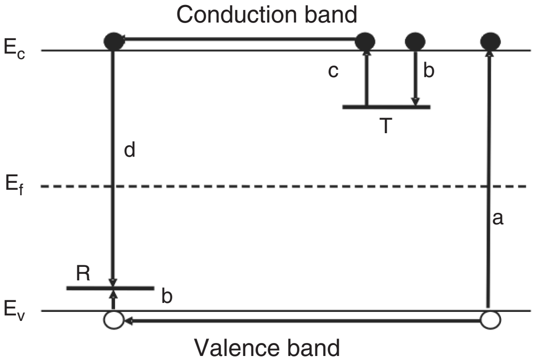

Figure 8.9 Electronic transitions in a TL material according to a two-level model: (a) generation of electrons and holes; (b) electron and hole trapping; (c) electron release due to thermal stimulation; (d) recombination. Solid circles represent electrons, open circles holes. Level T is an electron trap, level R is a recombination centre, E_v = valence band edge; E_c = conduction band edge

thermoluminescence (TL) was observed: the glow emitted by a diamond stone when warmed in the dark was reported to the Royal Society in 1663 by Robert Boyle.

In a simple TL model two levels are assumed, one situated below the bottom of the conduction band and the other situated above the top of the valence band (see Figure 8.9). The highest level indicated by T is situated above the equilibrium Fermi level (E_f) and is thus empty in the equilibrium state, i.e. before exposure to radiation and the creation of electrons and holes. It is therefore a potential electron trap. The other level (indicated by R) is a potential hole trap and can function as a recombination centre.

The absorption of radiation with $h\nu > E_g$ results in ionization of valence electrons, producing electron and holes that are then trapped respectively at T and R (transition b). The probability per unit time of releasing an electron from the trap can be described by the Arrhenius equation: $p = \phi \cdot e^{-E/KT}$ where ϕ is the frequency or the attempt-to-escape factor. In this simple model, ϕ is considered as a temperature independent constant with a value of the order of the lattice vibration frequency, namely $10^{12} - 10^{14}\ \mathrm{s}^{-1}$ and E is the trap activation energy. If $E \gg kT_0$, with T_0 the temperature of the device during irradiation, then any electron that becomes trapped will remain so for a long period of time after irradiation. By raising the temperature of the TL material above T_0, the probability of detrapping will increase: emitted charge carriers will then recombine at the centre R with emission of light. Assuming negligible retrapping [63, 64] during a heating scan where the temperature varies linearly with time with heating rate β the TL intensity is given by the well-known Randall–Wilkins first-order expression:

$$I_{TL}(t) = -\frac{1}{\beta}\frac{dn}{dt} = n_0\frac{\phi}{\beta}e^{-\frac{E}{kT}}e^{-\frac{\phi}{\beta}\int_{T_0}^{T} e^{-\frac{E}{kT}}\,dT} \tag{8.10}$$

where n_0 is the concentration of initially occupied traps.

The TLD materials most commonly used in medical applications are LiF:Mg,Ti, LiF:Mg,Cu,P and $Li_2B_4O_7$:Mn, because of their tissue equivalence. Other TLDs, used because of their high sensitivity, are $CaSO_4$:Dy, Al_2O_3:C and CaF_2:Mn [11]. Commercial TLDs need to be calibrated before they are used (thus they serve as relative dosimeters). To derive the absorbed dose from the thermoluminescence reading, a few correction factors have to be applied for effects such as energy, fading and dose response nonlinearity [11]. CVD diamond has been suggested as a potential alternative material to overcome these limitations. In Refs [65, 66] and later in Ref. [67], it was suggested that CVD-diamond films could be used as off-line dosimeters by monitoring their thermally stimulated current (TSC) instead of the TL response. A TSC off-line dosimeter has the same electrode configuration as an on-line diamond dosimeter. The response to the received dose is read-out by monitoring the current during a heating ramp with a constant rate β keeping the device in vacuum and in the dark. Considering a first order kinetics, with an applied electric field ε, and a device active area A, we obtain the following expression for the TSC signal:

$$I_{TSC}(t) = eA\mu\varepsilon\tau n_0 \frac{s}{\beta} e^{-\frac{E}{kT}} e^{-\frac{s}{\beta}\int_{T_0}^{T} e^{-\frac{E}{kT}}\,dT} \tag{8.11}$$

The results observed on CVD-diamond samples demonstrate that the TL and TSC peaks occur at similar temperatures, suggesting that similar detrapping phenomena are involved. Also good agreement is found between the trap parameters independently determined by TL and TSC analysis [68]. The TL response of an undoped polycrystalline CVD diamond after irradiation with a ^{60}Co γ-source at 50 cGy is shown as an example in Figure 8.10(a) (normalized to its maximum value) [69].

The glow-peak of diamond seems to exhibit the characteristics of a single peak, without any inflection points, which would indicate the presence of other overlapped peaks. The glow curve is spread over a wide temperature range (typically 50–300 °C), and is characterized by a dominant peak around 250 °C. A pronounced shoulder in the lower temperature range 50–200 °C is sometimes present, due to the emission from shallower energy levels. Investigating different kinds of diamond samples, the main differences are found in the shoulder structure located in this low-temperature region. These differences are due partly to the different growth conditions and partly to the fact that the

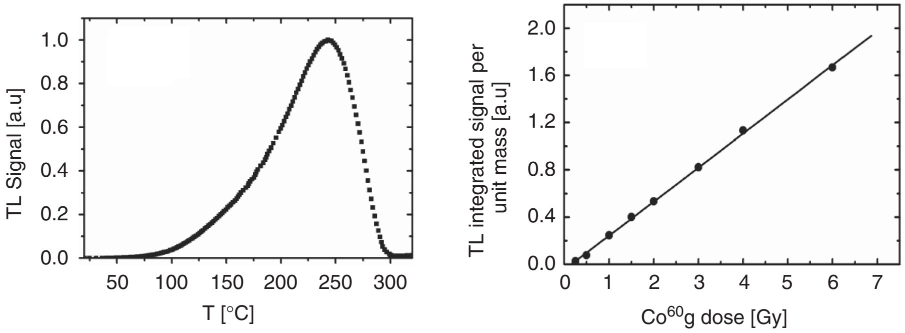

(a) (b)

Figure 8.10 (a) Normalized glow peak measured with a polycrystalline CVD diamond after exposure to γs from a ^{60}Co-radiotherapy beam. (b) Linearity of the TL integrated signal of the same sample with the absorbed dose in the range from 0.25 Gy to 7 Gy [69] shoulder is strongly dependent on the environmental conditions prevailing during the measurements [70]. It is quite easy to isolate the main peak located at high temperature by means of a preheat procedure (3 min at 220 °C), which is a very simple and practical procedure for dosimetry applications [71]. Glow-curve analysis after preheat treatments attribute the dominant peak to a single defect with energy of 1 eV and frequency factor $\phi = 10^7 - 10^9\ \mathrm{s}^{-1}$ [71]. After the heating pretreatment, good intersample and intrasample reproducibility has been shown in the TL response of polycrystalline CVD diamond films [72, 73]. A similar TL response for beta- and gamma-radiation has been reported [71, 74]. In [73], TL response versus dose was measured with 20-MeV electron beams, ^{60}Co photons and 22 MeV proton beams. In [75], diamond TLDs were shown to exhibit an energy-independent response for electron energies in the range 5–20 MeV. Linearity with dose has been reported by many authors [71–78] for different dose intervals selected within a wide range of exposures (from a few tens of mGy up to 10–100 Gy). In Figure 8.10(b) the linearity of the TL signal shown in Figure 8.10(a), integrated over time, is plotted in the absorbed dose range 0.25 Gy to 7 Gy [69]. Superlinearity is observed in some cases, while a sublinear trend followed by saturation is observed when the dose is increased up to a value when almost all the traps become filled [73, 76].

One inherent problem with CVD diamond is that the activation energy of the trap centres involved in TL is about 1 eV, which is below the photon energy in visible light. This means that, if exposed to ambient light, there can be significant changes in the carrier population of the sensor. This effect is called bleaching (or optical fading) and results in the progressive loss of the TL signal when diamond is illuminated in the spectral range 400–550 nm [79]. To minimize this effect, the diamond sensor should be kept in the dark or in an ambient where either the green part of the spectrum is filtered out or the illumination is only by red light [80]. The TL can also decay due to room temperature thermal excitation of relatively shallow traps (thermal fading). To reduce thermal fading and to better evaluate the integrated charge as a function of the dose, it is always recommended to undergo pretreatment heating to empty the shallow traps and to isolate the component that peaks at the highest temperature.

The TL response of diamond has been compared to LiF, a widely used commercial TLD dosimeter [71, 75, 77], which is characterized by several, overlapping, first-order TL peaks covering the range 50–220 °C [81]. The integrated TL/TSC response of diamond as a function of the dose compares favourably with that of LiF TLDs [82]. The CVD diamond sensitivity (the slope of the integrated charge as a function of the dose over the mass of the sample) has been calculated [71] as 0.43 C/J for a set of polycrystalline CVD-diamond films. This is comparable to the values observed in LiF TLD100 and TLD700 dosimeters, which are respectively 0.73 C/J and 0.54 C/J. In these diamond dosimeters, after the simple preheating procedure, the resulting TL glow curve consists of only one high temperature peak that is less sensitive to thermal fading than that of LiF dosimeters. To conclude this section, we observe that, in spite of the fact that numerous studies have proved that it is possible to produce CVD-diamond off-line dosimeters with comparable or sometimes even better performances than LiF TLDs, the considerably higher cost of commercial CVD diamond has prevented, so far, the competitive commercial use of synthetic diamond for this application.

8.4 CONCLUSIONS

Due to the close collaboration between fundamental research projects and technological developments in industry, which have taken place over the last 20 years, state-of-the-art diamond sensors have improved, reaching performances very close to the strict requirements of clinical radiotherapy. The most interesting application of diamond sensors is to direct-reading dosimetry since there is, at present, no other available tissue equivalent material to produce on-line dosimeters competitive with ionization chambers. On-line devices made on natural diamond stones are already commercially available, but are scarce and highly priced due to the difficulty of selecting stones with the proper dosimetric characteristics. CVD diamond devices have been proposed in their stead, since they can potentially be produced with high quality, at lower cost, and with reproducible properties. The most difficult task still to be overcome in the quest for a commercial, CVD-diamond, on-line dosimeter is a full understanding and control of the bulk impurities that influence properties such as signal stability and response dynamics. CVD-diamond sensors are especially appealing in modern radiotherapy techniques such as hadron therapy, stereotactic radiosurgery and photon IMRT. Their use would represent a remarkable advantage in small radiation field applications such as stereotactic therapy, where an IC does not have adequate spatial resolution and suffers from lateral electronic disequilibrium, resulting in a reduced response. In small radiation MV X-photon fields, a diamond dosimeter is more suitable than a Si diode because the spectral characteristic of a photon MV beam varies with changes in field size. In contrast to Si diodes, which are affected by these changes, diamond sensors (because of their energy independent response) should not be significantly affected. A comparison of TLD, Si diodes, ICs and diamond detectors in small fields of less than 4 cm demonstrated that diamond detectors exhibit a superior performance in the measurement of penumbra [57, 83]. Another important instrumentation frontier in clinical radiotherapy that could be faced in future by diamond dosimeters, concerns the manufacture of segmented devices to cover large bidimensional fields for IMRT and proton-therapy pretreatment verifications of dose [20]. Current state-of-the-art technology recently demonstrated that segmented detectors for tracking in high energy physics experiments can be processed on high-quality polycrystalline CVD-diamond 6-inch wafers [44] [see also Chapter 9 in this book]. As a reasonable perspective, once the present limitations of diamond dosimeters discussed above are overcome, we can expect that large-area, polycrystalline, CVD-diamond-segmented dosimeters will also become available for radiotherapy, profiting from the current developments in diamond detector technology.

ACKNOWLEDGEMENTS

The author wishes to express her sincere gratitude to Prof. Marta Bucciolini of the Dipartimento di Fisiopatologia Clinica, Università di Firenze, for all her helpful advice, the valuable hints to improve this chapter, and for her warm encouragement during their 10-year collaboration on the development of diamond sensors for clinical radiotherapy.

REFERENCES

[1] J. Barthe, R. Hugon, J.P. Nicolai, *Nucl. Instrum. Meth. A*, **583**, 1–8 (2007).

[2] S. Webb S, P.M. Evans, *Semin. Radiat. Oncol.*, **16**, 193–198 (2006).

[3] G. Aus, C.C. Abbou, M. Bolla *et al.*, *Eur Urol.*, **48**, 546–551 (2005).

[4] A.M. Evans, R.G. Moffat, R.D. Nash, H.F. Batho, S.A. Mibus, *J. Faculty Radiolog.*, **5**, 248–260 (1954).

[5] J.A. Del Regato, *Radiology*, **88**, 761–6 (1967).

[6] New prospects in radiotherapy: 15-million-volt linear accelerator at Barts, *The Lancet*, **265**, 909–911 (1955).

[7] M.A. Bagshaw, H.S. Kaplan, R.H. Sagerman, *Radiology*, **85**, 121–129 (1965).

[8] R.R. Wilson, *Radiology*, **47**, 487 (1946).

[9] L. Leksell, *Acta Chir. Scand.*, **102**, 2 (1951).

[10] D.W. Andrews, G. Bednarz, J.J. Evans, B. Downes, *Surg. Neurol.*, **66**, 559–564 (2006).

[11] E.B. Podgorsak, *Radiation Oncology Physics: A Handbook for Teachers and Students*, Available at: http://www-naweb.iaea.org/nahu/dmrp/syllabus.shtm.

[12] H.E. Johns, J.R. Cunningham, *The Physics of Radiology*, Charles C. Thomas Publisher, Springfield, Illinois, USA, 1983.

[13] M. Dosanjha, H.F. Hoffmann, G. Magrin, *Nucl. Instrum. Meth. A*, **571**, 191–194 (2007).

[14] G. Kraft, *Nucl. Instrum. Meth. A*, **454**, 1–10 (2000).

[15] A. Brahme, J.E. Roos, I. Lax, *Phys. Med. Biol.*, **27**, 1221–1229 (1982).

[16] C.C. Ling, J. Humm, S. Larson *et al.*, *Int. J. Radiat. Oncol. Biol. Phys.*, **47**, 551–560 (2000).

[17] M.J. Zelefsky, S.A. Leibel, P.B. Gaudin *et al.*, *Int. J. Radiat. Oncol. Biol. Phys.*, **41**, 491–500 (1998).

[18] M.J. Zelefsky, Z. Fuks, M. Hunt, *et al.*, *Int. J. Radiat. Oncol. Biol. Phys.*, **53**, 1111–1116 (2002).

[19] A.L. Zietman, M.L. DeSilvio, J.D. Slater *et al.*, *JAMA*, **294**, 1233–1239 (2005).

[20] D. Menichelli, M. Bruzzi, M. Bucciolini, C. Talamonti *et al*. *Nucl. Instrum. Meth. A*, **583**, 109–113 (2007).

[21] S.W.S. McKeever, *Thermoluminescence of Solids*, Cambridge University Press, Cambridge, 1985.

[22] R.C. Murty, *Nature*, **207**, 398–399 (1965)

[23] L.H. Gray, *Proc. R. Soc. A*, **156**, 578–596, (1936).

[24] G. Rikner, E. Grusell,, *Acta Rad. Oncol.*, **23**, (1984).

[25] G. Rikner, E. Grusell, *Phys. Med. Biol.*, **32**, 1109–1117, (1987).

[26] F.K. Bampton, *Industrial Diamond Review*, 55–59 (1976).

[27] B. Planskoy, *Phys. Med. Biol.*, **25**, 519 (1980).

[28] E.A. Burgemeister *Phys. Med. Biol.*, **26**, 269 (1981).

[29] E.A. Burgemeister, W. Schouten, *Radiat. Prot. Dosim.*, **6**, 145 (1984).

[30] R.J. Keddy, T.L. Nam, R.C. Burns, *Carbon*, **26**, 345–356 (1988).

[31] V.S. Khrunov, V.M. Kukushkin, S.S. Martynov, N.P. Marchenko, S.M. Vatnitskii, I.A. Ermakov, *Measurement Techniques* (English translation of Izmeritel'naya Tekhnika), **31**, 602–604 (1988).

[32] M. Bruzzi, M. Bucciolini, F. Nava, S. Pini, S. Russo, *Nucl. Instrum. Meth. A*, **485**, 172 (2002).

[33] A.B. Rosenfeld *Radiation Measurements*, **41**, S134–S153 (2007).

[34] S. Schnetzer *et al.*, *IEEE Trans. Nucl. Sci.*, **46**, 193 (1999).

[35] PTW-Freiburg GMBH, Lörracher Str. 7 79115 Freiburg, Germany, http://:www.ptw.de.

[36] F.C. Champion, *Adv. Phys.*, **5**, 383–411 (1956).

[37] C. De Angelis, S. Onori, M. Pacilio, G.A.P. Cirrone, G. Cuttone, L. Raffaele, M. Bucciolini, S. Mazzocchi, *Med. Phys.*, **29**, 248–254 (2002).

[38] M. Bruzzi, M. Bucciolini, G.A.P. Cirrone, G. Cuttone, S. Mazzocchi, S. Pirollo, S. Sciortino, *Nucl. Instrum. Meth. A*, **454**, 142–146 (2000).

[39] C. Descamps, D. Tromson, N. Tranchant, A. Isambert, A. Bridier, C. De Angelis, S. Onori, M. Bucciolini, P. Bergonzo, *Radiation Measurements*, **43**, 933–938, (2008).

[40] W.U. Laub, T.W. Kaulich, F. Nüsslin, *Phys. Med. Biol.*, **44**, 2183–2192 (1999).

[41] P. Blood, J.W. Orton, The Electrical Characterization of Semiconductors: *Majority Carriers and Electron States*, Academic Press, London, 1992.

[42] See Chapters 2 and 3 in this book.

[43] F. Borchelt, W. Dulinski, K. Gan, S. Han, J. Hassard, A. Howard *et al.*, *Nucl. Instrum. Methods, A*, **354**, 318–327 (1995).

[44] H. Kagan, *Nucl. Instrum. Methods A*, **541**, 221–227 (2005).

[45] A. Fidanzio, L. Azario, R. Kalish, Y. Avigal, G. Conte, P. Ascarelli, A. Piermattei, *Med. Phys.* **32**, 389 (2005).

[46] E.A. Konorova, S.F. Kozlov, *Sov. Phys.-Semicond.*, **4**, 1600–1605 (1971)

[47] S.F. Kozlov, E.A. Konorova, Y.A. Kuznetsov, Y.A. Salikov, V.I. Redko, V.R. Grinsberg, M.L. Meilman, *IEEE Trans. Nucl. Sci.*, **24**, 235–237 (1977).

[48] C. De Angelis *et al.*, *Nucl. Instrum. Meth. A*, **583**, 195–203 (2007).

[49] S.M. Sze, *Physics of Semiconductor Devices*, John Wiley & Sons, New York, 1981.

[50] M. Bruzzi, *IEEE Trans. Nucl. Sci.*, 48 (2001).

[51] S. Pini, M. Bruzzi, M. Bucciolini, E. Borchi, S. Lagomarsino, D. Menichelli, S. Miglio, F. Nava, S. Sciortino, *Nucl. Instrum. Meth. A*, **514**, 135–140 (2003).

[52] M. Bruzzi, H.F.-W. Sadrozinski, A. Seiden, *Nucl. Instrum. Meth. A*, **579**, 754–761 (2007).

[53] M. Bucciolini, E. Borchi, M. Bruzzi, M. Casati, P. Cirrone, G. Cuttone, C. De Angelis, I. Lovik, S. Onori, L. Raffaele, S. Sciortino, *Nucl. Instr. Meth. A*, **552**, 189 (2005).

[54] C. De Angelis, S. Onori, M. Bucciolini, M. Casati, I. Løvik, M. Bruzzi, S. Lagomarsino, S. Sciortino, *Radiat. Prot. Dosim.*, **38**, 120 (2006).

[55] M.J. Guerrero, D. Tromson, P. Bergonzo, R. Barrett, *Nucl. Instr. Meth. A*, **552**, 105 (2005).

[56] G.A.P. Cirrone, G. Cuttone, S. Lo Nigro, V. Mongelli, L. Raffaele, M.G. Sabini, L. Valastro, M. Bucciolini, S. Onori, *Nucl. Instr. Meth. A*, **552**, 197 (2005).

[57] M. Bucciolini, F:B. Buonamici, S. Mazzocchi, C. De Angelis, S. Onori, G.A.P. Cirrone, *Med. Phys.*, **30**, 2149–2154 (2003).

[58] D.A. Low, S. Mutic, J.F. Dempsey *et al.*, *Radiother. Oncol.*, **49**, 305–316 (1998).

[59] M. Bruzzi, M. Bucciolini, S. Lagomarsino, D. Menichelli, S. Miglio, S. Pini, S. Sciortino, *Physica Status Solidi A*, **193**, 563–571 (2002).

[60] M. Bruzzi, D. Menichelli, S. Pini, M. Bucciolini, J. Molnar, A. Fenyvesi, *Appl. Phys. Lett.*, **81**, 298 (2002).

[61] Eckhard Wörner, *Diamond Materials*, Freiburg, private communication, 2007

[62] J.F. Fowler, in *Radiation Dosimetry*, F.H. Attix, W.C. Roesch (Eds.), Academic Press, New York, 1966.

[63] J.T. Randall, M.H.F. Wilkins, *Proc. R. Soc. London A*, **184**, 366–389 (1945).

[64] J.T. Randall, M.H.F. Wilkins, *Proc. R. Soc. London A*, **184**, 390–407 (1945).

[65] E. Borchi, M. Bruzzi, M. Bucciolini, A. Guasti, S. Mazzocchi, S. Pirollo, S. Sciortino, *Nucl. Instr. Meth. A*, **426**, 181–184 (1999).

[66] M. Bruzzi, M. Bucciolini, G.A.P. Cirrone, G. Cuttone, A. Guasti, S. Mazzocchi S. Pirollo, M.G. Sabini, S. Sciortino, *IEEE Transaction on Nuclear Science*, **47** (2000).

[67] M. Rebisz, M.J. Guerrero, D. Tromson, M. Pomorski, B. Marczewska, M. Nesladekd, P. Bergonzo, *Diam. Rel. Mat.*, **13**, 796–801 (2004).

[68] A. Bizzarri *et al*. *Nucl. Instrum. Meth. A*, **426**, 169–172 (1999).

[69] M. Bruzzi, M. Bucciolini, S. Lagomarsino, D. Menichelli, S. Miglio, S. Pini, S. Sciortino, *Medium-to-high quality CVD Diamond Off-Line Dosimeters*, presented at Diamond 2002, Granada, September 2002.

[70] C. Furetta G. Kitis, C.-H. Kuo *Nucl. Instrum. Meth. B*, **160**, 65–72 (2000).

[71] E. Borchi, M. Bruzzi, C. Leroy, S. Sciortino, *J. Phys. D: Appl. Phys.*, **31**, 609–616 (1998).
[72] M. Benabdesselam P. Iacconi, J.E. Butler, J.M. Nigoul, *Diam. Rel. Mat.*, **12**, 1750–1754 (2003).
[73] S. Mazzocchi, M. Bruzzi, M. Bucciolini, G. Cuttone, S. Pini, M.G. Sabini, S. Sciortino, *Nucl. Instrum. Meth. A*, **476**, 713–716 (2002).
[74] O. Avila, A.E. Buenfil, M.E. Brandan, *Radiation Protection Dosimetry*, **58**, 61 (1994).
[75] G.J. Mosia, A.C. Chamberlain, *Nucl. Instrum. Meth. A*, **580**, 570–573 (2007).
[76] S. Gastélum *et al*. *Nucl. Instrum. Meth. B*, **260**, 592–598 (2007).
[77] F. Bogani, E. Borchi, M. Bruzzi, C. Leroy, S. Sciortino, *Nucl. Instrum. Meth. A*, **388**, 427–430 (1997).
[78] L.M. Apàtiga, J.I. Golzarri, J. Mumford, F. Alba, V.M. Castano, *Radiation Physics and Chemistry*, **54**, 223–228 (1999).
[79] E. Vittone, C. Manfredotti, F. Fizzotti, A. Lo Giudice, P. Polesello, V. Ralchenko, *Diam. Rel. Mat.*, **8**, 1234–1239 (1999).
[80] C.C. Liua, T.C. Chua, S.Y. Lina, J.P. Linb, *Applied Radiation and Isotopes*, **58**, 89–94 (2003).
[81] R.G. Fairchild, P.L. Mattern, K. Lengweiler, P.W. Levy, *J. Appl. Phys.*, **49**, 4523–33 (1978).
[82] S.W.S. Mckeever, M. Moscovitch, P.D. Townsend, *Thermoluminescent Dosimetry Materials*, Nuclear Technology Publishing, England, 1995.
[83] I.J. Das, M.B. Downes and A. Kassaee, *J. Radiosurgery*, **3**, 177–185 (2000).

9 Radiation Sensors for High Energy Physics Experiments

H. KAGAN

Department of Physics, Ohio State University, USA

W. TRISCHUK

Department of Physics, University of Toronto, Canada

9.1 Introduction 207
9.2 CVD diamond detectors 208
9.3 Radiation hardness studies with CVD diamond 213
9.4 Uses of CVD diamond in high-energy physics 214
  9.4.1 Pad detectors – BaBar, CDF and ATLAS beam conditions monitors 215
  9.4.2 Strip detectors 220
  9.4.3 Pixel detectors 222
9.5 Summary 223
References 225

9.1 INTRODUCTION

High-energy physics experiments investigate the properties and interactions of matter at very small distances. To investigate behavior at small distances requires large energies, and hence large accelerators; to observe the interactions at high energies requires complex detectors. The standard method of 'observing' a high-energy physics interaction is to assemble an array of detectors at precise locations and detect the ionization deposited by the remnants of the interaction in these detectors. The components of high energy physics experiments, both sensor material and electronics, need to be radiation tolerant and provide the high precision information required to observe and understand the physics. At present, detectors close to the interaction region are based on the mature silicon technology, which functions very well in relatively low radiation environments [1]. However, the practical limits of the radiation tolerance of silicon falls short of what is required for many future experiments.

CVD Diamond for Electronic Devices and Sensors Edited by Ricardo S. Sussmann
© 2009 John Wiley & Sons, Ltd. ISBN: 978-0-470-06532-7

Chemical Vapor Deposition (CVD) diamond has a number of properties that make it an attractive material for high-energy-physics detector applications. Its large band gap (5.5 eV) and large displacement energy (42 eV/atom) make it a material that should be inherently radiation tolerant with very low leakage currents. Its small dielectric constant (5.7) results in low detector capacitance and thereby, low-noise performance of the associated front-end electronics. Its large thermal conductivity, between four- and five-times that of copper at room temperature, make it a material whose devices may be operated without cooling. Its large charge carrier saturation velocity (220 μm/ns) and mobility, combined with a large breakdown field (10^7 V/cm), enables very fast signal response. Although diamond appears ideal in many respects, it does have one major limitation: the large band gap that produces many of its outstanding properties limits the number of electron–hole pairs created in the diamond by the passage of a charged particle. Additionally, charge trapping, if it exists in the material, may further limit the observed signal. While the energy required to create an electron–hole pair is an intrinsic property of diamond, significant improvements have been made over the years in growing CVD material of high electrical quality with reduced charge trapping for use in a large array of detector applications.

Progress in experimental high-energy physics depends crucially upon the ability to carry out experiments at high energies, to probe small distance scales, and high luminosities, to observe rare processes. These two conditions alone imply that high-energy physics experiments take place in harsh radiation areas. In order to perform these complex and expensive experiments, new radiation hard technologies are constantly being developed. Chemical vapor deposition diamond is one material being actively pursued as a radiation-tolerant material for use very close to the interaction region where detectors operate in extreme radiation conditions. During the past few years many CVD diamond sensors have been manufactured and tested. As a detector for high radiation environments, CVD diamond benefits substantially from its radiation hardness, very low leakage current, low dielectric constant, fast signal collection and ability to operate at room temperature. This chapter discusses the use of diamond detectors as radiation sensors for high-energy physics experiments.

9.2 CVD DIAMOND DETECTORS

During the 1960s and 1970s, the attractive properties of diamond detectors were demonstrated on highly selected, low impurity, natural diamonds with outstanding electrical properties [2, 3]. However, the size, cost and variability of natural diamonds limited their use at that time. The development of the chemical vapor deposition growth process [4] changed the situation since this process allowed diamond to be grown with large detector area, high purity, reduced cost and reduced variability. Hence diamond became a viable option for particle detectors and the first proposals were made for their use in the high-energy physics experiments [5].

Designs for diamond particle detectors are typically based on intrinsic CVD diamond, a few cm^2 in area, a few hundred micrometers thick, with electrical contacts deposited on opposite sides of the diamond bulk. Prior to depositing electrical contacts the diamond surfaces are polished to remove material from the substrate side and planarize the growth side. The geometry of the electrical contacts is application specific and is usually performed using a lithographic process. In this manner electrical structures may be constructed in the range tens of micrometers to centimeters. The electrical contact to the diamond bulk is made by evaporating or sputtering a carbide former, typically chromium, titanium or aluminum, which is then covered by an over-metal to facilitate an electrical connection, typically aluminum or gold. Contacts created in this manner can be removed from the diamond surface by appropriate measures, leaving the diamond surface in a state such that it can be remetalized. As a result, one may test the same diamond with different electrode patterns consecutively, e.g. a large pad, fine strips or small pixels, in the development of a specific device.

In Figure 9.1, we show the basic principle of using diamond as a particle detector. A voltage is applied across the diamond bulk to obtain an electric field of roughly 1 V/μm. When a charged particle traverses the diamond, atoms at crystal lattice sites are excited or ionized, promoting electrons into the conduction band and leaving holes in the valence band. On average, 3600 electron–hole pairs are created per 100 μm of diamond traversed by a minimum ionizing particle [3, 6]. These free carriers drift across the diamond in response to the applied electric field, inducing a current or charge on the electrodes that can be measured. After excitation of a diamond of thickness l, ideally the average measured charge, $\langle Q\rangle$, is related to the amount of charge generated in the material, Q_{ion}, the electron and hole mobilities, μ_e, μ_h, the electron and hole lifetimes, τ_{e}, τ_{h}, the mean distance the electrons and holes move apart, called the charge collection distance, *ccd*, and the applied electric field, E, by:

$$\langle Q\rangle = Q_{ion}\left(\frac{ccd}{l}\right) = \left(\frac{Q_{ion}}{l}\right)\left[\frac{(\mu_e\tau_e + \mu_h\tau_h)E}{l}\right] \tag{9.1}$$

The signal-induced current can be estimated using energy conservation or the Shockley–Ramo theorem [7, 8]. However, traps in the material may reduce the distance the electron–hole pairs move away from one another and hence the signal size. The *ccd* is a common figure of merit for the characterization of CVD diamond detectors. The charge collection distance [9] is related to the mean signal size $\langle Q\rangle$ by:

$$cdd = \frac{\langle Q\rangle[\mathrm{e}]}{36\ \mathrm{e}/\mu\mathrm{m}} \tag{9.2}$$

where 36 e/μm is the average number of electron–hole pairs generated by a minimum ionizing particle along 1 μm in diamond. Since the charge collection distance is usually

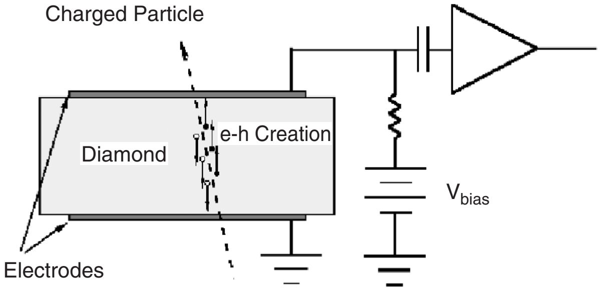

Figure 9.1 A schematic view of a diamond detector

smaller than the thickness of the CVD material, the collection distance serves as a useful tool for comparing diamonds.

Over the last ten years, there has been a substantial effort [10] to develop CVD diamond material with large collection distances and good uniformity. For most applications a charge collection distance of 200 μm, corresponding to a mean charge signal of 7200*e*, is required in order to have a large enough signal for good detection efficiency. The RD42 Collaboration [11] at CERN has been the main driver in this effort to achieve improvements in the charge collection distance and uniformity of CVD diamond. This work has now resulted in large-scale wafers of high quality polycrystalline CVD (pCVD) diamond and small pieces of single-crystal CVD (scCVD) diamond. The polycrystalline CVD diamond has grain boundaries that affect the charge collection distance, through the presence of traps, and the uniformity of signal response, through the presence of nonuniform electric fields in the material [12]. Since the collection distance increases with diamond thickness roughly linearly, with the substrate side having the poorest qualities and the growth side having the best qualities [13], diamonds for use as particle detectors are routinely thinned by removing material from the substrate side. By removing the poorest material, the effects of nonuniform electric fields are minimized and the overall charge collection distance of polycrystalline material is improved [14].

Figure 9.2 shows photographs of two recent polycrystalline CVD wafers [15] ready for test with contacts placed at 1-centimeter intervals on both sides of the wafer. In Figure 9.3 we show the measured collection distance and pulse height distribution, using a ^{90}Sr source, of a point on one of the as-grown wafers. The mean charge observed is 11340*e*, the most probable charge is approximately 8000*e* and 99 % of the distribution is above 4000*e*. The mean charge of 11340*e* corresponds to a charge collection distance of 315 μm [16].

In 2002 the first single-crystal diamond samples [15] grown using a chemical vapor deposition process [17] became available. These samples were synthesized with a microwave plasma-assisted CVD reactor using a specially prepared ⟨100⟩-oriented single crystal synthetic diamond substrate. These diamonds were typically 0.1–0.2 cm^2 in area

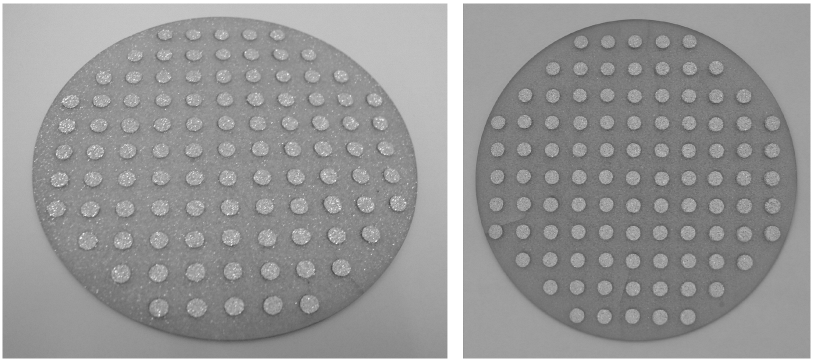

Figure 9.2 Photograph of the growth side of two full 12-cm wafers metalized with dots contacts 1 cm apart for testing. The charge collected was measured at each dot on the wafer using a ^{90}Sr source in the laboratory. The largest collection distances exceeded 300 μm on both wafers [16]. Reprinted from the RD42 Collaboration, Status Report 2006, "Development of Diamond Tracking Detectors for High Luminosity Experiments at the LHC," by H. Kagan et al, CERN/LHCC 2007-002, LHCC-RD012 (2007)

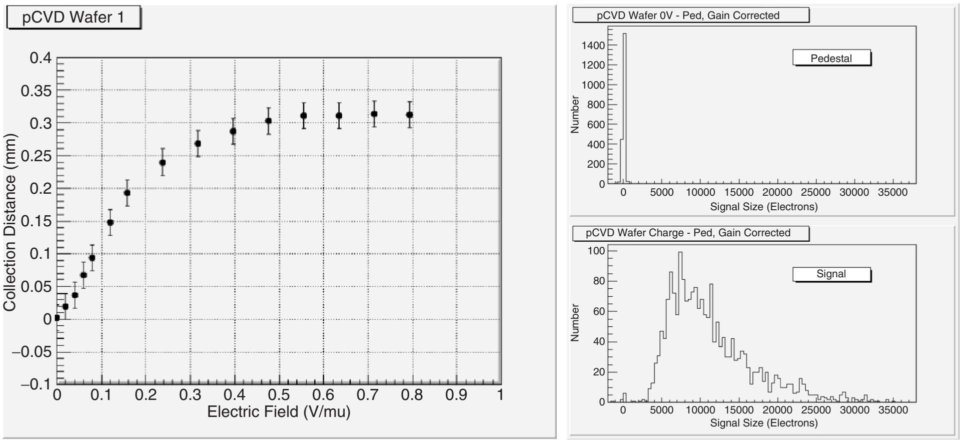

Figure 9.3 Charge collection distance as a function of electric field (left), and (right) Landau distribution measured with a ^{90}Sr source in the laboratory. The histogram shown is taken using every scintillator trigger. The upper histogram is the observed pulse height distribution with 0 V applied to the diamond. The lower histogram is the observed pulse height distribution at an electric field of 0.7 V/μm [16]. Reprinted from the RD42 Collaboration, Status Report 2006, "Development of Diamond Tracking Detectors for High Luminosity Experiments at the LHC," by H. Kagan et al, CERN/LHCC 2007-002, LHCC-RD012 (2007).

and 400–500 μm thick. In Figure 9.4 we show the pulse height spectrum observed from a 450-μm thick scCVD diamond [18]. The observed spectrum is consistent with full charge collection, i.e. a collection distance equal to the thickness of the material. The observed spectrum indicates that the most probable (MP) charge is 13400e, the Full Width at Half Maximum (FWHM) is 4000e, and there is more than a 10000e separation between the pedestal and the lowest observed pulse height. In Figure 9.5 we show the charge collection distance for scCVD diamond versus thickness of the material [18]. A clear linear relationship is evident demonstrating full charge collection out to thicknesses of 770 μm. The FWHM/MP for these single-crystal CVD diamonds is approximately 0.3, about one-third that of polycrystalline CVD diamond (compare Figures 9.3 and 9.4) and about two-thirds that of a correspondingly thick silicon detector. The narrow width of the signal spectrum indicates that single-crystal CVD detectors may be useful in spectroscopic applications. Measurements using α sources have confirmed this by demonstrating an energy resolution (FWHM) of $\Delta E/E = 0.0031$ [19].

For the development of CVD diamonds as charged particle detectors, it is useful to have a detailed understanding of the charge transport mechanisms in the material. The transient-current technique (TCT) [20] allows a direct measurement of the carrier lifetime, mobility, drift velocity, space charge, and electric field configuration in the material by observing the transient current pulse when a particle penetrates a diamond and stops near the entrance electrode. This method has been used on single-crystal CVD diamond to determine these basic semiconductor parameters of the material, including carrier lifetimes in excess of 30 ns, mobilities in excess of 1700 cm^2/Vs, and drift velocities in excess of 9×10^6 cm/s for both electrons and holes, with holes having larger mobility and drift velocity [21, 22]. These measurements explain why single crystal CVD material collects the full charge and may help in growing better polycrystalline material.

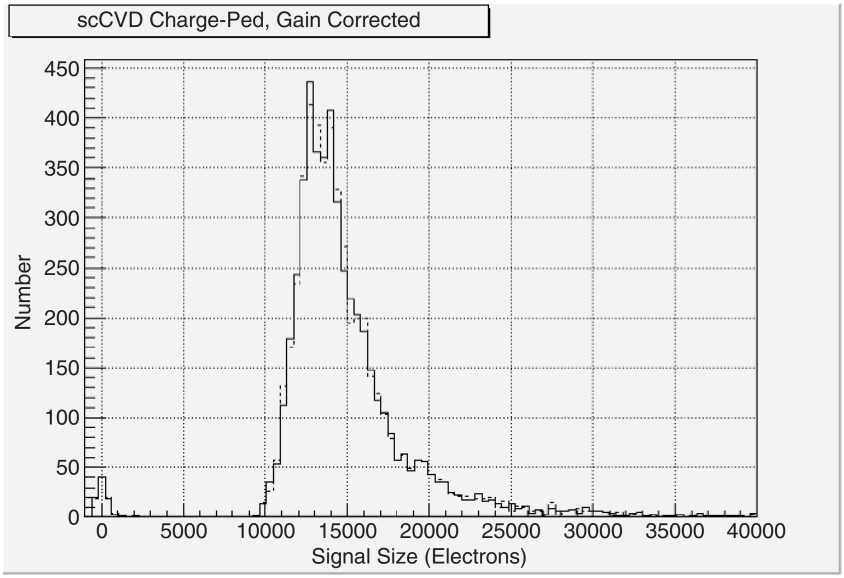

Figure 9.4 The pulse height distribution from a 450-μm thick scCVD diamond at an electric field of 1 V/μm. The two curves show the data at positive and negative bias voltages [18]. Reprinted from Nucl. Instr. and Meth., Radiation hard diamond sensors for future tracking applications by W. Adam et al , Copyright (2006) with permission from Elsevier

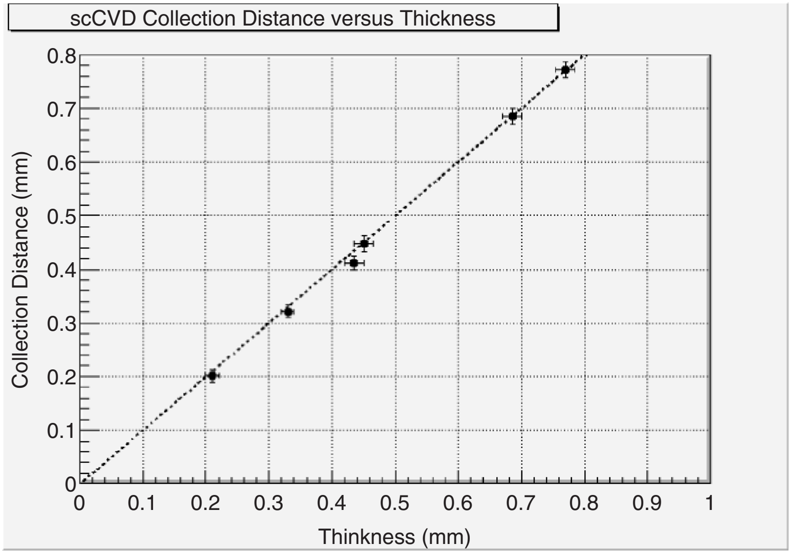

Figure 9.5 The charge collection distance versus thickness for scCVD diamonds. The line for full charge collection, i.e. charge collection distance, equals the thickness of the material and is also shown [18]. Reprinted from Nucl. Instr. and Meth., Radiation hard diamond sensors for future tracking applications by W. Adam et al , Copyright (2006) with permission from Elsevier

9.3 RADIATION HARDNESS STUDIES WITH CVD DIAMOND

In high-energy physics experiments, the detectors closest to the interaction must withstand the largest radiation dose. The absolute dose involved has changed dramatically over the years. For the ATLAS and CMS experiments at the Large Hadron Collider (LHC) of the European Organization for Nuclear Research (CERN), which will begin operation in 2009, the innermost detectors are required to withstand 50 Mrad of ionizing radiation and survive the damage due to nonionizing energy loss of 10^{15} particles/cm^2 accumulated over 10 years of operation [23]. The operational requirements for upgrades to the LHC called the superLHC (sLHC), which may begin operation as early as 2015, are an order of magnitude larger [23]. This sets the requirements for modern detector materials.

When a material is irradiated with high-energy charged and neutral particles, these particles displace atoms, producing vacancies and interstitials. The large band gap and large displacement energy of diamond make it an attractive material for these intense radiation environments. Results from proton irradiations [24, 25] show that up to 2.2×10^{15} p/cm^2 produce very little degradation in CVD diamonds with the collection distance decreasing at most 15 % while the spatial resolution improves by roughly 40 %. CVD diamonds have also been shown to withstand 250 Mrad of photon irradiation and neutron fluences of up to 3×10^{15} neutrons/cm^2 [26].

The RD42 group has now extended these irradiations to fluences up to 1.8×10^{16} p/cm^2 [27]. This corresponds to a dose of roughly 500 Mrad. At this fluence the pCVD diamond retains 25 % of its original pulse height. Figure 9.6 shows a summary of the proton irradiation results described above. In order to estimate the radiation damage effects on diamond as the collection distance increases, we have compared the collection distances for pCVD and scCVD samples before and after irradiation. The scCVD diamond is expected to be representative of the next generation high-quality polycrystalline material. By comparing the effective damage constants for the two different materials we can find the relationship between the two.

In Figure 9.6 we overlay the collection distance measurements of pCVD and scCVD samples, performed at an electric field of 1 V/μm, before and after irradiation so that zero on the x-axis corresponds to the unirradiated collection distance of the pCVD material. In addition, the scCVD fluences are shifted by -3.8×10^{15} p/cm^2. In effect, the scCVD material starts with a signal advantage that corresponds to a fluence of about 4×10^{15}. Another way of thinking of this is that our unirradiated pCVD material has that same number of trapping centers as the scCVD material after a dose of 4×10^{15} p/cm^2.

Figure 9.6 shows that all of the irradiations fall along a single damage curve given by:

$$1/ccd = 1/ccd_0 + k\phi \tag{9.3}$$

where ccd_0 is the initial collection distance, and k, the damage constant, is independent of the initial collection distance. This result now includes scCVD samples that have initial collection distances in excess of 400 micrometers. We do not expect the higher quality pCVD material to be any different. The data indicate that a single damage constant k describes the observations for both pCVD and scCVD diamond material, indicating that the damage due to irradiation is common to both.

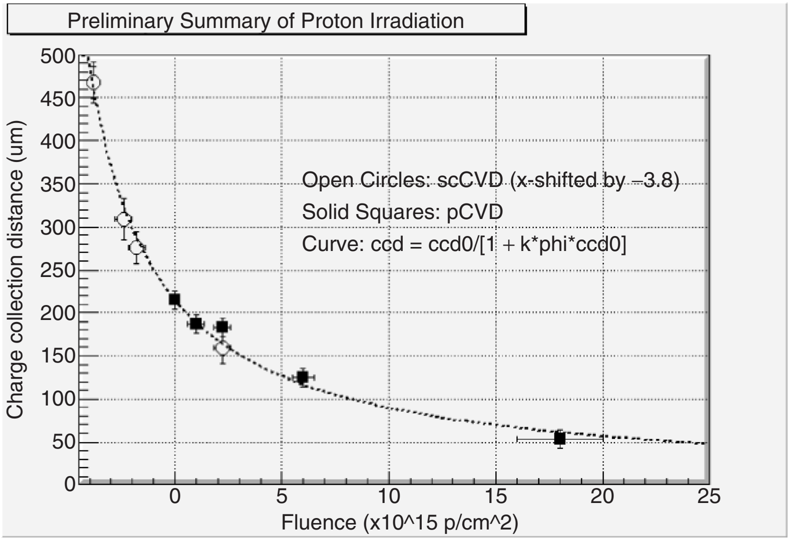

Figure 9.6 Summary of proton irradiation results for pCVD (solid squares) and scCVD (open circles) material operated at an electric field of 1 V/μm up to a fluence of 1.8×10^{16} p/cm^2. The curve is a classical radiation-damage curve given by $1/\text{ccd} = 1/\text{ccd}_0 + k\phi$ where ccd_0 is the initial charge collection distance, *k* is the damage constant and ϕ is the fluence. The scCVD data has been shifted to the left by a fluence of 3.8×10^{15}. With this shift the pCVD and scCVD data fall on a single curve, indicating that the damage due to irradiation is common to both [27]. Reprinted from the RD42 Collaboration, Status Report 2006, "Development of Diamond Tracking Detectors for High Luminosity Experiments at the LHC," by H. Kagan et al, CERN/LHCC 2007-002, LHCC-RD012 (2007)

9.4 USES OF CVD DIAMOND IN HIGH-ENERGY PHYSICS

Most detectors used in high-energy physics are based on structures that can be described as pads, strips or pixels. Figure 9.7 illustrates the three structures. Pad detectors are typically centimeters in scale and are used in measuring the general position of particles traversing a region. Specifically, this geometry is used in beam position monitors where the primary concern is how many particles are coming from beam−beam interactions versus background interactions. This type of detector may also provide timing information as to when a particle arrived at the detector.

Strip detectors were conceived to provide a high precision position measurement in one direction. The distance between the corresponding edges of the strips is called the pitch of the detector, which is typically tens to hundreds of micrometers. To provide a position measurement one compares the charge or pulse height on typically two strips. The position resolution attained depends on the signal-to-noise of the strips and ranges from $\sim$[pitch]/$\sqrt{12}$ when all the charge is on a single strip, to $\sim$[pitch]/(3.5−20) when the charge is shared between two strips. The improvement over simple digital resolution ([pitch]/$\sqrt{12}$) depends on the signal-to-noise on the charge readout of the neighboring strips [1]. Higher signal-to-noise improves the interpolation between strips enhancing the position resolution. Strip detectors are primarily used to provide tracking and vertexing information where the numbers of particles traversing the detector is not too large.

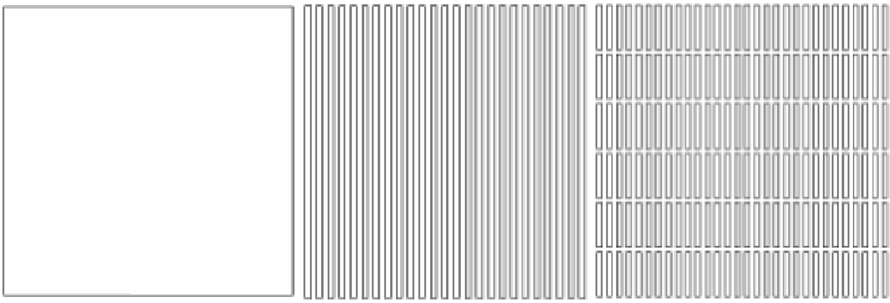

Figure 9.7 Schematic view of the main devices used in high-energy physics experiments: pad detector (left), strip detector (center), and pixel detector (right). The progression from little spatial information to two-dimensional spatial information goes from left to right

Pixel detectors were designed to provide high spatial resolution in two directions. By adjusting the pitch of a pixel detector in each direction, it is possible to tune the position resolutions in each direction. Relative to a pad detector (one element), the number of detector elements in a strip detector scales inversely with the pitch of the detector, while the number of detector elements in a pixel detector scales inversely with the product of the pitches in each direction. As a result pixel detectors are used for high precision tracking when the flux of particles is very large at the expense of a large number of electronic readout channels.

Detector prototypes based on all three geometries described above have been assembled and tested with diamond sensor material. Beginning in the early 1990s a diamond–tungsten sampling calorimeter [28] was constructed with 30 planes of 3 cm × 3 cm diamond each instrumented with three 1 cm × 3 cm pads. This prototype device achieved, for the first time, the expected energy resolution demonstrating the possibility of diamond as a charge sampling material. A few years later a 1 cm × 1 cm CVD diamond strip detector with 100 μm pitch strips was constructed and wire-bonded to a 128-channel VLSI sample-and-hold readout chip. This device achieved, for the first time, good signal-to-noise and position resolution demonstrating diamond as position sensing material [29]. Finally in the late 1990s, with the advent of reliable bump bonding connection technology, a 1 cm × 1 cm diamond was patterned with roughly 750 pixels and bonded using indium-bumps to a prototype LHC pixel detector readout chip with 50 μm × 433 μm readout pitch [30]. This device demonstrated that detectors with large numbers of channels could operate successfully in diamond. These early successes fostered the development of more sophisticated devices in each geometry as described below.

9.4.1 Pad detectors – BaBar, CDF and ATLAS beam conditions monitors

Radiation monitoring plays a crucial role in any experiment that operates a high precision tracking system close to the interaction region. Experience has shown that to protect the inner tracking detectors, systems must be provided that can abort the beams on large current spikes. In addition, radiation monitors may make measurements of the daily and integrated doses received by the inner tracking detectors and thus predict detector lifetimes, etc. At the LHC every experiment will have a diamond-based radiation monitoring system. We describe here the first diamond beam-loss monitoring system, the first system operational in a hadron collider and a unique state-of-the-art LHC system.

In 2002 the BaBar experiment [31] at the Stanford Linear Accelerator Center (SLAC) installed the first two pCVD diamond pad detectors to gain experience with the operation of diamond sensors for use as Beam Condition Monitors (BCM). The requirement was to abort the accelerator beams if the backgrounds at the experiment became too large. Diamonds were chosen as an add-on system since the then-installed silicon PIN-diode system was failing in regions of high radiation [32, 33]. The diamonds were 1 cm × 1 cm and had 8 mm × 8 mm pads. They were placed in the horizontal plane of the accelerator, 15 cm from the interaction region, 5 cm away from the PIN-diodes in the highest radiation region. The diamonds were read-out using the standard silicon PIN-diode readout board to measure the beam induced current. The main requirements of this application were small leakage current (background) after irradiation and linearity in the beam induced current (signal). Figure 9.8 is a photograph of one of the BaBar diamond detectors.

The two BaBar diamonds were operated for more than 5 years from the time they were installed until the accelerator was shut down. They are estimated to have received a dose of a few Mrad of radiation each; both performed reliably with leakage currents well below 0.1 nA and with beam-induced currents proportional to the dose rate. During the time period in which the diamonds were taking data, the two silicon PIN-diodes closest to the diamonds became radiation damaged and so BaBar relied on the diamonds to provide a measurement of the dose rates.

Figure 9.9 shows the operation of the accelerator Low Energy Ring (LER) current (upper trace), one diamond current (middle trace) and a silicon PIN-diode current near the diamond (lower trace) during the initial data taking of the BaBar experiment with diamond detectors. During the 8 hours displayed, two aborts occurred. The first abort was due to an acute spike in the dose rates; the second abort was due to a smaller but longer-lived increase in the dose rates. Both aborts are seen in the diamond and silicon sensors. During this data taking, before the silicon was radiation damaged, the signal

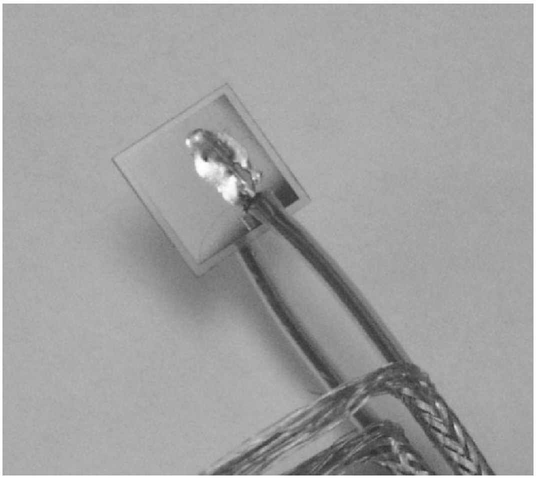

Figure 9.8 A photograph of one of the pCVD diamonds prepared for beam condition monitoring in the BaBar experiment. The pad contacts on the diamond had gold over metal so the electronic leads could be soldered to the pad

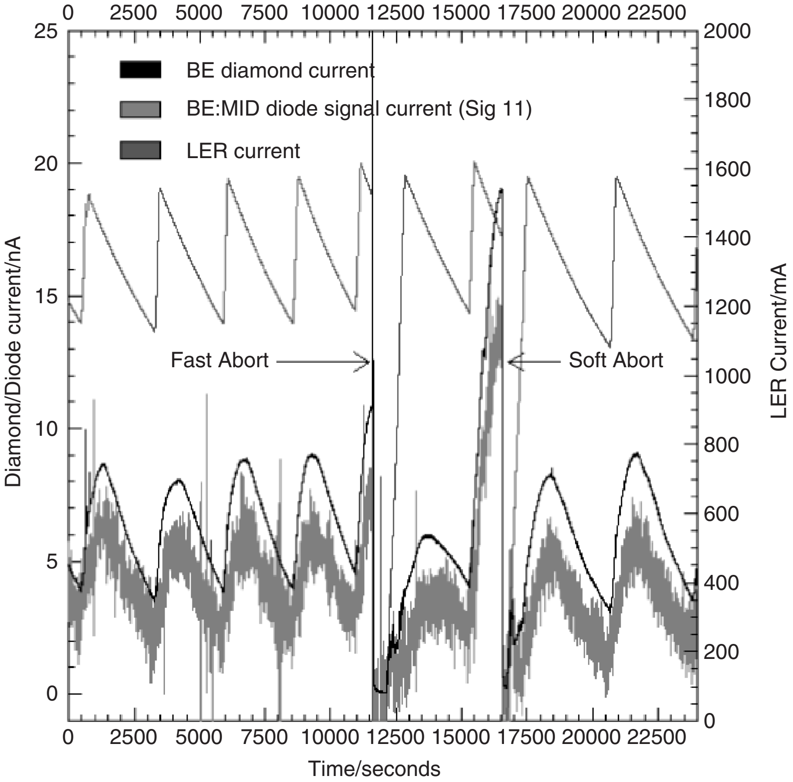

Figure 9.9 A comparison of a pCVD diamond sensor and a silicon PIN-diode monitoring radiation in the BaBar silicon tracker. During this data taking, the beam current (upper trace) gradually decreases between successive fills of the storage ring. The diamond sensor current (center trace) is comparable to that of the silicon PIN-diode (lower trace). At two points the beam is aborted. The first abort is due to an acute spike in the dose rates; the second abort is due to a smaller but longer lived increase in the dose rates. Both aborts are seen in the diamond and silicon sensors [33]. Reprinted from IEEE Trans. Nucl. Sci, Radiation monitoring with diamond sensors in BABAR by A. Edwards et al, IEEE Trans. Nucl. Sci. 51, 4, 1, 1808 Copyright IEEE (2004)

responses of the silicon detector and diamond detectors were similar. After exposure to a few Mrad the diamonds did not show any degradation of signal and performed as expected. The experience was the first use of diamonds in any high-energy physics experiment.

The performance of an experiment operating at a hadron collider can be severely degraded by beam instabilities where the high intensity, high energy, particle beams can be accidentally deflected into the experiment and hence damage important detector components. To protect the experiment from such accidents, fast, radiation hard beam condition monitoring detectors need to be installed which, if beam instabilities are detected, abort the beam safely and on the shortest time scale possible. Diamond detectors are ideal for this application. The largest beam monitoring system based on diamond sensors, currently in operation, protects the CDF experiment [34] at the Fermilab Tevatron. Thirteen 1 cm ×1 cm pCVD diamonds are installed in the CDF collision hall [35], and Figure 9.10

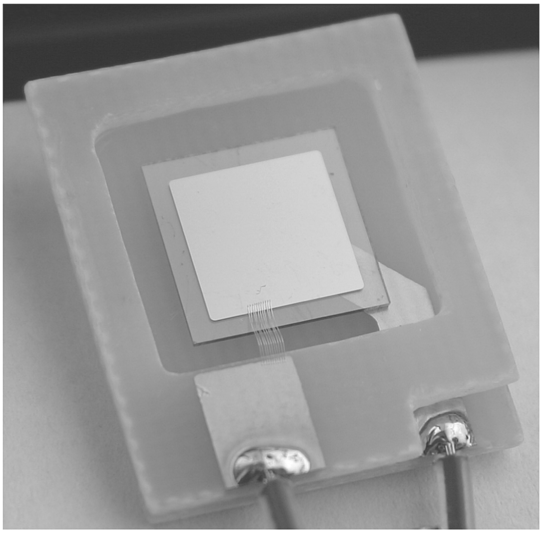

Figure 9.10 A photograph of one of the pCVD diamonds prepared for beam condition monitoring in the CDF experiment. The diamond was glued on a copper line and wire bonded to a second copper line. The pad contacts on the diamond were aluminum over metal so the pad could be wire bonded

shows one detector in an open package. Eight of these are immersed in the tracking volume in CDFs 1.4-T magnetic field. The tracking-volume diamonds are divided into two groups of four located upstream and downstream of the interaction point. Five additional diamonds are installed outside the CDF tracking volume, near the legacy abort system; a set of ionization chambers similar to those used monitor beam losses in others parts of the Tevatron accelerator.

The CDF diamonds are DC coupled and beam-induced currents are read out over 80 m of coaxial cable using custom built read-out boards that provide a time resolution of 20 μs. Figure 9.11 shows the response of two diamonds during the sequence of accelerator events leading to proton–antiproton collisions. One is located 2.0 cm from the beam inside the tracking volume, while the other is located 20 cm from the beam at a point outside the tracking volume. One can see the clear advantage of the diamond closer to the beam line and interaction point, as it is sensitive to the structure of all the accelerator events, while the diamond outside cannot resolve these. Both diamonds provide similar signals and are read out identically. However, the beam-induced current of the inner diamond is approximately an order of magnitude larger than the one outside, corresponding to the difference in radiation fields at the two locations. This system has been operational in CDF since 2006 and has been the primary abort system since 2007.

The ATLAS experiment [36] at the LHC has similar requirements for monitoring the conditions of the beams. Based on the BaBar experience, ATLAS decided in 2005 to build a BCM detector based on pCVD diamond sensors. The aim is to detect minimum ionizing particles with a good signal-to-noise ratio and a time resolution of about 2 ns. The choice of diamond sensors was motivated by the radiation hardness of diamonds, the high charge carrier velocity leading to very fast and short current signal, very narrow pulses due to short charge carrier lifetime, and very low leakage currents even after extreme irradiations.

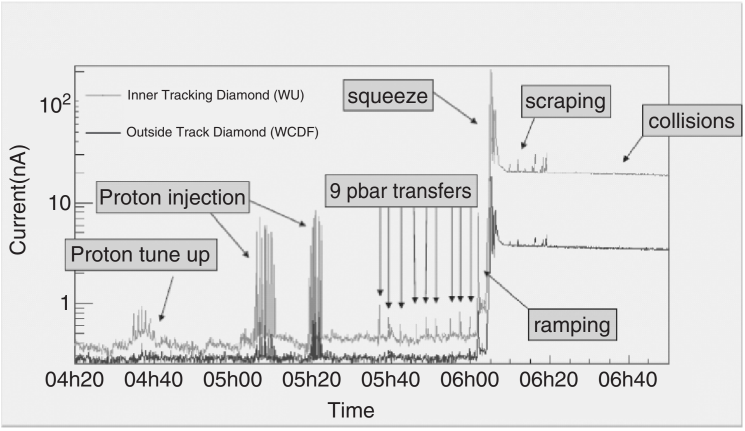

Figure 9.11 Diamond currents during beam injection at the Tevatron as a function of time. The upper trace shows the current of one of the diamonds inside the CDF tracking volume while the lower trace is the current from a diamond outside the tracking volume [35]. Reprinted from Nucl. Instr. and Meth.,Status of diamond detectors and their high energy physics applications by R. Wallny et al., Copyright (2007) with permission from Elsevier

No detector cooling is needed. The ATLAS BCM system uses fast timing information provided by the diamond to distinguish physics collisions from background. The key is that remnants from physics collisions arrive at the symmetrically located BCM stations, shown in Figure 9.12, at the same time ($\Delta t = 0$) while lost protons, or the showers they cause in the shielding surrounding the experiment, arrive on one side 6 ns before the nominal collision time and on the other 6 ns after the nominal time ($\Delta t = 12$ ns). To be able to distinguish between these two situations the BCM system must process the diamond signals, and return to baseline, in a few ns.

In the ATLAS system, a BCM module consists of a box housing two pCVD diamonds of 1 cm × 1 cm area with square contacts 8 mm × 8 mm mounted back to back. The signals from two sensors are fed in parallel into one channel of very high bandwidth

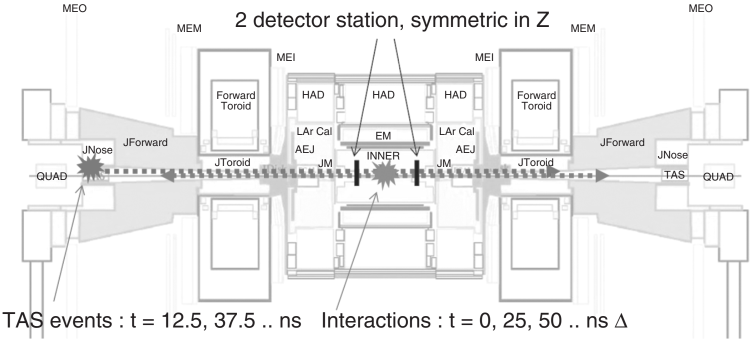
MEO
MEM
2 detector station, symmetric in Z
MEM
MEO
MEI
MEI
Forward Toroid
HAD
HAD
HAD
Forward Toroid
LAr Cal
EM
LAr Cal
JForward
JNose
AEJ
INNER
AEJ
JForward
JNose
JToroid
JM
JM
JToroid
QUAD
TAS
QUAD
TAS events : t = 12.5, 37.5 .. ns
Interactions : t = 0, 25, 50 .. ns Δ

Figure 9.12 A schematic view of the ATLAS experiment, showing the position of the symmetric BCM detector stations. Collisions occur at the star between the detector stations while background events are produced upstream (star at the far left) or downstream (not shown) of the ATLAS experiment

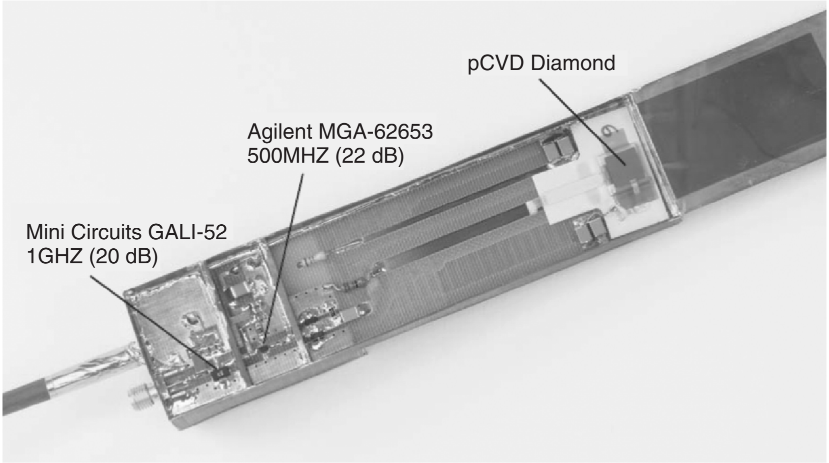

Figure 9.13 A photograph of the final module used by ATLAS for its BCM system

current amplifiers. The design aim of a module is a S/N ratio of ~10:1 in order to detect with high efficiency minimum ionizing particles [37]. The ATLAS system, consisting of 10 modules including spares, is complete and installed. Figure 9.13 shows a finished module. Figure 9.14 shows the test beam results for the timing of a final module indicating a time resolution better than 2 ns. The test also showed that for a 99.5 % efficiency the noise rate is 10^{-6}; at 97.5 % efficiency the noise rate is 10^{-9}. The final modules met all initial specifications.

9.4.2 Strip detectors

Every modern high-energy physics experiment has tracking near the interaction region. This tracking is usually designed with strip detectors to attain high precision spatial information for particles emerging from the interaction region. As stated above, the keys to high-precision spatial information are signal-to-noise and occupancy. The production of high quality polycrystalline CVD and single-crystal CVD material with charge collection distances larger than 250 μm furthered the development of tracking applications of diamond in high energy physics experiments. CVD diamond material is now of high enough quality that a typical diamond CVD strip detector has a signal to noise between 10:1 and 100:1, depending on the electronics used [38]. With a signal-to-noise in this range, diamond-based strip detectors are an option for high radiation areas.

Figure 9.15 is a photograph of a 25-μm pitch diamond strip detector. Figure 9.16 shows the spatial resolution of a diamond strip detector as a function of particle position between two strips measured using high-energy test beam particles. The test beam particle position is determined on an event-by-event basis using an external, high precision eight-plane tracking telescope. The precision of the tracking telescope is approximately 4 μm. Also shown in this figure are the positions of the strips relative to the track. Between the strips where the charge sharing is largest the spatial resolution is the best. When a particle passes through a strip the spatial resolution is the digital resolution [14.4 μm] indicating little or no charge sharing. This is the expected behavior.

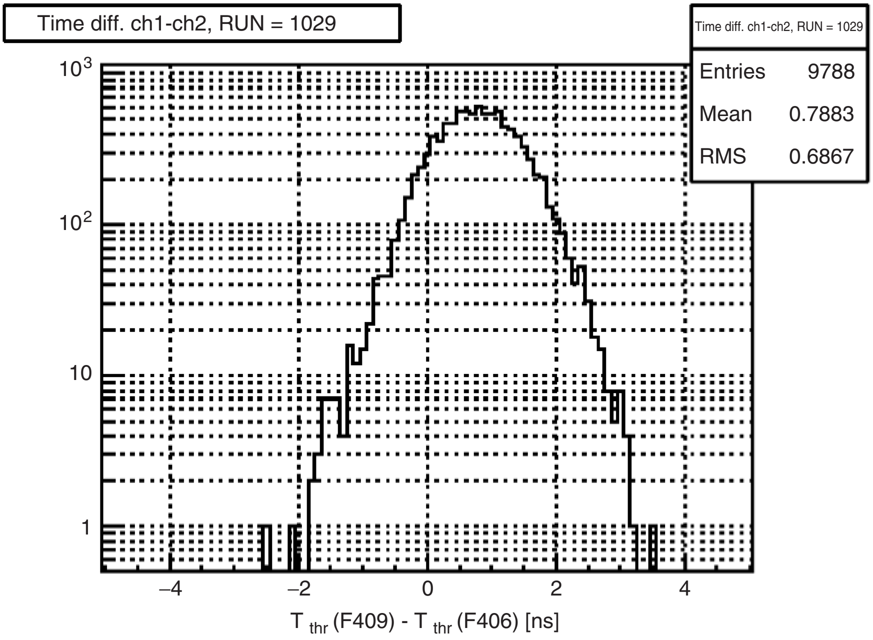

Figure 9.14 The timing difference distribution of two final ATLAS BCM modules. The RMS of the time difference distribution is 0.7 ns [37]. Reprinted from JINST 3, 02004, The ATLAS Beam Conditions Monitor by V. Cindro et al, Copyright Institute of Physics (2008)

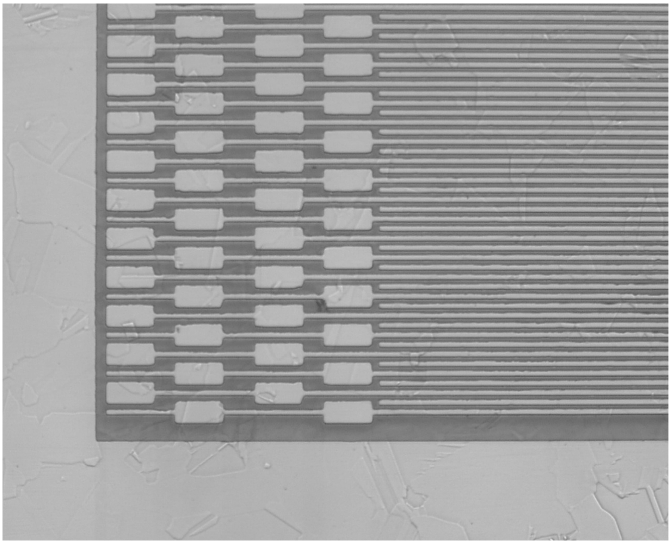

Figure 9.15 Photograph of a 25-μm pitch strip detector. The electronics is connected to the detector using the wire bond pads shown at the end of the strips

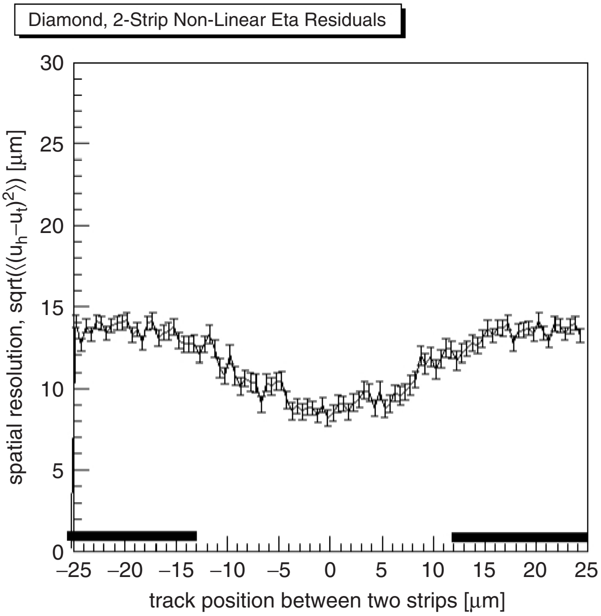

Figure 9.16 Spatial resolution versus particle position between two strips. The particle position is determined by an external, high precision, tracking telescope [38]. Reprinted from CVD Diamond Sensors for Particle Detection and Tracking, by Dirk Meier [38] Heidelberg University, http://atlasinfo.cern.ch/Atlas/documentation/thesis/thesis.html

9.4.3 Pixel detectors

At relatively low energy and low luminosity, high-precision tracking near the interaction region may be performed using strip detectors. However, as the energy and luminosity are raised the particle flux increases leading to occupancy problems, and the radiation level increases leading to detector damage. Both of these effects are lessened by smaller sensitive elements forcing the innermost layers to become pixel devices. This is the case at the LHC where the innermost detectors of every experiment are pixel detectors.

The super Large Hadron Collider (sLHC) is designed to increase the luminosity of the LHC by a factor of ten to 10^{35} cm^{-2} s^{-1}. In sLHC scenarios, the total expected fluence at a radius of about 5 cm will exceed 10^{16} particles/cm^2 [23]. Studies are now being performed to understand this radiation environment and the effect it will have on detectors. So far it has been found that at such high fluences the operational conditions are extreme. The availability of a very radiation-hard detector material and electronics will be a necessity in view of the future luminosity upgrades planned for the sLHC. Chemical vapor deposition diamond is one material being considered for such detectors [39].

The production of a pixel module requires the readout electronics to be connected to the sensors using a series of bump bonds. This connection technique, bump bonding, was developed by the Fraunhofer Institute for Reliability and Microintegration (IZM) [40]. With the connection technique in hand, the RD42 group constructed a range of diamond pixel detectors including a 2 cm × 6 cm full-diamond ATLAS pixel module (46 080 pixels) using pCVD diamond and a 1 cm × 1 cm single-chip diamond ATLAS

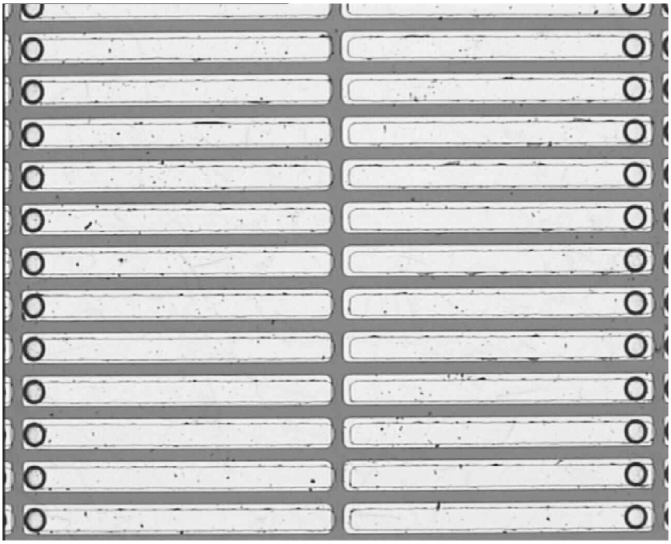

Figure 9.17 Photograph of the diamond pixel module pattern after the under-bump metal, the circles on the left and right, is deposited on the diamond

pixel module ($\sim$2000 pixels) using scCVD diamond, bump-bonded them to the ATLAS rad-hard electronics and tested the assemblies. Figure 9.17 is a close-up view of the metal pixel pattern on the diamond after the under-bump metal has been applied by the bump bonder. The bump bonding of the full module required 16 integrated circuit chips while the single-chip module required one integrated circuit chip.

Figure 9.18 shows the pulse height distribution from the single-chip module operated at an electric field of $E = 1$ V/μm for clusters with 1, 2 and 3 pixels hit [41]. The majority of clusters are single hit clusters. The signal distribution is narrow and well separated from the pedestal value. Figure 9.19 shows the tracking results from the full module obtained in the test beam. The spatial resolution observed in the full module is the digital resolution in both the x-view where the pixels have 50 μm pitch, and the y-view where the pixels are 400 and 600 μm long, since in this device there is very little charge sharing. Compared with a comparable silicon module, both single-chip and full-diamond modules exhibit smaller noise (136–145e) and operate at a lower threshold (1450–1700e) while attaining similar efficiencies (>97 %).

9.5 SUMMARY

Progress on the development of both polycrystalline and single-crystal CVD diamond detectors has been rapid. Pad, strip and pixel devices have been constructed using both pCVD and scCVD diamond. The signal size in pads, strip and pixel geometries, and their radiation resistance up to 1.8×10^{16} p/cm^2, has been characterized. Diamond sensors have found their first application in high-energy physics, beam-condition monitors. Research is underway to determine the applicability of diamond pixel detectors for the upgrade to the LHC. The next few years should see the development of larger single crystal CVD diamond devices, and additional applications for pixel and/or strip detectors.

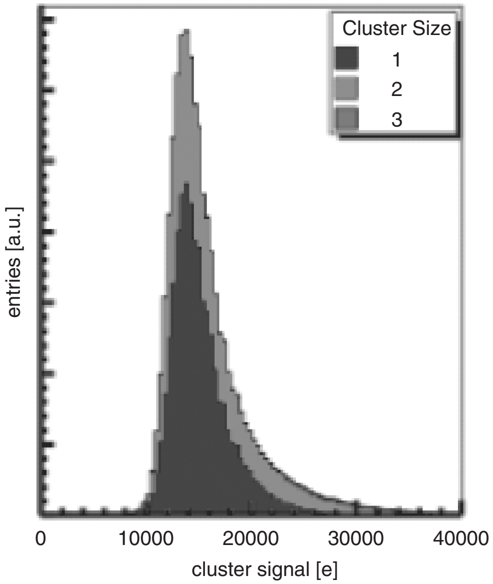

Figure 9.18 Signal charge distribution for particles projected into the scCVD single chip diamond pixel detector operated at $E = 1$ V/μm. The two distributions show the charge collected when charged particles leave signals on only one pixel (dark) or on two neighboring pixel (lighter). Almost invisible are the rare cases when signals are left on three (or more) pixels [41]. Reproduced from M. Mathes PhD thesis (2008) M. Mathes, Bonn University

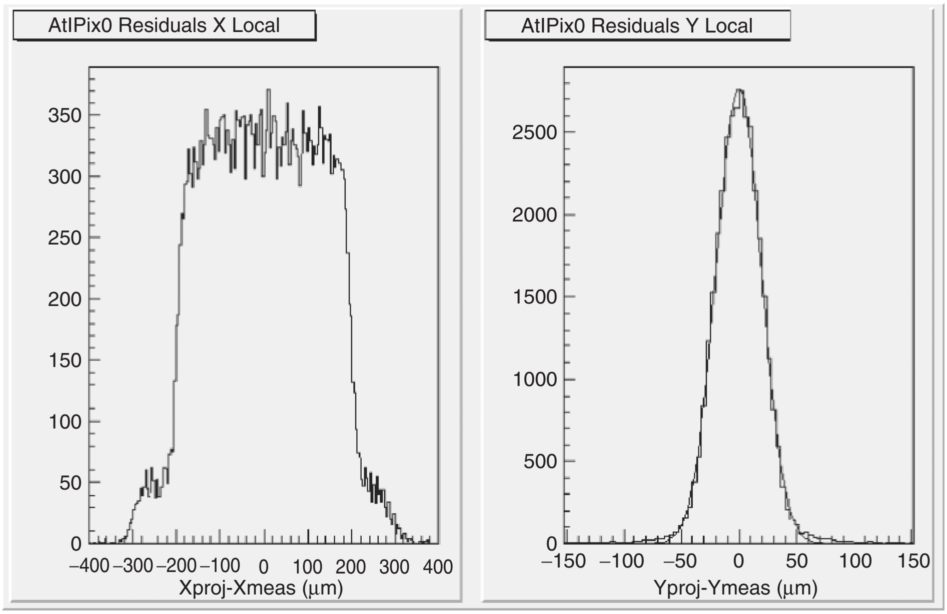

Figure 9.19 Pixel module residual distribution in both directions measured in the test beam. After unfolding the contribution from the tracking telescope the resolution is the digital resolution in both directions [41]. Reproduced from M. Mathes PhD thesis (2008) M. Mathes Bonn University

REFERENCES

[1] P. Weilhammer, *Nucl. Instr. Meth.* **A453**, 60 (2000).
[2] S.F. Kozlov *et al.*, *IEEE Trans. Nucl. Sci.* **42**, 160 (1975).
[3] C. Canali *et al.*, *Nucl. Instr. Meth.* **A160**, 73 (1979).
[4] J.C. Angus *et al.*, *J. Appl. Phys.* **39**, 2915 (1968).
[5] M. Franklin *et al.*, *Nucl. Instr. Meth.* **A315**, 39 (1992).
[6] S. Zhao, 'Characterization of the Electrical Properties of Polycrystalline Diamond Films,' PhD Dissertation, Ohio State University, 1994.
[7] W. Shockley, *J. Appl. Phys.* **9**, 635 (1938).
[8] S. Ramo, *Proc. IRE* **27**, 584 (1939).
[9] L.S. Pan *et al.*, *J. Appl. Phys.* **74**, 1086 (1993).
[10] The RD42 Collaboration, 'Development of Diamond Tracking Detectors for High Luminosity Experiments at the LHC,' CERN/DRDC 94-21/P56, (1994). RD42 is an ongoing research and development project of CERN, the European Center for Nuclear Research (http://www.cern.ch).
[11] RD42 status reports CERN/LHCC 97-3, 98-20, 2000-011, 2000-015, 2001-002, 2002-010, 2003-063, 2005-003, 2006-010, 2007-002, 2008-005.
[12] T. Lari *et al.*, *Nucl. Instr. Meth.* **A537**, 581 (2005).
[13] M.A. Plano *et al.*, *Appl. Phys. Lett.* **64**, 193 (1994).
[14] W. Adam *et al.*, *Nucl. Instr. Meth.* **A514**, 79 (2003).
[15] The diamonds shown were grown by Element Six Ltd., King's Ride Park, Ascot, Berkshire, SL5 9BP UK.
[16] The RD42 Collaboration, *Status Report 2006*, 'Development of Diamond Tracking Detectors for High Luminosity Experiments at the LHC,' CERN/LHCC 2007-002, LHCC-RD012 (2007).
[17] J. Isberg *et al.*, *Science* **297**, 1670 (2002).
[18] W. Adam *et al.*, *Nucl. Instr. Meth.* **A565**, 278 (2006).
[19] M. Pomorski *et al.*, *Phys. Stat. Sol.* **202**, 3152 (2006).
[20] M. Lampert and P. Mark, *Current Injection in Solids*, Academic Press, New York, 1970.
[21] H. Pernegger *et al.*, *J. Appl. Phys.* **97**, 073704 (2005).
[22] See also Chapter 2 by J. Isberg of this book.
[23] 1st Workshop on Radiation Hard Semiconductor Devices for Very High Luminosity Colliders, CERN, 28–30 Nov. 2001.
[24] D. Meier *et al.* (RD42 Collaboration), *Nucl. Instr. Meth.* **A426**, 173 (1999).
[25] W. Adam *et al.* (RD42 Collaboration), *Nucl. Instr. Meth.* **A447**, 244 (2000).
[26] P. Bergonzo *et al.*, *Phys. Stat. Sol.* **185**, 167 (2001).
[27] The RD42 Collaboration, *Status Report 2007*, 'Development of Diamond Tracking Detectors for High Luminosity Experiments at the LHC,' CERN/LHCC 2008-005, LHCC-RD016 (2008).
[28] R.J. Tesarek *et al.*, *Nucl. Instr. Meth.* **A349**, 96 (1994).
[29] F. Borchelt *et al.*, *Nucl. Instr. Meth.* **A354**, 318 (1995).
[30] W. Adam *et al.* (RD42 Collaboration), *Nucl. Instr. Meth.* **A436**, 326 (1999).
[31] B. Aubert *et al.* (BaBar Collaboration), *Nucl. Instr. Meth.* **A479**, 1 (2002).
[32] V. Re *et al.*, *Nucl. Instr. Meth.* **A518**, 290 (2004).
[33] A. Edwards *et al.*, *IEEE Trans. Nucl. Sci.* **51**, 1808 (2004); *Nucl. Instr. Meth.* **A552**, 176 (2005).
[34] F. Abe *et al.* (CDF Collaboration), *Nucl. Instr. Meth.* **A271**, 387 (1988).
[35] R. Wallny *et al.*, *Nucl. Instr. Meth.* **A582**, 824 (2007).
[36] G. Aad *et al.*, *JINST* **3**, S08003 (2008).
[37] V. Cindro *et al.*, *JINST* **3**, 02004 (2008).

[38] D. Meier, ‘CVD Diamond Sensors for Particle Detection and Tracking,’ PhD Dissertation, Heidelberg University, 1999.
[39] ATLAS Inner Detector R&D Proposal ATL-P-MN-002, ‘Diamond Pixel Modules for the High Luminosity ATLAS Inner Detector Upgrade,’ CERN EDMS ID 843181 (2008).
[40] Fraunhofer Institut Zuverlassigkeit Mikrointegration, Gustav-Meyer-Allee 25, D-13355, Berlin, Germany.
[41] M. Mathes, PhD Dissertation, Bonn University, 2008.

10 CVD-Diamond Detectors for Experiments with Hadrons, Nuclei, and Atoms

E. BERDERMANN AND M. CIOBANU

Gesellschaft für Schwerionenforschung (GSI) mbH Darmstadt, Germany

10.1 Introduction 227
  10.1.1 Physics background 229
  10.1.2 Heavy-ion research at GSI Darmstadt 230
  10.1.3 Future antiproton and ion research at FAIR 232
10.2 Ion interaction with diamond sensors 232
10.3 Signal processing and front-end electronics 234
10.4 Detector characterization 238
  10.4.1 Current−electric field characteristics 238
  10.4.2 Charge-collection efficiency 238
  10.4.3 Homogeneity of the detector response 242
  10.4.4 Time response 245
10.5 Applications 247
  10.5.1 Timing applications 247
  10.5.2 Ion-spectroscopy applications 250
  10.5.3 Tracking devices 251
10.6 Concluding remarks 252
10.7 Acknowledgements 253
References 253

10.1 INTRODUCTION

This chapter is dedicated to the understanding of the interaction of charged particles with CVD-diamond detectors over a wide range of ion species and energies. Specific attention is given to the description of the Front-End Electronics (FEE) used for the different applications, and to the joint operation thereof with the detector devices.

CVD Diamond for Electronic Devices and Sensors Edited by Ricardo S. Sussmann
© 2009 John Wiley & Sons, Ltd. ISBN: 978-0-470-06532-7

The progress that has been achieved on the quality of CVD-diamond throughout the last decade has shaped the history of the development of diamond detectors at GSI Darmstadt, one of the worldwide leading heavy-ion research centres. The R&D work is exclusively performed on diamond samples grown at Element Six, Ascot, UK, and supplied by Diamond Detectors Ltd (DDL), UK. The material specifications therefore refer to the denominations given by these companies (Table 10.1). The sensors are processed from freestanding films separated from the substrate used for the growth. The CVD-diamond types suitable for detector applications belong commonly to the category of electronic-grade materials, which are characterized by rather low density of atomic impurities.

The diamond programme at GSI started in the late 1990s with the development of heavy-ion beam-diagnostics detectors made of thin as grown polycrystalline CVD diamond (CVDD). Meanwhile, we have also been using detector-grade polycrystalline material, as well as homoepitaxial single-crystal CVDD grown on high-pressure high-temperature, synthetic-diamond substrates. Time-of-flight (ToF) devices for relativistic light ions and protons, or heavy-ion detectors providing particle identification in the space–charge limited current regime are made of spectroscopic-grade single-crystal material. The required thickness varies from a few micrometres for the detection of heaviest ions to about 500–700 μm for measurements of minimum-ionizing particles. Besides individual diamond-type features, the available sample area as well as cost issues are considered. Single-crystal diamond samples are small and therefore expensive for large-area devices. In close collaboration with the University of Augsburg, we recently began the investigation of wafer-scale, quasi-single-crystal diamond grown by hetero-epitaxy on iridium [1] (see also Chapter 6 by M. Schreck, in this book).

CVD diamond is currently a preferred detector material combining radiation resistance [2, 3] with many other unique detector properties [4, 5]. In this chapter, we have omitted the important radiation-tolerance discussion, which in the early 1990s motivated the development of diamond detectors for hot radiation environments [6]. Nonetheless, our current experience with CVD diamond used for strongly-ionizing and damaging radiation detection leads to the conclusion that even if diamonds are not ‘for ever’, they exhibit higher radiation resistance than do competing solid-state detector materials [7]. In contrast to the detector set-ups of colliding-beam experiments, the majority of the measurements in

Table 10.1 Denominations and Specifications of the Investigated CVDD Samples

Denominations	Specifications	Crystal structure
Intrinsic	Nondoped	Polycrystalline; single crystal
As grown	Both sides unpolished	Polycrystalline
Detector grade	Grown to ∼1 mm; subsequently lapped and polished down from the nucleation side to final thicknesses of ∼400–600 μm	Polycrystalline
Spectroscopic grade	Atomic impurities: $N < 5$ ppb; $B \ll 5$ ppb	Single crystal

hadron and nuclear physics research are performed with fixed-target spectrometers, each placed at the end of an individual beam line. The maintenance and (if unavoidable) the replacement of damaged detectors is thus easier. In the following, we will demonstrate that for almost all types and thicknesses of electronic-grade intrinsic CVD diamond of oxygen-terminated surface [8], a specific detector task can be addressed among the broad range of detector categories required in this field (Section 10.5).

10.1.1 Physics background

The central topic in the physics of hadrons and nuclei is the understanding of the structure of matter and of the fundamental interactions and forces that keep elementary particles together. These blend eventually into larger systems of dimensions that may range over 39 orders of magnitude. Quarks ($d < 10^{-18}$ m), nucleons ($d \sim 10^{-15}$ m) and nuclei ($d \sim 10^{-14}$ m), atoms ($d \sim 10^{-10}$ m) and crystals ($d \sim 10^{-9}$ m), the DNA ($d \sim 10^{-8}$ m), and the molecules ($d \sim 5 \times 10^{-8}$ m), up to the galaxies of dimensions $d \sim 10^{21}$ m, obey the same fundamental laws. Knowledge of the properties and the interactions of matter over the available range of interparticle distances in the laboratory, allows extrapolation to inaccessible regimes, providing new insights into the formation and evolution of the universe, and hence into the origins of our existence.

The basic particle families are hadrons and leptons. Hadrons are particles composed of quarks, bound by the fundamental strong force mediated by gluons. Quarks as well as electrons, muons, and neutrinos (the leptons), are elementary particles of half-integer spin that do not experience the strong nuclear force but weak interaction. Charged leptons are, in addition, subject to electromagnetic interaction, and these interactions are both described in the Standard Model of particle physics as two different aspects of a single fundamental electroweak interaction. Hadrons are classified in baryons and mesons. Baryons are neutrons and protons forming atomic nuclei and they consist of three quarks, whereas mesons are formed by a quark–antiquark pair. The confinement of quarks in hadrons is one of the remaining puzzles in particle physics research. The nucleon–nucleon interaction is mediated by light mesons (*pions*), and this nuclear force binds protons and neutrons in the nuclei.

It is therefore evident that in modern physics there is no fundamental separation between atomic-, nuclear- and high-energy physics. Only the amount of energy dissipated in the colliding systems differs, defining the species of the reaction products and their interaction distances. If the distance of closest approach between two interacting particles is large compared with the radii of the nuclei, the interaction is due to the transient electrostatic fields of the nuclei (Coulomb interaction). In the extreme opposite case of minimum-distance reactions, where very high temperatures and/or nucleon densities appear, physicists expect the quarks and their ‘bonding’ particles (the gluons) to move as free particles. It is likely that within a few fractions of a second after the ‘Big Bang’ the whole matter of the universe existed as a quark–gluon plasma [9].

In heavy-ion accelerator experiments we study the time-reversed evolution of the universe. In contrast to the primordial matter creation by fusion processes, high-energetic ion beams fragment both the projectile as well as the target nuclei to their smallest constituents by the dissipation of beam energy. In this context, every detector system used for the investigation of these constituents is a tool for a unified explanation of our existence. Diamond detectors are in demand for difficult tasks where classical sensors fail. The major drawbacks of classical semiconductor detectors operating in hot radiation environments are the progressive increasing leakage current as well as the type inversion of the doped layers building the junction. Both effects lead to a successive decrease of the sensors' depletion zone, and hence to deterioration of the detector response to impinging particles. In contrast to diamond detectors, which show a much better radiation resistance, the rate capability and the time resolution of classical devices are limited, since at least one of their charge carriers has rather low mobility (i.e., the holes in semiconductors and the ions in gaseous detectors). Plastic scintillator counters operate properly up to particle rates of about 1 MHz but become blind with radiation, whereas gas detectors are radiation hard but slow in performance, and this performance suffers at high ion rates due to space–charge effects.

The high atomic packing factor of the carbon atoms in the diamond lattice has two important consequences for diamond detectors: strong covalent bonds, which may be the key to the observed radiation hardness of diamond, and a wide band gap ($E_{\mathrm{g-Dia}} = 5.48\ \mathrm{eV}^{T=300K}$), which predict favourable detectors of very low dark current. Combined with the high chemical purity of CVDD materials, the intrinsic carrier density of diamond sensors at room temperature is $N_{\mathrm{i}} \approx 10^{-27}/\mathrm{cm}^3$, which is about 30 orders of magnitude lower than intrinsic silicon which has $E_{\mathrm{g-Si}} = 1.12\ \mathrm{eV}^{T=300K}$. Even far beyond room temperature, the sensor volume of high-quality intrinsic diamond detectors is naturally free from free charge carriers. Neither pn-junction nor cooling is required. These properties have also been confirmed after irradiation of single-crystal CVDD samples with 26-MeV protons up to fluences of about 10^{16} p/cm^2 [10]. In contrast, the depletion zone of narrow-gap semiconductor detectors (e.g., silicon) has to be controlled by a reverse-biased abrupt junction, usually consisting of a thin, heavily p-doped, and a thicker, weakly n-doped, layer. Since N_{i} depends strongly on the temperature, for a stable operation of such diode-devices at a low-noise level cooling is mandatory.

10.1.2 Heavy-ion research at GSI Darmstadt

Heavy-ion research at GSI covers an exceptionally wide range of objectives from nuclear, atomic and high-energy physics to plasma physics, material sciences, biophysics and nuclear medicine. The main probes used for the study of these topics are charged particle beams of ions from protons to uranium, accelerated from relatively low energies up to relativistic velocities. Nuclear matter is investigated over a wide range of nuclear densities (ρ) and temperatures (T). This includes normal conditions ($\rho/\rho_{\mathrm{o}} \leqslant 1$, $T < 100$ MeV, with ρ_0 the normal nuclear density), the hadronic gas phase ($\rho/\rho_{\mathrm{o}} \geqslant 2$ to 3, $T < 100$ MeV), the regime of cold neutron stars ($\rho/\rho_{\mathrm{o}} \sim 4$ and $T \approx 0$), up to the disintegration of the nuclear components into a quark–gluon plasma. Complex spectrometers are required, capable of identifying and tracking a very high number of particles per single collision at a repetition rate of more than 10^8 collisions per second.

Figure 10.1 shows, on the left-hand side, a schematic view of the existing accelerators UNILAC and SIS18, and on the right-hand side the future Facility for Antiprotons and Ion Research (FAIR) [11].

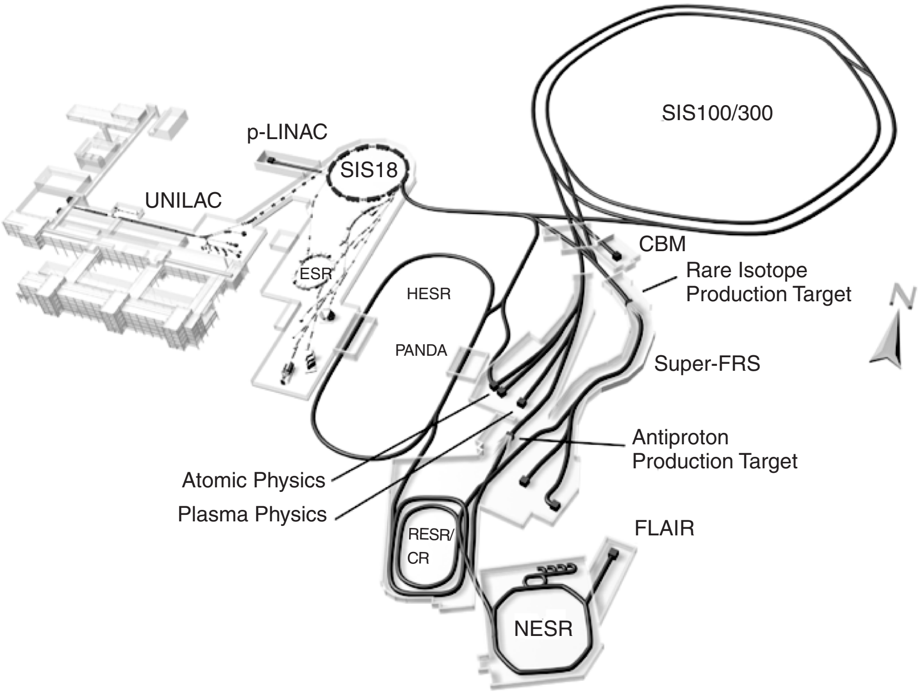

Figure 10.1 The future accelerator complex in Darmstadt. The existing accelerators (UNILAC, SIS 18) serve as injectors for the new international facility, FAIR. The double-ring synchrotron SIS100/300 will provide 10^{12} ions/spill of ion energies up to 30 AGeV, and proton energies up to 90 GeV. A system of storage-cooler rings ensures the brilliance of the beams. Each of the various experimental rings is dedicated to certain topics from the broad experimental programme [11]

For many practical reasons (not explained here) it is useful to give the energy E/A of a heavy-ion beam in units of MeV/amu or AMeV, which (classically) is a physical dimension proportional to the square of the ion velocity (β^2) giving the energy per accelerated atomic mass unit (amu = the mass number of the nucleons, i.e. proton and neutron). The kinetic energy E of a projectile with an atomic mass $A = N_\mathrm{p} + N_\mathrm{n}$ (with N_p, N_n, the number of protons and neutrons, respectively) is then E (MeV) = A × [E/A] (AMeV).

The UNILAC (Universal Linear Accelerator) produces beams of energies up to ~16 AMeV and is used for a number of low-energy atomic- and nuclear-physics experiments. The structure of neutron stars and the dynamics of core-collapse super novae are studied by observing the behaviour of condensed nuclear matter. Investigations of nuclei with extreme numbers of protons and neutrons (exotic nuclei) illuminate further the origins of the chemical elements and the processes during nucleosynthesis. UNILAC beams are post-accelerated in the SIS (SchwerIonen Synchrotron) up to 2 AGeV (ions) and up to 4 GeV (protons), respectively. Stored and cooled beams circulating in the ESR (Experimental Storage Ring) enable high-precision mass spectrometry as well as atomic physics with hydrogen-like heavy atoms, where quantum electrodynamics is tested for the highest atomic numbers [12]. Intense bunched beams impinging onto solid-state targets create hot and dense plasmas, the conditions of matter similar to those existing in stars or in the interiors of large planets. The behaviour of living cells under ion irradiation is the focus of the GSI biophysics group. The successful cancer treatment with carbon ions developed in Darmstadt [13] has led to the establishment of a clinical facility for cancer therapy with ion beams at the German Cancer Research Centre in Heidelberg (DKFZ).

10.1.3 Future antiproton and ion research at FAIR

The international facility FAIR at GSI is projected to go into service by 2012. The super-conducting synchrotrons SIS100/300 (Figure 10.1) provide primary-beam intensities of up to 10^{12} ions/spill. This will enable us to perform hitherto impossible investigations of radioactive nuclei and antiprotons with intense secondary beams, clarifying aspects of nucleosynthesis and the abundance of the elements in the universe. Ultra-slow antiproton beams in storage rings will be used to answer open questions in atomic physics. Using antiprotons as hadronic probes, the nuclear structure as well as the antinucleon–nucleon interaction will be studied with the PANDA (Antiproton Annihilations at Darmstadt) experiment. The Compressed Baryonic Matter (CBM) spectrometer is designed for the investigation of strongly interacting matter at highest possible baryon densities, where the transition from dense hadronic gas to a 'new state of matter' is expected. Fundamental aspects of quantum-chromo-dynamics, the restoration of chiral symmetry, the origin of hadron masses, or the confinement of quarks in hadrons are envisaged. Finally, there is great interest in the medical application of antiprotons for cancer therapy.

10.2 ION INTERACTION WITH DIAMOND SENSORS

Ions that slow down in matter (e.g. in diamond) undergo different processes, the strength of which depends on their kinetic energy. These are elastic collisions with the carbon atoms of the crystal lattice (Rutherford scattering), inelastic collisions with the carbon nuclei (nuclear reactions), and inelastic collisions with carbon electrons (ionization). Due to electron–nucleus interactions, the initial number of shell electrons of the projectile ions (i.e., their ionic charge state) alters in matter, making the interpretation of energy losses of partially ionized ions difficult (undefined Z_{eff} in Equation 10.1). This value equilibrates after a certain amount of material, which depends on the density of the target and on the velocity of the impinging ion.

Elastic scattering (identical in-going and out-coming ions) dominates at low energies, whereas at energies >100 AMeV the large inelastic cross-section results in the emission of additional products (Section 10.4.3). The major part of the energy dissipated in the crystal is converted to ionization. A number $N = \Delta E/\varepsilon_{\text{Dia}}$ of e–h pairs is created along the ion path given by the energy loss ΔE and by ε_{Dia}, which is the energy needed to create one e–h pair (e–h) in diamond. The non-ionizing part of ΔE is ultimately released to the lattice in the form of phonons or displacements. For a given energy deposition completely converted to ionization in totally correlated consecutive steps, the fluctuation of N would be zero. At the other extreme case, if the different competing energy-loss mechanisms contributing to ΔE were completely uncorrelated, Poisson statistics would apply with a corresponding variance of the expected number of e–h pairs $< N_0 >^2 = N_0$. Since the energy and momentum conservation law correlates lattice excitations with ionization, no one of these two pictures describes the case of real detectors. The actual variance of N is modified according Fano [14] to $< N >^2 = F \times < N_0 >^2 = F \times N_0$, where N_0 is the average number of created electrons and F is the *Fano factor* of a value between zero and one. The Fano factor would be zero for detectors where no fluctuations of N appear and unity where Poisson statistics apply. From experiments and theoretical calculations, $F \approx 0.1$ is estimated for silicon (${\varepsilon_{\mathrm{Si}}}^{300K} = 3.62$ eV) and germanium (${\varepsilon_{\mathrm{Ge}}}^{80K} = 2.95$ eV). Although no reliable measurements exist so far for the Fano factor of CVD diamond, a slightly lower value ($F_{\mathrm{Dia}} \approx 0.08$) is expected following the calculations published in Ref. [15].

The transient nonequilibrium condition produced by the ionizing energy loss in the sensors is specific for both the impinging ions of nuclear charge Z and velocity β and for the penetrated material with an ionization potential I. The Bethe formalism (Equation 10.1) describes the specific energy loss $\mathrm{d}E/\mathrm{d}x$ of ions for a wide range of velocities and ion species.

$$-\frac{dE}{dx} \propto \frac{Z_{eff}^2}{\beta^2} \cdot \left[\ln \frac{2m_e c^2 \beta^2}{I \cdot (1 - \beta^2)} - \beta^2 \right] \tag{10.1}$$

where Z_{eff} is the nuclear charge Z of the projectile modified by its atomic charge state, m_{e} is the mass of the electron, β and c are the ion and light velocities, respectively, and I the ionization potential of the target atoms.

The term $-\mathrm{d}E/\mathrm{d}x$ is also called the electronic stopping power of the detector material. New results obtained with modern spectrometers in the relativistic heavy-ion regime stimulated a more rigorous stopping power theory (Lindhard and Sørensen (LS) [16]) based on the Dirac equation. LS data are in good agreement with recent high-precision measurements carried out at GSI [17] and GANIL [18]. Relativistic ions are fully ionized ($Z_{\mathrm{eff}} = Z$) and deposit a uniform amount of energy per unit path length in matter. They lose only a few parts per thousand of their total kinetic energy in the detectors while forming a homogeneous ionization profile in the crystals. Relativistic collisions thus create mainly e–h pairs and high-energetic δ-electrons but cause very little damage, although the detector signals are high. At UNILAC energies, the ion interaction with matter differs substantially. Slow heavy ions deposit their full energy in the diamonds, and the ionization profile along the ion path is extremely inhomogeneous. The specific energy loss $\mathrm{d}E/\mathrm{d}x$ (Equation 10.1) as a function of the penetration depth shows a characteristic shape, which is called the Bragg curve (Figure 10.2) – named after the famous British physicist and chemist Sir William Henry Bragg (Nobel Prize in physics, 1915). The Bragg peak is of highest practical importance and exploited for various applications. Among them, the most prominent is cancer therapy using carbon ions and protons as developed in recent years at GSI and elsewhere. As opposed to classical treatments, ions deposit almost their full energy in the tumour volume, without damaging healthy tissue of the entrance channel. Figure 10.2 (left) shows a comparison of carbon-induced

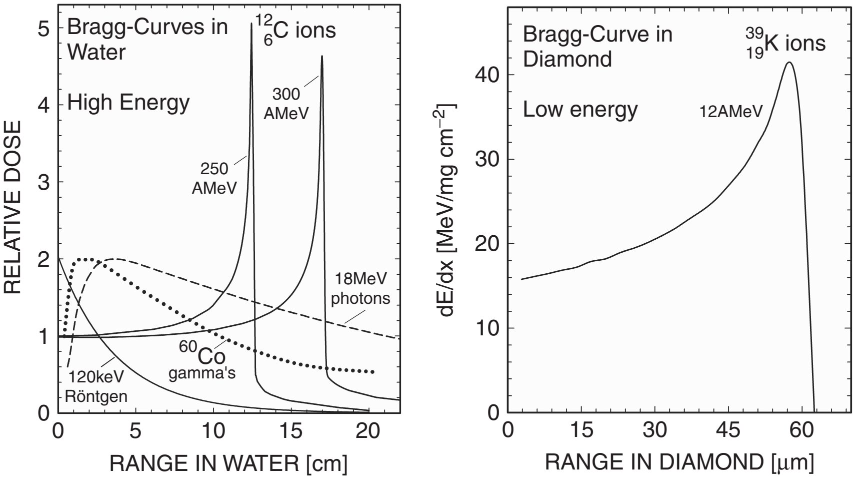

Figure 10.2 (left) Dose profiles of different ionizing-radiation sources in water phantoms. ^{12}C ions deposit the highest dose in the tumour volume (Bragg peak), adjusted by the beam energy. (right). Stopping power of ^{39}K ions of $E_{\mathrm{in}} = 12$ AMeV in diamond plotted against the ion range

dose profiles in water phantoms for two different carbon energies (^{12}C, 250 MeV, 300 MeV) compared with the irradiation profiles of γ-rays (^{60}Co of ~1.3 MeV, as well as high-energetic photons of 18 MeV) and X-rays (120 keV Röntgen). The right-hand side of Figure 10.2 is an example of a Bragg curve in diamond obtained with ^{39} K ions of 12 AMeV.

10.3 SIGNAL PROCESSING AND FRONT-END ELECTRONICS

The task of the electronic readout circuit is to maintain the original shape of the detector signal, thus enabling energy and time measurements (Sections 10.4 and 10.5) at minimum noise levels [19]. The original ultra-fast diamond-detector signal comprises a continuous frequency-dependent amplitude spectrum dominated by very high frequencies. The signal strength is given by the number of generated e–h pairs $N_{\mathrm{G}}(\text{e–h}) = Q_{\mathrm{G}}/q_{\mathrm{e}} = \Delta E/\varepsilon_{\mathrm{Dia}}$, where Q_{G} and q_{e} are the ion-generated and elementary charges, respectively, ΔE is the energy loss of the particle in the detector, and $\varepsilon_{\mathrm{Dia}}$ is the pair-production energy in diamond. Electronics applied for minimum-ionizing particle measurements has to cope with the high value of $\varepsilon_{\mathrm{Dia}}$ (~13 eV/e–h), hence the rather low number of electrons contributing to the detector signal. Conversely, for the detection of the heaviest ions, it has to support a rapid collection of the huge amount of transient space charge produced.

Figure 10.3 shows equivalent schemes of diamond-detector circuits, illustrating the signal processing in the two main biasing and readout modes used: the broadband readout (Figure 10.3a), and the charge-sensitive readout (Figure 10.3b), respectively.

In both cases, the parallel subcircuits consisting of the detector capacitance C_{D} and a current source I_{tr}, represent a diamond detector in the situation where a swift charged particle is traversing the sensor. The detector electrodes discharge promptly by the separation of the e–h pairs (signal rise time) and afterwards, they slowly recharge (signal

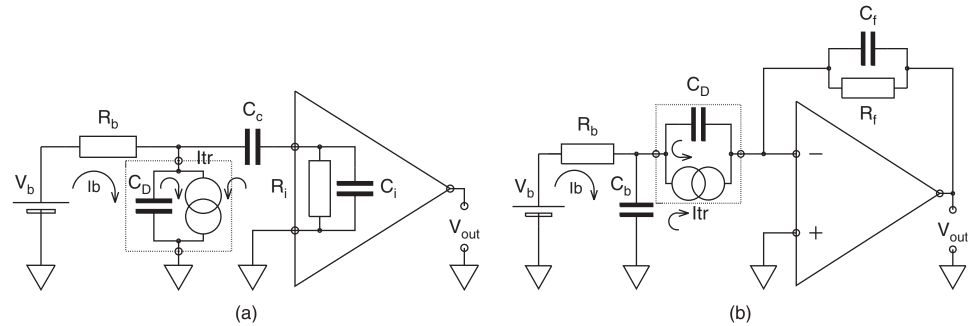

Figure 10.3 Schematics of the most used connection circuits for charged-particle detection: (a) the broadband readout, and (b) the charge-sensitive readout. The diamond detector is replaced by equivalent circuits, consisting of the detector capacitance C_D fed by a current source I_{tr} (t)

decay time) in accordance with Equation (10.2) by the flow of the transient current $I_{tr}(t)$ through the amplifier and the power supply:

$$I_{tr}(t) = dQ(t)/dt \tag{10.2}$$

where $I_{tr}(t)$ is the transient current, and $Q(t)$ is the corresponding time-dependent load of the detector capacitance C_D.

The recharge process contributes to the signal decay time with a time constant $R_b(C_D + C_P)$, where C_P (not drawn in the circuit schemes) represents the sum of stray capacitances. $I_{tr}(t)$ branches out, partially flowing through the detector and partially into the preamplifier. The biasing current I_b compensates the consumed charge until the excited circuit returns to the equilibrium state.

A typical broadband amplifier for diamond detectors [20] is an AC-coupled device, amplifying the input signal $v_i(t)$ according $v_{out}(t) = G_A v_i(t)$, where G_A is a voltage gain between 1 and 100. The capacitor C_C in Figure 10.3(a) couples $I_{tr}(t)$ into the amplifier while blocking DC current components, e.g. dark-current contributions. Broadband amplifiers have a frequency bandwidth $BW = f_H - f_L$ with $f_L \leqslant 1$ MHz and $f_H \geqslant 1.5$ GHz, a low input impedance $R_i = 50\ \Omega$ and an input capacitance C_i of ~2-5 pF, respectively. The resulting time constant R_iC_i is very short (0.1 to 0.25 ns) and the assembly is thus capable of operation at high beam intensities.

In contrast, a typical charge-sensitive amplifier (Figure 10.3b) is a DC-coupled-, inverting-, high-gain, high input-impedance amplifier with a so-called open-loop gain, $-A_0$. Due to the capacitor $C_b \gg C_D$, the noise at the amplifier input is reduced by coupling the noise produced by the bias resistor R_b to ground. Figure 10.3(b) is thus preferable for accurate energy measurements.

In order to perform charge integration, a feedback circuit consisting of a resistor R_f and a capacitance C_f is connected between the output and the input of the charge-sensitive amplifier. According to the Miller formalism [21], we evaluate the equivalent input impedance and capacitance from the equations $R_i = R_f/(1 - A_0)$ and $C_i = C_f(1 - A_0)$, respectively. For example, for $R_f = 1\ G\Omega$, $C_f = 1$ pF, and $A_0 = -10000$, the input values amount to $R_i = 100\ K\Omega$ and $C_i = 10$ nF. The resulting time constant is very long: $R_i \times C_i = 1$ ms.

Assuming a rectangular detector current pulse $I_{tr}(t)$, with I_0 the amplitude of the signal and t_{tr} the thickness-dependent transition time of the induced charge through the diamond bulk, the following Equations (10.3) give the input voltage to the amplifier:

$$\begin{aligned} 0 \leqslant t \leqslant t_{tr}: &\quad v_i(t) = I_0 \cdot R \cdot (1 - e^{-t/RC}) \\ t_{tr} \leqslant t \leqslant \infty: &\quad v_i(t) = I_0 \cdot R \cdot (e^{t_{tr}/RC} - 1) \cdot e^{-t/RC} \end{aligned} \tag{10.3}$$

The characteristic of the readout is defined by the relationship of t_{tr} to the time constant RC, with C the sum of all circuit capacitances $C = C_{\mathrm{D}} + C_{\mathrm{i}} + C_{\mathrm{P}}$, and R the sum of R_{b} and $R_{\mathrm{i}}(R = \mathrm{R_b} \times R_{\mathrm{i}}/(R_{\mathrm{b}} + R_{\mathrm{i}})$. In order to illustrate the different operation of a charge-sensitive and a broadband amplifier, we present in Figure 10.4 simulations, where a rectangular detector current pulse $I_{\mathrm{tr}}(t)$ is used as an input current to both types of amplifier (Figure 10.4a). The bottom graphs of the figure show the response to this input obtained from a charge-sensitive (Figure 10.4b) and from a broadband amplifier (Figure 10.4c), respectively. Three different cases of C_{P} are presented, corresponding to a close connection of the diamond detector with the amplifier (1 pF, dotted line), to a coaxial cable of 10 cm (10 pF, solid line), and to a cable of about 1 m length (100 pF, dashed line). Due to $C_{\mathrm{i}} \gg C_{\mathrm{P}}$ in the charge-sensitive amplifier case, the RC constant is very long, and the output pulse is independent of the stray capacitances assumed (Figure 10.4b). The output-voltage pulse of broadband amplifiers on the other hand, depends strongly on RC (Figure 10.4c). For RC $\ll t_{\mathrm{tr}}$ (i.e., when $C_{\mathrm{P}} = 1$ pF and 10 pF, respectively) the voltage pulse $v_{\mathrm{i}}(t)$ approximately follows the shape of the original current $I_{\mathrm{tr}}(t)$, whereas for large capacitances the signal is broader and of reduced amplitude.

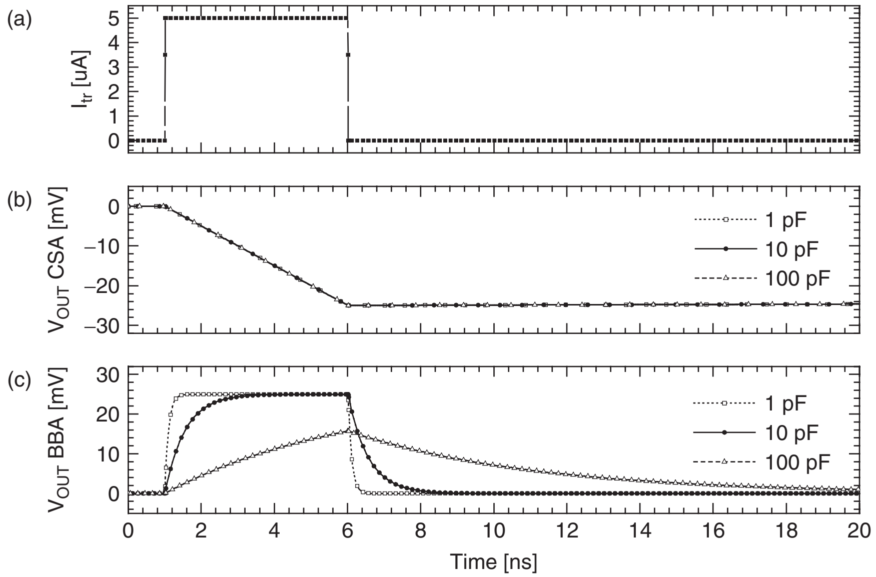

Figure 10.4 Simulations of signal processing using broadband- and charge-sensitive amplifiers. (a) Rectangular input signal in both amplifier types, representing an ion-induced charge $Q_{\mathrm{G}} = 25$ fC. (b) Output pulses of a charge-sensitive amplifier with $C_{\mathrm{f}} = 1$ pF ($S_{\mathrm{q}} = 1$ mV/fC) for three different values of stray capacitances C_{P} (1 pF, 10 pF and 100 pF, respectively). (c) Output pulses of a broadband amplifier of $R_{\mathrm{i}} = 50\ \Omega$ and $G_{\mathrm{A}} = 100$ for the same three stray capacitances. Contrary to the charge-sensitive amplifier case, the broadband amplifier response shows a significant dependence on C_{P}

In the charge-sensitive amplifier case, the ion-induced current is fully integrated at the feedback capacitance C_f, and the output signal amplitude $v_{\mathrm{out-peak}}$ obeys Equation (10.4):

$$v_{out-peak} = \frac{\int I_{tr}(t)\mathrm{d}t}{C_f} = \frac{Q_{ii}(\mathrm{e}, h)}{C_f} \tag{10.4}$$

The amplitude is here a direct measure of the ion-induced charge (i.e., the collected charge), and in the case of a complete charge collection, of the deposited energy as well. The output signals of a charge-sensitive amplifier are post-amplified by a shaping amplifier with pole-zero compensation networks. The pole-zero circuit performs a differentiation with the time constant τ_d, reducing the very long decay time of the output signal by almost two orders of magnitude. This feature of high-quality shaping amplifiers is necessary in order to prevent pile up at event rates approaching the $1/(2\pi \cdot R_\mathrm{f} \cdot C_\mathrm{f})$ limit. The differentiated signal is supplementary amplified by a low-pass filter of integration time constant τ_i. Usually $\tau_\mathrm{i} = \tau_\mathrm{d}$, and the ensemble performs a band-pass filtering (CR–RC filter) reducing further the noise. In the case of very weak signals, shaping amplifiers with multiple low-pass cells (CR–RC$^\mathrm{N}$ filter) are used.

The energy and time resolutions of a detector are high if the particle-induced signal (S) is significantly higher than the noise signal (N) of the FE amplifier. Any circuit component able to transport electrical current produces noise, the most important noise generating mechanisms in electronic devices being the thermal movement of electrons in resistive materials (thermal noise) and the fluctuations of the number of charge carriers traversing pn-junctions (shot noise). Both noise types are characterized by a white spectrum of Gaussian distributed intensity, meaning that the spectral density $P_\mathrm{n}/\Delta f = kT = v_\mathrm{n}^2/(R\Delta \mathrm{f}) = i_\mathrm{n}^2 R/\Delta f = \text{constant}$ [22]. Due to the wide diamond band gap, the detector dark current (thus the thermal noise) is negligible, and due to the absence of a junction (disregarding blocking contacts), the shot noise is negligible as well. Consequently, the S/N ratio of diamond detectors is limited by the noise of the front-end electronics.

The influence of the electronic noise to the energy resolution is described in more detail in Section 10.4.3. Regarding ToF measurements, the most important parameter is the intrinsic time resolution (σ_i) of a sensor, given by:

$$\sigma_i = \frac{\sigma_n}{\mathrm{d}v/dt} \tag{10.5}$$

where σ_n is the dispersion of the noise voltage, and $\mathrm{d}v/\mathrm{d}t$ the slope of the signal's leading edge at discriminator threshold [23, 24].

The transient-current (TC) signal slope of heavy-ion diamond detectors is very large (Section 10.4.4), at present a few orders of magnitude larger than any available broadband amplifier can follow. The electronic contribution limits the experimental rise time of the time signals (Figures 10.10 and 10.11), and thus σ_i as well as the corresponding ToF resolution (Figures 10.12 and 10.13).

10.4 DETECTOR CHARACTERIZATION

The discussions in the preceding sections show that the evaluation of a diamond sensor is inseparably linked to the intended application. CVD-diamond type and sample thickness are crucial parameters, likewise with the design of the electrodes as well as the characteristics and quality of the signal processing.

10.4.1 Current–electric field characteristics

For detector applications, the current–electric field (IE) characteristic serves to define the stable operation bias range at an acceptable leakage current. In this context, asymmetric IE behaviour is not *a priori* a crucial problem, however, it indicates some diamond or/and contact imperfections. The aim is to perform low-noise measurements at a safe positive or negative electric field for which the detector response is almost 'saturated'. This condition depends on the material quality (Section 10.4.2), and also on the actual ionization density in the diamond (Equation 10.1). For instance, a field higher than 1.5 V/μm is required in the case of polycrystalline CVDD heavy-ion detectors [25], whereas the corresponding value for measurements of minimum-ionizing particles amounts to $\sim$0.8 V/μm [26]. Note that the best performance of timing detectors is achieved at much higher electric fields than are needed for the saturation of the collected charge.

Various evaporated and/or sputtered contacts (Cr–Au, Ti–Pt–Au, Al, Pd) have been applied on polycrystalline as well as single-crystal CVDD samples to investigate possible variations in dark current behaviour and the detector signals. The present conclusion is that surface defects due to polishing [27] influence more strongly the long-term stability of the detector performance than do the species of metals applied. The signal size and shape is maintained after remetallization of the electrodes from an ohmic to a Schottky structure. Similar results have been obtained in a study with mixed electrodes. For transmission detectors readout in pulse mode, Schottky contacts are preferable. The more adhesive metal under heavy-ion irradiation is found to be pure aluminium. However, R&D on these issues is still ongoing, aiming at the elucidation of the dynamical altering properties of the diamond–contact interface [28, 29].

Figure 10.5 shows the IE-characteristics of polycrystalline (left graph) and single-crystal CVDD detectors (right graph), respectively, measured with Keithley electrometers while excluding parasitic currents, light-illumination, and humidity, as well as electrical pick-up.

Hysteretic behaviour is frequently obtained from polycrystalline sensors, whereas for single-crystal detectors this phenomenon is seldom observed. However, the presented data of those (in conjunction with the results of Section 10.4.3) contradict the expected dielectric strength of single-crystal CVDD ($\approx 1 \times 10^3$ V/μm). We therefore attribute the IE behaviour of some detectors of this type to the low quality of the diamond surface and of the detector electrodes.

10.4.2 Charge-collection efficiency

A crucial detector parameter is the electric-field dependent charge-collection efficiency CCE (E_D) of the sensor, which is the ratio of the collected charge Q_C to the charge

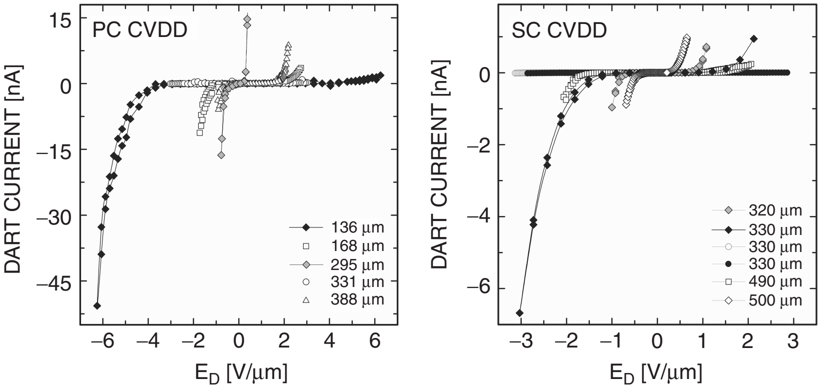

Figure 10.5 Electric-field dependence of the dark conductivity of as-grown polycrystalline diamond detectors (left) and of spectroscopic grade, single-crystal CVDD detectors (right), respectively. Although the single-crystal sensors show a factor of ~10 lower leakage current than as-grown films, the overall behaviour reveals many similarities (see text)

Q_G generated by the particle being detected. In 1932, Karl Hecht investigated the transition of charge carriers in the presence of trapping centres, studying the movement of photoelectrons in the electric field of biased AgCl crystals [30]. He discovered that the number of electrons N_x arriving at the anode decreased exponentially with the distance x of carrier generation for all the wavelengths of the excitation light source. The average carrier drift length $w_x(E)$ in the direction of the external E-field is defined as the drift distance where the number of the collected electrons has decreased to $1/e$ of N_G, and was named by Hecht the *Schubweg*. Nowadays the *Schubweg* is called the collection distance [31]. The value $1/w_x(E)$ can be understood as an E-field dependent absorption constant. Consequently, the collected charge Q_C obeys Equation (10.6a):

$$Q_C(E) = \int_0^x N_x(E)\cdot q_e\cdot\frac{\mathrm{d}x}{d_D} = \frac{N_G\cdot q_e\cdot w_x(E)}{d_D}\cdot\left(1-e^{\frac{-x}{w_x(E)}}\right) \tag{10.6a}$$

where $(q_e\cdot \mathrm{d}x/d_D)$ is the charge measured from one arbitrary electron moving a distance $\mathrm{d}x$ along E in a crystal of thickness d_D, and $w_x(E)$ is the corresponding *Schubweg*.

Equation (10.6b) is the same as Equation (10.6a) rewritten to introduce the detector parameter $CCE(E)$:

$$\frac{Q_C}{Q_G} = CCE(E) = \frac{w_x(E)}{d_D}\cdot\left(1-e^{\frac{-x}{w_x(E)}}\right) \text{ with } 0\leqslant x\leqslant d_D \tag{10.6b}$$

where $Q_G = N_G^* q_e$ is the ion-generated charge.

Hecht confirmed a proportional increase of $w_x(E)$ with E for small $w_x(E)$ values, and a saturation of the collected charge $Q_C(E)$ at $w_x(E)$ values much larger than the crystal thickness. He interpreted this observation as the approximately lossless collection of the generated charge at very high fields. Furthermore, he confirmed for the first time a significant improvement of $w_x(E)$ after blue-light irradiation of the AgCl crystals. This effect is known at present as priming or pumping of low-quality detectors (e.g.

polycrystalline CVDD sensors). It is explained as being a partial passivation of traps by previous exposure of the samples to moderate ionizing radiation [26].

The drift distance of charge carriers in solid-state detectors is, in general, a three-dimensional parameter $w(E_{x,y,z})$ described by:

$$w(E_{x,y,z}) = \sqrt{w_x^2(E_x) + w_y^2(E_y) + w_z^2(E_z)} \tag{10.7}$$

where $\mathrm{w_i}(E_i)$ are the independent drift-distance components in an arbitrary internal detector field $E = E(x, y, z)$.

Disregarding the attribute of $w_x(E)$ 'in the direction of the electric field', saturation-like bent $Q_\mathrm{C}(E)$ characteristics may be misinterpreted. Real saturation occurs only in perfect crystals biased with high fields, where charge carriers move undisturbed with a constant drift velocity in a homogeneous internal field E_x equal to the externally applied $E_\mathrm{D} = V_\mathrm{b}/d_\mathrm{D}$. In this ideal case $w(E) = w_x(E_x)$ and the $CCE(E)$ achieves a maximum value, in contrast, for instance, with the case of polycrystalline detectors revealing a small $w_x(E_x)$ while $Q_\mathrm{C}(E)$ may appear 'saturating' even at moderate bias.

In accordance with Equation (10.6b), the $CCE(E)$ is plotted in Figure 10.6 as a function of the ratio $x(E) = w_x(E)/d_\mathrm{D}$. The left-hand graph of the figure (double-logarithmic scale) shows the linear increase of $CCE(E)$ and thus of $Q_\mathrm{C}(E)$ for low values of x and w_x (implying low fields E). The right-hand graph of the figure (linear scale) illustrates the characteristics of both parameters for very high values x and w_x, which is the case for high-quality diamond detectors at high operation bias. The inset is a zoom of the high-efficiency range of the same data. The *Schubweg* $w_x(E)$ is finally extracted from the ratio $x(E)$ which belongs in Figure 10.6 to the measured $CCE(E)$. The estimation of the errors of very high $w_x(E)$ values is difficult, since a small uncertainty in the measurement of the collected charge leads to a very large variation in $w_x(E)$. However,

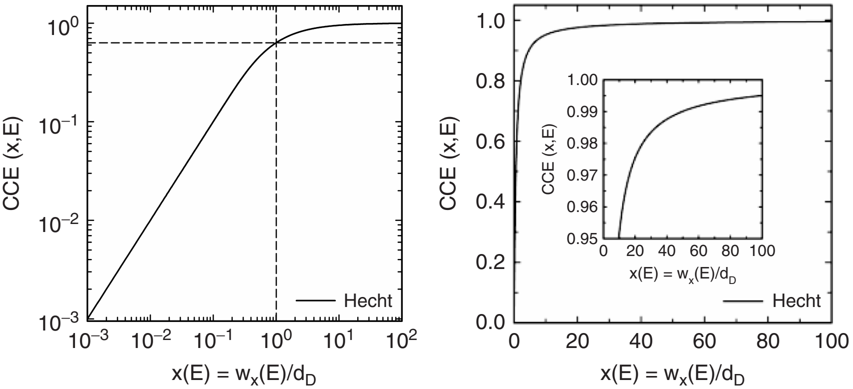

Figure 10.6 Hecht's function (Equation (10.6b)) plotted in double-logarithmic scale (left). For $w_x(E)$ much smaller than the detector thickness the CCE(E) increases linearly with $w_x(E)$ and thus with E. This is not valid anymore as $w_x(E)$ is approaching the detector thickness d_D (CCE(E) = 0.632). The same function is plotted in linear scale (right), showing in the inset a zoom of the high-efficiency range of Equation (10.6b). A CCE(E) = 0.950 is reached for $w_x(E) = 10\ d_\mathrm{D}$, whereas far beyond $w_x(E) = 100\ d_\mathrm{D}$, the still increasing CCE(E) is less than unity

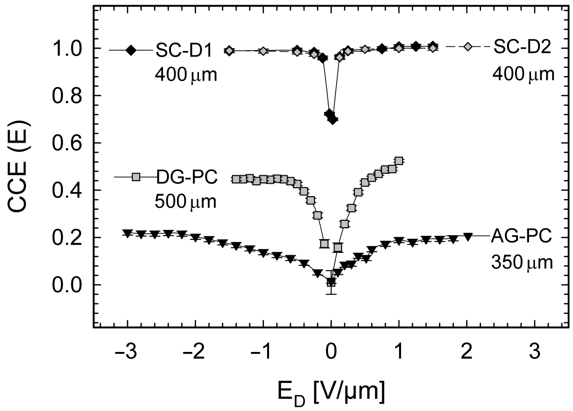

Figure 10.7 CCE(E) characteristics of various CVDD sensors. Two single-crystal detectors (SC-D1, SC-D2, diamond symbols) are compared with a detector-grade sensor (squares) and to an as-grown polycrystalline diamond detector (triangles), respectively. Both polycrystalline sensors were tested in the primed state (see text)

the detector task in a real experiment is to measure the ion-induced charge Q_C almost equal to the ion-generated charge Q_G, and this is possible with a precision of $\sim 1\,\%$, as will be demonstrated in Section 10.4.3.2.

The message of Hecht's equation is that for real detectors a *CCE(E)* equal to unity is impossible. For $w_x(E) = d_D$ the collected charge amounts to $Q_C = 0.632 Q_G$ and for $w_x(E) = 100\, d_D$ to $Q_C = 0.995 Q_G$. Figure 10.7 shows data measured with spectroscopic-grade, single-crystal CVDD detectors of 400 μm thickness (SC-D1, SC-D2, diamond symbols) as well as data from two primed polycrystalline CVDD sensors of quite different properties. One of those was produced from a diamond sample used as-grown (AG-PC, triangles) and the other from a film of detector-grade quality (DG-PC, squares), respectively (Table 10.1). In the case of the single-crystal CVDD detectors, the measurements were performed with ^{132}Xe ions of 400 AMeV, and in the case of the polycrystalline sensors with ^{90}Sr electrons of $E_\beta > 1$ MeV. The estimated *CCE(E)* errors are smaller than the symbols.

Even at highest bias, both types of polycrystalline sensor show an incomplete charge collection. In particular, the charge losses in the as-grown detector are huge, caused by the high trap density of the nucleation layers. Reproducibility of the growth process is demonstrated by the identical characteristics obtained from the spectroscopic-grade CVDD detectors. For both sensors, the onset of a high-level flat 'plateau' is observed at rather low electric fields. The results are summarized in Table 10.2.

The origin of the very high CCE values measured for both spectroscopic-grade counters is at present not clearly understood. Considering Hecht's message ($CCE < 1$), the following explanations are suggested: underestimation of the diamond stopping power for ^{132}Xe ions, $\varepsilon_{\text{Dia}} > 13$ eV/e–h, and/or charge injection from the contacts [19]. Note that the high low-field mobilities and deep-trapping lifetimes measured for single-crystal CVDD sensors [5] do not explain these results, since the $\mu \times \tau$ product (often used to evaluate polycrystalline CVDD of a collection distance much smaller than the detector thickness) has minor physical meaning for spectroscopic-grade sensors at operation bias.

Table 10.2 Charge-collection Parameters for Various Types of CVDD Detectors at $E = \pm 1$ V/µm (first-line data) and at Highest Possible Bias (Second-line data), Respectively

Diamond sample	CCE(E) CCE($E_{\max}$)	CCE($-E$) CCE($-E_{\max}$)	$x(E)$ $x(E_{\max})$	$x(-E)$ $x(-E_{\max})$	$w_x(E)$ $w_x(E_{\max})$	$w_x(-E)$ $w_x(-E_{\max})$
As grown	0.185 ± 0.01	0.140 ± 0.01	0.186 ± 0.01	0.140 ± 0.01	(65 ± 3.5) µm	(49 ± 3.5) µm
350 µm	0.195 ± 0.01	0.221 ± 0.01	0.196 ± 0.01	0.223 ± 0.01	(68 ± 3.5) µm	(78 ± 3.5) µm
Detector grade	0.490 ± 0.006	0.448 ± 0.007	0.595 ± 0.02	0.520 ± 0.01	(298 ± 6)µm	(260 ± 4)µm
500µm	–	0.448 ± 0.007	–	0.520 ± 0.01	–	(260 ± 4)µm
Spectroscopic grade D1	1.000 ± 0.008	0.989 ± 0.008	61.2	45.0	24.5 mm	18 mm
400 µm	1.000 ± 0.008	0.989 ± 0.008	61.2	45.0	24.5 mm	18 mm
Spectroscopic grade D2	1.002 ± 0.008	0.992 ± 0.008	81.8	61.2	32.7 mm	24.5 mm
400 µm	1.002 ± 0.008	0.992 ± 0.008	81.8	61.2	32.7 mm	24.5 mm

10.4.3 Homogeneity of the detector response

For ion identification in heavy-ion experiments, the detector response is required to be independent from the entrance position of the particle. Depending on energy and ion range, the amplitude A of the charge-sensitive amplifier output signal, which corresponds to the energy deposition, needs to be measured with an accuracy of 0.1–2 %. The originally narrow Gaussian energy-loss distributions are strongly affected by various detector properties: charge trapping, inhomogeneity of the film thickness, or varying electronic parameters [19]. The total experimental width δE_{Sum} of the spectral lines is given by:

$$\delta E_{Sum} = \sqrt{\delta E_G^2 + \delta E^2 + \delta E_{Dia}^2 + \delta E_{Noise}^2} \tag{10.8}$$

where δE_{G} is the uncertainty introduced by statistical fluctuations of the charge generation processes, δE the energy-loss straggling caused by different impact parameters, δE_{Dia} the diamond-crystal related term, and $\delta E_{\mathrm{Noise}}$ the electronic noise contribution.

Due to $\delta E_{\mathrm{G}} = \surd(F_{\mathrm{Dia}}\varepsilon_{\mathrm{Dia}}\Delta E)$, where F_{Dia}, $\varepsilon_{\mathrm{Dia}}$ are the diamond Fano factor and the pair-production energy, respectively, the charge-generation contribution is negligible (Section 10.2). Even for a high $\Delta E = 1$ GeV, being in the range of heavy-ion energy losses at SIS energies, $\delta E_{\mathrm{G}}/\Delta E \approx 10^{-5}$. The δE_{Dia} term assigned to the material quality is as broad as the variation of the collection distance (Section 10.4.2). Spectral lines that reveal, after noise correction, a width of the order of the tabulated energy-loss straggling δE indicate excellent spectroscopic properties of the detector material. For orientation,

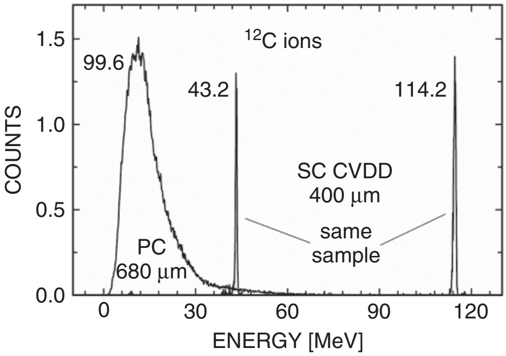

Figure 10.8 Energy spectra of monoenergetic ^{12}C ions of $E = 99.6$ MeV measured with an as-grown polycrystalline detector in the primed state (left-hand spectrum), and of ^{12}C ions of $E_1 = 43.2$ MeV (centre spectrum) and $E_2 = 114.2$ MeV (right-hand spectrum), respectively, measured with a spectroscopic-grade single-crystal CVDD sensor (see text)

δE increases proportionally with ΔE and it reaches, at SIS energies, values of $\delta E \sim 1\,\%\ \Delta E$.

10.4.3.1 Low-energy heavy-ion spectroscopy

Figure 10.8 shows energy distributions of low-energy ^{12}C ions of total kinetic energies $E_1 = 43.2$ MeV and $E_2 = 114.2$ MeV as measured with a spectroscopic-grade CVDD detector (right-hand side and mid distributions, respectively), as well as the corresponding spectrum of ^{12}C ions of $E = 99.6$ MeV measured with an as grown polycrystalline CVDD sensor in the primed state (left-hand spectrum). In all cases, the total kinetic energy of the ions is deposited in the crystals. The resolution $\delta E_{\mathrm{SUM}}/E$ of the polycrystalline sensor is equal to unity, whereas that of the single-crystal diamond detectors is 0.01 (E_1, left solid line) and 0.007 (E_2, right solid line), respectively.

The broad distribution obtained from the polycrystalline sensor responding to monoenergetic ions confirms the expected large dispersion of the collection distance, whereas its mean energy demonstrates the serious loss of ~50 % of the primary charge generated. In contrast, the narrow lines in the single-crystal diamond spectra reflect the total initial kinetic energy of the ions (plot parameter in MeV), and thus, the high potential of single-crystal devices for ion spectroscopy. However, the particle identification becomes challenging if multiple ionic charge states are involved (section 10.2, Equation 10.1). This is particularly the case for thin ΔE detectors in low-energy, heavy-ion experiments [17, 32] in which the charge states are often not equilibrated.

10.4.3.2 Ion spectroscopy at relativistic velocities

At the Fragment Separator (FRS) of GSI [17], ^{58}Ni ions of 650 AMeV were used to compare the particle-identification properties of as-grown polycrystalline sensors with the potential of silicon detectors (Figure 10.9, top graphs), and ^{132}Xe ions of 740 AMeV

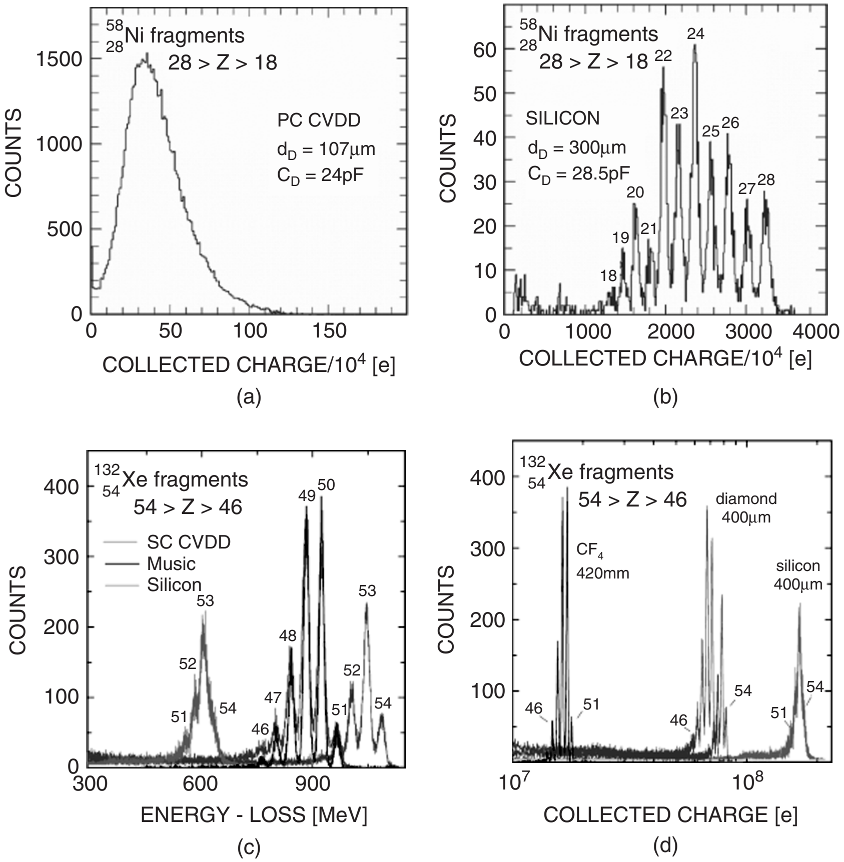

Figure 10.9 (a) and (b) ΔE spectra of ^{58}Ni fragments ($18 < Z_{\mathrm{frag}} < 28$) measured with an as-grown polycrystalline detector (left-hand plot) and with a silicon sensor (right-hand plot), respectively, calibrated in electrons. (c) and (d) ΔE spectra of ^{132}Xe fragments calibrated in MeV (left-hand plot) and in electrons (right-hand plot), respectively. Blue data belong to the single-crystal CVDD detector ($46 < Z_{\mathrm{frag}} < 54$), red data to the silicon sensor ($51 < Z_{\mathrm{frag}} < 54$), and black data to the MUSIC chamber ($46 < Z_{\mathrm{frag}} < 51$), respectively (see text). See plate 3

for a similar study with spectroscopic-grade single-crystal CVDD detectors (Figure 10.9, bottom graphs).

Projectile fragmentation [33] allows the simultaneous measurement of various ions, selectively transferred with a momentum resolution $\Delta(B\rho)/(B\rho) = 10^{-4}$ from the FRS target to the last focal plane. For a given setting of the FRS magnets, a limited range of fragments with corresponding magnetic rigidity is transferred, and the relative intensities of the transmitted ions measured are defined by the transport function of the FRS for that setting. In reality, the fragmentation cross-section decreases exponentially with Z.

Each fragment of nuclear charge Z ranging from Z_{proj} to Z_{proton} represents a different ionization density ($\propto Z^2/\beta^2$) in the counters. The velocity of heavy fragments is almost equal to the projectile velocity. The diagnostics used for particle identification includes Multiple-Sampling Ionization Chambers (MUSIC) placed in front and behind the test sensors. Note that MUSIC chambers [34] are the state-of-the-art detectors for the high-resolution spectroscopy of the heaviest ions. The FRS MUSICs operate with CF4 gas at atmospheric pressure and an active depth of 420 mm.

The data shown in Figure 10.9 are obtained using different FRS settings of individual transmission profiles, chosen to cover consecutive Z regions. The as-grown polycrystalline CVDD detector of 107µm thickness responds to every traversing particle in the range $18 < Z_{\mathrm{Frag}} < 28$ with a similar signal (Figure 10.9a), whereas the silicon sensor identifies, in this case perfectly, each of the fragments (Figure 10.9b). However, the silicon performance changes completely in the case of the space-charge limited current transients produced by fragments of $Z_{\mathrm{Frag}}\rangle 40$. The tracks of such highly ionizing ions in solid-state detectors are dense-plasma channels that seriously screen the electric field (space charge). Complex statistical processes lead to delayed charge-carrier drift and to long detector relaxation times (Section 10.4.4).

Figure 10.9(c) shows energy-calibrated, pulse-height distributions measured with a diamond detector for the ion ranges $46 < Z_{\mathrm{Frag}} < 51$ and $51 < Z_{\mathrm{Frag}} < 54$ (blue lines), respectively, along with spectra measured in the same experiment with a MUSIC detector for the range $46 < Z_{\mathrm{Frag}} < 51$ (black line) as well as with a silicon pin-diode sensor for the range $51 < Z_{\mathrm{Frag}} < 54$ (red line). Figure 10.9(d) shows the same data as Figure 10.9(c) calibrated in collected electrons. Due to the low $\varepsilon_{\mathrm{Si}}$ value the plasma density in silicon sensors is high (lower ΔE but higher ionization than in diamond), and due to the low hole mobility in silicon this space charge is persistent (very long relaxation times). The integration time of spectroscopy electronics is typically of a few microseconds, and hence only a part of the induced charge is measured, an effect known as the pulse-height defect of silicon sensors. In contrast, diamond detectors combining high pair-production energy with high mobility of both charge carriers are less affected by space charge (lower ionization, short relaxation time). The resolution $\delta E_{\mathrm{SUM}}/\Delta E = 0.013$ obtained from the single-crystal diamond sensor (Figure 10.9c, blue spectra) is almost equal to the expected energy-loss straggling δE (Section 10.4.3), and thus, astonishingly similar to the resolution of the MUSIC chamber (Figure 10.9c, black line). Both detector types reveal favourable insensitivity for high-energetic δ-electrons and background events, such as that produced, for instance, by ion interaction with the window of the vacuum system.

10.4.4 Time response

Figure 10.10 shows the transient current signals obtained from spectroscopic-grade, single-crystal CVDD detectors at different positive and negative biases. The HV potential was applied to the first electrode impinged by the particles. For the α-transients (left-hand graph) holes drift occurs for +HV (negative pulses) and electrons drift for −HV (positive pulses). Original nonamplified heavy-ion transient-current pulses are presented on the right-hand graph, whereas the α-signals are amplified with a broadband amplifier [20] of gain 100. In both studies and at every external field applied, the signal area corresponds to the expected ion-generated charge. Same coloured lines indicate equal bias.

The pulses induced by short-range (12 µm) ^{241}Am-α-particles represent the single-carrier drift at weak ionization (small-signal case), whereas the signals obtained from relativistic ^{132}Xe projectiles illustrate the dual-carrier drift at strong ionization (SCLC case). The shorter negative pulses in the α-case demonstrate the slightly faster drift of holes in diamond [5]. The almost equal rise and decay times of the trapezoidal signals

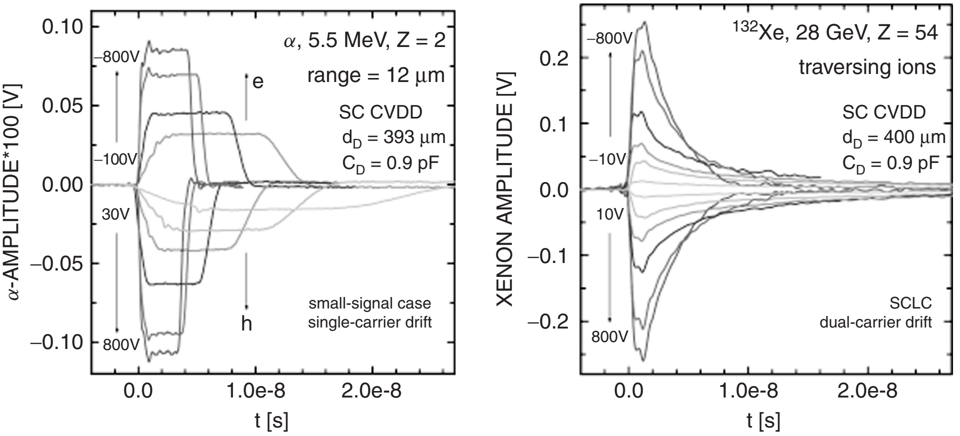

Figure 10.10 Development of the time response of spectroscopic-grade, single-crystal diamond detectors of $C_D = 0.9$ pF increasing the bias: (left) α-induced transients demonstrating the single-carrier drift in the small-signal case; (right) xenon-induced transients illustrating the dual-carrier drift at SCLC conditions. Same coloured lines indicate same bias (see text). See plate 4

reveal a fast absorption of the excess charge into the power supply. On the other hand, the decay time of the SCLC transients is dominated by the longer detector relaxation time $t_R (t_R \gg R_b(C_D + C_P)$, Section 10.3), being the time needed to expel all space charge from the counter. However, at operation bias the detector is back to equilibrium in a time $t \sim 10$ ns, which is much shorter than the integration time of the charge-sensitive amplifiers used for spectroscopy (>1 μs). Therefore, no pulse-height defects have been observed in the fragmentation spectra measured with single-crystal CVDD detectors (Section 10.4.3).

With respect to the time measurements, some additional issues have to be considered. The bias resistor R_b must be optimized to ensure constant voltage on the electrodes at all times. The 'speed' of a counter depends on the relationship of the ion-generated charge Q_G to the bias-induced charge $Q_b = C_D V_b$. The ultra-fast rise and decay time of the TC signals is supported if that charge reservoir reloading the electrodes is high enough. Important for ToF applications at relativistic velocities is the observation that the dual-carrier drift in the SCLC regime leads to a decreased FWHM of the signal while the signal rise time is almost maintained, slightly worse than in the small-signal case.

Figure 10.11 shows a similar study performed with primed as-grown polycrystalline sensors at constant external electric field. Two different samples were tested using 5.5 MeV α-particles (left-hand graph) and ^{84}Kr ions of 55 GeV (right-hand graph), respectively. The signal widths are in both cases dominated by the large detector capacitances.

Obviously, no significant difference is detected between the α-induced small signals and the SCLC transients of relativistic ^{84}Kr ions. The ion-generated charge is in both cases randomly quenched in the grain boundaries. However, if the amplitudes are well above discriminator threshold, polycrystalline CVDD devices providing narrower pulses than single-crystal sensors are preferable for high-rate counting and ion-ToF applications. In contrast, the noise of the broadband readout prevents its use for minimum-ionizing particle timing.

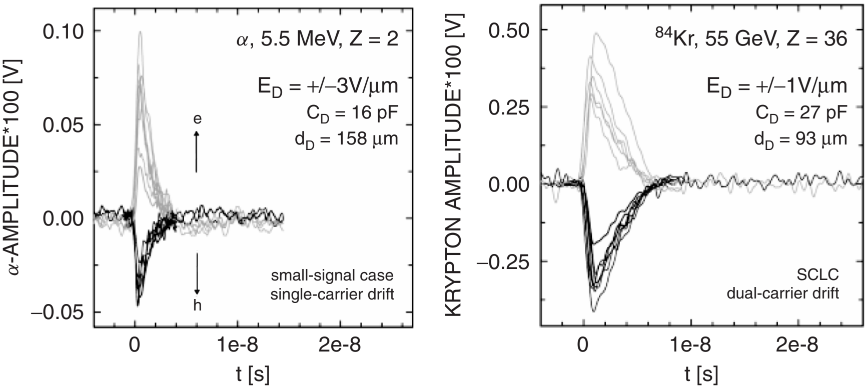

Figure 10.11 Time response of as-grown polycrystalline sensors at constant bias. (left) Response of a detector with $C_D = 16$ pF to 5.5 MeV α-particles obtained at $E_D = \pm 3$ V/μm. (right) Response of a sensor with $C_D = 27$ pF to ^{84}Kr ions of 55 GeV obtained at $E_D = \pm 1$ V/μm (see text)

10.5 APPLICATIONS

Due to the low Z of carbon, diamond sensors are advantageous low-background, front-end detectors. We classify diamond detectors with respect to the most important property concerned, which is the fast time response in timing applications (Section 10.5.1) and the homogeneous high-efficiency signal in spectroscopy applications (Section 10.5.2). Particle tracking is a mixed mode of operation (Section 10.5.3). In the following we present a selection of CVDD detectors developed at GSI Darmstadt.

10.5.1 Timing applications

Two subcategories of operation are distinguished: particle counting and ToF measurements. The short leading flank of the transient-current signal is used in both cases to define the time in which a particle traverses the detector. The optimization of the detector thicknesses and circuit capacitances is crucial. A large signal slope dv/dt is required in ion-ToF measurements (Section 10.3) in order to minimize the time walk $\Delta t(A)$ at the discriminator threshold (where A is the signal amplitude). This is particularly important in the case of polycrystalline sensors that show large variation of the signal shape (Figure 10.11). In addition, for particle counting and ToF of randomly impinging particles at ion rates beyond 100 MHz, the FWHM of the signals should be about 10-times shorter than the reciprocal value of the particle rate.

10.5.1.1 Beam-diagnostics detectors

As-grown polycrystalline CVDD detectors equipped with fast leading-edge discriminators can monitor single-ion rates up to 1 GHz per detector channel [35]. In order to adjust the single-channel rate to this value, detectors with adequate segmented electrodes defining the pad capacitance are applied. For heavy-ion beam profiling the monitors are equipped with strip/pixel motifs of sub-millimetre scale. However, the detection of highly focused beams (beam spots $\ll$ 1mm^2) with such sensors is not recommended. Instead, single-crystal sector devices metallized with quadrant electrodes are used, which control beam-size and position by the individual ratios of the sector signals [27].

At particle rates $>10^{10}$ ions/s, the pulses of individual ions overlap and the absolute number of single particles per bunch is extracted by normalizing the integrated bunch current to the current expected from a single ion. Due to their reduced collection efficiency, the polycrystalline sensors lead in this case to serious measurement errors. Thus, monitors made of single-crystal CVDD material are preferable. On the other hand, polycrystalline sensors are without competition in the high-frequency time-structure analysis of fast and slow extracted heavy-ion beams. A variety of beam-diagnostics detectors developed at GSI is presented in [35] and [36].

10.5.1.2 Ion-therapy detectors

Position-sensitive carbon-ion dosimetry of $\sim$1–2 % precision can be performed with large-area as-grown, polycrystalline, carbon-ion dosimeters operating as high-speed, single-particle, beam-monitoring devices [37]. This type of diamond is further considered for heavy-ion thermoluminescence dosimetry (TLD) [38], replacing the presently applied LiF detectors which show fast local saturation. For the clinical facility in Heidelberg, ionization chambers made of single-crystal CVD diamond are investigated for dosimetry over the full ion range ($1 < Z < 6$) provided.

10.5.1.3 Focal-plane detectors of ion spectrometers

The world's largest monolithic CVDD detector in operation is the 60 mm ×40 mm detector that was installed in August 2000 as the focal-plane detector of the magnetic ion spectrometer for atomic-physics studies [35]. The position-sensitive strip detector (32 strips of 1.7 mm width) enables high-resolution charge-state spectroscopy and lifetime measurements up to the heaviest ions by the measurement of the elastically scattered, projectiles in a target foil. The ejectiles of different, few electron, ionic-charge states emitted thereby are deflected by the magnetic field onto the focal plane of the spectrometer, where they are identified according to their magnetic rigidity by the position of the excited diamond detector strips.

10.5.1.4 Charge-exchange detectors for the ESR ion-storage ring

The properties of highly charged heavy ions were extensively studied with cooled beams stored in the ESR (Figure 10.1). At present, gaseous multi-wire proportional counters (MWPCs) are used to detect ions after charge exchange, when kicked out from the main trace of the particles circulating in the ring. A position-sensitive as-grown polycrystalline strip detector is currently investigated as a possible upgrade. A future design, capable of operation in the high-vacuum ($\sim 10^{-11}$ mbar) chamber of the ESR is also envisaged.

10.5.1.5 ToF detectors

For the mass identification of the reaction products, ToF measurements are combined with particle tracking in a magnetic field. The time $\Delta T = \text{ToF}$, which a certain particle requires to fly through a well-defined distance L, is measured with two detectors placed at $L(t=0)=0$ (start or time-zero detector) and at $L(t=T)=L$ (stop or often ToF detector), respectively. ToF spectra are obtained by feeding Time-to-Digital Converters (TDC) with the discriminator output signals of both detectors. For start and stop detectors of similar properties, the intrinsic time resolution of each sensor is estimated from $\sigma_\mathrm{i} = \sigma_\mathrm{ToF}/\sqrt{2}$. Figure 10.12 shows ToF spectra obtained with relativistic ^{27}Al ions of 2 AGeV using detector-grade polycrystalline sensors (left-hand graph) and spectroscopic-grade single-crystal devices (right-hand graph), respectively. Both detector sets were processed with the same FE electronics and the measured intrinsic resolutions were found to be equal ($\sigma_{i-\mathrm{PC}} = \sigma_{i-\mathrm{SC}} = 28$ ps). Considering the much better S/N ratio of single-crystal devices, it is obvious that this value is limited by the electronic noise and (in the specific measurement presented) by the 50 ps resolution of the TDC as well.

Among all fast applications, the most difficult task for a diamond detector is the timing of minimum-ionizing particles (MIP) with precision well-below 100 ps. In any case spectroscopic-grade single-crystal material is required. However, even if the CCE of this type of diamond detector is approaching unity, the low number of electrons created by a MIP in diamond (~36 e/μm) leads to a poor S/N ratio that does not match the inherent noise of the broadband readout (Section 10.3). Thick sensors create larger signals but longer dead time ($\approx$ FWHM), thus destroying the detector's rate capability (Section 10.4). Multi-layer sensors with intermediate common electrodes are useful in this case, maintaining a high signal size while decreasing significantly the rise time of the signals.

The best time resolution with minimum-ionizing particles is achieved with a ToF setup of monolithic diamond sensors (each of a thickness of 400 μm), by minimizing detector and stray capacitances. Equal intrinsic resolution of $\sigma_\mathrm{i} \gg 120$ ps was obtained with both kinds of MIP particles, high-energetic electrons from a ^{90}Sr source (Figure 10.13, left-hand graph) and relativistic 3.5 GeV protons (Figure 10.13, right-hand graph), respectively.

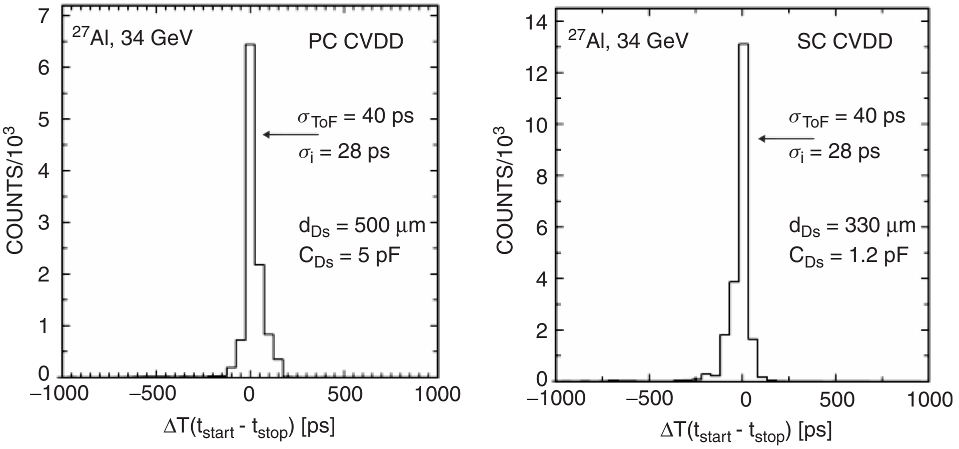

Figure 10.12 Performance of CVDD detectors in ToF measurements of relativistic light ions. ^{27}Al, 2 AGeV ToF spectrum, measured with detector-grade polycrystalline sensors (left) and with spectroscopic-grade single-crystal devices (right). The excellent intrinsic time resolution of 28 ps obtained from both detector types confirms the assumption that the ToF results are limited by the electronic noise

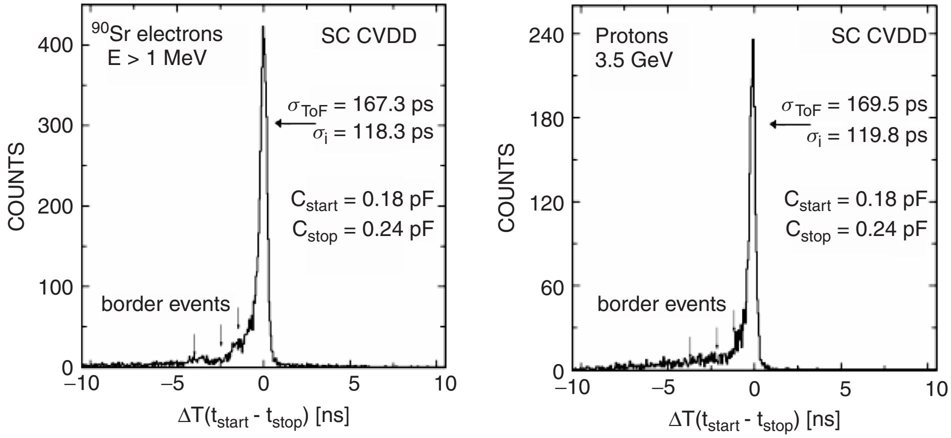

Figure 10.13 Timing properties of spectroscopic-grade CVDD detectors for minimum-ionizing particles. Intrinsic (σ_i) and ToF resolution (σ_{ToF}) measured with electrons of $E_\beta > 1$ MeV (left) and with protons of 3.5 GeV (right)

The tails of the ToF spectra are due to border events producing current transients of different timing and shape [39]. The tails can be reduced either by guard-ring electrodes, or preferably, by the use of detector samples larger than the beam spots.

10.5.2 Ion-spectroscopy applications

10.5.2.1 Target monitors

Spectroscopic-grade, single-crystal CVDD samples are developed for target monitoring of minimum kinematics walk. In UNILAC experiments, heavy-ion beams hitting thin target foils alter successively the structure and the thickness of the targets. For the correct interpretation of the experimental data, the stability of the beam energy and the target performance is monitored over a period of several weeks. The experimental set-ups are equipped with spectroscopy detectors of small area (usually silicon pin-diode sensors) placed at a certain scattering angle to the beam axis. They measure both the energy of the projectile after Rutherford scattering in the target foil and the energy of the back-scattered target ions. Shifts and broadening of the lines in the energy spectra indicate changing collision kinematics, and thus, changing target thickness and/or beam energy. Line shifting due to beam-monitor damage leads consequently to misinterpretation of the Rutherford spectra.

10.5.2.2 Energy-loss detectors

The high particle-identification potential of single-crystal diamond detectors via energy-loss spectroscopy in experiments with relativistic ions has been convincingly demonstrated as discussed in Section 10.4.3. Sensors of easy installation and operation are provided for every application where the limited size of that material is acceptable. In such measurements, diamond detectors are capable of replacing large-volume gaseous ionization chambers [39].

10.5.3 Tracking devices

The tracking of the same particle species requires only signal discrimination above the electronic threshold, which is the operation mode of a simple counting device. In experiments with various ions, the ToF resolution of diamond detectors is exploited (in addition to the ΔE signal) for particle identification. However, in measurements where the nuclear charge of the ions detected is similar, or where the interstrip chargesharing is used to improve the track resolution, the tracking devices operate similarly to ion-spectroscopy detectors.

10.5.3.1 Ion tracking at the high-energy branch of the super-FRS

For the R^3B project at FAIR, polycrystalline CVDD sensors will be used for high-intensity heavy-ion tracking through the Super-FRS up to the R^3B target. The in-beam detector device will perform tracking and ToF of exotic heavy ions at rates of $10^7 - 10^8$ HI/s, providing all coordinates (x, y, z, t) with sufficient resolution ($\Delta_{\mathrm{xyz}} \approx 100\mu\mathrm{m}$; $\Delta_{\mathrm{ToF}} < 50$ ps). In order to cover the wide range of the heavy-ions energy loss (Equation 10.1), diamond layers of different thickness will be applied, ranging from 200 μm for the lightest to 20 μm for the heaviest ions.

10.5.3.2 Ion tracking at the low-energy branch of the super-FRS

Tracking of slowed-down radioactive ion beams in NUSTAR experiments at FAIR require lowest ion-energy absorption, energy, and ToF resolutions, and high rate capability as well. A first in-beam evaluation of various polycrystalline and single-crystal CVDD detectors has been performed at the 3 MV tandem accelerator CNA-Seville. The conclusion is that single-crystal CVDD detectors are very promising for these purposes [32].

10.5.3.3 MIP tracking at FAIR

As opposed to the heavy-ion tracking devices in radioactive-beam experiments, the position resolution of the vertex device of the CBM spectrometer is required to be of the order of 3 μm. We will explore for this application the potential of quasi-single-crystal diamond grown on iridium. The challenge is to perform high-resolution, charged-particle tracking, secondary-vertex selection, and fast data readout with detectors of minimum material budget in the presence of up to 1000 charged particles at event rates of 10 MHz.

Two examples of CVDD detectors developed at GSI are shown in Figure 10.14. The largest monolithic polycrystalline sensor in use (left) which is described in Section 10.5.1.3, and a small single-crystal diamond beam monitor for highly focused beams (right) described in Section 10.5.1.1, respectively.

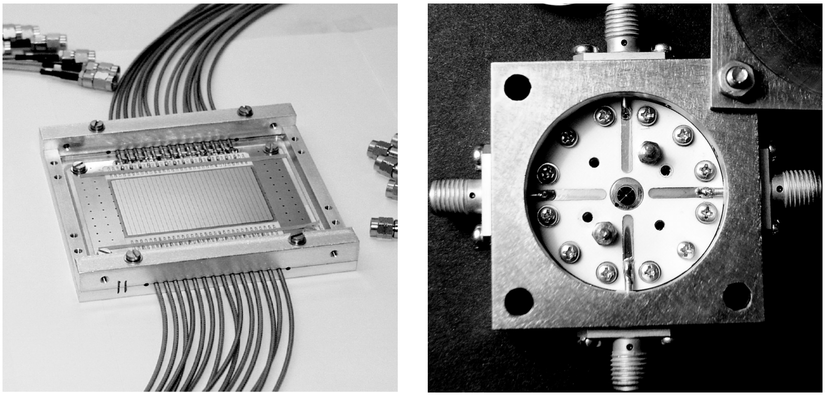

Figure 10.14 (left) The focal-plane detector of the magnetic spectrometer for high-energy atomic physics experiments, which is working since 2000 in the Cave A of GSI. The polycrystalline as grown CVDD sensor of 200 μm thickness has maximum dimensions 60 mm × 40 mm, and it is equipped with a strip electrode with 32 individually readout strips, each 1.7 mm wide. (right) Quadrant beam monitor, made of an ion-beam polished 3.5 mm × 3.5 mm single-crystal diamond plate of 50 μm thickness. The circular top electrode of 3 mm in diameter is segmented in four sectors separated by an isolation gap of 200 μm. This versatile device serves for monitoring of highly focused intense heavy-ion beams at GSI and for in-situ non-destructive X-ray beam control at the European Synchrotron Radiation Facility (ESRF) in Grenoble

10.6 CONCLUDING REMARKS

The intention of this article was to discuss the main categories of CVD-diamond detectors applied or projected in the framework of hadron, nuclear, and atomic physics research at GSI. The ultra-fast, low-background sensors meet the requirements of new-generation experiments perfectly where high particle rates are involved. The characteristic results presented in conjunction with the commonly used front-end electronics, underline the necessity to take the combined performance into account instead of considering solely the diamond quality. The crucial factor, which definitely limits the time resolution and rate capability of present diamond detectors, is the noise of available electronics with a wide bandwidth. We are confident that future sensors will benefit from the current development of microelectronic devices made of CVD diamond (See Chapters 12 to 14 in this book).

The limited size of single-crystal diamond samples is a serious drawback with respect to large-area detector systems (e.g., tracking devices). However, various important detector tasks are presented, where the actual size of the material is sufficient. The high pair-production energy of diamond is disadvantageous in measurements of minimum-ionizing particles but welcomed for the detection of highly ionizing ions. In timing measurements with ions heavier than carbon, the potential of as-grown polycrystalline sensors is higher than that of spectroscopic-grade detectors, in contrast to any particle-identification application via energy-loss spectroscopy, where polycrystalline sensors cannot be used.

10.7 ACKNOWLEDGEMENTS

This work belongs partially to the PhD thesis of Michal Pomorski, supported by the EC Project RII3-CT-2004-506078. We express our gratitude to Element Six and to DDL for the provision of excellent diamond material. We acknowledge the crew of GSI's target laboratory for sample metallization, Michael Träger for R&D support, and the NoRHDia Collaboration for fruitful joint work. We appreciate the increasing interest of the NoRHDia Users community in contributing challenging ideas for novel applications. We are grateful to A. Andronic, E. Badura, C. Kozhuharov, and C. Schmidt for comments on this manuscript. Special thanks from the corresponding author go to Christophor Kozhuharov for daily discussions concerning diamond work, and more.

REFERENCES

[1] S. Gsell, T. Bauer, J. Goldfuβ, M. Schreck, and B. Stritzker, A route to diamond wafers by epitaxial deposition on silicon via iridium/yttria stabilized zirconia buffer layers, *Appl. Phys. Lett.*, **84**, 4541 (2004).

[2] F. Hartjes for the RD42 Collaboration, Radiation tolerance of CVD diamond detectors for pions and protons, *NIM A*, **476**, 686–693 (2002).

[3] W. de Boer, J. Bol, A. Furgeri, S. Müller, C. Sander, E. Berdermann, M. Pomorski, and M. Huhtinen, Radiation hardness of diamond and silicon sensors compared, *Phys. Stat. Sol. (a)* **204**, 3004–3010 (2007).

[4] E. Berdermann, K. Blasche, P. Moritz, H. Stelzer, and B. Voss, The use of CVD-diamond for heavy-ion detection, *Diamond and Related Materials*, **10**, 1770–1777 (2001).

[5] M. Pomorski, E. Berdermann, A. Caragheorgheopol, M. Ciobanu, M. Kiš, A. Martemiyanov, C. Nebel, and P. Moritz, Development of single-crystal CVD-diamond detectors for spectroscopy and timing, *phys. stat. sol. (a)*, **203**, 3152–3160 (2006).

[6] M. Franklin, A. Frey, K.K. Gan, *et al.*, Development of diamond radiation detectors for SSC and LHC, *NIM A*, **315**, 39–42 (1992).

[7] M. Moll on behalf of the RD50 Collaboration, Development of radiation hard sensors for very high luminosity colliders, *NIM A*, **511**, 97–105 (2003).

[8] C.E. Nebel and J. Ristein, Thin-film diamond, in *Semiconductors and Semimetals*, Volume 77, R.K. Williardson and E.R. Weber (Eds), Elsevier Inc., San Diego CA, 2004.

[9] P. Braun-Munzinger and J. Stachel, The quest for the quark-gluon plasma, *Nature*, **7151**, 302–309 (2007).

[10] M. Pomorski, E. Berdermann, W. de Boer, A. Furgeri, C. Sander, and J. Morse, Charge transport properties of single-crystal CVD-diamond particle detectors, *Diamond and Related Materials*, **16**, 1066–1069 (2007).

[11] http://www.gsi.de/fair/experiments/index.html, last retr. 02/25/2008.

[12] Th. Stöhlker, A. Gumberidze, A. Kumar, R. Reuschl, and M. Trassinelli, in *Advances in Quantum Chemistry*, S. Salomonson and E. Lindroth (Eds), **53**, 57–65 (2007).

[13] G. Kraft for the Heavy-Ion Therapy Collaboration, Tumortherapy with ion beams, *NIM A*, **454**, 1–10 (2000).

[14] U. Fano, Ionization yield of radiations. II. The fluctuations of the number of ions, *Phys. Rev.*, **72**, 26–29 (1947).

[15] R.C. Alig, S. Bloom, and C.W. Struck, Scattering by ionization and phonon emission in semiconductors, *Phys. Rev. B*, **22**, 5565–5582 (1980).

[16] J. Lindhard, A.H. Sørensen, *Phys. Rev. A*, **53**, 2443 (1996).

[17] H. Geissel, H. Weick, C. Scheidenberger, R. Bimbot, D. Gardès, *NIM B*, **195**, 3–54, (2002).

[18] R. Bimbot, C. Cabot, D. Gardès, H. Gauvin, I. Orliange, L. De Reilhac, K. Subotic, and F. Hubert, *NIM B*, **44**, 1–19, (19899).

[19] E. Berdermann, A. Caragheorgheopol, M. Ciobanu, M. Pomorski, A. Pullia, S. Riboldi, M. Traeger, and H. Weick, Ion spectroscopy – a diamond characterization tool, *Diamond and Related Materials* **17**, 1159–1163, (2008).

[20] P. Moritz, E. Berdermann, K. Blasche, H. Stelzer, and B. Voss, Broadband electronics for Diamond Detectors, *Diamond and Related Materials*, **10**, 1770–1777 (2001).

[21] D. Johns and K. Martin, in *Analog Integrated Circuit Design*, John Wiley & Sons, Inc., New York, 1997.

[22] C.D. Motchenbacher, and J.A. Connelly, in *Low-Noise Electronic System Design*, John Wiley & Sons, New York, 1993.

[23] H. Spieler, Fast timing methods for semiconductor detectors, *IEEE Transactions on Nuclear Science*, **29**, 1142–1158 (1982).

[24] M. Ciobanu, A. Schüttauf, E. Cordier, N. Herrmann, K. D. Hildenbrand, Y. J. Kim, Y. Leifels, M. Marquardt, M. Kiš, P. Koczon, X. Lopez, M. Petrovici, J. Weinert, and X. J. Zhang, A Front-End Electronics Card Comprising a High Gain/High Bandwidth Amplifier and a Fast Discriminator for Time-of-Flight Measurements, *IEEE Transactions on Nuclear Science*, **54**, 1201–1206 (2007).

[25] E. Berdermann, K. Blasche, P. Moritz, H. Stelzer, B. Voss, and F. Zeytouni, First applications of CVD-diamond detectors in heavy-ion experiments, *Nucl. Phys. B* (Proc. Suppl.), **78**, 533–539 (1999).

[26] D. Meier, CVD diamond sensors for particle detection and tracking, *PhD Thesis*, Ruprecht-Karls University, Heidelberg (1999).

[27] J. Morse, M. Salomé, E. Berdermann, M. Pomorski, W. Cunningham, J. Grant, and V. O'Shea, Single-crystal CVD diamond as an X-ray beam monitor, *Diamond and Related Materials*, **16**, 1049–1055 (2007).

[28] E. Berdermann, A. Caragheorgheopol, M. Ciobanu, *et al.*, CVD-diamond detectors for spectroscopy and timing, *Proc. XLIII Int. Winter Meeting on Nuclear Physics*, I. Iori (Ed.), 371–381 (2005).

[29] R. Lovrincic and A. Pucci, Infrared spectroscopy of chromium film growth on single-crystal diamond, *GSI Scient. Report*, p197, (2006).

[30] K. Hecht, Zum Mechanismus des lichtelektrischen Primärstromes in isolierenden Kristallen, *Zeitschrift für Physik*, **77**, 235 (1932).

[31] S. Zhao, Characterization of the electrical properties of polycrystalline diamond films, *Ph.D Thesis*, The Ohio State University (1994).

[32] P. Bednarczyk, E. Berdermann, J. Gerl, *et al.*, Application of diamond detectors in tracking of heavy ion slowed-down radioactive beams, *Acta Physica Polonica B*, **38**, 1293–1296 (2007).

[33] W. Lynch, Nuclear fragmentation in proton and heavy-ion-induced reactions, *Ann. Rev. Nucl. Part. Sci.*, **37**, 493–535 (1987).

[34] H. Sann, Position sensitive detectors in heavy ion physics (at GSI), *NIM A*, **392**, 433–446 (1997).

[35] E. Berdermann, K. Blasche, H.W. Daues, P. Moritz, H. Stelzer, and B. Voss, The Diamond Project at GSI - Perspectives, *Proc., 7th International Conference on Advanced Technology and Particle Physics (ICATPP-7)*, M. Barone, E. Borchi, J. Huston, C. Leroy, P.G. Rancoita, P. Riboni, and R. Ruchti (Eds), pp. 246–251, World Scientific, 2001.

[36] J. Bol, E. Berdermann, W. de Boer, E. Grigoriev, F. Hauler, and L. Jungermann, Beam- monitors for TESLA based on diamond-strip-detectors, *IEEE Transactions on Nuclear Science*, **3**, 1566–1568 (2004).

[37] M. Rebisz, Alternative methods for heavy-ion therapy dosimetry, *PhD Thesis*, Ruprecht-Karls-Universität Heidelberg (2008), *GSI report Diss. 2008 -04 March*, unpublished.

[38] M. Rebisz and B. Voss, The response of thermally stimulated luminescence in CVD diamonds to heavy charged particles, *Radiation Measurements*, **42**, 628–631 (2007).

[39] E. Berdermann, M. Pomorski, A. Pullia *et al.* for the NoRHDia Collaboration, Performance of Diamond Detectors in a Fragmentation Experiment, *Proc. XLV Int. Winter Meeting on Nuclear Physics*, I. Iori (Ed.) (2007), http://wspig2.physik.uni-giessen.de:8000/Bormio2007/uploads/EleniBerdermann.pdf.

11 Neutron Detectors

G. VERONA-RINATI

Dipartimento di Ingegneria Meccanica, Università di Roma "Tor Vergata", Italy

11.1 Introduction 257
11.2 Experimental 258
11.3 Thermal neutron detection 259
11.4 Fast neutron detection 264
11.5 Radiation hardness 266
11.6 Neutron detectors for fission Reactor Monitoring 268
11.7 Neutron detectors for magnetic confinement fusion reactors 270
11.8 Conclusions 272
Acknowledgements 273
References 273

11.1 INTRODUCTION

Diamond is a very interesting material as an active element for radiation detection. In fact, diamond exhibits many outstanding properties such as high band gap, high break-down field, high carrier mobility and high radiation hardness [1–7]. These properties, in principle, make it possible to realize fast, low noise and radiation-hard detectors [8]. The recent development of synthesis processes for high quality single crystal homoepitaxial diamond prepared by Chemical Vapour Deposition (CVD), have resulted in considerable improvements in the detection performance of diamond devices for application in many different fields. As examples, interesting results have been obtained in UV and extreme UV detection for astrophysics and plasma physics [9–13], minimum ionizing particle detection in large accelerators [14, 15], beam monitoring [16–19], X- and gamma-ray detection, and dosimetry for radiology and radiotherapy [20–24].

A very promising application of diamond is in neutron detection, which is a primary issue when dealing with nuclear reactors for either fusion or fission [25–31]. Moreover, emerging radiotherapy techniques such as Boron Neutron Capture Therapy (BNCT) [32] and Fast Neutron Therapy (FNT) [33], which are based on neutron irradiation, need the

CVD Diamond for Electronic Devices and Sensors Edited by Ricardo S. Sussmann
© 2009 John Wiley & Sons, Ltd. ISBN: 978-0-470-06532-7

development of new neutron detectors with improved performance. An ideal neutron detector should be able to strongly discriminate neutrons from γ-rays; it needs to be compact (to allow for optimal positioning), free of fissile material (for security reasons and ease of operation), and be radiation and temperature hard (to allow operation in harsh environments). In addition, it should be sensitive to both thermal and fast neutrons. Traditionally used neutron detectors (fission chambers, gas counters, scintillator, silicon detectors) fail in at least one of these requirements. Diamond-based detectors could represent the ideal solution for neutron detection in the above-mentioned applications.

The recent development of single crystal CVD diamond detectors in a p-type/intrinsic/metal-layered configuration has allowed the production of devices with highly reproducible characteristics [34]. Under α-particle irradiation they have shown 100 % charge collection efficiency and a resolution of about 1 %. Moreover, these devices have shown a very stable and reproducible detection response and are thus extremely promising for application as neutron detectors.

In this chapter the properties and working principles of synthetic single crystal diamond neutron detectors in a p-type/intrinsic/metal-layered structure are extensively analysed. In such devices, fast neutrons with typical energy of 14.8 MeV are detected directly in the bulk of the intrinsic diamond layer through the $^{12}C(n,\alpha)^{9}Be$ reaction [25]. The produced ^{9}Be ions and α-particles have a total energy $E_\alpha + E_{Be} = E_n - 5.7$ MeV, where E_n is the energy of the impinging neutron. These ionizing particles interact mainly with electrons in the valence band, producing electron–hole pairs, which, due to the applied electric field, move towards the electrodes thus producing a measurable signal [44]. In order to achieve sensitivity to thermal neutrons, whose energy is lower than 100 meV, a converting layer (e.g. ^{6}LiF or ^{10}B), which could convert thermal neutrons into highly ionizing particles, is needed. The converting layer studied in this chapter was made by depositing on top of the upper electrode a 95 % enriched ^{6}LiF layer. The ^{6}LiF interacts with thermal neutron through the nuclear reaction $^{6}Li(n\alpha)T$ producing 2.73 MeV tritium and 2.07 MeV alpha-particles, which are easily detected by the diamond device.

11.2 EXPERIMENTAL

The devices were fabricated at the University of Rome ‘Tor Vergata’ laboratory using CVD diamond synthesized by microwave chemical vapour deposition (MWCVD). The structure of the single-crystal, diamond neutron detectors discussed in this paper is shown in Figure 11.1. A highly conductive boron-doped CVD diamond film, whose thickness is usually about 10–20 μm is first grown epitaxialy on a 4×4 mm^2 commercial high pressure–high temperature (HPHT) single crystal substrate. This B-doped layer is used as a back contact. An intrinsic diamond layer, which constitutes the element sensitive to the ionizing radiation, is then grown on the doped surface in a separate clean reactor in order to avoid boron contamination of the intrinsic layer. On top of the diamond-layered structure, a 2.5 mm diameter aluminium contact is then thermally evaporated and used as the top contact. This multilayer geometry allows separation of the response of the high quality intrinsic CVD sensing layer from any eventual response that may originate in the HPHT substrate, with no need to remove the substrate mechanically. This is because the detection signal originates only from the CVD layer where the electric field is confined. In order to achieve sensitivity to thermal neutrons, a ^{6}LiF or boron layer is deposited on

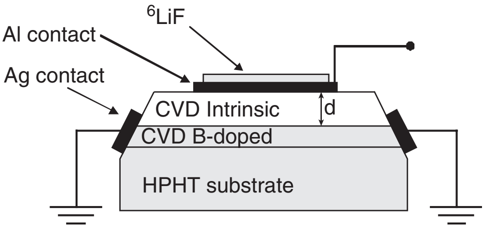

Figure 11.1 Scheme of the single crystal CVD-diamond neutron detector configuration

top of the aluminium contact by thermal evaporation. The device is finally mounted in a housing.

The typical readout electronics adopted for the characterization of the detector response is composed of a charge preamplifier, a shaping amplifier with, usually, a 1 μs shaping time and a multi-channel analyser (MCA) or a multi-channel scaler (MCS). The detector is typically biased with an electric field of about 2 V/μm with positive polarity on the top electrode [35]. Negative polarization of the devices always gives rise to a high dark current due to the highly rectifying properties of the adopted structure. The charge sensitive electronic chain was calibrated by using a 100 % collection efficiency Si detector, and the measured charge was related to the energy detected by diamond assuming 13.2 eV as the average energy for creating an electron–hole pair in diamond [36]. As a first stage, a standard characterization of the diamond device is performed by α-particle detection from a ^{241}Am source. In this configuration a 100 % charge collection efficiency and an energy resolution of approximately 1 % are routinely observed.

11.3 THERMAL NEUTRON DETECTION

A first neutron detection test was performed at the Frascati Neutron Generator [37] (FNG) – Frascati, Italy, which produces 14.1–14.8 MeV neutrons from the D–T reaction. A single-crystal, CVD diamond neutron detector as described in Section 11.2 was exposed to partially moderated neutron irradiation by introducing the diamond detector in a polymethylmethacrylate (PMMA) moderator, which serves to produce lower energy thermal neutrons. In this way both fast neutrons (14.8 MeV) and thermal neutrons are present in the neutron energy spectrum. The obtained pulse height analysis (PHA) spectrum is shown in Figure 11.2. The two sharp peaks at about 2 and 2.7 MeV are due to α-particles and tritium ions, respectively, produced by the interaction of ^{6}Li with thermal neutrons. At higher energies (see the inset in Figure 11.2, where a magnified view of the $5 \div 10$ MeV region is shown) the broader peak at about 9.1 MeV is due to the ^{12}C(n,α)^{9}Be reaction in diamond produced by the fast neutrons. Despite the reduced thickness of the CVD layer (approximately 25 μm), the Be + α ions peak, due to the interaction with fast neutrons, is clearly visible and well separated from the ^{12}C(n,n′)3α continuum at lower energies. This process will be discussed in detail in the next section. Since the thermal cross section ^{6}Li(n,α)T is four orders of magnitude higher than those of the other competing reactions occurring both in lithium and carbon [38], in the spectrum reported in Figure 11.2 the peaks due to thermal neutrons detection are much more intense than those

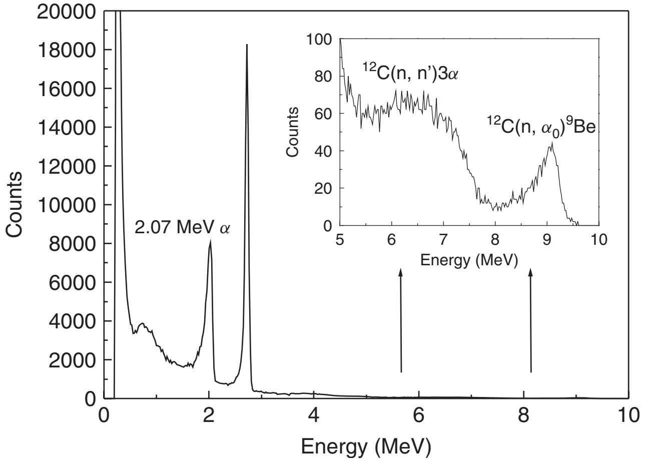

Figure 11.2 Spectrum of partially moderated 14.8 MeV neutrons acquired by the diamond neutron detector. In the inset a magnified, view of the 5 ÷ 10 MeV region is shown

due to fast neutrons, even using a very thin ^{6}LiF layer. Nevertheless, it is clear that the detector is fully capable of detecting simultaneously thermal and fast neutrons.

It can be seen from Figure 11.2 that the 2.07 MeV α peak is broader than the T peak at 2.73 MeV, and consequently less intense because the two peaks have the same area. This effect is due to the higher stopping power of α-particles in LiF as compared with tritium ions. The α-particles can lose a larger proportion of their energy inside the LiF layer before entering the diamond sensitive region and, depending on their generation point and their direction, this energy loss can vary within a range producing a broadening of the peak. This effect becomes more pronounced if the thickness of the LiF coating is increased. However, on the other hand the thicker the ^{6}LiF layer, the higher the conversion efficiency and the expected counting rate. Obviously, a saturation of the conversion efficiency as a function of the LiF layer thickness is expected when the thickness becomes comparable to the penetration depth of the reaction products in LiF (i.e about 34 μm for 2.73 MeV tritium ions and 6.1 μm for 2.07 MeV α-particles).

In order to select, for any given application, the optimum ^{6}LiF layer thickness it is necessary to perform a more detailed analysis of the reaction-product kinematics that will determine the trade-off between counting rate and energy resolution. For one particular case, the resolution of the peaks and the sensitivity of the detector to thermal neutrons for any given LiF thickness can be calculated from Monte-Carlo simulations. The procedure adopted for such simulations is described in the following. The Bragg curves of 2.07-MeV alphas and 2.73 MeV tritium ions in LiF were firstly approximated to the empirical function:

$$-\frac{dE}{dx} = \frac{Ae^{Bx}}{1 + e^{\frac{x-C}{D}}} \tag{11.1}$$

where the parameters A, B, C, and D were derived both for α-particles and tritium ions by the best fit of the above equation to the Bragg curves derived by the nuclear simulation program SRIM [39]. At this point, Monte-Carlo simulation of the released energy spectra was performed by randomly generating α-particles or tritium ions inside the ^{6}LiF layer with a homogeneous distribution of the creation point and isotropic distribution of emission angle, and then calculating the energy of the particle exiting the LiF layer. In the simulation, the path of αs and tritons is assumed to be a straight line. This is a good approximation of the first part of the particle path (close to the generation point) but the motion of the particles become more straggling close to the end of the path (low energies). However, the error produced by this assumption can affect only the energy calculation for α-particles and tritons whose energy close to the LiF–diamond interface is very low. These particles release only a small fraction of their starting energy inside the diamond. This means that only the very-low-energy part of the spectrum, usually not experimentally accessible due to the presence of noise and other low energy reactions, can be affected by the adopted approximation.

In Figure 11.3 the results of the simulations are shown (full lines) and compared with the experimental PHA spectra (dots) for three samples on which three different ^{6}LiF layer thicknesses were deposited: 0.5 µm, 1.55 µm and 3 µm, respectively. The only adjustable parameter in the calculated PHA spectra is the amplitude (i.e. the number of number of events), which was chosen in such a way as to have a good correspondence between calculated and experimental α-particle peak area. A very good agreement between simulation and experimental data was observed in all cases, except for the tritium ion peak

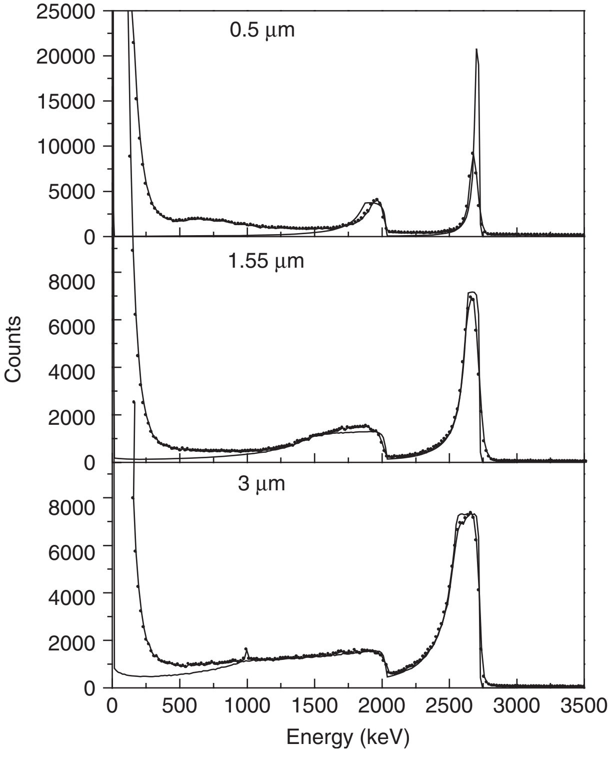

Figure 11.3 Experimental spectra (dots) under thermal neutron irradiation for three different ^{6}LiF layer thicknesses compared with numerical simulations (full lines)

measured by the sample with 0.5 μm thick LiF layer. The simulated peak is, in this case, much narrower, and therefore more intense, because the intrinsic broadening produced by the detector and the electronic chain were not taken into account in the simulation. However, in this case the total number of counts (i.e. the area) below this peak was equal for the simulation and the experimental spectrum. It will be noticed from Figure 11.3 that both the 2.73-MeV tritium ion and the 2.07 MeV α-particle peaks exhibit a broadening with increasing ^{6}LiF layer thickness, which is much more evident in the case of the α-particles than for tritium ions. This is because the stopping power of ^{6}LiF for 2.07 MeV α-particles is much higher than for 2.73 MeV tritium ions, so that the energy spread of the α-particles reaching the diamond sensitive layer is much higher and increases more rapidly with the thickness of the ^{6}LiF layer.

From the PHA simulations it is possible to calculate for any given LiF layer thickness the full width at half maximum (FWHM) for both the α-particle and the tritium-ion peaks. In Figure 11.4, the FWHM as a function of the LiF layer thickness is shown for both the α-particles and the tritium ions. As expected, due to the higher stopping power of α-particles compared with tritium ions, the α-particle peak is always much broader than that of tritium. In particular, while the tritium-ion peak retains significant energy resolution for thicknesses of several micrometres, in the case of α-particles a well defined peak (FWHM much lower than the peak energy) is observed only for thicknesses of the order of 2 μm or less.

Under normal operating conditions, a thermal neutron detector is used as a counter. In this detection mode, a signal amplitude threshold value is fixed and only pulses above this threshold are counted. The counting efficiency of such detectors has been simulated by choosing three different threshold values: 2.07 MeV, 1 MeV and 0.5 MeV. The higher threshold was chosen at just above the α-particle peak so that only tritium ions could be detected, while for the other two thresholds both α-particles and tritium ions were counted. The lower threshold (0.5 MeV) was chosen to be just above the experimental low-energy signal increase, which, in this case, is mostly due to a combination of elastic scattering of fast neutrons with carbon ions, protons ejected by the moderator and electronic noise. Figure 11.5(a) shows the simulated counting efficiency (defined as the counted events

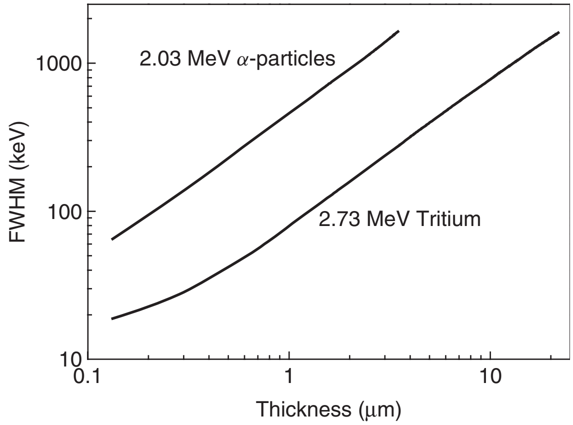

Figure 11.4 Calculated FWHM of the α and tritium peaks as a function of the ^{6}LiF layer thickness

divided by total number of ^{6}Li(n,α)T reactions produced in the LiF layer) as a function of the LiF layer thickness. For very low LiF thicknesses, the counting efficiency approaches 100 % for the two lower thresholds, while 50 % is the limit value for the highest threshold. This is because for the 2.07 MeV threshold only the tritium is detected, so that, for any ^{6}Li(n,α)T reaction, the produced tritium ions have 50 % probability to be directed toward the diamond sensitive layer, and 50 % probability to be directed outside the detector By increasing the LiF layer thickness, a greater proportion of the reaction takes place further from the diamond sensitive region. This results in an increase in the proportion of reaction products unable to reach the diamond region with an energy above the threshold value, with a consequent decrease in counting efficiency. From this simulation it is possible to calculate the detector sensitivity S per unit area defined as the ratio between counted and incident neutrons. Once the cross-section of the ^{6}Li(n,α)T reaction (which depends on the spectrum of the neutrons) is known, the detector sensitivity per unit area can be obtained by multiplying the counting efficiency by the reaction cross-section, the detector thickness and the ^{6}Li concentration. Figure 11.5(b) shows the counting sensitivity per unit area using a cross-section of 950 barn, which corresponds to the cross section of ^{6}Li with completely thermalized neutrons. The expected count rate R of a detector of area A under a neutron flux ϕ (neutrons per unit time per unit surface) can be extracted from

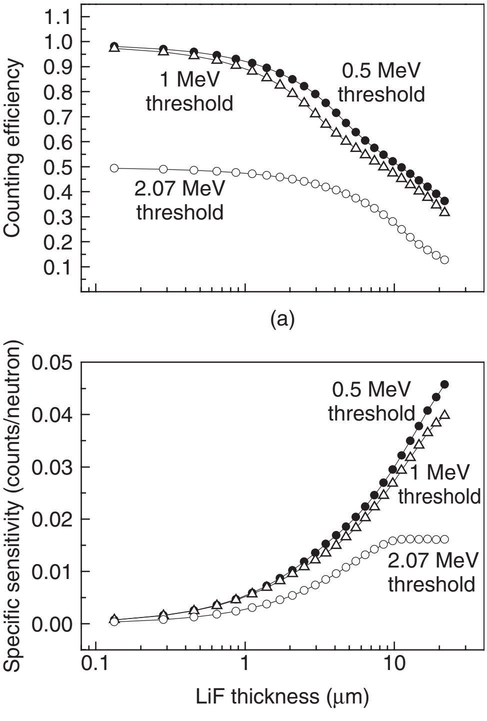

(b)

Figure 11.5 Simulated counting efficiency (a) under thermal irradiation as a function of the ^{6}LiF thickness for three different thresholds (500 keV, 1000 keV and 2070 keV). In (b) the sensitivity per unit area is reported

the value of S in Figure 11.5(b) as:

$$R = \phi A S \tag{11.2}$$

It will be noticed from Figure 11.5(b) that the counting sensitivity curve with 2.07-MeV threshold saturates for ^{6}LiF thicknesses above ~10 μm. This thickness is in fact the distance needed for the tritium ions to reduce their energy down to approximately 2.1 MeV. This implies that tritium ions generated at distances greater than 10 μm cannot be counted above this threshold and therefore will not contribute to the tritium ion counts. For the 0.55 MeV and 1 MeV thresholds, no saturation is observed because the distance needed to reduce the tritium energy below the threshold levels is greater than the maximum ^{6}LiF thickness (20 μm) used in the simulation.

11.4 FAST NEUTRON DETECTION

The most interesting reaction between fast neutrons and carbon is the above-mentioned ^{12}C(n,α)^{9}Be reaction. This reaction produces α-particles and ^{9}Be ions inside the diamond sensitive layer, which are simultaneously detected. The total energy of the reaction products is $E_\alpha + E_{Be} = E_n - 5.7$ MeV, where E_n is the energy of the impinging neutron (14.8 MeV in this test). The direct relationship between E_n and the energy of the reaction products allows spectroscopic measurements of the incident neutrons. However, especially for small intrinsic diamond layer thickness, some particles can escape from the detection volume, releasing only a fraction of their energy. This edge effect will be more pronounced if the diamond thickness is below, or comparable with, the penetration length of the produced α-particles and ^{9}Be ions: from 3 to 30 μm for α-particles and from 0.5 to 6 μm for Be ions, depending on their energies, which are related to the angle of emission. In order to evaluate this effect, the PHA spectra have been simulated by adopting the procedure below.

The stopping power curves of α-particles and ^{9}Be ions in diamond were firstly approximated to Equation (11.1) using the same procedure as reported previously. Monte-Carlo simulations were then performed by generating, inside the diamond layer, α-particle and ^{9}Be ion emission points. Because the mean free path of 14.8 MeV neutrons in diamond is approximately 3.8 cm (much larger than the typical diamond film thickness), the emission points were generated with an homogenous distribution. The distribution of the emission angle of the α-particle was chosen according to the differential cross section of the reaction ^{12}C(n,α_0)^{9}Be reported in Ref. [40]. The individual energies of both α-particles and ^{9}Be ions are calculated from the kinematics of the reaction. For each reaction, the energy released in the sensitive diamond layer by both α-particles and ^{9}Be ions, is finally calculated.

An interesting feature of fast neutron detection, visible in the spectrum reported in the inset of Figure 11.2, is the well defined ^{12}C(n,α)^{9}Be reaction peak at about 9.1 MeV. The width of this peak is the same as that of the FNG neutron-beam energy spread (about 0.5 MeV). At a first sight, a significant broadening of this peak, due to above mentioned edge effects, would be expected since the detector thickness is only 25 μm, comparable with the penetration depth of the ^{12}C(n,α)^{9}Be reaction products in diamond. In Figure 11.6, the simulated spectra of 14.8 MeV neutrons are shown for three different detector thicknesses. In order to take into account the energy spread of the 14.8 MeV neutrons produced at FNG, the results of the Monte-Carlo simulation

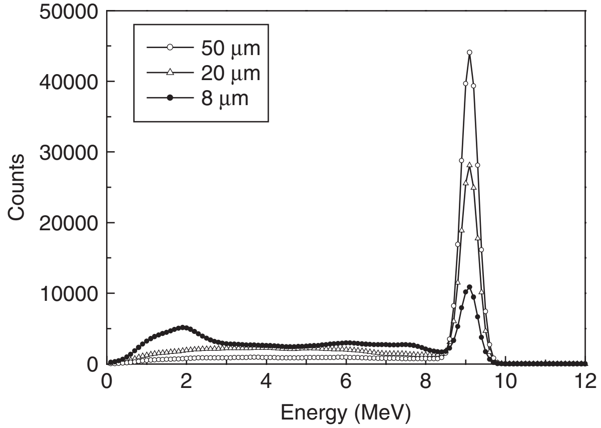

Figure 11.6 Simulated spectra under 14.8-MeV neutron irradiation relative to the $^{12}C(n,\alpha_0)^9Be$ peak for three different intrinsic diamond thicknesses (8 μm, 20 μm and 50 μm)

were convoluted with a 0.5 MeV FWHM Gaussian function. It is worth noting from Figure 11.6 that even for the lower thickness value a well defined peak is obtained from the simulation, and the only effect of reducing further the detector thickness is a gradual decrease of the peak height and a corresponding moderate increase of the background level. In particular, while the particles releasing all their energy inside the detector produce a well-defined peak, the particles that release only a fraction of their energy inside the device result in a very widespread energy distribution. As a consequence, the decrease of film thickness has the effect of removing counts from the well-defined 9.1 MeV peak and distributing them almost uniformly in the lower energy background. This results in negligible broadening of the peak but, on the other hand, when the thickness is reduced, many reaction events are lost in the low energy background, leading to reduced intensity of the $^{12}C(n,\alpha)^9Be$ peak. To characterize this aspect better, it is possible to define the peak efficiency as the ratio between the counts inside the $^{12}C(n,\alpha)^9Be$ peak and the total number of $^{12}C(n,\alpha)^9Be$ reactions. In a very similar way to what was obtained for thermal neutrons, the counting sensitivity per unit area can be easily derived from the peak efficiency by multiplying it by the cross-section of the $^{12}C(n,\alpha)^9Be$ reaction, the detector thickness and the ^{12}C atomic concentration. In Figure 11.7 the results of the simulations of the peak efficiency are shown as a function of the active diamond-layer thickness (full line). As expected, optimal collection takes place only for a device thickness much higher than the penetration depths of the reaction products. A comparison with experimental data (squares) is also reported in Figure 11.7. In particular, four different samples of thickness 25 μm, 53 μm, 74 μm, and 104 μm were tested under 14.8 MeV irradiation. Their peak efficiency was measured from the experimental PHA spectra by calculating the ratio between the counts in the $^{12}C(n,\alpha)^9Be$ peak and the number of $^{12}C(n,\alpha)^9Be$ reactions, where the latter is given by the total count number integrated over the whole spectrum multiplied by the cross-section of the $^{12}C(n,\alpha)^9Be$ reaction (72 mbarn) and divided by the total cross-section of 14.8 MeV neutrons in carbon (1.2 barn). The measured experimental points are in quite good agreement with the simulation results, thus confirming the adequacy of the proposed

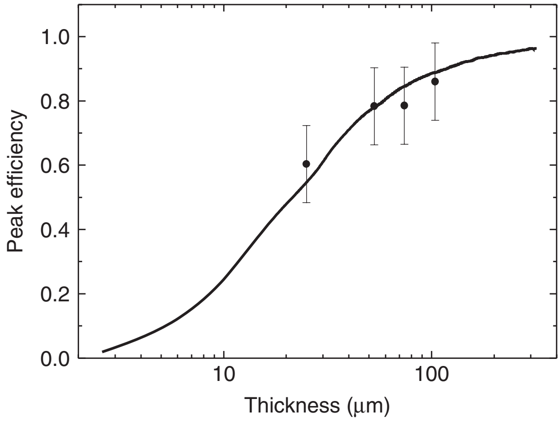

Figure 11.7 Counting efficiency of the $^{12}C(n,\alpha_0)^9Be$ peak (full line) as a function of the intrinsic diamond layer thickness under 14.8 MeV neutron. The circles are experimental data

model and allowing an estimate of detector performance for an arbitrary diamond layer thickness.

11.5 RADIATION HARDNESS

The expected radiation hardness of diamond is one of its most important features, which makes detectors based on this material extremely interesting for applications in fission and fusion facilities. Several studies on radiation damage have been already carried out on natural and synthetic diamond detectors [2–7]. However neutron radiation damage studies for synthetic diamond detectors have been performed mainly on polycrystalline CVD diamonds [3, 4, 6] and only recently on HPHT single-crystal diamond [7]. The radiation tolerance to fast neutrons has been demonstrated for natural diamonds, which could tolerate a neutron fluence of up to 1×10^{14} n/cm^2 before the spectroscopic properties started to degrade, and up to 3×10^{16} n/cm^2 before large efficiency changes occured [5]. Published data up to now report lower radiation tolerances for HPHT single-crystal diamonds in which a large degradation of the spectroscopic properties [7] was found for 14-MeV neutrons with a fluence of only 5.5×10^{13} n/cm^2.

In this section we report the results of a 14.8 MeV neutron-radiation tolerance study on a single-crystal CVD diamond detector of the type described in Section 11.2. In this study neutron fluences of up to 2.0×10^{14} neutrons/cm^2 were used.

The experiment was carried out using the Frascati Neutron Generator (FNG). The maximum neutron flux is obtained in the frontal position and very close to the neutron target, with a typical value of $1 \div 5 \times 10^9$ neutrons cm^{-2} s^{-1}. To reach the total fluence of 2.0×10^{14} neutrons/cm^2, seven irradiation sessions were performed. The high neutron fluence used for the present measurements provides relevant information for applications in fusion neutron diagnostic and high-energy physics accelerators since it is approximately one order of magnitude greater than the neutron fluence limit before failure in a conventional silicon radiation detector [41, 42].

Characterization measurements were carried out on the diamond detector under test before starting the heavy neutron irradiation, and subsequently after each irradiation step.

In particular, before and after each 14.8 MeV neutron irradiation step, an α-particle emission spectrum from a ^{239}Pu, ^{241}Am, ^{244}Cm mixed nuclides source and a 14.1-MeV neutron detection spectrum was acquired. The diamond detector was always operated and stored at room temperature and no thermal annealing was performed. The α spectra were acquired one or two days after the irradiation step, in order to allow for the decay of the main neutron-induced radioactivity in the device mainly arising from the detector housing and the connector.

The detector was not connected to the electronics during the irradiation. In order to determine the absolute neutron flux during heavy irradiation, the diamond detector was sandwiched between two pure aluminium foils, 5 mm in diameter, and 0.1 mm thick. After each irradiation the absolute neutron-induced activity of the two aluminium foils was measured with a calibrated high-purity germanium detector, and the average neutron flux impinging on the diamond film was derived using the value of 0.113 barn for ^{27}Al(n,α)^{24}Na cross section at 14.8 MeV [43].

In Figure 11.8 the mixed nuclide α-source spectrum, measured by the diamond detector after the last neutron irradiation step, is shown. A 100 % efficiency and an energy resolution of 0.5 % was extracted from the data shown in Figure 11.8, confirming the high radiation tolerance of diamond. In particular, it was observed from the α-particle spectra analysis, that after the first neutron irradiation, corresponding to a neutron fluence of 1.55×10^{12} n/cm^2, the energy resolution of the detector improved from approximately 1 % to 0.5 %. After this initial improvement, the response of the detector to α-particles remained stable for all subsequent irradiation steps up to the maximum neutron fluence. Evidence of this is shown in Figure 11.9, where the resolutions measured from the three main peaks of the α source are reported as a function of the total fluence. The same behaviour is observed for the neutron detection properties. In Figure 11.10 all the acquired neutron detection spectra are reported. All of them are perfectly superimposed with the exception of the first spectrum (before first irradiation), which exhibits a larger energy spread of the ^{12}C(n,α)^{9}Be peak. In particular, an initial improvement of the FWHM of the ^{12}C(n,α)^{9}Be, from 0.67 MeV to 0.34 MeV is observed and subsequently, the neutron detection performance remains stable

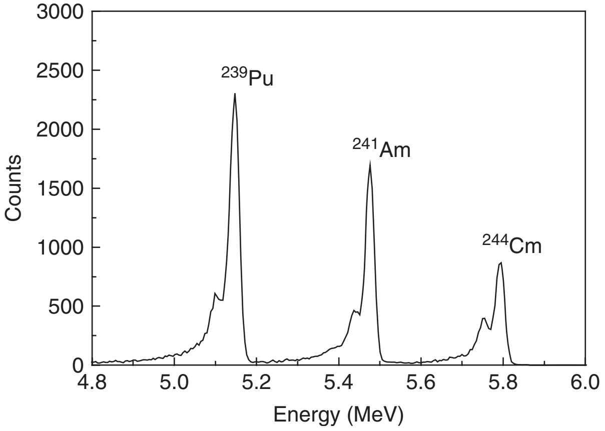

Figure 11.8 Pulse height spectra of the multi-isotope α source as acquired by the diamond detector after exposure to 2×10^{14} n/cm^2

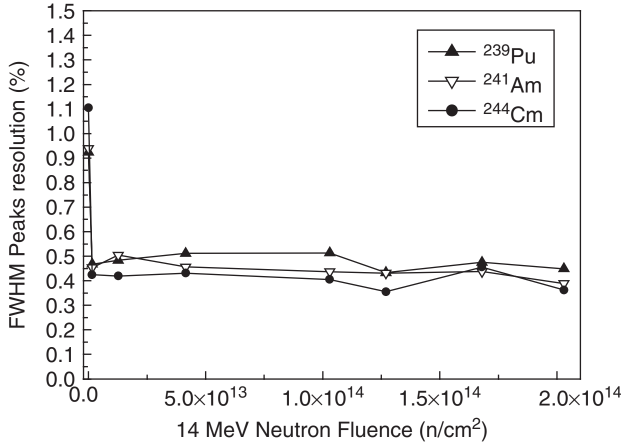

Figure 11.9 FWHM of the three α peaks as a function of the irradiated neutron fluence

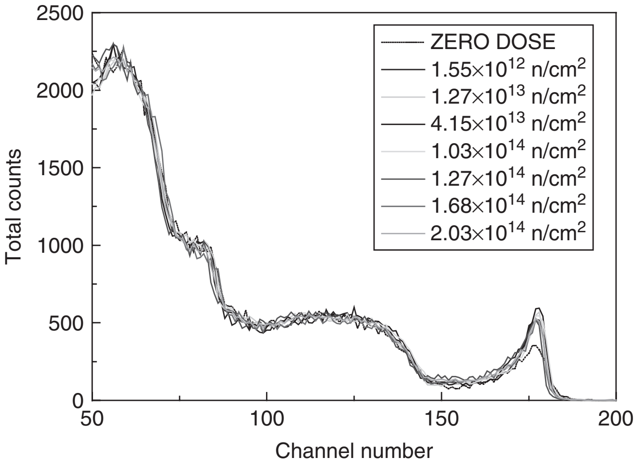

Figure 11.10 Pulse height spectra in the diamond detector irradiated by 14.1 MeV neutrons for different values of total fluence. The horizontal scale was not energy calibrated. The spectra have been normalized for an easier interpretation of the data

up to the maximum given neutron fluence. These results provide clear evidence that this type of diamond detector can sustain a very-high neutron fluence (at least up to 2×10^{14} n/cm^2) with no degradation in performance, thus demonstrating their possible use in high neutron flux environments. Work is in progress in order to increase the testing neutron dose and ascertain at which level of neutron fluence the devices start to degrade.

11.6 NEUTRON DETECTORS FOR FISSION REACTOR MONITORING

A first operative test in a harsh environment was performed at the TRIGA RC-1 fission research reactor of ENEA-Casaccia, Italy. In that experimental environment, besides high neutron flux, intense fluxes of gamma rays are also present. TRIGA RC-1 is a 1 MW pool thermal reactor, with core and reflector assemblies located at the bottom of an aluminium tank. The core diameter is 56.5 cm, while its height is 72 cm. The overall height of the tank is 7 m. The diamond detector was connected to a 10-m long cable and positioned 80 cm above the core midplane. The electronic chain consisted of an Ortec 142A charge preamplifier, a shaping amplifier with a 1 μs shaping time and a multichannel scaler (MCS). A fission chamber was also installed in the reactor and used as a reference. Due to its high sensitivity, the reference fission chamber was located in a different position to the diamond detector, further away from the core. In Figure 11.11 the neutron flux as measured by the diamond detector is reported and compared with that obtained by the reference fission chamber. During irradiation the reactor power was varied from 10 kW up to its maximum power of 1 MW through several steps. In order to take into account the pile-up effects present in the measurement, due to the 1 μs electronic time constant, the data in Figure 11.11 were corrected by the well-known pile-up correction formula for paralysable systems [44] following the procedure described in Ref. [30]. Since the fission chamber was positioned in a lower-neutron-flux region, a lower statistics was observed in its output. Despite this lower statistics, an excellent proportional agreement between the two detectors signals was observed, as shown in Figure 11.11. In particular, in the inset of Figure 11.11, where an expanded view of the fast decrease region of the reactor power region is reported, it can be appreciated that both detectors were able to follow the variation of the neutron flux in perfect agreement. The neutron flux at the diamond position was measured by the activation technique, using gold foils, and was 2.2×10^9 neutrons/cm^2 s at 1 MW reactor power. In this condition, the count rate of the diamond detector was about 150 000 counts per second, thus indicating a device sensitivity of 6.8×10^{-5} counts cm^2/neutron. In Figure 11.12, the count rate as measured by the diamond detector after the pile-up effect, is reported as a function of the count rate measured by the fission chamber. An excellent linearity of the diamond device response against

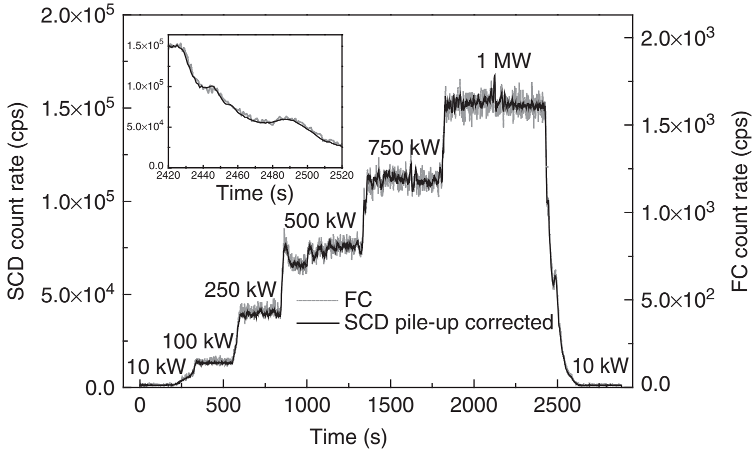

Figure 11.11 Comparison between the time traces of the pile-up corrected single crystal diamond detector (black line, left-hand vertical scale), and the fission chamber monitor (dotted line, right-hand vertical scale). In the inset is an enlarged view of the reactor's power fall from 1 MW to 10 kW

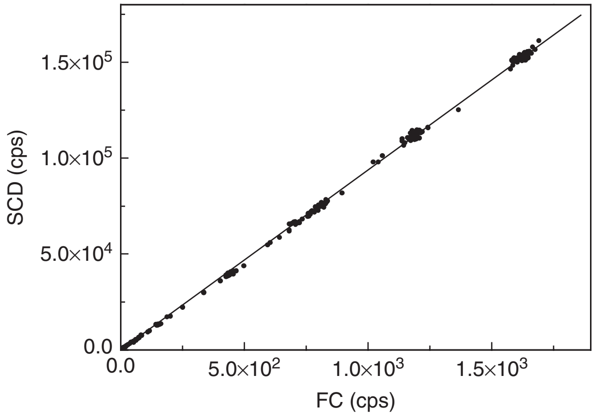

Figure 11.12 Single-crystal diamond, pile-up corrected, count rate as a function of the fission chamber response. The full line is the linear best fit

neutron flux is observed, demonstrating the possible use of diamond in nuclear fission reactors at least up to count rates of the order of 150 000 cps.

11.7 NEUTRON DETECTORS FOR MAGNETIC CONFINEMENT FUSION REACTORS

The detection of neutrons is one of the most important diagnostics of the fusion process since the total flux and the time dependence of the neutron emission, as well as the neutron energy, give fundamental information about the parameters of the burning plasma. One current difficulty in this type of experiment is that conventional neutron detectors suffer from many drawbacks at high levels of radiation. Its use therefore could problematic in the next generation fusion reactors such as the International Thermonuclear Experimental Reactor (ITER) due to the very high expected levels of neutron and gamma fluxes. For this reason a long-term test of the CVD diamond neutron detectors discussed in this chapter under operating conditions has been performed at the Joint European Torus (JET) at the Culham Science Centre, situated in Oxfordshire, UK. A diamond detector as described in Ref. [2], covered with a layer of ^{6}LiF has been operating inside the JET torus hall since April 2006 [29]. The detector is close to the main vertical port in Octant 1, about 4 m away from the plasma centre and connected to the JET acquisition system CODAS. Its data acquisition began from JET Pulse Number 66654. The detector worked with a bias of +3 V/μm for the whole duration of the JET experimental campaigns, which ended in April 2007.

The detector was directly connected to a charge preamplifier ORTEC Mod. 142A, and both detector and preamplifier were located inside a metallic box. The connection to a shaping amplifier and threshold discriminators, located outside the torus hall in the diagnostic area, was by means of long 50 Ω coaxial cables (about 100 m). The shaping amplifier worked with a shaping time of 1 μs. The logic signals produced by the discriminators were acquired as count rate versus time by the JET acquisition system CODAS. Two discrimination thresholds were set. The lowest (THR-1) was able to detect all the signals produced by the neutrons regardless of their energy (total neutron yield), the second threshold (THR-2) was set well above the first one in order to detect only the signals due to 14 MeV neutrons and produced by the $^{12}C(n,\alpha)^{9}Be$ reaction. To set this threshold a standard three-peak alpha source was used to calibrate the voltage output signal versus radiation energy.

The response of the CVD diamond detectors was compared to 14-MeV neutron data, usually measured at JET by silicon diodes, and to the JET total neutron yield measured by KN1 diagnostic. KN1 is the main system used at JET to measure the total neutron yield produced during a pulse. It consists of three sets of fission chambers arranged around the machine. Each set comprises a ^{235}U and ^{238}U chamber operating in pulse counting and current mode [45]. Both time-dependent response during single plasma pulses and the total number of counts for every JET pulse were recorded. It ought to be stressed that JET was operated with DD plasma, so 14 MeV neutrons were produced only by the so-called triton burn-up. The 14 MeV neutron yield under these conditions is very low, about 1 % of the total neutron yield.

In Figure 11.13 an example of the temporal response of the diamond detector both for total neutron emission and the 14 MeV emission is compared with the same quantities measured by KN1 and by silicon diodes, respectively. A good agreement is observed despite the low statistic, mainly due to the small diamond detector dimensions and the low yield of 14 MeV neutrons. Figure 11.13 demonstrates that by using a SCD detector covered with a ^{6}LiF film it is possible to discriminate between the total and the 14 MeV neutrons coming from triton burn-up This allowed, for the first time, using a single detector, simultaneous measurement of both the total and 14 MeV neutron yields as well as their time dependency.

In order to verify the linearity and stability of the devices, the total number of counts measured by the diamond detector for each JET pulse is reported in Figure 11.14 as a function of the JET neutron yield measured by KN1. In the plot more than 500 JET pulses, acquired during the 2006/2007 JET experimental campaign, are reported. A good linearity

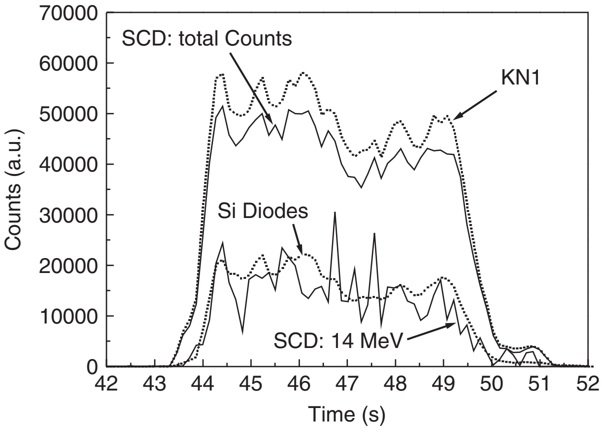

Figure 11.13 Time dependent total and 14 MeV neutron emission measured by the diamond detector as compared with the acquisition of the KN1 diagnostic (total yield) and of the silicon diodes (14 MeV)

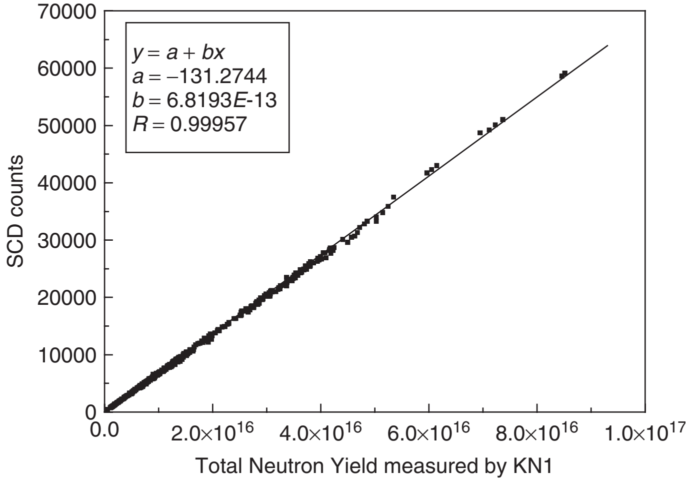

Figure 11.14 Diamond detector counts versus neutron yields measured by the KN1 diagnostic. The full line is the linear best fit of the experimental data

of the detector response and an excellent stability of the device over one year of uninterrupted operation were observed, demonstrating that CVD-diamond neutron detectors can be used reliably in large fusion facilities.

11.8 CONCLUSIONS

In this chapter we have presented a detailed study of the physics underlying the working principles of CVD single-crystal diamond neutron detectors in a p-type/intrinsic/metal configuration. Such detectors are capable of simultaneously detecting thermal and fast neutrons, exhibiting high linearity with dose and very high tolerance to radiation damage. Fast neutrons are detected directly in the bulk of the detector through the ^{12}C(n,α)^{9}Be reaction, while thermal ones are detected through the ^{6}Li(n,α)T reaction taking place in a thin ^{6}LiF deposit on top of the detector. An analysis of the nuclear reaction kinematics allows the resolution and sensitivity of the detector to be calculated for both fast and thermal neutrons, given the thickness of the diamond detector and of the ^{6}LiF layer. The experimental results are in good agreement with numerical simulations, thus confirming that this analysis allows the best choice of detector and ^{6}LiF layer thickness for any given application to be made.

Radiation hardness tests, performed by irradiating one of these devices with 14-MeV neutrons up to a maximum fluence of 2×10^{14} n/cm^2, provided evidence that after an initial improvement in the detector resolution, the performance of the device remained stable up to the maximum irradiated neutron fluence. This confirms the high radiation tolerance capability of diamond-based devices.

Tests performed at the TRIGA fission reactor confirm that diamond-based neutron detectors can be used in harsh environments, where high gamma-ray fluxes are also present. In addition, an excellent linearity of the neutron detector was observed even at high count rates, of the order of 150 000 cps.

Finally a long-term operative test conducted at the Joint European Torus (JET), where a diamond neutron detector was placed under continuous operation for one whole year, showed that the detector performance was extremely reliable and exhibited excellent stability throughout the test period. These results strongly suggest that detectors made with CVD single crystal diamond as reported in this work are, in principle, ready for reliable use in large nuclear facilities such as fission and fusion reactors.

ACKNOWLEDGEMENTS

The devices studied in this chapter were developed by the group of Rome University 'Tor Vergata' composed of Prof. Marco Marinelli, Prof. Enrico Milani, Dr Salvatore Almaviva, Dr Giuseppe Prestopino, Dr Claudio Verona and myself. I'd like to thank Dr Maurizio Angelone and Dr Mario Pillon, responsible for the Frascati Neutron Generator (FNG), whose contribution to the development of these devices was fundamental. They made possible the realization of all the neutron-detection measurements reported in this chapter and contributed to the analysis of the experimental results. I wish to thank as well the staff of the TRIGA and JET facilities who gave us the chance to perform neutron-detection tests in advanced fission and fusion reactor environments, and, in particular, Dr Roberto De Rosa and Dr Andrea Murari for skilful assistance and helpful discussion.

REFERENCES

[1] A. Paoletti, A. Tucciarone (editors) *The Physics of Diamond*, Proc. of the Int. School of Phys. 'Enrico Fermi', Course CXXXV, Varenna (Italy), 23 July–2 August 1996, IOS Press 1997.
[2] V.N. Amosov, A.A. Ivanov, Yu. Kaschuck, A.V. Krasilnikov, *Proc. of IEEE Nuclear Science Symposium & Medical Imaging Conference* **1**, (1997) 492.
[3] L. Allers, A.S. Howard, J.F. Hassard, A. Mainwood. *Diamond and Related Materials* **6** (2–4) (1997) 353.
[4] A. Oh, M. Moll, A. Wagner, W. Zeuner, *Diam. Relat. Mater.* **9**, 11 (2000) 1897.
[5] A. Alekseyev, V. Amosov, Yu. Kaschuck, A. Krasilnikov, D. Portnov, S. Tugarinov, *Nucl. Instrum. Meth. Phys. Res. A* **476**, (2002) 516–521.
[6] M. Angelone, M. Pillon, A. Balducci, M. Marinelli, E. Milani, M.E. Morgada, A. Tucciarone, G. Pucella, G. Verona-Rinati, K. Ochiai and T. Nishitani, *Rev. Sci. Instrum.* **77** (2006) 023505.
[7] T. Tanaka, J.H. Kaneko, Y. Kasugai, M. Katagiri, H. Takeuchi, T. Nishitani, T. Iida, *Diam. Relat. Mater.* **14**, (2005) 2031–2034.
[8] R.J. Trapper, *Rep. Prog. Phys.* **63** (2000) 1273.
[9] L. Barberini, S. Cadeddu, M. Caria, *Nucl. Instrum. Meth. Phys. Res. A* **460** (2001) 127.
[10] Y. Koide, M. Liao, J. Alvarez, *Diam. Relat. Mater.* **15** (2006) 1962.
[11] A. Kaiser, D. Kueck, P. Benkart, A. Munding, G.M. Prinz, A. Heittmann, H. Huebner, R. Sauer, E. Kohn, *Diam. Relat. Mater.* **15** (2006) 1967.
[12] A Mainwood, *Semicond. Sci. Technol.* **15** (2000) R55–R63.
[13] A. Balducci, M. Marinelli, E. Milani, M.E. Morgada, A. Tucciarone, G. Verona-Rinati, M. Angelone, M. Pillon, *Appl. Phys. Lett.* **86** (2005) 193509.
[14] W. Adam *et al.*, *Nucl. Instr. Meth. A* **465**, 1 (2001), 88–91.
[15] M. Pomorsky, E. Berdermann, M. Ciobanu, A. Martemyianov, P. Moritz, B. Marczewska, *Phys. Stat. Sol. A* **202**, (2005) 2199.
[16] P. Bergonzo, A. Brambilla, D. Tromson, R.D. Marshall, C. Jany, F. Foulon, C. Gauthier, V.A. Sole, A. Rogalev, J. Goulon, *Journal of Synchrotron Radiation* **6** (1999) 1.

[17] J. Morse, M. Salome, E. Berdermann, M. Pomorsky, W. Cunningham, J. Grant, *Diam. Relat. Mater.* **16** (2007) 1049.

[18] M. Marinelli, E. Milani, A. Paoletti, A. Tucciarone, G. Verona-Rinati, G. Luce, S. Albergo, V. Bellini, V. Campagna, C. Marchetta, A. Pennisi, G. Poli, R. Potenza, F. Simone, G. Sperduto, C. Sutera, *Diam. Relat. Mater.* **10** (2001) 706.

[19] G. Conte, G. Mazzeo, S. Salvatori, D. Trucchi, V. Ralchenko, *Nucl. Instrum. Meth. Phys. Res. A* **551** (2005) 83.

[20] Y. Garino, A. Lo Giudice, C. Manfredotti, M. Marinelli, E. Milani, A. Tucciarone, G. Verona-Rinati, *Appl. Phys. Lett.* **88** (2006) 151901.

[21] P. Cirrone, G. Cuttone, L. Raffaele, M.G. Sabini, C. De Angelis, S. Onori, M. Pacilio, M. Buccolini, M. Bruzzi, S. Sciortino, *Nucl. Phys. B (Proc. Suppl.)* **125** (2003) 179.

[22] M. Bucciolini, E. Borchi, M. Bruzzi, M. Casati, P. Cirrone, G. Cuttone, C. De Angelis, I. Lovik, S. Onori, L. Raffaele, S. Sciortino, *Nucl. Instr. Meth. A* **522** (2005) 189.

[23] M.J. Guerrero, D. Tromson, M. Rebisz, C. Mer, B. Banzin, P. Bergonzo, *Diam. Relat. Mater.* **13** (2004) 2046.

[24] A.J. Whitehead, R. Arey, C.M. Buttar, J. Conway, G. Hill, S. Ramkumar, G.A. Scarsbrook, R.S. Sussmann, S. Walker. *Nucl. Instr. Meth. A* **40** (2001) 20.

[25] M. Pillon, M. Angelone, A Krasilnikov, *Nucl. Instrum. Meth. Phys. Res. B* **101** (1995) 473.

[26] G.J. Schmid, R.L. Griffin, N. Izumi, J.A. Koch, R.A. Lerche, M.J. Moran, T.W. Phillips, R.E. Tuner, *Rev. Sci. Instrum.* **74** (2003) 1828.

[27] G.J. Schmid, J.A. Koch, R.A. Lerche, M.J. Moran, *Nucl. Instrum. Meth. A* **527** (2004) 554.

[28] J.H. Kaneko, T. Teraji, Y. Hirai, M. Shiraishi, S. Kawamura, S. Yoshizaki, T. Ito, K. Ochiai, T. Nishitani, T. Sawamura, *Rev. Sci. Instrum.* **75** (2004) 3581–3584.

[29] M. Pillon, M. Angelone, D. Lattanzi, M. Marinelli, E. Milani, A. Tucciarone, G. Verona-Rinati, S. Popovichev, R.M. Montereali, M.A. Vincenti, A. Murari, *Fus. Eng. Design* **81** (2007) 1174.

[30] M. Marinelli, E. Milani, G. Prestopino, A. Tucciarone, C. Verona, G. Verona-Rinati, M. Angelone, D. Lattanzi, M. Pillon, R. Rosa, E. Santoro, *Appl. Phys. Lett.* **90**, (2007) 183509.

[31] E. Pace, A. De Sio, *Nucl. Instrum. Meth. Phys. Res. A* **514** (2003) 93.

[32] D.W. Nigg, *Proc. Nucl. Energy* **35** (1999) 79 and references therein.

[33] R. L. Maughan, W.E. Powers, H.G. Blosser, *Med. Phys.* **21** (1994) 779 and references therein.

[34] M. Marinelli, E. Milani, G. Prestopino, M. Scoccia, A. Tucciarone, G. Verona-Rinati, M. Angelone, M. Pillon. D. Lattanzi, *Appl. Phys. Lett.* **89** (2006) 143509.

[35] A. Balducci, M. Marinelli, E. Milani, M.E. Morgada, A. Tucciarone, G. Verona-Rinati, M. Angelone, M. Pillon, *Appl. Phys. Lett.* **86** (2005) 253507.

[36] G.J. Schmid, J.A. Koch, R.A. Lerche, M.J. Moran, *Nucl. Instrum. Meth. A* **527** (2004) 554.

[37] M. Martone, M. Angelone, M. Pillon, *J. Nucl. Mater.* **212–215** (1994) 1661.

[38] JANIS-1.2, Java-based nuclear data display program, NEA OECD, 2004 (http://www.nea.fr/Janis)

[39] J. F. Ziegler, *Ion Implantation – Science and Technology*, Ion Implant Press (2006) (http://www.srim.org).

[40] R.C. Haight, S.M. Grimes, R.G. Johnson and H.H. Barschall, *Nucl. Sci. Eng.* **87** (1984) 41–47.

[41] E. Fretwurst, H. Herdan, G. Lindström, U. Pein, M. Rollwagen, H. Schatz, P. Thomsen. R. Wunstorf, *Nucl. Instrum. Methods A* **288** (1990) 1–12.

[42] Mara Bruzzi, *IEEE Trans. Nucl. Sci.* **48** (2001) 4.

[43] International Reactor Dosimetry File 2002: IRDF-2002. Vienna:International Atomic Energy Agency (2006) p. 24 (Technical reports series, ISSN 0074-1914; 452) STI/DOC/010/452, ISBN 92-0-105106-9.

[44] G.F. Knoll, Radiation Detection and Measurement, John Wiley & Sons, New York (2000).

[45] M.T. Swinhoe, O.N. Jarvis, *Nucl. Instrum. Methods Phys. Res.* **221** (1984) 460.

Part 3

Active Electronic Devices

CVD Diamond for Electronic Devices and Sensors   Edited by Ricardo S. Sussmann

© 2009 John Wiley & Sons, Ltd. ISBN: 978-0-470-06532-7

12 High-Power Switching Devices

JAN ISBERG

Division for Electricity Research, Uppsala University, Sweden

12.1 Introduction 277
12.2 High-Voltage/High-Power Diodes 279
  12.2.1 Schottky diodes 279
  12.2.2 Delta-doped Schottky diodes 283
  12.2.3 Edge termination 283
12.3 Photoconductive and Electron Beam Switches 285
  References 286

12.1 INTRODUCTION

For high-voltage and high-power applications, silicon is by far the dominant semiconductor material. However, silicon has a number of material related limitations, e.g. a moderate thermal conductivity, a bandgap of 1.1 eV that effectively limits operation to temperatures below 200 °C, and electric breakdown occurs at relatively low fields. Wide-band-gap materials, such as silicon carbide (SiC), gallium nitride (GaN) and diamond, offer the potential to overcome both the temperature and power handling limitations of silicon. Diamond is the most extreme in this class of materials. Going by the fundamental material properties alone, it offers the largest benefits as a semiconductor material for power electronic applications. The rapid progress in synthesis technology has made it is possible to produce 10×10 mm, high-purity, homoepitaxial diamond layers by CVD.

On the other hand, diamond has a problem with the large carrier activation energy of dopants, which necessitates specialised device concepts to allow room temperature (RT) operation. In addition, process technology for diamond is immature. Therefore the development of diamond power devices also poses great challenges. The global market for power semiconductor devices is estimated to be about $10 billion and growing by 8 to 10 % per year [1]. Common power devices include two-terminal devices such as rectifiers and fast recovery diodes as well as three-terminal devices, e.g. thyristors, GTOs (gate turn-off thyristor), MOSFETs and IGBTs (insulated gate bipolar transistor). Major application areas include electric power transmission and distribution systems, traction drives

CVD Diamond for Electronic Devices and Sensors Edited by Ricardo S. Sussmann
© 2009 John Wiley & Sons, Ltd. ISBN: 978-0-470-06532-7

and motor control, as well as switch-mode power supplies. Perhaps the most demanding application is within power distribution, where HVDC (high voltage direct current) converters operate at hundreds of kilovolts and hundreds of megawatt levels, but with low switching frequency, typically 50 or 60 Hz. Thyristors, and to some extent IGBTs, are used in these applications. Nearer to the other end of the spectrum are switch-mode power supplies. These operate at much higher frequencies (kilohertz) but with lower power loads (kilowatts). For such applications MOSFETs and IGBTs are commonly used.

For diamond, even though in its infancy as a semiconductor material, a wealth of proof-of-principle, two-terminal and three-terminal devices has been made and tested. Two-terminal electronic diamond devices described in the literature include: p–n diodes, UV emitting p–n diodes, p–i–n diodes, various types of radiation detectors, Schottky diodes and photoconductive or electron beam triggered switches. For high-power/high-voltage applications, high-voltage Schottky diodes and photoconductive or electron-beam triggered switches have attracted a lot of interest. This is described in more detail in the two following sections.

Regarding three-terminal diamond devices, the first transistor action in diamond was reported by Prins in 1981 [2]. He demonstrated a bipolar n–p–n transistor made from natural p-type diamond. The n-type regions were created by carbon ion-implantation, creating zones with high defect concentration that exhibited n-type behaviour. However, the current gain was very low.

More interesting for implementation in diamond are unipolar devices, such as MISFETs (metal-insulator-semiconductor field effect transistor), MESFETs (metal epitaxial semiconductor field effect transistor) and JFETs (junction field effect transistor). The experimental efforts in investigating such devices, however, have been largely focused on devices for RF applications. The development of diamond high-voltage/high-power devices poses some additional challenges since power devices require relatively large areas of near defect-free material. In addition, a high aspect ratio structure is necessary to allow for high forward currents. Geis *et al.* have demonstrated a high aspect ratio vertical MISFET using natural p-type diamond [3]. Its performance, however, was very far from the theoretical limits. Such devices (Figure 12.1) require etching of high aspect ratio mesas, or trenches, in diamond, which can be achieved by, for example, ion-beam assisted etching [4], reactive ion etching [5] or inductively coupled plasma etching [6].

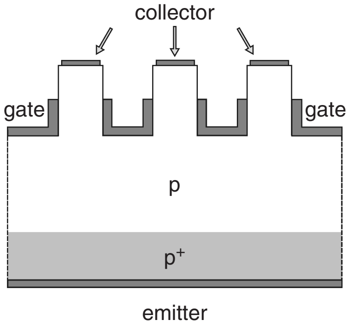

Figure 12.1 A possible vertical MESFET device structure for high-voltage/high-power applications. The narrow mesas, a few μm wide, are pinched off by applying bias to the Schottky metal gate

The present state of RF transistor development in diamond is described in the two following chapters: 13 by Kasu on H-terminated diamond field-effect transistors, and 14 by Kohn and Denisenko on doped diamond electronic devices.

12.2 HIGH-VOLTAGE/HIGH-POWER DIODES

One application where diamond diodes can be expected to deliver outstanding performance is as freewheeling diodes in power electronic systems, for example for motor control, switched mode power supplies or high-voltage, direct-current, transmission systems. Such diodes are connected anti-parallel with active switching devices such as IGBTs or MOSFETs. Freewheeling diodes are required to provide a path for the reverse current flow whenever inductive loads are switched off. This diode must have good reverse recovery characteristics with a small reverse recovery charge to keep the power dissipation low. Today, silicon p–i–n diodes are chiefly used for this purpose. Because of the relatively large amount of stored charge in bipolar devices, such as p–i–n diodes, the diode losses can be considerable. This is true in particular at high switching frequencies. Unipolar devices, such as Schottky barrier diodes (SBDs) have smaller stored charge and therefore exhibit better performance. This is due to the absence of minority carriers that otherwise have to be extracted at turn-off. Silicon carbide SBDs suitable for this application are, at the time of writing, commercially available with breakdown voltages of up to 600 V per junction. Due to the higher breakdown voltage and substantially higher carrier mobilities in diamond as compared with SiC, diamond Schottky diodes are expected to deliver even better turn-off performance and/or higher breakdown voltage. Their ability to operate at high temperatures is also very attractive. Other interesting applications for diamond SBDs include high-voltage, half wave and full wave rectifiers in power conversion applications.

12.2.1 Schottky diodes

In power devices it is desirable to combine a low specific on-state resistance (R_D) of the drift layer with a high breakdown voltage (V_{br}). For any given material there is a trade off between these two properties depending on the choice of doping concentration and thereby the depletion layer width at breakdown. For a SBD with a homogeneous p-doping in the drift layer and by neglecting any edge effects (i.e. field enhancement at the contact edge), the ratio V_{br}/R_D is given by:

$$\frac{V_{br}}{R_D} = \frac{1}{2} q E_{br} \mu_p p \tag{12.1}$$

where E_{br} is the breakdown field, μ_p the hole mobility and p the hole concentration in the drift layer. For diamond, the hole mobility is high. A μ_p above 1800 cm^2/Vs has been measured in boron doped material [7]. The breakdown field is also very high, $E_{br} > 10$ MV/cm is expected on theoretical grounds, but this requires an effective edge-termination structure and probably also nearly defect-free material. $E_{br} = 4$ MV/cm has been measured in intrinsic single-crystalline CVD diamond [8].

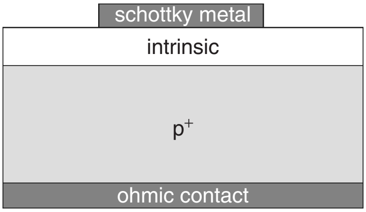

Figure 12.2 The basic m–i–p diode structure

From Equation (12.1) the situation seems very promising – at a first glance. However, due to the incomplete activation of the shallowest known dopant, boron, the hole concentration is much lower than the doping concentration (i.e. $p \ll N_A$) at RT. Thus, the situation is not as beneficial when comparing with semiconductor materials with shallow dopants, where complete activation can be achieved at RT. To overcome the problem associated with low activation, other device structures have been investigated. One particular structure that seems promising, is the metal–insulator–p$^+$ (m–i–p) structure, where an undoped (intrinsic) layer has been introduced between the Schottky metal contact and the doped layer in the traditional SBD structure (Figure 12.2). The doping concentration of the p$^+$ layer can be chosen to exceed 10^{19} atoms/cm^3, resulting in a high degree of activation in this layer due to the overlapping of the boron impurity band with the valence band.

One advantage with this structure is that the very high hole mobilities ($\mu_\mathrm{p} = 3800$ cm^2/Vs) and high breakdown field that have been measured in intrinsic diamond can be fully exploited. Another advantage is that the electric field is evenly distributed across the intrinsic region at reverse bias (compare the homogeneously doped SBD, where the field varies linearly over the depletion region). This is due to the lack of space charge at reverse bias in the intrinsic region.

In the m–i–p diode at low forward bias, the current is limited by thermionic emission over the Schottky barrier and the current–voltage characteristics obey the usual Schottky diode expression:

$$V = \frac{nkT}{q} \ln\left(1 + \frac{j}{j_0}\right) \text{ with } j_0 = A^* T^2 \exp\left(-\frac{\phi_B}{kT}\right) \tag{12.2}$$

Here V is the voltage drop, n the ideality factor, j the current density, k Bolzmann's constant, T the absolute temperature, A^* the effective Richardson constant, and ϕ_B the barrier height. At higher forward bias the current instead becomes limited by the free carrier space charge in the intrinsic layer and the voltage drop obeys the Mott–Gurney relationship:

$$V = \sqrt{\frac{8d^3 j}{9\varepsilon\mu}} \tag{12.3}$$

where V is the voltage drop over the intrinsic region, j is the current density, ε the dielectric constant of the material, and d the width of the intrinsic layer. In addition to the voltage drop over the intrinsic region, ohmic losses in the p$^+$ region and at the ohmic contact also contribute to the voltage drop. Empirically it has been found [8] that the total voltage drop over the m–i–p diode is well described (over many orders of magnitude in current) by the sum of Equations (12.2) and (12.3) and the ohmic voltage drop:

$$V = \frac{nkT}{q}\ln\left(1+\frac{j}{j_0}\right)+\sqrt{\frac{8d^3 j}{9\varepsilon\mu}}+rj \tag{12.4}$$

It is clear from this expression that in order to achieve a low voltage drop for a certain current requires a high mobility and, in particular, a thin intrinsic region. Since the width of the intrinsic region is determined by the required maximum blocking voltage of the reverse-biased m–i–p diode and the specific breakdown field strength of the material, it is clear that a high breakdown field is also necessary in order to obtain a low voltage drop. The ohmic voltage drop can be reduced by having a thin, highly doped, p^+ region and using a contact metallisation with a low specific contact resistance to boron-doped material. Very low contact resistances have been achieved in heavily boron-doped diamond, e.g. Werner *et al.* [9] measured a contact resistance $\rho_c = 2.3\times10^{-7}\ \Omega\,\text{cm}^2$ on heavily doped diamond with [B] $= 8\times10^{21}\ \text{cm}^{-3}$ and $\rho_c = 4.9\times10^{-3}\ \Omega\ \text{cm}^2$ for [B] $= 1\times10^{20}\ \text{cm}^{-3}$ using annealed Al:Si contacts. The low contact resistance is due to carbide formation (SiC in this case) at the metal/diamond interface. Other carbide forming contact metals, e.g. titanium, have also been reported to provide good ohmic contact to boron doped diamond after annealing.

In 1992 Denisenko *et al.* [10] first suggested the use of undamaged virgin insulating diamond as the hole drift layer and exploiting only the injection properties of p-type diamond in devices. Using natural diamond with boron impurities introduced by ion implantation, they demonstrated rectification in planar m–i–p structures with a breakdown voltage of about 100 V. As a result of a collaboration between ABB and Element Six Ltd, Isberg *et al.* in 2002 published results on a m–i–p^+ diode capable of blocking 2.5 kV at 1 mA/cm^2 leakage [11] (see also Figure 12.4). More details were later given in Ref. [8]. This diode consisted of a gold Schottky contact (Figure 12.3), an 18-µm thick layer of near intrinsic homoepitaxial diamond on which a thicker (300 µm) layer of boron-doped diamond had been deposited (Figure 12.4), and a Ti/Al/Au ohmic contact. The on-resistance was about 3 Ωcm^2 at 10 V forward bias, partly due to the thick p^+ layer in this device. Butler *et al.* [12] published data in 2003 on planar diode structures on low-doped homoepitaxial diamond. One of these devices was able to support 6 kV before breakdown occurred at the surface. No forward conduction data were given except that large forward resistances were measured, 300 Ωcm^{-2}. Substantially lower on-resistances were achieved later. Brezeanu *et al.* [13] report 0.5 Ωcm^2 at 5 V in m–i–p diodes with 10-µm intrinsic layer. Chen *et al.* [14] published values of 9.7 mΩcm^2 at RT and 4.7 mΩcm^2 at 873 K, both for a forward bias of 3 V. This device had a thin i-layer of 500 nm and was able to block about 40 V at 5 µA reverse leakage.

The trade-off between on-resistance and breakdown voltage obtained from simulations in this type of device is shown in Figure 12.5.

An attractive property of diamond is its ability to operate at very high temperatures. Vescan *et al.* [16] have demonstrated a diode with refractory W:Si Schottky contacts that functioned for temperatures up to 1000 °C in vacuum, where it failed most likely due to carbide formation at the metal/diamond interface.

A merged p–n/Schottky diode, or junction barrier Schottky (JBS) diode, with a nitrogen/boron doped p–n junction was described by Kubovitch *et al.* [17]. The intention was

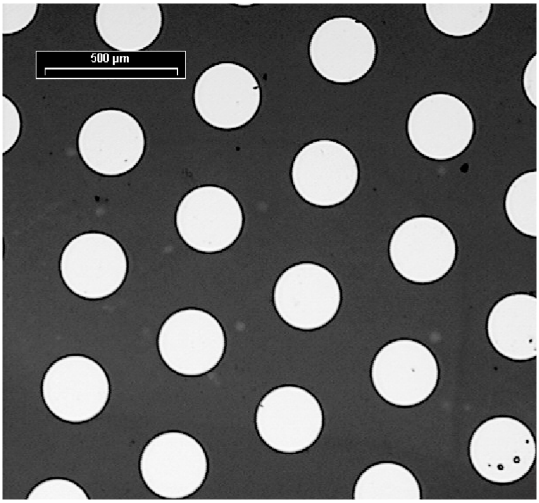

Figure 12.3 Small m–i–p diodes with gold Schottky contacts on single crystalline diamond

to combine the good blocking properties of a p–n junction (even though the activation energy of nitrogen is very large at 1.7 eV) with the low forward drop of the SBD. Such diodes were fabricated and tested, and the diode current–voltage characteristics showed some of both the Schottky and the p–n junction characteristics. The breakdown field was 2.5 MV/cm and the diode was able to operate up to 1000 °C in vacuum.

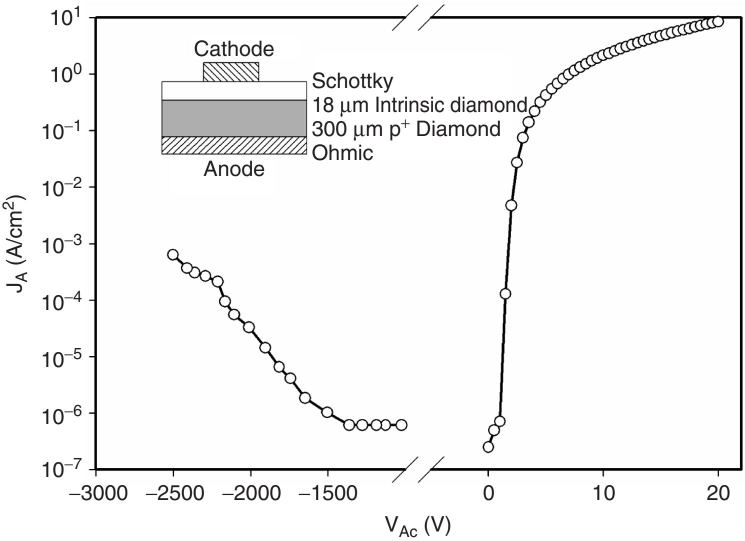

Figure 12.4 M–i–p diode in single crystalline diamond with high reverse breakdown voltage (from [8]). Reprinted from T-ED 2099B, IEEE Transactions on Electron Devices by D. J. Twitchen, A. J. Whitehead, S. E. Coe, J. Isberg, J. Hammersberg, T. Wikstrom and E. Johansson, 51, 826-828, by permission of the IEEE, Copyright 2004

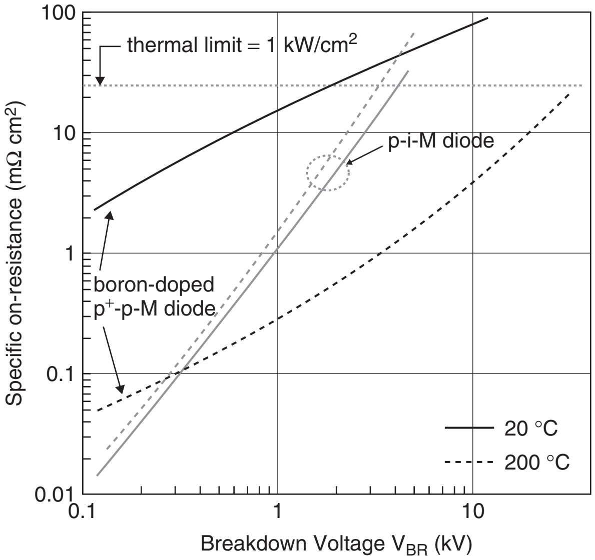

Figure 12.5 Simulations showing the trade-off between on-state resistance and breakdown voltage for m–i–p diodes and SBDs in diamond (from [15]). Reprinted from Diamond and Related Materials, Diamond Power Devices, Concepts and Limits, by A. Denisenko and E. Kohn, 14, 3-7, by permission of Elsevier, copyright 2005

12.2.2 Delta-doped Schottky diodes

A variation on the SBD scheme that may prove successful in the future is a diode with stacked delta-doped layers [15]. This has been suggested in order to achieve lower on-resistances and/or higher breakdown voltage. The delta doped layers are thin (ideally just a few atomic layers), very heavily doped layers with near complete RT thermal activation. Simulations show that such diodes would have a better breakdown voltage/on-state resistance trade-off than ideal SiC or GaN devices. See also Chapter 14 by Kohn and Denisenko.

12.2.3 Edge termination

For diamond Schottky diodes, the edge termination of the Schottky contact presents a difficult problem due to the lack of a shallow n-doping. Without effective edge termination, strong field enhancement at the contact edge cannot be avoided, which causes premature avalanche breakdown of the device. The role of edge termination is to distribute the field in the vicinity of the edge, thereby increasing the attainable blocking voltage, and is critical to the operation and reliability of the device. However, the experimental results described above were all accomplished with nonterminated structures.

Several different types of edge termination have been explored for Schottky diodes in wide-bandgap semiconductors. Some of the more common ones are shown in Figure 12.6, and include guard rings, metal field plates extending over an insulating surface layer, resistive Schottky barrier field plates (RESP), and junction-termination extension (JTE).

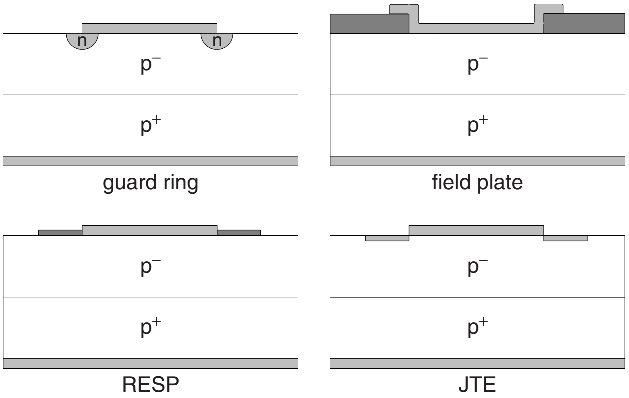

Figure 12.6 Different edge terminations for Schottky contacts: (upper left) guard rings; (upper right) metal field plate; (lower left) resistive Schottky barrier field plate; (lower right) implanted junction-termination extension

Guard rings (Figure 12.6) are commonly used in silicon power devices. Dopants are introduced by diffusion or ion implantation. The concept can be further improved by introducing several concentric so-called floating guard rings with optimised width and spacing, so that the field is shared equally between the rings. To achieve an effective guard ring termination, relatively deep guard rings are required. This method of termination is not a particularly attractive alternative for diamond Schottky diodes because of the lack of a shallow n-dopant, and the high implantation energies required for deep implantation. Diffusion is not an option, since it would require extreme temperatures, if at all possible.

A more promising edge termination for diamond Schottky diodes is to use field plates. As shown in Figure 12.6, the metal contact is extended over an insulating layer deposited on the surface. High fields can still occur at the edge of the field plate, especially if the insulating layer is thin and the surface layer has a low dielectric constant. Brezeanu *et al.* [18] tested the field plate edge termination on diamond m–i–p diodes. This was done in combination with a ramped insulating layer (SiO_2) to reduce the field enhancement further. Their oxide was ramped at a low angle of 11° to the surface and had a full thickness of 2.2 μm. They achieved a breakdown voltage of 1.1 kV for an i-layer of 13 μm. However, according to simulations, much better reverse performance was expected. In this context, this group also proposed the use of dielectrics with higher dielectric constant (high-*k* dielectrics), such as silicon nitride (Si_3N_4) and hafnium oxide HfO_2 to achieve better termination.

The resistive Schottky barrier field plate (RESP) termination (Figure 12.6) is another method of dispersing the surface potential at the edge of the junction. It consists of a resistive material on the semiconductor surface, connected to the metal contact. The high resistivity of the material causes a drop in potential from the main Schottky diode to the exterior of the RESP ring, leading to a spreading of the depletion region. This concept is very sensitive to the sheet resistivity of the resistive material. With a too high resistivity, the potential drop is similar to that of an unterminated diode. If it is too low, the potential at the end of the ring is comparable to that of the main contact and high fields are again expected at the edge. Consequently, the temperature dependence of the RESP resistivity has a strong influence on the performance. A low temperature dependence of the resistivity is also required for stable operation. For this reason RESP is a less viable alternative if the device has to operate over a wide temperature range. No RESP terminations on diamond diodes have been presented in the literature, but RESP terminations have been explored on e.g. 6H–SiC [19] using thermally oxidised titanium. The case is similar for the junction termination extension (JTE) shown in Figure 12.6. In this case, a highly resistive layer is formed by introducing a charge at the surface through controlled ion implantation. The high activation energy of available n-dopants in diamond may render this choice ineffective. JTE has however been used for n-type SiC Schottky diodes aimed for high voltage and high temperature [20].

12.3 PHOTOCONDUCTIVE AND ELECTRON BEAM SWITCHES

In the field of pulsed power, the issue is to accumulate electric energy over a relatively long period and release it during very short times, thereby creating very high power levels. This requires the use of various pulse forming techniques together with closing and/or opening switches that can handle extreme currents and often very high voltages. Typical applications include pulsed radar systems, generation of ultrashort X-ray pulses, driving Pockels cells for laser systems and inertial confinement fusion, just to mention a few. Common semiconductor power electronic devices, such as thyristors or IGBTs, are not suitable for more extreme applications that require switching of currents and voltages of several tens of kiloamperes and kilovolts, perhaps with nanosecond or sub-nanosecond risetimes. In such applications, different types of vacuum or gas-filled tubes such as krytrons, sprytrons or thyratrons are often used instead. Solid-state devices, such as photoconductive and electron-beam triggered switches, can however provide many advantages. Considerable efforts have been spent on the development of switches to meet tough demands on ultra-fast switching of high voltages with short risetimes and jitter-free operation. In its simplest form, such a solid-state switch consists of a piece of undoped semiconductor with two contacts. The switch is rendered temporarily conducting by the creation of charge carriers in the material by short pulse illumination or by pulsed e-beam excitation. The unique properties of diamond, particularly its high mechanical and dielectric strength together with its high carrier mobilities and thermal conductivity, suggest that the material should be an ideal semiconductor in such applications. Furthermore, as no doped layers are required, the lack of shallow dopants in diamond poses no problem. However, due to the high band gap in diamond (5.47 eV, corresponding to 226 nm), UV source illumination is required for photo-triggered devices.

Electron-beam triggered diamond devices have been studied by several groups, see e.g. [21–23]. Lin and Sverdrup in 1996 [24] demonstrated an electron-beam-activated (Figure 12.7) switch based on IIa natural diamond. This group achieved switching of up to 19 kA/cm^2 and peak powers up to 25 kW with a less than 100 ns risetime.

Fast opening switches are required for inductive energy storage (IES) in pulsed power applications. Compared with capacitive energy storage, IES provides up to ten-times higher energy density. Krishnan [25] described an e-beam controlled opening switch based on polycrystalline CVD diamond. This switch had an active area of 3 mm^2. The switch was able to interrupt 100 A at 500 V and was used to produce 7-kV, 30-ns, pulses when used as an opening switch in an inductive circuit.

Optically triggered, or photoconductive, diamond switches with similar performance have also been studied and are described in the literature (see e.g. [26–31]). Optical

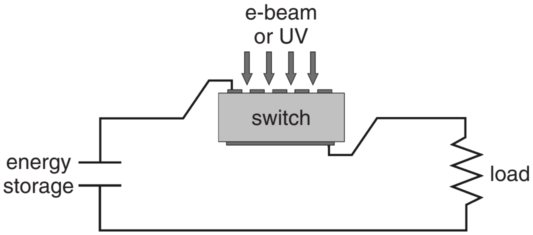

Figure 12.7 Schematic of a photoconductive or e-beam triggered closing switch

triggering has some advantages over e-beam triggers, e.g. operation in air is possible and lasers producing ultra-short pulses are readily available. However, the cost of short pulse UV lasers may be prohibitively expensive in many applications. Krishnan *et al.* [32] describes the development of a UV xenon flash lamp with strong output in the spectral interval 220–250 nm that can be used to produce submicrosecond pulses for diamond switches. Xu *et al.* [33] have investigated the use of polycrystalline CVD diamond in an entirely different kind of switch intended for a X-band microwave pulse compression system. The idea behind this switch is rapidly to modulate the conductivity of a diamond by UV laser illumination, thereby altering its reflectivity to microwaves. The highest reflectivity for 11 GHz microwaves was 38 %, achieved by illuminating the diamond with 10-ns, 160-mJ, pulses with a wavelength of 266 nm. For above-bandgap radiation, much higher reflectivities should be possible to reach.

Since the cost of the trigger source is a major part of the total cost for pulsed power switches, it is important to be able to control a large current with a small trigger current (for e-beam trigger) or photon flux (for optical trigger), i.e. a high gain is desired. In gallium arsenide (GaAs) closing switches, this can be achieved due to a lock-on effect in GaAs, which leads to a persistence of the current following a short trigger. Such GaAs switches with a diamond coating to improve contact performance have been described by Davanloo *et al.* [34, 35]. For diamond, an interesting possibility is to use a weak trigger pulse to initiate avalanche breakdown in the material. With such switches, very large current densities and short risetimes could be achieved following a relatively weak trigger pulse. Recent circuit simulations of triggered avalanche switches [36] and optically triggered Schottky barrier diodes in diamond [37] have yielded promising results. This was under the assumption that such devices can be biased to fields near the theoretical maximum without spontaneous breakdown. This puts severe demands on sample processing and requires the development of an effective edge termination to control the field at contact edges.

REFERENCES

[1] P.D. Taylor, D.J. Chamund and A. Garraway, *Industrial Diamond Review*, **66**, 19–22 (2006).
[2] J.F. Prins, *Applied Physics Letters*, **41**, 950–952 (1982).
[3] M.W. Geis, N.N. Efremow and D.D. Rathman, *J. Vac. Sci. Technol. A, Vac. Surf. Films (USA)*, 1953–1954 (1988).
[4] N.N. Efremow, M.W. Geis, D.C. Flanders, G.A. Lincoln and N.P. Economou, *Journal of Vacuum Science & Technology B: Microelectronics Processing and Phenomena*, **3**, 416–418 (1984).

[5] Y. Ando, Y. Nishibayashi, K. Kobashi, T. Hirao and K. Oura, *Diamond and Related Materials*, **11**, 824–827 (2002).

[6] J. Enlund, J. Isberg, M. Karlsson, F. Nikolajeff, J. Olsson and D.J. Twitchen, *Carbon*, **43**, 1839–1842 (2005).

[7] S. Yamanaka, D. Takeuchi, H. Watanabe, H. Okushi and K. Kajimura, *Phys. Status Solidi A*, **174**, 59–64 (1999).

[8] D.J. Twitchen, A.J. Whitehead, S.E. Coe, J. Isberg, J. Hammersberg, T. Wikstrom and E. Johansson, *IEEE Trans. Electr. Dev.*, **51**, 826–828 (2004).

[9] M. Werner, O. Dorsch, H.U. Baerwind, A. Ersoy, E. Obermeier, C. Johnston, S. Romani, P.R. Chalker, V. Moore and I.M. Buckley-Golder, *Diamond and Related Materials*, **3**, 983–985 (1994).

[10] A.V. Denisenko, A.A. Melnikov, A.M. Zaitsev, V.I. Kurganskii, A.J. Shilov, J.P. Gorban and V.S. Varichenko, *Materials Science & Engineering B: Solid-State Materials for Advanced Technology*, **B11**, 273–277 (1992).

[11] J. Isberg, J. Hammersberg, E. Johansson, T. Wikstrom, D.J. Twitchen, A.J. Whitehead, S.E. Coe and G.A. Scarsbrook, *Science*, **297**, 1670–1672 (2002).

[12] J.E. Butler, M.W. Geis, K.E. Krohn, J. Lawless Jr, S. Deneault, T.M. Lyszczarz, D. Flechtner and R. Wright, *Semiconductor Science and Technology*, **18**, 67–71 (2003).

[13] M. Brezeanu, T. Butler, N. Rupesinghe, S.J. Rashid, M. Avram, G.A.J. Amaratunga, F. Udrea, M. Dixon, D. Twitchen, A. Garraway, D. Chamund and P. Taylor, *IET Circuits, Devices & Systems*, **1**, 380–386 (2007).

[14] Y. Chen, M. Ogura, T. Makino, S. Yamasaki and H. Okushi, *Semiconductor Science and Technology*, **20**, 1203–1206 (2005).

[15] A. Denisenko and E. Kohn, *Diamond and Related Materials*, **14**, 491–498 (2005).

[16] A. Vescan, I. Daumiller, P. Gluche, W. Ebert and E. Kohn, *IEEE Electron Device Letters*, **18**, 556–558 (1997).

[17] M. Kubovic, H. El-Hajj, J.E. Butler and E. Kohn, *Diamond and Related Materials*, **16**, 1033–1037 (2007).

[18] M. Brezeanu, T. Butler, N.L. Rupesinghe, G.A.J. Amaratunga, S.J. Rashid, F. Udrea, M. Avram and G. Brezeanu, *Diamond and Related Materials*, **16**, 1020–1024 (2007).

[19] M. Bhatnagar, H. Nakanishi, S. Bothra, P.K. McLarty and B.J. Baliga, p. 89–94, 1993.

[20] D. Alok and B.J. Baliga, *IEEE Transactions on Electron Devices*, **44**, 1013–1017 (1997).

[21] G.M. Loubriel, F.J. Zutavern, M.H. Ruebush, D.J. Brown, M.W. O'Malley, W.D. Helgeson, R.R. Prasad, I.V. Tzonev, S.W. Gensler, N. Qi and M. Krishnan, *Proceedings of the Intersociety Energy Conversion Engineering Conference*, pp. 307–311, 1997.

[22] J. Achard, F. Silva, H. Schneider, R.S. Sussmann, A. Tallaire, A. Gicquel and M.C. Castex, *Diamond and Related Materials*, **13**, 876–880 (2004).

[23] R.P. Joshi, K.H. Schoenbach, C. Molina and W.W. Hofer, *Journal of Applied Physics*, **74**, 1568 (1993).

[24] S.-H. Lin and L.H. Sverdrup, *Materials Research Society Symposium – Proceedings*, pp. 383–393, 1996.

[25] M. Krishnan, X. Xu, J. Schein, N. Qi, R. Prasad and S. Gensler, *Digest of Technical Papers – IEEE International Pulsed Power Conference*, **2**, 1222–1225 (1999).

[26] S. Feng, P.T. Ho and J. Goldhar, *IEEE Transactions on Electron Devices*, **37**, 2511–2516 (1990).

[27] L.A. Vermeulen, J.F. Young, M.I. Gallant and H.M. van Driel, *Solid State Communications*, **38**, 1223–1225 (1981).

[28] R.R. Prasad, J. Schein, S.W. Gensler and M. Krishnan, *Digest of Technical Papers – IEEE International Pulsed Power Conference*, **1**, 142–145 (1999).

[29] J.F. Young, L.A. Vermeulen, D.J. Moss and H.M. van Driel, *Applied Physics Letters*, **42**, 434–436 (1983).

[30] P.T. Ho, C.H. Lee, J.C. Stephenson and R.R. Cavanagh, *Optics Communications*, **46**, 202–204 (1983).

[31] M.W. Geis, K.E. Krohn, J.M. Lawless, S.J. Deneault, M.F. Marchant, J.C. Twichell, T.M. Lyszczarz, J.E. Butler, D.D. Flechtner and R. Wright, *Applied Physics Letters*, **84**, 4620–4622 (2004).

[32] M. Krishnan, J.R. Thompson, D. Parks, A.N. Gerhan, E.H. Baksht, M.I. Lomaev and D.V. Rybka, *Proceedings of SPIE – The International Society for Optical Engineering*, p. 626310, 2006.

[33] X. Xu, J. Schein, N. Qi, R.R. Prasad, M. Krishnan, T. Fumihiko and S.G. Tantawi, *IEEE Transactions on Plasma Science*, **29**, 85–92 (2001).

[34] F. Davanloo, C.B. Collins and F.J. Agee, *IEEE Transactions on Plasma Science*, **30**, 1897–1904 (2002).

[35] F. Davanloo, C.B. Collins and F.J. Agee, *IEEE Conference Record of Power Modulator Symposium*, pp. 187–190, 2002.

[36] R.S. Balmer, I. Friel, S.M. Woollard, C.J.H. Wort, G.A. Scarsbrook, S.E. Coe, H. El-Hajj, A. Kaiser, A. Denisenko, E. Kohn and J. Isberg, *Philosophical Transactions of the Royal Society A: Mathematical, Physical and Engineering Sciences*, **366**, 251–265 (2008).

[37] M. Brezeanu, S.J. Rashid, T. Butler, N.L. Rupesinghe, F. Udrea, K. Okano, G.A.J. Amaratunga, D.J. Twitchen, A. Tajani, C. Wort and M.P. Dixon, *Diamond and Related Materials*, **14**, 499–503 (2005).

13 H-Terminated Diamond Field-Effect Transistors

MAKOTO KASU

NTT Basic Research Laboratories, Atsugi Japan

13.1 Introduction 289
  13.1.1 Why diamond RF power transistors? 289
  13.1.2 H-termination as p-type doping 291
  13.1.3 FET device structure 292
  13.1.4 Requirements of device substrate 292
13.2 Experimental Procedure 293
  13.2.1 FET fabrication process 293
  13.2.2 Measurement and analysis procedure 295
13.3 Results 295
  13.3.1 DC characteristics 295
  13.3.2 DC analysis: influence of crystalline properties 296
  13.3.3 RF small-signal characteristics 298
  13.3.4 RF noise characteristics 300
  13.3.5 RF large-signal characteristics 300
13.4 Discussion 302
  13.4.1 RF analysis: saturation velocity 302
  13.4.2 RF analysis: band diagram 303
  13.4.3 Device temperature during power operation 306
  13.4.4 Stability and reliability 307
13.5 Summary 309
  References 310

13.1 INTRODUCTION

13.1.1 Why diamond RF power transistors?

Diamond is one of the wide band-gap semiconductors. Table 13.1 summarizes the physical properties of wide band-gap semiconductors. Diamond has an indirect band gap, E_G, of

CVD Diamond for Electronic Devices and Sensors Edited by Ricardo S. Sussmann
© 2009 John Wiley & Sons, Ltd. ISBN: 978-0-470-06532-7

5.47 eV, and thereby a breakdown electric field strength, E_{BR}, in terms of a critical field for avalanche estimated to be >20 MV/cm [1]. High E_{BR} leads to high-voltage handling capability. Experimentally reported E_{BR} values range from 2 to 8 MV/cm [2, 3]. Reverse breakdown voltage of >6 kV in Schottky diode [4] and the drain breakdown voltage of ~200 V in field-effect transistor (FET) [5] have been reported.

In power operation, there is a need for high current capability, which is determined by the carrier concentration and the mobility, μ, in a low field, and the saturation velocity, v_{SAT}, in a high field. Extremely high carrier mobility μ (4500 cm^2/Vs for electrons and 3800 cm^2/Vs for holes) has been reported for single-crystal diamond formed by chemical vapor deposition (CVD) [6]. These μ values were measured by the time-of-flight method for undoped diamond (see Chapter 12 by Isberg in this book). Saturation velocities of 1.5×10^7 cm/s for electrons and 1.1×10^7 cm/s for holes [7] have been reported for natural diamond. These properties lead to a high radio-frequency (RF) power capability. In diamond FETs, a current-gain, cut-off, frequency [transition frequency (f_T)] of 45 GHz and a power-gain, cut-off, frequency [maximum frequency of the oscillation (f_{MAX})] of 120 GHz have been achieved [8]. The details are described in Section 13.3.3. A RF output power of 2.1 W/mm at 1 GHz in class-A operation has been reported [9].

High power levels lead to high power loss and thereby to self-heating and high device temperatures. The high thermal conductivity of diamond means that power devices can be fabricated on their intrinsically integrated heat spreader. Diamond possesses a thermal conductivity, λ, of 22 W/cm K (Table 13.1), which is the highest among materials. Owing to the high thermal stability, diamond will allow us to combine a device structure capable of generating an extremely high power density with an ideal heat sink. Little increase in temperature of diamond power FETs during power operation has been demonstrated [10]. The thermal device capability of diamond FETs is described in Section 13.4.3. Of course, if oxygen could be excluded because diamond easily reacts with oxygen, the temperature of chemical decomposition of diamond should be high. A diamond Schottky diode operating at 1000°C has been demonstrated [11]. High-power capability in a high-frequency range can be estimated in terms of Johnson's figure of merit (JFOM) [12]. The JFOM is related to the breakdown field, E_{BR}, and the carrier saturation velocity v_{SAT}:

$$\mathrm{JFOM} = (\mathrm{E_{BR} v_{SAT}}/2\pi)^2 \tag{13.1}$$

Table 13.1 Physical properties and JFOM device figures of merit for wide-band-gap semiconductors. E_G is the band gap energy, E_{BR} is the breakdown electric field strength, v_{SAT} is the saturation velocity, μ is the mobility, ε_r is the relative dielectric constant, λ is the thermal conductivity, and JFOM is Johnson's device figure of merit (normalized by silicon's value)

Material	E_G(eV)	E_{BR}(MV/cm)	V_{sat}($\times 10^7$ cm/s)	μ (cm^2/Vs)	ε_r	λ (W/cmK)	JFOM
Diamond	5.47	>20	1.5 (e) 1.1 (h)	~ 4500 (e) ~ 3800 (h)	5.7	22	5400 (h)
GaN	3.42	3	2.4 (e)	~ 2000 (e)	8.9	1.5	580
SiC	3.26	2.8	2.2 (e)	~ 1000 (e)	9.7	4.9	420
Si	1.12	0.3	1.0 (e)	~ 1350 (e)	11.9	1.5	1

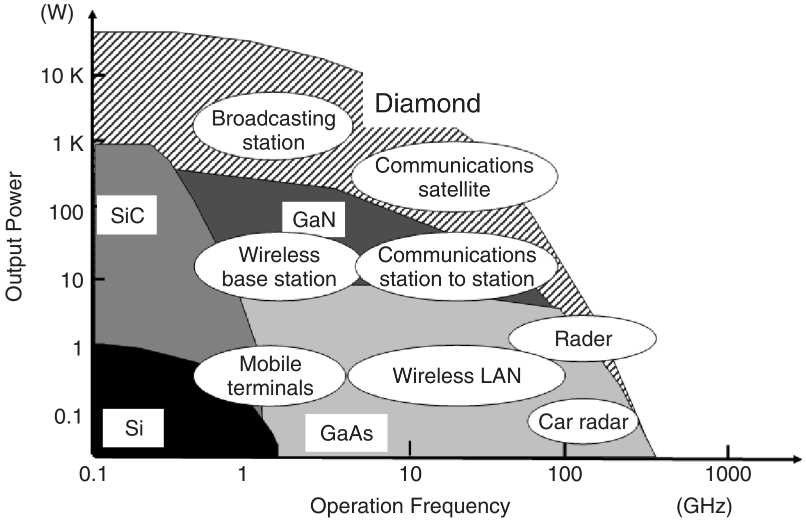

Figure 13.1 Output power and operation frequency currently required for specific devices in systems along with the semiconductor materials. Reprinted from Diamond and Related Materials, Diamond-based RF power transistors: Fundamentals and applications, by M. Kasu, K. Ueda, Y. Yamauchi, A. Tallaire, T. Makimoto, Vol 16, Iss 4-7, pgs 1010-1015 (2007) Copyright Elsevier

In the device characteristics, E_{BR} corresponds to the maximum voltage swing, and v_{SAT} is related to the maximum output current. The JFOM of diamond is about nine-times higher than for GaN and about thirteen-times higher than for SiC, and is the highest among semiconductors. Therefore, diamond is expected to show the highest power capability in a high-frequency range.

One field in which diamond devices could play an active part is wireless communications. Figure 13.1 shows the output power and operation frequency currently required for specific devices in systems, along with the semiconductor materials that have been or will be used to meet these requirements. Cellular phones, whose power amplifiers use GaAs heterojunction bipolar transistors (HBTs), require an output power and frequency of 0.9 W and 1.45 GHz, respectively. The base stations currently use GaAs FETs as output power amplifiers. On the other hand, broadcasting stations, communications satellites, and radars require output powers and frequencies that are unattainable with conventional semiconductor devices. They therefore still rely on traveling-wave tubes (TWT), which are problematic because of their weight. It is expected that diamond transistors will replace vacuum tubes in the future.

13.1.2 H-termination as p-type doping

As described in Section 13.2.1, in FETs the maximum current is limited by the maximum available carrier concentration and mobility. In diamond, because of its wide band gap, for p-type impurity, the activation energy of the B acceptor is 0.37 eV, and for n-type impurity, that for P and N donors are 0.6 [13] and ~1.7 eV, respectively (see Chapter 3 by A. Mainwood in this book). These values are much higher than the thermal energy at room temperature (RT), which is 26 meV. Therefore, the probability of carriers (electrons and holes) being released from the donor and the acceptor impurities is quite low ($<\sim10^{-6}$) at RT, and their dopants can not be used in transistors at RT.

An alternative method is to use a hole channel formed near the surface of H-terminated diamond [14, 15]. This is the most effective doping method known at present. The typical hole sheet concentration and mobility at RT are $(0.5-1) \times 10^{13}$ cm^{-2} and 50–150 cm^2/Vs, respectively, and thus the conductance is $\sim10^4$ Ωcm. Various explanations as to why the H-termination induces hole channels have been proposed [15–17] (see also Chapter 4 by Ley in this book), but they do not explain the results completely. However, the mobility and hole concentration result in a current level that is high enough for transistor action at RT. The details of the doping method are described in Chapter 4.

H-surface termination can be accomplished as an as-grown surface of diamond after microwave plasma CVD growth or through the exposure of diamond surface to H plasma in a microwave plasma CVD reactor. When the H-terminated surface is exposed to air, the sample shows p-type conductivity. Therefore, in addition to H surface termination, adsorbates from air are necessary.

The hole channel formed near the surface by the H surface termination is historically called the 'surface channel'. This term often confuses researchers because the rectifying properties of the metal/H-terminated diamond contact and the modulation of its conductivity by external gate bias cannot be straightforwardly explained in terms of the 'surface channel' [16].

13.1.3 FET device structure

FETs with H surface termination were pioneered by Kawarada [18]. There are two different FET concepts with different gate structures. In the first structure, the gate metal was evaporated directly onto the H-terminated diamond surface [5, 18]. In the other, it was evaporated on a thin insulator layer on H-terminated diamond surface [19–21]. The former structure is called a metal–semiconductor (MES) FET and the latter structure is called a metal–insulator–semiconductor (MIS) FET. In the latter, thin insulator layers, CaF_2 [19–21] and Al_2O_3 [22], have been used. MISFETs with a CaF_2 insulator layer show a large drop in RF current due to deep traps in the CaF_2 insulator layer [21] and therefore do not seem suitable as RF power devices. However, even for the former, the electrical properties show MISFET-like behavior, rather than MESFET. The details are described in Section 13.4.2.

13.1.4 Requirements of device substrate

The layer of a diamond FET is normally homoepitaxial diamond grown on a high-pressure, high-temperature (HPHT), synthesized diamond substrate. In comparison with polycrystalline diamond, the advantage of a homoepitaxial layer is that it has no grain boundaries and relatively low concentrations of impurities such as B and N. The surface orientation normally used is (001), but there are a few reports of (111) orientation [23]. For (111) orientation, twin crystalline defects form more easily. Generally, the hole concentration for (111) orientation is 1.5×10^{13} cm^{-2}, which is higher than that on (001) orientation [24], but the FET's drain current for (111) orientation is lower than that for (001) orientation. The problem with homoepitaxial diamond is that its size is limited by the size of the commercially available HPHT substrate (4×4 mm^2 square for (001) orientation and 3×3 mm^2 square for (111) orientation).

One idea for overcoming the small-size problem is to use diamond grown on foreign substrates. As example of this approach is highly oriented diamond (HOD) grown on a Si substrate. HOD supplied by Element Six is type-IIa polycrystalline diamond, in which ~90 % of the grain is oriented in the (110) direction [25]. The maximum drain current value obtained is 1.5-times higher than that of a homoepitaxial diamond FET. The f_T and f_{MAX} values are 45 and 120 GHz, respectively, the highest among diamond. HOD grown on (001) Ir-coated $SrTiO_3$ quasi-substrate has also been reported [26] (see also Chapter 6 by M. Schreck in this book). The thermal stress that develops between the Ir/SrTiO3 substrate and the diamond film upon cooling after growth may lead to delamination. This currently limits the obtainable surface area to approximately 1 cm^2 and often leads to cracks due to the uncontrollable lift-off process. Although the grain boundaries and defects remain on the surface, FETs showed good RF properties with f_T of 9.6 GHz and f_{MAX} of ~16 GHz [26]. Nanocrystalline diamond can also be grown on Si wafer, for which the size is not limited. FETs on nanocrystalline diamond have shown moderate RF properties of f_T and f_{MAX} of approximately 1 GHz [27].

13.2 EXPERIMENTAL PROCEDURE

13.2.1 FET fabrication process

Figure 13.2 shows photographs and a schematic cross-section of an H-terminated diamond FET fabricated by the University of Ulm and NTT. The sample has a homoepitaxial layer grown on HPHT-synthesized Ib-type ($3 \times 3 \times 0.5$ mm^3) substrate. Each device comprises a pair of FETs in order to double the channel width. In this case, a T-shaped gate with

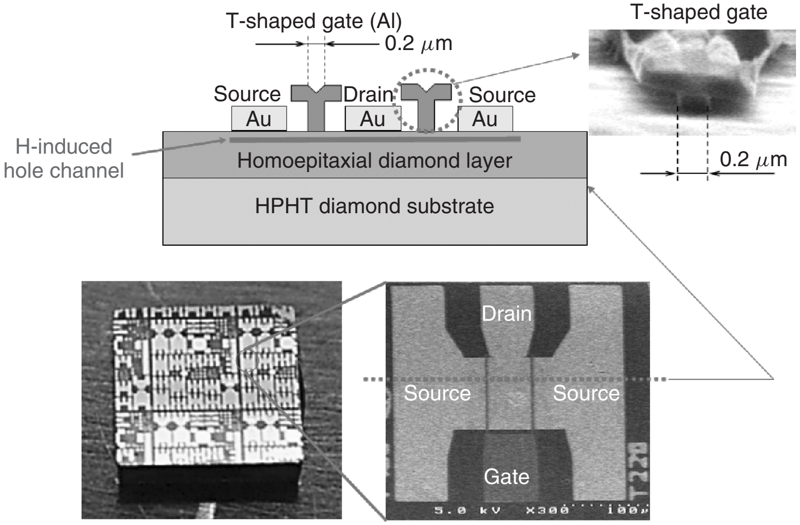

Figure 13.2 H-terminated diamond FET fabricated by the University of Ulm and NTT. Reproduced courtesy of Erhard Kohn

a length of 0.2 μm was fabricated by using electron-beam lithography. The T-shape can reduce gate resistance in RF and increase the cut-off frequency.

Figure 13.3 outlines the processes for fabricating H-terminated diamond FETs on a CVD homoepitaxial diamond layer. The CVD diamond layer is normally a 1-μm-thick homoepitaxial diamond layer on HPHT single-crystal (001) diamond substrate [Figure 13.3(a)]. The homoepitaxial layer is grown by using a microwave-plasma CVD system with a

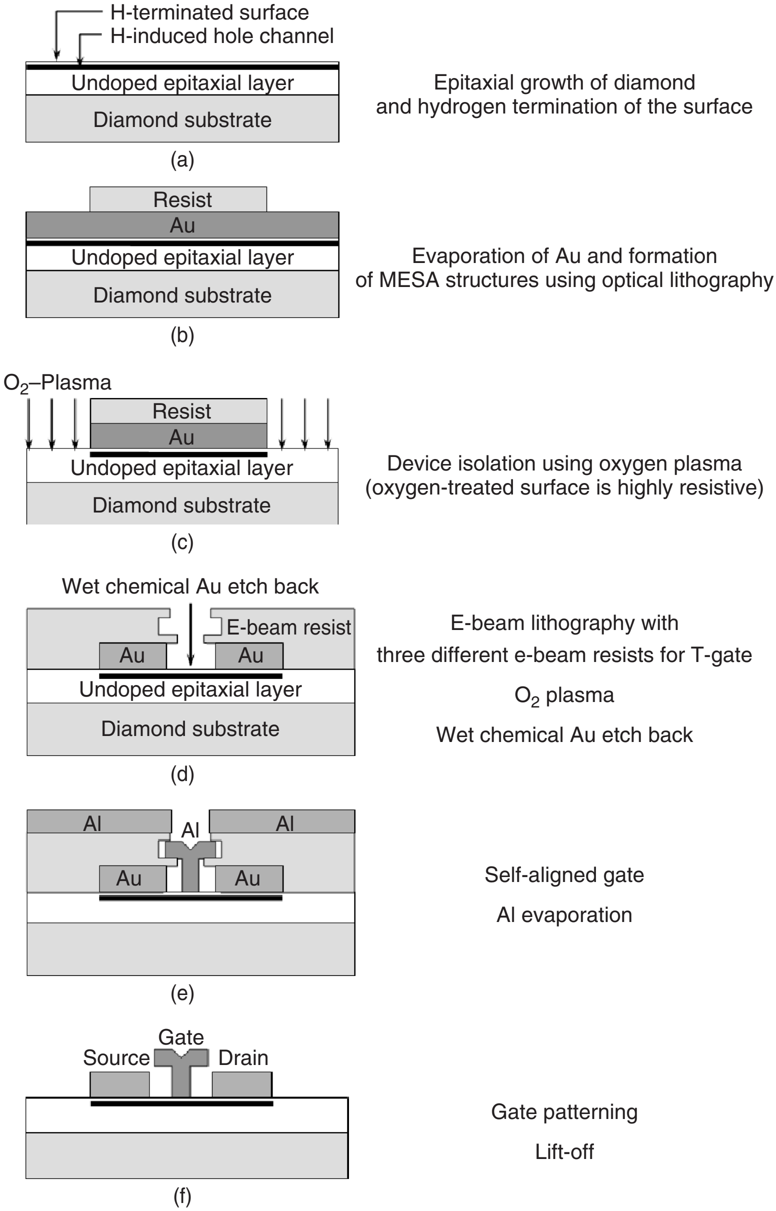
H-terminated surface
H-induced hole channel
Undoped epitaxial layer
Diamond substrate
Epitaxial growth of diamond and hydrogen termination of the surface
(a)
Resist
Au
Undoped epitaxial layer
Diamond substrate
Evaporation of Au and formation of MESA structures using optical lithography
(b)
O2–Plasma
Resist
Au
Undoped epitaxial layer
Diamond substrate
Device isolation using oxygen plasma (oxygen-treated surface is highly resistive)
(c)
Wet chemical Au etch back
E-beam resist
Au
Au
Undoped epitaxial layer
Diamond substrate
E-beam lithography with three different e-beam resists for T-gate
O2 plasma
Wet chemical Au etch back
(d)
Al
Al
Al
Au
Au
Self-aligned gate
Al evaporation
(e)
Gate
Source
Drain
Gate patterning
Lift-off
(f)

Figure 13.3 Fabrication procedure for H-terminated diamond FETs

microwave power of 1.3 kW and frequency of 2.45 GHz. As described in Section 13.2.2, H-surface termination is prepared as as-grown CVD surface. The H-terminated surface in air shows p-type conduction, and a hole channel therefore forms near the surface.

Next gold (Au) is evaporated directly on the entire H-terminated surface [Figure 13.3(b)], and photoresist is coated and developed to cover only the device area. For device isolation, by exposing the surface to O-plasma or ozone, the surface area around devices is terminated with oxygen (O-surface termination) and the hole channel is eliminated [Figure 13.3(c)]. Electron-beam (EB) resists are coated and then developed by EB lithography [Figure 13.3(d)]. The acceleration voltage of EB lithography of 100 kV enables us to develop a 0.1-μm-long gate area. Then with KI wet etchant [28], the Au in the gate area was etched back to make the gate area open. Then Al gate metal is evaporated [Figure 13.3(e)]. Next, after the lift-off process, Al gate contact is formed [Figure 13.3(f)].

The contact resistance of Au evaporated directly on H-terminated diamond is $10^{-6}\,\Omega\text{cm}^2$, which is low enough for device operation. The processes shown in Figure 13.3(e) and (f) are known collectively as the self-alignment technique [28], which is a way of minimizing the separation between the source contact and the gate contact, and thereby decreasing the source resistance (R_S). Consequently, an increase in the transconductance, g_m, is allowed, which is described in Section 13.3.1. The source resistance, R_S, is responsible for gate-source voltage drops. In the fabricated diamond FET, the two-dimensional hole gas (2DHG) channel is formed only below the H-terminated surface. The area around the devices is O terminated and a hole channel is not formed.

13.2.2 Measurement and analysis procedure

The small-signal (S-) parameters were measured with an Agilent 4156 network analyser system, whose frequency range was set from 1 to 30 GHz every 1 gigahertz for different gate-source voltage, V_{GS}, and drain-source voltage, V_{DS}, conditions. In the gigahertz frequency range, influence of parasitic elements, such as capacitance and inductance in contact pads on the S-parameters cannot be ignored. Normally, parasitic elements are extracted from S-parameter measurements of open- and short-circuit structures on the same wafer of measured devices and later numerically deleted from the measured S-parameters.

13.3 RESULTS

13.3.1 DC characteristics

DC drain current (I_{DS})–voltage (V_{DS}) characteristics at various gate voltages (V_{GS}) (output characteristics) are shown in Figure 13.4 for a CVD diamond FET with a gate length (L_G) of 0.1 μm. With increasing negative (forward) gate voltage, V_{GS}, the hole channel opens more widely and the negative drain current, I_{DS}, increases. The I_{DS} at a V_{GS} of 3.5 V reaches 550 mA/mm [8]. The maximum transconductance (g_m) is estimated to be 100–150 mS/mm. Here, the g_m is defined as $g_m = dI_{DS}/dV_{GS}$, and the intrinsic g_{m0}, which is calculated after removal of extrinsic components, was calculated to be 194 mS/mm.

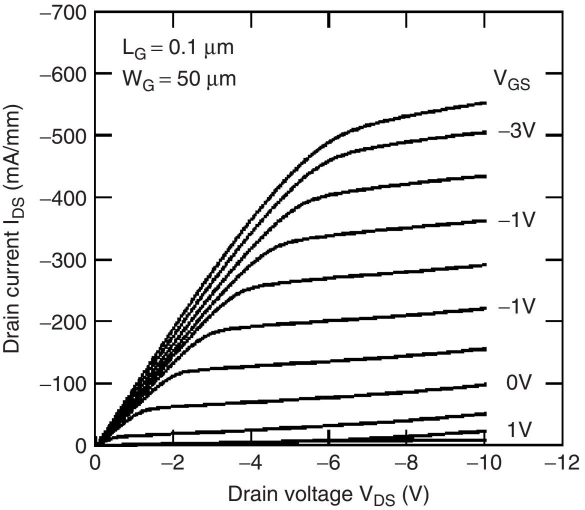

Figure 13.4 (a) DC drain current–voltage (output) characteristics and drain current–gate voltage (transfer) characteristics of polycrystalline CVD diamond FET. Reprinted from Diamond and Related Materials, Diamond-based RF power transistors: Fundamentals and applications, by M. Kasu, K. Ueda, Y. Yamauchi, A. Tallaire, T. Makimoto, Vol 16, Iss 4-7, pgs 1010-1015 (2007) Copyright Elsevier

The source resistance, R_S, which originates from the channel resistance between the source and gate contacts, causes a drop in V_{GS}. Eventually, R_S decreases the transconductance g_m as follows:

$$g_m = g_{m0} / (1 + g_{m0}R_S), \tag{13.2}$$

where g_{m0} is the intrinsic transconductance.

13.3.2 DC analysis: influence of crystalline properties

This section describes how crystalline properties influence the DC characteristics. As shown in Figure 13.5, the system can be regarded as being three layered, where the three layers are the surface, the bulk, and the environment. This section discusses how crystalline and surface properties influence FET properties. On the surface, the conduction for the device originates from holes generated by H termination. In the bulk, the diamond homoepitaxial layer contains crystalline defects, which have an influence on the FET. Further in the bulk, the diamond layer contains residual impurities that result in bulk conduction. In FET operation, both the bulk and the surface conduction occur in parallel. From the environment, adsorbates adsorb on the surface and influence the surface conduction.

Figure 13.6(a) shows $I_{DS} - V_{DS}$ characteristics of FETs on a homoepitaxial layer with a high defect density ($\sim 1\times10^6$ cm^{-2}) [29]. Reverse (positive) drain current, I_{DS}, flows even at the zero drain voltage, V_{DS}, as indicated by the arrow. This is gate current leakage. As shown in Figure 13.6(b), the reason for this is that the gate current, which apparently

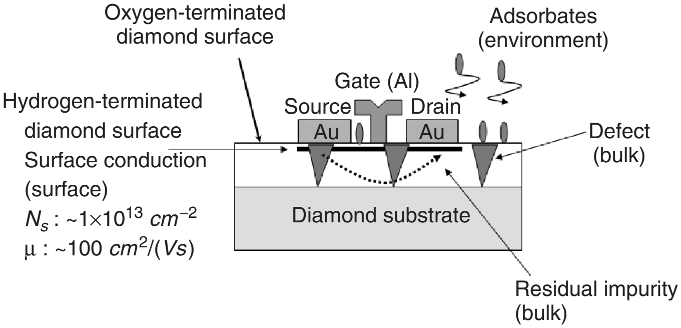
Oxygen-terminated diamond surface
Adsorbates (environment)
Gate (Al)
Hydrogen-terminated diamond surface
Source
Drain
Au
Au
Defect (bulk)
Surface conduction (surface)
N_s : ~1×10^{13} cm^{-2}
μ : ~100 $cm^2/(Vs)$
Diamond substrate
Residual impurity (bulk)

Figure 13.5 Influence of crystalline and surface properties on surface conduction in an H-terminated diamond FET on a homoepitaxial layer grown on a HPHT diamond substrate. Reprinted from Diamond and Related Materials, Influence of epitaxy on the surface conduction of diamond film by M. Kasu, M. Kubovic, A. Aleksov, N. Teofilov, Y. Taniyasu, R. Sauer, E. Kohn,T. Makimoto, N. Kobayashi, Vol 13, Iss 2, pgs 226-232 (2004) Copyright Elsevier

appears to have reverse I_{DS}, flows through an ohmic component between the Al gate and the hole channel.

Figure 13.7(a) shows $I_{DS} - V_{DS}$ characteristics for FETs on an unintentionally B-doped homoepitaxial layer (B concentration $\sim 1 \times 10^{16}$ cm^{-3}) [29]. Even at $V_{GS} = 0$ V in the reverse gate bias condition, I_{DS} cannot be cut. This is buffer leakage. Because the channel thickness is longer than the gate length, it is also called the short-channel effect. The reason for the buffer leakage is explained in Figure 13.7(b). In the homoepitaxial layer, one of the residual impurities commonly observed in low-temperature cathodoluminescence (CL) in the CVD diamond layer is B, which acts as acceptor. The origin of B has not been specified yet, but one candidate is the HPHT diamond substrate used for homoepitaxial growth [30], or the HPHT diamond powder used as seed for polycrystalline diamond growth, because the HPHT diamonds are made of graphite, which contains B impurities. When this type

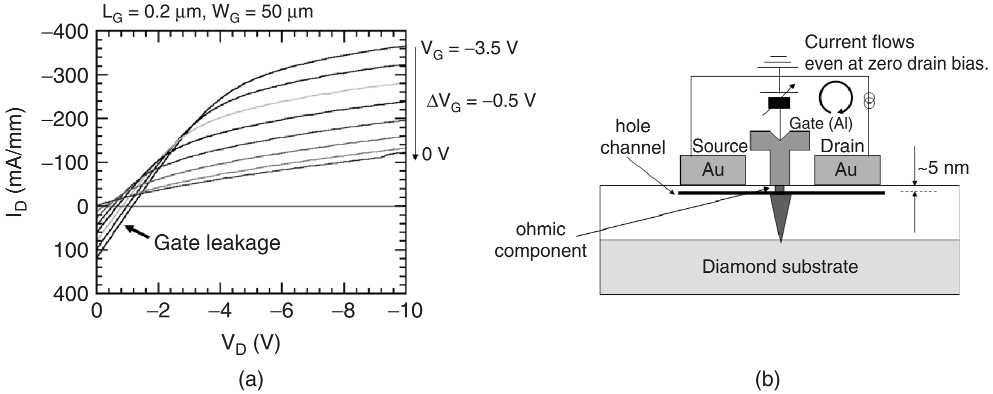

Figure 13.6 (a) $I_{DS} - V_{DS}$ characteristics for FETs on a homoepitaxial layer with a high defect density ($\sim 1 \times 10^6$ cm^{-2}). Reprinted from Diamond and Related Materials, Influence of epitaxy on the surface conduction of diamond film by M. Kasu, M. Kubovic, A. Aleksov, N. Teofilov, Y. Taniyasu, R. Sauer, E. Kohn,T. Makimoto, N. Kobayashi, Vol 13, Iss 2, pgs 226-232 (2004) Copyright Elsevier; (b) Explanation of how defects induce gate leakage

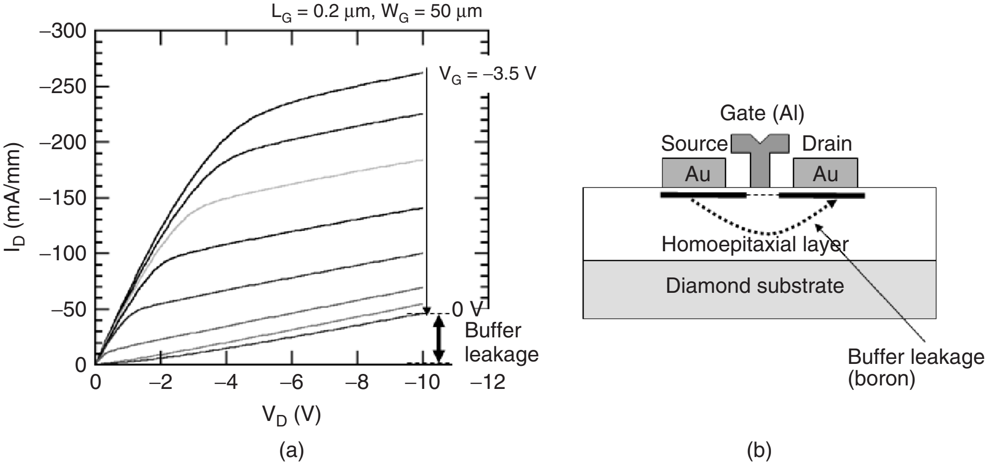

Figure 13.7 (a) $I_{DS} - V_{DS}$ characteristics for FETs on a homoepitaxial layer with unintentional B doping ($\sim 1\times10^6\text{cm}^{-3}$). Reprinted from Diamond and Related Materials, Influence of epitaxy on the surface conduction of diamond film by M. Kasu, M. Kubovic, A. Aleksov, N. Teofilov, Y. Taniyasu, R. Sauer, E. Kohn,T. Makimoto, N. Kobayashi, Vol 13, Iss 2, pgs 226-232 (2004) Copyright Elsevier; (b) Explanation of how residual B acceptors induce buffer leakage

of diamond which is used in the CVD chamber, the inside wall of the chamber becomes contaminated and this results in turn in the consequent B incorporation in any subsequent CVD diamond layer grown in that reactor. The accumulation of unintentionally doped B near the substrate has been observed [30]. Probably, high-density defects formed in a range of ~10 µm from the substrate promote B incorporation from the substrate. The B acceptors accumulated near the substrate interface will cause hole conduction in the bulk.

Consequently, the homoepitaxial layer of the H-termination exhibits two parallel hole conduction paths: one generated by the surface H termination (surface conduction) and one generated by residual B acceptors in the homoepitaxial layer (buffer conduction) [29]. The buffer conduction along the outside of the device cannot be changed by the gate bias in the device. Therefore, we observe buffer leakage current in (even unintentionally) B-doped (relatively thick) homoepitaxial layers.

13.3.3 RF small-signal characteristics

Figure 13.8 shows the frequency dependence of the current gain $|h_{21}|^2$ and the power gains, the maximum stable gain (MSG)/maximum available gain (MAG) and the unilateral (U) gains. The FET is the same as that with L_G of 0.1 µm in Figure 13.4. The cut-off frequency was extracted by the slope, −6 dB/oct, from the gain values at lower frequency, and the cut-off frequencies for current and power gains were obtained as 45 and 120 GHz, respectively [8], which are the highest reported for diamond FETs. The f_T value becomes the maximum near the pinch-off condition (I_{DS} becomes almost zero) [31], because C_{GS} drops faster than g_m. The f_{MAX} value increases with negative V_{DS}, because with negative V_{DS}, the depletion layer of the gate extends on the drain side and C_{GD}

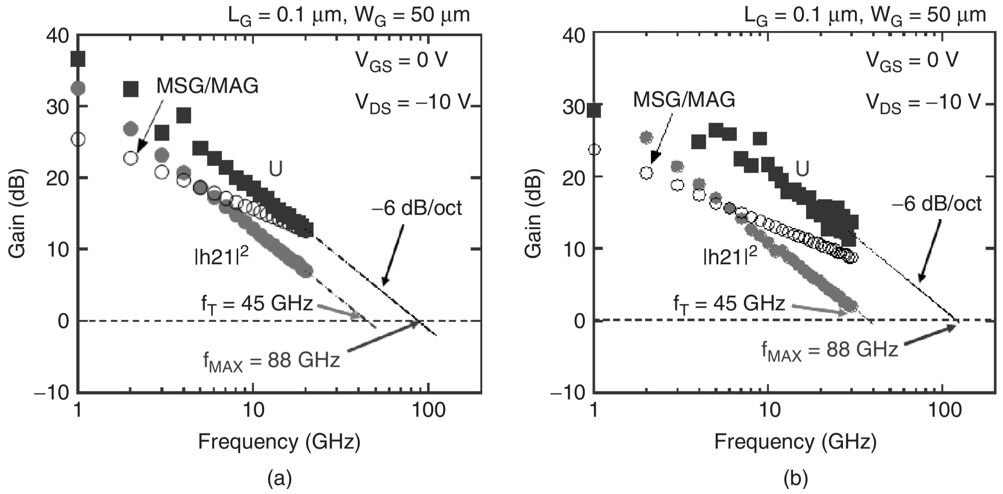

Figure 13.8 The frequency dependence of the current gain $|h_{21}|^2$ and the power gains (the maximum stable gain (MSG)/maximum available gain (MAG) and the unilateral (U) gains). Reprinted from Diamond and Related Materials, Diamond-based RF power transistors: Fundamentals and applications, by M. Kasu, K. Ueda, Y. Yamauchi, A. Tallaire, T. Makimoto, Vol 16, Iss 4-7, pgs 1010-1015 (2007) Copyright Elsevier; (a) $V_{GS} = 0$ V and $V_{DS} = -10$ V. (b) $V_{GS} = 0.5$ V and $V_{DS} = -18$ V. (a) and (b) reprinted from Electron Device Letters, Diamond FET Using High-Quality Polycrystalline Diamond with f_T of 45 GHz and f_{MAX} of 120 GHz, by K. Ueda, M. Kasu, Y. Yamauchi, T. Makimoto, M. Schwitters, D. J. Twitchen, G. A. Scarsbrook and S. E. Coe, Vol 27, Iss 7, pg 570-572 (2006) Copyright IEEE

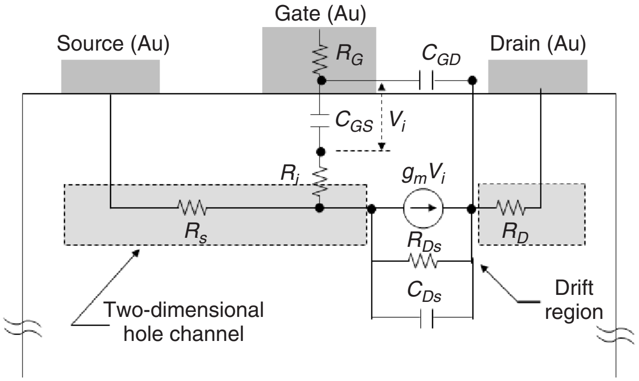

Figure 13.9 Equivalent circuit of the H-terminated diamond FET. Reprinted from Applied Physics Letters, Gate capacitance-voltage characteristics of submicron-long-gate diamond field-effect transistors with hydrogen surface termination by M. Kasu, K. Ueda, Y. Yamauchi, and T. Makimoto, Vol 90, Iss 4, pg 43509 (2007) Copyright American Institute of Physics

decreases. Another characteristics of H-terminated diamond FETs is a high $f_{\mathrm{MAX}}/f_{\mathrm{T}}$ ratio (~2.6), probably because of high drain conductance (the background resistance of diamond is extremely high). Figure 13.9 is the diamond-FET equivalent circuit extracted from an RF analysis [32].

13.3.4 RF noise characteristics

A low-noise amplifier (LNA) is used at the front end of RF receivers. The ability of LNA is qualified as the minimum noise figure, F_{min}. Low F_{min} means low noise is generated from inside the device during amplification. In Figure 13.10, the $\mathrm{F_{min}}$ value seems to increase linearly with frequency in the high frequency range [31]. This originates from quantum noise. A value F_{min} of 0.72 dB at 3 GHz (at I_{DS} of 45 mA/mm) was obtained near the pinch-off bias condition, i.e. at the bias point corresponding to that of the maximum f_{T} and f_{MAX} values. The F_{min} value (0.72 dB) is lower than Si MOSFET (0.88 dB at 2 GHz). Due to the high-impedance level at this bias condition, the optimum reflection coefficient Γ_{opt} had a very high magnitude of 0.951 and the noise resistance R_{n} was 151 Ω.

13.3.5 RF large-signal characteristics

Figure 13.11 explains how RF output power is extracted from the output (drain) voltage (V_{DS}) and current (I_{DS}). The high voltage and current result in high output power. The maximum voltage, V_{MAX}, is limited by the breakdown voltage, and the maximum current, I_{MAX}, is proportional to the product of the square of the maximum carrier concentration obtainable and the mobility. When specific applied output voltage (V_{O}) and load resistance (R_{L}) are chosen, V_{DS} and I_{DS} change following the load line as $V_{\mathrm{DS}} = V_{\mathrm{O}} - I_{\mathrm{DS}}.\mathrm{R_L}$. The loadline intercepts V_{O} and a slope $(-1/R_{\mathrm{L}})$. When the bias point is set at the middle point of I_{MAX} and V_{MAX} (Class A operation), the maximum RF output power is obtained without signal distortion. In Class A operation, the maximum output power is estimated

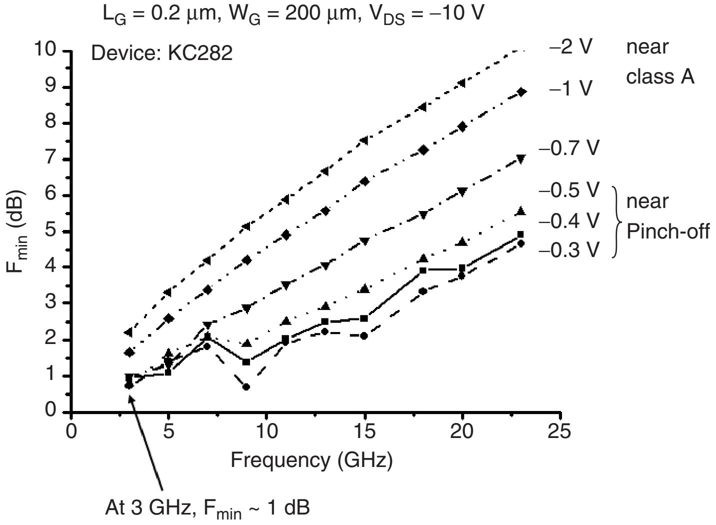

Figure 13.10 The minimum noise figure ($F_{\min}$) as a function of frequency. Near the pinch-off condition, the lowest $F_{\min}$ is obtained. Reprinted from Diamond and Related Materials, Microwave performance evaluation of diamond surface channel FETs by M. Kubovic, M. Kasu, I. Kallfass, M. Neuburger, A. Aleksov, G. Koley, M.G. Spencer, E. Kohn, Vol 13, Iss 4-8, pgs 802-807 (2004) Copyright Elsevier

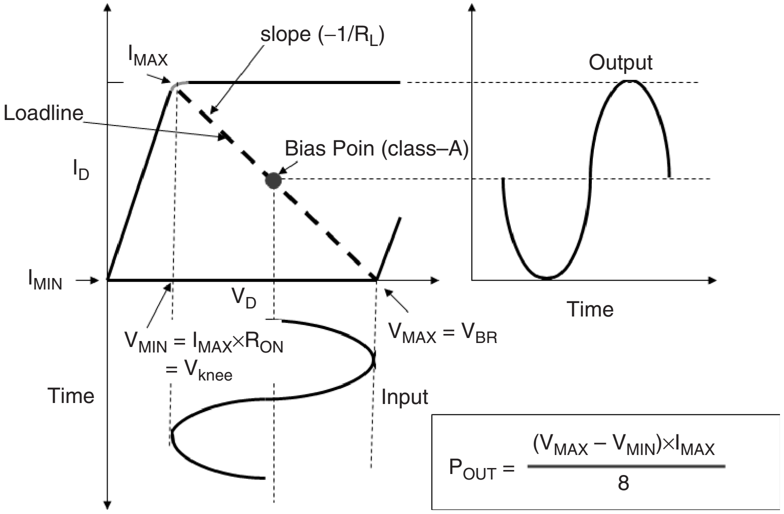
slope (−1/R_L)
I_{MAX}
Output
Loadline
Bias Poin (class–A)
I_D
I_{MIN}
V_D
Time
V_{MIN} = I_{MAX}×R_{ON} = V_{knee}
V_{MAX} = V_{BR}
Time
Input

$$P_{OUT} = \frac{(V_{MAX} - V_{MIN}) \times I_{MAX}}{8}$$

Figure 13.11 Relationship between DC signal and RF output power in drain current–voltage characteristics. Reprinted from Diamond and Related Materials, Diamond-based RF power transistors: Fundamentals and applications, by M. Kasu, K. Ueda, Y. Yamauchi, A. Tallaire, T. Makimoto, Vol 16, Iss 4-7, pgs 1010-1015 (2007) Copyright Elsevier

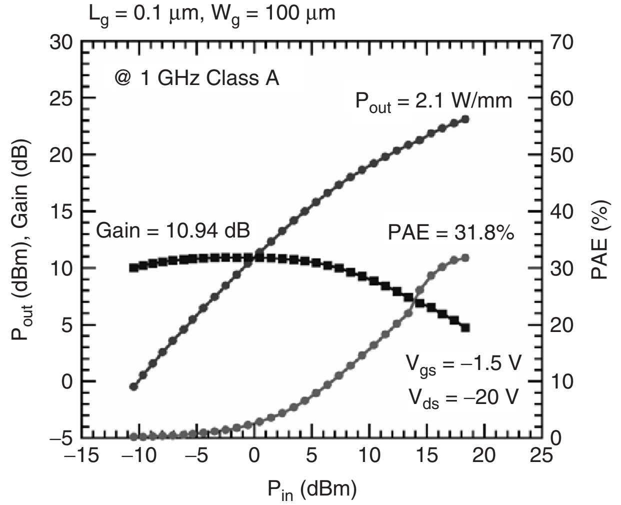

Figure 13.12 RF input–output power characteristics measured at 1 GHz in Class A operation of a homoepitaxial diamond FET. Reprinted from Diamond and Related Materials, Diamond-based RF power transistors: Fundamentals and applications, by M. Kasu, K. Ueda, Y. Yamauchi, A. Tallaire, T. Makimoto, Vol 16, Iss 4-7, pgs 1010-1015 (2007) Copyright Elsevier and from Electronics Letters, 2W/mm output power density at 1 GHz for diamond FETs by M. Kasu, K. Ueda, H. Ye, Y. Yamauchi, S. Sasaki and T. Makimoto, Vol 41, Iss 22, pgs 1249-1250 (2005) Copyright IET

as $P_{\mathrm{OUT}} = (V_{\mathrm{MAX}} - V_{\mathrm{MIN}}) \times I_{\mathrm{DMAX}}/8$. If V_{MAX} is set at V_{BR} and V_{MIN} is set at V_{KNEE}, the knee voltage, at which I_{DMAX} is obtained when the linear and saturation regions meet, P_{OUT} becomes the maximum (see Figure 13.11).

Figure 13.12 shows a RF (1 GHz) power sweep of a diamond FET in Class A operation [9]. The maximum output-power density, P_{OUT}, is 2.1 W/mm, and the power added efficiency (PAE) is 31 %. The maximum power gain is 10.9 dB (12 times). This P_{OUT} is twice that of widely used GaAs MESFETs, about 1 W/mm [33]. The diamond FET structure is a very simple structure that does not use a field plate to weaken the maximum field between the gate and the drain contacts. In contrast, the highest values reported for a GaN FET without and with a field plate are 10 W/mm at 30 V [34], and 32 W/mm at 120 V [35]. With a field plate and an optimized device configuration, the maximum RF output power of diamond FET with boron delta-doping is predicted to be 75 W/mm [36] [see also Chapter 14 in this book].

13.4 DISCUSSION

13.4.1 RF analysis: saturation velocity

Figure 13.13 shows plots of reported cut-off frequency f_{T} values as a function of gate length (L_{G}) [37]. In a high field region, f_{T} is expressed theoretically by L_{G} as:

$$\mathrm{f_T} = \mathrm{g_m} / 2\pi \mathrm{C_{GS}} = \mathrm{v_{sat}} / 2\pi \mathrm{L_G}, \tag{13.3}$$

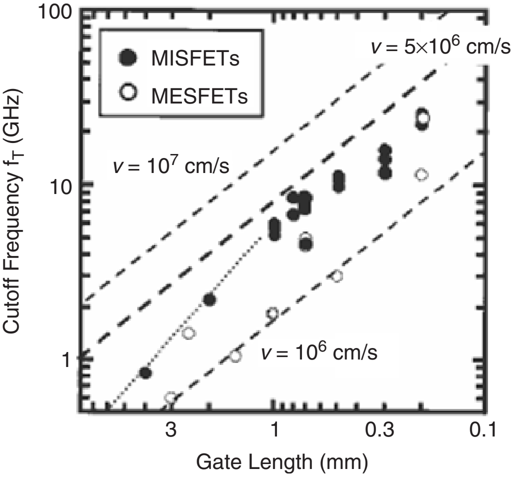

Figure 13.13 Transition frequency (f_T) value as a function of the gate length (L_G). Reprinted from International Electron Devices Meeting 2007 (IEDM 2007), Technical Digest, High-Performance p-channel Diamond MOSFETs with Alumina Gate Insulator by K.Hirama, H.Takayanagi, S.Yamauchi, Y.Jingu, H.Umezawa, and H.Kawarada, pgs 873-876, (2007) Copyright IEEE

where v_{sat} is the saturation drift velocity. The lines indicate the relationship between f_T and L_G expressed by Equation (13.3) assuming various v_{SAT} values. The data for $L_G < 1\,\mu\mathrm{m}$ seem to follow the line slightly below $v_{\mathrm{sat}} = 5\times10^6$ cm/s. The v_{sat} value of 5×10^6 cm/s is about a half of the value (1.1×10^7 cm/s) measured for natural diamond by the time-of-flight method [7].

13.4.2 RF analysis: band diagram

The gate-source capacitance, C_{GS}, and the transconductance, g_m, can be obtained from the S-parameter measurements. Figure 13.14 shows g_m and C_{GS} as a function of V_{GS} for a FET. The most interesting result is that C_{GS} shows a plateau for $-0.5\ \mathrm{V} < \mathrm{V_{GS}} < -2.0$ V [32]. This indicates that an energy barrier forms between the gate metal and 2DHG channel. Then, the results can be explained in terms of the band diagrams in Figure 13.15.

For $V_{GS} > -0.5$ V, as positive V_{GS} is increased, g_m decreases and C_{GS} decreases. This means that as positive V_{GS} is increased, the depletion layer below the energy barrier extends to the substrate side [Figure 13.15(a)]. The hole channel forms below this depletion layer and is three dimensional. For $-0.5\ \mathrm{V} < \mathrm{V_{GS}} < -2.0$ V, as V_{GS} is changed, C_{GS} does not change. This means that C_{GS} is almost equal to the energy-barrier capacitance, which is independent of the voltage. The hole channel is two dimensional, and therefore g_m stays high [Figure 13.15(b)]. For $V_{GS} < -2.0$ V, as negative V_{GS} is increased, g_m decreases and at the same time C_{GS} increases steeply. This indicates that because the energy barrier height is finite, in this V_{GS} range, the energy barrier becomes a triangular potential barrier [Figure 13.15(c)]. Then holes penetrate the energy barrier and consequently C_{GS} increases. Holes that penetrate the energy barrier are probably affected by impurity scattering in the energy barrier or roughness scattering at

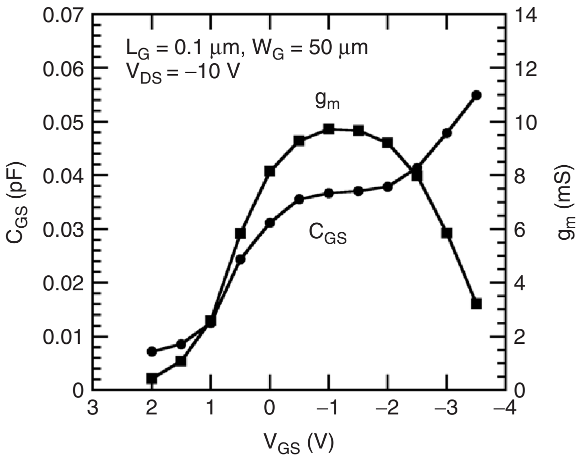

Figure 13.14 RF transconductance (g_m) and gate capacitance (C_{GS}) as a function of the gate voltage (V_{GS}). Reprinted from Applied Physics Letters, Gate capacitance-voltage characteristics of submicron-long-gate diamond field-effect transistors with hydrogen surface termination by M. Kasu, K. Ueda, Y. Yamauchi, and T. Makimoto, Vol 90, Iss 4, pg 43509 (2007) C

the interface between the 2DHG channel and the energy barrier and, eventually, g_m decreases.

The C_{GS} is 0.037 pF for $L_G = 0.1$ µm and $W_G = 50$ µm, and its corresponding capacitance per area is calculated to be 0.74 µF/cm^2. The value is similar to the value (1 µF/cm^2) measured from Cole–Cole plots for electrochemical diamond FETs [38]. From the C_{GS} value at the plateau, 0.74 µF/cm^2, the entire thickness of the energy barrier is estimated to be 6.8, 11 nm, assuming the relative dielectric constants of diamond (5.7) and Al_2O_3 (9).

In a cross-sectional transmission electron microscopy (TEM) image of the Al-gate contact layer and H-terminated diamond layer (Figure 13.16) [39], an interfacial layer is clearly seen between the Al layer and H-terminated diamond layer. Its entire thickness is 7–10 nm. In both the Al layer and the H-terminated diamond layer, lattices can be seen, indicating that both layers are crystalline. However, in the interfacial layer, lattices cannot be seen, suggesting that the interfacial layer is amorphous. Further, the boundary between the interfacial layer and the H-terminated diamond is not flat. This suggests that some chemical reaction has occurred during interfacial layer formation. These values are very similar to the thickness of the interfacial layer observed by cross-sectional TEM. Therefore, the interfacial layer observed in Figure 13.16 corresponds to the energy barrier found in the gate capacitance voltage characteristics. The chemical composition of the interfacial layer is not clear yet, but seems to be different from that of an Al_2O_3 insulator layer.

Figure 13.17 shows $I_{DS} - V_{GS}$ characteristics in the open channel condition. In this condition, the V_{GS} is applied to the interfacial layer. The breakdown occurs at $V_{GS} = -7.8$ V [38]. From the breakdown voltage and the interfacial-layer thickness (10 nm), the breakdown field of the interfacial layer is estimated to be ~8 MV/cm. This is comparable to the theoretically predicted breakdown field of diamond (10 MV/cm). In actual high-voltage FET operation, a high field is applied to the gate region and the high breakdown field

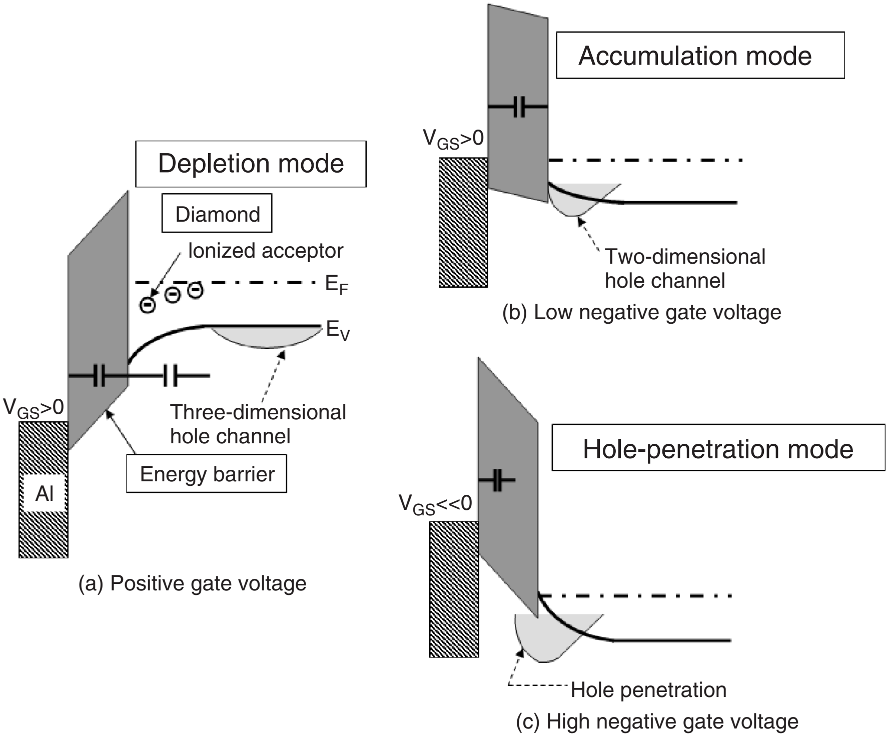
Depletion mode
Diamond
Ionized acceptor
E_F
E_V
$V_{GS}>0$
Three-dimensional hole channel
Energy barrier
Al
Accumulation mode
$V_{GS}>0$
Two-dimensional hole channel
Hole-penetration mode
$V_{GS}<<0$
Hole penetration

(a) Positive gate voltage

(b) Low negative gate voltage

(c) High negative gate voltage

Figure 13.15 Band diagrams under (a) zero gate bias and (b) flat band conditions. Reprinted from Applied Physics Letters, Gate capacitance-voltage characteristics of submicron-long-gate diamond field-effect transistors with hydrogen surface termination by M. Kasu, K. Ueda, Y. Yamauchi, and T. Makimoto, Vol 90, Iss 4, pg 43509 (2007) Copyright American Institute of Physics

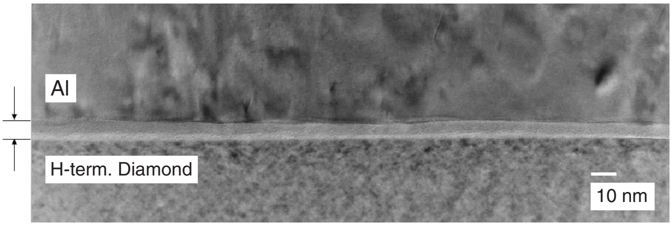
Al
H-term. Diamond
10 nm

Figure 13.16 Cross-sectional TEM image of the Al gate contact layer and H-terminated diamond layer. The interfacial layer is indicated by two arrows. Reprinted from Diamond and Related Materials, Gate interfacial layer in hydrogen-terminated diamond field-effect transistors by Makoto Kasu, Kenji Ueda, Hiroyuki Kageshima, Yoshiharu Yamauchi, Vol 17, Iss 4-5, pgs 741-744 (2008) Copyright Elsevier

of the interfacial layer will therefore be very favorable. When a V_{GS} value of −6V is applied (a large forward gate bias), degradation occurs because of gate breakdown (failure of the interfacial layer). However, when V_{GS} is is kept to values > -3.5 V, degradation is negligible.

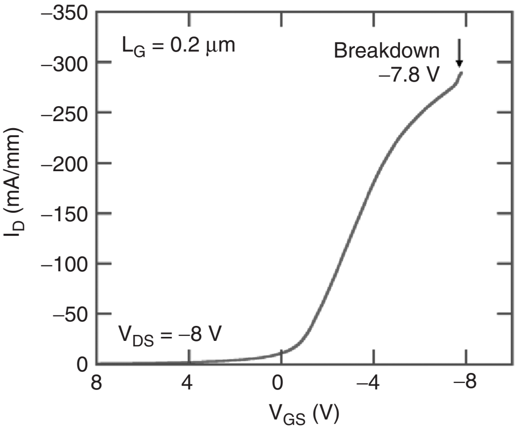

Figure 13.17 Gate breakdown. Drain current (I_{DS})–gate voltage (V_{GS}) characteristics (transfer characteristics) in the open channel condition ($V_{DS} = -8$ V). Reprinted from Diamond and Related Materials, Electronic surface barrier characteristics of H-terminated and surface conductive diamond by A.Kubovic, A.Denisenko, W.Ebert, M.Kasu, I.Kallfass, E.Kohn, Vol 13, Iss 4-8, pgs 755-760 (2004) Copyright Elsevier

13.4.3 Device temperature during power operation

As described in Section 13.1.1, one advantage of diamond over other semiconductors is its thermal conductivity (22 W/cm K for diamond, 4.9 W/cm K for SiC, and 0.46 W/cm K for GaAs). Even in GaN FETs fabricated on SiC or sapphire substrate, under the high drain current regime, drain current decreases gradually when drain voltage increases. A negative slope (drain conductance) in drain current–voltage characteristics is therefore observed [34]. This is because heat generated by the power consumption raises the temperature, the mobility decreases, and eventually the drain current is decreased. This negative slope becomes a high limit of the load line in Figure 13.11 and is, therefore, a serious problem in power operation. In contrast, diamond has superior heat spreading ability. Diamond FETs therefore exhibit no negative slope (drain conductance) in drain current-voltage characteristics (Figure 13.4).

Figure 13.18 shows infrared thermograph pictures of a diamond FET when the power is off and on. When power operation (total power: 0.84 W) starts, the device temperature rises only 0.64 degrees [10]. In a GaAs FET with similar output power, temperature increases 30 degrees. This extremely small temperature rise for diamond has been theoretically simulated [39]. From physics principles, the increase in temperature, ΔT, is inversely proportional to the thermal conductivity, λ, i.e., $\Delta T \propto W_{OUT}/\lambda$, where W_{OUT} is generated heat power.

Another aspect of power operation is that the available maximum output power is limited by the maximum device temperature (the temperature when the device burns out). Normally, devices in systems are designed for use at a maximum of 150°C. The maximum device temperature is determined by the balance between the device power consumption and heat spreading, thus the thermal conductivity of the substrate is important. In this point, the extremely high thermal conductivity of diamond is advantageous.

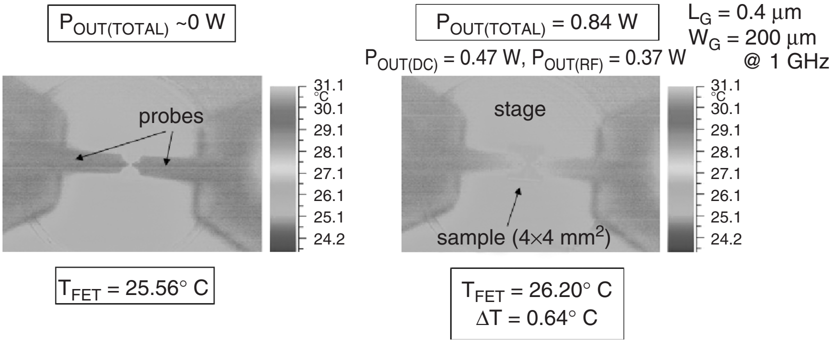

Figure 13.18 Infrared thermograph pictures of the device when the power is off and on. Reprinted from Diamond and Related Materials, High RF output power for H-terminated diamond FETs, by M. Kasu, K. Ueda, H. Ye, Y. Yamauchi, S. Sasaki, T. Makimoto, Vol 15, Iss 4-8, pgs 783-786 (2006) Copyright Elsevier. See plate 5

13.4.4 Stability and reliability

For device application, reliability is a critical issue. Unlike classical doping, the concentration of holes generated by H-surface termination changes with the amount of adsorbate on the surface [29]. This phenomenon is clearly observed when the sample is measured in air and in vacuum. Therefore, adsorbates are believed to come from air, and they are probably H_2O and/or CO_2 molecules [17], but this has not been confirmed as yet. A more critical issue is the long-term reliability, which is related to the presence of the adsorbates. It has been reported that the drain current decreased with each scan [22].

Figure 13.19 shows the microscopic image of a FET taken just before the drain breakdown [40]. Here, the (negative) drain voltage was increased while zero gate voltage was maintained. At the drain voltage at 100 V, drain breakdown occurred. Small protrusions on the drain contact (indicated by arrows) appeared. This suggests that hydrogen evaporates from the surface or from inside the diamond layer. One possible explanation for this is that holes accelerated by high drain voltage break C–H bonds. Another is that the high power consumption results in a local temperature rise. After such protrusion

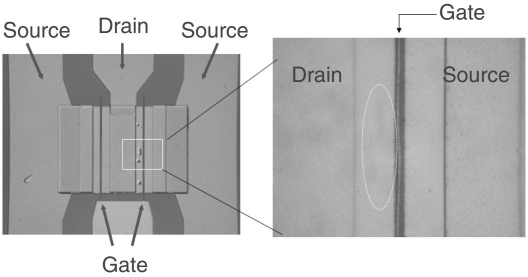

Figure 13.19 Optical microscope image of a FET just before drain breakdown. Protrusions, i.e., hydrogen bubbles, are indicated white circle (left figure). Reprinted from Diamond and Related Materials, Diamond-based RF power transistors: Fundamentals and applications, by M. Kasu, K. Ueda, Y. Yamauchi, A. Tallaire, T. Makimoto, Vol 16, Iss 4-7, pgs 1010-1015 (2007) Copyright Elsevier

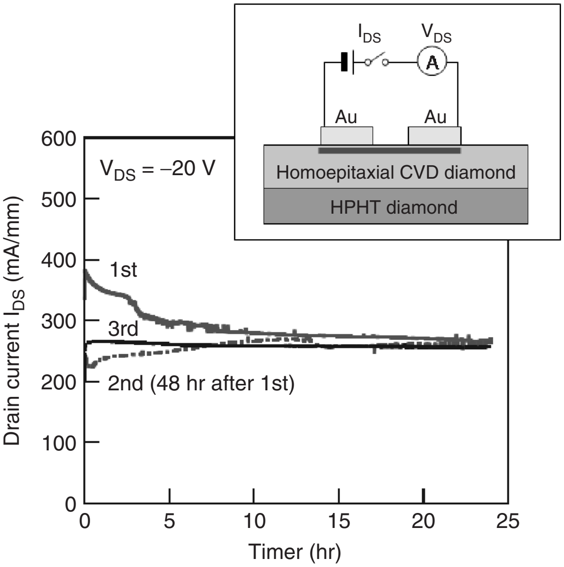

Figure 13.20 Time evolution of drain current for an ungated homoepitaxial diamond FET. Reprinted from Diamond and Related Materials, Diamond-based RF power transistors: Fundamentals and applications, by M. Kasu, K. Ueda, Y. Yamauchi, A. Tallaire, T. Makimoto, Vol 16, Iss 4-7, pgs 1010-1015 (2007) Copyright Elsevier

formation, the protrusions burst. This is drain breakdown in the H-terminated diamond FET. However, after they burst, we do not see any damage in the diamond crystal. This means that this phenomenon is not a breakdown of diamond itself.

As shown in Figure 13.20, drain current was measured continuously for 24 hours three times for an ungated FET, i.e., a FET structure without gate contact [40]. In all three measurements, the current at the initial stage was not so stable, but about 10 hours later, the current stabilized. For some 10 hours, no degradation was observed. The reason for the instability of the current in the early stage is that the adsorbates rearrange in the opened area on the surface between the source and gate contacts. However, eventually the current approaches the same value after approximately10 hours. This indicates that the H termination itself is very stable over the long term.

One advantage diamond has over GaN is that there is no RF current slump. In GaN, RF current is much lower than DC current. This RF slump phenomenon can be explained by a slow charge/discharge of donors near the surface [33]. This causes a long-term reliability problem. In contrast, with diamond no RF current slump has been observed [31]. This means that the gate metal/H-terminated diamond interface has no deep traps to induce current instability.

The gate leakage-induced degradation is shown in Figure 13.21 [40]. Here, when the gate and drain biases of a FET were off for a short time (3 s) (V_{GS} was changed from −3.5 to 0 V and V_{DS} was changed from −20 to 0 V at the same time) every 5 min, a drop in the drain current was observed, but a long time afterwards, the drain saturated. However, the saturated drain current decreased at each step, and at the same time, the gate current increased. This indicates that the decrease in drain current (the degradation) is closely related to an increase in the gate current.

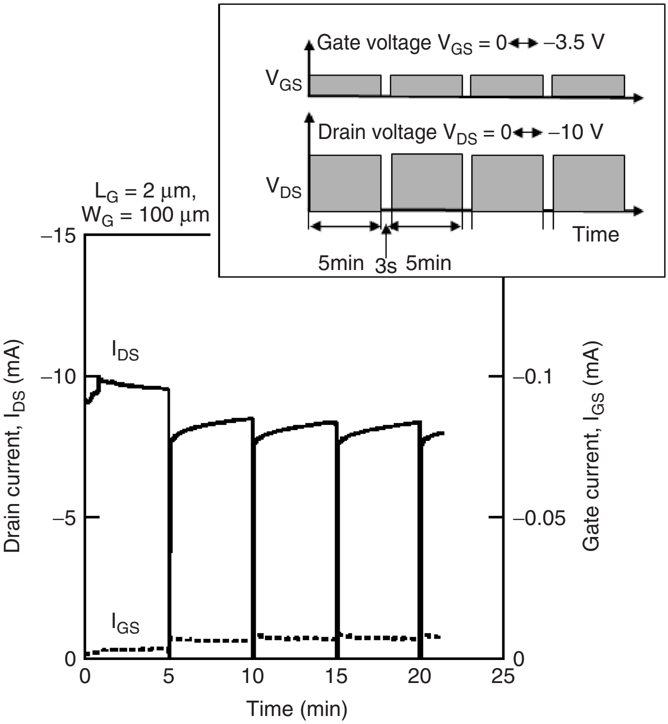

Figure 13.21 Time evolution of drain current for a gated homoepitaxial diamond FET. Every 5 minutes, the gate voltage and drain voltages (V_{GS}, V_{DS}) changed from (−3.5 V, −10 V) to (0 V, 0 V) for 3 s, which indicates the gate leakage-induced degradation. Reprinted from Diamond and Related Materials, Diamond-based RF power transistors: Fundamentals and applications, by M. Kasu, K. Ueda, Y. Yamauchi, A. Tallaire, T. Makimoto, Vol 16, Iss 4-7, pgs 1010-1015 (2007) Copyright Elsevier

13.5 SUMMARY

This chapter reviewed the present status and our current understanding of H-terminated diamond FETs. The drain current has reached 550 mA/mm, and the maximum transconductance (g_m) is estimated to be 100–150 mS/mm. A current-gain, cut-off frequency, f_T, of 45 GHz and a power-gain, cut-off frequency, f_{MAX}, of 120 GHz have been achieved. A minimum noise figure (F_{min}) of 0.72 dB has been achieved at 3 GHz. Output-power density of 2.1 W/mm at 1 GHz in Class A operation has been achieved. These values are sufficient for the efficient operation of RF devices, thus proving the very high potential for use of CVD diamond in RF power applications. The extremely small rise in device temperature during power operation, and the lack of a self-heating effect, which are characteristics observed in diamond FETs, would be highly desirable for any other semiconductor devices of this type.

However, although it is possible to use bare H-terminated surfaces for experimental devices, the observed level of degradation will have to be suppressed, or at least greatly reduced, before these devices can become commercially available. A reduction in degradation could be achieved by, for instance, passivating the H-terminated surface. However, to the best of my knowledge, none of the current interpretations of H-induced, p-type conduction fully account for all the H-termination-related electrical and FET properties, degradation processes, and nature of the naturally formed interfacial layer; all of these are discussed in this chapter. Therefore, I suggest that it should be possible through the further study of H-terminated diamond FETs, to improve or modify the H-termination, and find a more reliable doping technology so that these devices can be made with the required specifications to become a commercial reality.

REFERENCES

[1] L.R. Pan, D.R. Kania, *Diamond: Electronic Properties and Applications*, Kluwer Academic Publishers, 1995.

[2] W. Ebert, A. Vescan, P. Gluche, T. Borst, E. Kohn, *Diamond Relat. Mater.* **6** (1997) 329–332.

[3] V.K. Bazhenov, I.M. Vilkulin, and A.G. Gontar, *Sov. Phys. Semicond.* **19** (1985) 829–841.

[4] J.E. Butler, M.W. Geis, K.E. Krohn, J. Lawless Jr, S. Deneault, T.M. Lyszczarz, D. Flechtner, and R. Wright, *Semicond. Sci. Technol.* **18** (2003) S67–S71.

[5] P. Gluche, A. Aleksov, A. Vescan, W. Ebert, and E. Kohn, *IEEE Electron Dev. Lett.* **18** (1997) 547–549.

[6] J. Isberg, J. Hammersberg, E. Johansson, T. Wikstrom, D.J. Twitchen, A.J. Whitehead, S.E. Coe, and G.A. Scarsbook, *Science* **294** (2002) 1670–1672.

[7] L. Reggiani, S. Bosi, C. Canali, F. Nava, and S.F. Kozlov, *Phys. Rev. B* **23** (1981) 3050–3057.

[8] K. Ueda, M. Kasu, Y. Yamauchi, T. Makimoto, M. Schwitters, D.J. Twitchen, G.A. Scarsbrook, and S.E. Coe, *IEEE Electron Device Lett.* **27** (2006) 570–572.

[9] M. Kasu, K. Ueda, H. Ye, Y. Yamauchi, S. Sasaki, and T. Makimoto, *Electronics Letters Electronics Lett.* **41** (2005) 1249–1250.

[10] M. Kasu, K. Ueda, H. Ye, Y. Yamauchi, S. Sasaki, and T. Makimoto, *Diamond Relat. Mater.* **15** (2006) 783–786.

[11] A. Aleksov, A. Denisenko, M. Kunze, A. Vescan, A. Bergmaier, G. Dollinger, W. Ebert, and E. Kohn, *Semicond. Sci. Technol.* **18** (2003) S59–S66.

[12] E.O. Johnson, *RCA Rev.* **26** (1965) 163–177.

[13] S. Koizumi, T. Teraji, and H. Kanda, *Diamond Relat. Mater.* **9** (2000) 935–940.

[14] M.I. Landstrass and K.V. Rabi, *Appl. Phys. Lett.* **55** (1989) 975–977.

[15] H. Kawarada, *Surface Science* **26** (1996) 205–259.

[16] A. Denisenko, A. Aleksov, A. Probil, P. Gluche, W. Ebert, and E. Kohn, *Diamond Relat. Mater.* **9** (2000) 1138–1142.

[17] J. Ristein, F. Maier, M. Riedel, M. Stammler, and L. Ley, *Diamond Relat. Mater.* **10** (2001) 416–422.

[18] H. Kawarada, M. Aoki, and M. Itoh, *Appl. Phys. Lett.* **65** (1994) 1563–1565.

[19] Y. Yun, T. Maki, and T. Kobayashi, *J. Appl. Phys.* **82** (1997) 3422–3429.

[20] H. Umezawa, H. Taniuchi, T. Arima, M. Tachiki, K. Tsugawa, S. Yamanaka, D. Takeuchi, H. Okushi, and H. Kawarada, *Jpn. J. Appl. Phys.* **39** (2000) L908–910.

[21] H. Ishizaka, H. Umezawa, H. Taniuchi, T. Arima, N. Fujihara, M. Tachiki, and H. Kawarada, *Diamond Relat. Mater.* **11** (2002) 378–381.

[22] K. Hirama, S. Miyamoto, H. Matsudaira, K. Yamada, H. Kawarada, T. Chikyo, H. Koinuma, K. Hasegawa, and H. Umezawa, *Appl. Phys. Lett.* **88** (2006) 112117.

[23] M. Kasu, M. Kubovic, A. Aleksov, N. Teofilov, R. Sauer, E. Kohn, and T. Makimoto, *Jpn. J. Appl. Phys.* **43** (2004) L975–L977.

[24] M. Kasu, T. Makimoto, W. Ebert, E. Kohn, *Appl. Phys. Lett.* **83** (2003) 3465–3467.

[25] K. Ueda, M. Kasu, Y. Yamauchi, T. Makimoto, M. Schwitters, D.J. Twitchen, G.A. Scarsbrook, and S.E. Coe, Characterization of high-quality polycrystalline diamond and its high FET performance, *Diamond Relat. Mater.* **15** (2006) 1954–1957.

[26] M. Kubovic, A. Aleksova, M. Schreck, Th. Bauer, B. Stritzker, and E. Kohn, *Diamond Relat. Mater.* **12** (2003) 403–407.

[27] M. Kubovic, K. Janischowsky, and E. Kohn, *Diamond Relat. Mater.* **14** (2005) 514–517.

[28] A. Hokazono and H. Kawarada, *Jpn. J. Appl. Phys.* **36** (1997) 7133–7139.

[29] M. Kasu, M. Kubovic, A. Aleksov, N. Teofilov, Y. Taniyasu, R. Sauer, E. Kohn, T. Makimoto, and N. Kobayashi, *Diamond Relat. Mater.* **13** (2004) 226–232.

[30] A. Tallaire, M. Kasu, and K. Ueda, Thick diamond layers angled by polishing to reveal defect and impurity depth profiles, *Diamond Relat. Mater.* (in press) **17** (2008) 506–510.

[31] M. Kubovic, M. Kasu, I. Kallfass, M. Neuburger, A. Aleksov, G. Koley, M.G. Spencer, and E. Kohn, *Diamond Relat. Mater.* **13** (2004) 802–807.

[32] M. Kasu, K. Ueda, Y. Yamauchi, and T. Makimoto, *Appl. Phys. Lett.* **90** (2007) 043509.

[33] R.J. Trew, G.L. Bilbro, W. Kuang, Y. Liu, and H. Yin, *IEEE Microwave Magazine* March (2005) 56–66.

[34] Y.-F. Wu, D. Kapolnek, J.P. Ibbetson, P. Parokh, B.P. Keller, and U.K. Mishra, *IEEE Electron Device* **48** (2001) 586–590.

[35] Y.-F. Wu, A. Saxler, M. Moore, R.P. Smith, S. Sheppard, P.M. Chavarkar, T. Wisleder, U.K. Mishra, and P. Parikh, *IEEE Electron. Dev. Lett.*, **25** (2004) 117–119.

[36] A. Denisenko and E. Kohn, *Diamond Relat. Mater.* **14** (2005) 491–498.

[37] H. Matsudaira, S. Miyamoto, H. Ishizaka, H. Umezawa, and H. Kawarada, *IEEE Electron Device Lett.* **25** (2004) 480–482.

[38] M. Kubovic, A. Denisenko, W. Ebert, M. Kasu, I. Kallfass, and E. Kohn, *Diamond Relat. Mater.* **13** (2004) 755–760.

[39] M. Kasu, K. Ueda, H. Kageshima, and Y. Yamauchi, Gate interfacial layer in hydrogen-terminated diamond field-effect transistors, *Diamond Relat. Mater.* (in press) **17** (2008) 741–744.

[40] M. Kasu, K. Ueda, Y. Yamauchi, A. Tallaire, T. Makimoto, *Diamond Relat. Mater.* **16** (2007) 1010–1015.

14 Doped Diamond Electron Devices

E. KOHN AND A. DENISENKO

Department of Institute Electron Devices, University of Ulm, Germany

---

14.1 Introduction and Background 313
14.2 Delta-Doping Concept and Technology 318
  14.2.1 Delta-doping profiles 318
  14.2.2 Contacts and device technology 324
14.3 Field Effect Transistors 329
  14.3.1 Delta-channel field effect transistors 330
  14.3.2 P–I–P FETs 338
14.4 Diodes 342
  14.4.1 High voltage vertical diodes 343
  14.4.2 High temperature diodes 348
14.5 Electrodes and ION SENSITIVE FETS 354
  14.5.1 Electrodes 355
  14.5.2 ISFETs 360
14.6 Conclusion 365
14.7 Acknowledgements 366
References 367

14.1 INTRODUCTION AND BACKGROUND

Diamond may be considered as part of the family of wide band-gap semiconductors, which also contains SiC and GaN with its related heterostrutures, mainly AlGaN/GaN. Altogether they face competition from Si with its highly mature materials and device processing technologies [1]. However, the wide band gap in combination with a ceramic-like chemical stability predestines SiC, diamond and III-nitride heterostructures for extreme applications out of reach for Si, especially in respect of power-switching electronics, microwave power sources, high temperature electronics and sensing in harsh environments. As an example two figures of merit related to power electronic applications are given below:

CVD Diamond for Electronic Devices and Sensors Edited by Ricardo S. Sussmann
© 2009 John Wiley & Sons, Ltd. ISBN: 978-0-470-06532-7

Johnson figure of merit [2]:

$$JFM = \frac{F_{BR} v_s}{2\pi}$$

Baliga figure of merit [3] :

$$BFM = \varepsilon \cdot \mu \cdot E_G^3$$

The Baliga figure of merit relates to unipolar devices dominated by their conduction losses. Mostly used in microwave power generation is the JFM, which defines the transistor cut-off frequency and usable power. Here diamond is often quoted as superior semiconductor material in comparison with SiC and GaN heterostructures. However, reliable and representative data on breakdown field, low field mobility and the high field saturated velocity of holes and electrons in diamond devices are still very much in debate.

Thus, state-of the-art extreme device properties have been obtained for each material in the various fields. SiC has been mainly used in its hexagonal and rhombic configurations. It contains many modifications in its stacking order and although being highly temperature stable, stacking faults start to become mobile at high temperature causing device degradation. In addition, at an MOS interface with thermally grown native oxide, carbon generates deep surface-state levels, thus reducing inversion layer mobilities [4]. Despite these problems it is used industrially for advanced power applications, mostly power switching with voltages up to the 10 kV range. Devices developed for power switching applications include Schottky diodes [5], PIN diodes [6] junction barrier Schottky diodes (JSB) [7], bipolar transistors [8], thyristors [9], IGBTs [10], DMOSFETs [11], JFETs [12] and SITs [13]. For applications at microwave frequencies in the lower GHz-range MOSFETs [14] and MESFETs [15] have been realized. The output power of discrete bipolar transistors has reached 2.1 kW (at 425 MHz) in 2005 [16]. High temperature MOS gas sensors have been demonstrated for temperatures up to 1000 °C [17].

The III-nitrides are a GaN based materials system used with heterostructures reaching from InN to AlN, the workhorse being AlGaN/GaN. Due to its ceramic-like stability, this heterostructure has been proposed for high temperature gas sensing up to 800 °C [18]. Because of its high channel sheet charge density and carrier mobility it is used in present state-of-the-art microwave power FETs, with the highest power density of all semiconductor microwave devices at 42 W/mm [19]. The power level of discrete devices had reached nearly 0.8 kW (~3 GHz) in 2007 [20]. Breakdown voltages of up to 8.3 kV have been demonstrated [21]. However, the AlGaN layer is strained on GaN, and defects generated by piezo stress are presently considered to be the main degradation source at high power operation [22]. Using InAlN on GaN the system can be lattice matched ($In_{17}Al_{83}N$). In this configuration, high temperature stability has been obtained and the highest temperature of operation (of 1000 °C in vacuum) of any FET structure could be demonstrated with this materials configuration [23]. All III-nitrides in their hexagonal phase are highly polar and the polarization discontinuity developed at the heterostructure interface is used as a 2DEG-channel in the FET. Since this represents only the electronic charge component of the polarization dipole, the positive countercharge at the surface often referred to as surface donor [24], has always to be ionized. If this is not the case for the entire range of electrical field and temperature, instabilities will result, and indeed current compression and power slump are common phenomena in III-nitride based devices [25].

Diamond has been, up to now, mainly used in sensing, such as in high energy radiation and particle detection [26], electrochemical analysis (see [27] and chapters in the present book) and electrochemical waste water treatment [28]. However, the materials configuration is, in most cases, a polycrystalline or nanocrystalline layer configuration on a foreign substrate (mostly Si). Single-crystal applications are still confined to small substrate sizes of less than 1 cm^2. Diodes on single crystal substrates have been operated repeatedly up to 1050 °C limited by the test equipment (in vacuum to avoid 'burning' in oxygen), the highest temperature for any semiconductor diode configuration (see Section 14.4.2).

As mentioned already, diamond does not possess a large-area natural substrate and no large-area foreign substrate for single crystal heteroepitaxy. Although efforts are underway to deposite quasi-single crystal (100)-oriented layers on Ir, which by itself is deposited onto a support substrate, these experiments have not been successful for large area wafers like 4'-Si substrates (see [29] and Chapter 6 by Schreck in this book).

No shallow dopants have been found up to now (see Chapter 3 by A. Mainwood in this book). Nevertheless, most of the electronic device structures that have been developed in other semiconductors have also been investigated and fabricated in diamond, mostly on a very experimental level, however. The evolution of diamond technology and of the related device concepts during the first decades has already been described in a number of reviews and handbooks [30–35]. Examples of electronic structures investigated are Schottky diodes [36], pn-diodes [37], MOS-diodes [38], MESFETs [39] and MOSFETs [40, 41], PIP transistors [42], a vertical FET structure [43], a point contact transistor [44], a npn-transistor [45] and a permeable base transistor (PBT) [46] on the electronic side, vertical X-ray and particle detectors [47–49], planar DUV MSM detectors [50] and LEDs [51] on the optoelectronic and detector side. In addition, there have been electrochemical electrodes [52] and ion-sensitive and bio-sensitive FETs [53]. These structures have partially been realized on natural and synthetic single-crystal stones and on homoepitaxial layers, as well as on polycrystalline diamond (PCD), nanocrystalline diamond (NCD), and ultra-nanocrystalline diamond (UNCD) films grown on foreign substrates (mostly Si) by microwave plasma assisted CVD (MPCVD) or hot filament CVD (HFCVD). The doping technologies used include doping during epitaxy using gaseous sources [54] and solid sources [55, 56], ion implantation [57] and diffusion [58]. Doping from the gas phase is used mostly.

This chapter will concentrate on recent achievements related to the epitaxial growth of thin single-crystal layers and related doping technologies. The historical development will be touched on only briefly.

One of the main limitations in the device development has been the absence of shallow doping. Many chemical elements have been investigated for doping of diamond sometimes in conjunction with co-doping like N (D), Li (D), P (D), S (D), Sb (D), B (A), etc. [59–64]. In most cases either the energetic level was deep and/or the solubility and active site concentration low.

The element most commonly used is boron, an acceptor with an activation energy E_A of 0.37 eV and a solubility above 10^{21} cm^{-3}, first analyzed in 1971 [65]. At low acceptor concentrations, full activation is only obtained above about 600 °C [66–68]. At ambient temperature, activation is only in the lower percentage range, and at 77 K device characteristics are entirely frozen out. However, at high doping concentration the activation energy is reduced due to miniband formation and full activation is obtained at room temperature for concentrations above about 10^{20} cm^{-3} [69] (see Figure 14.1). This means

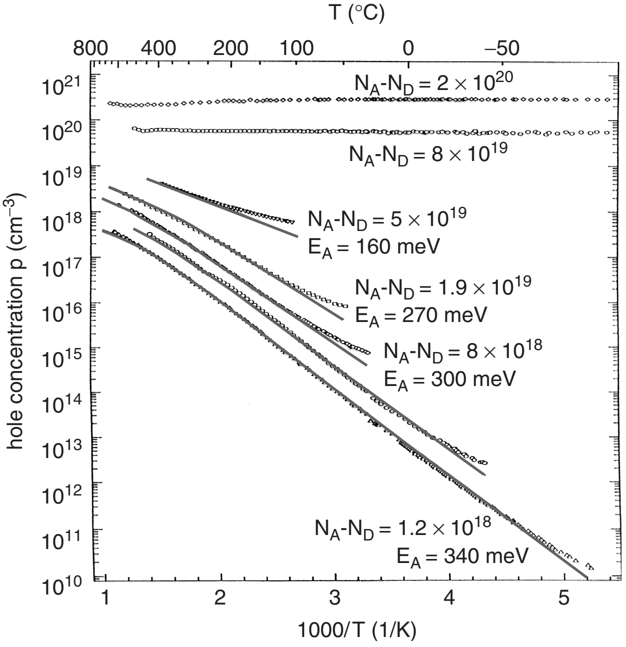

Figure 14.1 Carrier concentration as function of reciprocal temperature measured in boron-doped homoepitaxial diamond layers with different doping levels (after [66]). Reprinted from phys. Stat. solid. (a). Boron-doped homoepitaxial diamond layers: fabrication, characterization, and electronic applications by Borst, T.H. and O. Weis, Vol 154, 423. Copyright (1996) Wiley-VCH

also that ohmic contacts can be realized by tunneling on highly doped contact layers. However, boron is deposited from the H-rich gas phase mostly as BH_x precursor from B_2H_6 or $B(CH_3)_3$, and may thus also be incorporated as BH-complex. As BH-complex it will be electrically neutral [70]. Adding a second H-atom (deuterium) will make it a donor [71]. However both have only limited thermal stability. Furthermore, at high concentrations B can form a B_2 dimer, which is electrically inactive [72]. Thus, at high concentration (above about 5×10^{19} cm^{-3}), the chemical boron profile can differ substantially from the electrical profile due to incomplete activation despite miniband formation. Therefore, any doping technique has to take these complications into account. However, they can be widely avoided by choosing appropriate CVD growth parameters, as may be seen from a comparison of chemical doping profiles and CV-doping profiles as discussed in Section 14.2.1. A further problem accompanying all boron doping technologies is the mismatch (and related stress) that can be as high as $\Delta a/a \sim 10^{-3}$ at high doping, because of the different Bohr radius of carbon and boron atoms [73].

Donor doping of diamond is still a challenge. Two dopants have been investigated intensively and used in device structures. This is nitrogen with an E_D of 1.7 eV [74] and phosphorus with an E_D of 0.57 eV to 0.62 eV [75, 76]. Nitrogen cannot be activated at room temperature, and shows a solubility limit of about10^{18} cm^{-3} N_D when incorporated into a lattice site of only about 10^{18} cm^{-3} [77]. This means that a miniband cannot be formed, miniband conduction cannot be generated, and ohmic contacts based on tunneling cannot be realized. In device application, the nitrogen doped layer will appear as a lossy dielectric. Phosphorus has been incorporated mainly into [111]-oriented substrates, which is, however, not the usual semiconductor orientation and is difficult to prepare because of its hard surface. It has mainly been investigated for LEDs, where moderate activation can be tolerated [78] (see also Chapter 15 by Makino in this book), or experimental Schottky diodes [79]. For a phosphorus-doping concentration of 7×10^{16} cm^{-3}, an electron mobility of 660 cm^2/Vs has been measured [80]. Below 10^{16} cm^{-3}, films still seem to be highly compensated. The highest doping concentration measured up to now is 5×10^{19} cm^{-3} [81]. This means that a concentration close to miniband formation has been obtained, potentially enabling tunneling ohmic contacts. Thus, electronic devices based on these dopants would need substantial heating in the range above 300 °C and 500 °C respectively. However, at high temperatures deep-level defects will also be activated and increase leakage and redistribute fields.

In addition to extrinsically doped layers, a hole conductive layer (2DHG) can be generated at the surface, when it is hydrogen terminated [82] (see also Chapter 4 by Ley in this book). The acceptor configuration of the surface hole channel is not clear yet, but mostly related to surface adsorbates, and the channel related to transfer doping [83]. Field-effect transistors based on this channel concept have been the only ones, up to now, showing microwave gain and power performance. Both MESFETs and MISFETs have reached 2.1 W/mm output power densities, but become limited by surface breakdown, since the structures have not yet been passivated [84, 85]. The highest absolute power reached has been 1.27 W (at 1 GHz) [86]. However these structures are still plagued by instabilities and are restricted to operation at moderate temperatures [87, 88]. The concept is not easily suited to vertical device structures like high voltage diodes. Devices using this configuration are not the subject of this chapter and the reader is referred to Chapter 13, by Kasu, in this book.

The problem of obtaining full activation of extrinsic dopants in diamond has been an important part of the development of electronic device structures since the beginning. The outstanding potential of diamond in high power electronics, viewed from its ideal materials properties, had already been evaluated in the early 1990s [89]. At the same time, various transistor structures have been developed based on homoeptaxial growth and boron doping, such as MISFETs [41, 90, 91], MESFETs [92, 93] and JFETs [94]. This has already included first attempts at using FET channels based on pulse doping, and planar, recessed gate and backgate structures. An overview of some of these early activities can be found in [95]. A first application was thought to be in high-temperature logic elements [96, 97]. However, all these early structures were still suffering from low current levels or had to be operated at elevated temperatures, due to the rather immature growth and doping technologies used. The problem was in limiting the acceptor sheet charge density N_s to the 10^{13} cm^{-2} range in order to obtain full pinch-off before gate breakdown, while maintaining a peak concentration of 10^{20} cm^{-3} for full activation. This implied nm-narrow doping profiles, which in turn implies controling the epitaxial and doping processes down to the sub-nm range. This problem is discussed in Section 14.2.1.

On the other hand, full boron activation is also obtained for low doping concentrations, when the Fermi level crosses the acceptor level. This is the case for concentrations below about 10^{13} cm^{-3} (at room temperature). With such low doping levels, this is an attractive regime for high-voltage power diodes [98]. The challenge here was, of course, to obtain material with sufficiently low residual impurity and electrically active defect concentration to allow high space-charge limited current densities in the active layers.

Background doping concentrations below 10^{15} cm^{-3} and low defect densities had indeed been obtained by the early 2000s [99–102]. In turn, this has resulted in high mobilities of holes and electrons measured by time-of-flight experiments (see Chapter 2 by Isberg in this book). With such high-purity active layers on highly boron-doped contact layers, it has been possible to push the breakdown voltage of diodes into the kV region.

The development of electronic device structures has, therefore, mainly been built around boron doping technologies, and FET devices have been exclusively p-channel FETs. In respect to diodes, the emphasis has been on vertical mesa structures with unintentionally doped active layers of μm thickness to obtain high blocking voltages or high temperature performance. This was achieved mostly with barriers generated by Schottky contacts, in a few cases by a merged junction or a heterojunction (see below) with n-type ultra-nanocrystalline diamond (UNCD) (see below), hexagonal AlN [103] and cubic BN [104]. Very few attempts have been undertaken to realize epitaxial bipolar PNP device structures [105]; and indeed up to now the experimental performance reflects the doping problems already discussed.

Three fields of application will be discussed in detail in the following sections. In Section 14.3 the field effect transistor for RF power applications is the subject; the field of high voltage and high temperature diodes is discussed in Section 14.4, and electrochemical electrodes and ISFETs in Section 14.5.

14.2 DELTA-DOPING CONCEPT AND TECHNOLOGY

High performance electronic devices are usually realized on synthetic single crystal substrates and homoepitaxial active layers, generally by microwave plasma assisted CVD (MPCVD). This technology has developed into two distinctly different directions: high growth rates up to 100 μm/h for large volume stones [106], and slow growth down to monolayer control as in step-flow growth. Using an extremely low CH_4-content, down to 0.05 % in the H_2 gas phase, atomically flat surfaces can be obtained by the step-flow growth mode [107]. For device applications, slow growth processes dominate because of sub-nm thickness control and the low defect density requirement. However, despite high purity and related high carrier mobilities, the breakdown field of the material is still only a fraction of the theoretically expected value F_{br} of 10 MV/cm. In most published cases it is between 1.5 and 3 × 10 MV/cm [108, 109], in part because of unoptimized geometries, but also because of residual defects. This range is also in agreement with the analysis of the avalanche breakdown mechanism in high purity material [110]. The defect configuration causing this low value has, however, not yet been definitely identified.

14.2.1 Delta-doping profiles

To realize doping profiles that fulfill the requirements of simultaneous full activation and full channel pinch-off in an FET structure, nm-thin profiles are needed. This is illustrated by the example given in Figures 14.2 and 14.3 showing a calculated carrier profile within a box-like doping spike of 1.0 nm width and a peak concentration of 1×10^{20} cm^{-3}.

Figure 14.3 shows the relationship between the width d of the boron box-like doping profile for various peak-doping concentrations N_A^{peak}. Values of maximum profile thickness

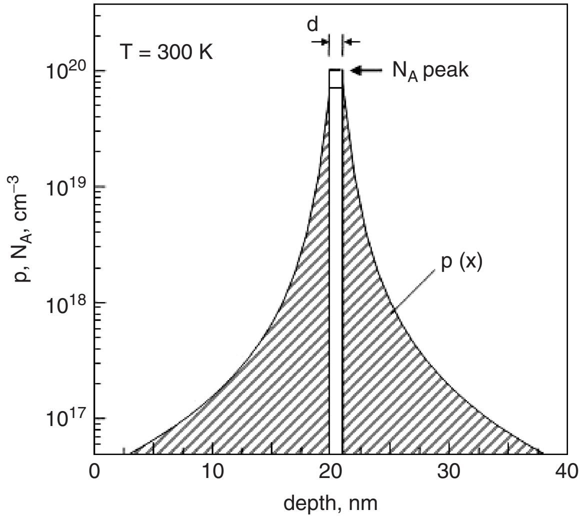

Figure 14.2 Calculated carrier profile for a box-like doping spike in diamond with a width d of 1.0 nm and the peak doping concentrations N_A^{peak} of 1.0×10^{20} cm^{-3} (Silvaco-Atlas solver). The amount of out-diffused carriers into the adjacent intrinsic diamond material with high carrier mobility is approximately 40 % (the dashed areas). This corresponds to a ratio L_D/d of Debye lengths $L_D = (2\varepsilon_s\varepsilon_0 \cdot kT/q \cdot N_A^{\text{peak}})^{1/2}$ to profile width d of about 0.22

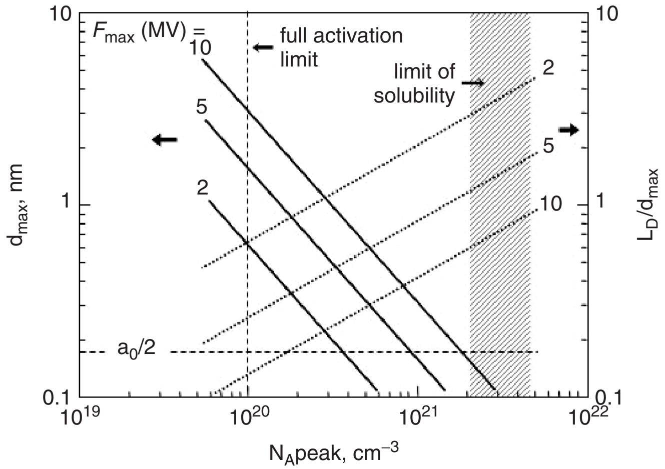

Figure 14.3 Dependence of maximum width of a box-like doping profile on peak acceptor concentration for various breakdown fields of 2 MV/cm, 5 MV and 10 MV/cm according to equation (14.1). Also shown is the ratio of Debye length (L_D) to doping profile width (d). Indicated in the plot is also the approximate window between full activation and solubility limit of boron in diamond (see text) and the tetrahedral unit cell dimension

d_{max} were calculated for the case of complete depletion of the doping spike prior to electrical breakdown of diamond, when the maximum field strength F_{max} is reached:

$$N_S = N_A^{peak} \cdot d_{min} = \varepsilon_s \varepsilon_0 F_{max}/q \tag{14.1}$$

where ε_s is the dielectric constant of diamond ($\varepsilon_s = 5.5$), q is the elementary charge and F_{max} is the electrical breakdown field.

Shown in the graph is the window in doping concentration within which for full pinch-off full activation can be reached inside the solubility limit. The boundary to full activation may be compared with Figure 14.1. The solubility limit of boron is assumed to be in the range of 2 to 5 × 10^{21} cm^{-3}, because of the high stress generated and the likelihood of defect and cluster formation, although experimental evidence points towards a density $\geqslant 1.4 \times 10^{22}$ cm^{-3} [111]. The solid lines are the calculated d_{max} versus N_A^{peak} relationships for three breakdown fields (F_{max}), between 10 MV/cm (theoretical value) and 2 MV/cm (likely value for defective substrates). For the case shown in Figure 14.2 with $N_A^{peak} = 1.0 \times 10^{20}$ cm^{-3} and $d = 1.0$ nm, the sheet charge density is $N_s = 1.0 \times 10^{13}$ cm^{-2} and the field for full depletion F_{depl} is 3.3 MV/cm. Another important figure is the ratio of profile width (d) to Debye length (L_D), which indicates the percentage of carriers moving outside the acceptor region with high mobility as illustrated in Figure 14.2. This ratio is also plotted in Figure 14.3. It can be seen that the profile width d is even more critical in the case of the highest possible sheet charge density $d_{max} \times N_A^{peak}$ within the F_{max} limit for obtaining an increase in mobility.

The goal of the technology is naturally to obtain a monolayer thin doping spike, which is also known as planar doping in III–V compounds semiconductor growth [112]. In Figure 14.3 this case is indicated by a dashed line representing the spacing of the carbon tetrahedron subunit cell with lattice constant a. Considering the lower full-activation limit of the boron acceptors in diamond of 10^{20} cm^{-3} [69], the average distance between the impurity atoms would be about 2 nm, which is sufficiently narrow to form a miniband in a monolayer doping profile. This will result in a sheet charge density of about 2.2 × 10^{13} cm^{-2} and the corresponding F_{max} for channel pinch-off of about 7 MV/cm. This sheet charge density is higher than the channel sheet charge densities commonly obtained with AlGaN/GaN heterostructures ($N_s \leqslant 1.5 \times 10^{13}$ cm^{-2}), and close to the densities obtained by the lattice-matched $In_{17}Al_{83}N$/GaN system ($N_s \approx 3 \times 10^{13}$ cm^{-2}) [113].

An additional benefit of delta doping is the spill-out of free carriers from the doping planes into the adjacent undoped material and the associated reduction of carrier scattering along the profile [114]. This effect has been considered as an effective mobility enhancement. In the case of an ideal delta-doping profile with no doping tails, no roughness and no clustering of impurity atoms, the low field mobility can be expressed as:

$$\mu_\delta = (1/\mu_{ph} + 1/\mu_I)^{-1} \tag{14.2}$$

where μ_{ph} represents phonon-assisted scattering and μ_I the scattering of ionized impurities along the direction of the doping plane. For diamond, the upper limit of μ_{ph} can be taken to be equal to the experimental value of 3800 cm^2/V s as recently measured at room temperature on high-quality homoepitaxial CVD layers [115]. Here, the concentration of residual impurities was estimated to be in the range of 10^{13} to 10^{14} cm^{-3}. The value of μ_I can be calculated using an ionized impurity scattering theory (Brooks–Herring model) for a bulk-doped semiconductor, and a mobility enhancement factor for a planar delta-doped channel. Using data from the literature on MBE-grown, planar-doped, Si, Ge, SiGe and GaAs [112], the enhancement factor of the mobility μ_{I} in thin (monolayer) delta- profiles has been estimated to be approximately 4:

$$\mu_{\mathrm{I(delta-profile)}} \gg 4\mu_{\mathrm{I(bulk\text{-}doped)}} \tag{14.3}$$

For $N_{\mathrm{S}} = 2.0 \times 10^{13}$ cm^{-2}, which corresponds to a peak boron concentration of about 1×10^{20} cm^{-3} in a monolayer doping profile, Equations (14.2) and (14.3) yield $\mu_{\delta} \sim 190$ cm^2/V s at room temperature.

Because of the sub-nm depth resolution requirement, the selection of the substrate sample and its polishing are important starting conditions. Indeed, polishing based on multi-step polishing [116], or a sequential process of mechanical polishing followed by polishing in the gas phase, has resulted in monolayer flat surfaces [117]. Figure 14.4 shows an AFM-profile of a (100)-surface of a selected commercial synthetic substrate before and after such a plasma treatment, followed by epitaxial growth of a 200-nm buffer layer at a growth rate of approximately 75 nm/h. The vertical scale is 2.5 nm and 2.0 nm per division and the pictures are therefore directly comparable.

As mentioned, pulse and delta-profile growth has been achieved by doping from the gas phase and from a solid source, namely a boron rod, inserted into the plasma for a short period of time. The experimental profiles discussed below and used in FET device structures are, in general, obtained by solid-source (boron rod) doping [55]. Device structures will usually contain a nominally undoped buffer layer, the delta-doping spike, and a nominally undoped cap layer. If all these parts are realized within one growth cycle, residual background boron in the chamber will cause doping tails and high background doping in the cap layer. Therefore, growth interruptions, and sometimes change of growth chamber,

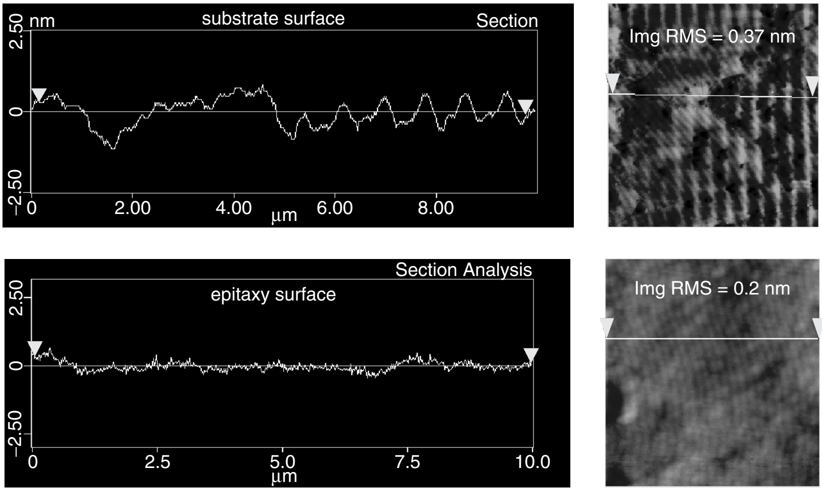

Figure 14.4 AFM images and scans illustrating the surface roughness of an exceptionally planar, commercial (100) oriented IB substrate, still with some remains of the original sawing grooves (upper part), and the same surface after H-plasma treatment followed by epitaxial growth of a 200-nm buffer layer

are needed. Fortunately, this is possible, because after growth the surface is hydrogen terminated, which is not lost when in contact with the atmosphere. This differs from SiC and III-nitrides, where conversion to oxygen coverage will occur naturally, even at ambient temperature. Therefore, steep profiles with a FWHM of 1 nm are usually grown in a complex sequence of growth steps, growth interrupts and boron deposition cycles.

A 1.1-nm wide profile will only contain six basic tetraedral unit cells so boron profiles are therefore not easily identified. Four methods have been widely used:

(i) profiling of the current and sheet resistance by differential mesa etching,
(ii) capacitance-voltage (CV) profiling in an electrolyte,
(iii) high resolution SIMS profiling, and
(iv) physical/chemical profiling by electron recoil detection (ERD).

The first method requires an etching process with sub-nm resolution and is therefore rather discrete [118]. It can only resolve the sheet resistance profile and μn-product. The second method is only possible within an electrochemical potential window of approximately some 3 volts and profiling is therefore limited in depth (for details see Section 14.5). The CV-measurement yields the mobile carrier (hole) profile, once the Helmholz double-layer characteristics in the liquid are extracted separately. The third method represents a chemical profile analysis, which relies on sputtering of material and is destructive. Even when using ultra-low energy, its resolution is limited by roughening during the sputtering process. The fourth method results also in a physical/chemical impurity profile with high spatial resolution determined by the energy (channel) resolution of the magnetic spectrograph. ERD utilizes Rutherford scattering of an energetic heavy ion beam on lighter target atoms. The heavy ions transfer part of their energy to the target element in an elastic scattering process. The particles are scattered under a forward scattering angle and identified by their nuclear charge or mass. From the energy signal, the initial depth of the counted atom can be calculated. For the calculation of the depth profile, only the scattering cross-sections and the energy loss of the ions and scattered atoms are needed [119]. Also this method is destructive. Figure 14.5 shows an ERD profile of a single delta profile with a full width at half maximum (FWHM) of 1.1 nm, grown by MPCVD and a solid boron source (rod) as described in Ref. [120]. The resolution in concentration is about 10^{-2}. Therefore, the profile is displayed on a linear scale. As can be seen, the peak carrier concentration is in the range of 1×10^{21} cm^{-3}.

Figure 14.6 shows the corresponding free carrier (hole) profile derived from CV measurements in an electrolyte, as described in the figure caption. Further details are given in Section 14.5. Due to the high resolution of this technique, the profile is displayed on a double logarithmic scale. The limit of resolution is given by the diffusion of mobile carriers forming a Debye tail with a Debye length of about 0.1 nm for 1.0×10^{21} cm^{-3}.

Indeed, the top part of the carrier profile in Figure 14.6 corresponds to the Debye tail; however, the bottom is still broadened. Thus, both profiles (ERD and CV) show peak concentrations of about 10^{21} cm^{-3} and a sheet charge density above 10^{13} cm^{-2}. Within the precision of the analysis, both profiles agree. This shows, that compensation by B_2-dimers [72] and passivation of boron by hydrogen (deuterium) [121] are not observed even at this high concentration.

The Hall measurements on profiles with a peak concentration up to 10^{21} cm^{-3} (like the one shown in Figure 14.5) yielded a Hall mobility of around 30 cm^2/V s at room

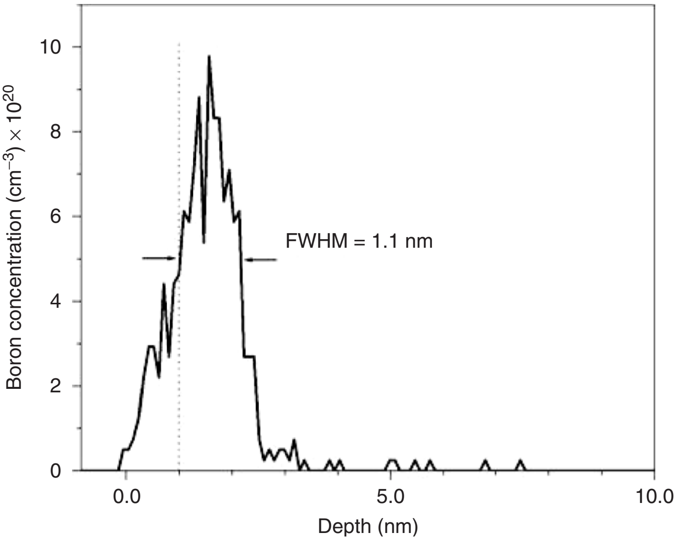

Figure 14.5 ERD profile of boron delta-doped profile. For the experiment the Q3D magnetic spectrograph at the Munich tandem accelerator with an energy resolution of $\Delta E/E = 7 \times 10^{-4}$ has been used, resulting in a depth resolution well below 1.0 nm. The detection limit in this experiment was about 5×10^{11} at/cm^2 (after [120]). Reprinted from Diamond and Related Materials, Characteristics of boron delta-doped diamond for electronic applications by H. El-Hajj, A. Denisenko, A. Bergmaier, G. Dollinger, M. Kubovic and E. Kohn, Vol 17, Iss 4-5 (2008) Copyright Elsevier

temperature. For comparison, the experimentally measured hole mobility in uniformly bulk-doped diamond with $N_A \cong 10^{20}$ cm^{-3} is only about 10 to 20 cm^2/Vs [68]. Nevertheless, the theoretical value of μ_δ given by Equations (14.2) and (14.3) would be about 90 cm^2/V s for such peak concentrations. This means that the experimental delta-doped layers are still do not have ideal planar profiles.

The above-discussed doping technology can also be applied to multiple delta-profile growth. A stack of delta-doped profiles could indeed substitute bulk-doped layers, providing a lower sheet resistance and lower strain [122]. A stack of four profiles is shown in Figure 14.7 [120], with a FWHM ranging from 1.1 nm to 2.5 nm, and grown in a similar way as described for the single delta-profile case. In this case the peaks were separated by intermediate, undoped, spacer layers of 7 nm. The peak concentration was in all cases between 5×10^{20} cm^{-2} and 7×10^{20} cm^{-2}. In this sequence, the length of the H_2/CH_4 growth pulse was varied between 3 s and 6 s. It can be seen that this is directly reflected in the FWHM width of the profiles (see Figure 14.7 inset). After growth of the entire stack, the surface roughness is not increased and still only 0.3 nm (rms). Such multiple delta profiles should be very beneficial in reducing stress, decreasing defect density, and improving mobility of bottom contact layers of vertical device structures such as high voltage and high temperature diodes, and has been used in the merged diode structure [123] discussed in Section 14.4.2.

Broadening of the profiles by diffusion is not observed even at high peak concentrations. Thus, profiles can also be overgrown with thin undoped cap layers without broadening of the delta profile. Diffusion coefficients quoted in the literature are 4.2×10^{-13} cm^2/s

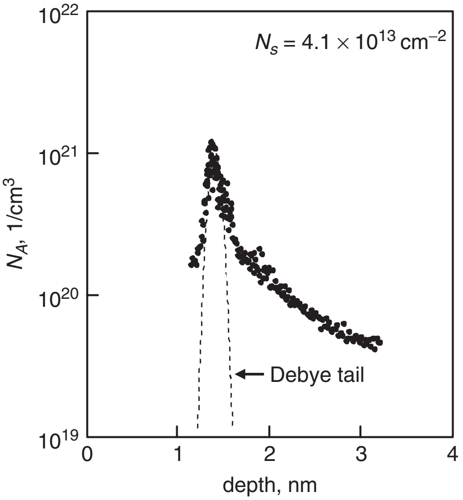

Figure 14.6 Electrochemical CV measurement of the delta-doped profile as characterized by ERD in Figure 14.5. The profile was extracted from capacitance voltage measurements of oxygen-terminated diamond in 0.1-M H_2SO_4 electrolyte at 1 kHz. The capacitance of the electrical double layer in the electrolyte and the corresponding voltage drop were derived by electrochemical impedance spectroscopy measurements. The dashed curve on the graph shows the Gaussian profile calculated for the Debye length corresponding to the peak concentration of 1.0×10^{21} cm^{-3}. The electrode area was 1 mm in diameter (after [120]). Reprinted from Diamond and Related Materials, Characteristics of boron delta-doped diamond for electronic applications by H. El-Hajj, A. Denisenko, A. Bergmaier, G. Dollinger, M. Kubovic and E. Kohn, Vol 17, Iss 4-5 (2008) Copyright Elsevier

at 850 °C (natural IIA diamond) [58] and less than 2×10^{-15} cm^2/s at 1200 °C with an estimated activation energy of 4.2 eV [124] and may therefore be strongly influenced by the quality of the material.

14.2.2 Contacts and device technology

Many of the processing steps of diamond devices are rather similar to those used on other semiconductor materials. A general difference however is the size of the substrate. The small size of single-crystal substrates of currently below 1 cm^2, together with sub-μm or nm-resolution in many cases, requires electron beam direct writing. Two processing steps may be addressed nevertheless, namely, ohmic contact formation and dry etching.

Metal contacts to diamond depend distinctively on the surface termination. On hydrogen-terminated surfaces the surface barrier between the metal and diamond depends on the work function difference and ohmic contacts can be realized with Au, while Schottky barriers can be formed using Al or Ni [125]. However the metal is not covalently bonded but rather weakly attached by van der Waal forces. Thus, adhesion is weak and this technology cannot be used for applications under extreme or harsh conditions. On oxygen-terminated surfaces, the surface potential is rather pinned at a level of about 1.2 to 2.0 eV above the valence band, depending on the oxidation technology [126-128]. The most common

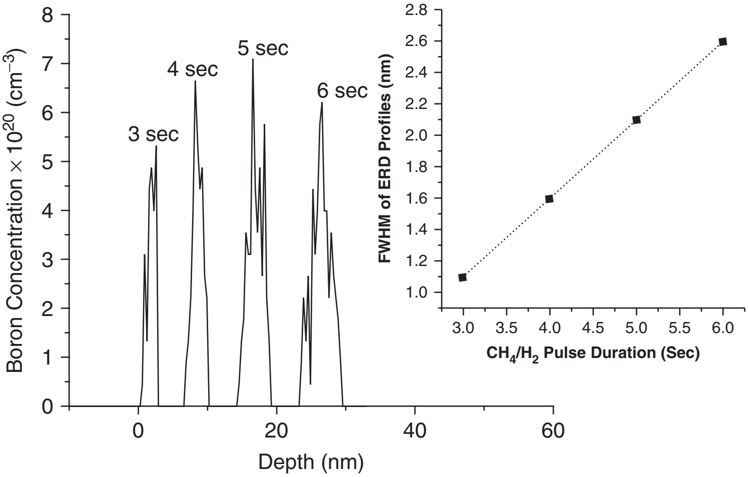

Figure 14.7 ERD analysis of a stack of multiple delta profiles grown as described in the text. Indicated is the time for which the solid boron source (a boron wire) was inserted into the plasma during the delta growth step. The inset shows the relationship between boron rod insertion time and the FWHM value of the profiles (after [120]). Reprinted from Diamond and Related Materials, Characteristics of boron delta-doped diamond for electronic applications by H. El-Hajj, A. Denisenko, A. Bergmaier, G. Dollinger, M. Kubovic and E. Kohn, Vol 17, Iss 4-5 (2008) Copyright Elsevier

barrier potential obtained in Schottky diodes, as discussed in Section 14.4.2, on technical surfaces prepared by plasma oxidation is around 1.7 eV. Nonrectifying contacts have therefore to be realized by tunneling. This implies a highly doped and fully activated contact layer. For boron (the only possible candidate up to now) this implies again an $N_A \approx 10^{20}$ cm^{-3} as discussed above. Thus, a large number of metals can be used, especially refractory metals like Ti, W, WSi and Ta, which can form carbide phases at the interface during contact annealing at temperatures above 600 °C [129–133]. The entire contact metallization stack usually also contains an Au overlayer and an appropriate diffusion barrier. Contact resistances down to $\rho_c \approx 10^{-5}$ Ω cm^{-2} are obtained [120] (seen also Figure 14.2). The definition of the contact resistance is that of the interfacial resistance of the semiconductor and metal interface. This implies that the current distribution in the semiconductor in front of the contact has to be correctly taken into account. This contribution may be a uniform series resistance in the case of a vertical mesa structure, a region of space-charge limited current flow in a high voltage diode, or the two-dimensional current distribution in the case of a planar contact.

In a planar configuration, the contact resistance is usually determined by a transmission line (TLM) structure measurement, employing planar resistors of different lengths [134] (see Figure 14.8). Here, the planar contact resistance R_c of the structure normalized on the contact width W is given by:

$$R_c \cdot W = \sqrt{\rho_c \cdot R_{sc}}\left(\coth L_c\sqrt{\frac{R_{sc}}{\rho_c}}\right) \quad \text{with } \coth L_c\sqrt{\frac{R_{sc}}{\rho_c}} \to 1 \text{ for } L_c\sqrt{\frac{R_{sc}}{\rho_c}} \geqslant 2 \tag{14.4}$$

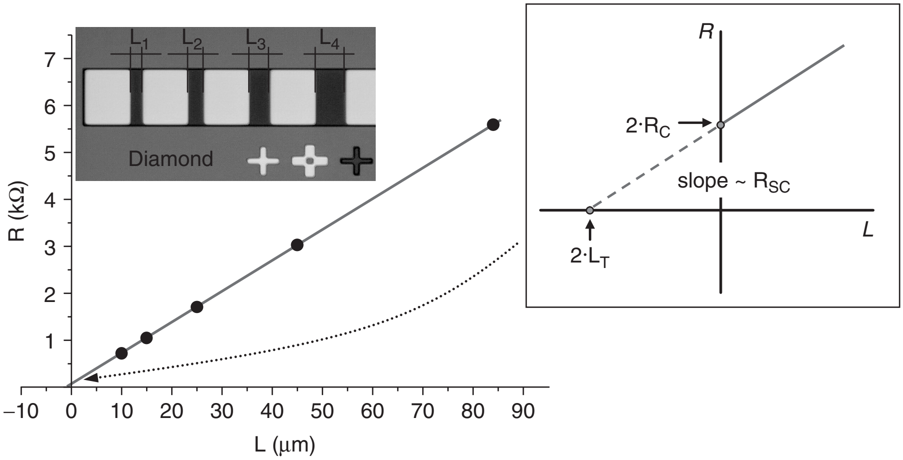

Figure 14.8 TLM measurement of epitaxial resistors of different lengths L as shown in the inset. The channel resistance is plotted against channel length. The slope of the fitted line represents the semiconductor channel sheet resistance R_s. The intercept with the vertical axis represents the contact resistance $2R_c$ (with two contacts to each structure). The extrapolated intercept with the horizontal axis represents the transfer length $2L_T$ (with two contacts to each structure). The active layer was a delta-doped profile. The sheet resistance was $R_s = 5.7\,\text{k}\Omega$, the transfer length $L_T = 0.4\,\mu\text{m}$, and the specific contact resistance $\rho_c = 9 \times 10^{-6}\,\Omega\,\text{cm}^2$ (after [120])

where ρ_c is the specific metal/semiconductor contact resistance, R_{sc} the sheet resistance of the active semiconductor layer underneath the contact, and L_c is the lateral length of the contact metallization. In many cases $\coth(x) \rightarrow 1$ can be set.

The sheet resistance underneath the contact layer, R$_{sc}$, may not be identical to that of the adjacent semiconductor region, R_s. On the one hand, if the contact metal is alloyed into the semiconductor material, the active layer cross-section will be changed. On the other hand, if the free or passivated surface causes surface depletion by a pinned surface potential (as in the case of the O-terminated surface), this will also alter the active layer cross-section. To distinguish between both sheet resistances R_{sc} and R_s, two independent measurements need to be performed, like an additional end-resistance measurement on a third contact [134]. This extended measurement technique also allows evaluation of the temperature behavior of the structure in detail, such as temperature-independent tunneling behavior of the contact and an exponential temperature dependence of active layers with doping levels below about 10^{19} cm^{-3} [133].

To escape this complication, it is often assumed that the semiconductor sheet resistance is not changed and that $R_{sc} = R_s$. In this simplified case, the contact resistance is often expressed by the transfer length L_T. Here the contact resistance is substituted by an additional piece of semiconductor with sheet resistance R_s and an ideal contact of zero resistance. The relationship between L_T and R_c is shown in Equation (14.5), neglecting the coth term:

$$L_T = \sqrt{\frac{\rho_C}{R_{SC}}} \tag{14.5}$$

To obtain a small R_c, contact areas are often separately doped. This may be achieved by ion implantation, diffusion, selective epitaxy or contact mesa etching of a stack of layers. Thus, in recessed gate FET devices the resistance of a planar contact is often described simply by $R_C\mathbf{W}$.

Blocking and rectifying contacts are pn-junctions, Schottky diodes and MIS contacts. pn-junctions and Schottky contacts are discussed in Section 14.4 as part of a vertical diode structure. In FETs they are employed as a gate dielectric, the limit of operation being determined by the ohmic loss and dielectric breakdown.

Experimentally, Schottky diodes have already been studied on natural boron doped stones and rectification has been observed only in some cases, the influence of the surface termination not yet being clear [36, 135]. In the beginning of the 1990s, Schottky diodes on boron-doped CVD layers have been studied more intensively and the influence of the surface preparation [136, 137], barrier characteristics and parasitics identified [138–140]. Already high current rectification ratios of up to 10^{12} at ± 10 V [141] and breakdown voltages up to around 500 V have been measured [129, 141–143]. Contact metals used have been mostly Au [136], but also Al [129, 136, 138], Pt [138, 145], W [144], WSi [146], and recently Ni [146], combined with various overlayers (mostly Au) and associated diffusion barriers and also Hg [141] for CV-probing. From the IV characteristics of the above collected experiments, ideality factors below $n = 1.1$ have been extracted, however often only at high temperatures [146]. Thus, in many cases the junctions are defect dominated at room temperature and the measured barrier height is not dominated by thermal emission only, but by field emission or even a tunnelling component. Thus, barrier heights extracted from IV-measurements seldom coincide with data extracted from CV-measurements. Such apparent IV-barrier heights have been between 1.2 and 2.3 eV as seen from Figure 14.9, where data (compiled from 18 references listed in the text) are shown. The dependence reflects different methods of preparation in the various laboratories rather than a dependence of the metal work function. After plasma

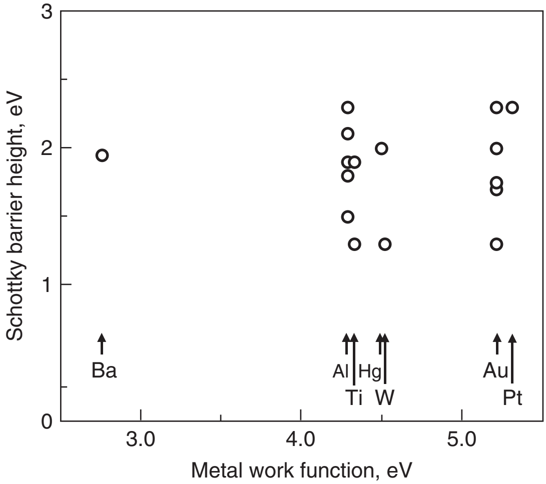

Figure 14.9 Schottky barrier height by IV measurements on oxygen terminated single crystal diamond surfaces compiled from the literature listed in the text

oxidation, mostly a barrier potential of about $\Phi_B \sim 1.7$ V is measured, which is equal to that of the free surface surrounding the contact and terminated by plasma oxidation [128].

Its reverse current characteristics depend strongly on the doping concentration, and low leakage, thin gate contacts are difficult to obtain. pn-junctions have been realized with donor doping by phosphorus and nitrogen. Phosphorous/boron doped structures have been mainly used in light emitting diodes (not discussed here; see Chapter 15 by Makino in this book), and nitrogen/boron doped structures as gate contact in FETs. Because of its deep level ($E_{DN} = E_C - 1.7$ eV) the nitrogen doped layer is not activated at room temperature and represents a lossy dielectric. Therefore a FET will operate similarly to a MISFET, however with a dispersion at around the dielectric cutoff of the N-doped layer.

The most efficient channel modulation and highest transconductance are obtained for a high-k dielectric layer no thicker than the tunneling limit. In the case of Si-MOSFETs the thickness of currently used gate oxides (about 2 nm) is already below the tunneling thickness. In this case the gate length has to be in the deep sub-μm range (about 100 nm) to realize high channel current densities. Nevertheless, the tunneling gate leakage current may be as high as 10 % of the open channel current. For diamond high power RF FET structures, this implies the use of a thin dielectric with a breakdown strength and a dielectric constant above that of diamond. Such a dielectric is Al_2O_3 (used on many semiconductors like Si, SiC, GaAs and GaN) and it has indeed been incorporated into delta-channel FETs (on O-terminated surfaces) [147], as well as surface channel FETs (on H-terminated surfaces) [85]. Its breakdown strength is 2 to 10 MV/cm and k (relative dielectric constant) is 7.5 to 9. These values differ with deposition parameters, since the material is in general amorphous but may contain nanocrystallites of different Al_2O_3 phases. Many deposition techniques have been used, such as sputtering, plasma deposition and ion beam deposition from Al_2O_3 targets, and atomic layer deposition (ALD) with monolayer control using a sequential gas inlet of the precursors [148, 149]. Precursors have been metalorganics for Al and O_3 or H_2O for oxide formation. Thin films (3 nm) have been generated by natural oxidation of evaporated Al [85]. Al_2O_3 has also been obtained by high temperature oxidation of AlN [150].

In any device structure, the reduction of parasitic elements is essential and in many cases this is related to the etching of profiles. This requires etching on the nm-scale. Since diamond cannot be etched in any (water based) wet solution, dry etching by oxygen is generally used. Since the strength of the diamond lattice is the highest of all carbon phases, any organic photoresist mask will etch faster than diamond and for deep profiles, metal oxide masks like TiO_2 are needed [151]. Further, defects are etched faster, and [100] surfaces attacked faster than (100)-surfaces, so that a rough surface or needles are usually formed. In addition, considering a technical surface with contamination from previous processing steps, most metallic residues will not be removed by an O-plasma. Therefore, additional species are often added to the plasma, like CF_4 [152] or Ar, adding a sputter component to the process [153]. Etch rates down to and below 1 nm/min have been realized and employed in recessed-gate FET structures [120]. In a previous paragraph the smoothing of surfaces by H-plasma processes is also mentioned. This process seems to be very much related to the different edge facets and a local field enhancement of the rough surface. At the power employed no noticeable etching after smoothing could be identified, even after H-treatment at high temperature (700 °C) over an extended period of time (h) as concluded by the electrochemical profiling of delta-doped profiles. As an indication of the stability of the diamond phase in H_2, an experiment in H atmosphere at 2200 °C may be worth mentioning [154].

14.3 FIELD EFFECT TRANSISTORS

High performance field-effect transistors need to be created with high mobility channels on high resistive substrates. In the case of diamond, these are mainly nitrogen-doped Type-1b (yellow) substrates with (100) oriented surface and less than 1 cm^2 surface area. Figure 14.10 shows a 4 mm ×4 mm commercial substrate with four fields of processed FET structures. Figure 14.11 shows a micrograph of a discrete transistor structure.

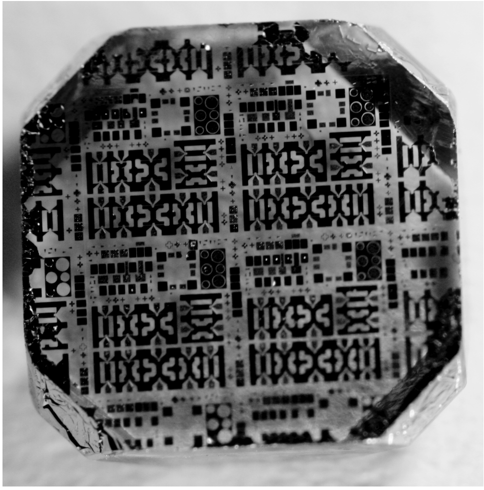

Figure 14.10 Micrograph of diamond single crystal substrate processed with FET devices. Substrate size approx. 4 cm × 4 cm

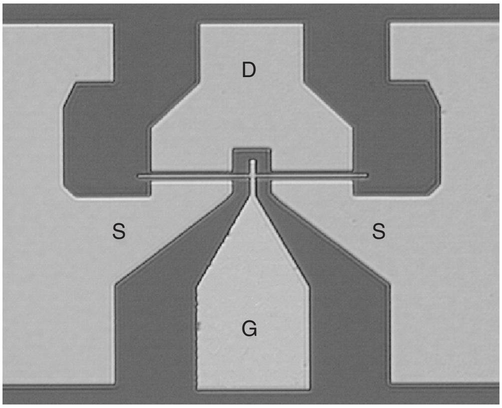

Figure 14.11 Micrograph of microwave FET in microstrip configuration. Gate length is 1.0 µm; gate width is 2 × 50 µm

14.3.1 Delta-channel field effect transistors

A boron delta-doped profile in diamond seems to be an attractive solution for RF power transistors, because it combines high activation with a limited sheet charge density. It uses a chemically and thermally stable conductive channel, which can be easily incorporated into conventional microwave power FET structure concepts, with gate recess and gate field plate using selective etching and regrowth techniques [155, 156]. A schematic cross-section of a planar delta-doped FET structure with a gate recess and gate field plate is shown in Figure 14.12. Since this structure has been analyzed theoretically in some depth, some dimensions are also indicated as used in the simulation of specific cases, resulting in the power design graph shown in Figure 14.14.

In general, using the stable O-terminated surface (with or without passivation), a gate recess is essential for efficient modulation of the entire delta-doped channel sheet charge density. In a planar configuration, the surface outside the gate contact will already be widely depleted by the pinned surface potential. However underneath the gate, the gate diode can be driven into a forward direction until the forward-gate threshold voltage is reached and the gate dielectric breaks down. Thus, the channel can be opened entirely, and charge accumulation may even be possible, depending on the density of surface

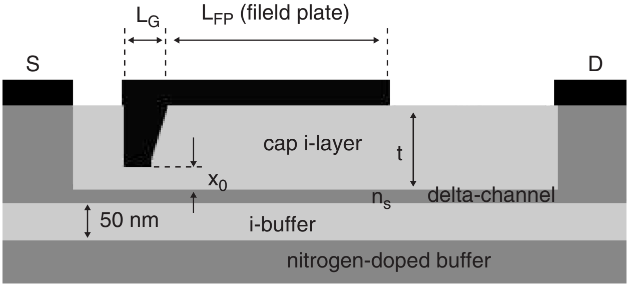

L_G = 0.1 µm

L_{FP} = 1 µm; 2 µm

t (cap layer) = 30 nm (planar gate FET)
= 150 nm (recess gate FET)

gate recess x_0 = 30 nm

angle of gate recess: 30°

potential of free surface: $\phi_{\text{surface}} = 1.7$ eV

Schottky barrier of gate: $\varphi_b = 1.7$ eV

Figure 14.12 Schematic cross-section of delta-doped channel FET structure with gate recess as used in the simulation (2-D Silvaco–Altas solver using the options of Fermi–Dirac statistic and incomplete ionization of the boron acceptors). The material parameters of the simulated device structure are listed in Table 14.1 (after [155]). Reprinted from Diamond and Related Materials, Diamond field effect transistors–concepts and challenges by A. Aleksov, M. Kubovic, N. Kaeb, U. Spitzberg, A. Bergmaier, G. Dollinger, Th. Bauer, M. Schreck, B. Strizker and E. Kohn, Vol 12, Iss 3-7 (2003) Copyright Elsevier

states, pinning the barrier potential. In this case the source and drain access regions will act as current limiters, thus, in essence preventing operation at forward gate bias (enhancement mode). In consequence, the parasitic series resistances will be high and the power handling capability seriously limited. Output power is developed in the high field drift region between gate and drain, which is the lateral space charge layer of the (reverse) biased gate contact developing towards the drain. The gate drain spacing must therefore accommodate this extension. In the output characteristics of the device this is the saturation region (see Figure 14.13).

The IV-operation is limited by the maximum allowed drain bias (V_D^{max}), which in turn is linked to the breakdown limit of the gate/drain diode. The quasi-static maximum RF output power generated in Class A operation (DC bias point at $I_{Dsat}/2$ and $V_D^{sat} + (V_D^{max} - V_D^{sat})/2$) is then given by:

$$P_{RF}^{max} = 1/8 \times [I_D^{max} \times (V_D^{max} - V_D^{sat})] \tag{14.6}$$

where V_D^{sat} is the knee voltage of current saturation, as illustrated in Figure 14.13. At high frequency the resistive load line and the output matching become complex.

As can be imagined, the highest field in the device structure is developed at the drain end of the gate. To lower the field at this point, commonly a field plate is used. In Figure 14.12 this is the gate contact overlapping from the gate footprint towards the drain. The field plate may be directly attached to the gate metal as shown in Figure 14.12, or may also be a separate contact biased on a separate potential, or left floating. In the case of GaN-based HEMTs up to two field plates have been added [157]. The penalty will be an effectively larger gate length, a larger channel transit time and thus lower f_T cut-off frequency.

Figure 14.14 shows the simulated maximum RF output power handling capability (based on the DC output current and voltage limits) of delta-doped channels, recessed gate structures as schematically shown in Figure 14.12 with various field plate configurations. The channel was an ideal delta-doped channel with monolayer doping (planar doping), which has not been achieved yet experimentally. With this assumption, the values of the maximum current density I_D^{max} were calculated using the gradual channel approximation for MOSFETs, taking into account the dependence of carrier velocity on the electrical field

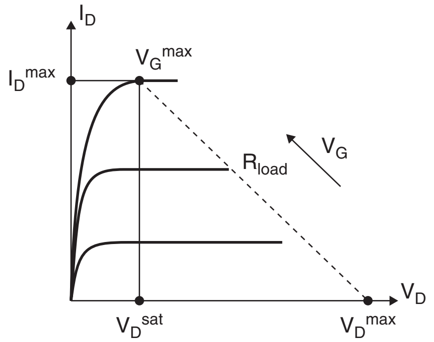

Figure 14.13 Schematic set of DC output characteristics explaining the modelled RF power handling characteristics shown in Figure 14.14. The value of V_G^{max} is determined by the onset of strong gate-current flow at forward bias. For p-channel devices all bias and current arrows indicate negative directions

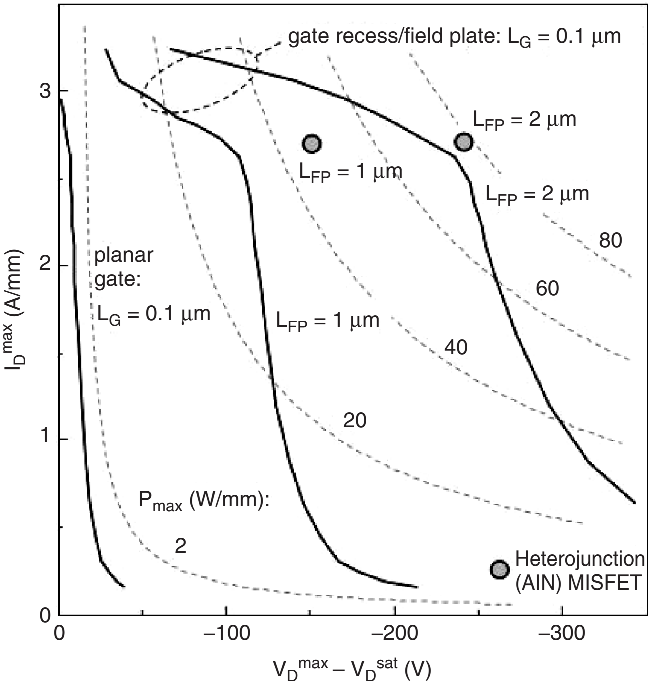

Figure 14.14 Theoretical RF power handling capabilities (I_D^{max} versus $V_D^{max} - V_D^{sat}$) for a planar gate and the recessed gate structure shown in Figure 14.12, calculated for 20 °C operating temperature. The dotted curves indicate various levels of constant RF power density ($P_{max} = 1/8(I_D^{max}[V_D^{max} - V_D^{sat}])$ for Class A operation. Also indicated by the open circles is the MISFET configuration with 1-μm field plate and 2-μm field plate as discussed in the text (based on [158]). Reprinted from Diamond and Related Materials, Diamond power devices. Concepts and Limits by A. Denisenko and E. Kohn, Vol 14, 491 (2005) Copyright Elsevier

Table 14.1 Material parameters of diamond at 300 K as used in the simulation of the recessed FET power performance in Figure 14.14 and discussed in the text (after [158])

Saturation velocity (holes)	1×10^7 cm/sec
Hole mobility (intrinsic diamond)	3800 cm^2/V s [115]
Electrical breakdown field	10 MV/cm
Relative dielectric constant	5.5
Activation energy E_A of boron acceptors in the delta-doped channel (eV):	$E_A = 0$ for $N_A > 10^{20}$ cm^{-3} $E_A = 0.37 - 8.6 \times 10^{-8} N_A^{1/3}$ [69]

similarly to the case of Si. The maximum drain bias V_D^{max} for pinch-off was assumed to be limited by electrical breakdown in diamond. These values were calculated by means of a 2-D numerical simulation (Silvaco–Blase solver®). Further assumptions are a Schottky gate contact on an oxygen terminated surface and a MISFET configuration with a 10-nm AlN dielectric gate layer and a set of materials parameters as listed in Table 14.1. The values of the sheet charge density N_s were varied within the range $9.0 \times 10^{12}/\text{cm}^{-2}$ to $2.3 \times 10^{13}/\text{cm}^{-2}$, crossing the critical doping for full boron activation at $2.1 \times 10^{13}/\text{cm}^{-2}$ [158].

To the first order, considering the configuration of a thin, planar, 2D-structure, the maximum lateral extension of the gate depletion layer towards the drain is inversely linked to the channel sheet charge density N_s. Thus, the gate/drain breakdown voltage, which is the maximum allowed drain voltage, is linked to N_s, which in turn is directly linked to the maximum drain current density in case saturated velocity is reached (lateral spreading model [159]). Thus, the maximum power-handling capability is determined by the product of breakdown field and saturated velocity of a given material ($P \sim F_{br} \times v_{sat}$), and output power can be equally generated by high current densities and low voltages as well as by high voltages and low current densities. Therefore, also inserted in Figure 14.14 are hyperbolas of constant power density by the dashed lines. As may also be seen from Figure 14.11, this tendency is indeed observed for the planar device configuration, however with very low output power levels of below 2 W/mm, due to the surface depletion problem discussed above. However, the situation can be improved by reshaping the gate/drain field distribution by a field plate as mentioned already. The field-plate approach allows combination of high current levels with high drain voltages due to an extension of the gate/drain breakdown condition. The field redistribution will be stronger for larger field-plate extensions (here the field plate is a direct DC-coupled extension of the gate). As can be seen, combined with a 0.1-μm footprint (to assure high speed operation with saturated carrier velocity domination) for a 1.0-μm field plate a power density of 34 W/mm is expected, for a 2.0-μm wide field plate this power density is 75 W/mm, ignoring thermal issues. This is more than 20-times the power, which is expected for a planar configuration. However, the field-plate extension will limit the high frequency performance and GHz-operation may limit the practical field plate extension to below 1 μm. The sheet charge density for optimum power density was about 2.0×10^{13} cm^{-2} (translating into $I_{Dmax} = 2.7$ A/mm), independent of field plate extension. The peak concentration is close to the full activation limit of a monolayer doping profile.

The breakdown behavior (and gate leakage-current level) can be further improved by inserting a gate dielectric as indicated by two configurations with 1-μm and 2-μm field plates respectively. In the simulated structure, a 10-nm thin AlN layer had been added onto the recess surface of the structure in Figure 14.12. As can be seen, the power handling capability is improved slightly further. However, in practice most important will be the reduction in gate leakage, when driving the gate deep into pinch-off as, for example, is required for class F operation with high efficiency.

The advantage of pulse doping for FET channels was realized early on, and thin, highly doped layers were attempted in the first generation of devices in the 1990s using gaseous precursors [92] as well as a solid sources [93]. However, the devices were still planar, the doping pulses were still rather wide, and to obtain full pinch-off, the peak concentration was still too low for full room-temperature activation. Output current operation in the mA/mm range was therefore only obtained at an elevated temperature (350 °C).

Further improvements in pulse doping (using a solid source) have resulted in delta profiles with full room-temperature activation and a variety of device configurations have been investigated. Probably the most complex one is sketched in Figure 14.15 [155] with the corresponding top view micrograph shown in Figure 14.16. It contains a backside nitrogen-doped, n-type shielding layer in the buffer, selectively grown highly boron-doped contact regions, a dry etched-gate recess, and a nitrogen/boron lossy dielectric pn-gate junction realized by overgrowth of the gate recess. Details of growth and processing are

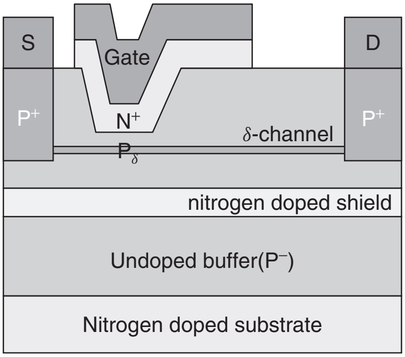

Figure 14.15 Schematic cross section of a recessed gate FET on single crystal diamond with nitrogen-doped lossy dielectric gate layer and gate field plate

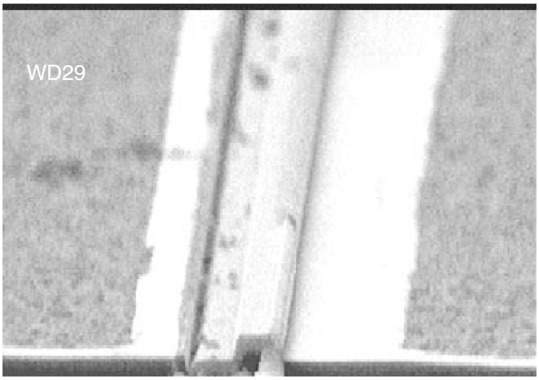

Figure 14.16 Top view micrograph of a recessed gate FET as shown schematically in Figure 14.15 and discussed in the text (courtesy of A. Aleksov)

given elsewhere [155]. The gate lossy dielectric pn-junction configuration was chosen because of high leakage of Schottky barrier contacts on the delta-doped channel. Indeed a gate barrier potential of 3.8 V was identified in a mode of operation as pn-junction [105]. The lossy dielectric gate junction built-in voltage is thus also 3.8 V, a value that is roughly twice that of the free surface potential. In conjunction with a recess, an enhancement mode of operation should be possible. By simulation of this structure with 0.2-μm gate length (along the path as described above), a maximum current density of 1.8 A/mm was extracted at a gate forward bias of −4 V, slightly above the lossy dielectric pn-junction threshold voltage, and a maximum drain bias of 130 V at pinch-off, resulting in a maximum RF output power of about 27 W/mm [105]. However the experimental output current level was far below expectations. Nevertheless, full pinch-off and operation in liquid nitrogen could be observed [105], indicating for the first time that delta-doped profiles providing pinch-off and full activation simultaneously, could be incorporated into sophisticated device structures. At low temperatures (in liquid nitrogen at around 77 K) approximately 75 % of the output current was obtained in enhancement mode, with a gate bias up to −4 V, verifying indeed the lossy dielectric pn-junction and recessed gate concept. The main problem was thought to be the difficulty in obtaining a smooth and defect-free recess region for uniform current flow.

To improve the characteristics discussed above, the technology has been re-evaluated, critical steps modified, and the precision of delta growth as well as dry etching improved along the lines, as described in Sections 14.2.1 and 14.2.2. In particular, to improve the gate leakage characteristics, the gate pn-junction was replaced by a thin Al_2O_3 dielectric layer, thus changing the configuration to a MISFET structure [147]. This avoided the overgrowth of a processed surface, which had previously resulted in a high defect density due to residual contamination. In addition, the Al_2O_3 film deposited by ion-beam deposition displayed a dielectric constant ε_r of 10, and an electrical breakdown strength estimated to be larger than 5 MV/cm. Thus, for the same FET input capacitance, the thickness of the dielectric gate to channel separation could be virtually doubled without sacrificing gate voltage drive capability.

The realization of the device may be briefly described as follows (details can be found elsewhere [147]). The roughness of the surface, after epitaxy, of a 250-nm buffer growth on a Type-1b substrate was 0.3 nm (rms), and thus lower than the estimated delta-profile thickness. The peak boron concentration of the delta profile was estimated to be about 4×10^{20} cm^{-3} and the modulated charge density N_s as 1.5×10^{13} cm^{-2}, both values were obtained from electrochemical profiling of associated test samples without an undoped cap. The effective activation energy of the delta-channel was 25 meV, confirming a peak doping level of full activation. Source and drain contacts were formed by a stack of refractory metals (WSi/WSiN/Ti/Au) on the oxygen terminated surface and annealed at 600 °C by RTA. The contact resistance was measured to 15.6 Ω mm, with an associated transfer length of 1.1 μm. Recess etching was performed by O-plasma with addition of 1 % of Ar, resulting in an etch rate of 1.0 nm/min. Recess etching was terminated in the 25-nm thick undoped diamond cap layer on top of the delta channel some 10 nm above the channel. The last step was the deposition of a 25-nm Al_2O_3 gate dielectric by ion-beam deposition, with a deposition rate of 2 nm/min, which also serves as surface passivation outside the gate recess. The gate metal was evaporated Al, the contact overlapping onto the unrecessed areas by 0.1 μm. The DC output characteristics of such a delta-channel, recessed gate, MISFET with 0.8-μm gate length are shown in Figure 14.17.

As can be seen, the device operates both in depletion and enhancement mode with more than 30 mA/mm maximum drain current density at −4 V forward gate bias. Such an enhancement mode of operation would not be possible without recess configuration. The pinch-off voltage is +5 V, measured at low drain bias. At higher drain bias, buffer layer leakage becomes noticeable, indicating residual boron doping in the buffer layer and a high defect density at the buffer layer/substrate interface. This limits the maximum drain-bias range to about 25 to 30 V, when breakdown is destructive.

The current drive capability of the structure is still low compared with the theoretical estimation. Therefore, the parasitic elements have been evaluated by equivalent-circuit modelling, especially taking the source and drain series resistances into account. Figure 14.18 shows the basic circuit used, and the fitting of the transfer characteristics at $V_D = -15$ V for the intrinsic device part, using a standard MOSFET equation with gradual channel approximation.

The analysis resulted in values of source and drain series resistances of 110 Ω mm compared with an intrinsic channel resistance of 3 kΩ mm. Due to the series resistances, the intrinsic gate bias was lowered and at $V_G = -4$ V, the intrinsic gate bias became

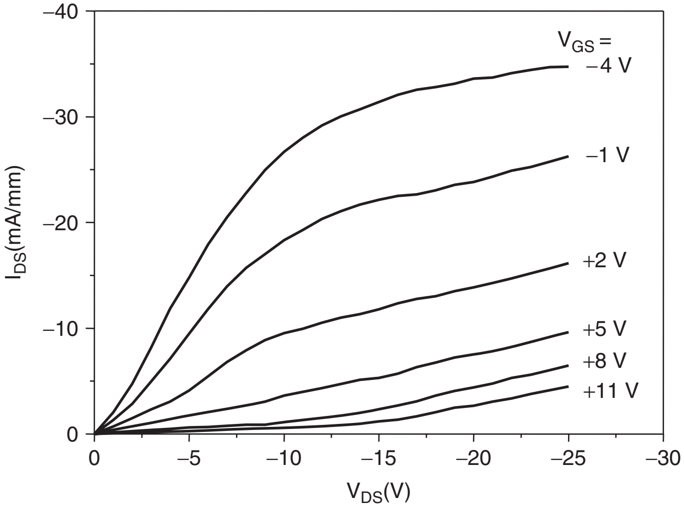

Figure 14.17 DC output characteristics of a MISFET structure with the gate recess and Al_2O_3 gate insulator and with a gate length of 0.8 µm measured at room temperature (after [147]). Reprinted from Diamond and Related Materials, Diamond MISFET based on boron delta-doped channel by H. El-Hajj, A. Denisenko, A. Kaiser, R. S. Balmer and E. Kohn, Vol 17, 1259 Copyright (2008), Elsevier

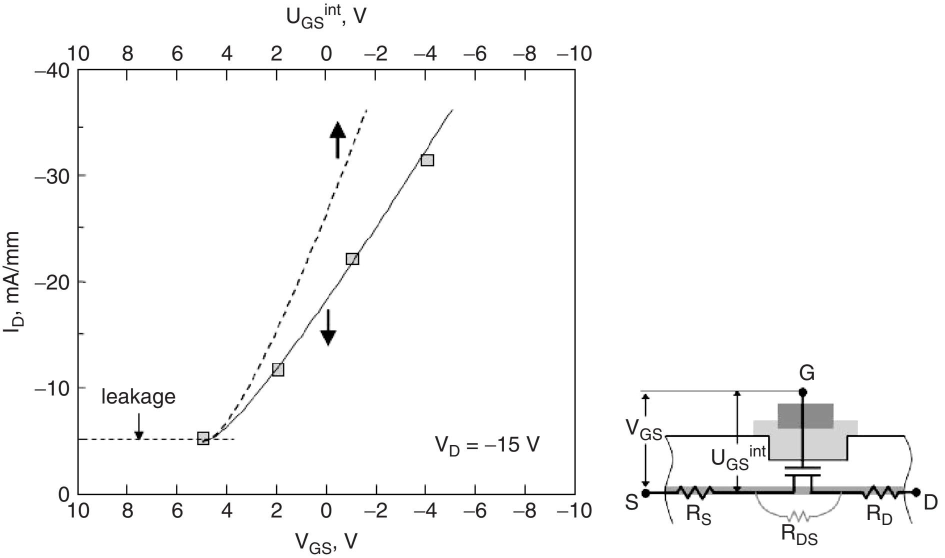

Figure 14.18 DC FET transfer characteristic (left) at $V_D = -15\,V$ and fitting by analysis of parasitic elements as indicated in the inset (right). The experimental data points are squares. The intrinsic transfer characteristic is shown as a dashed line (after [147]). Reprinted from Diamond and Related Materials, Diamond MISFET based on boron delta-doped channel by H. El-Hajj, A. Denisenko, A. Kaiser, R. S. Balmer and E. Kohn, Vol 17, 1259 Copyright (2008), Elsevier

-1.8 V. The intrinsic transfer characteristic is shown as a dashed curve. The analysis of the intrinsic transfer characteristics leads to a channel mobility of 20 cm^2/Vs. This low value is the main reason for the low output current density. In turn this means that the delta-channel carrier profile is still dominated by the Debye tail of the carriers and mobility enhancement is not yet seen. It seems therefore that the main remaining challenge is to realize still narrower doping profiles.

This structure has also allowed the first small signal, high speed, *s*-parameter measurements. In Figure 14.19 the extracted gain plots are shown. As can be seen, cut-off frequencies of $f_T \approx 1$ GHz and $f_{max} \approx 3$ GHz can be extracted. However, these gain curves are still parasitics dominated as can be seen by deviation from the 20 dB/dec slope in the frequency dependence. These data, although still parasitics dominated and obtained with a large gate length, are nonetheless the first microwave measurements on delta-channel devices and are in essence consistent with the DC data of the device structure.

The highest output current density ($I_D^{max} = 115$ mA/mm at $V_D = -20$ V) has been obtained with a junction FET of 2.0-μm source/drain contact separation, which represents also the gate length in this case [94]. Here, the channel was modulated by a nitrogen-doped diamond substrate operated as a back gate pn-junction. The high resistance of the diamond substrate restricted the operation of this back-gate FET to DC operation and temperatures above 200 °C. The technological advantage of this device concept had been the possibility of adjusting the delta-channel thickness by etching from the surface in a last step, while already monitoring the output characteristics.

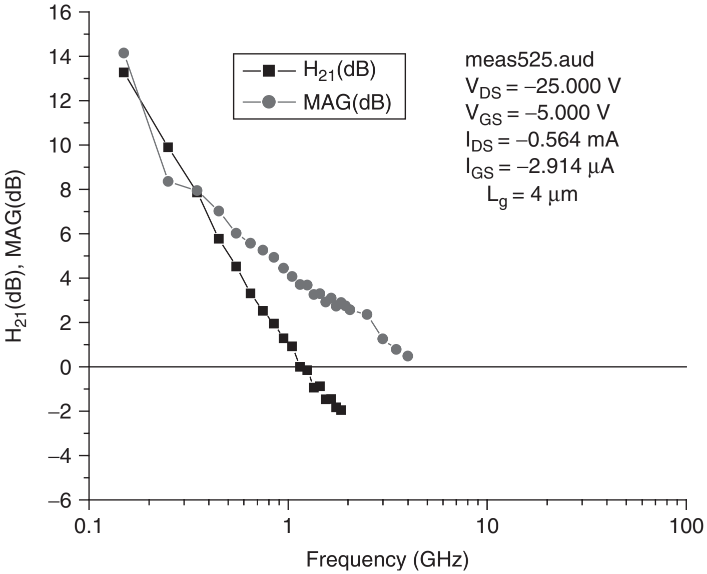

Figure 14.19 Current gain and maximum available gain versus frequency of recessed gate, delta channel, FET with 4-μm gate length (after [147]). Reprinted from Diamond and Related Materials, Diamond MISFET based on boron delta-doped channel by H. El-Hajj, A. Denisenko, A. Kaiser, R. S. Balmer and E. Kohn, Vol 17, 1259 Copyright (2008), Elsevier

14.3.2 P–I–P FETs

From the early days in the development of diamond FET technology, the difficulty of doping resulted in FET device concepts where doping was avoided, except for the contacts. One such concept is that of a space-charge injection triode, analogous to the vacuum triode [160]. Since no efficient electron injection mechanism for diamond has yet been developed, due to lack of shallow n-type doping (except by e-beam excitation), all investigated diamond device structures rely on hole transport. In the planar configuration this has been labelled PIP-transistor, owing to the fact that here the active transistor region is an intrinsic layer of material contacted by highly (P^+) doped regions. According to the Mott–Gurney law, the injection current in an ideal dielectric solid can be described by:

$$J \sim \mu \cdot V^2/L^3, \tag{14.7}$$

where μ is the low-field mobility of the injected carriers and L is the length of the i-layer between the contacts.

Essential for such PIP-structures is therefore a high hole mobility, short contact spacing and a highly uniform current flow as shown schematically in Figure 14.20 the gate resembling a grid in a vacuum triode.

Diamond is indeed a suitable material when considering hole transport with a mobility of up to $\mu_p = 3800$ cm^2/Vs at room temperature in intrinsic material [115]. However, such high mobilities have only been measured in time-of-flight experiments across a highly symmetrical, thick and exceptionally clean MPCVD-grown layer with a residual background doping concentration of the order of 10^{13} cm^{-3} [115, 161]. In practice, the proposed structures have generally been planar with a nominally undoped buffer layer grown onto a substrate, which often contains a high number of defects itself. The buffer layer may contain a certain residual boron level due to growth chamber contamination or memory effects. Both the intrinsic defects and residual boron may lead to a high degree of compensation. Thus, the nominally intrinsic channel of PIP-FETs may still contain deep states (traps) within the band gap. These defect-related states could become charged by the injected carriers and thus impose an electronic barrier, limiting the injection characteristics [162]. Besides, the charged states are likely to increase scattering of the injected carriers and reduce thereby the average mobility in the device channel. This situation is illustrated in Figure 14.21, where data of hole mobilities in diamond are plotted versus ionized impurity concentration. The solid curve is calculated by Equation (14.2) (phonon-assisted and ionized impurity scattering in bulk material) and fitted to experimental boundary conditions [115, 147].

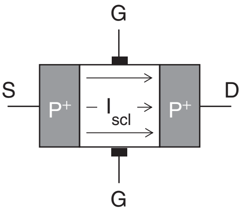

Figure 14.20 Cross-section of an ideal FET structure based on space-charge limited current flow as indicated

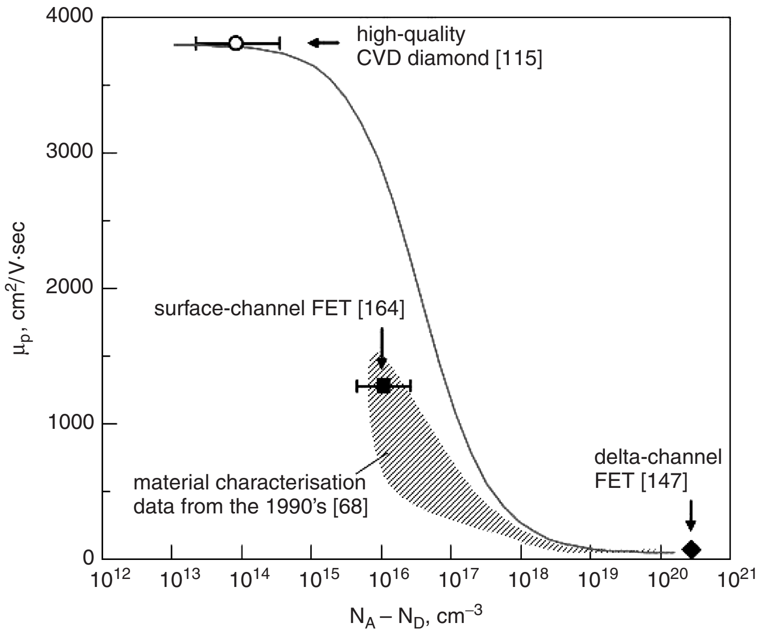

Figure 14.21 Hole mobility in diamond at room temperature versus the concentration of ionized impurities. Solid line derived from Equation (14.2) (phonon-assisted and ionized impurity scattering in bulk doped material), as described in Section 14.2. The shaded area shows the summary of data on hole mobility in diamond accumulated from work in the 1990s, from Ref. [68]. The high quality materials data are taken from Ref. [115]. The delta-doped channel data are from [147]

It can be seen that high values of mobility are only reached for material with a residual defect concentration below about 10^{15} cm^{-3}. On thick buffer layers with a background boron concentration of about 10^{15} cm^{-3}, mobilities between 800 cm^2/Vs and 1300 cm^2/Vs (at room temperature) have been measured [163, 164] which represent to date the typical range for high quality, nominally undoped, buffer layers.

The second important parameter is carrier velocity saturation. In diamond this saturated velocity is 1.0×10^7 cm/s for holes in an ideal intrinsic material [1, 165]. Serious deviations from the low field-mobility values may be expected for fields above 100 kV/cm. However, device related numbers are not available yet. An indication may be obtained from f_T cut-off frequency measurements of surface channel FET devices (on H-terminated surfaces), where v_{sat} values of about 5×10^6 cm/s could be extracted [85]. However, it should also be mentioned that in this case the 2D-channel hole mobility was below approximately 150 cm^2/Vs due to intensive surface scattering.

The translation of the ideal structure into a planar PIP-transistor structure is not straightforward as may be seen from Figure 14.22. Vertical structures have not been attempted yet, because of their technological complexity. In fact, the structure in the figure resembles that of a Si-MOSFET, where an inversion layer channel is modulated, if the active semiconductor layer is lightly doped. However, to generate an inversion layer, the interface state density at the semiconductor/dielectric interface has to be low, a condition that may also be described as 'unpinned'. Such a condition is only observed for the H-terminated surface and has led to surface channel FETs with a 2DHG-channel as discussed in

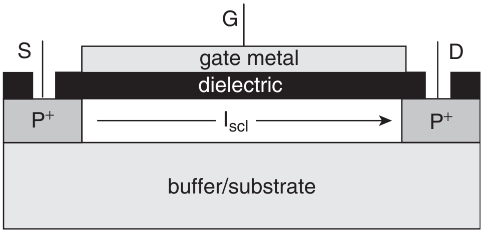

Figure 14.22 Basic planar PIP-MISFET cross section, also indicating the space-charge limited channel current flow (I_{scl})

Chapter 4 in this book. When the surface is O-terminated, the surface potential is pinned and the semiconductor highly depleted. Inversion-layer formation is not possible. Therefore a planar PIP-structure with an entirely oxygen-terminated surface will not convert to an inversion layer MOSFET structure, even if lightly doped. Nevertheless, the gate needs to overlap the source and drain contacts to avoid unmodulated free surface areas with high surface potential. To generate output power, drain bias is needed, which translates into a lateral drift region between gate and drain, which is not controlled by gate bias. Such a region has not yet been incorporated into the PIP-concept and therefore the development of such structures has concentrated on high current densities. The structure as shown, with short contact spacing and overlapping gate, will show a triode output characteristic at low drain bias before saturated velocity is reached, similarly to the characteristics of a static induction transistor (SIT) [12]. An extended saturated region is only expected with the incorporation of a gate/drain drift region.

Numerical simulation of this basic planar structure with ideal materials parameters (no traps in the active diamond layer, no oxide charges in the gate insulator, no pinned surface potential) has already been attempted in 1995 [166]. The structure contained embedded lateral contacts, a 0.1-µm ungated free surface separation of the gate and source/drain contacts, and a SiO_2 gate dielectric. For a contact spacing of 0.7 µm, a maximum output-current density of approximately 1.5 A/mm was extracted for an enhancement mode of operation, and for a spacing of 0.1 µm a current gain cut-off frequency f_T of about 50 GHz [166]. The structure was also evaluated for its power handling capability and compared by simulation with a delta-doped channel MESFET structure of similar geometry [167].

In general, the structure with charge injection across a lateral P^+/I-junction requires highly abrupt profiles with a low defect density at the interface and the adjacent intrinsic area. The contact areas need to be realized selectively, either by selective epitaxy into an etched pattern, by ion implantation or diffusion. This has been attempted by ion implantation, including a high-temperature anneal and removal of the damaged near surface area by a H-plasma process [168, 169]. For low gate leakage (of the overlapping gate metallization) the entire materials structure was overgrown with an undoped cap layer and then covered with an Al_2O_3 gate dielectric. The output characteristics indeed showed carrier injection characteristics at low bias and saturation at high bias. The device operated almost entirely in enhancement mode as predicted. For a gate length of 0.4 µm a maximum output current level of 3.7 mA/mm has been obtained (see Figure 14.23). A trap-filled limit (TFL [160]) region was not observed in the IV characteristics, indicating that the behaviour of the intrinsic channel area was notdefectlimited.

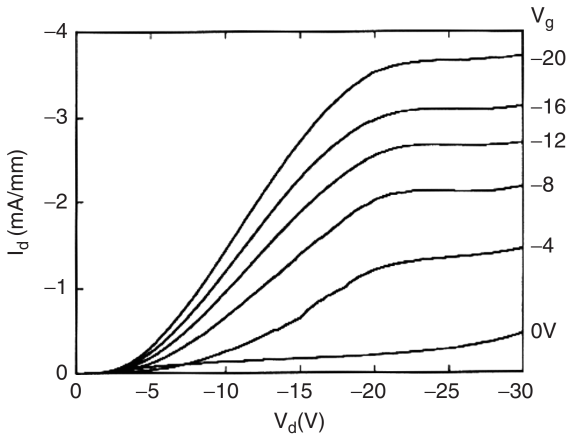

Figure 14.23 Output characteristics of experimental PIP-transistor with channel length of 0.4 μm at room temperature as described in the text (after [168]). Reprinted from Diamond and Related Materials,Fabrication of a submicron source-drain gap for p-i-p field effect transistors using epitaxial diamond layers by N. Kavakami, Y. Yokota, T. Taschibana, K. Hayashi, K. Inoue, K. Kobashi, Vol 13, 1939 Copyright (2004) Elsevier

Alternatively, the PIP-structure may be realized based on selective epitaxy, masking by Al_2O_3 and regrowth. This alternative technology is, however, highly complex and includes the overgrowth of already-processed surfaces. It has led to rather high output current levels, but also a high proportion of uncontrolled channel current [168]. Reducing the technological complexity, an alternative would be to use a recess structure as discussed in the case of the delta-doped channel approach with, however, a recess reaching through the entire delta profile into the substrate. This is illustrated in Figure 14.24.

In this case, the field distribution and related carrier injection from the P^+ contact areas into the intrinsic channel region are highly two-dimensional. The design of this region is therefore critical. This is illustrated in Figure 14.25, which shows the simulated current density of a PIP-transistor as function of etching depth beyond the doping profile into the i-layer, as schematically shown in Figure 14.24.

Over-etching quickly leads to an increase in the onset voltage for the injection and to a lower current in the space-charge regime. Thus, the etching depth is highly critical and

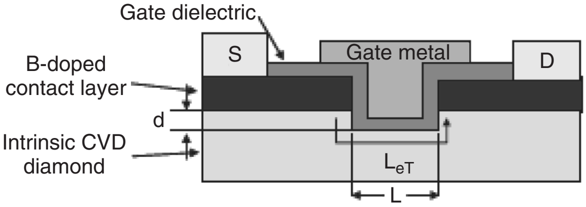

Figure 14.24 Planar PIP-FET structure based on i-channel layer recess etching as described in the text (after [156]). Reprinted from Philosophical Transactions of the Royal Society A, Unlocking diamond's potential as an electronic material by R. S. Balmer, I. Friel, S. M. Wollard, C.J.H.Wort, G.A. Scarsbrook, S.E.Coe, H. El-Hajj, A. Kaiser, A. Denisenko, E.Kohn and J. Isberg, Vol 1, 366 Copyright (2008) The Royal Society

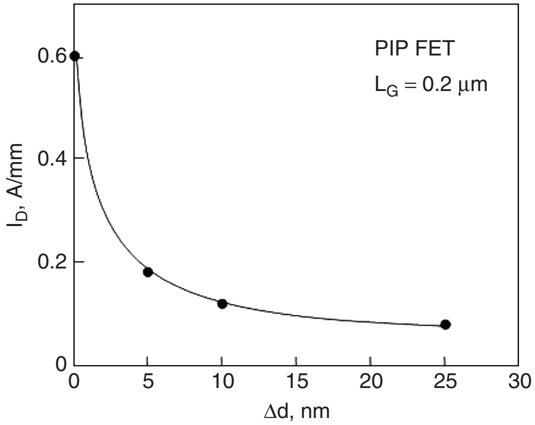

Figure 14.25 Maximum channel-current density of planar PIP-FET as function of over etching according to Figure 14.24 as evaluated by 2-D numerical simulation. The points are the calculated data

needs to be controlled to the nm level. On the other hand, this also means that the doping tail of the contact layer profile needs to be evenly controlled.

PIP structures have also been considered as capacitors and as tools for the study of high field transport properties. In the case of the capacitor configuration, this was a vertical epitaxial structure with a 1.6-μm thick, lightly boron doped, intrinsic layer sandwiched in between two heavily boron doped P^+ contact layers [170]. Analysis by impedance spectroscopy at various temperatures showed that the transport through the I-layer was by trap-assisted hopping. The second structure for high field analysis was a lateral structure where a 0.2-μm wide and 200-nm thick gap was cut into the P-contact layer by focused ion beam etching (FIB) [171]. This was followed by overgrowth of an I-layer. As such, the structure is that of an ungated PIP–FET. Fields up to 3 MV/cm could be applied, when the current started to rise sharply. This value is well in agreement with breakdown studies on thick high-purity layers [110] as well as on vertical Schottky diodes [108]. In both cases modulation of the channel current between the contact layers (by a gate) had not been attempted.

In addition to their use in high frequency power generation, the PIP-structure has been proposed as dosimeter for β-, γ- and neutron radiation [162].

14.4 DIODES

Most of the studied diode structures, except those used for the analysis of Schottky barrier characteristics, were realized in mesa configuration with vertical current flow. Figure 14.26 shows a micrograph of an array of vertical diode structures on a single crystal substrate patterned by mesa etching. Here, the diode surface is usually defined by the top metallization, serving as an etch mask and etched until contact is made with the highly boron doped back epitaxial contact layer.

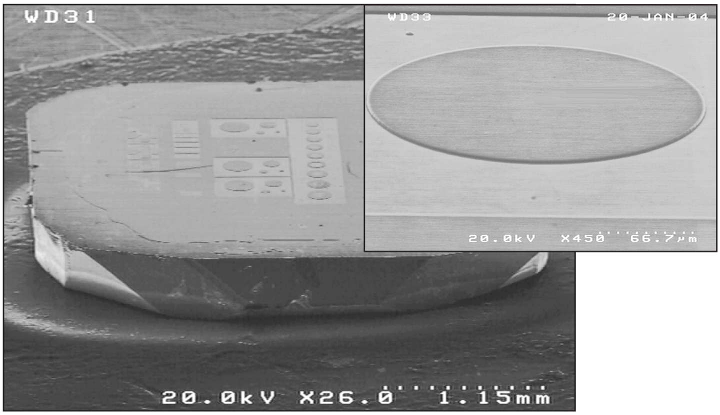

Figure 14.26 Micrograph of Schottky diode structures in mesa configuration on single crystal substrate. Reprinted from [168] with permission from Elsevier

14.4.1 High voltage vertical diodes

High voltage diodes certainly require an active layer material with high breakdown strength and a specific surface topography avoiding premature surface breakdown. In power rectifier applications, the goal is the combination of a high blocking voltage in reverse direction and a low loss in forward direction. These are two conflicting requirements and, therefore, different materials are usually evaluated by trade-off between on-resistance and blocking voltage.

A high reverse-blocking voltage implies a wide space-charge layer extension, which in turn means a low doped or intrinsic active layer in a vertical diode configuration. Here the advantage of diamond is quite obvious. With an ideal critical breakdown field F_{br} of 10 MV/cm, a 100-µm thick intrinsic layer would enable blocking of 100 kV. Even a conservative value for F_{br} of 2 MV/cm would enable blocking of 20 kV, a blocking voltage that has just been reached in SiC-based, high-voltage rectifier diodes [6]. For a space–charge layer extension of 100 µm, within the breakdown limit, the maximum doping concentration in the active region has to be below 3×10^{15} cm^{-3} or 5×10^{14} cm^{-3} respectively for the two breakdown limits mentioned above. However, as already extensively discussed, diamond does not posses a shallow dopant and thus the free carrier concentration may be essentially lower. This feature is addressed in Figure 14.27, which shows the dependence of the activation of boron acceptors on concentration and temperature. The graph shows that for room temperature operation of high voltage diodes with blocking voltages in the kV range, full carrier activation cannot be expected. On the other hand, at such low doping levels charge injection from a highly doped contact layer and the related space-charge limited current flow may dominate conduction through this layer (due to the high hole mobility) as already discussed in the case of the PIP-transistor structure.

A low forward loss implies a low threshold voltage and thus a low barrier potential in addition to the low series resistance as already discussed above. pn-junctions are not feasible for several reasons. Because of the lack of shallow donor doping, the n-layer will act as a severe series resistance or even as a dielectric for operation above the dielectric

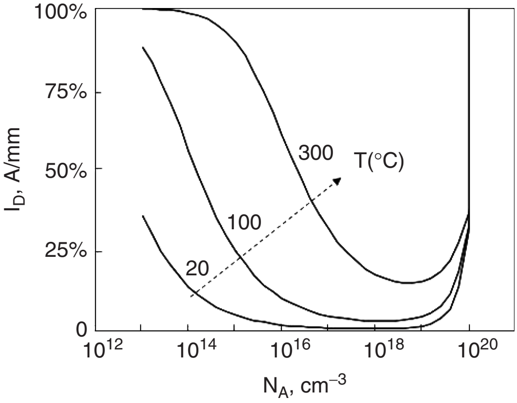

Figure 14.27 Thermal activation of boron acceptors in diamond as a function of concentration and temperature. The calculations are based on Fermi–Dirac statistics including the dependence of the activation energy of boron acceptors on concentration [69]

relaxation cut-off frequency. In addition, minority carrier storage will limit the switching speed and cause high switching current losses. Finally, because of the large band gap, the forward diode threshold voltage will be above −4 V for all configurations, resulting once more in high forward losses. For these reasons, most diamond diodes investigated for electronic switching applications have been designed as Schottky diodes with unipolar p-type carrier transport. Here, on the oxygen-terminated surface the barrier height and, thus, the diode forward threshold voltage will still be between 1.2 and 2.0 V.

The arguments discussed above have led to the frequently pursued concept of a diamond M/I/P (metal/intrinsic/p) diode. The discussion also leads to the conclusion that it is critical to evaluate diamond against other wide-band-gap materials such as SiC and GaN, and also to search for possible alternative structures. Such an evaluation has been performed in [158] and will be briefly summarized in what follows. Table 14.2 shows the set of parameters that have been used for the various materials.

The theoretical trade-off characteristics of diamond-based $M/P^-/P^+$ and $M/I/P^+$ diodes and the competitive structures on SiC and GaN are shown in Figure 14.28. Also shown is a power loss limit $I \times R^2$ of 1 kW/cm^2, reached at a forward bias of 5 V, which corresponds to a maximum current density of 200 A/cm^2, and which may be realistic assuming optimum thermal management [158]. The on-resistance is calculated for a forward bias of −5 V, assuming that it is dominated by the active layer resistance, and neglecting contact

Table 14.2 List of some material properties of diamond, GaN (wurtzite) and 6H-SiC used in the theoretical evaluation of power diode structures (after [158])

	Low-field mobility of free carriers in intrinsic (intentionally undoped) material at 300 K(cm^2/V s).	Saturated velocity v_{sat} at 300 K (cm/s)	Electrical breakdown field F_{br}(V/cm)
Diamond[115,165]	3800 (holes)	1.1×10^7	1×10^7
GaN(wurtzite)[165]	950 (electrons)	1.5×10^7	4.5×10^6
SiC (6-H)[165]	400 (electrons)	1.6×10^7	3×10^6

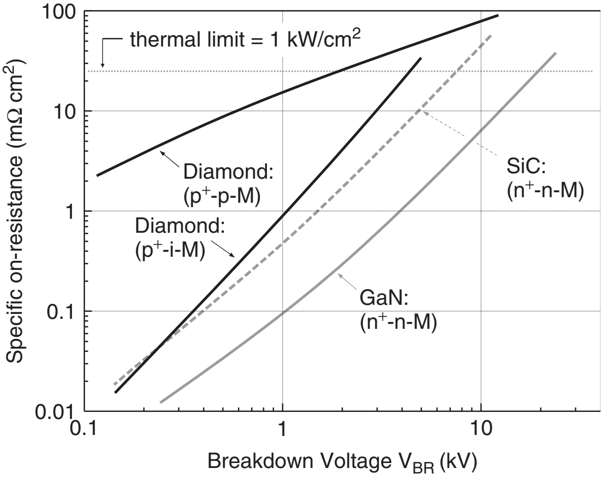

Figure 14.28 Trade-off between the on-resistance and the reverse breakdown voltage of a $P^+/P^-/M$ Schottky diode on diamond compared with equivalent structures on SiC and GaN (similar to [158]). Reprinted from Diamond and Related Materials, Diamond power devices. Concepts and Limits by A. Denisenko and E. Kohn, 14, 491, Copyright (2005) Elsevier

resistances. A forwards threshold voltage is not included in the calculation because this depends on the packaging technology and should ideally be negligible (see discussion below on merged diode structure). Each data point is calculated for the maximum doping concentration to reach breakdown with the lowest possible active layer resistance. Therefore the active layer resistance decreases with decreasing V_{br}. For the SiC and GaN diodes, Schottky contacts on n-type active layers with shallow doping are assumed; diamond diodes are calculated for boron doped active p-type layers. As can be easily seen, diamond $M/P^-/P^+$ diodes are not attractive due to the problem of boron acceptor activation, if operated at room temperature. To become competitive, the operating temperature needs to be raised to above 200 °C. However for P/I/M diodes, due to the high hole mobility for intrinsic diamond, high space-charge limited current densities can be expected at room temperature. However, since this current density decreases rapidly with increasing active layer thickness (see Equation 14.7) the main advantage is for small thicknesses and thus at low V_{br}.

Both competitors, SiC and GaN seem at least as attractive as diamond. However, for very high voltage diodes the materials quality may be decisive. Diamond layers have been realized with low background impurity concentration, basically owing to the fact that due to its small lattice constant and high lattice strength, most foreign impurities have a very low solubility and are not easily incorporated. For SiC, the hexagonal phase is almost exclusively used in electronic device structures. Within this phase coexist many modifications, each exhibiting different transport properties but in this discussion we will assume that there is a single 6H phase. One additional hurdle is that, as a compound material, it is difficult to realize uncompensated layers with low doping and with low defect density. GaN is also used in its hexagonal phase and usually contains a high defect density, but in this material these do not seem to dominate the electron transport properties. High quality GaN has been developed for optoelectronic applications but thick active layers of this material have not yet been combined with low on-resistance structures.

In the case of diamond, it seems that the breakdown voltage was mainly limited by boron doping in the active layer above approximately $N_A \geqslant 10^{17}$ cm^{-3}. At the time of these experiments, boron contamination in growth reactors was still a problem. Only in recent years have active layers of high purity been grown and the breakdown voltage of M–I–P$^+$ diodes be pushed into the kV-regime.

In recent years high purity diamond active layers with a residual acceptor doping concentration below 10^{15} cm^{-3} have been realized and incorporated into vertical diamond diode structures. This has lead to breakdown voltages of 2.5 KV [173] and 6.5 kV respectively [174]. In both cases the active layers have been grown using MPCVD and the structures carefully analyzed by physical/chemical and electrical methods. The 2.5-kV diode was realized on an active layer with a boron background below 10^{13} cm^{-3}. The hole mobility has been reported to be 4100 ± 400 cm^2/Vs, well in agreement with time of flight measurements on similar epitaxial material [115]. In the case of the 6.5-kV diode, the nitrogen donor compensation was 3×10^{13} cm^{-3}, the diode active layer boron doping between 10^{14} and 10^{16} cm^{-3}. Further analysis of breakdown conditions is difficult, since no detailed information on the structures has been provided. The blocking voltage of 6.7 kV is the highest of any semiconductor Schottky diode with comparable doping levels. The IV measurement of the diode with a breakdown voltage of 6.7 kV is shown in Figure 14.29. The characteristics have been measured in air (with breakdown by arcing) and oil, showing that breakdown may still be premature, since no edge termination has been used. However, edge termination of diamond diodes has already been considered theoretically [175].

As discussed in the preceding paragraphs, the concept of delta doping (or ideally planar doping) allows many problems arising from the inefficient activation of doping impurities, namely boron, to be circumvented. It has therefore also been proposed that this concept be incorporated into vertical, high-voltage, rectifier diode structures to raise the carrier density in the intrinsic active region as illustrated in Figure 14.30 [158].

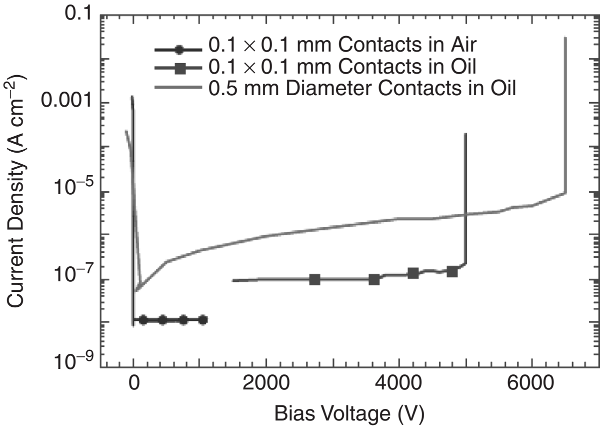

Figure 14.29 IV characteristics of diamond high voltage diode, after [173]. Shown are three measurements of contacts in air and oil. The breakdown of the contacts in air was caused by arcing. Reprinted from Semicond. Sci. Technol., Exceptionally high voltage Shottky diamond diodes and low boron doping by J. Butler, M. Geis, K. Krohn, J. Lawless, S. Deneault, T. Lyszczarz, D. Flechtner and R. Wright,18 S67, Copyright (2003) Institute of Physics

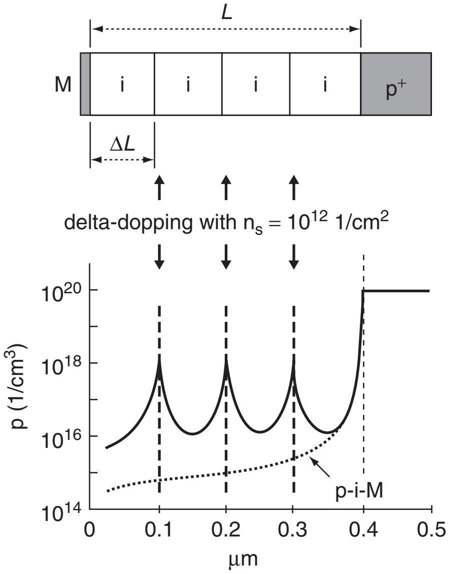

Figure 14.30 Schematic cross-section and carrier distribution by 2-D numerical simulation (Silvaco–Altas solver) across a stacked, delta-doped, diode with $L = 0.4\,\mu\text{m}$ and $\Delta L = 0.1\,\mu\text{m}$. For comparison, the calculated distribution of holes across a P–I–M diode with $L = 0.4\,\mu\text{m}$ is shown by the dotted curve [158]. Reprinted from Diamond and Related Materials, Diamond power devices. Concepts and Limits by A. Denisenko and E. Kohn, 14, 491, Copyright (2005) Elsevier

The issue addressed here is that of the low density of space charge carriers, after diffusion across a long distance (for a negligible low field). Shown is a M/I/P^+ diode, with an intrinsic layer into which planar doping sheets have been inserted at regular distances. The structure has been called a stacked delta-doped diode. It can be seen that, depending on the spacing of the planar doping sheets (with $N_s = 10^{12}$ cm^{-2}), the average carrier concentration can be raised to levels above 10^{16} cm^{-3}, whereas the diffusion tail would only result in a carrier concentrations below 10^{15} cm^{-3}, when reaching the metal contact. However, if the doping planes are spaced too closely, scattering on these planes would dominate over scattering within the intrinsic volume. The result of the scattering analysis indicates that the carrier mobility in the intrinsic material is preserved to 95 % if the separation of the doping planes is more than 80 nm, which is approximately the mean free path of carriers in high quality CVD diamond limited by phonon-assisted scattering (see also Figure 14.21). This is the reason for the spacing chosen in Figure 14.30. Of course the intrinsic layer shown is too thin for a high voltage diode and in practice the number of the doping planes and the total doping density has to be adjusted for each particular case of the breakdown characteristics.

This novel concept has been modelled against the conventional M/P^-/P^+ and M/I/P^+ structures in the same way as discussed in Figure 14.28. The trade-off characteristics of the three diode concepts are shown in Figure 14.31. As can be seen, the specific on-resistance of the stacked delta-doped diode can be lowered by more than one magnitude in comparison to the M/I/P^+ concept with the same breakdown voltage, due to redistribution of carriers in the intrinsic I-layer. This improvement makes this structure rather competitive with a SiC and GaN diode with a uniformly doped active layer [6]. The stacked,

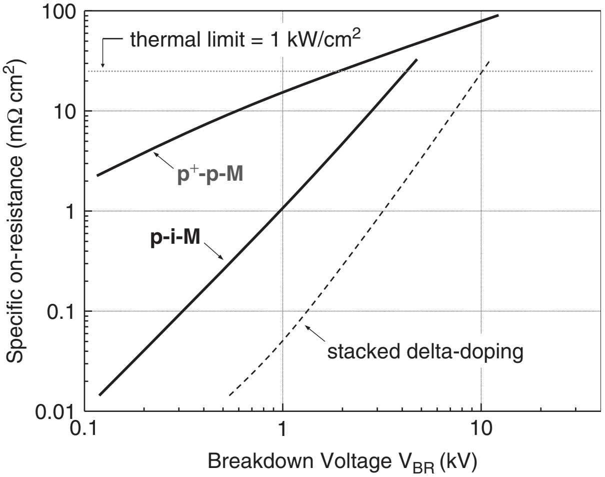

Figure 14.31 Specific on-resistance versus breakdown voltage for various diamond diode configurations as indicated. The performance of the stacked delta diode has been simulated assuming 30 planar doping sheets with a sheet charge density of 1×10^{12} cm^{-2} each and variable spacing above the critical value of 80 nm, where scattering on boron acceptors starts to dominate in the direction *perpendicular* to the doping planes. The total sheet charge density of 3×10^{13} cm^{-2} corresponded to the breakdown field of 10 MV/cm (similar to [158]). Reprinted from Diamond and Related Materials, Diamond power devices. Concepts and Limits by A. Denisenko and E. Kohn, 14, 491, Copyright (2005) Elsevier

delta-doped, diode on diamond may indeed be superior to a uniformly doped n-type SiC diode up to a breakdown voltage of 20 kV, neglecting thermal management problems. Within a voltage range below 3 kV, the projected characteristics are also comparable with or better than those of an ideal n-type GaN structure.

Besides the features addressed in this chapter, diamond diodes have shown exceptional temperature stability. The properties enabling this performance apply in part also to high voltage diodes. They are discussed in the next section.

14.4.2 High temperature diodes

Diamond is a meta-stable phase of carbon. Nevertheless it contains a high barrier for conversion to graphite and is therefore highly temperature stable. In a hydrogen atmosphere it has been shown to 'survive' 2200 °C [176]. However, it reacts with oxygen at high temperatures and etching is observed above about 600 °C, starting at defects. Therefore all high temperature measurements are usually performed in a vacuum. The properties of diamond Schottky diodes at elevated and high temperatures have been addressed since the early days of diamond device technology research. [36]. In the early 1990s, epitaxial Schottky diodes prepared by CVD were analyzed up to temperatures of approximately 580 °C. One of the motivations for this study was the poor performance encountered in a forward direction at ambient temperature due to the low boron activation [177]. In 1995, pn-diodes were operated at temperatures of up to about 900 °C [178].

A number of different diode configurations has been tested up to around 1000 °C for a short period of time without failure (reliability tests have not been published yet). These diodes have not yet been optimized for high breakdown voltages and moderately boron-doped active layers with a doping concentration in the range of 10^{17} cm^{-3} to 10^{18} cm^{-3} have been employed. The device structures were mesa type with Ti contact metallization and with no passivation or edge termination, as referenced below.

Even at this high temperature the intrinsic carrier concentration in diamond is of the same order as that of Si at room temperature. At room temperature, the specific resistivity of the intrinsic bulk material can be as high as TΩcm, and should still be close to GΩcm at 1000 °C. In fact high-temperature resistivity measurements have been proposed to assess the quality of diamond films [179]. For high purity material, rectifying characteristics would indeed be expected. However, for operation at such high temperature, two parameters become important: (i) defect activation in the active layer, and (ii) stability of contacts and contact interfaces. In fact all device structures tested at high temperatures suffer from a defect-activated increase in current levels, the actual level and activation energy depending on the specific case.

Since no shallow doping exists, it is important once more to consider carefully the activation of doping centres. This is best illustrated by Figure 14.32, which shows the temperature dependence of pn-junction characteristics realized by nitrogen and boron doping [178]. In this case, the nitrogen deep donor ($\Delta E_D = 1.7$ eV) and boron acceptor ($\Delta E_A = 0.37$ eV) levels result in a theoretical junction potential of 3.8 V [180].

As can be seen, the diode is highly insulating below about 600 °C, because neither nitrogen nor boron is fully activated. However, even for high temperature applications, rectifiers are usually expected to operate at temperatures below ambient temperature. As seen from the forward characteristics in the example shown in the figure, activation does not seem to be complete even at 900 °C, which is indeed to be expected since at this temperature nitrogen with a $\Delta E_D = 1.7$ eV, is not expected to be fully activated. Also seen in a forward direction is a threshold voltage between 1 and 2 V, which is less than the expected one (of 3.8 V [180]), indicating a high density of interface states. The strong leakage current observed in the reverse bias direction at high temperature reveals

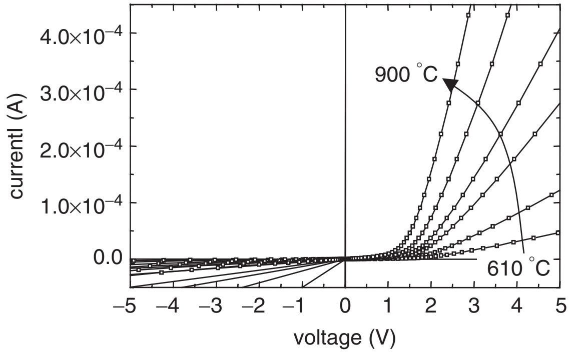

Figure 14.32 Characteristics of nitrogen/boron pn junction at various temperatures (after [178]). Reprinted from Applied Physics Letters, High-Temperature diamond pn-junction:B doped homoepitaxial layer on n-doped substrate by T. H. Borst, S. Strobel and O. Weis, 67. 2651, Copyright (1995) American Institute of Physics

the activation of defects. Using phosphorus ($\Delta E_D = 0.62$ eV) instead of nitrogen should improve the situation, but not to the point where high forward current densities could be expected at room temperature. Notwithstanding, phosphorous/boron junctions have been implemented into optoelectronic device structures for room temperature operation [181].

In contrast to buried pn-junctions with an interface of high crystalline quality, Schottky diodes rely on the integrity of the metal semiconductor interface, when driven to high temperatures. Therefore, refractory metal layers have been used, namely Pt [145], W [144] and W:Si [146] with an additional Si-based interfacial layer for chemical stabilization and defect passivation [182]. Nevertheless, a high activation of the reverse leakage current density with temperature has been observed, as shown in Figure 14.33 [146]. The diode failed during test at 1000 °C, and this was thought to be related to carbide formation at this temperature.

It has not been possible to fit the temperature behavior of the forward and reverse IV characteristics shown in Figure 14.33 and the CV results with one set of materials parameters. Therefore a heterogeneous case has been considered, consisting of a large-area Schottky contact (with a barrier height typical of O-terminated surfaces) on a semiconductor active layer (with a doping level consistent with the space-charge layer extension under reverse bias) in parallel with a small area defect diode dominating the reverse current behaviour. With this approach the forward current injection and the reverse leakage current behaviour could be associated with a defect density occupying only about 10^{-5}

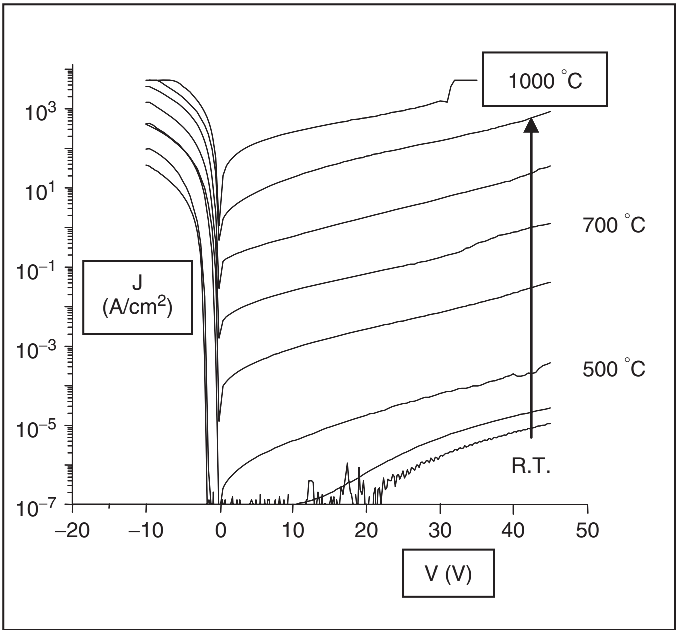

Figure 14.33 Semi-logarithmic plot of IV characteristics of a Schottky diode (with a W:Si based contact system) at various temperatures as indicated. The device was held for 30 min at each temperature and the temperature ramped as indicated. The diode failed during test at 1000 °C as can be seen from the top curve (after [146]). Reprinted from Electron Devices Letters, Very high temperature operation of diamond Schottky diode by A. Vescan, I. Daumiller, P. Gluche, W. Ebert and E. Kohn, 18, 556, Copyright (1997) IEEE

of the surface diode area [140], whereas the barrier height extracted from CV measurement coincided with the junction potential. In fact, a defect-induced current is thought to dominate the reverse current behavior of all diamond diodes fabricated up to now.

Further stabilization of the interface was attempted by an all-carbon interface. Such a structure was a diode where n-type UNCD (Ultra NanoCrystalline Diamond) was deposited onto the boron doped active layer. UNCD consists of diamond grains with a size of 3 to 10 nm imbedded in a graphitic grain boundary network with a grain boundary width of 0.2 to 0.4 nm. It is mostly grown by MPCVD in an Ar-plasma with a low methane and hydrogen content, under conditions generating a high renucleation rate [183, 184]. It can be n-type conductive through the grain boundaries when heavily nitrogen doped [185, 186]. The carrier concentration in the grain boundary paths is estimated at 10^{19} cm^{-3}. The conduction is room temperature activated with a low carrier mobility (10 cm^2/V s) as expected for a highly disordered system. Because of the high doping concentration, metal contacts display, in general, ohmic behaviour [187].

When interfaced with boron doped single crystal diamond, the material can be considered as a two-phase system, consisting of diamond grains and quantum size grain boundaries, and the interface will be heterogeneous [172]. The interface with the nano-grains will represent a pn-junction of the boron-doped substrate and the nitrogen-doped grains. These grains will be highly nitrogen doped but will not conduct at room temperature. The junction potential is expected to approximate to 3.8 eV. The graphitic grain boundaries act as Schottky barriers with a barrier potential of 0.7 eV, and both barriers act in parallel. Thus, the forward IV characteristics are determined by the parallel conduction of the two diodes. At low forward voltage the Schottky barrier dominates.

The all-carbon interface is indeed highly temperature stable.

Figure 14.34 shows an IV characteristic during operation at 1050 °C, the temperature being limited by the test set-up. Although at room temperature a current on/off ratio of 10^6 (for ± 10 V) was obtained, at maximum temperature this ratio is only about 10. Once more again, this low on/off ratio can be attributed to a defect-activated reverse current.

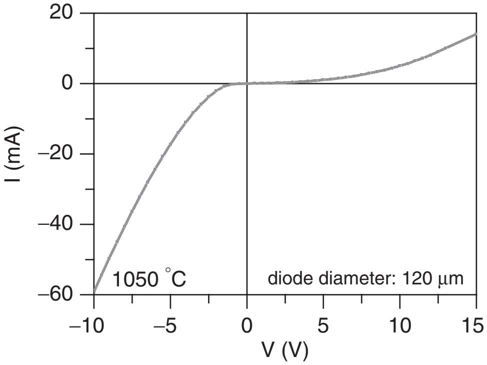

Figure 14.34 IV characteristics of UNCD/diamond pn-diode at 1050 °C in vacuum. Nitrogen content in the gas phase during growth was 15 %. The diode diameter was 30 μm (after [172]). Reprinted from Diamond and Related Materials, Ultra-nano crystalline/single crystal diamond heterostructure diode by T. Zimmermann, M. Kubovic, A. Denisenko, K. Janichowsky, O.A. Williams, D.M.Gruen, and E. Kohn 14, 416 Copyright, (2005) Elsevier

The diodes have been cycled repeatedly without failure or degradation, and represent therefore the diode structures with the highest thermal stability of all semiconductors.

To overcome the size limitation of single-crystal diamond substrates, the concept has also been realized on boron-doped nanocrystalline diamond (NCD) [188]. In this case the structure was grown by hot filament CVD on a 4-inch diameter Si-substrate using different growth regimes for the different layers. The grain size varied during subsequent deposition steps but was in all cases below 100 nm at the top of the grown layer. The p-type layer was boron doped, the n-type NCD material was grown with CH_4/H_2 chemistry and a high percentage of N_2 in the gas phase. The layer exhibited n-type conductivity, similar to UNCD. The electron concentration in the n-type layer was 3×10^{19} $cm^{-3,}$ and the electron mobility about 7 cm^2/Vs. Also in this case, two barrier potentials of 4.0 eV and 0.7 eV were identified. This suggested that the junction properties were similar those observed in the single crystal case. However, in this case the entire layer stack is highly disordered. This is reflected in a lower breakdown voltage, a lower current on/off ratio, and lower current densities in the forward direction, due to high series resistances. Defect-activated leakage is rather pronounced and rectifying behavior was only observed for temperatures below about 350 °C. These results suggest that such a highly disordered structure exhibits substantial parasitic effects and, therefore, in its present status, is not suitable for high performance electronic diode structures.

As discussed in the beginning, power rectifier diodes must combine two conflicting properties (high blocking voltage and low forward loss). It seems, therefore, reasonable to use a heterogeneous approach for an optimum compromise. The rational is to use a high barrier junction for low reverse leakage and high reverse breakdown voltage and low barrier for a low forward threshold voltage. To prevent the low barrier junction interfering with the reverse characteristics, its influence needs to be shielded in the reverse direction. This can be accomplished by lateral depletion of the low barrier junction, if it is confined to small (sub-μm) surface areas. Diodes combining these features have been labelled ‘merged diodes’ [189] and ‘junction barrier Schottky diodes’ [190] and are mainly found in SiC.

In diamond this concept can be realized by pn-junctions representing the high barrier junction with small, embedded, Schottky contacts representing the low barrier junction. Nevertheless the low barrier potential is still high in comparison to what can be obtained in SiC (where a dual metal approach and the embedding of nanoparticles has also been discussed [191, 192]). Since the Schottky contact areas have to be pinched-off laterally at reverse bias, their area has been realized as sub-μm spots (depending on doping concentration) which have been patterned in this proof-of-concept experiment by e-beam lithography [123]. As a consequence, the forward current flow is confined to these small areas only and current crowding in front of these spots may generate a relatively high series resistance. Thus an optimum design needs to take this aspect into account so as not to degrade the on-resistance of the diode. The investigated structure is shown in Figure 14.35.

The material structure contains a boron doped active layer covered with a thin nitrogen doped cap. The thickness of the nitrogen-doped layer was 10 nm so as still to allow high current flow at high forward bias. Into this layer stack small holes were etched to contact the active boron doped layer directly by the top metallization. The diameter of these Schottky contact spots was 0.6 μm.

Figure 14.36 shows the IV characteristics of the pn-diode without Schottky bypass and the merged diode. From the IV characteristics it can be seen that the thin nitrogen-doped

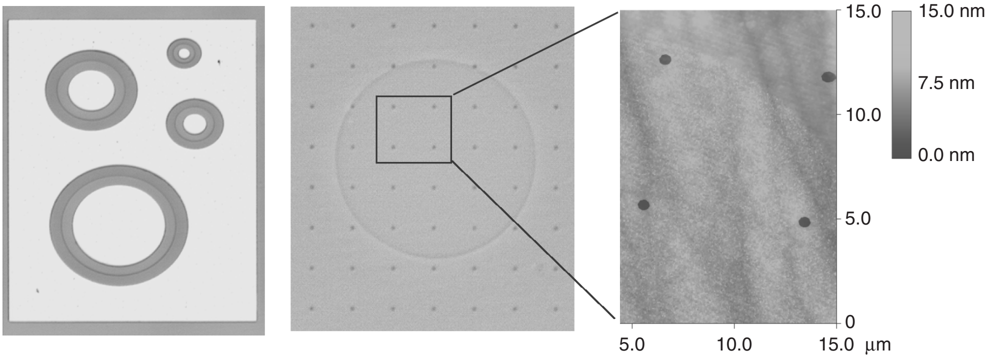

Figure 14.35 Topography of merged diode structure and details on embedded Schottky dot realization. After [123]. Reprinted from Diamond and Related Materials, Diamond merged diode by M. Kubovic, H. El-Hajj and E. Kohn, 16, 1033 Copyright (2007) Elsevier. See plate 6

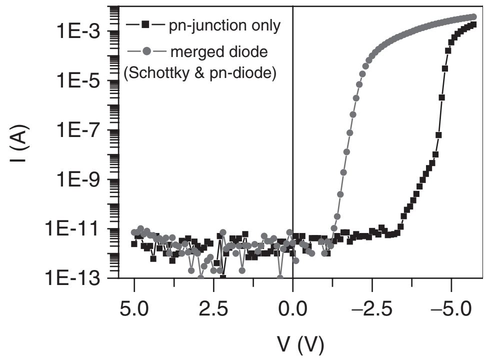

Figure 14.36 IV characteristics of the pn-diode without Schottky bypass and the merged diode (after [123]). Reprinted from Diamond and Related Materials, Diamond merged diode by M. Kubovic, H. El-Hajj and E. Kohn,16, 1033 Copyright (2007) Elsevier

cap layer of the pn-diode still conducts beyond the threshold voltage. Rectification is 10^9 (at ±5 V). However five orders of magnitude below the forward current level a shoulder appears, thought to be related to residual defects, causing an effectively lower barrier potential. Also shown is the merged diode configuration as pictured in Figure 14.35. As can be seen, the reverse diode characteristics remain unchanged. However, in forward direction the Schottky barrier potential dominates now.

The comparison of the two curves illustrates also that only a small part of the entire diode surface needs to be covered by the low barrier contact spots in order to dominate the (exponential) forward characteristics. This means, on the other hand, that a small density of defects will result in an essentially smaller barrier potential value as extracted from IV measurements than those extracted from CV measurements. If these defects also degrade the reverse characteristics, they cannot be entirely shielded by the surrounding material under reverse bias conditions. This may indicate, therefore, that these defects penetrate into the material (or through the entire active layer) and are not only confined to the surface.

An even further improved barrier could be realized by a heterostructure with other wide band gap cap materials such as AlN or cBN. Initial work on such heterostructures has been reported but has not yet progressed beyond proof-of-concept experiments [103, 104], the main problem being the materials quality of heteroepitaxial layers on diamond, which in general show a highly disordered interface.

The discussion of the various diode configurations shows that diamond faces serious competition, mostly from SiC- and GaN-based structures in the area of high voltage/high power diodes with kV blocking voltages. At high temperatures, however, diamond has shown exceptional stability, which may enable a new generation of ultra high temperature stable diodes. However, for these devices to be successful, passivation and packaging will be certainly be the next challenge [193, 194]. These features may also enable sensing in a harsh environment like high-energy particle detection. Indeed diamond is considered to be a next generation material for such applications [195–197] and associated chapters in this book.

14.5 ELECTRODES AND ION SENSITIVE FETS

Electrochemistry has become an established application for diamond in two fields, namely highly conductive electrodes for electrochemical sensors (see Chapter 17 by Foord in this book), and harsh environment applications, like waste water purification. The electrodes used in electroanalysis are mostly microcrystalline structured microelectrodes [198–200] or boron-doped epitaxial layers on single crystal diamond substrates [201]. The electrodes for wastewater treatment are mostly large area, free standing, polycrystalline sheets operating at high over-potentials [202–204].

The second field is biochemical sensing using functionalized diamond surfaces. In this case the starting material is mostly H-terminated diamond functionalized by photochemistry [205]. Active sensors with H-terminated surfaces often make use of the H-induced surface conductivity and operate in the mode of chemical-sensitive FETs [206].

The substrates and sensor devices based on H-terminated surfaces are discussed in Chapter 16 by Garrido in this book. The subjects in this section are electrodes and ion-sensitive FETs (ISFETs) based on boron-doped active layers. The level of doping in the structures discussed here is in the range between 10^{20} cm^{-3} to approximately 10^{21} cm^{-3}. The lower limit of 10^{20} cm^{-3} is given by the full activation of boron acceptors in diamond enabling high sensitivity of the ISFET, as discussed in Section 14.2 and electrodes with high electron transfer rates. The carrier transport at this doping level will occur within an impurity band (except in the delta-doped channel case). Such material is defined as a semiconductor with metal-like conductivity. However, with electrochemical behavior semiconducting rather than quasi-metallic properties are still dominant. For example, in electron-transfer reactions a semiconductor with quasi-metallic conductivity can still be described in terms of its depletion layer and surface barrier properties, and by its electronic surface states in the band gap [207]. Thus, ‘metal-like’ behavior is used with two distinctly different meanings, depending on whether bulk conduction or surface properties are meant. Doping of diamond with boron above 10^{21} cm^{-3} leads to high stress and the formation of an extended defect network and boron clusters. Such material may be considered metal-like in its electrochemical behavior, with the kinetics of electron transfer reactions being very close to that of pure metals. It will however, not display the extraordinary electrochemical stability of the pure diamond phase.

14.5.1 Electrodes

Boron-doped diamond (BDD) is the only semiconductor material used for electrochemical electrodes due to its high chemical inertness, wide potential window of water stability, and low background current [201, 208]. A typical voltammogram of a BDD electrode on single crystal substrate is shown in Figure 14.37, which also shows the window observed for technical Pt. The redox potential window of water dissociation for a Pt electrode is 1.23 eV. However in the case of diamond, water dissociation is suppressed for about 3 V. Nevertheless chemical activity is observed for many redox couples within the window. This allows, for example, detection of toxic molecules like phenols or biomolecules like dopamine at high anodic over-potentials. These molecules cannot be oxidized in water, before water itself has dissociated [202].

A critical issue with semiconductor-based electrodes is their chemical surface stability. The nature and arrangement of the surface bonds determines the chemical sensing characteristics as well as the electronic surface state distribution, where the surface states are the sites of electron transfer. In the case of diamond, two surface terminations have been commonly used up to now: hydrogen and oxygen termination. Both H-termination and O-termination have been used for electrochemical electrodes as well as for ion-sensitive field-effect transistors (ISFETs) [209, 210]. However, the H-terminated surface is only conditionally stable. At high anodic overpotentials, the H-terminated surface can be converted to an O-terminated one [211]. The O-terminated surface is highly stable and no further oxidation or etching is observed, even when operating in highly oxidizing media and under anodic polarization [212]. Oxygen can be attached to the surface in several ways, creating several types of carbon−oxygen functional groups like C–O–C bridges, C=O ketone and C–OH hydroxyl groups [213]. The carbon/oxygen ratio and the type of prevailing oxygen group can be influenced by applying wet chemical or anodic, plasma or thermal oxidation methods. More complicated polycarbonate groups (–CO–O–CO–) could be observed after ultrasonic treatment in oxidizing electrolytes [214]. Each type

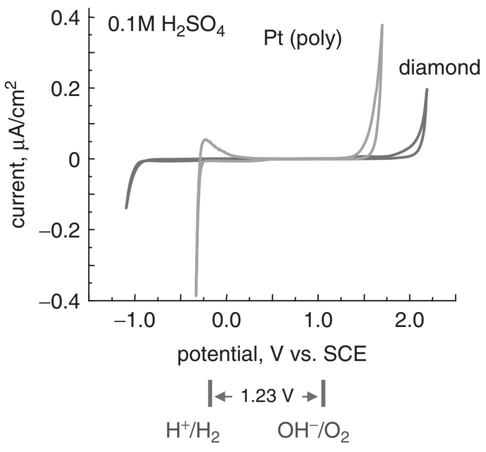

Figure 14.37 Cyclic voltammogram of boron-doped single crystalline diamond electrode in 0.1-M H_2SO_4 electrolyte. A voltammogram of technical platinum is shown for comparison. Also shown are the standard potenials of water dissociation

of surface bond exhibits its own energetic and kinetic parameters of redox reactions [211, 215], the reaction path being electron transfer across surface states [198, 207]. The activity of carbon–oxygen surface bonds is also responsible for the pH sensitivity of O-terminated diamond in electrolytes [216], the sensitivity being very close to the theoretical Nernst's limit of 59 mV/pH in a wide range of pH.

A schematic cross-section of the diamond–electrolyte junction is shown in Figure 14.38. Also shown is a basic, small signal, electrical equivalent circuit valid for simple electrolytes with no redox pair added. Such an equivalent circuit can be derived by electrochemical impedance spectroscopy analysis. C_{sc} represents the space–charge layer capacitance in the semiconductor with the associated loss R_{sc}. C_{dl} is the capacitance of the double layer in the electrolyte again with its associated loss R_{dl}. In case of high quality diamond with no chemically active defect sites, both R_{dl} and R_{sc} could be in the range of MΩcm^2 or above [201]. Thus, within the potential window of water electrolysis, the diamond-electrolyte interface will be similar to that of a MOS structure. In such a case, the distribution of the potential across the interface will be determined by the ratio of the depletion layer and double layer capacitances. For O-terminated single crystal diamond, the value of C_{dl} is about 10 µF/cm^2 [207]. For a wide range of doping concentrations up to 10^{21} cm^{-3}, the relationship $C_{dl} \gg C_{sc}$ holds. This enables doping profiling in diamond using capacitance–voltage (CV) measurements. However for correct analysis, the value of C_{dl} in series and the corresponding voltage drop across the Helmholtz layer on the semiconductor surface have to be taken into account. In a first approximation, the value of C_{dl} can be taken as bias independent. In such a case the CV analysis will be similar to the case of a MOS diode.

CV measurements corrected in this way have been used to derive the carrier profile in boron delta-doped layers as shown in Section 14.2.1. Although only approximate, these measurements remain the only nondestructive method for analysing thin and highly doped near-surface layers. The range of applied bias available for profiling is limited to about 3 V. At the onset of hydrolysis the conductances will dominate the equivalent circuit.

Figure 14.39 is a schematic energy-band diagram of the diamond–electrolyte junction using the electrochemical potential scale, adapted from Ref. [217]. It corresponds to the

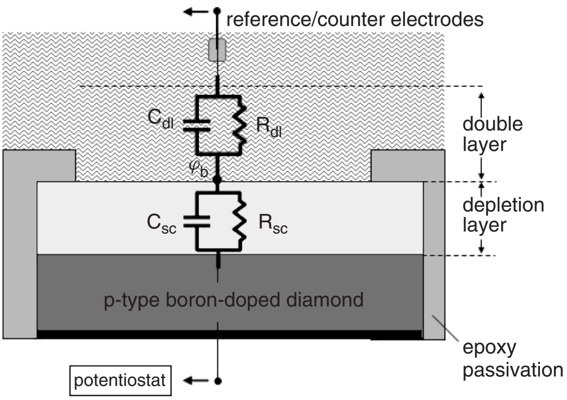

Figure 14.38 Schematic cross-section of the diamond–electrolyte junction in simple electrolytes and the corresponding equivalent circuit. The symbol φ_b denotes the surface potential at equilibrium, referring to Figure 14.39

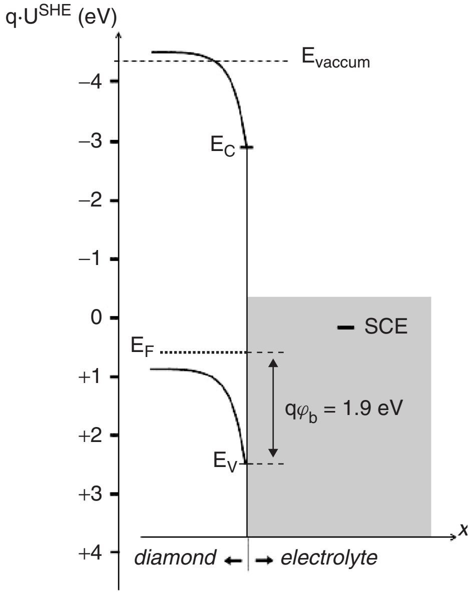

Figure 14.39 Schematic energy band diagram of diamond–electrolyte junction versus the electrochemical potential scale, adapted from Ref. [217]. The diagram is drawn for oxygen-terminated diamond by a wet chemical treatment as described in the text in equilibrium with pH 1 electrolyte. Reprinted from J. Appl. Phys., The electronic surface barrier of boron-doped diamond by anodic oxidation by A. Denisenko, C. Pientzka, A. Romanyuk, H. El-Hajj, E. Kohn, 103, 014904 Copyright (2008) American Institute of Physics

case of wet chemical oxidation of diamond in hot H_2O_2:H_2O:H_2SO_4 (1:2:2). This treatment induces a nearly 100 % coverage of the surface by hydroxyl (C–OH) and ether (C–O–C) bond structures, as revealed by X-ray photoemission spectroscopy. The electronic surface barrier of the oxidized surface in contact with the electrolyte was 1.9 eV, which correlates well with the case of a free surface and a Schottky junction [128]. The value of the electronic barrier in equilibrium remained constant in all electrolytes investigated. These results show that the oxidation of diamond induces electronic surface state pinning of the surface Fermi level, providing the pH sensitivity of the surface potential at the same time. The density of electronic states has been estimated at about 10^{13} cm^{-3} [128, 217]. Nevertheless, a surface potential of about 3.6 eV could be identified for oxidation in alkaline electrolytes [217].

Deviations from the behavior of the ideal (non-reactive) surface might be caused by surface defects. These defects, which may generate surface states within the band gap, are mostly secondary nucleation sites and dislocations on single crystal surfaces, and grain boundary defects and graphitic clusters on polycrystalline substrates. These defects may cause additional electrochemical activity within the potential window or reduce the potential window of water hydrolysis. These may also be responsible for a higher background current and cause instabilities and drift in sensitivity during long-term operation. The surface defects may be chemically less stable than the diamond substrate itself and may even be etched under certain conditions.

On the other hand, however, controlled patterning into microelectrodes has been used for increased sensitivity and complexity. Hence this chapter will address electrode systems (mostly designed for electroanalysis), which are realized in microtechnology on thin, highly doped layers. A conventional example of such a system is the microelectrode array based on metals (MEAs). An example of such an MEA in microstructured diamond is shown in Figure 14.40 [218]. Here the base was nanocrystalline diamond. The individual electrodes were realized on a boron-doped layer grown on an insulating diamond substrate and are isolated from each other by an added dielectric passivation layer. For electrode dimensions in the lower micrometer or sub-μm range, smooth surfaces and thin layers are needed, pointing towards the use of single crystal (or quasi-single crystal) substrates and boron pulse-doped or delta-doped layers, once large area surfaces become available. Similar arrays have been fabricated by the growth of stacks of highly doped active layers and undoped intrinsic layers only, as discussed elsewhere [219].

Thus, the manufacture of highly complex electrode arrays can be based on a technology rather similar to that of FETs and the technology may therefore be eventually extended into ChemFET arrays. However, all these arrays are realized on large area micro- or nanocrystalline material (with their respective defect densities), and adding FET structures means the transfer of the delta-doped channel technology into the nanocrystalline diamond regime. This subject is therefore also addressed below.

Even higher sensitivities can be generated by drawing advantage from the increased activity of specifically embedded nanospots. Such nanostructured electrodes have been applied to electrochemical analysis [220], to fuel cells [221] and to biosensors [222]. To realize such a nanopatterned electrode several parts need to be optimized. This consists firstly in the introduction of the nanospots themselves, usually in the form of nanoclusters. Basically, techniques similar to those used for the seeding of carbon nanotubes can be used [223]. Secondly, the surrounding areas should exhibit a low activity or be entirely

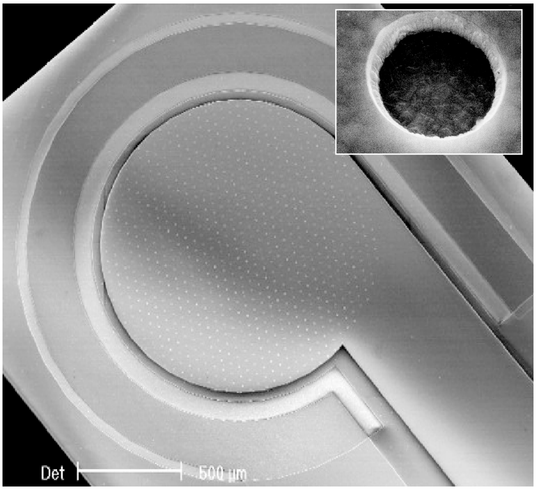

Figure 14.40 Microelectrode array on boron-doped microcrystalline diamond using an insulating diamond-like carbon layer for passivation of the individual electrode disks of 5 μm in diameter (see inset) (after [218]). Reprinted from Thin-Film Diamond II, Chapter 5, Industrial applications of diamond by W. Haenni, Ph. Rychen, M. Fryda, and C. Comninellis, Copyright (2004) Elsevier

inert so that their parasitic activity will not mask the signal of the nanospots. Nevertheless in the planar configuration all nanospots need to be electrically interconnected via a thin boron doped active layer.

Staying within the carbon materials system, active sites can also be generated by artificial defects that may contain local clusters of graphite or amorphous carbon. Such defects were introduced by damaging small areas by electrical discharge from a metal nanotip close to the surface in the electrolyte [224]. The size of such individually generated spots was estimated to be below 70 nm. The entire array of 50 nanospots covered about 1 % of the active electrode surface area of 10 × 10 μm, the surroundings of this field being passivated by Al_2O_3. Despite the small coverage, additional activity was clearly identified in the voltammogram and could be further refined by small signal characterization [224]. The admittance signal is shown in Figure 14.41 and compared to the signal before nanospot generation (of a similar sample). The induced carbon nanospots can then serve as discrete docking areas for biomolecules or metal clusters.

The background current of the diamond electrode substrate (surrounding the nanospots) can be reduced further by adding a thin, nominally undoped, cap layer on top of the boron-doped active layer. The reduction in background current is especially important for nanocrystalline diamond material, where the electrode background current is mostly related to activity of the grain boundaries (which may be boron cluster decorated in addition). In a first experiment [225], an 80-nm thick cap layer was overgrown onto a 2×10^{20} cm^{-3} boron doped layer of 100-nm thickness, on a nanocrystalline substrate with 60 nm average grain size. The related electrode characteristics (without nanospots)

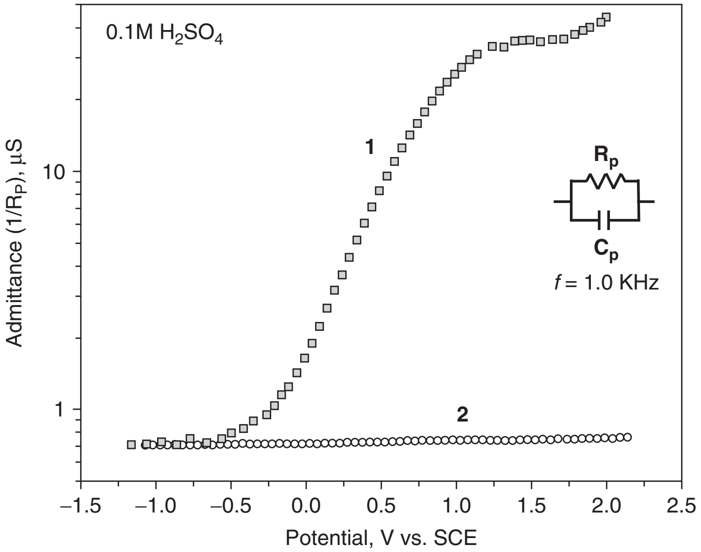

Figure 14.41 Admittance plots of a single crystal diamond electrode with 50 nanospots generated by electrical discharge (after [224]). Measurement was carried out in 0.1-M H_2SO_4 electrolyte at 1-kHz frequency. Curve 1 represents the processed surface with nanospots; curve 2 similar electrode areas without the nanospots. The equivalent circuit is shown in the inset. Reprinted from Diamond and Related Materials, Nanoscale surface modification of diamond for enhanced electrochemical sensing by F. Hernandez, A. Denisenko and E. Kohn,16, 867, Copyright (2007) Elsevier

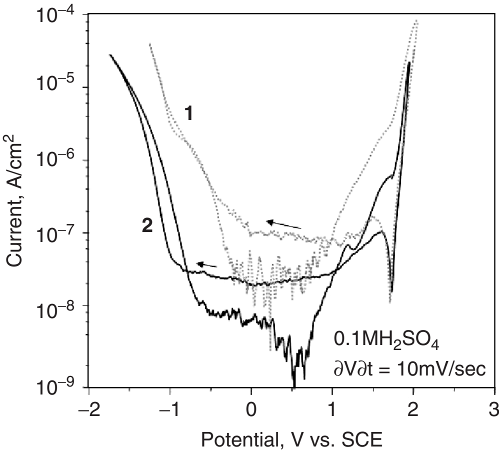

Figure 14.42 Cyclic voltammetry of nanocrystalline diamond electrodes grown by hot-filament CVD (after [225]). Curve (1): P^+ layer with boron acceptor concentration of 2×10^{20} cm^{-3}; curve (2) the same diamond film with an additional top cap layer of nominally undoped diamond with a thickness of about 80 nm and a residual boron concentration below 10^{16} cm^{-3}

are illustrated in Figure 14.42. Shown are the voltammograms on a semilogarithmic scale of an electrode with and without a cap layer. It can be seen that the presence of the nominally undoped cap layer reduced the background current by about one order of magnitude. At the same time, the onset of oxygen evolution reaction was not shifted. This means that the overgrowth of the cap layer did not induce an additional electronic barrier as parasitic potential drop at the interface, which might have blocked the carrier transport across the interface. A detailed analysis shows that despite the reduced background current level, a number of grain-boundary defects still remained active, which could then be electroplated by Au.

These experiments show that boron doped diamond electrodes can still be substantially improved and optimized by introducing specific doping profiles, surface patterning and surface modifications. The advantages of modifications in the nano-scale are quite obvious for single crystalline substrates; however, first experiments show that they are also very helpful for improving and tailoring the electrochemical performance of nanocrystalline substrates. The basis are boron-doped epitaxial layers with full room temperature activation.

14.5.2 ISFETs

As illustrated above, it seems straightforward to extend the diamond electrode technology into the technology of planar ISFETs with boron-doped channels. Many prerequisites can be transferred. However, the design of the channel doping profile of the ISFET device is more critical.

The characteristics of the ISFET gate electrode will be identical to the semiconductor/electrolyte interface explained above (see Figures 14.38 and 14.39). The channel is modulated by a field effect dominated by the space–charge layer capacitance C_{cs} of the oxygen terminated surface. The Helmholz double layer capacitance C_{dl} is often negligible or can be taken into account by a bias independent series capacitance (see Figure 14.38). On the other hand, the electron transfer in simple electrolytes is suppressed for a potential window of about 3 volts, limited by water electrolysis as also already discussed in detail in Section 14.5.1. Thus, gate leakage of the ISFET will be also suppressed within this range. To operate the ISFET efficiently, this bias range should roughly coincide with the gate voltage range between open channel condition and pinch-off.

On the other hand, at specific redox reactions, electron transfer will occur and gate current will flow. In this case the FET structure can be operated as a classical electrode (by shortening source and drain). In addition, if the transfer current is small compared with the channel current, this will represent a tolerable gate leakage and the analysis can be potentiometric and amperometric simultaneously with the same device.

The second requirement for the ISFET channel is the doping limit of full activation of boron acceptors in diamond, meaning a peak doping concentration in the ISFET channel above 10^{20} cm^{-3}. In conjunction with a maximum range of gate potential of about 3 volts, this will mean a sheet charge density of less than 1×10^{13} cm^{-2} and a width of the delta profile of less than 1 nm. This leads again to the concept of boron delta doping. A schematic cross-section of an ion-sensitive FET structure on diamond with boron-delta-doped channel is shown in Figure 14.43, after [210]. Also shown here is the equivalent circuit of an ideal gate–electrolyte interface operating in the potential window of water electrolytes. In such a case the resistive losses R_{sc} and R_{dl} across the interface (see Figure 14.38) can be ignored.

In this gate bias window of operation, the delta-doped ISFET on oxygen-terminated diamond will represent a MOSFET-like structure, where the potential of the surface ϕ_{S} in Figure 14.43 depends on pH. The pH sensitivity of the surface potential will be provided by carbon–oxygen functional groups on the surface of the FET electrode [216].

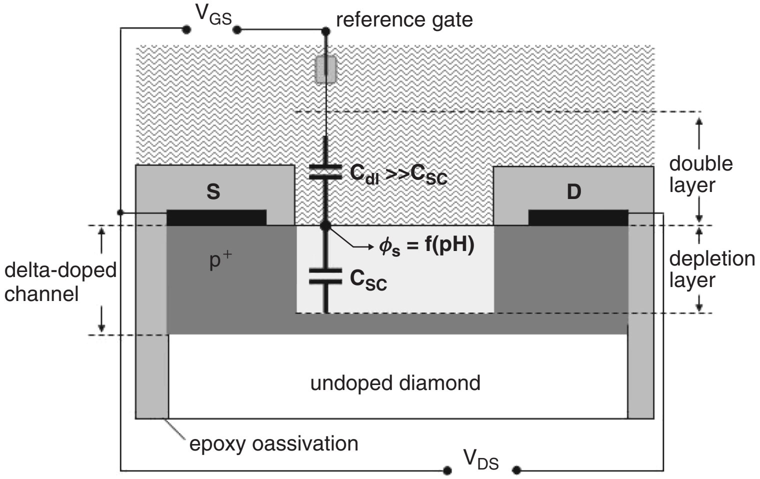

Figure 14.43 Schematic cross section of ion-sensitive FET structure on oxygen terminated diamond with boron delta-doped channel and the gate–electrolyte interface with ideal (MOS-like) characteristics. Reprinted from Diamond and Related Materials, pH sensor on O-terminated diamond using boron-doped channel by A. Denisenko, G. Jamornman, H. El-Hajj and E. Kohn, 16, 905, Copyright (2007) Elsevier

Due to the inertness and corrosion resistance of the diamond surface, the channel of the delta-doped ISFET can be in direct contact with electrolyte solutions and no barrier layers are needed, like in the case of Si-ISFETs [226]. This is a new degree of freedom for chemFET structures as compared with conventional Si-MOS-ISFETs up to now. Here, neither the gate oxide nor the metal-oxide electrode will allow gate current to flow. In addition, the diamond gate electrode can be operated in harsh environments, where metal-oxide electrodes, which are usually used as Si-ISFET electrodes, will fail. Thus, diamond can offer an essential advantage in electrochemical sensing in harsh environments beyond what has been demonstrated up to now with metal-oxide electrodes.

For first experiments, ISFET devices based on the oxygen-terminated surface and delta-doped channels, have been designed and fabricated on (100)-oriented, single-crystal substrates as well as on nanocrystalline substrates, and tested in 0.1M H_2SO_4 and 0.1M KOH solutions. The single crystal substrate served as a proof-of-concept experiment to identify the mode of operation on a surface of low defect density. The nanocrystalline substrate was chosen to evaluate whether or not it would be possible to include such an ISFET technology in today's large-area diamond-electrode arrays. Both experiments have been successful [210, 227] and will be discussed briefly below.

In both cases, the epitaxial growth was, in essence, identical to that described in Section 14.2, and contained a delta-doped channel grown by MPCVD directly onto the surface (but thicker in the nanocrystalline diamond case). The individual ISFET structures were defined by mesa etching. The source and drain ohmic contact metallization to the delta-doped channel was Ti/Au. The open gate electrode areas were embedded into a polyamide passivation layer patterned by lithography. The chip was protected and packaged using Teflon®-based adhesive tape. The passivated ISFET structure on single-crystal diamond and packaged ISFET device on nano-crystalline substrate respectively are shown in Figures 14.44 and 14.45.

The lowest pinch-off voltage had been obtained with the structure realized on a nanocrystalline substrate. Biased by a Pt electrode, operation in 0.1M H_2SO_4 in the linear region of the FET output characteristics is shown in Figure 14.46. The fabricated doping profile was characterized by the peak concentration of 3×10^{20} cm^{-3} and a full width at half maximum of about 1 nm, as revealed by CV-profiling in electrolyte [227]. The

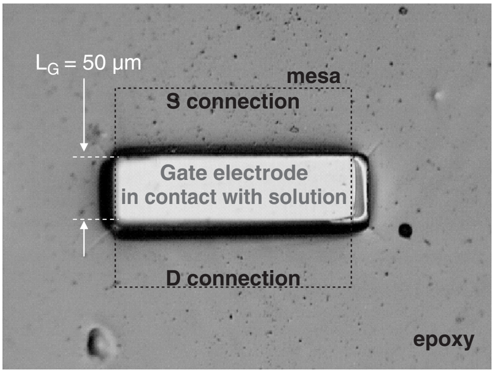

Figure 14.44 Micrograph of ISFET microstructure on (100) single-crystal diamond substrate. The delta channel is in direct contact with the solution in the gate electrode opening (after [210])

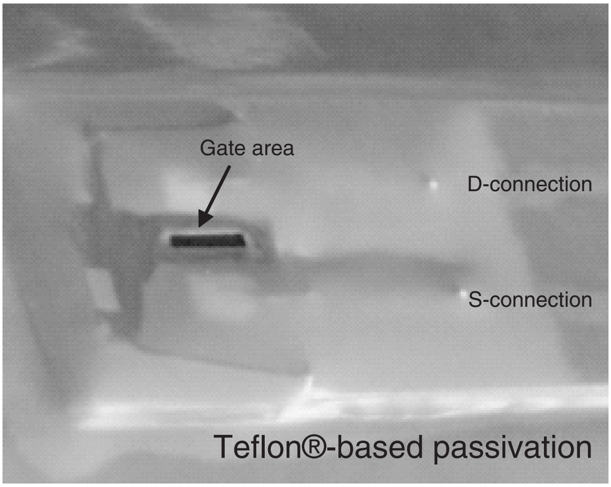

Figure 14.45 Micrograph of experimentally packaged delta-doped channel ISFET structure on nanocrystalline CVD diamond (after [227]). Reprinted from Diamond and Related Materials, O-terminated nano-diamond ISFET for application in harsh environment by M. Dipalo, C. Pietzka, A. Denisenko, H. El-Hajj and E. Kohn, Vol 17, 1241 Copyright (2008) Elsevier

surface of the ISFET channel was oxygen-terminated by wet chemical oxidation in hot H_2O_2:H_2O:H_2SO_4 (1:2:2). The window of gate bias operation was approximately 2 V, and was limited by the open channel conductance in the forward direction and gate leakage in the reverse direction. The gate length was 200 μm and the gate width 2.5 mm.

Within this range the channel current could be modulated by about 50 %. The built-in voltage of the gate electrode junction was determined by the high surface state density pinning the surface potential. It can be obtained by analyzing the characteristics of the diamond–electrolyte junction using capacitance–voltage, electrochemical impedance, spectroscopy and open-circuit potential measurements. In this case of wet oxidation, the barrier of the oxidized surface was about 1.9 eV, which in fact correlates well with the barrier potential of Schottky junctions [128]. The interpolated pH sensitivity was about 50 mV/pH between pH 1 and pH 13.

Oxygen-terminated electrodes show high electrochemical stability, with only slight changes in morphology and potential window even after extensive operation at high anodic overpotential in the amperometric regime. Therefore, the test was repeated several times as shown in Figure 14.47. An initial cycling experiment is shown, a second measurement after a 3-month exposure to atmosphere was followed by eight more cycles.

In the experiment a slight decrease in the current level was still observed, although the pH sensitivity was constant to about 15 %. It has been speculated that the slow degradation may be related to the polyimide and Teflon passivation and encapsulation. To prevent such interference it may be necessary to overgrow the parasitic areas entirely by undoped diamond.

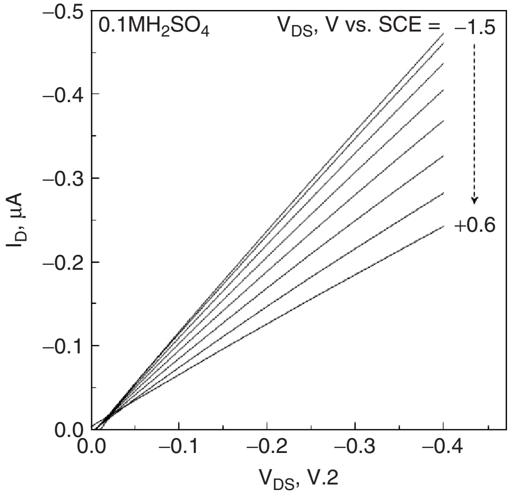

Figure 14.46 Output characteristics for low drain bias (linear region) of delta-channel ISFET on nanocrystalline diamond with a gate length of 200 μm and gate width of 2.5 mm in 0.1-M H_2SO_4 solution and biased by a Pt gate electrode with reference to a SCE electrode (after [227]). Reprinted from Diamond and Related Materials, O-terminated nano-diamond ISFET for application in harsh environment by M. Dipalo, C. Pietzka, A. Denisenko, H. El-Hajj and E. Kohn, Vol 17, 1241 Copyright (2008) Elsevier

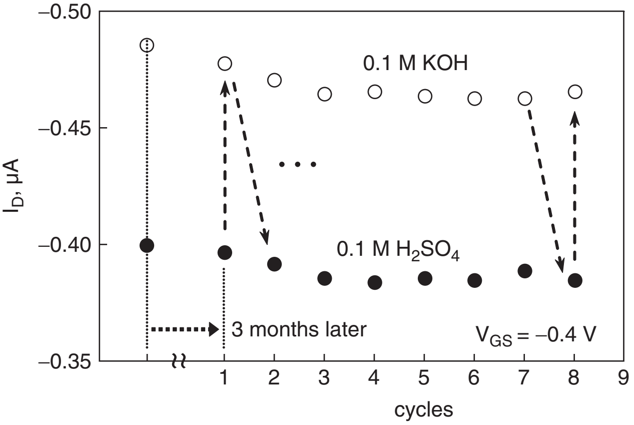

Figure 14.47 Stability test of the delta-doped channel ISFET on nanocrystalline diamond using the packaged structure as shown in Figure 1.46. The measurement points were recorded at a constant drain bias of $V_D = -0.5$ V and gate bias of $V_G = -0.4$ V against SCE (after [227]). Reprinted from Diamond and Related Materials, O-terminated nano-diamond ISFET for application in harsh environment by M. Dipalo, C. Pietzka, A. Denisenko, H. El-Hajj and E. Kohn, IN PRESS Copyright (2008) Elsevier

14.6 CONCLUSION

Diamond has been investigated as wide band gap semiconductor for several decades. During this time its materials and device technology have encountered many hurdles and difficulties, and despite its extraordinary promise it may still be considered a material for the future or, as also argued, 'the end of a dream'. Indeed, diamond does not possess a natural substrate of wafer-size single crystal growth, nor can it be doped with shallow impurities. However, despite these rather discouraging facts, in recent years new concepts have been developed to circumvent the many problems and extrapolate ideal device performances on semi-empirical grounds. In this chapter this progress has been reviewed.

In Section 14.2 doping is discussed. Boron is the workhorse and the section concentrated on this element. n-type doping is mainly used in optoelectronic structures, where moderate activation can be tolerated. It seems that it is still not ready to be implemented into high power diodes or transistors, where losses are extremely critical. Two distinct regions are of interest: delta-doped channels for layers with full activation and enhanced transport properties, and intrinsic drift regions for space–charge limited current flow. Not much lies in between. In the case of delta-doped profiles, the goal is planar doping of one monolayer. This has not quite been achieved yet, but the profiles are already as steep as the free carrier Debye tail. Mobility enhancement is therefore still moderate but not far out of sight. Undoped layers have already become very pure and of high crystalline quality. Nevertheless, the breakdown field is still only a fraction of the ideally expected one. The defect configuration responsible for this behavior needs still to be identified. Then indeed, diamond high voltage diodes, with their expected high robustness, can be attractive even in comparison to GaN.

Further, in Section 14.3, technological aspects are discussed and it is shown that neither ohmic or blocking contacts, nor their thermal stability pose a problem. However, the processing window for obtaining optimum performance is extremely tight and demands sub-nm dimensional control. The tools for achieving this precision are still experimental, especially since the availability of single-crystal surface area and materials quantity are still essentially limited.

Field effect transistors are one of the promising device structures for very high temperature and power operation. However, the competing materials systems, such as SiC or GaN, are already rather advanced, which also means on the other hand that their limitations and problems have gradually become apparent. These are mainly related to the fact that these materials systems are compound materials, which are influenced by both different modifications and stoichiometry-related defects. In contrast, the high bond strength of the diamond lattice results in a low solubility of most impurities and suppresses diffusion. Delta-doped profiles, useful for planar microwave devices (although with gate recess), have been demonstrated and GHz frequencies reached in a classical device configuration, which promises high robustness, and high thermal stability due to the built-in substrate heat spreader.

The development of diode structures has been driven by two applications: power switching with kV blocking voltages, and operation at extremely high temperatures. Both have been investigated in vertical device configurations. Diodes with more than 6-KV blocking voltage have been obtained with a low on-resistance due to a high mobility in the active layer. The target lies certainly above 10 kV and the experimental data obtained from the proof-of-concept experiments indeed allow extrapolation into this range with data entirely compatible with SiC and GaN devices. An essential part of the puzzle, which is the improvement of the breakdown field, is still missing. High temperature diodes still suffer from temperature-activated, reverse current by defects. However, this phenomenon is also common to SiC and GaN diodes and also limits their high temperature operation. Advanced diode concepts like that of a merged diode have been realized and show that such concepts can indeed be adapted to diamond. An all carbon pn-diode, where n-type UNCD was deposited onto a single crystal, boron-doped, active layer, has repeatedly been operated at 1000 °C (in vacuum) without degradation. Such stability has not been reached by any other materials configuration up to now. Similar stability may be expected from AlN based devises and it seems indeed attractive to combine these two materials in a heterostructure, the challenge being the deposition of a hexagonal phase on cubic diamond without high interface state density.

Finally, this chapter has addressed the electrochemical application of boron-doped diamond (BDD). BDD is the only semiconductor with high chemical inertness and corrosion resistance for amperometric operation in highly corrosive and hazardous media. Diamond electrodes have entered the industrial scale for wastewater treatment. So far the utilized material has been largely polycrystalline, except for proof-of-concept experiments. However, a single crystal substrate would allow the incorporation of a transistor function and combine amperometric and potentiometric operation, not possible with Si-based MOSFETs (with metal oxide electrodes). Indeed, first experiments on all-diamond ISFETs for harsh environments have been performed, based on the technology developed for electronic transistor structures.

All the examples above show convincingly that larger surface areas and a greater quantity of material will be required to pursue the development of diamond semiconductor devices with their technological complexity in a reproducible way. Nevertheless, it seems that no basic hurdles are left, projecting a ‘fulfilment of a dream’. Diamond will be able to operate under extreme conditions out of reach of the other alternative materials presently pursued. To identify and nurture these will be extremely important.

14.7 ACKNOWLEDGEMENTS

Many of the experiments discussed in this chapter have been performed in the laboratory of the authors over more than a decade. Therefore, the contributions of several generations of undergraduate students, PhD students, post-doctoral fellows and scientific visitors need to be readily acknowledged, as well as that of our technology support team in the Institute of Electron Devices and Circuits and the Microelectronics Technology Center. In addition this work would not have been possible without the continuous support by industry, the State of Baden-Württemberg, the German Research Society (DFG), and research programs of the European Union. Especially mention is made of the contributions by Element Six Ltd (UK) and Diamond Microwave Devices Ltd (UK). Furthermore the cooperation with many scientists working at international institutions is also worthy of mention, especially Dr Dieter Gruen (Argonne Laboratories, US), Dr Makato Kasu (NTT Basic Research, Japan) and Dr James E. Butler (Naval Research Laboratories, US).

REFERENCES

[1] M.N. Yoder, *Semiconducting Diamond Technology*; Naval Research Reviews, Office of Naval Research Two, 1987, XXXIX, p. 27.

[2] E.O. Johnson; *RCA Rev.*, **26**, (1963) 163.

[3] B.J. Baliga; Semiconductors for high voltage, vertical channel FETs; *J. Appl. Phys.*, **53** (1982) 1759–1764.

[4] V.V. Afanas'ev, A. Stesmans, M. Bassler, G. Pensi, M.J. Schulz; Shallow electron traps at the 4H-SiC/SiO2 interface; *Appl. Phys. Lett.*, **76** (2000) 336–338.

[5] J.H. Zao, P. Alexandrov, X. Li; Demonstration of the first 10-kV 4HsiC Schottky barrier diodes; *IEEE Electron Devices Lett.*, **24** (2003) 402–404.

[6] B.A. Hull, J.J. Sumakeris, M. Das, J. Richmond, J. Palmour; Progress on the development of 10kV 4H-SiC pin diodes for high current/high voltage power handling applications; *Mat. Sci. Forum*, **556–557** (2006) 895–900.

[7] A. Agarwal, S.-H. Ryu; Status of SiC power devices and manufacturing issues; *CS MANTEC Conf*. 2006, Vancouver, Canada, Proc. 215–218.

[8] Jian Hui Zhang, Jian Wu, P. Alexandrov, T. Burke, K. Sheng, J.-H. Zhao; 1836 V, 4.7 mΩ cm^2 high power 4H-SiC bipolar junction transistor; *Mat. Sci. Forum*, **527–529** (2005) 1417–1420.

[9] A. Agarwal, S. Krishnaswami, B. Damsky, J. Richmond, C. Capell, J. Palmour, S.H. Ryu; A 1cm ×1 cm, 5 kV, 100 A, 4H-SiC thyristor chip for high current modules; *Mat. Sci. Forum*, **527–529** (2005) 1397–1401.

[10] Q.Ch. Zhang, C. Jonas, B. Heath, M.l Das, S.H. Ryu, A. Agarwal, J. Palmour; 9kV 4H-SiC IGBTs with 88 mΩ cm^2 of $R_{\mathrm{diff,on}}$; *Mat. Sci. Forum*, **556–557** (2006) 771–773.

[11] S.-H. Ryu, S. Krishnaswami, M. O'Loughlin, J. Richmond, A. Agarwal, J. Palmour, Ben Damsky, A.R. Hefnner; 10-kV, 123-mΩ cm^2 4H-SiC power DMOSFETs; *IEEE Electron Devices Lett.*, **25** (2004) 556–558.

[12] Y.M. Sung, J.B. Casady, J.B. Dufrene, A.K. Agarwal; A review of SiC static induction transistor development for high-frequency power amplifiers; *Solid State Electronics*, **46** (2002) 605–613.

[13] G.I. Gudjonsson, F. Allerstam, E.Ö. Sveinbjörnsson, H. Hjelmgren, P.A. Nilsson, K. Andersson, H. Zirath, T. Rödle, R. Jos; Design and fabrication of 4H-SiC RF MOSFETs; *IEEE Trans. Electron Devices*, **54** (2007) 3138–3145.

[14] K. Andersson, M. Südow, P.A. Nilsson, E. Sveinbjörnsson, H. Hjelmgren, J.L Nilsson, H. Stähl, N. Rorsman; Fabrication and characterization of field-plated buried-gate SiC MESFETs; *IEEE Electron Device Lett.*, **27** (2006) 573–575.

[15] A. Agarwal, F. Husna, J. Haley, H. Bartlow, B. McCalpin, S. Krishnaswami, C. Capell, Sei Hyung Ryu, J. Palmour; First demonstration of 2.1 kW output power at 425MHz using 4H-SiC RF power BJTs; *Mat. Sci. Forum*, **527–529** (2005) 1413–1416.

[16] Yu Zhu Li, P. Alexandrov, Jian Hui Zhang, L.X. Li, J.H. Zhao; 10 kV, 87 mΩ cm^2 normally-off 4H-SiC vertical junction field-effect transistors; *Mat. Sci. Forum*, **527–529** (2005) 1187–1190.

[17] A.L. Spetz, A. Baranzahi, P. Tobias, I. Lundström; High temperature sensors based on Metal-insulator-silicon carbide devices; *Phys. Stat. Sol. (a)*, **162** (1997) 493.

[18] J. Song, W. Lu, J.S. Flynn, G.R. Brandes; Pt-AlGaN/GaN Schottky diodes operating at 800 °C for hydrogen sensing; *Appl. Phys. Lett.*, **87** (2005) 133501–1 to -3.

[19] Y.F. Wu, M. Moore, A. Saxler, T. Wisleder, and P. Parikh, 40 W/mm double field plated GaN HEMTs, in *IEEE DRC Conf. Dig.*, University Park, PA, p. 151, 2006.

[20] E. Mitani, M. Aojima, A. Maekawa, S. Sano; An 800-W AlGaN/GaN HEMT for S-band high power application; *CS MANTECH*, 2007, Austin (TX); Proc., pp. 213–216.

[21] Y. Uemoto, D. Shibata, M. Yanagihara, H. Ispida, H. Matsuo, S. Nagai, N. Batta, M. Li, T. Ueda, T. Tanaka, D. Ueda; 8300 V blocking voltage AlGaN/GaN power HFET with thick poly-AlN passivation; *2007 IEEE International Electron Devices Meeting*, Washington (USA) Dec. 10–12, 2007, *Technical Digest*, pp. 861–864.

[22] J. Joh and J. del Alamo. Mechanism for electrical degradation of GaN high electron mobility transistor, in *Proc. IEEE IEDM Tech. Digest*, 2006, 415.

[23] F. Medjdoub, J.-F. Carlin, M. Gonschorek, E. Feltin, M.A. Py, D. Ducatteau, C. Gaquiere, N. Grandjean, E. Kohn; Can InAlN/GaN be an alternative to high power/high temperature AlGaN/GaN devices?; 2006 *IEEE International Electron Devices Meeting*, San Francisco (USA) Dec. 11–13 2006, *Technical Digest*, Paper 35.7.

[24] J.P. Ibbetson, P.T. Fini, K.D. Ness, S.P. DenBaars, J.S. Speck, U.K. Mishra; Polarization effects, surface states, and the source of electrons in AlGaN/GaN heterostructure field effect transistors; *Appl. Phys. Lett.*, **77** (2000) 250–252.

[25] E. Kohn, I. Daumiller, M. Kunze, M. Neuburger, M. Seyboth, T.J. Jenkins, J.S. Sewell, J. Van Norstand, Y. Smorchkova, U. Mishra; Transient characteristics of GaN-based heterostructure field-effect transistors; *IEEE Trans. Microwave Theory and Techniques*, **51** (2003) 634–642.

[26] P. Bergonzo, R.B. Jackman; Diamond-based radiation and photon detectors; *Thin Film Diamond II (Semiconductor and Semimetals*, Vol. **77**), C. Nebel, J. Ristein (eds.) Chapter 6, Elsevier, 2004, pp. 197–311.

[27] G.M. Swain; Electroanalytical applications of diamond electrodes; *Thin Film Diamond II (Semiconductor and Semimetals*, Vol. **77**), C. Nebel, J. Ristein (eds.) Chapter 4, Elsevier, 2004, pp. 121–148.

[28] W. Haenni, P. Rychen, M. Fryda, C. Comninellis; Industrial applications of diamond electrodes; *Thin Film Diamond II (Semiconductor and Semimetals*, Vol. **77**), C. Nebel, J. Ristein (eds.) Chapter 5, Elsevier, 2004, pp. 149–196.

[29] S. Gsell, T. Bauer, J. Goldfuβ, M. Schreck, B. Stritzker; A route to diamond wafers by epitaxial deposition on silicon via iridium/yttria-stabilized zirconia buffer layers; *Appl. Phys. Lett.*, **84** (2004) 5441.

[30] G. Davis (ed.); *Properties and Growth of Diamond*, INSPEC, London, 1994.

[31] L.S. Pan, D.R. Kania (eds); *Diamond: Electronic properties and Applications*; Kluwer Academic Publishers, 1995.

[32] B. Dischler, C. Wild (eds); *Low Pressure Diamond–Manufacturing and Applications*, Springer, 1998.

[33] M.H. Nazare, A.J. Neves, *Properties, Growth and Applications of Diamond*; INSPEC, London, 2000.

[34] C. Nebel, J. Ristein (eds.) *Thin Film Diamond II (Semiconductor and Semimetals*, Vol. **77**, Elsevier, 2004.

[35] K. Kobashi: *Diamond Films*, Elsevier, Oxford, 2005.

[36] G.H. Glover; The C–V characteristics of Schottky barriers on laboratory grown semiconducting diamonds; *Solid-State Electronics*, **16** (1973) 973–983.

[37] Y.S. Vavilov; Semiconducting diamond; *Phys. Stat. Sol. (a)* **31** (1975) 11–26.

[38] M.W. Geis, J.A. Gregory, B.B. Pate; Capacitance–voltage measurements on metal–SiO_2–diamond structures fabricated with (100)- and (111)-oriented substrates; *IEEE Trans. Electron Devices*, **38** (1991) 619–625.

[39] W. Tsai, M. Delfino, D. Hodul, M. Riatziat, L.Y. Ching, G. Renolds, C.B. Cooper; Diamond MESFET using ultrashallow RTP boron doping; *IEEE Electron Devices Lett.*, **12** (1991) 157–159.

[40] C.R. Zeisse, C.A. Hewett, R. Nguyen, J.R. Zeidler, R.G. Wilson; An ion-implanted diamond metal–insulator–semiconductor field-effect transistor; *IEEE Electron Devices Lett.*, **12** (1991) 602–604.

[41] G.S. Gildenblat, S.A. Grot, C.W. Hatfield, A.R. Badzian; High-temperature thin-film field-effect transistor fabricated using a selective growth method; *IEEE Electron Devices Lett.*, **12** (1991) 37–39.

[42] T. Maki, S. Suzuki, T. Kobayashi; Preparation of P–I–P diamond unipolar-transistor structure and its hole-injection properties; *2nd International Conference on the Applications of Diamond Films and Related Materials*, MYU Tokyo 1993, pp. 311–316.

[43] D.L. Dreifus; Double diamond mesa vertical field effect transistor; US Patent 5 391 895 (1995).

[44] M.W. Geis, D.D. Rathman, D.J. Ehrlich, R.A. Murphy, W.T. Lindley; High temperature point-contact transistors and Schottky diodes formed on synthetic boron-doped diamond; *IEEE Electron Devices Lett.*, **8** (1987) 341–343.

[45] J.F. Prins, Bipolar transistor action in ion implanted diamond; *Appl. Phys. Lett.*, **41**, 1982, 950.

[46] M.W. Geis, N.N. Efremov, D.D. Rathman; Summary abstract: Device applications of diamonds; *J. Vac. Sci. Technol. A*, **6** (1988) 1953–1954.

[47] M. Zhang, Y. Xia, L. Wang, B. Gu, CVD diamond devices for charged particle detection *Semicond. Sci. Technol.*, **20** (2005) 555.

[48] S.F. Kozlov, R. Stuck, M. Hage-Ali, P. Siffert; Preparation and characteristics of natural diamond nuclear radiation detectors; *IEEE Trans. Nuclear Science*, **22** (1975) 160–170.

[49] D.R. Kania; M.L. Landstrass, M.A. Plano; Diamond radiation detectors; *Diamond and Realated Materials*, **2** (1993) 1012–1019.

[50] S.C. Binari, M. Marchywka, D,.A. Koolback, H.B. Dietrich, D. Moses; *Diamond and Realated Materials*, **2** (1993) 1020–10223.

[51] J.F. Prins; Cathodoluminescence and electroluminescence in ion implanted type II diamonds; *Diamond and Related Materials*, **3** (1994) 922–925.

[52] G.M. Swain, R. Ramesham; The electrochemical activity of boron-doped polycrystalline diamond thin film electrodes; *Anal. Chem.*, **65** (1993) 345–351.

[53] H. Kawarada, Y. Araki, T. Sakai, T. Ogawa, H. Umezawa; *Phys. Stat. Sol. (a)*, **185** (2001) 79.

[54] A. Deneuville; Boron doping of diamond films from the gas source; *Thin Film Diamond II (Semiconductor and Semimetals*, Vol. **77**), C. Nebel, J. Ristein (eds.) Elsevier, 2004.

[55] M. Kunze, A. Vescan, P. Gluche, W. Ebert, E. Kohn; Delta-doping in diamond; *Carbon*, **37** (1999) 787–791.

[56] T.H. Borst, P–C. Münzinger, O. Weis; Characterization of undoped and doped homoepitaxial diamond layers produced by microwave plasma CVD; *Diamond and Related Materials*, **3** (1994) 515–519.

[57] R. Kalish; Doping diamond by ion-implantation; *Thin Film Diamond II (Semiconductor and Semimetals*, Vol. **77**), C. Nebel, J. Ristein (eds.) Elsevier, 2004.

[58] G. Popovici, H.G. Wilson, T. Sung, M.A. Prelas, S. Khasawinah; Diffusion of boron, lithium, oxygen, hydrogen and nitrogen in type IIa natural diamond; *J. Appl. Phys.*, **77** (1995) 5103–5105.

[59] A.E. Alexenko, B.V. Spitsyn; Semiconducting diamonds made in the USSR; *Diamond and Related Materials*, **1** (1992) 705–709.

[60] T.H. Borst, O. Weis, Electrical characterization of homoepitaxial diamond films doped with B, P, Li and Na during crystal growth, *Diamond and Related Materials*, **4** (1995) 948–953.

[61] G. Braunstein, T. Bernstein, U. Carsenty, R. Kalish; Depth profile of antimony implanted into diamond; *J. Appl. Phys.*, **50** (1979) 5731.

[62] I. Sakaguichi, M. Gamo, Y. Kikuchi, E. Yasu, H. Haneda, T. Suzuki, T. Ando, Sulfur: A donor dopant for n-type diamond semiconductors; *Phys. Rev. B*, **60** (1999) R2139–R2141.

[63] S.C. Eaton, A.B. Anderson, J.C. Angus; Co-doping of diamond with boron and sulphur; *Proc. 7th Applied Diamond Conf./3rd Frontier Carbon Technology Joint Conf.*, 2003, NASA/CP-2003-212319, pp. 527–532.

[64] S. Koizumi, T. Teraji, H. Kanda; Phosphorous-doped chemical vapor deposition of diamond; *Diamond and Related Materials*, **9** (2000) 935–940.

[65] A.T. Collins, A.W.S. Williams; The nature of the acceptor centre in semiconducting diamond; *J. Phys. C.: Solid State Phys.*, **4** (1971) 1789–1800.

[66] T.H Borst, O. Weis; Boron-doped homoepitaxial diamond layers: fabrication, characterization, and electronic applications; *Phys. Stat. Solid. (a)*, **154** (1996) 423–444.

[67] J.-P. Lagrange, A. Deneauville, E. Gheeraert; A large range of boron doping with low compensation ratio for homoepitaxial diamond films; *Carbon*, **37** (1999) 807–810

[68] M. Werner, R. Locher, W. Kohly, D.S. Holmes, S. Klose, H.J. Fecht; The diamond Irvin curve; *Diamond and Related Materials*, **6** (1997) 308–313.

[69] J. Bourgoin, J. Krinski, B. Blanchard, Boron concentration and impurity-to-band activation in diamond; *Phys. Stat. Sol. (a)*, **52** (1979) 283.

[70] J. Chevallier; Hydrogen diffusion and acceptor passivation in diamond; in *Thin Film Diamond II (Semiconductor and Semimetals*, Vol. **77**), C. Nebel, J. Ristein (eds.) Chapter 1, pp. 1–36, Elsevier, 2004.

[71] Z. Teukam, J. Chevallier, C. Saguy, R. Kalish, D. Ballutaud, M. Barbe, F. Jomard, A. Tromson-Carli, C. Cytermann, J.E. Butler, M. Bernard, C. Baron, A. Deneuville; *Nature Materials*, **2** (2003) 482–486.

[72] E. Bourgeois, E. Bustarret, P. Achatz, F. Omnes, X. Blase, Impurity dimers in superconducting B–doped diamond: Experiment and first–principles calculations; *Phys. Rev. B*, **74** (2006) 094509.

[73] W.L. Wang, M. Polo, G. Sanchez, J. Cifre, J. Esteve, Internal stress and strain in heavily boron-doped diamond films grown by microwave plasma and hot filament chemical vapor deposition, *J. Appl. Phys.*, **80** (1996) 1846.

[74] S. Kajihara, A. Antonelli, J. Bernholc, R. Car, Nitrogen and potential n-type dopants in diamond, *Phys. Rev. Lett.*, **66** (1991) 2010.

[75] E. Gheeraert, S. Koizumi, T. Teraji, H. Kanda, M. Nesladek, Electronic states of phosphorous in diamond, *Diamond and Related Materials*, **9** (2000) 948.

[76] S. Koizumi, M. Suzuka; n-Type doping of diamond; *Phys. Stat. Sol. (a)*, **203** (2006) 3358–3366.

[77] R. Li, A molecular dynamics study of boron and nitrogen in diamond; *Solid State Commun.*, **135** (2005) 155.

[78] S. Koizumi, K. Watanabe, M. Hasegawa, H. Kanda; Ultraviolet emission from a diamond pn junction; *Science*, **292** (2001) 1899–1901.

[79] M. Suzuki, S. Koizumi, M. Katagiri, H. Yoshida, N. Sakuma, T. Ono, T. Sakai; Electrical characterization of phosphorous-doped n-type homoepitaxial diamond layers; *Diamond and Related Materials*, **13** (2004) 2037–2040.

[80] M. Katagiri, J. Isoya, S. Koizumi, H. Kanda; Lightly phosphorus-doped homoepitaxial diamond films grown by chemical vapor deposition; *Appl. Phys. Lett.*, **85** (2004) 6365–6367.

[81] T. Makino, H. Kato, S.G. Ri, Y. Chen, H. Okushi; Electrical characterization of homoepitaxial diamond p–n^+ junction; *Diamond and Related Materials*, **14** (2003) 1995–1998.

[82] H. Kawarada, Hydrogen-terminated diamond surfaces and interfaces, *Surface Science Reports*, **26** (1996) 205.

[83] P. Strobel, M. Riedel, J. Ristein, L. Ley, Surface transfer doping of diamond; *Nature*, **430** (2004) 439.

[84] M. Kasu, K. Ueda, Y. Yamauchi, A. Tallaire, T. Makimoto; Diamond-based power transistors: fundamentals and applications; *Diamond and Related Materials*, **16** (2007) 1010–1015.

[85] K. Hirama, H. Takayanagi, S. Yamauchi, Y. Jingu, H. Umezawa, H. Kawarada; High-performance p-channel diamond MOSFETs with alumina gate insulator; *International Electron Devices Meeting* (IEDM) 2007, Washington (DC) *Technical Digest*, pp. 837–876.

[86] M. Kasu, K. Ueda, H.Y. Yamauchi, S. Sasaki, T. Makimoto; High RF output power for H-terminated diamond FETs; *Diamond and Related Materials*, **15** (2006) 783–786.

[87] A. Aleksov, A. Denisenko, U. Spitzberg, T. Jenkins, W. Ebert, E. Kohn, RF performance of surface channel diamond FETs with sub-micron gate length; *Diamond and Related Materials*, **11** (2002) 382.

[88] H. Ye, M. Kasu, K. Ueda, Y. Yamauchi, N. Maeda, S. Sasaki, T. Makimoto; Temperature dependent DC and RF performance of diamond MESFET; *Diamond and Related Materials*, **15** (2006) 787–793.

[89] R.J. Trew, J–B. Yan, P.M. Mock; The potential of diamond and SiC electronic devices for microwave and millimetre-wave power applications; *Proc. IEEE*, **79** (1991) 598–620.

[90] J.S. Holmes, D.L. Dreifus; Field-effect transistors and circuits fabricated from semiconducting diamond; *International Electron Devices Meeting* (IEDM) 1994 San Francisco (CA) *Technical Digest*, pp. 423–426.

[91] S.A. Grot, G.S. Gildenblat, A.R. Badzian; Diamond thin-film recessed gate field-effect transistors fabricated by electron cyclotron resonance plasma etching; *IEEE Electron Devices Lett.*, **13** (1992) 462–464.

[92] H. Shiomi, Y. Nishibayashi, N. Toda, S. Shikata; Pulse-doped diamond p-channel metal semiconductor field-effect transistor, *IEEE Electron Dev. Lett.*, **16** (1995) 36.

[93] A. Vescan, P. Gluche, W. Ebert, E. Kohn; High-temperature, high-voltage operation of pulse-doped diamond MESFETs; *IEEE Electron Devices Lett.*, **18** (1997) 222–224.

[94] A. Aleksow, A. Vescan, M. Kunze, P. Gluche, W. Ebert, E. Kohn, A. Bergmaier, G. Dollinger; Diamond junction FETs based on δ-doped channels; *Diamond and Related Materials*, **8** (1999) 941–945.

[95] G.S. Gildenblat, S.A. Grot, A. Badzian; The electrical properties and device applications of homoepitaxial and polycrystalline diamond films; *Proc. IEEE*, **79** (1991) 647–668.

[96] J.S. Holmes, A.J. Tessmer, D.L. Dreifus; High temperature operation of diamond digital logic structures; *Proceedings, 2nd International High-Temperature Electronics Conference*, Charlotte (NC) VI-35–VI-40.

[97] J.R. Zeidler, C.A. Hewett, R. Nguyen, C.R. Zeisse; A diamond driver-active load pair fabricated by ion implantation; *Diamond and Related Materials*, **2** (1993) 1341–1343.

[98] S.J. Rashid, A. Tajani, L. Coulbeck, M. Brezeanu, A. Garraway, T. Butler, N.L. Rupesinghe, D.J. Twitchen, G.A.J. Amaratunga, F. Udrea, P. Taylor, M. Dixon and J. Isberg; Modelling of single-crystal diamond Schottky diodes for high-voltage applications; *Diamond and Related Materials*, **15** (2006) 317–323.

[99] S. Yamanaka, D. Takeuchi, H. Watanabe, H. Okushi and K. Kajimura; Low-compensated boron-doped homoepitaxial diamond films; *Diamond and Related Materials*, **9** (2000) 956–959.

[100] W. Huang, T.P. Chow, J. Yang, J. Butler; High voltage diamond Schottky barrier rectifiers; *Int. J. High Speed Electronics*, **14** (2004) 872.

[101] J. Isberg, J. Hammersberg, D.J. Twitchen, A.J. Whitehead; Single crystal diamond for electronic applications; *Diamond and Related Materials*, **13** (2004) 320–324.

[102] A. Tallaire, J. Achard, F. Silva, R. Sussmann, A. Gicquel, E. Rzepka, Oxygen plasma pre-treatments for high quality homoepitaxial CVD diamond deposition; *Phys. Stat. Sol. (a)*, **201** (2004) 2419.

[103] C. Miskys, J. Garrido, C. Nebel, M. Hermann, O. Ambacher, M. Eickoff, M. Stutzmann, AlN/diamond heterojunction diodes; *Appl. Phys. Lett.*, **82** (2003) 290.

[104] X.W. Zhang, H.-G. Boyen, N. Deyneka, P. Ziemann, F. Banhart, M. Schreck, Epitaxy of cubic boron nitride on (001)–oriented diamond; *Nature Materials*, **2** (2003) 312.

[105] A. Aleksov, A. Denisenko, E. Kohn, Prospects of bipolar diamond devices; *Solid State Electron.*, **44** (2000) 369.

[106] Ch. Yan, Y. Vohra, H–K. Mao, R.J. Hemely, Very high growth rate chemical vapour deposition of single crystal diamond; *Proc. Natl Acad. Sci.*, **99** (2002) 12523.

[107] D. Takeuchi, H. Watanabe, S. Yamanaka, H. Okushi, K. Kajimura; Homoepitaxial diamond films grown by step-flow mode in various misorientation angles of diamond substrates; *Diamond and Related Materials*, **9** (2000) 231–235.

[108] W. Ebert, A. Vescan, P. Gluche, T. Borst and E. Kohn; High–voltage Schottky diode on epitaxial diamond layer; *Diamond and Related materials* **6** (1997) 329–332.

[109] T. Teraji, S. Koizumi, Y. Koide, T. Ito, Electrical field breakdown of lateral Schottky diodes of diamond; *Jpn. J. Appl. Phys.*, **46** (2007) L196.

[110] J. Isberg, M. Gabrysch, A. Tajani, D.J. Twitchen; High-field electrical transport in single crystal CVD diamond diodes; *Advances in Science and Technology*, **48** (2006) 73–76.

[111] A. Deneuville, C. Baron, S. Ghodbane, C. Agnes; Highly and heavily boron doped diamond films; *Diamond and Related Materials*, **16** (2007) 915–920.

[112] E.F. Schubert (Ed.) *Delta–Doping of Semiconductors*, Cambridge University Press (1996) 604.

[113] J. Kuzmik, Power electronics on InAlN/(In)GaN: prospect for a record performance, *IEEE Electron Device Lett.*, **22** (2001) 510.

[114] K. Hess; Impurity and phonon scattering in layered structures, *Appl. Phys. Lett.*, **35** (1979) 484.

[115] J. Isberg, J. Hammersberg, E. Johansson, T. Wikstom, D. Twitchen, A. Whitehead, S. Coe, G. Scarbrook, High carrier mobility in single-crystal plasma deposited diamond *Science*, **297** (2002) 1670.

[116] J.E. Butler; Ultra smooth (100) diamond single crystal surfaces; *2nd International Industrial Diamond Conference*, April 2007, Rome (Italy), paper 257.

[117] K. Hayashi, S. Yamanaka, H. Okushi, K. Kajimura; Stepped growth and etching of [001] diamond; *Diamonds and Related Materials*, **5** (1996) 1002–1005.

[118] A. Vescan, W. Ebert, T.H. Borst, E. Kohn; Electrical characterisation of diamond resistors etched by RIE; *Diamond and Related Materials*, **5** (1996) 747–751.

[119] G. Dollinger, C.M. Frey, A. Bergmaier, T. Faestermann, Depth profile analysis with monolayer resolution using elastic recoil detection (ERD); *Europhys. Lett.*, **42** (1998) 19–24.

[120] H. El–Hajj, A. Denisenko, A. Bergmaier, G. Dollinger, M. Kubovic and E. Kohn, Characteristics of boron δ-doped diamond for electronic applications; *Diamond and Related Materials*, (2008) in press.

[121] R. Zeisel, C.E. Nebel, M. Stutzmann; Passivation of boron in diamond by deuterium; *Appl. Phys. Lett.*, **74** (1999) 1875–1876.

[122] T. Kobayashi, T. Ariki, M. Iwabuchi, T. Maki, S. Shikama, S. Suzuki; Analytical studies on multiple delta doping in diamond thin films for efficient hole exitation and conductance enhancement; *J. Appl. Phys.*, **76** (1994) 1977–1979.

[123] M. Kubovic, H. El–Hajj, J.E. Buttler, E. Kohn: Diamond merged diode; *Diamond and Related Materials*, 16 (2007) 1033–1037.

[124] T. Sung, G. Popovici, M.A. Prelas, R.G. Wilson; Boron diffusion coefficient in diamond; *Mat. Res. Soc.*, **416** (1996) 467–470.

[125] H. Kawarada, Hydrogen-terminated diamond surfaces and interfaces, *Surface Science Reports*, **26** (1996) 205.

[126] J. van der Weide, R. Nemanich, Influence of interfacial hydrogen and oxygen on the Schottky barrier height of nickel on (111) and (100) diamond surfaces; *Phys. Rev. B*, **49** (1994) 13629.

[127] F. Maier, J. Ristein, L. Ley, Electron affinity of plasma-hydrogenated and chemically oxidised diamond surfaces; *Phys. Rev. B*, **64** (2001) 16541.

[128] J. Shirafuji, T. Sugino; Electrical properties of diamond surfaces; *Diamond and Related Materials*, **5** (1996) 706–713.

[129] H. Shiomi, H. Nakahata, T. Imai, Y. Nishabayashi, N. Fujimori; Electrical characteristics of metal contacts to boron-doped diamond epitaxial film; *Jpn. J. Appl. Phys.*, **28** (1989) 758–762.

[130] Y. Zhu, B. Zheng, W. Yao, L. Cao; The interface diffusion and chemical reaction between a Ti layer and a diamond substrate; *Diamond and Related Materials*, **8** (1999) 1073–1078.

[131] J. Nakanshi, A. Otsuki, T. Oku, O. Ishiwata, M. Murakami; Formation of ohmic contacts to p-type diamond using carbide forming metals; *J. Appl. Phys.*, **76** (1994) 2293–2298.

[132] Y.G. Chen, M. Ogura, S. Yamasaki, H. Okushi; Investigation of specific contact resistance of ohmic contacts to B-doped homoepitaxial diamond using transmission line model; *Diamond and Related Materials*, **13** (2004) 2121–2124.

[133] A. Vescan, P. Gluche, W. Ebert, E. Kohn; Selectively grown ohmic contacts to δ-doped diamond films; *Electron. Lett.*, **32** (1996) 1419–1421.

[134] M. Werner, R. Job, A. Denisenko, A. Zaitsev, W.R. Fahrner, C. Johnston, P.R. Chalker, I.M. Buckley–Golder; How to fabricate low-resistance metal–diamond contacts; *Diamond and Related Materials*, **5** (1996) 723–737.

[135] C.A. Mead, T.C. McGill; Schottky barrier heights on p-type diamond and silicon carbide (6H); *Physics Letters*, **58A** (1976) 249–251.

[136] F.J. Himpsel, P. Heimann, D.E. Eastman; Schottky barriers on diamond (111); *Solid State Communications*, **36** (1990) 631–633.

[137] H. Kiyoto, H. Okushi, T. Ando, M. Kamo, Y. Sato; Electrical properties of a Schottky barrier formed on a homoepitaxially grown diamond (001) film; *Diamond and Related Materials*, **5** (1995) 718–722.

[138] V. Venkatesan, K. Das, J.A. Windheim, M.W. Geis; Effect of back contact impedance on frequency dependence of capacitance–voltage measurements on metal/diamond diodes; *Appl. Phys. Lett.*, **63** (1993) 1065–1067.

[139] W. Ebert, A. Vescan, E. Kohn; General diamond Schottky-barrier diode model from locus diagram analysis; *Diamond and Related Materials*, **3** (1994) 887–890.

[140] A. Vescan, W. Ebert, T. Borst, E. Kohn; I/V characteristics of epitaxial Schottky Au barrier diode on p^+ diamond substrate; *Diamond and Related Materials*, **4** (1995) 661–665.

[141] M.W. Geis, N.N. Efremov, J.A. von Windheim; High-conductance, low-leakage diamond Schottky diodes; *Appl. Phys. Lett.*, **63** (1993) 952–954.

[142] D.G. Jeng, H.S. Tuan, R.S. Salat, G.L. Fricano; Thin-film Al/diamond Schottky diode over 400-V breakdown voltage; *J.Appl. Phys.*, **68** (1990) 5902–5904.

[143] Y.G. Chen, M. Ogura, H. Okushi, Temperature dependence on current–voltage characteristics of nickel/diamond Schottky diodes on high quality boron-doped homoepitaxial diamond film; *Appl. Phys. Lett.*, **82** (2003) 4367–4369.

[144] H. Shiomi, H. Nakahata, T. Imai, Y. Nishibayashi, N. Fujimori; Electrical characteristics of metal contacts to boron doped diamond epitaxial film, *Jpn. J. Appl. Phys.*, **28** (1989) 758.

[145] J. von Windheim, V. Venkatesan, D. Malta, K. Das; Electrical characterisation of semiconducting diamond thin films and single crystals; *J. Electron. Mater.*, **22** (1993) 391.

[146] A. Vescan, I. Daumiller, P. Gluche, W. Ebert, E. Kohn; Very high temperature operation of diamond Schottky diode; *IEEE Electron Devices Lett.*, **18** (1997) 556–558.

[147] H. El-Hajj, A. Denisenko, A. Kaiser, R.S. Balmer, E. Kohn; Diamond MISFET based on boron delta-doped channel; *Diamond and Related Materials* (2008), to be published.

[148] N. Kawakami, Y. Yokata, T. Tachibana, K. Hayashi, K. Kobashi; Atomic layer deposition of Al_2O_3 thin films on diamond; *Diamond and Related Materials*, **14** (2005) 2015–2018.

[149] S. Jakschik, U. Schroeder, T. Hecht, D. Krueger, G. Dollinger, A. Bergmaier, C. Luhmann, J.W. Bartha; Physical characterization of thin ALD–Al_2O_3 films; *Appl. Surface Sciences*, **211** (2003) 352–359.

[150] J. Kolodzey, E.A. Chowdhury, T.N. Adam, Q. Guohua, I. Rau, J.O. Olowolafe, J.S. Suehle, C. Yuan; Electrical conduction and dielectric breakdown in aluminum oxide insulators on silicon; *IEEE Trans. Electron Devices*, **47** (2999) 121–128.

[151] D.S. Hwang, T. Saito, N. Fujimori; New etching process for device fabrication using diamond; *Diamond and Related Materials*, **13** (2004) 2207–2210.

[152] Y. Ando, Y. Nishibayashi, K. Kobashi, T. Hirao, K. Oura; Smooth and high-rate reactive ion etching of diamond; *Diamond and Related Materials*, **11** (2002) 824–827.

[153] J. Enlund, J. Isberg, M. Karlsson, F. Nikolajeff, J. Olsson, D.J. Twitchen; Anisotropic dry etching of boron doped single crystal CVD diamond; *Carbon*, **43** (2005) 1839–1842.

[154] S. Kumar, P. Ravindranathan, H.S. Dewan, R. Roy; Survival of diamond at 2000 °C in hydrogen; *Diamond and Related Materials*, **5** (1996) 1246–1248.

[155] A. Aleksov, M. Kubovic, N. Kaeb, U. Spitzberg, A. Bermaier, G. Dollinger, Th. Bauer, M. Schreck, B. Stritzker, E. Kohn; Diamond field-effect transistors – concepts and challenges; *Diamond and Related Materials*, **12** (2003) 391.

[156] R.S. Balmer, I. Friel, S.M. Woollard, C.J.H. Wort, G.A. Scarsbrook, S.E. Coe, H. El-Hajj, A. Kaiser, A. Denisenko, E. Kohn, J. Isberg; Unlocking diamond’s potential as an electronic material, *Philosophical Transactions of the Royal Society A*, **366** (2008) 1.

[157] H. Xing, Y. Dora, A. Chini, S. Heikman, S. Keller, U.K. Mishra; High breakdown voltage AlGaN–GaNHEMTs achieved by multiple field plates; *IEEE Electron Devices Lett.*, **25** (2004) 161–163.

[158] A. Denisenko, E. Kohn; Diamond power devices. Concepts and limits; *Diamond and Related Materials*, **14** (2005) 491.

[159] S.H. Wemple, W.C. Niehaus, H.M. Cox, J.V. DiLaurenzo, W.O. Schlosser; Control of gate-drain avalanche in GaAs MESFETs; *IEEE Trans. Electron. Devices*, **27** (1980) 1013–1018.

[160] M. Lampert and P. Mark, *Current Injection in Solids*, Academic Press, New York, 1970, p. 380.

[161] J. Isberg, A. Tajani, D. Twitchen; Photoionisation measurement of deep defects in single-crystalline CVD diamond using the transient-current technique, *Phys. Rev. B*, **73** (2006) 245207.

[162] A. Denisenko, W.R. Fahrner, U. Strähle, H. Henschel, R. Job; Radiation response of p–i–p diodes on diamond substrates of various types: Electrical properties of semiconductor–insulator homojunctions, *IEEE Trans. Nucl. Sci.*, **43** (1996) 3081.

[163] M. Kasu, N. Kobayashi; High mobility and high crystalline-quality chemical-vapor-deposition grown homoepitaxial diamond; *Diamond and Related Materials*, **12** (2003) 413–417.

[164] M. Kasu, N. Kobayashi; High mobility (1300 cm^2/ Vs) at room temperature in hydrogen-terminated (001) diamond; *Appl. Phys. Lett.*, **80** (2002) 3961–3963.

[165] *Properties of Advanced Semiconductor Materials GaN, AlN, SiC, BN, SiC, SiGe.* Levinshtein M.E., Rumyantsev S.L., Shur M.S. (Eds), John Wiley & Sons, Inc., New York, 2001.

[166] K. Miyata, K. Nishimura, K. Kobashi, Device simulation of submicrometer gate $p^+i–p^+$ diamond transistors, *IEEE Trans. Electron Dev.*, **42** (1995) 2010.

[167] K. Nishimura, K. Miyata, T. Kobori, K. Kobashi; Device simulation of diamond FETs with MES, P^+IP^+ and δ-doped structures in comparison with 6H-SiC MESFETs; *Electrochem. Soc. Proc.*, **95–4** (1995) 588–594.

[168] N. Kavakami, Y. Yokota, T. Taschibana, K. Hayashi, K. Inoue, K. Kobashi; Fabrication of a submicron source-drain gap for p–i–p field effect transistors using epitaxial diamond layers; *Diamond and Related Materials*, **13** (2004) 1939–1043.

[169] N. Kawakami, Y. Yokota, K. Hayashi, T. Tachibana, K. Kobashi, Device operation of p–i–p diamond metal-insulator-semiconductor field effect transistors with sub-micrometer channel; *Diamond and Related Materials*, **14** (2005) 509.

[170] T. Inushima, T. Matsushita, R.F. Mamin; Electrical measurements on p^+–p^-–p^+ homoepitaxial diamond capacitors; *Appl. Phys. Lett.*, **77** (2000) 1173–1175.

[171] M. Irie, S. Endo, C.L. Wang, T. Ito; Fabrication and properties of lateral p–i–p structures using single-crystalline CVD diamond layers for high electric field applications; *Diamond and Related Materials*, **12** (2003) 1563–1568.

[172] T. Zimmermann, M. Kubovic, A. Denisenko, K. Janischowsky, O.A. Williams, D.M. Gruen, E. Kohn, Ultrananocrystalline/single crystal diamond heterostructure diode; *Diamond and Related Materials*, **14** (2005) 416.

[173] D. Twitchen, A Whitehead, S. Coe, J. Isberg, J. Hammersberg, T. Wikstrom, E. Johansson; High voltage single crystal diamond diodes; *IEEE Trans. Electron Dev.*, **51** (2004) 826–828.

[174] J. Butler, M. Geis, K. Krohn, J. Lawless, S. Deneault, T. Lyszczarz, D. Flechtner, R. Wright, Exceptionally high voltage Schottky diamond diodes and low boron doping *Semicond. Sci. Technol.*, **18** (2003) S67.

[175] M. Brezeanu, T. Butler, N.I. Rupesinghe, G.A.J. Amaratunga, S.J. Rashid, F. Udrea, M. Avram, G. Brezeanu; Ramp oxide termination structure using high-k dielectrics for high voltage diamond Schottky diodes; *Diamond and Related Materials*, **16** (2007) 1020–1024.

[176] S. Kumar, P. Ravindranathan, H.S. Dewan, R. Roy; Survival of diamond at 2200 °C in hydrogen; *Diamond and Related Materials*, **5** (1996) 1246–1248.

[177] G.Sh., S.A. Grot, C.W. Hatfield, A.R. Badzian, T. Badzian; High temperature Schottky diodes with thin-film diamond base; *IEEE Electron Devices Lett.*, **11** (1990) 371–372.

[178] T.H. Borst, S. Strobel, O. Weis; High-temperature diamond p–n junction: B-doped homoepitaxial layer on N-doped substrate; *Appl. Phys. Lett.*, **67** (1995) 2651–2653.

[179] J.W. Vandersande, L.D. Zoltan; Using high-temperature electrical resistivity measurements to determine the quality of diamond films; *Diamond and Related Materials*, **4** (1995) 641–644.

[180] A. Aleksov, A. Denisenko, E. Kohn, First epitaxial pnp bipolar transistor on diamond with deep nitrogen donor; *Electronics Lett.*, **35** (1999) 20.

[181] K. Horiuchi, A. Kawamura, T. Ide, T. Ishikura, K. Nakamura, S. Yamashita; Efficient free-exciton recombination emission from diamond diode at room temperature, *Jpn. J. Appl. Phys.*, **40** (2001) L275.

[182] P. Gluche, W. Ebert, A. Vescan, E. Kohn; Si-Based Schottky contacts on diamond with high barrier height and thermal stability; *3rd International High Temperature Electronics Conference, Albuquerque*, (NM) June 1996, *Transactions*, P189–P194.

[183] D. Zhou, D.M. Gruen, L.C. Qin, T.G. McCauley, A.R. Krauss; Control of diamond film microstructure by additions to CH_4/H_2 microwave plasmas; *J. Appl. Phys.*, **84** (1998) 1981–1989.

[184] S. Jiao, A. Sumant, M.A. Kirk, D.M. Gruen, A.R. Krauss, O. Auciello; Microstructure of ultrananocrystalline diamond films grown by microwave Ar–CH_4 plasma chemical vapour deposition with or without added H_2; *J.Appl. Phys.*, **90** (2001) 118–122.

[185] S. Bhattacharyya, O. Auciello, J. Birrell, J.A. Carlisle, L.A. Curtiss, A.N. Goyette, D.M. Gruen, A.R. Kraus, J. Schlueter, A. Sumant, P. Zapol; Synthesis and characterization of highlyconductiing nitrogen-doped ultrananocrystalline diamond films; *Appl. Phys. Lett.*, **79** (2001) 1441–1443.

[186] S. Bhattacharyya; Mechanism of high n-type conduction in nitrogen-doped nanocrystalline diamond; *Phys. Rev. B*, **70** (2004) 125412–1 to–10.

[187] J.E. Gerbi, O. Auciello, J. Birrell, D.M. Gruen, B.W. Alphenaar, J.A. Carlisle, Electrical contacts to ultra–nanocrystalline diamond; *Appl. Phys. Lett.*, **83** (2003) 2001.

[188] T. Zimmermann, K. Janischowsky, A. Denisenko, F. Hernandez, M. Kubovic, D.M. Gruen, E. Kohn; Nanocrystalline diamond pn-structure grown by hot-filament CVD, *Diamond and Related Materials*, **15** (2006) 203.

[189] R. Held, N. Kaminski, E. Niemann; SiC merged p–n/Schottky rectifiers for high voltage applications; *Materials Science Forum*, **264–268** (1998) 1057–1060.

[190] R. Singh, D.C. Capell, A.R. Hefner, J. Lai, J.W. Palmour; High-power 4H-SiC JSB rectifiers; *IEEE Trans. Electron. Devices*, **49** (2002) 2054.

[191] F. Roccaforte, F. La Via, S. Di Franco, V. Raineri; Dual metal SiC Schottky rectifiers with low power dissipation; *Microelectronic Eng.*, **70** (2003) 524–528.

[192] S.-K. Lee, C.-M. Zetterling, M. Östling, I. Aberg, M.H. Magnusson, K. Deppert, L.-E. Wernersson, L. Samuelson, A. Litwin; Reduction of the Schottky barrier height on silicon carbide using Au nanoparticles; *Solid State Electron.*, **46** (2002) 1433–1440.

[193] S.P. McGeoch, F. Placido, Z. Gou, C.J.H. Wort, J.A. Savage; Coatings for the protection of diamond in high-temperature environment; *Diamond and Related Materials*, **8** (1999) 916–919.

[194] E. Savrun; Packaging considerations for very high temperature microsystems; *Sensors, 2002. Proceeding of IEEE*, Vol.2 (2002) 1139–1143.

[195] P. Lardon, C. Mer, P. Delacour, B. Bazin, D. Tromson, S. Normand, M. Nesladek, F. Foulon, P. Bergonzo; Investigations of high quality diamond detectors for neutron fluency monitoring in a nuclear reactor; *Diamond and Related Materials*, **15** (2006) 815–821.

[196] A. Balducci, M. Marinelli, E. Milani, M.E. Morgada, G. Pucella, M. Scoccia, A. Tucciarone, G. Verona–Rinati, M. Angelone, M. Pillon, R. Potenza, C. Tuve; Growth and characterization of single crystal CVD diamond film based nuclear detectors; *Diamond and Related Materials*, **15** (2006) 292–295.

[197] A. BenMoussa, J.F. Hochedez, U. Schühle, W. Schmutz, K. Haenen, Y. Stockman, A. Soltani, F. Scholze, U. Kroth, V. Mortet, A. Theissen, C. Laubis, M. Richter, S. Koller, J.-M. Defise, S. Koizumi; Diamond detectors for LYRA, the solar VUV radiometer on board PROBA2; *Diamond and Related Materials*, **15** (2006) 802–806.

[198] Diamond Electrochemistry, A. Fujushima, Y. Einaga, T. Rao, D. Tryk (Eds.) Elsevier, 2005, 586 pp.

[199] G.M. Swain; Electroanalytical applications of diamond electrodes, in *Thin Film Diamond II (Semiconductor and Semimetals*, Vol. **77**), C. Nebel, J. Ristein (Eds) Elsevier, 2004.

[200] K. Soh, W. Kang, J. Davidson, S. Basu, Y. Wong, D. Cliffel, A. Bonds, G. Swain, Diamond-derived microelectrodes array for electrochemical analysis; *Diamond and Related Materials*, **13** (2004) 2009–2015.

[201] Y. Pleskov, *The Electrochemistry of Diamond*, in *Advances in Electrochemical Science and Engineering*, Vol. **8**, by R. Alkire and D. Kolb (Eds) John Wiley & Sons, 1999, 366 pp.

[202] W. Haenni, Ph. Rychen, M. Fryda, Ch. Comninellis, *Industrial applications of diamond electrodes*, in *Thin Film Diamond II (Semiconductor and Semimetals*, Vol. **77**), C. Nebel, J. Ristein (eds.) Elsevier, 2004., 396 pp.

[203] J.J. Wilman, T.P. Mollart, S.E. Coe, G.A. Scarsbrook, H.P. Godfried, P.S. Bray; Industrial scale diamond electrochemical waste disposal; *International Conference on New Diamond and Nano Carbons* (NDNC) May 2007, Osaka (Japan) abstract 24–5 123.

[204] M. Fryda, Th. Matthee, A. Hampel, L. Schäfer, I. Tröster; Fabrication and application of Diachem electrodes; *Diamond and Related Materials*, **12** (2003) 1950–1956.

[205] T. Knickerbocker, T. Strother, M.P. Schwartz, J.N. Russell, Jr., J.E. Butler, L.M. Smith, and R.J. Hamers; DNA–Modified Diamond Surfaces.; *Langmuir*, 2003, **19** (2003) 1938–1942.

[206] K.W. Song, Y. Nakamura, Y. Sasaki, M. Degawa, H. Kawarada; pH-sensitive diamond field-effect transistors with directly aminated channel surface; *Anal. Chim. Acta*, **573** (2006) 3–8.

[207] J. van de Langemaat, D. Vanmaekelbergh, J.J. Kelly, Electrochemistry of homo epitaxial CVD diamond: energetics and electrode kinetics in aqueous electrolytes; *J. Electroanalyt. Chem.*, **475** (1999) 139–151.

[208] J. Angus, H. Martin, U. Landau, Y. Evstefeeva, B. Miller and N. Vinokur; Conducting diamond electrodes: Application in electrochemistry, *New Diamond Frontier Carbon Technol.*, **9** (1999) 175.

[209] H. Kawarada, V. Araki, H. Umezawa, Electrolyte-solution-gate FETs using diamond surface for biocompatible ion sensors, *Phys. Stat. Sol. (a)*, **185** (2001) 79–83.

[210] A. Denisenko, G. Jamornman, H. El_Hajj, E. Kohn; pH sensor on O-terminated diamond using boron-doped channel; *Diamond and Related Materials*, **16** (2007) 905–910.

[211] T. Kondo, K. Honda, D. Tryk, A. Fujishima; Covalent modification of single-crystal diamond electrode surfaces; *J. Electrochem. Soc.*, **152** (2005) E18–E23.

[212] H. Notsu, I. Yagi, T. Tatsuma, D. Tryk, A. Fujishima; Introduction of oxygen–containing functional groups onto diamond electrode surface by oxygen plasma and anodic polarisation, *Electrochem. Solid State Lett.*, **2** (1999) 522–524.

[213] J. Wilson, J. Walton, G. Beamson; Analysis of chemical vapour deposited diamond films by X–ray photoelectron spectroscopy; *J. Electron Spectroscopy Relat. Phenom.*, **121** (2001) 183–201.

[214] Ch. Goeting, F. Marken, A. Osborn, R. Compton, J. Foord; Surface modification of chemical vapour deposited diamond induced by power ultrasound; *Electrochem. Solid–State Lett.*, **4** (2001) E29–E31.

[215] H. Notsu, I. Yagi, T. Tatsuma, D.A. Tryk, A. Fujishima; Surface carbonyl groups on oxidized diamond electrodes; *J. Electroanalyt. Chem.*, **492** (2000) 31–37.

[216] T. Rao, D. Tryk, K. Hashimoto and A. Fujishima; Band-edge movements of semiconducting diamond in aqueous electrolyte induced by anodic surface treatment, *J. Electrochem. Soc.*, **146** (1999) 680–684.

[217] A. Denisenko, C. Pientzka, A. Romanyuk, H. El–Hajj, E. Kohn; The electronic surface barrier of boron–doped diamond by anodic oxidation; *J. Appl. Phys.*, **103** (2008) 014904–014912.

[218] A. Colley, C. Williams, U. D'Haenens Johansson, M. Newton, P. Unwin, N. Wilson, J. Macpherson; Examination of the spatially heterogeneous electroactivity of boron-doped diamond microarray electrodes; *Anal. Chem.*, **78** (2006) 2536–2548.

[219] A. Perret, W. Haenni, P. Niedermann, N. Skinner, Ch. Comninellis, D. Gandini; Diamond electrodes and microelectrodes, *Electrochem. Soc. Proc.*, **97** (1997) 275.

[220] F. Montilla, E. Morallos, I. Duo, Ch. Comninellis, J. Vazquez; Platinum particles deposited on synthetic boron-doped diamond surfaces. Application to methanol oxidation; *Electrochimica Acta*, **48** (2003) 3891–3897.

[221] Y. Zhang, S. Asahina, S. Yoshihara, T. Shirakashi; Oxygen reduciton on Au nanoparticle deposited boron-doped diamond films; *Electrochimica Acta*, **48** (2003) 741–747.

[222] J. Foord, W. Hao, S. Hurst; Studies of the chemical functionalisation of diamond electrodes; *Diamond and Related Materials*, **16** (2007) 877.

[223] J.A. Alonso, Structure and Properties of Atomic Nanoclusters, Imperial College Press 2006, 410.

[224] F. Hernandez, A. Denisenko, E. Kohn; Nanoscale surface modification of diamond for enhanced electrochemical sensing, *Diamond and Related Materials*, **16** (2007) 867–871.

[225] C. Pietzka, M. Dipalo, A. Denisenko, Z. Gao, E. Kohn, O-Terminated boron doped NCD electrode with low background current; *Proceedings of Hasselt Diamond Workshop–SBBD XIII*, 25–28 Feb. 2008, Hasselt (Belgium) Paper 10.5.

[226] P. Bergveld; Thirty years of ISFETOLOGY; *Sensors and Actuators, B* **88** (2003) 1–20.

[227] M. Dipalo, C. Pietzka, A. Denisenko, H. El–Hajj, E. Kohn, O-Terminated nano-diamond ISFET for application in harsh environment; *Diamond and Related Materials*, (2008) to be published.

15 Optoelectronic Devices Using Homoepitaxial Diamond p–n and p–i–n junctions

TOSHIHARU MAKINO AND HIROMITSU KATO

Nanotechnology Research Institute, Ibaraki, Japan

15.1 Introduction 379
15.2 Electrical properties of p- and n-type diamond films 381
15.3 (001)-oriented homoepitaxial p–n junction diodes 384
  15.3.1 Fabrication process and diode structure 384
  15.3.2 Electrical properties 385
  15.3.3 Light-emitting properties 387
15.4 (001)-oriented homoepitaxial p–i–n junction diodes 389
  15.4.1 Fabrication process and diode structure 389
  15.4.2 Electrical properties 391
  15.4.3 Light-emitting properties 393
15.5 Light-emitting mechanism 395
15.6 Summary 396
  Acknowledgements 396
  References 397

15.1 INTRODUCTION

Robust, nontoxic, and high-efficiency, deep-ultraviolet (UV), solid-state light sources, such as light-emitting diodes (LEDs) and laser diodes, have become the focus of intensive research and development as alternatives to large, toxic, low-efficiency, gas lasers and mercury lamps, because of their wide applications in biochemical detection, data storage, air–water purification, germicidal treatment and white-light generation via phosphor excitation.

Diamond exhibits near band-edge emission at 235 nm (5.27 eV) due to free-exciton recombination associated with transverse optical phonons [1–3]. The excitons in diamond have a large binding energy (80 meV) and small Bohr radius (1.57 nm) because of the

CVD Diamond for Electronic Devices and Sensors Edited by Ricardo S. Sussmann
© 2009 John Wiley & Sons, Ltd. ISBN: 978-0-470-06532-7

low relative dielectric constant (5.7). Therefore, it is expected that high-density excitons of over 10^{18} cm^{-3} can be generated even at room temperature (RT) (25 meV) [4, 5]. Actually, excitonic emission has been observed by cathodoluminescence and photoluminescence measurements even at RT for high-temperature and high-pressure (HTHP) synthetic diamond [1] and high-quality diamond thin films grown by CVD [4]. Moreover, it should be noted that if the density of excitons in the steady state becomes much higher than the density of deep levels, due to defect and impurity states, it should be possible to decrease the effective recombination rate via deep levels, and consequently accelerate the radiative recombination rate of excitons. This should make it possible, in principle, to achieve a high internal quantum efficiency comparable to that of direct-transition semiconductors (the details are given in Section 15.5) Thus, diamond is an attractive material for deep-UV LEDs, although diamond is an indirect-transition semiconductor.

Recently, $Al_xGa_{1-x}N$ systems (e.g. AlN [6]) have been studied as deep-UV light-emitting materials. For these systems, quantum-well and double-hetero-structures can be formed as the active layer of LEDs by heteroepitaxial growth of different compositional materials. Such band engineering increases the extraction efficiency because the cladding layers are optically transparent to the light emitted from the active layers. On the other hand, these systems contain high-density threading dislocations due to the lattice mismatch and the heterovalency between the substrates and the epitaxial films. Exceptionally, GaInN/GaN systems show high radiative efficiency, because fluctuations in the indium content in GaInN cause carriers to be localized in potential minima, thus preventing carriers from reaching dislocations. However, this effect cannot be expected in the deep-UV light region, and decreasing the dislocation density is the essential issue.

As for diamond, it is difficult to form quantum-well and double-hetero-structures at present, so the light extracting efficiency should be increased by designing another appropriate device structure. Diamond is a single element semiconductor, like silicon, which makes it possible to grow higher quality single crystals as compared with compound semiconductors. Indeed, high-quality diamond thin films have already been fabricated by homoepitaxial growth using chemical vapor deposition (CVD) [7, 8], and both p- [9] and n-type [10] conductivities with high mobilities have been controlled, as will be seen in Section 15.2. Also, diamond possesses excellent physical and electrical properties, such as high thermal conductivity and excellent radiation hardness [11]. These characteristics are suitable for the base material of deep-UV light LEDs, and are major advantages of diamond when compared with other competing materials.

The first report of a diamond deep-UV LED was presented by Koizumi *et al.* [12] in 2001, who succeeded in fabricating homoepitaxial diamond p-n junctions with boron (B)-doped p-type and phosphorus (P)-doped n-type layers on a HTHP-synthesized, B-doped (111) single-crystalline diamond substrate. Their p-n junction diodes showed good diode characteristics with a rectification ratio of over 10^8, and clear, sharp, deep-UV light emission due to free-exciton recombination was observed at RT. However, as will be seen in Section 15.2, LEDs structured using a (001)-oriented substrate would be more suitable for real applications.

On the other hand, Horiuchi *et al.* [13] developed diamond LEDs on (001)-oriented surfaces, using sulfur (S)-doped thin films as the n-type layer [14]. Although Hall-effect measurements did not show clear evidence of n-type conduction for the S-doped CVD diamond layer [15, 16], the junction showed a rectification ratio of 10^3 at RT, and a relatively high performance of excitonic emissions was obtained. Best performance values reported for this LED structure to date include a 0.027 % external quantum efficiency and 7-μW output power at 10 mA [17]. In order to attain higher efficiency and improve this LED, the S-doped layer needs to be improved.

In line with these research trends, we have continued to study exciton-related diamond deep-UV LEDs as well as the fundamental characteristics of excitons in diamond [13]. In order to make full use of the characteristics of excitons in diamond, in 2005 we developed (001)-oriented P-doped diamond films, which show clear n-type conductivity, by optimizing the conditions for CVD growth [18]. This was a significant breakthrough toward eliminating the restrictions on crystal orientation for n-type doping, and for fabricating LEDs for a wide range of applications. Indeed, LEDs with good diode characteristics have been fabricated on (001)-oriented substrate and high-efficiency, exciton-related, diamond LEDs have been realized [19, 20].

This chapter describes, the recent status of p- and n-type electrical properties for homoepitaxial diamond thin films, including the technical aspects of P-doped diamond growth. Next, fabrication processes and electrical and light-emitting characteristics of (001)-oriented homoepitaxial diamond p–n and p–i–n junction diodes are described. Finally, the light-emitting mechanism is discussed.

15.2 ELECTRICAL PROPERTIES OF P- AND N-TYPE DIAMOND FILMS

In order to develop LEDs, several fundamental technological issues must be improved upon, including intrinsic diamond growth, p- or n-type doping, contact fabrication, and etching technology. Especially, it remains difficult to optimize n-type doping and its associated technologies in diamond synthesis. Recent progress and remaining issues are summarized in Table 15.1.

For p-type diamond, the impurity boron is easily incorporated into both natural and synthetic diamond by CVD without any restriction on crystal orientation (see Chapter 3 by Mainwood in this book). Figure 15.1 shows typical temperature-dependent variations

Table 15.1 Crystal orientation dependence of characteristics for diamond

		Crystal orientation	
		(001)	(111)
Substrate	Mechanical polishing	easy	difficult
	Size	larger	limited (~2 mm × 2 mm)
	Electrical conductivity		
	p-type	$B(E_A: 0.37\ \text{eV})$	$B(E_A: 0.37\ \text{eV})$
	n-type	S (unclear)	
CVD film		$P(E_D: 0.57\ \text{eV})$	$P(E_D: 0.57\ \text{eV})$
	Ohmic contact		
	p-type	○ ($10^{-5}\ \Omega\text{cm}^2$)	○
	n-type	× ($10^{+5}\ \Omega\text{cm}^2$)	Δ (~ $10^{+3}\ \Omega\text{cm}^2$)
	Performance (Schottky, electrical, optical)	Performances on (001) sub. are better than those on (111) sub. for non-doped and *p*-type diamond.	

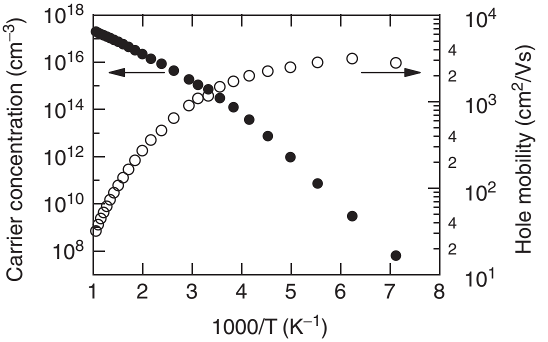

Figure 15.1 Typical temperature-dependent variations in carrier concentration and mobility for p-type diamond film with a boron concentration of ~2×10^{17} cm^{-3}

in carrier concentration and mobility for p-type diamond film on (001) orientation with a boron concentration of ~2×10^{17} cm^{-3} determined by Hall-effect measurements. The boron acceptor level was found to be ~0.37 eV above the top of the valence band. The mobility at RT of B-doped CVD diamond has now reached over 1000 cm^2/Vs. The compensation ratio was evaluated to be 0.2–0.5 %. As for (111)-oriented p-type films, the maximum mobility at RT and lowest compensation ratio are around 600 cm^2/Vs and 3 %, respectively [21]. The electrical properties of B-doped diamond film on (001) substrate are considered to be better than those on (111) substrate. For the Schottky junctions, a good ideality factor *n* of ~1.1 and undetectable leakage current can be achieved between various metals such as Al, Zn, Cr, Ni, Au or Pt and oxidized, B-doped, CVD diamond films. These results indicate that the quality of recent B-doped diamond films is at least comparable with that of conventional semiconductors such as Si and GaAs. The ohmic contacts for the p-type layer are easily produced by titanium carbide (TiC) alloys. The specific resistance of the contacts was analyzed by means of the linear transmission line model, and it can be reduced to ~10^{-5}–10^{-6} Ωcm^2 to satisfy the operational requirements of diamond electronic devices [22]. As noted here, technical aspects for p-type diamond have almost been established.

In contrast, n-type diamond is not present in nature, and controlled n-type doping had been considered almost impossible until 1997. Among the Group V elements, nitrogen was one of the candidates for n-type doping because of its similar covalent bond length (0.74 Å) to that of diamond (0.77 Å), but unfortunately, it forms a deep donor level at ~1.7 eV below the bottom of the conduction band, due to its structural distortion from the substitutional position in the diamond lattice [23]. Phosphorus has long been considered as another candidate for n-type doping. In 1997, Koizumi *et al.* [24] experimentally demonstrated the growth of n-type diamond on (111)-oriented diamond substrates by using phosphorus and CVD with a mixture of PH_3, CH_4, and H_2 gases. n-Type conductivity was identified by Hall measurements, and its temperature dependence revealed that the phosphorus donor level is ~0.57 eV. These achievements spurred efforts to grow high-quality, P-doped, n-type diamond films [10, 25–28], and mobilities have now reached ~660 cm^2/Vs by lightly phosphorus doping [10]. However, this discovery of phosphorus doping was restricted to the (111)-oriented diamond lattice structure. As shown in Table 15.1, to bring diamond electronic applications closer to real markets and to manufacture bipolar devices for a wide range of applications, it is necessary to control n-type doping using phosphorus on (001)-oriented crystals.

The process window for phosphorus doping is quite different between (001)- and (111)-oriented diamond growth [29]. Phosphorus doping on (001) substrate with parameters optimized for (111) doping does not result in any detectable incorporation of impurities (P, B, N, H, etc.) using secondary-ion mass spectroscopy (SIMS) analysis, owing to its quite slow growth rate around ~10 nm/h. Moreover, merely increasing phosphine PH_3 gas flow under (111) conditions did not lead to (001) phosphorus doping. The growth rate is thus a key parameter for impurity incorporation during CVD diamond growth. On the other hand, defect creation also depends on the growth rate. Defects that would compensate free carriers are considered to increase with an increase in the growth rate. Therefore, it is necessary to optimize methane (CH_4) gas flow rate as well as PH_3 in order to obtain the process window for (001) doping.

Based on this knowledge, phosphorus doping conditions were carefully optimized, and (001) n-type doping was finally achieved in 2005 by using different conditions compared with those used for (111) growth [18]. The phosphorus incorporation and its distribution were characterized by SIMS analysis. n-Type conductivity was confirmed by Hall-effect measurements over a temperature regime of 300–1000 K. Figure 15.2 shows typical temperature-dependent variations in carrier concentration and mobility for n-type diamond film with a phosphorus concentration of $\sim 5 \times 10^{17}$ cm^{-3} as determined by Hall-effect measurements. The highest mobility, up to 780 cm^2/Vs at RT, was obtained for (001) lightly P-doped diamond film. The donor level is ~0.57 eV, which is equal to that of (111) P-doped diamond, while the compensation ratio for (001) P-doped diamond is ~50–80 %, which is about one order of magnitude higher than that reported for (111) diamond. The concentration of free electrons at RT is as low as $\sim 10^{10}$ cm^{-3} owing to its deep donor level and large compensation ratio. Such carrier compensation is nonnegligible in (001) P-doped diamond. In addition, TiC contact did not show perfect ohmic current-voltage characteristics for the n-type layer. Usually in (111) diamond, phosphorus with a concentration exceeding $\sim 10^{19}$ cm^{-3} is introduced under the electrodes in order to form ohmic contacts [30], whereas heavy doping has yet to be achieved in (001) P-doped diamond [31]. The specific resistance for the n-type layer is around 10^3–10^5 Ωcm^2, which is significantly higher than that for the p-type layer ($\sim 10^{-5}$–10^{-6} Ωcm^2). The development

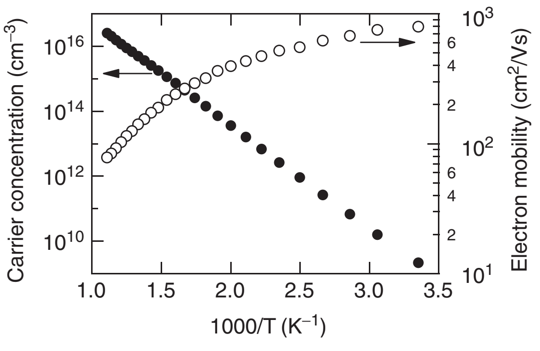

Figure 15.2 Typical temperature-dependent variations in carrier concentration and mobility for n-type diamond film with a phosphorus concentration of $\sim 5 \times 10^{17}$ cm^{-3}

of good ohmic contact with low specific resistance is the next key subject for n-type diamond research.

Phosphorus n-type doping of (111)- and (001)-oriented diamond has finally been achieved nearly 10 years after the discovery of phosphorus doping, and is a major step toward using diamond in bipolar electronic applications with p–n junctions. However, unfortunately, the electrical properties achieved for n-type diamond are still behind those for p-type. Continuing research and development on the technical aspects of n-type doping is necessary.

15.3 (001)-ORIENTED HOMOEPITAXIAL P–N JUNCTION DIODES

Based on the high quality of (001)-oriented, B-doped, CVD diamond films and successful control of n-type conductivity on (001)-oriented surfaces, we have fabricated (001)-oriented homoepitaxial diamond p-n junction diodes and characterized their electrical and light-emitting properties [20, 32].

15.3.1 Fabrication process and diode structure

B- and P-doped layers were independently grown by CVD using a mixture of CH_4 and H_2 gas on HTHP synthetic Ib (001) B-doped, single crystalline, diamond with a resistivity of approximately 10^{-2} Ω cm. The surface morphology of (001)-oriented diamond film is closely related to the misorientation angle of the substrate. We selected a substrate with a relatively large misorientation angle of about 3° to suppress the generation of nonepitaxial crystallites and pyramidal hillocks. As impurity source gases, PH_3 diluted with H_2 was used for phosphorus doping. The phosphorus concentration was estimated by SIMS to be $2–5 \times 10^{18}$ cm^{-3} using another specimen. Boron doping with a concentration of $2–4 \times 10^{16}$ cm^{-3} was achieved with CH_4 and H_2 plasma by an after-effect following heavy boron doping deposition by B_2H_6. The thicknesses of both the B- and P-doped layers were about 1 μm. Details of the growth conditions for both the B- and P-doped layers are summarized in Table 15.2.

After the growth, mesa-structures of 240 μm diameter were fabricated by conventional photo-lithography and inductively coupled plasma etching processes in order to reduce

Table 15.2 Growth conditions for each layer of the $p-n$ junction diode

		p-type layer	*n*-type layer
Gas flow rate	H_2:	399 sccm	397 sccm
	CH_4	0.8 sccm	1.6 sccm
	Impurity gas:	0 sccm[a]	(PH_3/H_2)[b] 1.6 sccm
	Gas pressure:	25 Torr	25 Torr
	Microwave power:	750 W	750 W
	Substrate temperature:	800 °C	900 °C

[a] For the B-doped layer, the residual B in the growth chamber was used as impurity gas.

[b] $PH_3/H_2 = 5\%$.

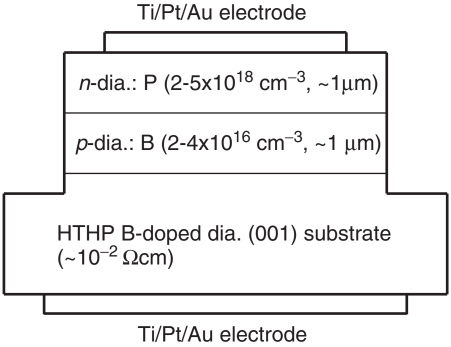
Ti/Pt/Au electrode
n-dia.: P (2-5x10^18 cm^-3, ~1μm)
p-dia.: B (2-4x10^16 cm^-3, ~1 μm)
HTHP B-doped dia. (001) substrate
(~10^-2 Ωcm)
Ti/Pt/Au electrode

Figure 15.3 Schematic diagram of the (001)-oriented homoepitaxial diamond p-n junction diode

the leakage current. Then, the p–n junction structures were kept in a mixture of H_2SO_4 and HNO_3 at 200 °C for 60 min to remove any surface contamination, and to terminate the surface with oxygen. Finally, Ti (30nm)/Pt (30nm)/Au (100nm) electrodes of 200 μm in diameter and 2.5 mm square were formed on the n-type layer and the back of the Ib (001) B-doped substrate, respectively, and were annealed at 420 °C for 30 min in Ar ambient atmosphere. Figure 15.3 shows a schematic diagram of the p–n junction diode.

15.3.2 Electrical properties

To assess the diode quality, we first observed the current–voltage ($I-V$) and capacitance–voltage ($C-V$) characteristics in detail. All electrical properties were measured in vacuum.

Figure 15.4 shows typical $I-V$ properties of the p–n junction diodes at RT. A clear rectification characteristic with a rectification ratio of about 10^6 at $\pm$ 30 V was observed. The reverse current level at -30 V was about 1×10^{-10} A, which might have been due to localized imperfections in the mesa-etched p–n junction area. The gradual increase in the current at the forward bias voltage originates from the high series resistance of the p–n junction diode, especially the n-type layer, with resistivity of the order of 10^6 Ω cm and/or higher [31]. The contact resistance is considered to be almost equivalent to or less than the device impedance.

We observed a $C-V$ characteristic predicted by conventional p–n junction theory, indicating the existence of a space–charge layer in the vicinity of the p–n junction diode. Figure 15.5(a) shows the capacitance at zero bias voltage as a function of frequency for the p–n junction diode at some typical temperatures. Two types of drop in capacitance values (i.e. the characteristic values of the capacitance starts to decrease) with frequency were clearly observed. One was observed at the frequency of 10^3 Hz at 25 °C (denoted by an open arrow), and the other was observed at 10^3 Hz at 200 °C (denoted by a solid arrow). These drops (denoted by open and solid arrows) originate from the slow thermal emission rate of deep dopants, such as boron acceptor level (E_A) located at 0.37 eV above the valence band maximum, and phosphorus donor level (E_D) at 0.57 eV below the conduction band minimum, respectively, which are unable to follow the high-frequency voltage modulation and so cannot contribute to the space–charge in the space–charge layer [33, 34]. At high temperatures, these characteristics are improved up to higher frequency, that is, the capacitance drop shifts to higher frequency as shown

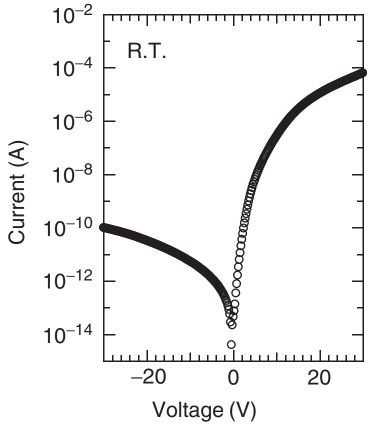

Figure 15.4 Typical current–voltage characteristics of the p–n junction diode at room temperature

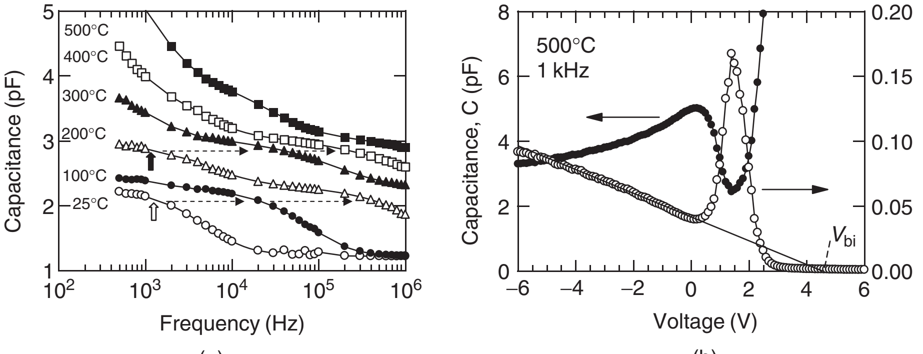

(a)

(b)

Figure 15.5 (a) Capacitance at zero bias voltage as a function of frequency for the p–n junction diode at some typical temperatures. (b) Capacitance–voltage characteristics for the p–n junction diode at 1 kHz and 500°C

by broken arrows in Figure 15.5(a), because the thermal emission rate of deep dopants becomes faster. Meanwhile, as shown in Figure 15.5(a), the capacitance value increases on the lower-frequency side at high temperatures of over 300 °C. This result originates from deep levels in the vicinity of the p–n junction as described later.

C–V measurements were carried out at sufficiently low frequency and/or high temperature in order to minimize deep dopant effects. Figure 15.5(b) shows the results of a C–V measurement at 1 kHz and 500 °C for the p–n junction diode. The $1/C^2$–V plot has good linearity in the reverse bias voltage region. The $1/C^2$ value, which is derived from the capacitance caused by the space–charge region for the p–n junction diode, can be written as:

$$\frac{1}{C^2} = \frac{2}{q\varepsilon_0\varepsilon_r S^2 N_i}(V_{bi} - V) \tag{15.1}$$

where N_i is the combined net space–charge density of both the p- and n-type layers, V_{bi} is the built-in potential, q is the elementary charge, ε_r is the relative dielectric constant of diamond, ε_0 is the permittivity of free space, and S is the electrode area. According to Equation (15.1), we estimated N_i as 2.5×10^{16} cm^{-3} from the reciprocal slope of the $1/C^2 - V$ characteristics at the reverse bias voltage, as shown by the fitting line in Figure 15.5(b). Also qV_{bi} was estimated as 4.7 eV from the extrapolation of the fitting line to zero. The estimated value of N_i is almost identical to the boron concentration of $2–5 \times 10^{16}$ cm^{-3}, and is two orders of magnitude lower than the phosphorus concentration of $2–5 \times 10^{18}$ cm^{-3}. Therefore, the N_i of the p–n junction diode corresponds to the boron acceptor density in the p-type layer. These results indicate that the space–charge layer extends practically to the p-type layer side. The estimated qV_{bi} is in good agreement with the expected qV_{bi} of about 4.3 eV, which was obtained with the simple equation $qV_{bi} = E_g - E_A - E_D$ at 500 °C, where E_g is the energy gap of diamond.

As shown in Figure 15.5(b), the $1/C^2 - V$ characteristics have a peak at the forward bias voltage near the zero current. This peak showed a strong frequency dependence. These characteristics indicate the existence of electrically active deep levels except for the boron acceptors and phosphorus donors in the vicinity of the p–n junction. The relatively high leakage current of $I - V$ characteristics as shown in Figure 15.4 would be affected by these deep levels.

15.3.3 Light-emitting properties

By injecting the carriers to the p–n junction diode under forward bias voltage, visible light emission was observed at over 0.7 mA, and the intensity increased gradually as the current was increased. At currents over 20 mA, we observed a sharp emission with a peak wavelength of 235 nm (5.27 eV), which was attributed to free-exciton recombination coupled with transverse-optical phonons (FE_{TO}). Figure 15.6 shows photographs of the

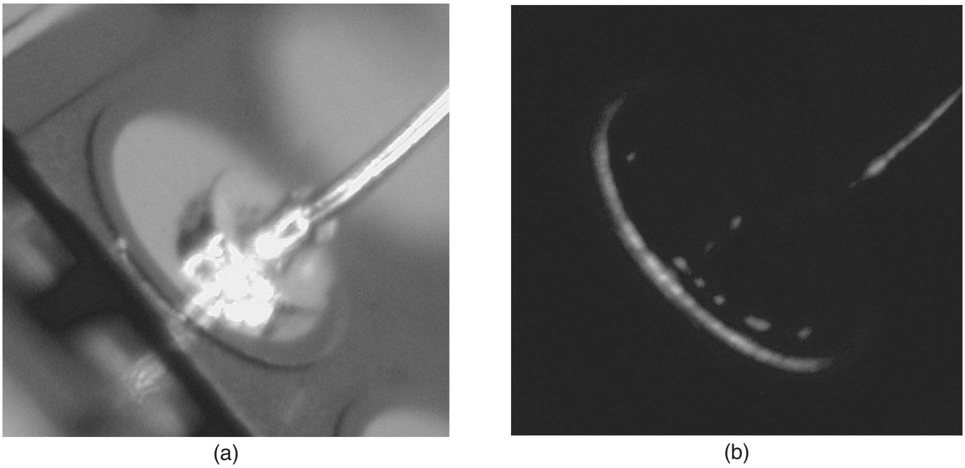
(a) (b)

Figure 15.6 (a) Photograph of the p–n junction diode by white-light illumination at zero bias voltage. (b) Deep-UV light emission without white-light illumination by forward current injection. Green light, which comes from the vertical sidewall of mesa-structure and around the electrode, can be seen at the same time as deep-UV light emission. A UV sensitive camera was not used to detect the light in photograph (b); however, we have confirmed that there is emission in the UV by measuring the electroluminescence spectrum at this forward current. See plate 7

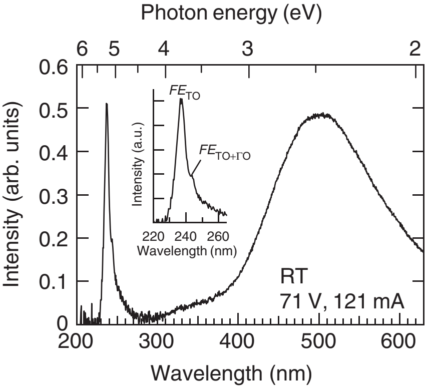

Figure 15.7 Typical light emission spectrum of the p–n junction diode under the bias voltage of 71 V and forward current of 121 mA at room temperature. The inset shows the spectrum expanded at around 235 nm

light emission. The visible light comes from the vertical sidewall of the mesa-structure, and around the electrode. Figure 15.7 shows the current-injected light emission spectra of the p–n junction diode under the forward bias voltage of 71 V and current of 121 mA at RT in vacuum. The light-emitting spectra were corrected according to the spectral sensitivity of the measurement system achieved by a standard halogen and deuterium lamps. As shown in Figure 15.7, strong emission of FE_{TO} and its phonon replica ($FE_{\text{TO}+\Gamma\text{O}}$) with the peak wavelength of 243 nm (5.1 eV) was observed. Broadband emissions from deep levels were also observed at the peak wavelengths of around 350 nm (3.5 eV) and 500 nm (2.5 eV) in the visible light region. The origin of these deep-level emissions has not yet been clarified, although 350-nm band emission is often observed by cathodoluminescence of B-doped [35] and (001)-oriented, P-doped, diamond thin films [31], and the extended defect related emission [36] such as band-A emission and the emission related to nitrogen-vacancy complexed defects [37] are well known as emissions in the visible region.

Figure 15.8 shows the ratio of the integrated intensity of the excitonic emissions relative to the deep level ($I_{\text{FE}}/I_{\text{deep}}$) as a function of the current. It was found that the relative

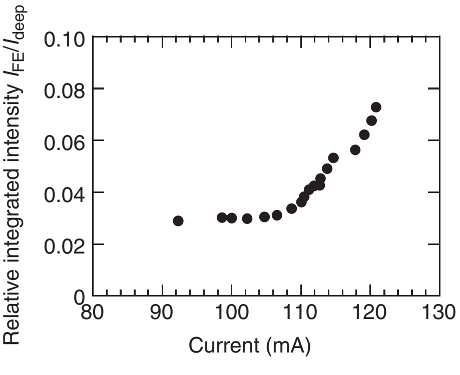

Figure 15.8 Relative integrated intensity of the excitonic emissions to deep-level emissions for the p–n junction diode as a function of the current

integrated intensity increases superlinearly as the forward current is increased. This trend would originate from the superior excitonic nature of diamond, such as the generation of high-density excitons of over 10^{18} cm^{-3} even at RT. We discuss this trend in detail in Section 15.5.

Thus, strong FE_{TO} emission could be realized by the good crystallinity of p- and n-type layers grown on the (001)-oriented substrate and good p–n junction diode characteristics. However, the relative integrated intensity is still only 7 %, even at the high current of 121 mA. The defect states related to the deep-level emissions would presumably exist in high concentration in the vicinity of the p–n junction as indicated from the electrical characteristics of the p–n junction diode. The key point in increasing the excitonic emission intensity is how to improve the crystallinity in the vicinity of the p–n junction.

15.4 (001)-ORIENTED HOMOEPITAXIAL P–I–N JUNCTION DIODES

In order to increase deep-UV light emission due to exciton recombination and to suppress the deep-level emission simultaneously, we fabricated (001)-oriented homoepitaxial diamond p–i–n junction diodes by sandwiching the intrinsic layer, which has a low impurity concentration and low density of deep levels, between p- and n-type layers, and characterized their electrical and light-emitting properties [19, 38].

15.4.1 Fabrication process and diode structure

The heavily B-doped p^+-type, B-doped p-type, intrinsic, and P-doped n-type layers were grown by CVD using a mixture of CH_4 and H_2 as source gases, and B_2H_6 and PH_3 as doping gases on HTHP synthetic Ib (001) single crystalline diamond, with a misorientation angle of about 1°. The p-type and intrinsic layers were grown in the same CVD chamber, and other layers were independently grown in other chambers. For the intrinsic layer, O_2 was added in the feeding gas to reduce the contamination of slight boron and other impurity atoms [39]. Details of the growth conditions for each of the p^+-, p-, intrinsic, and n-type layers are summarized in Table 15.3.

Table 15.3 Growth conditions for each layer of the $p-i-n$ junction diode

		p^+-type layer	p-type layer	intrinsic layer	n-type layer
Gas flow rate	H_2:	206 sccm	398 sccm	397 sccm	397 sccm
	CH_4:	2.4 sccm	2.4 sccm	2.4 sccm	1.6 sccm
	Impurity gas:	$(B_2H_6/H_2)^a$ 192 sccm	0 sccm[b]	(O_2) 1.0 sccm[c]	$(PH_3/H_2)^d$ 1.6 sccm
	Gas pressure:	50 Torr	50 Torr	50 Torr	25 Torr
	Microwave power:	1200 W	1200 W	1200 W	750 W
	Substrate temperature:	800–900 °C	800–900 °C	800–900 °C	900 °C

[a] $B_2H_6/H_2 = 0.01\%$.

[b] For the B-doped layer, the residual B in the growth chamber was used as impurity gas.

[c] For the intrinsic layer, O_2 was added to reduce the impurity contamination.

[d] $PH_3/H_2 = 5.0\%$.

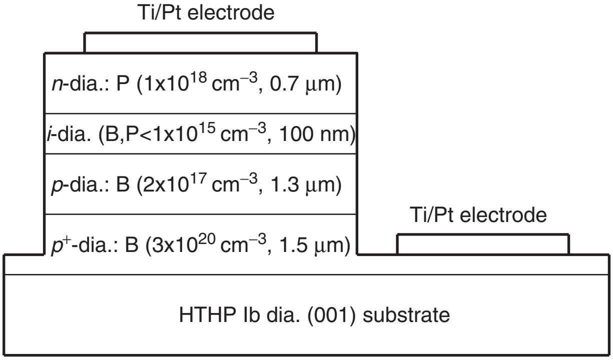
Ti/Pt electrode
n-dia.: P (1x10^18 cm^-3, 0.7 μm)
i-dia. (B,P<1x10^15 cm^-3, 100 nm)
p-dia.: B (2x10^17 cm^-3, 1.3 μm)
Ti/Pt electrode
p+-dia.: B (3x10^20 cm^-3, 1.5 μm)
HTHP Ib dia. (001) substrate

Figure 15.9 Schematic diagram of the (001)-oriented homoepitaxial diamond p–i–n junction diode

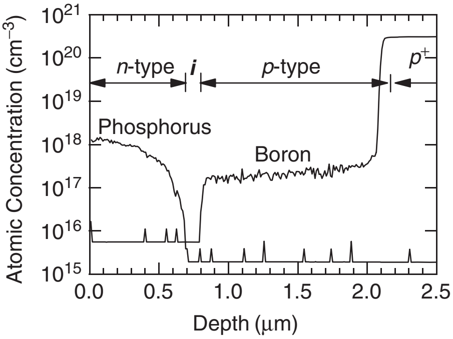

Figure 15.10 SIMS depth profiles of the p–i–n junction. The detection limits are 6×10^{15} cm^{-3}, 2×10^{15} cm^{-3} for boron and phosphorus atoms, respectively

The processes of fabricating mesa-structures and electrodes for the p–i–n junction diodes were almost the same as those for the p–n junction diode [20]. The size of mesa-structures was 120 μm in diameter. The sizes of Ti (30nm)/Pt (100nm) electrodes on the n-type and p^+-type layers were 100 and 400 μm in diameter, respectively. Figure 15.9 shows the schematic structure of the p–i–n junction diode.

To evaluate the impurity concentrations and thicknesses of each layer and interdiffusion, SIMS analysis was performed. Figure 15.10 shows SIMS depth profiles of the p–i–n junction. These profiles reveal that an intrinsic layer with a thickness of about 0.1 μm clearly forms between the p- and n-type layers without an intermixture area of boron and phosphorus atoms. The impurity concentrations of boron and phosphorus atoms in the intrinsic layer are below the detection limit of the order of 10^{15} cm^{-3}, indicating that O_2 in the feeding gas effectively suppresses the incorporation of impurity atoms during deposition of the intrinsic layer. The impurity concentration of p^+-, p-, and n-type layers was 3×10^{20} cm^{-3}, 2×10^{17} cm^{-3}, and 1×10^{18} cm^{-3}, respectively. The thickness of p^+-, p-, and n-type layers was ∼1.5 μm, 1.3 μm, and 0.7 μm, respectively.

15.4.2 Electrical properties

Figure 15.11 shows typical $I-V$ properties of the p–i–n junction diodes at RT. A clear diode characteristic with rectification ratio of about 10^{10} at ±25 V was observed. As described in Section 15.3.2, the gradual increase in the current at the forward bias voltage originates from the high series resistance of the p–i–n junction diode [31]. The contact resistance is considered to be almost equivalent to, or less than, the device impedance.

Figure 15.12(a) shows the capacitance at zero bias voltage as a function of frequency for the $p-i-n$ junction diode at some typical temperatures. Two types of drop in capacitance values (i.e. the characteristic values of the capacitance starts to decrease) with frequency were clearly observed. One was observed at the frequency of 10^3 Hz at 25 °C (denoted by an open arrow), and the other was observed at 800 Hz at 100 °C (denoted by a solid arrow). These drops in capacitance originate from the deep dopant effect of boron acceptor [34] and phosphorus donor [33], respectively, as described in Section 15.3.2. At higher temperatures, the capacitance drop shifts to a higher frequency as shown by broken arrows in Figure 15.12(a), because the thermal emission rate of deep dopants increases as the temperature increases. Meanwhile, as shown in Figure 15.12(a), the increase of the capacitance value on the lower frequency side at high temperature, which was seen for the p–n junction diode shown in Figure 15.5(a), was not observed for the p–i–n junction diode. This result indicates that the crystallinity in the vicinity of the p–i–n junction was improved.

As shown in Figure 15.12(a), the capacitance value on the lower frequency side almost saturated at temperatures higher than 300 °C. This trend could be explained by the temperature dependence of the bulk resistance of the p–i–n junction (R_{bulk}), especially the resistance of the n-type layer, as follows. From the simple equivalent circuit model shown in Figure 15.12(b), the capacitance measured by LCR meter (C_{meas}) at sufficiently lower frequency (ω) than 1 kHz for the p–i–n junction diode is given by:

$$C_{meas} = \frac{C_{pin}}{(1 + R_{bulk}/R_{leak})^2 + \left(\omega C_{pin} R_{bulk}\right)^2} \tag{15.2}$$

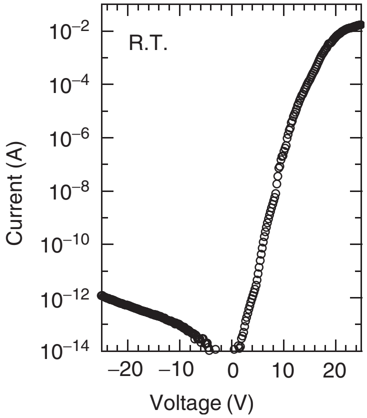

Figure 15.11 Typical current–voltage characteristics of the p–i–n junction diode at room temperature

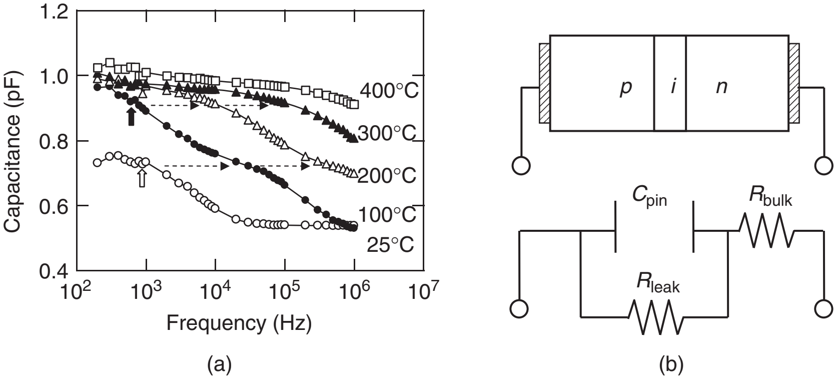

Figure 15.12 (a) Capacitance at zero bias voltage as a function of frequency for the p–i–n junction diode at some typical temperatures. (b) Model circuit representing the temperature dependence of capacitance at lower frequency

where C_{pin} is the combined capacitance due to the space–charge layer extending to the p-, i- and n-type layers, R_{leak} is the resistance of the leakage current path for the p–i–n junction diode. According to this equation, C_{meas} depends on R_{bulk}. We estimated that R_{bulk} decreased from the order of 10^6 to 10^2 Ω by Hall-effect measurements when the temperature increased from RT to 300 °C. Therefore, the influence of R_{bulk} could be neglected at temperatures higher than 300 °C, and so the value of C_{meas} is almost equivalent to C_{pin}.

Figure 15.13 shows the results of C–V measurement at a sufficiently low frequency of 1 kHz at the high temperature of 400 °C for the p–i–n junction diode. As shown in this figure, the capacitance increases gradually as the bias voltage is increased from −20 to +2 V (region I in Figure 15.13). This trend shows the existence of a space–charge layer extending to the p- and n-type layers and its narrowing as the bias voltage is changed from −20 to +2 V. At around 2–4 V, once the slope of the C–V curve becomes small (region II), the capacitance increases drastically as the bias voltage is increased (region III). The almost constant capacitance at around 2–4 V might correspond to that of the intrinsic layer, and the drastic increase of the capacitance for bias voltages higher than 4 V might correspond to the change due to the carrier injection in the intrinsic layer.

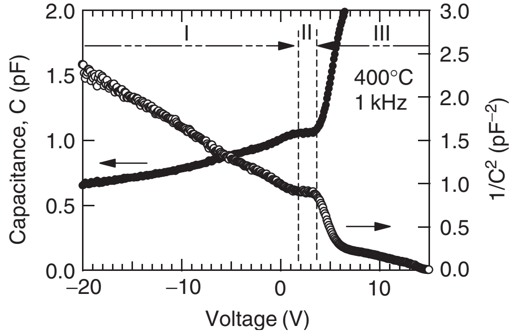

Figure 15.13 Capacitance–voltage characteristics for the p–i–n junction diode at 1 kHz and 400°C

The impurity (B and/or P) concentration in the intrinsic layer is less than 10^{15} cm^{-3}. However, the p–i–n junction diode has a few space charges in the intrinsic layer due to the presence of these few impurities. As a result, the $I-V$ and $C-V$ characteristics are complicated at a bias voltage higher than around 4 V (region III).

For the (001)-oriented diamond p–n junctions [32], $1/C^2-V$ properties had a peak at the forward bias near $1/C^2 = 0$. This characteristic indicates the existence of electrically active deep levels with a higher density than that of boron acceptors and/or phosphorus donors in the vicinity of the p–n junction. In the case of the p–i–n junction diodes as shown in Figure 15.13, there is no significant peak in the $1/C^2-V$ curve. Therefore, the density of deep levels could be decreased in comparison with that of the p–n junction diodes.

15.4.3 Light-emitting properties

At a forward current exceeding 5 μA, visible light emission began to be observed, and then deep-UV light emission was observed in the spectrum above 6 mA. Figure 15.14 shows a typical light emission spectrum of the p–i–n junction diode observed at RT. The spectrum was obtained by forward carrier injection under a current of 79 mA at a voltage of 30 V. Strong, sharp deep-UV emission with a peak wavelength of around 240 nm, which is attributed to FE_{TO} and $FE_{\mathrm{TO+\Gamma O}}$, can be clearly observed. What is significant in the present demonstration as shown in Figure 15.14 is that UV emission intensity is considerably higher than the emission due to deep levels, in other words, the emission due to deep levels is significantly suppressed. This result is supported by the analysis of SIMS data (Figure 15.10), the $I-V$ characteristic (Figure 15.11) and the $C-V$ characteristic (Figure 15.13).

A very interesting trend was found as shown in the inset of Figure 15.14, that is, the integrated intensity of excitonic emission (I_{FE}) increases superlinearly, whereas the slope of integrated intensity of deep-level emission (I_{deep}) decreases with increasing current. The same trend was observed for the p–n junction diodes. Figure 15.15 shows the relative integrated intensity of FE_{TO} and $FE_{\mathrm{TO+\Gamma O}}$ to the broadband due to deep levels ($I_{\mathrm{FE}}/I_{\mathrm{deep}}$) as a function of the forward current. It was found that $I_{\mathrm{FE}}/I_{\mathrm{deep}}$ increases nonlinearly

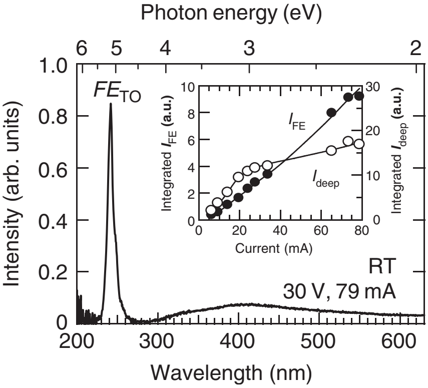

Figure 15.14 Typical light emission spectrum of the p–i–n junction diode under the bias voltage of 30 V and forward current of 79 mA at room temperature. The inset shows the integrated intensity of excitonic emission (I_{FE}) and deep-level emission (I_{deep}) as a function of the current

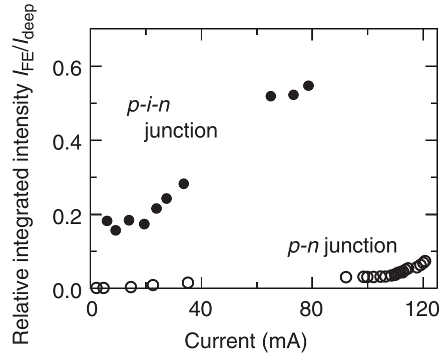

Figure 15.15 Relative integrated intensity of the excitonic emissions to the deep-level emissions (I_{FE}/I_{deep}) for the p–i–n junction diode as a function of the current. I_{FE}/I_{deep} for the p-n junction diode [21] is also shown for comparison

from 0.17 to 0.55 as current increases from 6 to 79 mA. On the other hand, for the p–n junction diodes, I_{FE}/I_{deep} increased from 0.002 to 0.08 as the forward current increases from 15 to 125 mA (see Figure 15.8). Thus, the value of I_{FE}/I_{deep} for the p–i–n junction improved about twentyfold compared with that of the p–n junction diodes. I_{FE}/I_{deep}, moreover, increased to 0.55 as the current was increased to ~79 mA. Thus, deep-UV light emission characteristics of homoepitaxial diamond LEDs could be significantly improved by sandwiching the high-quality intrinsic layer between p- and n-type layers.

Figure 15.16 shows the free-exciton emission spectra at the forward current of 30 mA for the p–i–n junction diode under various ambient temperatures, where the signal to noise ratio of the spectra is different from that in Figure 15.14 because the diode and the experimental conditions are different from those in Figure 15.14. No changes in spectral shape and intensity could be seen between RT and 200 °C. This result indicates that the actual junction temperature at 30 mA became at least 200 °C, even though the ambient temperature is RT. This high junction temperature originates from the Joule heat due to the high series resistance of the p–i–n junction diode. Then, the spectral shape and intensity of free-exciton emission would be not sensitive in this temperature range. Thus, the excitonic emission was observed even at higher temperatures than RT, which is a

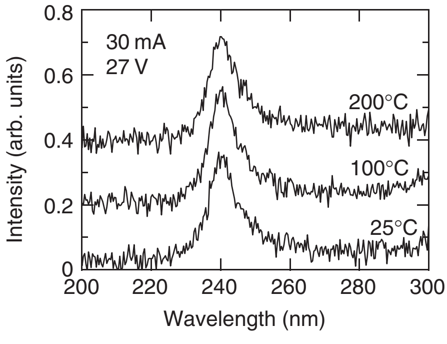

Figure 15.16 Excitonic emission spectra at the forward current of 30 mA for the p–i–n junction diode at different temperatures from 25°C to 200 °C

direct result of the specific properties of diamond such as a large exciton binding energy and a high thermal conductivity.

15.5 LIGHT-EMITTING MECHANISM

The actual lifetime of excitons in diamond τ_{ex} is given by:

$$\tau_{ex} = (\tau_r^{-1} + \tau_{deep}^{-1})^{-1} \tag{15.3}$$

where τ_{r} is the radiative recombination time of excitons and τ_{deep} is the trapping time of excitons to deep levels. For an indirect transition semiconductor, τ_{r} is much longer compared with τ_{deep} due to the requirement of momentum conservation in optical transitions. The τ_{r} of diamond has been reported to be of the order of microseconds [40], which is much longer than τ_{deep}, which is of the order of nanoseconds under low current injection for which deep levels are almost unoccupied. Therefore, most excitons should be trapped in the deep levels under this condition. However, we observed strong excitonic emission, and its nonlinear effects such as superlinearity of I_{FE} and sublinearity of I_{deep}, for the current dependence. In order to understand this phenomenon, we analyzed the kinetics, taking into account both exciton radiative recombination processes and exciton trapping and recombination processes via deep levels.

In the case of charged deep levels, bound carrier states are formed at those levels by the Coulomb potential of electric charge reduced by the screening effect of the permittivity. In a crystal with low relative dielectric constant, the screening effect of the Coulomb potential is weak and the energy level of the bound states is deep. In the case of diamond, Gheeraert *et al.* reported that the binding energies of second excited (2P) states for both donor and acceptor centers are about 80 meV by infrared absorption and photothermal ionization spectroscopy [41]. Thus, the bound states at charged deep levels in diamond should be considered when discussing the exciton transition to deep levels. The kinetic analysis based on this idea successfully explained the emission characteristics of diamond p–i–n junction diodes.

From this analysis, the following mechanisms for nonlinear emission characteristics were clarified. Generally, in Equation (15.3), τ_{deep} is inversely proportional to the unoccupied deep level density $N_{\mathrm{unoccupied}}$, i.e., $\tau_{\mathrm{deep}} = (C_{\mathrm{ex}} N_{\mathrm{unoccupied}})^{-1}$, where C_{ex} is the capture rate of excitons to deep levels. After the transition of excitons to deep levels, the occupied deep levels are charged and form the bound carrier states at those levels as described above, and the trapped carriers at deep levels recombine slowly with counter-charged carriers via the bound states. Under high excitation conditions, free-exciton density exceeds 10^{18} cm^{-3}, which is higher than the deep level density. Because the recombination of trapped carriers via bound states is relatively slow, almost-deep levels are trapped by part of the high-density excitons, that is, $N_{\mathrm{unoccupied}}$ becomes low and τ_{deep} becomes longer, and so the actual exciton lifetime τ_{ex} reaches the exciton radiative recombination lifetime τ_{r}. This indicates that the exciton radiative recombination rate increases. This is the mechanism of superlinearity of I_{FE} and sublinearity of I_{deep} for the current dependence. This condition derives from the superior excitonic nature of diamond, such as high density and high stability at high temperature. According to this kinetic analysis, a high internal quantum efficiency of excitonic emission should be expected, although diamond is an indirect-transition semiconductor. The quantum efficiency under high density exciton conditions has still not been evaluated experimentally. Further investigation is currently in progress.

15.6 SUMMARY

Diamond is one of the candidates for deep-UV light optoelectronic devices, because of its wide band-gap semiconductor and superior excitonic properties. After achieving phosphorus doping in diamond on (001)-oriented surfaces by optimizing the conditions for CVD growth, we fabricated high-quality homoepitaxial diamond p–n and p–i–n junction diodes on (001)-oriented surfaces, which has some advantages for actual applications, and investigated their diode and light-emitting properties.

For the homoepitaxial diamond p–n junction diodes, the rectification ratio was 10^6 at RT. The light emission spectra showed sharp deep-UV light emission at around 235 nm, attributed to free-exciton recombination coupled with TO phonon. The spectra were also associated with strong broadband emissions caused by crystalline defects, which would exist in the vicinity of the p–n junction as indicated by the capacitance–voltage measurements.

For the homoepitaxial diamond p–i–n junction diodes, the crystalline quality in the vicinity of the junction was improved, and the rectification ratio became 10^{10} at RT. Also, strong free-exciton emission and significantly suppressed deep-level emission were realized. The relative integrated intensities of free-exciton emission to deep-level emission increased about twentyfold compared to that of the p–n junctions. The free-exciton and the deep-level emission intensity increased superlinearly and sublinearly, respectively, for the current dependence. These light-emitting characteristics could be well explained by the kinetic analysis, taking into account the trapping and recombination processes of electron-hole pairs via bound states at charged deep levels, which is characteristic of materials with low relative dielectric constant like diamond. Moreover, strong excitonic emission was observed even at the high-junction temperature of over 200 °C.

Thus, our experimental results provide an interesting new insight into the light-emitting properties and mechanisms of (001)-oriented homoepitaxial diamond p–n and p–i–n junction diodes. Although diamond is an indirect transition semiconductor, the possibility of attaining high internal quantum efficiency deep-UV light emission was shown. Also, it was demonstrated that diamond has the potential for use in unique LEDs operating at high temperatures, which is hard to achieve with other commercially available LEDs. These characteristics are based on the superior excitonic properties of diamond (high density and high stability of excitons even at high temperatures) as well as the excellent thermal properties of this material. We believe that improvements, such as the ohmic contact properties of n-type diamond and an increase of the extraction efficiency, will enable the practical implementation of diamond deep-UV LEDs. Moreover, in the future, the full use of the characteristics of excitons will open the door to a unique exciton-related device, such as the diamond exciton laser.

ACKNOWLEDGEMENTS

This work was partly supported by the Japan Science and Technology Agency (JST) and the New Energy and Industrial Technology Development Organization (NEDO). We sincerely thank Dr H. Okushi, Dr S. Yamasaki, and Dr S. Kanno of the Nanotechnology Research Institute at AIST, Dr C. E. Nebel of the Diamond Research Center at AIST, Dr S. Koizumi of the Sensor Materials Center at NIMS, Dr T. Miyazaki of the Research Institute for Computational Sciences at AIST, Dr S.-G. Ri of the Nano Technology Innovation Center at NIMS, and all the members of the High Temperature Quantum Electronics (HTQE) Group of the Nanotechnology Research Institute at AIST for their valuable advice, encouragement and discussions. Please note that the present deep-UV diamond LED was realized by the many efforts of the HTQE group members. For the characterization of n-type diamond, appreciation is also extended to Dr M. Hasegawa of the Research Center for Advanced Carbon Materials at AIST, for his help in Hall-effect measurements.

REFERENCES

[1] P.J. Dean, E.C. Lightowlers, and D.R. Wight, *Phys. Rev.* **140**, A352–A368 (1965).
[2] A.T. Collins, M. Kamo, and Y. Sato, *J. Phys. Condens. Matter* **1**, 4029–4033 (1989).
[3] H. Kawarada, H. Matsuyama, Y. Yokota, T. Sogi, A. Yamaguchi, and A. Hiraki, *Phys. Rev. B* **47**, 3633–3637 (1993).
[4] H. Watanabe, K. Hayashi, D. Takeuchi, S. Yamanaka, H. Okushi, K. Kajimura, and T. Sekiguchi, *Appl. Phys. Lett.* **73**, 981–983 (1998).
[5] H. Okushi, H. Watanabe, and S. Kanno, *Phys. Stat. Sol. (a)* **202**, 2051–2058 (2005).
[6] Y. Taniyasu, M. Kasu, and T. Makimoto, *Nature* **441**, 325–328 (2006).
[7] H. Watanabe, D. Takeuchi, S. Yamanaka, H. Okushi, K. Kajimura, and T. Sekiguchi, *Diamond Relat. Mater.* **8**, 1272–1276 (1999).
[8] T. Teraji, *Phys. Stat. Sol. (a)* **203**, 3324–3357 (2006).
[9] D. Takeuchi, S. Yamanaka, H. Watanabe, and H. Okushi, *Phys. Stat. Sol. (a)* **186**, 269–280 (2001).
[10] M. Katagiri, J. Isoya, S. Koizumi, and H. Kanda, *Appl. Phys. Lett.* **85**, 6365–6367 (2004).
[11] R. Berman, Part 1 Solid State 1. Thermal Properties, and C.D. Clark, E.W.J. Mitchell, and B.J. Parsons, Part 1 Solid State 2. Colour Centers and Optical Properties, *The Properties of Diamond*, J.E. Field (Ed), Academic Press, London, 1979.
[12] S. Koizumi, K. Watanabe, M. Hasegawa, and H. Kanda, *Science* **292**, 1899–1901 (2001).
[13] K. Horiuchi, A. Kawamura, T. Ide, T. Ishikura, K. Nakamura, and S. Yamashita, *Jpn. J. Appl. Phys.* **40**, L275–L278 (2001).
[14] I. Sakaguchi, M.N. Gamo, Y. Kikuchi, E. Yasu, H. Haneda, T. Suzuki, and T. Ando, *Phys. Rev. B* **60**, R2139–R2141 (1999).
[15] R. Kalish, A. Reznik, C. Uzan-Saguy, and C. Cytermann, *Appl. Phys. Lett.* **76**, 757–759 (2000).
[16] J.A. Garrido, C.E. Nebel, M. Stutzmann, E. Gheeraert, N. Casanova, and E. Bustarret, *Phys. Rev. B* **65**, 165409–6 (2002).
[17] K. Horiuchi, A. Kawamura, Y. Okazima, and T. Ide, *New Diamond* **20**, 6–11 (2004) (in Japanese).
[18] H. Kato, S. Yamasaki, and H. Okushi, *Appl. Phys. Lett.* **86**, 222111–3 (2005).
[19] T. Makino, N. Tokuda, H. Kato, M. Ogura, H. Watanabe, S.-G. Ri, S. Yamasaki, and H. Okushi, *Jpn. J. Appl. Phys.* **45**, L1042–L1044 (2006).
[20] T. Makino, H. Kato, M. Ogura, H. Watanabe, S.-G. Ri, S. Yamasaki, and H. Okushi, *Jpn. J. Appl. Phys.* **44**, L1190–L1192 (2005).
[21] S.-G. Ri, H. Kato, M. Ogura, H. Watanabe, T. Makino, S. Yamasaki, and H. Okushi, *Diamond Relat. Mater.* **14**, 1964–1968 (2004).

[22] Y.G. Chen, M. Ogura, S. Yamasaki, and H. Okushi, *Diamond Relat. Mater.* **13**, 2121–2124 (2004).

[23] R. Farrer, *Solid State Commun.* **7**, 685–688 (1969).

[24] S. Koizumi, M. Kamo, Y. Sato, H. Ozaki, and T. Inuzuka, *Appl. Phys. Lett.* **71**, 1065–1067 (1997).

[25] H. Kato, W. Futako, S. Yamasaki, and H. Okushi, *Diamond Relat. Mater.* **13**, 2117–2120 (2004).

[26] M. Nesladek, *Semicond. Sci. Technol.* **20**, R19–R27 (2005).

[27] A. Tajani, E. Gheeraert, N. Casanova, E. Bustarret, J.A. Garrido, G. Rumen, C.E. Nebel, M.E. Newton, and D. Evans, *Phys. Stat. Sol. (a)* **193**, 541–545 (2002).

[28] T. Kociniewski, J. Barjon, M.-A. Pinault, F. Jomard, A. Lusson, D. Ballutaud, O. Gorochov, J.M. Laroche, E. Rzepka, J. Chevallier, and C. Saguy, *Phys. Stat. Sol. (a)* **203**, 3136–3141 (2006).

[29] H. Kato, S. Yamasaki, and H. Okushi, *Diamond Relat. Mater.* **14**, 2007–2010 (2005).

[30] T. Teraji, M. Katagiri, S. Koizumi, T. Ito, and H. Kanda, *Jpn. J. Appl. Phys.* **42** L882–L884 (2003).

[31] H. Kato, T. Makino, S. Yamasaki, and H. Okushi, *J. Phys. D: Appl. Phys.* **40**, 6189–6200 (2007).

[32] T. Makino, H. Kato, M. Ogura, H. Watanabe, S.-G. Ri, Y.G. Chen, S. Yamasaki, and H. Okushi, *Diamond Relat. Mater.* **15**, 513–516 (2006).

[33] M. Suzuki, S. Koizumi, M. Katagiri, T. Ono, N. Sakuma, H. Yoshida, T. Sakai, and S. Uchikoga, *Phys. Stat. Sol. (a)* **203**, 3128–3135 (2006).

[34] M. Suzuki, H. Yoshida, N. Sakuma, T. Ono, T. Sakai, M. Ogura, H. Okushi, and S. Koizumi, *Diamond Relat. Mater.* **13**, 198–202 (2004).

[35] S.C. Lawson, H. Kanda, H. Kiyota, T. Tsutsumi and H. Kawarada, *J. Appl. Phys.* **77**, 1729–1734 (1995).

[36] D. Takeuchi, H. Watanabe, S. Yamasaki, H. Okushi, H. Sawada, H. Ichinose, T. Sekiguchi and K. Kajimura, *Phys. Rev. B* **63** 245328–7 (2001).

[37] K. Iakoubovskii and A. Stesmans, *J. Phys.: Condens. Matter* **14**, R467–R499 (2002).

[38] T. Makino, N. Tokuda, H. Kato, M. Ogura, H. Watanabe, S.-G. Ri, S. Yamasaki, and H. Okushi, *Diamond Relat. Mater.* **16**, 1025–1028 (2007).

[39] M. Kadri, D. Araujo, M. Wade, A. Deneuville and E. Bustarret, *Diamond Relat. Mater.* **14**, 566–569 (2005).

[40] A. Fujii, K. Takiyama, R. Maki, and T. Fujita, *J. Luminescence* **94–95**, 355–357 (2001).

[41] E. Gheeraert, S. Koizumi, T. Teraji, H. Kanda, and M. Nesladek, *Phys. Stat. Sol. (a)* **174**, 39–51 (1999).

Part 4

Electrochemical and Biological Sensors

CVD Diamond for Electronic Devices and Sensors Edited by Ricardo S. Sussmann
© 2009 John Wiley & Sons, Ltd. ISBN: 978-0-470-06532-7

16 Biofunctionalization of Diamond Surfaces: Fundamentals and Applications

J. A. GARRIDO

Walter Schottky Institut, Technische Universität München, Germany

---

16.1 Introduction 401
16.2 CVD diamond materials 403
  16.2.1 Monocrystalline diamond 403
  16.2.2 Polycrystalline diamond 403
  16.2.3 Nanocrystalline diamond 404
  16.2.4 Ultrananocrystalline diamond 404
16.3 Functionalization of diamond surfaces 405
  16.3.1 Surface termination 406
  16.3.2 Photochemical, electrochemical and chemical methods 406
16.4 Biomolecules on diamond surfaces 415
  16.4.1 Protein physisorption 416
  16.4.2 Covalent grafting 419
16.5 Applications in biosensing 425
  16.5.1 Amperometric biosensors 425
  16.5.2 Enzyme Field Effect Transistors 427
16.6 Conclusions 430
  Acknowledgements 432
  References 432

16.1 INTRODUCTION

Recent years have witnessed a burst of interest in diamond as a substrate for applications in biosensors and biotechnology. However, compared to other semiconductors, metals, or even other carbon-related materials, the reports on bio-applications of diamond are still very scarce. The reason might be a combination of different factors

CVD Diamond for Electronic Devices and Sensors Edited by Ricardo S. Sussmann
© 2009 John Wiley & Sons, Ltd. ISBN: 978-0-470-06532-7

such as the relative primitive state of diamond technology, a limited commercial availability, and the lack of awareness about the potential of CVD diamond outside the diamond community. Should some of the issues related to diamond technology and availability be resolved, diamond will surely become a very attractive contender in the quest of suitable materials for applications in the field of biosensors and biotechnology. What are the properties which could make of diamond such an advantageous material for these particular applications?. Among the many exceptional attributes the ones that stand out are: the chemical stability of diamond surfaces in aqueous environment, its excellent electrochemical properties [1–3] (see also the chapter by Foord in this book), the possibility of strong covalent grafting of functional groups to diamond surfaces [4], a good biocompatibility [5], the control of surface termination, and the existence of surface conductivity in the case of H-terminated surfaces [6, 7] (see also the chapter by Ley in this book). A good chemical stability in an aqueous environment is an important prerequisite for most bio-applications. Unlike other semiconductors and metals, diamond shows a remarkable chemical stability of its surface, both in the oxidized and hydrogenated states. Its excellent electrochemical properties make diamond electrodes not only attractive for applications in which a large electrochemical potential window is required, but also for many bio-electrochemical applications, as will be discussed in this chapter. The ability to form strong covalent C–C bonds at its surface, a characteristic shared with other carbon materials, qualifies diamond to be very advantageous platform for the stable grafting of organic and bio-organic molecules. Although the term ‘biocompatibility’ is very broad and sometimes difficult to assess [8], it is generally recognized that diamond, similarly to other carbon-based materials such as diamond-like carbon, features a good biocompatibility [5]. The ability to prepare several stable surface terminations, among which the H-termination and the O-termination are the most commonly used ones, allows the modification of important surface-related properties such as hydrophobicity and conductivity. Compared with other materials, it is relatively easy to achieve the structuring of diamond surfaces with hydrophobic/hydrophilic patterns in order, for instance, to control protein adsorption. In addition, the electronic properties of H- and O-terminated surfaces are remarkably different: whereas O-terminated surfaces remain insulating, a hole conductive channel is generated at the surface of H-terminated diamond [7]. The existence of this surface conductive channel has stimulated the study of diamond-based solution Gate Field Effect Transistors (SGFETs) for biosensor applications [9–12].

In summary, the wide range of material properties of diamond make it a very attractive platform for different bio-applications. However, before the real potential of diamond is realized, much work will have to be performed to bring the bio-related activities of diamond close to the levels of development that have been reached using other materials, such as Au or Si. For instance, a much better understanding of the diamond/water interface is necessary; the biofunctionalization of diamond surfaces is still in its early development and more detailed investigation is needed. The same applies to an important issue such as the interaction between diamond and complex biosystems, such as proteins and cells. Additionally, the design, technology, and in some cases fundamental aspects of diamond-based sensors are still to be addressed. In this chapter we will describe the efforts that have been made to address some of these issues, with a special focus on the biofunctionalization of diamond surfaces. Important aspects related to the basic understanding of the diamond/water interface, or the detailed fabrication and characterization of diamond sensors, are not covered due to space restrictions. First, the different diamond materials available will be briefly presented, highlighting the correlation between their respective properties and suitable applications. Then, we will discuss the functionalization of diamond for the introduction of various functional groups on the weakly reactive diamond surface. The adsorption of biomolecules onto the diamond surface will be presented next, focusing on the covalent grafting of proteins. The last section deals with two applications of diamond biosensors, namely amperometric electrochemical sensors and enzyme-field effect transistors.

16.2 CVD DIAMOND MATERIALS

Currently, CVD diamond specimens of different quality, such as monocrystalline, polycrystalline, nanocrystalline (grain size around 100 nm), and ultrananocrystalline (grain size below 10 nm) are available either as coatings on various substrates, or as freestanding layers. The different properties of these diamond specimens enable different applications, i.e. monocrystalline diamond is not necessarily the best option for all applications. Several parameters can be used to identify the suitability of the diamond material depending on the application. Among them, surface morphology, electrical conductivity, capability of device fabrication, substrate nature (Si, quartz, diamond, metals, etc.) and dimensions, electrochemical properties (influenced by the sp^3/sp^2 ratio), possibility of surface conductivity, cost, etc. In the following, some relevant properties of the different diamond specimens are discussed.

16.2.1 Monocrystalline diamond

Nowadays, high quality, freestanding, monocrystalline diamond (or single crystalline diamond, SCD) is commercially available from a few sources. Unfortunately, the availability of highly conductive, B-doped SCD is very limited. Commercial SCD can be obtained with different surface polishing qualities. Figure 16.1(a) shows an AFM picture of a polished natural IIa diamond substrate with a low surface roughness ($\sim$0.3 nm rms). These surfaces are ideal for micro/nanopatterning, and for the study of structural properties of organic monolayers. In addition, the well-defined surface orientation enables a basic analysis of the surface chemistry. Monocrystalline diamond features the lowest sp^2 content of all diamond materials, which results in its excellent electrochemical performance, such as large electrochemical potential window and low background current [2]. Due to the very good surface quality, it is expected that the H-induced surface conductivity will reach the highest values (up to 10^{-4} S and higher) for intrinsic single crystalline diamond. This is especially interesting for the design of transducers based on electrolyte gate field-effect transistors. Besides the cost, which has recently become more competitive, the main disadvantages of single-crystalline diamond are the small size (typically below 5×5 mm^2) and the scarcity of commercially available, highly conductive, B-doped material.

16.2.2 Polycrystalline diamond

Both intrinsic and B-doped freestanding CVD polycrystalline diamonds (PCD) are commercially available either as large freestanding wafers or deposited on large area substrates. Due to its polycrystalline nature, and depending on the thickness, as-grown films exhibit

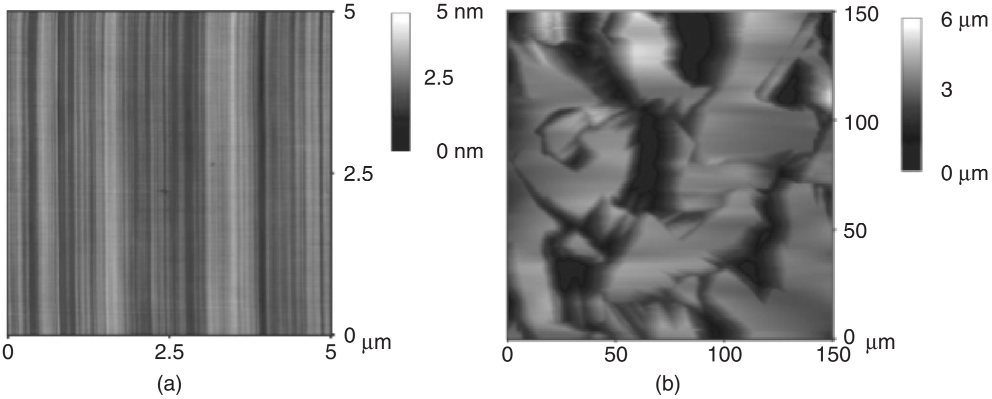

Figure 16.1 AFM characterization of (a) single crystalline and (b) polycrystalline diamond surfaces. See plate 8

a very high surface roughness (∼ µm) which hampers their use for those applications in which micro-/nano-patterning is important. However, these films can be smoothly polished, albeit at a higher cost. Figure 16.1(b) shows an AFM image of a polished polycrystalline diamond. Due to the availability of metal-like B-doped diamond films, and together with a relatively low sp^2 content (mostly located at the grain boundaries), this material is used commercially for electrochemical applications, and might be very attractive for amperometric biosensors. Intrinsic PCD has shown almost the same H-induced surface conductivity values to SCD. Thus, when polished, this material is also very attractive for the fabrication of EGFETs. The main disadvantages are the high roughness of as-grown films, the presence of grain boundaries, and a poorly defined surface orientation.

16.2.3 Nanocrystalline diamond

Nanocrystalline diamond (NCD) thin films on different substrates, mainly quartz and Si, have been increasingly available in recent years. It was shown that NCD can also be doped very efficiently with boron, so that metal-like films can be obtained [13], thus paving the way for several electrochemical applications [3, 14]. Compared with polycrystalline diamond, as-grown NCD exhibits a considerably lower surface roughness (∼10–20 nm), see Figure 16.2(a). Although H-terminated intrinsic NCD films also show surface conductivity, the large concentration of grain boundaries considerably reduce its value. Additionally, the large amount of sp^2-bonded carbon present in the grain boundaries is detrimental to the electrochemical properties [15]. However, B-doped NCD electrodes have considerable advantages compared with other carbon-related electrodes [16]. Thus, because of its low surface roughness and its relatively good electrochemical properties as compared with other carbon-based materials, B-NCD electrodes are very promising for bio-electrochemical applications.

16.2.4 Ultrananocrystalline diamond

The term ultrananocrystalline diamond (UNCD) was initially coined for the thin diamond films prepared from Ar-rich plasma and with a grain size below 10 nm [17]. It was shown

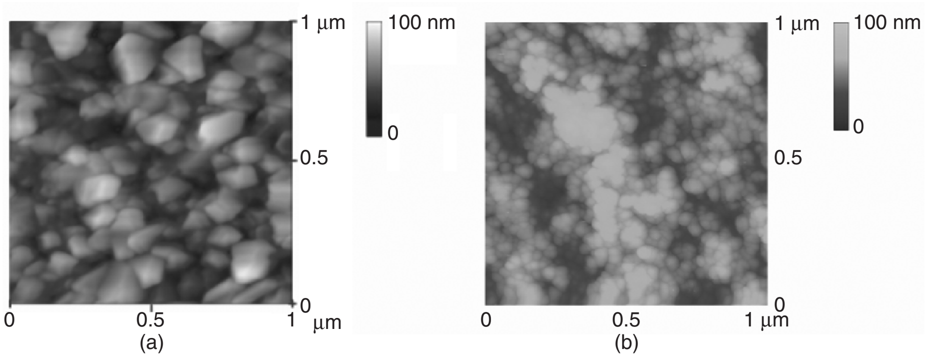

Figure 16.2 AFM characterization of (a) nanocrystalline and (b) ultrananocrystalline diamond surfaces. See plate 9

that the conductivity of these films could be readily controlled by the addition of nitrogen during growth. Nitrogen, however, does not act as a classical dopant; instead, it is thought to induce transport in a defect band located at the grain boundaries [18, 19]. UNCD films, with a roughness down to 5 to 10 nm rms, are available on standard substrates like Si and quartz, as well as on metals. UNCD films are expected to have the largest sp^2/sp^3 ratio of all the diamond materials discussed here; thus, the electrochemical properties of UNCD films are largely influenced by sp^2 bonds in the grain boundaries. Like NCD, UNCD films have clear advantages as compared with other carbon-related materials: UNCD electrodes exhibit a larger electrochemical potential window and lower background electrochemical current than do electrodes such as HOPG.

Finally, an interesting feature of UNCD, as well as of NCD, is the possibility of low temperature deposition [20], which might enable integration with other technologies or even the use of plastic substrates.

16.3 FUNCTIONALIZATION OF DIAMOND SURFACES

In the context of bio-applications, the modification of the surface generally addresses two main purposes: the introduction of functional groups and the alteration of surface properties. Thus, surface modification can pursue the grafting of functional biomolecules, like DNA or proteins, often used in biosensors, or, for instance, aim at the reduction of nonspecific adsorption of proteins, which is of relevance for biosensors and is also important in reducing undesirable responses to implants. In other cases, surface modification is necessary to promote cell adhesion; in this instance, the surface chemistry can be modified to enhance protein adsorption. For this the surface morphology can be changed, or even ligands promoting cell adhesion can be grafted onto the surface [8]. In the context used here, functionalization refers to the grafting of organic molecules to the diamond surface.

In the case of diamond, the frequently cited chemical stability of its surface has hampered more active research into the functionalization of diamond surfaces. In recent years, though, it has been shown that the surface of diamond can be functionalized using different methods, albeit under more aggressive conditions than required for other materials. Of special relevance for diamond functionalization is the surface chemistry, which can be modified by changes in the surface termination, as discussed in the following section.

16.3.1 Surface termination

Hydrogen- and oxygen-terminated diamond surfaces are the most common stable terminations. Recently, other surface terminations such as F-termination [21, 22], Cl-termination [22, 23], and NH_2-termination [22], have been reported.

H-termination of the diamond surface can be obtained upon exposure of the surface to H radicals, and is the usual termination of as-grown CVD diamond as it comes out of the growth reactor [24]. This termination is generally stable under atmospheric conditions, and is also thought to be stable in aqueous electrolytes. Upon hydrogenation, diamond surfaces are hydrophobic, with typical contact angles of around 90°. The most striking feature of H-terminated surfaces is their surface conductivity, which is developed when the surface is exposed to atmosphere and is related to the C−H surface dipole and the existence of surface adsorbates [7, 25] (see also the chapter by Ley in this book). The surface conductivity has enabled the design of diamond biosensors based on H-terminated surfaces.

O-terminated diamond surfaces can be obtained by different methods, such as O_2 plasma, ozone exposure, wet oxidation, anodic electrochemical oxidation, etc. The nature of the surface O-groups (ether, carbonyl, hydroxyl, etc.) depends on the oxidation process, the surface orientation, and the sp^2/sp^3 ratio [26]. O-Terminated surfaces are hydrophilic, but the degree of hydrophilicity obviously depends on the type of terminal O-group. When hydroxyl groups predominate, the surfaces are very hydrophilic with contact angles below 5°. Depending on the O-groups at the surface, different reactivities towards functionalization are expected for the O-terminated surfaces. The surface conductivity vanishes upon oxidation of diamond, which allows an easy method for the generation of conductive/nonconductive patterns at the surface.

F-termination of diamond has not received much attention, although it has been known for a long time [21]. F-Terminated surfaces can be obtained upon exposure to F radicals; so far, atomic and molecular beams [21], as well as CF_4 and C_4F_8 plasmas [27–30] have been used. F-Terminated surfaces have been reported to be stable in atmosphere and in aqueous electrolytes. Notably, the fluorination of diamond electrodes results in a much larger electrochemical potential window [30, 31]. In addition, the high hydrophobicity of F-terminated electrodes is interesting for tribological applications, and could be used to control adsorption of biomolecules.

Cl-terminated diamond surfaces have been obtained by different methods, such as plasma and photochemical or thermal decomposition of Cl-contaning gases [22, 23, 32]. Cl-Terminated surfaces are also hydrophobic, but their stability is an issue: C−Cl surfaces can react in air or water to form C−OH. However, this high reactivity of C−Cl surface bonds can be used as an intermediate state for surface functionalization [22, 33].

NH_2-terminated diamond surfaces have been prepared by the reaction of Cl-terminated or H-terminated surfaces with NH_3 gas under UV irradiation [22]. They have been proposed as intermediate states for further modification of diamond surfaces [34], as well as useful functional groups controlling the pH sensitivity of diamond surfaces [35].

16.3.2 Photochemical, electrochemical and chemical methods

The largest amount of work related to functionalization of diamond has dealt with the special case of H-terminated surfaces. Less frequent, by far, are the reports on the

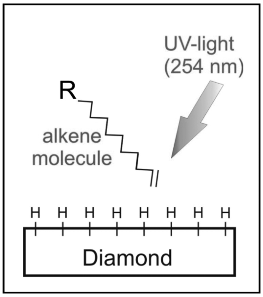

Figure 16.3 UV-light photochemical functionalization of H-terminated diamond using alkene molecules. The UV-light illumination is thought to induce electron injection into the liquid phase, forming reactive species that can react with the surface

functionalization of O-terminated surfaces. So far, three different approaches have been generally used to functionalize H-terminated diamond surfaces: photochemical, electrochemical, and chemical methods. For O-terminated surfaces, only chemical methods have been reported. Because of its relevance, the functionalization of H-terminated diamond surfaces is discussed first, followed by the functionalization of O-terminated surfaces.

16.3.2.1 Photochemical modification of H-terminated diamond surfaces

Hamers and coworkers have pioneered the photochemical functionalization of H-terminated diamond surfaces [4, 36]. The process is based on the reactivity of alkene molecules with a terminal double bond towards H-terminated diamond surfaces upon illumination with UV-light, as shown diagrammatically in Figure 16.3. A detailed explanation of the experimental details can be found in the references [4, 36]. In short, the H-terminated diamond surface is covered with a solution containing the desired alkene molecules, and illuminated with UV light (normally 254 nm) for several hours. Using careful X-ray photoelectron spectroscopy characterization, the Hamers group has reported monolayer surface coverage after approximately 10 hours of illumination [37]. The grafting process is thought to occur in the following steps: (i) electron injection from the diamond surfaces into the liquid phase, (ii) formation of reactive species such as radicals, and (iii) surface reaction. The exact origin of the ejected electrons is still under debate. Nichols *et al.* suggested that electrons from defect states are photoexcited into the conduction band and, due to the negative electron affinity of H-terminated diamond surfaces, can be ejected to the liquid phase [38]. Shin *et al.*, on the other hand, suggested that electrons are directly excited from the valence band of diamond into the molecular acceptor level of the alkene molecule [39]. In both cases, the negative electron affinity of diamond plays an important role, which explains the experimentally observed, strong specificity of this grafting mechanism for H-terminated surfaces.

16.3.2.2 Electrochemical modification of H-terminated diamond surfaces

Swain and coworkers reported for the first time on the covalent grafting of aromatic groups to diamond surfaces by the electrochemical reduction of phenyl diazonium salts in

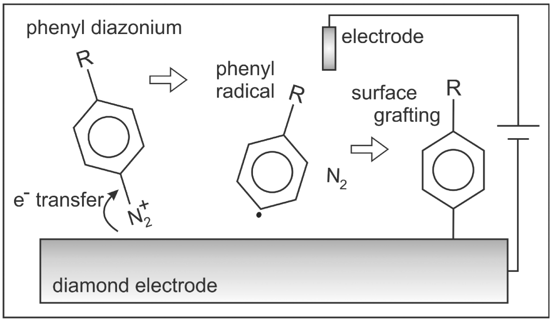

Figure 16.4 Electrochemical functionalization of diamond electrodes using aryl diazonium molecules; the process is typically performed in water-free solutions. Electrons from the electrode induce the electrochemical reduction of diazonium ions forming aryl radicals, which, after hydrogen abstraction, can be covalently grafted to the diamond electrode surface

acetonitrile at boron-doped diamond electrodes [40]. Recently, this surface modification scheme was used and extended by others [41, 42]. The grafting mechanism is schematically summarized in Figure 16.4, which shows the electrochemical reduction of a diazonium ion to form an aryl radical and a nitrogen molecule, followed by covalent bonding of the aryl radical to the diamond electrode surface after hydrogen abstraction. This grafting method is typically performed in water-free solutions (for instance, acetonitrile) and requires a conductive diamond electrode that can provide electrons during the anodic polarization to reduce the diazonium ion. Uetsuka *et al.* have reported that the electrochemically sustained formation of nitrophenyl layers on diamond is governed by 3D growth, i.e. the formation of multilayers [42]. The large amount of available aryl radicals, enabled by electrochemical polarization, can react with the diamond surface or with already grafted molecules. Thus, heterogeneous multilayer formation is expected for this electrochemical grafting method. Although most of the research has been carried out using H-terminated surfaces, Uetsuka *et al.* also reported the functionalization of O-terminated surfaces [42]. However, the surface coverage was not compared to the case of H-terminated surfaces. It is very plausible, though, that aryl radicals can also react with some of the oxygen surface groups, such as carboxyl or hydroxyl.

16.3.2.3 Chemical modification of H-terminated diamond surfaces

The spontaneous grafting of diazonium salts to Si, metals, and carbon surfaces has been known for some time [43]. Recently, the spontaneous grafting of diazonium monophenyls and biphenyls has also been successfully applied to diamond surfaces [44, 45]. Figure 16.5 summarizes the grafting process, for the case of diazonium biphenyls, which is believed to happen at the diamond surface. In order to reduce the diazonium salt the diamond surface should act as a reducing agent, and thus provide electrons. In the case of metals, it was suggested that the grafting efficiency was strongly dependent on the reducing capacity of the metal [46]. For highly reducing metals, disordered multilayers were observed, confirming that the faster the grafting the more disordered is the layer [46]. In the case of diamond surfaces, however, extremely long reaction times (∼72 hours) have been reported, together with monolayer coverage [44]. Figure 16.6 shows an AFM image of a

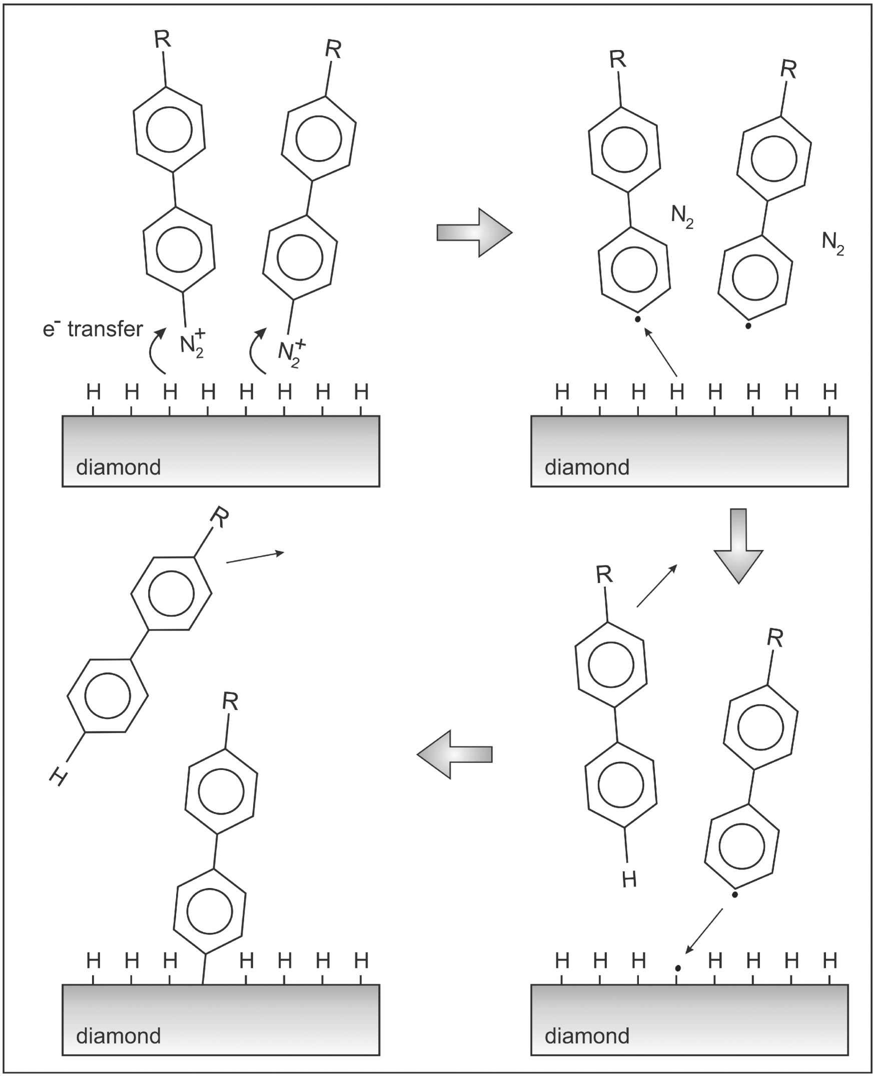

Figure 16.5 Schematic representation of the spontaneous grafting process. In order to reduce the diazonium salt the diamond surface acts as a reducing agent, spontaneously providing electrons. Biphenyl radicals are able to abstract hydrogen from the surface, allowing the reaction of the dangling bond with another radical

flat diamond surface (roughness <0.3 nm rms) modified with nitromonophenyl molecules. A scratching experiment, by removing the grafted layer in contact mode and then displaying the surface morphology in tapping mode, confirms the monolayer coverage. The evaluation of the trench depth reveals a layer thickness of about 0.6 nm, very close to the molecule length (0.74 nm). Similar experiments performed using biphenyl molecules showed a film thickness of 1 nm, again in good agreement with the molecule length (1.21 nm) [44]. The surface coverage was further investigated using X-ray photoelectron spectroscopy. Figure 16.7 shows three XPS spectra (in the N1s region) of a UNCD film

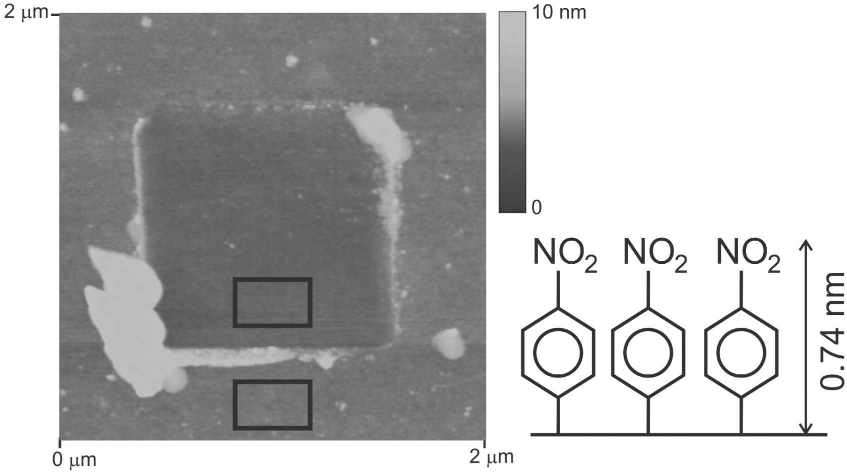

Figure 16.6 AFM shaving experiment performed on diamond surface modified with nitro-monophenyl molecules using spontaneous grafting. Scanning with the AFM in contact mode removes the grafted layer; the trench (1 × 1 μm^2) is then revealed by scanning in tapping mode. The evaluation of the trench depth, average height difference between the two black boxes in the figure, reveals a layer thickness of about 0.6 nm, very close to the molecule thickness (0.74 nm)

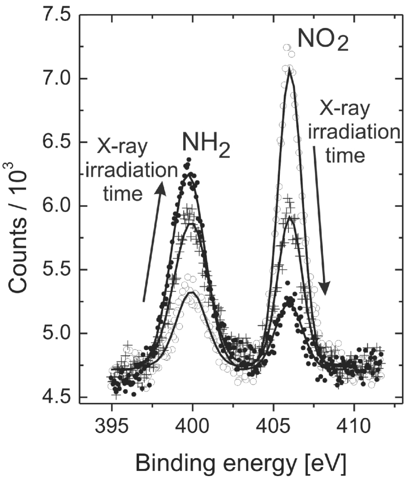

Figure 16.7 Subsequently recorded nitrogen 1s XPS spectra of a nitrobiphenyl modified diamond surface (spontaneous grafting) for increasing X-ray irradiation times. Longer radiation time induces a change in the chemical shift of the nitrogen photoelectron emission from an N–O to N–H binding configuration

modified with nitrobiphenyl molecules for different X-ray exposure times. The two peaks at 400 eV and 406 eV correspond to $-NH_2$ and $-NO_2$ groups, respectively. X-Ray irradiation induces the partial reduction of NO_2 groups to NH_2, as evidenced by the time dependent decrease of the NO_2/NH_2 peak ratio. Lud *et al.* have found that the NH_2 content increases from 20 % to 85 % [44]. At the same time, the total amount of nitrogen bonded to the surface decreases only slightly, with a total loss of nitrogen of about 10 % after 12 h of continuous irradiation. From the XPS analysis, a surface coverage of $5 \pm 0.5 \times 10^{-10}$ mol/cm^2 is obtained, which corresponds to 70–80 % of a full monolayer. The ability to control the reduction of the NO_2 terminal groups to NH_2 by means of irradiation can have interesting applications such as 'chemical lithography' for substrate nanostructuring [47].

In addition, it is well known that nitro functionalities can be electrochemically reduced to amino functionalities. Amino-terminal functionalities are particularly interesting because they can be used as anchor sites for the grafting of biomolecules. Thus, Lud *et al.* have proposed that diamond electrodes modified with nitrobiphenyl molecules are suitable platforms for *in situ* coupling of proteins to the electrode surface in physiological environment [44]. Figure 16.8 shows a cyclic-voltammetry experiment in which the terminal groups of nitrobiphenyl molecules grafted to the surface of UNCD films were electrochemically reduced. During the first sweep of the applied potential from 0 V versus Ag/AgCl towards negative values, the large cathodic current results from the electrochemical reduction of NO_2 groups. Integrating the total current under the cathodic peak (grey area in the figure) allows the estimation of the surface coverage, which in this case corresponds to $\approx 5 \times 10^{-10}$ mol/cm^2, in good agreement with XPS results.

A complete understanding of this grafting mechanism is still missing. An important open issue is the origin of the electrons necessary to reduce the diazonium ion. In the case of electrochemical grafting, electrons can be supplied during the cathodic polarization. In spontaneous grafting, however, no polarization is required. As was observed for the spontaneous grafting of diazonium monophenyls on metals, grafting efficiency is strongly correlated with the reducing capacity of the metal, i.e., the ability to provide electrons [46]. It is worth mentioning again that the observed reaction times for the spontaneous grafting of diazonium salts on diamond are far longer than on metals, suggesting that diamond surfaces show a considerably smaller reducing capacity than metal surfaces. Additionally, we have observed that the grafting efficiency on O-terminated UNCD surfaces is about 40 % lower than on H-terminated UNCD surfaces. Electrons from the diamond surface are available at the valence band and from mid-gap states; the later ones

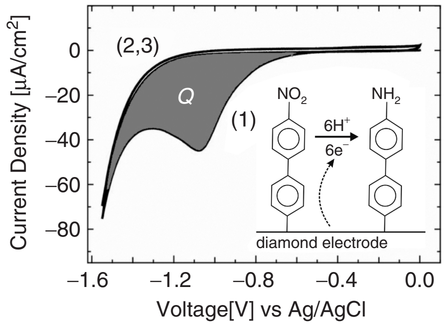

Figure 16.8 Electrochemical conversion of nitrobiphenyls. Cyclic voltammogram of a nitrobiphenyl-functionalized UNCD electrode recorded in 100-mM potassium chloride aqueous electrolyte solution. The first scan (1) shows an irreversible wave, peaking at −1.08V versus Ag/AgCl, corresponding to the reduction of the residual nitro groups (see inset). A surface coverage of about 5×10^{-10} mol/ cm^2 is obtained from the total current under the cathodic peak (grey area)

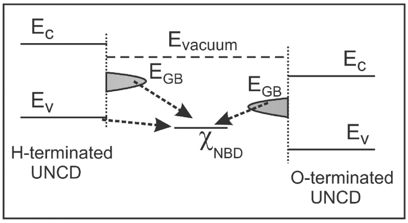

Figure 16.9 Schematic showing the band diagrams of H-terminated (negative electron affinity) and O-terminated (positive electron affinity) diamond surfaces, the LUMO level of the nitrobenzene diazonium molecule, and allowed electron transfer (dashed arrows)

are especially important in UNCD films where a significant density of mid-gap states is expected at the grain boundaries. Furthermore, the position of the bands and mid-gap states at the surface is largely determined by the surface electron affinity, which is negative for H-terminated surfaces (−1.3 eV) and positive for O-terminated surfaces (+1.7 eV). Figure 16.9 illustrates a possible scenario to explain the spontaneous grafting of diazonium salts to H- and O-terminated ultrananocrystalline diamond surfaces. The position of the LUMO level of the diazonium aromatic ion lies at about 4.4 eV below the vacuum level. In the case of H-terminated surfaces, both valence band and mid-gap states are able to provide electrons to the LUMO level. On the other hand, in the case of O-terminated UNCD only electrons from mid-gap states are able to reduce the diazonium salt. Thus, the different surface coverage observed for H- and O-terminated UNCD surfaces could be explained by the different reducing capacities of these two surfaces, which arise from their different electron affinities.

16.3.2.4 Chemical modification of O-terminated diamond surfaces

Several groups have investigated the chemical modification of O-terminated diamond surfaces [48, 49]. In contrast to H-terminated surfaces, an important chemical heterogeneity is expected at oxidized diamond surfaces. Indeed, it is well known that several oxygen-related surface groups (the most important are ether, carbonyl, and hydroxyl groups) are present at oxidized surfaces, whose chemical composition depends on the crystal orientation as well as on the oxidation process [26, 50]. Among these available groups, hydroxyls are very attractive because of their good reactivity; for example, the well-established alkoxysilane chemistry is based on the reaction with hydroxyl groups. An extensive review on the use of alkoxysilane chemistry for surface functionalization can be found elsewhere [51].

Figure 16.10 schematically summarizes the attachment of silanes to a hydroxyl-terminated diamond surface: the silane molecules, here 3-aminopropyl diethoxymethylsilane (APDEMS) dissolved in toluene, react with silanols in the water layer present on the hydrophilic diamond surface. These silanols immediately form covalent bonds to deprotonate hydroxyl groups at the surface, or can react with silanols of nearby molecules to form siloxane networks. The presence of hydroxyl groups on the hydrophilic surface is thus an essential requirement for the silanization process [52]. As mentioned above, the presence of hydroxyl groups at oxidized diamond surfaces depends on the crystal orientation and on the oxidation process used. Thus, UNCD surfaces, with randomly oriented, nanoscaled, diamond grains, are suitable substrates to investigate this grafting mechanism.

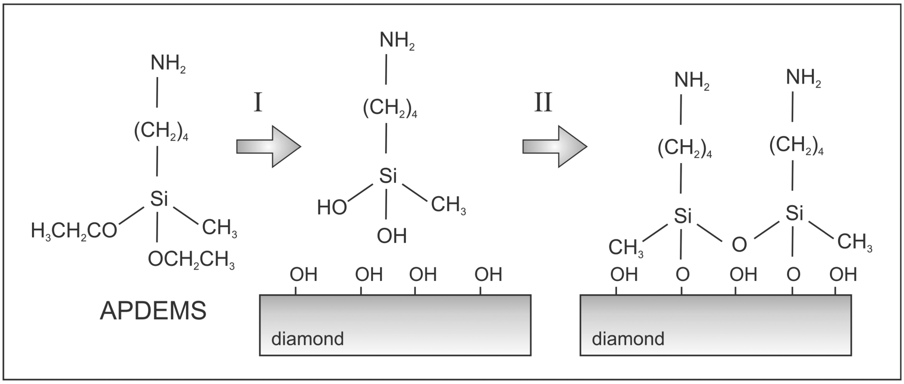

Figure 16.10 Silane chemistry on oxidized diamond surfaces. The ethoxy groups of the 3-aminopropyldiethoxymethylsilane (APDEMS) molecule react to silanols with the water layer present on the hydrophilic diamond surface (step I). These silanols can form covalent bonds with hydroxyl groups at the diamond surface (step II)

In the example discussed here, the oxidation was performed using an O_2-plasma (for more details see Ref. [49]): after the oxidation the static contact angle was below 5°. The very good hydrophilicity suggests the presence of hydroxyl groups at the surface, which are among the most hydrophilic of the O-groups. Fluorescence microscopy with fluorescent probes reacting selectively with the hydroxyl groups can be used to assess the availability as well as the reactivity of hydroxyl groups at the surface of O-terminated UNCD films. The fluorescence image in Figure 16.11(a) demonstrates the specific reactivity of

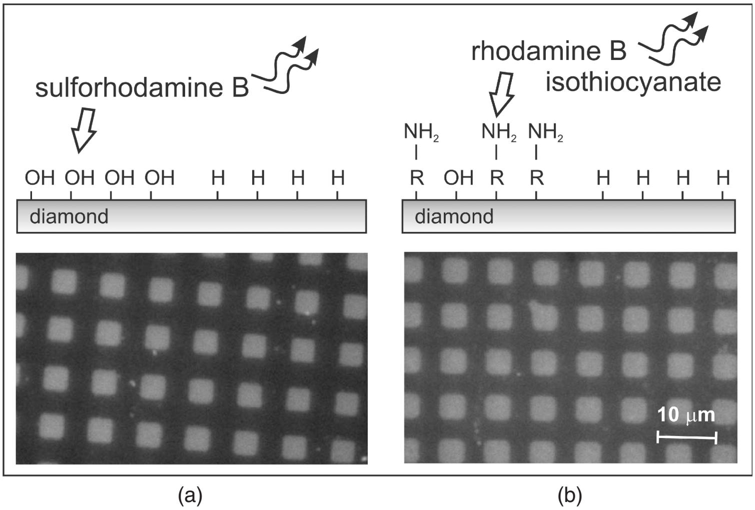

Figure 16.11 (a) Fluorescence image of a H/O patterned surface which has been reacted with sulforhodamine B. The fluorophore specifically reacts with hydroxyl surface groups, revealing their presence on the oxidized areas. (b) Fluorescence image of a H/O pattern onto which APDEMS were grafted and then reacted with rhodamine B isothiocyanate. This fluorophore specifically reacts with amino groups, confirming the presence and reactivity of the terminal amines of APDEMS molecules

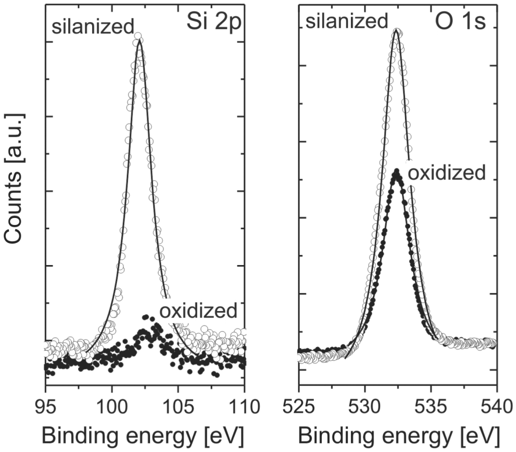

Figure 16.12 XPS spectra in the Si2p region (left) and N1s region (right) for oxidized (solid symbol) and APDEMS-modified (open symbol) nanocrystalline diamond surfaces

sulforhodamine B acid chloride on a patterned UNCD surface. The pattern is due to a H-terminated background onto which O-terminated regions with square shape are created by photolithography and oxygen plasma treatment [49]. As the image shows, the fluorescence probes only react with the O-terminated surface, thus confirming the presence of hydroxyl groups. A similar experiment using a fluorophore specific for carbonyl groups suggested that no reactive carbonyl groups are present.

X-ray photoelectron spectroscopy was used to investigate the surface coverage of the alkoxysilanes grafted to oxidized UNCD surfaces. Figure 16.12 summarizes representative results of this study. Upon functionalization, a clear Si 2p signal from the silane molecules is observed. In addition, the intensity of the O 1s peak increases after functionalization; the ratio between the O 1s signal for the silanized and oxidized surface is about 1.7, confirming that the grafting of APDEMS molecules does not result in multilayer formation [53]. The comparison between the C 1s signal and the Si 2p and O 1s signals indicates a surface coverage of $\sim 1.8 \times 10^{14}$ molecules/cm^2, which is about 50 % of the value expected for a dense monolayer [53].

The availability and reactivity of the amino-terminated APDEMS molecules on the diamond surface can again be assessed by fluorescence microscopy using fluorescent probes that react selectively with the amino terminal groups. This is the case for rhodamine B isothiocyanate, whose isothiocyanate group reacts with the primary amine grafted to the surface to form thiourea. The fluorescence image in Figure 16.11(b) confirms the specific reactivity of the fluorophore on a APDEMS-patterned UNCD surface. The pattern was prepared as discussed above: square-shaped, O-terminated, regions are created in a H-terminated UNCD surface by a combination of photolithography and oxygen plasma. Once patterned, the whole surface is reacted with APDEMS molecules as described above; from the previous discussion, the molecules are only expected to be grafted to the O-terminated regions. After thoroughly cleaning to remove physisorbed APDEMS molecules, the surface is again incubated with a solution containing rhodamine B isothiocyanate. As Figure 16.11(b) proves, fluorescence is only observed in the square-shape regions, confirming both the presence of the APDEMS molecules and the reactivity of the terminal amines [49]. As will be discussed in the next section, the availability of reactive amines is very attractive for further grafting of biomolecules.

16.3.2.5 Polymer brushes on diamond surfaces

The use of polymer coatings with multiple functions on a single grafted polymer chain is very attractive for biosensing applications, and its use has been demonstrate for various sensing principles [54]. A few studies on polymer coatings covalently attached to diamond can be found in the literature. Li *et al.* have reported on the functionalization of oxidized nanodiamond particles via atom transfer radical polymerization (ATRP) [55], Matrab *et al.* have reported on the ATRP of styrene and methyl methacrylate initiated by electro-grafted aryldiazonium salt on H-terminated UNCD [56], and Actis *et al.* have studied the electro-polymerization of pyrrole on oxidized boron-doped diamond electrodes modified by pyrrolyl units [57]. In all these studies, the surface had to be pre-modified with an organic layer, following an established procedure to introduce surface grafting and initiator functions for the surface-initiated polymerization (SIP). However, using a carbon substrate such as diamond offers the opportunity to directly introduce chemical functions or even a reactivity contrast by e.g. different surface activation, such as hydrogenation or oxidation. Hence, the formation of defined reactive interlayers such as SAMs is no longer necessary and the direct grafting of monomers on activated diamond surfaces can be realized in a one-step reaction. It has been shown that a broad variety of vinyl monomers can be directly grafted onto organic substrates by self-initiated photografting and photopolymerization (SIPGP) [58]. Based on the SIPGP approach, we have developed a straightforward method for the preparation of poly(styrene) (PS) coatings directly onto oxidized UNCD using styrene as the monomer. A detailed description of the experiments can be found in reference [59]. By preparing H/O patterns at the surface of UNCD films, it was observed that polymer grafts were only formed on the O-terminated surfaces. Infrared and X-ray photoelectron spectroscopy show characteristics fingerprints of poly(styrene). The exclusive formation of PS grafts on the oxidized areas can be explained by the energy difference required for the hydrogen radical abstraction from the oxidized and hydrogenated surface areas. Additionally, the possibility of further modification of the polymer grafts by incorporating additional functional molecules, such as fluorescent labels, was demonstrated [59]. Polymer brushes are expected to enable novel paths for designing more advanced biosensing schemes, incorporating multifunctional elements and a higher loading capacity for biomolecules.

16.4 BIOMOLECULES ON DIAMOND SURFACES

The precise control of the adsorption of biomolecules at solid surfaces is of particular relevance for most bio-related applications. Different methods of biomolecular adsorption are available and are often classified into nonspecific or specific adsorption, as well as strong or weak adsorption. Obviously, the choice of a particular method will depend on the application and the involved biomolecule. Nonspecific adsorption, such as physisorption, normally results in poor control over the orientation and activity of the biomolecules. Although it is a simple method, the stability is generally poor and in the case of proteins can result in undesired denaturation processes. On the other hand, nonspecific covalent immobilization, as for instance the grafting of proteins through the use of protein surface amines, can improve the stability and reduce denaturation; yet, it does not provide good control over the orientation and the activity. Specific covalent immobilization provides a satisfactory solution to most of these issues; however, it normally requires biomolecule engineering, which reduces the number of applications and makes the method much more sophisticated. Other noncovalent methods, such as that based on the biotin/avidin system, provide satisfactory stability and have been shown to be very flexible, although there are still some concerns about the *in-vivo* compatibility. Very interesting for certain proteins is the incorporation of these into supporting lipid bilayers, which can provide a stable environment for fragile proteins.

The solid support onto which the biomolecules are to be adsorbed plays an important role in the present discussion. Diamond surfaces offer a suitable platform for investigating different adsorption methods. For instance, covalent grafting is possible as shown in the previous section, and physisorption can also be influenced by controlling the surface termination (H- or O-terminated diamond). Thus, several groups have recently investigated physisorption of proteins on modified diamond surfaces [60–65], as well as the covalent grafting of biomolecules (proteins and peptides) [4, 66]. Current research also includes the study of cell growth onto diamond surfaces [67, 68]. In the following, we will start by discussing some aspects of the physisorption of proteins onto diamond surfaces and will conclude with a more detailed description of covalent grafting of biomolecules, with special emphasis on proteins.

16.4.1 Protein physisorption

Although nonspecific adsorption can be used to immobilized proteins onto surfaces, in many cases it is desirable to suppress it. In the case of biosensors, for instance, nonspecific adsorption results into surface fouling and, thus, sensor degradation. For *in-vivo* implants, the healing process improves when the implant surface is resistant to nonspecific adsorption. In other cases, however, protein adsorption is desirable to promote cell growth, as required in bone implants [8].

Nonspecific adsorption is a very complex process influenced by many factors related to electrostatic and hydrophobic interactions between substrate and molecule, as well as the surface morphology [69]. Among the important electrostatic interactions, one can mention the surface charge of the substrate, the acidity/basicity constant of surface groups at the biomolecule, and the pH and ionic strength of the solution. Hydrophobic interactions are not so well understood; experimentally determined relevant factors are the surface hydrophobicity and morphology, as well as the protein size and its local distribution of hydrophobic/hydrophilic surface groups.

In a revealing study, Whitesides and coworkers investigated the effect of surface wettability on the nonspecific adsorption of proteins to uncharged, self-assembled monolayers (SAMs) on gold [70]. They found that the adsorption to the SAM showed a general dependence on the wettability of the surface: proteins preferentially adsorbed to less wettable surfaces. Similarly, the effect of the wettability of the SAMs on the adsorption of proteins showed a dependence on the size of the proteins: small proteins (lysozyme) only showed adsorption to weakly wettable surfaces. Large proteins (fibrinogen), while adsorbing better to weakly wettable surfaces, showed adsorption on almost every type of surface [70].

What is the current knowledge about nonspecific adsorption of biomolecules in the particular case of diamond surfaces? Several groups have so far investigated the adsorption of proteins on diamond surfaces. Hydrophobic H-terminated nanocrystalline diamond surfaces have been reported to exhibit a low adhesion of plasma proteins, such as fibrinogen [60, 61]. On the other hand, hydrophilic O-terminated nanocrystalline diamond surfaces were shown to provide an exceptionally high affinity for proteins [62]. Steinmüller-Nethl and coworkers reported that O-terminated NCD is extremely efficient in adsorbing the bone morphogenetic protein-2 (BMP-2), due to the combination of suitable surface texture and hydrophilicity [63]. Interestingly, bound BMP-2 was found to be fully active, which shows that simple physisorption can be useful for medical implants as well as for innovative scaffolds in tissue engineering [63]. Similar results were obtained using oxidized diamond nanocrystals, with an excellent affinity for different proteins; lysozyme, for instance, strongly adsorbs on O-terminated nanodiamonds while maintaining its enzymatic activity [62].

Thus, it seems the case that for the particular case of diamond surfaces the lower the wettability the weaker the adsorption. However, this is in contradiction with the previously discussed report of Whitesides and coworkers [70], which demonstrated that hydrophobic surfaces are more prone to nonspecific adsorption of proteins. Therefore, these results suggest that in the case of diamond surfaces wettability is not the only parameter to consider. Other factors such as electrostatic interactions are able to influence the adsorption substantially. In contrast to other materials, the charge of diamond surfaces in contact with aqueous electrolytes has not been investigated in detail. Recently, we have studied the charge build-up at H-terminated and O-terminated diamond surfaces in aqueous electrolyte using electrokinetics experiments, from which the zeta potential could be calculated [71]. The zeta potential is commonly used for quantification of the electric charge at the double layer present at, for instance, the solid/liquid interface. It can be defined as the potential at the boundary between the immobile layer of adsorbed ions on a surface and the diffuse layer of mobile ions, i.e. the potential at the so-called shear or slipping plane [72]. However, it is important to realize that the zeta potential differs from the electric surface potential in the double layer. Yet, it can provide a good estimation of the electric charge of a surface in contact with an electrolyte. Figure 16.13 shows the pH dependence of the zeta potential of H-terminated and O-terminated diamond surfaces. The isoelectric point for O-terminated surfaces was found to be close to pH 1.5. On the other hand, the isoelectric point for the H-terminated surfaces was found to be slightly below pH 4. This means that at the physiological relevant pH, both surfaces are negatively charged. The negative charge at the O-terminated diamond surface could be induced by carboxyl or hydroxyl surface groups, as has been observed for metal oxides. More surprising is the negative charge observed at the H-terminated surfaces, where the number of those groups should be very small. Similar results have been observed for other hydrophobic surfaces, in which the measured isoelectric point was about pH 4 [73]. Thus, hydrophobic surfaces in contact with water acquire a net negative charge at physiological pH. It has been suggested that hydrophobic surfaces exhibit asymmetric adsorption of hydroxide (OH^-) and hydronium ions (H_3O^+), being hydroxide ions preferentially adsorbed to the surface [73]. The origin of such asymmetric adsorption at the hydrophobic/water interface, though, is still a matter of discussion. Initially, it was suggested that the conformation of water molecules and water ions at a hydrophobic surface might be the origin of this adsorption [71, 73]. More recently, molecular dynamics simulations of

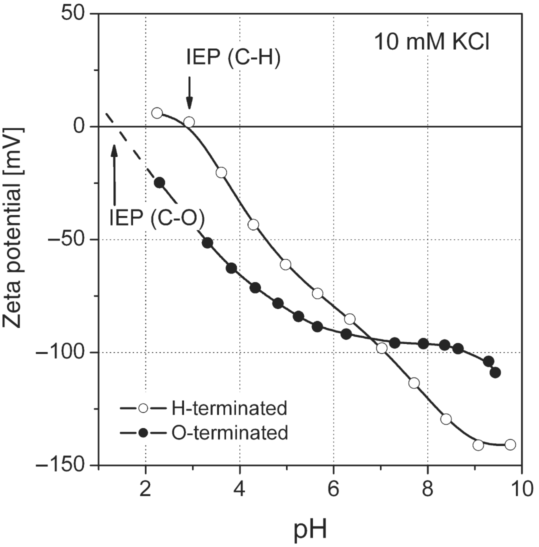

Figure 16.13 pH dependence of the zeta potential of H- and O-terminated diamond surfaces calculated from electrokinetics measurements [71]. The isoelectric point (IEP) for the H-terminated surface is close to pH 4, in agreement with the results obtained for other hydrophobic surfaces. On the other hand, the IEP of the O-terminated surfaces is well below pH 2

hydroxide and hydronium ions near a hydrophobic interface have suggested that both ions behave like amphiphilic surfactants [74]. However, due to the different molecular charge distribution in hydroxide and hydronium ions, the adsorption of OH^- to a hydrophobic surface is more favorable.

Therefore, surface charge cannot account for the different behaviour of H-terminated and O-terminated diamond surfaces in terms of protein adsorption; both surfaces are negatively charged but while O-terminated surfaces have a strong affinity for proteins, H-terminated surfaces show a much weaker affinity. In fact, protein adsorption can be strongly modified by the microscopic structure of water induced by certain surfaces. This is the case of ethylene-glycol (EG) based materials, which are extremely effective in preventing protein adsorption [70, 75]. It has been suggested that the structure and conformation of water molecules induced by EG play a crucial role in the nonfouling properties characteristic of EG [76]. Similarly, hydrophobic interactions between H-terminated diamond surfaces and water molecules could induce water structuring at the surface, as has been recently suggested [11, 71], thus resulting in weak protein adsorption. Hamers and coworkers have reported on the control of nonspecific adsorption of proteins to diamond surfaces by grafting EG-containing functional monolayers [64, 65]. In their experiments, they compared the adsorption of proteins on diamond, Si, and Au surfaces modified with functional monolayers. The substrate type was found to play a negligible role, only determining the properties of the functional monolayer, such as molecular order and packing. Interestingly, the adsorption of proteins (avidin in this particular experiment) onto EG-modified silicon surfaces (~0.055 pmol/cm^2) was found to be similar to the adsorption on bare H-terminated single crystalline diamond surfaces (~0.1 pmol/cm^2) [64], supporting the idea that the nonfouling characteristic of H-terminated diamond surfaces could arise from intrinsic hydration phenomena at these surfaces.

16.4.2 Covalent grafting

In contrast to physisorption, the covalent immobilization of proteins can help to prevent denaturation, results in better stability, and enables control over protein orientation. Proteins are in general very sensitive to the physiological environment and can be easily degraded or denatured by several physicochemical effects. In order to avoid degradation of the protein activity, the three-dimensional structure of proteins should be preserved after immobilization, which can be achieved by covalent immobilization of the proteins to a functionalized solid support. The schematic in Figure 16.14 is useful for discussing important aspects of covalent grafting of biomolecules to solid supports. Mono/multilayers of functional organic molecules are used in order to control the grafting of the biomolecules to surfaces. These functional layers can provide specific reactive groups to which the biomolecules can be grafted. In addition, the functional layers can be designed to control nonspecific adsorption of biomolecules, as discussed before. Thus, by selecting suitable functional groups and controlling their density at the surface, the orientation and grafting density of biomolecules can be engineered. Figure 16.15 shows a general scheme for covalent grafting of biomolecules to diamond surfaces. The surface of as-grown diamond films can be activated using different physical or chemical processes. As discussed in the surface functionalization section, different terminations such as H-, O-, F-, Cl- or NH_2-can be obtained at the diamond surface. Functional organic layers can be grafted to the activated diamond surface, as discussed above. The immobilized linker layers provide suitable functional groups for the immobilization of the biomolecules and, at the same time, introduce a separation between the surface and the biomolecules that can be helpful in preventing denaturation or nonspecific adsorption. Finally, depending on the surface functional groups introduced by the linker layer, several schemes are available for immobilizing the biomolecules. Figure 16.16 summarizes different strategies commonly used for protein immobilization [77]. Some of the strategies shown in Figure 16.16 have also been applied to immobilization of DNA on diamond surfaces. For instance, the Hamers group

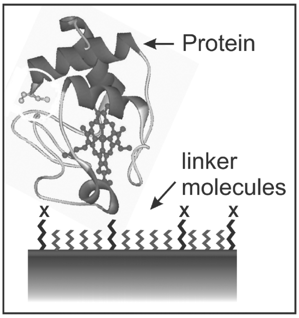

Figure 16.14 Schematic of the covalent grafting of a protein to a surface. Mono/multilayers of functional organic molecules are used in order to control the grafting of the biomolecules by providing specific reactive groups (X). By selecting suitable functional groups and controlling their density at the surface, the orientation and grafting density of proteins can be engineered

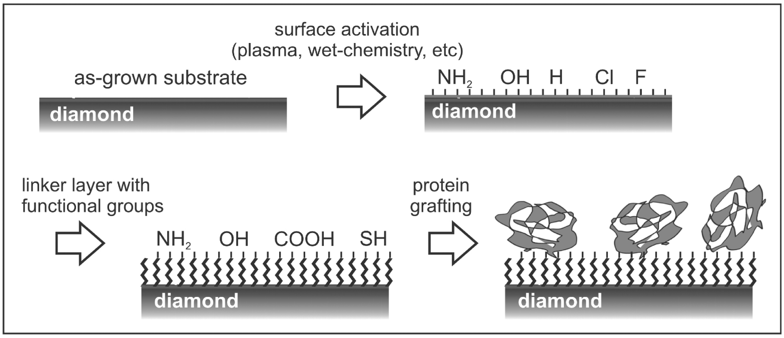
surface activation
(plasma, wet-chemistry, etc)
as-grown substrate
diamond
NH2 OH H Cl F
diamond
linker layer with functional groups
NH2 OH COOH SH
diamond
protein grafting
diamond

Figure 16.15 Immobilization scheme of biomolecules onto diamond surfaces. Different surface modification methods can be used to activate the surface of as-grown diamond substrates. A linker layer with a variety of functional groups is covalently grafted to the activated surface. Finally, the proteins can be grafted to reactive terminal groups of the linker layer

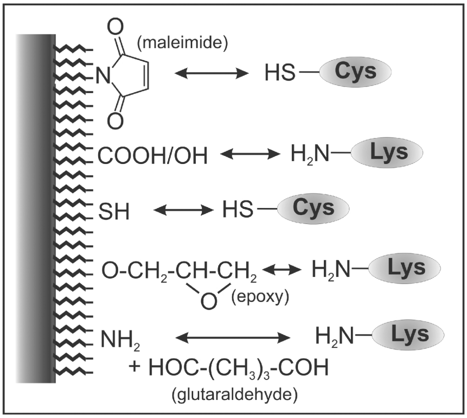
(maleimide)
N
O
O
HS–Cys
COOH/OH
H2N–Lys
SH
HS–Cys
O-CH2-CH-CH2
O (epoxy)
H2N–Lys
NH2
H2N–Lys
+ HOC-(CH3)3-COH
(glutaraldehyde)

Figure 16.16 Different strategies for covalent grafting of proteins, using two different reactive groups available at the protein surfaces: the amine of surface lysine residues and the thiol of surface cysteine residues

reported on the covalent grafting of thiol-modified DNA to ultrananocrystalline diamond surfaces activated with amino groups using a heterobifunctional crosslinker containing a maleimide group [4]. Thiol groups react very efficiently with the maleimide terminal, forming a thioether bond. The same grafting method was used by Nebel and coworkers, who also investigated the mechanical stability of the grafted DNA molecules [78]. A different method was employed by Kawarada and coworkers, who reported on the covalent immobilization of amino-modified DNA to amino-functionalized diamond surfaces [79]. In this case, the reaction between the two terminal amino groups is enabled by the bifunctional crosslinker glutaraldehyde. Christiaens *et al.* tethered amino-modified DNA probes to nanocrystalline diamond surfaces previously activated with carboxyl-terminated fatty acids. Carbodiimide-mediated coupling enabled the reaction between the NH_2-DNA and the HOOC-fatty acid [80]. In all these reports, the estimated density of DNA molecules immobilized onto the diamond surface was of the order of 2 to 6×10^{12} molecules/cm^2.

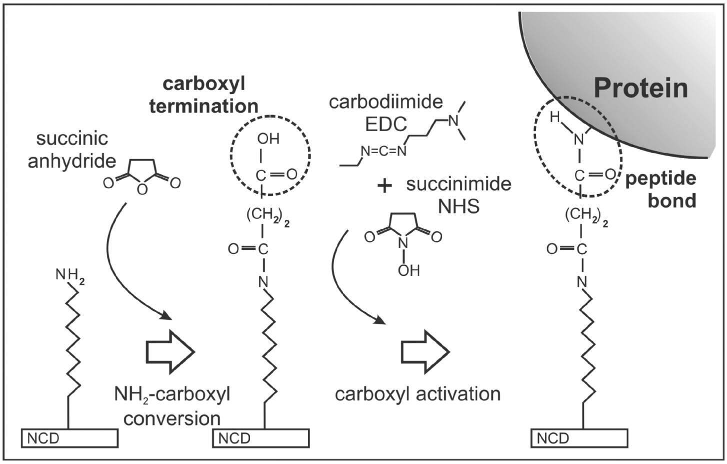

Figure 16.17 Example of a grafting protocol used for the covalent immobilization of proteins to diamond surfaces that have been previously modified with amino-terminated organic molecules. Succinylation of the primary amine introduces a carboxyl group at the modified diamond surface. Carbodiimide-mediated coupling enabled the reaction between amine residues at the protein surface and the carboxyl group at the diamond surface, forming a peptide bond

In the case of proteins, the chosen grafting scheme (see Figure 16.16) depends on the different reactive groups available at the protein surface. In most cases, the selected reactive group is the amine group of surface lysine residues. Due to the large density of available surface amines, this grafting method will result in a random orientation of the protein. Figure 16.17 schematically summarizes a grafting protocol that we have used for the covalent immobilization of proteins to diamond surfaces that have been previously modified with amino-terminated organic molecules [66]. Succinylation of the primary amine using succinic anhydride introduces a carboxyl group at the modified diamond surface. Carbodiimide-mediated coupling enables the reaction between amine residues at the protein surface and the carboxyl group at the diamond surface, forming a peptide bond. Using this protocol we have immobilized the green fluorescence protein (GFP) to nanocrystalline diamond surfaces [66].

Starting from the H-terminated diamond surface and using a combination of photolithography and oxygen plasma, the surface was patterned into hydrogenated/oxidized regions. Amino-terminated molecules were selectively grafted to the hydrogenated surface by using the previously described photochemical grafting of alkene molecules. GFP were reacted with the whole surface using the protocol shown in Figure 16.17. Thus, GFP is expected to be grafted only to the initially H-terminated diamond surface. Figure 16.18 shows a fluorescence image of the GFP-modified diamond surface. As expected, a GFP fluorescence signal is visible from areas that were initially hydrogenated and to which the linking molecules were grafted. The dark regions in the image correspond to initially oxidized diamond areas, where linking molecules are not expected and thus no GFP can be covalently bound. This simple experiment proves the successful immobilization and confirms that GFP is still active even if immobilized to a solid support [66].

Alternatively, electrochemical methods, such as cyclic voltammetry, can be used to verify the grafting of redox enzymes to the surface of diamond electrodes. Charge transfer

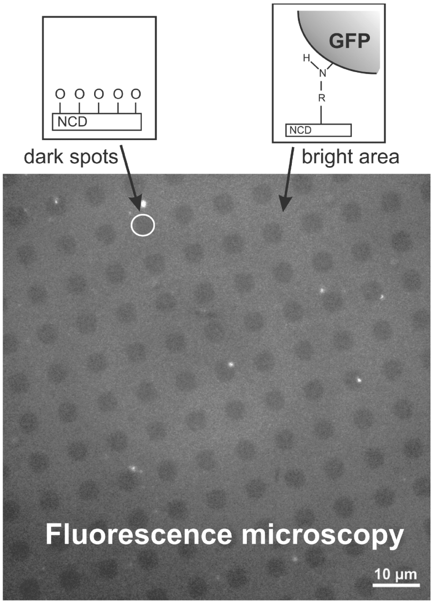

Figure 16.18 Fluorescence image of the GFP-modified diamond surface (see text). The GFP fluorescence signal is mainly visible from areas that were initially hydrogenated and to which the linking molecules were grafted. The dark regions in the image correspond to initially oxidized diamond areas, where the linking molecules are not expected and thus no GFP can be covalently bound

between the redox active group of the immobilized enzyme and diamond provide a definite fingerprint for the activity of the enzyme, enabling, in addition, the estimation of the surface coverage. Figure 16.19 shows cyclic voltammograms measured with a UNCD electrode to which cytochrome c enzymes were immobilized using a grafting method based on disulphide bridges (see Figure 16.16) [81]. The anodic and cathodic peaks correspond to the oxidation and reduction of the redox active heme group of the enzyme, confirming the successful immobilization of cytochrome c to the UNCD electrode. The position of the anodic and cathodic peaks is very close to that reported for the enzyme in solution, which indicates that the immobilization process does not alter significantly the enzyme structure. Integration of the anodic/cathodic current can be used to estimate the density of active enzymes grafted to the surface; in this particular case the surface coverage is about 6×10^{12} enzymes/cm^2, which amounts to about 60 % of a full monolayer. The peak shape analysis indicates an almost ideal electron transfer process between the surface-localized redox protein and the conductive diamond substrate, suggesting a highly oriented and dense enzyme layer [81]. An efficient electron transfer between enzyme and electrode is crucial to improving the performance of amperometric-based diamond biosensors, as will be discussed later in this chapter.

However, many enzymes relevant for biosensor applications are not able to transfer charge to a nearby electrode, making their detection by direct charge transfer impossible. In this case, colorimetric methods are helpful for evaluating enzyme kinetics and surface coverage. The colorimetric detection method uses incubation of the enzyme-modified surface with an analyte that reacts with such an enzyme. During the reaction between

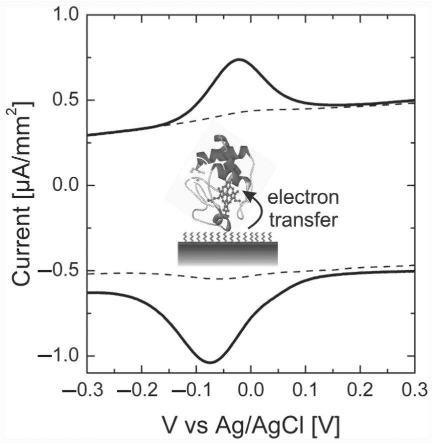

Figure 16.19 Cyclic voltammograms measured with a bare UNCD electrode (dashed line) and a UNCD electrode (solid line) to which yeast cytochrome *c* enzymes were immobilized. The anodic and cathodic peaks correspond to the oxidation and reduction of the redox active heme group of the enzyme

analyte and enzyme, one of the generated products further reacts with a dye added to the solution where the experiment is performed. Thus, the enzyme kinetics can be obtained under certain conditions by measuring the change in the optical absorption of the solution with a spectrophotometer. We have used this method to investigate the kinetics of the enzyme acetylcholinesterase grafted to single crystalline diamond surfaces [82]. Acetylcholinesterase (AChE) is a relevant enzyme in neuronal signal transduction, which hydrolyses the neurotransmitter acetylcholine (ACh). Figure 16.20 shows a schematic of the colorimetric set-up together with the expected reactions in the solution. In this experiment, acetylthiocholine (ATCh) was used as an analyte instead of acetylcholine. At

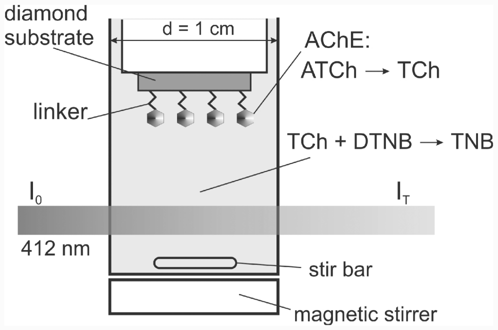

Figure 16.20 Colorimetric set-up used to investigate the activity of acetylcholinesterase (AChE) enzymes immobilized to diamond surfaces. At the diamond surface, acetylthiocholine (ATCh) is degraded to thiocholine (TCh) and acetate by AChE. The generated TCh is detected via the reaction with dithiobisnitrobenzoic acid (DTNB), in which the transparent DTNB solution turns yellow due to the generation of nitromercaptobenzoic acid (TNB). The change in the optical absorption of the solution, which is continuously stirred to ensure a homogeneous spatial distribution of all reagents, is measured with a spectrophotometer

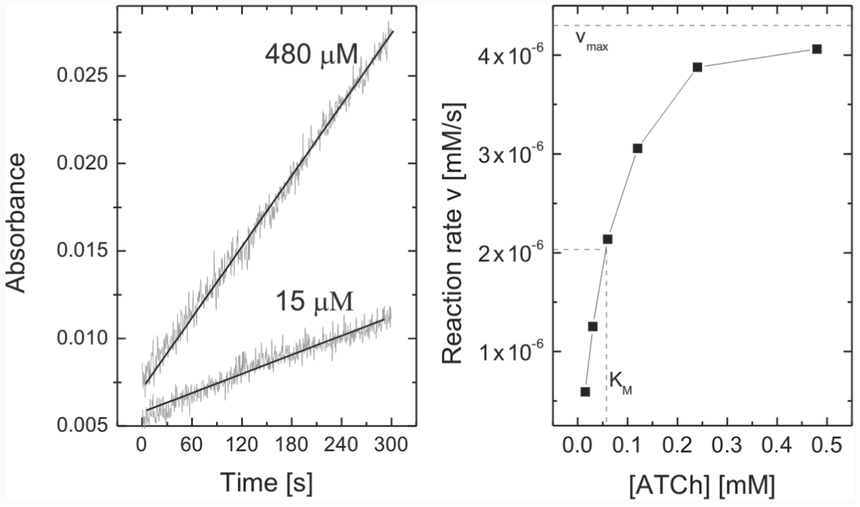

(a) (b)

Figure 16.21 Results of the colorimetric experiments assessing the activity of immobilized acetylcholinesterase enzymes. (a) Absorbance versus time plot showing the response of the solution, in which the enzyme-modified diamond sample is immersed, to the addition of 15 μM and 480 μM of acetylthiocholine. (b) Calculated reaction rates for different concentrations of ATCh, showing the typical Michaelis–Menten kinetics enzyme-catalysed reaction

the surface of the enzyme-modified diamond, acetylthiocholine is degraded to thiocholine (TCh) and acetate by AChE. The generated thiocholine can be detected via the reaction with dithiobisnitrobenzoic acid (DTNB), in which the transparent DTNB solution turns yellow due to the generation of nitromercaptobenzoic acid (TNB) [83]. The change in the transparency of the solution, which is continuously stirred to ensure a homogeneous spatial distribution of all reagents, was measured with a spectrophotometer. During the experiment, the absorbance of TNB at 412 nm was monitored over time, which increased due to the enzyme-induced generation of TNB. Figure 16.21(a) shows the variation of the absorbance measured for two different concentrations of ATCh in the solution. The change in absorbance is directly proportional to the amount of generated TNB, which corresponds to an equal amount of TCh released in the enzymatic degradation of ATCh. Thus, by performing this experiment with different concentrations of ATCh, the kinetics of the enzyme activity can be studied, as the reaction rate is proportional to the variation of TCh concentration. Figure 16.21(b) shows plots of the so-determined reaction rates for different analyte concentrations, illustrating the typical behaviour corresponding to an enzyme-catalyzed reaction as described by Michaelis–Menten kinetics [84]. For low analyte concentration the reaction is diffusion limited, and thus an increase of [ATCh] causes a proportional increase in the reaction rate. At high analyte concentration the reaction rate is limited kinetically and the reaction rate approaches its saturation value, $\nu_{\max}$, which is proportional to the number of active enzymes and the catalytic rate constant, k_2, $\nu_{\max} = k_2[\mathrm{E}]$. In order to estimate the surface coverage, the value of the catalytic rate constant should be known. However, the activity of immobilized enzymes is controversially discussed in the literature [85, 86]. A tenfold decrease of enzymatic activity has been recently reported for immobilized AChE with respect to the free enzymes. This was attributed to a diffusion barrier for the analyte into and out of sterically hindered catalytic sites of the immobilized AChE [87]. Using this assumption, and using the measure $\nu_{\max}$ of free enzymes, we estimated a surface coverage of active AChE of about 10–25 % of a full monolayer [82].

16.5 APPLICATIONS IN BIOSENSING

As mentioned before, diamond offers a very interesting platform for the fabrication of bioelectrochemical sensors due to its excellent chemical stability and electrochemical properties, together with the presence of the surface conductive channel. Amperometric and potentiometric biosensors using diamond electrodes have been reported by different groups [49, 66, 88–92]. In addition, using the sensing capability of surface conductive diamond films, DNA-hybridization [93] and enzyme-based sensors have also been reported recently [82, 94]. Here, we will describe our own work on two types of biosensors: enzyme-modified amperometric sensors and enzyme-field-effect transistors.

16.5.1 Amperometric biosensors

The working principle of amperometric biosensors, illustrated in Figure 16.22, is based on an electrochemical method that measures charge transfer across the electrode interface. It requires conductive electrodes plus active control of the interfacial potential. The bioreceptor element of the biosensor is an enzyme that catalyzes the conversion of the analyte into the product(s). Two different detection mechanisms can be implemented based on (i) direct charge transfer between the enzyme redox group and the electrode, and (ii) charge transfer between generated product/s and the electrode. As for the direct charge-transfer mechanism, the charge state of the enzyme redox group is modified during

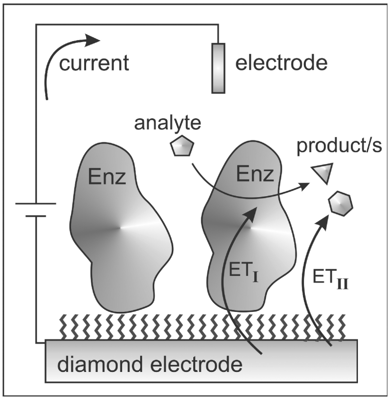

Figure 16.22 Working principle of an amperometric biosensor. The bioreceptor element of the biosensor is an enzyme that catalyses the conversion of the analyte into the product(s). The detection principle is based on the measurement of the electron transfer across the electrode interface, which is related to the catalytic reaction. Two different detection mechanisms can be implemented based on direct charge transfer between the enzyme redox group and the electrode (ET$_I$) and charge transfer between generated product/s and electrode (ET$_{II}$), as detailed in the text

the analyte-to-product reaction. Given that direct charge transfer between the electrode and the enzyme is effective, any charge provided by the electrode is able to return the redox group to its initial charge state, resetting the enzyme for a new catalytic reaction. Thus, measuring the current across the electrode directly provides information about the analyte concentration [95]. In many cases the direct charge transfer between the redox enzyme and electrode is hindered, making the detection based on the previously discussed method difficult. Yet, sometimes, one of the generated products can be reduced/oxidized at the electrode so that the reduction/oxidation current can be directly related to the amount of analyte in the solution [95].

In the case of direct charge transfer between the enzyme and the electrode, the current in the electrode is governed by electron tunnelling across the interface. The tunnelling process is characterized by the electron transfer rate constant, which is given by $k_{ET} = k_0 \exp(-\beta d)$, where d is the distance separating the electrode and the redox group of the enzyme, k_0 is the electronic rate constant at $d = 0$, and β is the electronic decay coefficient [96]. Thus, several factors related to the functionalization method strongly influence the electron transfer rate constant. For instance, the protein orientation influences the position of the redox group of the enzyme respect to the surface and thus the distance d. Also the linker molecules used to immobilize the protein to the surface will affect k_{ET}, by changing d (depending on the molecule length) and β (depending on the electronic properties of the used molecules). Indeed, the proper choice of the linker molecules can have very drastic consequences on k_{ET}, and thus on the total current, determining the device sensitivity. For instance, it is well known that the value of β differs for conjugated and nonconjugated molecules, because of the strong overlap between π orbitals in the case of conjugated molecules. Typical values of β for conjugated molecules are $\beta_{conj} \approx 0.2–0.5$ Å^{-1} and for nonconjugated molecules $\beta_{non-conj} \approx 1.1–1.5$ Å^{-1} [97]. This relatively small difference in β has a large influence on k_{ET} due to the exponential tunnelling factor. Assuming a value of $d = 1$ nm, k_{ET} will be three to four orders of magnitude larger for the case of conjugated molecules, underlining the importance of choosing the appropriate linker molecule.

To provide a proof of concept for diamond-based amperometric biosensors, horseradish peroxidase (HRP) enzymes were immobilized on the surface of UNCD electrodes. The immobilization process was been carried out on H-terminated (using the photochemical grafting of alkenes) and O-terminated (based on APDEMS) surfaces [49, 88]. In the case of the HRP on the H-terminated UNCD electrode [88], the cyclic voltammetry experiments showed reduction/oxidation waves, which have been attributed to the direct charge transfer between the diamond electrode and the redox centre of the enzyme. HRP is an enzyme that is widely used in bioelectrochemistry as a sensor for H_2O_2. The analyte H_2O_2 will oxidize the redox center of the HRP, which can be reduced to its initial state with two electrons provided by the electrode; thus, the measured current is directly related to the concentration of H_2O_2 in the solution. Figure 16.23(a) shows a typical amperometric experiment performed at a fixed potential of 0.05V against Ag/AgCl using a HRP-UNCD diamond electrode. The step-like increase of the cathodic current corresponds to the addition of H_2O_2 aliquots to the solution. Figure 16.23(b) shows the dependence of the cathodic current on the concentration of H_2O_2 [88]. These results show that enzyme-modified diamond electrodes can be used for the development of amperometric biosensors featuring a high selectivity by working at low potentials.

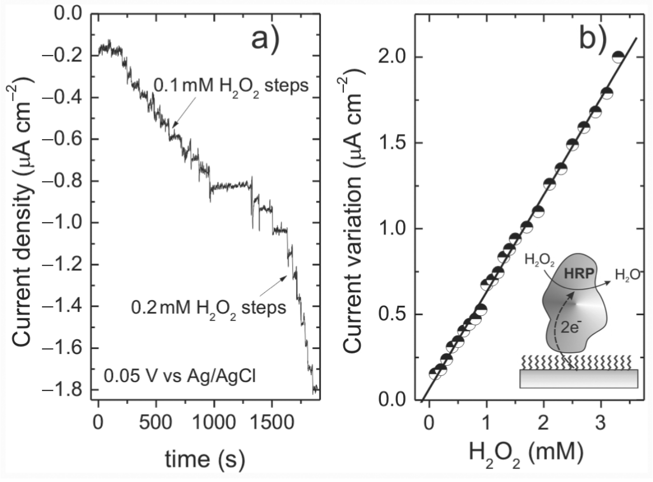

(a) (b)

Figure 16.23 Electrochemical response of a UNCD electrode modified with the enzyme horseradish peroxidase (HRP). H_2O_2 oxidizes the redox centre of the HRP, which can be reduced to its initial state with two electrons provided by the electrode. The measured current is directly related to the concentration of H_2O_2 in the solution. (a) Amperometric experiment performed at a fixed potential of 0.05 V versus Ag/AgCl. The step-like increase of the cathodic current corresponds to the addition of H_2O_2 aliquots to the solution. (b) Calibration curve; dependence of the cathodic current on the concentration of H_2O_2 added to the solution

16.5.2 Enzyme Field Effect Transistors

The working principle of enzymatically coupled ion-sensitive field effect transistors (ENFETs), initially proposed by Janata in 1976 [98], relies on the immobilization of enzymes on top of the active area of an electrolytic solution gate, field-effect transistor (SGFET), see Figure 16.24. The catalytic activity of the immobilized enzymes towards certain analytes alters the chemical composition of the solution close to the active area. In some cases, the enzymatic reaction induces a local change of the pH, which can be detected by the SGFET. Until now, reports on Si-based ENFETs have dominated the literature [99, 100], but there are still major problems with the stability of such devices. Due to its chemical stability and biocompatibility, diamond offers an attractive platform for the fabrication of ENFETs. In addition, the unique feature of its spontaneous surface conductivity induced by hydrogen termination offers a novel detection mechanism. SGFETs on H-terminated diamond surfaces have been successfully demonstrated, exhibiting a clear sensitivity to both pH and the ionic strength of the solution [10, 71]. It has been shown that the surface conductivity of H-terminated diamond can be modulated in an electrolyte by using a gate electrode [9, 11]. Under the control of the gate electrode, and in a certain potential range, the hydrogenated diamond/electrolyte interface behaves like an almost ideal capacitor, allowing the capacitive charging of the interface [11]. Interestingly, a surface conductive diamond SGFET behaves like a MOSFET device (with the metal replaced by the solution gate) in which there is no insulating layer preventing carriers crossing the interface. Figure 16.25(a) shows the typical transistor curves of a SGFET fabricated on a IIa-type single crystalline diamond; complete pinch-off of the drain source

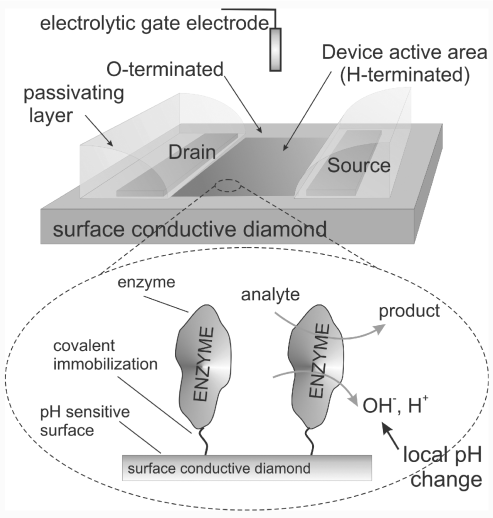
electrolytic gate electrode
O-terminated
passivating layer
Device active area (H-terminated)
Drain
Source
surface conductive diamond
enzyme
analyte
product
covalent immobilization
ENZYME
ENZYME
pH sensitive surface
OH⁻, H⁺
local pH change
surface conductive diamond

Figure 16.24 Working principle of a surface conductive diamond enzymeFET

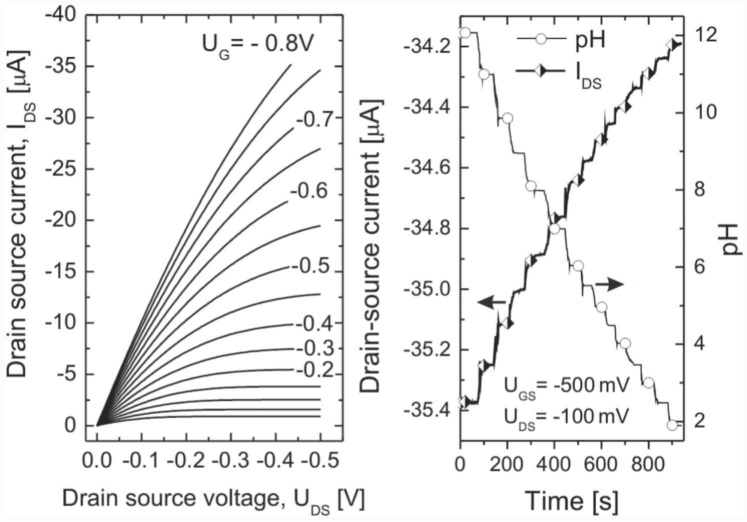

Figure 16.25 Characterization of a solution gate field-effect transistor based on surface conductive diamond substrates. (a) Typical transistor characteristics, drain-source current versus drain source voltage for different gate voltages (the gate voltage is referred to a Ag/AgCl reference electrode). (b) pH response of the SGFET; a pH decrease results in a decrease of the surface conductivity, and thus of the drain-source current

current below the threshold gate potential, and drain-source current saturation for large drain-source voltages are clearly visible. The pH sensitivity of surface conductive diamond SGFETs has been studied in different laboratories. Initially, Kawarada *et al*. reported that H-terminated diamond surfaces are not pH sensitive [9]. Later on, it was shown that the introduction of certain groups at the surface of H-terminated diamond resulted in a pH sensitivity and that a decrease of the pH resulted in a decrease of the surface conductivity, see Figure 16.25(b) [10]. Different possibilities have been suggested to explain the pH sensitivity of surface conductive diamond SGFETs. For instance, it has been shown that by using a description of the diamond/water interface based on the site-binding model in which amphoteric hydroxyl groups are present at the diamond surface, the correct pH dependence can be explained [10]. In addition, the adsorption of OH^- and H_3O^+ ions onto the H-terminated diamond surface could also explain such a pH dependence [71]. However, a detailed microscopic understanding of the pH sensitivity of diamond surfaces is still missing [11].

For the fabrication of diamond-based ENFETs, we have covalently tethered acetylcholinesterase (AChE) enzymes to the active area of a pH-sensitive, surface-conductive, diamond SGFET [82], as shown schematically in Figure 16.24. As mentioned above, AChE hydrolyzes the neurotransmitter acetylcholine (ACh) into choline and acetate. The latter is hydrolyzed very quickly to acetic acid, a process that releases a proton and thus changes the local pH of the surrounding electrolyte in the vicinity of the enzymes. Due to the pH sensitivity of diamond SGFETs, the variation of the pH in the direct vicinity of the sensitive surface can be monitored as a variation of the drain–source current. Thus, the measured variation of the drain–source current is proportional to the local pH change and, in turn, also proportional to the concentration of analyte (here acetylcholine).

For the fabrication of diamond ENFETs, the enzymes were covalently grafted to the active area of the diamond SGFET, which was previously modified using the photochemical method for tethering amino-terminated alkene molecules, as described in the section on functionalization of surfaces). In this particular case, the enzymes were immobilized to the aminated surface by using glutaraldehyde crosslinking. The experiments were performed in an electrolyte solution containing a Na-based phosphate buffer, $MgCl_2$, and NaCl, at a pH of 8. A detailed description of the experimental methods can be found in Ref. [82]. Figure 16.26(a) shows the variation of the source–drain current and of the macroscopic pH value of the electrolyte solution plotted versus time, while different concentrations of the analyte, acetylcholine chloride, were added to the solution. By increasing the concentration of the acetylcholine the drain-source current decreases, due to the lowering of the local pH, which results from the released protons during the acetylcholine hydrolyzation. The results in Figure 16.26(a) demonstrate that the detection limit is below 1 μM of acetylcholine. Figure 16.26(b) shows a calibration curve, in which the change in I_{sd} is plotted versus the concentration of substrate. From the linear slope in the lower substrate concentration range, the sensitivity of the ENFET can be derived. With the help of the transistor characteristics, a sensitivity value of about 500 μV/μM was obtained. As expected, this value is strongly dependent on the buffer concentration, solution pH, temperature, etc. [82]. In addition, several control experiments were performed to ensure that the device response in fact originated from the covalently bound enzymes. For devices without enzymes a negligible response to acetycholine of about 1.1 μV/μM was found, most probably induced by minimal pH variation of the electrolyte upon analyte addition. To confirm the importance of the covalent grafting, ENFETs devices were fabricated in which the enzymes were merely physisorbed, without the use of linker molecules and cross-linking. The sensitivity then dropped to values as low as 3.7 μV/μM, demonstrating that a proper covalent attachment is needed. Stability tests were also conducted; after 5 days of storage in standard electrolyte at 4 °C, a decrease in the sensitivity of about 20 % was observed for the AChE-diamond FETs [82]. AChE proteins are known to be quite

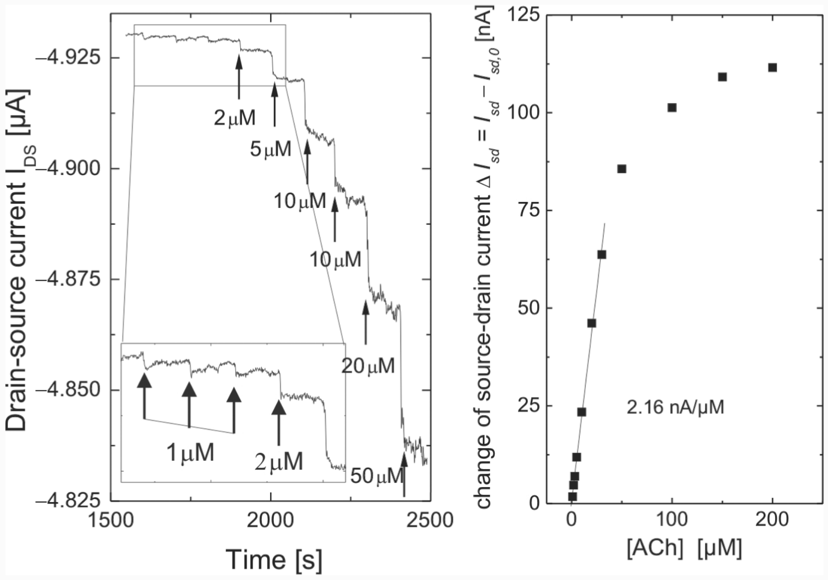

(a) (b)

Figure 16.26 Characterization of the acetylcholinesterase (AChE) diamond ENFET. (a) Drain source current response of the device to addition of acetylcholine (ACh) to the solution. By increasing the concentration of ACh, a decrease of the drain-source current is observed. During the catalytic activity of AChE in the presence of ACh, protons are released close to the diamond surface, which locally decreases the pH of the solution. As a result, the drain-source current decreases. (b) Calibration curve showing the variation of the drain-source current with the concentration of ACh

delicate enzymes, and thus extremely sensitive to the environment. By using the more robust penicillinase enzymes, we have been able to demonstrate an almost unchanged response of the ENFETs after more than 1 month of storage at 4 °C.

All these experiments show that diamond-based SGFET devices in combination with various linking and cross-linking methods, offer a versatile and stable platform for applications in the field of biosensors. The stability and performance, of course, depends on the particular biomolecule used for the specific sensing application.

16.6 CONCLUSIONS

The functionalization of diamond surfaces with biomolecules is of special relevance for applications in the field of biotechnology and biosensors. In this chapter, different strategies for the modification of diamond surfaces with organic molecules are described. For instance, photochemical modification of H-terminated diamond surfaces with alkene molecules, or electrochemical and chemical (spontaneous) modification using aryl diazonium molecules. While it has been reported that the photochemical and chemical methods result in sub/monolayer coverage, multilayer formation was observed using the electrochemical method. For O-terminated surfaces, we have shown that silane chemistry can be used, provided that hydroxyl groups are available at the diamond surface.

Due to the large contrast for grafting molecules onto oxygen- and hydrogen-terminated surfaces, most of the functionalization methods discussed above can be used to produce patterned surfaces. Surface polymerization has been briefly discussed as an alternative route for introducing functional groups to diamond surfaces; we have shown that the preparation of patterned surfaces is also possible using self-initiated photografting and photopolymerization.

We have also discussed the adsorption of proteins on these functionalized diamond surfaces, paying special attention to the immobilization via covalent bonds. Even if immobilized on the diamond surface, the proteins (at least partially) maintain their catalytic activity, as clearly demonstrated by fluorescence microscopy (in the case of the green fluorescence protein), electrochemical characterization (for cytochrome c on diamond electrodes), and colorimetric experiments (for acetylcholinesterase). Finally, two applications have been discussed, namely amperometric enzyme sensors and enzyme field effect transistor (ENFET) biosensors. In the case of the amperometric device, horseradish peroxidase enzymes were grafted onto the surface of conductive UNCD electrodes. The charge transfer between the active redox centre of the enzyme and the electrode surface enable the detection of H_2O_2 at very low overpotentials, demonstrating that enzyme-modified diamond electrodes can be used for the development of third-generation biosensors, based on the direct charge transfer between the enzymes and the electrode. In the case of ENFETs, the active area of surface conductive, solution gate field-effect transistors was modified with acetylcholinesterase enzymes, in order to develop biosensors for the detection of neurotransmitters. These are preliminary prototypes but they demonstrate that together with different linking and crosslinking methods, they offer a versatile and stable platform for applications in the field of biosensors.

However, considerably more work will still be required in order to improve further our understanding of the functionalization of diamond surfaces. A detailed knowledge of the microscopic mechanisms enabling the functionalization methods discussed here is still missing. Furthermore, these functionalization methods have to be further refined in order to obtain a better control over the whole process. Most of the functionalization methods discussed here will allow the preparation of monofunctional monolayers of biomolecules. Surface polymerization, on the other hand, is a relatively simple method that enables the fabrication of porous polymer layers, which can accommodate different functionalities and a larger amount of biomolecules, opening the way for novel designs. A research field which is still in its infancy is the interaction of biomolecules with bare and modified diamond surfaces; for instance, while O-terminated surfaces have shown strong affinities for proteins, H-terminated surfaces show remarkably good nonfouling characteristics. The origin of this is not clearly understood. Other terminations, such as fluorinated diamond, have not yet been explored in this context, and might reveal interesting nonfouling properties, as demonstrated for fluorinated diamond-like carbon films. The interaction of living systems, i.e. cells, with diamond surfaces is very important for both *in-vitro* and *in-vivo* applications. However, so far, not much is known about this subject, partially due to the lack of understanding at the level of protein/diamond interactions. This fascinating challenge will surely be one of the most relevant fields of research for those interested in biorelated applications of diamond.

ACKNOWLEDGEMENTS

This work was partially supported by the EU through the research projects DRIVE (Diamond Research on Interfaces and Versatile Electronics) and DREAMS (Diamond to Retina Artificial Micro-Interfaces Structures), and by the Deutsche Forschungsgemeinschaft (DFG) under projects GA 1432/1-1 and SFB 563. I am particularly grateful to Prof. Martin Stutzmann for critical reading of the manuscript.

REFERENCES

[1] Y. V. Pleskov, A. Y. Sakharova, M. D. Krotova, L. L. Bouilov and B. V. Spitzyn: Photoelectrochemical properties of semiconductor diamond, *Journal of Electroanalytical Chemistry* **228**, 19 (1987).

[2] H. B. Martin, A. Argoitia, J. C. Angus and U. Landau: Voltammetry studies of single-crystal and polycrystalline diamond electrodes, *Journal of the Electrochemical Society* **146**, 2959 (1999).

[3] G. M. Swain, A. B. Anderson and J. C. Angus: Applications of diamond thin films in electrochemistry, *MRS Bulletin* **23**, 56 (1998).

[4] W. Yang, O. Auciello, J. E. Butler, W. Cai, J. A. Carlisle, J. E. Gerbi, D. M. Gruen, T. Knickerbocker, T. L. Lasseter, J. N. Russell, L. M. Smith and R. J. Hamers: DNA-modified nanocrystalline diamond thin-films as stable, biologically active substrates, *Nature Materials* **1**, 253 (2002).

[5] Robert A. Freitas Jr., *Nanomedicine*, Volume IIA: *Biocompatibility*, Landes Bioscience, 2003.

[6] M. I. Landstrass and K. V. Ravi: Resistivity of chemical vapor deposited diamond films, *Applied Physics Letters* **55**, 975 (1989).

[7] F. Maier, M. Riedel, B. Mantel, J. Ristein and L. Ley: Origin of surface conductivity in diamond, *Physical Review Letters* **85**, 3472 (2000).

[8] D.G. Castner, B.D. Ratner, Biomedical surface science: Foundations to frontiers, *Surface Science* **500**, 28 (2002).

[9] H. Kawarada, Y. Araki, T. Sakai, T. Ogawa and H. Umezawa: Electrolyte solution-gate FETs using diamond surface for biocompatible ion sensors, *Physica Status Solidi (a)* **185**, 79 (2001).

[10] J.A. Garrido, A. Härtl, S. Kuch, M. Stutzmann, O. Williams and R. Jackmann: pH sensors based on hydrogenated diamond surfaces, *Applied Physics Letters* **86**, 073504 (2005).

[11] J.A. Garrido, A. Härtl, M. Dankerl, A. Reitinger, M. Eickhoff, A. Helwig, G. Müller, M. Stutzmann, The surface conductivity at the diamond/aqueous electrolyte interface, *J. Am. Chem. Soc.* **130**, 4177 (2008).

[12] C. E. Nebel, B. Rezek, D. Shin and H. Watanabe: Surface electronic properties of H-terminated diamond in contact with adsorbates and electrolytes, *Physica Status Solidi (a)* **203**, 3273 (2006).

[13] M. Nesladek, D. Tromson, C. Mer, P. Bergonzo, P. Hubik, and J.J. Mares, Superconductive B-doped nanocrystalline diamond thin films: Electrical transport and Raman spectra, *Appl. Phys. Lett.* **88**, 23211 (2006).

[14] Y. Show, M. A. Witek, P. Sonthalia, and G. M. Swain, Characterization and electrochemical responsiveness of boron-doped nanocrystalline diamond thin-film electrodes, *Chem. Mater.* **15**, 879 (2003).

[15] J. A. Bennett, J. Wang, Y. Show, and G. M. Swain, Effect of sp^2-bonded nondiamond carbon impurity on the response of boron-doped polycrystalline diamond thin-film electrodes, *J. Electrochem. Soc.* **151**, E306 (2004).

[16] A. E. Fischer, Y. Show, and G. M. Swain, Electrochemical performance of diamond thin-film electrodes from different commercial sources, *Anal. Chem.* **76**, 2553 (2004).

[17] D. M. Gruen: Nanocrystalline diamond films, *Annual Review of Materials Science* **29**, 211 (1999).

[18] S. Bhattacharyya, O. Auciello, J. Birrell, J.A. Carlisle, L.A. Curtiss, A. N. Goyette, D. M. Gruen, A. R. Krauss, J. Schlueter, A. Sumant *et al.*, *Appl. Phys. Lett.* **79**, 1441 (2001).

[19] P. Achatz, O.A. Williams, P. Bruno, D.M. Gruen, J.A. Garrido, and M. Stutzmann, Effect of nitrogen on the electronic properties of ultrananocrystalline diamond thin films grown on quartz and diamond substrates, *Phys. Rev. B* **74**, 155429 (2006).

[20] X. Xiao, J. Birrell, J. E. Gerbi, O. Auciello and J. A. Carlisle: Low temperature growth of ultrananocrystalline diamond, *J. Appl. Phys.* **96**, 2232 (2004).

[21] A. Freedman and C. D. Stinespring: Fluorination of diamond (100) by atomic and molecular beams, *Appl. Phys. Lett.* **57**, 1194 (1990).

[22] J. B. Miller and D. W. Brown: Photochemical Modification of Diamond Surfaces, *Langmuir* **12**, 5809 (1996).

[23] A. Freedman: Halogenation of diamond (100) and (111) surfaces by atomic beams, *J. Appl. Phys.* **75**, 3112 (1993).

[24] H. Kawarada: Hydrogen-terminated diamond surfaces and interfaces, *Surface Science Reports* **26**, 205 (1996).

[25] R. S. Gi, T. Mizumasa, Y. Akiba, Y. Hirose, K. T. and M. Iida: Formation mechanism of p-type surface conductive layer on deposited diamond films, *Japanese Journal of Applied Physics* **34**, 5550 (1995).

[26] P.E. Pehrsson and T.W. Mercer, Oxidation of the hydrogenated diamond (100) surface, *Surface Science* **460**, 49 (2000).

[27] G.-J. Zhang, K.-S. Song, Y. Nakamura, T. Ueno, T. Funatsu, I. Ohdomari and H. Kawarada: DNA micropatterning on polycrystalline diamond via one-step direct amination, *Langmuir* **22**, 3728 (2006).

[28] V. S. Smentkowski, J. John T. Yates, X. Chen and I. William A. Goddard: Fluorination of diamond–C_4F_9I and CF_3I photochemistry on diamond (100), *Surface Science* **370**, 209 (1997).

[29] H. B. Martin, A. Argoitia, J. C. Angus and U. Landau: Voltammetry studies of single-cristal and polycrystaline diamond electrodes, *Journal of the Electrochemical Society* **146**, 2959 (1999).

[30] T. Kondo, H. Ito, K. Kusakabe, K. Ohkawa, Y. Einaga, A. Fujishima and T. Kawai: Plasma etching treatment for surface modification of boron doped diamond electrodes, *Electrochimica Acta* **52**, 3841 (2007).

[31] S. Ferro and A. D. Battisti: The 5-V window of polarizability of fluorinated diamond electrodes in aqueous solutions, *Anal. Chem.* **75**, 7040 (2003).

[32] S. Hadenfeldt and C. Benndorf, Adsorption of fluorine and chlorine on the diamond (100) surface, *Surface Science* **404**, 227 (1998).

[33] T. Ando, M. Nishitani-Gamo, R. E. Rawles, K. Yamamoto, M. Kamo and Y. Sato: Chemical modification of diamond surfaces using a chlorinated surface as an intermediate state, *Diamond and Related Materials* **5**, 1136 (1996).

[34] K. Song, M. Degawa, Y. Nakamura, H. Kanazawa, H. Umezawa and H. Kawarada: Surface-modified diamond field-effect transistors for enzyme-immobilized biosensors, *Japanese Journal of Applied Physics* **43**, L814 (2004).

[35] K. Song, Y. Nakamura, Y. Sasaki, M. Degawa, J. H. Yang, and H. Kawarada, pH-sensitive diamond field-effect transistors (FETs) with directly aminated channel surface, *Anal. Chim. Acta* **573**, 3 (2006).

[36] T. Strother, T. Knickerbocker, J. Russell, J. N., J. Butler, L. M. Smith and R. Hamers: Photochemical functionalization of diamond films, *Langmuir* **18**, 968 (2002).

[37] B. Nichols, J. Butler, J. Russell, J.N. and R. Hamers: Photochemical functionalization of hydrogen-terminated diamond surfaces: A structural and mechanistic study, *Journal of Physical Chemistry B* **109**, 20938 (2005).

[38] B. M. Nichols, K. M. Metz, K.-Y. Tse, J. E. Butler, J. N. Russell, Jr., and R. J. Hamers. Electrical bias-dependent photochemical functionalization of diamond surfaces. *Journal of Physical Chemistry B* **110**, 16535–16543 (2006).

[39] D. Shin, B. Rezek, N. Tokuda, D. Takeuchi, H. Watanabe, T. Nakamura, T. Yamamoto, and C. E. Nebel, Photo- and electrochemical bonding of DNA to single crystalline CVD diamond, *Physica Status Solidi (a)* **203**, 3245 (2006).

[40] T.-C. Kuo, R.L. McCreery, G. M. Swain, electrochemical modification of boron-doped chemical vapor deposited diamond surfaces with covalently bonded monolayers, electrochem. *Solid-State Lett.*, **2**, 188 (1999).

[41] J. Wang, M. A. Firestone, and J. A. Carlisle, Surface functionalization of ultrananocrystalline diamond films by electrochemical reduction of aryldiazonium salts, *Langmuir* **20**, 11450 (2004).

[42] H. Uetsuka, D. Shin, N. Tokuda, K. Saeki, C. E. Nebel, electrochemical grafting of boron-doped single-crystalline chemical vapor deposition diamond with nitrophenyl molecules, *Langmuir* **23**, 3466 (2007).

[43] J. Pinson, F. Podvorica, Attachment of organic layers to conductive or semiconductive surfaces by reduction of diazonium salts, *Chem. Soc. Rev.* **34**, 429 (2005).

[44] S. Q. Lud, M. Steenackers, R. Jordan, P. Bruno, D. M. Gruen, P. Feulner, J. A. Garrido, and M. Stutzmann, Chemical grafting of biphenyl self-assembled monolayers on ultrananocrystalline diamond, *J. Am. Chem Soc.* **128**, 16884 (2006).

[45] W. Yang, S.E. Baker, J. E. Butler, C.-S. Lee, J. N. Russell, L. Shang, B. Sun, and R.J. Hamers, Electrically addressable biomolecular functionalization of conductive nanocrystalline diamond thin films, *Chem. Mater.* **17**, 938 (2005).

[46] A. Adenier, N. Barré, E. Cabet-Deliry, A. Chaussé, S. Griveau, F. Mercier, J. Pinson and C. Vautrin-Ul, Study of the spontaneous formation of organic layers on carbon and metal surfaces from diazonium salts, *Surface Science* **600**, 4801 (2006).

[47] W. Eck, V. Stadler, W. Geyer, M. Zharnikov, A. Golzhauser, M. Grunze, Generation of surface amino groups on aromatic self-assembled monolayers by low energy electron beams −a first step towards chemical lithography, *Adv. Mater.* **12**, 805 (2000).

[48] H. Notsu, T. Fukazawa, T. Tatsuma, D.A. Tryk, and A. Fujishima, Hydroxyl groups on boron-doped diamond electrodes and their modification with a silane coupling agent, *Electrochem. Solid-State Lett.* **4**, H1 (2001).

[49] J. Hernando, T. Pourrostami, J. A. Garrido, O. A. Williams, D. M. Gruen, A. Kromka, D. Steinmueller, M. Stutzmann, Immobilization of horseradish peroxidase via an amino silane on oxidized nanocrystalline diamond, *Diamond and Related Materials* **16**, 138 (2007).

[50] S. Ferro, M. Dal Colle and A. De Battisti, Chemical surface characterization of electrochemically and thermally oxidized boron-doped diamond film electrodes, *Carbon* **43**, 1191 (2005)

[51] J. Sagiv: Organized monolayers by adsorption. 1. Formation and structure of oleophobic mixed monolayers on solid surfaces, *J. Am. Chem. Soc.* **102**, 92 (1980).

[52] A. Ulman: Formation and structure of self-assembled monolayers, *Chemical Reviews* **96**, 1533 (1996).

[53] J. H. Moon, J. W. Shin, S. Y. Kim, J. W. Park, Formation of uniform aminosilane thin layers: an imine formation to measure relative surface density of the amine group, *Langmuir* **12**, 4621 (1996).

[54] G. Harsanyi, Polymeric sensing films: new horizons in sensorics? *Materials Chemistry and Physics* **43**, 199 (1996).

[55] L. Li, J. L. Davidson, C. M. Lukehart, Surface functionalization of nanodiamond particles via atom transfer radical polymerization, *Carbon* **44**, 2308 (2006).

[56] T. Matrab, M.M. Chehimi, J.P. Boudou, F. Benedic, J. Wang, N.N. Naguib and J.A. Carlisle, Surface functionalization of ultrananocrystalline diamond using atom transfer radical polymerization (ATRP) initiated by electro-grafted aryldiazonium salts, *Diamond and Related Materials* **15**, 639 (2006).

[57] P. Actis, M. Manesse, C. Nunes-Kirchner, G. Wittstock, Y. Coffinier, R. Boukherroub and S. Szunerits, Localized electropolymerization on oxidized boron-doped diamond electrodes modified with pyrrolyl units, *Phys. Chem. Chem. Phys.* **8**, 4924 (2006).

[58] H. L. Wang, H. R. Brown, Self-initiated photopolymerization and photografting of acrylic monomers, *Macromolecular Rapid Communications* **25**, 1095–1099 (2004).

[59] M. Steenackers, S.Q. Lud, M. Niedermeier, P. Bruno, D.M. Gruen, P. Feulner, M. Stutzmann, J.A. Garrido, R. Jordan, Structured polymer grafts on diamond, *J. Am. Chem. Soc.* **129**, 15655 (2007).

[60] W. Okrój, M. Kamińska, L. Klimek, W. Szymański and B. Walkowiak, Blood platelets in contact with nanocrystalline diamond surfaces, *Diamond and Related Materials* **15**, 1535 (2006).

[61] J. M. Garguilo, B. A. Davis, M. Buddie, F. A. M. Köck and R. J. Nemanich, Fibrinogen adsorption onto microwave plasma chemical vapor deposited diamond films, *Diamond and Related Materials* **13**, 595 (2004).

[62] X. L. Kong, L. C. L. Huang, C.-M. Hsu, W.-H. Chen, C.-C. Han, and H.-C. Chang, High-affinity capture of proteins by diamond nanoparticles for mass spectrometric analysis, *Anal. Chem.* **77**, 259 (2005).

[63] D. Steinmüller-Nethl, F.R. Klossb, M. Najam-Ul-Haq, M. Rainer, K. Larsson, C. Linsmeier, G. Köhler, C. Fehrer, G. Lepperdingeg, X. Liu, N. Memmel, E. Bertel, C. W. Huck, R. Gassner and G. Bonn, Strong binding of bioactive BMP-2 to nanocrystalline diamond by physisorption, *Biomaterials* **27**, 4547 (2006).

[64] R.J. Hamers, J.E. Butler, T. Lasseter, B.M. Nichols, J.N. Russell, K.-Y. Tse and W. Yang, Molecular and biomolecular monolayers on diamond as an interface to biology, *Diamond and Related Materials* **14**, 661 (2005).

[65] T.L. Clare, B.H. Clare, B.M. Nichols, N.L. Abbott, and R.J. Hamers, Functional monolayers for improved resistance to protein adsorption: oligo(ethylene glycol) modified silicon and diamond surfaces, *Langmuir* **21**, 6344 (2005).

[66] A. Härtl, E. Schmich, J. A. Garrido, J. Hernando, S.C.R. Catharino, S. Walter, P. Feulner, A. Kromka, D. Steinmüller, and M. Stutzmann, Protein-modified nanocrystalline diamond thin films for biosensor applications, *Nature Materials* **3**, 736 (2004).

[67] C. G. Specht, O. A. Williams, R. B. Jackman, and R. Schoepfer, Ordered growth of neurons on diamond, *Biomaterials* **25**, 4073 (2004).

[68] K. F. Chong, K. P. Loh, S. R. K. Vedula, C. T. Lim, H. Sternschulte, D. Steinmüller, F.-S. Sheu, and Y. L. Zhong, Cell adhesion properties on photochemically functionalized diamond, *Langmuir* **23**, 5615 (2007).

[69] M. Mrksich and G. M. Whitesides, Using self-assembled monolayers to understand the interactions of man-made surfaces with proteins and cells, *Ann. Rev. Biophys. Biomol. Struct.* **25**, 55 (1996).

[70] G.B. Sigal, M. Mrksich, and G.M. Whitesides, Effect of surface wettability on the adsorption of proteins and detergents, *J. Am. Chem. Soc.* **120**, 3464 (1998).

[71] A. Härtl, J. A. Garrido, S. Nowy, R. Zimmermann, C. Werner, D. Horinek, R. Netz, and M. Stutzmann, The ion sensitivity of surface conductive single crystalline diamond, *J. Am. Chem. Soc.* **129**, 1282 (2007).

[72] J. J. Lyklema, *Fundamentals of Interface and Colloid Science*, Volume 2, Academic Press, 1995.

[73] R. Zimmermann, S. Dukhin, and C. Werner, *Phys. Chem. B.* **105**, 8544 (2001).

[74] K.N. Kudin and R. Car, Why are water-hydrophobic interfaces charged? *J. Am. Chem. Soc.* **130**, 3915 (2008).

[75] K.L. Prime and G.M. Whitesides, Self-assembled organic monolayers: model systems for studying adsorption of proteins at surfaces, *Science* **252**, 1164 (1991).

[76] J. Zheng, L. Li, S. Chen, and S. Jiang, Molecular simulation study of water interactions with oligo (ethylene glycol)-terminated alkanethiol self-assembled monolayers, *Langmuir* **20**, 8931 (2004).

[77] G. T. Hermanson, *Bioconjugate Techniques*, Academic Press, 1996.

[78] B. Rezek, D. Shin, C.E. Nebel, Properties of hybridized DNA arrays on single-crystalline undoped and boron-doped (100) diamonds studied by atomic force microscopy in electrolytes, *Langmuir* **3**, 7626 (2007).

[79] G.-J. Zhang, K.-S. Song, Y. Nakamura, T. Ueno, T. Funatsu, I. Ohdomari, and H. Kawarada, DNA micropatterning on polycrystalline diamond via one-step direct amination, *Langmuir* **22**, 3728 (2006).

[80] P. Christiaens, V. Vermeeren, S. Wenmackers, M. Daenen, K. Haenen, M. Nesládek, M. vandeVen, M. Ameloot, L. Michiels and P. Wagner, EDC-mediated DNA attachment to nanocrystalline CVD diamond films, *Biosensors and Bioelectronics* **22**, 170 (2006).

[81] S.Q. Lud, M. Stutzmann, J. A. Garrido, in preparation.

[82] A. Härtl, B. Baur, M. Stutzmann, and J.A. Garrido, Enzyme-modified field effect transistors based on surface-conductive single crystalline diamond, *Langmuir* **24**, 9898 (2008).

[83] G. L. Ellman, K. D. Courtney, V. Andres and R. M. Featherstone: A new and rapid olorimetric determination of acetylcholinesterase activity, *Biochemical Pharmacology* **7**, 88 (1962).

[84] A. Cornish-Bowden, *Fundamentals of Enzyme Kinetics*, Third Edition, Portland Press, 2004.

[85] S. Letant, B. Hart, S. Kane, M. Hadi, S. Shields and J. Reynolds: Enzyme immobilization on porous silicon surfaces, *Advanced Materials* **16**, 689 (2004).

[86] J. K. Mbouguen, E. Ngameni and A. Walcarius: Organoclay-enzyme film electrodes, *Analytica Chimica Acta* **578**, 145 (2006).

[87] A. Hai, D. Ben-Haim, N. Korbakov, A. Cohen, J. Shappir, R. Oren, M. E. Spira, and S. Yitzchaik, Acetylcholinesterase-ISFETs based system for the detection of acetylcholine and acetylcholinesterase inhibitors, *Biosensors and Bioelectronics*, **22**, 605 (2006).

[88] J. Rubio-Retama, J. Hernando, B. López-Ruiz, A. Härtl, D. Steinmüller, M. Stutzmann, E. López-Cabarcos, and J.A. Garrido, Synthetic nanocrystalline diamond as third generation biosensor support, *Langmuir* **22**, 5837 (2006).

[89] H. Notsu, T. Tatsuma and Akira Fujishima, Tyrosinase-modified boron-doped diamond electrodes for the determination of phenol derivatives, *J. Electroanal. Chem.* **523**, 86 (2002).

[90] J. Wang and J. A. Carlisle: Covalent immobilization of glucose oxidase on conducting ultrananocrystalline diamond thin films, *Diamond and Related Materials* **15**, 279 (2006).

[91] Y. L. Zhou, R. H. Tian and J. F. Zhi, Amperometric biosensor based on tyrosinase immobilized on a boron-doped diamond electrode, *Biosensors and Bioelectronics* **22**, 822 (2007).

[92] W. Yang, J.E. Butler, J.N. Russell, and R. J. Hamers, Direct electrical detection of antigen-antibody binding on diamond and silicon substrates using electrical impedance spectroscopy, *The Analyst* **132**, 296 (2007).

[93] K.-S. Song, G.-J. Zhang,, Y. Nakamura, K. Furukawa, T. Hiraki, J.-H. Yang, T. Funatsu, I. Ohdomari, and H. Kawarada, Label-free DNA sensors using ultrasensitive diamond field-effect transistors in solution, *Phys. Rev. E* **74**, 041919 (2006).

[94] K.-S. Song, T. Hiraki, Hitoshi Umezawa, H. Kawarada, Miniaturized diamond field-effect transistors for application in biosensors in electrolyte solution, *Appl. Phys. Lett.* **90**, 063901 (2007).

[95] A. J. Bard, M. Stratmann, *Encyclopedia of Electrochemistry: Bioelectrochemistry*, Volume 9, Wiley-VCH.

[96] A. M. Kuznetsov and J. Ulstrup, *Electron Transfer in Chemistry and Biology*, John Wiley & Sons, 1999.

[97] S. Creager, C. J. Yu, C. Bamdad, S. O'Connor, T. MacLean, E. Lam, Y. Chong, G. T. Olsen, J. Luo, M. Gozin, and J. F. Kayyem, Electron transfer at electrodes through conjugated 'molecular wire' bridges, *J. Am. Chem. Soc.* **121**, 1059 (1999).

[98] J. Janata and S. D. Moss: Chemically sensitive field-effect transistors, *Biomedical Engineering* **11**, 241 (1976).

[99] M. J. Schöning and A. Poghossian: Recent advances in biologically sensitive field-effect transistors (BioFETs), *Analyst* **127**, 1137 (2002).

[100] S. Dzyadevych, A. Soldatkin, Y. Korpan, V. Arkhypova, A. El'skaya, J.-M. Chovelon, C. Martelet and N. Jaffrezic-Renault: Biosensors based on enzyme field-effect transistors for determination of some substrates and inhibitors, *Analytical and Bioanalytical Chemistry* **377**, 496 (2003).

17 Diamond Electrochemical Sensors

JOHN S. FOORD

University of Oxford, Department of Chemistry, UK

17.1 Introduction 439
17.2 Electrochemical measurements 441
17.3 Advantages of diamond electrodes 442
17.4 Influence of growth conditions on electrode properties 443
17.5 Influence of surface termination on electrode properties 449
17.6 Sensing using macroscopic diamond electrodes 453
  17.6.1 Stripping voltammetry 453
  17.6.2 Solution phase voltammetry 455
  17.6.3 Functionalised diamond electrodes 461
17.7 Other aspects of diamond electrochemistry 462
17.8 Concluding remarks 464
References 465

17.1 INTRODUCTION

Electrochemistry is concerned with the investigation and applications of chemical processes involving electron transfer across an interface, normally formed between an electrically conducting solid, the electrode, and a solution, the electrolyte [1]. The subject plays an important role in research on basic scientific phenomena, such as corrosion, and in large-scale chemical processes such as those involved in the production of aluminium and chlorine and in electroplating. It also underlies various types of electrical device such as electrochemical sensors, e.g. for blood glucose, batteries and fuel cells, and electrochromic displays. Extremely large-scale commercial markets are associated with this broad field.

The choice of the electrode material is an important one in many electrochemical processes. The electrodes themselves can vary hugely, depending on the application. Bulk electrochemical production processes may involve electrodes, which may be square metres in area, whereas an electrochemical sensor may be based on a length scale a

CVD Diamond for Electronic Devices and Sensors Edited by Ricardo S. Sussmann
© 2009 John Wiley & Sons, Ltd.
ISBN: 978-0-470-06532-7

million times smaller. The former electrode may be required to last many months; the latter may be discarded after a single use. Numerous properties of the electrode need to be considered in making an optimal selection. Since electrochemical conditions can be quite hostile, robustness, strength and resistance to corrosion and erosion processes can be important. A problem with many potential electrochemistry applications is that the electrode becomes poisoned by adsorption of electrically insulating films on the surface; an inherent resistance to 'electrode fouling' is therefore sometimes needed. In electrochemical sensor applications such as the amperometric sensor, the need is often to be able to catalyse a particular redox process at an applied potential, and produce a measurable and reproducible current that is not masked by background interferences arising from unwanted capacitance in the circuit or competing electrochemical reactions. Commercial considerations also obviously arise.

Most people are familiar with diamond as a highly insulating material, or more recently as a semiconductor in the various potential applications that thin film diamond possesses in modern device technologies, such as power electronics. However, when highly doped with boron, the material takes on almost metallic properties and, in particular, exhibits an electrical resistance that is comparable to, or less, than that exhibited by many electrode materials that are in widespread use in electrochemistry today. This means that diamond has the potential to be used as an electrochemical material [2–5].

In Figure 17.1, historical data on the annual number of scientific publications concerning diamond electrochemistry is compared with that of a very well established analogous electrode material, namely glassy carbon (note the scaling factor). Prior to the mid-1990s, electrochemical studies of diamond were something of a scientific curiosity. However, the material began to be taken seriously by electrochemists in general around 1995, prompting a rapid rise in the number of publications. After this initial phase, the variation in

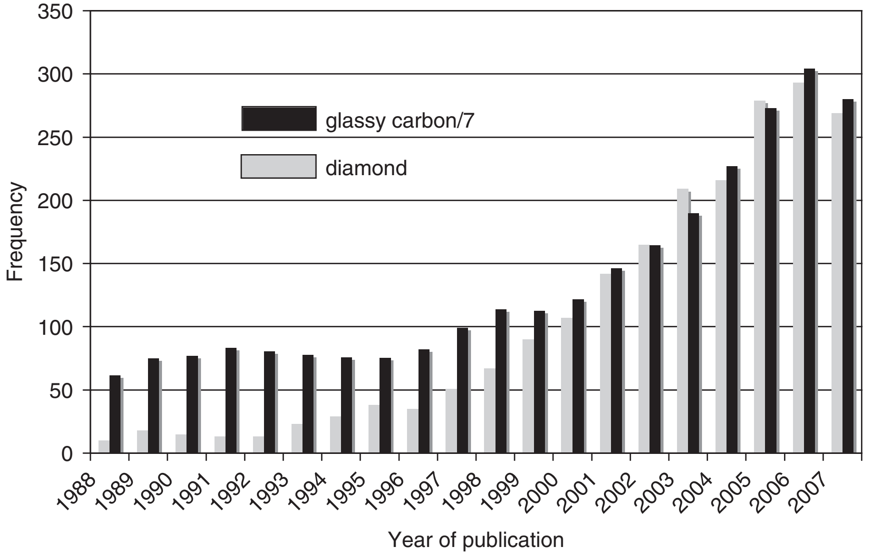

Figure 17.1 Historical data for the period 1988–2007, illustrating the annual number of scientific publications concerning diamond electrochemistry in comparison to similar data for glassy carbon. The figures for glassy carbon have been divided by a factor of 7

'diamond' activity has broadly tracked that of the electrochemical field as a whole, and it now has a significant, if not dominant, usage in this field. The main part of the published body of research is concerned with fundamental studies of diamond electrochemical systems, and with the development of electrochemical approaches for various chemical sensing technologies. In this chapter, the information to come out of this research will be reviewed, with a focus on the important results and developments in the field.

17.2 ELECTROCHEMICAL MEASUREMENTS

Since electrochemistry involves charge transfer across an interface between the electrode and solution phase, it is sensitive to any change in electrostatic potential across the interface concerned. If two dissimilar electrodes that are connected via a high input impedance digital voltmeter, are immersed in the solution phase, then the difference between the two interface potentials can be simply measured under conditions of essentially zero current flow where equilibrium exists at each electrode surface. The potential of the electrochemical cell thereby established will depend on the standard electrode potentials of the electrochemical couples comprising the cell, and on the solution concentrations of the electroactive species present. This forms the basis of the potentiometric approach to electroanalysis, in which the electrode potential of an indicator electrode, the potential of which depends on solution concentration, is measured against a reference electrode. If the indicator electrode can be made truly selective to one species, then an accurate electrochemical sensor can be produced. The most familiar potentiometric sensor is the glass electrode for the measurement of pH.

Problems with potentiometric sensors arise if, as is commonly the case, the electrode is not sufficiently selective to the target chemical species. A more versatile electrochemical approach is therefore based on voltammetry, in which the current flowing at an electrode is measured as a function of an applied potential. This provides very sensitive detection limits, down to picomolar, and enables several species to be distinguished and detected at once if they react at differing potentials. The most rigorous measurement technique here is based on the use of three electrodes rather than the two electrodes for the case above. Put simply, a potentiostat is used to measure the current flowing through the electrode of interest, the so-called working electrode, as a function of the potential applied between it and a reference electrode through which no current flows; instead a third electrode, known as an auxiliary or counter electrode, is used to provide a balancing counter current to that flowing through the working electrode.

The most common measurement method employing this set-up is known as cyclic voltammetry, where the current to the working electrode is measured as its potential is varied linearly with time between two limits, V_1 and V_2, after which the direction of potential scan is immediately reversed to return the potential to V_1. This corresponds to one complete voltammetric cycle. An example of such cyclic voltammetry data is shown in Figure 17.5A. The y-axis (current) refers to the current flowing through the working electrode of interest, in this case diamond. The x-axis is the potential applied to the diamond electrode versus a reference electrode. In this case the reference electrode is the so-called standard calomel electrode (SCE). In trace (i), the potential is first swept from -1.0 V to $+2.0$ V. At a potential of about 1.0 V, hydroquinone present in the cell in the vicinity of the electrode becomes oxidised, producing an oxidative peak in the voltammetry trace; as the potential is swept back to -1.0 V, a reductive peak is seen as some of this oxidised hydroquinone is reduced. From the magnitude of these current peaks, the concentration of hydroquinone can be deduced, and furthermore the hydroquinone peaks can be distinguished from those associated with other species, provided they occur at other potentials. The electron transfer kinetics are represented by the peak separation between the oxidative and reductive peaks. If the kinetics are fast, the two peaks are almost coincident, a peak separation of down to 57 mV being observed. As the kinetics get slower, so the peak separation rises as a greater electrical driving force ('overpotential') is needed. The voltammetric data therefore provides the basic scientific characterisation of the electrochemical system, which underpins the production of an electrochemical sensor relating to that system. Hence cyclic voltammetry is very commonly used for the early assessment of electrochemical properties for electroanalytical applications. In practical applications, greater sensitivity can be achieved if pulsed potential waveforms are employed, which has given rise to the existence of several alternative voltammetric methods, closely related to the cyclic voltammetry approach described above. Further details can be obtained from standard texts dealing with so-called dynamic (i.e. electrochemical measurement during current flow) electrochemistry such as Ref. [1].

17.3 ADVANTAGES OF DIAMOND ELECTRODES

There is a combination of reasons as to why diamond electrodes frequently show improved performance in comparison with other electrode materials, notably glassy carbon and graphitic electrodes, which have frequently been utilised for amperometric sensor applications, where a rapid, sensitive, reproducible and easily measured signal response are the primary requirements [2–5]. Most obviously, diamond electrodes display a minimal background signal in these types of application, enabling sensitive measurement of the desired signal to be made. The background signal has several origins, one of which is the double-layer capacitance that tends to be smaller ($\sim$10 μF cm^{-2}) for diamond. Secondly, many types of carbon electrode have a high concentration of ionisable or redox active groups on the surface, most typically oxygen–carbon functionalities, which give rise to distinct background peaks or a pseudo-capacitive background to the voltammetry data. These features seem to be absent from a diamond electrode. Thirdly, at higher potentials, most electrodes tend to exhibit extremely large background currents due to the decomposition of the electrolyte. For example, in water, hydrogen evolution sets in at negative potentials whilst oxygen evolution occurs at positive potentials. Due to the magnitude of these currents, electroanalysis cannot be carried out in such regimes, so essentially a 'potential window' is defined, within which the electrode can operate. For a Pt electrode this window is small, around 1.5 V. Complex electrochemical processes, such as are associated with solvent decomposition, tend to be very slow at diamond electrodes; a large electrochemical driving force or 'overpotential' is needed for them to occur. In Figure 17.2, it can be seen that these processes only occur significantly at diamond electrodes below -1 V or above 2 V versus SCE, meaning that redox processes over a much wider potential range than for conventional electrodes can be followed, using diamond.

One of the problems associated with electrochemistry is electrode fouling; adsorption of insulating deposits occurs at the electrode–electrolyte interface that can gradually poison the electrode response, a particular problem in biological media. Electrodes such as glassy carbon tend to be polar, hydrophilic and have chemically reactive oxygen functionalities that promote adsorption. In contrast, the diamond surface is chemically rather inert –

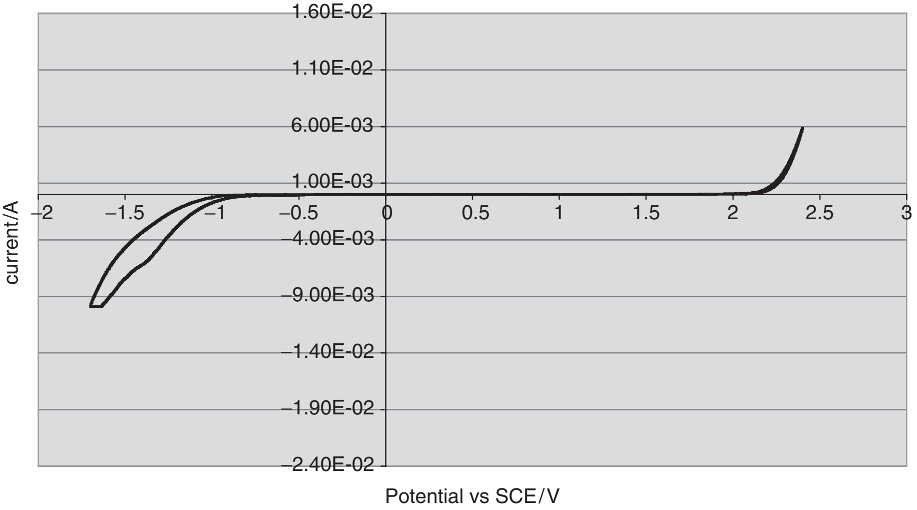

Figure 17.2 Background cyclic voltammogram versus SCE, 0.1 V s^{-1}, for a 3-mm diameter diamond electrode in 0.1-M HNO_3 at 300 K in the presence of dissolved oxygen

there is generally low electrostatic polarity and a lack of very reactive groups at the surface – so adsorption tends to be minimised. This means that diamond electrodes can preserve their activity for longer when in rather hostile solutions. This has been shown to be the case in a number of studies that have examined the activity of diamond electrodes in comparison with glassy carbon in solutions that bring about fouling, such as bovine serum albumin [6]. Typical results are shown in Figure 17.3. Whereas the glassy carbon electrode exhibits significant poisoning, making quantification of a sensor response quite difficult, this is not the case for the diamond electrode, which is scarcely affected by the presence of the adsorbing species. A general problem with many carbon electrodes is that the oxygen functionalities and microstructure can be quite variable, and complicated preconditioning routines are often used. As a result, reproducibility tends to be poor and the electrode performance can change quite markedly during use due, for example, to changes in the oxygen functional groups that are present. One of the striking features of diamond electrodes is the high degree of reproducibility that they exhibit without the need to resort to complicated activation routines. Finally, the robustness of the material can also be exploited. This has been demonstrated nicely in studies on the use of power ultrasound in electrochemical studies of diamond. Ultrasound is employed in electrochemistry since cavitational processes serve both to enhance mass transport to the electrode surface, thus enhancing sensitivity, and to prevent the build up of adsorbed layers. Unfortunately at the power densities required, many electrode materials are eroded away. Diamond, in contrast, is unaffected and so is the material of choice for this electrochemical application.

17.4 INFLUENCE OF GROWTH CONDITIONS ON ELECTRODE PROPERTIES

The general trend to emerge from studies of diamond electrodes (see [2–5] and references therein), is that they exhibit electron transfer kinetics for simple ‘outer sphere’ (electron

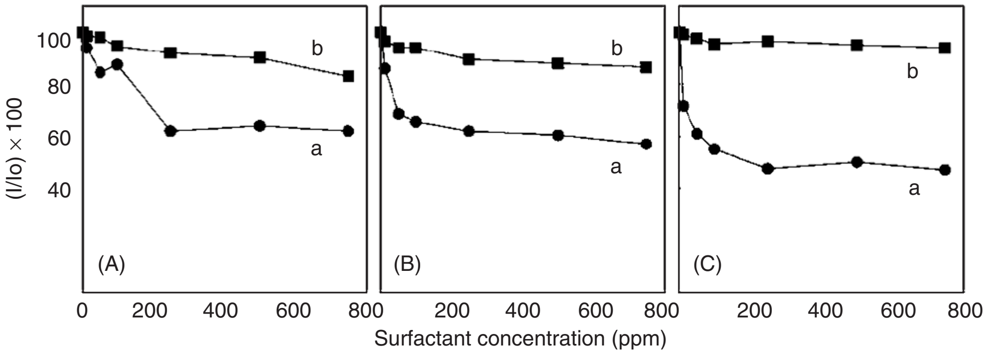

Figure 17.3 Graphs showing the variation in peak current in square-wave voltammetry for the oxidation of ascorbic acid with variation in the concentration of: (A) bovine serum albumin; (B) gelatin; (C) Triton X-100. (a) refers to a glassy carbon electrode and (b) to one fabricated from diamond. Reproduced with permission from D. Shin, D. A. Tryk, A. Fujishima, A. Merkoci and J. Wang, Electroanalysis, 17, 305–311 (2005) Copyright Wiley-VCH Verlag GmbH & Co.

transfer processes which occur with little change in bonding configuration) redox couples such as Ru $(NH_3)_6{}^{3+/2+}$ and $IrCl_6{}^{2-/3-}$, which are comparable to those observed from other active electrodes such as edge-plane graphite or activated glassy carbon, although more careful investigation suggests that features arise that are not expected for a uniform, conductive electrode material. In contrast, for more complex electrochemical processes, unusual selectivity effects can arise in comparison with other electrode materials, which for example gives rise to the wide potential window. The exact electrochemical properties of a given diamond electrode are influenced by the conditions used in CVD to prepare it, since these control the properties of the deposited diamond.

The term ‘diamond electrode’ encompasses a broad range of diamond-based materials, which vary with respect to the phase purity of the diamond, the microstructure of the crystallites that comprise the polycrystalline film, and dopant concentration, normally boron, which is used to impart conductivity. Each of these features is controlled by the choice of growth conditions, with low methane–hydrogen ratios in the reactor feedstock favouring phase-pure materials with large grain sizes, and higher methane content producing the opposite result. Most diamond electrodes are grown by hot-filament or microwave-assisted CVD, but the choice between these two growth techniques does not appear especially to influence the electrochemical properties.

Although some single crystal studies of diamond electrodes have been performed, the majority of the work has been done with polycrystalline materials that appear to perform similarly if the phase purity is high. Of the polycrystalline forms that are used, two particular types can be distinguished: large grain size materials with grain sizes in the range of typically 5–10 μm, and so-called nanocrystalline deposits with a grain size below 1 μm, typically several hundred nanometres. Typical electron micrographs [7] are shown in Figure 17.4. Raman spectra, as expected, confirm a high degree of phase purity for the large grain sample, whilst the Raman analysis of the small grain material shows the complicated spectrum associated with nanocrystalline diamond. This indicates the presence of a significant amount of graphitic and polyacetylene-type species within the confines of the film. Unsurprisingly the electrochemical properties of the different diamond phases are rather different from each other.

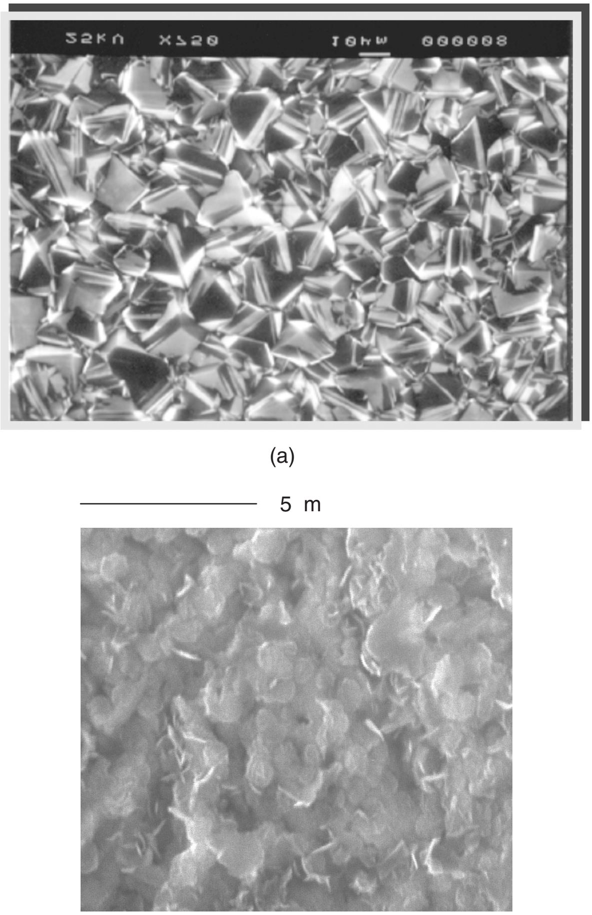

Figure 17.4 Secondary electron micrographs of: A, a macrocrystalline diamond electrode; B, a nanocrystalline diamond electrode. Reproduced with permission from C.H. Lau, K.J. Grehan, R.G. Compton, J.S. Foord and F. Marken, Journal of the Electrochemical Society, 150, E59–E65 (2003)

The large grain diamond electrode shows the extreme features of diamond electrochemistry that were highlighted in the previous section, whereas the properties are somewhat degraded for the nanocrystalline material. For example, if we compare the width of the potential window as the phase purity is changed, it is reduced from 3–4 V for phase-pure diamond down to around 2.5 V for the nanocrystalline material. This simply represents a reduction in the electrochemical selectivity of the electrode. Phase-pure diamond exhibits good electrochemical responsivity for simple electron transfer processes, but chemically complicated steps such as the decomposition of water are rather slow, presumably because intermediates cannot be stabilised by bonding to the inert electrode surface. This selectivity is shown rather nicely in the voltammograms in Figure 17.5, which compare the behaviour of diamond and platinum as electrodes in liquid ammonia [8]. Chemically complex processes occur at potentials more positive than 0.8 V, so the catalytic Pt electrode

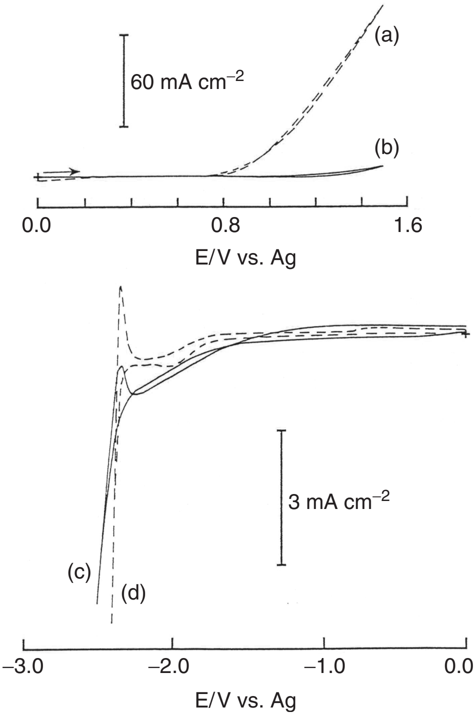

Figure 17.5 Voltammetric data using liquid ammonia with iodide background electrode, scanning to positive and negative potentials versus Ag. Scans (a) and (d) are for a Pt electrode; scans (b) and (c) denote a diamond electrode. Reproduced with permission from C.H. Lau, K.J. Grehan, R.G. Compton, J.S. Foord and F. Marken, Journal of the Electrochemical Society, 150, E59–E65 (2003)

exhibits much higher electrochemical activity in this regime. In contrast, at negative potentials the process is very simple: electrons from the electrode become solvated within the ammonia phase. As a consequence, the diamond and the platinum behave in a very similar fashion. As the phase purity drops, the selectivity disappears and the potential window is reduced.

One of the reasons, nevertheless, why nanocrystalline diamond is of interest is that it appears possible to combine some of the advantages of a diamond electrode with the advantages of other electrode materials by use of this form of diamond. In particular, the electrochemical responsivity can be enhanced by using nanocrystalline formulations [7]. In Figure 17.6, some examples of this are given. In Figure 17.6(a), the oxidation and reduction of hydroquinone in 0.1 M KCl is compared at a nanocrystalline and a macrocrystalline electrode. For the latter, a much wider peak separation between the oxidation and reduction peaks of hydroquinone indicates a lower electrode activity. Interestingly, at nanodiamond electrodes, two redox systems are detected, as indicated by the double peaks in positive- and the negative-going scans. A plausible explanation for the additional response is the presence of a partially deprotonated form of hydroquinone in aqueous 0.1-M KCl solution. This form of hydroquinone is not detected separately at kinetically slower electrode surfaces such as the macrocrystalline diamond. A similar conclusion concerning electrode activity can be drawn for ascorbic acid oxidation. Figure 17.6(b) shows

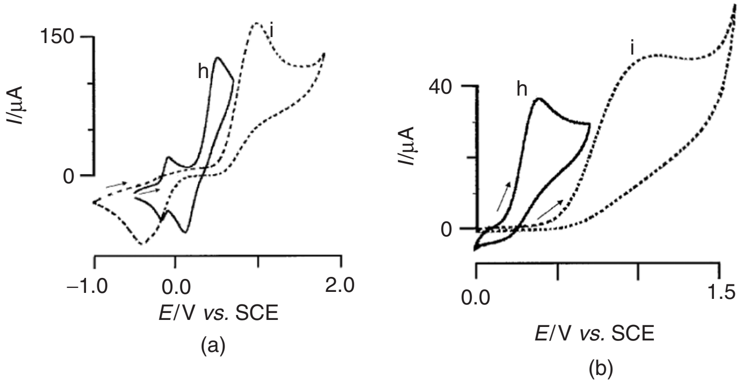

Figure 17.6 Cyclic voltammograms (0.1 Vs^{-1}) for the oxidation of: A, hydroquinone; B, ascorbic acid, at 300 K at (h), a nanodiamond electrode, (i), a microcrystalline diamond electrode. Reproduced from C.H. Lau, K.J. Grehan, R.G. Compton, J.S. Foord and F. Marken, Journal of the Electrochemical Society, 150, E59–E65 (2003) with permission from The Electrochemical Society

cyclic voltammograms for the oxidation of 2-mM ascorbic acid in aqueous 0.1-M KCl at a nanodiamond electrode. A well-defined, diffusion-controlled, voltammetric signal for the oxidation is detected at 0.36 V versus SCE. Comparison of the ascorbic acid oxidation response at the macrocrystalline diamond electrode shows a considerable difference in reactivity, with the much larger electrochemical driving force needed for the oxidation (overpotential) shifting the wave by 0.5 V to more positive potentials.

The differences between the electrochemical activity of the nanodiamond and microcrystalline diamond mean that some sensor applications can be achieved successfully with the former whilst not with the latter. The differences that arise are likely to be traced to the presence of sp^2 diamond impurities in the nanodiamond, for example in grain boundaries. These provide more chemically active sites than are present at the pure diamond electrodes, thus providing improved catalytic activity. As noted above, the potential window is not as great at nanodiamond electrodes in comparison with the phase-pure material. It seems likely that some of the other noted advantages of diamond are also degraded. What this gradation of diamond properties seems to offer, however, is the ability to ‘tune’ the electrode activity by control of the grain size and phase purity to an optimal formulation for a particular application. For example, this has been done for the detection of indoles [9], where the use of nanodiamond has enabled electrode activity to be achieved, whilst providing much improved resistance to electrode fouling in comparison with conventional carbon-based electrodes.

The second area where the properties of the film influence the electrochemistry observed, relates to the electrical activity of the film, as influenced (normally) by the B-doping level. Although B forms an acceptor level around 0.35 eV above the valence band when present at low concentrations ($\sim 10^{17}$ cm^{-3}), most electrodes for electrochemistry have much higher B content (10^{19}–10^{21} cm^{-3}) where the B centres interact and broaden into an impurity band that moves towards the valence band and mediates conduction, as the B concentration rises. At the lower B levels, the electrode can have poor conductivity, leading to a ‘stretching’ of the voltammograms and increased peak separations due to uncompensated resistance in the electrode. If the electrochemical properties are to be understood, it is important that the more highly B-doped materials are used or the effects of electrode resistance implicitly taken into account.

Even when this is done, there would still appear to be a broad trend for the electron transfer kinetics of simple 'outer sphere' electron transfer processes to speed up with an increase in B, and to approach those for electrodes such as activated glassy carbon for the higher B concentrations. This seems to suggest that the availability of band-gap states, as introduced by B and other impurities (such as H) and defects in the film, mediate the charge transfer with the available density of states limiting the maximum rate available. However the situation is rather more complex. Polycrystalline diamond electrodes normally expose a range of crystal facets due to a random orientation of the grains at the surface. This leads to considerable nonuniformity in the B concentration across the film, since the B uptake during CVD growth is much greater for some growth sectors than for others. For example, the B concentration in the {111} growth sectors is at least 5-times that in the {100} sector, so that diamond electrodes are electrically fairly heterogeneous. Indeed, studies of diamond electrodes using scanning electrochemical microscopy [10] show that the electrochemical activity tends to be focussed on 'hot-spots' at the electrode surface, such as shown in Figure 17.7. Another factor, especially at lower B concentration, which limits the electrochemical activity, may therefore be that significant areas of the electrode are inactive. Under these circumstances the voltammetric response will depend to an extent on the exact distribution of the active areas, the concentration of the redox species, and the timescale of the experiment. As has been addressed previously in simulations of heterogeneous electrodes, at short timescales (fast scan rates) the diffusion layer at the electrode surface is small compared with the separation of the active areas, so the effective area of the electrode is simply the geometric area of the hot spots. At long timescales the converse holds, with the diffusion fields overlapping and leading to linear diffusion and an effective area equal to that of the entire electrode. In intermediate regimes, radial diffusion effects contribute. This probably underlies why the diamond electrode response often cannot be satisfactorily modelled using semi-infinite linear diffusion models.

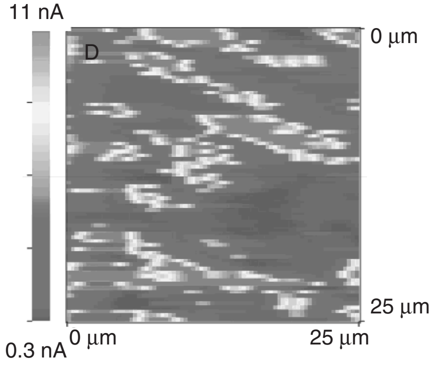

Figure 17.7 Scanning electrochemical microscope image of a boron-doped diamond electrode monitoring the spatial variation in activity for the reduction of 1.4-mM $Ru(NH_6)^{3+}$ in 0.1-M KCl. The light regions represent areas of high activity. Reprinted with permission from K.B. Holt, A.J. Bard, Y. Show, and G.M. Swain, Journal of Physical Chemistry B, 108, 15117–15127 Copyright American Chemical Society (2004)

In summary, it is now well established that significant variations in electrode properties can arise as a result of changes in B concentration, crystallinity and phase purity of the diamond material used. It is therefore important that these properties are carefully chosen and controlled if reproducible and predictable results are to be obtained.

17.5 INFLUENCE OF SURFACE TERMINATION ON ELECTRODE PROPERTIES

Because of the reduced atomic coordination of carbon atoms at the diamond surface, diamond surfaces in vacuum normally undergo a reconstruction to form a π-bonded atomic array to restore the normal valence. However such surfaces are quite reactive chemically, so tend to react when they come into contact with other phases to lift the reconstruction and form chemisorbed species. Because the diamond CVD process involves the use of atomic hydrogen, which forms extremely strong bonds to diamond, CVD diamond is normally completely terminated with chemisorbed hydrogen atoms when it emerges from the reactor, although some more weakly chemisorbed hydrocarbons are sometimes also found on the surface.

This chemisorbed hydrogen phase is quite stable chemically; in vacuum or an inert atmosphere the diamond has to be heated to temperatures in excess of 800 °C in order to desorb it and produce the reconstructed surface. Although diamond does readily oxidise if heated in air, the hydrogen-terminated surface is kinetically relatively stable in air at room temperature, and even after several hours the hydrogen termination persists. On a timescale of weeks however, slow oxidation does take place to replace the hydrogen with chemisorbed oxygen [11]. The exact forms in which these oxygen species are bonded to the surface are less well known, but the available evidence would indicate that ether and carbonyl linkages dominate when diamond is in contact with dry oxygen; in the presence of hydrogen or moisture, surface hydroxyl groups are probably present [12]. It follows that most 'as-received' diamond electrodes are probably mainly terminated with these various oxygen functionalities.

Changes in the surface termination, however, undoubtedly occur during electrode usage, which can influence the electrode performance. Detailed studies [e.g. 12] of how diamond electrode surfaces that have been freshly hydrogenated in a H plasma are modified by the electrochemical environment have been performed. Typical XPS spectra are illustrated in Figure 17.8, which presents the C 1s spectra from diamond surfaces subject to differing treatments. The changes in profile arise from chemical shift effects due to bonding to oxygen. If the potential is maintained within the electrochemical window, the hydrogenated surface is quite stable in solution for a period of hours and very little oxygen is observed on the surface after it is withdrawn from solution. However, if potentials outside this window are employed then rapid oxidation of the surface occurs. It can be seen that anodic treatment of the surface produces a spectrum rather similar to that from oxygen plasma treatment. Analysis of the spectrum shows approximately monolayer concentration of oxygen at the electrode surface, with highly oxidised centres such as carboxylic acid terminations (–COOH) present as well as the range of oxygen species noted above. Since anodic polarisation of the electrode produces species such as oxygen and hydroxyl radicals at the electrode, it is perhaps unsurprising that the electrode becomes oxidised. What is more surprising is that even electrode usage in the hydrogen evolution (cathodic polarisation) regime also produces some surface oxidation. The oxygen coverages are

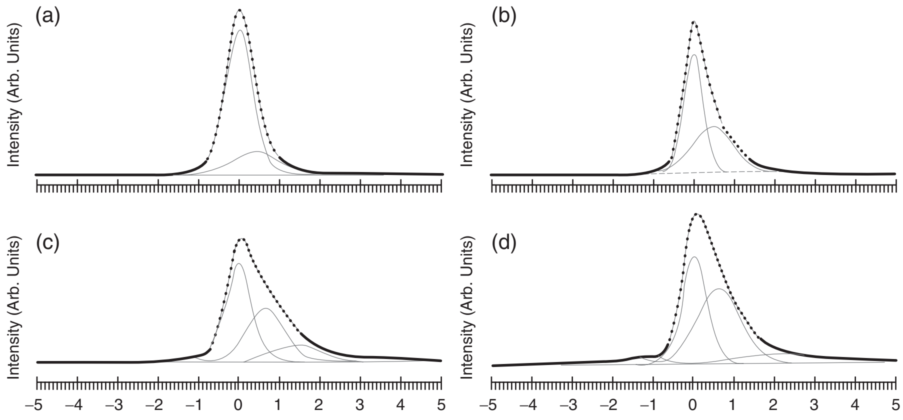

Figure 17.8 XPS spectra showing the C 1s peak profile plotted against binding-energy shift from the parent bulk diamond C 1s component: (a) diamond after H plasma treatment; (b) after cathodic treatment at −1.5 V versus SCE in 0.1-M H_2SO_4; (c) after oxygen plasma treatment; (d) after anodic treatment at +1.7 V versus SCE

below what is seen in the anodic polarisation regime, and highly oxidised centres such –COOH are not produced, but nevertheless the oxidation is significant.

There is a range of literature on diamond electrochemistry, based on the misplaced assumption that the electrodes in aqueous solution can be switched between H and O 'termination' simply by cathodic or anodic pretreatment. This is incorrect. Electrodes freshly treated by H plasma to achieve H-termination can be used, in the short term, in that condition in solution provided extreme potentials are not employed. All other electrodes are normally fairly oxidised when received, and remain in an oxidised form during electrochemistry, although the degree of oxidation does vary with differing anodic and cathodic polarisations.

These changes in surface termination can influence the electrochemistry observed, presumably since they change the electronic structure and the ability of the surface to form bonds to intermediates. A simple example of this is illustrated in Figure 17.9, arising from experiments on the electrochemical detection of Ag using stripping voltammetry [13]. The micrograph was taken after Ag deposition on a patterned diamond surface, with the dark area corresponding to an oxidised region and the light area to the hydrogen-terminated diamond. The small particles are Ag nanoparticles that are localised in the hydrogen-terminated region; the overpotential for Ag nucleation is significantly higher on the oxidised region of the electrode.

This variation in redox kinetics with surface termination is not observed for 'outer sphere' processes, where the chemical interaction between the relevant species and the surface is minimal, but is otherwise a significant feature of the diamond electrochemistry. A useful couple which displays this feature is the $Fe(CN)_6^{3-/4-}$, system which is quite sensitive to the nature of the surface of carbon electrodes in general. Although there are some conflicting results, the electron transfer kinetics can change by several orders of magnitude with the electrode termination [14]. Typical results are indicated in Figure 17.10. It seems likely that the main origin of the variation in kinetics is the electrostatic repulsion between the negatively charged $Fe(CN)_6^{3-/4-}$ species and the negatively charged functionalities on the surface, when the surface becomes oxidised. For example,

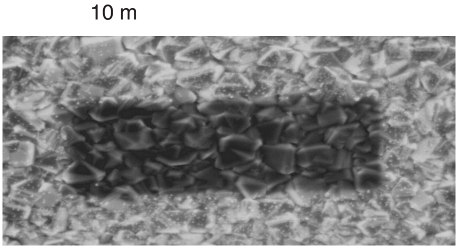

Figure 17.9 SE micrograph showing selective area electrodeposition of Ag nanoparticles on the hydrogenated area of a patterned diamond sample, with hydrogenated (light) and oxidised (dark) regions. C.H. Goeting, F. Marken, C. Salter, R.G. Compton and J.S. Foord, Chemical Communications, 17, 1697–1698 (1999) Reproduced by permission of The Royal Society of Chemistry

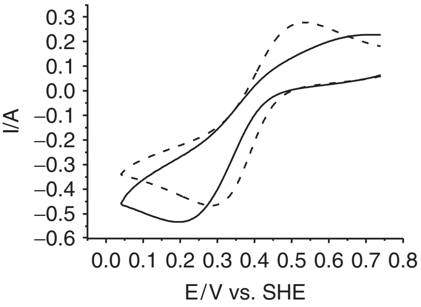

Figure 17.10 A Cyclic voltammograms of 1-mM $Fe(CN)_6^{3-/4-}$ at diamond surfaces with differing surface treatments. B. Rotating disk voltammetry data of 1-mM $Fe(CN)_6^{3-/4-}$ from an oxidised diamond surface at differing pH. Reprinted from Electrochimica Acta, 50, McEvoy, James P. and Foord, John S., Direct Electrochemistry of blue copper proteins at boron-doped diamond electrodes, 2933–2941, (2005) with permission from Elsevier

results in Figure 17.10 show rotating disc voltammetry data as a function of pH, illustrating that the signal response is reduced at high pH. Analysis of the data indicates the pK_a of the active group responsible for deactivation of the electrode is consistent with –COOH functionalities.

This variation in the signal response with pretreatment can be used to good effect in order to obtain selective electrochemical sensor action. For example, in physiological measurements, there is interest in the detection of dopamine in the presence of excess ascorbic acid. Although both can be detected by electrochemical oxidation individually, the problem is that the waves for the two species are closely overlapping at many electrodes. This can be seen in Figure 17.11 for an untreated diamond surface where the oxidation wave for dopamine is less than 100 mV below that for ascorbic acid [15]. However, after an anodic treatment to oxidise the diamond electrode, it is found that the ascorbic-acid signal is shifted to much higher positive potentials than the dopamine. This then allows selective analysis of this chemical even when ascorbic acid is in large excess. In other examples of the effect of pretreatment, it has been reported that electron transfer kinetics to small redox proteins such as cytochrome c and azurin, can be dramatically increased by oxidative treatments produced by polishing.

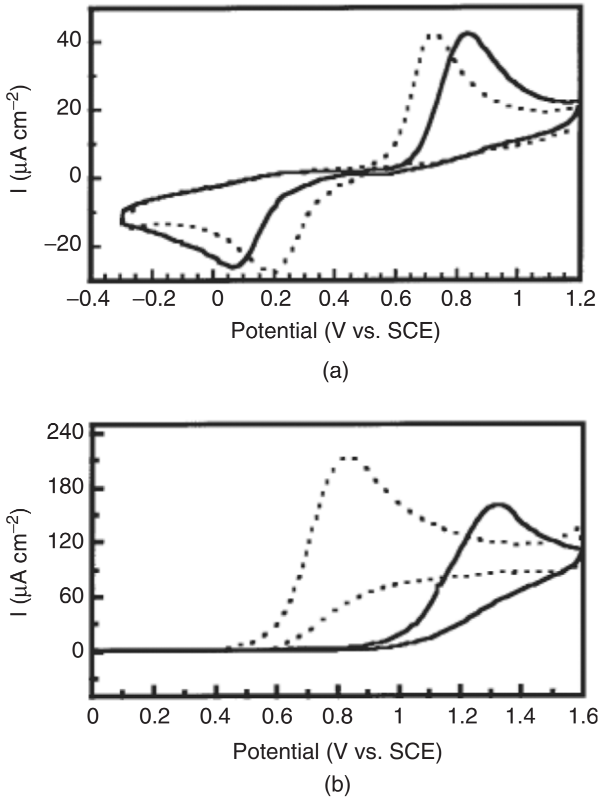

Figure 17.11 Cyclic voltammograms (0.1 Vs^{-1}) for: A, 0.1-mM dopamine; B, 1-mM ascorbic acid. Dashed lines are the as-received diamond electrode and solid lines after an oxidative treatment to the surface. Reprinted from Electrochemical and Solid-State Letters, E. Popa, H. Notsu, T. Miwa, D.A. Tryk and A. Fujishima, 2, 49–51 (1999) by permission of the Electrochemical Society

Other studies on the effects of anodic and cathodic pretreatments show that the influence can be even greater if they are carried out in nonaqueous media [16]. For example in Figure 17.12, the reduction of benzoquinone in acetonitrile is compared at a boron-doped diamond electrode before and after cathodic pretreatment in ethanol. Although, addition of the first electron to benzoquinone (BQ/BQ^{-}) is not affected by the pretreatment, the reduction in separation between the cathodic and anodic waves for the addition of the second electron (BQ^{-}/BQ^{2-}) shows that the kinetics of this second step are increased by a factor of five compared with the electrode surface prepared in aqueous solution. Interestingly, detailed XPS analysis of the treated surface in ethanol showed very little difference from the ‘as-received’ electrodes or those treated in water. This suggests that obvious chemical differences over the main area of the electrode are not solely responsible for these changes in electrode kinetics that the pretreatments bring about. Possibly, a small concentration of very active sites is implicated, which are not easily detected in area-averaged spectroscopies such as XPS, or alternatively, subtle changes in the electronic structure of the electrode may be involved.

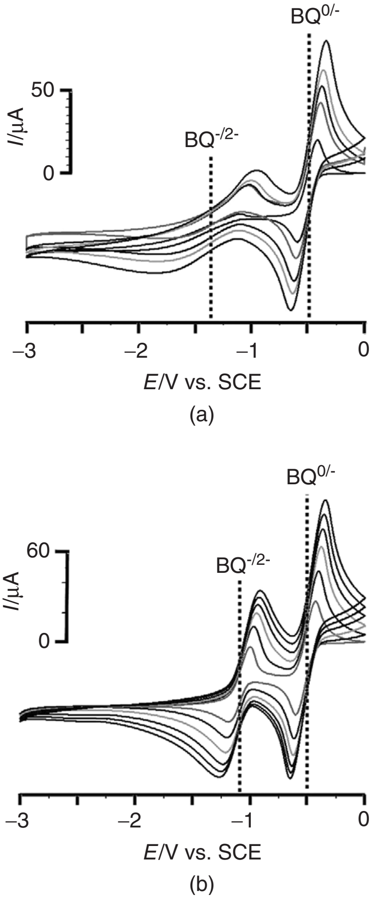

Figure 17.12 Cyclic voltammograms for the reduction of benzoquinone at: A, untreated diamond electrode; B, same electrode after cathodic pretreatment in ethanol. Reprinted from the Journal of Electroanalytical Chemistry, Kulandainathan, M. Anbu; Hall, Clive; Wolverson, Daniel; Foord, John S.; MacDonald, Stuart M. and Marken, Frank. 606, 2, 150–158 (2007) with permission from Elsevier

17.6 SENSING USING MACROSCOPIC DIAMOND ELECTRODES

There are now numerous examples of chemical sensor applications using diamond electrodes, which will be briefly described below.

17.6.1 Stripping voltammetry

Stripping voltammetry is an important electrochemical technique for the detection of trace levels of a species in solution that can be electrochemically and reversibly deposited on an electrode material. The basis of the technique is as follows. The species of interest is first concentrated by electrodeposition on an electrode, which is set to an appropriate potential to oxidise or reduce the species concerned. Because the species may be at the trace concentration level, this process may take an appreciable period of time (e.g. several minutes) and may not give rise to a detectable current-above-background. After this preconcentration process, the material then undergoes electrodissolution ('stripping') by scanning the electrode potential to positive or negative values in order to drive the reverse electrochemical process. The charge passed then enables the amount of material deposited on the electrode to be evaluated; using a suitable calibration, this can then be used to calculate the original solution concentration. If several electrochemical waves are observed, then the chemical identity of the species can be deduced from the stripping potentials observed. The technique can easily detect nanomolar concentration levels in favourable circumstances. The original electrode used in this area was liquid mercury in droplet or thin film form, but due to toxicological properties this is now not permissible, so other electrode materials need to be found. Diamond seems to represent an ideal replacement for mercury.

Stripping voltammetry is particularly suited to the detection of heavy metals, such as Pb and Cd, in solutions such as environmental groundwaters. An example [17] is the detection of Mn, for which typical data is shown in Figure 17.13. In this work Mn^{2+} (aq) is preconcentrated onto the diamond electrode at a potential of 0.85 V versus SCE. At this positive potential, Mn(II) is oxidised to Mn(IV), which deposits on the electrode surface as MnO_2. On scanning the potential negative, MnO_2 is then stripped from the electrode back into solution, thus producing the observed wave at 0.5 V versus SCE. As can be seen, a linear signal response is observed over an extremely wide dynamic range, enabling the determination of Mn in solution down to the picomolar level.

Swain and coworkers have compared the performance of diamond- and mercury-coated glassy carbon electrodes in this sensor application [18]. Stripping voltammetry data for these two electrodes are shown in Figure 17.14, from aqueous solutions containing 100 ppb of various heavy metals (Ag, Cu, Pb, Cd and Zn). Whereas Ag can be detected at the diamond electrode due to the wide potential window, the stripping potential is too

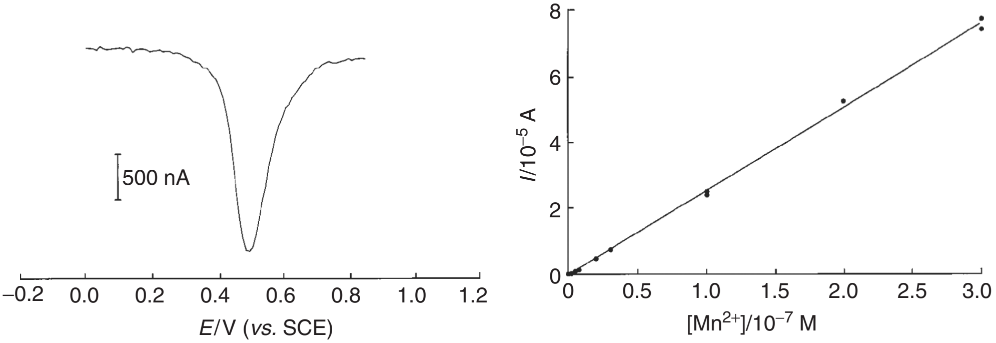

Figure 17.13 A, Differential pulse cathodic stripping voltammogram following preconcentration of Mn in the form of MnO_2 on the electrode surface, from an aqueous solution containing 10^{-8} M Mn^{2+}. B, Calibration plot of the peak current stripping signal versus Mn^{2+} concentration. A.J. Saterlay, J.S. Foord and R.G. Compton, Analyst, 124, 1791–1796, 2001, Reproduced by permission of The Royal Society of Chemistry

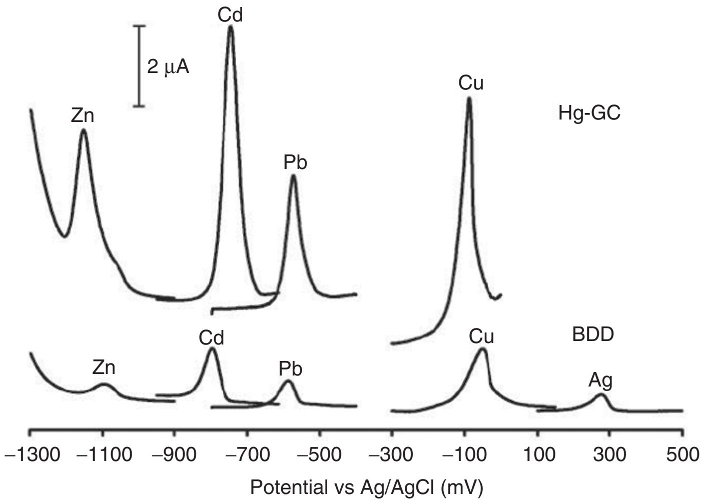

Figure 17.14 Stripping voltammetric (*I* versus potential) curves after preconcentration from a solution containing 100 ppb of the indicated metals. Top traces: Hg-coated glassy carbon electrode; Bottom traces: boron-doped diamond electrode. Reprinted from Analytica Chimica Acta, E.A. McGaw and G.M. Swain, 575, 180–189, (2006) with permission from Elsevier

anodic for the mercury electrode to be used in this application. Although the peaks are smaller for the diamond electrode, the background signals and reproducibility are much better and, as a result, the diamond electrode shows better detection figures of merit, as well as benefiting obviously from being nontoxic!

Another nice example of the use of diamond electrodes in this area is the detection of inorganic As in drinking water, which is a major hazard to human health in various areas of the world. The maximum contaminant level of As allowed in drinking water is 10 ppb so any useful analytical method needs to detect As to below this level. Au is the optimal material on which to electrodeposit, due to the reversible formation of an Au–As intermetallic compound, so the relative performance of diamond and glassy carbon electrodes when coated with Au particulates has been compared with an Au foil. Results [19] for the Au-coated diamond electrode are shown in Figure 17.15 for the detection of As(III); similar results were achieved for the detection of As(V) if this species is first prereduced. A limit of detection of 0.05–0.08 ppb was found, significantly lower than at the Au-coated glassy carbon electrode or the Au foil. The improvement brought about by the diamond electrode, which supports the Au particulates, was attributed to its better phase stability. Although there are numerous physical methods for the detection of As, none are as simple or offer all of the performance advantages that this simple application of stripping voltammetry offers.

17.6.2 Solution phase voltammetry

In an alternative approach to stripping voltammetry, where the substance of interest is concentrated at the electrode surface, an alternative electroanalytical approach is simply to measure an amperometric current associated with a redox process, in which the species

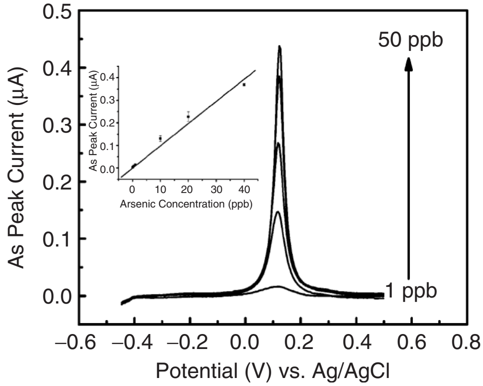

Figure 17.15 Stripping voltammograms obtained from solutions of As(III) with indicated concentrations. The inset shows the calibration plot. Reprinted with permission from Y. Song and G.M. Swain, Analytical Chemistry, 79, 2412–2420. Copyright American Chemical Society, 2007

involved diffuse between the bulk solution to be analysed and the electrode surface. The maximum measurable current is limited by the rate of bulk diffusion to the electrode surfaces, but under favourable conditions concentrations well below 10^{-6} M are detectable using this approach.

Many organic molecules can be detected by the current arising from electrochemical oxidation, but a problem at many electrodes is that this process occurs in the same potential region as oxygen evolution from water, which therefore masks the electroanalytical signal. Also the organic species in solution or, especially, the products of oxidation, tend to adsorb at the electrode surface and consequently block its activity. Diamond is thus an ideal electrode for use in such an application in view of the wide working potential window and resistance to fouling. There are numerous examples in the literature of molecular sensing of organics via electroxidation using diamond. A representative example is the detection of 4-chlorophenol (4-CP) [20]. The chlorophenols represent a serious problem in aquatic environments and are 'priority pollutants', with limits in human drinking water of around 1 µg L^{-1}. It was observed that 4-CP could be oxidised selectively, in comparison to water, at potentials around 1.3 V versus SCE, and amperometry data for the oxidation of 4-CP of aliquots added to the inlet to a flow cell incorporating a diamond electrode are shown in Figure 17.16. Analysis of this and similar data shows that a linear response for concentrations of up to 50 µM is observed, with a detection limit of 10^{-8} M, around the limit of permissible concentration in potable water. At higher concentrations or electrode potentials, even diamond was found to become passivated by the oxidation products from 4-CP due to adsorption and polymerisation. It was shown that the use of power ultrasound in a cell as illustrated in Figure 17.17 was able to eliminate this, extending the detection limit up to 300 µM [21]. Microjets, as a result of ultrasound-induced cavitation processes near the electrode, essentially scour the electrode and maintain its activity. Here, a further advantage of diamond electrodes is exploited, namely the hardness and dimensional stability of the material; whilst most other electrode materials are rapidly eroded at the ultrasound powers needed to maintain activity, this is not the case with diamond.

Although in the above case, the analytical signal associated with 4-CP did not suffer interference from other important pollutants such as nitrite or sulfite, a problem with

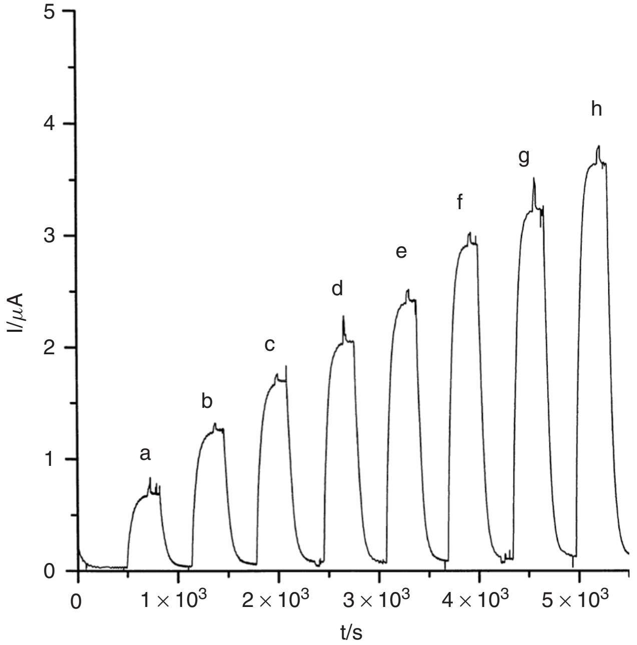

Figure 17.16 Chronoamperometry at 1.5 V versus SCE, monitored using a diamond electrode in flow-injection analysis of a sample spiked with [(a)–(h)] 4-chlorophenol injections corresponding to increasing concentrations in the range 4–20 μ M.C. Prado, G.G. Murcott, F, Marken, J.S. Foord and R.G. Compton, Electroanalysis, 2002, 14, 975–979. Copyright Wiley VCH Verlag GmbH & Co. KGaA. Reproduced with permission

detecting organics by electroxidation is that many different organic species may be present in the analyte that undergo oxidation at very similar potentials, thus making their differentiation rather difficult. Liquid chromatography techniques can be used to separate the organic species, and then an electrode can be employed to detect the presence of the organic of interest as it flows out of the chromatograph. This forms the basis of so-called electrochemical detection chromatography as opposed, for example, to more common methods based on optical detection variants. The electrochemical detection method has several advantages, and its use in microanalysis systems such as capillary electrophoresis has attracted particular interest. Shin and coworkers [22] compared the behaviour of diamond, screen-printed carbon and glassy carbon electrodes in such an application for the detection of aromatic amines, which are produced as unwanted by-products in various industrial processes. Results for these three electrode materials are shown in Figure 17.18, where the better resolution and improved signal/noise ratio of the diamond electrode is apparent. Overall, the study identified that the diamond electrode showed lower noise levels, better limits of detection and much reduced passivation effects as compared with the other electrode materials investigated. A similar conclusion was reached by Wang and coworkers in investigating diamond electrochemical detectors in CE for detection of phenols, nitroaromatic explosives and organophosphate nerve agents [23]. Again, some illustrative data comparing the performance of different electrode materials is shown in Figure 17.19. The better resolution of the diamond electrode, presumably through weak

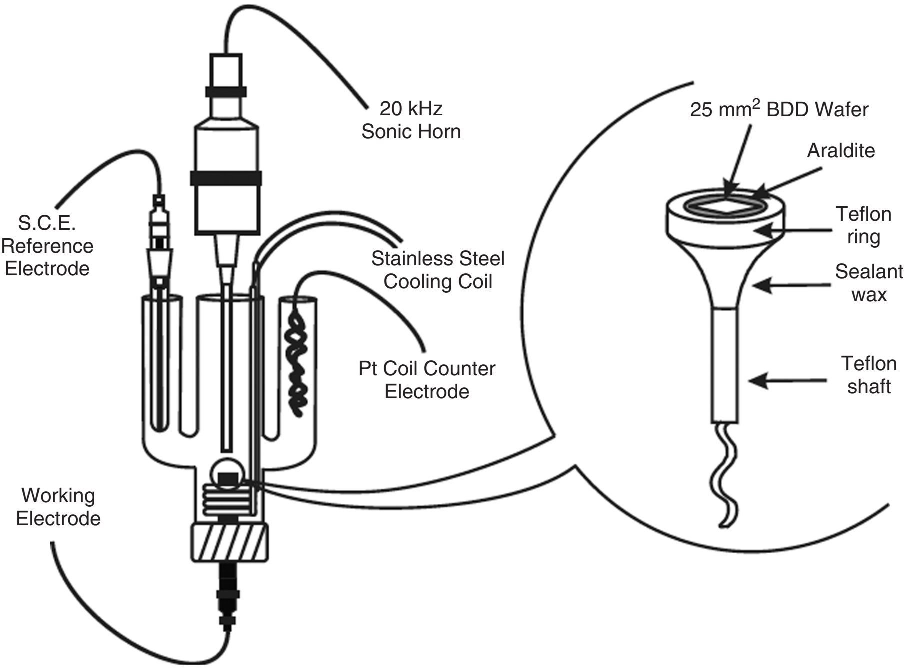
20 kHz
Sonic Horn
S.C.E.
Reference
Electrode
Stainless Steel
Cooling Coil
Pt Coil Counter
Electrode
Working
Electrode
25 mm² BDD Wafer
Araldite
Teflon
ring
Sealant
wax
Teflon
shaft

Figure 17.17 Schematic diagram of apparatus for power sonoelectrochemistry using diamond electrodes. A.J. Saterlay, J.S. Foord and R.G. Compton, Electroanalysis, 2001, 13. 1065–1070. Copyright Wiley VCH Verlag GmbH & Co, KGaA. Reproduced with permission

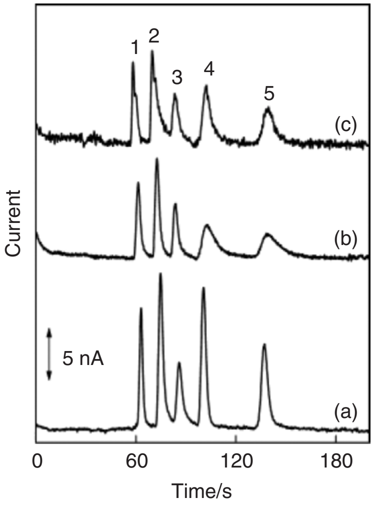

Figure 17.18 Capillary electrophorograms of five different aromatic amines using electrochemical detection and differing electrode materials: (a) diamond; (b) screen-printed carbon; (c) glassy carbon. D. Shin, D.A. Tryk, A. Fujishima, A. Muck Jr., G. Chen and J. Wang, Electrophoresis, 2004, 25 3017–3023. Copyright Wiley-VCH Verlag GmbH & Co, KGaA. Reproduced with permission

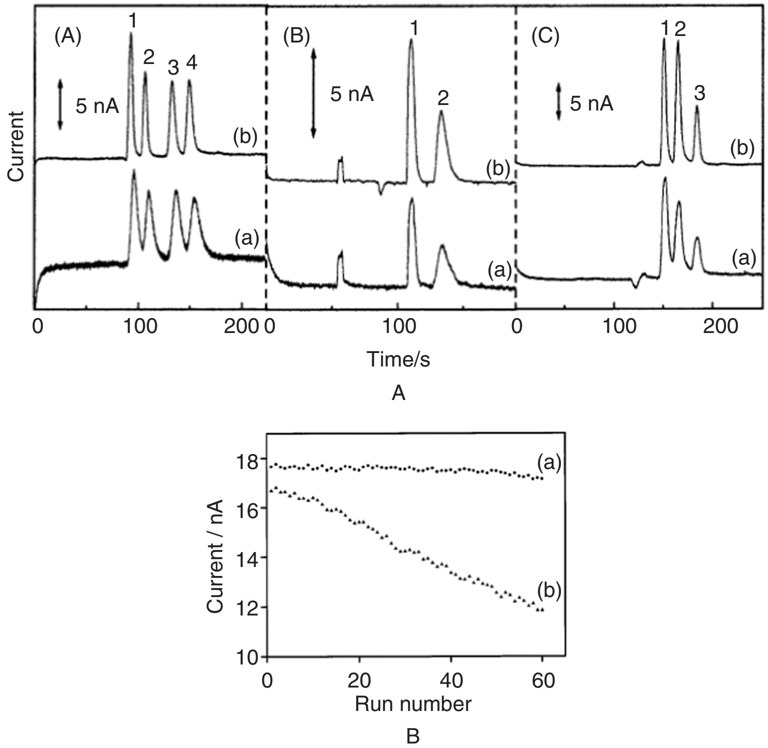

Figure 17.19 A: Capillary electrophorograms for various phenols (A), nerve agents (B), and explosives (C), recorded using screen-printed carbon electrode (a) and diamond electrode (b) electrochemical detection. B: Stability of the response for repetitive flow-injection analysis of 5 ppm TNT at a (a) diamond and (b) screen-printed carbon electrode. Reprinted with permission from J. Wang, G. Chen, M.P. Chatrathi, A. Fujishima, D.A. Tryk and D. Shin, Analytical Chemistry, 75, 935–939, Copyright American Chemical Society, 2003

adsorption effects, is apparent. Of particular note is the observation in Figure 17.19B, which shows that the diamond electrode retains virtually constant activity over more than 60 scans, whereas the screen carbon electrode loses more than 35 % of its activity in this period.

Although electro-oxidation is the most frequently used method for the electrochemical sensing of organics, if reducible functional groups are present, the potential window of diamond in the cathodic region can again be exploited advantageously for electrochemical sensing. An example is the detection of Parathion, a harmful pesticide with a maximum permissible concentration in drinking water of around 35 $\mu g\ L^{-1}$. The molecule has a reducible nitro group (NO_2) in the structure that undergoes reduction at about −0.7 V versus SCE. As shown in Figure 17.20, this can be used to develop a sensitive analytical procedure for the detection of Parathion [24]. A limit of detection in pure water was found to be 2.9 $\mu g\ L^{-1}$, well below the maximum permissible concentration, somewhat better than was achievable using a more conventional hanging mercury drop electrode (HMDE). The investigators also studied the detection of Parathion in real polluted water samples (Figure 17.20). Whilst the other pollutants have a small effect on the detection of Parathion

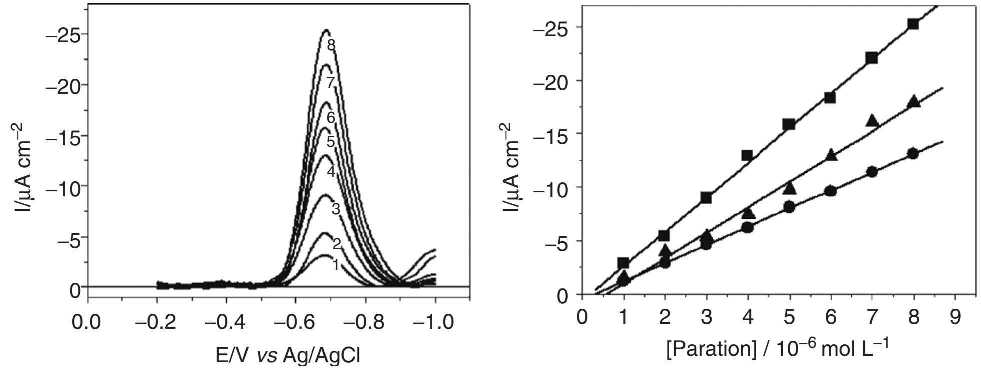

Figure 17.20 A: Square-wave voltammetry of the reduction of Parathion at variable concentrations in the range 1–8 µM at a diamond electrode. B. Plots of peak current versus Parathion concentration from samples dissolved in Milli-Q water (square) and polluted water samples (triangle, circle). V.A. Pedrosa, D. Miwa, S.A.S. Machado and L.A. Avacaa, Electroanalysis, 2006, 18, 1590–1597. Copyright Wiley-VCH Verlag GmbH & Co, KGaA. Reproduced with permission

at the diamond electrode, due to the resistance to adsorption, much greater effects were seen at the HMDE electrode, thus highlighting the advantages of using diamond in this type of application.

Solution-phase electrochemistry can also be used for the detection of inorganic species. An early example here is the work of Swain *et al.* concerning the detection of azide (N_3^-), which, historically, has been used as a propellant in automotive airbags and is a potential pollutant as a result of their disposal [25]. Azide can be oxidised to nitrogen and/or nitrogen oxides at positive potentials and voltammograms comparing the diamond and glassy carbon electrodes are shown in Figure 17.21. At the positive potentials required, the glassy carbon electrodes show a large background current due to oxygen evolution from water and electro-oxidation of the electrode. As a consequence, it is hard to achieve the sensitive detection of azide, since the associated current sits on a large background. In contrast, the background current is far smaller for diamond, so the detection of azide is much more easily achieved. Detection limits of around 0.1 µM were observed, with the

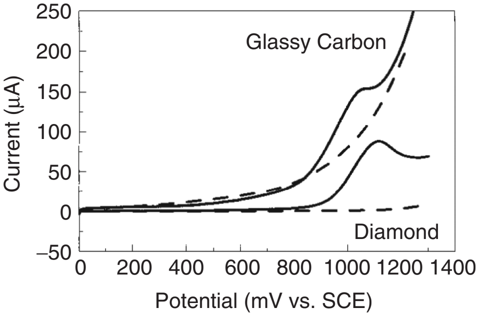

Figure 17.21 Linear sweep voltammograms utilising glassy carbon and diamond electrodes for the detection of 1-mM sodium azide. Dashed curves denote the background sweep in the absence of analyte. Reprinted with permission from J. Xu and G.M. Swain, Analytical Chemistry, 70, 1502–1510. Copyright American Chemical Society, 1998

diamond electrode demonstrating superior sensitivity, dynamic range, response sensitivity and response variability.

17.6.3 Functionalised diamond electrodes

A fundamental requirement for a chemical sensor in many applications is that the device gives a selective response to the target analyte without yielding a false signal due to the presence of other interfering species in solution. Although electrochemistry can, in principle, distinguish between differing species on the basis of the half-wave potential of the redox process, or other more subtle characteristics such as the rate of diffusion to the electrode surface, this is often too limited to separate out chemically similar species. The problem can be solved if some prior step (such as chromatography – see above) can be used to separate out the various chemical species in solution, or if a selective membrane is employed so as only to permit the target species to reach the electrode surface. However an alternative approach is to impart some form of 'molecular recognition' to the surface, such that any measured electrochemical signal is associated only with the target molecule. This can be achieved if a chemical functionalisation step is used to bind specific molecular species to the electrode surface. There are several successful approaches based on the thermal reaction of diamond with carbenes, the photochemical reaction with alkenes, or electrochemical reduction of relevant compounds to bring about this functionalisation.

A very simple example of this concept in action is associated with the detection of neurotransmitters such as dopamine and its metabolites in the present of interfering species such as ascorbic acid. Fujishima and coworkers [26] have shown that the response to ascorbic acid can be shifted to a potential below and removed from that of dopamine oxidation, if a cationic polymer (N,N)-dimethylaniline is first electrodeposited on the diamond surface. It is believed that the electrostatic interaction between the polymer backbone and the negatively charged ascorbic acid species at the detection pH is sufficient to concentrate the analyte at the electrode surface, thus promoting electron transfer.

Very high specificity is possible if biologically active molecules such as enzymes are covalently attached to the diamond surface. Since this normally involves formation of a strong C–C bond, such functionalisations are extremely stable on diamond. In one investigation, a diamond electrode surface was first treated in an oxygen plasma to oxidise the surface and form –OH groups on the surface. This was then reacted with an amino alkoxy silane linker molecules, which reacts with surface hydroxyl groups to attach amino end-groups to the electrode. Finally, these amino groups were used to attach the enzyme horse-radish peroxidase (HRP) to the surface. HRP catalyses the reduction of hydrogen peroxide at electrode surfaces at potentials of about 0 V, thus forming the basis for the detection of hydrogen peroxide and molecules such as glucose if the chemistry is linked to enzymes such as glucose oxidase. The attachment of the enzyme to the diamond surface thus significantly increases the response of the electrode to hydrogen peroxide as shown in Figure 17.22 [27]. Although the performance observed is somewhat below other optimised state-of-the-art electrodes utilizing HRP, this example illustrates some of the possibilities that can be achieved by using standard methods for covalent bond formation to diamond.

A somewhat different electrochemical approach comes from the work of Nebel and coworkers [28]. These investigators used a photochemical reaction between diamond and alkene compounds to, again, attach amino functionalities to the diamond surface, which are then reacted with a cross-linker and thiol-modified single stranded DNA (ssDNA) to

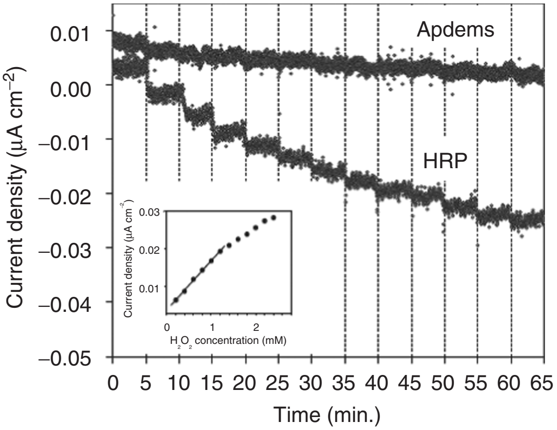

Figure 17.22 Amperometry comparing the response at 0 V versus SCE of an aminosilane-modified (APDEMS) and a HRP-modified diamond electrode to the addition of 0.2-mM aliquots of H_2O_2. Reprinted from Diamond Related Materials, J. Hernando, T. Pourrostami, J.A. Garrido, o.A. Williams, D.M. Gruen, A. Kromka, D. Steinmuller and M. Stutzmann, 16, 138–143, 2007 with permission from Elsevier

attach DNA to the diamond surface covalently. This then forms the basis of the biosensor since the probe DNA molecule on the diamond surface will efficiently bind to ssDNA in solution if it has the complementary base sequence. This DNA hybridisation process forms the basis of modern array technologies for DNA sequencing, which are normally read-out using optical methods. By attaching the DNA to an electrode surface, it is instead possible to obtain a rapid electrical readout. Binding of the complementary DNA to the surface can be verified by the reduction in the electrochemical response of test redox species in cyclic voltammetry that arises as a result of the blocking of diffusion of the species the electrode surface; other electrical methods such as impedance spectroscopy can also be used in this regard.

17.7 OTHER ASPECTS OF DIAMOND ELECTROCHEMISTRY

The work presented above discusses the electrochemical properties of macroscopic boron-doped diamond electrodes, which represents the main body of work in this field. For completeness, two bodies of work outside this main area will be briefly addressed. The first is associated with surface conductive diamond [29]. It has been known for many years that although bulk diamond is an extremely good insulator when undoped, the surface often displays quite a high electrical conductivity in the ambient atmosphere when it is hydrogen terminated (see Chapter 4 by L Ley in this book). This is associated with the fact that hydrogenated diamond has an unusually low ionisation energy and thus the transfer of electrons from the valence band to adsorbate species with a high electron affinity occurs, creating p-type conductivity in the diamond. For diamond in air, these acceptors are believed to be various electrochemical couples associated with species within a hydration layer at the diamond surface. Surface conductivity can also exist in solution when a sufficiently positive potential is applied to the hydrogenated diamond, especially in the

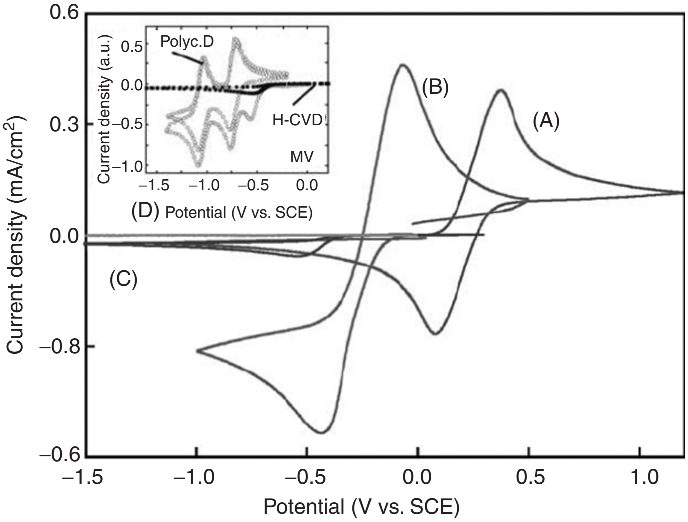

Figure 17.23 Cyclic voltammetry data for $Fe(CN)_6^{3-/4-}$ (A), $Ru(NH_3)_6^{2+/3+}$ (B), methyl viologen (C), and Co $(sep)^{3+/2+}$ (D) at a hydrogenated, undoped, diamond electrode. The inset contrasts the methyl viologen response with that seen at a boron-doped diamond electrode. C.E. Nebel, B. Rezek, D. Shin and H. Watanabe, Physcia Status Solidi (a), 2006, 203, 3273-3298. Copyright Wiley-VCH Verlag GmbH & Co, KGaA. Reproduced with permission

presence of more oxidising couples. Under these circumstances, the diamond can exhibit electrochemistry as seen in Figure 17.23. At negative potentials, transition to a more insulating state occurs, and no electrochemistry is exhibited with more negative redox couples, again as seen in Figure 17.23. If the surface is oxidised, the conductivity is also lost and the diamond becomes electrochemically inert. Great care needs therefore to be exercised to maintain the hydrogen termination, for example by ensuring that the electrode is always maintained within the 'potential window' when in aqueous solution.

A second area that will most likely become of great practical interest is the development of diamond microelectrodes and arrays. The term 'microelectrode' normally refers to an electrode with a lateral scale below 100 μm, whilst those below 10 μm are referred to as ultramicroelectrodes. Both are extremely useful in analytical electrochemistry for several reasons. Firstly, because of their small area, they draw a correspondingly small current, so can be used in highly resistive media without background electrolyte, since the potential drop in solution is relatively small because of the low current flowing. Secondly, rapid spherical diffusion of reactants to the electrode takes place, allowing better quantification and lower detection limits than at macroscopic electrodes, which display slow linear diffusion. Thirdly, spatially localised electrochemical measurements can be performed, for example as in scanning electrochemical microscopy or *in vitro* and *in vivo* measurements of biological tissues. Early progress is now being made in the development of diamond microelectrodes. This has taken on two aspects. Firstly, diamond microelectrode arrays have been demonstrated, comprising conducting boron-doped microelectrodes in an insulating matrix comprising silicon dioxide or insulating diamond. Secondly, single diamond micro- and ultramicro-electrodes have been produced and used in biological applications [30]. Here the diamond CVD process is used to coat fine needles, which after appropriate

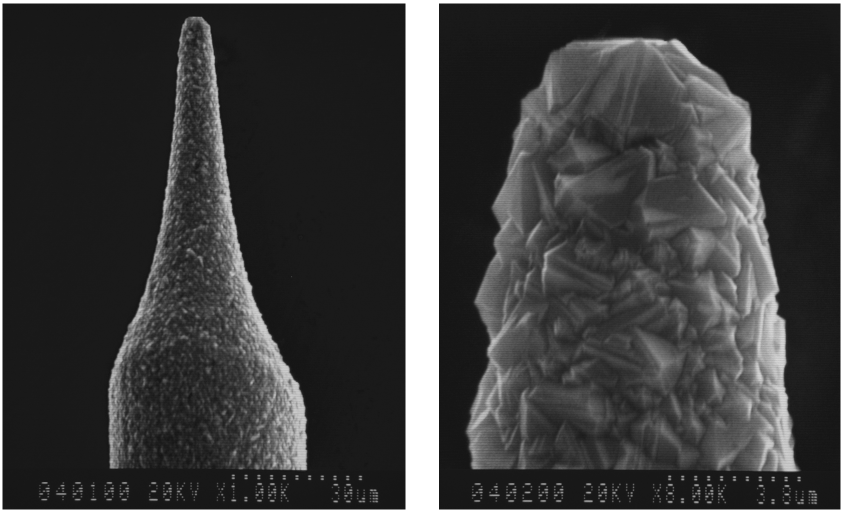

Figure 17.24 Low and higher resolution SE micrographs of diamond ultramicroelectrodes with a tip radius of 2–3 mm

insulation can be used to produce active diamond electrodes down to ~1 microkmetre. A typical diamond microelectrode before insulation is shown in Figure 17.24. At present, diamond microelectrodes have not been used extensively simply because they are not yet generally available, but when this situation changes their use can be expected to rise rapidly.

17.8 CONCLUDING REMARKS

The current field of diamond electrochemistry for chemical sensing applications has been reviewed. It has been observed that CVD diamond can be produced in variable bulk forms with differing surface chemical terminations, and both these factors have a significant influence on electrochemical properties and so need to be carefully controlled if predictable results are to be obtained. Varied applications of diamond sensors in electrochemical analysis have been shown, where superior performance is observed on account of the distinctive electrochemical characteristics that diamond displays.

Despite showing superior performance in many applications, there are probably a couple of reasons why diamond will remain as just one of several carbon-based electrode materials for electrochemical sensing. Firstly, diamond displays pronounced selectivity in the electrochemical processes it catalyses, and this selectivity is sometimes hard to predict and is not well understood. This means that it can work well in many applications, whilst performing poorly in others. A second feature, which at present also controls usage of diamond in this field, is the commercial availability of the material: although six or so suppliers exist worldwide, the availability is well below that of many other electrode materials. Overall, however, the evidence would suggest that diamond should normally be considered as a serious candidate, along with other carbon-based materials, when an electrode material for a sensor application is being chosen.

REFERENCES

[1] A. J. Bard and L. R. Faulkner, *Electrochemical Methods: Fundamentals and Applications*, John Wiley & Sons,New York, 2001.
[2] R. G. Compton, J. S. Foord and F. Marken, *Electroanalysis*, **15**, 1349–1363 (2003).
[3] G. M. Swain, *Electroanal. Chem.*, **22**, 181–277 (2004).
[4] J. C. Angus, Y. V. Pleskov and S. C. Eaton, *Semicon. Semimet.*, **77**, 97–119 (2004).
[5] Y. Einaga, R. Sato, H. Olivia, D. Shin, T.A. Ivandini and A. Fujishima, *Electrochim. Acta.*, **49**, 3989–3995 (2004).
[6] D. Shin, D.A. Tryk, A. Fujishima, A. Merkoci and J. Wang, *Electroanalysis*, **17**, 305–311 (2005).
[7] C.H. Lau, K.J. Grehan, R.G. Compton, J.S. Foord and F. Marken, *J. Electrochem. Soc.*, **150**, E59–E65 (2003).
[8] F.J. Del Campo, C.H. Goeting, D. Morris, J.S. Foord, A. Neudeck, R.G. Compton and F. Marken, *Electrochem. Sol. St. Lett.*, **3**, 224–227 (2000).
[9] J.S. Foord and A. Chatterjee, *Phys. Stat. Sol. A*, **202**, 2110–2115 (2005).
[10] K.B. Holt, A.J. Bard, Y. Show and G.M. Swain, *J. Phys. Chem. B*, **108**, 15117–15127 (2004).
[11] J.S. Foord, L.C. Hian and R.B. Jackman, *Diam. Rel. Mater.*, **10**, 710–714 (2001).
[12] C.H. Goeting, F. Marken, A. Guierrez-Sosa, R.G. Compton and J.S. Foord, *New Diam. Front. Carb. Technol.*, **9**, 207–228 (1999).
[13] C.H. Goeting, F. Marken, C. Salter, R.G. Compton and J.S. Foord, *Chem. Commun.*, **17**, 1697–1698 (1999).
[14] J.P. McEvoy and J.S. Foord, *Electrochim. Acta*, **50**, 2933–2941 (2005).
[15] E. Popa, H. Notsu, T. Miwa, D.A. Tryk and A. Fujishima, *Electrochem. Sol. St. Lett.*, **2**, 49–51 (1999).
[16] M.A. Kulandainathan C. Hall, D Wolverson, J.S. Foord, S.M. MacDonald, and F. Marken, *J. Electroanal. Chem.*, **606**, 150–158 (2007).
[17] A.J. Saterlay, J.S. Foord and R.G. Compton, *Analyst*, **124**, 1791–1796.
[18] E.A. McGaw and G.M. Swain, *Anal. Chim. Act.*, **575**, 180–189 (2006).
[19] Y. Song and G.M. Swain, *Anal. Chem.*, **79**, 2412–2420 (2007).
[20] C. Prado, G.G. Murcott, F. Marken, J.S. Foord and R.G. Compton, *Electroanal.*, **14**, 975–979 (2002)
[21] A.J. Saterlay, J.S. Foord, and R.G. Compton, *Electroanal.*, **13**, 1065–1070 (2001).
[22] D. Shin, D.A. Tryk, A. Fujishima, A. Muck Jr, G. Chen, and J. Wang, *Electrophoresis*, **25**, 3017–3023 (2004).
[23] J. Wang, G. Chen, M.P. Chatrathi, A. Fujishima, D.A. Tryk and D. Shin, *Anal. Chem.*, **75**, 935–939 (2003).
[24] V.A. Pedrosa, D. Miwa, S.A.S. Machado and L.A. Avacaa, *Electroanal.*, **18**, 1590–1597 (2006).
[25] J. Xu and G.M. Swain, *Anal. Chem.*, **70**, 1502–1510 (1998).
[26] P.R. Roy, M.S. Saha, T. Okajima, S. Park, A. Fujishima and T. Ohsakaa, *Electroanal.*, **16**, 1777–1784 (2004).
[27] J. Hernando, T. Pourrostami, J.A. Garrido, O.A. Williams, D.M. Gruen, A. Kromka, D. Steinmuller and M. Stutzmann, *Diam. Rel. Mater.*, **16**, 138–143 (2007).
[28] C.E. Nebel, B. Rezek, D. Shin and H. Watanabe, *J. Phys. D: Appl. Phys.*, **40** 6443–6466 (2007).
[29] C.E. Nebel, B. Rezek, D. Shin and H. Watanabe, *Phys. Stat. Sol. (a)*, **203**, 3273–3298 (2006).
[30] J. Park, V. Quaiserova-Mocko, B.A. Patel, M. Novotny, A. Liu, X. Bian, J.J. Galliganbc and G.M. Swain, *Analyst*, **133**, 17–24 (2008).

Part 5

Micro-Electro-Mechanical Systems

CVD Diamond for Electronic Devices and Sensors Edited by Ricardo S. Sussmann

© 2009 John Wiley & Sons, Ltd. ISBN: 978-0-470-06532-7

18 CVD Diamond MEMS

J. KUSTERER AND E. KOHN

Department of Electron Devices, Institute for Electron Devices and Circuits, University of Ulm, Germany

18.1 Introduction 469
18.2 Transducer elements 472
  18.2.1 Transducers, sensors, and actuators 472
  18.2.2 Diamond for sensors and actuators 473
  18.2.3 Thermal transducers 473
  18.2.4 Mechanical transducers 478
18.3 Technological building blocks 486
  18.3.1 Diamond material preparation 487
  18.3.2 Characterisation of materials properties 492
  18.3.3 Diamond patterning 498
  18.3.4 Integration concepts 506
18.4 Sensor and actuator applications 508
  18.4.1 Mechanical sensors 509
  18.4.2 RF applications 512
  18.4.3 Fluidic applications 526
18.5 Conclusions 535
  Acknowledgements 536
  References 536

18.1 INTRODUCTION

Presently, the world of microelectromechanical systems (MEMS) is dominated by silicon technologies. Indeed, it is the only material to combine sensors and actuators with passive and active electronics for signal readout, data conversion, data processing, data storage, etc. Silicon materials and the related fabrication technologies have reached a nearly ideal status in terms of quality and yield, not atleast because of the available large surface area substrates. However, in applications under extreme conditions like, for instance, high temperatures, aggressive media, or high-energy particle radiation, Si may fail. In this case ceramics and wide band gap semiconductors with ceramic-like stability have an important role to play [1, 2].

CVD Diamond for Electronic Devices and Sensors Edited by Ricardo S. Sussmann
© 2009 John Wiley & Sons, Ltd. ISBN: 978-0-470-06532-7

One candidate in this respect is diamond, besides SiC and III-nitrides. It is extremely hard and stiff, mechanically and temperature stable, chemically inert and corrosion resistant, piezoresistive, and has the highest thermal conductivity (at room temperature) of all natural solids. Its mechanical material properties, like Young's modulus and hardness, remain constant within a wide temperature range. Its resistivity range can be varied by doping by about 15 orders of magnitude from highly insulating to quasi-metallic. Although diamond does not posses any shallow dopant, the quasi-metallic electrical conductivity is nearly temperature independent within typical operation regimes of MEMS (due to miniband conduction). Overviews concerning specific diamond characteristics and concerning its general use in MEMS can be found in the literature [3–15].

The absence of shallow dopants has, however, prevented so far the development of CMOS-like electronics in diamond. In general, the technology of diamond transistors is still immature and not ready for use in signal and data processing circuitry. Current growth conditions of diamond films generally do not allow a monolithic integration of diamond devices with silicon technologies. The only exception to date is the growth of ultrananocrystalline diamond (UNCD) with high grain boundary content at temperatures as low as 350 °C, which has opened a way for integration with Si-CMOS technologies of such material [10]. Here, work has concentrated on RF-MEMS applications, namely GHz-resonators.

In the majority of cases, diamond MEMS have therefore been discrete devices and integration has been achieved by means of hybrid technologies. The first concepts based on the use of surface mount technologies (SMTs) have already been proposed [16–18]. Using such mounting technologies, hybrid integration may be possible using various substrate materials including semiconductors like Si, GaN or SiC, and others such as ceramics, glasses, or even plastics.

Smart sensor chips, integrating the transducer with signal-conditioning and signal-processing circuitry, based on Si technologies are the workhorses of sensor systems to date. The field of diamond sensors and actuators has therefore to find applications outside the conventional Si territory. This will be needed because the limits of Si as substrate material are now clear: a small band gap, relatively low surface corrosion resistance, limited hardness mechanical high temperature characteristics.

Diamond can scale macroscopic discrete device structures into the microscale while largely preserving their performance. Being a wide band-gap semiconductor with a higher stability than most ceramics, it can substitute some of the ceramics, refractory metals and semiconductors currently used in MEMS structures, thus avoiding complicated materials stacks and associated thermal, mechanical and electrical stress problems. Altogether this allows operation at high power and energy densities enabling the downscaling mentioned above. Thus, current diamond MEMS device structures have been developed as discrete devices for very specific applications in very diverse fields, such as high-energy particle detection, high power/high temperature stable RF-microsystems, and electrochemistry in harsh environments. Because special electronics for extreme applications is the goal of many efforts in SiC and GaN, the hybrid integration of diamond MEMS with GaN or SiC electronics may indeed enable a new generation of smart sensors operating in extreme conditions in the future.

Nanocrystalline films on foreign substrates are nearly exclusively used in diamond-based microsystems. Monocrystalline diamond substrates are currently limited to square centimetre size. The only possibility of obtaining quasi-single crystal films is by heteroepitaxy on Ir (see Chapter 6 by Schreck in this book). However, Ir itself needs a foreign substrate like $SrTiO_3$ and the entire materials stack is difficult to balance in respect to thermal mismatch. Therefore, this alternative is also at present limited to a surface area of about 1 cm^2. Therefore, both are unattractive for MEMS fabrication. The foreign substrate for the nanocrystalline films is mostly Si, because of its well-developed micromachining technologies.

Nanocrystalline diamond (NCD) films can exhibit diverse properties. With nucleation densities above or around 10^{12} cm^{-2}, films coalesce within several tens of nm, and depending on the nucleation method used, films can be highly conformal on 3D-structures. Growth of the nucleated films can occur in different crystalline orientations by the use of different gas chemistries, and the various growth morphologies are best described by α-parameter engineering. Two growth techniques are commonly used, microwave plasma assisted CVD (MPCVD) and hot filament CVD (HFCVD). These synthesis techniques can produce a large family of material configurations, including films with sub-µm grain size to films with nm-grain size. If the grain size is below 10 nm, these films are labelled ultrananocrystalline diamond films. Films can be grown with rather constant grain size or in a columnar structure. These configurations have been labelled 3D-NCD and 2D-NCD respectively. It is therefore not unexpected that these films can vary substantially in their properties. This wide range of growth conditions makes it possible, in many cases, to reach near ideal properties optimised for a specific application. 3D-NCD for instance may exhibit a higher fracture strength than a single crystal substrate, which could be dominated by an internal stress profile and a high defect density. Varying the conditions during growth allows, for example, stress engineering of films, which is an important aspect in the fabrication of mechanical structures.

In the following chapter concepts for discrete MEMS device structures will be discussed. This will include sensing and actuation principles, microtransducer elements, possible system integration concepts, and already-realised systems. The chapter is divided into four major parts. Firstly we will discuss the physical background of different transducer schemes that are commonly used in MEMS. In each case the physical aspects will be related to the practical layout properties, which are relevant for diamond as transducer material. The following section will address diamond substrate preparation issues, which include heteroepitaxial growth and characterisation of the bulk and surface properties of the film. In the next section processing techniques will be reviewed and their suitability for the fabrication of particular device structures will be compared. Finally, we will present a number of diamond microsystems that have been fabricated and tested.

We will describe and review the state-of-the-art of diamond-based microelectromechanical systems. Other MEMS related structures, like radiation detectors or electrochemical electrodes and ChemFETs, are however beyond the scope of this chapter (see elsewhere in this book). Although many examples described represent device structures developed in the institute of the authors, we have aimed to describe the broader field and to acknowledge the contributions of the many international groups, without whom this field would not have been developed to its present state.

18.2 TRANSDUCER ELEMENTS

18.2.1 Transducers, sensors, and actuators

Transducers convert one form of energy into another. When the transducer works as a sensor, the input energy consists of environmental signals such as temperature, electromagnetic field, mechanical force, radiation, taste or smell, which are converted into the energy used for signal processing and transmission. In the case of microelectromechanical systems (MEMS), this matrix is restricted to the conversion of a mechanical to an electrical signal realised by micro systems technology (MST). However, with time the MEMS acronym has become more general and it will be used here for the conversion of mechanical and thermal input signals into electrical output signals, since they are mostly strongly linked. Conversely, a MEMS actuator will convert electrical signals into a mechanical or thermal response, the structure again being realised by MST. Examples of either are force, acceleration or thermal sensors with electrical output or switches and inkjets with electrical input.

However, for many device structures a strict classification depends on the specific application. In many cases the principle used is reciprocal, and a device can be used either as a sensor or an actuator. For instance, a resistor can be a thermal sensor measuring temperature by a change in electrical conductivity or, by applying an external voltage, induce an electrical current to generate heat and make a thermal actuator. Another example is a bimetal cantilever beam, which can sense thermal overloads as a high temperature fuse by closing or opening an electrical contact. Alternatively, in a switch application it closes or opens a signal or power path in a circuit in response to a thermal input. Table 18.1 lists some examples of microtransducers corresponding to their mode of energy conversion, which are commonly used in microsystem technologies. From the matrix it can also be seen that besides mechanical and thermal sensors and actuators labelled above as MEMS

Table 18.1 Examples of some transducers in micro systems

Input\output	Electrical	Mechanical	Thermal	Chemical	Radiating
Electrical	Electronics	**Electrostatic actuator**	**Micro heater**	Battery electrode	LED
		SAW, LCD, DLP			LASER
Mechanical	**Piezo resistor** piezoelectric sensor	Microgear	Friction sensor		
Thermal	**Thermistor** thermo pile	**Bimetal actuator**	Heat spreaders		
Chemical	ISFET	Combustion engine		Bio-signal transmission	Chemiluminescent marker
Radiating	Photo/radiation detector	Optical tweezers	Thermal radiator	Photo-chemical etchants	Fluorescent marker

devices, a number of other transducer elements, like radiation detectors or electrochemical sensing elements exist, which however, will not be covered by this chapter. In the table, those discussed in this chapter are highlighted by bold letters.

18.2.2 Diamond for sensors and actuators

For many transducers diamond is a suitable base material that may have either an active or a passive function. An example of an active function is the case of a conductive layer in a piezoresistor, where the physical effect is developed within the diamond film itself. In a passive function it can be used as a carrier material because of its thermal, mechanical, and chemical stability, as is the case in a piezoelectric actuator where a PZT piezoceramic is the active layer. One main aspect, which will be addressed throughout this chapter, is the use of diamond transducers in harsh environments. It should be pointed out that although diamond is highly temperature stable in the absence of oxygen (it has been shown to survive 2200 °C in H_2-atmosphere [19]), and that it is also chemically inert and highly corrosion resistant, if it is heated in an oxygen-containing atmosphere, it will degrade by graphitisation and even burn at temperatures above 500–600 °C.

The following paragraph will give an overview of fundamental physical effects and design considerations that are relevant for diamond-based microtransducers. It will concentrate on components that have been successfully realised with polycrystalline diamond films (PCD) of various grain sizes, on average mostly below 100 nm. Films with grain sizes below 100 nm and above 10 nm are mostly labelled nanocrystalline diamond (NCD), whereas films below 10 nm are labelled UNCD. In detail these devices are heaters, thermistors, mechanical sensors and actuators, piezoresistors, and piezoelectric sensors. Also mentioned, although not discussed in detail, are acoustic transducer devices (SAWs, FBARs) [20–28], optical DUV sensors [29, 30], radiation detectors [31–33], electrochemical electrodes [34–38], and ISFETs (ion sensitive field effect transistors) [39–42].

18.2.3 Thermal transducers

18.2.3.1 Heaters

In many MEMS applications heaters play an important role. They are, for instance, the heart of bubble-jet elements and bimetal actuators. The heat in such devices is generated by the dissipation of electrical power, typically within an ohmic resistor. The amount of heating power is given by:

$$P_{th} = \frac{W_{th}}{t} = P_{el} = I^2 R = \frac{V^2}{R} \tag{18.1}$$

where P_{th} denotes the thermal power, W_{th} the generated heat, t the time of applied electrical power, P_{el} the electrical power, I the electric current, R the ohmic resistance, and V the externally applied voltage.

From this equation it can be seen that for a given voltage the generated thermal power increases as the ohmic resistance is decreased. For a rectangular geometry this resistance is given by:

$$R = \rho \frac{l}{A} = \rho \frac{l}{wt} \tag{18.2}$$

where ρ is the electrical resistivity, l the length of the resistor in the direction of the electric current, A the cross section traversed by electric current, and w and t the width and height of a rectangular cross-section.

Accordingly, small resistances can be realised with materials having high electrical conductivity, such as metals. However, extremely thin metal layers have to be used when higher values of resistance are required. In addition, for local heating, supply lines to the heaters must be significantly wider and thicker in size to prevent parasitic heating. Hence, for metal heaters operating in the lower voltage range, their layer thicknesses have to be in the nm range. This requires precise control of thickness and specific resistivity of the metal by its deposition method, including recrystallisation effects at high temperatures. Phase changes imply structural modifications, which may also result in the generation of intrinsic stresses. Passivation is needed to prevent oxidation, which again changes the overall resistivity and may render the entire film insulating with time.

In semiconductors, electrical conductivity is controlled by doping. Highly doped or quasi-metallically doped semiconductors usually exhibit three orders of magnitude higher resistivity values than metals. Thus, for the same heater surface dimensions, layer thicknesses can be increased from the nm range into the μm range, enabling tighter control and reproducibility. Wiring of such semiconductor heater elements can then be realised by metal lines with negligible self-heating. In many semiconductors, chemical instabilities (like phase changes) and corrosion (through oxidation or etching) are observed. In contrast, nanocrystalline diamond films are highly stable. No change in phase has been observed even under operation at 1000 °C (in vacuum). In air, oxidation (and etching) of grain boundaries is known to start at about 600 °C [43], before the grains themselves are attacked. In water, microcrystalline diamond is used as electrochemical electrode in electroanalysis with high anodic overpotentials, or in waste water treatment without degradation over an extended period of time (see Chapter 17 by Foord in this book). Obviously, the performance will depend on the graphitic grain boundary content of the film and UNCD may be less stable than NCD or microcrystalline films. NCD heaters have been used in contact with acidic and alkaline solutions, withstanding for example the ejection of H_2SO_4 in a bubble-jet configuration without degradation. Figure 18.1 illustrates the use of a diamond heater element working as a microfountain by applying a microsecond electrical pulse (in the case shown with a power density close to 1 MW/cm^2) to the heater. The height of the water column was about 20 cm [17, 44]. Such types of heater have been the heart of diamond bubble-jet devices (see Section 18.4.3.2).

To obtain high electrical conductivity in nanocrystalline diamond films, two possible doping schemes can be considered. One is doping with boron. Boron acts as an acceptor within the diamond grains (see Chapters 3 by Mainwood and 2 by Isberg in this book) and can be also incorporated within the grain boundaries. In the crystal bulk it is a deep acceptor with an activation energy of 370 meV [45]. However, at a concentration above about 10^{19} cm^{-3} the activation energy is reduced by miniband formation (see Figure 18.2). This activation energy is, in many cases, also preserved in NCD films. If the grains are highly defective, a larger activation energy may be observed at concentrations below 10^{18} cm^{-3} due to compensation by n-type defects. In most cases the influence of the

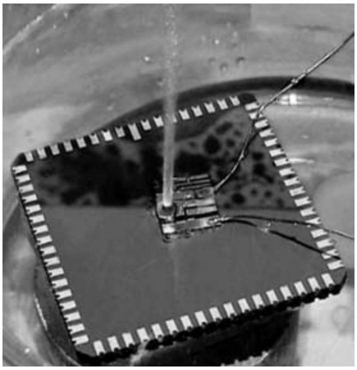

Figure 18.1 Water fountain generated by pulsed stimulation of a boron doped, nanocrystalline diamond micro heater located slightly beneath a water surface. Height of the water column is about 20 centimetres. Details on the operation can be found in Ref. [17]. Reprinted with permission from Comprehensive Microsystems, Chapter 1.06, by Erhard Kohn. Copyright (2007) Elsevier. See plate 10

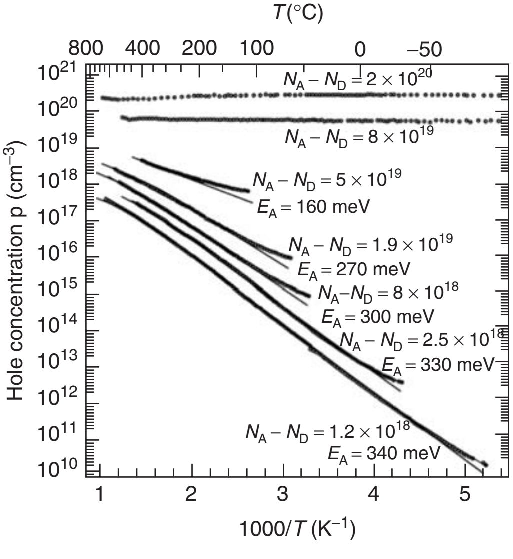

Figure 18.2 Free hole concentration in bulk diamond dependent on temperature for different doping levels. For levels in the range of 10^{20} cm^{-3} and above, no temperature dependence is observed [45]. Reprinted with permission from phys. stat. sol a, Boron-Doped Homoepitaxial Diamond Layers: Fabrication, Characterization and Electronic Applications by Borst and Weis, 154, pgs 423–444. Copyright (1996) Wiley-VCH

grain boundaries is small, except at high concentrations above 10^{21} cm^{-3}, when the influence of boron clusters becomes noticeable. Thus, boron doped films can be used in two applications: at low concentrations they can be used for thermistors (see Section 18.2.3.2), and with high concentrations ($N_A > {\sim}10^{20}$ cm^{-3}) as heaters with a temperature independent resistivity [46].

The second possibility for achieving conduction is through the grain boundary network itself. In NCD and UNCD films with a grain boundary content in the percentage range, conductivity can be obtained by nitrogen doping. In this case nitrogen in a concentration of a few percent is added to the gas phase during growth. Nitrogen is incorporated into the grain boundaries, causing graphitic grain boundary conduction. This conductivity is comparable to that of quasi-metallically doped boron films, nearly temperature independent and also stable at high temperatures [44, 48–51]. NCD and UNCD films 'doped' in this way have been stably operated up to 1000 °C (in vacuum). Within the bulk, nitrogen acts as donor with an activation energy of 1.7 eV [47] and is, therefore, not electrically activated at all practical working temperatures. NCD films grown with low nitrogen content in the gas phase have high resistivity and may be considered a lossy dielectric with a known position of its Fermi level.

Considering again the temperature stability of heaters, it is important to achieve good adhesion between different layers of the materials stack. In particular, high thermal mismatch results very often in cracks in the heterostructures and to peeling of parts of the films. An obvious advantage in the use of diamond is the possibility of fabricating nearly all layers of the stack from one identical material, avoiding thermal mismatch issues. Only the wiring lines will be made of (refractory) metals, but are, in general, located outside thermal hotspots and thus not considerably strained.

For MEMS devices that employ the bimetal effect (see Section 18.2.4.2), it is important to specify the calibration of temperature increase. The amount of thermal energy needed to obtain a defined temperature rise is determined by the specific heat capacity. This amount of energy has to be dissipated again, when returning to ambient condition. Therefore static and dynamic aspects have to be considered. Table 18.2 shows specific heat capacity values for electrically conductive, solid state materials used for MEMS. It can be seen that metals such as Pt consume very little energy during heating. On the other hand, thermal conductivity is much higher in diamond or SiC, resulting in faster heat dissipation during dynamic operation or after switching the device off. Consequently, the best compromise for fast driven thermoelectric device structures is offered by diamond [52] or a combination of diamond and metals. Compared to Si and SiC, diamond has a lower specific heat capacity and, at the same time, the highest thermal conductivity. It should be mentioned here that for heterogeneous systems consisting of diamond and metals, the adhesion is critical and linked to covalent bonding and carbide formation at the interface.

Table 18.2 Minimum electrical resistivity, specific heat capacitance, and thermal conductivity of different MEMS materials (at room temperature)

	Conductive diamond	Si	3C–SiC	Pt
Minimum electrical resistivity (Ωcm)	$\sim 10^{-3}$	$\sim 10^{-3}$	$\sim 10^{-2}$	10.6×10^{-6}
Specific heat (J/gK)	0.509	0.710	0.690	0.130
Thermal conductivity (W/mK)	>2000	150	360	72

18.2.3.2 Thermistors

As described in the previous section, the electrical resistance of lightly boron-doped diamond layers changes nearly exponentially with temperature. Thus, a lightly doped diamond resistor, side by side with a quasi-metallically doped heater, can serve as thermistor and temperature controller. The temperature dependency of the electrical resistance of a thermistor is typically expressed as [53]:

$$R(T) = R_0 e^{\beta\left(\frac{1}{T} - \frac{1}{T_0}\right)} \tag{18.3}$$

where $R(T)$ is the temperature dependent resistance, T_0 a reference temperature at which $R(T) = R_0$, and β a material parameter known as the characteristic temperature.

Diamond doped with boron concentrations below approximately 10^{18} cm^{-3} exhibits very high β parameters and thus a high sensitivity to changes in temperature over a wide temperature range (see Figure 18.2) [43, 45, 54]. For films of low doping concentrations (in the range of $10^{16} - 10^{17}$ cm^{-3}) a mobility dependence of about $T^{-2.8}$ must also be considered in the temperature interval of 400 to 800 K [55], in addition to possible compensation by defects.

Figure 18.3 shows the temperature dependence of a heater with integrated thermistor, which was operated within the temperature range from room temperature to 500 °C. The heater resistance still exhibits a small temperature dependence, the dependencies of both elements being nearly exponential (the small deviation most likely being caused by the temperature dependence of the mobility). The resistance variation of the thermistor is five orders of magnitude. In the same temperature interval, the conductivity of the heater increases only by about a factor of two. For the temperature readout a meter with an amplifier spanning five orders of magnitude is needed.

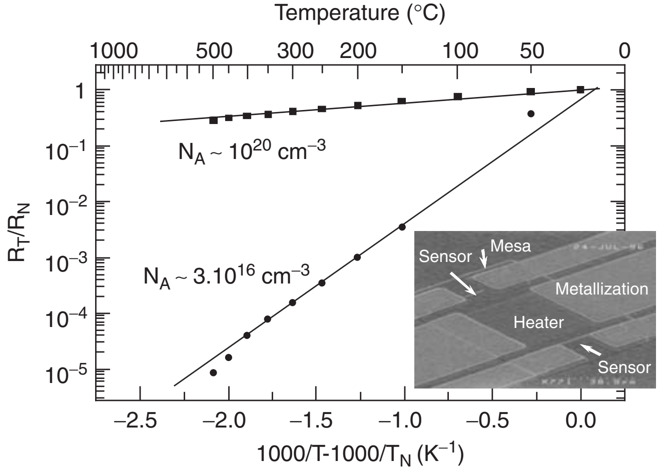

Figure 18.3 Temperature dependent resistance of a low-doped diamond thermistor (dots) integrated with a highly doped heating element (squares). Nearly exponential behaviour can be observed within a temperature range from room temperature to approximately 500 °C. Reference temperature for the Arrhenius plot is room temperature (22 °C) [53]. Reprinted with permission from Microsystem Technologies Volume 1–3, by P. Gluche, 5,1, pgs 38–43. Copyright (1969) Springer

18.2.4 Mechanical transducers

Mechanical transducers convert movable static or dynamic mechanical forces into electrical signals or vice versa. Effects discussed in this section are electrostatic coupling, bimetallic effects, piezoresistive effects, and the use of piezoelectric materials.

18.2.4.1 Electrostatic actuators

In MEMS, mechanical actuators are movable parts, typically cantilever beams, bridges or membranes, which act as switches or resonators, as well as gears, or hinges to move mirrors. One driving mechanism is electrostatic actuation. Using the Coulomb force, two plates of opposite electrical polarity attract each other. For an ideal, rectangular, parallel-plate system this force is given by [57]:

$$F_{el} = \frac{\varepsilon_0 A V^2}{2d^2} = \frac{\varepsilon_0 w l V^2}{2d^2} \tag{18.4}$$

where F_{el} is the Coulomb force, ε_0 the permittivity in vacuum, A the area of the plates with width w and length l, V the applied voltage, and d the distance between the plates.

This equation shows that the force is reciprocally proportional to the square of the distance between the plates. This means that for a wide separation the force is small, but for very narrow separations the force becomes extremely high and the plates snap. Hence this effect is often used for switches but not for actuators that require a smooth controllable displacement.

In electrostatic MEMS actuators, the Coulomb force F_{el} is mostly employed in a cantilever beam configuration, frequently known as a parallel-plate actuator (also a bridge-like configuration is possible; however moderate control voltages can only be obtained by very small electrode separations). Such a cantilever, which is fixed at one end, is pulled down when an electrical field between the top and bottom electrodes is applied. The threshold voltage for this type of drive can be approximated for the quasi-static case by [58]:

$$V_{th} = \sqrt{\frac{18 E I g^3}{5 \varepsilon_0 l^4 w}} \tag{18.5}$$

where V_{th} denotes the threshold voltage, E the Young's modulus of the cantilever material, I the geometrical moment of inertia, g the separation between the electrodes (air gap), l the cantilever length, and w its width.

An insulating layer between the beam and the bottom electrode prevents current flow in the closed state. This isolation can be realised by a passivation layer covering the bottom electrode or by an insulating cantilever material having an electrode on its top. Equation (18.5) is only valid for geometries where the isolation layer is thin compared with the separation distance, i.e. the gap capacitance C_{gap} dominates with respect to the isolation capacitance C_{iso}. In most cases this assumption is valid. For thick isolation layers, C_{iso} acts in series to C_{gap}. For a detailed analysis, see Ref. [59].

Equation (18.5) shows that small driving voltages of an electrostatic actuator are possible for thin and wide cantilevers that possess low stiffness. In particular, long cantilevers and small air gaps contribute essentially to low actuation forces. Obviously, a small cantilever spring constant will be obtained with these parameters. However, in turn, a small spring constant is associated with a small reset force, which effects the release of the cantilever beam after the electrical load is switched off. Therefore, for fast dynamic operation it is preferable to use stiff materials with a high Young's modulus, although this will require higher actuating voltages. In addition, many dielectrics used for insulation suffer from charging, which keeps the cantilever in contact even after an applied voltage is turned off. Already during fabrication processes, especially with wet chemical procedures, soft cantilevers are attracted by surface tension effects and may be 'glued' to other parts of the device.

When diamond is used as cantilever beam material, these circumstances can be mostly avoided. Because of its high Young's modulus, thin and stiff beams can be fabricated with moderate actuation voltages, in the range of some tens of volts [60]. The influence of the high restoring force on the reset of the cantilever is shown in Figure 18.4 [61], comparing diamond with silicon. It can be seen, that a diamond cantilever reaches its initial position more than twice as fast. However, this behaviour will only be observed in vacuum. In atmosphere, air damping reduces the speed because a large beam surface is needed in order to achieve a large capacitance. To minimise air damping, the beams either contain many openings or the devices need to be vacuum packaged. A more detailed study on the contribution of air damping and intrinsic stress in diamond cantilever actuators can be found in Refs [16, 62].

The resonance frequency is a commonly used figure of merit for describing the operation of electrostatic and other types of mechanical actuators. In a resonator application, the resonant frequency is in fact the frequency of operation (see Section 18.4.2.1); in an electromechanical switch application (see Section 18.4.2.2) devices can be operated close

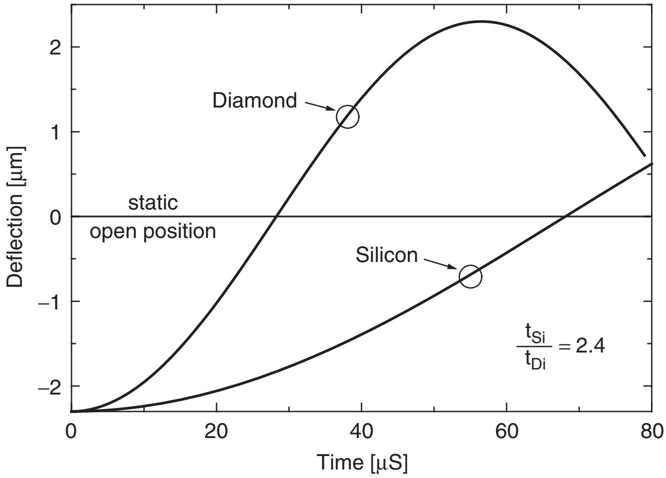

Figure 18.4 Comparison of dynamic behaviour by FEA (finite-element analysis) of a deflected diamond and silicon cantilever of identical geometry, when the deflection force is turned off. Inducing an oscillating characteristic, the diamond structure passes its quiescent position more than twice as fast as does the silicon one [61]. Reprinted with permission from Diamond and Related Materials, Diamond electro-mechanical micro devices – technology and performance by E. Kohn, M. Adamschik, P. Schmid, S. Ertl and A. Flöter, 10, 9–10. Copyright (2001) Elsevier

to the resonance frequency, but actual resonance has to be avoided because it is an unstable condition.

The first order resonance frequency $f_{res,0}$ of a single material cantilever beam is given by [63]:

$$f_{res,0} = \frac{\lambda_i^2}{4\pi}\sqrt{\frac{E}{3\rho}}\frac{t}{l^2} \cong 0.16\sqrt{\frac{E}{\rho}}\frac{t}{l^2} \tag{18.6}$$

where $\lambda_i = 1.875$, E the Young's modulus, ρ the mass density, t the beam thickness, and l the beam length.

For a given geometry, a maximum $f_{res,0}$ can be obtained for a material with a high ratio of Young's modulus to density, which in thin solid films is also approximately the speed of sound in the longitudinal direction. In Table 18.3 these MEMS parameters are compared for different materials. It can be seen that diamond exceeds all other materials and factors of more than 2 compared to silicon and about 1.7 compared to SiC and AlN can be expected for an identical geometry.

18.2.4.2 Bimetal actuators and sensors

In bimetal transducers, two or more layers of different materials are stacked on top of each other. Owing to their different coefficients of thermal expansion, a temperature variation generates mechanical stress and bending moments. Hence, freestanding parts of the layer stack can bend or buckle.

The amount of thermal expansion ε_{th} of a material is given by:

$$\varepsilon_{th} = \int_{T_0}^{T_1} \alpha_{th}(\vartheta)\mathrm{d}\vartheta \tag{18.7}$$

where T_0 and T_1 are the lower and the upper temperature limits and α_{th} is the (temperature dependent) coefficient of thermal expansion (CTE).

As can be seen from Figure 18.5, the temperature dependence of the thermal expansion itself is not linear. However, for small temperature differences, which are typical for bimetallic MEMS actuators, a linear approximation by a CTE is often used.

Considering now a cantilever actuator with bimetal stimulation, the generated thermal strains in both materials are converted into intrinsic stress, which implies a bending

Table 18.3 Young's modulus, density of mass, and square root ratio of these values for various MEMS materials

	Diamond	Silicon	3C–SiC	AlN	Ni
Young's modulus (E) (GPa)	1050	165	307	331	210
Density (ρ) (g/cm^3)]	3.52	2.33	3.21	3.26	8.91
$\sqrt{E/\rho}$ (10^3 m/s)	18.3	8.4	9.8	10.1	4.7

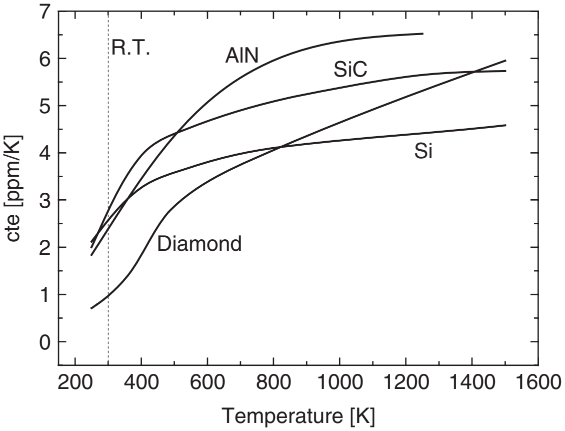

Figure 18.5 Temperature dependence of the coefficient of thermal expansion α_{th} for some MEMS materials from room temperature to >1000 K

moment M_{th}, which in an ideal case can be described by [64]:

$$M_{th} = \frac{\Delta T}{2} \frac{E_1 w_1 t_1 E_2 w_2 t_2}{E_1 w_1 t_1 + E_2 w_2 t_2} (t_1 + t_2)(\alpha_2 - \alpha_1) \tag{18.8}$$

where ΔT is the temperature difference, E_1 and E_2 the Young's moduli, w_1 and w_2 the beam widths, t_1 and t_2 the beam thicknesses, and α_1 and α_2 the coefficients of thermal expansion.

This bending moment initiates a deflection of the cantilever tip. According to Hooke's law, stiff materials (high Young's moduli) stimulate high stress values, therefore, an often used figure-of-merit for thermal stress generation is the product of the Young's modulus and the coefficient of thermal expansion [16]. In order to obtain large moments, and thus large cantilever deflections, two materials with a large difference in these figures are desirable. In Table 18.4, values for diamond and other MEMS materials are listed. It shows that particularly metals such as Ni or Cu in combination with diamond are well suited for such an application. With these pairs, cantilever bending can be achieved already with moderate temperature changes.

Table 18.4 Young's moduli, coefficients of thermal expansion, and products of these values for various MEMS materials

	Diamond	Silicon	3C–SiC	AlN	Ni	Cu
Young's modulus (E) (GPa)	1050	165	307	331	210	130
Coefficient of thermal expansion at RT (α_{th}) (ppm/°C)	1	4.2	3.8	4.6	13.4	16.5
$E \cdot \alpha_{th}$ (10^3 m/s)	1050	693	1167	1523	2815	2145

For optimum performance of a bimetal transducer, a maximum bending moment is obtained for the case that the generated forces of each single layer are identical, i.e. if:

$$\frac{t_2}{t_1} = \sqrt{\frac{E_1}{E_2}} \tag{18.9}$$

where t_1, t_2 are the layer thicknesses, and E_1, E_2 the respective Young's moduli [65].

In any other case, the induced thermal stress is partly converted into a constant compressive or tensile strain within the layers. In an extreme case, where the thickness ratio and/or the Young's moduli ratio are very high, the thicker and/or stiffer layer dominates. As a result, negligible bending, but stretching or compression of the 'weaker' layer is observed. Typical examples for this case are thin films deposited onto much thicker substrates (as in the case of strained layer epitaxy).

Thus, it can be concluded that ideal thermal MEMS transducers consist of two materials with a similar Young's modulus, but a large difference in thermal expansion. For fast dynamic operation (see Equation (18.6)) the capability for high thermal power dissipation is also needed, again pointing towards diamond. In general, a diamond/Cu or diamond/Ni bimetal stack is a highly suitable combination.

18.2.4.3 Piezoresistive sensor elements

When deforming a conductive material, a change of resistance can be observed. This effect was first studied in 1856 for copper and iron wires and was named piezoresistivity.

The amount of change in the material resistance is usually described by its gauge factor K (or GF) defined as [66]:

$$K = \frac{\Delta R/R}{\varepsilon} \tag{18.10}$$

where R is the electrical resistance and ε the mechanical strain.

The physical origin of this effect can be separated into two parts. One is the geometrical variation in the structure dimensions and the other is the modification of the band structures and associated carrier redistribution in case of semiconductors. Hence, Equation (18.10) can be rewritten as [67]:

$$K = 1 + 2\nu + \frac{1}{\varepsilon}\frac{\Delta\rho}{\rho} \tag{18.11}$$

with the Poisson's ratio ν and resistivity ρ.

According to Equation (18.11), the geometrical piezoresistive effect, which is represented by the terms $1 + 2\nu$, is limited to a gauge factor of $K = 2$ because of a maximum achievable Poisson's ratio of 0.5. It is therefore the value for many metals.

In n-type or p-type semiconductors, a deformation of the crystal lattice redistributes the density of states of electrons and holes in the transversal and longitudinal parts of the conduction or valence band respectively [68]. Accordingly, a repopulation of free carriers and a change of effective mass are induced. This results in an increased or a reduced mobility, depending on the doping level. The diamond lattice is similar to silicon and a similar directionality should be observed for its piezoresistive coefficients. Generally, conductivity is enhanced in the direction of compressive stress and reduced in the direction of tensile stress. Thus, for symmetry reasons, the piezoresistivity of semiconductors with a diamond lattice can be separated into longitudinal, transversal, and shear effects, independent of the crystallographic orientation and therefore piezoresistivity will be equally observed for randomly oriented polycrystalline or nanocrystalline films.

In diamond, only p-doping by boron is relevant for piezoresistors. Ideally the valence band density of states distribution is isotropic and no directionality should be observed. However, it is slightly distorted with a symmetry related to the main axes. The main contribution in boron-doped diamond is caused by a shift of the light-hole valence band under mechanical stress (see Figure 18.6) [69, 70]. Also here, compression leads to an increase in conductivity, whereas stretching results in a decrease. A longitudinal gauge factor as high as 1000 [71] has been extracted and has been found to vary significantly with doping concentration, approaching the value for metals at high doping concentrations [72]. In experimental, nanocrystalline, sensor elements (as discussed in Section 18.4.1) the gauge factor is usually below 20, mainly because relatively high boron concentrations are needed for significant activation at room temperature. In part, these low values have also been attributed to losses in the grain boundaries, although gauge factors determined on individual crystallites of highly oriented diamond layers (see Figure 18.7) have not shown essentially larger values either [66]. A complication in the determination of the gauge factor is the nearly exponential temperature dependence of the boron acceptor activation. Therefore, care has to be taken in the interpretation of the temperature dependence of the piezoresistivity [69, 73]. Sometimes, a decrease of resistivity has been observed from room temperature to about 300 °C, increasing again for higher temperatures (measured up to 500 °C) [74]. Thus at least two compensating effects overlap: the piezoresistive effects and carrier activation.

18.2.4.4 Piezoelectric actuators

Piezoelectricity can be found in many insulating materials that lack an axis of symmetry and are also birefringent. This was discovered in 1880 by the brothers Jacques and

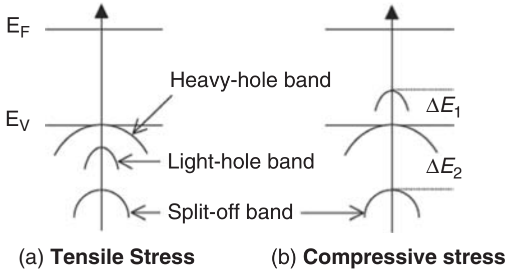

Figure 18.6 Origin of the change of p-type conductivity due to piezoresistive effect in diamond [69]. Deformation of the crystal induces a redistribution of the particular valence bands and thus a repopulation of free carriers. Reprinted with permission from Journal of Physics: Condensed Matter, A theoretical calculation of the piezoresistivity and magnetoresistivity in p-type semiconducting diamond films by C. Y. Kong, W. L. Wang, K. L. Liao, S. X. Wang and L. Fang, 14,8, 1765–1774. Copyright (2002) Institute of Physics

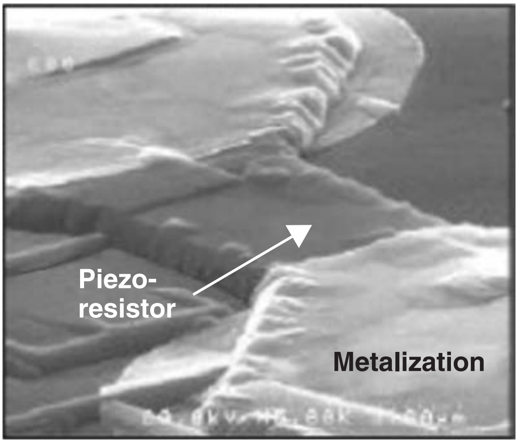

Figure 18.7 Structure for determination of piezoresistivity in diamond crystallites. The piezoresistor in this SEM micrograph contains only one grain boundary [66]. Reprinted with permission from Diamond and Related Materials, Analysis of piezoresistive properties of CVD-diamond films on silicon by M. Adamschik, R. Muller, P. Gluche, A. Floter, W. Limmer, R. Sauer and E. Kohn, 10, 9–10. Copyright (2001) Elsevier

Pierre Curie in their studies of tourmaline crystals. Materials showing distinctive piezoelectric behaviour are ceramics with the perovskite structure, such as $BaTiO_3$, $SrTiO_3$, or $Pb(Zr,Ti)O_3$ labelled as PZT. For high temperature applications, materials such as AlN, $LiNbO_3$, langasite ($La_3Ga_5SiO_{14}$), langanite ($La_3Ga_{5.5}Nb_{0.5}O_{14}$), or langatite ($La_3Ga_{5.5}Ta_{0.5}O_{14}$) [75] may be especially suited since they possess high Curie temperatures and a thermal stability of more than 1000 °C. In these materials the piezo coefficients and the coupling coefficients, which represent the amount of mechanical energy converted into electrical energy and vice versa, are, however, lower as compared with PZT.

Diamond, because of the symmetry of its lattice, is not piezoelectric and can only be used as a carrier material for this application. Because piezoceramics are mostly brittle and have low stiffness, diamond is an excellent complementary carrier material and can be employed to develop mechanically stable actuators with high resonance frequencies. Bilayers with a piezoelectric overlayer on a mechanical support layer are common in microsystem technologies and are called unimorphs. Figure 18.8 shows calculated, first order, resonance frequencies of multilayer cantilevers consisting of PZT, NCD, and PZT on NCD. Additionally, some FEA data, which take the additional influence of the metal electrode into account, are also included. As can be seen, the resonance behaviour is largely determined by the diamond supporting film, while the actuation is generated by the PZT overlayer. An Al-overlayer electrode will degrade these properties only marginally.

The prerequisite for piezoelectricity in a material is an asymmetric lattice configuration, which implies spontaneous polarisation. By applying mechanical loads, the dipole lengths in the crystal are varied, which generates an electrical charge dipole at the surfaces. By adding metal electrodes to the surfaces, an electrical voltage can be measured, which is the direct piezoelectric effect. Conversely, by applying a potential onto the electrodes the polar crystal can be distorted; this is consequently called inverse piezoelectric effect. Both options are used for MEMS transducers either to detect mechanical deformation of

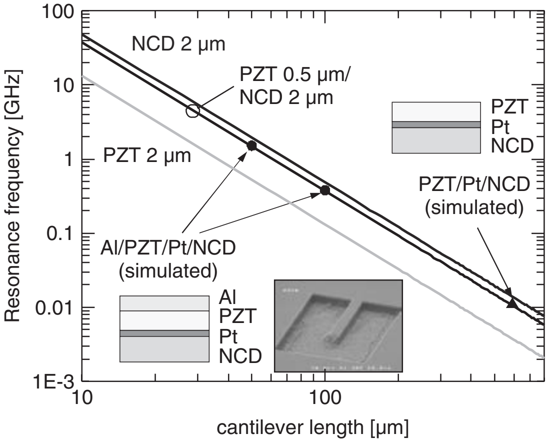

Figure 18.8 Calculated resonance frequencies of cantilevers out of PZT, NCD, and PZT on NCD. The dots and the triangles are finite-element analysis (FEA) data, which include also thin metal layers. The inset shows a fabricated 50-μm long cantilever made of such a layer stack [76]. Reprinted with permission from Diamond and Related Materials, Piezo-actuated nanodiamond cantilever technology for high speed applications, by J. Kusterer, A. Luker, P. Herfurth, Y. Men, W. Ebert, P. Kirby, M. O'Keefe and E. Kohn, 17, 7–10, 1429–1433, Copyright Elsevier

a structure or to actuate deflection. The piezoelectric effect can be applied by two modes d_{31} and d_{33}, as illustrated in Figure 18.9. The quantity of generated electrical charge or piezoelectrically induced mechanical strain can be expressed according to Refs [63, 77] by:

$$D_{3,t} = d_{31} \cdot \sigma_{11} \tag{18.12}$$

$$\varepsilon_{x,t} = d_{31} \cdot E_{el,z} \tag{18.13}$$

for transversal mode or by

$$D_{1,l} = d_{33} \cdot \sigma_{11} \tag{18.14}$$

$$\varepsilon_{x,l} = d_{33} \cdot E_{el,x} \tag{18.15}$$

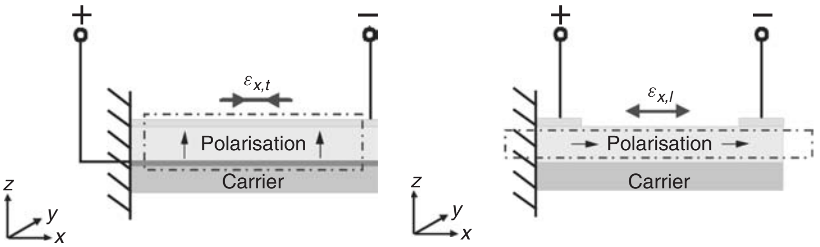

Figure 18.9 Effect of transversal (left) and longitudinal (right) effect in piezoelectric actuators [76]. Reprinted with permission from Diamond and Related Materials, Piezo-actuated nanodiamond cantilever technology for high speed applications, by J. Kusterer, A. Luker, P. Herfurth, Y. Men, W. Ebert, P. Kirby, M. O'Keefe and E. Kohn, 17, 7–10, 1429–1433, Copyright Elsevier

for longitudinal devices (see Figure 18.9), where $D_{3,t}$, $D_{1,l}$ and $\varepsilon_{x,t}$, $\varepsilon_{x,l}$ are respectively the dielectric displacement and mechanical strain for transversal and longitudinal configuration, σ_{11} the mechanical stress in the piezoelectric film, $E_{el,x}$, $E_{el,z}$ the applied electrical field between two electrodes, and d_{31}, d_{33} the piezoelectric coefficients (for mechanical sensors, Equations (18.13) and (18.15), the first index of the piezoelectric coefficients describes the direction of the cause, whereas the second one that of the effect. For mechanical actuators, Equations (18.12) and (18.14), this is the other way round).

The use of diamond in such a device offers several advantages as compared with other materials. In mechanical actuators the use of diamond results in the highest resonance frequency for a given geometry (compare Table 18.3). This can be employed for the development of microresonators with high operating frequencies or for high-speed micromechanical switches. However, only a factor of approximately two compared with other MEMS materials can be expected (see Section 18.2.4.1). On the other hand, as in the case of electrostatic actuators, the high stiffness of diamond permits a fast switching-off action as long as diamond dominates as a carrier material [76]. Combined with a proper piezoelectric material it might permit high sensitivity for sensor applications at high temperature and in corrosive environments. Examples are high-pressure sensors (see Section 18.4.2), high acceleration sensors, mass flow detectors for high gas or liquid flows, vibration sensors, or shock detectors.

The first piezoelectric actuators consisting of diamond and PZT have recently been reported, including an actuator using a UNCD carrier [78] (see Figure 18.10) and another one with an NCD carrier [76]. In both studies resonance frequencies in the MHz range have been demonstrated.

18.3 TECHNOLOGICAL BUILDING BLOCKS

This section will describe the fabrication technology for diamond sensors and actuators in microsystems technology. It will give information about diamond film deposition and

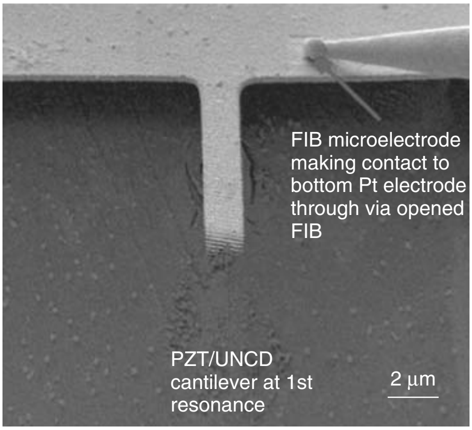
FIB microelectrode making contact to bottom Pt electrode through via opened FIB
PZT/UNCD cantilever at 1st resonance
2 μm

Figure 18.10 PZT/UNCD unimorph, operating at the first order resonance frequency [78]. Reprinted with permission from Appl. Phys. Lett., Piezoelectric/ultrananocrystalline diamond heterostructures for high-performance multifunctional micro/nanoelectromechanical systems by S. Srinivasan, J. Hiller and B. Kabius, 90, 134101, Copyright (2007) Elsevier

the surface termination of these films. The section continues with analytical methods for NCD diamond film properties that are of special interest to MEMS, such as Young's modulus, intrinsic stress, fracture strength, and thermal conductivity. Depending on the type of diamond film, these characteristics can deviate considerably from the ideal case. In the second part of the section, device-manufacturing techniques like diamond patterning, structure release, and system integration concepts are discussed.

18.3.1 Diamond material preparation

18.3.1.1 Diamond deposition

As already discussed, diamond films in MEMS devices are generally nanocrystalline and mostly deposited on Si substrates. Thus, although not single crystalline, these are still labelled heteroepitaxial. Their growth conditions are commonly optimised for the set of properties that is important for the application. In some cases, these heteroepitaxial films can attain properties close to single crystal diamond [79] such as high hardness, high Young's modulus, high thermal conductivity, and corrosion resistance. Thin polycrystalline diamond films on silicon or glass are already commercially available on cost-effective, large-scale wafers with diameters of up to 12 inches [80]. However, in such films the grain size increases with increasing thickness and the surface becomes increasingly rough. Therefore, in most cases these films are polished afterwards, complicating the fabrication process. Typical layer thicknesses for diamond MEMS are in the micron range with grain sizes in the same order. Therefore these types of films are known as microcrystalline diamond (MCD) [81]. In the submicron range these are nanocrystalline diamond (NCD) films [82], and in the lower nanometer range ultrananocrystalline diamond (UNCD) films [83]. Deviations from ideal single crystal behaviour can be largely traced back to the influence of the grain boundary network. This is illustrated in Figure 18.11 for the case of thermal conductivity. This figure shows that for a given grain size some films

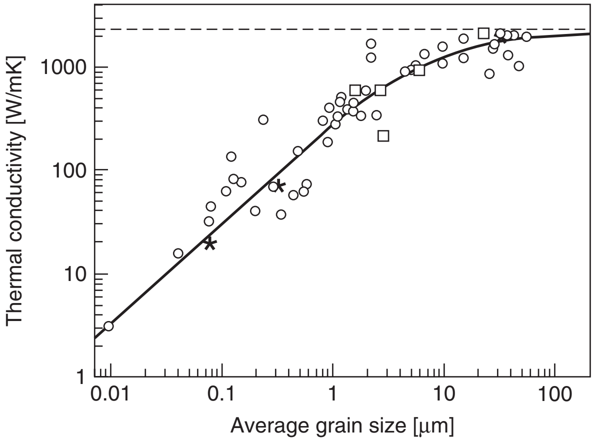

Figure 18.11 Relationship between thermal conductivity (at room temperature) of polycrystalline diamond films and grain size. The line shows a theoretical calculation, taking account of the various scattering mechanisms; symbols represent measured data [17, 64]

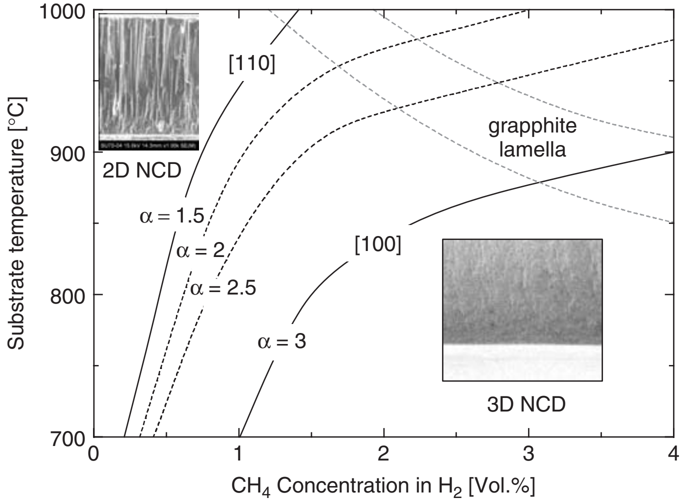

Figure 18.12 Illustration of the formation of different morphologies of epitaxial diamond by the α-diagram. The diagram is based on growth in methane/hydrogen atmosphere. The insets show regimes of columnar nanocrystalline growth [106] (2D-NCD) and strong twinning during nanocrystalline growth (3D-NCD) on silicon (based on Ref. [110]). Reprinted with permission from Journal of Physics: Condensed Matter, The effect of oxygen and nitrogen additives on the growth of nanocrystalline diamond films by C. J. Tang, A. J. Neves, A. J. S. Fernandes, J. Gracio and M. C. Carmo, 19, 38, 6236-1 to 6236-9. Copyright (2007) Institute of Physics. Reprinted with permission from Diamond and Related Materials, Oriented CVD Diamond Films: twin formation, structure and morphology by C. Wild, R. Kohl, N. Herres, W. Müller-Sebert and P. Koidl, 3, 4-6. Copyright (1994) Elsevier

exhibit higher than average values of thermal conductivity. As pointed out earlier, nanodiamond may be grown randomly as 3D-NCD or textured as 2D-NCD (see Figure 18.12). Thus, for example, columnar grown films can combine an nm-smooth surface with high thermal conductivity.

The first critical issue in the growth process of heteroepitaxial films is adhesion to their carrier substrates. MEMS elements will experience thermal and mechanical stresses with the substrate basis and must tolerate vibrations, resonance behaviour and shock. Therefore, nucleation procedures on the foreign substrates must form covalent bonding or alloying. Two methods are generally utilised, namely ultrasonic seeding with nanodiamond powder embedded in a thin amorphous carbon layer predeposited onto the base substrate, which is mostly Si [84–87], and bias enhanced nucleation (BEN) [88–91]. With both techniques densities of 10^{12} nuclei/cm^2 can be obtained. In the plasma, the amorphous carbon interlayer film is consumed and the seeds are firmly bonded to the Si substrate. Ultrasonic seeding with nanodiamond particles may cause ultrasonic damage on the substrate surface if no interlayer is used. The seeds may be polycrystalline by themselves, directly influencing the subsequent growth process. A surface smoothness of this initial seeding layer of 5–10 nm rms is typical [92]. BEN requires a carbide forming substrate material, which is electrically conductive at the nucleation temperature (mostly above 500 °C). During nucleation, carbide clusters are formed through gas phase reactions with the substrate, and within the thin carbide interlayer (like SiC on Si) diamond nuclei are formed. Also here a surface smoothness of around 5 to 10 nm is typical for this interlayer.

With both methods, conformal coatings with 3D-topographies have been obtained. However, with BEN, bias needs to be applied to the substrate surface, which may be complicated in cases where dielectrics like SiO_2 are used. By BEN the nuclei can be oriented with respect to the substrate orientation, namely [100]-oriented Si. Therefore, this technique is used to grow highly oriented diamond HOD films [93]. In this case the surface is [100]-textured and in case of thick films large quasi-single crystal areas may be obtained. Due to the oriented growth of the individual crystallites, a stress profile is, in general, incorporated [94], leading to concave bending of the Si-substrate as well as to upward bending of free standing cantilevers [61].

A promising approach is the nucleation of diamond on iridium. However, Ir itself needs to be deposited onto a foreign substrate, and the entire material stack is difficult to balance in respect to thermal stresses upon cooling from the growth temperature. The technique is, therefore, at present still confined to substrate sizes of about 1 cm^2. However, on such substrates quasi-single crystalline layers have been obtained [95–97] (see also Chapter 6 by Schreck in this book). Due to the small substrate size, to our knowledge, these have not yet been used in MEMS devices.

For the growth of diamond films, two techniques are commonly used. One is the growth in a microwave-produced plasma. Several acronyms are used such as MWCVD (Microwave Chemical Vapour Deposition), MWPECVD (Microwave Plasma Enhanced Chemical Vapour Deposition, or MWPACVD (Microwave Plasma Assisted Chemical Vapour Deposition). For growth a high density of H-radicals is needed, which is generated by a high-energy microwave plasma of usually 2.45 GHz. The second technique is hot filament chemical vapour deposition, where H_2 is cracked thermally by refractory metal wires heated to a temperature of 1500–2500 °C [17, 98–100]. In addition to these two techniques, diamond growth has been also reported by pulsed laser deposition [101] or DC arc jet deposition [102]. The precursor gas is, in most cases CH_4, which is diluted in H_2 for the growth of both microcrystalline and nanocrystalline diamond. UNCD growth is achieved in plasma by the addition of a high concentration of Ar in the gas phase [103, 104]. Additives to the gas mixture such as N_2, O_2, or CF_4, also affect the growth mechanism and may lead (as in the case of nitrogen) to grain boundary conduction. Hence, morphology, microstructure, texture, and crystalline quality are influenced by species like CH_3, CH_2, CH, C_2 and CN, or HCN radicals [105–109]. In addition, films grown using particular gas mixtures, but at different reaction temperatures, will also show specific and distinctively different properties.

Different growth modes resulting in different textures are usually described by the α-parameter [110], which represents the ratio of growth velocity in the [100]-direction with respect to the [111]-direction (Figure 18.12) for the case of a CH_4-based growth chemistry as a function of gas composition and growth temperature. Also shown in the inset of Figure 18.12 is the change of crystallite shape from cubic for $\alpha = 1$ to octahedral for $\alpha = 3$. Three basic regimes can be observed. Columnar NCD growth is usually obtained with moderate methane concentrations, which is sometimes labelled 2D-NCD [50]. For high methane contents at lower temperatures, 3D-NCD growth is obtained, which is composed of crystallites having similar dimensions in all three spatial directions. In between, a regime of textured polycrystalline diamond growth can be observed. The insets in the figure show cross-sections of 2D and 3D NCD layers on silicon.

18.3.1.2 Diamond surfaces

The surface properties of diamond may determine adhesion, wetting behaviour of liquids, interface characteristics of metal contacts, and electrochemical activity. After growth the diamond surface is usually hydrogenated (see also Chapters 4 by Ley and 16 by Garrido in this book). The termination with hydrogen is stable in atmosphere at ambient temperature but is, chemically, the most active diamond surface. When heated in air (or oxygen), treated with highly oxidising acids or basic solutions, exposed to an oxygen plasma or exposed to UV radiation, the H-termination may convert to an oxygen-termination. Such H-terminated surfaces are therefore also the starting point for defined and specific surface functionalisations, mostly through UV photochemistry. The change is usually accompanied by a change in wetting behaviour. A fully oxidised surface may form a wetting angle of $\alpha < 5^\circ$ as compared with 93° for a fully H-terminated surface [111, 112]. For fluorinated surfaces the wetting angle could be as high as 106°. Treatment time in an oxygen plasma can be as short as 1 minute for nearly full exchange of termination [113]. Fluorine, oxygen, and hydroxyl groups show strong bonding, whereas hydrogen is less stable [114]. In Figure 18.13 the contact angles of oxygenated, hydrogenated, and fluorinated diamond films with water are illustrated. For MEMS the liquid phase is often present and is especially important when considering capillaries and bubble-jet operation. The surface termination also strongly affects the behaviour of metal contacts, their electrical characteristics as well as their adhesion properties. It is equally reflected in the interfacial properties of passivation layers.

In a biological environment, the wettability has a pronounced influence on cell attachment and cell growth [115]. For instance, most neuron cells do not grow on hydrogenated, hydrophobic diamond NCD-layers, whereas growth of neural dendrites and synopses is seen on oxygen-terminated surfaces. Figure 18.14 shows such an example of a patterned substrate with cell coverage after cell attachment and cell growth after 20 days incubation *in vitro*, made visible by the fluorescence image of neuron cell markers. The pattern was an oxygen-terminated grid by an oxygen plasma treatment with H-terminated square windows on a NCD film grown by HFCVD.

Differences are also found in the longtime mechanical stability of hydrogen- and oxygen-terminated surfaces [116]. Experiments on cavitation damage have shown that a hydrogenated surface is more affected by bubble collapse than is an oxygenated surface. The reason is attributed to the hydrophilicity of oxygen-terminated surfaces, where bubbles are difficult to form.

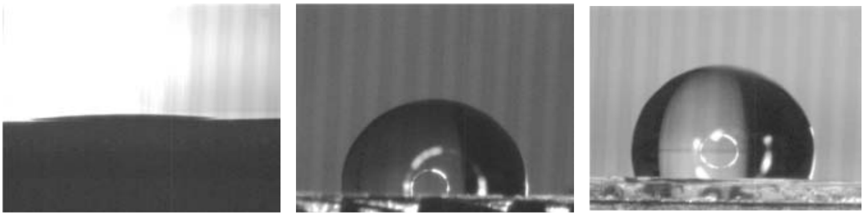

Figure 18.13 Contact angles of sessile water droplets on oxygenated (left), hydrogenated (centre), and fluorinated (right) diamond surfaces (courtesy of A. Pasquarelli, University of Ulm, Germany). Reprinted courtesy of Alberto Pasquarelli

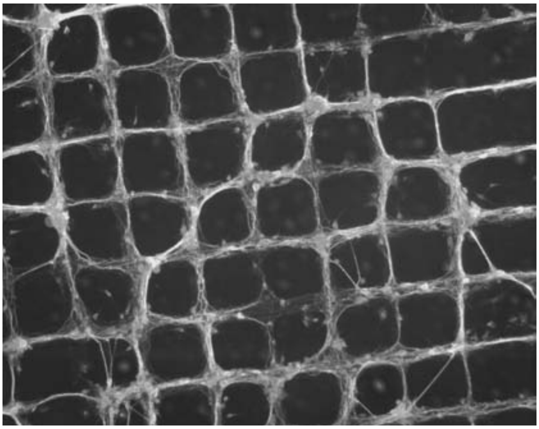

Figure 18.14 Fluorescence mapping of hippocampal cells (rat embryo, 18 days of gestation, 20 days incubation *in vitro*) on NCD with patterned surface termination; the grid was oxygen terminated, the windows in between hydrogen terminated (courtesy of T. M. Böckers, University of Ulm, Germany). Reprinted courtesy of Professor Böckers. See plate 11

Essential part of all MEMS devices is metal–diamond interfaces for ohmic or rectifying contacts. According to the Mead and Spitzer rule [117] Schottky barrier heights for covalent p-type semiconductors are about one-third of the band gap, i.e. in the range of 1.8 eV for boron-doped diamond. Indeed, for oxygen-terminated surfaces the surface potential is pinned at approximately 1.7 eV (although in special cases also dependent on the type of oxidation), which is then also seen as the Schottky barrier potential. Rectifying contacts are consequently observed for metal contacts on oxygen-terminated diamond films with low and medium boron doping levels [118, 119]. For Al metallisations on oxygen-terminated surfaces a transition from Schottky to ohmic behaviour can be observed after high temperature treatments, which is attributed to a formation of Al_3C_4 at 1020 K [120]. However, for clean self-terminated surfaces in vacuum (see [121]) or hydrogenated surfaces, surface potential values ranging from 0.1 eV to 1.0 eV have been reported [122]. In the latter case, the surface was most likely partially hydrogen, partially oxygen terminated. H-Terminated surfaces are mainly used in biochemical applications. For applications at high temperature or under highly corrosive environments, oxygen-terminated surfaces are nearly exclusively used. Schottky barriers are not frequently used in MEMS devices. A more detailed analysis of this subject can be found in Chapter 14 by Kohn and Denisenko in this book.

Ohmic characteristics on H-terminated surfaces can be obtained for metals with a low work function difference like Au. The contact is only weakly attached by van der Waals forces and peels off easily. Furthermore, the contacts are not high-temperature stable. However, rather generally employed in MEMS devices are quasi-metallically doped films [123]; and here ohmic contacts can be realised by tunnelling. Many metals and alloys have been used, such as Ti, Cr, Mo, Co, Pd, TiWN, AlSi [123], Cu, or WSi. Specific contact resistivities can be as low as 10^{-7} Ωcm^2, as determined by TLM measurements [124]. For good adhesion and operation at high temperatures, carbide-forming materials are especially suited, the interface being often stabilised by annealing above 600 °C [125].

18.3.2 Characterisation of materials properties

Depending on application and utilisation, the properties of the materials used in the various MEMS elements need special optimisation. Such properties are the Young's modulus, intrinsic stress, fracture strength, and thermal conductivity, among others. As already mentioned, the properties of the films strongly depend on growth parameters, crystallite size, grain boundary configuration, etc. Because of this large variance, the determination of these properties and their reproducible realization is important and will therefore be discussed below.

18.3.2.1 Young's modulus

The Young's modulus, or modulus of elasticity, describes the stiffness of a material. Apart from geometrical parameters it specifies the spring constant of mechanical actuators. Together with the density, it also determines the mechanical resonance frequency. For polycrystalline diamond films, values close to that of a perfect single crystal of 1143 GPa have been realised [126]. For nanocrystalline layers with an average grain size of less than 100 nm, a Young's modulus of 1120 GPa has been determined [127], and for UNCD 960 GPa have been reported [128]. The Young's modulus of diamond is, moreover, temperature stable up to at least 750 °C [129, 130]. These Young's moduli have been determined by various measurement techniques such as:

(i) strain-stress measurements,
(ii) cantilever resonance measurements, and
(iii) surface acoustic wave dispersion measurements.

In the first method, a mechanical load is applied to a cantilever or bridge structure and simultaneously the resulting deflection recorded [123, 131]. According to the beam layout, the data can be observed into mechanical stress and strain of the structure. When plotting strain versus stress, a linear relationship according to Hooke's law would be expected for the elastic regime, the slope being the Young's modulus. In fact, in nanocrystalline diamond films no plastic regime can normally be identified up to fracture.

The first-order resonance is usually determined with single ended cantilever beams like the one in Figure 18.10. Resonance can be stimulated externally, e.g. with the help of a piezooscillator. The quality factor Q of diamond cantilevers is generally high and the resonance sharp, hence it is easily identified optically when the beam structure becomes blurred [132]. Surface acoustic waves are used in acoustic-wave dispersion measurements, where the calculated nonlinear dispersion relationship is fitted to the measurement [127, 133].

An interesting fact, which was analysed in Ref. [127], is the dependence of the Young's modulus on nucleation density. High nucleation densities of more than 10^{12}cm^{-2} have resulted in Young's moduli close to the theoretical limit for polycrystalline films, whereas densities below 10^{10}cm^{-2} have resulted in roughly half the value. This has revealed indeed that a high nucleation or seed density is needed to take advantage of the high stiffness of diamond films, regardless of the growth technique.

18.3.2.2 Intrinsic stress

Thermal mismatch between deposition temperature and operating temperature, as well as high doping concentrations, dislocations within crystallites and especially the changing shape of the individual crystallites during growth, induce residual stress within heteroepitaxial diamond layers [134–139]. In polycrystalline films on silicon, intrinsic stress can vary from −300 MPa (tensile) [140] to about +500 MPa (compressive). In highly boron-doped diamond films, values up to +1200 MPa are possible [135]. A thick substrate is hardly affected if its thickness is orders of magnitude larger than that of the thin film. Stress within grain boundaries, together with stress developed in the grains, plays an important role in NCD and UNCD layers. Since growth can be performed in various ways (see α-parameter engineering, Section 18.3.1.1 and Figure 18.13), the stress profile can also be influenced by the growth conditions. This leads to distinctive stress engineering of the films. Layers with highly compressive stress are needed, for example, for the fabrication of buckled beams that have a bistable characteristic (see Section 18.4.2.3). Conversely, the use of tensile stressed films within a clamped structure is needed, when buckling has to be prevented. Depending on seeding and growth conditions, different types of diamond films can contain different stress profiles. For 2D-NCD and 3D-NCD films with uniform morphology, stress is typically uniform across the layer thickness [141]; textured films generally possess gradual stress, because of their increased grain size or changed shape during columnar growth [142].

Various methods to determine residual stress have been used, such as Raman spectroscopy, measurement of wafer curvature or X-ray diffractometry. For NCD and UNCD thin films used in MEMS devices, usually specific test structures are incorporated in the layout [143]. For compressive stress a ‘harp’ structure can be used, in which double anchored beams with various lengths are arranged side by side. At a critical length l_c of:

$$l_c = t\pi\sqrt{\frac{E}{3\sigma_0}} \tag{18.16}$$

such bridge structures buckle, depending on Young’s modulus E, film thickness t, and residual stress σ_0 [144].

Two examples of such an array of Euler bars are shown in Figure 18.15 for a highly stressed film of approximately 500 GPa (left), and a quite moderately stressed layer of about 230 MPa internal stress (right). It can also be seen that because of diamond’s transparency, the critical cantilever length can conveniently be determined under an optical polarising microscope.

Euler buckling, however, only occurs within compressive stressed layers. For determination of tensile strain often rotation tips (see Figure 18.16) are used (with this structure compressive stress can also be determined). In the presence of stress the indicator beam rotates, because of an asymmetric arrangement of its suspensions. The centre of rotation is located in the centre between the suspensions. According to Figure 18.16, the tip of the pointer turns anti-clockwise in case of tensile strain, i.e. when the suspending arms contract. A clockwise deflection is initiated by compressive strain caused by an expansion of the arms. The correlated tip deflection gives information on the built-in stress σ_0 in

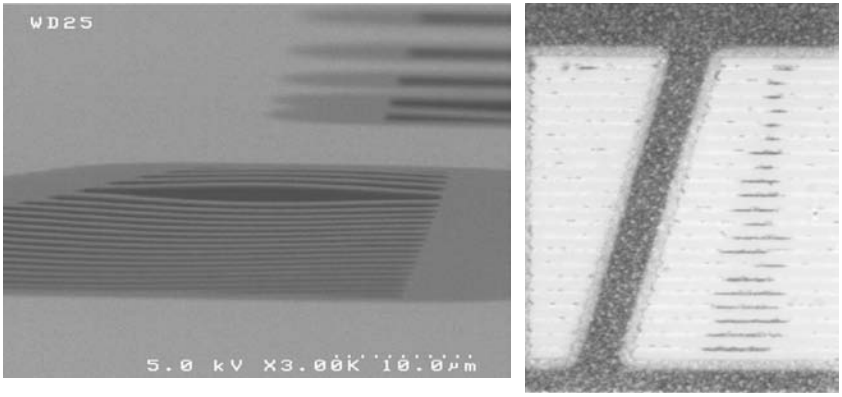

Figure 18.15 Examples for Euler bars within a 'harp' structure. The left-hand picture shows an SEM graph, where all beams are buckled either upwards or downwards; the right-hand picture shows the top view of a polarisation microscope, where buckling can be observed as a dark shade of the beams in their centre [61]. Reprinted with permission from Diamond and Related Materials, Diamond electro-mechanical micro devices - technology and performance by E. Kohn, M. Adamschik, P. Schmid, S. Ertl and A. Flöter, 10, 9–10. Copyright (2001) Elsevier

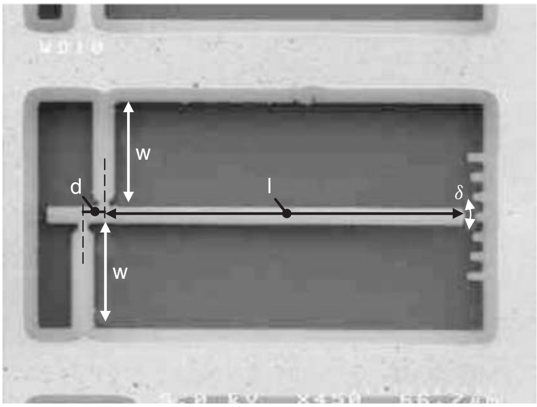

Figure 18.16 Rotation tip structure for determination of tensile or compressive stress in diamond film. In the case shown, no turning of the released rotation tip can be observed, since the film was stress balanced by growth engineering with residual stress beyond the detection limit (50 MPa). The layer thickness was approximately 250 nm

the film according to [145] by:

$$\sigma_0 = E\frac{d}{2wl + wd}\delta \tag{18.17}$$

the geometrical parameters are as labelled in the figure and the width of the pointer being small with respect to the arm lengths w.

However, rotation tips and Euler bars are only suitable indicators for uniform stress across the film thickness. In the case of a gradual vertical stress profile, only the average stress can be detected. Therefore, additional cantilever beams, which are fixed at one end only, need to be used. They bend upwards or downwards depending on a positive or negative vertical stress gradient.

Therefore, all stress profiles can be separated into a vertically constant and a gradual component, which has an average stress value of zero, i.e.:

$$\sigma(z) = \sigma_{const} + \sigma_{grad}(z) \tag{18.18}$$

where σ_{const} equals the value of σ_0 determined by Euler bars or rotation tips, and z denotes the vertical direction.

The constant part expresses then the value of stress, which causes *in-plane* deformation; i.e. expansion or contraction in the case of single-fixed cantilevers and buckling in the case of such double-fixed beams that comply with Equations (18.16) or (18.17). On the other hand, the gradual component $\sigma_{grad}(z)$ does not contribute to either of these effects, but represents the *out-of-plane* deflection of a singe-fixed beam. In case of a linear stress profile, the slope $\mathrm{d}\sigma/\mathrm{d}z$ of the gradual component can be determined from a cantilever of length l by means of its tip deflection δ according to [146] by:

$$\frac{\mathrm{d}\sigma}{\mathrm{d}z} = \frac{2E}{l^2}\delta \tag{18.19}$$

and

$$\sigma_{grad}(z) = \frac{\mathrm{d}\sigma}{\mathrm{d}z}z \tag{18.20}$$

where the origin is in the middle of the layer.

From the equations it can also be concluded that for a layer without a constant component the neutral line, which is free of stress, is located in the middle of the layer.

A higher order stress distribution can be determined by measuring the tip deflections of a cantilever that is stepwise etched. By this, the stress in the etched layers is removed and does not contribute to the tip deflection anymore. By superposition of the individual stress contributions, which correspond to the individual changes in tip deflection, the initial stress gradient can be calculated stepwise. Consequently, for a complete computation of the entire stress profile, the constant stress component has to be added [146].

By specific variation of growth conditions and the incorporation of chemical doping elements during growth, distinct stress profiles in diamond films can be generated. Moreover, patterning of these films allows local stress distributions to be established, which result in various shapes of freestanding structures. As an example an S-shaped cantilever beam is shown in Figure 18.17. The stress gradient in the layer has been changed from negative to positive at about two-thirds of the cantilever length, resulting in the curvature shown.

18.3.2.3 Fracture strength

The ultimate limit for the operation of a device is obviously its physical destruction. For a mechanical device, where internal and external loads play a significant role, destruction can be caused by rupture of one or more parts. The critical point for such a case is reflected in the fracture strength of the utilised materials. In this respect NCD and UNCD

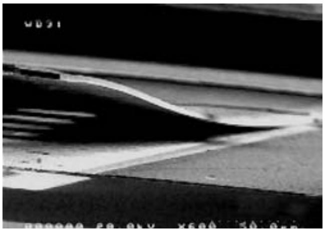

Figure 18.17 Cantilever realised in a stress-engineered diamond film. The 'S'-shape curvature of the beam was obtained by local variation of the vertical stress profile

Table 18.5 Fracture strength of MEMS materials

	Single-crystalline diamond	Highly oriented diamond	Nano-crystalline diamond	Ultranano-crystalline diamond	Poly-Si	Poly-crystalline 3C-SiC	Cu
Fracture strength (GPa)	2.8 [147]	2.7 [131]	3.9 [141]	4.1 [148]	3.4 [149]	1.2–6.5 [150, 151]	<0.5 [152]*

*Ultimate tensile strength

possess very high mechanical stability, and are only exceeded by 3C–SiC among typical MEMS materials (Table 18.4). However the spread in available data for 3C–SiC is very wide.

A method used to determine the fracture strength is to apply a force to the tip of a rod or cantilever in the direction of its length. Fracture strength σ_{fract} is reached for the case of rupture and can be expressed by Hooke's law in the absence of a plastic range as:

$$\sigma_{fract} = \frac{F_{\max}}{A} \tag{18.21}$$

where $F_{\max}$ is the maximum load and A the cross-section of the rod or cantilever, respectively.

For microstructures this method is difficult to apply, since forces are typically small and the mounting of fixtures for a load application is complicated. A general way is the three point bending technique [153]. Here, a mechanical load is applied to a bridge structure, while recording the strain–stress behaviour. However, in this case the stress–strain relationship is highly nonlinear because of an uneven stress distribution. However, since diamond is transparent with a high refractive index, interference fringes can be seen when free standing films are bent. This has been used in [128] and an optical method has been developed to identify the beam deflection under an optical microscope (see Figure 18.18) while the bridge structure is loaded with the help of a nanoindenter until the beam breaks.

18.3.2.4 Thermal conductivity

The heart of thermal sensors and actuators is the generation and dissipation of temperature gradients. The relevant materials parameters are thermal conductivity and specific heat.

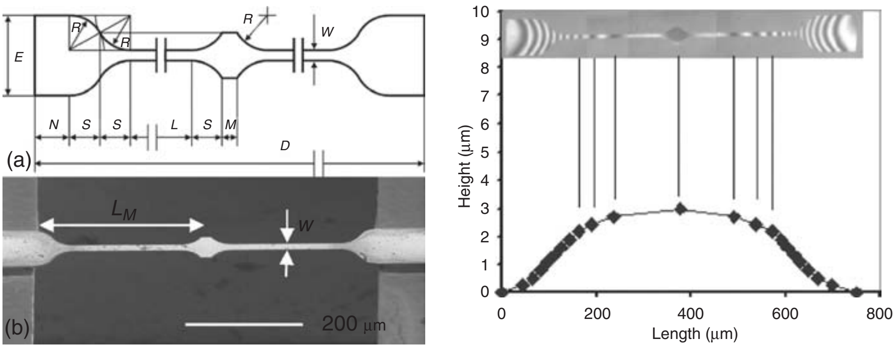

Figure 18.18 A structure for the determination of the fracture strength of freestanding UNCD films (left) with geometry as indicated. In the experiment, the deflection of the loaded bridge is identified by interference fringes within the beam, made visible under a microscope (right) [128]. Reprinted with permission from Journal of Microelectromechanical Systems, A new methodology to investigate fracture toughness of freestanding MEMS and advanced materials in thin film form by H. D. Espinosa and Bei Peng, 14, 1, 153–159, Copyright (2005) IEEE

Single crystal diamond possesses an extraordinarily high thermal conductivity, although being an insulator (if undoped), the heat is transported by phonons (and not electrons as in the case of metals). Hence, grain boundaries have a substantial influence and the thermal conductivity of polycrystalline layers depends strongly on their morphology and the grain boundary network configuration [64, 154, 155]. A decrease in grain size is typically associated with a decrease of thermal conductivity as discussed before and shown in Figure 18.11. For grains in the nm-range, the decrease in thermal conductivity is linear with grain size. Smooth surfaces and large fracture strength are not easily combined with a high thermal conductivity. However, as already mentioned, by using specific growth modes as in the case of 2D-NCD, smooth layers may still possess high thermal conductivity in the vertical direction; laterally the phonon mean free path length should be still determined by the lateral grain size. The specific growth modes also allow the design of films for high or low thermal conductivity. Low thermal conductivity may be desirable in cases where loss of thermal energy to a substrate needs to be minimised.

There is a number of techniques for determining the thermal conductivity of thin diamond films such as:

(i) The 3ω *technique*. Here, a metal line located on the test substrate serves as heater and thermistor, and is driven with an AC current of angular frequency ω. The oscillation of heating is independent of polarity and thus 2ω. The voltage, which can be measured across the thermistor, is the superposition of AC current and resistance variation and results in an angular frequency of 3ω. This voltage is therefore proportional to the temperature variation with 2ω, which is in turn dependent on the thermal conductivity of the test substrate. By measuring the voltage at different actuation frequencies f, the thermal conductivity σ_{th} can be calculated as [156–158]:

$$\sigma_{th} = \frac{V^3 \ln \frac{f_2}{f_1}}{4\pi l R^2 (V_2 - V_1)} \frac{dR}{dT} \tag{18.22}$$

with V being the rms voltage at the angular frequency ω, V_1 and V_2 the measured rms voltages at frequencies f_1 and f_2 (corresponding to 3ω), R the average resistance, and $\mathrm{d}R/\mathrm{d}T$ the resistance dependence on temperature T.

(ii) The *laser flash technique (LFT)* [127]. Here, a thermal wave is excited in the film by a laser pulse and its propagation time through a particular geometry is determined.

(iii) Thermal resistance measurements on anchored cantilevers, which are heated in the tip area, and the thermal response measured at the anchor point by a thermistor.

(iv) Deflection measurement of a bimetal actuator of appropriate geometry, where the bending moment depends on the temperature difference in respect to the surroundings [64].

18.3.3 Diamond patterning

18.3.3.1 Diamond etching

Reactive ion etching

Because of the chemical inertness of diamond, wet chemical patterning is not practically possible. Thus, plasma processes like reactive ion etching (RIE) using an oxygen-based chemistry are common. In most cases a sputtering component is created by adding argon in order to obtain smooth surfaces. Without argon, differences in the etching rates of different facets and the grain boundary network often lead to a roughened or spiked surface. Reasonable etch rates can be obtained for high power densities at moderate pressures, which imply high self-bias voltages. Volatile products are carbon dioxide and carbon monoxide.

Hard masks must be chemically stable oxide layers, such as TiO_2, Al_2O_3 and SiO_2, or nitrides such as Si_3N_4, and also oxide forming metals like Ti, Cu, or Al. Their etch selectivity in respect to diamond depends basically on the sputter component of the etch gas mixture. In general, metal oxide masks are less attacked than are silicon oxide or silicon nitride. As a consequence, less erosion of the mask edges and thus steeper sidewalls of patterned diamond films, are obtained with oxidised metal masks. In fact, for fabrication of small openings with high aspect ratios, as for example for small nozzles, metal hard masks are more appropriate. However, redeposition of sputtered material onto areas to be etched often prevents homogenous and high aspect ratio etching [159]. If materials that form carbides at the interface (like Ti and Si) are used, complete removal of the mask after diamond etching can be difficult. Therefore, in many cases, mask layers are stacks of silicon nitride or oxide and inert metals. As an example, Figure 18.19 shows a transmitted light image of a 3-micrometre thick NCD-membrane structure during processing as described in the figure caption, and in which a hole of approximately 2 μm in diameter had been etched in the centre. The hard mask employed was a stack of Si_3N_4/Ti. Further improvements for decreasing of redeposition are chlorine or fluorine based ‘etch flashes’ between diamond etching steps, which remove redeposited material [160]. Also, small additives of these gases directly into the diamond etching chemistry are useful as long as adequate selectivity is still provided.

For improved resolution and accuracy of sub-μm structures, hard masks patterned by direct e-beam writing have also been used [161]. In this technique the hard mask material (e.g. hydrogen silsesquioxane, HSQ) is deposited by spin-coating and subsequently baked

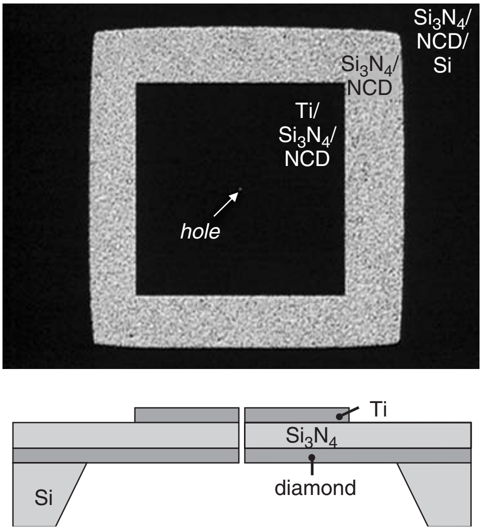

Figure 18.19 (Top) Diamond membrane (bright area) fixed in a silicon frame (outer dark area). The image was taken under transmitted light microscopy. The inner dark area represents the field where a combined mask of Ti/Si_3N_4 was used to fabricate a very small hole in its centre. (Bottom) Diagrammatic cross-section

out. Electron beam lithography can then be directly used to expose the mask areas, which initiates the loss of hydrogen and thus a subsequent cross-linking. With an appropriate developer the desired areas to be etched can then be removed. The remaining parts, i.e. the hard mask, have a consistency similar to silicon dioxide.

Etching in inductively coupled plasma

Compared with an RIE system, the plasma density in an inductive coupled plasma (ICP) system is typically two orders of magnitudes higher. In addition to capacitive coupled RF power (as in RIE), a magnetic coil surrounding the etch chamber is used to generate additional active species. Charged particles are drawn onto a spiral path by the Lorentz force down the electrical potential in the reaction chamber. This results in an avalanche effect and plasma densities in the range of more than 10^{11} ions/cm^2 are typical [162]. With this method, diamond patterning with extremely fast etch rates can be realised under low self-bias conditions [163], i.e. with moderate physical sputter influence [164]. Hard masks are less attacked and less redeposition is seen. ICP systems are generally equipped with a high gas flow rate capability, which additionally prevents redeposition due to effective dissipation of sputtered hard mask particles. Altogether, homogeneous and fast etching as well as steep sidewalls have been realised by oxygen based ICP etching as shown in Figure 18.20. Here, an NCD-film pattern of a 1.7-micrometre thick film has been etched by ICP. The hard mask was Al (converted to Al_2O_3 at its surface).

Nano patterning by focused ion beam

In focused ion beam (FIB) systems an ionised gas, the most used element being gallium, is focused to a beam with a diameter in the nanometre range by electrostatic lenses. This

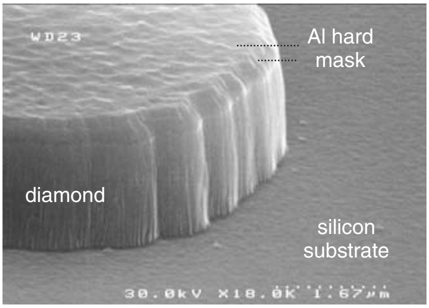

Figure 18.20 NCD layer patterned by ICP etching using an Al hard mask. The sidewalls are nearly rectangular and the silicon surface shows practically no diamond residues. The etching time in this experiment was 5 minutes

beam can be used either for surface analysis (analysing sputtered target material) or to sputter etch (mill) the surface locally (at higher ion energies).

In respect to etching, a major benefit of this technique is the direct writing of the etch pattern avoiding lithographic steps or hard masks. The technique is hardly dependent on the material to be etched and thus widely unselective, and enables high aspect ratios and very small feature sizes, making ‘direct’ 3D-micromachining possible [165]. It allows *in-situ* process monitoring when combined with a scanning electron microscope in a dual dystem. On the other hand, the method is not suited for high throughput or for the etching of large areas, and is therefore mostly used in nanostructures and proof-of-concept experiments. Figure 18.21 illustrates an inclined opening in a 2-micrometre thick NCD membrane with a diameter of approximately 550 nm at one side and 120 nm at the other side.

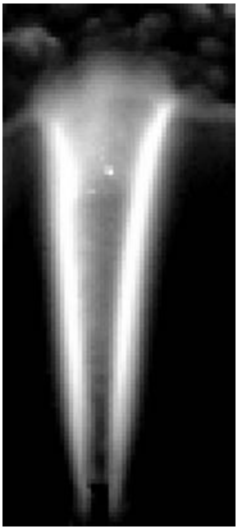

Figure 18.21 FIB etched pin-hole in a 2-µm thick NCD membrane (courtesy U. Kaiser and A. Chuvlin, Electron Microscopy Group of Materials Science, University of Ulm and Carl Zeiss AG, Germany)

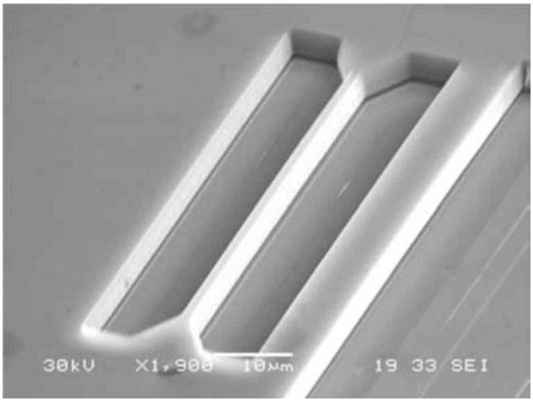

Figure 18.22 Single-crystal diamond bridge released by wet chemical etching of a buried graphitised layer. The graphitic layer was produced by ion implantation of helium ions into the diamond substrate using FIB [166]

FIB can also 'indirectly' assist 3D-patterning of monocrystalline diamond [166–168]. In this case, highly accelerated He ions are implanted into diamond films in order to damage the structure. After a subsequent annealing step a thin buried graphite layer is formed. With the help of small trenches, which are directly milled by FIB to define the shape of the structures, the graphitic parts can be removed by a wet chemical etch. Using this technique freestanding structures have been realised as seen in Figure 18.22. In the case shown, the substrate material was a single-crystal diamond substrate.

18.3.3.2 Selective growth

An alternative method for patterning diamond films is selective growth [169, 170]. As discussed in Section 18.3.1, this needs a patterned or selectively deposited seeding or nucleation layer. While diamond will nucleate and grow on carbide forming seed layers, it will not easily nucleate onto inert surfaces like copper, gold, or stable oxides or nitrides (which cannot be reduced or etched by the high H-radical density in the gas phase during the high temperature nucleation step). Such materials have therefore been used as masks for selective growth on diamond itself or on carbide forming metals. Aluminium oxide has been used in this way, and for thicknesses up to a few micrometres so have SiO_2 and Si_3N_4. Critical issues for thick layers are long deposition times and the appearance of thermal stresses after cooling. Hence, such passivation layers very often crack or peel off. However, electroplated copper was found to tolerate conformal overgrowth of rather thick contours and has been used extensively as sacrificial layer material (see below) in the realisation of all-diamond capillary systems and the all-diamond inkjet (see Sections 18.4.3.1 and 18.4.3.2). In Figure 18.23 the result of a structure fabricated in this way is shown. It displays a vertical capillary with a diameter of approximately 1 μm in a diamond membrane of 2 μm thickness. The image shows the nucleation side of the membrane after wet chemical release. The utilised copper micropost, which was used for the selective growth of the membrane surrounding the capillary, can also be seen.

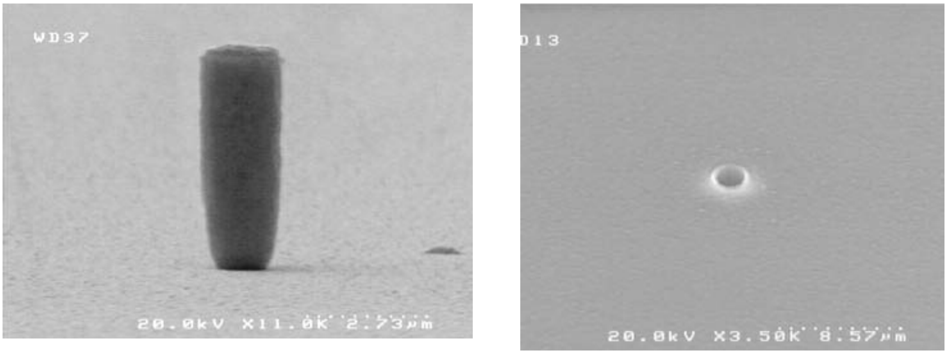

Figure 18.23 (Left) Copper micro-pillar on a 200-nm NCD film on silicon prepared for selective growth surrounding the pillar. (Right) Top view of the vertical capillary realised by etching the Cu-sacrificial pillar embedded in a 2-μm NCD film after removal of the Si substrate, membrane fabrication, and removal of the lower 200 nm NCD. The surface shown is the nucleation side of the diamond film [231]. Reprinted with permission from Diamond and Related Materials, A diamond-on-silicon patch-clamp-system by J. Kusterer, A. Alekov, A. Pasquarelli, R. Müller, W. Ebert, F. Lehmann-Horn and E. Kohn, 14, 11–12, Copyright (2005) Elsevier

18.3.3.3 Diamond micromoulding

In some microsystem applications like AFM probes, 3D-structures of a specific shape are required. To manufacture such structures moulding techniques have been used [171–174]. The process starts with a prepatterning step of the host substrate. In the case of a silicon substrate, crystallographic etching on <100>-oriented substrates (see Section 18.3.3.5) results in pyramidal openings, which can be nucleated by BEN or seeded with nanoparticles. Subsequently the etch pyramids are coated and filled with nanocrystalline diamond. After removing the silicon host, a diamond cast of the pyramid pattern is obtained. In Si, spherical moulds have been achieved by isotropic etching (as mentioned above), cubical shapes have been obtained by ASE™ (advanced silicon etching). Besides UNCD-AFM

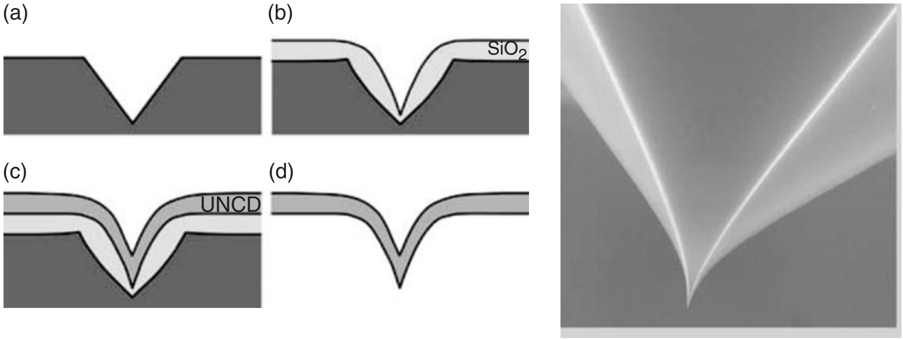

Figure 18.24 Illustration of diamond micromoulding technique. Using a two-step mould preparation by crystallographic silicon etching and subsequent surface oxidation, the deposited diamond casts appear in a pyramidal shape with a sharp peak of around 10-nm radius at the tip of an AFM probe [175, 176]. Reproduced with permission from http://www.thindiamond.com/NaDiaProbes.asp, brochure NaDiaProbeTM. Courtesy of Advanced Diamond Technologies, Inc.

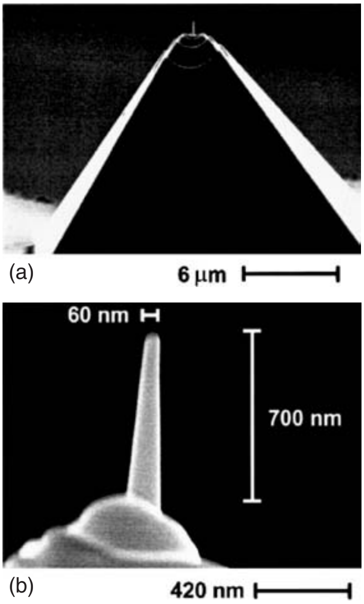

Figure 18.25 SEM images of a modified diamond probe tip. The silicon moulding cast was prepared by crystallographic etch and subsequent FIB milling. Diamond deposition into the mould and cast release resulted in a pyramid with a sharp peak of about 60 nm at the tip [177]. Reprinted with permission from Journal of Vacuum Science and Technology B: Microelectronics and Nanometer Structures, High aspect ratio all diamond tips formed by focused ion beam for conducting atomic force microscopy by A. Olbrich, 17, 4, 1570–1574, Copyright (1999) AVS The Science & Technology Society

probes for AFM-applications (see Figures 18.24 and 18.25) [175–177], capillary systems have also been realised by this technique [172].

18.3.3.4 Sacrificial layer technology

Freestanding moveable parts in MEMS mechanical actuators are commonly realised by a sacrificial layer technology [178]. Starting with a substrate, which may already include patterned areas, a sacrificial layer is deposited and locally structured. By overgrowth of this layer a connection to the substrate is provided at the prepatterned sites. After structuring of this top layer, the sacrificial layer is removed (‘sacrificed’) and the freestanding parts are released (see Figure 18.28). It is obvious that the sacrificial layer has to withstand the overgrowth cycle and needs to be removed selectively after overgrowth from a cavity. Traditionally, SiO$_2$ has been the sacrificial layer material in many MEMS technologies, being chemically highly stable and etched by HF.

Also for diamond, SiO$_2$ has been mainly employed [178]. An example of such a process used in the making of electrostatic cantilever switches is shown in Figure 18.26. However, thick layers of SiO$_2$ tend to develop stress with the overgrown diamond film and may crack or peel off. Therefore in our laboratory a sacrificial-layer technology based on electroplated copper has been developed and used in high aspect ratio structures like capillaries and the all-diamond inkjet (see Sections 18.4.3.1 and 18.4.3.2). The inkjet

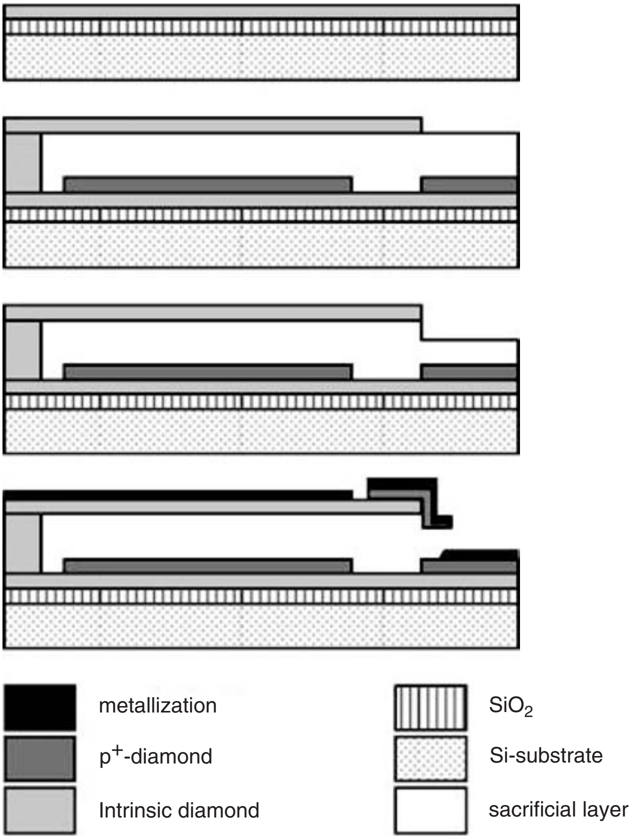
metallization
p+-diamond
Intrinsic diamond
SiO2
Si-substrate
sacrificial layer

Figure 18.26 Schematic processing sequence of diamond cantilever fabrication with the help of a SiO_2 sacrificial layer [59]

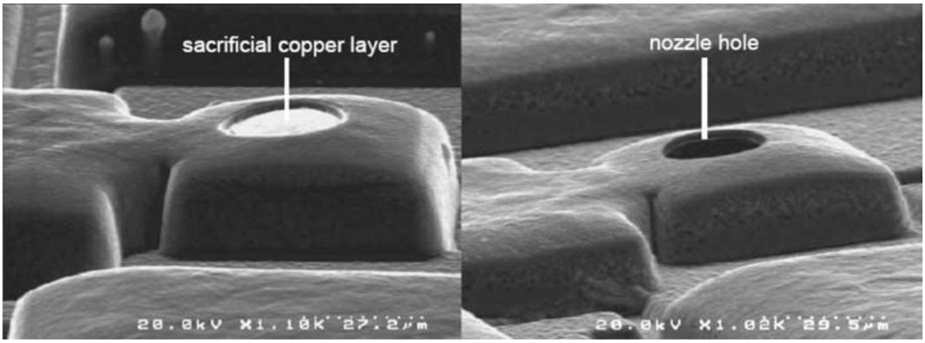
sacrificial copper layer
20.0kV X1.10k 27.2μm
nozzle hole
20.0kV X1.02k 29.5μm

Figure 18.27 Example of sacrificial layer technology using copper. An all-diamond bubble jet chamber was fabricated with a chamber height of about 20 μm (compare Section 18.4.3.2) [180]. Reprinted with permission from Diamond and Related Materials, An “all-diamond” inkjet realized in sacrifical layer technology by R. Müller, R. Gronmaier, K. Janischowsky, J. Kusterer and E. Kohn, 14, 3–7, Copyright (2005) Elsevier

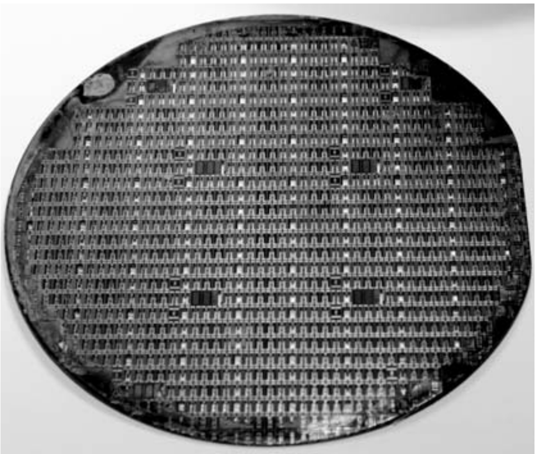

Figure 18.28 MEMS actuators released by bulk machining with the help of ASE^{TM}. The two inch wafer includes approximately 1000 devices [219]. Reprinted from Nanodiamond Microbridges for RF-Applications, presented at the 2nd International Diamond Conference in Rome 2007, with permission from Diamond At Work Ltd

sacrificial technology is illustrated in Figure 18.27. On the left-hand side of the figure, the overgrown inkjet chamber is still filled with Cu. On the right-hand side the Cu filling has already been etched out with nitric acid.

In both cases, direct nucleation is not possible and either seeding with nanopowder [179] or the insertion of a thin interfacial nucleation layer is needed. In both illustrated examples BEN has been used in conjunction with a special, thin, interfacial nucleation layer.

18.3.3.5 Structure release by bulk machining

Often membranes and freestanding structures are realised on a bulk substrate, which is Si in most cases. Here, the freestanding structure can either be realised by undercut etching from the front side or substrate etching from the rear.

Frontside release

Because of the high chemical stability of diamond, all silicon patterning methods are selective to diamond and are therefore possible. Hence, silicon can be chemically wet etched using isotropic silicon etch (ISE; mixture of HF, HNO_3, and CHOOH), or by plasma etching in fluorine or chlorine based gas mixtures. Nevertheless, some considerations have to be taken into account concerning these techniques. First of all, diamond MEMS also include components made of other materials such as metal feeding wires, bimetals, dielectrics, or piezoelectrics. It is necessary that these materials also withstand the etching process or need to be passivated. In this respect, wet chemical etching processes mostly fail, since only very few materials configurations are immune. Chlorine-based plasmas also strongly affect most of the commonly used metals and dielectrics. In contrast, fluorine-based isotropic plasma etching is mostly possible and therefore commonly used.

Another critical point is the resulting shape of isotropic etching process. The etchant starts to act only upon all exposed areas in the beginning of etching. In the course of this process an undercut spreads laterally. This means, firstly, that suspended areas must be significantly larger than the structures to be released in order to avoid release at the anchor point. Secondly, the actual position of the beam fixture moves during undercut etching. This needs to have been taken into account at the mask design level.

Rearside release

Free-standing components are often also released from the rear of the substrate. In this way the complete bulk material beneath the micromechanical component needs to be removed. Thus, highly selective etching processes with high etch rate are needed. In the case of Si, the substrate thickness is mostly above 0.5 mm. Both wet chemical etching and dry etching techniques may be used.

On [100]-oriented Si-substrates, wet etching in solutions of KOH (caustic potash) or TMAH (tetramethylammonium hydroxide) will result in [111]-oriented edge pyramid shaped facets. To obtain high etch rates, hot KOH needs to be used and adequate hard masks are needed at the rear, typically based on Si_3N_4.

Dry etching can result in perpendicular walls and is therefore a preferred technique. However, the profile can be adjusted by the plasma parameters, especially pressure. The shape can be isotropic, when using fluorine- or chlorine-based plasma etches, or anisotropic by ASE^{TM}. Steep sidewalls, however, permit smaller structures and therefore higher device densities. Figure 18.28 shows both sides of a wafer including bridge actuators, which were released by ASE^{TM}.

18.3.4 Integration concepts

For operation in given environments and for signal processing, transducers may need to be directly integrated into circuitries including active and passive components. Two basic ways of integration are possible, namely *monolithic* and *hybrid* integration.

18.3.4.1 Monolithic integration

Typically, monolithic integration means transducer and electronic circuit integration on a common semiconductor substrate, which may be Si or GaAs, GaN or SiC, in one process flow. Components include microcontrollers, memories, oscillators, mixers, matching networks, phase-locked loops, analogue interfaces, realised in ‘mixed technology’. Monolithic integration allows high integration density, parasitic impedances can be kept small, and losses can be minimised. For realisation, practically all technological patterning and deposition methods as described above could be utilised. However, to date the heart of any monolithic system is CMOS signal conditioning and signal processing circuitry. Thus, diamond deposition would need to be compatible with CMOS processing, with a temperature limit of about 350 °C, whereas most nanocrystalline films are deposited within a temperature range of 700–900 °C in an environment of high H-radical density. Only UNCD has been deposited at a temperature of 400 °C with a reasonable growth rate but with a high content of graphitic grain boundaries [181], and it has therefore been only used for mechanical MEMS structures like resonators. However, it is an important first step in bringing diamond MEMS device applications into the Si-based mainstream MEMS field.

18.3.4.2 Hybrid integration

Traditionally, when sensor systems are scaled down from the macroscopic field, the first step is hybrid integration into the signal-conditioning environment. Therefore, many technologies for hybrid integration, such as surface mount technologies (SMTs) have been developed. Another driving force for the development of efficient hybrid mount technologies has been opto-electronic and fibre-optic systems with individually optimised components.

The deposition of diamond films is not yet compatible with CMOS technologies, but since diamond is considered to be the preferred material for applications in extreme and harsh environments, concepts for hybrid integration of diamond based MEMS will be the first step in their systems integration.

A key technological building block in this respect is the attachment of the component onto a base substrate. For diamond in applications at high temperatures or aggressive surroundings this means high temperature and chemically stable attachments. Glueing is therefore not an option in most cases and a high temperature stable soldering process is needed. In a first attempt in our laboratory, a solid-liquid interdiffusion soldering process (SLID) has been used, originally developed for the stacking of thinned Si chips [18]. Here two surfaces are joined by Cu/Sn layers, which are firstly alloyed into a low temperature eutectic at about 400 °C, and then transformed into a high temperature stable eutectic during the process by diffusion, forming a joint stability of approximately 600 °C.

Figure 18.29 illustrates this technique with the creation of a diamond detector chip, which was alloyed onto a silicon substrate including electrical through connections [182, 183]. Due to the high stability of the final joint, many layers can be stacked. In this case this was a diamond-on-Si detector chip on a Si-CMOS base plate. Further details can be found in the literature [18,184–186]. Because of the low thermal budget during the SLID process, many base plate materials are possible, as for example Si, SiGe, GaN, SiC, RF ceramics, or LTCCs (low temperature co-fired ceramics).

Another example for the application of this technique is shown in Figure 18.30 in conjunction with a microelectromechanical diamond actuator switch. Here a diamond bridge actuator, which has been realised in a silicon frame, has been soldered onto a

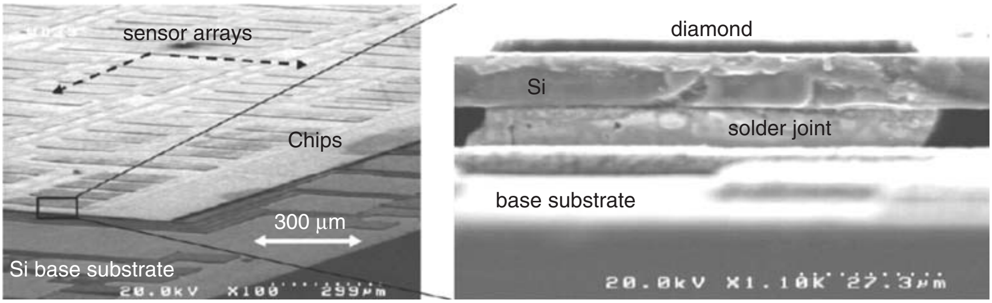

Figure 18.29 Hybrid integrated DUV diamond detector system consisting of a diamond-on-silicon sensor chip soldered onto a silicon CMOS base substrate. The soldering process was the Cu/Sn based SLID process [182]. Reprinted from Diamond and Related Materials, Concept for 3-D integrated UV sensor by A. Kaiser, D. Kueck, P. Benkart, A. Munding, G. M. Prinz, A. Heittmann, H. Huebner, R. Sauer and E. Kohn, 15, 11–12, Copyright (2006) Elsevier

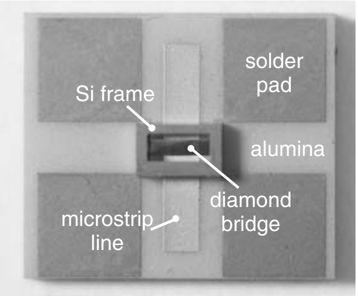

Figure 18.30 Diamond bridge actuator within silicon frame, which has been integrated into a microstrip test line by means of the SLID process. Four solder pads on both the diamond device and the alumina substrate are connected and are used for power supply to the actuator

Au-microstrip transmission line on a microwave alumina substrate. Details of this device structure are discussed in Section 18.4.2.3 below.

18.4 SENSOR AND ACTUATOR APPLICATIONS

In the following sections examples of MEMS components are discussed, based on the sensing and actuation principles discussed in Section 18.2 and the basic fabrication processes described in Section 18.3. Most of the structures have been realised in the laboratory of the authors and have therefore been based on similar design and realisation concepts. However this does not mean that the routes described are the only possible ones. Alternative building blocks as well as different technologies based on alternative processing tools can certainly also be envisaged. The list is certainly not complete, but will give an indication of how the strengths and weaknesses of diamond compare with competing materials.

This section focuses on diamond as a material of high chemical stability, fracture strength and high stiffness. However, during the discussion it should be remembered that diamond is only one of several superhard materials.

Another material of high chemical and mechanical strength is SiC. Indeed with this material many MEMS device structures have also been developed, mainly for applications at elevated temperature up to 600 °C [187]. For these applications SiC is often used in its cubic phase, whereas active electron devices, like field-effect transistors, are exclusively realised on hexagonal phases, which offer an essentially lower defect density. The growth of cubic-phase layers on Si substrates can be single crystalline, but the surface is rather rough and textured [188]. Freestanding SiC structures are therefore frequently realised after surface polishing. Nevertheless, despite these problems the technology has been developed to a state where first foundry services are being offered [189].

GaN offers two advantages compared with diamond and SiC. Firstly it is a highly polar material when used in its hexagonal phase, which is nearly exclusively the case. Secondly it allows the growth of heterostructures ranging from AlN to InN via AlGaN, AlInN and InGaN. It is, therefore, the first complex piezoelectric semiconductor materials system. It has been well developed for optoelectronic and electronic applications and many materials problems have been solved in the past. Applications in mechanical MEMS with built-in piezoelectric properties have, however, not yet passed the proof-of-concept phase.

A rather general comparison of the three wide band gap materials systems, diamond, SiC and GaN in respect to applications in harsh environment can be found in Ref. [17].

18.4.1 Mechanical sensors

Diamond sensor structures for the measurement of mechanical effects, namely pressure and acceleration, have been designed around piezoresistive and piezoelectric transducer elements. In the case of piezoresistors, these were realised by boron doped mesa structures. As well as nanocrystalline diamond, highly oriented diamond films have been used as a materials base to minimise the influence of grain boundaries (see Figure 18.7). With such micrometer-sized piezoresistors a gauge factor K of 20 has been obtained. The main reason for this small gauge factor is the fact that relatively high boron-doping levels are needed in order to obtain a reasonable activation and a corresponding low sheet resistance. In the case of high sheet resistances, the effect of thermal activation by self heating may be stronger than the piezoresistive response.

The readout of the piezoresponse is normally obtained with a Wheatstone bridge circuit. The largest differential signal can be expected if one piezoresistor in one branch is located on a compressive part of the structure and the other one is located on a tensile part. This usually determines the layout, especially on membranes. An orientation dependence of their individual resistor is not expected if the orientation of the individual crystallites is random, as is usually the case for nanocrystalline films.

In the case of a piezoelectric element, these are typically cantilever unimorphs as discussed in Section 18.2.4.4.

18.4.1.1 Pressure sensors

Most pressure sensors are based on hermetically sealed membrane structures that detect a pressure difference by bowing. In the case of diamond, the membrane is mostly realised with a diamond-on-silicon substrate, where the Si substrate is etched by a bulk machining process, serving as frame for the mask [190–193]. Detection mechanisms can be capacitive, by optical beam deflection or using piezoresistors. The first method requires the integration of an RF circuit, the second the hybrid integration of a micro-optic system and the third a readout bridge on the membrane. Piezoresistors have commonly been used in diamond. In the example discussed below, they were deposited on top of the membrane surface and positioned to make use of the longitudinal piezo-effect. For an increase of differential pressure the membrane may buckle downwards and the resistors in the centre are compressed, while the outer ones are stretched. For signal readout they were implemented within a Wheatstone bridge configuration (see Figure 18.33; left).

The major benefit of diamond in this application is the high membrane stability without creep or fatigue. It can be used for detection of very high pressures in combination with high durability and reliability. The disadvantage for many applications, stemming from the high stiffness, is its low sensitivity to small pressure differences. A fabricated device and its sensor characteristics are illustrated in Figure 18.31 [190]. From the diagram a linear relationship between the output voltage of the Wheatstone bridge and the variation of ambient pressure can be observed. This linear characteristic is in agreement with the expected behaviour of longitudinal diamond piezoresistors used in this case.

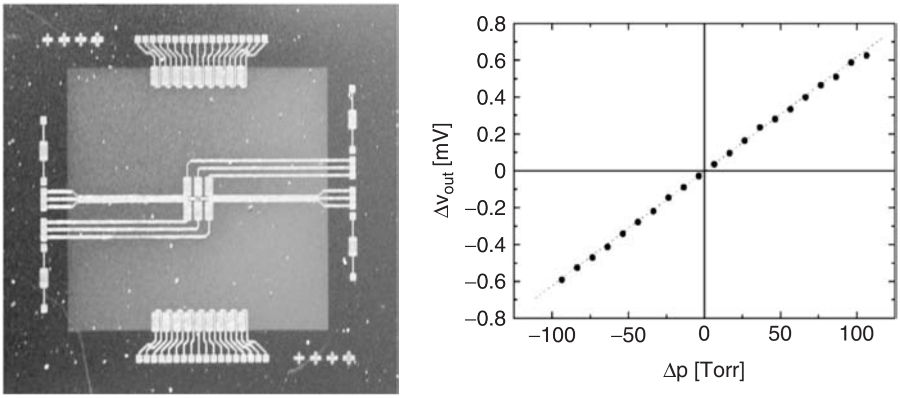

Figure 18.31 Image of a diamond membrane pressure sensor (left). Piezoresistors in the centre and at the outside border of a square diamond membrane are used to detect the membrane deformation. The diagram shows the output signal of the Wheatstone bridge as function of pressure variation with atmosphere as a quiescent condition [66]. Reprinted with permission from Diamond and Related Materials, Analysis of piezoresistive properties of CVD-diamond films on silicon by R. Adamschik, R. Muller, P. Gluche, A. Floter, W. Limmer, R. Sauer and E. Kohn, 10, 9–10. Copyright (2001) Elsevier

Another approach used to detect local pressures has been the piezoelectric cantilever actuator. In this case the pressure may be transmitted mechanically to the tip of a cantilever by micro gears or it may the pressure of a gas flow. Such a gas flow pressure sensor has been realised on the base of an AlN/NCD unimorph, where AlN represents the active piezoelectric layer [194]. By measuring the dynamic impedance and phase shift of the electrical signal of the piezoelectric layer, operated in the d_{31}-mode (compare Section 18.2.4.4), a shift in resonance frequency, owing to the influence of the drag force, was used for detection. A linear decrease of resonance frequency with pressure has been observed with a sensitivity of 0.155 Hz/mbar. Figure 18.32 shows this behaviour in a nitrogen atmosphere in a window of flow-induced pressure from 1.5 to 7 bar.

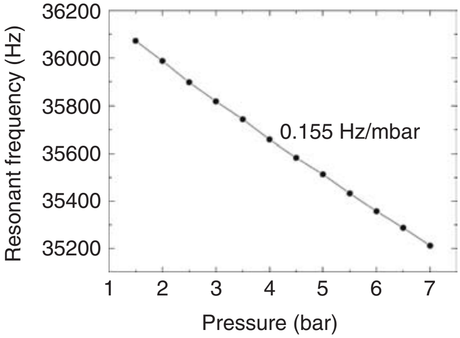

Figure 18.32 Variation of first order resonance frequency of an AlN/NCD piezo-actuator in ambient nitrogen atmosphere and superimposed gas flow pressure. The structure for this experiment was 320 μm long, 70 μm wide with an NCD thickness of 0.6–0.7 μm, an AlN thickness of 1 μm, and electrode thicknesses of 0.1 μm [194]

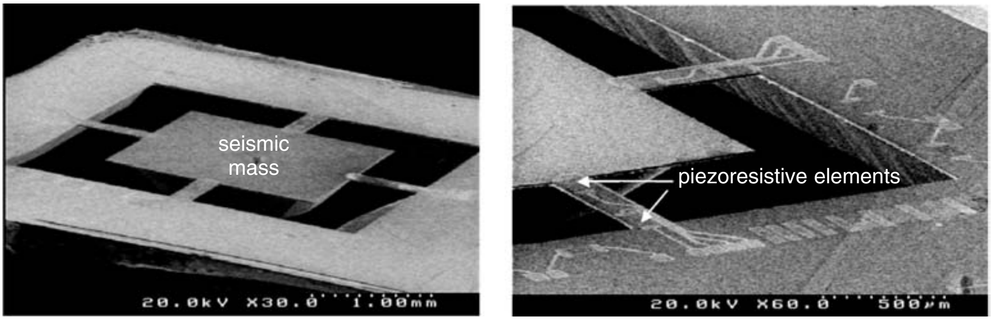

Figure 18.33 Diamond acceleration sensor including a seismic mass and piezoresistive sensor elements. The silicon was etched by wet etching [9]. Reprinted with permission from Diamond and Related Materials, Diamond MEMS- a new emerging technology by E. Kohn, P. Gluche and M. Adamschik, 8, 2–5, Copyright (1999) Elsevier

18.4.1.2 Acceleration sensors

Because of their high fracture strength and stiffness, diamond films can withstand high acceleration and shock. Such a sensor structure has indeed been realised based on the movement of a centre seismic mass suspended on four arms, representing the bridges to the surrounding frame. The transducer elements were piezoresistors located on the four suspended bridges and arranged as a Wheatstone bridge as can be seen from Figure 18.33. The suspended bridge sensor structure was realised by bulk machining. Firstly, a membrane was produced with a process analogous to that used for the realization of the pressure sensor structure by wet chemical etching of Si. Next, the bridges were made by dry etching of the diamond film in an oxygen plasma [190]. The thickness of the diamond bridges was 15 µm. The sensor was mounted into a hybrid assembly and integrated with an instrumentation amplifier for signal readout. Figure 18.34 shows the response to a shock experiment, where the sensor was dropped on the floor. Simulation, based on the

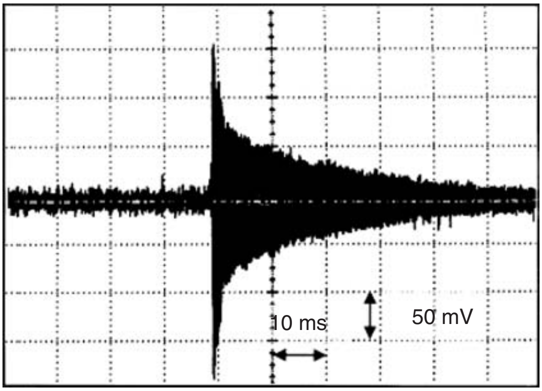

Figure 18.34 Shock response of the diamond acceleration sensor shown in Figure 18.33 [9]. Reprinted with permission from Diamond and Related Materials, Diamond MEMS- a new emerging technology by E. Kohn, P. Gluche and M. Adamschik, 8, 2–5, Copyright (1999) Elsevier

materials parameters obtained from test structures also located on the wafer, indicated a theoretical limit for fracture at an acceleration of 7000 $\boldsymbol{g}$.

As mentioned before, the important parameters for the use of diamond as a mechanical force, pressure or acceleration sensor are its high linearity with the absence of any plastic range, its high thermal stability in not turning soft at high temperatures, its high fracture strength, and its high stiffness. It is therefore a prime candidate for applications in extreme environments as encountered in crash accidents, in the control of explosive events or in other harsh environments, where Si may fail. The sensing under such conditions is still exceptional and devices used here are mostly discrete and circuits implemented in a hybrid configuration. This means also that mechanical diamond MEMS cannot compete with their Si-counterparts, where integration of signal conditioning and signal processing is a major part and the chip is a smart sensor system. In the comparison of the two materials it needs to be mentioned that Si can be processed in its single crystal phase, where the grain structure will not limit miniaturisation into the sub-μm and nm-ranges.

18.4.1.3 AFM cantilever probe tips

In atomic force microscopy (AFM), commonly silicon, silicon nitride, or diamond-coated silicon cantilevers are used for mapping surfaces. Three modes are typically used, namely contact, tapping, and force modulation. Probes made entirely of diamond have also been developed and are already commercially available (NaDiaProbe$^{\text{TM}}$) [176, 195–197]. These diamond tips have several advantages compared with other standard tips:

- mechanical stability and high hardness enable long lifetimes even in contact mode.
- tip radii of 7 nm allow high resolution;
- high Young's moduli imply high resonance frequencies for tapping mode;
- chemical inertness permits the use in aggressive and biological environments;
- doping with boron permits use in potential mode.

The diamond tips are mainly realised by micromoulding as described in Section 18.3.3.3. Here, in general, [100]-oriented surfaces are etched by wet etching and a pyramid relief structure with [111]-oriented sidewalls obtained. An array of such diamond AFM cantilever probes is shown in Figure 18.35. A plot of resolved feature size of a silicon nitride and an UNCD probe during 100 scans is also shown in the figure. It demonstrates the robustness and hence reliability of diamond tips for this application.

18.4.2 RF applications

RF microsystems have become an essential part of many RF and microwave systems due to their low intrinsic losses and parasitics. They can substitute active elements like transistor switches, and represent lumped as well as distributed passive elements like inductors or filters. In most cases the structures are suspended or else use air or vacuum gaps with intrinsically low leakage and low permittivity. The basic material for these

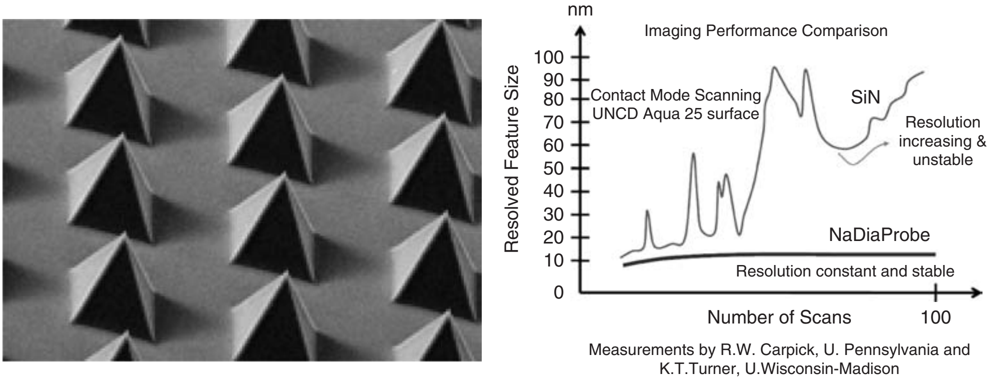

Figure 18.35 Array of UNCD AFM probes (left). Reproduced with permission from http://www.thindiamond.com/NaDiaProbes.asp, brochure NaDiaProbeTM. Courtesy of Advanced Diamond Technologies, Inc. In the diagram on the right the reliability of such tips is demonstrated by comparison with a silicon nitride probe [176]. Reproduced with the kind permission of Professor Robert Carpick

RF microsystems is largely Si, relying on technologies very similar to those used in, for example, automotive MEMS applications. On the other hand, at high frequencies, high temperatures and high power, other semiconductors have started to replace Si, which is rapidly reaching its ideal material and structural limits. The competing materials, as mentioned before, are SiC and GaN. A comparison of active electronic device structures of the three wide-band-gap materials with emphasis on diamond is given in Chapter 14 by Kohn and Denisenko in this book. Most of the device structures discussed there are still discrete. Nevertheless, in many cases they need to be switched on and off, tuned and matched, which is often achieved by hybrid integration with discrete components on a carrier. Thus, in these cases it is indeed attractive to add MEMS components, especially electromechanical switches, using hybrid technologies. Within this context the prospects of diamond based MEMS device structures for RF applications have been discussed by a number of authors in recent years [198–201].

In the following section, examples of diamond discrete RF-MEMS structures, such as resonators, switches and switchable inductors, which have been realised in various technologies will be discussed. This will be complemented with a short discussion on diamond as a low loss microwave substrate (and elements of vacuum microelectronics based on diamond).

18.4.2.1 Mechanical resonators

The most important materials parameters for mechanical resonators are stiffness (Young's modulus) and mass density, as discussed in Section 18.2.4. For diamond, both lead to high resonance frequencies and to a high sensitivity to changes in mass, for example when used as a cantilever to detect adsorbed species. The development of diamond resonators has therefore been oriented towards electronic applications at GHz frequencies on one hand and on the other hand towards the use as a mass sensor in chemistry and biology [202]. The actuation principle has been by electrostatic and piezoelectric actuation [203].

The material dependence of the resonance frequency is given by Equation (18.6) (Section 18.2.4.1), which allows either a direct comparison between different materials of identical geometry or, equally, can be used to describe the influence of geometry on an identical performance material. Diamond seems to be the most appropriate material for high frequency applications. The influence of the material parameters in scaling is however only by the square root. Therefore, differences are rather moderate and may be overruled by the resolution limits of the respective processing technologies.

Another important aspect is the quality factor Q, which reflects the losses at resonance; a high Q-factor representing low losses. Q will depend on mechanical losses like internal friction, which may be mainly associated with grain boundaries, or external friction such as air damping. However, at the small geometries needed for high speed applications, inhomogeneities such as surface roughness may become important [204]. At sub-μm geometries, the boundary conditions, mostly determined by the geometrical layout, need also to allow the resonance to develop with maximum efficiency. Mechanical matching becomes important [205]. Therefore microwave resonators have been built with nano- or ultrananocrystalline diamond [206], but may have to compete with single-crystal Si technologies.

A test structure for diamond resonator performance can be seen in Figure 18.36 [206]. NCD bridge structures with a length ranging from 1 to 8 μm (often also called clamped–clamped or double ended beams), are fixed within a diamond frame similar to an Euler bar test structure, (see Section 18.3.2.2). However, in contrast to an Euler bar, as a resonator the bridge needs to be stress free (or stress balanced), since built-in stress will lower the resonance frequency. It can be seen from the diagram, that with decreasing beam length the resonance frequency increases to 640 MHz for a length of 2 μm. The film thickness was 180 nm. The square root relationship between length and resonance frequency is well preserved. The first order resonance of double-clamped cantilevers is approximately six times higher than in the case of a single-ended cantilever as discussed in Sections 18.2.4.1 and 18.2.4.4. It should be noted that the beams have been covered by a metallisation layer, used for electrostatic actuation with the help of a counter electrode

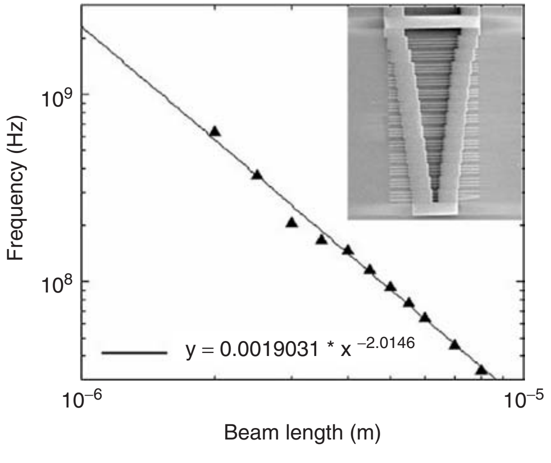

Figure 18.36 Frequency measurements of various long NCD resonator structures [206]. Reprinted with permission from Applied Physics Letters, Nanomechanical resonant structures in nanocrystalline diamond by L. Sekaric, 81, 23, 4455–4457, Copyright (2002) American Institute of Physics

on the substrate. Certainly the resonance frequencies have been lowered by its influence (compare also with Figure 18.8). The mechanical quality factors have thereby been evaluated to be in the range 2500–3000. Using UNCD, quality factors up to 116000 have been reported [203].

For frequencies in the GHz range (e.g. for wireless RF applications) either further down-scaling into the sub-μm range is needed, or operation at higher modes, which can be well developed in disk resonators. Such an approach is that of the radial contour mode disk resonator, which has been realised in NCD [205]. The first order resonance is characterised by the radial contour becoming elliptic (compare Ref. [207]). Acoustic anchor losses across the fixture of the NCD disk have been suppressed by using a fixture of a different material (polysilicon) [205]. Vibrating disk and suspension are therefore acoustically mismatched and only very little energy is lost through transfer. With such a resonator, a resonance frequency of 1.51 GHz has been demonstrated with a quality factor of 11 555. At a lower resonance frequency of 498 MHz a *Q* value of 55 300 (in vacuum) has been obtained. Besides the quality of the films, of equal importance is the dynamic isolation to the support by a mechanical mismatch at resonator frequency as mentioned.

Recently, the first diamond resonator arrays have been developed for broadband applications [161]. Paddle and ring resonators have been made within a weakly coupled array. In these applications flexible square and ring shape structures are fixed on silicon dioxide pillars and are interconnected by thin diamond springs. In Figure 18.37 an SEM micrograph of ring resonators (Figure 18.37 top) and their resonances in different modes of vibration (Figure 18.37 bottom) are illustrated. Three resonant modes can be seen, ranging from 35.6 to 38.0 MHz with a separation of 1.2 MHz, i.e. a discretisation of approximately 3 %. The diamond layer thickness was in the range of 100 nm and the ring diameters were 20 μm.

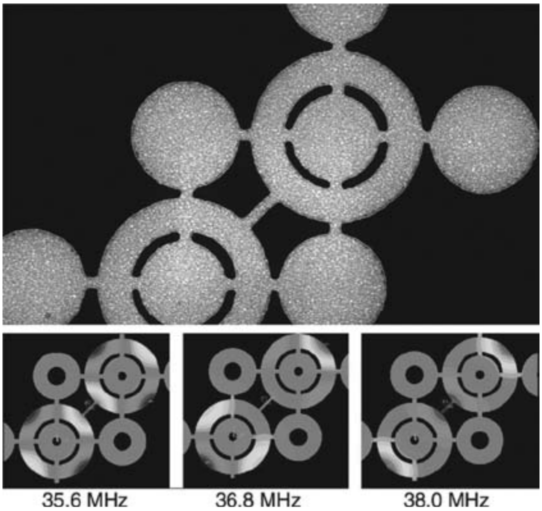

Figure 18.37 SEM micrograph of a ring resonator array and FEA images of three different resonance modes [161]. Reprinted from Diamond and Related Materials, Nanocrystalline diamond resonator array for RF signal processing by J. W. Baldwin, M. K. Zalalutdinov, T. Feygelson, B. B. Pate, J. E. Butler and B. H. Houston, 15, 11–12, Copyright (2006) Elsevier. See plate 12

18.4.2.2 Electrostatic switches

Many RF MEMS switches are usually based on electrostatic actuators and this type of actuator has also been used for diamond switches since the early development work [208–212]. Figure 18.26 shows a basic layout of a single anchored cantilever switch. The circuit is closed when the tip contact pad touches the base-plate contact pad and the current flows through the cantilever to the base plate. Thus, the cantilever top surface needs to be metallised. The top and bottom electrode need to be electrically isolated by an insulator, in this case an undoped diamond cantilever.

Such basic, electrostatically actuated, single ended cantilever switch structures have been used to evaluate the capability of diamond switches. For diamond devices, tests of operation under extreme conditions are important.

- Cantilever switches have been operated by electrostatic actuation at temperatures of 650 °C in vacuum [209]. During the experiment no change in switching voltage has been observed, indicating no change in Young's Modulus (see Figure 18.38). The top metallisation is Au with limited thermal stability. Therefore switching at higher temperatures up to 850 °C was performed by mechanical actuation with a needle. No mechanical fatigue or sticking was observed.
- To assess the thermal stability of the contact at the cantilever tip, an overdrive experiment was performed on a low-impedance DC load. As can be seen from Figure 18.39, the contact was burned off as expected and a hole marks the position of the tip contact. The Au overlayer melted around the burned hole. Nevertheless, the contact could still be switched, as shown in the inset of Figure 18.39. Thus, despite the high temperature developed by the ohmic switching loss, no contact alloying and no oxide isolation were induced.

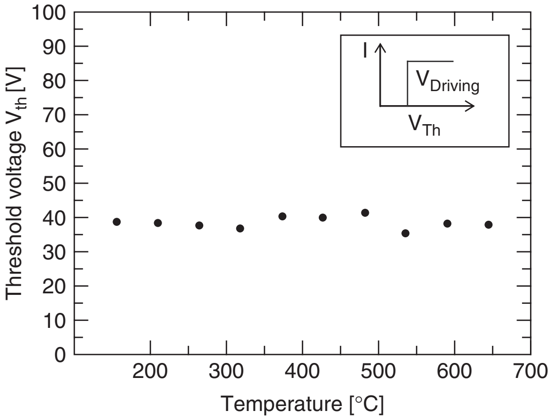

Figure 18.38 Measured temperature dependence of the threshold voltage of a cantilever switch, indicating no change in Young's modulus at least up to 650 °C (redrawn after [61]). Reprinted with permission from Diamond and Related Materials, Diamond electro-mechanical micro devices - technology and performance by E. Kohn, M. Adamschik, P. Schmid, S. Ertl and A. Flöter, 10, 9–10. Copyright (2001) Elsevier

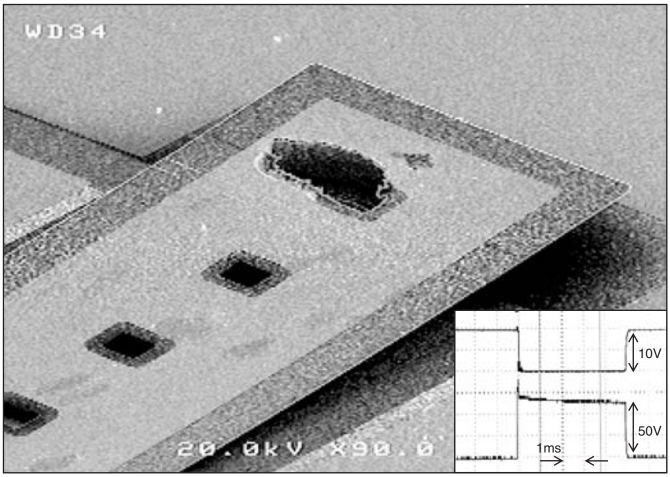

Figure 18.39 SEM of a cantilever switch after electrical overdrive. The inset shows the switching characteristic after the experiment, confirming that it was still operational

These experiments illustrate that diamond is suitable for high power switches that can be operated rapidly (indicated by a high resonance frequency) and at high temperatures. Diamond can be used in these structures as a quasi-metallic contact material, as an insulator and as the conductive plate of the electrostatic actuator. Furthermore, it does not require any passivation layer, except when operated under an oxygen atmosphere at high temperature. This suggests that diamond could replace other, more complicated, layer stacks as used in other technologies.

Figure 18.40 shows two examples of single anchored cantilever switches in coplanar waveguide configuration for the on and off switching of microwave signals. In this RF application, an interrupted waveguide centre line is bridged by the switch, which therefore needs to contain two contacts electrically in series. The devices were fabricated using a sacrificial layer technology and have been monolithically integrated into a diamond-on-Si substrate pattern. The integration into the waveguide was performed in two different ways.

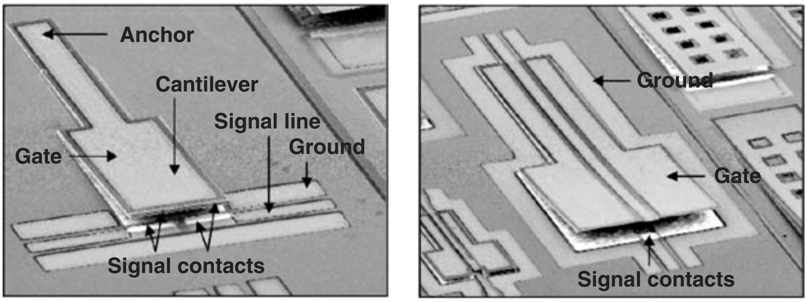

Figure 18.40 Different monolithic integrated electrostatic actuator concepts and layouts within a coplanar RF waveguide. The left cantilever actuator closes a gap in a signal line from the side; on the right, the signal line is part of the beam itself [208]. Reprinted from Diamond and Related Materials, Diamond microwave micro relay by M. Adamschik, J. Kusterer, P. Schmid, K. B. Schad, D. Grobe, A. Flöter and E. Kohn, 11, 3–6. Copyright (2002) Elsevier

In a first design the switch was located perpendicularly to the waveguide. In this lateral configuration the electrostatic actuator capacitor can be located outside the waveguide structure as seen from Figure 18.40 (left). To obtain high switching forces and speeds the capacitor needs to have a relatively large surface area. This however results in slow switching due to air damping [16, 64]. Therefore the actuator capacitor plate usually incorporates a number of holes, as illustrated in the right hand side of Figure 18.40.

In a second approach, the entire cantilever is part of the coplanar waveguide pattern. Here, the ground plane of the RF line also served as one electrode of the parallel-plate actuator as shown in Figure 18.40 (right). With this in-line structure, only one contact pad is needed, resulting in principle in a lower insertion loss of the contact. The connection of the cantilever ground plane to the common ground of the circuit and any changes in wave guide geometry, such as the holes to reduce air damping, need to be considered carefully in the layout because at microwave frequencies changes in waveguide geometry are generally associated with changes in impedance.

The RF performance of an RF in-line switch in a configuration as shown in Figure 18.40 (right) is shown in Figure 18.41. This shows the attenuation in the on-state and off-state, which are the insertion losses and isolation respectively, calculated from S-parameter measurements.

The insertion loss of 0.4 dB at low frequency represents an ohmic contact resistance of about 5 Ω within the 50-Ω-line. At higher frequencies, the contact is additionally capacitively coupled, but the loss increases because current flow is increasingly confined to the surface by the skin effect. In the off-condition, the isolation at low frequency is higher than −65 dB, which corresponds to a resistance in the gigaohm range, reflecting the air gap isolation. At higher frequencies the gap becomes capacitively coupled and resonances appear periodically. At 10 GHz the isolation is still approximately 35 dB. The lowest DC contact resistances in such diamond-based cantilever switches was 200 mΩ, where the metallisation of the beam had reached the contact tip by side evaporation [210].

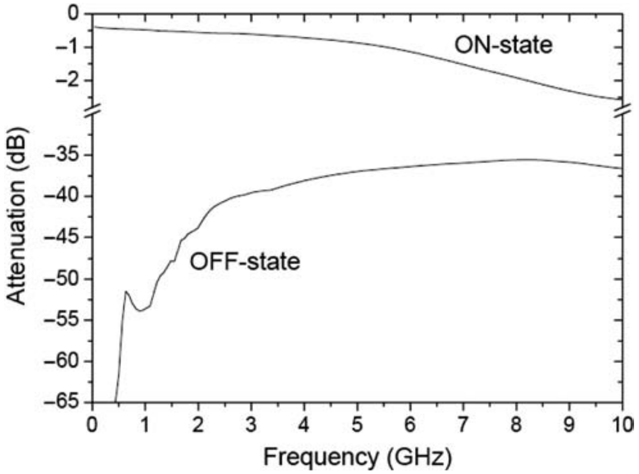

Figure 18.41 RF performance of the diamond microwave switch as shown in Figure 18.40 (right) [211]. Reprinted with permission from Microwave Symposium Digest, 2003 IEEE MTT-S International, Evaluation of CVD Diamond for heavy duty microwave switches by E. Kohn et al., Volume 3, 8–13 June 2003, pages 1625–1628, Copyright (2003) IEEE

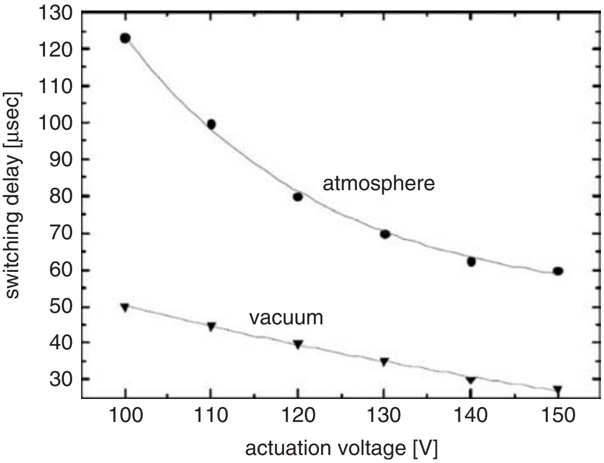

Figure 18.42 Transient behaviour of diamond microswitches (experimental points). Owing to air damping, switching speed in vacuum is a factor of about 2 higher [213]

As already indicated, the switching speed is determined by the intrinsic materials parameters as well as by air damping. The influence of air damping on the single-ended cantilever switch from Figure 18.17 is shown in Figure 18.42 by its transient switching behaviour. The cantilever analysed had a length of 1200 µm and was based on an anchor height (and thus cantilever separation at the anchor point) of 2 µm. At the tip end, the separation was about 50 µm. Thus, the beam was bent by built-in stress. For closing, various driving voltages above the threshold voltage of about 100 V were applied, a higher driving voltage resulting in a higher switching force. As can be seen, in vacuum the switching time can be as low as 30 µs. However, in air the speed is reduced by a factor of more than two by air damping, if no openings are included in the cantilever structure.

The investigation into the resonance performance of such cantilevers with piezoelectric actuation indicated that switching speed in the upper ns-range may be obtainable upon scaling into the lower µm-range (see also Figure 18.8).

18.4.2.3 Electrothermal switches

Power consumption in electrothermal actuators (Section 18.4) is typically rather high, especially when power needs to be applied during stand-by. Thus, single ended cantilevers as discussed above are not attractive, unless perhaps operated as fuses, where the switch is normally closed and opened only at overdrive.

It is therefore very advantageous to find an actuator layout that can provide two stable positions, and where switching between these conditions is possible [214–220]. Such a bistable layout can be realised by a buckled beam (Euler bar; see Section 18.3.2.2). Compressive stress in such a bridge configuration leads to buckling into either an up-state or a down-state position. Switching between these states can be achieved by bimetal actuators positioned on the beam to develop the appropriate bending moments. Figure 18.43 shows such an actuator realised in a silicon frame. It has been fabricated using a technology that

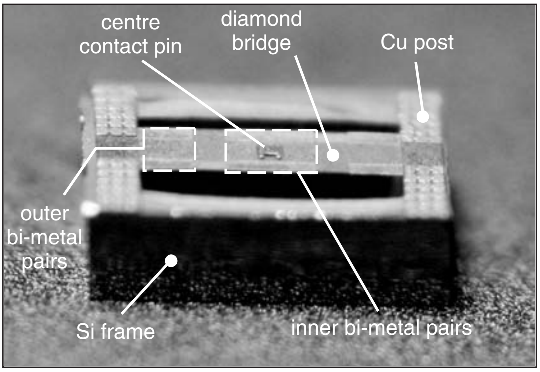

Figure 18.43 Fabricated and diced electrothermal bridge actuator in silicon frame [219]. Reprinted from Nanodiamond Microbridges for RF-Applications, presented at the 2nd International Diamond Conference in Rome 2007, with permission from Diamond At Work Ltd

is very similar to that of the acceleration sensor, including bulk machining and diamond film dry etching. The bimetal elements are Cu-diamond pairs heated by diamond resistors. These pairs need to develop upwards and downwards bending moments and are therefore located around the beam centre and near the anchor points, respectively. More details on the design can be found elsewhere [16].

Two stable positions are developed only within a certain window of built-in compressive stress. If the stress is too low the bridge will not buckle; if the stress is too high, it will bounce back after actuation (see Ref. [218]). Stress engineering of the film is therefore an essential part of this technology.

The actuator design as shown in Figure 18.43 is well suited for assembly into a MEMS component by hybrid integration onto various substrates. Figure 18.44 shows a bistable bridge actuator, which is assembled in the coplanar structure of an aluminium nitride RF substrate. The actuator frame was additionally equipped with copper pads, which are used

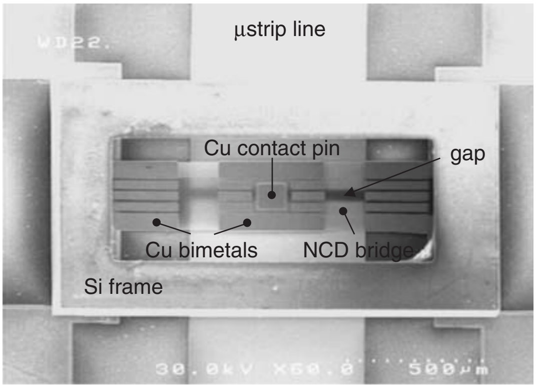

Figure 18.44 Bistable diamond bridge actuator integrated into an RF microstrip line on AlN. The figure shows the diamond bridge within a silicon frame from the top. The transparency of the thin diamond bridge in this SEM view the identification of the bimetals, contact pin, and gap in the microstrip line underneath

as spacers as well as for the bias connections. An electrically isolated copper pin in the centre of the bridge is used as the contact to close a gap in the centre line of the coplanar waveguide (see also Figure 18.30).

The actuator frame has been mounted onto the substrate upside-down using the SLID soldering technique as described in Section 18.3.4.2. The thickness of this solder joint is critical since it also represents the spacer thickness for up and down movement of the bridge. Figure 18.45 illustrates the two stable positions of the assembled switch in a side view with opened (left) and closed (right) position. Typical gap heights are in the micrometre range. Therefore only minor capacitive coupling in the off-state is expected. In the on-state, the buckling induces a rather high contact force, resulting in a low-loss contact.

The assembled switch was tested at a frequency of 2.1 GHz with transmitted input power of up to 50 W (limited by the generator maximum output power). Figure 18.46 shows the performance during the power sweep. Two power sweeps were carried out without change or degradation in the transmission characteristics. The maximum RF power density is mostly concentrated around the contact pin. Its density has therefore been estimated to

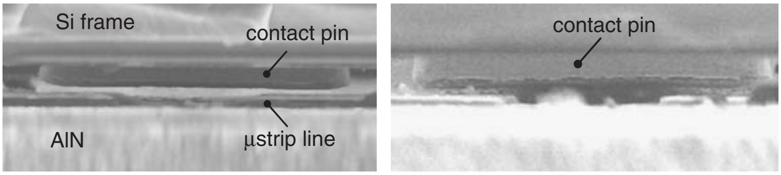

Figure 18.45 SEM side views of the contact pin of the bistable diamond bridge actuator of Figure 18.44 in open (left) and closed (right) states. The image was taken by viewing into the gap between the small side of the silicon frame and the AlN substrate

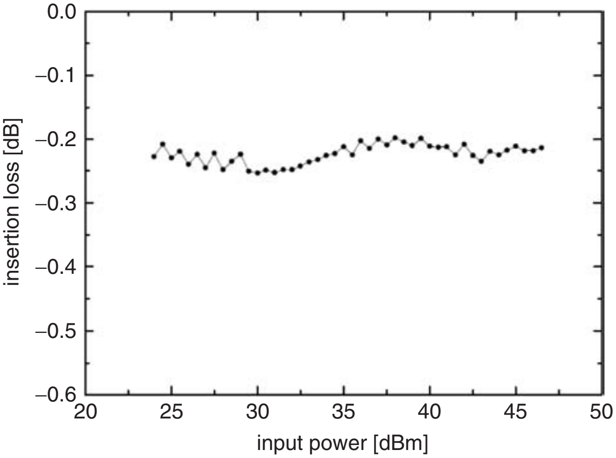

Figure 18.46 Insertion loss of transmitted RF power at 2.1 GHz of a bistable diamond MEMS switch. The substrate was a microstrip line on alumina. The extraction is based on scattering parameter (s_{21}) measurements in the on-position of the switch. The insertion loss is essentially unchanged [219]. Reprinted from Nanodiamond Microbridges for RF-Applications, presented at the 2nd International Diamond Conference in Rome 2007, with permission from Diamond At Work Ltd

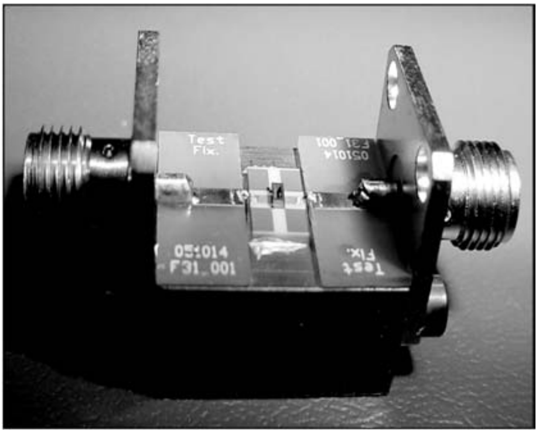
Test
Fix.
051014
F31_001

Figure 18.47 Diamond RF switch mounted into a test fixture, which was used for the measurement shown in Figure 18.46 (courtesy S. Balachandran and T. Weller, University of South Florida, Tampa, USA)

be in the range of MW/cm^2. The RF substrate in this experiment was alumina possessing moderate thermal conductivity. Thus, self-heating has certainly occurred, but did not result in any switching instability. Switching under RF power, robustness and reliability have not yet been studied in these first experiments.

In addition to RF applications, the bridge actuator may be used for several other purposes. By using various shapes of contact pin the actuator can be considered as a movable micro- or nano-tool that may serve a variety of tasks [218]. Figure 18.48 shows an overview of what may be possible. In a fluidic device, a function can be that of a dipping electrode (left picture). Herein, the microtool can act either in a passive way as a valve or as a throttle to stop or regulate the liquid flow in a capillary. It can be an active electrochemical electrode, causing chemical reactions, or operate as a sensor, e.g. within an ISFET configuration. Also heating of the liquid inside such a microchannel could be considered by employing a microtool possessing a diamond heater (see Section 18.2.3.1)

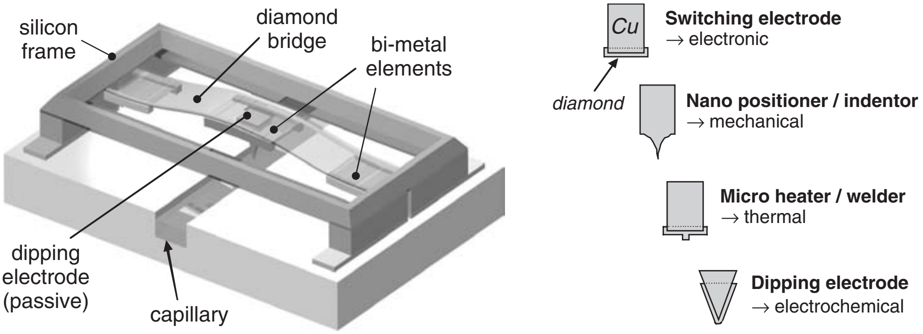
silicon frame
diamond bridge
bi-metal elements
dipping electrode (passive)
capillary
Cu
diamond
Switching electrode
→ electronic
Nano positioner / indentor
→ mechanical
Micro heater / welder
→ thermal
Dipping electrode
→ electrochemical

Figure 18.48 Schematic illustration of a possible bridge actuator within a microfluidic device (left), and various tool shapes (right) [218]. Reprinted from Diamond and Related Materials, Bi-stable micro actuator based on stress engineered nano-diamond by J. Kusterer, F.J.Hernandez, S. Haroon, P. Schmid, A. Munding, R. Müller and E. Kohn, 15, 4–8. Copyright (2006) Elsevier

Table 18.6 Possible applications for an actuator bridge with different tool shapes

Tool shape	Base plate	Function	Field of application
Needle	Capillary plate	Dipping electrode	Electrochemical or electrophoretic mass flow control
		Needle valve/throttle	
		Nano indenter	Penetration of molecules
	Hole plate	Stamping tool	Micro stanza
	Capillary plate	Watervalve	Switching of channels in mixers
		Nano indenter	
	'Micro workbench'	Micro heater	Deformation of biomolecules
Cube/cylinder			
			Micro welding
		Stamping tool	Micro bonding
			Micro punching
Specific	'Micro workbench'	Stamping tool	Nano imprinting

at its tip. It is also possible to envisage a steerable electrode to move and separate charged and bipolar molecules in the liquid by an electrical field (electrophoresis). In some cases, direct contact and penetration of small molecules by a sharp and spiky tip of the microtool may be desired. It may therefore be termed a multipurpose instrument for the micro- and nano-scale. Table 18.5 presents a few examples of uses for the actuator tool.

18.4.2.4 Switchable inductors

Switches and switching networks can perform various functions in RF circuits, including the switching on and off of transmission lines, switching between impedances, phase angles or inductances for matching and tuning as is, for instance, needed when frequency ranges are changed. In a first circuit application, the bistable diamond bridge actuator has been used to switch inductances [220].

In Figure 18.49 the concept of an inductor switch is illustrated. A coplanar waveguide has been modified by three parallel discontinuities, of which two possess an in-line gap. In this application the diamond actuator is equipped with two isolated contact pins that close the gaps of the line in case of contact (bridge in down-state). All three parallel discontinuities have been designed for a certain inductance, depending on frequency (see Figure 18.50). If the bridge is switched to the open up-state, the inductance is changed, since it is mainly the centre discontinuity that is effective. According to the diagram, on–off inductance ratios of between 1.4 (at 1 GHz) and 2.2 (at 30 GHz) have been obtained. The absolute inductance values were in the range 100 pH to just over 1 nH.

18.4.2.5 Microwave substrate

As has been discussed in the previous sections, diamond is well suited as a substrate for RF microsystems, especially for high power application, where thermal management is

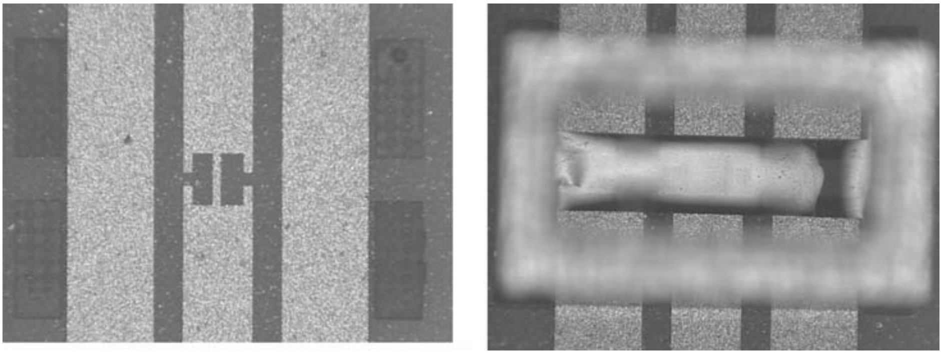

Figure 18.49 A switchable RF inductor. A coplanar waveguide is modified by discontinuities (in the centre of the graph), which can be altered by a diamond bridge actuator mounted on top of it. The RF waveguide is realised by gold lines on alumina (courtesy S. Balachandran and T. Weller, University of South Florida, Tampa, USA)

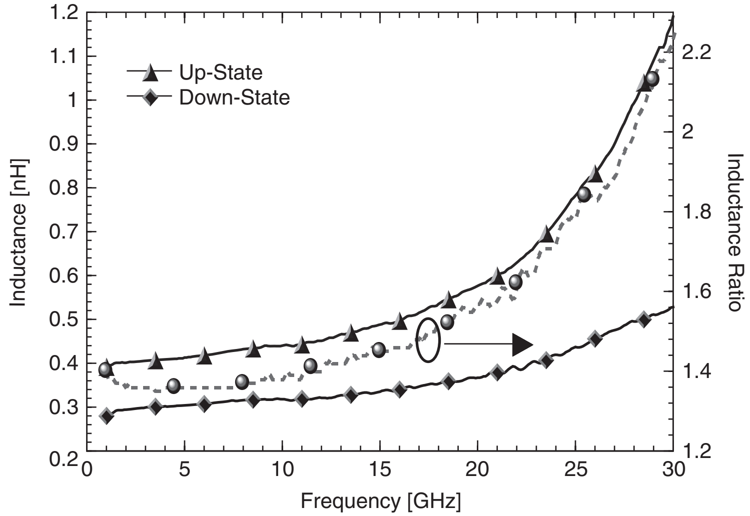

Figure 18.50 Measured inductances and related inductance ratios of a switchable diamond bridge RF inductor [220]. Reprinted with permission from Microwave Symposium Digest, 2003 IEEE MTT-S International, Thermally Activated Nanocrystalline Diamond Micro-Bridges for Microwave and High-Power RF Applications by S. Balachandran, J. Kusterer, R. Connick, T. M. Weller, D. Maier, M. Dipalo and E. Kohn, Volume 3, 8–13 June 2003, pages 367–370, Copyright (2003) IEEE

important. An example may be a passive RF switch circuit for beam steering of high-power and high-resolution phased array radars. Considering Figure 18.30, the microwave substrate of the switch was alumina (amorphous Al_2O_3). Despite the low thermal conductivity of this substrate, 50 W could be transmitted. Similarly, sapphire (crystalline Al_2O_3) is the substrate for many (inexpensive) GaN-based FETs and indeed limiting the output power so that the advantage of the wide band-gap properties can only be drawn marginally. Therefore, (hexagonal) SiC is used for high power devices but do not suffice for thermal management at the high power density end and diamond heat sinks are therefore in

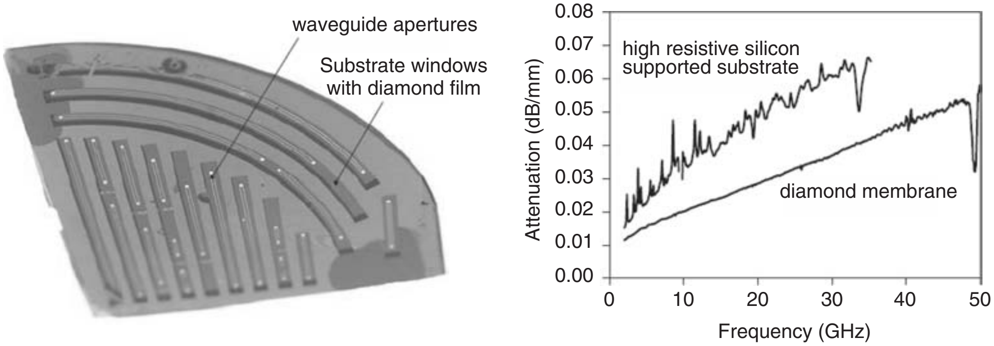

Figure 18.51 RF coplanar waveguides on a diamond substrate (left) [211]. Reprinted with permission from Microwave Symposium Digest, 2003 IEEE MTT-S International, Evaluation of CVD Diamond for heavy duty microwave switches by E. Kohn et al., Volume 3, 8–13 June 2003, pages 1625–1628, Copyright (2003) IEEE, which was used to study RF transmission loss of diamond (right) (courtesy of D. Grobe, University of Ulm). The dark spots on both ends of the diamond wafer result from glue used to fix the sample onto a glass holder. Reproduced courtesy of Dirk Grobe

discussion [221]. The present choice for hybrid, integrated, planar microwave power circuits is AlN [222], however as ceramics with a much reduced thermal conductivity as compared with the single crystalline phase. Thus, only diamond substrates will allow the utilisation of the full potential of high power diamond RF-microsystems in passive circuits.

However, substrate losses usually increase with frequency (see Figure 18.51) [201, 211, 223]. It is therefore important to analyse the losses of polycrystalline quasi-substrates (which are mostly polished) and nanodiamond, which is grown with a process optimized for high thermal conductivity in respect to the residual losses mostly incurred by grain boundary effects. Thus, diamond has been investigated, mostly with coplanar waveguide structures with lateral ground-to-ground coupling, over a broad frequency range from 1 GHz to above 100 GHz [223]. On freestanding polycrystalline wafers that have been polished on both sides, a total attenuation of less than 0.1 dB/mm has been measured above 100 GHz. It was thought that this residual attenuation was induced by power leaking into higher surface modes. No evidence was found for attenuation due to the polycrystalline nature of the diamond substrate [223]. Coplanar waveguide structures were also investigated up to 50 GHz on highly oriented diamond (HOD) films on Si, patterned directly after growth without polishing [201]. Thus, the influence of the Si-substrate could also be identified. Figure 18.52 shows a quarter of a 2-inch diameter Si-substrate coated with a 30-μm thick HOD film. The transmission line and resonator structures are located on membranes etched into the Si. With the various geometries, different frequency ranges have been addressed. In the right-hand graph of Figure 18.52 the attenuation is shown up to 50 GHz for a waveguide on a membrane with a loss of approximately 0.05 dB/mm at 50 GHz. By simulation, a diamond permittivity of 5.8 could be extracted, compared with a static relative dielectric constant of 5.7. The losses induced by the supporting Si-substrate (with a specific resistivity >10 kΩcm) are also shown in the graph by the overlaid curve.

Further evidence for the exceptionally low loss of diamond films and freestanding substrates, at GHz frequencies may be taken from the application as gyrotron windows. A gyrotron is a vacuum tube for the generation of sub-mm wave, high power, pulses as

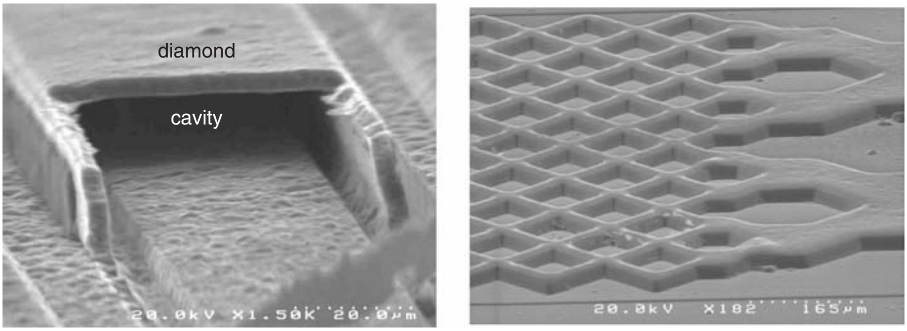

Figure 18.52 High aspect ratio NCD capillaries for microfluidic applications (left: [227]. Reprinted with permission from Device Research Conference Digest, 2005, DRC ’05. 63rd, “All diamond inkjet” for dispension of aggressive liquids by R. Müller, W. Berger, K. Janischowksy and E. Kohn, Volume 1, June 20–22, pages 229–230. Copyright (2005) IEEE; right: courtesy of Ralph Müller. Reproduced courtesy of Ralph Müller)

needed for fusion experiments. The separation of the tube vacuum from the atmosphere is realised by a dielectric window. For pulse transmission up to RF-power densities in the MW/cm^2 range, diamond windows have been used [225]. Two features have been important: the absence of dark spots, which originate from grain boundary defects and which absorb and result in local hotspots; and the high thermal conductivity for effective heat removal.

18.4.3 Fluidic applications

In electronics, as with automotive and at high frequencies, the devices are well passivated and shielded when used in a package, which may be realised in plastic or by a vacuum sealed ceramic housing. However, many microsystems are also used in direct contact with a liquid environment, namely in chemical, pharmaceutical, biological, and medical applications, as well as waste water analysis and printing. These systems contain a distributing network of capillaries and are fed by liquid reservoirs. Active elements are heaters, as used in inkjets, or electrochemical sensors used for analysis. In the following section, the first fluidic applications based on diamond in direct contact with a liquid are discussed. The emphasis in this discussion is on microsystems technology aspects. The active elements, such as ChemFETs and electrochemical electrodes, are discussed in Chapter 17 by Foord and Chapter 14 by Kohn and Denisenko in this book.

Three applications will be described where diamond exhibits clear advantages over Si, the current choice for most MEMS applications. These are inkjet elements, micropumps, and patch-clamp systems. In contrast to currently available systems, these devices can be used for handling aggressive media like strong acids, bases, salty solutions, reductives, and oxidants.

18.4.3.1 Capillaries

Microchannels or capillaries are essential elements in microfluidic devices. They transport liquids from one active or passive section to another. They are used in inkjets to deliver ink to the printing head, in microfluidic mixers to feed the individual liquids into the mixer, or in micropumps to guide a liquid through the pumping element.

Hence, different requirements have to be considered. Firstly, they have to be liquid tight, then, they must withstand the operating pressures, and their sidewalls have to be smooth enough not to cause turbulence or lock in larger molecules. The surface needs, furthermore, to be chemically inert and corrosion resistant as well as inactive with respect to electrochemical surface reactions. With respect to adhesion of biological molecules or cells they may be hydrophilic, hydrophobic (lipophilic), or amphiphilic. In many cases, especially in biomedical applications, inspection is done optically by fluorescence. Thus, the walls have to be transparent to the wavelengths used, which may be in the UV wavelength range when used in the biochemical environment. Most of these requirements can be met by plastics and glass, which are therefore the most commonly used carrier materials. Si is used if the active element is an ISFET or a metallic microelectrode. In contact with the liquid is usually (besides the passivation) a noble metal or a metal oxide, many metal oxides being stable under biochemical conditions. However, in harsh environments such as highly corrosive media, like concentrated hot salt solutions, most of the above mentioned materials fail. For such applications all-diamond capillary technologies have been developed mostly realised by moulding techniques or sacrificial layer technologies, and the use of NCD or UNCD films and diamond-on-Si substrates [226].

Described here will be a copper sacrificial layer technology for the fabrication of high aspect ratio and large cross-section channels by overgrowth with thin NCD films and subsequent etching The basic process has already been introduced in Section 18.3.3.4 [180, 226]. Figure 18.54 shows two examples of such all-diamond capillaries, which have been developed for bubble-jets and micropump structures (see below).

18.4.3.2 Bubble-jet structures

Bubble-jet or inkjet elements are widely used in printing [228]. They generally contain a heater, which is surrounded by a compartment or cavity, and ink supply channels. The heater consists typically of a stack of layers that are addressed individually as resistive heaters, electrical isolation, passivation, protection against cavitation damage, or adhesion between layers. In conventional inkjets the fluidic components are mostly made of plastics. In addition, usually inkjet modules based on Si-technologies are arranged as arrays and include the driver circuitry for the heater elements.

For diamond, individual bubble-jet elements as well as arrays have been realised but with no monolithic integration of the driver electronics. Several generations of technology have been developed that tackle many of the problems of use in aggressive media. Originally, the diamond nozzle plate was fabricated separately and connected to the heater compartment by gluing. However, this connection has limited the types of liquids to be used and the overall lifetime. Using a sacrificial layer technology as discussed in Section 18.3.3.4, an all-diamond inkjet has been developed, where only the diamond surface is in contact with the liquid in the capillary supply network as well as in the inkjet chamber [180]. Figure 18.27 in Section 18.3.3.4 shows details of such an element. An inkjet element with its integrated feeding capillary is shown in Figure 18.53.

Figure 18.54 shows the process of droplets ejection with the help of a pseudo-cinematographic recording (compare Ref. [52]). Beside the ejected droplet a satellite drop is also seen, which often develops depending on the viscosity of the liquid. The velocity of

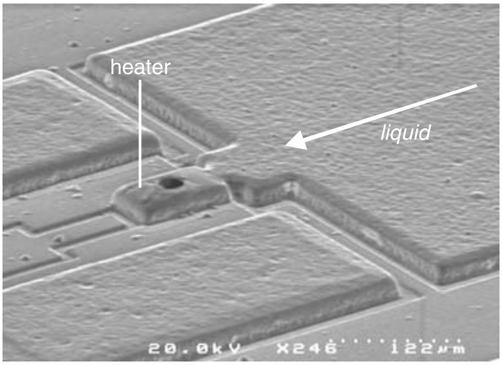

Figure 18.53 All-in-diamond bubble-jet element with integrated liquid feed line [227]. Reprinted with permission from Device Research Conference Digest, 2005, DRC '05. 63rd, "All diamond inkjet" for dispension of aggressive liquids by R. Müller, W. Berger, K. Janischowksy and E. Kohn, Volume 1, June 20–22, pages 229–230. Copyright (2005) IEEE

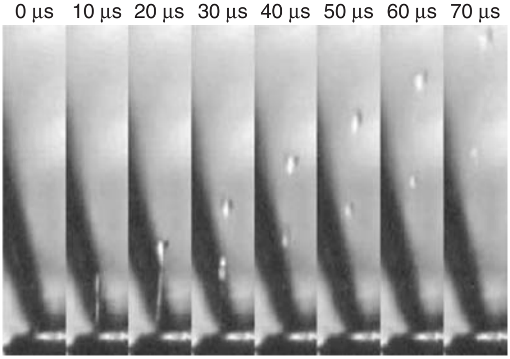

Figure 18.54 Visualisation of operation of the diamond bubble-jet shown in Figure 18.53. The particular image stripes were taken by pseudo-cinematographic recording [180]. Reprinted with permission from Diamond and Related Materials, An "all-diamond" inkjet realized in sacrifical layer technology by R. Müller, R. Gronmaier, K. Janischowsky, J. Kusterer and E. Kohn, 14, 3–7, Copyright (2005) Elsevier

the ejected droplets depends mainly on the mass density of the liquid, which here was purified water, and was 9.1 m/s for a heating pulse of 4.8 μs [180]. The maximum ejection frequency could be increased to 10 kHz, before the speed of the ejected bubble started to drop. This high frequency reflects two conditions. Firstly, the diamond resistor heats up fast and only a small fraction of the heating energy is lost to the substrate. This was possible because 3D-NCD with low thermal conductivity was used as base film. Secondly, after the pulse is switched off the heat is effectively dissipated due to the high thermal conductivity of the top diamond capillary system, realised as 2D-NCD.

Since in this technology a boron-doped diamond heater was monolithically integrated into an all-diamond chamber, the system was tested in aggressive acids. Since Cu was the sacrificial layer material and had been removed by nitric acid, high inertness of the system could be expected. However, during operation the liquid is ejected by an explosive phase transition at the spinodal temperature, which is 312 °C for water [229]. Due to the

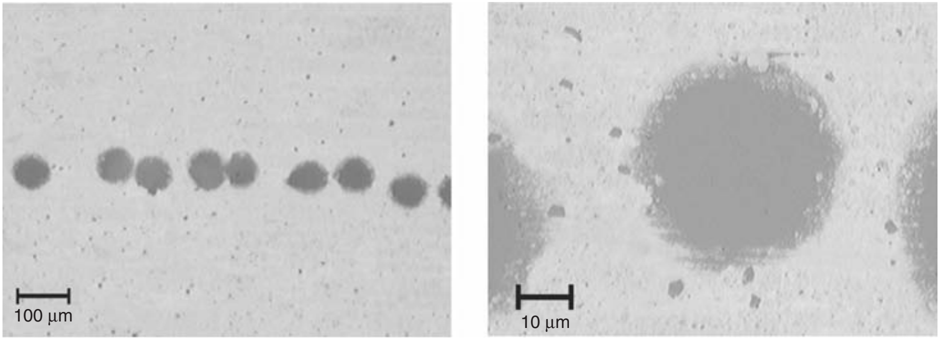

Figure 18.55 View through a copper-coated cover slip under a microscope. Circular openings in the metal film have been derived by printing with 40 % concentrated sulfuric acid etchant with a distance of bubble-jet and cover slip of 10 mm [227]. Reprinted with permission from Device Research Conference Digest, 2005, DRC '05. 63rd, "All diamond inkjet" for dispension of aggressive liquids by R. Müller, W. Berger, K. Janischowksy and E. Kohn, Volume 1, June 20–22, pages 229–230. Copyright (2005) IEEE

high frequency of the ejection process at 10 kHz [227], the diamond surface may reach higher temperatures. Nevertheless, sulfuric and nitric acids could be ejected and Cu films etched as shown in Figure 18.55 [227]. The droplets were ejected onto a copper coated, cover-slip substrate, while moving the substrate stage. Figure 18.55 shows microscope views through the glass substrate onto the rear of the copper film after an experiment with sulfuric acid. It can be seen, that the droplets of acid have etched the copper in circles of roughly 50 micrometres in diameter.

These experiments indicate that devices based on diamond thin films can operate in harsh liquid environments. Their advantages may be summarised as follows:

- high speed of operation, owing to effective heat dissipation of diamond after each droplet generation;
- no thermal stress generation between individual layers of the system;
- perfect adhesion to the substrate, since the connection to the Si template is realised by a SiC interface of high mechanical strength;
- very small nozzles and hence extremely small droplets made possible by the high fracture strength of the diamond nozzle plate material;
- high corrosion resistance because of chemical inertness of the diamond surface even without passivation;
- no cavity damage even without any overlayer, due the high mechanical stability of the diamond cavity walls.

Such a bubble-jet system has been used for biochemical oligonucleotide synthesis, where several chemical steps were performed during the attachment cycle of an additional base to the oligonucleotide [52]. Therefore, the system contained a double inkjet chamber in an array of 10 inkjet pairs. The bubble-jet chip was mounted onto a stainless steel carrier, supplying the liquid through etched via connections through the Si substrate and a front side channel system. The driver electronics was hybrid integrated. A micrograph of the entire module is shown in Figure 18.56 [52].

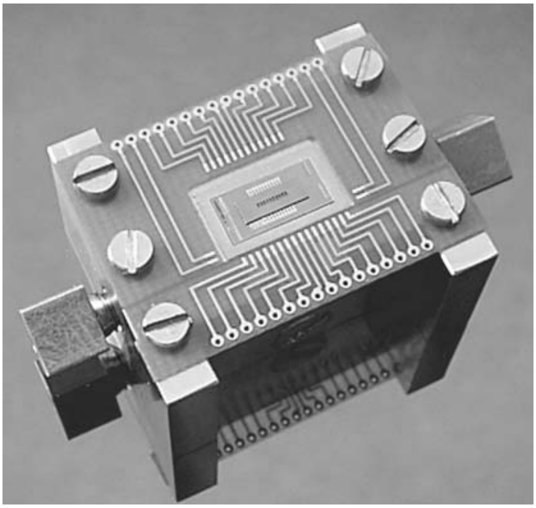

Figure 18.56 Assembled diamond-based print head including bubble-jet chip, PCB for wire connection, and carrier, which contains fluidic elements for input of two different liquids [52]. Reprinted from Diamond and Related Materials, Diamond micro system for bio-chemistry by M. Adamschik, M. Hinz, C. Maier, P. Schmid, H. Seliger, E. P. Hofer and E. Kohn, 10, 3–7. Copyright (2001) Elsevier

18.4.3.3 Micropumps

Pumps are generally used to feed microfluidic elements with liquids of defined pressure or for extraction of liquids by suction, and most cases the pumps are added externally. MEMS technologies offer the possibility of direct integration of such elements. Two concepts are common: the peristaltic pump and the membrane pump. Both of these concepts have been realised in diamond as described below.

Peristaltic pump

A peristaltic pump has been designed and realised to obtain a side shooter bubble-jet [180]. In this case, a linear array of heaters is operated dynamically to accelerate a compressed liquid domain towards the side opening of the chip, to be ejected with high speed. Thus, at the heart is a cascade of diamond heater elements that are connected by diamond capillaries. Once this channel is filled with liquid, the heaters can be driven in a sequential mode, pushing a liquid domain along the cascade. An example of a side-shooter print head with integrated peristaltic micropump is shown in the SEM micrograph in Figure 18.57.

Membrane pump

Another micropump concept is that of a membrane pump. For its realisation in diamond the electrothermal bimetal actuation principle was chosen (as discussed in Section 18.2.4.2). Here, a monostable diamond membrane is actuated by four bimetallic nickel elements. The height of the membrane deflection is force dependent and thus

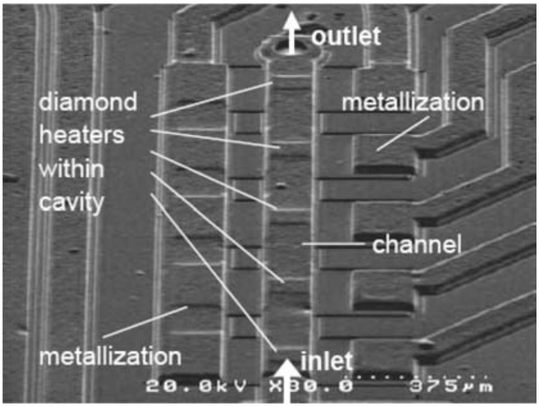

Figure 18.57 NCD bubble-jet side shooter with monolithically integrated peristaltic micropump. Timed heating of the linear diamond heater cascade accelerates a liquid domain towards the outlet for high-speed droplet ejection [180]. Reprinted with permission from Diamond and Related Materials, An "all-diamond" inkjet realized in sacrifical layer technology by R. Müller, R. Gronmaier, K. Janischowsky, J. Kusterer and E. Kohn, 14, 3–7, Copyright (2005) Elsevier

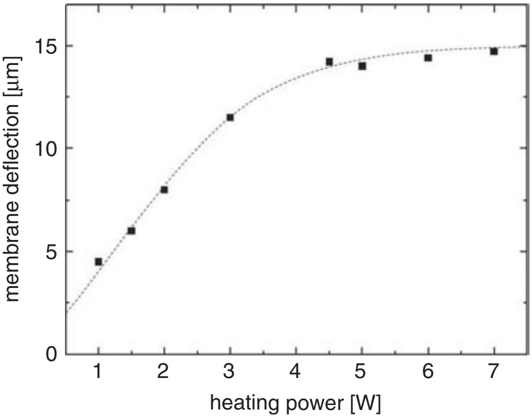

Figure 18.58 Membrane deflection as a function of total electrical input power of the bimetal heaters. The side length of the square membrane was 500 µm (redrawn after [226]). Reprinted from Diamond and Related Materials, Elements for surface microfluidics in diamond by R. Müller, P. Schmid, A. Munding, R. Gronmaier and E. Kohn, 13, 4–8. Copyright (2004) Elsevier

dependent on the heating power, as shown in Figure 18.58. As can be seen, relatively high power, and hence power density, is needed to reach the required force for full deflection. Once more it is important to consider the heat dissipated by the diamond film.

The membrane represents the lid of the pumping chamber with opposite positioned input and output ports that have to act as directional valves. These have been realised as wedge-shaped nozzles without moving parts [226]. Unfortunately, with such valve structures only a small directional efficiency can be obtained, resulting also in a low pumping efficiency. Figure 18.59 shows a realised pumping module with pumping chamber and input and output valves.

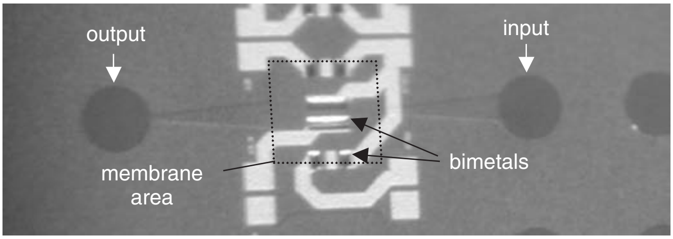

Figure 18.59 Micrograph of realised micropump including input and output valves and capillary opening to connect liquid input and output reservoirs

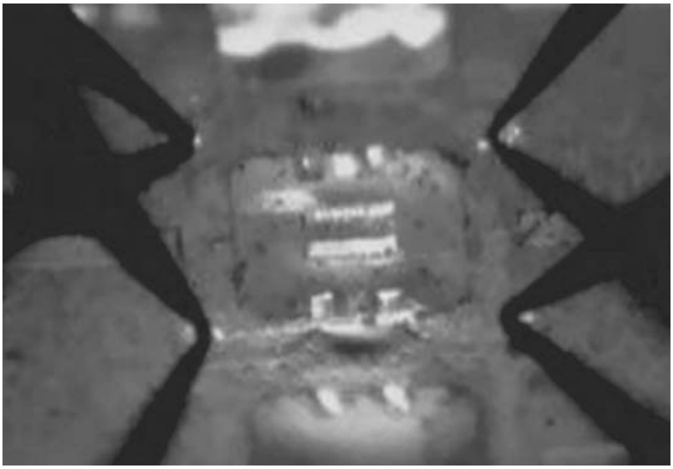

Figure 18.60 Micrograph of pumping chamber during operation. In the picture the membrane is buckled upwards by the heated bimetals in its centre (compare Figure 18.59) [226]. Reprinted from Diamond and Related Materials, Elements for surface microfluidics in diamond by R. Müller, P. Schmid, A. Munding, R. Gronmaier and E. Kohn, 13, 4–8. Copyright (2004) Elsevier

Figure 18.60 illustrates a chamber under an applied DC voltage showing the location of the bimetal elements and contact pads being contacted by needles. The reflection on the surface indicates that the membrane is in upwards position. During operation with an AC signal the net liquid flow is to the left. The pump can be operated with a vibration frequency of approximately 2 kHz, however, with small throughput. More details on the operation can be found in Ref.[226].

18.4.3.4 Patch-clamp systems

The patch clamp technique has been developed to analyse ion channels in cell membranes. A potential difference is applied across the cell membrane (between the extracellular solution and the intracellular solution). These channels are protein molecules, which react to the potential difference and allow the passage of ions when open, thus initiating an electrical charge transfer.

The common method of detecting the action potential of the cell opening and closing is by clamping a small area of the cell surface ('patch') to the tip of a pipette by suction.

Both cell and pipette are in a cellular solution. Using electrochemical electrodes, action potentials and current pulses are tapped. Potential levels and action current pulses are usually small and need to be resolved by special low-noise amplifiers. Patch clamping by capillaries is time consuming and needs professional skills, therefore planar patch-clamp systems based on membranes with a small centre opening to clamp the cell have been developed. Such systems usually contain a large number of compartments and many cells can be analysed in parallel [230]. Membrane materials are glass, silicon nitride, plastic, or PMDS (Polydimethylsiloxane). They need to be electrically highly insulating, providing a GΩ-seal around the patch clamp hole. For the integration of active elements directly adjacent to the clamp hole, semiconductor materials have not yet been used for two major reasons: (i) it is difficult to combine high insulation characteristics with the doping levels needed for electrode operation. (ii) The material needs to be of high mechanical strength to sustain the pressure differences for clamping with low leakage.

None of these limitations apply to diamond, which can combine all the required mechanical, electronic and electrochemical properties. This raises the potential for developing patch-clamp array systems with integrated active elements like electrochemical electrodes, heaters, thermal sensors, and ISFET sensors [231]. In addition, nanocrystalline diamond films are optically transparent, offering the possibility of combining electrochemical with optical fluorescence analysis. Electrochemical microelectrodes can suppress water dissociation across a large potential window in combination with extremely low background current. Surface functionalization allows identification of specific biomolecules. These properties are discussed in other chapters of this book (see Chapter 16 by Garrido) and will be only briefly discussed here.

To evaluate diamond in this application, a first patch clamp array has been realised in diamond-on-Si technology with technological elements similar to those used in membrane and cantilever fabrication. A micrograph of the chip is shown in Figure 18.61. The membrane consists of a 2-micrometre NCD film with a clamping hole in the centre. Since the fracture strength of NCD increases as the thickness of the membrane is reduced, very thin membranes are possible even in combination with a compartment size of a few square micrometres in area. The hole usually has a diameter of about 1 μm to balance resolution, hole through-resistance and GΩ-isolation. Utilizing thin diamond membranes, the clamp-holes diameter could be reduced well into the nm range. Clamp holes of various diameters have been realised using various technologies, such as selective growth in combination with a sacrificial layer technology (see Figure 18.23) [231], dry etching using hard masks (see Figure 18.19) and focused ion beam etching (see Figure 18.21)

The array shown in Figure 18.61 consists of 10 compartments of various membrane areas in order to evaluate adequate volumes for cell analysis. The chip was also equipped with metal electrodes on both sides for current detection. Since the thin diamond membrane is transparent to electron beam exposure, both electrodes are easily visible.

The chip was mounted onto a plastic fixture and sealed with a gasket. On top, an elastomer mould was added for volume extension of the compartments. The fully assembled module is shown in Figure 18.62. For measurement, the upper compartments were filled with a solution similar to an extracellular solution, and the bottom chamber with an electrolyte similar to an intracellular solution. Subsequently a low pressure is applied at the bottom chamber, which results in a suction of the cell to the clamp hole. A very critical issue in this respect is the insulation of the top and bottom solutions by a GΩ-seal. Leakage currents passing through the clamp hole outside the cell are, in general, much

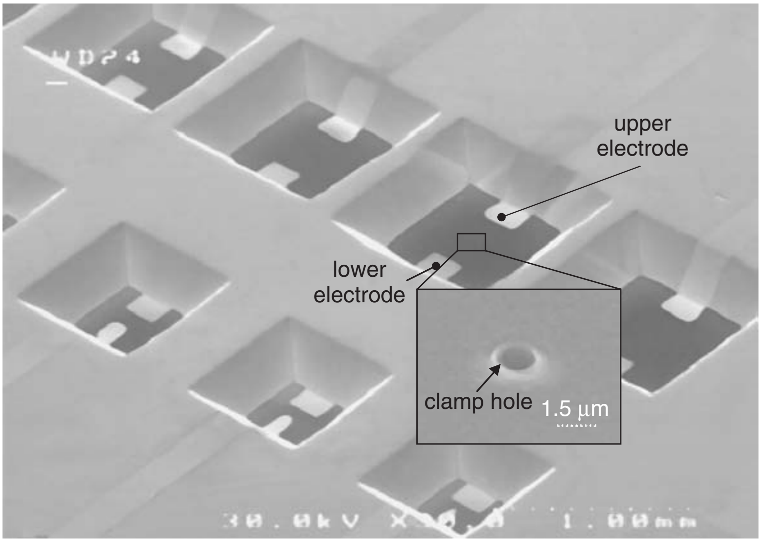
upper
electrode
lower
electrode
clamp hole
1.5 µm
30.0kV
1.00mm

Figure 18.61 Image of patch-clamp test chip. Visible are compartments of different volumes with an NCD membrane at their base. Front as well as rear electrodes can also be seen because of the e-beam transparency of the membranes [231]. Reprinted with permission from Diamond and Related Materials, A diamond-on-silicon patch-clamp-system by J. Kusterer, A. Alekov, A. Pasquarelli, R. Müller, W. Ebert, F. Lehmann-Horn and E. Kohn, 14, 11–12, Copyright (2005) Elsevier

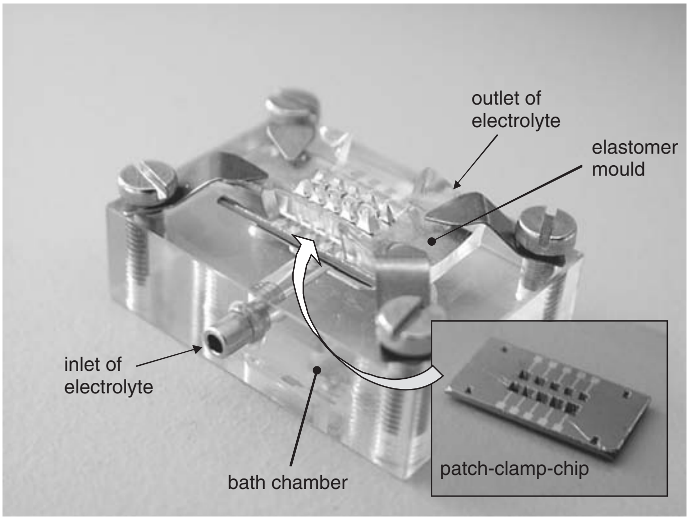
outlet of
electrolyte
elastomer
mould
inlet of
electrolyte
bath chamber
patch-clamp-chip

Figure 18.62 Assembled patch-clamp system including test-chip (see Figure 18.61), plastic fixture, and elastomer mould [231]. Reprinted with permission from Diamond and Related Materials, A diamond-on-silicon patch-clamp-system by J. Kusterer, A. Alekov, A. Pasquarelli, R. Müller, W. Ebert, F. Lehmann-Horn and E. Kohn, 14, 11–12, Copyright (2005) Elsevier

higher than the currents to be detected. Therefore, it is necessary for there to be a very smooth membrane surface around the hole, which was achieved in this case by using the nucleation side of the NCD layer. In the case analysed in detail, the circular hole was fabricated by selective growth around a Cu micropillar, which was made from selective electroplating within a photo resist mask (compare Figure 18.25).

Electrochemical analysis using electrolytes similar to intracellular fluid showed that the values of through-resistance is in proportion with the through-hole volume [231]. As a result, typical clamp-hole diameters of 1.5 μm have through resistances of approximately 300 kΩ. Without electrolyte, the series resistance was in the TΩ-range. Compartments without clamp hole exhibited an isolation resistance of 240 GΩ in electrolyte, indicating the absence of any leakage through pinholes.

18.5 CONCLUSIONS

In this chapter we have described the development of diamond-based microstructures used as actuators and sensors and usually known as MEMS. Many of these are realised by surface rather than bulk technologies and their technology is therefore based on diamond thin films, largely grown on silicon substrates. These films are polycrystalline and, for micrometer-sized geometries, nano and ultrananocrystalline. If optimised for specific applications, the relevant properties of these films approach closely the single crystal phase. The films can be doped by boron with characteristics similar to single crystal layers (except of a lower mobility). Boron-doped films are, therefore, one the basic components in active MEMS functions. Because this material is not yet suitable for the fabrication of efficient transistors, it is not possible at present to obtain first level integration for signal conditioning. Therefore, up to now, diamond microsystems are discrete components and monolithically integrated smart sensors or actuators have so far not been developed.

This is one of the reasons why the microsystems discussed in this chapter have not been able to date to compete with monolithically integrated Si systems in conventional applications. However, diamond exhibits many exceptional attributes for application in harsh and extreme environments, which cannot be easily served by silicon. This chapter discusses several of these applications based on mechanical structures where Si-surface and bulk machining technologies are used. As can be seen, the areas where diamond could be used in microsystems are highly diverse, but to break away from niche applications it will necessary to realise full monolithic integration with signal conditioning and signal processing CMOS-like circuits.

For integration, low temperature deposition of diamond on silicon will compromise many of the exceptional properties of diamond and may not be a practical solution. The only remaining possibility is the combination with another wide-band-gap semiconductor with ceramic-like stability. Diamond growth on SiC-electronics (using the hexagonal phase) has not been evaluated successfully yet. Another option is the combination with III-nitride heterostructures. Overgrowth of nitrides at high temperature in a H-radical rich atmosphere is difficult and has resulted in many cases in their decomposition. However the overgrowth of thin InAlN surface barrier layers with diamond has recently been achieved without degrading the relevant electronic properties of the InAlN/GaN heterostructure, namely its polarisation-induced, interfacial, two-dimensional electron gas property, the basis of InAlN/GaN field-effect transistors. A further successful development of this technology will enable a new class of fully integrated microsystems for extreme applications out of the reach of any presently known semiconductor technology.

However, this is still highly speculative and with currently available technology, diamond MEMS devices have only two options: discrete MEMS devices or hybrid integration with conventional electronics. Examples of both have been discussed in this chapter including numerous examples of advanced prototype state-of-the-art structures.

ACKNOWLEDGEMENTS

This work contains many contributions from our diamond technology group realised over many years of research. The authors would like to thank all the PhD students, who contributed to the development of MEMS technology. Especially we would like to mention Mario Adamschik, who developed the first generation technology and devices, without which further developments would not have been possible. Equally important is the contribution of Philipp Schmid, now with Microconsult Ltd, who developed fundamental calculations and finite-element analyses in diamond mechanics and thermodynamics. We would also like to acknowledge the cooperation with Dieter Gruen at Argonne Laboratories regarding the ultrananocrystalline diamond materials that have been investigated and implemented into device structures during our work. We are also grateful to our scientists, technicians, and master students for their cooperation in the technical realisation of diamond devices. We are also grateful to the institutions that supported us in the fabrication and analysis of our devices, namely the Institute for Microwave Techniques of Professor Menzel at the University of Ulm, the Center for Wireless and Microwave Information Systems of Professor Weller at the University of South Florida in Tampa, and microGaN Ltd in Ulm. Last but not least, many stimulating discussions within the scientific community should not be left unmentioned. This work has been supported financially in part by the European Union, the German Ministry of Education and Research (BMBF) and the German Research Society (DFG).

REFERENCES

[1] V. V. Buniatyan, V. M. Aroutionian, *J. Phys. D: Appl. Phys.* **40** (2007) 6355–6385.
[2] C. A. Zorman, M. Mehregany, Materials for microelectromechanical systems, in The Handbook of MEMS, M. Gad-el-Hak (Ed.), CRC Press, London (2002).
[3] G. Davis, Properties and Growth of Diamond, INSPEC, London (1994).
[4] M. H. Nazare, A. J. Neves, Properties, Growth and Applications of Diamond, INSPEC, London (2000).
[5] C. Nebel, J. Ristein, Thin-Film Diamond I, Elsevier, San Diego (2003).
[6] C. Nebel, J. Ristein, Thin-Film Diamond II, Elsevier, San Diego (2003).
[7] K. Kobashi, Diamond Films, Elsevier, Oxford (2005).
[8] B. Dischler, C. Wild, Low-Pressure Synthetic Diamond: Manufacturing and Applications, Springer, Berlin (1998).
[9] E. Kohn, P. Gluche, M. Adamschik, *Diam. Rel. Mat.* **8** (1999) 934–940.
[10] O. Auciello, S. Pacheco, A. V. Sumant, C. Gudeman, S. Sampath, A. Datta, R. W. Carpick, V. P. Adiga, P. Zurcher, Z. Ma, H-C. Yuan, J. A. Carlisle, B. Kabius, J. Hiller, S. Srinivasan, *IEEE Microwave Magazine* Dec. (2007) 61–75.

[11] J. K. Luo, Y. Q. Fu, H. R. Le, J. A. Williams, S. M. Spearing, W. I. Milne, *J. Micromech. Microeng.* **17** (2007) S147–S163.

[12] E. Kohn, M. Adamschik, P. Schmid, A. Denisenko, A. Aleksov, W. Ebert, *J. Phys. D: Appl. Phys.* **34** (2001) R77–R85.

[13] O. Auciello, J. Birell, J. A. Carlisle, J. E. Gerbi, X. Xiao, B. Peng, H. D. Espinosa, *J. Phys.: Condens. Mat.* **16** (2004) R539–R552.

[14] E. Kohn, M. Adamschik, P. Schmid, S. Ertl, A. Flöter, *Sixth Applied Diamond Conference/Second Frontier Carbon Technology Joint Conference* (ADC/FCT, 2001), Proceedings, pp. 90–97.

[15] M. Werner, G. Grötz, H. Möller, M. Eickhoff, P. Gluche, M. Adamschik, C. Johnston, P. R. Chalker, *Sensors Update* **5** (1), (2001), 141–190.

[16] J. Kusterer, P. Schmid, E. Kohn, *New Diamond and Frontier Carbon Technology* **16** (6) (2006) 295–321.

[17] E. Kohn, in *Harsh Environment Materials in Comprehensive Microsystems*, Y. Gianchandani, O. Tabata, H. Zappe (Eds), Elsevier (2007). 131–181

[18] A. Munding, B. Benkhart, A. Kaiser, E. Kohn, Cu/Sn solid–liquid interdiffusion bonding, in *Wafer Level 3-D ICs Process Technology*, C. S. Tan, J. R. Gutmann, L. R. Reif (Eds), Springer, Berlin (2008) in press 131–169.

[19] S. Kumar, P. Ravindranathan, H.S. Dewan, R. Roy, *Diam. Rel. Mat.* **5** (1996), 1246–1248.

[20] M. B. Assouar, O. Elmazria, P. Kirsch, P. Alnot, V. Mortet, C. Tiusan, *J. Appl. Phys.* **101** (2007), 114507–1 to 114507–5.

[21] B. Paci, A. Generosi, V. R. Albertini, M. Benetti, D. Cannatà, F. Di Pietrantonio, E. Verona, *Sens & Act. A* **137** (2007), 279–286.

[22] M. B. Assouar, F. Bénédic, O. Elmazria, M. Belmahi, R. J. Riobóo, P. Alnot, *Diam. Rel. Mat.* **10** (2001) 681–685.

[23] M. El Hakiki, O. Elmazria, F. Bénédic, P. Nicolay, D. Monéger, R. Azouani, *Diam. Rel. Mat.* **16** (2007) 966–969.

[24] V. Mortet, O. Elmazria, M. Nesládek, M. El Hakiki, G. Vanhoyland, J. D'Haen, M. D'Olieslaeger, P. Alnot, *Phys. Stat. Sol. (a)* **199** (2003) 145–150.

[25] P. Kirsch, M. B, Assouar, O. Elmazria, *Appl. Phys. Lett.* **88** (2006) 223504–1 to 223504–3.

[26] L. Le Brizoual, T. Lamara, F. Sarry, M. Belmahi, O. Elmazria, J. Bougdira, M. Remy, P. Alnot, *Phys. Stat. Sol (a)* **202** (2006) 2217–2223.

[27] S. Bensmaine, L. Le Brizoual, O. Elmazria, J.J. Fundenberger, M. Belmahi, B. Benyoucef, SAW devices based on ZnO inclined c-axis on diamond, *Diam. Rel. Mat.* (in press).

[28] L. A. Francis, W. Pan, C. Geuens, A. Kromka, H. A. C. Tilmans, D. Steinmüller-Nethl, C. Van Hoof, *16th MicroMechanics Europe Workshop MME* (2005), Leuven, Belgium, *Proceedings*, pp. 232–235.

[29] P. Gluche, O. Kohn, M. Binder, W. Ebert, A. Vescan, E. Rohrer, C. E. Nebel, E. Kohn, *Proceedings of the 16th IEEE/Cornell Conference on Advanced Concepts in High–Speed Semiconductor Devices & Circuits*, (1997), Ithaca, NY, USA, pp. 314–321.

[30] M. Liao, Y. Koide, J. Alvarez, *Appl. Phys. Lett.* **88** (2006), 033504–1 to 033504–3.

[31] H. Kagan, *Nuclear Instruments and Methods in Physics Research Section A: Accelerators, Spectrometers, Detectors and Associated Equipment*, **546** (2005) 222–227.

[32] A. De Sio, E. Pace, G. Cinque, A. Marcelli, J. Achard, A. Tallaire, *Spectrochim. Acta Part B: Atomic Spectroscopy* **62** (2007) 558–561.

[33] J. H. Kaneko, T. Teraji, Y. Hirai, M. Shiraishi, S. Kawamura, S. Yoshizaki, T. Ito, K. Ochai, T. Nishitani, T. Sawamura, *Review of Scientific Instruments* **75** (2004) 3581–3584.

[34] A. Fujishima, Y. Einaga, T. N. Rao, D. A. Tryk, *Diamond Electrochemistry*, Elsevier, Amsterdam (2005).

[35] A. Denisenko, C. Pietzka, A. Romanyuk, H. El-Hajj, E. Kohn, *J. Appl. Phys.* **103** (2008) 014904–1 to 014904–8.

[36] A. Kraft, *Int. J. Electrochem. Sci.* **2** (2007) 355–385.

[37] D. A. Tryk, H. Tachibana, H. Inoue, A. Fujishima, *Diam. Rel. Mat.* **16** (2007) 881–887.

[38] F. Hernandez, A. Denisenko, E. Kohn, *Diam. Rel. Mat.* **16** (2007) 867–871.

[39] A, Denisenko, G. Jamornmarn, H. El-Hajj, E. Kohn, *Diam. Rel. Mat.* **16** (2007) 905–910.

[40] M. Dipalo, C. Pietzka, A. Denisenko, H. El-Hajj, E. Kohn, O-terminated nano-diamond ISFET for applications in harsh environment, *18th Conference on Diamond, Diamond–like Materials, Carbon Nanotubes, and Nitrides*, 9–14 September (2007), Berlin, Germany.

[41] J. A. Garrido, A. Härtl, S. Kuch, M. Stutzmann, O. A. Williams, R. B. Jackman, *Appl. Phys. Lett.* **86** (2005), 073504–1 to 073504–3.

[42] B. Rezek, D. Shin, H. Watanabe, C. E. Nebel, *Sens & Act. B* **122** (2007) 596–599.

[43] P. R. Chalker, C. J. Johnston, M. Werner, *Semicond. Sci. Technol.* **18** (2003) S113–S116.

[44] M. Dipalo, J. Kusterer, K. Janischowsky, E. Kohn, *Phys. Stat. Sol. (a)* **203** (2006) 3036–3041.

[45] T. H. Borst, O. Weis, *Phys. Stat. Sol. (a)* **154** (1996) 423–444.

[46] A. Deneuville, C. Baron, S. Ghodbane, C. Agnès, *Diam. Rel. Mat.* **16** (2007) 915–920.

[47] A. T. Collins, *Semicond. Sci. Technol.* **4** (1989) 605–611.

[48] S. Bhattacharyya, O. Auciello, J. Birrell, J. A. Carlisle, L. A. Curtiss, A. N. Goyette, D. M. Gruen, A. R. Krauss, J. Schlueter, A. Sumant, P. Zapol, *Appl. Phys. Lett.* **79** (2001) 1441–1443.

[49] S. Bhattacharyya, *Phys. Rev. B* **70** (2004) 125412 to 1125412–10.

[50] T. Zimmermann, K. Janischowsky, A. Denisenko, F. J. Hernández Guillén, M. Kubovic, D. M. Gruen, E. Kohn, *Diam. Rel. Mat.* **15** (2006) 203–206.

[51] T. Zimmermann, M. Kubovic, A. Denisenko, K. Janischowsky, O.A. Williams, D.M. Gruen, E. Kohn, *Diam. Rel. Mat.* **14** (2005) 416–420.

[52] A. Kaiser, M. Hintz, M. Adamschik, P. Schmid, R. Müller, C. Maier, H. Brugger, E. P. Hofer, H. Seliger, E. Kohn, Diamond based injection system for spotting and synthesis in biochemistry, *AICHE Annual Meeting, Symposium Sensor Technology*, November (2002), Indianapolis, USA, *Proceedings* 175185.

[53] P. Gluche, R. Leuner, A. Vescan, W. Ebert, E. Kohn, C. Rembe, S. aus der Wiesche, E. P. Hofer, *Microsystem Technologies* **5** (1998) 38–43.

[54] M. Aslam, G. S. Yang, A. Masood, *Sens. & Act. A* **45** (1994) 131–137.

[55] E. Klugmann, M. Polowczyk, *Mat. Res. Innovat.* **4** (2000) 45–48.

[56] R. Sauer, *Cryst. Res. Technol.* **34** (1999) 227–241.

[57] H. J. De Los Santos, G. Fischer, H. A. C. Tilmans, J. T. M. van Beek, *IEEE Microwave Magazine* Dec. (2004) 36–49.

[58] K. E. Petersen, *IEEE Trans. Electr. Dev.* **25** (1978) 1241–1249.

[59] M. Adamschik, *PhD thesis*, University of Ulm, Germany (2001).

[60] M. Adamschik, P. Schmid, S. Ertl, P. Gluche, A. Flöter, E. Kohn, Performance of High Speed Diamond Micro Switch, *International Conference on Micro Materials Micromat* (2000), 17–19 April (2000), Berlin.

[61] E. Kohn, M. Adamschik, P. Schmid, S. Ertl, A. Flöter, *Diam. Rel. Mat.* **10** (2001) 1684–1691.

[62] P. Schmid, M. Adamschik, S. Ertl, E. Kohn, Dynamic Performance of Diamond Microswitches, *EURO–DINAME '99, Ulm Research Conferences*, 11–16 July (1999), Schloss Reisensburg (Günzburg), Germany, *Proceedings* 179–185.

[63] Q.–M. Wang, Q. Zhang, B. Xu, R. Liu, L.E. Cross, *J. Appl. Phys.* **86** (1999) 3352–3360.

[64] P. Schmid, *PhD thesis*, University of Ulm, Germany (2006)

[65] Q.–M. Wang, L. E. Cross, *Ferroelectrics* **215** (1998) 187–213

[66] M. Adamschik, R. Müller, P. Gluche, A. Flöter, W. Limmer, R. Sauer, E. Kohn, *Diam. Rel. Mat.* **10** (2001) 1670–1675.

[67] M. Werner, P. Gluche, M. Adamschik, E. Kohn, H.–J. Fecht, Review on Diamond Based Piezoresistive Sensors, *IEEE International Symposium on Industrial Electronics*, July (1998), *Proceedings* 1 (7–10), 147–152.

[68] S. M. Sze, *Physics of Semiconductor Devices*, Wiley–Interscience, New York (1981).

[69] C. Y. Kong, W. L. Wang, K. L. Liao, S. X. Wang, L. Fang, *J. Phys.: Condens. Matter* **14** (2002) 1765–1774.

[70] Y. Tang, *PhD thesis*, Michigan State University, USA (2006).

[71] M. Aslam, I. Taher, A. Masood, M. A. Tamor, T. J. Potter, *Appl. Phys. Lett.* **60** (1992) 2923–2925.

[72] W. L. Wang, X. Jiang, K. Taube, C.-P. Klages, *J. Appl. Phys.* **82** (1997) 729–732.

[73] W. L. Wang, K. J. Liao, B. Feng, G. Sánchez, M. C. Polo, J. Esteve, *Diam. Rel. Mat.* **7** (1998) 528–532.

[74] A. Yamamoto, N. Norio, T. Takahiro, *Diam. Rel. Mat.* **16** (2007) 1670–1675.

[75] J. Stade, L. Bohatý, M. Hengst, R. B. Heimann, *Cryst. Res. Technol.* **37** (2002) 1113–1120.

[76] J. Kusterer, A. Lüker, P. Herfurth, Y. Men, W. Ebert, P. Kirby, M. O'Keefe, E. Kohn, Piezo-actuated nanodiamond cantilever technology for high-speed applications, *Diam. Rel. Mat.* **17** (2008) 1429–1433.

[77] Y. Jeon, R. Sood, L. Steyn, S.-G. Kim, Energy Harvesting MEMS Devices Based on d_{33} Mode Piezoelectric Pb((Zr, Ti)O_3 Thin Film Cantilever, *CIRP Seminar on Micro and Nano Technology*, 13–14 Nov. (2003), Copenhagen, Denmark.

[78] S. Srinivasan, J. Hiller, B. Kabius, *J. Appl. Phys.* **90** (2007) 134101–1 to 134101–3.

[79] Z. Zhong, N. P. Hung, *Mat. and Manufact. Proceedings* **15** (2000) 853–865.

[80] http://www.sekicvdsolutions.com/microwave-plasma/reactors.html

[81] T. Hara, T. Yoshitake, T. Fukugawa, L. Yun Zhu, M. Itakura, N. Kuwano, Y. Tomokiyo, K. Nagayama, *Diam. Rel. Mat.* **13** (2004) 679–683.

[82] O. A. Williams, M. Nesládek, *Phys. Stat. Sol. (a)* **203** (2006) 3375–3386.

[83] A. R. Krauss, O. Auciello, D. M. Gruen, A. Jayatissa, A. Sumant, J. Tucek, D. C. Mancini, N. Moldovan, A. Erdemir, D. Ersoy, M. N. Gardos, H. G. Busmann, E. M. Meyer, M. Q. Ding, *Diam. Rel. Mat.* **10** (2001) 1952–1961.

[84] Y. Avigal, A. Hoffman, *Diam. Rel. Mat.* **8** (1999) 127–131.

[85] H. Liu, D. S. Dandy, *Diam. Rel. Mat.* **4** (1995) 1173–1188.

[86] S. S. Rotter, Growth of conformal thin diamond films by CVD for coating application, *Appl. Diamond Conf./Frontier Carbon TechnologiesADC/FCT* 99, Tokyo, Japan, *Proceedings* 2527.

[87] A. V. Sumant, P. U. D. A. Gilbert, D. S. Grierson, A. R. Konicek, M. Albrecht, J. E. Butler, T. Feygelson, S. S. Rotter, R. W. Carpick, *Diam. Rel. Mat.* **16** (2007) 718–724.

[88] K. Janischowsky, W. Ebert, E. Kohn, *Diam. Rel. Mat.* **12** (2003) 336–339.

[89] B. W. Sheldon, R. Csencsits, J. Rankin, R. E. Boekenhauer, Y. Shigesato, *J. Appl. Phys.* **75** (1994) 5001–5008.

[90] B. R. Stoner, G.–H. M. Ma, S. D. Wolter, J. T. Glass, *Phys. Rev. B* **45** (1992) 11067–11092.

[91] R. C. Hyer, M. Green, K. K. Mishra, S. C. Sharma, *J. Mat. Sci. Lett.* **10** (1995) 515–518.

[92] S.-M. Huang, H.-C. Hsu, M.-S. You, F. C.-N. Hong, *Diam. Rel. Mat.* **15** (2006) 22–28.

[93] A. Flöter, H. Güttler, G. Schulz, D. Steinbach, C. Lutz–Elsner, R. Zachai, A. Bergmaier, G. Dollinger, *Diam. Rel. Mat.* **7** (1998) 283–288.

[94] Y. von Kaenel, J. Stiegler, J. Michler, E. Blank, *J. Appl. Phys.* **81** (1997) 1726–1736.

[95] P. Bernhard, C. Ziethen, G. Schönhense, M. Schreck, T. Bauer, S. Gsell, B. Stritzker, *Jpn. J. Appl. Phys.* **45** (2006) L984–L986.

[96] J. C. Arnault, G. Schull, M. Mermoux, B. Marcus, A. Crisci, R. Polini, *Phys. Stat. Sol. (a)* **202** (2005) 2073–2078.

[97] J. C. Arnault, F. Vonau, J. Faerber, J. Arabski, G. Schmerber, F. Wyczisk, P. Legagneux, *Phys. Stat. Sol. (a)* **199** (2003) 27–32.

[98] G. F. Zhang, V. Buck, *Surf. Coat. Techn.* **160** (2002) 14–19.

[99] P. W. May, *Phil. Trans. R. Soc. Lond. A* **358** (2000) 473–495.

[100] M. Werner, R. Locher, *Rep. Prog. Phys.* **61** (1998) 1665–1710.

[101] T. Hara, T. Yoshitake, T. Fukugawa, L. Yun Zhu, M. Itakura, N. Kuwano, Y. Tomokiyo, K. Nagayama, *Diam. Rel. Mat.* **13** (2004) 622–626.

[102] M. H. Loh, M. A. Cappelli, *Diam. Rel. Mat.* **2** (1993) 454–461.

[103] W. Tang, J. Liu, T. Huang, F. Lu, *Diam. Rel. Mat.* **10** (2001) 327–331.

[104] J. E. Gerbi, J. Birell, M. Sardela, J. A. Carlisle, *Thin Solid Films* **473** (2005) 41–48.

[105] S. Jiao, A. Sumant, M. A. Kirk, D. M. Gruen, A. R. Krauss, O. Auciello, *J. Appl. Phys.* **90** (2001) 118–122.

[106] C. J. Tang, A. J. Neves, A. J. S. Fernandes, J. Grácio, M. C. Carmo, *J. Phys.: Condens. Matter* **19** (2007) 386236–1 to 386236–9.

[107] E. J. Corat, V. J. Trava-Airoldi, N. F. Leite, M. C. A. Nono, V. Baranauskas, *J. Mat. Science* **32** (1997) 941–947.

[108] C. J. Tang, A. J. Neves, S. Pereira, A. J. S. Fernandes, J. Grácio, M. C. Carmo, *Diam. Rel. Mat.* **17** (2008) 72–78.

[109] J. T. Paci, T. Belytschko, G. C. Schatz, *Phys. Rev. B* **74** (2006), 184112–1 to 184112–9.

[110] C. Wild, R. Kohl, N. Herres, W. Müller-Sebert, P. Koidl, *Diam. Rel. Mat.* **3** (1994) 371–381.

[111] T. Kondo, H. Ito, K. Kusakabe, K. Ohkawa, Y. Einaga, A. Fujishima, T. Kawai, *Electrochem. Acta* **52** (2007) 3841–3848.

[112] L. Ostrovskaya, V. Perevertailo, V. Ralchenko, A. Dementjev, O. Loginova, *Diam. Rel. Mat.* **11** (2002) 845–850.

[113] T. Kondo, H. Ito, K. Kusakabe, K. Ohkawa, K. Honda, Y. Einaga, A. Fujishima, T. Kawai, *Diam. Rel. Mat.* **17** (2008) 48–54.

[114] D. Petrini, *PhD thesis*, Uppsala Universitet, Sweden (2007).

[115] C. G. Specht, R. Schoepfer, O. A. Williams, R. B. Jackman, *Biomaterials* **25** (2004) 40734078.

[116] C. Haosheng, L. Jiang, L. Fengbin, C. Darong, W. Jiadao, *Wear* **264** (2008) 146–151.

[117] C. A. Mead, W. G. Spitzer, *Phys. Rev.* **134** (1964) A713 – A716.

[118] Y. G. Chen, M. Ogura, H. Okushi, *Appl. Phys. Lett.* **82** (2003) 4367–4369.

[119] J. E. Butler, M. W. Geis, K. E. Krohn, J. Lawless Jr., S. Deneault, T. M. Lyszczarz, D. Flechtner, R. Wright, *Semicond. Sci. Technol.* **18** (2003) S67–S71.

[120] D. A. Evans, O. R. Roberts, A. R. Vearey-Roberts, D. P. Langsteff, *Appl. Phys. Lett.* **91** (2007) 132114–1 to 132114–3.

[121] P. K. Baumann, R. J. Nemanich, *Phys. Rev. B* **58** (1998) 1643–1654.

[122] S. C. Erwin, W. E. Pickett, *Solid State Communications* **81** (1992) 891–894.

[123] M. Werner, *Semicond. Sci. Technol.* **18** (2003) S41–S46.

[124] M. Werner, C. Johnston, P. R. Chalker, S. Romani, I. M. Buckley-Golder, *J. Appl. Phys.* **79** (1996) 2535–2541.

[125] A. Vescan, I. Daumiller, P. Gluche, W. Ebert, E. Kohn, *Diam. Rel. Mat.* **7** (1998) 581–584.

[126] C. A. Klein, G. F. Cardinale, *Diam. Rel. Mat.* **2** (1993) 918–923.

[127] J. P. Hess, P. Hess, T. Feygelson, J. E. Butler, S. Chattopadhyay, K. H. Chen, L. C. Chen, *J. Appl. Phys.* **93** (2003) 2164–2171.

[128] H. D. Espinosa, B. Peng, *J. Microelectromech. Sys.* **14** (2005) 153–159.

[129] M. Werner, S. Klose, F. Szücs, Ch. Moelle, H. J. Fecht, C. Johnston, P. R. Chalker, I. M. Buckley-Golder, *Diam. Rel. Mat.* **6** (1997) 344–347.

[130] F. Szuecs, M. Werner, R. S. Sussmann, C. S. J. Pickles, H. J. Fecht, *J. Appl. Phys.* **86** (1999) 6010–6017.

[131] P. Gluche, M. Adamschik, A. Vescan, W. Ebert, F. Szücs, H. J. Fecht, A. Flöter, R. Zachai, E. Kohn, *Diam. Rel. Mat.* **7** (1998) 779–782.

[132] J. Kusterer, E. Kohn, A. Lüker, P. Kirby, M. F. O'Keefe, Diamond high speed and high power MEMS switches, *4th EMRS DTC Technical Conference* (2007), Edinburgh, UK, *Proceedings* A1.

[133] P. Hess, *Appl. Surf. Sci.* **106** (1996) 429–437.

[134] J. Michler, M. Mermoux, Y. von Kaenel, A. Haouni, G. Lucazeau, E. Blamk, *Thin Solid Films* **357** (1999) 189–201.

[135] N. G. Ferreira, E. Abramof, E. J. Corat, N. F. Leite, V. J. Trava-Airoldi, *Diam. Rel. Mat.* **10** (2001) 750–754.

[136] Q. H. Fan, A. Fernandes, E. Pereira, J. Grácio, *J. Appl. Phys.* **84** (1998) 2989–3428.

[137] T. R. Anthony, *Diam. Rel. Mat.* **4** (1995) 1346–1352.

[138] C. T. Kuo, C. R. Lin, H. M. Lien, *Thin Solid Films* **290–291** (1996) 254–259.

[139] J. K. Krüger, J. P. Embs, S. Lukas, U. Hartmann, C. J. Brierley, C. M. Beck, R. Jiménez, P. Alnot, O. Durand, *J. Appl. Phys.* **87** (1) (2001) 74–77.

[140] H. Li, B. W. Sheldon, A. Kothari, Z. Ban, B. L. Walden, *J. Appl. Phys.* **100**, 094309–1 to 094309–9.

[141] F. J. Hernández Guillén, K. Janischowsky, J. Kusterer, W. Ebert, E. Kohn, *Diam. Rel. Mat.* **14** (2005) 411–415.

[142] F. J. Hernández Guillén, K. Janischowsky, W. Ebert, E. Kohn, *Phys. Stat. Sol. (a)* **201** (2004) 2553–2557.

[143] J. Zhang, J. W. Zimmer, R. T. Howe, R. Maboudian, *Diam. Rel. Mat.* **17** (2008) 23–28.

[144] H. Guckel, T. Randazzo, D. W. Burns, *J. Appl. Phys.* **57** (1985) 1671–1675.

[145] B. P. van Drieënhuizen, J. F. L. Goosen, P. J. French, R. F. Wolffenbuttel, *Sens. & Act.* **37–38** (1993) 756–765.

[146] E. H. Yang, S. S. Yang, A new technique for quantitative determination of the stress profile along the depth of p^+ silicon films, *The 8th International Conference on Solid–State Sensors and Actuators, and Eurosensors IX*, 25–29 June (1995), Stockholm, Sweden, *Proceedings* pp. 68–71.

[147] J. E. Field, The Properties of Diamond, Academic Press, London (1979).

[148] H. D. Espinosa, B. Peng, B. C. Prorok, N. Moldovan, O. Auciello, J. A. Carlisle, D. M. Gruen, D. C. Mancini, *J. Appl. Phys.* **94** (2003) 6076–6084.

[149] H. Kapels, R. Aigner, J. Binder, *IEEE Trans. Electr. Dev.* **47** (2000) 1522–1528.

[150] K. M. Jackson, J. Dunning, C. A. Zorman, W. N. Sharpe, *J. Microelectromech. Sys.* **14** (2005) 664–672.

[151] W. Zhou, J. Yang, G. Sun, X. Liu, F. Yang, J. Li, *J. Microelectromech. Sys.* **17** (2008) 453–461.

[152] S. R. Agnew, B. R. Elliott, C. J. Youngdahl, K. J. Hemker, J. R. Weertman, *Mater. Sci. Eng. A* **285** (2000) 391–396.

[153] F. X. Lu, Z. Jiang, W. Z. Tang, T. B. Huang, J. M. Liu, *Diam. Rel. Mat.* **10** (2001) 770–774.

[154] S. Barman, G. Srivistava, *J. Appl. Phys.* **101** (2007) 123507–1 to 123507–8.

[155] W. L. Liu, M. Shamsa, I. Calizo, A.A. Balandin, R. Ralchenko, A. Popovich, A. Saveliev, *Appl. Phys. Lett.* **89** (2006), 171915–1 to 171915–3.

[156] D. G. Cahill, R. O. Pohl, *Phys. Rev. B* **35** (8) (1987) 4067–4073.

[157] J. H. Kim, A. Feldman, D. Novotny, *J. Appl. Phys.* **86** (1999) 3959–3963.

[158] S. Ahmed, R. Liske, T. Wunderer, M. Leonhardt, R. Ziervogel, C. Fansler, T. Grotjohn, J. Asmussen, T. Schuelke, *Diam. Rel. Mat.* **15** (2006) 389–393.

[159] G. F. Ding, H. P. Mao, Y. L. Cai, Y. H. Zhang, X. Yao, X. L. Zhao, *Diam. Rel. Mat.* **14** (2005) 1543–1548.

[160] T. Yamada, H. Yoshikawa, H. Uetsuka, S. Kumaragurubaran, N. Tokuda, S.-I. Shikata, *Diam. Rel. Mat.* **16** (2007) 996–999.

[161] J. W. Baldwin, M. K. Zalalutdinov, T. Feygelson, B. B. Pate, J. E. Butler, B. H. Houston, *Diam. Rel. Mat.* **15** (2006) 2061–2067.

[162] http://www.axinst.com

[163] J. Enlund, J. Isberg, M. Karlsson, F. Nikolajeff, J. Olsson, D. J. Twitchen, *Carbon* **43** (2005) 1839–1842.

[164] D. S. Hwang, T. Saito, N. Fujimori, *Diam. Rel. Mat.* **13** (2004) 2207–2210.

[165] A. Stanishevsky, *Thin Solid Films* **398–399** (2001) 560–565.

[166] P. Olivero, S. Rubanov, P. Reichart, B. C. Gibson, S. T. Huntington, J. Rabeau, A. D. Greentree, J. Salzman, D. Moore, D. N. Jamieson, S. Prawer, *Adv. Mater.* **17** (20) (2005) 2427–2430.

[167] P. Olivero, S. Rubanov, P. Reichart, B. C. Gibson, S. T. Huntington, J. Rabeau, A. D. Greentree, J. Salzman, D. Moore, D. N. Jamieson, S. Prawer, *Diam. Rel. Mat.* **15** (2006) 1614–1621.

[168] C. F. Wang, E. L. Hu, J. Yang, J. E. Butler, *J. Vac. Sci. Technol. B* **25** (2007) 730–733.

[169] R. Ramesham, *Thin Solid Films* **340** (1999) 1–6.

[170] Y. Fu, H. Du, J. Miao, *J. Mat. Proc.Technol.* **132** (2003) 73–81.

[171] J. Andersson, *PhD thesis*, Uppsala University, Sweden (2004).

[172] H. Björkman, R. Rangsten, P. Hollman, K. Hjort, *Sens. & Act.* **73** (1999) 24–29.

[173] T. Takida, K. Inoue, S.G. Ri, H. Kimura, H. Kiyota, I. Saito, T. Kurosu, M. Iida, *Jpn. J. Appl. Phys.* **9** (2000) L56–L58.

[174] T. Shibata, Y. Kitamoto, K. Unno, E. Makino, *J. Microelectromech. Sys.* **9** (2000) 47–51.

[175] K.-H. Kim, N. Moldovan, C. Ke, H. D. Espinosa, X. Xiao, J. A. Carlisle, O. Auciello, *small* **1** (2005) 866–874.

[176] http://www.thindiamond.com/NaDiaProbes.asp, brochure NaDiaProbe$^{\text{TM}}$.

[177] A. Olbrich, B. Ebersberger, C. Boit, Ph. Niedermann, W. Hänni, J. Vancea, H. Hoffmann, *J. Vac. Sci. Technol. B* **17** (1999) 1570–1574.

[178] M. Adamschik, P. Schmid, S. Ertl, W. Ebert, N. Käb, E. Kohn, CVD-diamond for high temperature MEMS applications – first example: diamond micro switch, *5th International High Temperature Conference (HiTEC)*, 12–15 June (2000), Albuquerque, NM, USA, *Proceedings*.

[179] H. Björkman, P. Rangsten, K. Hjort, *Sens. & Act.* **78** (1999) 41–47.

[180] R. Müller, R. Gronmaier, K. Janischowsky, J. Kusterer, E. Kohn, *Diam. Rel. Mat.* **14** (2005) 504–508.

[181] X. Xiao, J. Birrell, J. E. Gerbi, O. Auciello, J. A. Carlisle, *J. Appl. Phys.* **96** (2004) 2232–2239.

[182] A. Kaiser, D. Kueck, P. Benkhart, A. Munding, G. M. Prinz, A. Heittmann, H. Huebner, R. Sauer, E. Kohn, *Diam. Rel. Mat.* **15** (2006) 1967–1971.

[183] H. Hübner, O. Ehrmann, M. Eigner, W. Gruber, A. Klumpp, R. Merkel, P. Ramm, M. Roth, J. Weber, R. Wieland, Face-to-face chip integration with full metal interface, *Advanced Metallization Conference, AMC* (2002), San Diego, CA, USA, MRS *Proceedings* 18, 5358.

[184] A. Munding, *PhD thesis*, University of Ulm, Germany (2007).

[185] A. Kaiser, *PhD thesis*, University of Ulm, Germany (2007).

[186] P. Benkhart, *PhD thesis*, University of Ulm (2008).

[187] R. S. Okojie, G. M. Benheim, G. J. Saad, E. Savrun, Characteristics of a hermetic 6HSiC pressure sensor at 600 °C, *AIAA Space (2001) Conference and Exposition*, Albuquerque, NM, USA, Abstract AIAA (2001)–4652 August (2001), 1–8.

[188] L. Cheng, M. Pan, J. Scofield, A. J. Steckl, *J. Electr. Mat.* **31** (2002) 361–365.

[189] M. Mehregany, C. A. Zorman, *Thin Solid Films* **355–356** (1999) 518524.

[190] E. Kohn, W. Ebert, M. Adamschik, P. Schmid, A. Denisenko, *New. Diam. Front. Carbon Technol.* **11** (2001) 81–100.

[191] M. Adamschik, P. Gluche, A. Flöter, W. Ebert, E. Kohn, The potential of CVD–diamond films for sensor and actuator applications, *9th International Trade Fair and Conference for Sensors Transducers and Systems*, 18–20 May (1999), Nuremberg, Germany, *Proceedings* 287–292.

[192] P. R. Chalker, C. Johnston, *Phys. Stat. Sol. (a)* **154** (1996) 455–466.

[193] D. R. Wur, J. L. Davidson, *J. Microelectromech. Sys.* **4** (1995) 34–41.

[194] V. Mortet, K. Haenen, J. Potmesil, M. Vanecek, M. D'Olieslaeger, *Phys. Stat. Sol. (a)* **203** (2006) 3185–3190.

[195] Ph. Niedermann, W. Hänni, N. Blanc, R. Christoph, J. Burger, *J. Vac. Sci. Techn. A* **14** (1996) 1233–1236.

[196] A. Malavé, E. Oesterschulze, W. Kulisch, T. Trenkler, T. Hantschel, W. Vandervorst, *Diam. Rel. Mat.* **8** (1999) 283–287.

[197] E. Oesterschulze, A. Malavé, U. F. Keyser, M. Paslaer, R. J. Haug, *Diam. Rel. Mat.* **11** (2002) 667–671.

[198] Y. Gurbuz, O. Esame, I. Tekin, W. P. Kang, J. L. Davidson, *Solid-State Electronics* **49** (2005) 1055–1070.

[199] A. Aleksov, M. Kubovic, M. Kasu, P. Schmid, D. Grobe, S. Ertl, M. Schreck, B. Stritzker, E. Kohn, *Diam. Rel. Mat.* **13** (2004) 233–240.

[200] E. Kohn, A. Aleksov, M. Kubovic, P. Schmid, J. Kusterer, M. Schreck, M. Kasu, A new material base for future ultra high power RF electronics, *The International Conference on Compound Semiconductor Manufacturing Technology*, (2004), *Proceedings* 2.5.

[201] P. Schmid, D. Grobe, J. Kusterer, A. Adamschik, S. Ertl, A. Flöter, C. Warns, W. Menzel, E. Kohn, An investigation into diamond for microwave applications, *Modern Technique and Technology Conference MTT* (2002). *8th International Scientific and Practical Conference of Students, Post-graduates and Young Scientists*, May (2002), *Proceedings*.

[202] N. Sepulveda, D. Aslam, J. P. Sullivan, *Diam. Rel. Mat.* **15** (2006) 398–403.

[203] N. Sepulveda, *PhD thesis*, Michigan State University, East Lansing, MI, USA (2005).

[204] G. Palasantzas, *J. Appl. Phys.* **103** (2008) 046106–1 to 046106–3.

[205] J. Wang, J. E. Butler, T. Feygelson, C. T.-C. Nguyen, 1.51 GHz polydiamond micromechanical disk resonator with impedance-mismatched isolating support, *17th International IEEE Electro Mechanical Systems Conference*, 25–29 January (2004), Maastricht, The Netherlands, *Proceedings* 641–644.

[206] L. Sekaric, J. M. Parpia, H. G. Craighead, T. Feygelson, B. H. Houston, J. E. Butler, *Appl. Phys. Lett.* **81** (23) (2002) 4455–4457.

[207] L. Yan, J. Wu, W. C. Tang, Piezoelectric micromechanical disk resonators towards UHF band, *IEEE International Ultrasonics, Ferroelectrics, and Frequency Control Joint 50th Anniversary Conference*, 23–27 August (2004), Montréal, Canada. *Proceedings* 926–929.

[208] M. Adamschik, J. Kusterer, P. Schmid, K. B. Schad, D. Grobe, A. Flöter, E. Kohn, *Diam. Rel. Mat.* **11** (2002) 672–676.

[209] E. Kohn, W. Ebert, A. Aleksov, A. Denisenko, M. Adamschik, P. Schmid, Diamond technology for electronics and MEMS review of status and perspectives, *23rd International Conference on Microelectronics (MIEL 2002)*, 12–15 May (2002), Niš, Yugoslavia, *Proceedings* 59–66.

[210] P. Schmid, J. Kusterer, D. Grobe, M. Adamschik, W. Menzel, E. Kohn, Diamond MEMS technology for microwave switches, *23rd International Conference on Microelectronics (MIEL 2002)*, 12–15 May (2002), Niš, Yugoslavia, *Digest*.

[211] E. Kohn, W. Menzel, F. J. Hernandez–Guillen, R. Müller, A. Munding, P. Schmid, D. Grobe, J. Kusterer, Evaluation of CVD diamond for heavy duty microwave switches, *IEEE MTT–S International Microwave Symposium (2003)*, 8–13 June (2003), Philadelphia, PA, USA, *Digest* 1625–1628.

[212] P. Schmid, M. Adamschik, E. Kohn, *Semicond. Sci. Technol.* **18** (2003) S72–S76.

[213] J. Kusterer, *diploma thesis*, University of Ulm (2001).

[214] P. Schmid, F. J. Hernández-Guillén, E. Kohn, *Diam. Rel. Mat.* **12** (2003) 418–421.

[215] P. Schmid, F. J. Hernández–Guillén, E. Kohn, Simulation of a diamond-based bistable thermal microswitch, *2003 Nanotechnology Conference and Trade Show Nanotech* (2003), 23–27 February, San Francisco, CA, USA, *Proceedings* 380–383.

[216] R. Müller, P. Schmid, A. Munding, F. J. Hernández–Guillen, E. Kohn, Bi-stable thermal actuators based on CVD diamond, *Seventh Applied Diamond Conference/Third Frontier Carbon Technology Joint Conference (ADC/FCT 2003)*, 18–21 August (2003), Tsukuba, Japan, *Proceedings*.

[217] J. Kusterer, S. Haroon, E. Kohn, Bi-stable diamond-bridge actuator, *Microsystem Technologies MST (2005)*, 5–6 October (2005), Munich, Germany, *Proceedings*.

[218] J. Kusterer, F. J. Hernández-Guillén, S. Haroon, P. Schmid, A. Munding, R. Müller, E. Kohn, *Diam. Rel. Mat.* **15** (2006) 773–776.

[219] J. Kusterer, S. Balachandran, D. Maier, M. Dipalo, R. Connick, T. M. Weller, E. Kohn, Nanodiamond microbridges for RF applications, *2nd International Diamond Conference*, 19–20 April (2007), Rom, Italy, *Proceedings* A.5.3.

[220] S. Balachandran, J. Kusterer, R. Connick, T. M. Weller, D. Maier, M. Dipalo, E. Kohn, Thermally actuated nanocrystalline diamond micro-bridges for microwave and high power RF applications, *IEEE MTT–S International Microwave Symposium (2007)*, 3–8 June (2007), Honolulu, HI, USA, *Proceedings*.

[221] J. G. Felbinger, M. V. S. Chandra, Y. Sun, L. F. Eastman, J. Wasserbauer, D. Babic, D. Francis, F. Ejeckam, *IEEE Electr. Dev. Lett.* **28** (2007) 948–950.

[222] A. Kaiser, K. Ruess, B. Holl, J. Vanselow, E. Feurer, J. Kusterer, Improved thermal management in high power applications by utilizing novel 'filled vials' thin film substrate technology, *Proceedings of The 40th International Symposium on Microelectronics IMAPS (2007)*, 11–15 Nov. (2007), San Jose, CA, USA.

[223] F. Steinhagen, W. H. Haydl, T. Krems, W. Marsetz, R. Locher, C. Wild, P. Koidl, A. Hülsmann, T. v. Kressenbrock, P. Heide, *Microwave Symposium Digest* (1998) IEEE MTT–S International, pp. 1065–1068.

[224] D. Grobe, S. Ertl, E. Kohn, C. Warns, W. Menzel, *Proceedings of the 19th European Conference on Diamond, Diamond–like Materials* (2002).

[225] M. Thumm, *Int. J. Ifrared and Millimeter Waves* **19** (1998) 3–14.

[226] R. Müller, P. Schmid, A. Munding, R. Gronmaier, E. Kohn, *Diam. Rel. Mat.* **13** (2004) 780–784.

[227] R. Müller, W. Berger, K. Janischowsky, E. Kohn, All-diamond-inkjet for dispensing of aggressive liquids, *Proceedings of the (2005) Device Research Conference*, June 20–22 2005, Santa Barbara, CA, USA.

[228] J. S. Aden, J. H. Bohorquez, D. M. Collins, M. D. Crook, A. Garcia, U. E. Hess, *Hewlett–Packard Journal* Feb. (1994) 41–45.

[229] S. v. Stralen, R. Cole, *Boiling Phenomena*, Vol. **1**, McGraw–Hill, New York (1979).

[230] A. Finkel, A. Wittel, N. Yang, S. Handran, J. Hughes, J. Costantin, *Journal of Biomolecular Screening* **11** (2006) 488–496.

[231] J. Kusterer, A. Alekov, A. Pasquarelli, R. Müller, W. Ebert, F. Lehmann-Horn, E. Kohn, *Diam. Rel. Mat.* **14** (2005) 2139–2142.

[232] M. Adamschik, M. Hinz, C. Maier, P. Schmid, H. Seliger, E. P. Hofer, E. Kohn, *Diam. Rel. Mat.* **10** (2001) 722–730.

Part 6

Superconductivity in CVD Diamond

CVD Diamond for Electronic Devices and Sensors Edited by Ricardo S. Sussmann
© 2009 John Wiley & Sons, Ltd. ISBN: 978-0-470-06532-7

19 Superconductivity in Diamond

YOSHIHIKO TAKANO

National Institute for Materials Science, Tsukuba, Japan

19.1 Introduction to Superconductivity 549
19.2 Carrier Doping into Diamond 550
19.3 Insulator–Metal–Superconductor Transition in Boron-Doped Diamond 551
19.4 Growth of Superconducting Diamond 552
  19.4.1 Man-made diamond using high-pressure, high-temperature method 552
  19.4.2 Synthetic diamond using the CVD method 553
  19.4.3 Homoepitaxial (111) and (100) films 554
  19.4.4 T_C as a function of boron concentration 555
  19.4.5 Effective carrier concentration 556
19.5 Superconducting Properties 557
  19.5.1 Inelastic X-ray scattering 557
  19.5.2 X-Ray absorption spectroscopy 557
  19.5.3 Superconducting gap properties 558
19.6 Summary 560
References 560

19.1 INTRODUCTION TO SUPERCONDUCTIVITY

Superconductors exhibit three important unique phenomena: zero resistivity, the Meissner effect, and the Josephson effect. In the superconducting state, electrical current can flow without resistivity. In a solenoid made of a superconducting material, a very high current can flow and generates a very high persistent magnetic field because of zero resistivity. These superconducting magnets are employed, for example, in magnetic resonance imaging (MRI), magnetic levitation trains and cyclotrons. One of the expected future applications is in the superconducting computer. The switching devices using superconductors are Josephson junctions, which can be assigned to the diode and transistor in semiconductors. Superconducting computers can calculate very rapidly and their energy consumption is expected to be very low.

CVD Diamond for Electronic Devices and Sensors Edited by Ricardo S. Sussmann
© 2009 John Wiley & Sons, Ltd.
ISBN: 978-0-470-06532-7

I would like to give a short account of the history of superconductivity. In 1911, superconductivity was discovered by Heike Kamerlingh Onnes at Leiden University [1]. He found the zero resistivity in mercury when the sample was cooled to below 4.2 K using liquid helium, since he had succeeded in liquefying helium gas in 1908. After this discovery, many superconductors were found in other pure metals. The highest superconducting transition temperature T_C among them is 9.2 K for niobium.

In 1957, Bardeen, Cooper and Schrieffer postulated the BCS theory that explains the mechanism of superconductivity [2]. The phonon induces an attractive force between two electrons and makes a Cooper pair. According to the McMillan equation, T_C is proportional to the Debye temperature [3]. Materials that have a high Debye temperature are strong candidates for superconductors with a high transition temperature T_C.

In 1986, Johannes Georg Bednorz and Karl Alexander Müller discovered a high-T_C superconductor in the perovskite cuprate of LaBaCuO system [4]. Soon after this discovery, superconducting temperatures were found to increase dramatically in new high-T_C superconductors, i.e. $YBa_2Cu_3O_{7-d}$ with $T_C \sim 90$ K, above liquid nitrogen temperature, and $Bi_2Sr_2Ca_2Cu_3O_{10}$ with $T_C \sim 110$ K. The highest T_c is currently 135 K, that of mercury-based perovskite cuprate $HgBa_2Ca_2Cu_3O_y$. Since the discovery of mercury-based high-T_C superconductors, the record T_C has not been broken. Superconductivity started with mercury and the currently highest T_C was achieved by mercury-based perovskite cuprates.

The dream in research on superconductivity is to find a room temperature superconductor that would be one of the key technologies in solving the world energy problem. If the world were connected with room-temperature superconducting networks, we could supply electricity without loss. It would be possible to generate electricity in a desert using solar cells during the day and send it to countries on the other side of the world during their nighttime. With such a dream, researchers working on superconductivity are making efforts to find new superconductors in new materials [5–9].

As everybody knows, diamond is the hardest material in the world. It also has the highest thermal conductivity at around room temperature, because of its remarkably high Debye temperature due to its strong phonon. This makes diamond a strong candidate for a superconductor. However, diamond is an insulator, and thus cannot superconduct. The first aim is to obtain metallic diamond by impurity doping.

19.2 CARRIER DOPING INTO DIAMOND

Pure diamond is an electrical insulator having a wide band gap of 5.5 eV between the valence band and the conduction band (see Chapter 1 by G. Davies in this book). Because of the wide gap, diamond is transparent to a wide range of light wavelengths, from IR to UV. For electrical device applications, p-type and n-type semiconducting diamonds are required.

To make diamond a p-type semiconductor, boron is doped into the diamond lattice (see Chapter 3 by Mainwood in this book). One doped boron atom corresponds to one free hole carrier in diamond, because boron has one fewer electrons than does carbon. The doped boron acts as an acceptor, and the acceptor level is 0.37 eV. Since the doping range of boron is very wide and the acceptor level is not deep, boron doping is the only method of obtaining metallic type conductivity in diamond.

By contrast, phosphorus doping makes diamond an n-type semiconductor, since the dopants act as donors and the donor level is ~0.57 eV [10]. However, metallic n-type diamonds have not been obtained, because of the narrow doping range. Boron and phosphorus doped semiconducting diamond (p–n type) is now being investigated for applications such as UV emitters and detectors (see Chapter 15 by Makino in this book).

19.3 INSULATOR–METAL–SUPERCONDUCTOR TRANSITION IN BORON-DOPED DIAMOND

With boron doping, diamond becomes a semiconductor, and shows a beautiful blue color. The conductivity increases for an increase in boron concentration. When the boron concentration increases beyond the metal–insulator transition concentration $N_B = 3.0 \times 10^{20} cm^{-3}$, diamond shows metallic properties, and the color turns black [11, 12].

It is important to characterize the electronic structure of the highly boron doped diamond to understand the mechanism of superconductivity and metal–insulator transition. Soft X-ray, angle-resolved, photoemission spectroscopy (ARPES) was performed using a photon energy of 800 eV in SPring-8, which is a large synchrotron radiation facility in Japan [13]. Band dispersions around the gamma point of homoepitaxial CVD diamond thin films with boron concentrations of $N_B = 2.88 \times 10^{20}$ cm^{-3}, $N_B = 1.18 \times 10^{21}$ cm^{-3}, and $N_B = 8.37 \times 10^{21}$ cm^{-3}are presented in Figure 19.1. Together with the band dispersion, we plotted the temperature dependence of the resistivity for each sample. The band structures of heavily boron-doped diamonds show good agreement with the curves that are the calculated energy band dispersion for pure diamond. It was found that the band structure of heavily boron-doped diamond is basically consistent with that of pure diamond.

The left-hand figure, diamond sample (a), with the lowest boron concentration of $N_B = 2.88 \times 10^{20}$ cm^{-3}, which is just below the metal–insulator transition, shows semiconductive transport properties. The top of the diamond valence band of this sample lies slightly below the Fermi level, which is not representative of metallicity.

In contrast, for the diamond (b) in the figure, which contains boron above the metal–insulator transition concentration, the energy bands of diamond shift toward the higher binding energy regions and are found to cross the Fermi level. The resistivity was suppressed significantly and dropped at a low temperature corresponding to the beginning of superconductivity.

For an increasing boron concentration, the valence band dispersion of the diamond (c), with a boron concentration of $N_B = 8.37 \times 10^{21}$ cm^{-3} shows a large shift toward the higher binding energy. The resistivity is found to decrease dramatically and the superconducting transition temperature exhibits a remarkable increase.

These results indicate that the metallicity of the boron-doped diamond is due to the underlying diamond original band structure. If the heavily boron-doped diamond were a 'conventional' superconductor, the superconductivity would originate from holes in the valence band due to the boron doping. The carrier densities for samples (b) and (c), estimated from the band dispersion, are $N = 6.6 \times 10^{20}$ cm^{-3} and $N = 1.9 \times 10^{21}$ cm^{-3}, respectively. It is noted that the carrier densities estimated from ARPES results are found to have significantly lower values compared with the boron concentrations obtained

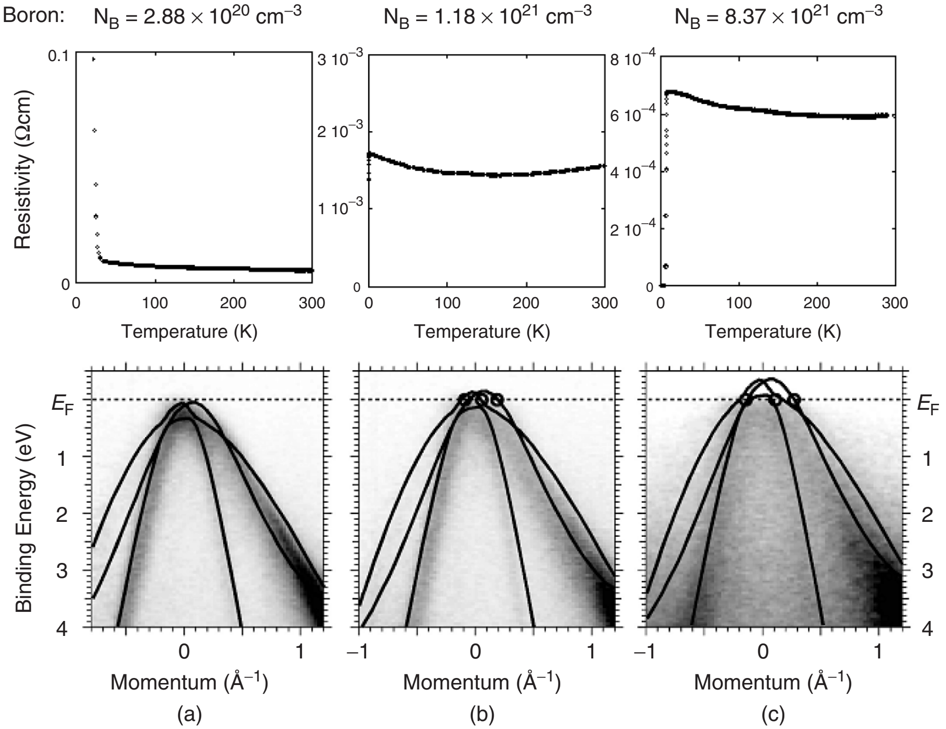

Figure 19.1 Temperature dependence of resistivity and band dispersions around the gamma point for boron doped homoepitaxial CVD-diamond thin films

from secondary-ion mass spectrometer (SIMS) measurements. This may be related to the local boron conditions. We discuss effective carrier densities and T_C in the next section.

19.4 GROWTH OF SUPERCONDUCTING DIAMOND

19.4.1 Man-made diamond using high-pressure, high-temperature method

When it was found that natural diamond was produced under high-pressure and high-temperature conditions deep in the ground, many scientists engaged in synthesizing artificial diamond using high-pressure high-temperature (HPHT) apparatus. The first success of man-made diamond was achieved by the GE company in 1955, published in *Nature* [14–16]. In this method, iron and nickel were used as metal catalysts. Seven years later, boron-doped diamond was grown using the HPHT method with a metal catalyst [17]. Applications of diamond to electrical devices were already one of the targets. However, superconducting diamond cannot be obtained using this method, since the boron concentration is not sufficient for superconductivity.

Direct conversion of graphite to diamond, using static pressure, was achieved by the GE group in 1962 [18, 19]. In the following year, boron-doped diamond was produced using the direct conversion HPHT method [20, 21]. Although high boron doping was also reported, superconductivity was not observed at that time, since it was not expected in diamond and thus the properties of diamond at low temperatures were not examined.

In 2004, the news of superconductivity in heavily boron-doped diamond synthesized using direct conversion HPHT, 8–9 GPa and 2500–2800 K for 5 s sintering, by Ekimov *et al.* was received with considerable surprise [22, 23]. Polycrystalline diamond was formed at the interface between graphite and B_4C. The sample showed zero resistivity at 2.3 K, and the upper critical field and coherence length were estimated to be 3.4 T and 10 nm. Synthesis under much higher pressure was also performed [24]. To open up new possibilities for diamond-based electrical devices, these phenomena need to be clearly investigated.

19.4.2 Synthetic diamond using the CVD method

The big news of Chemical Vapor Deposition (CVD) growth of diamond film using a hydrocarbon gas such as methane, was reported by Spitsyn *et al.* [25]. In this paper, the authors mentioned not only pure diamond but also boron-doped diamond. The CVD equipment is simpler than that for the high-pressure method, and is useful for device applications since thin films and wafer-shape diamond can only be grown using the CVD method.

To obtain high quality diamond thin films, much effort has been given to improving the CVD method, since diamond is a promising material for electronic devices. The microwave-plasma CVD method was further developed by Kamo *et al.*, who constructed a simple and sophisticated CVD system [26]. The microwave was radiated through the wave guide and the source gas mixture was introduced into the quartz tube piercing the wave guide.

The first superconducting CVD-diamond thin film was successfully made using this type of microwave plasma CVD method in 2004 [27, 28, 11, 30]. The superconducting transition temperature significantly increased as $T_{Conset} = 7.4$ K and $T_{Czero} = 4.2$ K, which were above liquid helium temperature. Detailed superconducting properties are discussed later. The heavily boron-doped polycrystalline diamond thin film was deposited on a silicon (001) substrate. Deposition was carried out under 50 Torr chamber pressure, 500 W microwave power, and 800–900°C substrate temperature, using a dilute gas mixture of methane and trimethylboron (TMB) in hydrogen. The methane concentration was 1–3 % in hydrogen with a B/C ratio of 2500–12000 ppm.

Nanocrystalline-diamond thin films with a thickness of 60–500 nm were grown using a microwave CVD system, and Raman spectra were studied. The superconducting transition temperature in these nanocrystalline diamond films is about 1.66 K [29].

The advantages of the CVD method for producing superconducting diamond are: (i) the boron concentration can be controlled over a wide range, and (ii) the diamond films can contain boron at relatively high concentrations due to the wide range of the solubility limit of boron introduced into diamond. For applications to actual devices, diamond needs to be made into the form of wafers or thin films. The only procedure currently available to this end is the low-pressure CVD synthesis process.

19.4.3 Homoepitaxial (111) and (100) films

Boron-doped homoepitaxial diamond thin films were synthesized in our group by the microwave plasma CVD method. These films were deposited on polished (111) and (100) surfaces of single-crystal HPHT synthesized Ib diamond substrates. The source gases for boron doping were hydrogen, methane, and TMB. The boron concentration was controlled by changing the mixing ratio of carbon/boron source gases.

The homoepitaxial (111) thin film was deposited under 3 % methane and 6000 ppm TMB. The boron concentration was estimated from SIMS measurements to be $N_B = 8.4 \times 10^{21}$, which corresponds to about B/C = 5 %. The temperature dependence of resistivity is plotted in Figure 19.2(a). At zero magnetic field, the resistivity is found to decrease due to the onset of superconductivity at around 11.4 K (T_{Conset}), and zero resistivity was obtained at 8.4 K (T_{Czero}), which is the highest reported value of T_{Czero} for diamond superconductivity [30–32].

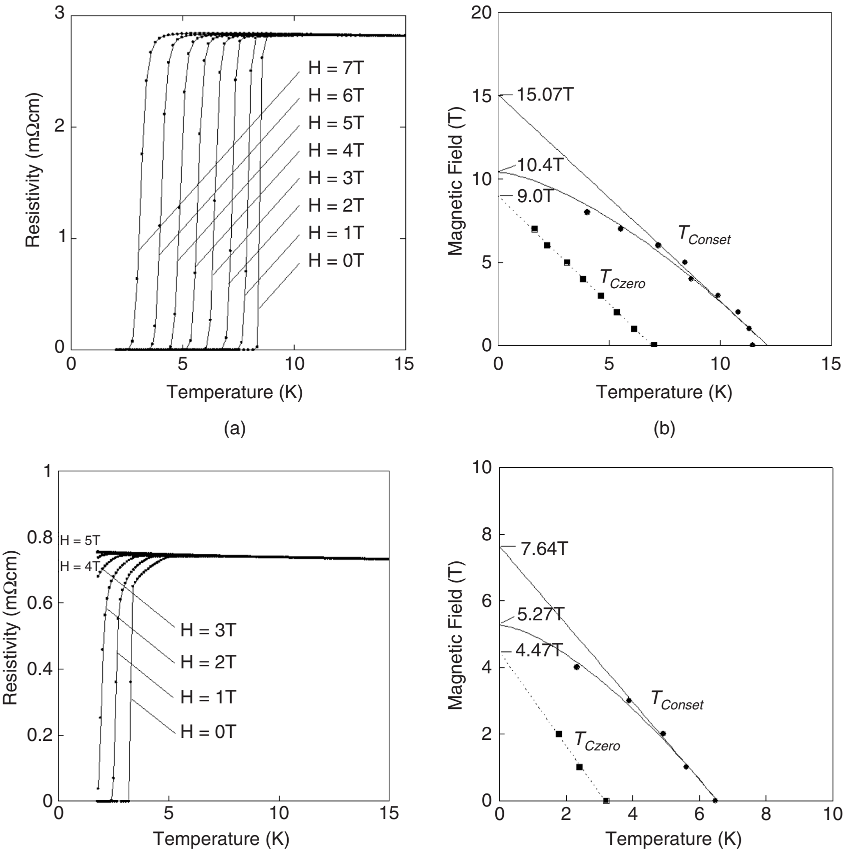

(a) (b)

(c) (d)

Figure 19.2 Superconducting properties of homoepitaxial (111) and (100) films. Temperature dependence of resistivity for homoepitaxial (111) films (a), and (100) films (c). Phase diagram of the upper critical field H_{C2} and irreversibility field H_{irr} for (111) films (b) and (100) films (c)

With increasing applied magnetic field, the superconducting transition temperature is found to shift toward lower temperatures. In Figure 19.2(b), the T_{Conset} and T_{Czero} are plotted in the temperature versus magnetic field diagram to estimate the upper critical field H_{C2} and the irreversibility field H_{irr}, where H_{C2} is the maximum magnetic field in which superconductivity can survive and H_{irr} is the maximum magnetic field where zero resistivity can be obtained.

Assuming that the superconductivity is in the dirty limit, H_{C2} is approximated to be 10.4 T using the equation $H = H_{C2\mathrm{WHH}}(1 - T/T_C)^{1.5}$. Here, it was found that this equation could be used for an approximation of the WHH theory [33]. The coherent length was also determined from H_{C2} to be $\xi = 5.51$ nm using the equation $\xi = (\varphi 0/2\pi H_{C2})^{1/2}$. The irreversibility field was estimated at $H_{\mathrm{irr}} = 9.0$ T from the linear extrapolation of T_{Czero}. The variation in resistivity with temperature above T_C is very flat, which suggests that the transport properties are not those of a simple metal.

In contrast, for homoepitaxial (100) films, the superconducting transition temperatures $T_{Conset} = 6.3$ K and $T_{Czero} = 3.2$ K, which are about half those obtained for the (111) thin film, were obtained even at the same boron concentration as shown in Figure 19.2(c). From the temperature versus magnetic field diagram of T_{Conset} and T_{Czero}, upper critical field and irreversibility field were estimated to be $H_{C2} = 5.27$ T and $H_{\mathrm{irr}} = 4.47$ T, and the coherent length $\xi = 7.89$ nm (Figure 19.2d). These results indicate that the superconductivity in homoepitaxial (100) films is significantly suppressed [30, 34]. The reason for the significant difference in superconductivity observed for the (111) and (100) thin films is discussed in the next section.

19.4.4 T_C as a function of boron concentration

As mentioned above, the superconducting properties were found to be strongly dependent on the crystal growth orientation of (111) and (100). The boron concentration dependence of the superconducting transition temperature is summarized in Figure 19.3 [22,

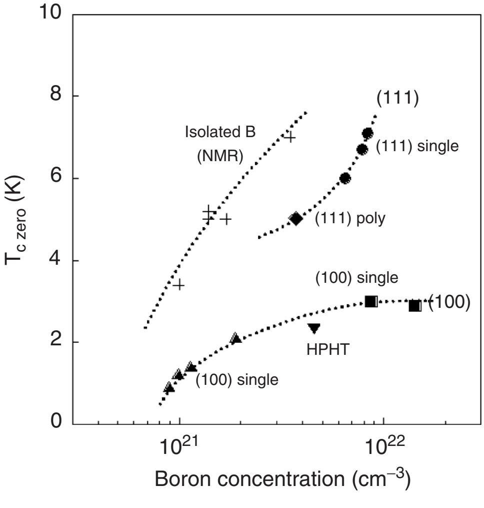

Figure 19.3 Superconducting transition temperature T_C as a function of boron concentration N_B

30–32, 34]. It was shown that the T_{Czero} of the (111) thin films significantly increases when the boron concentration is increased, which corresponds to an increase in the carrier concentration. The optimum doping condition may be reached at even higher boron concentrations.

In contrast, the (100) thin films show, in general, a significantly lower T_{Czero} compared to the (111) thin films. The T_C of the (100) thin films reaches a maximum at around 10^{22} cm^{-3} and is expected to decrease with a further increase in boron concentration. Boron does not act as an effective acceptor for carrier doping, which suppresses the superconductivity in the (100) thin films. The HPHT-synthesized diamond sample fits the (100) thin-film curve; this suggests that the growth orientation of the HPHT sample is in the (100) direction, which may limit the superconducting transition temperature.

19.4.5 Effective carrier concentration

The superconducting transition temperatures of the homoepitaxial (111) and (100) thin films are significantly different even at the same boron concentration, which suggests that the effective carrier density responsible for superconductivity is different between the (111) and (100) films. To estimate the effective carrier density, the detailed local boron condition was analyzed using nuclear magnetic resonance (NMR) measurements.

Figure 19.4 shows NMR spectra of superconducting boron-doped diamond (111) and (100) thin films [35]. The spectrum is composed of two peaks, a sharp peak and a broad peak. The sharp peak corresponds to the isolated boron substituting the carbon site of diamond lattice, where the electric gradient is very small due to the symmetric site. On the other hand, the broad peak may be corresponding to the B–B pair and B–H complex because the electric gradient is significantly large due to the lower symmetry. According to the proton decoupling measurements using 1-GHz high magnetic field NMR, the B–B

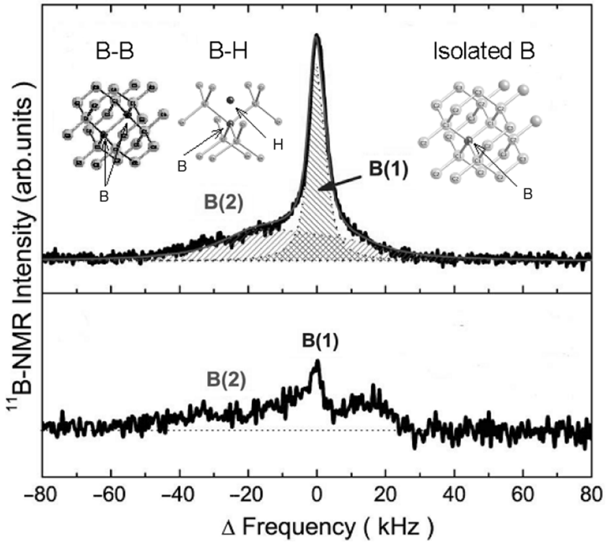

Figure 19.4 NMR spectra for (111) and (100) films

pair is found to contribute largely to the broad peak [36]. Hard X-ray photoemission spectroscopy also suggests that a significantly large number of B–B pairs exist in the boron doped diamond [37].

The effective free carrier was introduced only by substitutional isolated boron, because the B–B pair or B–H complex does not contribute to free carrier doping as suggested by band calculations [38]. The superconducting transition temperature was plotted as a function of isolated boron concentration in Figure 19.3. The data points of (111) and (100) films were plotted in a unique line 'Isolated B', which suggests that the effective carrier doping responsible for superconductivity is the substitutional isolated boron. We also found that the carrier densities estimated by soft X-ray ARPES show good agreement with the isolated boron concentrations determined using NMR [39]. To achieve a higher T_C in diamond, we have to increase the concentration of isolated substitutional boron.

19.5 SUPERCONDUCTING PROPERTIES

19.5.1 Inelastic X-ray scattering

The optical phonon dispersion of boron-doped diamond samples was measured using an inelastic X-ray scattering (IXS) in SPring-8 [40]. Heteroepitaxial (100) boron-doped diamond thick films were prepared on SiC substrates using the microwave plasma CVD method, of which the boron concentration was $N_B = 3.8 \times 10^{21}$ cm^{-3}. The longitudinal optical (LO) phonon was found to be softened as much as ~8 meV near the Γ-point, where the softening is suppressed toward the zone-boundary point L. This suggests that strong electron–phonon interactions contribute to the superconductivity in diamond. The electron–phonon coupling parameter has been determined as approximately $\lambda = 0.33$, considering some theoretical approximations.

Although in some publications [41–46] it is highlighted that superconductivity in diamond is explained by the BCS theory, the softening rate of the optical phonons predicted from the VCA (virtual crystal approximation) is much higher than the experimental values. It has also been found that the softening of the optical phonons, determined from *ab initio* pseudopotential calculations using a 10 × 10 × 10 supercell, is in good agreement with the experimental result [44]. Many parameters characterized from experiments will be employed to develop further the exiting theories.

19.5.2 X-Ray absorption spectroscopy

Figure 19.5 shows X-ray absorption spectra (XAS) of the highly boron-doped diamond [47]. Using the XAS spectra, the electronic properties of unoccupied states can be observed. A wide band gap of 5.5 eV is clearly observed between the valence and conduction bands. The peak I is located around 0.37 eV above the valence band maximum, which is consistent with the boron acceptor level. Peak I increases remarkably with increasing boron concentration, and it seems to merge with the valence band. Baskaran was the first to propose superconductivity because of the boron-impurity band, based on the resonating valence band (RVB) theory [48].

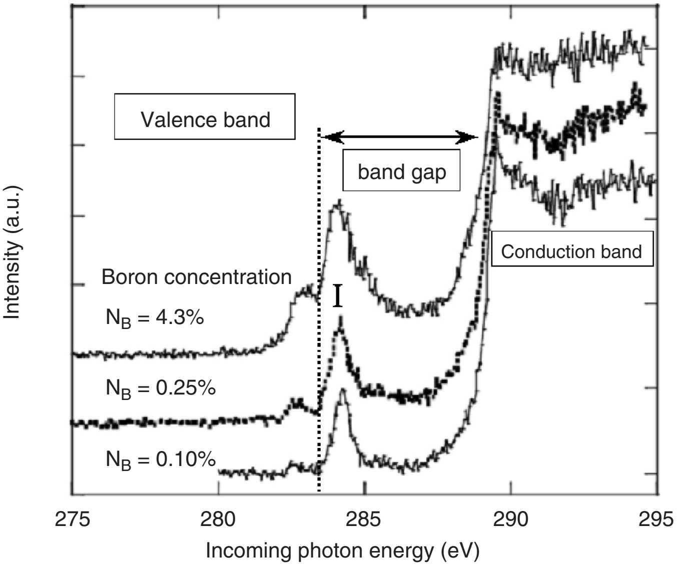

Figure 19.5 X-ray absorption spectra of boron doped diamond films

19.5.3 Superconducting gap properties

The superconducting gap properties were observed using several techniques such as laser photoemission spectroscopy, sub-terahertz spectroscopy, and scanning tunneling spectroscopy (STS). The characteristics of the superconducting gap properties are summarized to elucidate the mechanism of superconductivity in diamond, which leads to the understanding of superconductivity uniquely observed in doped semiconductors.

Laser-excited photoemission spectroscopy of boron doped superconducting diamond was performed [49]. As shown in Figure 19.6, superconducting gap properties were observed above 10 K, which is consistent with the T_{Conset} of the transport measurements. The gap properties become dominant with decreasing temperature. The estimated gap parameters at 4.5 K are $\Delta(4.5\ \mathrm{K}) = 0.78$ meV and $2\Delta(0)/k_B T_C = 3.56$, which are in good agreement with the typical values for weakly coupled BCS superconductors. A broadening parameter of the spectrum $\Gamma = 0.7$ meV is remarkably large, suggesting some effects of disorder due to the boron doping.

The reflectivity of boron-doped superconducting diamond film was measured down to 5 cm^{-1} by sub-terahertz spectroscopy using coherent synchrotron radiation [50]. The opening of an optical gap was observed below T_C, which provides $2\Delta/k_{\mathrm{B}}T_C \sim 3$, in satisfactory agreement with the BCS prediction.

Low temperature STM measurements were performed on homoepitaxial (111) thin films with a $T_{Cmag} = 5.4$ K determined from magnetization measurements [51]. An atomic image of a (111) surface was clearly observed at 0.5 K as shown in Figure 19.7(a) inset. The scanning tunneling spectroscopy (STS) in the area where the atomic image was obtained shows the spectrum indicating the superconducting gap properties (Figure 19.7(a)). The obtained gap parameters $\Delta(0) = 0.87$ meV, and $2\Delta/k_B T_C = 3.7$ are close to the BCS values. The

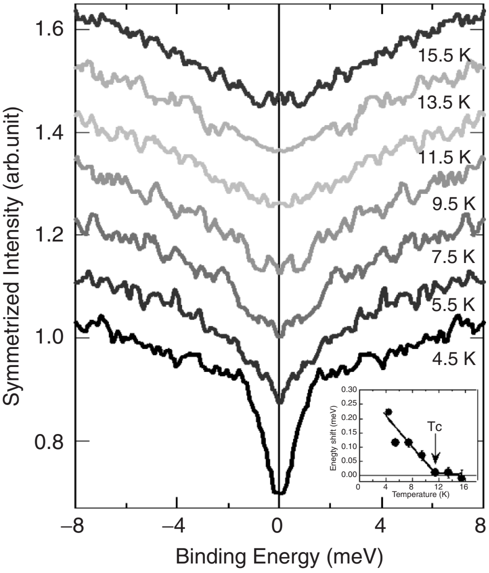

Figure 19.6 Laser-excited photoemission spectroscopy of homoepitaxial (111) film

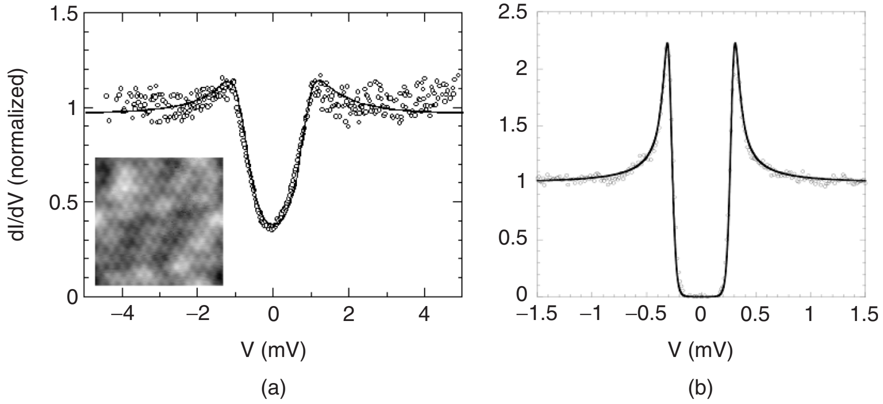

(a)

(b)

Figure 19.7 The scanning tunneling spectroscopy for homoepitaxial (111) film (a) and (100) film (b)

shape of the gap is broad, similar to that of the photoemission spectroscopy, and the broadening parameter is estimated as $\Gamma = 0.38$ meV. These results are similar to those of granular superconductors and indicate a disorder induced by the boron doping.

For a homoepitaxial (100) thin film with a low $T_C = 1.9$ K and a lower boron concentration of $N_B = 2.1 - 3.1 \times 10^{21}$ cm^{-3}, a typical s-wave superconducting gap $\Delta = 0.285$ eV was observed (Figure 19.7(b)) [52]. This clearly demonstrates that boron-doped diamond is well described by s-wave BCS superconductivity with a measured ratio $2\Delta / k_B T_C = 3.48$ characteristic of weak coupling. The vortex properties were also clearly observed under a magnetic field of 1200–1900 Oe. The spatial distribution of vortices is strongly disordered, which suggests that the existence of many pinning centers for vortices, even though a typical s-wave superconducting gap was clearly observed.

These differences in the spectral shape of the superconducting gap can be related to boron concentrations and superconducting transition temperatures. STS measurements of (100) thin films with the same boron concentration as that of the (111) thin film will reveal the difference in the superconducting properties between the films, and the effect of the disorder induced because of the boron doping [53].

19.6 SUMMARY

Superconductivity is rarely observed in semiconductors where the free carriers are the result of impurity doping. To date, to the best of the author's knowledge, only four semiconductors (diamond, Si, SiC, and $SrTiO_3$) have been found to exhibit superconductivity. It is of great interest that diamond exhibits superconductivity with a T_C above 10 K, whereas for the other three the value of T_C is as low as 1 K.

For fabricating a Josephson junction, a narrow bridge 1 μm in width was fabricated in a polycrystalline CVD diamond to include a single grain boundary, using a focused ion-beam (FIB) etching machine. The current–voltage characteristics observed, including hysteresis, were typical of a superconductor–insulator–superconductor (SIS) Josephson junction [28]. Employing the characteristics of superconductivity in a semiconductor, integrated superconductor–semiconductor based novel devices could be produced in the future.

When doped with boron that produces free charged carriers, diamond is metallic and superconductivity is observed. However, the boron introduces disorder and this disorder is thought to suppress superconductivity. In recent years, theoreticians have predicted that it would be possible to reach remarkably high superconducting transition temperatures if the disorder is removed. Although it is currently extremely difficult to introduce free carriers by impurity doping without inducing disorder, we believe it should be possible in the future to fabricate a higher transition temperature superconductor.

REFERENCES

[1] H. Kamerlingh Onnes, *Leiden Commun*. 120b, 122b, 124c (1911).

[2] J. Bardeen, L. N. Cooper, and J. R. Schrieffer, *Phys. Rev.* **108**, 1175 (1957).

[3] W.L. MacMillan, *Phys. Rev.* **167**, 331 (1968).

[4] G. Bednorz and K. A. Muller, *Z. Phys.* **B64**, 189 (1986).

[5] J. Nagamatsu, N. Nakagawa, T. Muranaka, Y. Zenitani, and J. Akimitsu, *Nature* **410**, 63 (2001).

[6] Y. Takano, H. Takeya, H. Fujii, H. Kumakura, T. Hatano, K. Togano, H. Kito and H. Ihara, *Appl. Phys. Lett.* **78**, 2914 (2001).

[7] K. Takada, H. Sakurai, E. Takayama-Muromachi, F. Izumi, R.A. Dilanian, and T. Sasaki, *Nature* **422**, 53 (2003).

[8] Y. Takano, S. Takayanagi, S. Ogawa, T. Yamadaya, and N. Mori, *Solid State Commun.* **103**, 215 (1997).

[9] Yoichi Kamihara, Hidenori Hiramatsu, Masahiro Hirano, Ryuto Kawamura, Hiroshi Yanagi, Toshio Kamiya, and Hideo Hosono, *J. Am. Chem. Soc.* **128**, 10012 (2006).

[10] S. Koizumi, H. Ozaki, M. Kamo, Y. Sato, and T. Inuzuka, *Appl. Phys. Lett.* **71**, 1065 (1997).

[11] Y. Takano, M. Nagao, T. Takenouchi, H. Umezawa, I. Sakaguchi, M. Tachiki, and H. Kawarada, *Diamond Relat. Mater.* **14**, 1936 (2005).

[12] K. Thonke, *Semicond. Sci. Technol.* **18**, S20–S26 (2003).

[13] T. Yokoya, T. Nakamura, T. Matsushita, T. Muro, Y. Takano, M. Nagao, T. Takenouchi, H. Kawarada, and T. Oguchi, *Nature* **438**, 647 (2005).

[14] F. P. Bundy, H. T. Hall, H. M. Strong, and R. H. Wentorf, Jr., *Nature* **176**, 51–55 (1955).

[15] H.P. Bovenkerk, F.P. Bundy, R.M. Chrenko, P.J. Codella, H.M. Strong, and R.H. Wentorf jr., *Nature* **365**, 19 (1993).

[16] H. B. Bovenkerk, F. P. Bundy, H. T. Hall, H. M. Strong, and R. H. Wentorf, Jr., *Nature* **184**, 1094–1098 (1959).

[17] R. H. Wentorf, Jr. and H. P. Bovenkerk, *J. Chem. Phys.* **36**, 1987 (1962).

[18] P. S. DeCarli and J. C. Jamieson, *Science* **133**, 1821 (1961).

[19] F. P. Bundy, *Science* **137**, 1057 (1962).

[20] F. P. Bundy, *J. Chem. Phys.* **38**, 631–643 (1963).

[21] R. H. Wentorf, Jr., *J. Phys. Chem.* **69**, 3063–3069 (1965).

[22] E. A. Ekimov, V. A. Sidorov, E. D. Bauer, N. N. Mel'nik, N. J. Curro, J. D. Thompson and S. M. Stishov, *Nature* **428**, 542 (2004).

[23] E.A. Ekimova, V.A. Sidorov, A.V. Rakhmanina, N.N. Mel'nik, R.A. Sadykov, and J.D. Thompson, *Sci. Technol. Adv. Mater.* **7**, S2–S6 (2006).

[24] N. Dubrovinskaia, G. Eska, G. A. Sheshin, and H. Braun, *J. Appl. Phys.* **99**, 033903 (2006).

[25] B.V. Spitsyn, L.L. Builov and B.V. Deryagin, *J. Cryst. Growth* **52**, 219 (1981).

[26] M. Kamo, Y. Sato, S. Matsumoto, and N. Setaka, *J.Cryst. Growth* **62**, 642 (1983).

[27] Y. Takano, M. Nagao, I. Sakaguchi, M. Tachiki, T. Hatano, K. Kobayashi, H. Umezawa, and H. Kawarada, *Appl. Phys. Lett.* **85**, 2851 (2004).

[28] Y. Takano and H. Kawarada, *Solid State Phys. 'Kotaibutsuri'* **41**, 457 (2006).

[29] M. Nesládek, D. Tromson, C. Mer, P. Bergonzo, P. Hubik and J. J. Mares, *Appl. Phys. Lett.* **88**, 232111 (2006).

[30] Y. Takano, T. Takenouchi, S. Ishii, S. Ueda, T. Okutsu, I. Sakaguchi, H. Umezawa, H. Kawarada, M. and Tachiki, *Diamond Relat. Mater.* **16**, 911 (2007).

[31] H. Umezawa, T. Takenouchi, Y. Takano, K. Kobayashi, M. Nagao, I. Sakaguchi, M. Tachiki, T. Hatano, G. Zhong, M. Tachiki, and H. Kawarada, condmat/0503303 (2005).

[32] H. Umezawa, T. Takenouchi, K. Kobayashi, Y. Takano, M. Nagao, M. Tachiki, T. Hatano, and H. Kawarada, *New Diamond and Frontier Carbon Technology*, **17**, 1 (2007).

[33] N. R. Werthamer, E. Helfand, and P. C. Hohenberg, *Phys. Rev.* **147**, 295 (1966).

[34] E. Bustarret, J. Kacčmarcčik, C. Marcenat, E. Gheeraert, C. Cytermann, J. Marcus, and T. Klein1, *Phys. Rev. Lett.* **93**, 237005 (2004).

[35] H. Mukuda, T. Tsuchida, A. Harada, Y. Kitaoka, T. Takenouchi, Y. Takano, M. Nagao, I. Sakaguchi, T. Oguchi, and H. Kawarada, *Phys. Rev. B* **75**, 033301 (2007).

[36] M. Murakami, T. Shimizu, M. Tansho, Y. Takano, S. Ishii, E. Ekimov, V. Sidorov, H. Kawarada, and K. Takegoshi, *Jpn. J. Appl. Phys.* **46**, L1138 (2007).

[37] T. Yokoya, E. Ikenaga, M. Kobata, H. Okazaki, K. Kobayashi, A. Takeuchi, A. Awaji, Y. Takano, M. Nagao, I. Sakaguchi, T. Takenouchi, K. Kobayashi, H. Kawarada, and T. Oguchi, *Phys. Rev. B* **75**, 205117 (2007).

[38] Oguchi *et al.*, to be published.

[39] T. Yokoya, T. Nakamura, T. Matushita, T. Muro, H. Okazaki, M. Arita, K. Shimada, H. Namatame, M. Taniguchi, Y. Takano, M. Nagao, T. Takenouchi, H. Kawarada and T. Oguchi, *Sci. Technol. Adv. Mater.* **7**, S12 (2006).

[40] M. Hoesch *et al.*, *Sci. Technol. Adv. Mater.* **7**, S31 (2006).

[41] L. Boeri, J. Kortus, O. K. Andersen, *Phys. Rev. Lett.* **93**, 237002 (2004); *Sci. Technol. Adv. Mater.* **7**, S54 (2006).

[42] K. W. Lee, W. E. Picket, *Phys. Rev. Lett.* **93**, 237003 (2004).

[43] X. Blase, Ch. Adessi, and D. Conne'table, *Phys. Rev. Lett.* **93**, 237004 (2004).

[44] H. J. Xiang, Z. Li, J. Yang, J. G. Hou, and Q. Zhu, *Phys. Rev. B* **70**, 212504 (2004).

[45] K.-W. Lee and W. E. Pickett, *Phys. Rev. B* **73**, 075105 (2006).

[46] M. Cardona, Solid State Communications **133**, 3–18 (2005); *Sci. Technol. Adv. Mater.* **7**, S60 (2006).

[47] J. Nakamura *et al*., cond-mat/0410144.

[48] G. Baskaran, *J. Supercond. Nov. Magn*. **21**, 45 (2008). *Sci. Technol. Adv. Mater.* **7**, S49 (2006).

[49] K. Ishizaka *et al*., *Phys. Rev. Lett.* **98**, 047003 (2007).

[50] M. Ortolani, S. Lupi, L. Baldassarre, U. Schade, P. Calvani, Y. Takano, M. Nagao, T. Takenouchi, and H. Kawarada, *Phys. Rev. Lett.* **97**, 097002 (2006).

[51] T. Nishizaki, Y. Takano, M. Nagao, T. Takenouchi, H. Kawarada and N. Kobayashi., Sci. Technol. Adv.Mater. S22 (2006); *Physica C*, 460–462, **210** (2007).

[52] B. Sacépé, C. Chapelier, C. Marcenat, J. Kacčmarcčik, T. Klein, M. Bernard, and E. Bustarret, *Phys. Rev. Lett.* **96**, 097006 (2006).

[53] T. Shirakawa, S. Horiuchi, Y. Ohta, and H. Fukuyama, *J. Phys. Soc. Jpn.* **76**, 014711 (2007).

Index

Page references in bold refer to tables. Those in italics refer to figures.

acceleration sensors 511–512
acetylcholinesterase (AChE) 423–425, 429
acoustic deformation potential 34–35
actuators 472–473
  piezoelectric 483–486
adsorbates
  charge transfer with diamond surface 81–85
  buckminsterfullerene 85–91
  see also proteins
alkenes, functionalization of H-terminated surfaces 407
alpha particles 264
aluminium gallium nitride 314
amino groups, as surface terminator 406, 411
3-aminopropyldiethoxymethylsilane (APDEMS) *413*, 414–415
amplifiers, broadband 235
angle-resolved soft-emission spectroscopy (ARPES) 549
aromatic groups, functionalization of H-terminated surfaces 407–408
Arrhenius equation 200
arsenic 455
ATLAS experiment 218–220
atomic force microscopy (AFM), probe tips 512
azide 460–461

BaBar experiment 216–218
background current 193
Baliga figure of merit 314
band gap 20
  materials with wide **290**
  and temperature 22–23
band profile
  hydrogen-terminated surfaces 76–81
  see also carriers
baryons 229
Beam Condition Monitor detectors 216–220
  heavy-ion 247–248
beryllium ions, generated by fast neutron collisions 264
beta-scission mechanism 114–115
Bethe formalism 233
bias enhanced nucleation (BEN) 128–129
  on iridium 141–143
  for microelectromechanical systems 488–489
  on silicon 133–134
    models 134–135
bimetal transducers 480–482
biosensors 354
  adsorption of biomolecules 415–416
    DNA 420
    proteins 416–425
  advantages of diamond 402
  applications, amperometry 425–426
  electrochemical 461–462
  materials 403–405
blind to optical light detectors (BOlD) 166
Blu-Ray DVD players 179
bone morphogenic protein-2 417

CVD Diamond for Electronic Devices and Sensors Edited by Ricardo S. Sussmann
© 2009 John Wiley & Sons, Ltd. ISBN: 978-0-470-06532-7

boron
  deuterium complex 58
  as dopant 30, 51, 315–316
    activation 317
    charge carrier scattering 36
    in electrodes 355–360
    Hall effect 44–45
    and superconductive transition temperature 553–554
    in thermal transducers 474–475
boron nitride, as substrate 130
boron-doped diamond (BDD) *see* boron
brachytherapy 185
Bragg curve 233–234
Brillouin scattering 7–8
broadband amplifiers 235
bubble-jet structures 474, 527–529

cadmium 454
cancer 185–187
cantilevers *504*
  beams 479
  switches 516–519
capacitance H-terminated FETs 303–305
capacitance-voltage characteristics
  electrodes, measurement 356
  homoepitaxial p-i-n LEDs 391–393
  homoepitaxial p-n LEDs 385–387
carbon
  glassy 442–443
  isotopes 4
    S13sC 6
carrier-velocity saturation, P-I-P FETs 339
carriers
  concentration
    at high temperatures 349
    boron-doped diamond 381–382
    and conductivity 30–33
    H-terminated diamond 78
    superconductors 554–555
  density, depth-integrated, hydrogen and oxygen-doped surfaces 80
  drift velocity 38–39
  electron holes 23–24
  mobility, boron-doped diamond 382
  in particle detectors 211
  scattering 33–38
    by dislocations 37
    by grain boundaries 37
    by ionised impurities 35–36
    by neutral impurities 36–37
    and delta-doping 320
    intervalley 35
  space-charge density, H-terminated surfaces 79–81
  space-charge limited current 41–42
  trapping by defects 61
  velocity saturation 40–41
Centronic UV detectors 172–173
characterization methods
  charge carrier properties 42–46
  crystalline nanolayers 144–145
  elasticity 7–8
  enzyme grafting 421–423
  intrinsic stress 493–495
  microwave-activated gas mixtures 108
  superconductivity 549–550
  surface functionalization 414–415
  Young's modulus 492
charge carriers *see* carriers
charge-sensitive amplifiers 235
chemical vapor deposition
  carbon surface migration 115–117
  etching 114–115
  gas-phase chemistry 104–105
  kinetic Monte Carlo modeling 117–120
  reaction rate 109
  standard model 104
  for superconductivity 551–554
  surface growth
    radical incorporation 108–111
      insertion across dimer troughs 112–113
      insertion into dimer reconstruction 111–112
chlorine, as surface terminator 406
4-chlorophenol 455–456
cobalt 62, 130–131
collection distance 239
colorimetry 422–424
Compressed Baryonic Matter (CBM) spectrometer 232
compression strain 7
conductivity
  electrical 30–33
    effect of ionizing radiation 191–192
    and fullerenes adsorbed at surface 85–91
    through grain boundary network 476
  photoconductivity 165–170
  thermal 18–20, 290
    characterization 496–498
  see also superconductivity

contacts 324–328
  boron-doped surfaces 324–329
  H-terminated surface 324
  O-terminated surface 324
  for particle detectors 238
Coulomb force 478
crystal orientation
  and carrier scattering 35
  and conductivity 35
  and superconductive transition temperature 553–554
cube edge length 4
  and temperature 5
current-voltage characteristics
  homoepitaxial p-i-n LEDs 391
  homoepitaxial p-n diodes 385
CVD *see* chemical vapor deposition
cyclic voltammetry 441–442
cytochrome c 422

DC characteristics, H-terminated FETs 295–298
Debye temperature 35
  from specific heat 17
deep level transient spectroscopy (DLTS) 58–59, 61
defects
  electrodes 357
  heteroepitaxic growth on iridium 148
  nickel-induced 61–62, 62
  and photoconductivity 168–169
  silicon-induced 60
  transition-metal induced 62
  trapping and scattering of carriers 58–59
  UV scattering and trapping 169
  vacancies 59–60
delta-doping 283
  in diodes 346–348
  profiles 318–324, *319*
  stacked 323
deuterium 58
Diamond Detectors Ltd. 228
dielectric properties 24–25
diodes 342–348
  high-temperature 348–354
  high-voltage vertical 343–348
  high-voltage/high-power 279–285
  homoepitaxial, p-i-n, electrical properties 391–393
  light-emitting *see* light-emitting diodes
  m-i-p 344
  Schottky *see* Schottky diodes
dislocations, charge carrier scattering 37
DNA 462–463
dopants
  activation 317
  complexes 54–55, 57–58
  complexes with vacancies 55–56
  electron acceptors, boron 51
  and electronic properties 30–33
  hydrogen complexes 57–58
  other 54
  phosphorus, Hall effect 44
  see also boron
doping
  delta-doping 318–324, *319*, 346–348
  and electrical conductivity 30
  electron donors 316–318
  for superconductivity 548–549
drift velocity 38–39, 38–40

elastic scattering 232–234
elasticity 7–9
  and resonance 480
elasticity, and temperature 8
electrochemical sensors
  advantages of diamond 442–443
  growth conditions and electrode properties 443–449
  measurements 441–442
  overview 439–441
electrochemistry 462–463
electrodes 355–360
  advantages of diamond 442–443
  in ISFETs 363
  macroscopic 453–462
  microscopic 463–464
  standard Salome 441–442
  surface functionalization 461–462
  surface patterning 358–360
electron acceptors, and band structure 77–81
electron affinity
  hydrogen and oxygen-terminated surfaces 77
  surfaces with fullerenes 88
electron beam switches 285
electron beams, in radiotherapy 186
electron scattering 33–34
electron transfer doping model 93–98
electron-hole condensate 23–24
electronic stopping power 233

electrons, *see also* carriers
electrostatic switches 516–519
electrothermal switches 519–523
Element Six 228
energy-loss detectors, ion spectroscopy 250–251
ENFETs 427–430
environmental sensing 454–455, 455–456
enzymes
  charge transfer in amperometric biosensors 425–426
  in FETs 427–430
  grafting 421–423
epitaxy, on silicon 135–137
ESA Solar Orbiter 166, 180–181
etching
  focused ion beam (FIB) 499
  inductively coupled plasma (ICP) 499
  P-I-P FETs 341–342
  reactive ion etching 498–499
  of substrate 505–506
  in surface growth 114–115
  see also selective growth
explosives, electrochemical sensing 457–459

FAIR facility 232
Fermilab Tevatron 217–218
field effect transistor (FET) *see* transistors
field plates, Schottky diode edge termination 284
fission reactors, neutron detectors 268–269
fluorescence spectroscopy 414–415
fluorine, surface terminator 406
focused ion beam (FIB) etching 499
Frascati Neutron Generator 259–264
  radiation tolerance experiment 266–268
Frenklach growth model 117–118
fullerenes
  adsorbed 84
    and surface conductivity 85–91
    thermal stability 90
functionalization *see* surface functionalization
fusion reactors, neutron detectors 270–271

gallium nitride
  in high-voltage diodes 345
  in microelectromechanical systems 508–509
Gibbs free energy 109
gold, on H-terminated diamond 295
grain boundaries
  carrier scattering 37
  and thermal conductivity 497
green fluorescence protein (GFP) 421
Grüneisen effect 16–17
Grüneisen parameter 12
GSI Darmstadt 228–229
  FAIR facility 232
  Fragment Separator 243–245
  heavy-ion research 230–232
guard rings 284
gyrotrons 525–526

hadron colliders, beam condition monitors 217–218
hadrons 229–230
Hall effect 42–46
halogens 54
harmonic vibration 10
Harris mechanism 112–113
heaters 473–477
heavy metals 454–455
heteroepitaxy 126–127
  nucleation 127–130
  properties and applications 153–155
high-energy physics
  applications of CVD diamond 214–220
  pixel detectors 222–223
  strip detectors 220–221
high-pressure high-temperature (HPHT) diamond 550–551
  growth 126
  as substrate for FETs 292–293
hole mobility, P-I-P FETs 338–339
homoepitaxial growth, for superconductivity 552–554
horseradish peroxidase 426, 461
hybrid integration 507
hydrogen
  complexes with dopants 57–58
  as surface terminator 291–292, 317
    contacts 324
    effect on band profile 76–81
    electrochemistry 462–463
    in microelectromechanical systems 490
    negative electron affinity 73–76, *75*
    and surface conductivity 69–73
    and surface functionalization 406

hydrogen-terminated surfaces, band profile 76–81
hydroxyl groups, on O-terminated surfaces 413–414

III-nitrides 314
impurities
  charge carrier scattering 35–37
  and thermal conductivity 19
indium aluminium nitride (InAlN) 314
inductively coupled plasma (ICP) etching 499
inelastic X-ray scattering (IXS) 555
integration (of MEMs) 506–507
intensity-modulated radiotherapy (IMRT) 186–187, 197–198
interfacial layer, between Al contact and H-terminated diamond 304–305
intrinsic stress 493–495
ion beams
  etching (FIB) 499
  heavy particles 230–232
  interaction with sensors 232–234
ionization, microwave-activated gas mixtures 106
ionization chamber 188
iridium
  as substrate 131–132
    development of domain patterns 145
    for microelectromechanical systems 489
    nucleation models 146–148
    nucleation and pattern formation 141–143
    texture improvement 148–151
    topographic features 143–144
  substrates for 151–153
ISFETs 360–363, *364*
  stability 363, *364*
isotopes
  effect on lattice dimensions 6–7
  effect on Raman spectrum 16–17
  and lowest energy gap 23
  and thermal conductivity 19

JFETs 278
Johnson figure of merit 314
Joint European Torus (JET) 270–271
junction barrier Schottky (JBS) diode 281–282

kinetic Monte Carlo (KMC) modeling 117–120
KN1 diagnostic 271

Large Hadron Collider (LHC) 215–220, 222–223
lattice
  coefficient of expansion 5–6
  defects *see* defects
  dimensions 4–5
  thermal expansion 5–6
lattice misfit
  in heteroepitaxic growth 126–127
  silicon 138
lead 454
light-emitting diodes (LED) 179, 380–381
  homoepitaxial
    p-i-n
      electrical properties 391–393
      fabrication 389–390
      light-emitting properties 391–393
    p-n
      electrical properties 385–387
      fabrication 384–385
      light-emitting properties 387–389
    light-emission mechanism 395–396
lithium, as dopant 54
lithium fluoride 262–264
low energy electron diffraction (LEED) 144

mass spectrometry, ToF 38–39, 248–250
membrane pumps 530–532
MEMS *see* microelectromechanical systems
MESFETs 70, 278
mesons 229
metal-insulator-semiconductor field-effect transistors (MISFET) 278
metal-semiconductor field-effect transistors (MESFET) 70, 278
methane 104
  desorption from surface during etching 114
methyl radicals
  at surface 110, **111**
  insertion across dimer troughs 112–113
microchannels 526–527
microelectrode arrays 358, 463–464
microelectromechanical systems (MEMS)
  bubble-jet structures 527–529
  capillaries 526–527
  electrostatic switches 516–519
  electrothermal switches 519–523
  fabrication, material preparation 487–490
  fluid pumps 530–532
  integration, monolithic 506

microelectromechanical systems (MEMS) (*Continued*)
  material properties, Young's modulus 492
  patch-clamps 532–535
  resonators 513–515
  sensors
    acceleration 511–512
    pressure 509–510
  silicon carbide 508
  surfaces 490–491
  switchable inductors 523
  transducers
    electrostatic actuators 478–480
    heaters 473–476
    metal bilayer 480–482
    thermistors 476–477
microfluidics
  bubble-jet structures 527–529
  capillaries 526–527
  patch-clamps 532–535
  pumps 530–532
micromoulding 501–502
microwave systems, substrate 523–526
microwave-activated gas mixtures
  modeling 105–108
  optical diagnosis 108
minimum-ionizing particles (MIP) 249
MISFET 278
monocrystalline diamond, for biosensors 403
monolithic integration 506
Monte Carlo modeling
  CVD processes 117–120
  neutron detector converting layer thickness 261
mosaic spread
  heteroepitaxial growth on iridium *149*
  on silicon substrate 140
Mott-Gurney law 42, 280
Multiple-Sampling Ionization Chambers (MUSIC) 244–245

nanocrystalline diamond (NCD) 471
  for biosensors 404
  in electrodes 445–446
NE8 defect 62
negative electron affinity (NEA), hydrogen-doped surfaces 73
neutron detectors
  overview 257–258
  converting layer 258, 260, 262
  fission reactors 268–269
  fusion reactors 270–271
  radiation hardness 266–268
neutrons
  fast 264–265
  thermal 259–264
nickel 61–62
  as heteroepitaxic substrate 130–131
nitrogen 52
  at grain boundaries 476
  as dopant 316–317
  in lattice 5
  and photoconductivity 168–169
nitrogen-vacancy centre 56–57
nitrogen-vacancy-hydrogen centre 60
noise
  in H-terminated FETs 300, *301*
  in particle detectors 237
nuclear reactors 257–258
  fission, neutron detectors 268–269
  fusion, neutron detectors 270–271
nucleation 127–130
  for microelectromechanical systems 488–489
  on silicon 133–135

optical phonon charge carrier scattering 35
oxygen
  as surface terminator 76–77
    and contact deposition 324–325
    functionalization by chemical modification 412–415

pad detectors 214, 215–220
PANDA experiment 232
parallel-plate actuator 478–479
Parathion 459–460
particle detectors
  basic principles 208–212
  heavy-ion
    applications 247–250, 250–252
    charge-collection efficiency 238–240
    current-field characteristic 238
    detector response
      homogeneity 242–245
      with time 245
  for high-energy physics
    basic principles 208–212
    applications of CVD diamond 214–220
    pixel detectors 222–223

    - strip detectors 220–221
  - neutron
    - overview 257–258
    - converting layer 258, 260, 262
    - fusion reactors 270–271
    - radiation hardness 266–268
- patch-clamp systems 532–535
- peristaltic pumps 530
- phenols, electrochemical sensing 457–459
- phonons
  - absorption and emission probability 10
  - dispersion curves 10–11
  - Raman scattering
    - three phonons 16
    - two phonons 14–17
  - and Raman spectroscopy 11–12
  - scattering of charge carriers 34–35
- phosphorus 52–53
  - as dopant 316–317
    - Hall effect 44
    - in LEDs 382–384
- photo-Hall measurements 43–44
- photoconductive switches 285–286
- photoconductivity 165–170
  - and defects 168–169
- photolithography
  - ultraviolet 166
  - UV 179–180
- photons, interactions with matter *189*
- piezoelectric actuators 483–486
- piezoresistivity 482–483
- pixel detectors 222–223
- planar doping 320
- plasmas, modeling 106–108
- platinum, as heteroepitaxic substrate 130–131
- polycrystalline diamond
  - for biosensors 403–404
  - in electrodes 444–447
  - thermal conductivity 19
  - in UV detectors 170–174
- polymer surface coatings 415
- potentiometry 441
- power distribution 278
- pressure sensors 509–510
- priming, radiation dosimeters 194
- projectile fragmentation 244–245
- proteins
  - covalent grafting 419–425
  - physisorption 416–419
- proton beams, in radiotherapy 186
- pumping, radiation dosimeters 194
- pumps 530–532

- quantum information processing (QIP) 50

- radiation dosimeters 187–190
  - off-line configuration 199–202
  - on-line configuration 191–199
    - diamond vs. silicon 193–194, **194**
    - response stability 195–196
- radiation hardness 213–214
  - and neutron detection 266–268
- radiotherapy, overview 185–187
- Raman frequency 11–13
- Raman scattering, isotope effects 16–17
- Raman spectroscopy 10–11, 11–13
  - electrodes 444
  - two- and three-phonon scattering 14–16
- reflection coefficient 25
- reflection high energy electron diffraction (RHEED) 144
- refractive index 25
- resistance, electrical, contacts 325–327
- resistive Schottky barrier field plate (RESP) 284
- resonance (mechanical) 513–515
  - micromechanical parts 479–480
- resonators 513–515
  - disk 515
- rhenium, as heteroepitaxic substrate 131

- sacrificial layers 503–505, *504*
- sapphire, as heteroepitaxic substrate 130
- Schottky diodes 279–282, 324–325, 327
  - delta-doped 283
  - edge termination 283–285
  - junction barrier (JBS) 281–282
- Schubweg 239
- SchwerIonen Synchrotron (SIS) 231–232
- scratching, to enhance heteroepitaxial nucleation 128
- selective growth 501
- self-assembled monolayers (SAM) 416–419
- semiconductors
  - properties for power diodes **344**
  - wide band-gap **290**
- sensors 472–473
  - biosensors *see* biosensors
  - piezoresistive 482–486
  - *see also* particle detectors

shear strain 7
Shockley-Ramo theorem 209
signal-to-noise ratio, particle detectors 237
silanes, functionalization to O-terminated surfaces 412–415
silicon
  defects induced 60
  as heteroepitaxic substrate 131, 135–137
    growth 132–133
    nucleation 133–135
  as substrate, structural limitations 139–140
silicon carbide
  4H 30
  in high-voltage diodes 345
  in microelectromechanical systems 508
  as substrate, structural limitations 139–140
sodium, as dopant 54
space charge density, hydrogen and oxygen-doped surfaces 78–79
space-charge limited current 41–42
specific heat capacity 17–18
standard calomel electrode 441–442
Stanford Linear Accelerator Center (SLAC) 216
stress 8
  intrinsic 493–495
substrates 130–132, *132*
  etching 506–507
  for FETs 292–293, 329
  HPHT diamond 292–293
  iridium *see* iridium
  for microelectromechanical systems 488–489
  for microwave systems 523–526
  silicon 131–137
sulfur 53–54
super Large Hadron Collider (sLHC) 222–223
superconducting gap 556–558
superconductivity 547–548
  boron-doped diamond 549–550
  transition temperature 553–554
superconductors
  boron concentration and transition temperature 553–554
  doping 548–549
  properties, X-ray scattering 555
surface conductivity
  electron transfer model 92–98
  fullerene-induced 85–91
  see also hydrogen, as surface terminator
surface functionalization 405
  by chemical modification 408–412
    O-terminated surfaces 412–415
  by electrochemical modification 407–408
  by photochemical modification 407
  electrodes 461–462
surface termination 406
  effect on electrode properties 449–452
  see also hydrogen, oxygen
surfaces
  carrier scattering 37
  for microelectromechanical systems 490–491
switching devices 285–286
  for power 314

target monitors, ion spectroscopy 250
temperature, and band gap 22–23
thermal conductivity 18–20, 290
  characterization 496–498
thermal expansion, in bimetal transducers 480–482
thermal neutron detection 259–264
thermally stimulated current 201
thermistors 476–477
thermoluminescence 188
  off-line radiation dosimeters 199–200, 201–202
thermoluminescence detectors 188
titanium carbide, as heteroepitaxic substrate 131
ToF detectors 38–39, 248–250
transconductance, gate-source, H-terminated FETs 303–305
transducers **472**
  mechanical
    bimetal 480–482
    electrostatic actuators 478–486
    piezoelectric actuators 483–486
    piezoresistive sensors 482–483
  thermal 473–476
  see also particle detectors
transient response
  particle detectors 245
  polycrystalline UV detectors to white light 173
transient-current measurement 211
transistors 69–70
  characteristics, DC 295–298
  delta-channel 330–337

  - delta-doped, RF characteristics 331–332
  - device structure 292
  - ENFETs 427–430
  - enzyme-coupled 427–430
  - H-terminated
    - fabrication process 293–295
    - gate-source capacitance 303–305
    - operating temperature 306
    - RF characteristics 300–302
    - stability and reliability 307–308
  - HPHT diamond as substrate 292–293
  - P-I-P 338–342
  - ISFETs 360–364, *364*
  - JFETs 278
  - MESFETs 70, 278
  - MISFET 278
- transmission electron microscopy (TEM) 144
- TRIGA RC-1 reactor 268–269

- ultrananocrystalline diamond (UNCD) 351
  - for biosensors 404–405
  - functionalization by chemical modification 409–411
  - O-terminated, silanation 412–415
- unimorphs 484
- Universal Linear Accelerator (UNILAC) 230–232
- unsealed source radiotherapy 185
- UV detectors
  - contacts 167–168
  - future prospects 178–181
  - photosensitivity **178**
  - polycrystalline 170–174
  - single crystal 174–177
- UV LEDs 380–381
- UV light, scattering and trapping by defects 169

- vacancy-hydrogen centre 60
- valence band 20–22
  - lowest band gap 22–23
- valence bands 20–22
- velocity saturation 40–41
- vibration, dispersion curves 10–11
- vibrations, overview 9–10
- voltammetry 441
  - solution-phase 455–461
  - stripping 453–455

- X-ray absorption near-edge structure (XANES) 145
- X-ray absorption spectroscopy 555
- X-ray diffraction, and stress 8–9
- X-ray photoelectron diffraction (XPD) 145
- X-rays, in radiotherapy 186

- Young's modulus 8, 480
  - characterization 492

- zero-point energy 6